NASA Technical Memorandum 4210

Reports of Planetary Geology and Geophysics Program—1989

Henry Holt, *Editor*
NASA Office of Space Science and Applications
Washington, D.C.

National Aeronautics and
Space Administration
Office of Management
Scientific and Technical
Information Division

1990

Foreword

This is a compilation of abstracts of reports from Principal Investigators of NASA's Office of Space Science and Applications, Solar System Exploration Division, Planetary Geology and Geophysics Program.

The purpose of this publication is to document in summary form research work conducted in this program over the past year (1989). Each report reflects significant accomplishments within the area of the author's funded grant or contract.

No attempt has been made to introduce editorial or stylistic uniformity; on the contrary, the style of each report is that of the Principal Investigator and may best portray his research.

Joseph Boyce
Discipline Scientist
Planetary Geoscience Programs

CONTENTS

CHAPTER 1

VENUS

THE GEOLOGY OF VENUS: A PRE-MAGELLAN SYNTHESIS AND KEY QUESTIONS FOR MAGELLAN

James W. Head and Larry S. Crumpler, Dept. of Geological Sciences, Brown Univ., Providence, RI 02912

A fundamental question in planetary science has been the nature of volcanic and tectonic activity on Venus, and mechanisms of lithospheric heat transport on a planet that is similar to Earth in size, density, and position in the Solar System(1). Acquisition and analyses of high resolution data from Earth-based observatories and the Venera 15-16 missions have permitted more detailed characterization of numerous regions of Venus initially defined by PV data, and the sharpening of questions for Magellan.

Observations and Synthesis: High topography can be produced by a variety of mechanisms (tectonic crustal thickening, volcanic construction, thermal uplift, etc.) each of which has distinctive geologic and tectonic signatures (1). For example, Beta Regio is a regional near-equatorial rise 2000 x 2300 km in dimension rising >5 km above mpr, containing a central N-S linear trough (Devana Chasma) 200-300 km wide within which is a concentration of faults; Arecibo data indicate that Theia and Rhea Montes are shield volcanoes linked to and both predating and postdating the faulting (2). Devana Chasma bifurcates in the vicinity of Theia Mons, with rift zones connecting south to Phoebe Regio and extending west toward Aphrodite Terra, giving the region of southern Beta the distinct appearance of a tectonic junction focused at Theia Mons (3-5). Several flanking plateaus have radar and morphologic characteristics similar to the tessera terrain (6). Synthesis of these data suggest that Beta Regio is the site of a distinctive mantle thermal anomaly (plume or hot spot) that is linked to uplift, regional lithospheric extension and rifting, and associated volcanism. As yet undetermined, and subject to investigation using Magellan data, is the exact nature and structure of the mantle anomaly, the amount and significance of regional lithospheric extension, the role of the tessera-like flanking plateaus, the significance of the tectonic junction, and the relationship of its arms to other regions (Phoebe and Aphrodite) and their tectonic styles.

Aphrodite Terra is part of the Equatorial Highlands and extends for up to 16,000 km from Western Aphrodite to Atla Regio. Detailed analysis showed the presence of parallel cross-strike discontinuities (CSD's) and analysis of topographic profiles in directions parallel to the CSD's showed evidence for bilateral symmetry about an axis that was often characterized by a distinctive linear trough. These characteristics, together with other data, led to the proposal that Western Aphrodite Terra was the site of crustal spreading along a segmented rise crest, that the CSD's represented the equivalent of ocean-floor fracture zones, and that on the basis of the characteristics of topographic profiles, spreading was occurring at rates of the order of a few centimeters a year (7). In this hypothesis, the plateaus superposed on the rise represent zones of enhanced upper mantle temperature and crustal production (mantle plumes or hot spots), analogous to Iceland in the North Atlantic.

Assessment of terrestrial spreading centers under Venus conditions (8) predicted that crust on Venus produced at average spreading centers would be about 15 km thick. Using PV gravity and topography data, this model was applied to test the hypothesis that Western Aphrodite was the site of crustal spreading (7). The symmetric average topography on the plateau provided a fit to thermal boundary layer topography comparable to that seen in spreading centers on Earth, with a spreading rate of about 1.0 cm/yr. The steep topographic slopes at the edge of the Iceland-like plateau could be explained by variations of about 15 km in crustal thickness, with the crust being thicker in the plateau region. Analysis of the gravity data in a manner similar to that for the topography showed that the maximum gravity values coincide with the ridge axis (the center of topographic symmetry), and that elevated upper mantle temperatures and thicker crust could account for the large apparent depth of compensation (9) characterizing this region (8). Analysis of Eastern Aphrodite Terra shows the presence of many of the elements that are characteristic of Western Aphrodite Terra, although some elements (e.g., Iceland-like plateaus) do not occur, the altitude of the rise crest is lower, the gravity values are different, and the patterns of CSD's and rise crests are apparently more complex (10). Thus, evidence for crustal spreading exists in Eastern Aphrodite Terra and it appears that it represents more nominal spreading processes associated with normal upper mantle temperatures, and that it may be complex in nature, not necessarily representing a single pair of rigid plates (11). As yet undetermined, and subject to investigation with Magellan data, is the detailed nature of the CSD's in terms of possible plate boundary complexities, the implications for the details of

poles of rotation and possible plate-like kinematics, the relationship between surface features and upper mantle flow patterns, the geometry and role of variability of the upper mantle temperature along the rise crest, the relative roles of crustal thickness variations and dynamic uplift in the gravity and topography signatures, and the relationship of Aphrodite Terra to other parts of the equatorial highlands.

In contrast to Beta and Aphrodite, Ishtar Terra shows evidence for extensive development of convergence and compressional deformation (12-16) in the form of orogenic belts (13), adjacent foredeeps of possible flexural origin (15), crustal underthrusting (15) and large-scale regional crustal thickening (16). Not yet determined is the detailed nature of convergence and crustal loss processes and the regional and global significance of such processes. Data on the size-frequency distribution of impact craters on Venus (27, 28) has been interpreted to mean that the average age of the surface observed thus far is less than one billion years, and could be less than the 450 my average age of the Earth's crust. Not yet determined, and subject of investigation with Magellan data, is the global distribution of craters and local and regional trends of crater density and ages.

Ridge belts are linear deformation belts (12) up to 200 km wide, having two different modes of occurrence (17), extending a total length of about 40,000 km in the Venera coverage, and proposed to be of compressional (18) or extensional (19) origin. A critical challange for Magellan analysis is to determine their global distribution and their mode(s) of origin. Corona are 160-670 diameter features characterized by an annulus of deformation and associated volcanism and interpreted to be related to mantle upweling or hot spots (20,21). Questions center on their global distribution, their relationship to regions of larger-scale mantle upwelling, and other possible explanations for their formation. Plains regions make up the vast majority of the surface observed thus far (22,6,23) and are of volcanic origin based on associated flows, domes, large volcanic edifices, and embayment relationships. Not yet determined is the thickness of plains deposits, the nature of the substrate on which they occur, the contribution of plains volcanism to crustal formation and growth (24), the significance of local areas of enhnaced volcanic sources, and their relationship to regions of interpreted crustal spreading. A complex ridge and grooved terrain known as tessera (12, 25) makes up about 14% of the Venera region and has a number of possible origins including focused deformation and crustal thickening, gravity sliding, and processes similar to those producing the generally orthogonal patterns of fracture zones and abyssal hills on the terrestrial sea floor. It has been proposed that the trough-and-ridge tessera may have originated through processes analogous to those responsible for the ocean floor fabric on Earth, forming at rise crests and evolving to its present morphology and configuration through processes of crustal spreading. In this scenario, the plateau-like nature of the trough-and ridge tessera could be the result of localized crustal thickening during the spreading process, producing elevated Iceland-like plateaus whose texture is preserved from subsequent lowland volcanic flooding (26). In summary, the nature of the trough-and-ridge tessera suggests that at least some of the intervening terrain between regions of spreading and zones of convergence may have originated through processes analogous to sea-floor spreading. Left unresolved is why sea-floor-like fabric is concentrated on plateaus rather than throughout the plains, whether or not the fabric underlies a local volcanic veneer over larger portions of the surface of Venus, and how this fabric links to tectonic zones in the intervening regions.

Summary: On the basis of these regional analyses, we can conclude that there is evidence for a variety of characteristics and processes operating on the surface of Venus as presently known. Evidence has been presented for crustal spreading in Aphrodite Terra and local Iceland-like plateaus representing regional superposed areas of elevated upper mantle temperatures or 'hot-spots' (e.g., Ovda and Thetis Regiones). Zones of convergence and possible crustal loss, and distinctive orogenic belts, have been identified in the Ishtar Terra region. There is evidence for a latitudinal variation in styles of tectonism and volcanism, with the equatorial region being characterized by extensional deformation (29) and the northern high latitudes (particularly Ishtar Terra) being characterized by compresisonal deformation. The equatorial region has large shield volcanoes associated with the extensional deformation (Rhea, Theia, Sif, Gula Montes). Plateaus of tessera characterized by complex deformation and some seafloor-like fabric occur in intervening areas between zones interpreted to be spreading and zones of convergence. These regions and other regional zones of convergence and crustal thickening suggest major horizontal movement and deformation of the crust. Size-frequency distributions of impact craters observed in the northern high latitudes (27,28) and in regions covered by Arecibo data (6) indicate a relatively young age for the surface of Venus, with an average age of less than one billion years. Gravity data (9) reveal a positive correlation of gravity and topography at long wavelengths in the equatorial region, show variable apparent depths of compensation within the highlands (9,30), and show local regions of high amplitude anomalies (e.g., Beta, Atla Regio) where the apparent depth of compensation is so high that some type of dynamic support, such as large-scale mantle upwelling, or mantle plumes, seems plausible.

Questions for Magellan: Recent analyses have focused some key geological questions for Magellan as follows: What is the global distribution and age of hot spots, crustal spreading centers, zones of convergence, upland plateaus, and volcanoes, and what are their relationships? What are the mechanisms of crustal formation and recycling? Is there a globally interconnected tectonic network and what is its relationshop to processes of crustal formation and loss? What is the thermal structure of Venus and is there evidence for globally significant lithospheric plates and plate tectonics? What is the distribution of gravity anomalies and how do they relate to surface topography and geology? What is the relationship of surface features to mantle processes? Can we make more quantitative estimates of different mechanisms of Venus heat loss?

References: 1. S. Solomon and J. Head, *J. Geophys. Res. 87*, 9236 (1982); 2. D. Campbell *et al.*, *Science 226*, 167 (1984); 3. E. Stofan *et al.*, *Geol. Soc. Am. Bull. 101*, 143 (1989); 4. D. Senske and J. Head, *Lunar Planet. Sci. 20*, 986 (1989); D. Senske and J. Head, *Lunar Planet. Sci. 19*, 1063 (1988); 5. G. McGill *et al.*, *Geophys. Res. Lett. 8*, 737 (1981); 6. D. Campbell *et al.*, *Science 246*, 373(1989); 7. J. Head and L. Crumpler, *Science 238*, 1380 (1987); L. Crumpler and J. Head, *Tectonophys.*, in review (1989); 8. C. Sotin *et al.*, *Earth Planet. Sci. Lett.*, in press (1989); 9. W. Sjogren *et al.*, *J. Geophys. Res. 88*, 1119 (1983); 10. L. Crumpler and J. Head, *Lunar and Planet. Sci. 19*, 233 (1988); 11. R. Grimm and S. Solomon, *J. Geophys. Res. 94*, 12103 (1989); 12. A. Basilevsky *et al.*, *J. Geophys. Res. 91*, D399 (1986); 13. L. Crumpler *et al.*, *Geology 14*, 1031 (1986); 14. R. Vorder Bruegge *et al.*, *J. Geophys. Res.* in press (1989); 15. J. Head, *Geology*, in press (1989); S. Solomon and J. Head, *Lunar Planet. Sci. 20*, 1030 (1989); 16. R. Vorder Bruegge and J. Head, *Geophys. Res. Lett. 16*, 699 (1989); 17. S. Frank and J. Head, *Lunar Planet. Sci. 19*, 350 (1988); 18. V. Kryuchkov,*Lunar Planet. Sci. 19*, 649 (1988); 19. A. Sukhanov and A. Pronin, *Proc. Lunar Planet. Sci. Conf 19*, 335 (1989); 20. E. Stofan and A. Pronin, submitted to *Icarus* (1989); 21. E. Stofan *et al.*, *Lunar Planet. Sci. 19*, 1129 (1988); 22. V. Barsukov *et al.*, *J. Geophys. Res. 91*, 378 (1986); 23. D. Senske, thesis, Brown University, Providence, R.I. (1989); 24. J. Head, Venus Crustal Formation and Evolution (this volume); 25. D. Bindschadler and J. Head, *J. Geophys Res.*, in review (1989); 26. J. Head, *ibid.*, in press (1989); 27. B. Ivanov *et al.*, *J. Geophys. Res. 91*, 413 (1986); 28. G. Schaber, E. Shoemaker, R. Kozak, *Sol. Syst. Res. 21*, 144 (1987); 29. G. Schaber, *Geophys. Res. Lett. 9*, 499 (1982); 30. W. Kiefer *et al.*, *Geophys. Res. Lett. 13*, 14 (1986); B. Bills *et al.*, *J. Geophys. Res. 92*, 10335 (1987); R. Herrick *et al.*, *Geophys. Res. Lett. 16*, 543 (1989).

THE NORTHERN QUARTER OF VENUS: AVAILABILITY OF NEW USGS OPEN-FILE GEOLOGIC/GEOMORPHIC AND STRUCTURE MAPS.

Gerald G. Schaber and Richard C. Kozak, U.S. Geological Survey, Flagstaff, AZ 86001

Introduction. Geologic/geomorphic and structural maps of the northern quarter of Venus have recently been compiled at 1:15,000,000 scale as part of a pre-Magellan investigation of the geology and tectonics of Venus [1,2]. These maps, on two sheets with accomplanying text and unit descriptions, have been released prior to formal publication as a USGS Open-File Report to expedite availability to the planetary geoscience community prior to start of Magellan mapping of Venus in August, 1990. The maps show an alternative interpretation of the same region of Venus that was covered by the geomorphic/geologic map of Sukhanov et al. [3], which was published by the USGS as part of a 1:15,000,000-scale map series [4] under a joint US/USSR cooperative agreement [5].

Our open-file maps are the result of photogeologic interpretation of medium-resolution (1.5-2 km) images of the northern quarter of Venus acquired by the two Soviet spacecrafts, Venera 15 and 16. The mapped area covers 111.4 X 10^6 km^2 and is centered on the North Pole. Processing and mosaicking of the Venera 15/16 radar data [6,7] were done by the Institute for Information Transmission Problems of the USSR Academy of Sciences. We mapped the resulting 27 1:5,000,000-scale quadrangles [8,9] at a reconnaissance level prior to compilation on a 1:15,000,000-scale image mosaic [3, sheet 2]. Supplementary data used in mapping included a topographic dataset of combined Pioneer Venus (PV) and Venera 15/16 altimetry data [L. Soderblom and E. Eliason, pers. commun., 1989]. This dataset was used along with the Venera radar mosaic to create a synthetic stereoimage [10] that greatly facilitated geologic and structural interpretation during mapping [11].

Geologic/Geomorphic Map Units. We mapped 34 geologic/geomorphic units within 14 general terrain types. Our geologic/geomorphic map was digitized and co-registered with other datasets (e.g., combined PV/Venera altimetry dataset) to determine various statistics for the mapped units, including percentage of total mapped area covered (Table 1).

Acknowlegments. Research was supported under NASA PG Contract W-15,514 to the USGS.

References. [1] Schaber, G.G. and Kozak, R.C., 1990, USGS Open-File Report 90-24, Denver, Colo., scale 1:15,000,000; [2] Schaber, G.G. and Kozak, R.C., 1990, *Abstrs. of Papers Submitted to the Twenty-First Lunar and Planet. Sci. Conf.*, Houston, Texas - in press; [3] Sukhanov, A.L., and 11 others, 1989, *USGS Misc. Inv. Ser. Map I-2059*, scale 1:15,000,000; [4] USGS, 1989, *Misc. Inv. Ser. Map I-2041*, 3 sheets, scale 1:15,000,000; [5] Basilevsky, A.T., Burba, G.A., and Batson, R.B., 1989, *In Abstrs. of Papers Submitted to the Twentieth Lun. Planet. Sci. Conf.*, Houston, Texas, 46-47; [6] Alexandrov, Yu. A. and 10 others, 1985, *Geodeziya i Kartografiya, v. 1985, no. 9*, 41-48; [7] Bockstein, I., Chochia, P., and Kronrod, M., 1988, *Earth, Moon, and Planets, v. 43*, 233-259; [8] USSR Acad. of Sciences, 1987, *Photomap of the Venusian surface,*

sheets B-2 to B-27, Moscow, GUGK (Main Administration of Geodesy and Cartography), scale 1:5,000,000; [9] USSR Acad. of Sciences, 1988, *Photomap of the Venusian surface, sheet B1*, Moscow, GUGK (Main Administration of Geodesy and Cartography), scale 1:5,000,000; [10] Batson, R.B., Edwards, K., and Eliason, E.M., 1976, *Photogram. Eng. and Remote Sens., v. 42*, 1279-1284; [11] Kozak, R.C. and Schaber, G.G., 1988, *In Abstrs. of Papers Sumbitted to the Nineteenth Lunar and Planet. Sci. Conf.*, Houston, Texas, 513-514. [12] Barsukov, V.L., and 29 others, 1986, *Proc. 16th Lunar Planet. Sci. Conf., part 2, J. Geophys. Res., v. 91, no. B4* , D378-D398; [13] Schaber, G.G., and Kozak, R.C., 1989, *In Abstrs. of Papers Submitted to the Twentieth Lunar Planet. Sci. Conf.*, Houston, Texas, 954-955.

Table 1. PERCENT AREA COVERAGE BY MAP UNIT AND TERRAIN CATEGORY.

MAP UNIT Symbol (see [1] for description)	% OF MAP AREA	TERRAIN CATEGORY
ps	33.03	SMOOTH PLAINS
psl	0.83	
pi	8.51	OTHER PLAINS
pm	4.91	
pc	2.78	
pt	3.96	
tl	3.40	TESSERA
twf	1.79	
tef	0.96	
th	0.23	
tg	0.04	
tf	0.47	
tu	2.75	
ml	0.68	MARGINAL BELTS
mt	1.17	
l_1	6.32	LINEATED AND FRACTURED TERRAIN
l_2	6.06	
f	1.23	
btd	0.68	DOMED TERRAINS OF BETA AND BELL REGIONS
bld	1.06	
s	2.69	SHIELDS, DOMINAL HILLS/MESAS, AND PATERAE
dh	3.34	
dm	0.05	
cp	0.86	
co_1	1.07	CORONAE
co_2	0.37	
r	0.30	RIDGE BELTS AND RIDGED PLAINS
rb_1	5.46	
rb_2	0.53	
rs	2.75	
rc	1.33	
c	0.06	CRATERS (>45 KM IN DIAMETER) AND MISCELLANEOUS TERRAINS
ce	0.12	
h	0.23	

VENUS: SOUTHERN HEMISPHERE TERRAINS AND A SURFACE AGE ESTIMATE FROM NEW ARECIBO RADAR IMAGERY

D.B. Campbell[1] and J.W. Head[2]. [1]National Astronomy and Ionosphere Center, Cornell University, Space Sciences Building, Ithaca, NY 14853. [2]Department of Geological Sciences, Brown University, Providence, RI 02912.

Introduction. The Arecibo 12.6 cm wavelength radar was used to image most of the surface of Venus 'visible' during the close approach of the planet to the earth in 1988. To date, processing of the data has provided 1.5 to 2.5 km resolution, 25 look, imagery of the surface in the approximate longitude range 270° to 20° and latitude bands 12°N to 66°N and 10° to 66°S. The incidence angle at which the radar viewed various portions of this area varied over the approximate range of 12° to 66° with the lowest incidence angles being at low latitudes near longitude 330° and the highest ones near the peripheries of the images. Image quality is also a function of incidence angle since the signal-to-noise ratio decreases with incidence angle due to both scattering law effects and increased atmospheric absorption.

Southern Hemisphere Terrains. The area covered in the southern hemisphere by the new imagery includes all or part of four upland areas, Alpha Regio, Phoebe Regio, Themis Regio and Lada Terra, three prominent montes, Hathor, Innini and Ushas plus parts of three lowland planitia, Navka/Guinevere, Lavinia and Helen. The new data (1) show that Alpha Regio is characterized by a system of 5 to 10 km wide lineaments, probably corresponding to ridges and troughs, whose dominant orientation is generally N-S and whose length ranges from 15 to over 100 km. A second set of less prominent linear structures is observed which has an orientation approximately orthogonal to the N-S system. Oval to linear patches of radar dark plains 20-200 km in extent oriented parallel to the major structural trends are also observed. On the basis of observations from the Pioneer-Venus orbiter, Alpha Regio was predicted to be similar to the terrains designated as Tessera in the Venera 15/16 imagery of high northern latitudes (2). This new data strongly supports this interpretation. Topographically, Phoebe Regio consists of two SE trending linear rises extending towards Lavinia Planitia and including a southern extension of the Beta Regio rift system (3,4). The western linear rise is characterized by a 200 km wide linear zone disrupted by bright lineaments on and parallel to the rise crest; this zone has many similarities to the Devana Chasma rift. On the basis of this similarity it is interpreted as a rift zone. Several associated volcanic centers are also observed. The eastern linear rise has similar characteristics (bright lineaments on and parallel to the rise crest) but the structure is not as radar-bright and appears to be generally more subdued. Themis Regio is characterized by two major types of features, concentric ring to oval structures 250 to 400 km in diameter, and volcanic edifices(5). Several densely packed and interconnected ring/oval structures and superposed volcanoes form Themis itself and a chain of ring/oval structures and volcanoes extends from Themis to the east for about 2200 km. These structures are similar to coronae(6) in size and presence of concentric annular ridges, but differ in their polygonality, close spacing and chain-like nature. These structures are separated from

Hathor Mons by a prong of Lavinia Planitia. The structure of Themis is similar to the Beta-Eisila Deformation Zone(6), but neither the origin of the circular/oval structures, nor their exact relationship to the corona structures seen in Venera data(7), are clear at the present time. Only the northernmost border of Lada Terra (the south polar highland region rising up to 2 km above mpr) is seen. It is characterized by radar-dark plains and by a 150-200 km wide linear belt of bright lineaments paralleling the slope at the northern edge of Lada and having some similarities to ridge belts seen in the Venera data(8). Additional belts of bright lineaments are seen to the north of Lada Terra on the southern slopes of Lavinia Planitia. Three prominent Montes (Ushas, Innini, Hathor) form a generally N-S trending upland rise between Navka/Guinevere and Lavinia Planitia. These peaks rise 1.5-2 km above mpr, are separated from each other by 800-1200 km, are the locus of flow-like deposits that often appear to embay surrounding structure, and they are interpreted to be volcanic edifices similar to volcanoes seen in the northern hemisphere (Sif, Theia, etc.)(9). Several types of structures are radial to these features, including paired bright lineaments forming 20-40 km wide zones, and broader zones of bright lineaments 50-150 km wide one of which extends south into Lavinia Planitia. These are tentatively interpreted as zones of extension.

The Planitiae are low in elevation (< mpr) and form broad areas of plains of apparent volcanic origin between the upland/highlands and montes. Navka and Lavinia contain several apparent volcanic sources (domes, flow center, etc.) and Lavinia is disrupted by abundant linear deformation zones, features also seen in the northern Venus plains(3,8). Few features are visible in the small eastern part of Helen Planitia covered by the new images. Instead this region has unusual surface properties which result in a radar image showing primarily 'speckle' with a slowly varying mean. Further examination of the data is needed to better describe and understand this phenomenon.

Crater Counts. A total of forty-two circular features with diameters greater than 8 km have been identified in the 50 $10^6 km^2$ covered by the new Arecibo images in the southern hemisphere. This count resulted from a search for possible impact craters and excluded a very small number of circular features whose general appearance and close association with the large volcanic mountains made classifications an impact craters extremely doubtful. This is not to say that all of the remaining 42 craters are being interpreted as impact craters. Rather, the count is a probable upper limit on the number of impact craters in this region and corresponds to a number density of 0.8 craters per $10^6 km^2$. Comparing this with the average density of 1.3 per $10^6 km^2$ for probable impact craters greater than 8 km in diameter obtained for the northern most quarter of the planet from the Venera 15/16 data(10) indicates that the density of impact craters measured from the Venera 15/16 images may not be representative of the planet as a whole. A size-frequency distribution has been obtained for the 42 craters identified in the Arecibo images of the southern hemisphere and this is shown in Fig. 1 in comparison with a similar plot obtained from the Venera 15/16 data for northern latitudes. For diameters larger than approximately 30 km, the curves indicate similar crater retention ages. However, at smaller diameters there appears to be a significant deficiency of craters in the southern hemisphere compared with the north.

References: (1) D. Campbell *et al.* (1990) LPSC XXI, 161; (2) D. Bindschadler *et al.* (1990), Distribution of Tessera Terrain on Venus: Prediction for Magellan, GRL, in press; (3) D. Campbell *et al.* (1989) Science, 246, 373; (4) G. McGill *et al.* (1981) GRL, 8, 737; (5) E. Stofan *et al.* (1990), LPSC XXI, 1210; (6) E. Stofan *et al.* (1990), LPSC XXI, 1208; (7) E. Stofan and A. Pronin (1989), Coronae on Venus, Morphology, Classification and Distribution, submitted to Icarus; (8) A. Basilevsky *et al.* (1986), JGR, 91, D399; V. Barsukov *et al.* (1986), JGR, 91, D378; (9) S. Keddie *et al.* (1990), LPSC XXI, 615; (10) Basilevsky *et al.* (1987), JGR, 92, 12,869; (11) W. Hartmann *et al.* (1981) in "Basaltic Volcanism on the Terrestrial Planets", 1049, Pergamon Press.

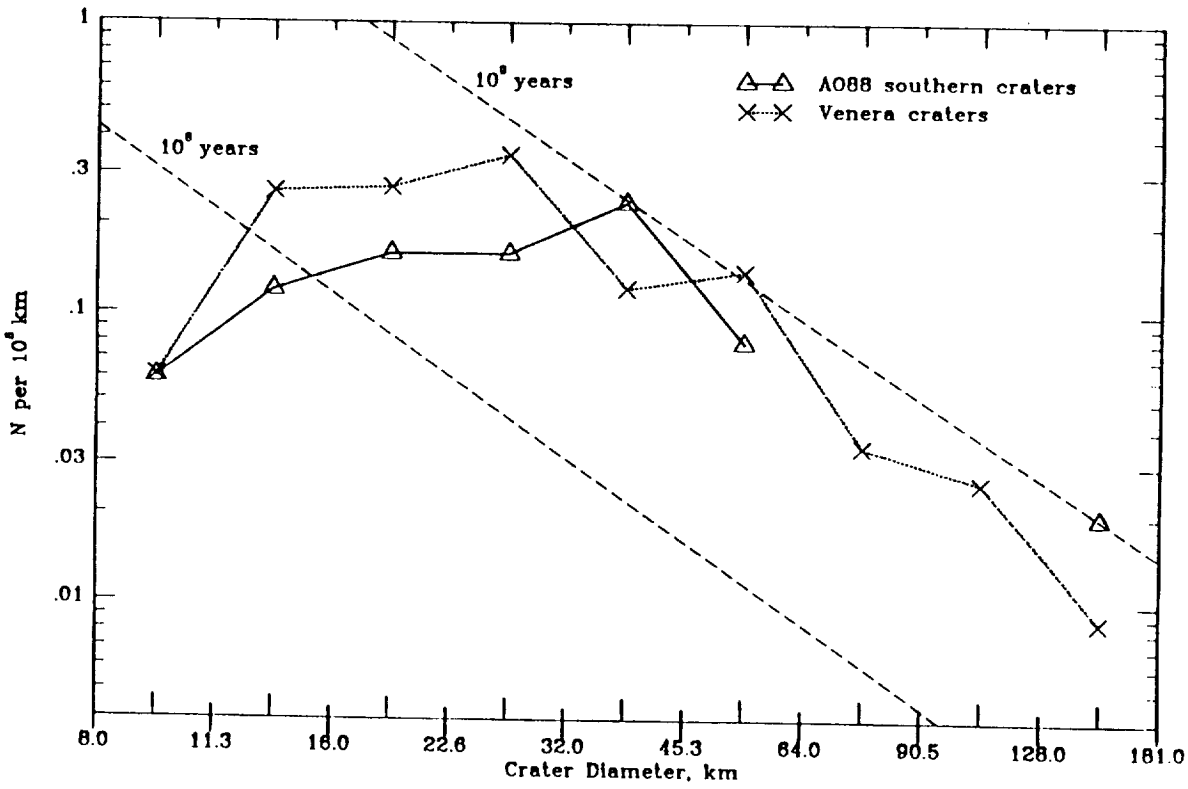

Figure 1. Comparison of the size-frequency distributions for the 42 craters observed in $50.10^6 km^2$ of the southern hemisphere with the Arecibo radar system and for the 146 craters observed from the Venera 15/16 spacecraft over $115.10^6 km^2$ at latitudes north of 30°N. The 10^8 and 10^9 year isochrons shown for comparison are based on the lunar impact rate derived by Hartmann(11).

VENUS CRUSTAL FORMATION AND EVOLUTION: AN ANALYSIS OF TOPOGRAPHY AND CRUSTAL THICKNESS VARIATIONS

James W. Head, Department of Geological Sciences, Brown University, Providence RI 02912

Morgan and Phillips[1] tested the hypothesis that conductive heat loss is an efficient heat loss mechanism and showed that most of the topography of Venus (about 93%) could result from spatially varying thermal expansion in response to spatially varying heat flow (hot spots). They proposed that the remaining topography (at high elevations) could be accounted for by crustal thickness variations. In this study the complementary hypothesis that the topography of Venus could result largely from crustal thickness variations is tested. Existing data for Venus (composition, hypsometry, regional topography, regional slopes, geology) are consistent with a basaltic crust with a wide range of thickness for the planet as a whole, but a narrow range in terms of crustal thickness frequency distribution, with the vast majority of the planet having crustal thicknesses within ±5 km of the mean value.

CRUSTAL THICKNESS: On the basis of observed wavelengths of tectonic features combined with theoretical models of deformation of the lithosphere, Zuber[2] developed constraints on the near-surface thermal gradient, and using rheological models of the crust and upper mantle, estimated the thickness of the crust. For a range of geologic features primarily in the lowlands and rolling plains, Zuber[2] estimated an upper limit of crustal thickness of 30 km, and in a later study[3] which incorporated growth rate similarity requirements, she refined the upper limit of allowable crustal thickness to about 20 km. Using observed impact crater depths and models of viscous relaxation of crater relief, Grimm and Solomon[4] calculated thermal gradients and derived upper bounds to crustal thickness of 10-20 km in regions of low to intermediate elevations. Larger values for crustal thickness (generally in excess of 100 km) have been proposed or are permissible on the basis of 1) parameterized convection models which are subject to boundary or initial condition assumptions, 2) apparent depths of compensation of long wavelength topography which are thought to be overestimates due to components of dynamic compensation, and 3) the depth of the basalt/eclogite phase change which is applicable only as an upper limit. Although these higher estimates cannot be ruled out, crustal thicknesses in the Venus lowlands and rolling uplands seem more likely to lie in the range of less than about 20-30 km, on the basis of the analyses cited above.

CRUSTAL THICKNESS VARIATIONS: Venus terrain and topography can be subdivided into lowlands and rolling plains, upland plateaus, and highlands. Geologic evidence, such as the presence of orogenic belts[5] and compressional deformation in Ishtar Terra[6], is consistent with most of the highest topography being due to variations in crustal thickness. Geologic evidence leading to reasonable hypotheses for the origin of other regions of intermediate to high topography (the tessera terrain) are also consistent with crustal thickness variations[7], although not uniquely so. Geologic evidence indicates that a portion of Venus (primarily the Equatorial Highlands) is the site of extensional deformation[8] and that the topography can be explained by a combination of crustal thickness variations (plateaus)[9] and thermal sources (broad rise)[1,10]. Although crustal thickness is not uniquely determined, abundant evidence[2-4] points to a crustal thickness for the Venus lowlands of less than about 20 km. Using these observations and interpretations, a simple model of Airy isostasy using global Venus topography can assess the potential significance of crustal thickness variations in explaining the topography of Venus. The distinctive unimodal hypsometric curve can be expained by: 1) a crust of relatively uniform thickness (less than 20 km thick) comprising over 75% of the surface, 2) local plateaus (tessera) of thickened crust (about 20-30 km) forming <15% of the surface, 3) regions (Beta, Ovda, Thetis, Atla Regiones and Western Ishtar Terra) forming <10% of the surface showing 30-50 km modelled crustal thickness, which can be explained on the basis of geologic observations as combinations of crustal thickening (plateaus) and thermal effects, and 4) areas in which Airy isostasy predicts crustal thicknesses in

excess of 50 km (the linear orogenic belts of Western Ishtar Terra). It is concluded that crustal thickness variations linked to crustal formational and modificational processes can account for the vast majority of the observed topography. Regional variations in heat flux (lithospheric thickness variations) are very significant locally, as along the rise crest of the Equatorial Highlands. More subtle thermal variations (e.g., very broad low thermal rises analogous to the Pacific superswell[11], and the flanks of spreading centers between rise crest and thermal equilibrium)[9] can also obviously contribute to variations in topography. Gravity and topography data from Magellan will permit the further delineation of the contributions of thermal effects and crustal thickness variations for local regions.

The most significant factors in accounting for the differences in the hypsometric curves between Venus and Earth appear to be related to crustal thickness variations and their distribution on Venus and Earth.[16] These factors include: 1) the larger percentage of continental crust on the Earth (41%) relative to highland crust on Venus (<10%), 2) the greater average thickness of Earth's continental crust (about 40 km) relative to Venus uplands and highlands (about 30-35 km); 3) the greater average thickness of the Venus lowland/rolling upland crust (about 15 km) relative to the Earth's oceanic crust (5-6 km); 4) the greater percentage of lowland/rolling upland crust on Venus (about 75%) relative to oceanic crust on Earth (59%); and most importantly, 4) the greater contrast in average thickness difference between the crusts of the two terrains on Earth (5/40 = 35 km) and Venus (about 15/30 = 15 km), about 20 km difference between Venus and Earth. This latter factor appears to cause the fundamental separation of the two peaks on Earth relative to Venus.[16] The average compositional difference between the continental crust and the oceanic crust on the Earth contributes only about 20% of the separation between peaks on Earth, but is not as important a factor as the crustal thickness differences, which contribute about 80% of the elevation difference.

CRUSTAL FORMATION AND EVOLUTION: As yet not uniquely determined is the mechanism or mechanisms for crustal formation and evolution. Impact-related early crustal differentiation seems unlikely because of the young age of the surface of Venus observed thus far. A crust of impact origin buried by subsequent vertical differentiation and volcanic flooding requires at least 6-8 km thickness of lava to obscure the early record of impact craters and basins. Such a process would require that the present crust is primarily the result of vertical differentiation processes. Presently observed rates of resurfacing (4 km/b.y.)[12] are sufficient to obscure such an early crust, but the early impact-derived crust must be very thin (<5-10 km) if the total average crustal thickness is less than 20 km.

Vertical differentiation processes are plausible mechanisms for the formation and evolution of the observed crust. If such processes are the dominant mechanism, then some implied crustal growth rates are (in average thickness and volumes) 2-4 km/b.y. (1-2 km^3/yr) for a crust produced by surface volcanism,[12,13] at least 9-18 km/b.y. (4.5-9 km^3/yr) for crustal thicknesses limited by melting, and at least 17 km/b.y. (8.5 km^3/yr) for a crustal thickness limited by negative buoyancy. Vertical differentiation models require abundant local volcanic sources which vary in space and time, which produce a generally homogeneous crustal thickness, and which permit sufficient lateral crustal movement to yield the observed orogenic belts and regions of compressional deformation. If vertical differentiation processes are in fact the predominant mechanism for production of the crust on Venus, then the estimates of present average crustal thickness of less than about 20 km discussed above constrain vertical differentiation models. Models which invoke crustal thicknesses limited by basal melting (about 40-80 km) or negative buoyancy (about 75 km) are not consistent with the <20 km crustal thickness number. Rates for vertical recycling models based solely on addition of surface volcanic deposits[12,13] (1-2 km^3/yr) could produce the presently observed crust over the history of the planet. However, this would require that essentially no crust has been recycled, and that surface volcanic deposits are by far the major contribution to the crust. This seems unlikely because underplating and intrusion usually dominate volumetrically over extrusion (the ratio of intrusion to extrusion for Earth is about 5:1 for oceanic

regions and about 10:1 for continental regions[14]). In order for this model to be viable, it would require that the average volcanic flux on Venus in the past be considerably less than 2 km^3/yr,[12] or that some type of crustal recycling take place. The average crustal thickness of less than about 20 km would seem to rule out global vertical crustal recycling by melting or negative buoyancy, and presents several problems for models of vertical resurfacing, requiring anomalously low early resurfacing rates or an unspecified method of crustal recycling.

Crustal spreading models provide a mechanism: 1) to produce a geologically young global crust of less than about 20 km thickness (about 15 km average thickness[10]), 2) to produce Icelandic-like plateaus of locally thickened crust[9], 3) to explain the generally extensional deformation of the regions where a thermal component to topography seems most likely (Equatorial Highlands)[8], and 4) to move the crust and plateaus laterally to produce the observed areas of convergence, orogenic belts, and compressional deformation. Crustal spreading models require that crustal recycling is taking place at zones of convergence and crustal thickening, and require the identification of areas of crustal loss in addition to the presently observed regions of orogenic belts.

SUMMARY AND CONCLUSIONS: It is concluded that Venus hypsometry can be reasonably explained by a global crust of generally similar thickness with variations in hypsometry being related to: 1) crustal thickening processes (orogenic belts and plateau formation) and 2) local variations in the thermal structure. Vertical differentiation and crustal spreading processes are the most likely candidates for the formation and evolution of the crust, and there is abundant evidence that both have been operating in recent geologic history.[9,15] Of these two, crustal spreading processes are interpreted to be most consistent with the observations derived from presently available data. Determination of the exact proportion of the topography of Venus that is due to the thermal effects[1] and crustal thickness variations (discussed here), and determination of the type of crustal thickening processes operating, must await new data and further study. In particular, global imaging data showing the age of the surface, the distribution and age of regions of high heat flux, and evidence for the global distribution of processes of crustal spreading and crustal loss, would permit better estimates of this proportion. Together with geological data derived from images, global gravity and topography data would permit modelling of crustal thickness variations and thermal contributions and tests of the various concepts of crustal growth, which would lead to regional understanding of these processes, and assessments of their contribution to the global values.

References: 1) P. Morgan and R. Phillips (1983)JGR, 88, 8305; 2) M. Zuber (1987) JGR, 92, E541; 3) M. Zuber and E. Parmentier (1989) Icarus, in press; 4) R. Grimm and S. Solomon (1988) JGR, 93, 11911; 5) L. Crumpler *et al.* (1986) Geology, 14, 1031; 6) R. Vorder Bruegge and J. Head (1989) GRL, 16, 699; 7) D. Bindschadler and J. Head (1989) Models for the origin and evolution of tessera terrain, Venus, submitted to JGR; 8) G. Schaber (1982) GRL, 9, 499; 9) J. Head and L. Crumpler (1987) Science, 238, 1380; 10) C. Sotin *et al.* (1989) EPSL, 95, 321; 11) M. McNutt and K. Fischer (1987) in Seamounts, Islands, and Atolls, B. Keating *et al*, ed., AGU, 25; 12) R. Grimm and S. Solomon (1987) GRL, 14, 538; 13) B. Fegley and R. Prinn (1989) Nature, 337, 55; 14) J. Crisp (1984) J. Vol. Geotherm. Res., 20, 177; 15) D. Campbell et al (1989) Science, 246, 373; 16) J. Head (1990) Venus hypsometric curve: An assessment of its components and comparison to Earth, LPSC XXI.

A Model for the Initiation of Subduction, with Results for Venus

D.L. Herrick and E.M. Parmentier, Division of Geological Sciences, Box 1846,
Brown University, Providence, RI 02912

Plate tectonics requires that the generation of new lithospheric material at spreading centers be balanced by consumption of the lithosphere at subduction zones. While the dynamics of an extant system of plate tectonics are rather well understood (Forsyth and Uyeda, 1975), the means of inception of plate motions are less clear. Crustal production via mantle upwellings at mid-ocean ridges or lithospheric hotspots is possible for a one-plate planet (for example, Mars or the early Earth), and the thermal subsidence of this material provides both a gravity spreading force that causes lateral migration, and a density increase that promotes an approach toward negative buoyancy. In the case of the Earth, the compressive stresses associated with lithospheric spreading forces have acted in concert with the density increase to cause nucleation and development of zones of subduction. However, theoretical analyses of the initiation process for subduction (for example, McKenzie, 1976) suggest that the forces promoting the return of material to the interior are at the outset outweighed by interplate friction and the elastic restoring force associated with plate flexure. Because these forces which resist subduction initially exceed the driving forces, the presence of terrestrial subduction zones indicates a deficiency in our theoretical understanding of the factors involved in initiating subduction.

The present study expands upon McKenzie's conceptual approach to modelling the relative magnitudes of the driving and resisting forces associated with a lithospheric slab attempting to subduct. The thermal lithosphere is assumed to consist of a basaltic crust and the upper portion of a peridotite mantle. The crust is further divided into gabbro, granulite, and eclogite phases with increasing depth. Superposition of an error function temperature profile on this structure, with due allowance for density changes as a result of thermal expansion, permits the numerical computation of a lithostatic pressure profile, which may be combined with the thermal model to yield the depths of crustal phase changes. It is then possible to determine the mean density of the thermal lithosphere, which is compared with the density of the asthenosphere immediately below it in order to assess the relative buoyancy of the lithosphere. Negative lithospheric buoyancy is a minimum requirement for the initiation of subduction. The results of this calculation, for a variety of total crustal thicknesses and lithospheric cooling ages, are shown in Figure 1 for the case of the planet Venus. Since the question of whether Venus has a system of plate tectonics is still unresolved, we feel that a first application of the model to this planet is most appropriate. Applications to the Earth and other planets will be made in the near future.

The forces incorporated into our model of subduction are illustrated schematically in Figure 2. Each can be classified as either a driving or a resisting force with respect to the initiation of subduction. Figure 3 shows (again for Venus) how the sum of the driving stresses compares with the sum of the resisting stresses as a function of the amount of plate that has been subducted. Note that the resisting stresses exceed the driving stresses at every stage of the subduction process. This turns out to be the case for any reasonable cooling age and crustal thickness that we might consider. The conclusion to be drawn is that the contribution of lithostatic pressure to the frictional stress at the plate interface prohibits the initiation of subduction, and thus the development of plate tectonics, on Venus under any circumstances. However, since this model would predict a similar fate for the Earth, we are forced to rethink the contribution of lithostatic pressure to the interplate shear stress.

McKenzie (1976) took the effective shear stress between the plates to be 0.1 kbar, based on the maximum stress drops measured in terrestrial earthquakes. If we adopt this value for Venus, the results are as indicated in Figure 4. Because it is not clear that a shear stress of 0.1 kbar is appropriate for Venus, perhaps a better approach to this problem would be to determine the largest shear stress that could act on the fault between the plates without allowing the resisting stresses ever to exceed the driving stresses and thus pinch off the subduction process. In the case of Figure 4, this maximum allowable shear stress would be about 0.25 kbar. Contours of this parameter are plotted in Figure 5 as a function of cooling age and crustal thickness.

Several avenues of inquiry concerning this model will be pursued in the coming weeks. One is the effect of asthenospheric shear, which could act as either a driving or a resisting force depending on whether convection is taken to be a cause or a consequence of plate tectonics. Once this force is incorporated, calculations of the requirements for the development of subduction zones will be extended

from Venus to the Earth, and ultimately to other large solid bodies in the solar system. It is important that our model demonstrate not only the feasibility of plate tectonics for the Earth (and perhaps Venus), but also the difficulty of initiating subduction on other planets. Finally, we plan to assess the effects of crack propagation theory on our results. If the driving forces of subduction are sufficient to initiate the process along a short segment, the relative vertical motion would produce stress concentrations at the tips of the segment. In this manner a tearing-mode propagation of the subduction zone parallel to its axis might result at an energy cost significantly less than for a simultaneous initiation of subduction along the entire mature length of the trench. This scenario would prove especially attractive if the present model still cannot account for the initiation of terrestrial subduction.

References

Forsyth, D.W., and Uyeda, S., On the relative importance of the driving forces of plate motion, Geophys. J. R. Astr. Soc. 43, 163-200, 1975.

McKenzie, D.P., The initiation of trenches: a finite amplitude instability, in A.G.U. Ewing Series 1, 57-61, 1976.

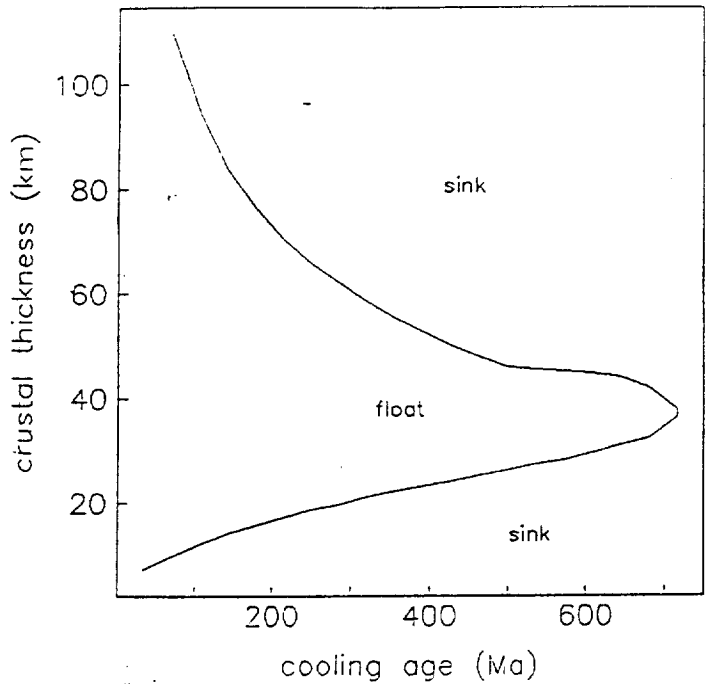

Figure 1 (left). Buoyant tendency of the thermal lithosphere of Venus as a function of crustal thickness and lithospheric cooling age. Note that crustal thicknesses in the range of 25-50 km remain quite buoyant for a long time and thus greatly inhibit subduction of the lithosphere as a whole. This reflects a maximum contribution from low-density gabbroic crust to the buoyancy of the slab.

Figure 2 (below). Stresses acting on the plates in the zone of convergence. Driving forces include the gravity spreading force associated with a distant thermally elevated region, slab pull due to both thermal and phase-change sources of positive density contrast with the asthenosphere, and an isostatic contribution resulting from the excess thickness of negatively buoyant lithosphere in the region of plate overlap. Subduction is resisted by elastic restoring forces and by friction at the interface between the two plates. The primary contributor to this frictional stress is the lithostatic overburden imposed by the overriding plate, with minor contributions from the gravity spreading and elastic forces, and a small negative contribution from slab pull.

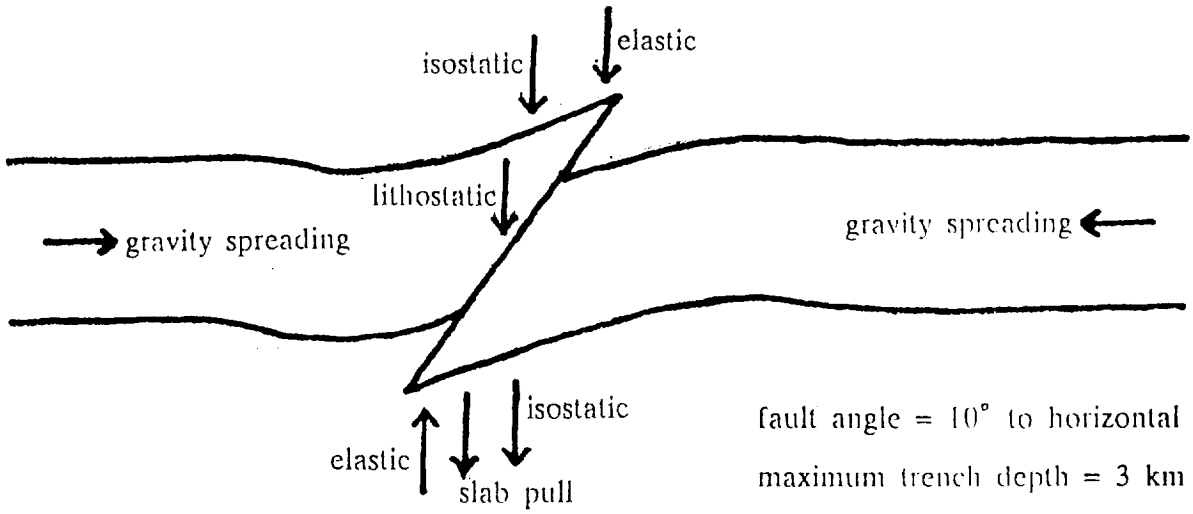

Figure 3 (left). Total driving and resisting stresses versus plate convergence for a lithospheric cooling age of 600 Ma and a crustal thickness of 20 km. The primary contribution to the driving stress is the gravity spreading force, which remains constant with the amount of subducted lithosphere. The resistance to subduction is dominated by the lithostatic contribution to the interplate friction. As one plate overrides the other, the lithostatic pressure at the plate contact increases in proportion to the integrated column density of material above it. The pressure levels off after the full topography of the subduction zone has been built up. For the 3 km trench and 10 degree dip angle illustrated in Figure 2, this transition occurs after 34 km of plate has been subducted. Note that the resisting stresses exceed the driving stresses at every stage of the subduction process.

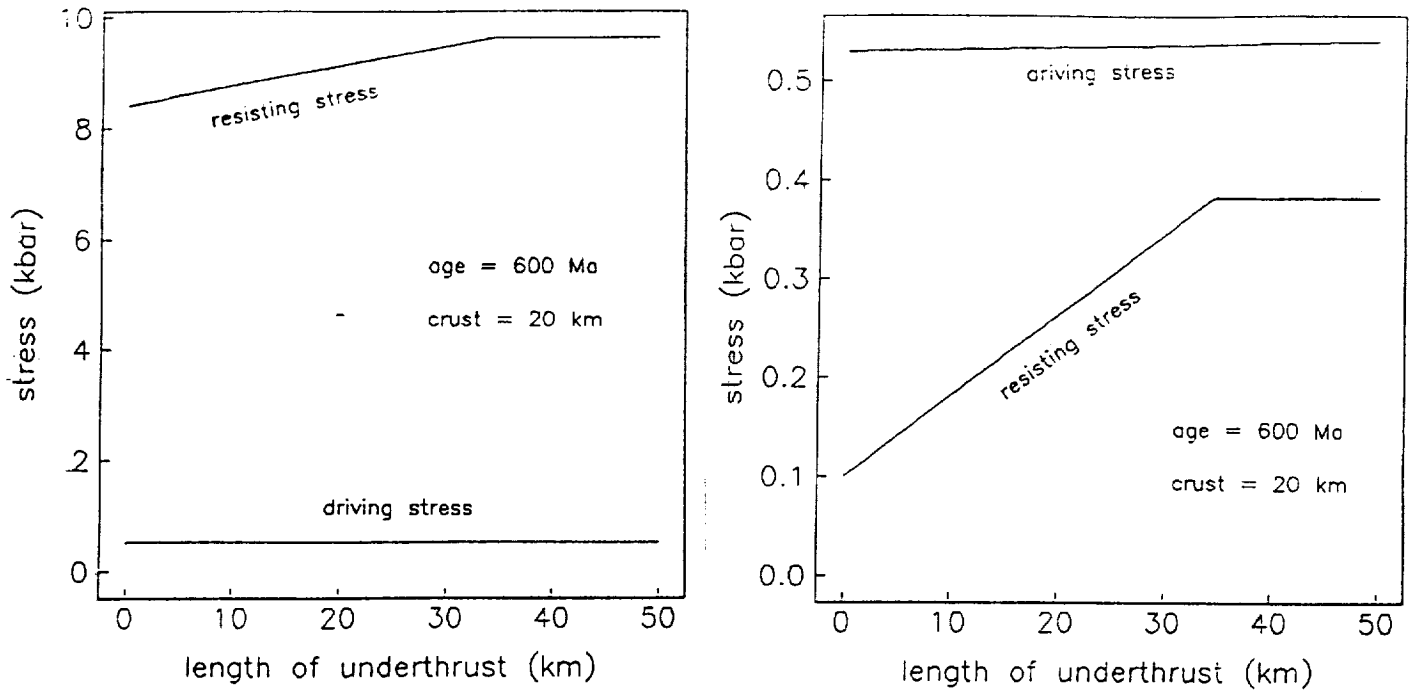

Figure 4 (right). Same as Figure 3, but with shear stress fixed at 0.1 kbar. The driving stress is unchanged, whereas the resisting stress, initially equal to the specified 0.1 kbar, increases because of the growing work done against elasticity in bending the plates, and then levels off as before when the mature geometry of the system has been attained. In this example (600 Ma cooling age, 20 km crust), the driving stress always exceeds the resisting stress, and a subduction zone can therefore become established.

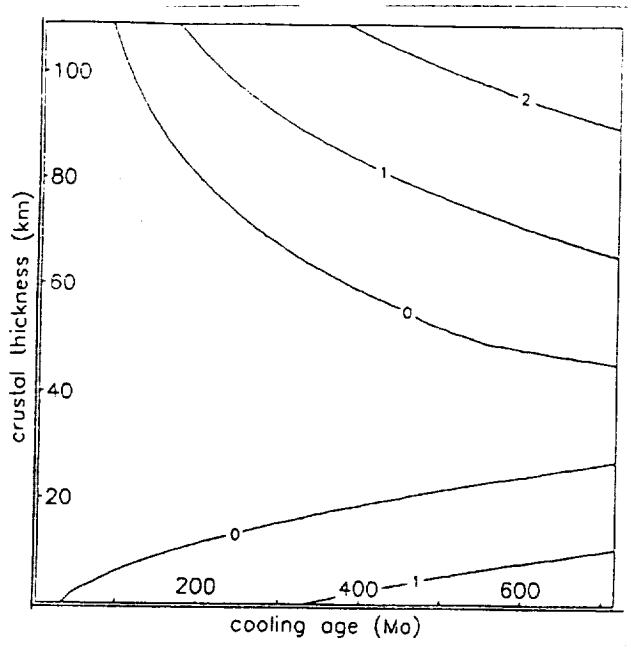

Figure 5 (left). Largest possible interplate shear stress (in kilobars) that would still permit initiation of subduction, plotted as a function of crustal thickness and cooling age. For points lying to the left of the zero contour, the driving stress (primarily gravity spreading stress) is insufficient to prevent the immediate or eventual superiority of the resistive elastic bending stress even in the case of free slip. Crustal thicknesses from about 25 to 50 km again prove to be the most difficult to subduct.

BASALTIC CRUST GENERATION ON VENUS

R.J. Phillips and R.E. Grimm, Department of Geological Sciences, Southern Methodist University, Dallas, TX 75275.

Introduction. Terrestrial basaltic magmas are generated at divergent plate margins by pressure-release partial melting of ascending mantle material. A by-product of this melting is a relatively magnesium-rich residuum due to the preferential fractionation of iron into basaltic magmas. This residuum is more buoyant than its parent undepleted mantle [1,2]. In the Earth's ocean basins, the residuum is attached to the mechanical plate and, along with newly-created basaltic crust, is moved away from sites of partial melting. Significant crustal generation is ongoing because fresh material is continuously drawn to high levels (i.e., low pressure regions) of the mantle.

On Venus, two factors may inhibit crustal generation. If the lithosphere is unable to subduct and therefore unable to drive significant horizontal motion and lithospheric divergence, easy access to the surface will be lost. Furthermore, the residuum generated by partial melting may accumulate in the upper mantle, where it is buoyantly stable. If the ascending mantle cannot penetrate this residuum, then the melting process will eventually shut down as the residuum (and basaltic crust) limit the minimum depth to which mantle can rise. To first order, convection will not penetrate the residuum if the chemical density anomaly of the residuum exceeds the thermal density anomaly of the ascending mantle material. Here we show how this process works and apply it to Venus.

Method. We have combined a global parameterized convection calculation [3] with solutions to the differential equation for the mass fraction of partial melting as a function of temperature and pressure [4,5]. The lateral extent of partial melting is governed by the horizontal velocity of an upper boundary layer. The velocity is obtained by equating the heat delivered by convection to the heat lost by thermal diffusion out of the boundary layer, assuming unit aspect ratio to the convection cell. The convecting temperature of the mantle is obtained by integrating the energy conservation equation with time, and the upper-mantle temperature is obtained by extrapolating upward along an adiabat. The system was calibrated by finding the value of A in $\mu = \mu_o \exp(A/T)$ for the Earth such that at t = 4.6 Ga, the heat flux is 84 mW/m^2 and the upper-mantle temperature is 1300JC. The value obtained for A is 65,000 K with μ_o = 165 m^{2}s^{-1}. For Venus, 0.6 Ma passes before basaltic crust is allowed to accumulate, supposing that it would be remixed into the mantle before that. The crustal accumulation will be only modestly diminished if the starting point is moved forward in time. At each 5 Ma increment, the amount of accumulated crust and residuum is calculated, heat sources are preferentially removed from the mantle, and the outer radius of the convecting mantle is reset according to the crust and residuum thicknesses. We assume that heat can diffuse from the crust at the same rate it is delivered, so that the temperature T_L at the top of the boundary layer does not build up. A simple diffusion calculation shows that this is true to first order, and, in any event, the crustal accumulation is insensitive to T_L (Figure 1).

Results. Figure 1 shows the results of our calculations for Venus with varying values of T_L. Each calculation was run until the change in crustal thickness in a 5-Ma increment was less than 10 m. As expected, the process

shuts down, here at about 16 km of crust and in about 100 Ma. The temperature T_L affects the rate of crustal buildup but has only a small influence on the asymptotic value. Higher temperatures lead to faster buildup.

In Figure 1 it was assumed the mantle did not penetrate the residuum at all. In Figure 2, we compare for T_L = 1300 K, the effects of 0%, 25%, and 50% penetration. That is, this is the fraction of residuum that is entrained in the convective flow and does not stabilize at the top of the mantle. For 50% assimilation, a 40-km-thick crust accumulates in 300 Ma.

Discussion. The residuum density can be calculated from the mass fraction of partial melt [6]. The magnitude of the average density contrast is at a maximum early in the melting sequence, when most of the magma is being generated. For T_L = 1300 K, the average residuum density contrast $\Delta\rho_c$ for the first 10 of 16 km is 16 kg m^{-3}. For a coefficient of thermal expansion $\alpha = 3 \times 10^{-5}$ K^{-1}, this corresponds to a thermal density contrast of about 160 K. In an internally-heated mantle, the temperature contrast of ascending material might be less than 100 K. Whole-mantle plumes might have temperature anomalies in excess of 300 K [7], reflecting the hot boundary layer at the core-mantle interface. Thus in the calculations here, plumes would penetrate the residuum, but possibly not the upper part if the residuum is stably stratified. On Earth, hot rising mantle plumes are predicted to generate large amounts of basalt [8]. Our calculations show that increasing the upper-mantle temperature from the mean convecting temperature (as might be expected in a plume) will not have strong effect on the final crustal thickness: with higher temperatures both thicker crust and thicker residuum will be generated, leading to a shutdown. For example, a 200J increase in upper-mantle temperature leads to a crustal thickness of 23 kilometers for T_L = 1300 K and a 300J difference will actually decrease the final crustal thickness. We have not taken into account the role of melting in removing heat from the boundary layer. This effect would lower the horizontal velocity of the layer and decrease the lateral extent of melt, which will decrease the average crustal thickness. The residuum density contrast estimates may increase when this effect is considered.

Conclusions. Because of various assumptions and approximations used at this point, the absolute magnitudes of the numbers in Figure 1 and 2 should not be taken too seriously. The results do show, however, the self-limiting nature in basaltic crustal generation on a planet without seafloor spreading. Clearly, the most sensitive parameter here is the fraction of assimilation of residuum into the convecting mantle. Future work will include a quantitative look at penetration of the residuum by convection, as well as the stability of the residuum.

References. [1] O'Hara, M.J., *Nature, 253*, 708, 1975; [2] Jordan, T.H., in Boyd *et al.*, (eds.), *The Mantle Sample: Inclusions in Kimberlites and Other Volcanics*, AGU, 1, 1979; [3] Phillips, R.J., and M.C. Malin, in Hunten *et al.* (eds.), *Venus*, 159, 1983; [4] McKenzie, D.P., *J. Petrol., 25*, 713, 1984; [5] McKenzie D., and M.J. Bickle, *J. Petrol., 29*, 625, 1988; [6] Finnerty, A.A. *et al.*, *JGR, 93*, 10225, 1988; [7] Richards, M.A., and B.H. Hager, *JGR, 93*, 7690, 1988; [8] White R., and D. McKenzie, *JGR, 94*, 7685, 1989.

Figure 1

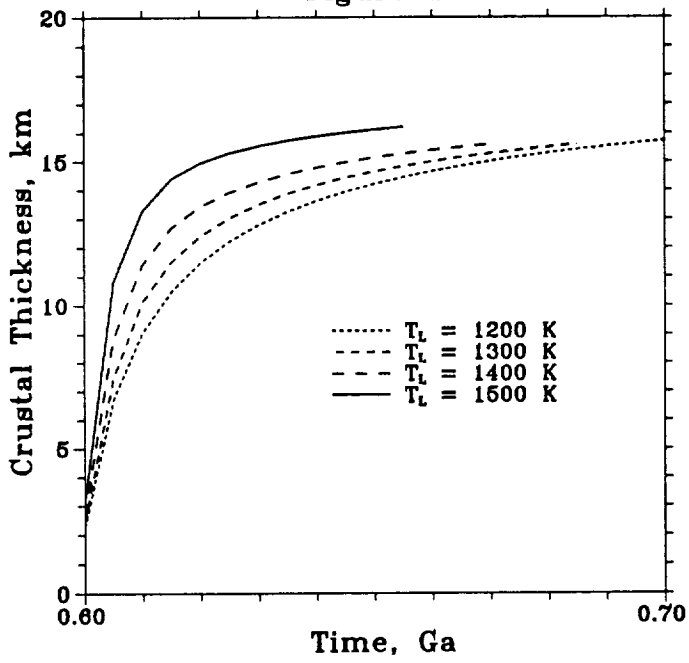

Figure 2

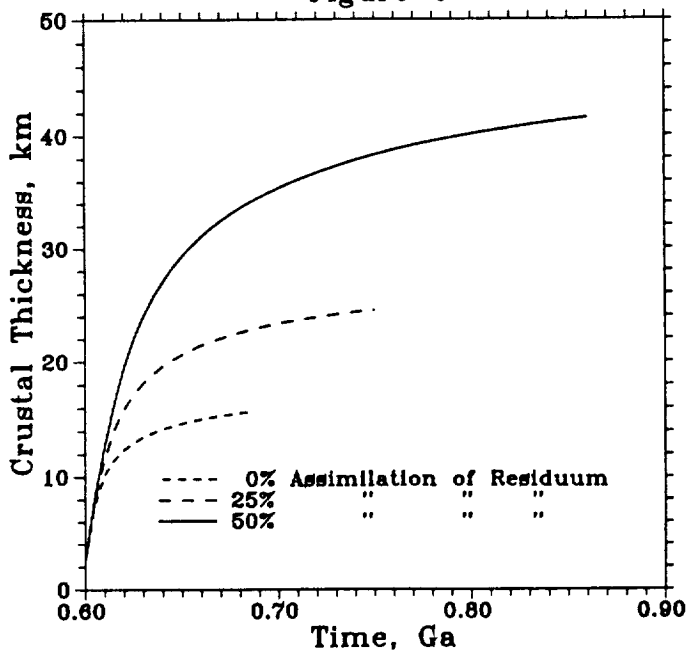

GLOBAL MANTLE CONVECTION PLANFORM PATTERN FOR VENUS

R.R. Herrick, and R.J. Phillips, Department of Geological Sciences, Southern Methodist University, Dallas, TX 75275

Introduction. Recent work [1,2] has suggested that, for a fairly robust set of conditions, the pattern of mantle convection for an Earth-sized planet should be that of isolated upwellings amidst an interconnected network of sheetlike downwellings. Because it has been argued that long-wavelength topography on Venus reflects, at least in part, the effects of mantle convection [3], this planet may be an ideal place to examine this concept despite the lack of seismic information. We have tested this idea by constructing a model that assumes that the Venusian long-wavelength topography and gravitational potential are caused by density anomalies due to convection and near-surface effects. Near-surface effects may include crustal thickness variations, lithospheric density or temperature anomalies, etc., but will hereafter be lumped into the term "crustal thickening". At the long wavelengths used, near-surface effects cannot be resolved from one another with the available data. Using inversion techniques, we have transformed spherical harmonic models of the Venusian topography [4] and gravitational potential [5] into global maps of crustal thickening and the mantle convection pattern. These maps can be used further to identify large-scale topographic features that are dynamically maintained.

Procedure. Crustal thickening can be represented by variations in surface density on a spherical shell located at the mean depth of the base of the crust (assumed to be 15 km below mean planetary radius [6]). Assuming Airy isostasy, a simple linear relationship exists between the spherical harmonic coefficients (SHCs) of the crustal shell and those of the resulting topography and potential [7]. For the potential this relationship is different for each spherical harmonic degree. A crustal density of 2900 kg/m^3 was assumed.

Most of the contribution to dynamically supported topography and geoid signals comes from density structure due to mantle temperature anomalies associated with the upper boundary layer of convection [8]. Thus we represent mantle contribution to the geoid and topography by a second shell of varying surface density placed at an appropriate depth in the upper mantle. In the calculations a depth of 200 km was used. We follow previous work [9,10] that has solved simplified forms of the Navier-Stokes equations to develop equations for kernels that relate the SHCs of the shell to the surface gravitational potential and the geoid to topography ratio. The model assumes that the mantle is a Newtonian, incompressible viscous fluid. The core is assumed to be inviscid and a free-slip condition is used at the core-mantle boundary. The core was assigned a radius of 3300 km and a density of 9900 kg/m^3. The mantle was assumed to be isoviscous with a viscosity of 1.0×10^{21} Pa s and was assigned a density of 4400 kg/m^3. A value of 8.87 m/s^2 was used for gravitational acceleration throughout the mantle. The calculated kernels were used to develop a linear relationship between the SHCs of the mantle shell and the SHCs of the topography and potential field. This relationship is different for each spherical harmonic degree.

The result is that for each spherical harmonic degree a 2 x 2 matrix relates the two SHCs of the surface density shells to the SHCs of the topographic and potential fields. We inverted each of these matrices and multiplied by the SHCs of the topography and gravitational potential to calculate the SHCs for the crus-

tal thickening and mantle convection shells. A 5 x 5 degree grid spacing was used to produce the global maps to degree and order 10 of crustal thickening and upper mantle density pattern shown in Figures 1 and 2. The mantle convection shell was then forward transformed to produce SHCs for only the dynamic contribution to the topographic field. This is shown in Figure 3 with the total topography to degree and order 10 shown in Figure 4 for comparison. The crustal thickening contribution to topography can be found by dividing the values in Figure 1 by the negative of the crustal density.

Discussion. The mantle flow field has a pattern of isolated upwellings (unshaded) amidst an interconnected network of downwellings in reasonably good agreement with the predictions of [1] and [2]. Figure 3 shows that the only large-scale, high-elevation features that are predicted to be primarily dynamically supported are Thetis (-20N, 130E), Atla (0N, 195E) and Beta (30N, 280E) Regiones. Figure 1 shows that Ovda Regio (-5N, 90E) and Ishtar Terra (70N, 0E), for example, appear to be supported primarily by near-surface effects.

References. [1] Bercovici, D., *et al.*, 1989, *Science, 244*, 950-955. [2] Bercovici, D., *et al.*, 1989, *GRL, 16*, 617-620. [3] Phillips, R.J., and M. Malin, 1984, *Ann. Rev. Earth Planet. Sci., 12*, 411-443. [4] Bills, B., *et al.*, 1987, *JGR, 92*, 10,335-10,351. [5] Bills, B., and M. Kobrick, 1985, *JGR, 90*, 827-836. [6] Grimm, R., and S. Solomon, 1988, *JGR, 93*, 11,911-11,929. [7] Phillips, R.J., and K. Lambeck, 1980, *Rev. Geophys. Space Phys., 18*, 27-76. [8] Parsons, B., and S. Daly, 1983, *JGR, 88*, 1129-1144. [9] Richards, M. and B. Hager, 1984, *JGR, 89*, 5987-6002. [10] Hager, B., and R. O'Connell, 1981, *JGR, 86*, 4843-4867.

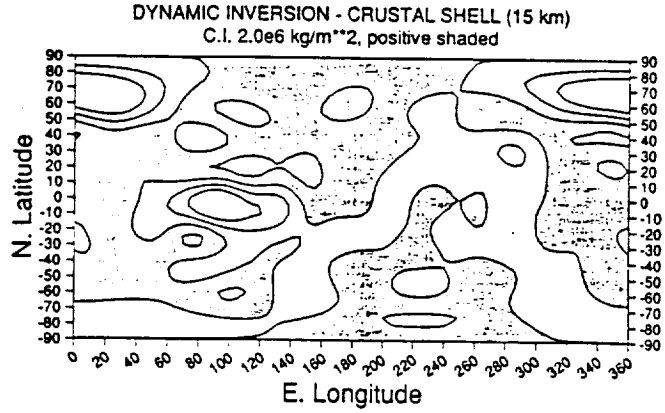

Figure 1

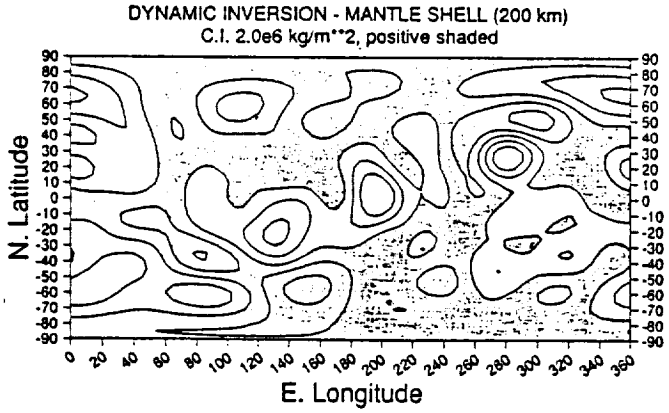

Figure 2

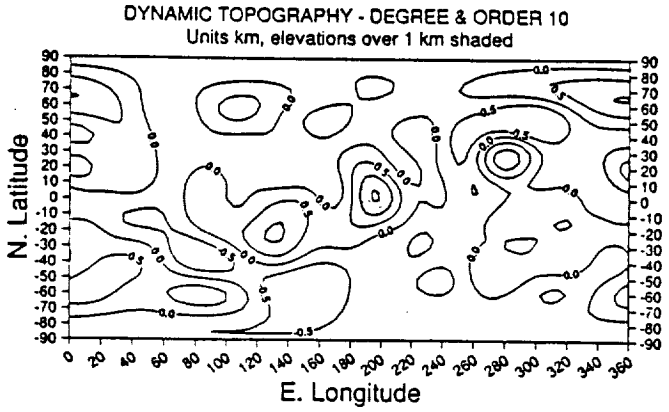

Figure 3

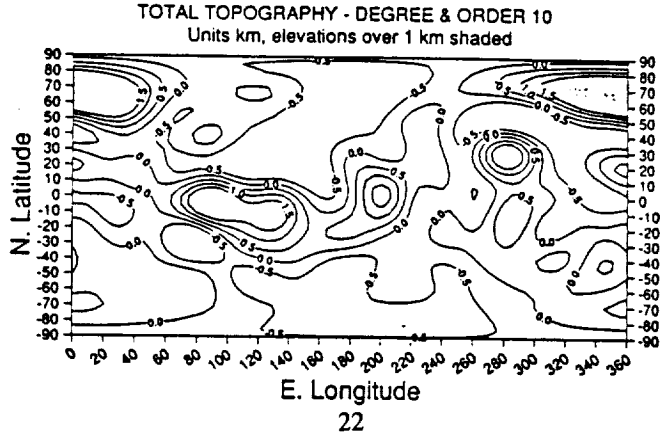

Figure 4

STRESS ANALYSIS OF TELLUS REGIO, VENUS, BASED ON PIONEER VENUS ALTIMETRY AND GRAVITY DATA AND COMPARISON WITH VENERA 15/16 RADAR IMAGES.

David R. Williams and Ronald Greeley, *Department of Geology, Arizona State University, Tempe, AZ 85287*

The Tellus Regio highland offers a unique opportunity to model the lithospheric and sublithospheric structure on Venus. Because the region is covered by the Venera 15/16 radar images (1,2) as well as the Pioneer Venus (PV) altimetry (3) and gravity (4,5), a comparison among these data can be made. Furthermore, Tellus Regio is located at the southern margin of the Venera 15/16 coverage, where the PV altitude was still low enough (300-600 km) to allow for reasonably good resolution gravity measurements. The comparison is made using a lithospheric model developed for global stress calculations by Banerdt (6), and modified to incorporate regional stresses (7). The stress distributions estimated from this model are then compared to the surface morphology revealed in the Venera 15/16 radar images to constrain the relevant parameters.

The first step involves a radargeologic interpretation of Tellus Regio. The highland area consists generally of a gently sloping dome about 1500 km in diameter. A geologic sketch map has been produced from this image, showing 6 major units (see figure). The dome field unit (df) at the western edge of the map is characterized by small domical hills within smooth plains. The relatively featureless smooth plains unit (ps) is in the southeast and southwest map area. Embayment relations indicate the smooth plains to be relatively young. Complex plains (cp), found to the north, are similar to the smooth plains except for a more mottled appearance. This unit contains irregular craterforms, some with associated flowlike features, interpreted as possible eruptive centers. The highland area of the map is dominated by the tesserae unit (t). This unit is characterized by series of parallel fractures which have disrupted the surface in a blocky, "parquet" terrain. The map shows the major structural trends within the tesserae, as well as Elliot Patera, an irregular craterform mapped as a volcano (2). A ridge belt unit (rb) is observed in the southwest corner of the map. A number of scarps cut across the tesserae on its eastern and western margins, and appear to have formed subsequent to the tesserae terrain. They are inferred to result from intrustion of material along major fracture systems following deformation of the tesserae terrain. The complex terrain (dc), occuring in the northwestern part of the map, is similar to the complex plains with the addition of "cobweb"-like radar-bright features. Based on emplacement, cross-cutting and superposition, it appears the oldest unit is the complex terrain, followed in age by the complex plains, tesserae terrain, ridge belts, smooth plains, and dome terrain. The final stage of tectonic deformation appears to consist of large scale extension, forming the ridge belts.

Stress models are calculated for comparison with the sketch map. The stress distribution is calculated in two parts, a global, long-wavelength stress (harmonic degrees $l \leq 7$) and a regional, shorter wavelength stress ($7 \leq l \leq 30$). Harmonic degrees greater than 30 are beyond the resolution of the available gravity data. The global stresses are solved for using the two-level compensation model of Banerdt (6). The lithosphere is assumed to be a thin, elastic spherical shell, and toroidal stresses are ignored. The harmonic coefficients for degrees 1-7 of PV topography (8) and equipotential anomaly (9) are used to calculate the net vertical load, equipotential anomaly at the crust-mantle boundary, crustal thickness anomaly, mantle density anomaly, and scalar load potential. The lithospheric flexure w is assumed to be related to the topography, H, by a degree of compensation constant, k: w=kH. This constant is one of the free parameters in the equation which can

be varied to try and fit the observed stress patterns. The other free parameters are the crustal thickness, c, lithospheric thickness, L, and depth of the mantle to which density anomalies support surface stresses, M. For given values of these parameters, a global stress distribution is obtained.

The regional stresses are calculated in a similar manner, except that the equations have been recast in terms of two-dimensional Fourier coefficients. The coefficients of the topography are calculated from the PV altimetry. The equipotential anomaly coefficients are obtained from an inversion of the PV line-of-sight (LOS) gravity data. The long and short wavelength coefficients are filtered out, and the degree 7-30 equivalent coefficients are calculated in a similar manner to the global solutions. Regional stress distributions are then obtained for values of c, L, M, and k. For a given set of values, the regional and global stress solutions are combined, giving a stress distribution for Tellus Regio for harmonic degrees 1-30. Varying the free parameters individually has shown that the crustal thickness has negligible effect on the stress distribution for Tellus Regio. Unless the mantle support is concentrated close to the surface, the depth of the mantle support also has little effect. The assumed lithospheric thickness and degree of compensation do have a large effect on the model stress distribution, however, and are therefore the best constrained parameters.

Comparison of model stress distributions with the geologic sketch map shows that the best fit occurs for a degree of compensation between 0 and 0.5 (i.e. the lithospheric flexure is from zero to half the topographic relief) and a lithospheric thickness greater than 5 km. The figure shows the stress distribution for k = 0.3 and L = 20 km, overlain on the geologic sketch map. The arrows show the deviatoric principal tensional and compressional stress directions. Where only one arrow is shown, the conjugate stress is vertical. Note the good agreement between the tensional stresses and the ridge belts and faults in the tesserae terrain, The highland area is underlain by anomalously thick crust and dense mantle, and the stresses are of the order of 20 to 30 MPa. The compensation is nearly isostatic, and is concentrated close to the surface.

Bearing in mind the limitations of the data and the assumption that the most recent features observed at Tellus Regio reflect the present day stress distribution, the following interpretation is possible. The denser mantle beneath Tellus Regio represents a cooler, downwelling mantle region. The horizontal mantle flow towards the stagnation point above this downwelling has entrained hot mobile crustal material, which is maintained in this region. The buoyancy of the crustal material caused upwarp and extension, as well as intrusive activity, inflation of the lithosphere, and surface volcanism. This interpretation can account for the observed surface features, inferred stress distribution, and calculated dense mantle and thick crust below the highland region. Note that this area is different from other regions of Venus, and so this interpretation does not necessarily apply to all highland areas.

References: (1) Barsukov et al., 1986, *J. Geophys. Res.*, 91, D399. (2) Basilevski et al., 1986, *J. Geophys. Res.*, 91, D373. (3) Masursky et al.,1980, *J. Geophys. Res.*, 85, 8232. (4) Sjogren et al., 1980, *J. Geophys. Res.*, 85, 8295. (5) Sjogren et al., 1983, *J. Geophys. Res.*, 88, 1119. (6) Banerdt, 1986, *J. Geophys. Res.*, 91, 403. (7) Williams and Greeley, 1990, submitted to *J. Geophys. Res.*. (8) Bills and Kobrick, 1985, *J. Geophys. Res.*, 90, 827. (9) Mottinger et al., 1985, *J. Geophys. Res.*, 90, C739.

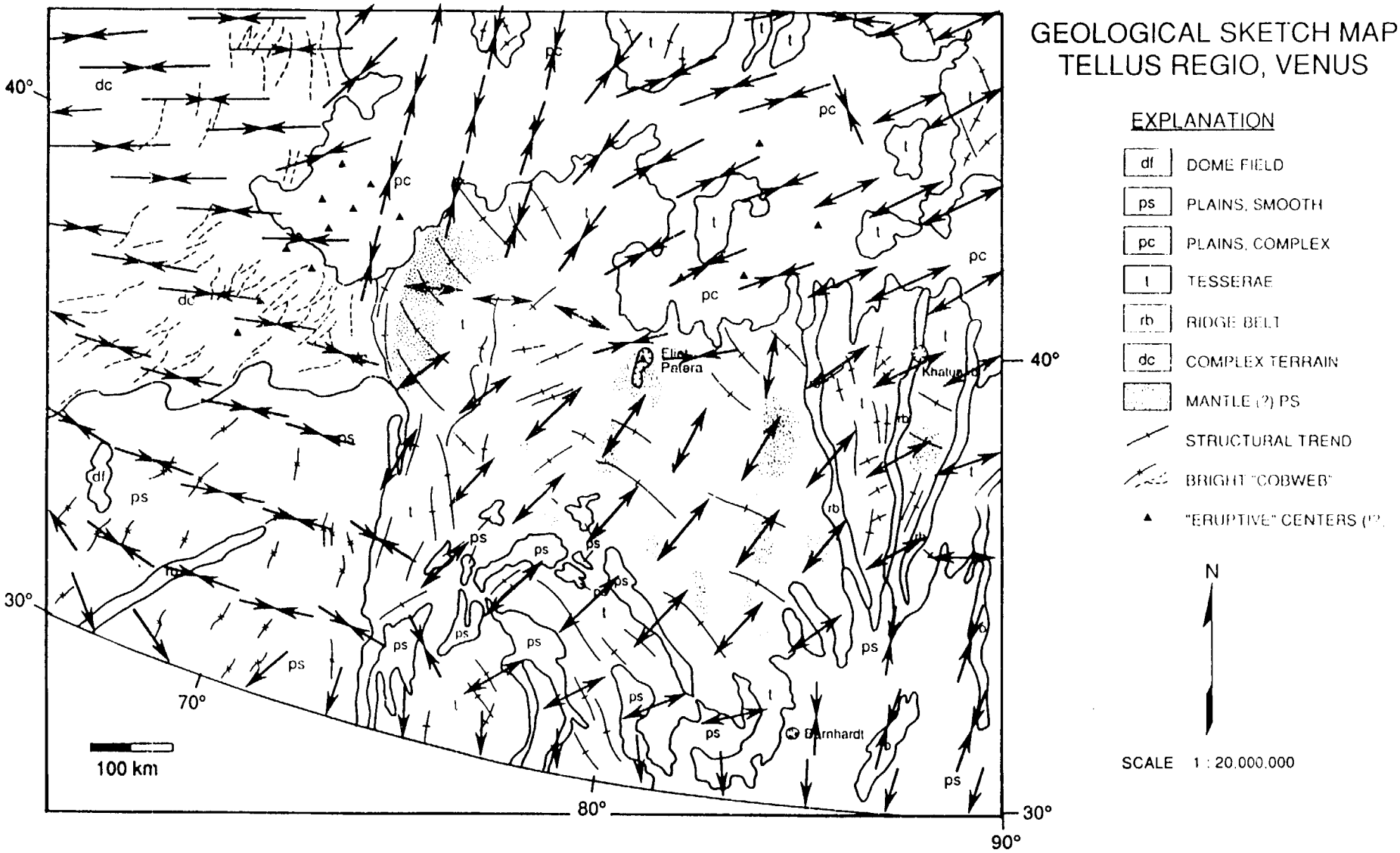
GEOLOGICAL SKETCH MAP
TELLUS REGIO, VENUS
EXPLANATION
df DOME FIELD
ps PLAINS, SMOOTH
pc PLAINS, COMPLEX
t TESSERAE
rb RIDGE BELT
dc COMPLEX TERRAIN
MANTLE (?) PS
STRUCTURAL TREND
BRIGHT "COBWEB"
"ERUPTIVE" CENTERS (?)
N
SCALE 1 : 20,000,000
40°
30°
70°
80°
90°
100 km
Eli
Patera
Khalu
Barnhardt

GRAVITY ANOMALY CONSTRAINTS ON THE GEODYNAMICS OF LAKSHMI PLANUM, VENUS

Robert E. Grimm and Roger J. Phillips, Department of Geological Sciences, Southern Methodist University, Dallas, TX 75275.

Introduction. Among the highland regions on Venus, Ishtar Terra, in particular the Lakshmi Planum region, is unique and may play a key role in understanding the geology of Venus. Although Lakshmi contains abundant volcanic features as do other highlands, the mountainous banded terrain bordering Lakshmi sets it apart from other regions. Gravity data can provide constraints on the internal processes responsible for these differences. We calculate the geoid anomaly at constant altitude over Lakshmi, and then test these data, together with the observed elevation, regional strain pattern, and inferred age against geodynamic models.

Gravity Inversion. The area under study here is approximately 55J - 70J N, 310JE - 15JE. We use ORBSIM [1] and a linearized inversion technique to calculate a set of discrete surface masses that satisfy the observed line-of-sight accelerations. The geoid anomaly at uniform altitude z_0 may be evaluated from this mass distribution. The geoid-to-topography ratio (GTR) was calculated in the spatial domain by linear regression and the long-wavelength apparent depth of compensation (ADC) was found from ADC = $(GTR)g/2\pi G\rho_c$.

The ADC as a function of z_0 was also calculated for Bell Regio, a smaller but representative "hotspot" of Venus, using a similar point-mass inversion [2]. The ADC for Bell varies from 130 km at z_0 = 250 km to 270 km at z_0 = 700 km. This strong change with altitude indicates that longer-wavelength components are compensated at increasingly greater depths and suggests that the thickness of the compensation zone is at least several hundred kilometers. The ADC for Lakshmi, however, is smaller and much more constant, 130 +/- 10 km for z_0 = 500 to 1400 km. Since the formal standard errors are small (given 1 mgal LOS measurement errors), it is difficult to reject the hypothesis that Lakshmi is indeed supported at nearly a single depth.

Geodynamic Models. We consider three broad hypotheses for the origin of Lakshmi Planum, but these models are not entirely mutually exclusive. Under *local mantle upwelling* [3,4], Lakshmi is the surface expression of a hotspot which produces topography both dynamically and by volcanic construction. This model holds that the mountain belts form as a result of incipient downward mantle return flow. Under *local mantle downwelling* [5,6], cold sinking mantle beneath Lakshmi induces shear tractions on the crust, which thicken and elevate it; volcanism is the result of basal crustal remelting. Lithospheric delamination is related to this hypothesis, having contributions to topography from both sinker-induced shear thickening and thermal buoyancy of hot mantle replacing the lithosphere. The exact mechanism for formation of mountain belts remains to be tested. A third scenario, *regional compression*, may be distinguished from the second in that Lakshmi is simply a locus of strain accumulation and crustal thickening from regional stress fields; neither broad downward mantle flow nor lithospheric subduction need occur. The formation of mountain belts and uplift of the plateau have been considered analogous to the Himalayas and Tibet [7,8]. The principal question for such a model is the source and magnitude of stress. Such forces could include "slab pull" (in this case probably beneath Lakshmi and hence resembling scenario 2),

"ridge push" from extinct thermally elevated terrain, or shear tractions exerted by mantle flow. Since global lithospheric divergence and consumption is likely difficult to develop on Venus, it is possible that limited horizontal motions are driven by regional stresses until choked off. Localization of compressive forces could be due to structural or thermal heterogeneities in the crust or lithosphere, or due to variations in the velocity gradients of mantle flow.

Model Calculations. An endmember hypothesis, applicable to any of the three principal models, is that the plateau relief is entirely supported by *thickened crust*, either due to volcanic construction or crustal shortening. This extreme corresponds to simple Airy isostasy, and so the ADC represents the crustal thickness about which observed deviations are measured. A crustal thickness of 130-160 km beneath Lakshmi Planum and 100-130 km in the rolling plains is necessary. Such a value is unlikely given prior estimates of 10-30 km crustal thicknesses in the plains [9-11], analysis of long-term creep stability [12], and the transition to denser eclogite at ~ 70 km depth [13]. Isostatic support by a crust of *distinct composition* (perhaps more felsic) may also be rejected as a Pratt mechanism requires thicknesses > 250 km. *Lithospheric thinning or delamination* will yield ADCs of only about 50 km. Moreover, only about 1.5 km of relief can be achieved by this mechanism [14]; if the remainder is accomplished by Airy-compensated volcanism, the net ADC will be even shallower. Supplemental dynamic compensation is required.

We extend a simple two-dimensional halfspace formulation [11] to model the dynamic effect of a cosine-bell-shaped surface mass anomaly at depth. A suite of exploratory calculations uses three constant-viscosity layers: crust/lithosphere to 20 km, upper mantle to 700 km, and lower mantle. The uppermost layer may have a distinct density. We find that either upwelling or downwelling mantle may produce the geoid and topography observed for Lakshmi Planum, but under very different conditions. An *upwelling* (centroid 160 km, buoyancy stress 100 MPa) is acceptable if the crust does not strongly couple with the flow (i.e., its density contrast is ignored) and if the mantle is not layered. A deeply-seated *downwelling* (400-600 km, buoyancy stress > 200 MPa) can give the same effect, provided that the crust can be shear-thickened by mantle flow and that a more viscous lower mantle exists. The ADC does not have as narrow a mode as a function of z_0 as in the upwelling model. Incorporation of the effective viscosities of diabase and olivine [11] further suggests that uplift above a plume will be rapid, but that the thermal gradient must be high (~20 K/km) over the sinker so that substantial uplift will be attained in 0.1-1.0 b.y. Neither model, however, yields the surface stress distribution necessary to form the banded terrain as a primary consequence of the uplift: Azimuthal extension is predicted to a radius of 400-1200 km, followed by a zone of strike-slip deformation. Radial compression does not occur until distances > 1300 km, i.e., in the surrounding plains. *Regional compression* can evidently deform the margin of Lakshmi into mountain belts, but its geoid signature is problematic. There is no evidence to date for a substantial gravity anomaly over Tibet, which is consistent with simple peripheral compression and isostatic crustal thickening [15]. If underthrust lithosphere is invoked to provide the large geoid anomaly over Lakshmi, the dynamic flow induced by the slab must be reckoned with.

Discussion. A more complex model than those analyzed in detail here is needed to produce both the correct stress and ADC. Because of the narrow range of ADCs, we favor upwelling models in which a mantle plume has flattened out and the surface has been subsequently deformed. Lakshmi must be distinguished from other paradigm hotspots on Venus by different environmen-

tal conditions (lithospheric heterogeneity?) or by being in a different stage of hotspot evolution. In this latter case, Lakshmi may represent an older hotspot; its crust may be somewhat thicker and its lithosphere weakened due to a protracted thermal history. An anomalously weak Lakshmi Planum could serve as a "strain magnet" which regional stress fields are able to deform.

References. [1] R.J. Phillips et al., *JGR, 83*, 5455, 1978; [2] S. Smrekar and R.J. Phillips, *LPSC XX*, 1028, 1989; [3] A.A. Pronin, *Geotectonics, 20*, 271, 1986; [4] A.T. Basilevsky, *Geotectonics, 20*, 282, 1986; [5] D.L. Bindschadler and E.M. Parmentier, *LPSC XX, 78*, 1989; [6] W.S. Kiefer and B.H. Hager, *LPSC XX*, 529, 1989; [7] L.S. Crumpler et al., *Geology, 14*, 1031, 1986; [8] J.W. Head, *LPSC XVII*, 323, 1986; [9] M.T. Zuber, *Proc. LPSC 17th, JGR, 92*, E541, 1987; [10] W.B. Banerdt and M.P. Golombek, *JGR, 93*, 4759, 1988; [11] R.E. Grimm and S.C. Solomon, *JGR, 93*, 11911, 1988; [12] R.J. Phillips et al., *Science, 212*, 879, 1981; [13] W.M. Kaula, *Science*, in press, 1990; [14] W.M. Kaula and R.J. Phillips, *GRL, 8*, 1187, 1981; [15] P. Molnar and P. Tapponier, *JGR, 83*, 5361, 1978.

THERMAL EVOLUTION OF VENUS MOUNTAIN BELTS. Noriyuki Namiki and Sean C. Solomon, Department of Earth, Atmospheric, and Planetary Sciences, Massachusetts Institute of Technology, Cambridge, MA 02139.

Introduction. The linear moutain belts of Ishtar Terra were recognized from *Pioneer Venus* topography to be distinctive landforms not found on the smaller terrestrial planets [1]. Arecibo radar images showed that much of Akna, Freyja, and Maxwell Montes consist of banded terrain [2] indicative of large-scale compressive deformation [3]. The improved resolution of the imaging and topographic data from *Venera 15* and *16* [4,5] led to better definition of the deformational features and initial hypotheses regarding the origin and evolution of the mountain belts [6,7]. From an analysis of radar images and topographic data from the Freyja Montes, Head [8] proposed that the mountain belt formed as a result of a sequence of large-scale underthrusts of the lithosphere of the North Polar Plains beneath Ishtar Terra.

We are developing thermal models for the evolution of the mountain ranges of Ishtar Terra, with initial focus on Freyja Montes. There are several motivations for such models. If Freyja Montes formed in response to large-scale horizontal convergence by the development of major underthrusts [8], then whether the imbricated blocks between sequential thrust zones originated as layers of underthrust lithosphere or only as upper crustal layers stripped off from the lower lithosphere at a weak ductile zone in the middle to lower crust is closely tied to the mechanical properties of the thrust zone and their dependence on the time-dependent thermal evolution of crust and mantle in the region. The thermal structure of the convergence zone is also intimately tied to the origin and nature of volcanism in Ishtar Terra. Volcanic activity has been widespread on Lakshmi Planum [1,4]. The sequence of tectonic and volcanic events that occurred in the region [7,9] suggest that the volcanism may be at least partly related to the heating and partial remelting of a crustal layer thickened by convergence and underthrusting.

Approach. We adapt the numerical method of Bird and others [10,11] to test quantitatively this lithospheric convergence hypothesis. We solve the two dimensional heat equation

$$\rho C_P \frac{\partial T}{\partial t} = \nabla (k \nabla T) + A$$

where T is temperature, t is time, ρ is density, C_P is specific heat, k is thermal conductivity, and A is heat production. The kinematics of convergence and underthrusting are specified *a priori* (Fig. 1), and this equation is solved by a finite difference technique.

Model Assumptions and Parameter Ranges. We assume a geometry as indicated in Fig. 1 and a constant surface temperature T_s. Frictional heating along the brittle portion of the main boundary thrust is included as constant heat flux $v\tau$, where v is the convergence rate and τ is the shear stress; adiabatic heating of underthrusting plate is neglected. The properties of crust and mantle (Table 1) are assumed to be those of basalt and peridotite on the basis of the Venera lander results [12] and of the assumed gross similarity in bulk composition of Venus and Earth. The base of the lithosphere is taken to be the point at which the temperature reaches 0.9 T_m, where T_m is the melting temperature of peridotite. The asthenosphere is assumed to be convecting vigorously, so that an adiabatic gradient applies. The temperature distribution in the asthenosphere is assumed to be unaffected by underthrusting.

Obvious key parameters are the crustal thickness h_C, surface heat flux q_S, crustal heat production A_C, τ, v, and the geometry and evolution of underthrusting. The ranges of h_C , q_S, and τ are constrained from previous inferences on the thickness of the Venusian elastic lithosphere [13-15]. A_C is calculated from the U, Th, and K contents of surface rock at the Vega 1-2 and Venera 9-10 landing sites [16]. The range of v is determined so that it includes the estimates of divergence rates in the equatorial highlands [17-19]. The dip angle δ of underthrusting is constrained only by terrestrial analogy. The ranges of these variable parameters are summarized in Table 2.

Assessment. Initial models are aimed toward understanding the factors that control the thermal assimilation of any mantle portion of underthrust segments of lithosphere, the development of a weak ductile layer in the middle to lower crust which might provide nucleation zones for new thrust fault systems, and the initiation of partial remelting in the lower crust. Results to date indicate that these processes depend strongly on the thermal structure and crustal thickness of the lithosphere prior to underthrusting and on the convergence rate.

References. [1] H. Musursky et al., *JGR, 85*, 8232, 1980; [2] D.B. Campbell et al., *Science, 221*, 644, 1983; [3] S.C. Solomon and J.W. Head, *JGR, 89*, 6885, 1984; [4] V.L. Barsukov et al., *JGR, 91*, D378, 1986; [5] Yu. N. Alexandrov et al., *Science, 231*, 1271, 1986; [6] L.S. Crumpler et al., *Geology, 14*, 1031, 1986; [7] A.A. Pronin, *Geotectonics, 20*, 271, 1986; [8] J.W. Head, *Geology*, in press, 1990; [9] K.P. Magee and J.W. Head, *LPS, 19*, 713, 1988; [10] P. Bird et al., *JGR, 80*, 4405, 1975; [11] M.N. Toksöz and P. Bird, *Tectonophysics, 41*, 181, 1977; [12] Yu. A. Surkov et al., *JGR, 89*, B393, 1984; [13] M.T. Zuber, *JGR, 92*, E541, 1987; [14] R.E. Grimm and S.C. Solomon, *JGR*, 93, 11911, 1988; [15] S.C. Solomon and J.W. Head, *LPS, 20*, 1032, 1989; [16] Yu. A. Surkov et al., *JGR, 92*, E537, 1987; [17] W.M. Kaula and R.J. Phillips, *GRL, 8*, 1187, 1981; [18] J.W. Head and L.S. Crumpler, *Science, 238*, 1380, 1987; [19] R.E. Grimm and S.C. Solomon, *JGR, 94*, 12103, 1989.

Table 1. Properties of Crust and Mantle

Parameters	Crust	Mantle
density [kg/m^3]	$\rho_c = 2900$	$\rho_m = 3400$
thermal conductivity [W/m-K]	$k_c = 2.0$	$k_m = 3.0$
specific heat [J/mol-K]	$C_{pc} = 700$	$C_{pm} = 850$
heat production [W/kg]	(see Table 2)	$A_m = 1.5 \times 10^{-12}$
melting temperature [K]	1453 + 7.25 P[kbar]	1423 + 12.5 P[kbar]
surface temperature [K]	$T_s = 750$	

Table 2. Ranges of Key Parameters

h_c	5 -100 [km]
q_S	20 - 200 [mW/m^2]
τ	0 - 100 [MPa]
A_c	(15 - 650) x 10^{-12} [W/kg]
v	1 - 100 [mm/yr]
δ	15° - 60°

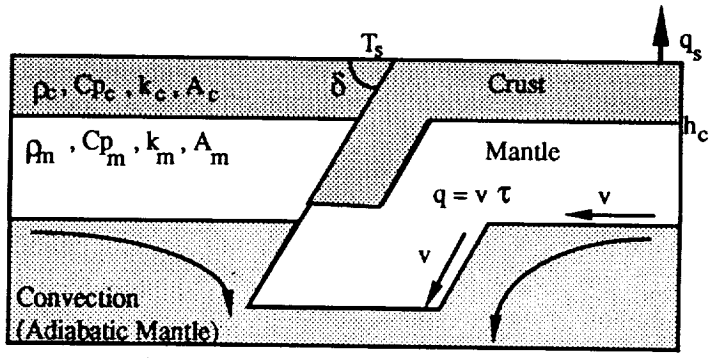

Fig. 1. Schematic of thermal evolution model

TEPEV MONS AND THE ELASTIC LITHOSPHERE OF VENUS: AN ASSESSMENT OF FLEXURE MODELS.

Sean C. Solomon, Dept. of Earth, Atmospheric, and Planetary Sciences, Massachusetts Institute of Technology, Cambridge, MA 02139, and James W. Head, Department of Geological Sciences, Brown University, Providence, RI 02912.

Introduction. An important but unresolved issue for Venus is the magnitude of the heat flux from the interior. The mean heat flux is closely related to the bulk composition and thermal history of the planet [1], while variations in heat flux within and among tectonic provinces - if known - would constrain the formative processes for different tectonic regimes and the mode of interaction of mantle convection with the Venus lithosphere [2]. One indirect measure of heat flux is the thickness T_e of the elastic lithosphere inferred from the flexural response to surface loading, since the lithospheric thickness is limited by the temperature-dependent depth at which ductile behavior dominates brittle behavior at flexural strain rates [3]. Janle et al. [4] first drew attention to an approximately annular depression surrounding the volcano Tepev Mons in Bell Regio. Under the assumption that this depression is of flexural origin, Janle et al. inferred from the radial position and depth of the depression that the elastic lithosphere is 30-100 km thick beneath the volcano.

This range of values for T_e presents a problem. With the assumption that such an elastic lithosphere thickness exceeds the thickness of the crust [5,6], so that the ductile strength of the lower lithosphere is limited by the flow law for dry olivine [3], T_e may be converted to the equivalent depth T_m to the base of the mechanical lithosphere [7] and the average lithospheric thermal gradient [8]. If T_e is 30-100 km and the characteristic flexural strain rate is 10^{-16} s^{-1}, the implied lithospheric thermal gradient is 3-8 K/km [8]. For thermal conductivities of 2.5 and 4 W/m-K for crustal and mantle material, these gradients are equivalent to heat flow in the range 10-27 mW/m^2, values substantially less than the global average of 74 mW/m^2 expected by scaling from Earth [1] and also less than that implied by the thickness of the elastic lithosphere indicated by the flexural response to underthrusting of the North Polar Plains of Venus beneath Freyja Montes [8]. There is no reason to expect that the thermal gradient and heat flow in the Tepev Mons region of Bell Regio should be less than in the North Polar Plains to the north of Freyja Montes, a region near the planetary modal elevation [9]. To the contrary, the broadly elevated rise of Bell Regio, the numerous associated volcanic constructs [10,11], and the large apparent depth of isostatic compensation of relief [12,13] suggest that Bell Regio is a site of mantle upwelling and a heat flux that is greater than the global average or that typical for plains units.

In this paper we reevaluate the topographic and geological evidence relevant to lithospheric flexure beneath Tepev Mons. We reexamine the lithospheric thickness and thermal gradient implied by the flexure hypothesis, and we assess the validity of that hypothesis.

Geological Setting. Venera radar imaging and altimetry indicate that Bell Regio is a broad uplift variously faulted by limited extension and partial subsidence [11,12]. The elevated region includes a number of distinct volcanic centers as well as two exposed areas of tesserae older than the plains units that constitute much of the surface (Fig. 1). Venera 15 and 16 altimetric data provide the highest resolution topographic information for the region, but because southern Bell Regio is near the southern limit of coverage, track-to-track spacing is a rather large 140 km. On only a single Venera 16 orbit was the topography of the central Tepev Mons construct sampled (Fig. 2). The depressions outward of Tepev Mons to the NW, NE, SE and S (Fig. 1) are similarly coarsely sampled in the E-W direction, and most of these

depressions may simply be relative lows between Tepev Mons and high-standing terrain to the east (a broad volcanic center [14]), north (tessera), and west. Whether these depressions form a quasi-continuous annulus and whether this annular deep is of flexural origin [4] are open to question.

Flexural Interpretation of Topography. If we disregard other potential sources of topography exterior to Tepev Mons, then we may test the hypothesis [4] that the depressions arranged approximately circumferential to the construct are signatures of lithospheric flexure. The only reliable topographic profile with which to assess the hypothesis is that obtained along the single orbit that sampled the volcano itself. Even that profile (Fig. 2) indicates that the topography outward of the construct is asymmetric, with a depression indicated on the northern limb but no clear depression to the south.

We have fit the northern limb of the profile in Fig. 2 to a flexural loading model for Tepev Mons. For a circularly symmetric approximation to the volcano profile, we represented the volcano as a stack of coaxial cylinders of density 3.0 g/cm^3. For a range of assumed values for T_e, we calculated the deflection profile [15] outward of the volcano, after scaling the total load to account for subsidence beneath the construct itself [16]. A comparison of these profiles with the observed topographic profile north of Tepev Mons (Fig. 3) indicates that a value for T_e of about 30 ± 10 km provides the best fit. This value is at the lower limit of the range suggested by Janle et al. [4]; in particular, much of their range (e.g., T_e = 50-100 km) can be excluded by Fig. 3. As noted above, T_e = 30 km would imply dT/dz = 8 K/km and a heat flux q = 24-27 mW/m^2 for a crustal thickness in the range 10-20 km [5,6].

Assessment of the Flexural Interpretation. While the topographic profile in Fig. 3 can - as demonstrated - be interpreted in flexural terms, the absence of symmetry in the depression (Fig. 2) and the high-standing tessera to the immediate north of the volcano (Fig. 1,3) cast the

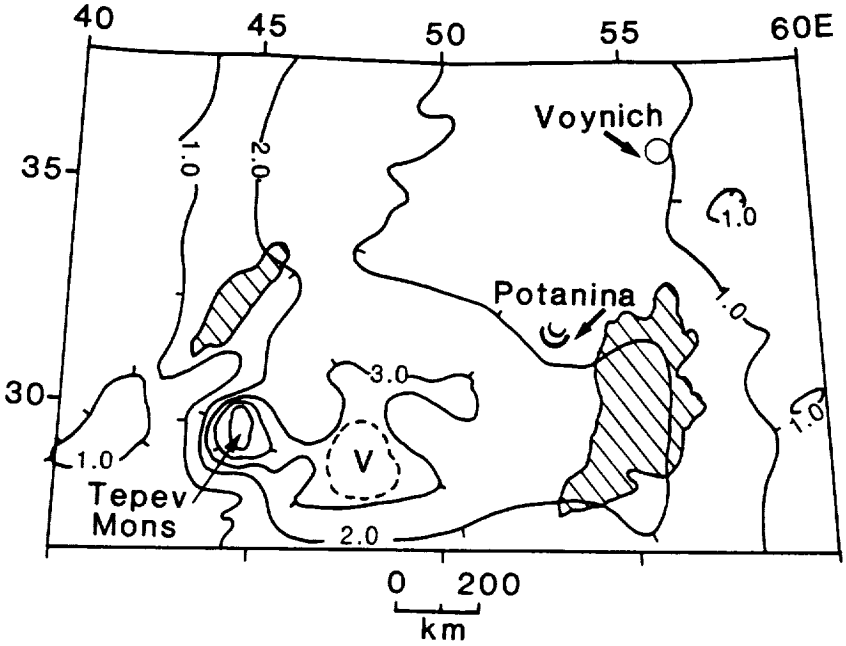

Fig. 1. Simplified topographic map of the Tepev Mons region of southern Bell Regio [12]. Contours are elevation in km with respect of a planetary radius of 6051 km. Shading denotes tesserae. A very broad volcanic construct east of Tepev Mons is indicated by the V. Two impact craters are also noted.

flexural hypothesis into doubt. As noted above, other depressions flanking Tepev Mons can also be interpreted as relative lows between the volcanoes and neighboring high terrain arising from construction or thickened crust and Airy isostasy. We conclude that Tepev Mons is not sufficiently isolated spatially from other nearby highs to derive a meaningful estimate of elastic lithosphere thickness from the topography alone.

References. [1] S.C. Solomon and J.W. Head, *JGR, 87*, 9236, 1982; [2] P. Morgan and R.J. Phillips, *JGR, 88*, 8305, 1983; [3] C. Goetze and B. Evans, *GJRAS, 59*, 463, 1979; [4] P. Janle et al., *Earth Moon Planets, 41*, 127, 1988; [5] M.T. Zuber, *JGR, 92*, E541, 1987; [6] R.E. Grimm and S.C. Solomon, *JGR, 93*, 11911, 1988; [7] M.K. McNutt, *JGR, 89*, 11180, 1984; [8] S.C. Solomon and J.W. Head, *LPS, 20*, 1032, 1989; [9] R.O. Kuz'min et al., *Sol. Syst. Res., 21*, 8, 1987; [10] M.S. Markov et al., *Sol. Syst. Res., 21*, 8, 1987; [11] A.T. Basilevsky and P. Janle, *Sol. Syst. Res., 21*, 672, 1987; [12] P. Janle et al., *Earth Moon Planets, 39*, 251, 1987; [13] S. Smrekar and R. J. Phillips, *LPS, 20*, 1028, 1989; [14] B.A. Campbell and R.C. Kozak, *LPS, 19*, 158, 1988; [15] S.C. Solomon and J.W. Head, *JGR, 84*, 1667, 1979; [16] R.P. Comer et al., *Rev. Geophys., 23*, 61, 1985.

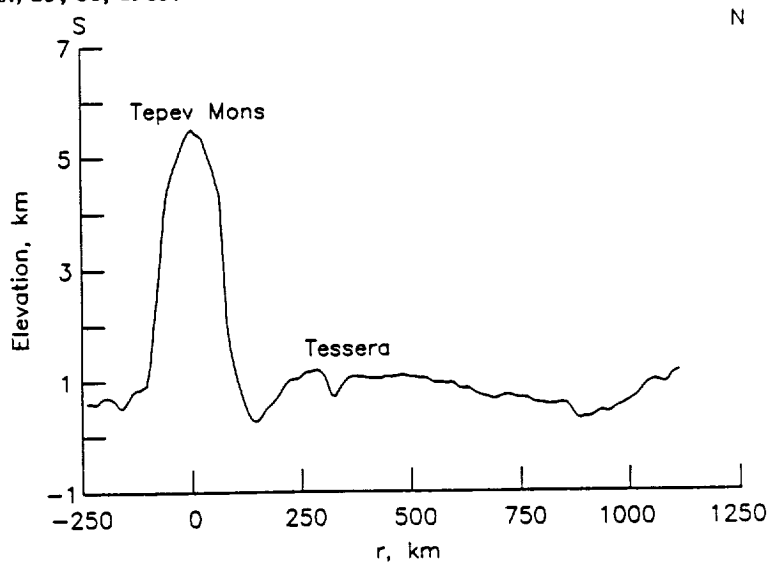

Fig. 2. Venera 16 topographic profile across Tepev Mons (orbit 29). The orbit track passes through the volcano at an azimuth of about N03°W.

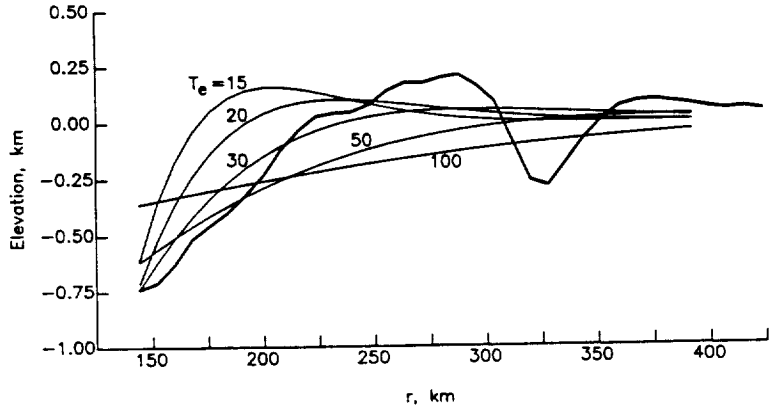

Fig. 3. Fit of the topographic profile from Fig. 2 northward of Tepev Mons to models of lithospheric flexure for a range of values of T_e. The datum for the topography far from the volcano has been set to zero.

GEOID TO TOPOGRAPHY RATIOS FOR SELECTED VENUSIAN FEATURES: IMPLICATIONS FOR COMPENSATION MECHANISMS

S.E. Smrekar, and R.J. Phillips, Department of Geological Sciences, Southern Methodist University, Dallas, TX 75275.

Introduction. Compensation depths and interpreted mechanisms can be used as a guide to the dominant heat loss mechanisms on Venus. Various studies have found apparent compensation depths for seven features on Venus [1-5]. As compensation depth is model dependent, some care must be used in comparing compensation depths from different studies. Spherical harmonic models provide a single, global view of the planet, but group all geological provinces together and have fairly low resolution. Here we use calculated apparent depths of compensation to estimate geoid to topography ratios (GTRs). One advantage of our study is that we look at a large number of features using the same approach, including many regions too small to be resolved with current spherical harmonic models. Using a geoid to topography ratio (GTR) also allows us to easily compare our results both to terrestrial values for oceanic hotspots and plateaus, and to compensation models.

Method. The Geophysical Data Facility (GDF) at the Lunar and Planetary Institute was used to calculate apparent depths of compensation (ADCs) for 11 highland regions: Alpha, Asteria, Bell, Beta, Gula, Phoebe, Sappho, Tellus and Ulfrun Regiones, plus Nokomis Montes and an unnamed feature north of Ulfrun Regio. We refer to it as North Ulfrun Regio. One orbit with the largest, most symmetric anomaly was modeled for each region. We used a topographic density of 3000 kg/m^3. The compensation surface is the negative of the height density product of the topography. The GDF calculates the dynamic gravity anomaly using the ORBSIM program [6]. Using 10 km increments in the ADC, the smallest residual fit to the actual gravity was found for a range of ADCs. We also use ADCs for Atla, Thetis and Ovda Regios from a similar study [2].

Using these ADCs, we estimate their GTRs. As the ADCs were calculated assuming a crustal compensation model, we use the long wavelength, Airy approximation for the GTR. In this approximation, $\Delta N/h = 2\pi G\Delta\rho D/g$, where ΔN is the geoid anomaly, h is the topography, G is the gravitational constant, $\Delta\rho$ is the density contrast, D is the depth of compensation, and g is the gravitational acceleration (8.7 m/s^2 for Venus). Long wavelength thermal compensation models have the same form. The usefulness of this approach is verified by our direct calculation of the GTR at Bell Regio. At Bell Regio we inverted the line of sight gravity data to obtain a vertical gravity map [7]. The least squares fit of geoid to topography yielded a GTR of 19.8, +/- 0.4 m/km. The value found using this approach is 24.6 m/km, which is in reasonable agreement.

Results. The GTRs are plotted against topographic height, measured to the nearest 0.5 km, in Figure 1. The new data points calculated for this study increase the average GTR range for Venus above the value found if only previously published ADCs are used to estimate GTRs [8]. Data for 53 terrestrial oceanic hotspots and plateaus [9] are plotted for comparison. If the oceans were removed from these same terrestrial features, the GTRs would increase by a factor of 1.5. Even if with this correction, the majority of the Venusian values are much larger than the terrestrial values. The GTRs are plotted against average diameter in Figure 2. This plot suggests two populations of GTRs, both of which show GTR increasing with diameter, but with different slopes and aver-

age values. This relationship is supported by statistical analysis of the two trends. The correlation coefficient for a least squares line fit to the upper trend is 0.837, and 0.967 for the lower branch. A t-test shows that both correlations are significant at the 95% confidence level. No significant linear fit exists for the entire data set. Analysis of the correlation between GTR and average height, GTR and maximum height, and maximum height and diameter for the two trends are discussed below.

Discussion. The lower trend on the GTR versus diameter plot may represent regions which are predominantly supported in the lithosphere, by either crustal or thermal compensation. Airy models with a crustal density of 3000 kg/m^3 can produce a GTR range of 1 to 19 m/km, as observed for the lower trend, if the crustal thickness varies from 10 to 130 km. Thermal isostatic models require a similar range of lithospheric thickness. No correlation exists between GTR and maximum height, or between height and diameter. The full equation for the geoid for a crustally compensated area predicts a slight increase in GTR with increasing h: $\Delta N = (2\pi G\rho/g)h(2D - h\rho_m/\Delta\rho)$, or, GTR = $\Delta N/h = (2\pi G\rho/g(2D - h\rho_m/\Delta\rho)$, where ρ_m is the mantle density. The thermal equation has the same form. Thus this lack of correlation between GTR and height is not inconsistent with a crustal compensation model. The lack of correlation between height and diameter for the lower trend also agrees with this interpretation, in the sense that there is no physical process which relates the height and the diameter of a crustal or lithospherically compensated region.

The upper GTR versus diameter trend may represent regions which are dynamically supported. The expected relationship for dynamic processes between GTR and height or diameter is unclear. The points which make up the upper trend also show a correlation between maximum height and diameter. This is the relationship predicted for transient mantle plumes [10], although height decays with time while diameter increases. Convection solutions appear to be the only models capable of fitting the large range of GTRs observed in the upper trend. An upper mantle convection model [11], scaled to Venusian values, can fit a GTR range of 14 to 27, with a Raleigh number of 10^6, and a conductive lid thickness of 0 to 150 km. Fitting the largest GTR values, up to 40 m/km, is problematic. Decreasing the Raleigh number by an order of magnitude only increases the GTR a few m/km. For a Raleigh number of 10^6, boundary layer thicknesses of 200-300 km are necessary to fit GTRs of 30-40 m/km. Such large thicknesses are in conflict with the idea of dynamic support. As the thickness of the conductive lid does not scale with the depth of convection, it does not appear that simply going to whole mantle convection will produce larger GTRs. Other possible ways of increasing the GTRs include non-steady state behavior and variable viscosity models.

In summary, the majority of Venusian GTRs are much larger than terrestrial values. Plotting GTR against the diameter of individual features suggests two linear trends, although further error analysis must be done to verify this. These trends may be related to the compensation mechanism of the two groups. The lower trend agrees fairly well with the trends and GTR ranges expected for crustal or thermal compensation. The upper trend may correspond to dynamically supported features. Although the lower range of GTRs in this trend can be fit by an upper mantle, constant viscosity model, we do not have a model which can fit the larger values with a reasonable parameter range.

References: [1] Esposito, et al., *Icarus, 51*, 448-459, 1982. [2] Herrick, et al., *Geophys. Res. Lett., 16*, 543-546, 1989. [3] Janale, et al., *Earth Moon Planets, 39*, 251-273, 1987. [4] Phillips and Malin, in *Venus*, Univ. AZ Press,

1984. [5] Sjogren, et al., *Geophys. Res. Lett., 11*, 489-491, 1984. [6] Phillips, et al., *J. Geophys. Res., 83*, 5455-5465, 1978. [7] Smrekar and Phillips, *Lunar Planet. Sci. Conf. XX*, 1028-1029, 1989. [8] Smrekar and Phillips, *EOS, 70*, 1334, 1989. [9] Sandwell and McKenzie, *J. Geophys. Res., 94*, 7403-7418, 1989. [10] Olsen and Nam, *J. Geophys. Res., 91*, 7181-7191, 1986. [11] Ceuleneer, et al., *Earth Planet. Sci. Lett., 89*, 84-102, 1978.

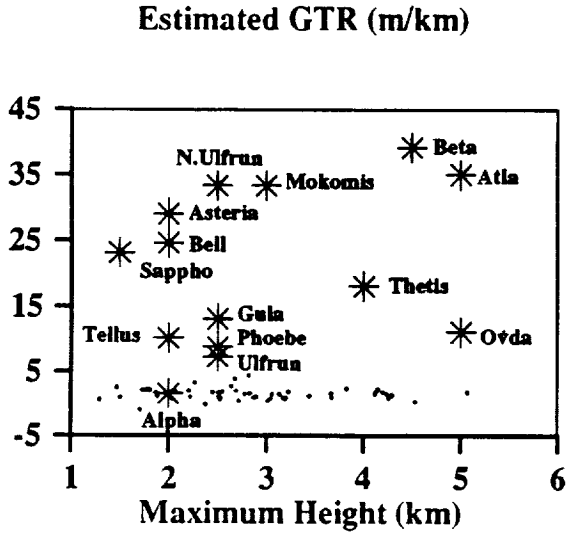

Figure 1. GTR vs topographic height. Stars indicate venusian features, dots indicate terrestrial values.

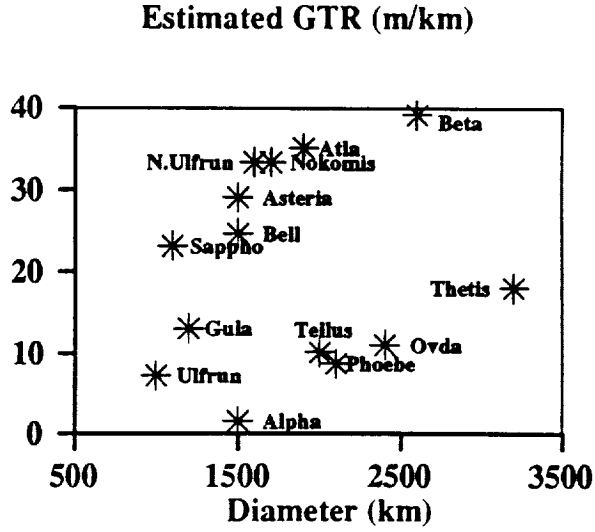

Figure 2. GTR vs average diameter.

VOLCANISM IN NW ISHTAR TERRA, VENUS

L.Gaddis and R. Greeley, Department of Geology, Arizona State University, Tempe, AZ 85287

Venera 15/16 radar data for an area in NW Ishtar Terra (74°N, 313°E; at the intersection of Akna and Freyja Montes) show an area with moderate radar return and a smooth-textured surface which embays low-lying areas of the surrounding mountainous terrain (figure.1). Although this unit may be an extension of the lava plains of Lakshmi Planum to the southeast, detailed study suggests a separate volcanic center in NW Ishtar Terra. Lakshmi Planum, on the Ishtar Terra highland, exhibits major volcanic (Barsukov *et al.*, 1986; Magee and Head, 1988a, b; Gaddis, 1989) and tectonic (Crumpler *et al.*, 1986; Head, 1988; Vorder Breugge and Head, 1988) features. It is a smooth-surfaced plateau (3 to 5.5 km in elevation) surrounded by major mountain belts including Akna, Freyja, and Maxwell Montes. Volcanic features on Lakshmi Planum include calderas of Colette (130x180 km) and Sacajawea (120x200 km) Paterae, lava flows (Colette flows average 15 km in width, 100-300 km in length; Magee and Head, 1988b), and associated smaller vents. These volcanoes may be the surface expression of hot spots, as observed in Hawaii, in which the growing volcanic edifice deformed the surrounding areas (Pronin, 1986); alternatively, compressional deformation may have resulted in crustal thickening and melting, and the formation and deposition of volcanic materials (Magee and Head, 1988b).

On the Venera radar image (figure 1) radar brightness is influenced by slope and roughness; radar-facing slopes (east-facing) and rough surfaces (~8 cm average relief) are bright, while west-facing slopes and smooth surfaces are dark. The moderate radar return indicates a smooth unit embaying low-lying areas of the adjacent "ridge-and-trough" terrain; these characteristics are consistent with a volcanic origin for this unit. To the northwest, bright, lobate features extend further northwestward more than 300 km. A geologic sketch map (figure 2) shows smooth terrain for the volcanic units, and the darker units represent adjacent, possibly associated volcanic flows.

A series of semi-circular features, apparently topographic depressions, do not conform in orientation to major structural trends in this region of NW Ishtar Terra. Topography[9] (figure 3; after Fotokarta Veneri B4) shows elevations from about 5.5 km in the SE (toward Lakshmi Planum) to 2 km (to NW). If the 3.0 km elevation is assumed to be the outer boundary of a complex caldera in the center of the smooth terrain, a feature about 200 x 250 km in size is measured; the smaller depression to the southeast (an associated vent?) is about 50 km in diameter.

The large depression (caldera?) in NW Ishtar Terra is similar to the calderas of Colette and Sacajawea Paterae, as all three structures are large irregular depressions. Although Colette and Sacajawea have been described as shields, their flank slopes are low (<0.5°). All 3 calderas have depths of 1 to 1.5 km, but the caldera in NW Ishtar is both more complex and larger than Colette (130x180 km) and Sacajawea (200x120 km). If a relationship between caldera diameter and magma chamber diameter and depth exists for Venus (Wood, 1984), then the chamber under the NW Ishtar caldera is larger/deeper than those of Colette and Sacajawea. Although the types and volumes of volcanic products from the structures and the presence or absence of rifting and associated volcanism cannot be constrained with Venera data, the large calderas indicate that centralized eruptions were predominant. Age relationships are difficult to establish; although the muted appearance and lower relief of Sacajawea support an older age than for Colette, it is not possible to determine a relative age for the NW Ishtar Terra volcano.

NW Ishtar Terra appears to be the site of a volcanic center with a complex caldera structure, possibly more than one eruptive vent, and associated lobed flows at lower elevations. The morphologic similarity between this volcanic center and those of Colette and Sacajawea suggests that centralized eruptions have been the dominant form of volcanism in Ishtar. The location of this volcanic center at the intersection of two major compressional mountain belts and the large size of the caldera (with an inferred large/deep magma source) support a "crustal thickening/melting" rather than a hot-spot origin for these magmas.

References Cited: Barsukov *et al.*, 1986, LPSC Proc. 16th, JGR, 91, D378; Crumpler *et al*, 1986, Geology, 14, 1031; Fotokarta Veneri B4, Lakshmi Planum, 1987; Gaddis, 1989, LPSC XX, 317; Head, 1988, LPSC XIX, 469 ; Magee and Head, 1988a, LPSC XIX, 711; Magee and Head, 1988b, LPSC XIX, 713; Pronin, 1986, Geotektonika, 4, 26 (in Russian); Vorder Bruegge and Head, 1988, LPSC XIX, 1218; Wood, 1984, JGR, v. 89, 8391.

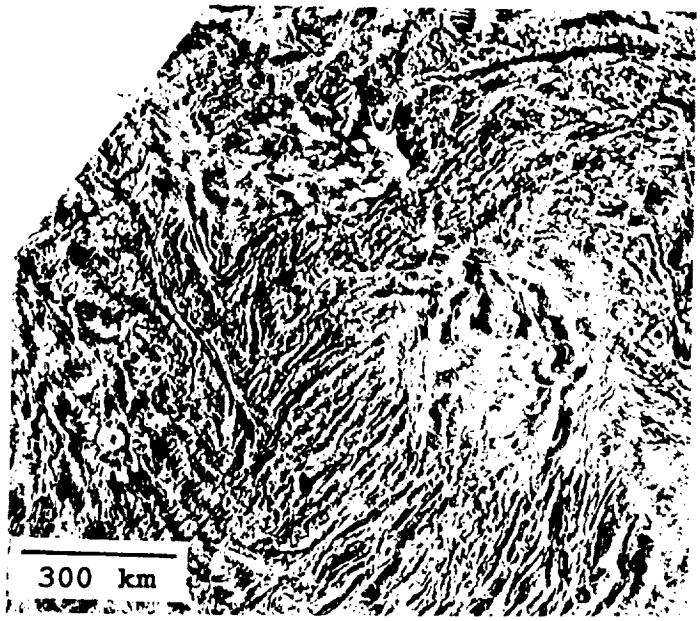

Figure 1

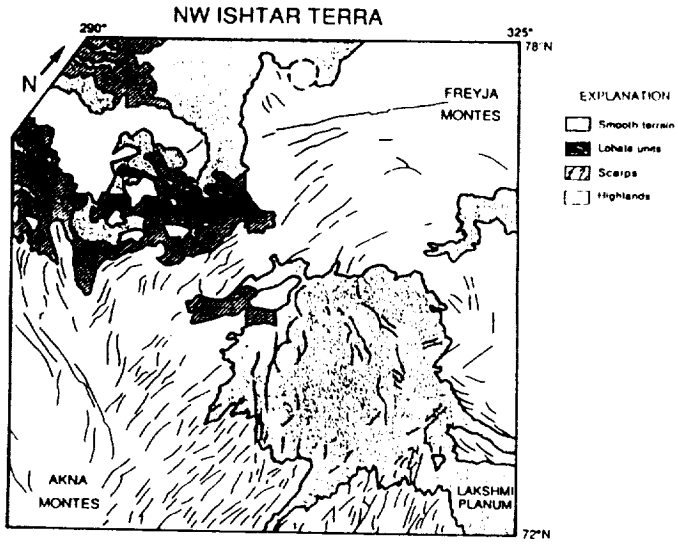

Figure 2

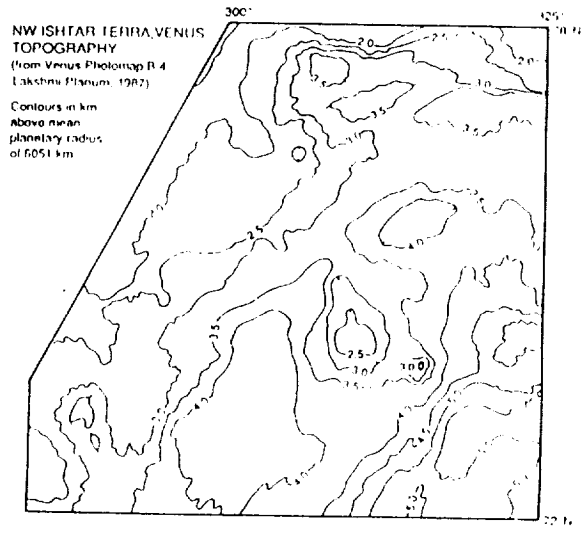

Figure 3

FORMATION AND EVOLUTION OF PLUME PLATEAUS ON VENUS

L. S. Crumpler and James W. Head, Department of Geological Sciences, Brown University, Providence, RI 02912

Introduction: Plateau-like areas with dimensions in the range of several hundreds to several thousands of kilometers are relatively common on Venus and are characterized by several of the following features: broad regional rises, linear boundaries, locally relatively steep sides, associated volcanic edifices and deposits, rifting, complex surface structure and texture (often tessera-like), and tectonic junctions(1-4). Plateaus can be classified into several types, some associated with the Equatorial Highlands (Beta, Atla, the sites of tectonic junctions; Western Eisila, the site of localized volcanism; Ovda and Thetis, the site of rifting and apparent crustal spreading), and others at mid to high latitudes and not obviously associated with rifting at present (Tellus, Alpha, Eastern Fortuna, Laima)(3,4). Here we examine the origin of the plateaus at Ovda and Thetis, and propose a model for their evolution and how they may be linked to the characteristics and evolution of plateaus elsewhere on Venus.

Crustal Spreading, Mantle Plumes, and the Formation of 'Plume Plateaus': Crustal spreading in Western Aphrodite Terra is interpreted from linear cross-strike discontinuities (CSDs) thought to represent fracture zones, which segment Aphrodite into domains characterized by bilateral symmetry parallel to the linear discontinuities. The centers of symmetry of the domains have central depressions and form linear rises that are oriented normal to the CSD's, terminate against them, and are offset at them in an en echelon manner (5), in patterns comparable to spreading centers in the Earth's ocean basins. On the basis of these data and analysis of topographic profiles, Aphrodite Terra appears to be the site of spreading at the present time at rates of the order of 1.5-3 cm/yr (5,6). Analysis of the nature of the process of crustal spreading in the Venus environment indicates that the enhanced upper mantle temperature (about 1500°C) caused by high surface temperature should result in a crustal thickness of about 15 km, a factor of 2-3 greater than that for the Earth (6). Material formed at the rise crest and moved laterally would become lower topographically as it cooled and would be modified by subsequent volcanism and tectonism. Localized plateaus along the Equatorial Highlands, such as Ovda and Thetis Regiones, are interpreted to be the site of elevated upper mantle temperatures, enhanced melting, and greater crustal thicknesses (5,6). Specifically, these Iceland-like pleateus could be formed by increased upper mantle temperatures of about 100°C, which would produce a 30 km thick crust characterized by an increase in isostatically supported elevations of about 1.5 km (6). Models of Ovda Regio that are consistent with both topography and gravity data suggest that such a process is plausible, with upper mantle temperatures of about 1600°C and spreading rates of about 1 cm/yr (6). The most likely mechanism for the enhanced upper mantle temperature is a localized upwelling of the mantle, and the geometry of the plateaus suggests that it may be a mantle plume or 'hot spot' similar to the one thought to underlie the Icelandic plateau (7). The size of Ovda Regio (2000 km wide) and the interpreted spreading rates suggest that this mantle plume has been active for the past 200 million years (6).

Evolution of 'Plume Plateaus': Cessation of the enhancement of upper mantle temperature at the site of a mantle upwelling or hot-spot would return the spreading environment to a more normal condition of spreading (if nominal, to a crustal thickness of about 15 km, and isostatically compensated topography of 1-1.5 km less than previously). In this case continued spreading would split the 'plume plateau', separate it, and move it laterally off the thermal rise into the adjacent lowlands at rates comparable to the spreading rates (8,9). Although the split and separated plateau would become topographically lower as it evolved thermally, its enhanced crustal thickness and its correspondingly increased isostatic topography, would result in the plateau remaining elevated above the adjacent surrounding plains by an amount related to crustal thickness variations. There are several possible modifications that might be expected as plateaus split, separate, and are moved laterally. The following predictions from the model are compared to some observations of Venus plateaus: 1) Presence of plateaus with predicted characteristics; about 10-15% of the area covered by Venera 15/16 data show the presence of plateaus which have at least some of the characteristics outlined above, and other areas of the surface have plateaus which are characterized by tessera-like fabrics (10); 2) Marginal deformation of plateaus caused by localization of deformation along

potential zones of weakness at edges of plateaus (e.g., crustal thickness differences, fracture zone boundaries of plateaus); possibly initiated by changes in tectonic geometry. Marginal deformation is observed along the borders of western Tellus and Alpha. 3) Accretion with other plateaus may occur when two plateaus converge; if underthrusting and crustal loss occur (11), then when zones of thicker crust converge, they may resist further underthrusting and coalesce to form a larger plateau. Such a situation has been porposed for the Clotho Tessera/Danu Montes region of Ishtar Terra (12). 4) Collage accretion would occur when plume plateaus with thick crust become the locus of accretion and continue to grow by collection of plume plateaus and associated deformation. Such collages of plume plateaus might be viewed as 'protocontinents'. This situation may be occurring in Ishtar Terra, where various segments of thickened crust appear to be converging and accreting into a larger upland plateau with associated orogenic belts and suture zones (13). 5) Volcanic flooding and embayment would be expected and low elevation plateaus (relatively thin crust) might be partially to wholly buried depending on the off-rise volcanic contribution. Many of the topographically low regions of tessera are distinctly embayed and partially buried, and almos all show embayment relationships by surrounding plains.

Predictions: Are the plateaus in middle to high latitudes remnants of thick crust originally created at rise crests ('plume plateaus') and transported laterally to their present positions? This hypothesis makes several predictions that can be tested: 1) shallowly compensated evolved plume plateaus (depths related to crustal thickness); 2) textures and structures that can be linked to plateau origin at rise crests (e.g., analogs to fracture zones and abyssal hills on Earth's seafloor); 3) symmetry of plateaus about their point of origin should be observed if they are split and rifted; 4) internal structures should be observed consistent with their mode of formation and direction of splitting and spreading; 5) plateau size frequency distribution and shapes consistent with plume production. Many of these predicitons can be tested with observations from the upcoming Magellan mission.

Possible relationships to the Earth: Oceanic plateaus are a well-known phenomenon in the Earth's ocean basins (14) and Iceland is a clear example of the formation of a plateau at a rise crest (7). Some presently off-axis oceanic plateaus are thought to have formed at rise crests and been moved laterally (8). Oceanic plateaus have been proposed to be important in continental accretion because of crustal thickness differences and suturing during subduction (15). We are presently analyzing oceanic plateaus on Earth for clues as to basic processes of their formation and evolution which might aid in the understanding of plateaus formed on Venus.

References: 1. A. Basilevsky *et al.*, *J. Geophys. Res.* **91**, D399 (1986); 2. V. Barsukov *et al.*,*J. Geophys. Res.* **91**, D378 (1986); 3. D. Senske, thesis, Brown University, Providence, R.I. (1989); 4. D. Senske and J. Head, *Lunar Planet. Sci.* **20**, 984 (1989); 5. L. Crumpler *et al.*, *Geophys. Res. Lett.* **14**, 607 (1987); L. Crumpler and J. Head, *J. Geophys. Res.* **93**, 301 (1988); J. Head and L. Crumpler, *Science* **238**, 1380 (1987); 6. C. Sotin *et al.*, *Earth Planet. Sci. Lett.* **95**, 321 (1989); 7. J. Schilling, *Nature* **242**, 565 (1973); 8. L. Crumpler and J. Head, *LPSC XIX*, 235 (1988); 9. J. Head and L. Crumpler, A crustal spreading/mantle plume model for the tectonics of Venus, *LPSC XXI* (1990); 10. D. Bindschadler *et al.*, Distribution of tessera terrain on Venus: Prediction for Magellan, *Geophys. Res. Lett.* in press (1990); 11. J. Head, The formation of mountain belts on Venus: Evidence for large-scale convergence, undrthrusting, and crustal imbrication in Freyja Montes, Ishtar Terrain , *Geology* in press (1989); 12. R. Kozak and G. Schaber *Geophys. Res. Lett.*, 16, 175 (1989); J. Head and J. Burt, The Danu Montes deformation zone of southern Ishtar Terra: Evidence for convergence and crustal underthrusting, *LPSC XXI* (1990); 13. R. Vorder Bruegge and J. Head, *Geophys. Res. Lett.* **16**, 699 (1989); R. Vorder Bruegge *et al.*, in press, Jour. Geophys. Res. (1990); R. Vorder Bruegge and J. Head, *LPSC XXI* (1990); 14. A. Nur and Z. Ben-Avraham, *Jour. Geophys. Res.* **87**, 3644 (1982); 15. Z. Ben-Avraham *et al.*, *Science* **213**, 47 (1981).

TWO GLOBAL CONCENTRATIONS OF SMALL DOME-LIKE HILLS ON VENUS

Jayne C. Aubele, Department of Geological Sciences, Brown University, Providence, RI 02912

Introduction. Small dome-like hills are among the smallest resolvable features with distinguishing characteristics in Venera 15/16 images of Venus[1]. More than 22,000 small dome-like hills have been mapped in the 20% of the surface imaged by Venera and they are the most numerous identified single morphologic feature on Venus. Domes are defined and identified on the basis of their positive topographic form, generally circular planimetric outlines, diameters in the range 1-2km to 20km, and slopes of ≤10° (and probably ≤5°) [2]. Associated characteristics include summit pits, radar bright slopes and aprons, and basal topographic platforms [3].

On the basis of an assessment of their individual and cluster characteristics, their overall surface distribution and associations[3], and theoretical analyses of the eruption conditions for magmas on Venus[4], domes have been shown to be analogous to the characteristics of small shield volcanoes constructed from multiple centralized effusive eruptions consiting of discrete volumes of material erupted over short time intervals. On the basis of their overall abundance, regional distribution, individual characteristics, and associated geologic terrain units, they are interpreted to be similar to seamounts on Earth [3].

In this study, we show that domes on Venus predominantly occur in their greatest concentration in two regions that are near Beta Regio and Thetis Regio. These well-known global topographic rises have been previously interpreted, on the basis of a variety of characteristics, to represent potential hot spots and regions of anomalous heat flow, associated rifting, and dynamic topography. The concentration of domes in these two areas may represent increased volcanic productivity associated with enhanced regional thermal budgets, perhaps in association with large scale regions of mantle convective upwelling.

Global Distribution. Dome density contour maps produced by Slyuta *et al.* [2] show local and regional clustering of domes in specific areas, particularly in the Akkruva Colles area. For the present study, detailed maps of dome location, number and distribution for every Venera quadrangle have been prepared in which all domes larger than 5 km are identified and digitized. Only bright features showing a paired dark side were interpreted to be domes and included in the data set. The resultant dome point map shows two significant areas of major dome concentrations approximately 180° longitude apart: (i) the largest concentration occurs in the Akkruva Colles area of Niobe Planitia centered at approximately 45°N/120°E and including Ananke, Kutue and Shimti Tesserae and Uni Dorsa (east of Tellus Regio, and just north of the flanks of the Thetis Regio rise), and (ii) another significant concentration occurs in northwestern Guinevere Planitia centered at approximately 35°N/300°E and including Lachesis Tessera (north flank of Beta Regio rise). Because these areas lie adjacent to the limits of Venera image coverage, the extent of these regional clusters is known only for their north, east, and west margins. In addition to these major areas of concentrations, domes occur in smaller concentrations throughout the imaged area of Venus, generally in association with known local scale volcanic edifices, calderas [5], and certain features (corona) interpreted to be volcanic in origin [6].

Global Association. The Akkruva and Beta dome concentration areas are also anomalous in other respects. Both areas predominantly consist of intermediate elevations (6051-6053) and show relatively prominent regional orthogonal tectonic patterns analogous to those associated with tessera. These characteristics stand in contrast to surrounding regions of relatively smooth low-lying plains and to the complexly disturbed and elevated surfaces of adjacent areas of true tessera and imply that the surfaces on which the two significant dome concentrations occur have a more complex origin than do the simple smooth low elevation plains.

Both areas generally coincide with the unit designated Rolling Plains [7] and with the Plains-Corona-Tessera, Plains, and Plains-Corona Assemblages [7]. These assemblages can be characterized in a tectonic sense as having formed predominantly from vertically directed deformational forces [7] as opposed to significant lateral deformation known to occur elsewhere [8]. The Beta concentration has been imaged by Arecibo high-resolution radar and, on this basis, large volcanic edifices[Campbell et al. 1989] are known to occur in association with domes in this area. Analysis of Pioneer-Venus radar properties [9] also distinguishes these areas as smooth to transitional in roughness and low to intermediate in reflectivity, which has been interpereted [9] as implying a predominant surface material ranging from porous material such as soil to a material comparable to terrestrial rock. These characteristics are consistent with surface exposure of rough to smooth plains-forming lava flows with variable degrees of surficial weathering products overlying smooth surfaces and infilling small-scale surface roughness elements.

Discussion. Both of the regional dome concentrations occur on the slopes, or in proximity to, significant regional topography that correlates with positive anomalies in the gravity potential field [10]. Both the Beta Regio and Thetis Regio-Eastern Aphrodite areas have been shown previously to be characterized by topography/gravity correlations [10] and correspondingly deep apparent depths of compensation commonly interpereted to represent deep convective upwelling, dynamically supported topography, and associated dynamic tectonic deformation. These characteristics are large enough to show considerable expresssion even at low harmonic degrees [11] (long wavelengths), implying that their origin is significant at global scales, and that the effects of the perturbing underlying mantle may be expressed over areas larger than the topographic influences alone.

Predicted influences of significant dynamic mantle upwelling include enhanced regional heat flow associated with the correspondingly warm upwelling mantle, and local lithospheric thinning, associated rifting, a significant increase in shallow mantle melting, corresponding increases in magma production, and increase in surface volcanic production rates and crustal thickness. The presence of numerous small effusive volcanoes in these areas on Venus is interpreted to

represent enhanced regional and global scale distribution of advective heat flow in association with two areas of large scale dynamic mantle upwelling.

Global scale clustering of volcanic edifices on this scale is known to occur on Earth and may represent similar large scale mantle convective processes. On Earth a degree 2 pattern of hot spot concentrations (Pacific and Africa-North Atlantic hot spots centered 180° apart) is known to correlate with degree 2 variations in upper mantle temperature, and, once corrected for shallow density variations in the lithosphere, corresponding geoid highs can be shown as well [12]. These observations have been interpreted to reflect large scale patterns of mantle **convective** upwelling on Earth [13], associated increased upper mantle temperatures and hemispheric regions of enhanced volcanism (antipodal hot spot concentrations).

Conclusions. Two global scale regions of dome concentration occur on Venus, one near Beta Regio and another north of Thetis Regio, and are interpreted to be exceptionally large concentrations of numerous small effusive shield volcanoes. Corresponding associated anomalous geologic unit characteristics, intermediate (neither "lowland nor highland") regional elevation of the surface, proximity to large regional highlands, and correlated long wavelength positive gravity anomalies are all associated characteristics of both of these areas. On the basis of the regional positive gravity and topography correlations and associated geologic characteristics indicative of rifting and tectonic extension, the nearby highland areas of Beta and Thetis Regio have been commonly interpreted as potential regions of dynamic mantle support of overlying topography, buoyant mantle upwelling and increased mantle heat flow. If so, the concentration of effusive volcanic activity near these areas is suggested to reflect two areas of regionally enhanced thermal budgets, increased shallow melting, and relatively enhanced higher volcanic production and eruption.

Questions that remain include the following: (i) is the apparent longitudinally antipodal concentration of regional volcanic activity an artifact of the limited area and limited resolution currently available for Venus?; (ii) are other areas interpreted to be characterized by the geological and geophysical characteristics of dynamic mantle upwelling also areas of enhanced volcanic effusive activity?; and (iii) what is the dome global distribution, abundance, size-frequency distribution, and changes in these characteristics with latitude? Increased resolution of small domes less than 2 km in diameter and increased areal identification from Magellan data will enable a more thorough assessment of these questions.

References. [1] Barsukov, V.L., *et al.*, 1986, *Proc. LPSC XVI, J.G.R.* **91**, B4, D378; [2] Slyuta, *et al.*, 1988, *LPSC XIX*, 1097; Aubele, J.C., *et al.*, 1988, *LPSC XIX*, 21. [3] Aubele, J.C., 1989, *LPSC XX*, 28; [4] Head, J.W. and L.Wilson, 1986, *J.G.R.* **91**, 9407; [5] Magee, K.P., and J.W.Head, 1988, *LPSC XIX*; [6] Stofan, E.R., and J.W.Head, 1988, *LPSC XIX*, 1127; [7] Head, J.W., 1989, *LPSC XX*, 392; [8] Head, J.W., *et al.*, 1989, *LPSC XX*, 396; [9] Head, J.W., 1985, *J.G.R.* **90**, 6873; [10] Bills, B.G.,*et al*; 1987, *J.G.R.* **92**, 10335; [10] Sjogren, W.L., *et al.*, 1983, *J.G.R.* **88**, 1119; [11] Williams, B.G., *et al.*, 1983, *Icarus* **56**, 578 [12] Richards, M.A., *et al., 1989, Science* **246**, *103*; [13] Cazenave, A., *et al.*, 1989, *Nature* **340**, 54.

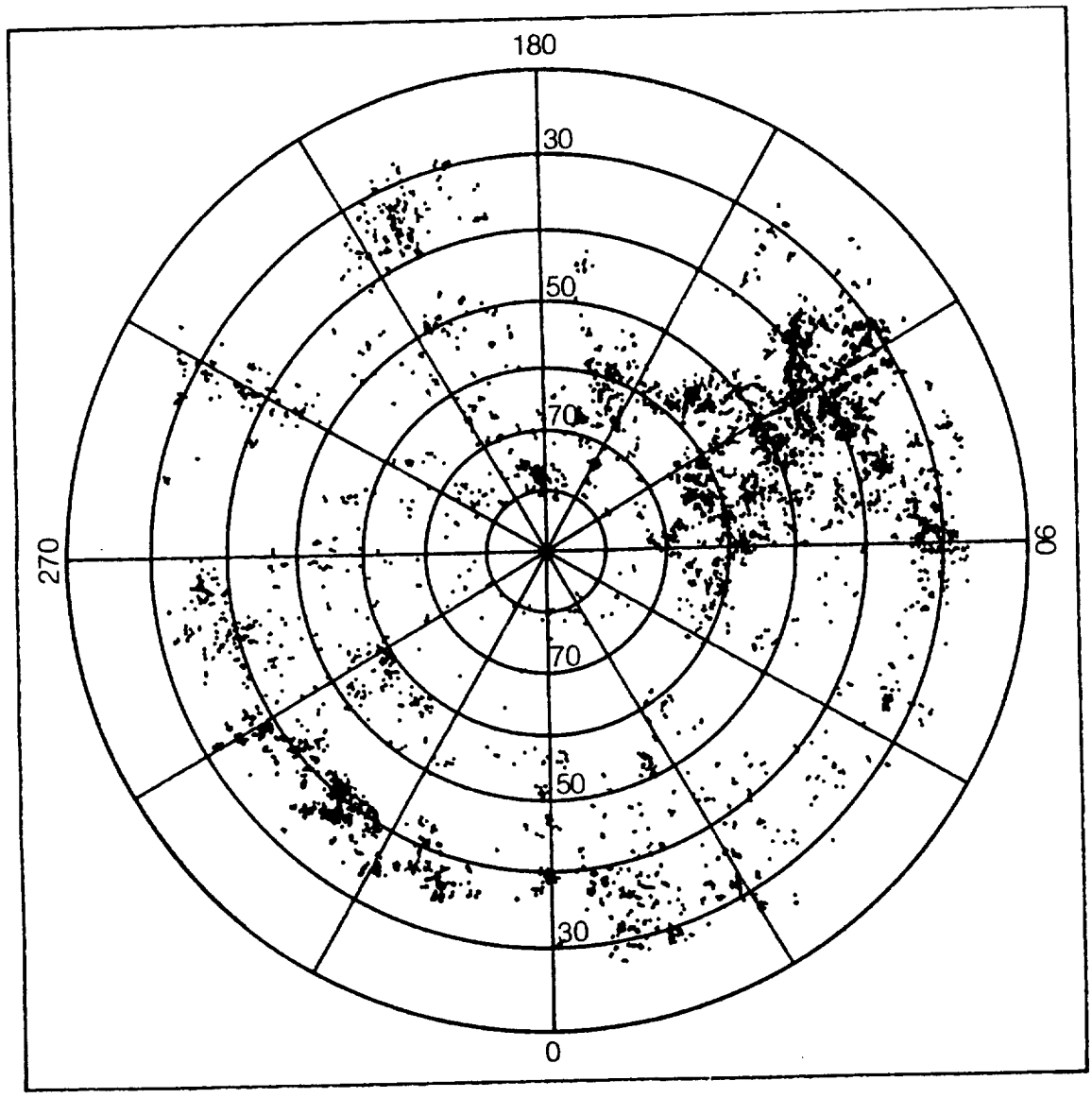

Dome location map. All domes larger than 5 km were mapped on Venera quadrangles, digitized and re-projected to a polar projection. Venera image coverage ends at approximately 20° latitude. Domes primarily occur in rolloing plains terrain. Two major areas of dome concentration occur at 120° longitude, north of Thetis Regio in the Akkruva Colles area and at 300° longitude, northeast of Beta Regio in Guinevere Planitia. Dome abundance is depleted in the areas of predominant ridge belts and in the area of Lakshmi Planum. Total number of domes plotted is 7000.

THE POTENTIAL FOR AEOLIAN STRUCTURES ON VENUS: A SYNOPSIS OF EVIDENCE FROM EXPERIMENTAL INVESTIGATIONS WITH THE VENUS WIND TUNNEL

John R. Marshall and Ronald Greeley
Department of Geology, Arizona State University, Tempe, AZ 85287

There are basically two requirements for the formation of aeolian structures on a planetary surface: a supply of loose sediment and winds in excess of the sediment mobilization threshold. The high temperatures and chemical reactivity of the venusian atmosphere have the potential for indurating surface materials by chemical welding and by processes related to solid-state diffusion such as cold welding and sintering. Conversely, the high temperatures should tend to destroy electrostatic interparticle forces which contribute to sediment cohesion on Earth; sediment cohesion on this planet is also partly a function of forces exerted by traces of interstitial moisture. These latter forces would, of course, be absent on Venus.

Thus, arguments could be made both for and against the existence of loose sediments on Venus. However, Venera spacecraft recorded dust mobilization upon contact with the venusian surface (Ksanfomaliti et al., 1983). Venera landers also recorded wind speeds equal to, or in excess of, wind speeds theoretically required (Iversen et al., 1976) to mobilize sediments. Because the spacecraft instruments functioned for no more than a few hours, the wind speed data cannot be considered truly representative; it seems unlikely that the instruments fortuitously recorded maximum wind speeds for the planet.

Because a reasonable case can be made for the potential for aeolian action on Venus, simulations of the venusian environment have been made with the Venus Wind Tunnel (VWT). These simulations (Greeley et al., 1984a,b) have demonstrated two important facts: first, sediments ranging in size from silt to coarse sand are readily mobilized by winds of the strength measured by Venera craft and second, this mobilization, almost without exception, leads to the formation of small-scale sediment structures whose orientation with respect to wind direction is a strong function of wind strength.

The VWT is a closed-circuit wind tunnel with a flow-path circumference of ~12 m. The test section is 1.2 m long and 0.2 m in diameter. The tunnel is pressurized with carbon dioxide to (typically) 30 bar which produces an atmospheric density equivalent to that on Venus at the geodetic datum where temperature and pressure are 770 K and 95 bar respectively. VWT experiments have succeeded in determining threshold wind speeds for various sediment sizes, the behavior of particles in motion, sediment flux, and the role of wind speed, wind duration, particle size, particle size distribution, particle density, and atmospheric density in determining the character of small-scale aeolian structures.

At very low wind speeds (~0.4 m/s) when particles intermittently roll or saltate, sand-size materials produce ridge and furrow structures oriented parallel with the wind direction. When slightly higher wind speeds produce a fully-developed saltation cloud, the aeolian structures become transverse to the wind. These transverse features vary somewhat in their morphology, depending upon prevailing conditions, but they always occur in regularly-spaced trains with the individual bedforms having lengths of several tens of centimeters and heights of a few centimeters. The morphology of the structures is most sharply defined when wind speeds are close to saltation threshold; here the structures, which are referred to as microdunes (Greeley et al., 1984b), have well developed slip faces, gentle stoss slopes, and various other characteristics reminiscent of full-scale terrestrial dunes.

As wind speeds are raised to about three times threshold speed, the microdunes grade into more symmetrical ridges and waves which ultimately give way to a plane bed. The same type of transition is observed as particle size becomes larger; coarse sand (mm size) does not develop structures. When atmospheric density is reduced, there is again a similar transition in bedform morphology; the structures have disappeared entirely by the time atmospheric density reaches ~0.03 g/cm^3 (coincidentally, the minimum value for Venus). The addition of dust-size material to a bed of sand, or the mixing of sand into bimodal populations, again detracts from the microdune configuration and gives rise to various ridge and wave morphologies. Thus, the "optimum"

development of transverse structures (i.e., the formation of microdunes) occurs for well-sorted, fine sand at wind speeds close to threshold with an atmospheric density approaching the maximum for Venus (higher gas densities than those capable of being tested (presumably) would also be conducive to microdune formation). Deviations from these conditions cause progressive changes in bedform morphology that terminate in the disappearance of the bedforms.

Although the potential development of bedforms on Venus is clearly constrained by a number of variables, it is to be noted that as the "optimum" set of conditions is approached, the set of conditions most likely to prevail on the planet is also approached. Most entrainment will probably occur close to threshold, particles will tend to become well sorted with time, the size of materials most readily forming transverse structures is approximately the same as the optimum size for transportation, and most of the planet's surface has atmospheric densities approaching 0.065 g/cm^3. This fortuitous combination of circumstances strongly suggests that transverse aeolian structures would be found on the surface of Venus, unless there are, as yet, unknown negating factors involved.

With respect to the tendency for entrained particle populations to approach unimodality on Venus, this would not be a unique trend; all fluids in any planetary environment (that are engaged in transporting sediments) exercise the ability to sort materials by size or density, unless transport occurs catastrophically. In VWT experiments with mixtures of particle sizes and mixtures of particle densities, the sorting of materials occurs very rapidly in the presence of transverse bedforms. During the development of a microdune, fine sediments or relatively dense materials become concentrated in the upper layers of the structure; the cycling of material through the structure as it migrates downstream proves to be a very efficient mechanism for sediment discrimination. Thus, not only do transverse structures develop in mixed sediments, they also have a tendency to improve their viability through the mechanism of internal sediment sorting.

Well-developed, highly asymmetrical microdunes have characteristics reminiscent of large terrestrial dunes as noted above. They also have characteristics of current ripples formed in subaqueous environments. Most noteworthy of these characteristics are the size of the structures, the mode of particle transport over the structures, and the presence of a deep scour hollow in the wake of the lee slope. The similarity between microdunes and current ripples is not wholly unexpected, given that the venusian atmosphere and water both constitute dense fluids, at least by comparison with terrestrial or martian atmospheres. A current ripple is believed to be the smallest end member of a continuum or family of subaqueous bedforms that can reach many tens of meters in length (Allen, 1984). If there is any merit to the comparison between microdunes and current ripples, it might be reasonable to postulate the existence of structures on Venus that are considerably larger than those observed in the VWT. In fact, in VWT experiments, there was evidence to suggest that microdunes were capable of growing beyond the sizes observed. Dimensional limitations of the tunnel itself restricted direct investigation of this possibility.

It is concluded that there is a high probability for the presence of aeolian structures on Venus on the basis of VWT experiments. These experiments have demonstrated that transverse bedforms readily develop in an atmosphere with a density equivalent to that on Venus, that the bedforms develop most readily when wind speeds are close to entrainment threshold, and that the bedforms have a self-sustaining ability resulting from their sediment-sorting efficiency. VWT experiments and comparison of results with subaqueous phenomena both suggest that venusian structures may achieve wavelengths considerably greater than those observed in the laboratory.

References:

Allen, J.R.L., *Sedimentary Structures.* Elsevier, Amsterdam, 1984.

Greeley, R. et al., Windblown sand on Venus: preliminary results of laboratory simulations. *Icarus, 57,* 112-124, 1984.

Greeley, R. et al., Microdunes and other aeolian bedforms on Venus; wind tunnel simulations. *Icarus, 60,* 152-160, 1984.

Iversen, J.D. et al., Windblown dust on Earth, Mars, and Venus. *J. Atmos. Sci., 33,* 2425-2429, 1976.

Ksanfomaliti, L.V. et al., Wind velocity near the surface of Venus from acoustic measurements. *Cosmic Res., 21,* 161-167, 1983.

CHAPTER 2

OUTER PLANET SATELLITES AND RINGS

CHARGED-PARTICLE INDUCED ALTERATIONS OF SURFACES IN THE OUTER SOLAR SYSTEM

R.E. Johnson, School of Engineering and Applied Science
University of Virginia, Charlottesville, Virginia 22903-2442

Solar system surfaces unprotected by an atmosphere can be modified by plasma bombardment. This knowledge can be used to establish the age of the surface layer and the rates for geologic processes. The list of possible irradiation effects is long and, indeed, the list is likely to be increased as the data on Uranus, Halley, and Pluto are further analyzed. In addition there is the renewed interest in the lunar surface for which plasma effects are well documented but only partially understood. In this work we make accurate assessments of surface of objects for which relevant laboratory information on irradiation effects is available or can be successfully extrapolated. Until sample return missions are possible, the limitations of observations to the outer layers of solid objects requires careful evaluation of the surface modifications which can affect interpretations of remote sensing data. Sputtering and other irradiation effects have been used to account for many initially uncertain observations, and often these initial guesses have been wrong. Our models for our laboratory data, therefore, provide important constraints and we have shown that plasma interactions are important for interpreting solar system observation in a number of cases.

In the previous two years we placed strong emphasis on describing the plasma interaction with possible Io surface constituents SO_2, sulfur, and Na_2S in order to interpret polar darkening by radiation and ejection of species into the atmosphere and torus. More recently we have calculated the plasma bombardment profiles of the surfaces of the icy Saturnian satellites to interpret reflection spectra. In the last funding period we evaluated the effect of charged particles on the surfaces (mantles) of Pluto and of comets in the Oort cloud. These surfaces have been irradiated for 4.6×10^6 years by galactic cosmic rays and there has been considerable speculation as to the ramifications of this irradiation process.

Pluto's exposure to cosmic rays results in a slow alteration on the reflectance of the methane condensed on its surface and the UV absorbed in the atmosphere can produce precipitates. If the atmosphere is global then the galactic cosmic rays are the dominant source for inducing alterations in the absence of local fields which might produce particle precipition. We showed that, depending on the rates of the competing regolith processes and the rates of replenishment of the methane the surface can appear bright, 'red' or 'dark'. Using laboratory data we showed that the amount of darkening occurring in one orbit is small. Therefore, transport, burial and re-exposure of organic 'sediments' must control the reflectance and the average reflectance is established by the radiation altered species accumulated over many orbits with the observed spatial and, possibly temporal differences in albedo due to transport. The cosmic rays although producing changes in reflectance slowly, do so inevitably. Therefore, the fact that the surface is not dark everywhere implies that it is active and the exposure rates vs. depth into the surface given in the paper on Pluto can be used to constrain turnover rates.

Comets in the Oort cloud experience similar effects. This irradiation processing occurs in competition with a number of surface alteration processes evaluated by Stern. First, we corrected the many different estimates of cosmic ray dose that have led to 'primordial' mantles varying from 50 m to a few cm. The cosmic-ray-induced refractory mantle should be of the order of 30 gm/cm^2. Including the other surface alteration processes will not seriously affect this estimate. These discussions are summarized in a review chapter in the Bamburg proceedings. Recently, experimental data have been used by us to show that this crust will survive the comet's entrance into the inner solar system.

Finally, our most recent effort has been an evaluation of the coupling between the atoms and molecules in lunar corona with the composition of the local surface. Directly sputtered species were shown to give an energetic corona indicative of the average composition of the moon's surface and those sputter species interacting with the regolith will give local (~100 km) information using atmospheric instruments on the Lunar Orbiter.

References

Pospieszalska, M.K. and R.E. Johnson Magnetospheric Ion Bombardment Profiles of Satellites: Europa and Dione Icarus 78 1-13 (1989).

Johnson, R.E. Application of Laboratory Data to the Sputtering of a Planetary Regolith Icarus 78 206-210 (1989)

Johnson, R.E. The Effect of Irradiation on the surface of Pluto Geo. Res. Lett. 16 1233-1236, 1989.

Strazzulla, G. and R.E. Johnson Irradiation Effects on Comets and Cometary Debris. Bamburg Proceedings in Press, 1990.

Johnson, R.E. Report of the Lunar Atmosphere Working Group of LExSWG (in preparation)

The Effect of Volume Phase Changes, Vapor Transport and Sunlight Penetration on the Thermal Regime of Icy Regoliths

Fraser P. Fanale and James R. Salvail, Hawaii Institute of Geophysics, University of Hawaii, Honolulu, Hawaii 96822 U.S.A.
Dennis L. Matson and Robert H. Brown, Jet Propulsion Laboratory, California Institute of Technology, 4800 Oak Grove Drive, Pasadena, California 91109 U.S.A.

The thermal regime of porous ice can be modified by phase changes and vapor transport taking place throughout its volume. Sunlight can also penetrate to considerable depths in high albedo, translucent ice. When this insolation is absorbed below the surface and cannot radiate from below the surface, which is the case for water ice, a "solid state greenhouse" results. The effect of phase changes, vapor transport and sunlight penetration and absorption on the temperature profile of the ice can vary considerably depending upon the thermal and optical properties of the ice and the available illumination. These processes have been known and studied for years in terrestrial snowpacks, but they have not been included in a single, unified model. Previous thermal models of surface volatiles for extraterrestrial applications have generally assumed that sublimation occurs only at the boundary of materials containing volatiles. However, it is clear that for any porous material containing ices, both sublimation and condensation can occur at any gas-solid interface within the material. Just as the latent heat can significantly affect the surface temperature of a frost covered body, sublimation and condensation throughout the bulk material can also produce significant changes in the volumetric temperature distribution. Convection can also affect the temperature distribution inside porous materials, although in most natural settings, the effect is considerably less than the latent heat. Sublimation and condensation can also cause at least temporary variations in certain physical properties of a porous icy medium, such as porosity, density and thermal conductivity.

The "solid state greenhouse effect" has been recently modeled by Brown and Matson (1987) and Matson and Brown (1989). Clow (1987) considered the implication of this effect for frost on Mars, and Carr (1983) included it implicitly in his calculations for the stability of streams and lakes on Mars. However, none of these models included the effect of volumetric phase changes and vapor transport.

A model that includes the effects of volumetric phase changes, vapor transport and sunlight penetration has been developed and applied to the Jovian satellite Europa. Europa has a high albedo icy surface, which is implied by observations to have a low density and a very low thermal conductivity (100 ergs/cm-s-K). The core of our model is an energy equation that includes the effects of conduction, convection, sublimation/condensation and insolation penetration. Vapor flux equations for the free molecular regime and the continuum regime are included. The thermal conductivity and the insolation extinction coefficient are considered as free parameters, and reasonable ranges of these parameters are considered. The domain under consideration is assumed to be pure water ice. The surface boundary condition includes the effects of radiation, latent heat and heat conduction. Insolation is not included in the boundary condition because the model, to be consistent, requires that insolation be absorbed by a finite thickness of ice. Therefore, the surface is heated from below by upward conduction. The boundary condition at depth is a small upward heat flow. The pores of the ice contain vapor which, when at equilibrium with the ice, is maintained at the vapor pressure governed by the local temperature. The temperature variation with depth results in a pressure variation. The pressure gradient induces a flow which momentarily perturbs the vapor pressures away from the equilibrium values. When this occurs, ice is sublimed or vapor is condensed, depending on the direction of the

pressure perturbation, at a rate such that the local equilibrium vapor pressure is maintained.

Temperatures, vapor fluxes and volumetric rates of ice sublimation or condensation were computed as functions of depth and time of day for a regolith column at 0 latitude and an albedo of .6. Various cases were computed using thermal conductivities of 100 and 1000 ergs/cm-s/K, insolation extinction coefficients of .1 an .2 cm and pore sizes of 1 and 10 microns in various combinations. Sample results are shown in figures 1 and 2. The temperature for the time of day that gives the maximum surface temperature is shown in figure 1 for various cases, and the vapor fluxes for the same conditions and cases are shown in figure 2.

The thermal conductivity is the most important parameter in determining the magnitude of the "solid state greenhouse effect". A very low thermal conductivity of 100 ergs/cm-s-K results in temperatures reaching the triple point of water at depths greater than 7 to 15 cm on Europa depending on time of day. Maximum surface temperatures range from 98 to 108 K for these cases. A thermal conductivity of 1000 ergs/cm-s K results in maximum temperatures of 141 to 174 K depending on the optical opacity. Maximum surface temperatures are slightly less than 110 K for these cases. Phase changes and vapor transport in the porous ice greatly reduce the "solid state greenhouse effect in water ice compared to that which would occur in translucent, nonvolatile materials. Maximum vapor fluxes are 4*10**(-7) or 4*10**(-8), for 10 and 1 micron pore sizes, and occur at depths slightly above where the triple point of water is reached for the cases of low thermal conductivity. Maximum vapor fluxes are five to seven orders of magnitude less for the cases of high thermal conductivity. Above the depth of maximum vapor flux, the vapor fluxes decrease rapidly as the surface is approached, and vapor is condensed, possibly causing the density of the ice very near the surface to slowly increase with time.

Although temperatures near the surface reach the melting point of water ice for the cases of low thermal conductivity, the vapor in the pores at these depths is transported to colder locations nearer to the surface where it condenses. This acts as a release mechanism to permit gas to escape from ice at higher temperatures. Almost no gas can escape at the very cold surface, since it condenses before it gets there. Additional heat supplied to the ice at the melting point of water ice can be carried away with the escaping vapor, maintaining the gas pressure in the pores at the equilibrium vapor pressure. As liquid water droplets form, they are quickly vaporized to maintain the equilibrium vapor pressure against the escaping gas. At greater depths, the pressure of the overlying crust would compress the ice, reducing the porosity and eliminating the flow passages in the ice. The vapor would no longer have access to colder locations where it can condense. Under these conditions, the pressure can increase, allowing liquid water to exist as a stable phase at greater depths.

References

Brown, R.H. and D.L. Matson. Thermal effects of insolation penetration into the regoliths of airless bodies, Icarus 72, 84-94, 1987.

Carr, M.H. Stability of streams and lakes on Mars. Icarus 56, 476-495, 1983.

Clow, G.D. Generation of liquid water on Mars through the melting of a dusty snowpack. Icarus 72, 95-127, 1987.

Matson, D.L. and R.H. Brown. Solid state greenhouses and their implications for icy satellites. Icarus 77, 67-81, 1989.

Table 1. Cases Studied

Case No.	Phase Changes and Convection Included	κ (erg cm $^{-1}$ sec^{-1} K^{-1}	ζ (cm)	r_o (μm)
1	No	100	5	N/A
2	Yes	100	5	10
3	Yes	100	5	1
4	Yes	100	10	1
5	Yes	1000	5	10
6	Yes	1000	10	1
7	Yes	1000	5	1

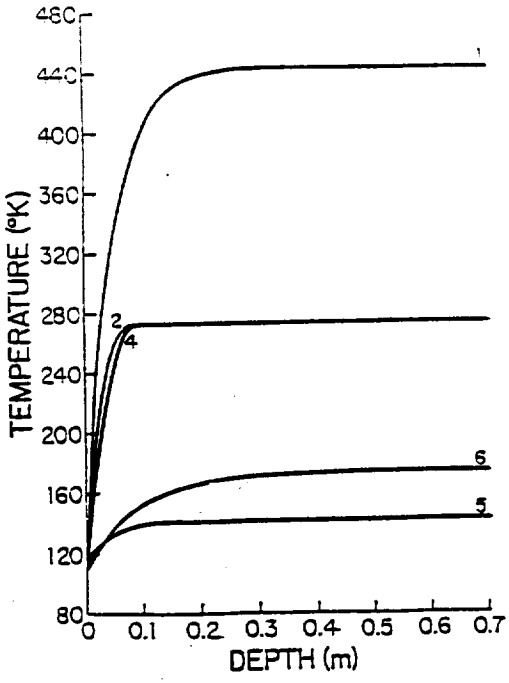

Fig. 1. Ice temperature vs. depth for time of day of maximum surface temperature for cases indicated.

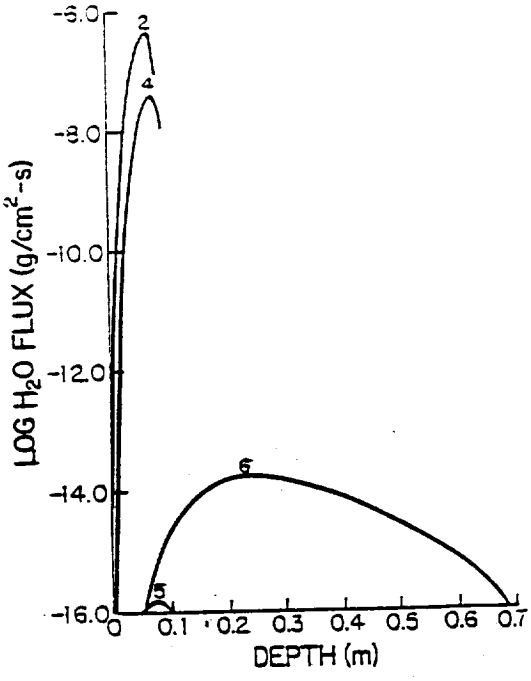

Fig. 2. Water flux vs. depth for time of day of maximum surface temperature for cases indicated.

PROGRESS IN SOLID-STATE GREENHOUSE MODELS FOR ICY SATELLITES. Robert Hamilton Brown (JPL/Caltech)

Telescopic Constraints on Models

Recently, models of the subsurface temperature distributions of icy satellites have suggested the possibility of a solid-state greenhouse effect. (Brown and Matson 1987; Matson and Brown, 1989). The effect arises primarily because insolation is absorbed over a finite distance in a regolith, rather than at the surface as is assumed by most classical thermophysical models. The magnitude of the effect, and the subsurface temperatures achieved as a result, may have important implications for geophysical models of high-albedo, icy bodies. This is because actual boundary-layer temperatures may in fact be significantly higher than those assumed in previous studies, facilitating interior melting of such bodies.

Because sunlight is allowed to be absorbed over a finite distance in an icy regolith, solid-state greenhouse models predict different shapes for both the cool-down and warm-up flux curves as compared to those predicted by models that don't allow for surface penetration of sunlight. Therefore, observations of eclipses of icy satellites in the thermal infrared can, in principle, constrain their near-subsurface temperatures. To this end several models, including solid-state greenhouse models, were fit to recently obtained, narrow-band observations of eclipses of Europa and Ganymede at 8.7 μm. These two bodies were chosen for the initial work because their albedos suggest that sunlight may penetrate their regoliths deeply enough to cause substantial subsurface heating beyond what is predicted by a classical thermal diffusion model. The new models are more detailed that those used in previous analyses of eclipse heating and cooling curves (see chapter by Morrison in *Planetary Satellites*). These models not only include solid-state greenhouse effects, but also take into account the fact that the Jupiter-facing hemispheres of Europa and Ganymede see eclipses during each orbit, while the anti-Jupiter faces do not. The models also take account the effects of the Jovian penumbra and the finite size of the satellite as Jupiter's shadow sweeps across it during eclipse ingress and egress.

Several models of the eclipse flux curves of Europa that assume no sunlight penetration into the regolith were examined, as well as models that allow sunlight penetration. To date I have not been able to find satisfactory matches to the eclipse flux curves with non-greenhouse models that either assume uniform thermal properties with depth or assume two-layers--an upper layer of low density and a lower layer of high density (similar to those used by Morrison and Cruikshank, and Hansen for Ganymede and Callisto). It is possible, however, to match the flux curves of Europa at 8.7 microns with a model that has uniform properties with depth and allows sunlight penetration with a scale length of about 1 centimeter. The resulting predicted greenhouse temperature of the subsurface at Europa's equator is ~140 $\pm$ 30 K and the predicted penetration scale length for sunlight is about 1 cm.

Laboratory Constraints

In a further effort to understand the solid-state greenhouse effect from a laboratory perspective, a series of simple laboratory experiments was performed. The experiments study the temperature response of 800-μm soda-lime glass beads in a vacuum of about 10^{-5} torr with carefully monitored boundary conditions such as the effective temperature of the radiation field seen by the surface of the bead bed. Preliminary measurements under vacuum indicate that inversions in the subsurface temperature profile are significant and permanent, providing strong confirmation of the solid-state greenhouse effect.

Using quartz halogen lamps as an illumination source with incident fluxes of about 0.1 w/cm^2 a solid-state greenhouse temperature inversion of ~70 ° K was observed peaking at about 6 mm below the surface of the bead bed. The inversion established itself within 30 minutes of the onset of illumination and was nearly 70 °K when the experiment was shut down 7.5 hours later. A simple greenhouse model that uses thermal parameters appropriate for soda-lime glass beads in a vacuum at pressures lass than about 10^{-5} torr matches quite well the transient response of the bead bed to the incident light. Although it was not possible to measure the temperature of the bead bed for the ~48 hours that it would have taken to approximately reach steady state, the model runs matching the transient behavior predict a steady state temperature inversion of ~150 K for this experiment. The modeling and measurements are ongoing.

Applications

One of the great surprises of the Voyager encounter with Neptune and Triton was the discovery of active volcanism on Triton. At least two active plumes were discovered, as well as several dark streaks in Triton's south polar regions. The dark streaks, although not seemingly active at present, may well be the recent remains of plumes similar to those that are presently active. The bulk of the dark streaks are concentrated in the regions near Triton's south pole at latitudes south of about -30 °. Because the active plumes are concentrated in areas presently in permanent sunlight, and because those latitudes are nearing summer solstice in the southern hemisphere, insolation as an energy source (or a trigger) for this volcanism is an attractive hypothesis.

I have been studying the efficacy of insolation-only mechanisms that involve trapping of solar radiation below a translucent, low-conductivity surface layer (variations on the solid-state greenhouse theme) and subsequent release of that energy in the form of latent heat of sublimation, as plausible candidates for driving Triton's plumes. Preliminary calculations show that either a classical solid-state greenhouse consisting of exponentially absorbed insolation in a layer of frozen nitrogen contaminated with small amounts of dark particulates, or a "super" greenhouse consisting of a relatively pure layer of solid nitrogen over a dark absorbing layer could provide large enough temperature differences to drive Triton's plumes.

Mechanisms involving geothermal heat, either in combination with insolation or as the sole energy source, could also be viable under certain conditions, but have the drawback that they do not readily explain the

latitudinal distribution of Triton's plumes and streaks. This difficulty can be mitigated to some extent if geothermal heat is thought to participate in a mechanism that is triggered by the added energy input of seasonal cycles of insolation.

CRYOVOLCANISM ON TRITON J.S. Kargel and R.G. Strom, Lunar and Planetary Laboratory, University of Arizona, Tucson, AZ 85721

Introduction. The Voyager 2 images of Triton revealed evidence of past cryovolcanic activity, some of it very recent in relative geological terms [1,2]. Observations of atmospheric plumes and associated dark streaks vented from the surface allow the possibility that explosive cryovolcanism was occurring at the time of the encounter (although non-volcanic explanations are also plausible [1]). Here we discuss some of Triton's cryovolcanic morphologies and a model of volatile-driven explosive ammonia-water volcanism.

Cryovolcanic morphologies. The most dramatic cryovolcanic features on Triton are the vast smooth-floored, closed depressions (Figure 1). Clearly some type of cryogenic "lava" has been extruded and contained by the lakes' walls. A complexly pitted region occurs near the center of the lava lake; an associated feature may be a collapsed lava tube. Similar pitted areas occur in Triton's other lava lakes. These pits could be indicative of late cryoclastic (explosive) volcanism. Low-relief domes are scattered across the lakes' floors. The morphologies of the lava lakes and of adjacent terrains indicate a multi-staged history of tectonic collapse and cryovolcanic flooding, sometimes with overflow onto adjacent regions.

Figure 2 shows a region characterized by deep, irregular, rimless volcanic depressions, with adjoining smooth areas. A highly viscous substance (or one with a high yield strength) produced flow front escarpments several hundred meters high and flowed around obstacles of comparable height. Two cryovolcanic craters in the region have associated collapsed lava tube-like features. One volcanic crater has a central lava dome, another indication of the immobile character of these cryolavas. Tectonic alignment of several craters suggests a similarity to terrestrial fissure eruptions. Triton's fissures are part of a global volcano-tectonic grid. Elsewhere, this grid is expressed as viscous dike-like intrusions and dike swarms (FDS 11396.27), broad linear volcanic plateaus, and lobate fissure flows, in one case 34 km long and 28 km wide (FDS 11394.51).

The unique "cantaloupe terrain" [1] consists of linear to quasi-circular ridges, aligned pits, and pitted ridges, all forming a net-like pattern crossed by the global volcano-tectonic grid. Thick flow-like features appear to emanate from the global fracture zone, extending for over 200 km and inundating parts of the cantaloupe terrain. Pitted ridges may be fissures along which explosive eruptions have occurred. Interspersed through this and other terrains are shorter dark flow-like features with little or no observable vertical relief. These units include the darkest material on Triton [1], suggesting a radiation-darkened carbonaceous composition quite distinct from the other, more predominant and apparently more viscous flows. Evidence for cryoclastic deposits include a major fracture which appears to be subdued by mantling material at its northeast end (FDS 11395.09), and other smooth, subdued terrain nearby.

Cryolava compositions. The high apparent viscosities of the erupted liquids argues against liquid N_2, CH_4, or CO, or mixtures of them, as the dominant chemical constituent. Pure water, even with suspended ice, is probably also much too fluid to generate the thick lava flows and domes observed on Triton. Ammonia-water liquids containing other chemical constituents or suspended ice might have the required rheology [3]. Croft argues persuasively on independent grounds that Triton's cryolavas are fundamentally aqueous [4]. The similarities of the flow thicknesses on Triton, Miranda, and Ariel, especially after gravity scaling, suggests similar cryolava compositions.

Volatile-driven explosive cryovolcanism. Volcanic craters and plumes on Triton may indicate that many eruptions were explosive. This would require a minor or trace volatile component such as CH_4 or N_2 acquired, for instance, by partial melting in the presence of methane clathrate. Unfortunately, the solubility of these gases in ammonia-water mixtures is unknown; however, gas solubility data exist for pure water and liquid ammonia solvents [5-10]. The solubilities of CH_4 and N_2 in ammonia-water mixtures should be on the order of 0.1-2.0% by mass at 176 K and 500-1000 bars (corresponding to likely conditions of partial melting). The bubble content of an ascending magma increases rapidly as it nears the surface because of the pressure dependence of gas solubilities. The magma disintegrates into an accelerating gas-driven spray of cryoclastic particles if the bubble content exceeds about 75% by volume [11].

To illustrate the potential for explosive cryovolcanism on Triton, consider a simple model. Equate the hydrostatic pressure, P_{ext}, to the lithostatic pressure, $q_c gh$, where q_c is the crustal density (0.95 g cm-3), g is the gravitational acceleration (78 cm s^{-2}), and h is the depth. This simplifying assumption implies a specific shape to the conduit [13], but the general qualitative outcome of the model should not be lost for its specificity. The internal gas pressure in a bubble, P_{int}, has two components, P_{ext} and P_c, where the

latter is due to surface tension. An expression may be derived giving the volume fraction, u, of gas in the foaming liquid:

$u = [(XRT)/M(q_c gh+2c/r)]/\{[(XRT)/M(q_c gh+2c/r)] + 1/q_l\}$,

where X is the mass fraction of the volatile component, R is the gas constant, T = 176K, M is the volatile's molecular mass (16 for CH_4), q_l is the density of the liquid in the absence of suspended bubbles (about 0.95 g cm^{-3}), c is the surface tension of the liquid at 176 K = 72 dynes cm^{-1} [13], and r is the radius of the bubbles (we assume two values, 0.01 and 1 cm). Figure 3 shows that the critical 75% volume fraction of bubbles required for magmatic disintegration is achieved at a depth of about 40 meters for 0.1% CH_4 and 800 meters for 2% CH_4, almost independent of bubble size (surface tension turns out to be unimportant for satellites as large as Triton).

The salient point of Figure 3 is that explosive eruptions of ammonia-water magmas may produce craters some hundreds of meters deep and may vent ash clouds into the atmosphere of Triton if the magmas contain approximately 1% volatiles. Alternatively, phreato-magmatic interactions of ammonia-water liquids with surficial methane or nitrogen ice [14] may produce explosive cryovolcanic landforms.

Acknowledgements. We thank Steven Croft for hours of stimulating discussions. The first author gives special thanks to the Voyager Imaging Team for inviting me to participate in the last greatest encounter.

References. [1] Smith, B.A. et al., 1989, Science 246, 1422-1450. [2] Strom, R.G., S.K. Croft, and J.M. Boyce, 1990, LPS XXI. [3] Kargel, J.S. and S.K. Croft, 1989, LPS XX, 500-501, and submitted to Geochim. et Cosmochim. Acta. [4] Croft, S.K., 1990, LPS XXI. [5] Bolshakov, P.E. and E.S. Lebedeva, 1940, Acta Physicochimica U.R.S.S., 12, 501-512. [6] Davis, D.S., 1941, Ind. Eng. Chem., 33, 1454-1455. [7] Culberson, O.L., 1951, Petroleum Transactions, AIME, 192, 223-226. [8] Pray, H.A., C.E. Schweikert, and B.H. Minnich, 1952, Ind. Eng. Chem., 44, 1146-1151. [9] Lefrancois, B. and C. Vaniscotte, 1960, Genie Chimique, 83, 139-145. [10] Dean, J.A. (ed.), 1979, Lange's Handbook of Chemistry, 12th ed., Table 10-1. [11] Houghton, B.F. and C.J.N. Wilson, 1989, Bull. Volcanol. 51, 451-462. [12] Wilson, L. and J.W. Head III, 1981, Jour. Geophys. Res., 86, 2971-3001. [13] Efremov, Yu.V. and I.F. Golubev, 1962, Zh. Fiz. Khim. 36, Part 2, 999-1000. [14] Stevenson, D.J., 1982, Nature, 298, 143-144.

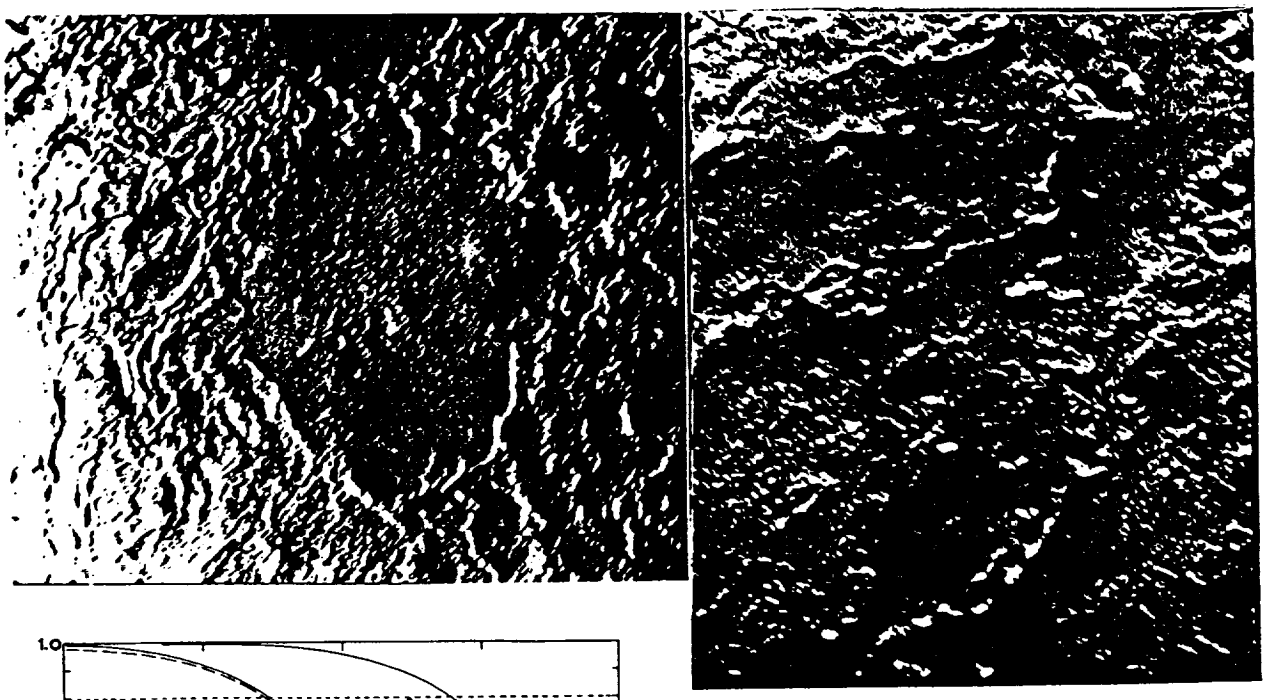

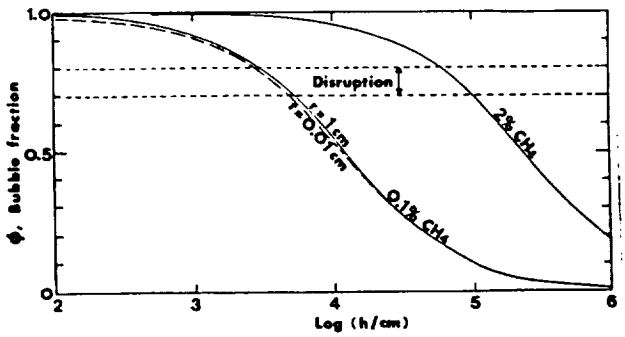

Figure 1. Cryogenic "lava" lake on Triton (above, left).

Figure 2. Volcano-tectonic fissures, explosive vents, flow fronts, and flow-mantled terrains on Triton (above).

Figure 3. Volatile exsolution model for 0.1% and 1.0% CH_4 in ammonia-water magma ascending in Triton (left).

Triton: Geology and Geologic History

S.K. Croft, Lunar and Planetary Laboratory, University of Arizona, Tucson, AZ, 85721.

Triton was revealed by Voyager 2 to have one of the most complex assemblages of surface features found on the icy satellites (1). An equally complex geologic history is implied. A preliminary geologic map (from which the simplified map in 1 is taken) and history are presented here.

Geologic Units. Figure 1 is a geologic sketch map based on the orthographic photomosaic in 1. Many of the units are gradational into each other, so some of the boundary lines are approximate. The "cantaloupe " terrain is divided into two subunits: 1) ridged plains (Cr) characterized by linear ridge segments with rugged, often pitted, crests separated by smooth topographic lows, and 2) the dimpled plains (Cd), which also contain numerous sub-circular dimple-like depressions. The origin of the dimples is unknown, suggestions include circular volcanic constructs and old mantled impact craters. Three subunits of smooth plains are mapped: 1) smooth valley plains (Sv) occur on the floors of four terraced depressions, or "lakes". The plains are very smooth and embays all irregularities of the lakes' rims. A cluster of irregular pits (generally with a largest central pit) is found on each deposit. 2) The laminated smooth materials (Sl) occur in a zone around the equatorial lakes and consist of irregular flat areas at different elevations separated by scarps a few hundred meters high. Some of the scarps may be tectonic. 3) The high smooth plains (Sh) are flat to undulating smooth materials around several large quasi-circular depressions and strings of irregular rimmed and rimless pits reminiscent of terrestrial cinder cones along erupting fissures. The unit superposes everything else (except small impact craters) and appears to stand somewhat above the surrounding terrains. The patchy smooth (Ps) unit consists of rugged and pitted ridges surrounding patches of smooth material in topographic lows. The unit appears transitional between the smooth plains and the cantaloupe terrain, which it borders. The knobby materials (Tk) occur in large patches within and around the high smooth plains and consist of groups of roughly equidimensional knobs 3 - 5 km across located on the floors of irregular depressions. The mottled hummocky (Th) materials occur in a band south of the high smooth plains and appear to emerge from underneath the smooth materials. The "hummocks" include domes and smooth ridges typically 10 km across, and a few lobate structures associated with the raised ridge. The mottling is most apparent near the boundary with the polar units. The dark smooth material (Sd) is gradational with the darker material of the mottled hummocky materials, which it borders. The linear ridge materials (Rl) occur in strips of single or multiple ridges 20-25 km wide, a few hundred meters high, and up to 1000 km long. The ridge materials are smooth and may have lobate edges. The bright spotted terrain (Bs) is a polar unit characterized by a matrix of very high albedo materials within which darker spots shaped like water droplets on oil occur. The dark spots stand high, and are quite rigid: impact craters are preserved in them. The bright materials have variable thicknesses: the coating on the spots is thin enough (a few meters) to allow the darker albedo to show through, whereas in the lows between the spots, the materials are thick enough (tens to a hundred meters) to bury piece-wise a 5 km wide ridged trough that passes from the smooth dark terrain into the polar deposits. The bright rough terrain (Br) is also a matrix of bright material with imbedded dark rugged ridges. The unit appears to be ridged cantaloupe terrain with bright polar material filling the topographic lows. The bright streaked terrain (Bst) is relatively featureless except for the oriented dark streaks. The features of the spotted and rough bright units disappear gradually into the streaked unit, suggesting burial with increasing southern latitude by an ever thickening layer of polar materials. Dark lobate materials (Ld) are very dark (albedo 0.2) deposits occurring in small patches typically a few kilometers wide and up to 10 km long. The patches occur in a broadly elongate field about 800 by 1000 km near the center of the map. The deposits superpose everything except the bright deposits, so they are geologically late.

The bright materials are interpreted to be seasonal (1). The various smooth, knobby, linear ridge, and dark lobate deposits are interpreted as cryovolcanic (1,2). The origin of the cantaloupe terrain is uncertain, particularly the dimples. Proposals include heavily modified impact craters and some form of cryovolcanism.

Geological History. Crater-count statistics are poor on Triton (3), thus geochronologies must rely primarily on superposition relationships. The presumed earliest stage of Triton's history, the era of heavy cratering, has largely been erased. The oldest recognized surface on Triton is the cantaloupe terrain. The ridged and dimpled units grade into each other, so their relative ages are uncertain. The

dimples exhibit a range of preservation states, so they are among the last features to form on the formed on the unit. The cantaloupe terrain is superposed by all adjacent units, but its original extent is poorly constrained. If the bright rugged terrain is merely blanketed cantaloupe terrain, then the unit may have originally covered much of Triton's surface. The linear ridges are generally superposed on the cantaloupe terrain, though at least one dimple overlaps a ridge. The mottled hummocky terrain overlies the cantaloupe terrain at their single contact near the "Y" ridge, and buries the ridge itself to the east. The smooth dark terrain appears to overlie the hummocky terrain, though the contact is gradational. The association of the smooth unit with the ridge suggests a genetic relation. The relation between the hummocky materials and the patchy-smooth unit is indicated by a graben which crosses the former units but disappears in the patchy smooth materials. The smooth units to the north superpose the hummocky materials and at least some of the patchy smooth materials. The highland unit is the oldest of the smooth units, based on crater counts (the only relation so established). It is associated with the strings of rimless and rimmed irregular pits and represents a major phase of volcanic activity. The laminated terrain units are contiguous with and in part younger than the highland unit. The youngest of all is the valley smooth units on the floors of the "lakes". The knobby materials, which appear as collapsed sections of the smooth units formed sometime during the deposition of the smooth terrains. The dark spot materials also formed fairly late in this era. The bright polar units are the last form. The bright material of all polar units and the equatorial bar (not mapped) appears to mantle pre-existing units by varying thicknesses roughly correlated with the distance from the pole. The dark streaks, which lie on the bright materials. Unfortunately, an absolute age cannot be established. They may have been active in recent times. They may also be related to the extrusion of the indefinitely late dark lobate deposits to the north. The equatorial bar of bright material appears to overlie everything, and is thus the most recent feature.

References. 1. Smith, B.A. and the Voyager Imaging Team (1989) Science,246:1422-1449. 2. Croft, this volume. 3. Strom, R.A., S.K. Croft and J. Boyce, this volume.

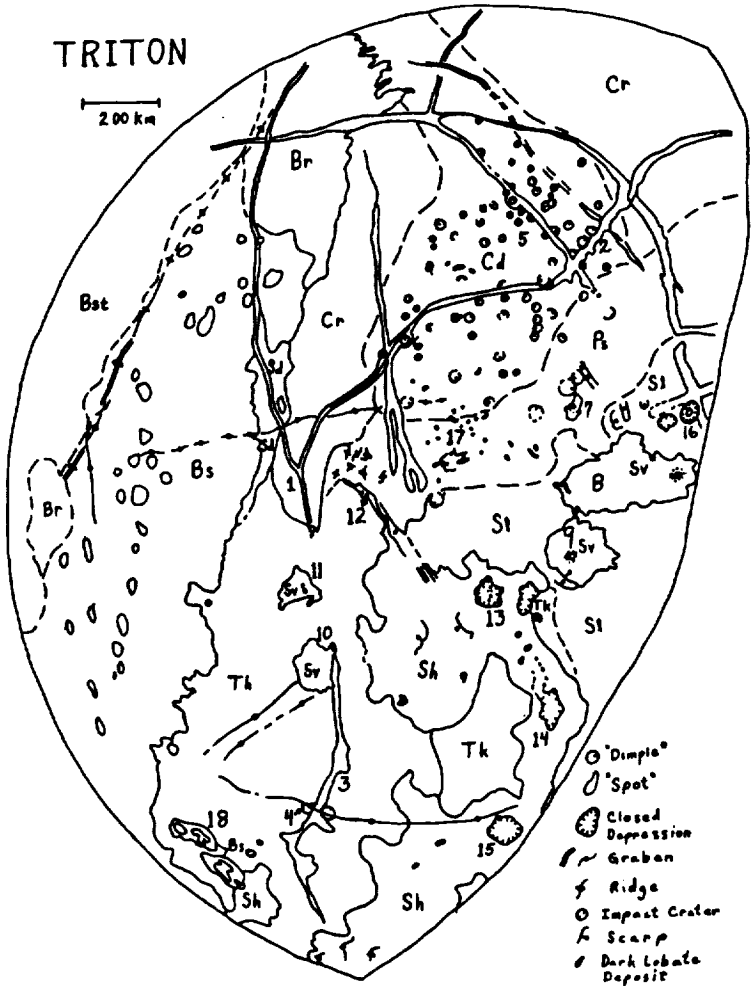

Fire and Ice on Triton: models for Cryovolcanism and Glaciology

Steven K. Croft, Lunar and Planetary Laboratory, University of Arizona, Tucson AZ, 85721.

The majority of features on Triton's surface can be interpreted as cryovolcanic in origin based on morphology and distribution (1,2). Several important facets of the physical and chemical nature of the extrusive activity can be addressed on the basis of the morphology, remote chemical sensing, comparisons with terrestrial volcanological phenomena, and estimates of bulk composition.

Bulk Composition and Interior Structure. The density of Triton is 2.07 g/cm^3, near that nominally predicted for objects formed in the solar nebula, as contrasted with objects formed in local planetary nebulae which would have densities near 1.3, like the smaller saturnian satellites. Solar nebular objects consist primarily of water ice and (presumably) carbonaceous chondritic rock, but are somewhat poorer in H_2O ice than planetary nebular objects because carbon is primarily in the form of CO (and nitrogen is in the form of N_2), which "absorbs" a lot of oxygen that would otherwise form H_2O. In planetary nebular objects, carbon is primarily in the form of CH_4 and nitrogen is in ammonia. Triton is not a purely a solar or planetary object since both nitrogen, associated with solar nebular materials, and methane, usually associated with planetary nebular materials, have been detected in Triton's atmosphere. Neither ammonia nor CO have been directly detected, but the presence of their respective nebular counterparts, methane and N_2, in the atmosphere suggests both may be present (there is indirect evidence for ammonia, see below). The high density of Triton precludes significant incorporation of the pure ices of CO, N_2, or CH_4 ices (which would yield a density near 1.2), but all of these ices could have been incorporated in minor amounts in Triton during accretion as trapped molecules in a dominant water-ice clathrate or as ammonia hydrate.

H_2O has not been detected on Triton's surface. However, surface topography implies the presence of water ice. Observed vertical topography of cliffs, ridges, knobs, and depressions in all of Triton's surface units except the polar and smooth "lake" materials is typically hundreds of meters up to near 800 meters. Impact craters are preserved in the smooth materials, ranging in depths from hundreds of meters to near 1.5 km. Based on the measured rheological properties, such topography could only be preserved for a few years if the crust and smooth materials were composed primarily of solid methane, even at Triton's frigid temperatures. Only bumps and ledges a few meters high could be preserved for millions or billions of years if methane were the primary crustal material. Measurements of the viscosity of pure solid ammonia indicate ammonia to be even "softer" than methane at Triton surface conditions, in spite of ammonia's significantly higher melting point. The rheology of solid N_2 and CO have not been measured, but estimates of their creep properties based on isomechanical scaling (3) with other molecular ices (H_2, neon, argon, krypton, CH_4, NH_3, CO_2, and H_2O) indicates that they should be two to three orders of magnitude softer than methane under similar conditions. Of the likely crustal ices, only water ice or water-dominated ammonia-water ice can preserve the observed topography, thus H_2O must be the primary component of both the crustal materials and the smooth "lake" deposits.

The extensive resurfacing on Triton implies that its interior is largely differentiated. The resurfacing by water ice implies that ice did not dominate Triton's interior convective heat transport, allowing temperatures to rise sufficiently to melt and drive out interstitial ices. Once begun, differentiation would tend to fall into a positive feedback loop: removing ice from the core would raise the effective viscosity, which would force the temperature up, which would tend to remove more ice, etc., driving the differentiation to near completion. This must be tested by further modeling, however. If differentiated, Triton's interior consists of two layers: a primarily H_2O ice mantle about 350 km thick over a rocky core about 1000 km in radius. (There is probably a thin layer of mixed rock-ice at the boundary.) This assumes a rock density of 3.6 g/cm^3 and an ice density of 0.92 g/cm^3; various assumptions about the hydration state of the rock do not greatly affect this result. The pressure at the bottom of the ice layer is about 1 kb, thus no ice II or higher density phases were present in this model when the ice mantle formed, though a thin layer of ice II may have formed later as the satellite cooled off. The computed thickness of any ice II layer is strongly dependent on the adopted phase boundary between ice Ih and ice II, which is poorly known at temperatures relevant to Triton's upper crust. The central pressure for this model is about 19 kb and the corresponding mass fraction of rock is about 0.72. The heat driving the differentiation may be due to radioactive heating or a Goldreich-type tidal heating event(4). In either case, differentiation would have begun near the center, first driving out any pure deposits of the light ices CO, N_2, or CH_4, then any ammonia in an ammonia-water melt, then the rest of the light ices and water ice as the clathrate melted. The sequence of melting would have repeated as melting progressed outward. The materials comprising the observed cryovolcanism probably came from the outermost (and last) layer of mixed ices and rock to melt, after the bulk of the ice crust had formed. Thus the observed cryovolcanism may have involved all of molecular ices. Interestingly, the rock core itself is large enough to have undergone some melting of interior rocks, possibly leading to localized rock volcanism at the ice/rock interface. Since the ice crust is relatively thin, the surface may be affected by such an episode. Speculatively, the large "lakes" may represent local remelting of the ice crust over a rock volcanism zone.

Minor Compositions of the Cryomagmas. The morphologies of some of the cryovolcanic deposits provide indirect indicators of composition. There is a range of viscosities represented by the cryovolcanic deposits. The smooth material of the "lakes" is very flat (except for a few clusters of depressions that may be due to subsurface drainage) and embays all bordering irregularities without visible topographic "lips" to the limit of resolution. Thus this material had low viscosities at the time of emplacement. Conversely, the high-standing linear ridges and light lobate deposits in the patchy-smooth and hummocky materials appear to be extruded materials hundreds of meters thick, indicating high viscosities at the time of emplacement. Direct estimates of the internal viscosities of the thick flows cannot be made, but the thicknesses of the edges of the flows imply yield strengths at the time of flow stagnation of the order of a few tenths of a bar, in the middle of the observed range of yield strengths for terrestrial lava flows. For

terrestrial magmas, internal viscosities correlate roughly with yield stresses (the physical relationship is not well understood). Since the mechanics and yield stresses of the flows on Triton (though certainly not the compositions) are apparently similar to those of terrestrial flows, the viscosities of the flows on Triton are probably also similar, of order 10^6 poise. The viscosities of pure molecular liquids (i.e., pure methane, water, etc.) are very low (order 10^{-2} poise). Viscosities high enough to generate very thick deposits have been found only in partially congealed mixtures of substances: to date only ammonia-water and mixtures of ammonia-water with small amounts of other substances have been confirmed to generate viscosities sufficiently high(5). Thus the ridges and lobate deposits may indicate the presence of small amounts of ammonia mixed in the melts. Crater statistics and superposition indicate that the smooth "lake" materials are generally younger than the ridges and lobate deposits. Thus the more viscous materials may represent early melts containing ammonia, while the late "lakes" materials may be water-rich melts that were generated after the ammonia was exhausted in the melt-generating regions. The composition of the "spots" and the lobate dark deposits are unknown. Their morphologies are different from the other cryovolcanic materials, suggesting a distinct composition. The melts are stratigraphically late, suggesting that they are late, high temperature (200 - 300 K?) melts. One possibility for the composition of these deposits are the paraffin-like compounds found in small amounts in carbonaceous materials. Such compounds have appropriate melting points, densities low enough to rise through an ice crust, viscosities high enough to make the lobate forms, and carbon capable of darkening with time to the observed albedos.

Nature of the "Volatiles". Several morphologic forms indicate cryoclastic and possibly explosive cryovolcanism (2), which implies the presence of materials much more volatile than H_2O. The primary candidates are CH_4, CO, and N_2. At eruption temperatures characteristic of water-rich cryomagmas (270 K), these gases dissolve at levels similar to H_2O in terrestrial magmas. Solubility increases with increasing pressure, reaching concentrations of several weight % at one kilobar, the approximate pressure at the presumed last melt zone at the rock/ice interface. Exsolution of the gases at these concentrations upon nearing the surface will generate particulate ejection velocities of 300 to 500 m/s, just in the range needed to produce cryroclastic ejecta blankets in the observed diameter range of a few hundred kilometers. The liquids of CH_4, CO, and N_2 are all buoyant in an H_2O crust and will exist as liquids at depths of a few to a few tens of kilometers in Triton's crust for likely thermal gradients. The vapor pressures of N_2 and CO at 270 K are 5-10 kb (comparable to steam in terrestrial magmas), sufficient to blast off lids of ice several kilometers thick. Thus liquid water penetrating pods of liquid N_2, CH_4, or CO at depth would be capable of maar-like explosions, possibly producing features like the dimples of the cantaloupe terrain.

Vent Shape. One of the surprises on Triton was the presence of circular cryovolcanic vents similar to terrestrial vents in addition to the linear vents characteristic of cryovolcanism on the other icy satellites. Mechanism changing the initial linear vents on earth to circular vents include: a) thermal stress driving wall failure, b) volatiles in the wall rocks driving wall failure by vaporization, and c) thermal melting and erosion of the walls. These mechanisms have not yet been thoroughly evaluated for cryovolcanism in an ice crust. Thermal stresses are apparently not important since similar temperature rises would occur during cryovolcanic intrusion on all the icy satellites, whereas circular vents are not common. Volatile expansion may be the case on Triton, but this implies no "volatiles" on the other icy satellites. Thermal erosion may work if Triton's cryomagmas are water-rich while those on the other icy satellites are not. Work on this problem is in progress.

"Glaciers"?. The rheological differences between water ice and other molecular ices indicate that the roll water ice plays in Triton's geology is similar to the roll of rock on Earth, while the roll of methane and nitrogen ices is similar to the roll of temperate water ice; in other words, layers of methane and nitrogen ices more than a few meters thick on Triton would flow downhill in a glacier-like fashion and collect in low spots. No "glaciers" or glacial features have been seen on Triton. However, the stresses at the bases of layers of methane and nitrogen snow thick enough to flow are very small (of order 10_{-3} bars), hence little mechanical erosion of the kind associated with terrestrial glaciers is expected. Also, fissures and surface deformations associated with the very thin elastic layers (of order a few meters) would be small, probably below the resolution available for Triton, thus "glacial" deposits on Triton would be difficult to recognize. However, many surfaces on Triton are characterized by isolated rugged ridges separated by smooth-floored valleys. The bright material of the polar caps, which are probably "snows" of methane and nitrogen, preferentially occupy low spots near the edge of the polar cap. Such low-lying smooth materials may represent methane and nitrogen ices that have flowed "glacially" onto the topographic lowlands, obscuring any pre-existing roughness.

References. 1. Smith B.A. et al. (1989) Science 246: 1422-1449. 2) Croft, S.K. Physical volcanism on Triton. This volume. 3) Frost, H.J. & M.F. Ashby (1982) Deformation-mechanism Maps: the plasticity and creep of metals and ceramics. 4) Goldreich P. et al. (1989) Science 245:500-504. 5) Kargel J. et al., in preparation.

Physical Cryovolcanism on Triton

Steven K. Croft, Lunar & Planetary Laboratory, University of Arizona, Tucson, AZ 85721.

Triton has a bewildering variety of surface features and resurfaced areas that are cryovolcanic in origin. Cryovolcanism is differentiated from ordinary volcanism in that the fluid materials are molecular ices such as water, ammonia, methane, etc., rather than silicate rocks. Probably most of the basic physical processes are the same in cryovolcanism and volcanism, but there may be some differences due to differences in the material properties of the "working fluids". Comparison of volcanological landforms on the icy satellites and the terrestrial planets should give clues to the similarities and differences between cryo- and terrestrial-volcanic processes. Many of the features on Triton are remarkably similar to terrestrial volcanic forms (1), implying similar processes, whereas some of the extrusive forms have no known terrestrial counterparts. This abstract describes the variety of morphologic forms and possible mechanisms; another abstract (2) describes models and materials. The features discussed are located by an identifying number in the geologic sketch map in (3).

Linear Ridges and Troughs: These features form an open, somewhat rectilinear, network over nearly the entire imaged face of Triton. Individual ridges range from several hundred to at least 2000 km long. The widths vary from about 10 to about 30 km, and the heights up to a few hundred meters. The structures range from parallel paired ridges (near #1 in ref. 3) to triple and multiple ridges (#2), to single, broad ridges (#3). The ridges have been interpreted as leveed flows or dikes in various stages of extrusion of viscous ($\approx 10^6$ poise) materials. The preferred interpretation here is that of dike extrusion. However, the dikes are too long to be surface piercements of fluid-filled penny-shaped elastic cracks, so they are interpreted to be laterally propagating dikes similar to the Abitibi dike in Canada or the Great Dike in Africa. At least one recognizable lobate flow (#4) connects directly back to one of the broad ridges. Numerous small hummocks and lobate ridges morphologically similar to the lobate flow fill the adjacent area to the south, suggesting an extended area of deposition from the ridge.

Cantaloupe Dimples and Pits: The dimples in unit Cd (around #5) form a field about 1000 km across of similar-dimension structures typically 20-40 km in diameter. Individual dimples are typically fairly shallow, quasi-circular depressions with raised rims. The dimples show a variety of morphologies: floors are rough, smooth, pitted, or contain small mounds; the depressions are single, double concentric, and overlapping; the rims are simple concentric ridges and rugged, irregular peaks. The area has been interpreted as a heavily modified portion of heavily cratered terrain or as a collection of some type of cryovolcanic craters. I suggest that the craters are maar-like explosion craters grouped in a typical volcanic field similar to the Pinacate or Hopi Butte volcanic fields on Earth. Terrestrial maars show the variety of morphologies seen in the dimples. At least one dimple (#6) is doubled, with the outer ring being cut by a linear ridge and the inner ring cutting the ridge, indicating at least two distinct periods of activity in the same location, a situation most easily explained by endogenic activity. The normalized size distribution and field-diameter/crater-diameter ratio is similar to that of terrestrial maars, and, interestingly, the mean diameter of the dimples is 25 - 35 times the mean diameter of maars on the Earth, whereas the ratio of surface density times surface gravity on Earth to Triton is about 30-35, implying similar pressures for explosive formation. Superposition relations between the dimples and the linear ridges indicate that there was partial contemporaneity between the two sets of features. The temporal mix of non-explosive features (the ridges) and explosive ones (the dimples) is similar to the mix in the terrestrial volcanic fields, implying time-variability in the explosive fluids at depth. The numerous smaller pits and craters (nominally 5-10 km across) in the cantaloupe terrain tend to occur in chains and along the rugged ridges. These features may represent smaller cryovolcanic structures such as degraded (cryo-)cinder cones, collapse pits, pseudocraters, or smaller explosion pits (*). At the eastern boundary of the cantaloupe terrain, an increasing portion of the low spots in the terrain appears flooded with a variety of smoother deposits that grade into the smooth deposits around the larger caldera (see below). Some of these features (e.g.,#7) appear as bulbous deposits with rounded edges a few hundred meters high that are distinct in texture from the other floor deposits. These may be local extrusions from vents in the craters in which the deposits lie. Their exact origin is unknown: #7 has a distinct lobate edge and lip at the eastern end and a pit (the source vent?) in the middle of the main lobe. The material may be very viscous flows from the pit, but there is no obvious lip on the boundaries of the deposit on the western end where it extends into an irregular crater with a rugged rim. Thus the source may be in the crater and the pit may be some type of explosion crater due to overriding a deposit of a volatile (solid N_2?). Alternatively, the deposit may be a (cryo-)volcanic dome, or a succession of thinner ground-hugging flows like a cryo-"nuees ardentes".

"Lake Caldera". There are four quasi-circular structures with smooth floors bounded with inward

facing scarps (#8,9,10,11). The smooth materials embay all irregularities and have no visible lips. Thus these materials were extruded at low viscosity, in contrast to the higher viscosities of the linear ridge material. Feature #9 has one well defined terrace at the eastern end indicative of at least two episodes of collapse. The overall structure bears considerable similarity to large caldera such as Kilauea and Olympus Mons. The circular portions of these features are all 150 - 200 km in diameter, comparable to the thickness of the underlying ice crust. Features #8-10 have small fields of rimless pits surrounding a largest pit about 20 km in diameter. It is suggested that these represent collapse depressions near the main source vent for each smooth floor deposit caused by drainback at the end of the eruption after the surface of the smooth deposit had solidified. Feature #11 has three equidimensional pit aligned along the old trend of the nearby linear ridge. The smooth deposit is not entirely contained by an inward-facing scarp, and extends without sharp boundaries into the hummocky terrain. The structure may be transitional between the "Lake " caldera and the "collapse" caldera (see below). Smooth material like the smooth floors of the "lakes" also occurs in a long fissure or graben (#12), indicating a possible fissure eruption of the low viscosity material.

"Collapse" Caldera. Another class of structures similar to terrestrial volcanic structures are features 13,14,15, and associated irregular pits and chains of pits. These features are quasi-circular depressions with smaller pits and depression within. They are surrounded by quasi-circular deposits of smooth materials that extend out 100 to 200 km from the main depressions. The entire ensemble is strongly reminiscent of collapse caldera and chains of eruption and collapse pits seen in linear volcanic zones on the Earth such as the Laki Fissure area in Iceland. The trends of the pit chains on Triton, like those on Earth, are along extensions of visible surface fractures, suggesting linear tectonic failure zones as ready vents for the cryomagmas. Indeed, there is a strong correlation between the location of most cryovolcanic structures and tectonic failure features on Triton. These smooth highland deposits are at least partially cryoclastic in nature: a) the edges feather out irregularly into the surrounding terrains, and b) topography near the edges of the deposits are "softened", the best example being feature #12 which has sharp, rugged topography at the western end that becomes progressively rounded and less distinct as it continues into the smooth deposit. Feathered edges and terrain softening are characteristic of lofted deposits rather than ground flows.

Dark Lobate Flows. Dark lobate materials are very dark (albedo 0.2) deposits that occur in small, sub-circular to elongate patches typically a few kilometers wide and up to 10 km long. The patches primarily occur in a broadly elongate field about 800 by 1000 km around #17. Individual patches occur as domes (like cinder cones) and lobate tongues in the hollows of the very rough cantaloupe and patchy smooth terrains. The features are reminiscent of very viscous extrusions on the Earth. A possible analog, even in terms of size, is the Chao Dacite flow in Chile.

Dark Spots. In contrast to the above features which have recognizable parallels in terrestrial volcanism, the dark spots are unlike anything else seen in the solar system. The dark spots are oval to somewhat irregular shaped spots with smooth, convex-upward edges scattered between about 20 and 40° south. The larger spots range from 30 to 80 km in diameter. The spots are reminiscent in shape and distribution of droplets of water splashed across an oil-covered surface. The spots are often (always?) surrounded by a border of lighter material. The prototype example of this feature is #18. Other unmistakable examples occur farther to the east and south. A broad band of oval spots extends through the southern half of the bright spotted polar terrain. These spots are partially obscured by a thin coat of bright material, but their shapes, distributions, and albedo are similar to the dark droplet type materials. In addition, many of the spots in the polar unit have bright borders recognizable under the thin coating. Thus the polar spots are also inferred to be dark droplet materials. If this interpretation is correct, then these materials are quite widespread, and the process forming them is an important one. The droplet materials are quite solid despite their appearance: the type areas have several well-preserved superposed craters. It is speculated that the units are extrusive, the borders being possibly thermally metamorphosed crustal materials (though at typical widths of several tens of kilometers the mechanics are obscure). If this is the case, the convex edges (order 100 m high) imply a fairly high viscosity at the time of emplacement.

References. 1)Smith B.A. and the Voyager Imaging Team (1989) Science 246:1422-1449. 2) Croft, S.K. (1990) Fire and Ice on Triton. This Volume. 3) Croft, S.K. (1990) Triton geology and geologic history. this volume. 4) Kargel J. and R.G. Strom (1990) This volume.

TITAN AND TRITON: THE BEHAVIOR OF ICES MORE VOLATILE THAN WATER

David J. Stevenson, Division of Geological and Planetary Sciences
Caltech, Pasadena, CA 91125 U.S.A.

Water ice is the most common volatile in the solar system and is the dominant component determining the morphology and behavior of most observable satellite surfaces in the outer solar system . However, there are at least two very interesting counterexamples where more volatile ices are playing a very important role: Titan and Triton. This is interesting for a variety of reasons, the most important being the insight that we can gain into the origin and early history of these bodies. I report below some recent efforts concerning Titan and Triton.

Hydrocarbon Storage on Titan It has been known since the Voyager encounter of Saturn that Titan must have a large reservoir of methane on or near the surface. This follows unavoidably from the observations of methane photolysis (and hydrogen escape) and the significant mixing ratio of methane in the troposphere. The equivalent of a global ocean $\sim$ 1 km in depth is required. Over geologic time, this ocean becomes more ethane rich (Lunine et al, 1983) thereby lowering the methane partial pressure in the atmosphere (but not the photolysis rate). Recent radar observations (Muhleman et al, 1990) strongly suggest that there is no global ocean: They find a strong reflection at least part of the time, analogous to that observed for water ice-dominated surfaces such as Ganymede. How can we reconcile the atmospheric and radar observations? The best prospect is subsurface storage of liquid hydrocarbons in a "regolith" of water ice. The macroporous regolith could be due to impact-generated rubble that has imperfectly sintered and compacted over geologic time, or it could be due to erosion: chemical weathering of the ice by the liquid.

Janusz Eluszkiewicz and I have modeled quantitatively these two processes. Compaction by itself is drive by power-law creep and is naturally more effective at depth where the overburden is greater. It is also possible that the temperature is larger at several kilometers depth. However, we find that the hydrocarbon "ocean" can undergo thermal convection in the permeable regolith, reducing the temperature gradient to an adiabat which is close to isothermal. Under these circumstances, a 3 km thick regolith that stores the equivalent of a 1 km thick ocean can survive for the age of the solar system at $T \lesssim 95$K. The biggest uncertainty with this model lies in the issue of whether the regolith was ever this thick. The process of cavernous weathering works in the opposite sense to compaction: It creates porosity at depth because the water ice is probably more soluble in methane that is under pressure than in methane that is unpressured. The parameters characterizing this process are exceedingly poorly known (and even the direction of the effect is conceivably wrong), but geologically-relevant erosion timescales are possible and may aid storage of the hydrocarbons. Storage in this fashion has many virtues: It satisfies radar constraints, tidal evolution constraints and is physically plausible. Cassini and the Huygens probe will test the correctness of this picture.

Thermal Evolution of Triton The remarkable images returned by Voyager pose several questions concerning the structure and history of Neptune's large moon. Amar Gandhi and I have sought to understand the history of Triton by constructing parametered convection calculations based on rock core and water ice-dominated mantle rheologies. Although the severe heating that accompanies capture may have melted all the water

ice, this heat spike is short-lived and does not seem to be relevant for understanding the regions of Triton surface that exhibit low crater counts. Instead, the high rock/ice ratio ($\sim$70:30) implies an unusually high chondritic heating and a long delay in the cooling and freezing of a water-rich ocean underlying an Ice I outermost shell. If NH_3 is present in the ocean then it becomes progressively concentrated as cooling progresses; at some point, the liquid becomes comparable or equal in density to the overlying ice and volcanism can take place. This resurfacing is late in geologic time and strictly related to radiogenic heating and the presence of ices more volatile than water. It is possible that the volcanism persists even now, but the "geyser" activity is probably unrelated to this because it is very shallow.

Rheology of Nitrogen and Methane Clearly the flow properties of these ices are important for understanding Triton's present surface and its evolution. Janusz Eluszkiewicz and I have constructed deformation maps, using existing data for methane and theoretical arguments based on homologous scaling for nitrogen. In both cases, we find that the creep is non-Newtonian (exponent $\sim$3) at the stress levels corresponding to kilometer topography. The relaxation time for this topography is short, typically of order 10^6 years for the relevant temperature ($\sim$ 40-50K), demonstrating that the observed topography must be supported by water ice-dominated materials. Conversely, an arrangement of nitrogen ice over methane ice is gravitationally unstable because the former is twice as dense as the latter. This "salt dome" behavior may lead to patchy exposure of CH_4 at the surface, despite the tendency of solar heating to place N_2 on top. Patches of methane may heat up relative to N_2 because they sublime less; these localized temperature variations may be relevant to understanding the "geysers".

References

Eluszkiewicz, J. and Stevenson, D.J. (1990a) submitted to G.R.L.
Eluszkiewicz, J. and Stevenson, D.J. (1990b) LPSC XXI Abs, 323.
Lunine, J.L., Stevenson, D.J. and Yung, Y. (1983) Science 222, 1229.
Muhleman, D.O. et al (1990) Science, in press.
Stevenson, D.J. and Gandhi, A. (1990) LPSC XXI Abs, 1202.

Pluto's Atmosphere is not Pure Methane: Composition and Cosmochemistry

Jonathan I. Lunine, University of Arizona, Tucson AZ 85721

Cosmochemical overview: The compositions of the atmospheres of Titan, Triton and Pluto contain information on the chemical state of the gases and solids which were present in the outer solar nebula at the time of formation. Although these bodies are all more highly evolved than comets, thereby obscuring the primordial record to some extent, they have the "advantage of place": relative to comets, we are fairly confident of the approximate location of formation of these three bodies. Models of the physical and chemical evolution of the surface and atmosphere are required in order to come closer to an estimate of the "bulk" initial volatile abundance than the atmospheric composition will provide. In the case of Titan, the sum total of the Voyager data can be used to construct a model of the surface, estimate the rate of photochemical conversion of methane to higher hydrocarbons, and derive an initial volatile budget for the surface-atmosphere system (1,2). This yields a CH_4 to N_2 ratio of order 10, as opposed to the atmospheric ratio of order 0.1. The atmospheric CO to N_2 ratio is 10^{-4}, and is probably photochemically-controlled (3). Together with the bulk density, these data indicate that Titan is very likely a product of the highly-reduced gas characterizing a proto-satellite nebula around the early Saturn, with the N_2 perhaps formed from ammonia (4). The recent Voyager flyby of Triton permitted the first assessment of that body's atmospheric composition; the CH_4 to N_2 ratio is 10^{-4} (vapor-pressure controlled) and an upper limit on CO/N_2 is 10^{-2}. Although Triton's bulk density and orbit are strongly suggestive of formation in the relatively-oxidized solar nebula, in which CO should be very much more abundant than CH_4, the atmosphere appears to be strikingly similar to that of Titan (correcting for vapor-pressure effects). A means of sequestering large amounts of CH_4 from the solar nebula gas has been suggested (5), but the absence of CO relative to N_2 is striking. It is in this context that the composition of Pluto's atmosphere is of high interest.

Detection of a heavier gas: While Pluto has long been known to have CH_4 on its surface or in an atmosphere (6), the first direct detection of an atmosphere was made by a stellar occultation observed from the ground in June, 1988 (7,8). Although such an occultation yields temperature and molecular weight as a combined quantity, it is possible to separate the two if the temperature profile can be computed. Assuming the atmosphere is at least partially methane allows a simple temperature profile to be constructed based on absorption and reradiation of solar infrared photons. From such a calculation (9), Roger Yelle and the author concluded that Pluto's atmosphere has a mean molecular weight of between 22 and 28, significantly higher than that of methane. On the basis of the surface temperature, and vapor pressure considerations, nitrogen and carbon monoxide are the two likely candidates. Unfortunately, one cannot distinguish between the two; yet knowing whether the heavier gas is predominantly CO or N_2 is clearly of the highest interest.

The temperature profile and the occultation light curve: The light curve recorded by the KAO during the stellar occultation shows a break in slope near the base of both the ingress and egress curves; below the break the decrease in starlight becomes much steeper. William Hubbard, in collaboration with Yelle and the author (10), used the temperature profile derived in (9) to synthesize occultation light curves. They showed that the steep decrease in temperature from the region of methane heating down to the surface could reproduce the occultation curves. An alternative proposal is that near-surface haze may be dimming the starlight. John Stansberry and Marty Tomasko, in collaboration with the author (11), constructed a model of photochemical haze production in Pluto's atmosphere; they concluded that for all but extreme conditions, such a haze could not produce sufficient optical extinction ot explain the shape of the occultation curve.

State of volatiles on Pluto's surface: The total pressure at Pluto's surface, combined with a temperature in the 50 to 55 K range (12), suggest that atmospheric methane is in saturation equilibrium with surface frosts of predominantly methane composition. Conversely, both nitrogen and carbon monoxide are so volatile that, in pure form, their surface ices would have vapor pressures of millibars at Pluto's surface temperature. The restriction on surface pressure implies that these gases are not in equilibrium with surface ices. Any methane ice on the surface would accomodate a few tenths of a percent of either CO or N_2 measured pressure; if the methane ice is sufficiently thick this could be a significant reservoir. Alternatively, the CO or N_2 may be supplied from a clathrate hydrate or subsurface outgassing, or CO may be derived chemically from CO_2. In any event, escape calculations suggest that these gases, like methane, must be resupplied to the atmosphere.

References (1) Lunine, Stevenson and Yung, Science 222, 1229, (1983); (2) Lunine, in The Atmospheres of Saturn and Titan, ESA SP-241, 83 (1985); (3) Samuelson et al., JGR 88, 8709 (1983); (4) Atreya, Donahue and Kuhn, Science 201, 611 (1978); (5) Lunine, in Origin and Evolution of Planetary Systems, Cambridge, 213 (1989); (6) Cruikshank, Pilcher and Morrison, Science 194, 835 (1976); (7) Hubbard et al., Nature 336, 453 (1988); (8) Elliot et al, Icarus 77, 148 (1989); (9) Yelle and Lunine, Nature, 339, 288 (1989); (10) Hubbard, Yelle and Lunine, Icarus, in press (1990); (11) Stansberry, Lunine and Tomasko, GRL 16, 1221 (1989); (12) Sykes et al., Science 237, 1336 (1987).

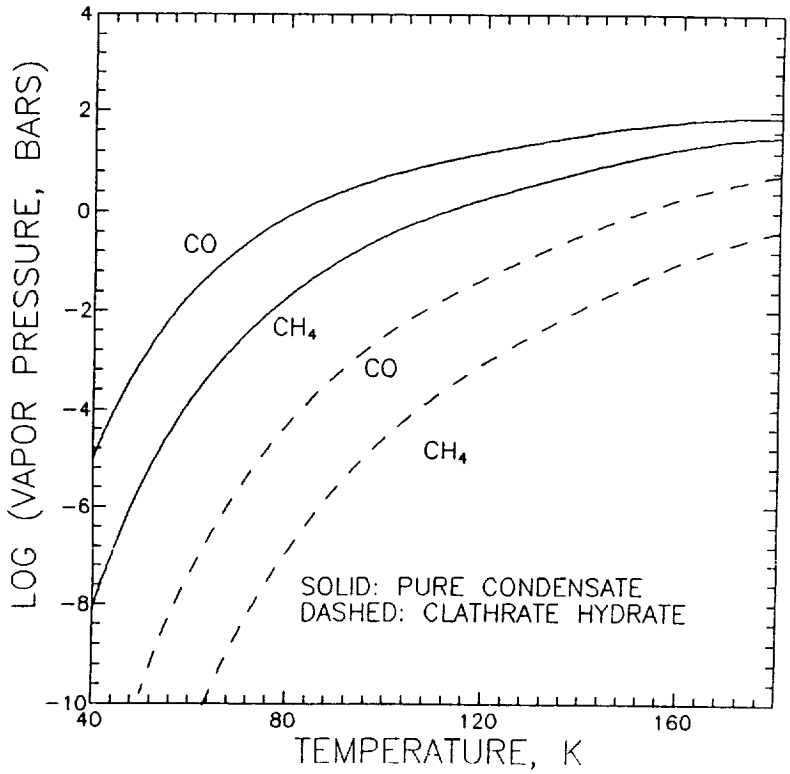

Figure 1: Vapor pressures versus temperature for CH_4 and CO (N_2 is very similar to CO on this scale). The temperature of Pluto's surface is between 50 and 55 K. From (10).

A POST-VOYAGER VIEW OF NEPTUNE'S RING ARCS.

Philip D. Nicholson, Space Sciences Building, Cornell University, Ithaca, NY 14853.

In July 1984 Neptune joined the family of 'ringed' planets, with the discovery during a stellar occultation of a narrow, asimuthally extended, partially transparent structure orbiting the planet at a distance of ~ 67000 km,or 2.8 R_n. The most puzzling aspect of this observation was the lack of any detectable feature in the data at the point where the star again crossed this orbital radius, which led Hubbard *et al.*, (1986) to dub this feature an 'arc', rather than a ring. Since 1984, data from ~ 20 stellar occultations by Neptune have been examined, at least 6 of which have yielded additional evidence for incomplete rings, or arcs. In only 3 cases, however, was the putative arc occultation observed at more than one telescope, and for 2 of these the data are of relatively poor photometric quality. The sole remaining unambiguous arc observation occurred on 20 August 1985. In no experiment has a complete ring been observed.

Voyager images have now revealed the actual distribution of ring material around Neptune: the'arcs' or incomplete rings inferred from ground-based stellar occultations now appear to be due to three longitudinal clumps in the outer ring, 1989N1R (radius = 62900 km), each 4-10 deg long, and spanning a total range of 33 degrees. Further data has come from the UV stellar occultation observed by the Voyager UVS and PPS instruments (Broadfoot *et al.*, 1989; Lane *et al.*, 1989), which both detected the leading arc; the measured width of 15 km and mean optical depth of 0.05 are compatible both with the ground-based near-IR data and with parameters inferred from visual images (Smith *et al.*, 1989).

With the revised Neptune pole direction inferred from Voyager tracking of the inner satellites (Owen, 1989, *priv. comm.*), the radii of three ground-based arcs from 1984-1985, including both of the independently confirmed observations, are found to match the radius of the outer ring to ± 100 km. Moreover, these same three cuts fall within a narrow longitude range of 12.6 deg, when extrapolated to a common epoch using the Voyager-derived arc mean motion. An examination of all the available occultation data has shown only two additional cases in which a star crossed the 33 deg arc region, apparently threading a gap between the arcs. By extending the time baseline of the Voyager arc model to include the ground-based occultation data, an improved arc mean motion of 820.1185 deg/day has been derived (Nicholson *et al.*, 1990), corresponding to a semi-major axis of 62932.3 km. The distribution of ground-based occultation cuts across the arc region of 1989N1R is compared in Figure 1 with the Voyager arc model, as a function of the assumed mean motion.

REFERENCES:

Broadfoot, A. L., *et al.* (1989). *Science* **246**, 1459.

Hubbard, W. B., *et al.* (1986). *Nature* **319**, 636.

Lane, A. L., *et al.* (1989). *Science* **246**, 1450.

Nicholson, P. D., *et al.* (1990). *Icarus* (in press).

Smith, B. A., *et al.* (1989). *Science* **246**, 1422.

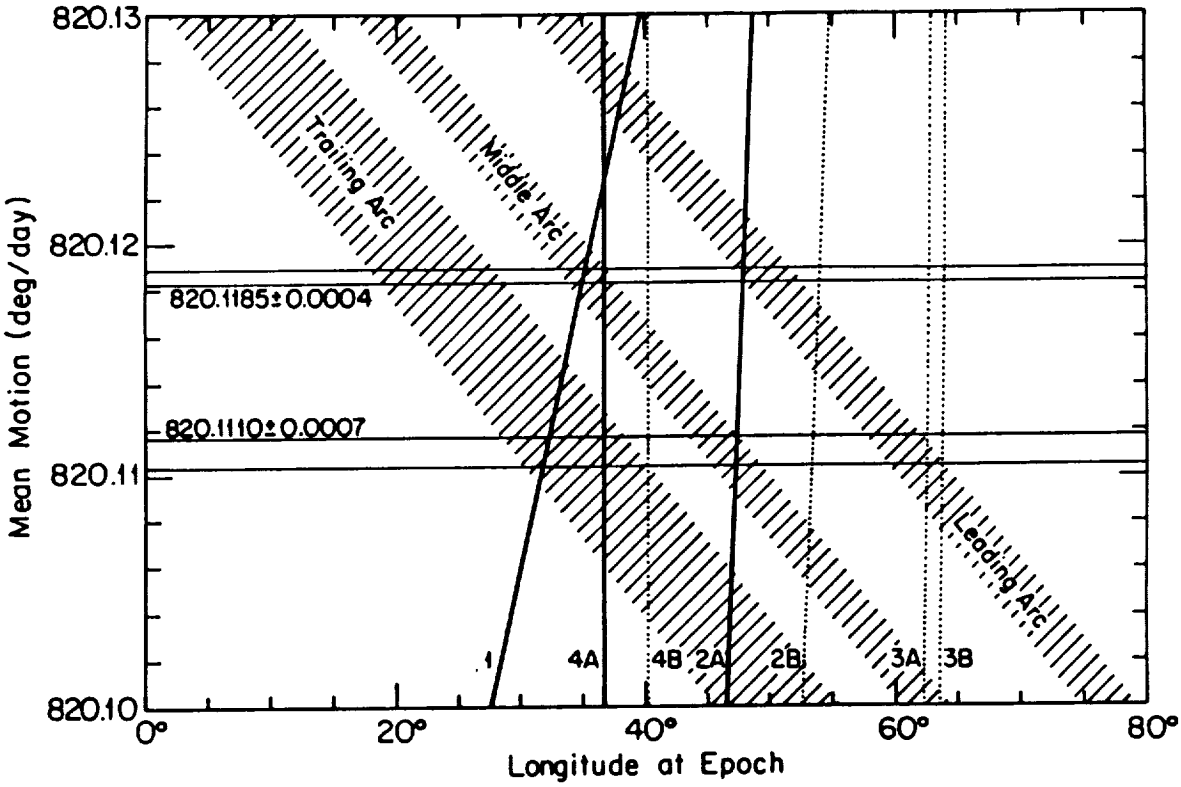

Figure 1. Longitudes of stellar occultation cuts across the Neptunian ring 1989N1R, corrected to a common epoch of 20 August 1985, 6:53:49.3 UTC. Solid lines indicate positive arc observations; dotted lines cuts for which no arc occultation was observed. The hatched diagonal bands indicate the three arcs observed in Voyager images in August 1989, projected back to the same epoch. Matches between the occultation data and the Voyager images occur for mean motions of 820.1185 and 820.1110 deg/day. Key: 1 = 22 July 1984; 2 = 7 June 1985 (two stars); 3 = 30 July 1985 (IRTF and Palomar Mtn.); 4 = 20 August 1985 (IRTF and Lowell Obs.).

SMALL SATELLITES OF NEPTUNE: SIZES, SHAPES, AND WHOLE-DISK PHOTOMETRY

P. Thomas and J. Veverka, Center for Radiophysics and Space Research, Cornell University, Ithaca, NY 14853.

The small satellites of Neptune fall into two groups: Nereid, which has a distant eccentric orbit, and six others with circular orbits less than five planetary radii from Neptune (Smith et al., 1989). Some of the innermost of the new small satellites appear to be connected intimately with the planet's rings. Only the largest of the newly discovered satellites, 1989N1, was resolved well enough by Voyager 2 to show surface features; the second largest, 1989N2, was imaged well enough to obtain its approximate shape; for two others, 1989N3, N4, only an estimate of size was possible (Table 1).

Table 1: Small Satellites of Neptune

Satellite	a(10^3 km)	Mean Radius (km)	Geometric Albedo	Best Resolution (km/pxl)
Nereid	5110.0	170 ± 25	0.14 ± 0.04	43.3
1989N1	117.6	209 ± 8	0.062 ± 0.01	1.3
1989N2	73.6	95 ± 10	0.057 ± 0.01	4.1
1989N3	52.5	75 ± 10	0.063 ± 0.02	16.9
1989N4	62.0	80 ± 10	0.063 ± 0.01	18.4
1989N5	50.0	40 ± 8		17.4
1989N6	48.0	27 ± 8		17.3

For 1989N1 the shape (Fig. 1) can be determined well from available images. An ellipsoidal approximation gives radii of 220, 208, and 200 (± 4) km. Tracking the large 200 km crater (Smith et al., 1989) near (10°S, 20°W) shows that the satellite is within 5% of synchronous rotation. For 1989N2 the long axis radius is about 100 km, the short axis radius, about 85 km. The intermediate axis cannot be determined from Voyager data. Mean radii for 1989N3 and N4 can be measured from a few images with sufficient resolution but with some smear. The sizes of 1989N5 and N6 must be estimated indirectly from the total brightness, assuming that these two inner satellites have albedos identical to those of the other four (Table 1).

In terms of shape, limb roughness, and relative size of the largest crater, 1989N1 is typical of other small satellites (Thomas et al., 1986). There is no evidence in the Voyager image of any past internal geologic activity or of structural readjustment due to internal processes. It is worthwhile to point out that 1989N1 is larger than Mimas and not much

smaller than Enceladus, and that it is the ellipsoidal shape of Mimas rather than the irregular form of 1989N1 that requires explanation (Johnson and McGetchin, 1973; Dermott and Thomas, 1988).

Geometric albedos can be measured directly for four of the inner satellites (Table 1): all give values close to 6%. Thus, these satellites appear to be similar in albedo to the ring particles (Smith et al., 1989) and to the small satellites of Uranus (Thomas et al., 1989), but are definitely darker than Nereid, the geometric albedo of which is about twice as high (Table 1). Since Voyager observations of the small satellites are restricted to phase angles between about 10° and 50°, a major uncertainty in the geometric albedos given in Table 1 concerns the extrapolation of the phase curves to opposition. For 1989N1, N2, N3, and N4, adequate phase curves can be derived; that for 1989N1 is shown in Fig. 2. All four satellites have phase coefficients between 0.03 and 0.04 mag/deg between phase angles of 10° and 50°.

Color measurements with the Voyager Cameras for Nereid and 1989N1 and by the Voyager Photopolarimeter for 1989N2 indicate that these satellites all have flat, gray spectra similar to those of the ring particles (Smith et al., 1989; Lane et al., 1989).

This research was supported by NASA Grant NSG 7156.

References:

Dermott, S. F., and P. Thomas (1988). The shape and internal structure of Mimas. *Icarus 73*, 25-65.

Johnson, T. V., and T. R. McGetchin (1973). Topography on satellite surfaces and the shape of asteroids. *Icarus 18*, 612-620.

Lane, A. L., et al. (1989). Photometry from Voyager 2: Initial results from the Neptunian atmosphere, satellites and rings. *Science 246*, 1450-1454.

Smith, B. A., et al. (1989). Voyager 2 at Neptune: Imaging science results. *Science 246*, 1422-1449.

Thomas, P., J. Veverka, and S. Dermott (1986). Small satellites. In *Satellites* (Burns and Matthews, eds.). U. of Arizona Press.

Thomas, P., C. Weitz, and J. Veverka (1989). Small satellites of Uranus: Disk-integrated photometry and estimated radii. *Icarus 81*, 92-101.

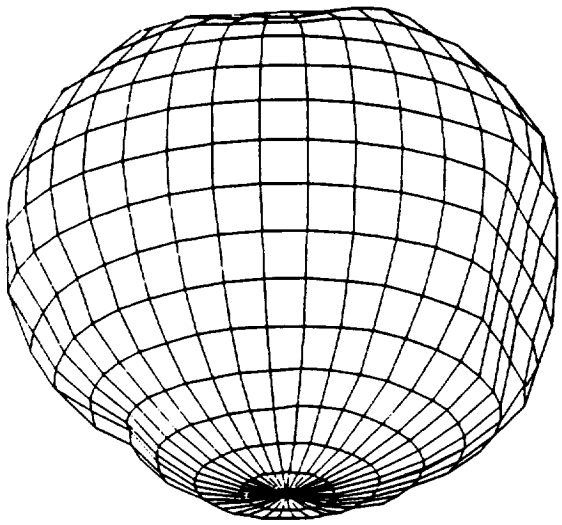

Fig. 1. Shape of 1989 N1 from three best Voyager image sequences, as seen from 25°S, 95°N. The shape is typical of heavily cratered small satellites. The largest crater (located at 10°S, 20°W), is 200 km across, a scale comparable to the mean radius of the satellite.

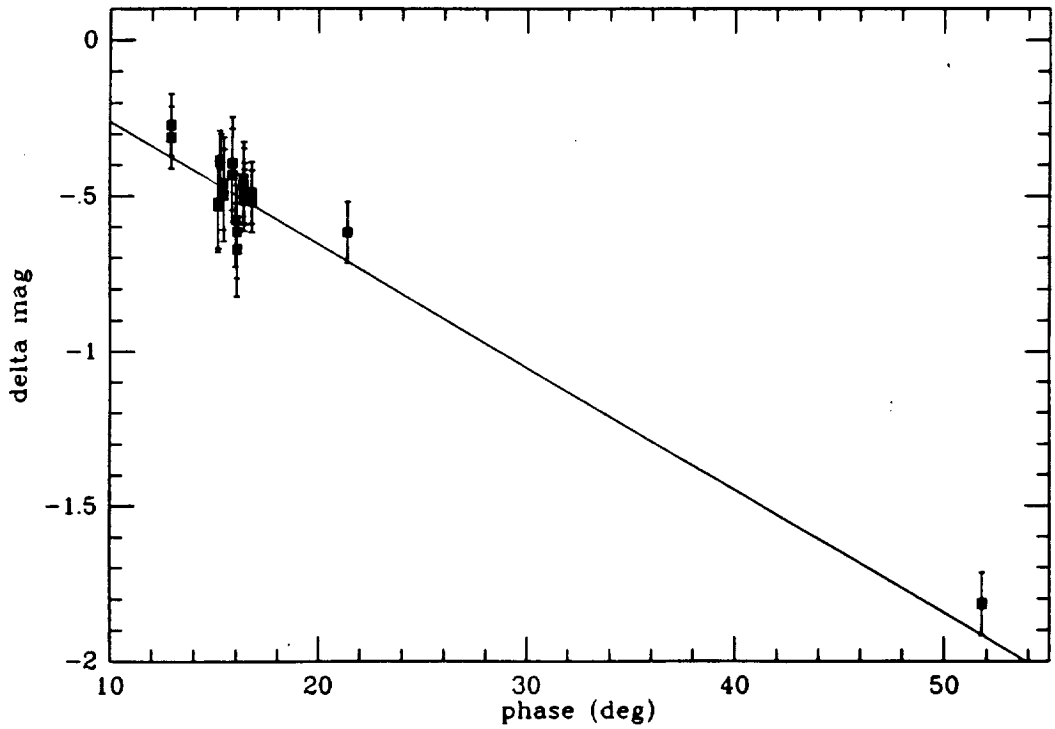

Fig. 2. Disk-integrated phase curve for 1989N1; Clear filter. Error bars are approximate measurement uncertainties and do not include corrections for a light curve, which may have an amplitude of 0.1 mag. The fitted phase coefficient is 0.039 mag/deg.

MODELS FOR RIDGE AND TROUGH TERRAIN ON ICY SATELLITES AND THE ORIGIN OF RIDGES IN ELSINORE CORONA, MIRANDA

***Robert Pappalardo and Ronald Greeley**, Department of Geology, Arizona State University, Tempe AZ 85287*

A terrain common to four icy satellites of Jupiter, Saturn, and Uranus is "ridge and trough terrain," which consists of subparallel ridges and troughs, most often within resurfaced regions. Such terrain includes the "grooved terrain" of Ganymede [1], the "ridged plains" of Enceladus [2], the coronae of Miranda, and a variety of areas on Ariel. The morphologies of ridges and troughs on icy satellites, which we have classified [3], differ among the icy satellites and can vary on a single icy body. Different processes might produce terrains of comparable ridge and trough morphology on icy bodies. Here we discuss the candidate processes for forming ridge and trough terrain and tests to distinguish among them.

Nine geological processes are considered capable of producing alternating ridges and troughs: 1) tension fracturing, 2) normal faulting (either horst and graben faulting or block faulting), 3) thrust faulting, 4) folding, 5) strike-slip tectonics (wrenching and bend duplexing), 6) fissure volcanism, 7) fissure extrusion of solid-state material (extrusive diapirism), 8) near-surface intrusion, and 9) surface folding of a flow. Each process creates distinct landforms. However, there must be clear understanding of each process in order to extrapolate observed terrestrial morphologies to cold, low gravity bodies and icy surface materials. If parameter values can be determined, models for the development of terrestrial landforms can be applied to icy satellites, their viability tested, and the effects of changes in parameter values evaluated. Both morphological and theoretical models for the creation of ridge and trough landforms are currently being tested against the observations of ridge and trough terrain.

1) Tension Fracturing. The high length/width and Ridge-width/Trough-width ratios of some ridge and trough types are compatible with their being tension fractures. However, no observed trough sets show the length and spacing distribution characteristic of tension fractures, predicted to follow a decaying exponential [4,5]. In addition, the widths of troughs observed on icy satellites predict depths so large [4] that it is unlikely that any are true tension fractures. Morphometric parameters are indicators of the stress necessary to produce a fracture, and stress models are being used to evaluate the fracture hypothesis.

2) Normal Faulting. Normal faults, commonly manifest as horst and graben topography or tilted block faults, can take on a range of morphologies, and many varieties of ridge and trough terrain may be the result of normal faulting. Theoretical faulting models are being used to constrain ridge and trough types that can result from this process.

3) Thrust faulting. Thrust belts are morphologically distinct in that they display strike-slip tear faults and fault blocks show a common direction of convexity where they intersect the surface. Some ridges and troughs bounding Inverness Corona, Miranda are candidate thrusts; however, they lie in topographically low regions and are likely normal faults instead.

4) Folding. Folding models relate fold (ridge) spacing to the thickness of the folded plate. The maximum plate thickness that permits folding is directly related to the plate's compressive strength and inversely related to gravity. On Earth, ice sheets greater than 0.3 m in thickness do not fold, but fail brittley [6]. The increased compressive strength of very cold ice and the low gravity of icy satellites will permit folding of thicker ice sheets upon sufficient compressive stress, perhaps allowing folding to be a viable model for ridge and trough terrain.

5) Strike-slip tectonics. Wrench tectonism forms a braided pattern of surface faults upon small strike-slip displacements. Braided and sinuous types of ridges and troughs [3] might have formed by this process. Bends along strike-slip faults may result in fault-bounded duplexes whose parallel interior faults trend obliquely to its bounding faults [7]. This may account for the oblique trends of some ridge and trough sets on Ganymede, relative to sulcus bounds.

6) Fissure volcanism. In regions of high extension rate and rapid quenching, such as along the East Pacific Rise, fissure eruptions can produce linear volcanic constructs ~2 to 15 km wide and up to 200 km long. A crestal graben is characteristic (due to pressure reduction and subsequent keystone collapse) and volcanic peaks can be found along-axis [8]. Marginal troughs may develop

beside volcanic ridges which are initially uncompensated. These constructs are possible analogues to "Large Ridges" on Enceladus, "Elsinore Ridges" on Miranda, and "Curvilinear Ridges" on Ariel [3].

7) Extrusive diapirism. Diapirism has been shown to be a viable model for creating regularly spaced ridges and troughs [3]. In plan view, diapiric walls may pinch and swell and be discontinuous along their length, and their rim synclines take the form of bounding troughs. Diapiric walls may be an appropriate analogue to "Elsinore Ridges" on Miranda and "Curvilinear Ridges" on Ariel.

8) Near-surface intrusion. Near surface intrusion warps the overlying surface in a ridge-trough-ridge style [9] consistent with morphologies that have been observed on icy satellites [10]. However, to produce surface deformation on the scale appropriate to some Ganymede troughs, a 1 km wide dike would require a driving pressure $>10^4$ bar. Intrusions by tabular dikes or diapiric ridges can arch their cover in the style of an anticlinal laccolith [11]. Preliminary results indicate that wide laccoliths (~10 km) may form under a shallow cover (~100s m) on icy satellites in response to magma driving pressures of a few bars.

9) Surface folding. Flow ridges are, theoretically, a viable analogue for ridge and trough terrain [12]. Flow ridges are predicted to have a ridge-width/trough-width ratio ~1, to have convex-up ridge morphology, and to trend parallel to their source and to topographic slope. Flow ridges may truncate intervening troughs, but troughs do not truncate ridges. "Sinuous Ridges and Troughs" bounding a "Large Ridge" on Enceladus (near 10°N, 330°) meet these morphological requirements. It has been suggested that "Close-Packed Ridges and Troughs" in Inverness Corona, Miranda, are flow ridges [13]. However, some display flat-floored troughs, and some are gradational from "Asymmetrical Ridges and Troughs" that we interpret to be extensional block faults, suggesting that normal faulting is a more appropriate model.

The origin of Miranda's coronae and the ridges and troughs contained within has been the subject of much debate. Ridges in the outer bands of Elsinore Corona, located in the western hemisphere of Miranda, have been suggested to be folds [14], horsts [14,15], or linear volcanic constructs [13,16]. Presently, the morphological predictions and theoretical constraints of the geologic models are being applied to test formation hypotheses. Summarized here is a preliminary analysis of the origin of subparallel ridges and troughs in the outer bands of Elsinore Corona based upon morphological constraints.

A sketch map of the types of ridges and troughs observed in Elsinore Corona ([17], Figure 1) shows that two landforms, here called Elsinore Ridges and Straight Troughs, dominate the corona's outer bands, giving the "ridged" (and/or "grooved") appearance. Elsinore Ridges are ~10 to 50 km long and typically 2 to 3 (but up to 6) km wide. They are morphologically similar to some Ganymede ridges in that they can be sharp-crested and terraced in profile [10] and are of essentially the same scale. However, Elsinore Ridges are distinct in that they pinch and swell, can be discontinuous along their length, and blend into the level of surrounding terrain where one or both of their bounding troughs terminate. They also may end with a convex terminus. Elsinore Ridges display the largest Ridge-width/Trough-width ratio (~0.5) of all types, resulting in a "ridged" (rather than "grooved") appearance. Analysis of of "grooved terrain" near the south pole of Ganymede shows that it is also "ridged," with a Ridge-width/Trough-width ratio ~0.8 [18]. Elsinore Ridges are observed to occur only in the east-west trending band of Elsinore Corona (hereafter the "Ridged" band), subparallel to the corona's boundaries.

The linear, "ridged" morphology of Elsinore Ridges and apparent lack of strike-slip displacement discounts their being formed as the result of tension fracturing, thrust faulting, strike-slip tectonics, or surface folding.

The morphology of Elsinore Ridges is generally consistent with their being folds [14], but bounding troughs are difficult to explain in a folding model. Furthermore, the geological associations to Elsinore Ridges argue an extensional, rather than compressional, origin. Straight Troughs, which may bound Elsinore Ridges and which occur throughout the Ridged band, are linear, narrow (~1 km) troughs typically separated from each other by broad and relatively flat regions. Their wide spacing and the flat topography of the intervening terrain argues that Straight

Troughs are true negative relief features. In the adjacent north-south trending band, a set of Straight Troughs disappears into the terminator. Elsinore Ridges do not appear in this north-south band. Neither Elsinore Ridges nor Straight Troughs can be unambiguously traced across the juncture of the two bands; instead, some Straight Troughs of the north-south band terminate against a mottled unit ([17], Figure 1). Of the possible formation processes, horst-and-graben faulting can best explain the morphology of Straight Troughs. Local extension might occur in a compressional stress regime (along fold crests), but the lack of candidate compressional features in the north-south band means that there is no clear evidence for compression there, only extension.

Sinker and riser models [14] predict identical stress states in the north-south and the Ridged bands. Thus, the evidence for extension and the lack of evidence for compression in the north-south band calls the compressional model into question. Additional arguments can be made for the outer bands of Elsinore Corona having formed in an environment of extensional stress. 1)Straight Troughs, which are probably graben, also occur in the Ridged band. 2)It has been argued that Elsinore Corona is at least partially volcanically resurfaced [19], suggesting an extensional regime. 3)Limb profiles [20] show that topographic depressions bound Elsinore Corona on its three visible sides. Prominent bounding troughs are predicted to occur at the margins of rift zones [21], and the presence of similar structures has been used to argue an extensional origin for Ganymede's ridge and trough terrain. Beyond the bounding trough, Elsinore Corona is bordered by a rise of ~1 km [20] that might be an isostatic response to adjacent normal faulting [22]. 4)Within its southern boundary, the Ridged band contains troughs that are arranged *en echelon*, indicative of oblique extension.

Elsinore Ridges may be horsts, linear extrusions of melt or of solid-state (diapiric) material, or anticlinal laccoliths lifted by large-scale linear intrusions. Topographic lows adjacent to Elsinore Ridges do not appear flooded, arguing against formation of these ridges by extrusion of low-viscosity material. Ridges do not exhibit smooth parabolic profiles and lobate termini, as would be expected of viscous extrusions. No evidence exists for associated circular plan extrusions or intrusions, arguing against formation of ridges by diapiric extrusion or by laccolithic intrusion of diapiric walls [c.f. 17]. Bounding troughs and convex termini argue against Elsinore Ridges being horsts. Further morphological and theoretical tests are being applied to constrain the origin of Elsinore Ridges. The presence of Elsinore Ridges in the Ridged band and their absence in the north-south band may be due to differences in lithospheric thickness at the times of band formation, in amount or rate of extension, or in degree or timing of volcanic resurfacing.

The process of applying terrestrial geologic models to the icy satellites continues, with emphasis turning toward theoretical constraints of the geologic models. Morphological and theoretical constraints will be applied to each of the ridge and trough types [3] observed on icy satellites, and evaluation and ranking of the formation models will be made for each type. A synthesis will be produced in which the derived classification will be finalized and cross-referenced to the interpreted formational process, and conclusions will be developed as to the role ridge and trough terrain may play in the general evolution of outer planet satellites.

[1]Smith *et al.*, *Science* **204**, 945 (1979).
[2]Smith *et al.*, *Science* **215**, 504 (1982).
[3]Pappalardo and Greeley, *Uranus Colloq.*, 5.20 (1988).
[4]Nur, *J. Struct. Geol.*, *4*, 31-40, 1982.
[5]Gudmundsson *Tectonophys.*, *139*, 295-308, 1987; *J. Struct. Geol.*, *9*, 61-69, 1987.
[6]Kerr, in *Physics and Mechanics of Ice* (Tryde, ed.), 163 (1980).
[7]Woodcock and Fischer, *J. Struct. Geol.* **10**, 725 (1988).
[8]Lonsdale, *Tectonophys.* **116**, 255 (1985).
[9]Pollard *et al.*, *Tectonophys.* **94**, 541 (1983).
[10]Squyres, *Icarus* **46**, 156 (1981).
[11]Pollard and Johnson, *Tectonophys.* **18**, 311 (1973).
[12]Fink and Fletcher, *J. Volcanol. Geotherm. Res.* **4** 151 (1978); Fink, *Geology* **8**, 250 (1980); Croft *et al.*, *in preparation.*
[13]Croft, *LPSC Abstr. XVIII*, 207 (1987).
[14]Janes and Melosh, *JGR* **93**, 3127 (1988).
[15]McKinnon, *Nature* **333**, 701 (1988).
[16]Schenk, in press.
[17]Pappalardo and Greeley, *LPSC Abstr. XX*, 820 (1989).
[18]Squyres, Ph.D. thesis, Cornell Univ., 1981.
[19]Smith *et al.*, *Science* **233**, 43 (1986).
[20]Thomas, *Icarus* **73**, 427 (1988).
[21]Gibbs, *J. Geol. Soc. London* **141**, 609 (1984).
[22]Jackson and McKenzie, *J. Struct. G* **5**, 471 (1983).

Thermal Stress Tectonics on the Satellites of Saturn and Uranus

John K. Hillier and Steven W. Squyres
Center for Radiophysics and Space Research
Cornell University, Ithaca, NY 14853

Most of the satellites in the saturnian and uranian systems appear to have undergone extensional tectonism and resurfacing. Only Iapetus and Umbriel do not exhibit clear evidence of at least some such activity (1,2), and even in these cases the lack of evidence may be due to insufficient image resolution. We examine here the internal stress distribution produced by the thermal evolution of the saturnian and uranian satellites following their formation, and consider the conditions necessary to produce near-surface extensional stresses large enough to cause failure.

Starting from an initial accretional temperature profile (3), the satellites are allowed to evolve thermally by radiation to space and conduction. Solid state convection, when it occurs, is handled following the technique of Ellsworth and Schubert (4). The effects of both radiogenic heating in the silicate fraction of the satellite (assuming a carbonaceous chondritic compostion) and the release of latent heat from ice phase transitions are included in the model.

The stresses built up in the satellites are calculated assuming that the satellites have a viscoelastic rheology, and that deviatoric stresses are initially zero. The radial, σ_r, and tangential, σ_T, stresses in excess of the lithostatic stress are found by integrating:

$$\frac{d\sigma_r}{dt} = \frac{2E}{1-\nu}\left[\frac{1}{R_{Sat}^3}\int_0^{R_{Sat}} r^2\frac{d\alpha}{dt}dr - \frac{1}{r^3}\int_0^r r^2\frac{d\alpha}{dt}dr - \left\{\frac{\sigma_r}{12\mu} + \int_0^{R_{Sat}}\frac{\sigma_r}{12}\frac{d(\frac{1}{\mu})}{dr}dr - \int_0^r \frac{\sigma_r}{12}\frac{d(\frac{1}{\mu})}{dr}dr\right\}\right],$$

$$\frac{d\sigma_T}{dt} = \frac{E}{1-\nu}\left[\frac{2}{R_{Sat}^3}\int_0^{R_{Sat}} r^2\frac{d\alpha}{dt}dr + \frac{1}{r^3}\int_0^r r^2\frac{d\alpha}{dt}dr - \frac{d\alpha}{dt} - \left\{\frac{\sigma_T}{12\mu} + \int_0^{R_{Sat}}\frac{\sigma_r}{12}\frac{d(\frac{1}{\mu})}{dr}dr - \int_0^r \frac{\sigma_r}{12}\frac{d(\frac{1}{\mu})}{dr}dr\right\}\right],$$

where

$$\alpha = \alpha_l \Delta T + \frac{1\Delta\rho_{pt}}{3\rho}U(r - r_b(t)),$$

E is Young's modulus, ν is Poisson's ratio, α_l is the linear coefficient of thermal expansion, μ is viscosity, ΔT is the change in temperature from the initial temperature, $\Delta\rho_{pt}$ is the difference in density between the ice I and ice II dominated regions, r_b is the position of the ice I - ice II phase boundary, U is the step function and t is time. In the expression for α, the first term takes into account the effects of thermal stresses, while the second accounts for shifts in the position of the ice I - ice II phase boundary. The total stress is found by subtracting the lithostatic stress from σ_T and σ_r. Lithostatic stress is calculated assuming a simple two-layer model with a constant-density ice II - rock core and ice I - rock mantle. The position of the ice I - ice II phase boundary is determined from the equilibrium relation (4):

$$P(\mathrm{MPa}) = 0.917T(\mathrm{K}) - 1.762,$$

and is found after each time step using an iterative procedure until a self-consistent solution is obtained.

We find that large extensional surface stresses can be produced early in the thermal histories of these satellites. The most important sources of stress are *(a)* thermal stresses caused by rapid cooling and contraction of outer regions that were warm at the end of accretion, and *(b)* global expansion caused by ice II $\rightarrow$ ice I phase changes. Table 1 shows the maximum near-surface extensional tangential stresses reached in each of the major satellites within the first 200 Myr. In

all cases, the radial stresses remain nearly lithostatic. The results shown in the table are for an initial temperature profile produced by gas-free accretion. On the smaller satellites, only small stresses develop, probably insuffcient in strength to fracture ice. However, if accretion occurs in a warm gaseous nebula, allowing a large post-accretional temperature drop, extensional stresses of at least several MPa develop very quickly (within a million years) on these satellites, sufficient in strength to fracture ice. On the intermediate to lage satellites, extensional stresses of several tens of MPa accrue within 200 million years, easily strong enough to fracture ice.

An important characteristic of the temperature and stress distributions that we find is that the material immediately underlying the zone where failure is expected is the warmest in the satellite, and its temperature commonly is close to or greater than the H_2O-NH_3 eutectic temperature. Hence, it may be buoyant and mobile enough to reach and flow out onto the surface through any fractures that are created. We believe, therefore, that thermal stresses may be able to account for both extensional tectonism and resurfacing on many of the saturnian and uranian satellites.

Table 1

Satellite	$\sigma_T$max(MPa)	Satellite	$\sigma_T$max(MPa)
Iapetus	51.6	Oberon	53.7
Rhea	30.0	Titania	62.9
Dione	6.6	Umbriel	18.4
Tethys	3.4	Ariel	28.1
Enceladus	0.4	Miranda	0.0
Mimas	0.2		

References

1) Squyres, S.W. and S.K. Croft (1986), in *Satellites* (J.A. Burns, Ed.), 293-341.

2) Smith, B.A. (1986), *et al.*, *Science* **233**, 43-64.

3) Squyres, S.W., *et al.* (1988), *JGR* **93**, 8779-8794.

4) Ellsworth, K. and G. Schubert (1983), *Icarus* **54**, 490-510.

ALBEDO AND COLOR MAPS OF THE SATURNIAN SATELLLITES

B. J. Buratti, J. A. Mosher, and T. V. Johnson
JPL/Caltech

Color and albedo maps of the five medium sized Saturnian satellites - Mimas, Enceladus, Tethys, Rhea, and Dione - were recently completed (Buratti et al., 1990). One of the areas we investigated in detail was the cause of the albedo dichotomies found on the outer three of these objects (see also Verbiscer and Veverka, 1989). Originally, we thought that the areas were "coated" by Saturn's E-ring; however, by comparing our results with the model of Shoemaker and Wolfe (1982), we concluded that brighter leading sides of the satellites may be caused in part or totally by preferential micrometeoritic gardening. This idea is still not entirely satisfactory, because Plescia and Boyce (1982) showed that craters are not preferentially placed on the trailing side.

There is evidence for an unusual exogenic deposit on Tethys. Two dark "patches" exist on this satellite: a reddish longitudinal feature centered on the antapex of motion, and a bluish equatorial region centered near the apex of motion. We suggest that the former feature is primordial, or possibly caused by magnetospheric interactions, whereas the blue patch is an exogenic deposit, possibly caused by a collision with a comet or a cloud of particles similar to those that have been purported to exist in the Saturnian region (Burns et al., 1989).

The other conclusions we report are:

1. There is a general lack of correlation of albedo and color with geologic features, except in the case of Rhea and the trailing side of Dione.

2. There is no appreciable leading/trailing color dichotomy for these satellites, except for Tethys.

3. UV photolysis may have altered the surfaces.

REFERENCES

1. Buratti, B. J., J. Mosher, and T. Johnson (1990). Icarus, accepted for publication.

2. Burns, J. A. et al. (1989). B.A.A.S. 21, 930.

3. Shoemaker, E., and R. Wolfe (1982). In Satellites of Jupiter (D. Morrison, ed., Tucson, Univ. Of Arizona Press) 277.

4. Verbiscer, A. and J. Veverka (1989) Icarus 82, 336.

THE CRATERING RECORD AND GEOLOGICAL HISTORY OF ENCELADUS

S. Pozio[1] and J.S. Kargel[2]; 1 Reparto Planetologia, Viale Universita, 11-00185 Rome, Italy; 2 Lunar and Planetary Laboratory, University of Arizona, Tucson, AZ 85721

Introduction. The saturnian satellite Enceladus shows a variety of tectonic features and a wide range in crater densities indicative of a dynamic history [1-5]. In a previous paper we examined the tectonics of Enceladus [5]. Here, we construct a geological history based on crater densities and our previous tectonic mapping. Figure 1 shows the surface of Enceladus divided into four major terrains, each of which is sharply bounded by major tectonic contacts: cratered plains, ridged plains, rifted terrain, and banded terrain. Two terrains are further subdivided on the basis of tectonics or internal variations in cratering.

Cratering record. Figure 2 shows a cumulative crater density plot for Enceladus and its terrain units, and Figure 3 is an "R-plot" comparing Enceladus with other icy satellites. Observational losses are minor for craters larger than 5.7 km (image resolution is about 2 km/l.p.). Table 1 gives cumulative crater statistics for craters larger than 5.7 km in diameter for the major terrain units and their subdivisions.

The ridged plains (Rp) include a long system of curvilinear ridges of likely compressional or volcano-tectonic origin [5]. The Rp are almost devoid of craters. Only two small craters have been identified in this entire area (109,000 km^2), indicating complete and geologically recent re-surfacing.

The cratered plains (Cp) exhibit over an order of magnitude variation in crater densities. The lower crater densities are found at the lower latitudes (Cp1, Cp2, and Cp11), while progessively (gradationally?) higher crater densities occur to the north (Cp 3-10). No obvious cryovolcanic flow fronts are visible in the Cp, nor are obvious "ghost" craters present, although such features might be found with better resolution. A tectonic alignment of pits in Cp4-6 may relate to tectonically-controlled cryoclastic volcanism [7]. The absence of craters larger than about 30 km means that even the most heavily cratered surfaces are devoid of "Population 1" craters [2], indicating that even these old regions were probably resurfaced. The crater density in the most heavily cratered regions is similar to that on Mimas and the heavily cratered surfaces of Tethys (Figure 3).

The Cp are everywhere dominated by extensional tectonics, although locally the tectonic style may include trans-tensional faulting [5]. Many fractures are very fresh, although other fractures have been cratered, suggesting that an extensional tectonic regime prevailed in the Cp for a considerable time.

A sub-unit of cratered plains, Cp12, exhibits unusual appearing craters. Small craters have been preserved, while large craters are very shallow and have bowed up floors, indicative of viscous relaxation [4]. The crater density of this region is similar to the adjacent, normal appearing regions of heavily cratered plains; since no sharp tectonic contact is apparent, Cp12 appears to have been derived from typical cratered plains by a laterally gradational enhancement in heat flow.

A north-trending rifted terrain (Rf) is characterized by sub-parallel extensional fractures, cryovolcanic flooding, and possibly "stretched" craters, and the whole unit has been tectonically down-dropped. Rf was derived by volcano-tectonic processes at the expense of cratered plains. The density of post-rifting craters is spatially non-uniform, suggesting protracted or episodic rifting. Cp tectonically abutts Rf on both east and west, and at one time Cp was apparently continuous across the region now occupied by Rf.

The banded terrain (Bt) is crossed by en echelon bands of uncertain origin [5]. The Bt has a low but variable crater density, indicating that it was generated over a substantial interval of time. Bt1 has about the same crater density as the rifted terrain and Cp4, while the sparse cratering of Bt2 is comparable to Cp1-3. The morphology and cratering record of the Bt are consistent with either multiple over-lapping cryovolcanic flows or with imbricated thrust sheets.

Absolute and relative ages. The observed crater density in the ridged plains is roughly 0.2% that of the heavily cratered regions. Part of this exceedingly low crater density is probably accounted for by unfavorable illumination of much, but not all, of the ridged plains. Even so, the actual crater density of the ridged plains is probably less than 1% that of the heavily cratered terrain. Assuming the heavily cratered terrain is of the order of 4×10^9 years old, and assuming a constant flux of Population 2 projectiles since that time, then the age of the ridged plains is of the order of 10^7-10^8 years old.

The absolute ages of other terrains can not be usefully constrained due to our current insufficient understanding of the impact flux through time. Table 1 provides some indication of relative ages, though one must be mindful of problems with apex-antapex asymmetries in cratering rates and possible shifts in Enceladus' rotation axis through time. We note, however, that the ridged plains are centered in the trailing

C12

hemisphere, which should have the largest and most energetic flux of impactors; hence, the freshness of the Rp is a true indication of its youthfulness. Also, abrupt lateral contrasts in crater density always correlate with tectonic boundaries on Enceladus.

Geological History. (1) Very early in Enceladus' history, global re-surfacing obliterated all evidence of the heavy bombardments related to accretion and Population 1 craters [6]. Subsequently, only Population 2 projectiles impacted Enceladus. For conceptual simplicity one may imagine that all of Enceladus' surface once consisted of cratered plains bearing only Population 2 craters. The oldest surviving remnants of these plains may now be found at high northern latitudes (Cp5-10). (2) Rifting resulted in fracturing, cryovolcanic flooding, and possibly viscous relaxation and stretching of impact craters in the Rifted terrain; this event may have been co-eval with plains formation in Cp4 and the emplacement of Bt1. (3) Continued cryovolcanism and extensional fracturing generate the younger sub-units of the cratered plains (Cp1-3), and emplacement of the youngest sub-unit of the banded terrain (Bt2). (4) Ridged plains were formed by a combination of compressional tectonics and widespread cryovolcanism.

References. [1] Smith, B. et al., 1982, Science, 215, 504-537. [2] Plescia, J.B., and Boyce, J.M., 1983, Nature, 301, 666-670. [3] Squyres, S. et al., 1983, Icarus, 53, 319-331. [4] Passey, Q.R., 1983, Icarus 53, 105-120. [5] Pozio, S. and Kargel, J.S., 1989, abstract, Lun. Planet. Sci. XX, 864-865. [6] Strom, R.G., 1987, Icarus, 70, 517-535. [7] Kargel, J.S., 1984 (abstract), Lun. Planet. Sci. XV, 427-428.

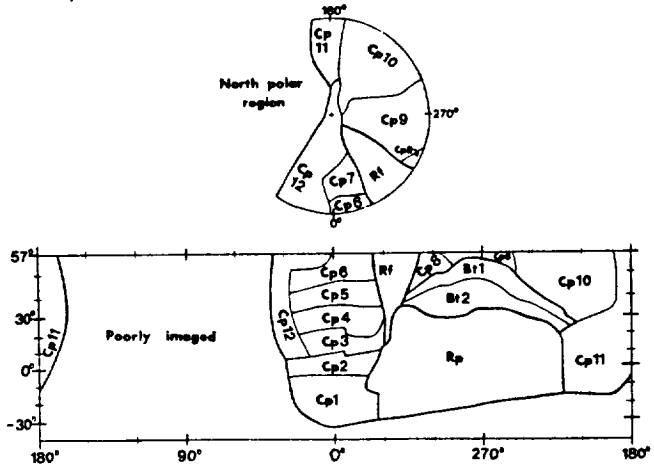

Figure 1. Terrain units and sub-divisions; Cp= Cratered Plains; Rp= Ridged Plains; Rf= Rifted Terrain; Bt= Banded Terrain.

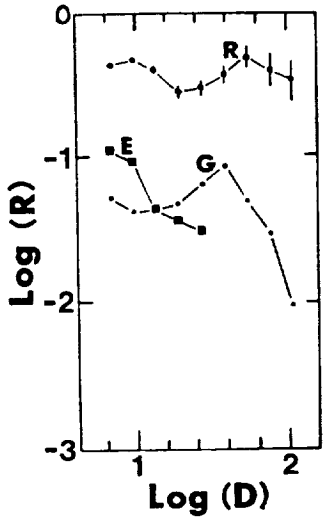

Figure 3. "R"-plot. E = Enceladus; R = Rhea showing population 1 and 2 superimposed [6]; G = Ganymede cratered terrain.

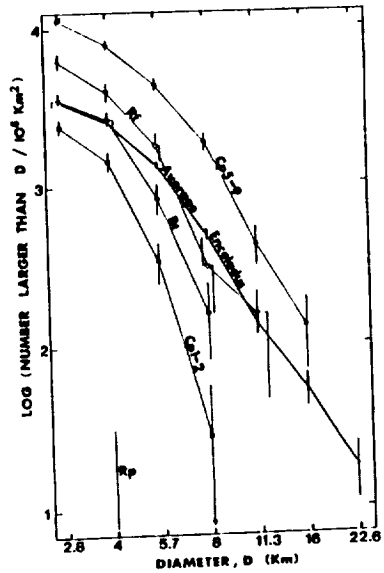

Figure 2. Cumulative crater density plot.

Table 1. Cumulative numbers of craters larger than 5.7 km per 10^6 km^2

Terrain	Sub-unit	Area(km^2)	Density	Uncertainty
	Cp1	22,400	450	+- 140
	Cp2	13,000	150	110
	Cp3	11,440	790	260
	Cp4	12,000	2080	420
	Cp5	7,940	4160	720
	Cp6	6,340	3790	770
	Cp7	2,850	4210	1220
	Cp8	2,440	3690	1230
	Cp9	11,080	5050	680
	Cp10	28,900	3220	330
	Cp11	53,000	1190	150
	Cp12	21,400	3510	410
Cp Average		192,790	1960	110
	Bt1	9,370	1600	410
	Bt2	15,900	380	150
Bt Average		25,270	830	180
Rp Average		109,000	0	
Rf Average		12,900	1780	370
Enceladus Avg.		349,960	1340	60

IO: A VOLATILE-RICH SATELLITE

Alfred S. McEwen, U.S. Geological Survey, Flagstaff, AZ 86001 and Jonathan I. Lunine, Lunar and Planetary Laboratory, Tucson, AZ 85721.

Hapke (1989) showed that the spectral properties of Io can be matched by combinations of basalt, SO_2, polysulfur oxide (PSO), and S_2O. He proposed that the surface is dominantly basaltic with only thin (on the order of a micrometer) coatings of SO_2 (except for thicker patches covering ~10% of the surface) and its dissociation products PSO and S_2O and that elemental sulfur is not present in significant amounts. However, observations and models of the active volcanism indicate that volatiles such as sulfur and SO_2 must be more abundant than envisioned by Hapke (McEwen and Lunine, 1990).

In Hapke's model, the surface of Io is as volatile poor as possible, yet it is consistent with the spectral observations. However, models richer in volatiles also match the spectral observations. The fundamental problem is that reflected light provides information on only the uppermost particles of the surface. Io's bulk density and topography suggest a dominantly silicate crustal composition. However, the size and temporal variability of the active volcanic plumes and the hot-spot infrared spectra indicate that volatiles must be more abundant than only those of a thin surface coating. Furthermore, the rates of formation of PSO and S_2O as dissociation products of SO_2 are probably much lower than the volcanic resurfacing rate; unless they condense directly from volcanic gases, they are probably minor components of the surface.

PSO Abundance and Volcanic Resurfacing.

Critical to Hapke's model is the assumption that the volcanic resurfacing of Io is local and intermittent, so that optically thick layers of PSO or S_2O have time to accumulate (as dissociation products of SO_2) between resurfacing events. Hapke stated that the areas altered by the active plumes observed by Voyager make up about 2.5% of Io's surface. However, he based this statement on data given by Johnson et al. (1979), which was obtained prior to the Voyager 2 encounter and did not include the very large eruption deposits from Aten, Surt, and the greatly enlarged east Loki plumes; the radius of Pele's deposit was also underestimated. These corrections increase the area of Io's resurfacing by plumes to about 12% in only a 4-month period. Little PSO/S_2O is likely to accumulate from dissociation of SO_2 prior to volcanic resurfacing, unless it condenses directly on the cold surface from SO or S_2O gas in the plumes.

Active Volcanism.

Hapke stated that "The hot spots and plumes are silicate volcanoes and associated fumaroles." The active plumes on Io had eruption velocities ranging from 0.5 to 1.0 km s^{-1} (Smith et al. 1979), so they should not be characterized as fumaroles, which are low-energy gas vents. The point that Hapke seemed to attempt to make is that only small quantities of SO_2 and no elemental sulfur need be present to explain Io's volcanism. However, the presence of significant volatiles is required to drive explosive volcanism. Io's surface is highly depleted in H_2O and CO_2 (Cruikshank et al. 1978, Pollack et al. 1978). Because H_2O and CO_2 drive terrestrial explosive eruptions, other volatiles such as SO_2 or S probably drive the volcanism, although recent evidence for H_2S (Nash and Howell 1989, Salama et al., 1990) may indicate the presence of some subsurface H_2O. Kieffer (1982) analyzed the plumes in terms of the thermodynamics of SO_2 and S working volcanic fluids, and the matches between her predictions and the Io

observations (cf. McEwen and Soderblom 1983) have been considered a strong argument that the plumes are driven by these materials. Furthermore, the longevity (most likely several years' duration) of the Prometheus-type plumes, which are probably driven by SO_2, indicates that a substantial reservoir of SO_2 must be available.

Significance of Hot-Spot Emissions.

Hapke attached significance to the notion that hot-spot temperatures are consistent with basaltic flows, but he dismissed the parallel argument for sulfur. Lunine and Stevenson (1985) constructed a detailed model from the hypothesis that the Loki hot spot is a convecting, molten sulfur lake heated from below by molten silicates. The convection model took account of the peculiar viscosity behavior of sulfur and the hydrodynamics of evaporation of sulfur from the lake surface and recondensation of the vapor over a wide area surrounding the lake. They concluded that (1) the maximum temperature in the Loki hot spot is very tightly controlled by evaporation of sulfur from the lake surface, through the strong dependence of vapor pressure on temperature; (2) the energetics of the hot spot are consistent with the maximum steady-state energy flux derivable from a convecting silicate magma chamber; and (3) the infrared spectrum emitted from such a surface sulfur lake and the surrounding recondensed sulfur fits rather well the Voyager IRIS spectra (no more than 5% discrepancy). It should be emphasized that conclusion (2) does not imply that exposed molten silicates at the surface would fit the IRIS data; in fact, they would produce relatively too much flux at high wave numbers compared with the IRIS spectra for Loki. Carr (1986) performed a parallel calculation for a molten silicate flow. He synthesized IRIS spectra from his model temperatures and areas for active and inactive silicate flow regions. Comparison of his models with the IRIS Loki data shows discrepancies of up to a factor of 2 at a given wave number. More specifically, the model flux is relatively low in the 600 to 1800 cm^{-1} wave-number range and relatively high in the 1800 to 2400 cm^{-1} range, depending on how the hot-spot area (or eruption rate in Carr's model) is adjusted. Therefore the model predicts either too small an area at temperatures of 200°-500°K or too much area at temperatures in excess of 500°K. Carr suggested that volatiles such as sulfur or sulfur compounds might be outgassing on parts of the flow and might redistribute the power to lower wave numbers. This would require that at least half of the total excess emission from Loki would result from this outgassing. The sulfur lake model is, in a sense, a version of that suggestion in which all of the excess emission is explained by sulfur outgassing.

Disk-integrated Spectrum of Io.

Hapke demonstrated a good match between the average disk-integrated spectrum of Io from 0.2-0.8 μm and a linear mixture of the spectra of 50% PSO, 10% SO_2, 15% S_2O, and 25% basalt powder. Other workers have demonstrated a good match in this spectral region from different materials. We suggest that fits to a portion of the disk-integrated spectrum that does not contain diagnostic absorption features may not allow a unique interpretation; this problem is shared by proponents of both elemental sulfur and PSO/S_2O.

Disk-Resolved Spectra.

McEwen (1988) produced multispectral mosaics of Io from the five Voyager colors from 0.32 to 0.62 μm. The intrinsic spectral variability of Io, as seen in a series of two-dimensional histograms, is continuous among three major

spectral end members. One end member corresponds to the spectrum of SO_2 frost, the second corresponds spatially to Pele-type plume deposits, and the third consists of relatively low albedo materials. Basalt powder and S_2O fall well outside the Io data, so they are probably not present as nearly pure components on a scale of 1 km or larger. The PSO spectra, which are similar to those of various forms of elemental sulfur, fall within the data swarm and near the second end member. However, the spatial relations show that unit 2 materials are closely associated with deposits from the Pele-type plumes; these deposits were minutes to months old at the times of the Voyager observations. Their age is inconsistent with gradual formation as a dissociation product of SO_2. If unit 2 is PSO rather than elemental sulfur, then it must form at the time of deposition, perhaps as a condensate of gaseous SO as discussed by Sill and Clark (1981) and Hapke (1989). If so, then the presence of PSO does not imply a volatile-poor Io.

REFERENCES

Carr, M. H. 1986. Silicate volcanism on Io. J. Geophys. Res. 91, 3521-3532.

Cruikshank, D. P., T. L. Jones, and C. B. Pilcher 1978. Absorption bands in the spectrum of Io. Astrophys. J. 225, L89-L92.

Hapke, B. 1989. The surface of Io: A new model. Icarus 79, 56-74.

Johnson, T. V., A. F. Cook, C. Sagan, and L. A. Soderblom 1979. Volcanic resurfacing rates and implications for volatiles on Io. Nature 280, 746-750.

Kieffer, S. W. 1982. Dynamics and thermodynamics of volcanic eruptions: Implications for the plumes on Io. In Satellites of Jupiter (D. Morrison, Ed.), pp. 647-723. Univ. of Arizona Press, Tucson.

Lunine, J. I., and D. J. Stevenson 1985. Physics and chemistry of sulfur lakes on Io. Icarus 64, 345-367.

McEwen, A. S. 1988. Global color and albedo variations on Io. Icarus 73, 385-426.

McEwen, A. S., and J. I. Lunine 1990. Comment on "The surface of Io: A new model" by Bruce Hapke. Icarus 84, 268-274.

McEwen, A. S., and L. A. Soderblom 1983. Two classes of volcanic plumes on Io. Icarus 55, 191-217.

Nash, D. B., and R. R. Howell, 1989. Hydrogen sulfide on Io: Evidence from telescopic and laboratory infrared spectra. Science 244, 454-457.

Pollack, J. B., F. C. Witteborn, E. F. Erickson, D. W. Strecker, B. J. Baldwin, and T. E. Bunch 1978. Near-infrared spectra of the Galilean satellites: Observations and compositional implications. Icarus 36, 271-303.

Salama, F., L. J. Allamandola, F. C. Witteborn, D. P. Cruikshank, S. A. Sandford, and J. D. Bregman 1990. The 2.5-5.0μm spectra of Io: Evidence for H_2S and H_2O frozen in SO_2. Icarus 83, 66-82.

Sill, G. T., and R. N. Clark 1981. Composition of the surface of the Galilean satellites. In Satellites of Jupiter (D. Morrison, Ed.), pp. 174-212. Univ. of Arizona Press, Tucson.

Smith, B. A., E. M. Shoemaker, S. W. Keiffer, and A. F. Cook 1979. The role of SO_2 in volcanism on Io. Nature 280, 738-743.

SULFUR ON IO: CALORIMETRIC ANALYSES OF LABORATORY ANALOGS

James L. Gooding[1] and Douglas B. Nash[2]
[1]SN21/Planetary Science Branch, NASA/Johnson Space Center, Houston, TX 77058
[2]San Juan Institute, San Juan Capistrano, CA 92675.

Introduction. Vacuum-weathered sulfur, produced by differential sublimation of ordinary sulfur under high vacuum, has been proposed as a candidate surface material on the Jovian moon, Io [1,2]. We previously used differential scanning calorimetry (DSC) [3] to characterize the differences in phase composition among different sulfur analogs prepared in the laboratory [1,2]. Here we report new DSC data that provide a direct test of the hypothesis [1] that vacuum-weathered sulfur is predominantly polymeric in form.

Experimental Procedure. Replicate samples of Crystex (90% polymeric sulfur; Stauffer Chemical Company, Westport, CT) were analyzed with a Perkin-Elmer DSC-2C as 1-5 mg aliquots in loosely-covered aluminum pans. Heat-flow curves were acquired as each sample was heated over the 300-480 K range at 5 K/min under continuous purge (4 cm^3/min) of high-purity Ar gas, followed by quench cooling to 300 K. Results were compared with those obtained previously for vacuum-weathered sulfur and its unweathered parental substrate [3]. DSC temperature and heat-flow calibrations were established by analysis of indium metal (U. S. National Institute of Standards and Technology, GM-758), assuming T(melt) = 429.76 K and ΔH(melt) = 3.264 kJ/mol (6.794 cal/g) [4].

Results. Heat-flow curves for the three sulfur analogs are compared in Fig. 1 and corrected thermodynamic values are summarized in Fig. 2. We have previously interpreted peaks *a-c* as solid-state phase transitions, peak *d* as bulk melting, and peak *e* as a liquid-lambda transition related to polymerization of the melt [3]. The major observation is that vacuum-weathered sulfur resembles, but does not exactly match, polymeric sulfur in its phase composition.

DSC peak *e* is absent from both the vacuum-weathered and polymeric samples, suggesting that their melt structures are similar and distinctively different from that of ordinary sulfur. Nonetheless, peak *a*, which is diagnostic of vacuum-weathered sulfur, is absent from polymeric sulfur. Also, peak *b* for vacuum-weathered sulfur is shifted to a higher temperature relative to both polymeric and ordinary sulfur. Finally, peak *d* in vacuum-weathered sulfur represents a relatively low enthalpy change whereas integrated values of peak *d* are comparable for both polymeric and ordinary sulfur. In detail, the respective values for temperature and enthalpy of fusion of polymeric sulfur appear to be intermediate between corresponding values for vacuum-weathered and ordinary sulfur. Broadening of peak *d* in the heat-flow curves of both the polymeric and vacuum-weathered samples suggests either an unresolved component (e.g., incomplete resolution of peaks *c* and *d*) or an intrinsic signature of the polymeric allotrope that is not characteristic of ordinary sulfur. Additional DSC analyses at lower scan rates (to increase temperature resolution), along with further analyses of peak shapes, should provide a direct test of these alternative interpretations.

In summary, these new results indicate that vacuum-weathered sulfur is not identical to polymeric sulfur but that the vacuum-weathered sulfur probably contains a significant polymeric fraction. Precise phase identification of the of vacuum-weathered sulfur will require additional work.

References: [1] Nash D. B. (1987) *Icarus, 72,* 1-34. [2] Nash D. B. and Moses J. I. (1988) *Geophys. Res. Lett., 15,* 697-700. [3] Nash D. B. and Gooding J. L. (1989) *Lunar Planet Sci. XX,* Lunar and Planetary Institute, Houston, 760-761. [4] Robie, R. A. et al. (1979) *U. S. Geol. Surv. Bull. 1452,* 456 p.

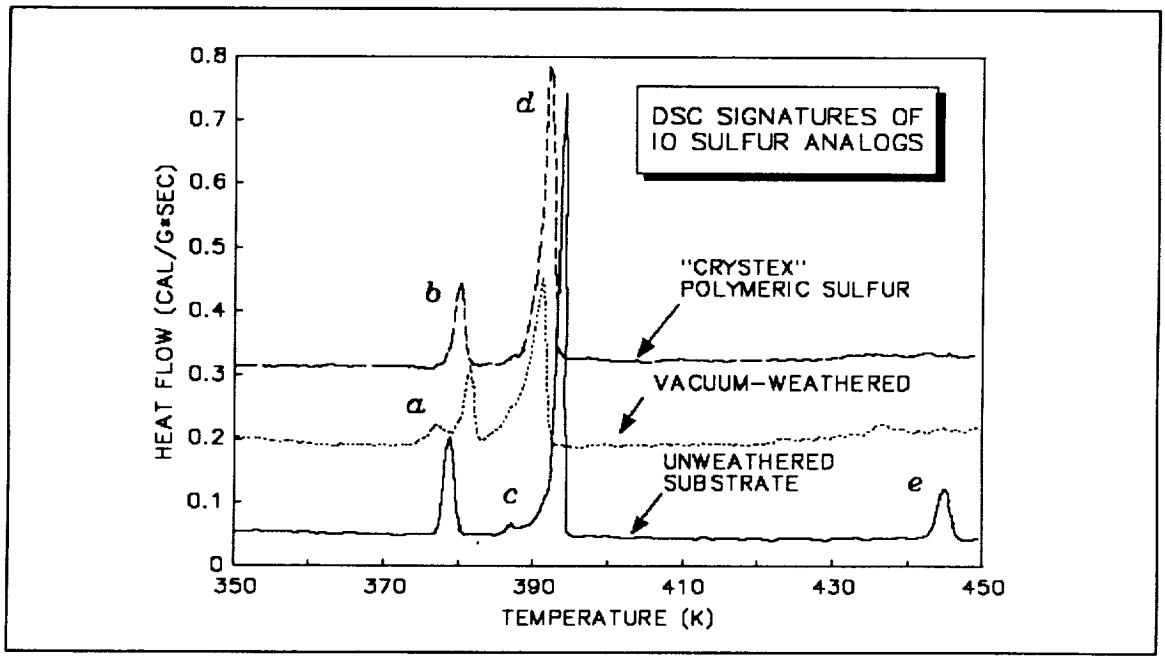

Figure 1. DSC heat-flow curves for first-run heating of sulfur analogs. Heat-flow data have been mass-normalized so that the three curves are directly comparable. For display clarity, the three curves have been artificially staggered along the vertical scale. Peaks a-e are the same as depicted in Fig. 2.

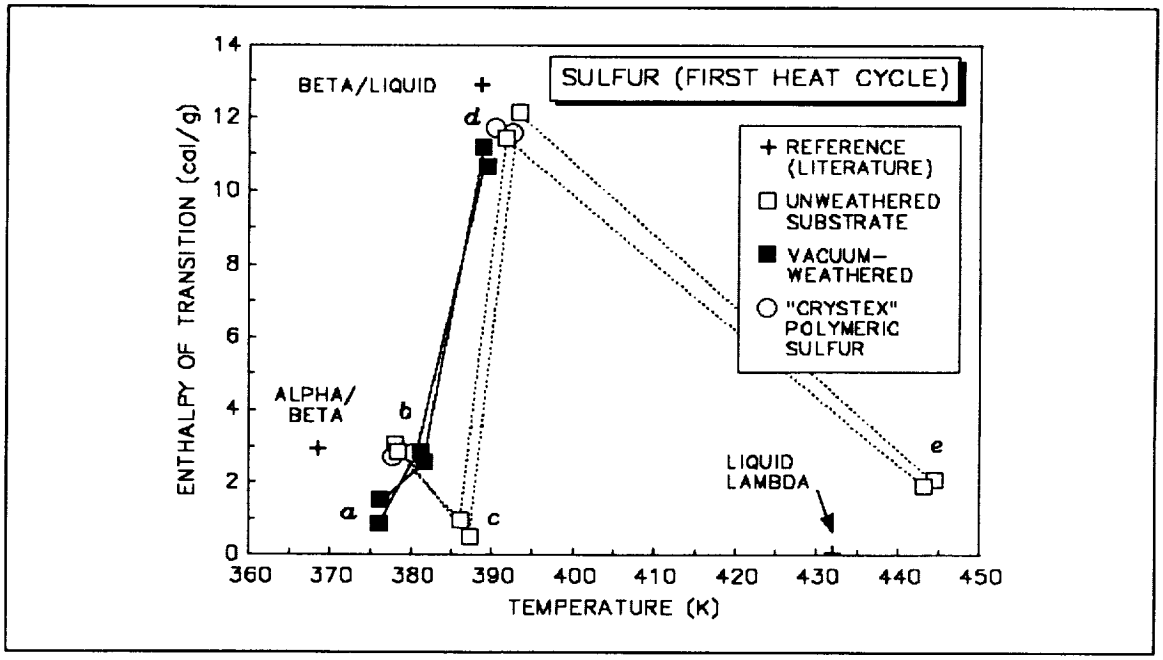

Figure 2. Corrected phase-transition data derived from DSC heat-flow curves after calibration. Duplicate analyses are represented for each analog material.

REFLECTANCE MODELING OF CALLISTO TO DETERMINE ICE ABUNDANCES AND MINERALOGY OF THE NON-ICE COMPONENT

Wendy M. Calvin and Roger N. Clark, U.S. Geological Survey, MS 964,Box 25046, Denver, CO 80225

In the planetary community there has been some controversy regarding the amount of water ice present in the optical surface of Callisto. In order to help resolve this controversy an extensive modeling study was undertaken. In contrast to previous studies this effort concentrated on matching all the ice bands as well as the albedo of Callisto by using simultaneous intimate mixtures of ice and rock in an areal combination with pure rock. For the rock component either carbonaceous or enstatite chondrite meteorites were used as they are spectrally flat in the 0.5 to 2.5-μm range, and have a drop in reflectance from the visible to the ultra-violet, similar to Callisto. Given the great range of parameters we wished to explore, an empirical study was not practical, therefore model spectra were calculated according to equations presented by Hapke (1981).

First the carbonaceous chondrite meteorites were used in the models, but were found to be much too dark. This effect can not be countered by simply reducing the grain size as features caused by the larger-grained ice are suppressed even for very small abundances of the meteorite. Next the enstatite chondrites were used in the models, as they have reflectance levels that are higher than the carbonaceous chondrites while remaining spectrally flat between 0.5 and 2.5 μm. Models which attempted to fit the 3-μm band using a small ice grain size poorly matched the depths of the ice bands shorter than 2.5 μm. Extensive modeling has shown that ice with grain sizes smaller than 0.01 cm can not be included without compromising the fit of these spectral bands. Also, models which fit the depths of the ice bands shorter than 2.5 μm indicate that surface ice is insufficient to account for the 3-μm band, so that in this spectral region other hydrated minerals must dominate.

After modeling over 250 thousand combinations fairly narrow limits for the ice grain size and weight fractions were obtained. The best fitting models contain 20-45 wt% ice in the optical surface, in reasonable agreement with results of a separate modeling study performed by Roush et al., 1990. The Calvin and Clark study (1988, 1990) indicates that the ice component of the surface is fairly large grained. The best matches to the observed spectrum used one component of ice with a grain size on the order of millimeters to centimeters and another ice component with grain sizes in the range of 200-500 μm. The non-ice material must have a grain size larger than or approximately equal to 50 to 100 μm in order to avoid suppressing the weaker ice bands in calculated spectra. The best fitting models are those of a surface that has patches of ice and rock intimately mixed and patches of pure rock.

These limits on the abundance and grain size of the ice in the optical surface allow an inversion of the model calculations to remove this amount of ice from the observed reflectance spectrum. This results in the reflectance spectrum for the non-ice material on the surface in which three broad absorption features of mineralogical origin are observed:

1) a broad absorption centered over 1 μm, which is associated with both oxidation states of iron,
2) a drop in reflectance from 0.7 to 0.3 μm (the "red edge") with an indication of ferric spin forbidden bands, and
3) a strong absorption from 2.8 to 4 μm associated with adsorbed water.

Given the ancient appearance of Callisto's surface it might be expected that the non-ice material is similar to meteoritic material, and after examining spectra from the meteorite classes presented by Gaffey (1976) we found that the spectral absorption bands in the Callisto non-ice material resemble those observed in the spectra of primitive carbonaceous chondrites. Among the primitive (type CM and CI) carbonaceous chondrites we found the CM meteorite Nogoya provided the best match. However, these primitive chondrites are much to dark spectrally to be considered as reasonable analogs to the Callisto non-ice material. However, materials present in the matrix of these meteorites may in fact be reasonable candidates.

The 1-μm absorption in the Callisto non-ice material coupled with the spin forbidden absorptions in the visible indicate both ferric and ferrous iron. Barber (1981) has discussed that the hydrous silicates present in the matrix of the CM chondrites include iron-rich serpentines and berthierines. These silicates contain both ferric and ferrous iron and are hydrated and are therefore reasonable candidates for the Callisto non-ice material. Few of these matrix materials have been characterized spectrally as they are fairly uncommon terrestrially. An examination of Fe- and Mg-endmember serpentines (Calvin and Clark, 1989) revealed that a combination of the the two will provide a reasonable spectral match to the Callisto non-ice material up to 1.5 μm. The Fe-serpentine can match the 0.35 μm spin forbidden absorption and the broad 1-μm absorption. The Mg-serpentine can duplicate the spin forbidden features at 0.30 and 0.43 μm. There are discrepancies beyond approximately 1.5 μm which may be alleviated by the inclusion of other matrix phases or opaque minerals on the surface of Callisto.

Recent observations from the NASA Infrared Telescope Facility on Mauna Kea undertaken under the Planetary Astronomy Program should assist in further constraining the nature of the non-ice material on Callisto. These new data were obtained with the CGAS spectrometer using the "D" grating with a resolving power of approximately 300. Observations were made covering the wavelength range from 1.9 to 4.8 μm.

Barber, 1981, *Geochim. Cosmochim. Acta*, **45**, 945-970. Calvin and Clark, 1988 *BAAS*, **20**, 876. Calvin and Clark, 1989, *Meteoritics*, **24**, 257-258. Calvin and Clark, 1990, submitted to *Icarus*. Gaffey, 1976, *J. Geophys. Res.*, **81** 905-920. Hapke, 1981, *J. Geophys., Res.*, **86**, 3039-3054. Roush et al., 1990, *Icarus*, in press.

Callisto: New Evidence for a Hemispheric Difference in Surface Texture

Bonnie J. Buratti (JPL/Caltech)

One of the most important goals of remote sensing observations is the derivation of surficial textural properties of planetary surfaces. These properties -- which include the compaction state of the optically active portion of the regolith, the scale and extent of macroscopically rough features, as well as the shape and size distribution of surficial particles -- are indicators of the present structure and past evolution of the body. Moreover some planets and satellites exhibit significant differences in these properties at various locations on their surfaces.

Telescopic observations of the Galilean satellite Callisto indicate that marked differences exist between its leading and trailing hemispheres. Polarization measurements suggest that the leading side is covered with pulverized dust whereas the trailing side consists of dust-free rock or gravel (Dollfus, 1975). The optical data are particularly intriguing: the leading hemisphere is usually darker, but it undergoes a large opposition surge to become brighter than the trailing hemisphere when its face is fully illuminated. In the absence of a scattering model for planetary surfaces, the available optical observations have never been properly interpreted. Fortunately, in the past several years, radiative transfer models (e.g., Hapke, 1986) have been developed and applied to a large number of airless planets and satellites. If accurate photometric measurements are obtained over a wide range of scattering geometries, estimates to better than 10% can be made of the following physical parameters: the single scattering albedo (w), the mean slope angle of rough features (θ), the Henyey-Greenstein asymmetry factor in the single scattering phase function (g), and the fraction of space occupied by particles in the regolith (f).

Voyager imaging observations of Callisto have been reduced and combined with ground based telescopic data to product complete solar phase curves of both its leading and trailing hemispheres. These curves have been fit to a scattering model to yield the results shown in the Table. We find that the leading side of Callisto is composed of particles which are more strongly backscattering and less highly compacted than the trailing side.

We attribute this hemispheric difference to enhanced micrometeoritic bombardment of the leading side, and note that Europa has the opposite dichotomy (i.e., the trailing side is fluffier; see Buratti et al., 1988) possibly because of enhanced magnetospheric interactions in its vicinity.

A similar analysis for Ganymede has shown that its surface texture is hemispherically uniform.

TABLE

	w(± 0.03)	θ(± 0.03)	g(± 0.02)	f(%)	p(geom.albedo ± 0.02)
Callisto					
Leading Side	0.43	0.36	-0.23	8	0.23
Trailing Side	0.45	0.29	-0.17	12	0.20

Buratti, B. et al. (1988). Nature 333, 148.
Dollfus, A. (1975). Icarus 25, 416.
Hapke, B. (1986). J.G.R. 86, 3039.

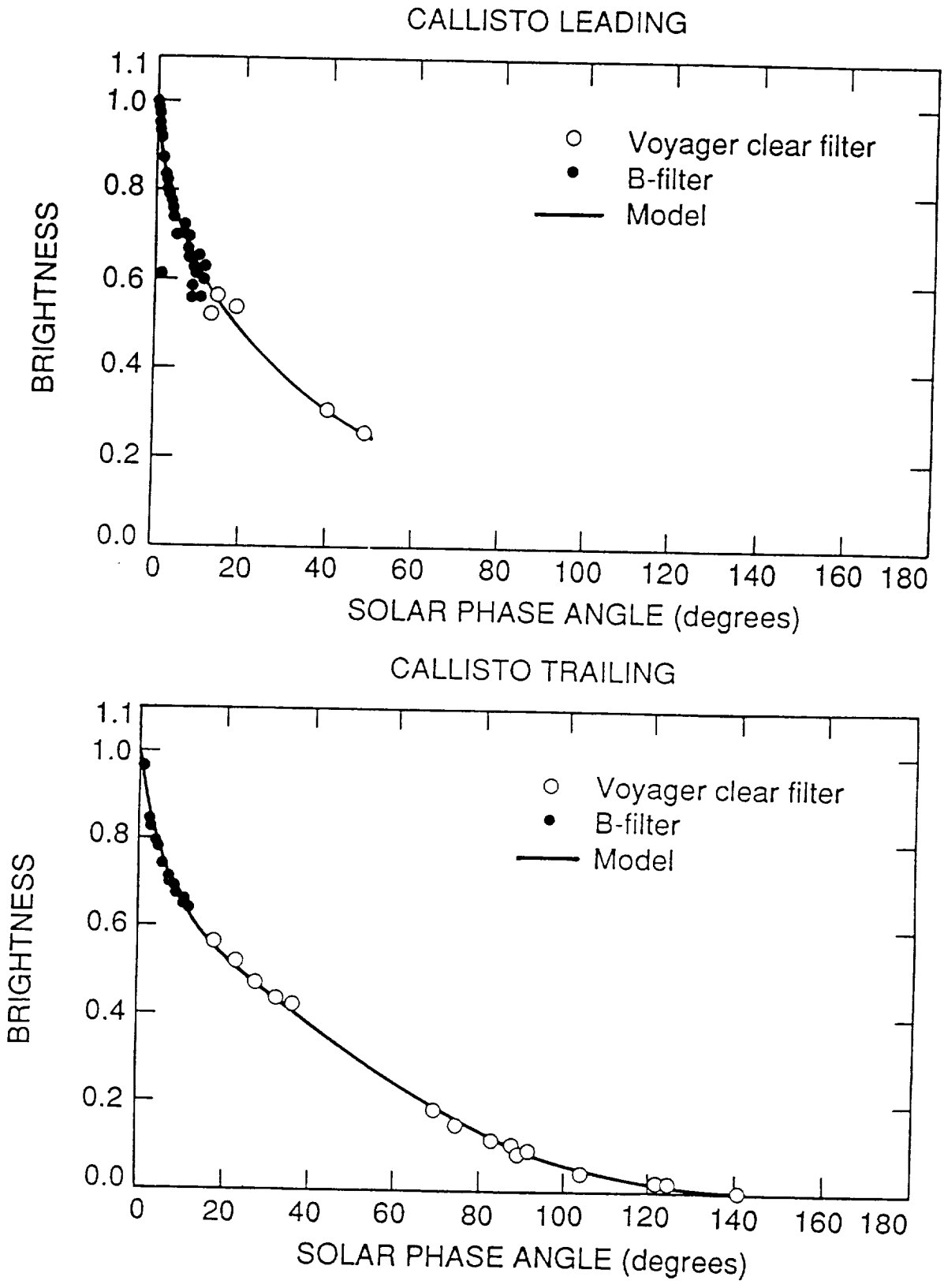

Figure. The model fit from the Table shown with the available observations of the leading and trailing sides of Callisto.

Physical Processes in Planetary Rings

Joseph A. Burns, Cornell University, Ithaca, NY 14853

Summary of Research Progress. Substantial advances have been made during the last twelve months on a variety of research topics supported by the above listed grant. Here I will first catalog seven of the topics that were addressed during the past year and then highlight three of them, those in which the most scientific advances were made. 1) In an attempt to understand the cause of Saturn's F ring's bizarre structure, we analyzed a selection of the best images to search for periodic features that might be produced by nearby moonlets. 2) We considered the dynamical fate of dust lost from Phobos, including solar radiation and electrical forces, in an attempt to understand the possible detections of debris by the PHOBOS spacecraft; the latter forces occur because the grains rapidly become charged and move through the solar wind's magnetic field that is convected past Mars. 3) We investigated the dust and debris hazards faced by spacecraft flying past asteroids and through Saturn's E ring. 4) We introduced "collisions" into a numerical code that we have been developing over the past few years for the history of a narrow ring as perturbed by shepherd satellites that may move along elliptical or inclined orbits. 5) We studied the possibility that corotational Lorentz resonances might determine the location of the two outer narrow Neptunian dust rings. 6) We made major revisions to a general review of planetary rings that was last revised in the early 1980s and that is appearing in the third edition of a popular survey of the solar system, and we contributed to a review of the properties of the rings of Uranus. 7) In research partly supported by this grant, we completed a review of the contradictory evidence coming from dynamics versus that from physical properties as to the origin of the Martian satellites. Various visitors to Cornell, who received living stipends partially from this grant, carried out research on the dynamics of Pluto, the orbital histories of the known Earth-crossing asteroids, and numerical simulations of the Neptunian arcs.

1. Periodic Structures in Saturn's F Ring

Kolvoord, Burns and Showalter examined Voyager narrow angle frames of Saturn's F ring for clumps and azimuthal periodicities. Using a collection of overlapping Voyager 1 images (FDS 35044.24 - 35045.36) that span $\sim$ 140° in longitude with an average radial resolution of $\sim$ 60 km/pixel, we have measured the equivalent width $\int I / Fdr$ of a strip surrounding the F ring as a function of azimuth, after appropriate calibration and background subtraction. A Fast Fourier Transform of these data shows several discrete wavelengths rather than the range of values described in the initial Voyager reports. The strongest signal in this data corresponds to the spacing of two bright clumps that are perhaps the signatures of embedded satellites with dislodged regolith. Since nearby satellites should produce periodic features with $\lambda = 3\pi\Delta a$, where Δa is the separation in semimajor axes of perturber and perturbee (Showalter and Burns, *Icarus* **52**, 526-544), we can identify the perturbations of proximate moons. The gravitational signature of Prometheus (inner adjacent moon) is strong, while that of Pandora (outer adjacent moon) is absent, as expected since Prometheus is both more massive and closer to the ring. Other features may indicate the presence of as-yet unseen nearby moonlets (cf. Cuzzi and Burns, *Icarus* **74**, 284-324); since the separation in semimajor axes is specified by λ, the strength of the signatures requires that the moonlets

be on elliptical ($e \sim 10^{-2}$ - 10^{-3}) orbits so that they pass close to the ring. Voyager 2 data give similar, but less convincing, identifications.

2. Fate of Dust Lost from Phobos

Horanyi, Burns, Tatrallyay, and Luhmann investigated the dynamics of small dust grains ejected from the Martian satellites, considering both the solar radiation perturbation and electromagnetic forces since the grains move in a magnetized plasma. Lorentz forces can dramatically change the nature of the trajectories, resulting in, for example, prolonged lifetimes for submicron-sized grains moving through our idealized model. Though temporal changes of the solar wind were ignored and we only followed grains for 20 *days* or less, we suggest that a permanent, non-uniform and time-dependent dust halo of grains predominantly around 0.1μm may exist about Mars.

3. Debris Hazards about Asteroids and Saturn

Future missions to the outer solar system are planned to make close approaches to asteroids, subjecting the spacecraft to unknown hazards from possible orbiting debris. In an effort to assess the extent of this increased risk, *Hamilton and Burns* have numerically investigated orbits around an asteroid in the circularly restricted three-body problem using a mass ratio $\mu = 5\text{x } 10^{-12}$ which corresponds to an asteroid with $R \sim 100$ km and $\rho \sim 2.9 g/cm^3$. The asteroid's orbit was taken to be circular with a semimajor axis of 2.55 AU. Retrograde orbits remain bound more than twenty years when started on circular orbits of distances less than 44,500 km, although the particles reach distances of 49,500 km due to orbital eccentricities that develop. For prograde motion over 300 years, these values are 22,000 km and 36,000 km. Distances should scale with the Hill radius $(\frac{\mu}{3})^{1/3}$ or with R for application to other asteroids.

Working in a system rotating with the asteroid's mean motion, we find quasi-periodic orbits that separate regions of nearly circular motion from escape orbits for both prograde and retrograde motion. Since prograde and retrograde orbits differ so greatly, we explored escape as a function of orbital latitude. Only retrograde orbits of low inclination are unusually stable; thus, if an ensemble of particles were started at all radial locations with all possible velocity orientations, the region in which particles would remain many years later would be roughly spherical up to about 50° latitude and then flat across the top. For this reason, we suggest that spacecraft flybys take place over the pole of the asteroid's orbital plane. This investigation did not address mechanisms for population of such distant orbits.

Burns, Kolvoord, and Hamilton studied the likelihood of particles being found along the orbital paths of Saturnian satellites. Such co-orbital material may give clues about accumulation processes and may affect a satellite's recent bombardment history. Also, with Cassini planned to maneuver close to many satellites for observations and for gravity assists, the mission could be jeopardized by any mm particles that reside along satellite orbits.

We have applied past numerical and analytical results on the three-body problem to consider the stability of co-orbiting particles in Hill's limit (mass ratio μ of satellite/Saturn $\rightarrow 0$). For the various Saturnian moons, we calculate regions that are populated by stable tadpole ($\Delta r \sim \mu^{1/2}$) and horseshoe orbits ($\Delta r \sim \mu^{1/3}$) as well as zones of chaos ($\Delta r \lesssim \mu^{2/7}$) and of gravitational wakes ($\Delta r > \mu^{2/7}$); Δr is the radial separation between the orbits of a

satellite and a particle. These trajectory types do not differ much for small out-of-plane motion.

Co-orbital material other than the known Lagrangian moonlets of Dione and Tethys might cause some of the abrupt absorptions of charged particles noticed when spacecraft passed through the L- shells of Mimas, Enceladus, and perhaps Dione. We interpret these absorptions in terms of the lost regolith model of Cuzzi and Burns (*Icarus* **52**, 284-324), and we find debris clouds with τ L $\geq$ 10 km (τ = optical depth and L = cloud length); the likelihood of crossing a debris cloud is $<10\%$; typical widths are 10^3 km. To absorb Mev electrons, the constituents of these clouds must be at least a few mms in diameter. We thereby bound the likelihood that Cassini could be hit by such grains.

References

J. A. Burns, R. A. Kolvoord and D. P. Hamilton (1989). An assessment of potential hazards to the Cassini spacecraft from debris along satellite orbits. In Cassini Mission Proposal Information Package (JPL PD 699-11) **13**, 6-1 to 6-23. Abstract in *BAAS* **21**, 930.

D. P. Hamilton and J. A. Burns (1990). Orbital stability zones around asteroids. Rough draft prepared for submittal to *Icarus*. Abstract in *BAAS* **21**, 969.

M. Horanyi, J. A. Burns, M. Tatrallyay, and J. G. Luhmann (1990). On the fate of dust lost from the Martian satellites. *Geophys. Res. Ltrs.* To appear.

R. A. Kolvoord, J. A. Burns and M. R. Showalter (1990). Periodic features in Saturn's F ring. Submitted to *Nature*. Abstract in *BAAS* **21**, 929-930.

An Analysis of Arc Ring Dynamics

S. J. Peale (UCSB)

The confinement of planetary ring particles in a small range of longitudes near the line of apsides of a satellite in an eccentric orbit which is coplanar with that of the rings is investigated by determining the motion of a massless test particle in orbital resonance with the satellite (satellite/planet mass ratio = 10^{-7}), where the ratio of mean motions is close to $j/(j+1)$, (j=integer). The two lowest order eccentricity–type resonance terms in the disturbing function, commonly referred to as Lindblad and corotational resonances, as well as the lowest order secular terms are retained in the Hamiltonian, which is transformed into a constant of the motion by a series of canonical transformations. The transformations also reduce the problem to two degrees of freedom. The stable stationary point of the system corresponds to completely damped libration of both resonance variables where the Hamiltonian has its maximum value. The libration of the corotational resonance angle $\theta_2 = j\lambda_1 - (j+1)\lambda_2 + \varpi_2$ confines the particle to a narrow range of longitudes about any of j sites around the orbit. The surfaces of section for the $j = 2$ case, with θ_2 and its conjugate variable being the coordinates, for various values of the Hamiltonian do not overlap greatly and their superposition resembles the a level curve diagram for a single resonance except the separatrix between libration and circulation is replaced by a wide chaotic zone. The resonances are more strongly interacting as j is increased and superposition of the surfaces of section is no longer possible. Quasiperiodic libration prevails in the $j = 4$ case up to amplitudes of about 30° in real space (Maximum amplitude = 45° for $j = 4$ before adjacent libration zones overlap.), but nearly the entire libration zone is chaotic for larger amplitudes. Even for small amplitude libration, the amplitude varies wildly from one libration to the next. The complex motion induced by the interaction of the resonances in quasiperiodic libration and even more so in the chaotic zones implies that an ensemble of particles in an arc ring will be continuously mixed with the subsequent dissipation of energy via collisions. If we model this dissipation as a constant rate of decrease in the orbital energy while conserving angular momentum on the average for a representative particle of the ensemble, the mean amplitude of libration is reduced as the Hamiltonian climbs toward its maximum value at the stationary point. The effects of the perturbing satellite may thus stabilize arc rings against the tendency for them to disperse because of interparticle interaction.

This work was motivated by the observation of probable arc rings around Neptune through stellar occultations before the arrival of Voyager 1. The approach used here differs from that of Goldreich *et al.*, who also proposed a corotational orbital resonance as the confining mechanism in that eccentricity–type resonances rather than inclination–type were used and the phase space of the motion of a test particle trapped in the resonance was thoroughly investigated with surfaces of section. The limited region of non chaotic libration was therby revealed.

In August observations made by the Voyager 1 spacecraft revealed an arc ring system consisting of 3 close but distinct segments. The ring system was close to a j=4 orbital resonance with one of the newly discovered satellites. But apparently the rings are not in this or any other orbital resonance, and the existence of three short, close segments is not consistent with a confinement in longitude by a corotational orbital resonance. The above theory of confinement therefore probably does not apply to the observed arc rings of Neptune, although it remains a viable mechanism for such a confinement. Unfortunately, the precise orbital periods for the various satellites has not been released as of this writing. The information that the rings were not in any orbital resonance with a satellite was obtained from P. Goldreich (private communication, 1989).

Structure of Saturn's Rings: Collisional Properties of Water Ice Particles

Frank Bridges,* D.N.C. Lin,# K. Williams,* and J. Truher*
*Physics Department, University of California, Santa Cruz, Santa Cruz, CA 95064
#Astronomy/Astrophysics Department, University of California, Santa Cruz,
Santa Cruz, CA 95064

The formation and continuing evolution of the Saturnian ring system (and other ring systems) depends crucially on the dynamics of the constituent particles. The energy losses in very low velocity collisions, the erosion and aggregation processes, as well as their dependence on the surface properties of the particles, all play an important role. For zero-impact-parameter collisions, we have shown previously[1] that the coefficient of restitution, ε, varies substantially with particle velocity and approaches $\varepsilon = 1$ at velocities below 0.05 cm/s. However, ε is very dependent on the surface properties -- the roughness of the surface and the amount and thickness of surface frost. Generally, freshly frosted surfaces have a low value for ε initially; repeated collisions that compact the frost result in relatively high values of ε. Similarly, we have found[2] that in such collisions the amount of mass transferred per collision is strongly dependent on the surface properties; however, the erosion as a result of collision is extremely slow at velocities typical of the velocities in Saturn's rings.

Recently[3] we have shown that the sticking forces between particles in low velocity, zero-impact-parameter collisions, can be quite large but again depend on the characteristics of the surface. At low temperatures, 100 - 140K, frost free ice particles do not stick at velocities down to 0.005 cm/s. For frosted surfaces, sticking can occur at velocities as high as 0.1 cm/s. The measured sticking force depends on the velocity of impact the thickness of the frost, and on the amount of compaction from previous collisions. For low velocity collisions (0.02 cm/s) with freshly deposited frost, the sticking force is small, typically less than 5 dynes for a 2.5 cm radius sphere on a flat surface. At somewhat higher velocities the measured sticking force is much larger. This suggests that the sticking force is dependent on the amount of interpenetration of the two frosted surfaces. At still higher velocities of impact (1 cm/s), the frost becomes compacted, the sticking force is zero, and remains very small in subsequent collisions. At lower velocities, compaction is slow and sticking occurs for many collisions, with a slowly decreasing sticking force.

At low velocities, when sticking occurs, the particle oscillates on the surface for a few cycles, with an initial amplitude of order 10 microns. From the period of the oscillations an estimate of an effective spring constant can be calculated. Once sticking occurs, if a small force is applied to the ice particle the displacement of the ice particle changes linearly with the applied force until the contact breaks. This indicates that the frost layer is somewhat fluid-like and it's thickness varies by 10's of microns.

Preliminary measurements of the coefficient of restitution for water ice particles coated with CO_2 frost have been carried out at low temperatures between 100 and 150K. At the lower temperatures ε is similar to that measured for frosted water ice particles. However, at somewhat higher temperatures (140K), ε is clearly smaller and appears to decrease more rapidly with velocity than for similar measurements for water frost. This suggests that the CO_2 frost is softer above 140K. If the temperature of the surface of ring particles approaches 140K and contains appreciable CO_2, a lower value of ε is expected. Further measurements are in progress.

In each of the investigations described briefly above, the collisions have been zero-impact-parameter collisions. How might the results change in glancing collisions? Is the coefficient of restitution smaller? Does sticking occur in glancing collisions? To address such problems we have

developed a 2-D pendulum system that allows glancing collisions (but does not allow rotations of the ice particle). Over the last year, the pendulum has been built, the new electronics to measure the ice ball position in both x and y directions has been completed, and some of the new software to control the experiment has been developed. The pendulum must now be mounted in the cryostat and procedures developed for balancing the pendulum and for calibrating the position sensors at low temperatures. Measurements at glancing angles will be more realistic and provide better estimates of how these parameters vary with impact parameter.

References

1. Hatzes, A.P., F. Bridges, and D.N.C. Lin 1988. Collisional Properties of Ice Spheres at low Impact Velocities. Mon. Not. R. Astr. Soc. **213**, 1091-1116.
2. McDonald, J.S.B., A.P. Hatzes, F. Bridges, and D.N.C. Lin 1989. Mass Transfer During Ice Particle Collisions in Planetary Rings. Icarus **82**, 167-179.
3. Hatzes, A.P., F. Bridges, D.N.C. Lin, and S. Sachtjen, Coagulation of Particles in Saturn's Rings: Measurements of the Cohesive Force of Water Frost, submitted for publication.

Dynamics and Structure of Planetary Rings

Richard G. French
Department of Astronomy, Wellesley College

During the past year, the PI's efforts have been devoted primarily to planning, conducting, and analyzing observations of the July 3, 1990 Saturn occultation of 28 Sgr obtained from McDonald Observatory using the 2.1m and 2.7m telescopes. On the 2.1m telescope, a 4-channel high speed aperture photometer was used with U, B, V, and R filters, along with a fifth channel that monitored the guide star intermittently throughout the observations. Because of the large contribution of reflected light from Saturn and its rings, and differences in the albedo of the planet and rings at these wavelengths, color correction methods have been employed to extract the normalized stellar signal from the data. An example of the efficacy of this technique is shown in Fig. 1 of the F ring region. The central and bottom panels show data from red and blue channels, in which the ring is concealed by atmospheric scintillation and by seeing variations. The top panel shows the occultation light curve reconstructed by combining data from both channels, exploiting the red color of the scar relative to the rings. The F ring is now clearly visible, near point 780. A refined version of this technique is now being applied to the entire data set.

The U. of Texas IR camera (58 x 62 pixels, at a plate scale of about 1"/px) was used on the 2.7m telescope to record the occultation at a central wavelength of 2.1 μm, where the signal from the highly reddened star could be discriminated against the reflected solar signal from the planet and rings, and where the background due to thermal radiation and absorption was relatively constant. Observations were made at a rate of 5 frames/sec for the time intervals 5:52 – 7:51 UT (spanning the ring system from just outside the F ring to the atmospheric immersion), 7:31 – 7:51 UT (covering the expected region for the central flash due to focussing of starlight around the limb of the oblate planet), and 8:18 – 9:34 UT (including atmospheric emersion and the ring system out to the F ring).

Photometric reduction of the nearly 40,000 individual frames is well underway. As an example of the scientific questions that can be addressed by these observations, we can compare the wavelength-dependence of the opacity of the outer C ring (a relatively low optical depth region) and the inner B ring (which is significantly more opaque). Voyager RSS and UVS occultation observations of this region are shown in Figure 2, along with the infrared (K-band) light curve of the 28 Sgr occultation obtained by the PI. The Voyager observations were normalized, converted to normal optical depth, and then transformed to the *predicted* intensity for the occultation geometry of the 28 Sgr occultation.

Figure 2(a) shows the Voyager RSS observations, scaled to correspond to the 28 Sgr geometry. The C ring structure is clearly shown, but because of the grazing incidence angle and the high optical depth, little structure can be seen in the B ring. Figure 2(b) shows the preliminary 28 Sgr light curve. The structure in the C ring corresponds very closely with what was seen in the predicted RSS curve, but there is additional structure revealed in the inner B ring as well. Figure 2(c) shows the scaled UVS observations, computed assuming that the predicted optical depths for the 28 Sgr occultation should be multiplied by a factor of two to correct for signal losses due to diffraction for the far-field Earth-based observations. Porco and Nicholson (*Icarus* **72**, 437, 1987) showed that this factor of two resulted in good agreement between the RSS and PPS observations of the outer C ring. This is confirmed Figure 2(c), where the scaled C ring structure nicely matches the RSS and 28 Sgr observations. However, the inner B ring structure does *not* match the other light curves – scaling the optical depth by a factor of two in this region predicts much more extinction than is actually observed. In Figure 2(d), the scale factor applied to the UVS-derived normal optical depth is one, instead of two. As expected, the derived C ring profile is more transparent than the actual ground-based data, but the B ring is now in much closer agreement.

From this comparison, we can see that the scattering properties of the inner B ring and outer C ring are quite different. This was not known on the basis of Voyager data alone. Once the 28 Sgr data have been properly calibrated, it will be possible to investigate a variety of plausible explanations for this difference. If this is due to a particle size effect, it would mean that the B ring has a significantly higher population of micron-sized particles than the C ring. This would have an important bearing on the evolution of the ring system since small particles have very short lifetimes against destructive processes in the rings.

Additional work in progress on the 28 Sgr observations includes analysis of the central flash, accounting for the effects of signal attenuation by passage of occulted starlight through the ring system. Figure 3 shows a comparison of the predicted intensity of the central flash scan as observed from McDonald Observatory ignoring (thick line) and including (thin line) the effects of the rings. Atmospheric occultations have also been analyzed to determine stratospheric temperature profiles, and a joint astrometric solution for the orbits of the rings and the direction of Saturn's pole is in progress.

We have also completed an extensive search for excited normal modes in the Uranus ring system in addition to the well-known m=0 mode in the γ ring and the m=2 mode in the δ ring. No additional normal modes have been found. This search will be revisited during July 1990, by which time we expect to have acquired important new observations of the rings by observations at the IRTF of the brightest stellar occultation in several years by this ring system.

Figure 1

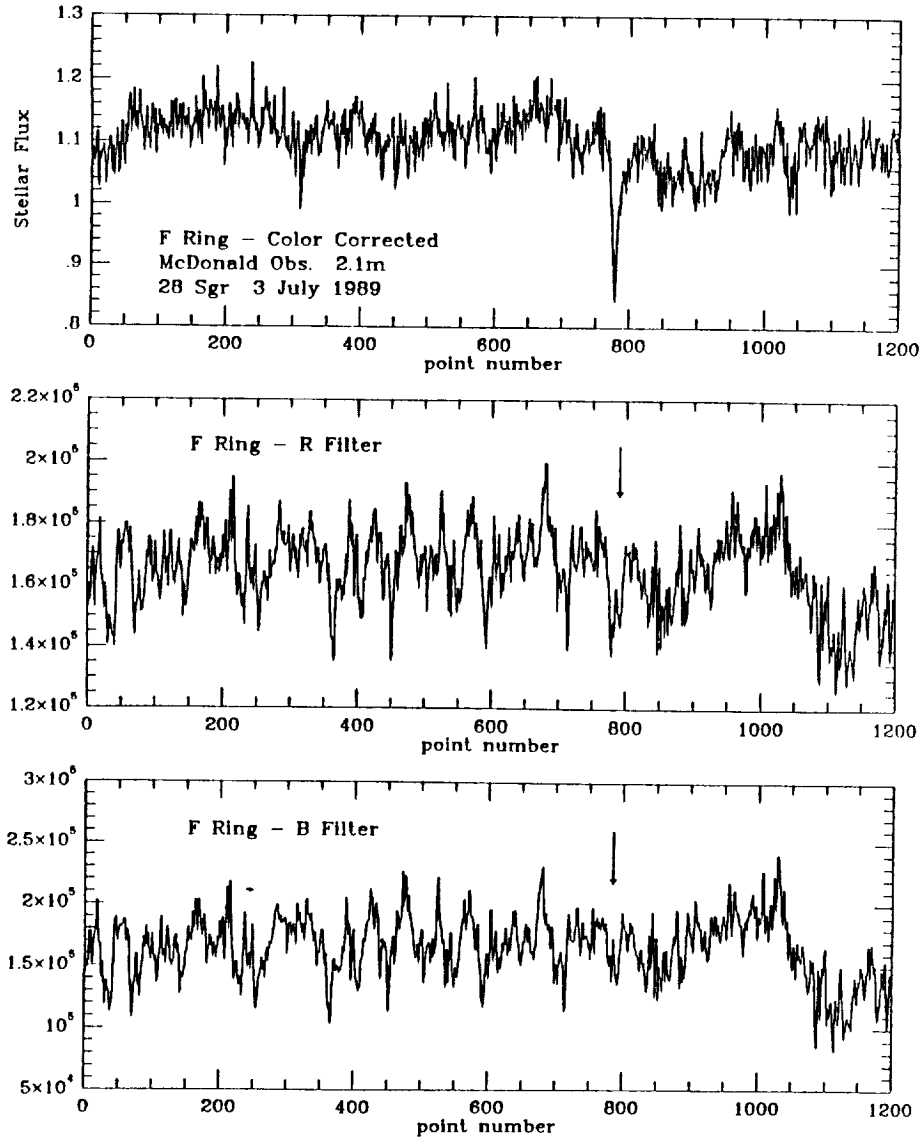

Figure 2

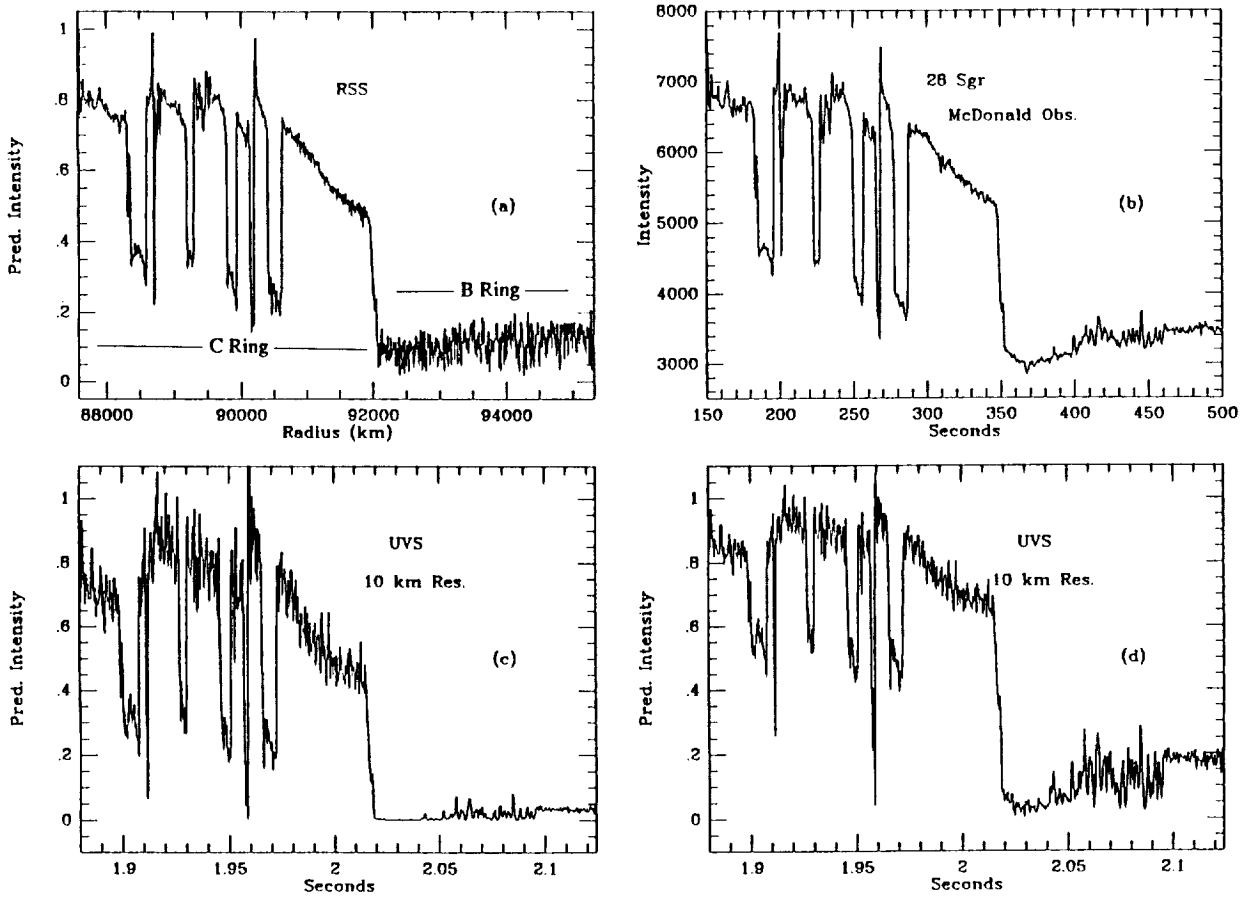

Figure 3

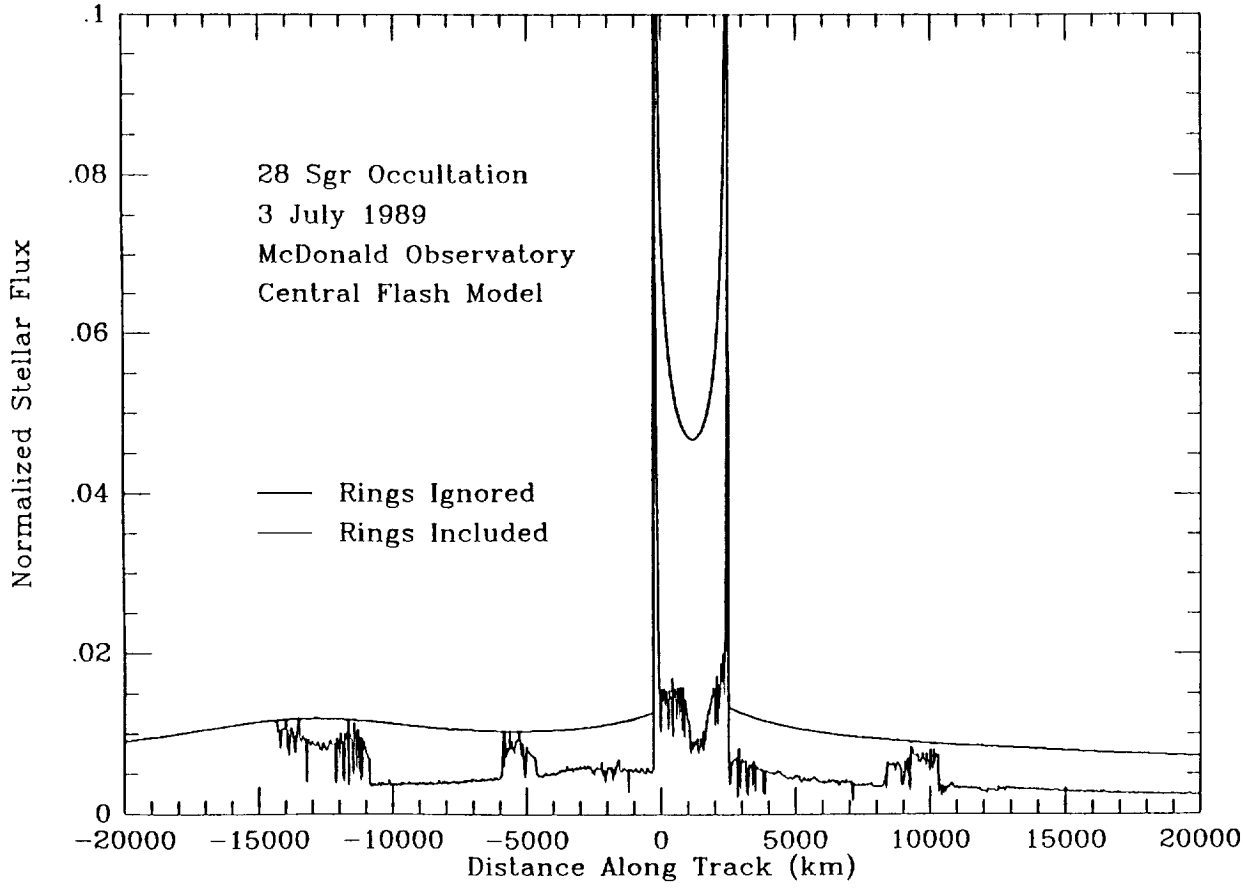

CHAPTER 3

COMETS AND ASTEROIDS

EARTH-CROSSING ASTEROIDS UPDATE; E.M. Shoemaker, C.S. Shoemaker, R.F. Wolfe, and H.E. Holt, U.S. Geological Survey, Flagstaff, AZ 86001.

The year 1989 marked a high point in the discovery of Earth-crossing asteroids. Fourteen new Earth crossers were found during the year, five of them in one remarkable dark-of-the-Moon observing period in late October and early November. These new discoveries plus an Apollo asteroid discovered in January, 1990, bring the total of known Earth crossers to 98, including 9 Atens, 62 Apollos, and 27 Earth-crossing Amors. Of these asteroids, 59 have precisely determined orbits and are now numbered, 10 are lost, and most of the remainder have been discovered too recently to have been observed on a second apparition.

Two discoveries in 1989 of special interest were 1989 AC and 1989 FC. Found on January 4 by J.-L. Heudier, R. Chemin, A. Maury, and C. Pollas at Caussols, France, 1989 AC is the sixth brightest known Earth crosser (H = 14.2). It was followed at about 20 observatories around the world. An early preliminary orbit permitted C.S. Shoemaker to find and measure prediscovery positions from films taken by H.R. Holt and T.A. Rodriquez at Palomar on July 17, 1988. This increase in the length of the observed arc enabled C.M. Bardwell to link 1989 AC with 1934 CT, which was observed on two nights in February, 1934, at Uccle, Belgium. Hence, 1989 AC was actually the second Apollo asteroid to be observed at the telescope.

1989 FC was discovered at Palomar by H.E. Holt and N.G. Thomas on March 31, 1989, eight days after it had passed within about 690,000 km of the Earth. This is the closest known approach of any asteroid to Earth. A campaign of observations organized by E. Bowell of Lowell Observatory resulted in a good preliminary orbit based on a 66-day arc; this orbit should be sufficient to permit recovery observations of 1989 FC in 1990, which are needed to assure that this very faint object will not be lost. At H = 21.0, 1989 FC and 1988 TA are the faintest known asteroids with relatively accurate orbits. If they are S-type asteroids, as are the majority of known Earth crossers, they are about 200 m in diameter.

Our estimate of the population of Earth-crossing asteroids to H = 17.7, based on discoveries to date, is shown in Table 1.

Table 1. Earth-crossing asteroids discovered through February, 1990

	Number discovered		Percent Discovered	Estimated Population
	Total	$H \leq 17.7$	$H \leq 17.7$	$H \leq 17.7$
Atens	9	5	(5.8)	90 ± 40
Apollos	62	41	5.8	690 ± 300
Earth-crossing Amors	27	15	(5.8)	250 ± 130
Total Earth crossers	98	61	5.8	1030 ± 470

The total population is based on the rate of discovery of Earth crossers with the 46-cm Schmidt camera at Palomar Observatory, and the proportions of Atens, Apollos, and Earth-crossing Amors is based on their proportions among the discovered objects. Present evidence suggests that the discovery of Earth-crossing asteroids is complete at H = 13.24, the magnitude of the brightest known object. For Earth crossers fainter than mag 15.8, the slope of the magnitude-frequency distribution is assumed to be similar to that of main-belt asteroids (cumulative frequency approximately proportional to $e^{0.92H}$), as shown in Fig. 1. The frequency evidently drops precipitously for objects brighter than mag 15.8 (cumulative frequency roughly proportional to e^{2H}).

A check on the inferred magnitude-frequency distribution of the Earth-crossing asteroids is provided by the frequency with which Earth crossers have been accidently rediscovered (Table 2). Nine have been rediscovered or recovered without deliberate search. The probability of rediscovery is a strong function of absolute magnitude. Rediscovered asteroids are all brighter than H = 16.25; most are mag 15 or brighter. The brightest Earth crosser, (1627) Ivar, was discovered in 1929, then lost, rediscovered in 1957, and serendipitously recovered in 1985 with the Palomar 46-cm Schmidt. Another Earth-crossing asteroid as bright as or brighter than Ivar is unlikely to have escaped detection. Four out of 11 known objects in the magnitude range 13.0-14.9 have been accidentally rediscovered, which suggests that completeness of discovery to H = 14.9 is about 36%; the completeness indicated in Fig. 1 is 36%. Four out of 21 known objects, or 19%, have been rediscovered in the magnitude range 15.0-15.9. This may be compared with the ratio of 12% for the number discovered to the population predicted in this range. Within the large uncertainty due to small statistics for rediscoveries, the two ratios are similar. One object out of 29 (3.4%) has been discovered in the magnitude range 16.0-17.7, as compared with a rediscovery rate of 3.5% predicted from Figure 1.

Table 2. Rediscoveries of Earth-crossing asteroids

Range of magnitude (H)		H	Fraction rediscovered	
	1627 Ivar	13.24		
13.0-14.9	4179 1989 AC	14.2	4/11	(36%)
	3122 1981 ET3	14.3		
	4183 1959 LM	14.6		
	3573 1986 TO	15.0		
15.0-15.9	2201 Oljato	15.56	4/21	(19%)
	1620 Geographos	15.61		
	1863 Antinous	15.81		
16.0-17.7	2100 Ra-Shalom	16.21	1/29	(3%)

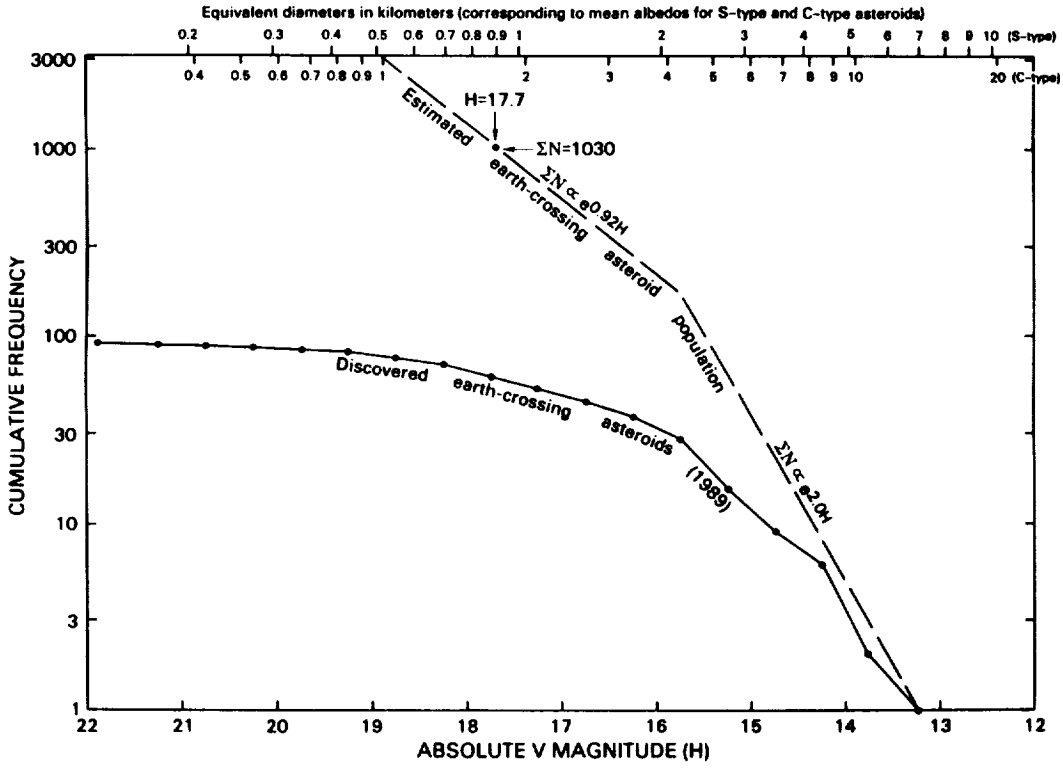

Figure 1. Magnitude-frequency distribution of Earth-crossing asteroids

We have updated our estimates of probabilities of collision with the Earth for Earth-crossing asteroids, using the equations of Shoemaker et al. [1]. Where we were unable to derive the collision parameters from secular perturbation theory, we used the equations of Opik [2]. The frequency distribution of collision probabilities is strongly skewed (Fig. 2): half a dozen asteroids have collision probabilities substantially exceeding 10^{-8} yr^{-1}. Mean probability of collision is 10.7 x 10^{-9} yr^{-1} for Atens, 4.1 x 10^{-9} yr^{-1} for Apollos, and 1.4 x 10^{-9} yr^{-1} for Earth-crossing Amors. The grand mean probability of collision obtained for all categories of Earth-crossing asteroids is 4.2 x 10^{-9} yr^{-1}. The uncertainty in this estimate probably is about 40%.

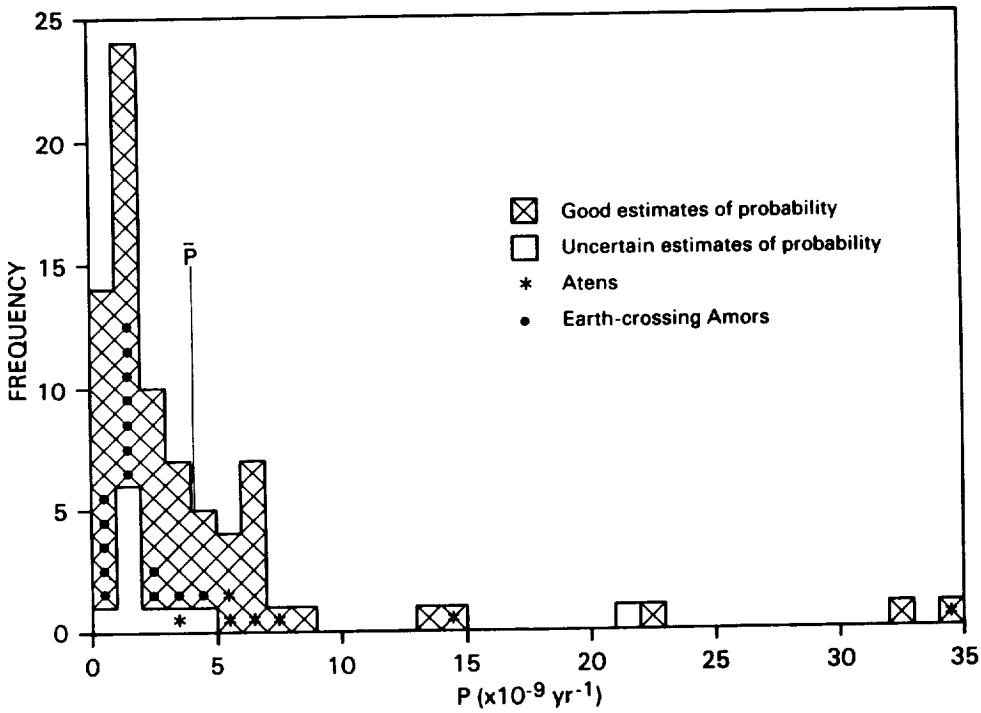

Figure 2. Frequency distribution of probabilities of collision with Earth for Earth-crossing asteroids

A correction should be made to the observed distribution of collision probabilities to account for observational selection in the discovery of Earth-crossing asteroids. The probablility of discovery of near-Earth asteroids is proportional to their dwell time in the Earth's neighborhood. For Earth crossers, the dwell time is inversely proportional to the velocity of the asteroid relative to the Earth near the time of encounter. The mean collision probability obtained by weighting the observed probabilities by the encounter velocities provides an accurate correction for observational selection. The corrected mean is $3.4 \times 10^{9} yr^{-1}$, about 20% lower than the observed mean.

Multiplying the corrected mean collision probability by the estimated population at H = 17.7, we estimate the present rate of collision for Earth-crossing asteroids to be $(3.5 \pm 1.8) \times 10^{6} yr^{-1}$, about 10% higher than that reported by Shoemaker et al. [1]. The colliding flux consists of about 70% Apollos, 20% Atens, and 10% Amors. Using improved data on the proportion of S- and C-type asteroids and the rms impact speed, weighted according to collision probability, of 17.9 km s^{-1}, we estimate that the production rate of asteroid impact craters larger than 10 km in diameter is $(1.4 \pm 0.7) \times 10^{-14} km^{-2} yr^{-1}$, somewhat lower than that given by Shoemaker et al. [1] and Shoemaker [3]. The collision rate of Earth crossers to H = 15.8 (roughly equivalent to S-type asteroids with diameters greater than 2 km) is about $6 \times 10^{7} yr^{-1}$; the rate to H = 13 (asteroids roughly 9 km in diameter and larger) is about $3 \times 10^{9} yr^{-1}$.

References: [1]Shoemaker, E.M., Williams, J.G., Helin, E.F., and Wolfe, R.F., 1979 in Gehrels, T., ed., Asteroids, Tucson, Univ. Arizona Press, p.253-282. [2]Opik, E.M., 1951, Proc. Roy. Irish Acad. 54A, p. 165-199. [3]Shoemaker, E.M., 1983, Ann. Rev. Earth Planet. Sci., v. 11, p. 461-494.

SOLAR SYSTEM DYNAMICS

J. G. Wiliams and J. Gibson, Jet Propulsion Laboratory, California Institute of Technology, Pasadena, CA, 91109

This report will discuss two efforts, one a study of the Alexandra asteroid family and the other the measurement of positions of comets and asteroids.

Like other asteroid families, the Alexandra family presumably originated when a parent asteroid suffered a collision. From the volume of the known fragments, the diameter of the parent was at least 230 km. One of the curiosities about this family is that most (93%) of the volume of the observed fragments remains in three large pieces: 54 Alexandra with a diameter of 171 km, 145 Adeona (155 km), and 70 Panopaea (127 km). The three large pieces are roughly aligned, with Alexandra and Panopaea at opposite end of the family. Somehow these two large remnants were separated at several hundred meters/sec, the remainder of the fragments spilling out between them, but managed to survive as large pieces. While normal asteroid families represent events from modest cratering events to total destruction, the Alexandra family is a case of considerable violence without total destruction. The most curious fact about the family is that Adeona, the more centrally located of the three large asteroids, is in a disk-like distribution of asteroids. This disk is seen in proper element space and it implies a disk-like distribution in velocity space. The thickness of the disk is about 1/10 the size of the family. About half of the family members are in the disk. All of the family members are dark except one; the three large objects are C class and one disk member is a rare T-class object. These facts have been reported (Williams, 1988).

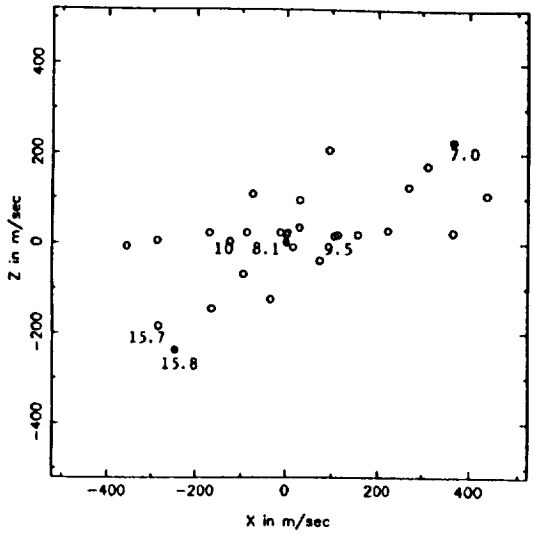

Further studies of the family during the past year have provided further knowledge. Six members of the family have measured rotation periods and the periods, in hours, are indicated in the figure. Two of the periods have been provided by Harris (private communication, 1989); the others may be found in Lagerkvist et al. (1989). The disk is seen edge on and the three large asteroids are marked by filled circles. There appears to be a correlation between the rotation period and the position in the family with the fastest spinning at the Alexandra end of the family and the slowest spinning at the Panopaea end. This correlation makes sense since the strength of the forces and their gradients which acted on the fragments at the time of breakup should both depend on the distance from the site of impact. The fragments should rotate away from the site of impact. Laboratory impact experiments have seen this clearly (Fujiwara and Tsukamoto, 1981). From the spin rates and speeds of separation it can be estimated that only 1/10,000 of the kinetic energy went into spin compared to the speeds.

Other facts about the family have been learned. The size distribution of small fragments (D<100 km) was determined from numbered asteroids and a faint survey, allowing for completeness. The differential number versus diameter has an exponent of -4, steeper than the belt. This is at the boundary between finite and infinite total volume if extrapolated to zero size (the distribution must change slope at some small size) so only a 230 km lower limit can be set for the diameter of the parent body. Larger than 10 km, 200 Alexandra family members are expected. Taking into account the speeds of separation and the potentials of the bodies (using an assumed density of 2.5 gm/cm^3) the energy density was $4x10^8$ ergs/gm. This does not include the work which went into breaking up the parent body. Normal to the disk the rms scatter of disk members is 11 m/sec. This is so thin that eventually it may be possible to detect warping of the disk if it was formed in the gravity field of either Adeona or the parent body. Both the Alexandra family and its disk remain an enigma. The disk probably did not arise from rotational breakup because the spin periods are too slow. Neither does material orbiting the parent body seem likely because the speeds are too high. It may have originated from the geometry of the breakup, but this is not clear at all. The Alexandra family and its unique disk deserve further study.

During the past year positions of 11 planet crossing asteroids and 12 comets were reported. Included were positions for 10 comet recoveries and several asteroid recoveries. Positions of a 2:1 librating asteroid were also reported.

References

Fujiwara, A. and A. Tsukamoto, Rotation of fragments in catastrophic impact, Icarus, 48, 329-334, 1981.

Lagerkvist, C.-I., et al., Asteroid lightcurve parameters, in Asteroids II (eds. Binzel, Gehrels, and Matthews), Univ. Arizona Press, 1162-1179, 1989.

Williams, J. G., The unusual Alexandra family, Lunar and Planetary Science XIX, 1277-1278, 1988.

UNDERSTANDING ASTEROID COLLISIONAL HISTORY THROUGH EXPERIMENTS AND NUMERICAL STUDIES

Donald R. Davis and Eileen V. Ryan,
Planetary Science Institute, 2421 E. 6th St., Tucson, Arizona 85719 U.S.A.

The overall goal of this program is to better understand solar system history through interpretation of the observed size and spin distributions of asteroids, along with other constraints. A wealth of new data has accumulated on asteroids in the past two decades: sizes and rotation rates for different sized asteroids now exist not only for the entire population but also for the major taxonomic types of asteroids (Gradie et al. 1989; Binzel et al. 1989). New studies of dynamical families (Zappalà, et al. 1990) continue to refine our knowledge of the number and membership of these groupings. Asteroids of the M and A taxonomic classes are widely believed to be produced by large scale asteroid collisions, yet other bodies--Vesta in particular--seem to demand that collisions have not even significantly punctured a thin basaltic veneer on their surface. A fuller understanding of the asteroid complex (as with most other solar system bodies) will spring from integrating observations and data from many different disciplines into a coherent paradigm. For example, studies of the collisional evolution of asteroid sizes alone tells us little about the primordial asteroid population since many hypothetical initial populations collisionally relax to the present population (Chapman and Davis 1975; Davis et al. 1985). Only by invoking other constraints, such as the collisional evolution of asteroid spin rates, the preservation of Vesta's basaltic crust, the formation of dynamical families, and observed crater populations in the inner solar system, we can better reconstruct the asteroid population in the early solar system. We have developed a computer model for studying asteroid collisional evolution (Davis et al. 1985) and much of our recent work consisted of modification and application of this code, along with carryout of experiments and developing scaling laws.

As noted above, understanding asteroid collisional history requires linking many observational clues into an integrated model. Spurred by this realization, we, in association with colleagues in Italy have developed a numerical code that models the collisional evolution of both sizes and spins of the asteroid population. Our initial results reported at the Asteroids II meeting in March, 1988 reported on the changes in asteroid spin rates produced by large, disruptive collisions and by smaller cratering impacts.

However, for one important type of collisional outcome there existed no available model for calculating spin rates. This is a collision that shatters and partially disperses the fragments, leading to the formation of a "rubble pile" structure. To correct this deficiency, we modified the semiempirical model of Paolicchi et al. (1989) to calculate the spin rate of a partially reaccumulated "rubble pile." This model shows that there is a preferential loss of high angular momentum material in the direction of rotation, which we term the angular momentum "splash" effect somewhat analogous to the angular momentum drain for cratering impacts (Dobrovolskis and Burns 1984). This effect slows down asteroids in the size range where rubble piles are most common, thus offering an explanation for the fact that asteroids in this size range are observed to be rotating most slowly.

Incorporating this effect into our spin evolution model gives a comprehensive algorithm for calculating the spin rate changes for asteroids of all sizes. In order to understand the effects of the five important parameters of the model on the changes to both asteroid sizes and spins, we carried out a systematic exploration of parameter space. All cases starting with the same initial population and all bodies were rotating with an eight-hour period initially. Results of this analysis are:

- Asteroid spins have been affected considerably by collisions over solar system history, except perhaps for the largest asteroids.
- There is a large coupling between the change in asteroid sizes and rotational changes for most choices of the model parameters.
- The observed spindown at asteroid sizes of ~100 km likely results from the angular momentum "splash" effect (Cellino et al. 1990).
- Small asteroids are spinning slower than predicted from laboratory experiments and theoretical consideration. Whether or not this is related to the bifurcated nature of many small asteroids as revealed by recent studies (Ostro, 1989) remains to be determined.

We also developed and published a collision interpretation of the size distribution of asteroid taxonomic types. New work on the size distribution of the major taxonomic types of asteroids (Gradie et al. 1989) has revealed several different forms: The numerous C asteroids show a non-power law distribution, characterized by a relative peak on the size frequency distribution around 100 km diameter, while the S and M types show near-power law distribution. The P asteroids show a gentle curvature to the size distribution, with a decreasing slope with decreasing size. We developed and published an interpretation of these asteroid size distributions from the perspective that they are the products of collisional evolution and that these distributions tell us about the dynamic strengths characterizing the different taxonomic types of asteroids. This paper also predicted that the P asteroids would show a size distribution similar to that of the C types when further data are available on small P asteroids.

We carried out experiments at the Ames Gun Range designed to study collisional disruption of "rubble pile" structures and energy partitioning in disruption impacts. The motivation for using artificially constructed aggregates as targets is to simulate early solar system planetesimals, gravitationally-bound asteroid "rubble piles," and perhaps even comets. For the May 1989 AVGR run, two types of aggregate targets were used in 18 impact experiments. The first type consisted of weakly bonded gravel of a relatively restricted particle size. The second type is created by gluing together fragments from previously shattered cement-mortar targets (Davis and Ryan, 1990). The basic structure of these two types of aggregates is the same: strong constituent particles weakly bonded together.

Surprisingly, we found that these weak bodies behaved collisionally as if they were about as strong as basalts. This held true for the preshattered targets even after twice repeated impacts. Disruption of the glued-gravel aggregates resulted in many large fragments, much larger than the size of the constituent grains. The size distributions showed the expected two-slope power-law behavior, but they were slightly more discontinuous and irregular for the glued-gravel aggregates.

Finally, we collaborated on modifying and testing a two-dimensional numerical hydrocode model for studying large scale collisional outcomes. A numerical routine for simulating two-body collisions based on the Los Alamos two-dimensional hydrocode 2-D SALE (Amsden et al. 1980) was modified by E. Ryan in collaboration with H. J. Melosh and E. Asphaug to include material strength effects. Grady and Kipp's (1980) equations for time-dependent fragmentation resulting from tensile stress in one dimension were adapted for

the 2-D code. Output from this code includes a complete fragmentation summary for each cell of the modeled target: fragment size distributions, vector velocities of particles, peak values of pressure and tensile stress, and peak strain rates associated with fragmentation.

The first step in validating the new 2-D model was to compare it to the 1-D numerical results of Melosh (1987). As a test we injected a uniform compressive pulse into the bottom of a 300 m. x 1 m. rectangle of material (anorthositic basalt). Such a pulse corresponds to the Grady-Kipp model's implicit assumption of uniform strain-rate. The 2-D code results matched the 1-D predictions of Melosh (1987). In addition, when we used a cylindrical projectile impacting a spherical target, we accurately reproduced analytical solutions of Grady and Kipp for maximum tensile stress versus strain-rate, and fragment size versus strain-rate. The fragment size distributions displayed the characteristic two-slope power law behavior commonly seen in laboratory impact experiments.

The next step was to use the 2-D code with the initial conditions and parameters (energy, momentum) necessary to simulate a laboratory impact. A convenient experiment was a basalt-basalt collision done by W. K. Hartmann at the AVGR (1979, unpublished) where we knew the specifics of projectile/target mass, density, impact velocity, etc. The code was started with the same collisional energy and momentum as the 3 cm. cylindrical projectile impacting at ~250 m/sec the 3 cm. basalt target in the laboratory. The figure below shows the cumulative fragment size (mass) distribution predicted by the code in comparison to the actual laboratory results.

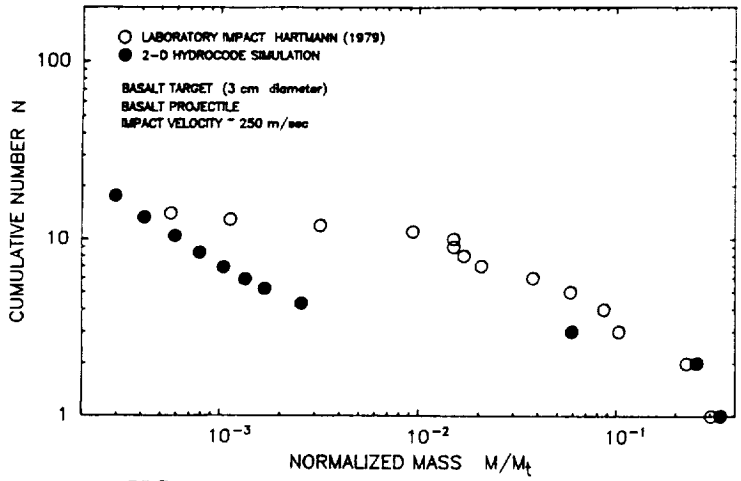

No other model has come this close to predicting fragment size distributions, and with minor adjustments we expect the correlation to be greatly improved. This, of course, was an initial trial and we will compare the code with numerous impact experiments and target materials and continue refining the algorithm accordingly.

REFERENCES

Binzel, R. P. et al. 1989, in Asteroids II, 416; Davis, D. R. et al. 1989, in Asteroids II, 805; Chapman, C. R. and Davis, D. R. 1975, Science 190:553-556; Davis, D. R. 1989, in Asteroids, Comets, Meteors III, 39-44; Paolicchi, P. et al. 1989, Icarus 77:187-212; Zappalà, V. et al. 1990, submitted to The Astronomical Journal; Davis, D. R. and Ryan, E. V. 1990, Icarus 83:156-182; Cellino, A. et al. 1990, submitted to Icarus; Melosh, H. J. 1989, Impact Cratering; Amsden, A. A. et al. 1980, Los Alamos Scientific Lab Report LA-8095; Grady, D. E. and Kipp, M. E. 1980, Int. J Rock Mech. Min. Sci. and Geomech. Abstr. 17; Dobrovolskis, A. and Burns, J. A. 1984, Icarus 57:464-476.

INVESTIGATION OF THE TROJAN ASTEROIDS; C.S. Shoemaker, E.M. Shoemaker, and R.F. Wolfe, U.S. Geological Survey, Flagstaff, AZ 86001

Our serendipitous discovery in 1984 of the high-inclination, bright L5 Trojan 3317 Paris (diameter 127 ± 8 km) led us to the realization that the dispersion of orbital inclinations of Trojan asteroids is greater than had been recognized and that a significant number of Trojans bright enough to be observed with the Palomar 46-cm Schmidt remain to be discovered [1]. By slightly modifying our ongoing Palomar asteroid and comet survey, we could search most of the L4 and L5 libration regions when these regions are favorably located in the sky. Accordingly, we initiated a search of the L4 region in the fall of 1985 [2]. The availability in 1987 of Kodak's high-resolution technical pan emulsion on a stiff base (film 4415) improved the threshold of detection for asteroids by a full magnitude and thereby increased the number of Trojans accessible to the 46-cm Schmidt by a factor of about 2.5. Renewed work was begun on the L4 region in 1988, and an intensive examination of the L5 region was made in the fall of that year. We are continuing the survey for bright Trojans with the goal of finding all Trojans brighter than H = 10.25 and of obtaining precise, multiple-opposition orbits for all known bright Trojans. Concurrently, surveys for faint Trojans are being carried out by L.M. French, S.J. Bus, and E. Bowell, using the Cerro Tololo 61 cm Schmidt and by E. Bowell and K. Russell, using the U.K. 1.2-m Schmidt [3].

To date, 53 Trojans have been found with the 46-cm Schmidt (Table 1). In 11 cases, previously known Trojans with short-arc orbits were rediscovered; multiple opposition orbits were thus obtained. Five Trojans found independently at Palomar were discovered nearly simultaneously at other observatories. Our new discoveries have increased the number of known L5 Trojans brighter than H = 10.25 by about 60%.

A question of considerable interest has been the relative sizes of the populations of the L4 and L5 swarms. Degewij and van Houten [4] suggested that L4 Trojans are about 3.5 times more numerous than L5 Trojans. The magnitude-frequency distribution of all discovered L5 Trojans brighter than B(1,0) = 11.25 (H < 10.25) is shown in Fig. 1. From our survey of the L5 region, we conclude that discovery is probably now complete to B(1,0) ≈ 10, the approximate magnitude of the brightest object that we found in 1988. At this magnitude, the cumulative numbers of objects in the L4 and L5 swarms are nearly the same. At fainter magnitudes, we suggest that the magnitude-frequency distribution of the L5 population follows the dotted line shown in Fig 1, which has been drawn parallel with the distributions estimated for L4 [1] and which extends from the observed frequency at B(1,0) = 10. Although we have found roughly equal numbers of new L4 and L5 Trojans, the mean magnitude of our L4 Trojans is about 0.2 mag brighter than that of our L5's. This difference is the consequence of exceptionally good observing conditions in the fall of 1988. It is clear that L5 Trojans are less numerous than L4's at magnitudes fainter than B(1,0) ≈ 10.25, but the difference is only about 30%, at least for Trojans brighter than B(1,0) = 11.25. Our suggested curve for the L5 population is close to that estimated by van Houten et al. [5] for L4. By extrapolation, we infer that there are about 100 L5 Trojans brighter than B(1,0) = 12.

The mean inclination of the Trojans found with the 46-cm Schmidt is 17.2 degrees in the L4 swarm and 16.1 degrees in L5. These values are slightly less than that of the total Trojan population (17.7 degrees) estimated by Shoemaker et al. [1] probably because of lack of coverage of the libration regions at high southern ecliptic latitudes.

Since mid 1988, the total number of known Trojans has increased from 157 to 257; 141 are in the L4 swarm and 116 in L5. This increase is due chiefly to new discoveries with the Palomar 46-cm Schmidt and with the Cerro Tololo 61-cm Schmidt. Altogether, 61 Trojans are now numbered, and multiple opposition orbits have been obtained for 121 Trojans, 54 in the L4 swarm and 67 in L5. Two-month-arc orbits are available for an additional 19 Trojans. The large increase in multiple opposition orbits available for L5 Trojans has made possible, for the first time, a successful search of the L5 swarm for dynamical pairs and groups of possible collisional origin. We calculated proper elements by analytical methods presented in [1] for 67 multiple opposition orbits and 11 two-month arc orbits of L5 Trojans. Libration amplitude (D), proper eccentricity (e_p), and proper inclination (i_p) obtained by analytical methods are closely similar to the same proper elements obtained by Bien and Schubert by numerical integration for 21 numbered L5 Trojans [6]. Ten fairly closely matched dynamical pairs, one dynamical group of three Trojans, and three somewhat tentative pairs were found (Table 2). Calculated velocities of separation for all recognized pairs and within the group of three are comparable with separation velocities between members of main asteroid belt families. The most closely matched pair includes the numbered Trojan 2241 and 1988 TU1, a fairly bright Trojan discovered with the Palomar 46-cm Schmidt.

Table 1. Trojans discovered with the Palomar 46-cm Schmidt

	H	Epoch	M	Peri.	Node	Incl.	e	a	Arc	O	Source
L4 Trojans											
3596 Meriones*	9.5	851114	12.54	66.27	355.97	23.58	0.0753	5.1249	---	--	MPC11835
3709 Polypoites	9.8	808277	38.21	246.97	186.48	19.61	0.0636	5.2648	---	--	MPC14165
3793 Leonteus	8.8	880827	14.69	261.46	199.81	20.96	0.0922	5.1667	---	--	MPC12956
3794 Sthenelos	9.9	880827	94.08	34.29	342.62	6.07	0.1458	5.1887	---	--	MPC12956
4007 Euryalos*	10.0	891001	56.98	78.99	6.08	11.02	0.0582	5.1486	---	--	MPC14326
4068 Menestheus*	9.5	891001	0.66	312.65	177.29	17.48	0.0791	5.2571	16yr	18	MPC14598
1973 SQ1* (89 AO2)	10.0	891001	160.37	127.22	212.60	6.16	0.0251	5.1584	16yr	8	MPC14343
1973 SW1* (89 CJ2)	10.5	891001	17.50	103.10	29.19	10.61	0.0380	5.1226	16yr	13	MPC14942
1985 TG3	10.0	880827	66.58	86.05	307.96	11.72	0.0516	5.2622	2yr	10	MPC12786
1986 TR6* (89 EY4)	10.0	891001	73.69	149.80	277.32	12.01	0.0523	5.1055	3yr	15	MPC15067
1986 TS6* (89 BX)	10.0	891001	77.70	73.84	347.22	11.01	0.0759	5.2262	3yr	13	MPC14351
1988 AK * (89 AQ1)	9.0	891001	46.74	6.62	86.11	22.12	0.0636	5.3092	9yr	12	MPC14354
1988 BW1	10.0	880209	209.73	206.54	58.39	21.90	0.0471	5.2683	57	8	MPC13034
1988 BX1	9.5	880827	63.54	344.87	77.50	31.50	0.0662	5.2637	83	12	MPC13171
1988 BY1	10.0	880827	66.51	9.64	43.36	21.53	0.1345	5.2244	81	10	MPC13171
1989 AU1*	10.0	890114	356.49	231.81	247.53	5.86	0.0871	5.2954	40	10	MPC14461
1989 AL2	9.5	890203	104.40	278.71	100.96	34.55	0.0850	5.2522	59	4	MPC14461
1989 AM2 = 75XX3	9.5	891001	73.47	350.58	75.40	28.43	0.1362	5.2447	14yr	11	MPC14954
1989 AN2	10.0	890203	37.48	274.06	169.72	9.07	0.0451	5.2189	58	6	MPC14906
1989 AV2	10.0	890203	62.16	123.02	285.14	19.08	0.0942	5.2798	56	6	MPC14749
1989 BL *	10.5	891001	39.00	29.20	77.62	8.53	0.1047	5.2329	38yr	20	MPC14358
1989 BW	9.5	890203	55.23	355.00	70.51	17.48	0.1504	5.2053	58	5	MPC14461
1989 BB1	10.5	901105	279.41	193.45	66.77	15.92	0.0758	5.1895	11mo	6	Bardwell
1989 CK1	9.5	890203	15.07	33.50	81.36	19.45	0.0110	5.1514	56	6	MPC14906
1989 CQ1 = 77AP1	10.0	891001	87.76	85.36	324.71	14.74	0.0954	5.0842	12yr	7	MPC14794
1989 CH2	10.0	890203	14.56	0.39	115.75	29.83	0.0280	5.2112	56	6	MPC14906
1989 CK2	10.0	890203	43.00	341.14	102.09	20.26	0.0875	5.2018	57	6	MPC14906
1990 DK	10.5	900129	33.08	228.68	253.50	7.45	0.0509	5.1387	27	4	Bardwell
L5 Trojans											
3317 Paris	8.4	851201	348.28	147.42	135.33	27.90	0.1260	5.1924	---	--	MPC10036
4348 1988 RU	9.0	891001	9.52	157.98	219.50	7.96	0.0995	5.2395	---	--	MPC15694
1988 PY	10.3	901105	40.00	64.39	309.55	7.11	0.1241	5.1668	11mo	24	MPC16027
1988 PB1	10.5	891001	304.15	164.16	260.74	25.91	0.0460	5.2092	85	8	MPC14952
1988 QE	10.0	901105	350.95	168.10	241.35	7.70	0.0461	5.1436	11mo	9	MPC16028
1988 QY	10.5	880827	15.94	92.03	222.21	29.67	0.0743	5.1480	26	5	MPC13674
1988 RO *	10.5	880827	347.55	157.19	209.16	15.59	0.0941	5.1909	12	8	MPC13843
1988 RT	9.4	901105	32.66	102.96	280.43	6.97	0.0603	5.3013	1yr	11	MPC16028
1988 RV	10.0	880827	214.00	129.80	352.30	14.85	0.0409	5.2183	53	6	Bardwell
1988 RA1*	10.0	880916	16.18	18.52	316.20	15.88	0.1101	5.2057	32	10	MPC13674
1988 RF1	11.0	880916	6.76	337.89	1.54	22.38	0.1199	5.1134	28	4	MPC14156
1988 RG1	10.5	881006	28.89	161.46	159.17	23.81	0.0636	5.2850	59	6	MPC14156
1988 RK1	10.0	881006	16.12	283.04	61.43	9.34	0.0924	5.2588	58	7	MPC14157
1988 RM1	10.7	901105	65.89	122.59	221.43	8.63	0.0494	5.1021	11mo	12	MPC16028
1988 TA3 = 88RJ1	9.8	901105	167.75	90.36	155.37	10.88	0.1058	5.2969	14mo	7	MPC15893
1988 TH1	10.5	881026	29.78	169.98	171.55	10.79	0.0529	5.2101	36	6	MPC14595
1988 TU1	9.5	881006	23.12	206.35	134.62	19.09	0.1432	5.2068	52	6	MPC14157
1988 TZ1	10.0	881006	45.92	22.02	295.19	24.97	0.1117	5.2794	53	6	Bardwell
1988 TU2 = 54UM1	9.0	901105	82.61	93.03	252.69	25.59	0.0220	5.1437	34yr	14	MPC15892
1989 SZ = 88 RN1	9.5	901105	160.04	275.87	334.51	27.15	0.0161	5.1666	14mo	10	MPC15895
1989 SC7	10.0	891001	16.77	110.14	241.83	15.68	0.0107	5.2885	64	7	MPC15757
2035 T-3* (88 RW)	11.5	880827	23.07	338.94	337.08	6.56	0.1493	5.1576	11yr	16	MPC13688
4271 T-3* (88 TZ2)	10.0	880827	328.83	313.91	64.39	8.81	0.1131	5.2270	11yr	19	MPC14028
5010 T-3* (88 RH1)	10.0	891001	32.22	204.05	154.75	12.38	0.0112	5.1288	11yr	18	MPC14206
5191 T-3* (88 RX)	10.5	880827	23.43	170.96	140.53	12.76	0.1308	5.2367	11yr	10	MPC14029

*rediscovered or independently discovered

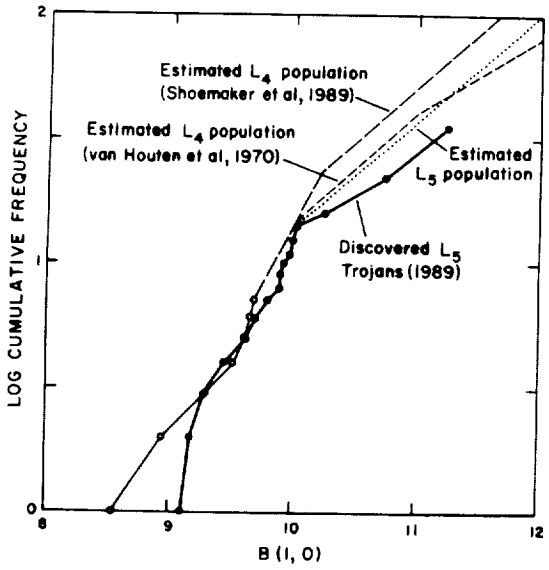

References: [1] Shoemaker, E.M., Shoemaker, C.S., and Wolfe, R.F., 1989, in Binzel, R.P., Gehrels, T., and Matthews, M.S., eds., Asteroids II, Tucson, Univ. Arizona Press, p. 487-524. [2]Shoemaker, C.S., and Shoemaker, E.M., 1988, Lunar and Planet. Sci. 19, p. 1077-1078. [3] French, L.M., Vilas, F., Hartmann, W.K., and Tholen, D.J., 1989, in Binzel, R.P., Gehrels, T., and Matthews, M.S., eds., Asteroids II, Tucson, Univ. Arizona Press, p. 468-486. [4] Degewij, J., and van Houten, C.J., 1979, in Gehrels, T., ed., Asteroids, Tucson, Univ. Arizona Press, p. 417-435. [5] van Houten, C.J., van Houten-Groeneveld, I., and Gehrels, T., 1970, Astron. Jour., v. 75, p. 659-662.[6] Bien, R., and Schubert, J., 1987, Astron. Astrophys., v. 175, p. 292-298.

Fig.1 Cumulative frequency distributions of L4 and L5 Trojans

Table 2. Candidate collisional pairs or groups in the L5 Trojan swarm

		D		e_p		i_p		H
		[6]	[1]	[6]	[1]	[6]	[1]	
	1988 RG1		32		.017		23.2	10.5
	1988 RO10		28		.027		23.1	13.4
2241	1979 WM	25	26	.101	.098	17.9	17.9	8.66
	1988 TU1		25		.102		18.0	9.5
	4035 T3		23		.074		17.5	12.1
	1988 SA3		35		.082		17.9	12.8
2223	Sarpedon	28	29	.038	.038	16.8	16.7	9.41
	1988 RR10		39		.029		16.7	13.5
884	Priamus	22	22	.087	.090	10.1	10.2	8.89
	1988 TA3		37		.099		10.2	9.8
	1988 RT		38		.062		8.3	9.4
	1988 RK1		27		.056		8.4	10.0
	4271 T3		8		.101		7.8	10.0
	1988 PY		18		.107		8.3	10.3
	1988 RG10		26		.028		4.5	11.8
	1988 RD12		25		.022		4.8	11.9
	1989 UQ5		40		.030		4.5	12.1
	4179 T3		17		.061		4.0	11.8
	1988 RP12		10		.063		3.8	12.8
2674	Pandarus	14	16	.088	.088	2.1	2.1	9.0
	1988 RL10		28		.084		2.6	12.5
	1988 RS10		27		.063		1.8	12.4
	1988 RH11		32		.059		2.2	13.3
	Tentative pairs							
1208	Troilus	21	27	.046	.055	33.0	32.8	9.0
2363	Cebriones	36	35	.033	.037	32.7	32.8	8.8
1867	Deiphobus	35	34	.029	.026	28.2	28.2	8.6
	1989 SZ		20		.043		27.9	9.5
3317	Paris	10	11	.079	.088	26.6	26.8	8.4
	1988 PB1		25		.077		27.2	10.0

Notes: Proper elements in columns headed with [6] are from reference [6]; proper elements in columns headed [1] were derived by the methods described in reference [1].

New Families Containing Faint Asteroids

R.F. Wolfe, U.S. Geological Survey, Flagstaff, AZ 86001

Since early in this century, many and often conflicting divisions of asteroids into families have been advanced (Hirayama, 1928; Brouwer, 1951; Arnold, 1969; Linblad and Southworth, 1971; Williams, 1979, 1989). The present study extends the work of J. G. Williams. Williams has linked asteroids into more than 100 families, using his proper elements, for about the first 2100 numbered asteroids and for Palomar-Leiden Survey (PLS) asteroids with one-month-arc orbits (Williams and Hierath, 1987).

The original impetus for the present study was to determine family membership of faint asteroids discovered by S. J. Bus in 1981 during the United Kingdom-Caltech Asteroid Survey (UCAS). This survey led to the determination of relatively precise orbits for about 1200 new faint asteroids. It was expected that examination of such a population of faint asteroids for family membership would shed considerable light on relative ages of families and on the collisional breakup process.

At present, multiple-opposition orbits have been calculated for about 6000 asteroids. The availability of this large number of precise orbits makes it possible to recognize and to study details of family structure more readily than ever before. Using osculating orbital elements from B. G. Marsden of the Minor Planet Center for numbered asteroids through number 4060 and for all multiple-opposition unnumbered objects, I calculated proper elements by the method of Williams (1969). In addition, I calculated proper elements from osculating elements of the UCAS asteroids. After removing all asteroids falling within Williams' family boundaries in semi-major axis, eccentricity, and inclination, I combined the remainder with all other non-family members for which proper elements had been calculated. From this sample, using both graphics and computer analysis, I have found over 30 new candidate families . Some of these families consist solely of faint PLS and UCAS asteroids. Table 1 lists proper elements of some of these new families.

The formation of a family in the asteroid belt by impact is the equivalent of the formation of an impact crater on a planet. Each family is the result of a discrete impact event. Collision of a small asteroid with a larger asteroid commonly disrupts the larger object completely; a number of smaller bodies are moderately dispersed in orbital element phase space by the impulses acquired during the impact. The distribution of family members in proper element phase space is illustrated for two families in Fig. 1. Relative sizes of the asteroids shown are based on infrared diameters, where available, and otherwise on absolute magnitudes and assumptions about the average albedo of the family. The Astraea Family illustrates the results of a cratering event without catastrophic disruption of the parent. Since all the family members except No. 5, Astraea, are typically a few kilometers in diameter, this family probably represents a relatively young (post heavy bombardment) impact event. In older families, such small members may be expected to have been destroyed by further collisions.

The Tiflis Family (Fig. 1) is a group of Mars crossers. (753) Tiflis itself is a shallow Mars-crossing asteroid with a crossing depth of -.015 (Table 1). From impulses acquired in the collisional breakup of the parent, most of the smaller fragments have become deeper Mars crossers. Their orbital elements, as would be expected, appear to have been further dispersed by Mars encounter. Thus, there is a greater spread in proper elements, particularly inclination, than in non-planet-crossing families. The fact that we can still recognize this family indicates that it must be fairly young, because encounter with Mars should lead to still larger dispersion of orbital elements in a period of on the order of a few hundred million years.

Asteroids such as Tiflis, which just graze the orbit of Mars, are an important source of deep Mars crossers. Most of these very shallow Mars crossers are found in a relatively stable region of proper-element space remote from resonances. They have very long dynamical lifetimes, and they may have occupied shallow crossing orbits from the time of heavy bombardment. Collisions with these shallow-crossing asteroids probably are a significant source not only of deeper Mars crossers but also of Earth-crossing asteroids, as further Mars encounters can deliver asteroids to Earth-crossing orbits. In the Tiflis family, we see evidence for the first stages of injection of collision fragments into deeper crossing orbits.

References: Arnold, J. (1969) Astron J. 74, 1235-1242; Brouwer, D. (1951) Astron. J., 56, 9-32; Hirayama, K. (1928) Jap. J. Astron. Geophys. 5, 137-162; Linblad, B.A., and Southworth, R.B. (1971) in Physical Studies of Minor Planets, T. Gehrels, ed., NASA SP-267, 337-352; Williams, J.G. (1969) Ph.D. Thesis, Univ. of Calif. Los Angeles; Williams, J.G. (1979) in T. Gehrels, Ed., Asteroids (Univ. of Arizona) 1040-1063; Williams, J.G. (1989) in R. Binzel, T. Gehrels, and M. Matthews, eds., Asteroids II (Univ. of Arizona) 1034-1075; Williams, J.G., and Hierath, J. (1987) Icarus, 72, 276-303.

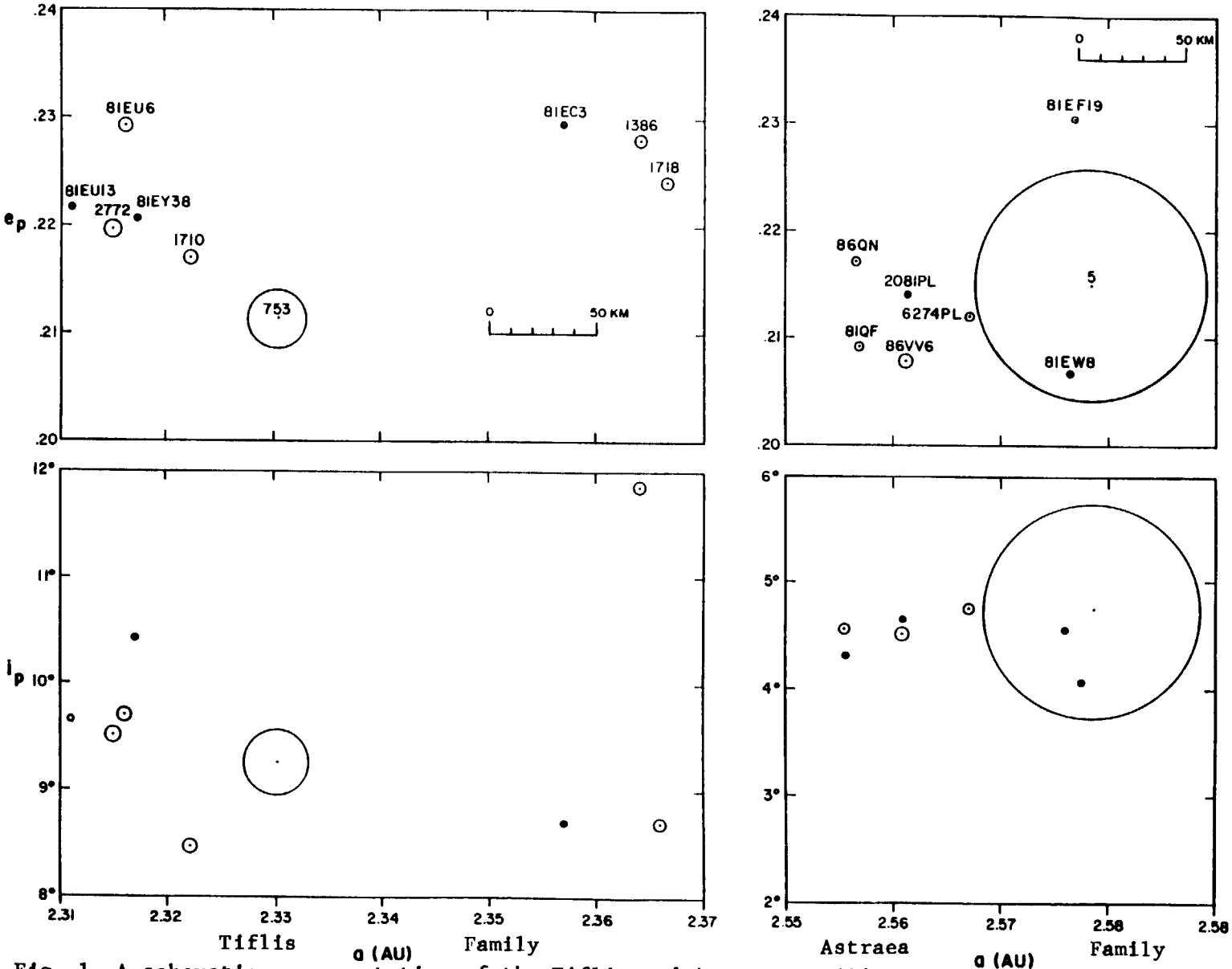

Fig. 1 A schematic representation of the Tiflis and Astraea Families

Astraea Family

Asteroid	a(AU)	e	i(deg)	d wbar	d node	mag	diam
86QN	2.5561	0.2170	4.5771	46.409	-57.195	14.00	(5)
81QF	2.5565	0.2089	4.2955	46.532	-56.482	14.60	(4)
2081PL	2.5610	0.2140	4.6461	46.600	-57.200	16.10	(2)
86VV6	2.5610	0.2079	4.4966	46.641	-56.638	12.70	(9)
6274PL	2.5670	0.2120	4.7610	46.700	-57.400	14.90	(2)
81EW8	2.5761	0.2066	4.5713	47.338	-57.477	16.00	(2)
81EF19	2.5769	0.2304	4.0485	47.816	-60.178	15.50	(2)
5	2.5780	0.2150	4.7610	47.300	-58.500	7.24	116
Means	2.5666	0.2140	4.5196	46.917	-57.634	number in family	8

Tiflis Family (Mars crossing)

Asteroid	a(AU)	e	i(deg)	d wbar	d node	mag	diam	Marsx
81EU13	2.3110	0.2218	9.6541	33.234	-42.707	16.00	(2)	-0.064
2772	2.3149	0.2196	9.5495	33.425	-42.767	13.09	(7)	-0.05
81EU	2.3162	0.2293	9.6948	33.287	-43.288	13.50	(6)	-0.081
81EY38	2.3171	0.2204	10.4164	32.851	-42.693	15.00	(3)	-0.063
1710	2.3220	0.2170	8.4531	34.500	-43.200	13.40	(6)	-0.032
753	2.3300	0.2110	9.2650	34.100	-42.700	10.34	(26)	-0.015
81EC3	2.3574	0.2295	8.6965	35.511	-45.739	16.00	(2)	-0.029
1386	2.3640	0.2280	11.8295	33.100	-45.000	13.50	(6)	-0.051
1718	2.3660	0.2240	8.6849	35.800	-45.700	13.60	(6)	-0.010
Means	2.3332	0.2223	9.5826	33.979	-43.755	number in family	9	

Ingeborg Family (Phocaea Region)

Asteroid	a(AU)	e	i(deg)	d wbar	d node	mag	diam
2055	2.3110	0.2500	25.2773	17.200	-40.000	13.50	(6)
83AG2	2.3170	0.2345	25.2140	16.899	-38.920	13.00	(8)
391	2.3200	0.2550	24.8346	17.900	-40.900	11.10	(19)
81EJ48	2.3241	0.2422	25.4676	16.885	-39.742	16.50	(2)
2050	2.3260	0.2550	26.1677	16.400	-40.700	12.79	(9)
83VQ1	2.3352	0.2628	25.8681	17.126	-41.922	15.50	(2)
64VE	2.3400	0.2500	25.0030	17.864	-41.241	14.50	(4)
87SG3	2.3413	0.2452	25.6391	16.941	-40.628	14.50	(4)
86CB	2.3464	0.2430	25.2457	17.428	-40.764	14.00	(5)
86AK	2.3479	0.2569	25.5311	17.496	-41.945	12.50	(10)
Means	2.3309	0.2495	25.4248	17.214	-40.676	number in family	10

Lemaitre Family (Phocaea Region)

Asteroid	a(AU)	e	i(deg)	d wbar	d node	mag	diam
3401	2.3688	0.2444	25.9254	16.858	-41.619	13.00	(8)
2078	2.3690	0.2527	25.2330	17.983	-42.545	12.70	(9)
84SR	2.3715	0.2507	25.6581	17.420	-42.359	15.00	(3)
2044	2.3790	0.2560	26.0401	17.300	-43.300	13.20	7.87
1565	2.3930	0.2420	25.7853	17.200	-42.500	12.50	(10)
86JZ	2.3934	0.2526	24.6580	19.027	-43.852	13.50	(6)
88EF	2.3988	0.2524	25.4359	18.062	-43.757	13.50	(6)
2075	2.4041	0.2344	25.9636	16.845	-42.253	13.70	(6)
Means	2.3847	0.2482	25.5874	17.587	-42.773	number in family	8

Siva Family (Phocaea Region)

Asteroid	a(AU)	e	i(deg)	d wbar	d node	mag	diam
2937	2.3200	0.2208	25.2393	16.514	-37.971	13.09	(7)
77RL	2.3208	0.2098	26.0019	15.225	-37.055	13.00	(8)
85HS1	2.3248	0.2029	24.0981	17.573	-37.245	14.00	(5)
81EE31	2.3257	0.2123	24.2865	17.580	-37.891	16.00	(2)
1170	2.3260	0.2120	24.1420	17.800	-38.000	12.52	12.3
3267	2.3290	0.2194	24.9546	16.936	-38.282	12.90	(8)
86JA1	2.3397	0.2188	26.3594	15.210	-38.325	12.50	(10)
1816	2.3400	0.2100	25.9126	15.400	-37.800	13.60	(6)
86RB	2.3428	0.2133	25.8362	15.745	-38.153	12.50	(10)
3397	2.3495	0.2111	24.4816	17.538	-38.555	14.30	(4)
81TR	2.3531	0.2102	24.4690	17.583	-38.697	14.50	(4)
81GP	2.3533	0.2236	25.4485	16.664	-39.389	13.50	(6)
3913	2.3570	0.2072	24.9609	16.869	-38.466	12.00	(12)
1192	2.3650	0.2240	24.9609	17.500	-40.100	12.93	(8)
Means	2.3391	0.2140	25.0822	16.724	-38.281	number in family	14

Alauda Family

Asteroid	a(AU)	e	i(deg)	d wbar	d node	mag	diam
702	3.1940	0.0410	21.7773	20.600	-64.100	7.23	202
3246	3.1979	0.0475	22.0676	19.506	-64.318	11.47	(30)
81EH21	3.2065	0.0505	22.0552	19.623	-65.041	13.00	(15)
1838	3.2100	0.0420	21.5307	22.000	-65.600	10.80	(42)
81DZ1	3.2302	0.0501	22.4000	17.423	-65.624	13.50	(12)
4045	3.2306	0.0479	22.4320	17.097	-65.394	11.40	(31)
4653PL	3.2400	0.0480	21.8390	20.000	-67.100	13.90	(10)
6673PL	3.2420	0.0520	21.6540	21.300	-67.900	13.10	(14)
1101	3.2430	0.0500	21.7773	20.400	-67.500	10.80	41
Means	3.2216	0.0477	21.9481	19.772	-65.842	number in family	9

Table 1. Proper elements of representative New asteroid families. Diameters in parentheses were calculated from their magnitudes.

CLASSIFICATION OF ASTEROID AND METEORITE SPECTRA BY PRINCIPAL COMPONENTS ANALYSIS. Daniel T. Britt[1], David J. Tholen[2], Jeffrey F. Bell[3], and Carle M. Pieters[1]; (1) Dept. of Geological Sciences, Box 1846, Brown Univ., Providence RI 02912; (2) Institute for Astronomy, Univ. of Hawaii, 2680 Woodlawn Dr., Honolulu HI 96822; (3) Hawaii Institute of Geophysics, Univ. of Hawaii, 2525 Correa Rd., Honolulu HI 96822.

Introduction: Several quantitative techniques have been used to classify asteroids on the basis of their spectral and albedo characteristics [eg. 1,2,3]. All of these methods have been successful in separating the bewildering spectral variety of the asteroids into a number of distinct classes in statistical or albedo/color-ratio space. The validity of these classes is strongly supported by the distinct and relatively limited zones in the main asteroid belt occupied by each class [4]. A logical next step is to extend this successful line of analysis to direct classification comparisons between the asteroids and their compositional analogs, the meteorites.

Methodology: To quantitatively classify the spectral characteristics of both asteroids and meteorites we used the technique principal components analysis as applied by Tholen [1]. This statistical technique can quantify the variance in a data set and represent this variance by projecting it into an arbitrary space of orthogonal principal components where distance between samples is a measure of dissimilarity [5]. Asteroid spectra for the study were taken from the 8-color survey of Zellner et al. [6] and the meteorite spectra were taken from the extensive laboratory study of Gaffey [7]. The high-spectral resolution laboratory meteorite spectra were converted into the 8-color system by a computer resampling routine using digital versions of the filter band passes of the 8-color system. All spectra were scaled to unity at 0.55 microns to remove albedo as a factor in the analysis. The spectra of 412 asteroids and 116 meteorites were used in this analysis.

Results and Discussion: Shown in **Figure 1** is a plot of the total data set. Asteroids are represented by the letter of their Tholen class (see [8] for an explanation of classes), and the meteorites are represented by symbols. To simplify this plot, **Figure 2** is an enlargement of the densest portion of **Figure 1.** The individual asteroid data points have been eliminated and the zones of principal component space occupied by each asteroid spectral class are outlined. Only the individual meteorites are represented by symbols. In this analysis the first principal component tends to be sensitive to the general slope of the spectrum with red slopes having positive values and flat slopes having negative values. The second principal component is correlated with the strength of absorption bands in the IR and UV regions. A few general points can be made about the distribution of meteorites in principal component space. First, the analysis was successful in identifying basic similarities; mineralogically similar meteorites tend to plot near each other and meteorite groups tend to occupy definite areas. Second, the wider distribution of meteorites in principal component space demonstrates there is more variance in the meteorite spectra than is seen in the asteroid spectra.

Looking in detail at the relative positions of asteroids and meteorites tends to confirm some theories, but it also produces some surprises. Eucrites display substantial variance and plot away from the main body of asteroids and near the position of the asteroid Vesta, their suggested analog [9]. Ordinary chondrites also show large variance and overlap the area occupied by the eucrites. However, they also tend to plot near their suggested analog, the Q-class asteroid Apollo [10,11]. The other suggested analog for the ordinary chondrites, the S-class asteroids, are offset to the right and above the ordinary chondrites due to their weaker one-micron bands and red continuum slope.

The CM and CI carbonaceous chondrites, which have traditionally been linked with the C-class asteroids, plot near them but slightly below and offset to the right. They generally correspond to Tholen's G-class, which has a slightly deeper UV absorption than the C-class. The optically altered black chondrite meteorites also tend to plot with the low-albedo C and G-class asteroids [12]. Several authors have suggested that CO and CV carbonaceous chondrites may be analogs for some S-type asteroids and they argue for the creation of an new class "K" to represent these objects [2,13]. In this analysis the CO and CV chondrites plot in lower left of the S-class field along with those S-class asteroids suggested as possible members of the K-class. This supports the interpretation of class K asteroids (and the Eos asteroid family which contains most of them) as a possible source of the CO's and CV's [13,14]. The placement of the iron meteorites is surprising. Their suggested analogs are the M-class asteroids (shown as X in the plots), but these asteroids tend to be systematically less red sloped than their meteorite analogs. This may be due to the fact that Gaffey's spectra of iron meteorites were obtained from cut surfaces rather than powdered samples and probably do not adequately reproduce the scattering properties of real metal asteroidal regoliths [15]. The enstatite chondrites are also offset from their suggested analogs, the E-class asteroids. Perhaps the most interesting result is that no meteorites plot with the F, B, P, or D-class asteroids, tending to confirm work that points to meteorite collections sampling a relatively limited portion of the asteroid belt [16].

Conclusions: In general, this analysis provides semi-quantitative support for most compositional interpretations of asteroids based on qualitative visual comparisons of spectra. The offset seen in iron, enstatite chondrite, and carbonaceous chondrite meteorites from their common asteroid analogs suggests a systematic suppression of the spectral red slope in these asteroids, perhaps due to regolith processes. For example, particle size has been shown to strongly affect the spectra of carbonaceous chondrites [17], and the particle size distribution on

asteroids is poorly constrained. The results of this analysis support the concept that the meteorite collection samples a relatively limited zone in the asteroid belt. The lack of similarity between the meteorites and the F, B, P, and D-class asteroids confirm a bias in the meteorite collections toward sampling the inner belt.

References: [1] Tholen D.J. (1984) *Asteroid Taxonomy From Cluster Analysis of Photometry*. Ph.D. Thesis, Univ. of Ariz., Tucson. [2] Tedesco et al. (1989) *Astronomical Journal 97*, 580-606. [3] Barucci M.A. et al. (1987) *Icarus 72*, 304-324. [4] Bell J.F. et al. (1989) *Asteroids II*, Univ. of Arizona Press, 921-945. [5] Davis J.C. (1986) *Statistics and Data Analysis in Geology*. Wiley, NY. [6] Zellner B. et al. (1985) *Icarus 61*, 355-416. [7] Gaffey M.J. (1976) *JGR 81*, 905-920. [8] Bell J.F. (1986) *LPS XVII*, 985-986. [9] McCord T.B. et al. (1970) *Science 168*, 1445-1447. [10] Mcfadden L.A. et al. (1984) *Icarus 59*, 25-40. [11] Bell J.F. and Keil K. (1988) *Proc. LPSC 18th*, Cambridge Univ. Press, 573-587. [12] Britt D.T. and Pieters C.M. (1989) *LPS XX*, 111-112. [13] Bell J.F. (1988) *Meteoritics 23*, 256-257. [14] Chapman C.R. et al. (1989) *Asteroids II*, Univ. of Arizona Press, 386-415. [15] Britt D.T. and Pieters C.M. (1988) *Proc. LPSC 18th*, Cambridge Univ. Press, 503-512. [16] Wetherill G.W. and Chapman C.R. (1988) *In Meteorites and the Early Solar System*. Kerridge J.F. and Matthews M.S. Eds, Univ. of Arizona Press, 35-67. [17] Johnson T.V. and Fanale F.P. (1973) *JGR 78*, 8507-8518.

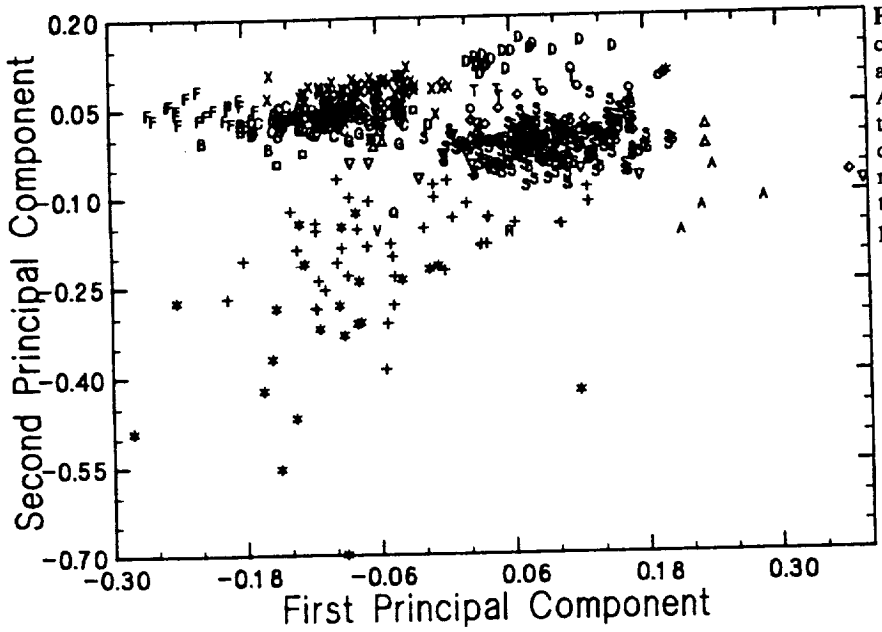

Figure 1: The first two principal components of a combined asteroid and meteorite spectral data set. Asteroids are denoted by the letter of their Tholen class and meteorites are denoted by symbols. The letter "X" refers to E, M, and P-class asteroids that tend to occupy the same principal component space.

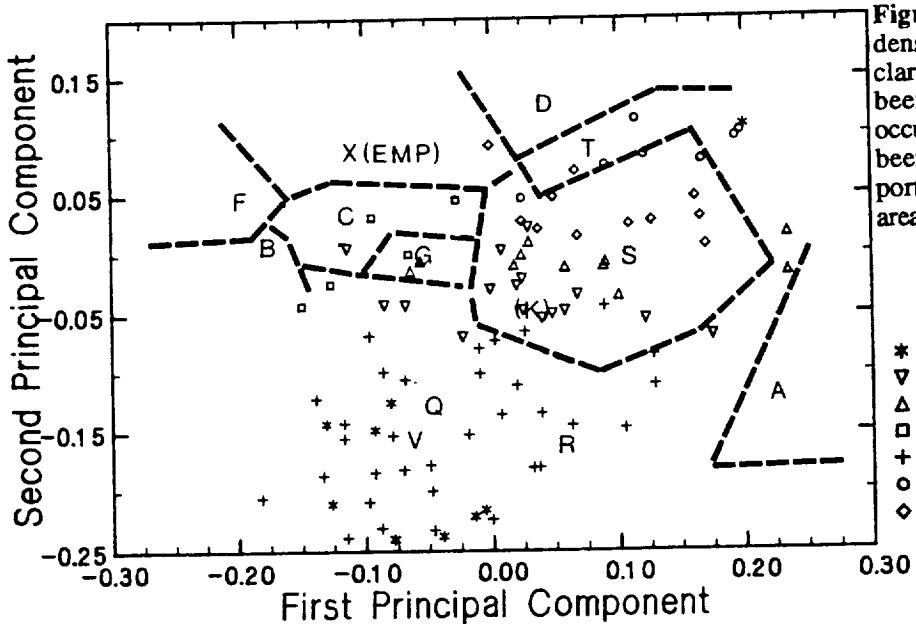

Figure 2: An enlargement of the densest portion of Figure 1. For clarity individual asteroids have been eliminated and the area occupied by each asteroid class has been outlined. The lower left portion of the S-class area is the area for the proposed K-class.

THE DISTRIBUTION OF PETROLOGIC TYPES AND FALL FREQUENCY OF BLACK CHONDRITE METEORITES. D.T. Britt and C.M. Pieters, Brown University, Providence, R.I. 02912.

Introduction: Black chondrite meteorites are ordinary chondrites that are characterized by an extremely active shock history which has contributed to the alteration of their optical properties. Although they are chemically indistinguishable from the range of normal ordinary chondrites they exhibit pervasive shock features such as brecciation, optical alteration (blackening), and low gas-retention ages [1,2,3]. The presence of these features make black chondrites invaluable samples of the effects of the space environment on ordinary chondrite material. Since shock can be a major contributor to regolith processes, black chondrites can provide insight into the optical effects of regolith processes on ordinary chondrite parent bodies. Black chondrites have been shown to be spectrally similar to some low-albedo C-type asteroids [2], raising the possibility that parent bodies of ordinary chondrites could be covered with an optically altered regolith and may be "hiding" in the population of C-type asteroids [4]. It is important to answer some of the basic questions about the fall frequency and distribution petrologic types of these optically altered meteorites to determine whether optical alteration is a major surface process on ordinary chondrite parent bodies.

Data Collection: We have initiated a program to identify and catalogue the optically altered black chondrite falls held by some of the major meteorite collections. Black chondrites are identified on the basis of three criteria. First, that the meteorite meet our functional definition of a black chondrite "any ordinary chondrite meteorite exhibiting distinctly low reflectance (≥ 0.15) in hand sample (example Farmington), or with major portions of the meteorite containing such low reflectance material (example Paragould)". Sample reflectance was determined by calibrating a Kodak gray scale (KODAK publication Q-13) to absolute reflectance using RELAB and comparing hand sample color with the gray scale. Second, that there was sufficient sample mass (>5 grams) and interior exposure to make a reliable reflectance determination. Third, that terrestrial weathering and rust were minimized. This was accomplished by restricting the survey to observed falls and rejecting any sample that exhibited visible rust (The Catalogue of Meteorites [5] was used as authority for falls and petrologic type). In addition, since this survey focused on black chondrites only, we excluded from the study all samples that had been previously identified as gas-rich ordinary chondrites, a total of 39 falls [6,7,8], and all unequilibrated ordinary chondrites, a total of 18 falls [5] (note that 7 unequilibrated ordinary chondrite falls are also gas-rich). Both of these meteorite types also contain low reflectance matrix material that would bias any selection.

Results and Discussion: To date the meteorite collections of Harvard University, the Smithsonian Institution's Department of Mineral Sciences, and the USSR Academy of Sciences have been surveyed. After eliminating meteorites that did not meet the sampling criteria, a total of 339 ordinary chondrite falls were checked and a total of 48 black chondrites were identified. The statistics of the distribution of these meteorites between the petrologic types are summarized in **Table 1** and the meteorites are listed in **Table 2**. A number of surprising insights are apparent in this data. First, there are a relatively large number of black chondrites. A review of available literature at the start of this project revealed only 15 falls cited as black chondrites [1,5,9-11]. This survey has examined a little over half of the total ordinary chondrite falls and has more than tripled the number of identified black chondrites. These results suggest that black chondrites constitute about 14% of ordinary chondrite falls. If gas-rich ordinary chondrites are included, this suggests that 23 % of all ordinary chondrite falls have been optically altered by regolith or regolith-like processes. Second, black chondrites are roughly equally distributed between petrologic type. Of the 15 black chondrite falls cited in the published literature, 2/3 are L-chondrites. But this survey shows that black chondrites are least common among the L-chondrites and that all types are within $\pm$ 6% of the mean. Finally, these results show no strong trend between the metamorphic grades, suggesting that the proportion of black chondrites in each metamorphic grade is not significantly different from the proportions in all other grades. The trends of black chondrite fall frequency among the petrologic and metamorphic types suggests that all ordinary chondritic material is being subjected to roughly equal levels of shock-alteration.

Conclusions: Previous work has shown that black chondrite meteorites may provide important spectral information on the optical effects of regolith processes on ordinary chondrite parent bodies. This study shows that: (1) Black chondrites are a numerically important sub-set of ordinary chondrites. (2) Black chondrites are found in roughly equal proportions in all petrologic and metamorphic types of ordinary chondrites. (3) No single shock event provides a dominant proportion of black chondrites. All these factors combine to suggest that optical alteration in general, and black chondrites in particular, can be very important, both in understanding the optical effects of asteroidal regolith processes and in the search for ordinary chondrite parent bodies in the main asteroid belt.

Acknowledgments: The authors are indebted to G.J. MacPherson and T. Thomas of the Smithsonian Institution, C.A. Francis of Harvard University, and M.I. Petaev of the Meteorite Committee of the USSR Academy of Sciences for providing access to their respective meteorite collections and for their assistance during this research. We gratefully

acknowledge the financial support of NASA grant NAGW-28. RELAB is supported as a multi-user facility under NASA grant NAGW-748.

References: [1] Gaffey M.J. (1976) JGR, 81, 905-920. [2] Heymann D. (1967) Icarus, 6, 189-221. [3] Britt D.T., et al. (1989) Proc. 19th Lunar Planet. Sci. Conf., 537-545. [4] Britt D.T., et al. (1989) LPC XX, 109-110. [5] Graham A.L. et al. (1985) Catalogue of Meteorites. Univ. of Ariz. Press. [6] Schultz L. and Kruze H. (1983) Helium, Neon, and Argon in Meteorites: A Data Compilation. Preprint. [7]Schultz L. and Kruze H. (1986) Supplement to Helium, Neon, and Argon in Meteorites: A Data Compilation. Preprint. [8] Bell J.F. and Keil, K (1988) Proc. 18th Lunar Planet. Sci. Conf., 573-580. [9] Fredriksson K. (1963) Space Research, 3, 974-983. [10] Dodd R.T. and Jarosewich E. (1979) Earth Planet. Sci. Let., 44, 335-340. [11] Ehlmann A.J. et al. (1988) Proc. 18th Lunar Planet. Sci. Conf., 545-554.

TABLE 1

TYPE	# CHECKED	# BLACK	PERCENTAGE
H4	32	6	18.8%
H5	66	9	13.6%
H6	41	7	17.1%
Total H	**139**	**22**	**15.8%**
L4	11	2	18.2%
L5	29	5	17.2%
L6	130	13	10.0%
Total L	**170**	**20**	**11.8%**
LL4	2	0	0.0%
LL5	8	1	12.5%
LL6	20	5	25.0%
Total LL	**30**	**6**	**20.0%**
Grand Total	**339**	**48**	**14.16%**

TABLE 2

Alphabetical Listing of Black Chondrites (To Date)

Akbarpur H4
Andura H6
Appley Bridge LL6
Atarra L4
Athens LL6
Beddgelert H5
Bielokrynitschie H4
Blansko H6
Canellas H5
Castalia H5
Cereseto H5
Chantonnay L6
Chicora LL6
Djati-Pengilon H6
Ensisheim LL6
Ergheo L5
Farmington L5
Gopalpur H6
Gorlovka H3-4
Hedeskoga H5
Hedjaz L3-6
Kabo H4
Karkh L6
Kendleton L4
Kunashak L6
Limerick H5
Malakal L5
Moti-ka-nagla H6
Nakhon Pathom L6
Ojuelos Altos L6
Olmedilla de Alarcon H5
Orvinio L6
Paragould LL6
Paranaiba L6
Pervomaisky L6
Rancho del la Presa H5
Rose City H5
Salles H6
Sena H4
Seres H4
Sevrukovo L5
Shytal L6
Suchy Dul L6
Sultanpur L6
Supuhee H6
Tadjera L5
Uden LL6
Walters L6

DISPERSED OPAQUES IN BLACK ORDINARY CHONDRITES: THE SPECTRAL EFFECTS OF OPTICAL ALTERATION. D.T. Britt and C.M. Pieters. Department of Geological Sciences, Brown University, Box 1846, Providence, RI, U.S.A..

Introduction: Meteorites are often our only source of ground truth information and insight into a myriad of solar system processes. Some are especially useful as a record of the effects of the space environment on the surface material of atmosphereless bodies; i.e. regolith processes on asteroids and moons. A thorough understanding of these effects is important for the interpretation of imaging and spectroscopic data from a whole suite of future missions and current telescopic observations. Regolith processes tend to be dominated by shock. The optically altered black chondrite meteorites can provide significant clues to the effects of shock processes in the space environment on common rock-forming minerals. Black chondrites are, as the name implies, ordinary chondrites that exhibit significantly lower reflectance than normal ordinary chondrites. In addition they are characterized by very subdued absorption bands in their reflectance spectra, low gas-retention ages, and pervasive brecciation and shock features [1]. About 13% of ordinary chondrite falls can be classified as black [2]. Black chondrites have been shown to have strong spectral similarities to the spectra of some low-albedo C-class asteroids [3]. In this study we will analyze the structure of the opaque components in two black chondrites, Farmington (L5) and Pervomaisky, (L6) and model the optical effects of these materials on the spectral characteristics of normal ordinary chondrites.

Meteorite Samples: The meteorites chosen for this initial study represent the two major morphologies seen in black chondrites. Farmington shows darkening throughout the entire meteorite, although, as discussed below, there is significant variation in the degree of optical alteration at the chondrule scale. Pervomaisky exhibits the light and dark macrostructure common in many black chondrites: large areas of light, unaltered material co-existing with large areas of darkened, optically altered material. The spectra of samples from light and dark portions of Pervomaisky are shown in **Figure 1**. These samples were taken from areas less than a centimeter apart and the bulk chemistry of the two areas are identical [4]. The spectrum of the dark portion exhibits a strong attenuation of both albedo and absorption features while the light portion shows a spectrum similar to normal ordinary chondrites of the same petrologic type [5]. In thin section the light portion of Pervomaisky is characterized by broken chondrules and fragments of chondrules ranging between 70 μm to 1 mm in diameter. Opaques are irregular blebs of troilite and Fe-Ni metal 100-200 μm in diameter and some veins of the same material. Average particle size is approximately 200 μm for the chondrules and 150 μm for the opaques. In the dark portion of Pervomaisky the chondrules exhibit the same basic structure and size, but the form of the opaque component is dramatically different. In contrast to the large blebs seen in the light portion, opaques in the dark portion are drawn out into a network of fine, thin veins and veinlets. The veins are generally 1-5 μm thick and are often surrounded by a cloud of minute opaque particles with diameters of < 0.5 μm. Examination of thin sections shows veins are directly associated with areas opaque to transmitted light and appear to be primarily composed of troilite. To estimate vein density a series of random traverses 100 μm in length were examined in thin section. The average number of veins crossing the traverses were 5.4, indicating that optical path lengths of greater than 20 μm would be strongly attenuated by the veins. The total abundance of opaque components estimated from chemical analysis are 6.4 wt.% FeS and 9.18 wt.% Fe-Ni [4].

In thin section Farmington is characterized by broken chondrules and fragments of chondrules ranging from 20 to 400 μm in diameter. Transparent and opaque chondrules are randomly intermixed with about 70% of the chondrules showing at least some opacity. In contrast to Pervomaisky, the opaque fraction of Farmington consists of relatively few irregular clumps of Fe-Ni metal and troilite 50-100 μm in diameter, and a pervasive dusting of finely dispersed droplets ranging from 5 to < 0.5 μm in diameter. It is thought that these "dusty" opaques were dispersed as a result of shock processes [5]. These finely dispersed droplets are primarily composed of troilite and are directly associated with the opaque chondrules [6]. Chemical analysis reports the total abundance of opaques as 4.79 wt.% FeS and 7.46 wt.% Fe-Ni [6]. To estimate the particle density of the droplets a series of areas 100 x 100 μm in opaque material were examined in reflected light and the numbers of droplets were counted. Average droplet population was approximately 400 droplets per 10,000 sq. μm area. With this density of droplets, a photon would have an 0.21% probably of traversing 100 μm of this material without encountering an opaque particle. The average path length through this material would be 11.6 μm.

Spectral Mixture Modelling: To examine the optical effects of the distribution of the opaque material we used a two-component intimate mixture program [7] based on the reflectance model of Hapke [8]. The end-members for this mixture are the spectrum of normal ordinary chondrite material such as the light material of Pervomaisky and the spectrum of a troilite separate from the iron meteorite Munbrabilla [9]. The spectrum of these end-members are shown in **Figure 1**. Photometric scattering properties for this material were assumed for purposes of this study to be similar to those measured for magnetite [7]. Although the scattering properties of troilite are almost certainly not the same as magnetite, the effect of the forward or backward scattering properties is probably secondary to the effect of particle size on photon path length. For all simulations the density of the ordinary chondrite material was set at 3.0 g/cm^3 and for troilite was 4.5 g/cm^3. The weight percent of troilite was fixed at 6% to simulate the

approximate concentration reported by chemical analysis. Average particle diameter was set at 100 μm for the ordinary chondrite material and varied for the shock darkened portion to determine the effect of particle size on the optical properties of the mixture.

Discussion: Shown in **Figure 2** are the results of three simulations run with ordinary chondrite and troilite end-members. The first simulation fixed troilite particle size at 100 μm. This is similar to the distribution of opaques in normal ordinary chondrites and the light portions of Pervomaisky. In this case the effect of the opaque end-member on the mixture spectrum is very modest. Simulation number two reduced the troilite particle size by an order-of-magnitude to 10 μm. The effect on the mixture spectrum is now more pronounced as the smaller particle size increases the optical effectiveness of the opaque component. The final simulation is with a troilite particle size of 1 μm, within the actual range of opaque particle sizes seen in thin sections of optically altered material. The spectrum of this simulation shows that small particle size in opaques strongly attenuates the albedo and absorption bands of normal ordinary chondrite material, producing a spectrum very similar to the attenuation seen in optically altered black chondrites.

Conclusions: In thin section fine structures of small-diameter (< 5 μm), shock dispersed opaques are pervasive throughout darked portions of optically altered ordinary chondrites. These structures tend to be composed primarily of troilite and are directly associated with optical opacity in the chondrules and matrix. The process or processes that mobilizes, disaggregates, and disperses this material into the silicate fraction of the meteorite is a key in understanding the conditions for optical alteration on asteroidal surfaces and will be a focus of future work. Intimate mixture modelling using realistic parameters confirms the importance of opaque particle size in the attenuation of albedo and absorption bands. A two (or more) order-of-magnitude difference in particle sizes between the silicate and opaque phases in optically altered ordinary chondrites allows a very small component of opaque material to dominate the optical properties of these meteorites.

REFERENCES: [1] Heymann D. (1967) *Icarus 6*, 189-221, [2] Britt D.T. and Pieters C.M. (1990) *Meteoritics*, in press. [3] Britt D.T. and Pieters C.M. (1989) *LPS XX*, 111-112. [4] Migdisova L.F. and Petaev M.I. (1990) Work in progress. [5] Gaffey M.J. (1976) *JGR 81*, 905-920. [6] Buseck P.R. et al. (1966) *G&C Acta 30*, 1-8. [7] Mustard J.F. and Pieters C.M. (1989) *JGR 94*, 13619-13634. [8] Hapke B. (1981) *JGR 86*, 3039-3054. [9] Bell et al. (1990) Work in progress.

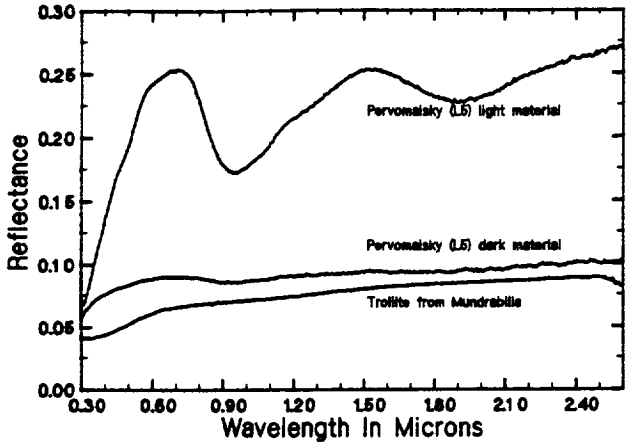

Figure 1: Bidirectional reflectance spectra of dark and light portions of the L6 ordinary chondrite Pervomaisky and troilite separates from the iron meteorite Mundrabilla. In mixing simulations described in the text the spectra of the light portion of Pervomaisky and troilite from Mundrabilla were used as end-members.

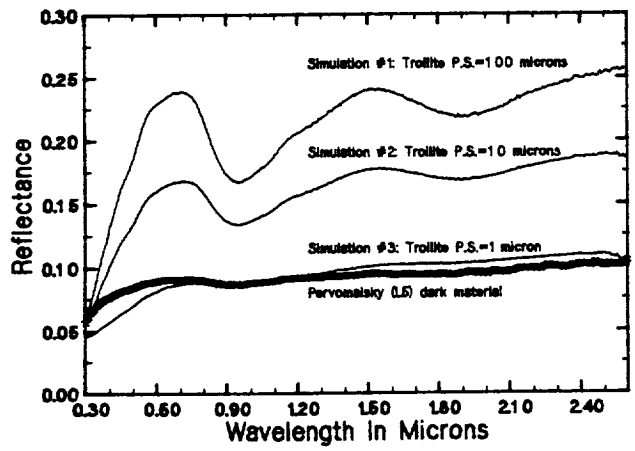

Figure 2: The results of three spectral mixing simulations compared to the spectra of the dark portion of Pervomaisky. The spectra of the light portion of Pervomaisky and troilite from Mundrabilla were used as end-members.

On the Relationship of Shocked Ordinary Chondrites to Asteroids

Jeffrey F. Bell and Klaus Keil (Hawaii Institute of Geophysics, Univ. of Hawaii, Honolulu HI 96822) and Dan Britt (Dept. of Geology, Brown University, Providence RI 02912)

Background

Most work on asteroid composition has been based on an implicit assumption that the spectra of asteroids can be simulated by selecting a meteorite thought to represent the bedrock of the asteroid of interest, and pulverizing it to simulate the upper layer of the asteroid regolith which is optically visible to a telescope. In many cases this method can provide an adequate spectral match, allowing for small variations due to particle size differences and photometric geometry. However, there remain spectral classes of asteroids which have no meteoritic analogs and several classes of meteorites whose laboratory spectra do not match those of any observed asteroids. The case which has attracted the most attention over the years is that of the ordinary chondrites. While these are the most common meteorites falling on the Earth's surface at present, only a few unusual asteroids have been suggested as possible spectral matches for them. The most popular recent candidate for an OC source body is the small Earth-crossing asteroid 1862 Apollo. This asteroid has unique spectral features which caused Tholen (Ph.D. thesis, Univ. of Arizona, 1984) to erect a new asteroid class "Q" of which Apollo is the only unambiguous member. However, many workers find the apparent lack of any Q-type asteroids in the main asteroid belt a serious objection to this identification. It would be much more satisfying to identify OCs with some very common main-belt asteroid type. The traditional candidates have been S-type asteroids. A variety of "space weathering" processes have been proposed which might alter the regolith of an OC parent body to produce the highly reddened spectra observed in typical S asteroids. However, OC regolith breccia matrix material which is rich in implanted solar-wind gases, does not show the characteristic red slope of S asteroids. Since this material acquired solar gases during previous residence at the uppermost surface of a regolith, it must be representative of the optical surface of the parent body. Thus the lack of spectral similarity of this material to S asteroids is very strong evidence against the "space weathering" hypothesis in its "classic" form.

Another class of OC material is known to possess an unusual spectrum more easily reconciled with a common asteroid type. The so-called "black chondrites" are meteorites with abundant evidence of severe shock effects due to impact events on their parent bodies. In addition to a small fraction of OCs which are entirely composed of such material, many others have narrow veins of shocked material between clasts of normal OC appearance. Spectra of the shock-blackened material possess much lower albedos and shallower absorption bands than unshocked OC material. In some cases of high degrees of shock-melting, the spectra are very similar to those of carbonaceous chondrites and C-type asteroids. It has recently been proposed that the elusive OC parent bodies could be hiding among the C asteroid population, if their uppermost regoliths were composed mostly of shocked "black chondrite" material. While this OC = C-type hypothesis lacks some of the superficial charm of the classic OC = S-type space weathering theory, in that it links OCs with an asteroid class which already has an accepted meteoritic analog (CI/CM chondrites), it is in fact much more reasonable in that it appeals to clearly real asteroidal impact processes and is consistent with the existing meteorite spectral data. We therefore chose to explore this hypothesis by obtaining lab spectra of highly shock-blackened portions of ordinary chondrites.

Measurements

Figure 1 compares the spectral reflectance of the most highly shock-blackened portions of each meteorite studied. They are all very different from the spectra of normal, unshocked OC material. Common features include the reduction of albedo to the 0.05-0.10 level, great or total suppression of the silicate absorption bands near 1 and 2 μm, and a residual absorption in the 0.3-0.6μm region. As previously shown, this material spectrally resembles unshocked carbonaceous chondrite material.

Implications For Asteroids

Are ordinary-chondrite parent bodies hidden among the C-type asteroids? Our results agree with previous suggestions that highly shocked OC material could spectrally mimic some C-type asteroids. This is only relevant to interpretation of asteroid telescopic spectra if such shocked material covers a large fraction of an asteroid's optical surface. There are several lines of evidence which bear on this important question.

More important than the overall abundance of the shock-blackened material is the question of where this material occurs in a typical asteroid. It has been suggested that the optical surfaces of the OC parent bodies are largely covered with a thin layer of shock-blackened material, which gives them the appearance of C-type asteroids. This hypothesis does not require that the actual shock-blackened meteorites in our collections be former surface material, only that they have experienced a similar blackening process to that in the uppermost regolith. However, it does imply that most or all of the solar-gas-rich regolith breccias in the OC collection would be shock-blackened, since the presence of trapped solar wind in these meteorites establishes that they contain material that was once at the top of the regolith. However, the gas-rich matrix material does not generally exhibit extreme blackening. Typically, the gas-rich regions in these meteorites exhibit clearly recognizable absorption bands which are still about half as deep as the bands in gas-free clasts in the same sample. There seems to be a real distinction in spectral characteristics between gas-rich regolith breccias and true shock-blackened breccias. This distinction is probably due to the differing mechanics of impact in different regions of the target material. Rock below the impact is compressed against underlying rock and strongly shocked, while the material which ends up in the ejecta blanket has been disrupted and thrown out at low velocity.

However, our knowledge of the physics of the blackening process, and the detailed distribution of shock effects and solar-wind effects in the meteorite breccias is currently inadequate to rule out such an effect. For instance, even the most gas-rich material found in meteorites contains only about 20% actual ex-surface material when the individual grains are examined for solar-wind effects. It is possible that the true optical surface could exhibit much stronger blackening effects than found in the breccias. A possible means of investigating this hypothesis would be to obtain spectra and gas-rich grain abundances for a variety of samples and extrapolate the correlation (if any) found to a composition of 100% gas-rich grains. This would be an exceedingly laborious task, but probably the best line of future research in this area.

Are Class K asteroids ordinary-chondrite parent bodies? Another group of asteroids have spectra similar to some of the shock-blackened material measured in this study. Several members of the Eos asteroid family have flat featureless spectra in the 1-2.5μm range, even though their visible (0.3-1μm) spectra were similar to those of S-type asteroids and they were almost all classified S in the system of Tholen. This unusual spectral signature is very similar to that of some of the less strongly shocked black OC material in Fig. 1. The average albedo of Class K asteroids is about 0.09, also consistent with some of our meteorites. From a purely spectroscopic view, the K class is as likley to be composed of shocked OC material as any member of the C class.

However, we do not believe that this is a reasonable interpretation. In addition to all the general reasons given above for C-type asteroids, there is the fact that every asteroid in the Eos family, with rare exceptions, shares the unusual Class K spectrum. This implies that the entire mass of the 120km parent body of the family was converted to black chondrite material, presumably during the impact which shattered it to create the current asteroid family. From the meteorite record, it does not appear that such catastrophic disruptions result in a large fraction of blackened material. For instance, a large fraction of the H chondrites appear to have experienced a source body disruption about 5 million years ago, yet these meteorites do not exhibit an anomalously high proportion of shock-blackened material.

For the K-type asteroids there is also a ready alternative interpretation. The spectrum of 221 Eos, the best-observed K asteroid, is almost identical to that of the CO chondrites. The origin of these meteorites has always been a mystery, as they are too bright to match C-type asteroids. The discovery of the K class provides them with a reasonable asteroidal parent body.

Are Phobos and Deimos shock-blackened OCs? The recent outburst of interest in the satellites of Mars occasioned by the Soviet mission to Phobos has led to suggestions that Phobos and Deimos may be examples of ordinary-chondrite-like bodies covered with a superficial layer of shocked material, which disguises them as carbonaceous chondrites. The meteoritical evidence cited above is less directly relevant here, since it is unlikely that any known meteorite is from Phobos or Deimos. However, we do have some direct evidence of the nature of the regoliths on these bodies. In the Viking photographs both show signs of a very deep regolith which heavily blankets features in the bedrock. The standard explanation of this is that the large amount of low-velocity ejecta from impacts on the satellites does not escape the Mars gravity well, but recollides with the satellite at low velocity after a few orbits. This extra component of low-velocity secondary projectiles should bias the total impact environment very strongly toward low-velocity impacts which simply dig up fresh bedrock and create little or no shocked material. The special dynamical environment of Phobos and Deimos thus implies that the average surface region is even more free of shocked material than the main-belt asteroids considered above. There seems to be no reason to revise the traditional interpretation of Phobos and Deimos as carbonaceous chondrite analogs.

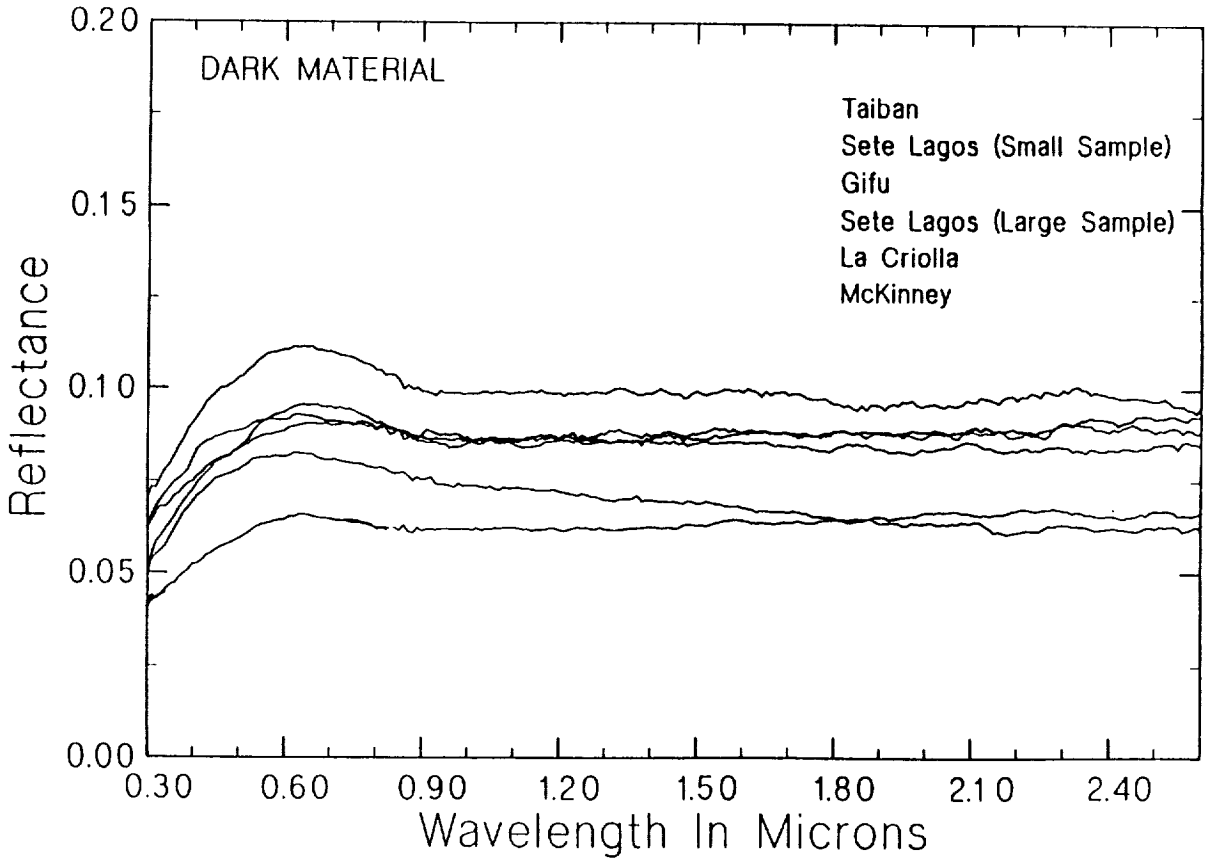

The Evolution of the Water Regime of Phobos

Fraser P. Fanale and James R. Salvail, Hawaii Institute of Geophysics, University of Hawaii, Honolulu, Hawaii 96822 U.S.A.

There are several reasons for believing that Phobos once contained a significant amount of water in its interior. Phobos appears to be generally similar to C class asteroids and some carbonaceous chondritic meteorites (Veverka and Thomas, 1979; Veverka and Burns, 1980). Some of these meteorites are known to contain phyllosilicate minerals, which contain water of hydration. Some of the phyllosilicates are thought to have been produced by solid-gas interaction in the pre-planetary nebula. They could also have been produced by the action of liquid water on anhydrous minerals after planetary formation. Geochemical studies of matrix materials have suggested that all the phyllosilicates may have had the latter (secondary) origin (Du Fresne and Anders, 1962). These and other observations suggest that asteroids accreted as a mixture of relatively anhydrous minerals, organics and water ice (Jones et al., 1988), which represents one source of free water. Measurements of the fundamental O-H stretch band in the optical surface materials of many C-class asteroids revealed a relatively weak correlation between band depth and heliocentric distance. This indicates that a major electromagnetic induction heating event could have raised the temperature of the interior of Phobos high enough to free the bound water in some of the phyllosilicates on a time scale of 10**4 to 10**5 years (Herbert and Sonnett, 1979). If Phobos was captured from the outer solar system, the electromagnetic heating may not have caused massive water loss and hydration of the optical surface. In that case, diffusion would have been the primary means of water migration and loss. Thus, there may be two sources of free water within Phobos. Images of Phobos show that it has sets of craters with raised rims aligned along grooves, which suggest volatile venting associated with impact events (Thomas and Veverka, 1979). The small size of Phobos, its low albedo and its heliocentric distance are conditions that might lead to a significant if not complete loss of water from Phobos over geological time.

Phobos was modeled as a sphere of radius 9 km, which is half of its minimum width. The orbit of Phobos is in the equatorial plane of Mars, and its rotation is synchronous with its orbital period. Therefore, its obliquity must be approximately the same as that of Mars. The time variation of the obliquity of Phobos was assumed to have been the same as that of Mars. The obliquity and eccentricity variations of Mars were first computed by Ward (1979), but the approximate formulae given by Fanale et al. (1986) were used. The increasing solar power output over geologic time was also accounted for (Gough, 1977). For most cases of interest, the current depth of subsurface ice turns out to be small compared to the minimum dimension of Phobos. In these cases a one dimensional thermal model would yield acceptably accurate temperatures for those depths relevant to the computation of water fluxes and ice depths. Interior temperatures were calculated for a one dimensional thermal model using spherical coordinates. The surface boundary condition includes the annual average insolation, the infrared radiation from the surface and the heat conduction into the ground. The boundary condition at the ice interface maintained continuity of heat flow through a boundary separating two domains having different thermal properties due to the presence or absence of ice, and it also accounted for the insignificant amount of heat released by sublimation of the ice. At the center of the sphere, the adiabatic boundary condition was used.

The nonvolatile material was assumed to exist as a coherent, porous matrix with water ice occupying a fraction or all of the pore space. Ice near the surface sublimes and flows through the tortuous passages to the surface where it is lost to space. The

gas flux is a function of the changing temperature of the ice front, the instantaneous depth of the ice front and the properties of the porous matrix, namely, the porosity, the pore size and the tortuosity. The flow of vapor in the porous matrix is always in the free molecular/Knudsen regime. The ice boundary recedes at a rate determined by the gas flux, the bulk density of the porous matrix and the mass ratio of nonvolatiles to ice. Integrating this rate numerically over time gives the new ice depth at the end of a time step within a given obliquity cycle. Temperatures, gas fluxes and ice depths were computed for a selected number of obliquity cycles, each representing an epoch in the history of Phobos. This was done since it would be impractical to calculate temperatures continuously over geologic time. However, since the ice depth is an integral over time, it was necessary to obtain a relatively accurate estimate of the ice depth at the end of an epoch. This was done by computing the average water flux over the obliquity cycle at the beginning of the epoch and assuming that this average flux would be the same for all obliquity cycles comprising that epoch. The solar power output would increase slightly during this period. This would increase temperatures slightly and would tend to increase water fluxes during an epoch. However, the recession of the ice would tend to decrease water fluxes due to the increased diffusion path length. Thus, the two effects would tend to offset each other.

We have investigated cases in which water ice is evenly distributed and cases in which ice is concentrated in a near surface layer and fills all the pore spaces down to a depth that depends on the bulk density, the assumed average porosity of Phobos and on the mass fraction of water initially allocated to Phobos. The geologic history of Phobos was divided into 75 epochs each having a length of 6 X 10**7 yrs and each containing 50 long term obliquity cycles. Detailed calculations were performed only for the first obliquity cycle of each epoch, and the results were assumed to characterize that epoch. The solar constant was calculated at the beginning of each epoch, and it was assumed to remain constant throughout the obliquity cycle for which it was used. The solar insolation was calculated at 100 evenly spaced points in time throughout the obliquity cycle for a particular latitude using the time dependent obliquity and eccentricity functions. Temperatures, water fluxes and ice depths were calculated throughout the selected obliquity cycle. The results for this obliquity cycle were used to calculate the depth of the ice at the end of the epoch.

Annual average temperatures were affected significantly over geologic time by the increasing solar power output, and over a 10**5 to 10**6 year time scale by the obliquity cycle and to a lesser extent by the eccentricity cycle. These effects cause the insolation and the resulting annual average surface temperatures to vary in a highly complex manner. These variations are propagated to great depths due to the long time scales. The most significant results are summarized in figures 1 and 2. These show the current depth of ice as a function of latitude for the surface concentrated cases and for both cases of porosity and pore size. Depth limits are given for the initial mass fractions of water indicated. The results show that if Phobos was initially endowed with 1% water ice , the ice could still be retained in pores at depths of hundreds of meters at lower latitudes to only tens of meters at high latitudes. This is so despite Phobos' low albedo, proximity to the sun, and periodically high obliquity. The possibility of shallow ground ice on Phobos could be an important consideration in the planning of future manned missions to Mars.

References

Du Fresne, E.R. and E. Anders. On the chemical evolution of the carbonaceous chondrites. Geochim et Cosmochim Acta 26, 1085-1114, 1962.

Fanale, F.P., J. R. Salvail, A.P. Zent and S.E. Postawko. Global distribution and migration of subsurface ice on Mars. Icarus 67, 1-18, 1986.
Gough, D.O. Theoretical predictions of variations in the solar output. In "The Solar Output and Its Variation, (O.R. White,ed.), Colorado Assoc. Univ. Press, Boulder, CO., 1977.
Herbert, F. and C.P. Sonnett. Electromagnetic heating of minor planets in the solar system. Icarus 40, 483-493, 1979.
Jones, T.D., L.A. Lebofsky and J.S. Lewis. The 3 micron hydrated silicate signature on C class asteroids: Implications for origin of outer belt objects. Proc. Asteroids II Conf., Tucson, AZ, 1988.
Thomas,P. and J. Veverka. Grooves on Phobos: Their distribution, morphology and possible origin. J. Geophys. Res. 84, B14, 8457-8477, 1979.
Veverka J. and P. Thomas. Phobos and Deimos: A preview of what asteroids are really like?, in Asteroids, (t. Gehrels ed.), 628-651. 1979.
Veverka J. and J.A. Burns. The moons of Mars. Ann. Rev. Earth Planet Sci. 8, 527-558, 1980.
Ward, W.R. Present Obliquity oscillations of Mars: Fourth order in orbital E and I. J. Geophys. Res. 84, 237-241, 1979.

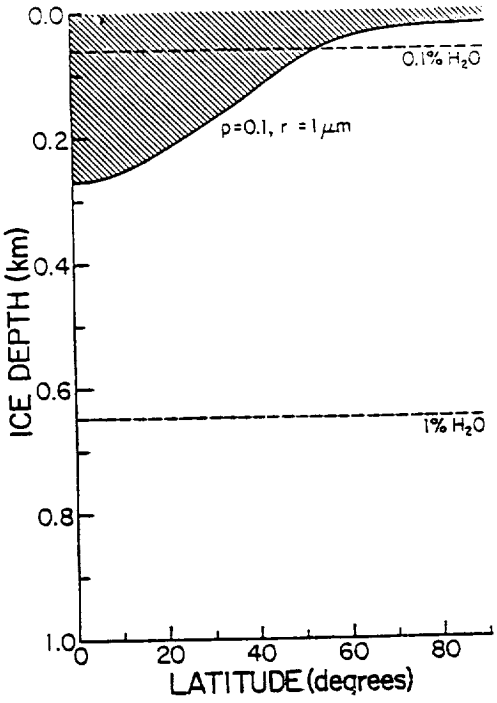

Fig. 1. Ice depth vs. latitude at present for the surface concentrated case of .1 porosity, 1 micron pore size. Depth limits for indicated mass fractions of water are shown.

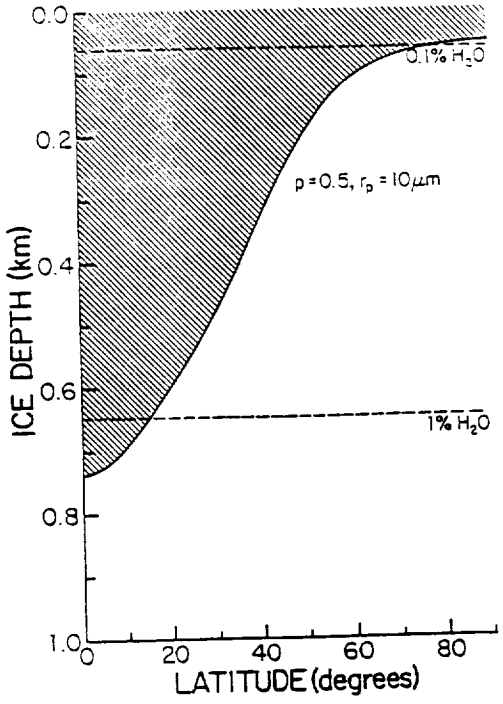

Fig. 2. Ice depth vs. latitude at present for the surface concentrated case of .5 porosity, 10 micron pore size. Depth limits for indicated mass fractions of water are shown.

Small Satellites and Asteroids: Scale Variation of Topography and Shapes.

P. C. Thomas, Center for Radiophysics and Space Research, Cornell University, Ithaca, NY 14853

The shapes and surface topography of satellites are dependent on the objects' mean radii. Although a size dependence is hardly a surprise (Johnson and McGetchin, 1973), the quantitative data now available provide clues to the shaping processes and histories of rocky and icy satellites, and for asteroids. Limb topography provides a standard method of comparison of overall shapes and roughnesses (Thomas, 1989). The primary characteristics of satellite shapes are: 1) Icy satellites >200 km radius are all smooth ellipsoids, except for 1989N1, mean radius 208 km. 2) Smaller icy satellites and 1989N1 have limb roughnesses of 2-8% of mean radius, a characteristic that does not vary with size below 200 km radius (Fig. 1). 3) Rocky satellites smaller than 200 km radius are also rough (Fig. 1b). Rocky satellites larger than 200 km are all greater than 1700 km radius, and are smooth ellipsoids. Two asteroids with many good photoelectric occultation chords (Millis et al., 1981) are consistent with the small satellite data. The largest asteroid is very much rougher than icy satellites of the same size.

The shapes of these objects probably derive mostly from one or more processes: impacts, downslope movement, viscous relaxation. The two main modelling questions are: 1) can reasonable crater densities and morphologies explain the roughness of small satellites, and 2) are predicted changes in crater morphology adequate to explain the drastic differences in shapes of small and large icy objects and/or the shape trend of rocky objects? To address these questions limb topography from impacts has been calculated using gravity-dependent morphologic parameters for crater morphology on icy and rocky objects from the work of Schenk (1989). Initial shapes were spheres, and craters were randomly placed on the objects. Depth/diameter ratios, crater size distributions, and crater densities were varied. By running models with different distributions of craters, we obtained mean roughnesses for different diameters to compare with the roughness data. The models and data are compared in Fig. 1. Fig. 2 illustrates the appearance of a calculated small satellite limb. The onset of complex craters with low depth/diameter ratios (depth increases as a small power of diameter) greatly reduces the roughness of the icy objects; it nearly follows the icy satellite data. The multiple model lines in Fig. 1 emphasize that a general model may have enough free parameters to render comparison with any one satellite meaningless. In some cases, the observed geology renders the model of limited application: Miranda and Enceladus, both of which have obvious internal heating and tectonics. Mimas remains the difficult object to explain. It is an equilibrium ellipsoid (Dermott and Thomas, 1988), yet there is no evidence for, or expectation of, internal heating.

For rocky objects, the meager data are consistent with the impact model through the size of the largest asteroid. The prediction from these data is that asteroids that lack significant melting will be as rough as their length of cratering allows (that is, redistribution of ejecta has not smoothed them off).

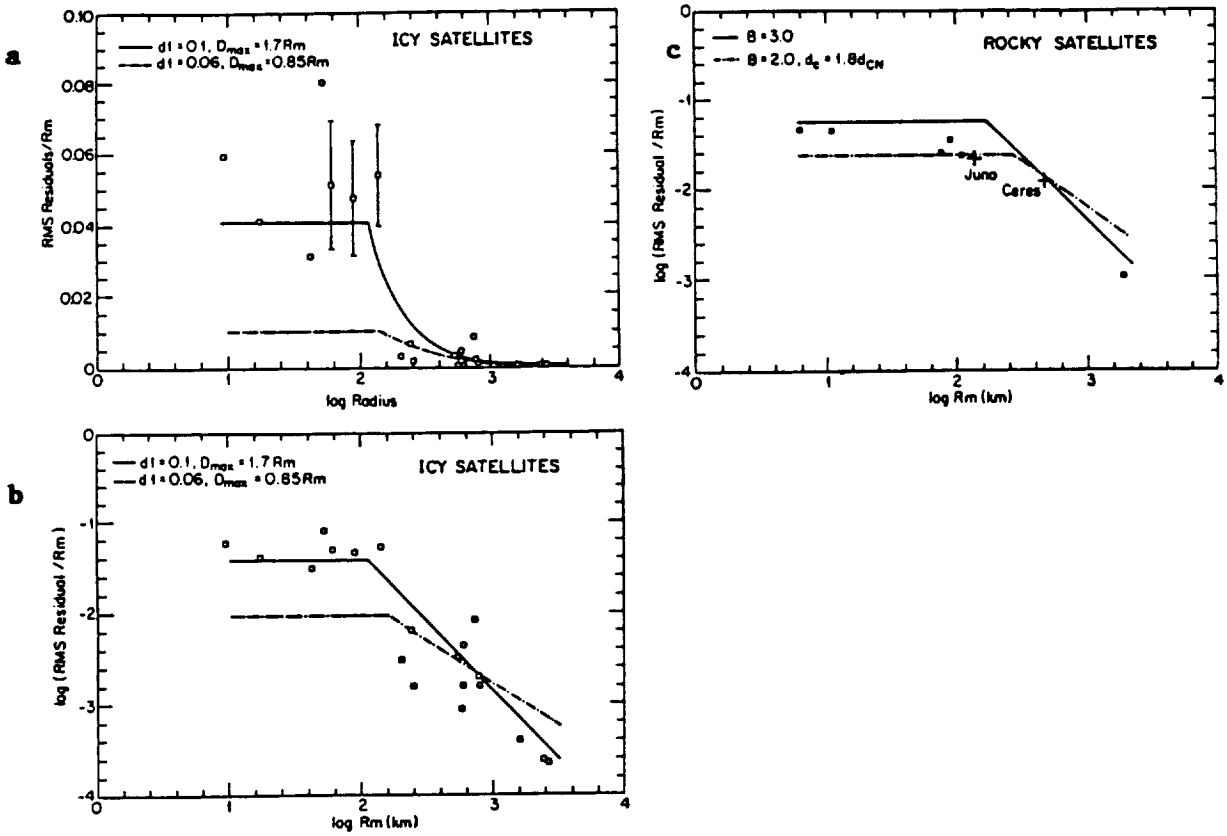

Figure 1. Comparison of data on satellite limb roughnesses with model results. Rocky and icy satellites are treated differently.

Variables in the models are: Maximum crater diameter as a fraction of mean radius; crater depth at 1 km diameter; 0.1 or 0.06 used for icy satellites; 0.2 for rocky ones (see Schenk; 1989); crater density distribution expressed as slope of cumulative curve (2 or 3 in these models).

a-b. Icy Satellites. Roughness is the rms residuals to ellipsoidal fits of the limb coordinates, as a fraction of the mean radius. Points with several views are marked by mean values and extremes. The drastic difference between small and large satellites is well illustrated by this linear plot. The two different model curves show the effects of different crater densities (i.e., largest crater size), and depth of craters. The models show that roughness of small satellites is easily approximated by bowl-shaped craters of normal depths. Larger satellites are also consistent with the model, but these usually have the largest crater <0.85 Rm. These larger satellites are smooth enough from internal effects that the cratering model is usually not applicable.

c. Comparisons of two models with the shape data for rocky satellites and two asteroids (latter from Millis et al., 1981; 1987). The crater density slopes are varied, as is the size of onset of complex craters, to illustrate that many families of models may apply to the rocky objects. The largest object plotted is Io (Moon would be similar). The largest asteroid is not significantly different from the other data and can be satisfied with many different cratering models; it is rougher than icy satellites of similar diameter.

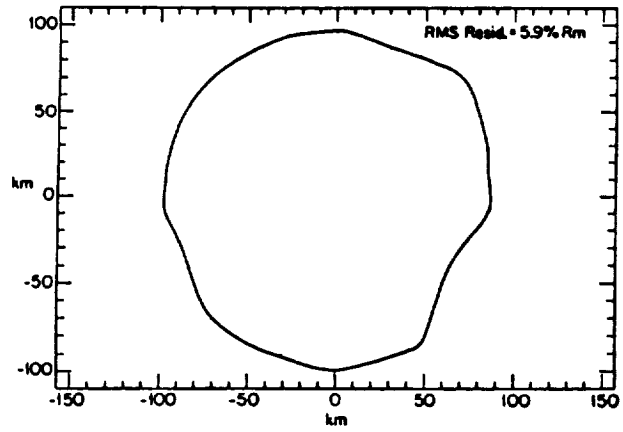

Figure 2. Example of a limb profile with a roughness of 5.9% Rm; compare with Fig. 1a data.

References:

Dermott, S. F. and Thomas, P. C. 1988. The shape and internal structure of Mimas. *Icarus 73*, 25-65.

Johnson, T. V. and McGetchin, T. R. 1973. Topography on satellite surfaces and the shape of asteroids. *Icarus 18*, 612-620.

Thomas, P. 1989. The shapes of small satellites. *Icarus 77*, 248-274.

Schenk, P. H. 1989. Crater formation and modification on the icy satellites of Uranus and Saturn: Depth/diameter and central peak occurrence. *J. Geophys. Res. 94*, 3813-3832.

Supported by NASA grant NAGW-111.

THE SHAPE OF ASTEROID 433 EROS

S. J. Ostro, K. D. Rosema, and R. F. Jurgens
Jet Propulsion Laboratory, Caltech, Pasadena, CA 91109

Introduction

433 Eros, discovered by G. Witt in 1898, is distinguished by being the first known Mars-crosser, the first asteroid to show a lightcurve, and the first asteroid to be observed while occulting a star. The discovery of Eros' large orbital eccentricity attracted considerable interest and catalyzed a series of dynamical studies, and triangulation of the distance to Eros and analyses of perturbations on Eros' orbit provided the most reliable pre-radar values for the AU. Eros made its closest approach to Earth in this century (0.15 AU) on January 13, 1975, and was favorably placed for telescopic investigation within several months of that date. A campaign was organized to seize this opportunity using available astronomical techniques, and the May 1976 issue of *Icarus* was devoted to papers reporting the observations. Zellner (1976) noted that no other solar system body in its size range had been so thoroughly observed.

The constraints on Eros' shape, derived primarily from optical lightcurves (e.g., Dunlap 1976; Millis et al. 1976) and 3.5-cm radar observations (Jurgens and Goldstein 1976, hereafter JG76), were obtained within the framework of some assumed, axisymmetric model. Such approaches were appropriate first approximations, but their inadequacy was apparent from the presence of odd harmonics in the lightcurves and in the rotational-phase dependence of the radar signatures. In analyzing the latter, JG76 used a homogeneous, triaxial ellipsoid model (Jurgens 1982), but they warned of that model's inability to accommodate a strong, predominantly first-harmonic wobble in the echo spectral shape. The presence of the fundamental Fourier component indicated that Eros' figure and/or it's radar scattering properties are not axisymmetric.

Recently, Ostro et al. (1988a) introduced a theoretical approach to asteroid echo-spectral analysis that follows naturally from the geometric relation between spectral edge frequencies and the shape of a rotating asteroid. This approach uses the *extent* of the spectra to determine the convex envelope, or hull, of the asteroid's polar silhouette -- a pole-on projection of the asteroid with concavities "filled in." Ostro et al. (1988a) showed how to estimate the hull, developed error-analysis techniques, and studied the relation between the accuracy of a hull estimate and the parent dataset's signal-to-noise ratio.

The Convex Hull of Eros' Pole-on Silhouette

Ostro, Rosema, and Jurgens (1990) use the 1975 Goldstone radar spectra to estimate Eros' hull and then use the results to evaluate, and in a few instances refine, the 1976 constraints on the asteroid's physical properties. We also address certain practical aspects of hull estimation not confronted by Ostro et al. (1988a). For example, for a given set of echo spectra, the accuracy of a hull estimate turns out to depend on the data set's frequency resolution and rotational-phase resolution. The Eros data (199, 3.5-cm spectra in the OC polarization) are "over-resolved" in each domain, so it was necessary to smooth the data and to search for the best phase/frequency filter.

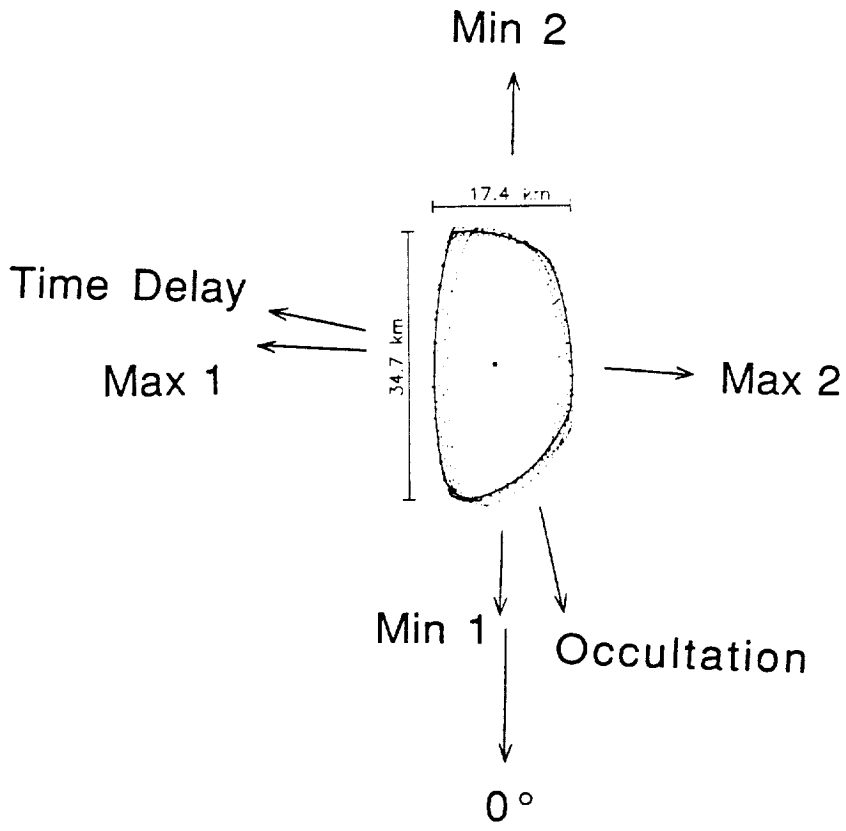

The above figure shows the resultant estimate of Eros' hull (solid curve), which is "quasi-trapezoidal" in shape; the dotted curves convey the estimation error. A dot indicates the hull's center of rotation (Eros' center of mass) while a larger symbol indicates the hull's centroid. Arrows indicate orientations at epochs of lightcurve extrema (Millis et al. 1976), a radar time delay measurement by Campbell et al. (1976), and stellar occultation observations (O'Leary et al. 1976). The silhouette is clearly non-axisymmetric, suggesting that some of the odd-harmonic character of Eros' lightcurves and radar echoes are due to shape.

Lightcurve Inversion: Eros' Mean Cross Section

Ostro et al. (1988b) show that under certain ideal conditions, one can use "convex-profile inversion" of a lightcurve to estimate a profile which, *unlike the hull*, is a two-dimensional *average* of the asteroid's shape. That profile is called the mean cross section, $\underline{C}$, and is defined as the average of the envelopes on all the surface contours parallel to the equator. The ideal conditions for estimating $\underline{C}$ include Condition GEO, that the scattering is uniform and geometric; Condition EVIG, that the viewing-illumination geometry is equatorial; and Condition PHASE, that the solar phase angle ϕ is known and nonzero. These conditions collapse the three-dimensional lightcurve inversion problem, which cannot be solved uniquely, into a two-dimensional problem that can. During late Jan 1975, the sub-Sun and sub-Earth points were near Eros' equator and, given the 9° solar phase angle, the scattering was probably almost geometric.

Convex-profile inversion of an Eros lightcurve obtained by Tedesco (1976) on 1975 Jan 20 yields the estimate of $\underline{C}$ (solid curve) shown in the following figure. This average of Eros' shape rotates clockwise and is shown at the same rotation phase as in the hull figure. The Earth's direction is toward the bottom and the Sun's is 9° clockwise from there.

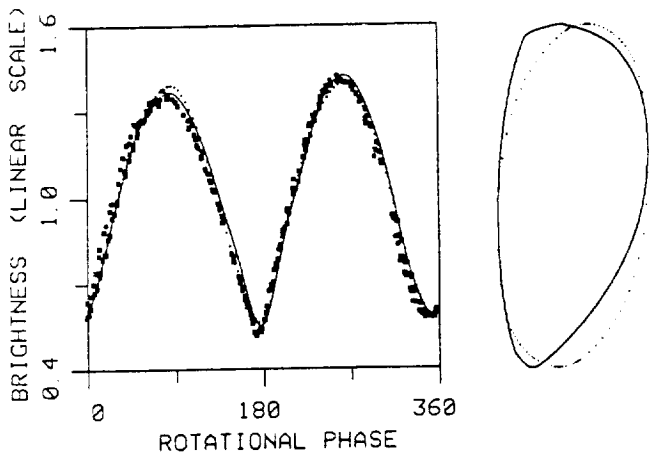

The mean cross section is a weaker shape constraint than the hull. However, visual and thermal-IR lightcurves are *disc-integrated* mappings of precisely those *average* shape characteristics conveyed by the mean cross section. The estimate of Eros' mean cross section is "tapered," and some support for the validity of this result is offered by Lebofsky and Rieke (1979), who argue that a tapered shape can help to explain aspects of the asteroid's thermal-infrared signature observed by those authors and by Morrison (1976). In this context, Eros' mean cross section reveals shape characteristics responsible for odd-harmonic components of thermal-IR "emission" lightcurves as well as phase differences between emission and "reflected-light" curves. The estimates of Eros' hull and mean cross section have their longest sides on the receding limb at zero rotational phase. Perhaps that face of Eros lacks prominent positive relief. For the other sides, the apparent differences between the curvatures of the hull and the mean cross section might arise from non-equatorial topography.

REFERENCES

Campbell, D. B., et al. 1976. Icarus 28, 17-20.
Dunlap, J. L. 1976. Icarus 28, 69-78.
Jurgens, R. F. 1982. Icarus 49, 97-108.
Jurgens, R. F., and R. M. Goldstein 1976. Icarus 28, 1-15.
Lebofsky, L. A., and G. H. Rieke 1979. Icarus 40, 297-308.
Millis, R. L., et al. 1976. Icarus 28, 53-67.
Morrison, D. 1976. Icarus 28, 125-132.
O'Leary, B., et al. 1976. Icarus 28, 133-46.
Ostro, S. J., and R. Connelly 1984. Icarus 57, 443-463.
Ostro, S. J., et al. 1988a. Icarus 73, 15-24.
Ostro, S. J., et al. 1988b. Icarus 75, 30-63.
Ostro, S. J., K. D. Rosema, and R. F. Jurgens 1990. Icarus, in press.
Tedesco, E. F. 1976. Icarus 28, 21-28.
Zellner, B. 1976. Icarus 28, 149-153.

On the Physics and Origin of Cometary Nuclei

Fred L. Whipple, Smithsonian Astrophysical Observatory,
60 Garden Street, Cambridge, MA 02138

Studies with members of the Halley Multicolor Camera Team of the Giotto Mission show that three major jet sources can account for 71 percent of the dust jet activity of Halley's comet at the time of the Giotto passage. Each jet's azimuthal intensity is well represented by a Gaussian curve out to an azimuthal distance of 60° - 90° from the center. The assumption that each jet arises from an area of a few square kilometers with a number of subsources, each with a cone half angle of ~ 10°, leads to a radial intensity distribution consistent with the observations. This intensity distribution follows a 1/R law for distance R from the nucleus greater than 20 km but falls below this relationship at smaller distances. The above rather natural solution for the problem obviates the need for solutions for the break-up of grains or their acceleration near the nucleus although there is other evidence for break-up.

It is not clear whether some 26 percent of the scattered dust background around the nucleus arises from a jet on the far side directed away from the spacecraft or whether it arises from less active areas spread broadly over the sunlit side.

The strongest jet at the time of the Giotto mission was centered 41° south of the projected sunward direction and apparently arose from a polar region. Probably a nutation of the pole with a 7.4 day period caused this activity to change with that period while the major rotation rate near 2.2 days was around a minor axis more or less perpendicular to this direction.

The nature of the jet activity on the Halley comet nucleus and the battered appearance of the nucleus support the idea that comets grew from the encounters of cometesimals, perhaps up to ~ 1000 meters in dimension. High velocity encounters above perhaps ~ 100 m/s would release latent energy of amorphous ices and chaotic chemicals and be rather destructive. Lower velocity encounters would produce matrix material shattered by the encounter with pristine remnants of cometesimals left embedded in it. Probably the matrix material would be less consolidated and more friable than the cometesimals, containing larger globs that could be blown out more easily by the gas in dust jets. Thus relatively large volumes of matrix material might be lost to produce chasms, craters and general "wasting" effects on steep slopes.

Current calculations of the capture of comets from the Oort Cloud indicate that such captures could not produce the short-period (SP) comets because of the low inclinations of their orbits to the plane of the ecliptic. Hence the suggestion has been made that the SP comets are derived from comets in longer period orbits formed in the main disc of the Laplace nebula and still moving in low-inclination orbits with perihelia well beyond the outer planets.

If this concept is true and the Oort Cloud comets were formed in the Uranus-Neptune region of the Laplace nebula before being thrown out to great distances, these long-period (LP) comets should have been formed in a warmer region than the SP comets. Also they might have been more battered by mutual collisions during their growing stages. Hence the LP comets might contain fewer amorphous ices and less highly volatile material than the SP comets. On the other hand, the outer layers of some "new" LP comets appear to have a thin outer layer of very volatile material, probably formed by cosmic rays.

If the above scenario is valid, one has reason to seek observational differences between LP and SP comets. This search is complicated by major changes in the structure and even the composition of comets induced by:

a) differential collisional effects depending on the velocity of the collisions;

b) dimensional effects involving radioactivity for larger comets that might move the volatiles from the core to outer regions;

c) aging effects involving the warming of the entire short-period comets by solar radiation and differences in the nature of the core material seen at the surface of very old SP comets and the near-surface material of the younger comets; and

d) other effects of the environmental character that might change the comets, including supernovae, bright nearby stars, the interstellar medium, etc.

In spite of a number of observing programs and statistical studies, no differences of significance have been found in the composition of SP comets compared with LP comets. On the other hand, there is strong evidence that LP comets have a tendency to brighten earlier than the SP comets as they approach the Sun, but tend to fall in brightness in much the same fashion after perihelion. This difference might be attributed solely to radial differences in the nuclei of comets, the SP comets generally being more reduced by sublimation than the LP comets. There is also indirect evidence from the non-gravitational forces that newer (LP) comets are more active than average SP comets, but this effect might well arise from the same cause as the light-curve differences.

A search continues for observable differences between LP and SP comets. Because the orbits of LP comets are statistically somewhat a measure of their age since capture into orbits of small perihelion distances, the light curve differences can be used to indicate the reality of an aging effect, not merely between "new" and SP comets but also among LP comets generally. Unfortunately, we have no orbital age criteria for SP comets, an objective greatly to be sought.

It is possible that the direction of the major axes of LP comets may in some way distinguish their origin (and possibly aging), in view of recent evidence that the "galactic tidal force" is probably more important than passing stars in perturbing Oort Cloud comets into visibility. The dearth of major axes of "newer" comets pointed near the galactic poles and equator support this assumption.

Two groups of LP comets are of interest in this regard: one by Biermann, Heubner and R. Lust with aphelia in the region of galactic longitude (l) and latitude (b) defined by $180^{o} \leq l \leq 248^{o}$ and $-2^{o} < b < +38^{o}$, the <u>BHL cluster</u>; and the other by Delsemme, the <u>D Cluster</u>, extending for many degrees through the galactic pole. The distribution of the semi-major axes suggests that the BHL cluster is older than the D cluster. Delsemme stresses the important point that members of his cluster have predominant motions at aphelion that are "almost perpendicular to the plane of the ecliptic," this suggests galactic tidal forces, at least at moderate galactic latitudes. The members of the BHL cluster are moving almost at random at aphelion. This and their older age compared to the D cluster suggest that they were brought in by a passing star sometime ago and, therefore, that we are <u>not</u> presently in a "comet shower" induced by the relatively close passage of a star.

The 18 members of a special group with aphelia lying within 10^{o} of the galactic plane are of interest. The periods (P) are peculiarly, distributed half in the range

$10^3<P<10^4$ yr, with only 3 in the range $10^4<P<10^5$ yr and only one apparently new, viz., the very dusty C/Arend-Roland 1957 III. Here we have a suspicion of a relatively old stellar passage or passages. In any case these comets apparently were not brought in by the galactic tide and not "recently".

The BHL cluster is interesting because it contains the aphelia of P/Halley, the infamous C/Kohoutek, 1973 XII, C/Morehouse, 1908 III, two of the 5 comets (of 209) with 100<P<200 yr and, if slightly enlarged the Kreutz sungrazers and 10 of the 20 comets listed as "Great" in Marsden's 1986 catalogue. On the other hand, the newer D cluster contains no comets of especial interest. We might conclude that in the BHL cluster we find large interesting comets of an older "comet shower", whereas the "new" cluster contains average comets.

Of the 209 comets with high quality orbits only 8 with $i<35^o$ and $1/a<10^{-4}(AU)^{-1}$ are relatively new and possible progenitors of SP comets. Of these 8, 5 were well observed, of which 2 split, 2 developed a conspicuous disk at solar distances r > 5AU and the fifth is C/Kohoutek. In the BHL cluster there are 7 (the GE group) with aphelia concentrated near the intersection of the galactic and ecliptic planes. All have direct motion ($i<79^o$) and P<16,500 yr. They possibly represent comets on their way towards short periods.

For a full discussion see "The Forest and the Trees" to appear in the Proceedings of the Colloquium "Comets in the Post-Halley Era" held in Bamberg, FRG, April 1989.

Cometary Cratering Rates on the Terrestrial Planets.

G. W. Wetherill, DTM, Carnegie Institution of Washington, Washington, D.C. 20015

The larger terrestrial planet and lunar impact craters are produced by astronomically observable planet-crossing bodies. These bodies are derived from collisions in the main asteroid belt as well as from the sources of comets in the outermost solar system ($35 - 10^5$ A.U.). It has been shown that the asteroidal region probably supplies about 1/3 of the cratering flux, the remainder being cometary (Wetherill, 1989). Although the contribution from active comets is significant (Weissman et al., 1989) most of the impacting cometary population probably consists of extinct or at least dormant comets of asteroidal appearance, primarily in orbits only barely distinguishable statistically from those of Apollo-Amor objects of asteroidal origin.

These conclusions have been augmented by new Öpik-Arnold Monte Carlo calculations of the probability of gravitationally decoupling short-period comets from Jupiter's influence by close encounters with Earth and Venus. The probability of decoupling is found to be $\sim 3 \times 10^{-3}$. When combined with observational data on the observed number of active short period comets and the observed number of Apollo-Amors, a model of planetary cratering is obtained that is also consistent with the mass flux and orbital distribution of the survivable small-size end member Earth-crossing population, the meteorites.

Duncan et al. (1988) have shown by numerical integration that the orbital distribution of Jupiter family comets corresponds to that expected from an otherwise unobserved "Kuiper belt" of comets just beyond Neptune, and is inconsistent with the earlier hypothesis of capture of long-period Oort cloud comets by Jupiter. By use of more approximate Monte Carlo methods, this work has been extended to include the entire cometary source region. It is found that any highly flattened inclination distribution, such as may be expected to be found for cometary aphelia as large as ~ 2000 A.U., is acceptable, but no isotropic distribution corresponding to derivation of short period comets by capture of an isotropic distribution from either the inner or outer Oort cloud at greater aphelia agrees with the observed orbital distribution of short period comets. This new work also suggests the speculation that the approximate factor of two discrepancy between the observed lunar and terrestrial cratering rates could be a stochastic effect of the most deeply penetrating passing star having perturbed the most distant portion of the inner non-isotropic region (aphelion ~ 2000 A.U.) about 500 m.y. ago, supplying a moderate pulse of Neptune-crossing comets with dynamic lifetimes $10^8 - 10^9$ years, that then slowly evolved into Jupiter family comets and Apollo objects.

References:

Wetherill G.W. (1989) Cratering of the terrestrial planets by Apollo objects. In press, *Meteoritics*.

Weissman P.R., A'Hearn M.F., McFadden L.A., and Rickman H. (1989) Evolution of comets into asteroids. In press, *Asteroids II*, Univ. of Arizona Press.

Duncan M., Quinn T., and Tremaine S.D. (1988) Origin of short period comets. *Astrophys. J.* **328**, L69–L73.

COMETARY PHYSICS AND DYNAMICS

Paul R. Weissman, Jet Propulsion Laboratory, Pasadena, CA 91109

The study of comets has wide ranging implications for many other areas of planetary science. Comets are the best obtainable source of preserved solar nebula material and thus contain a cosmo-chemical record of conditions at the time of planetary formation. Comets were likely the planetary building blocks for Uranus, Neptune, and the outer planets' satellites, and may constitute a significant fraction of the mass in the outer solar system. Cometary bombardment of the terrestrial planets (and Titan) likely contributed a significant fraction of the volatile reservoirs of these planets. Subsequent cometary impacts on the Earth may have played a role in initiating global biological extinction events. This report details a number of areas studied in the past year.

Cometary Masses and Terrestrial Impact Rates: The spacecraft flybys of Comet Halley in 1986 showed that cometary nuclei were much larger and darker than previously expected (Sagdeev et al., 1986; Keller et al., 1986), leading to a sharp revision upward in the predicted mass of the nuclei. The average nucleus mass is now estimated at 3.8×10^{16} grams (Weissman, 1990a). This revision has a number of important implications. For example, the estimated total mass of comets in the Oort cloud increased sharply. Based on current dynamical simulation results (Duncan et al., 1987; Heisler, 1990) the population of the Oort cloud is now estimated to be 7.2×10^{12} comets with a total mass of 45 to 50 Earth masses. Estimated cratering rates for comets on the Earth are also increased substantially. It is found that the majority of cometary impacts occur during comet showers caused by random passing stars and encounters with giant molecular clouds in the galaxy. Showers account for approximately 17% of terrestrial craters $\geq$ 10 km diameter, versus the steady-state flux of long and short-period comets which provides about 12% of the cratering flux (Weissman, 1990b). Finally, estimates of the total mass of cometary volatiles which may have bombarded the Earth in its early history have also increased, in some cases exceeding the current total mass of the Earth's oceans.

An Upper Limit on the Mass of the Kuiper Belt: The existence of a cometary belt beyond the orbit of Neptune has been suggested based on hypotheses of solar system formation (Cameron, 1962), and on dynamical arguments with regard to the origin of short-period comets (Duncan et al., 1988). A unique test of the existence of that belt can be made using Pluto's satellite Charon. It is observed that Charon's orbit has a very low eccentricity, $< 10^{-3}$ (Tholen and Buie, 1988). Charon's orbit is tidally damped and the only significant perturbation on it would come from impacts by cometary nuclei. Detailed estimates of the expected impact rates for both long-period comets and comets in the proposed belt beyond Neptune, called the Kuiper Belt, show that the Kuiper Belt comets clearly dominate (Weissman et al., 1989). The forced eccentricity in Charon's orbit caused by the summing of many random impacts leads to an upper limit of about 5 Earth masses of comets in the Kuiper Belt, based on the current upper limit on the observed eccentricity. This is comparable to the limit which was set based on radio tracking of Pioneer 10 and 11 (Anderson and Standish, 1986), and somewhat more than the limit based on the lack of distant perturbations on the aphelion of Comet Halley (Yeomans, 1986). Continued observation of Pluto-Charon eclipse events may lead to a refinement in the eccentricity, which could in turn provide a better constraint on the estimated Kuiper Belt mass.

Comet Halley Brightness Asymmetries: Comet Halley was anomalously bright at large distances from the Sun, in particular on the post-perihelion leg of its orbit where it was four magnitudes brighter than when inbound at comparable distances. Newburn's (1984) empirical photometric model for converting visual magnitudes to gas production rates was used on 826 magnitude observations ranging from 11.0 AU inbound to 8.2 AU outbound, compiled by Green and Morris (1987). The results were compared with the expected gas production from a

sublimating ice sphere with surface area of the Halley nucleus and with 30% of the surface active, and with the albedo, pole orientation, and rotation period (2.2 days) of Halley. The increased gas production immediately post-perihelion is explained by seasonal effects on an obliquely rotating nucleus, where the large change in true anomaly as the comet goes through perihelion results in a rapid change in the latitude of the sub-solar point (Weissman, 1987). The northern hemisphere of the nucleus is poorly illuminated pre-perihelion and is then suddenly fully illuminated right at the comet's closest point to the Sun. This causes substantial thermal stresses in the nucleus surface, breaking up the existing crust and greatly increasing the fraction of active area on the nucleus surface.

The proposed explanation for the continued brightness at large solar distances outbound is more speculative. Radar observations of comets show evidence of large clouds of debris around nuclei, including Comet Halley (Campbell et al., 1989). It is possible that these clouds of icy-silicate-hydrocarbon conglomerate act as a secondary source of coma gases and dust, continuing to sublimate at very low rates far from the Sun, but with a vastly increased total surface area. These large particles are blown off the nucleus during the comet's most active phase around perihelion, and thus are only seen on the outbound leg. By the time Comet Halley returns to perihelion, the cloud of debris has dispersed and only the primary nucleus remains. This matches estimates by Sykes et al. (1986) that debris discovered in short-period comet orbits by the IRAS satellite may be tens of years old, long compared to the orbital periods of most Jupiter family short-period comets, but short compared to the 76-year orbital period of Comet Halley.

Physical Processing of Cometary Nuclei: The common perception of cometary nuclei is that they are unprocessed interstellar and proto-solar nebula material, aggregated at low velocity and at very low temperature. However, a detailed examination of the expected physical processing that comets have likely encountered over the history of the solar system shows that this is not the case (McSween and Weissman, 1989), and that the expected processing is in many ways similar to, though more subtle than, that for meteorites. Alteration processes may occur during comet formation in the outer planets region, during their dispersal to or residence within the Oort cloud, and after their return to the planetary region. Processes that may have significantly modified cometary nuclei include heating, impacts, and irradiation. Possible consequences include phase changes in ices, hydration reactions in silicates, synthesis of organic compounds, collisional disruption and reaccretion, shock and irradiation effects in minerals and ices, cosmogenic nuclide formation, redistribution or loss of volatiles, and formation of a refractory veneer. A model of cometary nuclei that emerges from these considerations provides a framework for understanding observations of comets and future samples.

References: Anderson, J. D., and Standish, E. M., In *The Galaxy and the Solar System*, eds. R. Smoluchowski et al., Univ. Arizona Press, Tucson, pp. 286-296; Cameron, A. G. W. (1962) Icarus **1**, 13-69. Campbell, et al. (1989) Astrophys. J., in press; Duncan, M., et al. (1987) Astron. J. **94**, 1330-1338; Duncan, M., et al. (1988) Astrophys. J. **328**, L69-L73; Green, D. W. E., and Morris, C. S. (1987) Astron. Astrophys. **187**, 560-568; Heisler, J. S. (1990) Icarus, in press; Keller, H. U., et al. (1986) Nature **321**, 320-326; McSween, H. Y., and Weissman, P. R. (1989) Geochim. Cosmochim. Acta **53**, 3263-3271; Newburn, R. L. (1984) Adv. Space Res. **4**, 185-188; Sagdeev, R. Z., et al. (1986) Nature **321**, 262-266; Shoemaker, E. M., et al. (1979) In *Asteroids*, ed. T. Gehrels, Univ. Arizona Press, Tucson, pp. 253-282; Shoemaker, E. M., et al. (1988) In *Global Catastrophes in Earth History*, Snowbird Utah, October, 1988, pp. 174-176 (abstract); Sykes, M. V., et al. (1986) Science **232**, 1115-1117; Tholen, D. J., and Buie, M. W. (1988) Astron. J. **96**, 1977-1982; Weissman, P. R. (1987) Astron. Astrophys. **187**, 873-878; Weissman, P. R., et al. (1989) Geophys. Res. Lett. **16**, 1241-1244; Weissman, P. R. (1990a) In *Comets in the Post-Halley Era*, eds. R. Newburn et al., Kluwer, Amsterdam, in press; Weissman, P. R. (1990b) In *Global Catastrophes in Earth History*, eds. V. Sharpton and P. Ward, GSA Special Paper **247**, in press; Yeomans, D. K. (1986) In *Exploration of Halley's Comet*, eds. B. Battrick et al., ESA SP-250 **2**, 419-425.

Rotation of Halley's Comet

S. J. Peale(UCSB) and Jack J. Lissauer(SUNY at Stony Brook)

The two distinct periodicities of 2.2 days and 7.4 days inferred from the coma structure and light curves of Halley's comet together with the irregular shape of its nucleus suggest that the nucleus is not in a state of principal axis rotation. We model this situation using numerical simulations supported by analytic calculations. It is easy to numerically generate light curves from modulated jets of material which exhibit both periodicities if we choose initial conditions for a representative nucleus such that the shorter period is the rotation period and the longer period is that of precession of the spin vector in the body frame of reference. The dominant spectral power in such curves most often corresponds to the 7.4 day period unless the amplitude of precession is very small. Although curves similar to those observed over short time intervals are obtained for precession about either of the axes with extreme moments of inertia, the observed marked seasonal changes in the light curve are only produced for precession about the axis of maximum moment of inertia. The generation and stability of a wobble–type rotation state is investigated by numerically solving Euler's equations for the reaction torque from a jet of ejected material. A nonprincipal axis rotation is easy to excite from an initial rotation about the axis of maximum moment of inertia (minimum energy) only if the nucleus is nearly axisymmetric. Except for almost perfect axial symmetry, excitation of a precession about the axis of minimum moment of inertia is always frustrated by an initial precession about the axis of maximum moment of inertia. In the more probable case of significant triaxiality, even a precession of the spin about the axis of maximum moment of inertia is difficult to excite from an initial minimum energy state, and it can change only slowly from the jet–induced torques. However, this slow change could suffice to generate a substantial amplitude wobble from the cumulative effects of many apparitions. The damping time for the wobble is $O(10^6 \text{ to } 10^8)$ years, which rules out a primordial origin of a wobble but allows a gradual excitation. Significant changes in the spin angular momentum can occur in a single apparition, but the stability of the amplitude of precession about the axis of maximum moment of inertia means that a rotation state which is relatively stable over many apparitions is not unreasonable. The improbability of exciting a spin precession about the axis of minimum moment of inertia, the relative instability of this state to the jet–induced torques and the small probability of observing significant seasonal changes in the light curve in this state all favor the model in which Halley's nucleus precesses about the axis of maximum moment of inertia.

On the Density of Halley's Comet

S. J. Peale(UCSB)

The density of Halley's Comet is determined as a function of a parameterized time of visibility of ejected material, as a function of the angular deviation α from the Sun–comet direction of the averaged reaction force due to jets of ejected material when α is assumed independent of orbital position, and as a function of thermal inertia for a variable α. The variation of the averaged gas ejection rate from the nucleus as a function of orbital true anomaly is estimated by using the light curve of Green and Morris (1987) calibrated by the ejection rate at 1.28 radians past perihelion (0.89 AU) found from the spacecraft flybys. Estimates of the H_2O production rate deduced from several observational data sets are scattered around the gas production rate determined from the light curve except very near perihelion where the observationally based estimates are scarce and generally fall below the rate determined from the light curve. Although some of the densities obtained by this procedure are in reasonable agreement with intuitive expectations of densities near 1 g/cm^3, the uncertainties in several parameters and assumptions expand the error bars so far as to make the constraints on the density uninformative. So many of these uncertainties apply to all procedures proposed for determining the density that we conclude that secure, informative constraints on the density of any cometary nucleus must await the time of spacecraft rendezvous with that nucleus. In particular, the suggestion that cometary nuclei tend to be very fluffy, underdense objects should not yet be adopted as a paradigm of cometary physics.

IS COMET HALLEY A SOLAR NEBULA CONDENSATE ? S. Engel, J.S. Lewis, and J.I. Lunine (LPL/U. of Arizona)

Comets are the best probes of the physical and chemical conditions in the outer solar nebula during planet formation despite the controversy regarding their formation environment. This paper will address whether they are products of the same condensation sequence whereby planets and asteroids formed, or if they are agglomerations of interstellar grains.

Since water-ice is stable at roughly 5 AU comet formation may have occured relatively close to the sun. Dynamical studies do not seem to confirm this, since Jupiter and Saturn tend to eject the majority of icy planetesimals to interstellar space and not to the Oort cloud [1]. Hence cometary formation zones further out in the Uranus-Neptune region (20 to 30 AU) or regions far out in the solar nebula (10^2 and more) were suggested [2].

Carbonaceous dust on the surface may give comets low albedos and red spectral properties. Similar spectral properties are observed in outer belt asteroids (spectral classes D,P and C). It was suggested, that some of these asteroids are extinct or dormant comets based on dynamical and spectroscopic grounds [3]. More clues for a connection between comets and meteorites were found in interplanetary dust particles (IDPs) collected in the Earth's stratosphere. Comets are the major source of IDPs, but it is not known to what extent asteroids contribute to that number [4]. Spectral signatures of IDPs are consistent with carbonaceous dust found in comets but are also in agreement with the composition of outer solar system asteroids. This might suggest that some asteroids and comets accreted in the same surrounding in the outer solar nebula.

The comet Halley data show high abundances in CH_4, CO_2 and NH_3 which seem at first glance inconsistent with a solar nebula origin. However, when physical and chemical interactions of CO and N_2 molecules with their surroundings are considered, more CH_4, CO_2 and NH_3 are available in the outer solar nebula than was predicted by earlier simple models of chemical processes. A model was developed to explain the volatile composition (CO, CH_4, CO_2, N_2, NH_3) in comet Halley as a solar nebula condensate. In these investigations the CO/CH_4, CO/CO_2 and N_2/NH_3 ratios will be discussed. Assumed was a CO-N_2- dominated outer solar nebula and elemental abundances were calculated for a distance 20 AU from the sun. Mixing rates applied range from inefficient mixing to efficient mixing.

Besides calculating gas phase abundances at certain temperatures a number of other processes were included in the model: 1) a change in the elemental O to C ratio to lower values in the inner region of the nebula due to diffusive redistribution of water vapor [5], 2) surface catalyzed reactions on metal grains which lower quench temperatures [6], 3) mixing of molecular species from the inner, chemically active part of the nebula to the

region of comet formation [7,8] 4) fractionation due to clathrate-hydrate formation and condensation of volatiles in the outer (colder) part of the nebula.

For a quench temperature of 700 K and roughly 10% mixing efficiency for CH_4 and CO_2 from the inner solar nebula into the CO-rich outer solar nebula the carbon composition in comet Halley can be explained with our model. Unfortunately the same scenario doesn't explain the nitrogen abundances. The N_2/NH_3 ratio measured in comet Halley is lower then the one calculated for the solar nebula. A possible explanation is that the abundances of CH_4 and NH_3 are determined in a proto-planetary subnebula [9]. A problem with this theory is that the dynamical aspects of mixing these components out of such a subnebula remain highly speculative. On the other hand, an interstellar origin for NH_3 seems to be possible. Icy planetesimals could have been accreted in molecular clouds that show high abundances in NH_3, CO, CO_2 and H_2CO. These cometesimals then would have been mixed with cometesimals formed in the outer solar nebula and accreted into a cometary parent body. In general this would support the view of a comet as an agglomerate.

Our results show that while some molecules (CO, CH_4, CO_2) indicate a solar nebula origin for comet Halley, others suggest contamination by interstellar material (NH_3, H_2CO). This would imply, that at least in the outer part of the nebula mixing was imperfect.

References:

[1] Fernandez J.A. and W.-H. Ip (1981) Icarus 47, 470.

[2] Weissman P.R. (1985) in Protostars and Planets II, Univ. of Arizona Press, 895.

[3] Hartman W.K., D.J. Tholen and D.P. Cruikshank (1987) Icarus 69, 33.

[4] Bradley J.P., S.A. Sandford and R.M. Walker (1988) in Meteorites and the Early Solar System, Univ. of Arizona Press.

[5] Stevenson D.J. and J.I. Lunine (1988) Icarus 75, 146-155.

[6] Vannice M.A. (1975) J. Catalysis 37, 146.

[7] Stevenson D.J. (1988) submitted to Astrophys. J..

[8] Prinn R.G. (1988) submitted to Astrophys. J..

[9] Prinn R.G. and B. Fegley (1988) in Origin and Evolution of Planetary and Satellite Atmospheres, Univ. of Arizona Press, in press.

The Influence of CO Ice on the Activity and Near Surface Differentiation of Comet Nuclei

Fraser P. Fanale and James R. Salvail, Hawaii Institute of Geophysics, University of Hawaii, Honolulu, Hawaii 96822 U.S.A.

Recent observations of comets, especially Comet Halley (Festou et al., 1986; Woods et al., 1986), have indicated the presence of significant concentrations of CO, suggesting that CO ice may be a more abundant component of cometary ice than was previously thought. CO may be responsible for the activity of comets at large distances from the sun, where the volatility of H2O is too low to account for the observed activity (Delsemme, 1982). This seems to be particularly true for comets passing through the inner solar system for the first time. CO2 has generally been regarded as being the second most abundant cometary ice next to H2O, but the weight of current observational evidence seems to indicate that CO may be as abundant or even more abundant than CO2. Free CO ice can be mixed with H2O and other ices, or CO molecules can be trapped in H2O lattices to form a clathrate. It has been shown that CO sublimes from the clathrate at a higher temperature than in the free state and that the presence of CO in an H2O matrix increases the effective volatility of H2O ice (Sandford and Allamandola, 1988). Amorphous H2O ice has also been shown to trap more volatile gases (Bar-Nun et al., 1985 and 1987).

Houpis et al. (1985) were the first to develop a detailed thermal model of the chemical differentiation of a comet nucleus composed of two ices, H2O and CO2, plus nonvolatiles. Fanale and Salvail (1987) developed an improved model that additionally accounted for the effects of a spherical nucleus shape, nucleus rotation, orientation of the rotation axis, heat conduction into the interior of the nucleus, restriction of the gas outflow by the H2O ice and dust, the use of thermal conductivities for both amorphous and crystalline H2O ice and tracking of the boundary between the amorphous and the crystalline H2O ice. These models calculate the ice temperatures, the fluxes of CO2 and H2O gases and the depth of CO2 ice as functions of heliocentric distance. Both of these models are based on the assumption that the ice is a coherent matrix with a significant tensile strength. This assumption is controversial, since it is widely believed that cometary material is a mixture of loose or very weakly cohering particles held together primarily by gravity. If this is true, the highly volatile ices would eject all the overlying H2O ice grains, and no material differentiation could occur. Also, H2O ice grains should have been observed much more frequently than has been the case. If the ices composing cometary material are structured and sufficiently coherent, a layer of H2O ice and dust will be produced as the volatile ices are sublimated and lost from the nucleus. This layer would continue to grow until a comet is within a few AU from the sun, at which time H2O sublimation becomes significant. Then the water ice layer becomes eroded, and a thin layer of coarse nonvolatile particles accumulates on the surface. If the perihelion is inside 1 to 2 AU of the sun, all the nonvolatile particles are ejected from the nucleus. On the outbound part of the orbit the processes are reversed in sequence, and the water and dust layer thickens again.

The computer program used in our previous work (Fanale and Salvail, 1987) has been adapted to model a comet nucleus containing CO ice instead of CO2 ice, in addition to the H2O ice and dust, and having the orbit of comet Halley. Temperatures of the H2O and CO ice surfaces, the fluxes of CO and H2O gases and the depth of the CO ice have been calculated for various cases of pore size, porosity and the fraction of CO ice. The pressure of subsurface CO gas has also been calculated and related to the stability of the H2O ice and dust mantle and the possibility of H2O ice grain emission.

For our model it was found that CO gas production exceeds H2O gas production for heliocentric distances greater than 2.5 AU. CO gas production from comets on their first orbit is greater than that for succeeding orbits for distances less than 10 to 12 AU before perihelion, and the difference can be as much as three orders of magnitude. After perihelion there is little difference in CO gas production between the first and succeeding orbits. It was also found that for a Halley type of orbit CO ice should always exist within three meters from the surface. Shortly after perihelion CO ice may exist within a few tens of centimeters from the surface. This has important implications for design of in situ elemental nucleus analysis experiments. The CO gas output has not been found to depend significantly on the permeability of the H2O ice and dust mantle. CO ice is only 15 to 20% deeper for a mantle with an average pore size of 10 microns than for one having and average pore size of 1 micron. The reason is that the higher temperatures in a low permeability mantle tend to compensate for the reduced area of the flow passages in the porous ice. The subsurface CO gas pressure is much less than is needed to rupture a mantle of annealed water ice. If the H2O ice is in the form of small ice grains having negligible tensile strength, no stable H2O ice mantle could be maintained in the presence of the large CO gas pressures unless some cohesive forces such as those observed among silicate 'mantle' grains in several comet simulation experiments are operating. Such cohesive forces may be comparable to our suggested range of CO pressures based on laboratory experiments. This may account for episodic changes in regional activity. If loose, dusty H2O ice grains exist on a cometary surface, they can be ejected in the micron size range by CO gas for most of a Halley type orbit.

References

Bar-Nun, A., J. Dror, E. Kochavi and D. Laufer. Amorphous water ice and its ability to trap gases. Phys. Rev. B. 35, 2427-2435, 1986.

Bar-Nun, A., G. Herman, D. Laufer and M.L. Rappaport. Trapping and release of gases by water ice and implications for icy bodies. Icarus 63, 317-332, 1985.

Delsemme, A.H., Chemical composition of comet nuclei. In "Comets" (L.L. Wilkening, ed.), Univ. of Arizona Press, Tucson, AZ., 85-130, 1982.

Fanale, F.P. and J.R. Salvail. The loss and depth of CO2 ice in comet nuclei. Icarus 72, 535-554, 1987.

Festou, M.C., P.D. Feldman, M.F. A'Hearn, C. Arpigny, C.B. Cosmovici, A.C. Danks, L.A. McFadden, R. Gilmozzi, P. Patriarchi, G.P. Jozzi, M.K. Wallis and H.A. Weaver. IUE observations of Comet Halley during the vega and Giotto encounters. Nature 321, 361-363, 1986.

Houpis, H.L.F., W.H. Ip and D.A. Mendis. The chemical differentiation of comet nuclei: the process and its consequences. Astrophys. J. 295, 654-667, 1985.

Sandford, S.A. and L.J. Allamandola. The condensation and vaporization behavior of H2O:CO ices and implications for interstellar grains and cometary activity. Icarus 76, 201-224, 1988.

Woods, T.N., P.D. Feldman, K.F. Dymond and D.J. Sahnow. Rocket ultraviolet spectroscopy aof Comet Halley and abundance of carbon monoxide and carbon. Nature 324, 436-438, 1986.

CHAPTER 4

COSMOGONY AND DYNAMICS

A THREE-DIMENSIONAL PROTOSTELLAR COLLAPSE MODEL INCLUDING RADIATIVE TRANSFER

Elizabeth Myhill and William M. Kaula
Department of Earth and Space Sciences,
University of California, Los Angeles.

We have developed a three-dimensional Cartesian code for protostellar collapse which is second-order accurate and treats the effects of radiative transfer through the Eddington approximation. The principal equations governing the collapse are the mass, momentum, and energy conservation equations. The source terms in these equations are evaluated with a second-order centered difference method, while the advection terms are calculated with the Van Leer upwind interpolation scheme (1). The source and advection terms are evaluated separately with an update of momentum in between because this has been found to suppress numerical noise (2). To determine the gravitational potential of the density distribution, a method involving Fourier transforms and Green's functions is used to invert Poisson's equation (3). The mean intensity equation, which is needed to determine the radiative flux, and the equations of state for the energy and pressure are solved following Boss (4). The gas is assumed to be a mixture of hydrogen, helium, and heavier elements. The dissociation of hydrogen molecules and the ionization of hydrogen atoms are both considered. The mean opacity values are given by Pollack et al (5). To test the second-order finite difference scheme, we compared our calculations to the analytical solutions for isothermal, pressureless collapse (6). To further check the isothermal code, which does not include the effects of radiative transfer, we used the standard test case by Bodenheimer and Boss (7) for the self-gravitating collapse of a rotating, isothermal protostellar cloud. Our results agree with their calculations. We began with a roughly spherical cloud in a 31x31x31 grid point box. The initial ratios of thermal to gravitational energy and of rotational to gravitational energy were set to .25 and .20 respectively. We imposed an m=2 mode density perturbation and ran the code for 1.39 free fall times, where one free fall time is the time that it would take a cloud to collapse to a singularity if thermal pressures were ignored. Figures 1 and 2 show the diffuse binary which formed after .81 and 1.39 free fall times.

References

(1) Van Leer, B. 1977. J. Comp. Phys. 23, 263.
(2) Williams, H.A. 1988. PhD Thesis, Louisiana State University.
(3) Hockney, R.W. 1970. Meth. Comp. Phys. 9, 135.
(4) Boss, A.P. 1984. Astrophys. J. 277, 768.
(5) Pollack, J.B., C.P. McKay, and B.M. Christofferson 1985. Icarus 64, 471.
(6) Hunter, C. 1962. Astrophys.J. 136, 594.
(7) Bodenheimer, P. and A.P. Boss 1981. Mon. Not. R. Astr. Soc. 197, 477.

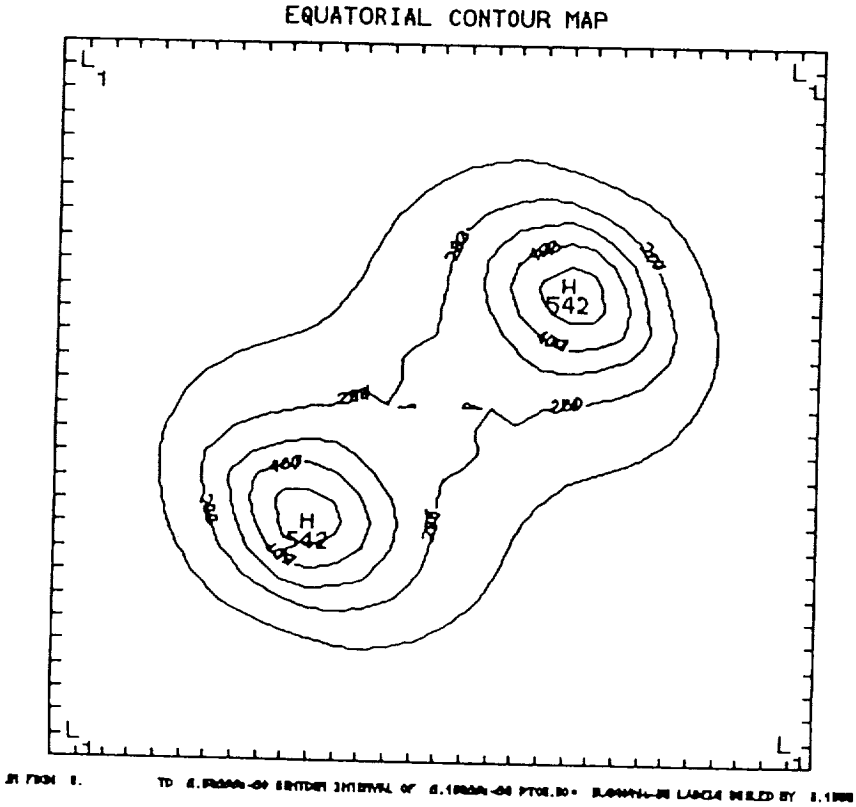

.81 free-fall time

- initially, the density perturbation pinches off and forms a diffuse binary
- here, the collapsing cloud has gone on to form a "bar-like" structure
- the density maxima are growing very slowly

Figure 1

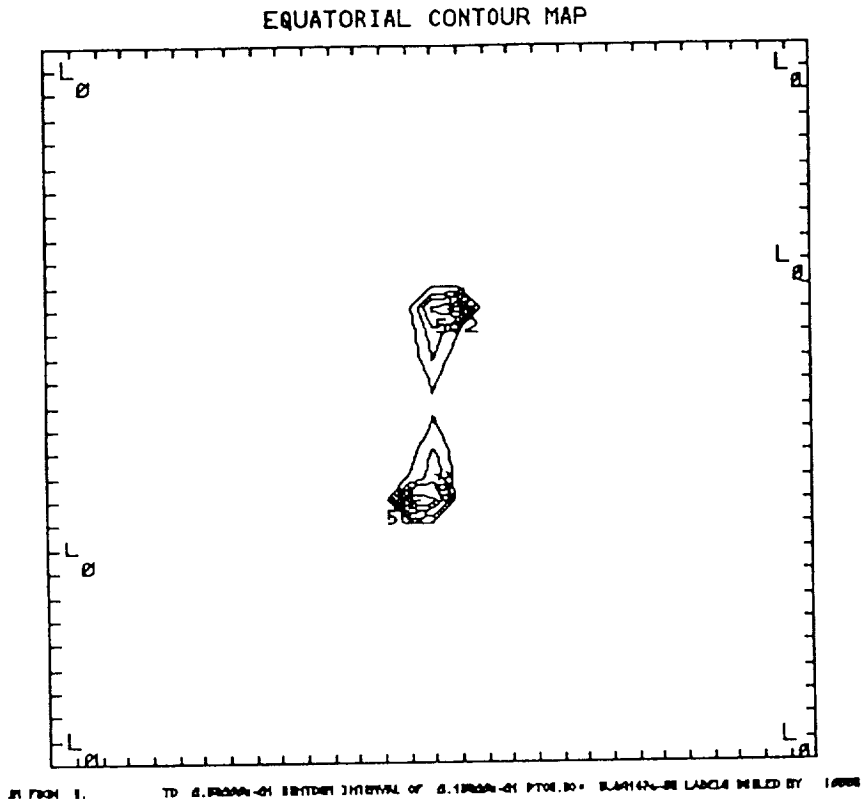

1.39 free-fall time

- a well-defined binary system has formed
- the density maxima are now approximately 600 times the initial value
- the binary has rotated roughly 90 degrees

Figure 2

NUMERICAL INVESTIGATION OF DYNAMICAL STABILITY IN THE SOLAR SYSTEM ON A LARGE PARALLEL PROCESSOR

William I. Newman[1], William M. Kaula[1],
Eugene Y. Loh[2], and Gary D. Doolen[3]

Exploration of the stability of test particles, both between the planets and near Lagrangian points, has been undertaken on the CM-2 Connection Machine Computer. The CM-2 is capable of $2^{16} = 65{,}536$ simultaneous independent calculations. Hence eccentricities up to 0.35 and inclinations to $\sin^{-1} 0.7$ are being tested.

Experience in the Jupiter-Saturn band (Weibel et al, 1990) indicates that runs for a band near a planet of mass m will have to extend at least 10^5 (m_J/m) revolutions, where m_J is the mass of Jupiter. Hence: one band at a time is being be explored; planet orbits interior to the inner planet of a band represented by Fourier Series; and the terrestrial planets combined with a Sun for integrations beyond Jupiter (or in its Lagrange regions). Because the parallel processor is difficult to adapt to non-uniform time steps, particles perturbed into collision (or ejection) trajectories are discarded and replaced by ones close to survivors, in order to sample regions of possible stability more densely. The tests for collision take into account longitude differences at orbit crossings so as to preserve any chance resonances (analogous to the Trojans and Pluto).

Most important, care has been taken to develop an accurate and efficient integrator. The round-off and stability characteristics of Cowell-Stormer type integration schemes have been thoroughly investigated, extending the procedures of Henrici (1962). We established the formal stability properties of these integration methods for orders 2-18, and obtained important results germane to accumulated round-off error. Our analysis indicates:

- o the maximum stable integration step systematically diminishes with the order of the integration scheme; but
- o the cumulative round-off error steadily increases with the order of the integration scheme; so
- o the range of admissible integration steps strongly diminishes with order.

Rules are being developed for choosing the optimum combination of time step and order for each integration.

References

Henrici, P. 1962: *Discrete Variable Methods in Ordinary Differential Equations.* Wiley, New York.

Weibel, W.M., W.M. Kaula, & W.I. Newman 1990: A computer search for stable orbits between Jupiter and Saturn. *Icarus* **83**, 392-390.

[1]University of California, Los Angeles, CA
[2]Thinking Machines Corporation, Cambridge, MA
[3]Los Alamos National Laboratory, Los Alamos, NM

PLANETARY ACCRETION RATES: ANALYTIC FORMULAE CONFIRMED BY A VARIETY OF NUMERICAL SIMULATIONS

R. Greenberg and W.F. Bottke, Lunar and Planetary Lab, Univ. of Arizona, Tucson

The dynamics of encounters of planetesimals with growing planetary embryos have been traditionally modelled using a two-body approximation (1). Greenberg *et al.* (2) discovered that random velocities V (corresponding to orbital eccentricities and inclinations) during accretion dropped so low, relative to the embryos' escape velocities V_e, that approaches were governed predominantly by keplerian shear rather than by the random motion. They noted that the traditional methods for estimating impact rates needed to be re-examined before use in this low- velocity regime.

Comparison of numerical integration of orbital motion with results of the two-body method, led Wetherill and Cox (3) to conclude empirically that the latter did not work for $V/V_e \lesssim 0.1$. However, Greenberg *et al.* (4) found that two-body behavior is a good approximation of encounters even at such low velocities, if one takes into account the way that the approach trajectory sets up the encounter geometry.

This discovery provided the foundation for an analytic evaluation of impact rates (5), which takes into account the transition from governance of approach by random motion to governance by keplerian shear. It was found that this transition takes place near $V/V_e \sim (2\pi\rho a^3/3M)^{-1/6}$ or about 0.1, which explains the limit found in (3). (Notation here follows (5).) For larger V/V_e (Regime A), the usual formula with two-body gravitational cross-section applies:

$$\text{Impact rate} \sim \pi r^2(1 + V_e^2/V^2)\sigma n/2 \qquad (A)$$

For smaller V/V_e (Regime B), approach dynamics enhance the accretion by an additional factor $\propto V/V_e$ (5):

$$\text{Impact rate} \sim \pi r^2 V_e^2 \sigma/(4m/M)^{1/3} V a \qquad (B)$$

We note further that once the gravitational cross-section is larger than the disk thickness, which occurs for $V/V_e \lesssim (2\pi\rho a^3/3M)^{-1/3}$ (Regime C), the two-dimensional formula applies:

$$\text{Impact rate} \sim 4r\sigma V_e \qquad (C)$$

These analytic formulae, although intended to be only approximate, agree very well with impact rates found by three-body orbital integration (3,6,7). Several examples of the agreement are shown on the next page. The predictive success of these formulae indicates that we now have a reasonably good understanding of some of the fundamental processes controlling impact rates.

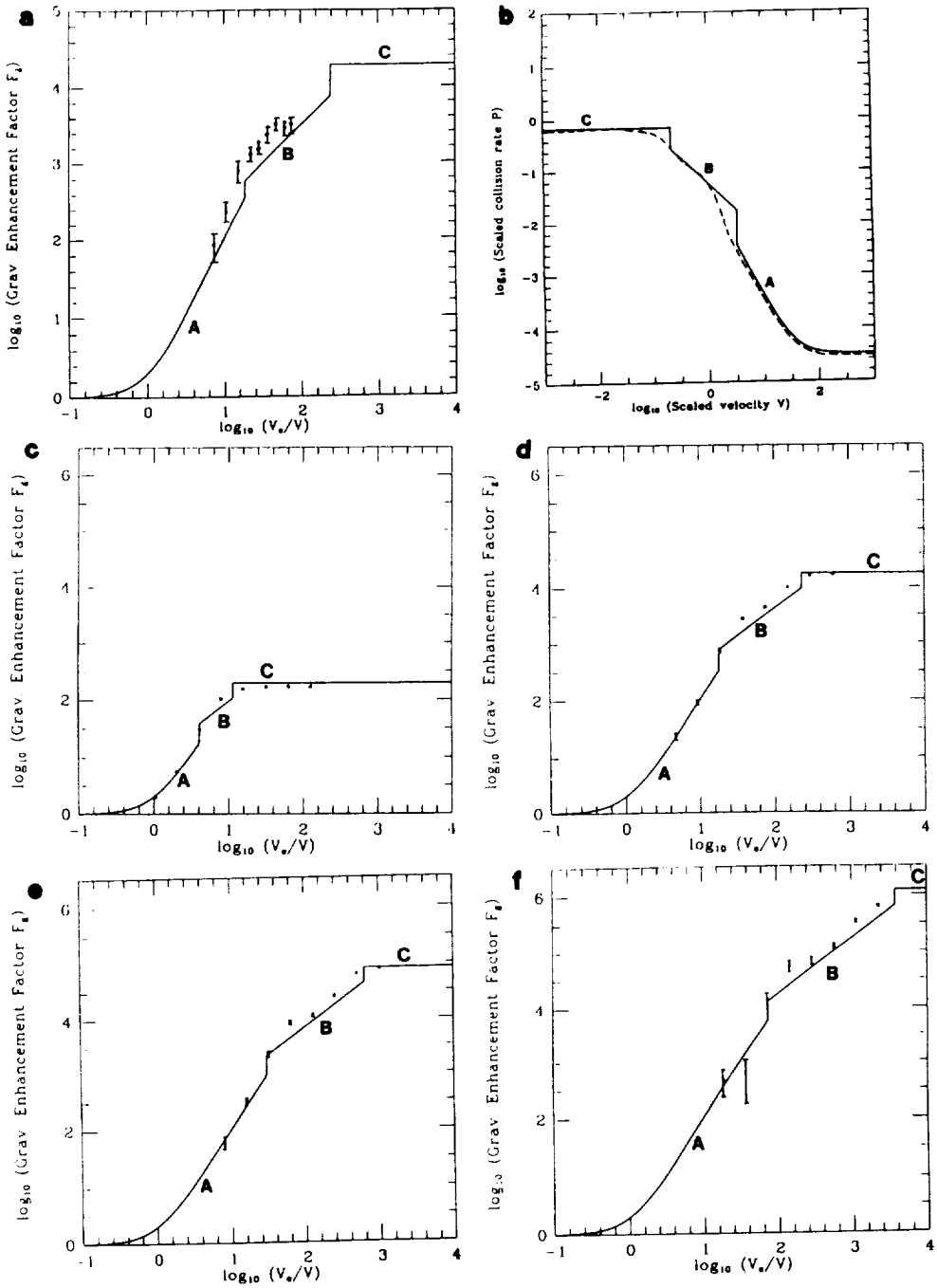

Figures: Plots of impact rates for cases studied in numerical experiments (3,6,7) for a variety of values of a, q, and m. Solid lines are our analytic model in regimes A, B, and C. Scaling matches that used in each numerical study. Data points in (a) are from Fig. 9 of (3), in (b) are from Fig. 2 of (8) based on (6), and in (c,d,e,f) are from Figs. 8a,b,c,d of (7).

References: (1) e.g. Safronov, V.S., 1972, NASA TT F-677; (2) Greenberg, R., *et al.* 1978, Icarus **35**, 1; (3) Wetherill, G.W., and Cox, L.P. 1985, Icarus **63**, 290; (4) Greenberg, R., *et al.*, 1988, Icarus **75**, 1; (5) Greenberg, R., *et al.*, 1988, LPSC XIX, 425; (6) Ida, S., and Nakazawa, K., 1989, Astron. Astrophys. **224**, 303; (7) Greenzweig, Y., and Lissauer, J.J., 1989, Accretion cross-sections of protoplanets, Preprint, submitted to Icarus. (8) Ohtsuki, K., and Ida, S., 1989, Runaway growth with collision rate in the solar gravitational field, Preprint PPSG-34, submitted to Icarus.

MAPPING EFFECTS OF DISTANT PERTURBATIONS ON PARTICLE-PLANET ENCOUNTERS

W.F. Bottke and R. Greenberg, Lunar and Planetary Lab.
Univ. of Arizona, Tucson
G.B. Valsecchi and A. Carusi, IAS Reparto Planetologia, Rome

The Öpik method (1) for estimating the effects of gravitational encounters of a particle (*e.g.* planetesimal) with a planet or a planetary embryo breaks down for small encounter velocities because the distant-approach trajectories are slightly modified by perturbations of the heliocentric orbits (2), not because of a breakdown (suggested in 3) of the two-body approximation at encounter. According to (2), the distant perturbations change the geometries of arrival at the planet, usually keeping the same arrival relative velocity as the unperturbed trajectory, but shifting the approach path parallel to the unperturbed one. Thus a beam of particles on initially parallel paths targeted to be centered on a head-on collision was generally shifted by distant approach perturbations so particles near the edge of the beam actually encountered the planet head-on (2). It was speculated (2) that this shift might conserve the outcome statistics by replacing particles shifted away from the planet by others shifted closer.

To test that hypothesis, for a variety of cases we have numerically followed the evolving distant perturbations of a beam of particles en route to a planet. At any point in their approach, their orbits can be represented by the arrival paths they would have if allowed to proceed unperturbedly to the planet. Thus a beam of particle that actually followed the Öpik approximation would be represented by a set of unchanging parallel arrival vectors. A shifted beam as described in (2) would appear to shift gradually sideways, while retaining its formation.

We plot the characteristics of such an approaching beam as a set of darts hitting a target plane (or "b-plane") centered on the planet. The length and direction of a dart show its relative velocity and the tip is at the arrival position. The plots show a view direction normal to the target plane. Information on the length of a dart is given by the size of a dot on its tail. The plots shown here show the initial trajectory set needed in order to arrive as a centered parallel beam at a planet.

We can only show a couple of sample results without quantitative consideration, due to short space. Fig. 1 shows a case where the beam is simply shifted sideways by distant approach perturbations. Fig. 2 shows a much more complex evolution because the particles are on orbits with extremely low eccentricities. Units of distance are in terms of the planet's orbital radius. Analysis of our extensive set of such evolution diagrams is providing insight into the statistical mechanics of encounters, which will be useful in modeling planetary accretion.

Figure 1

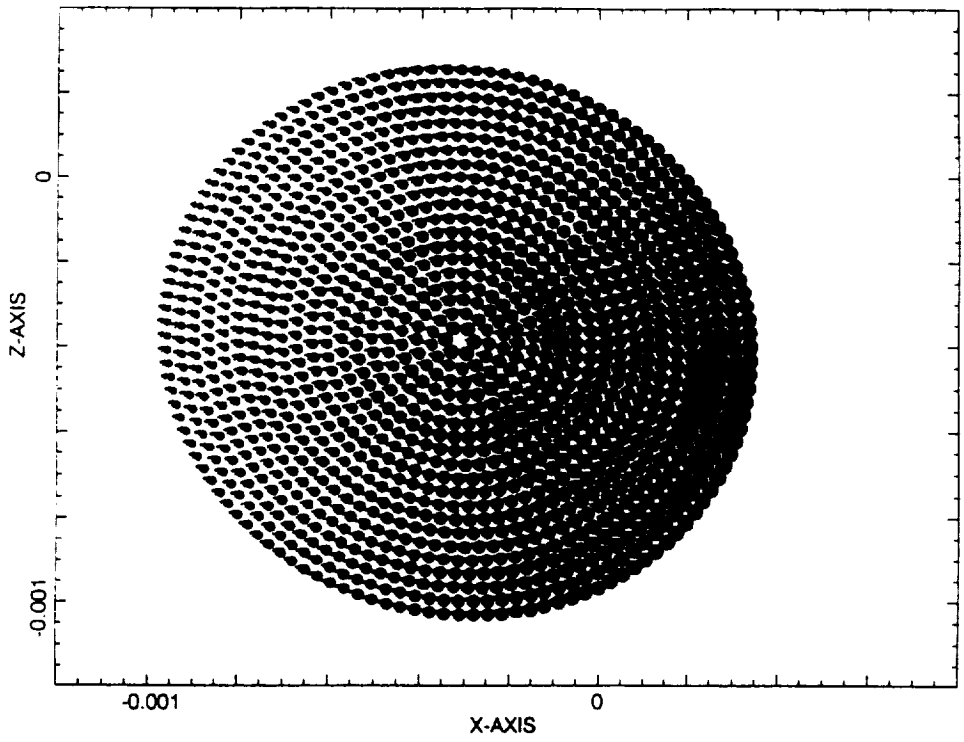

Figure 2

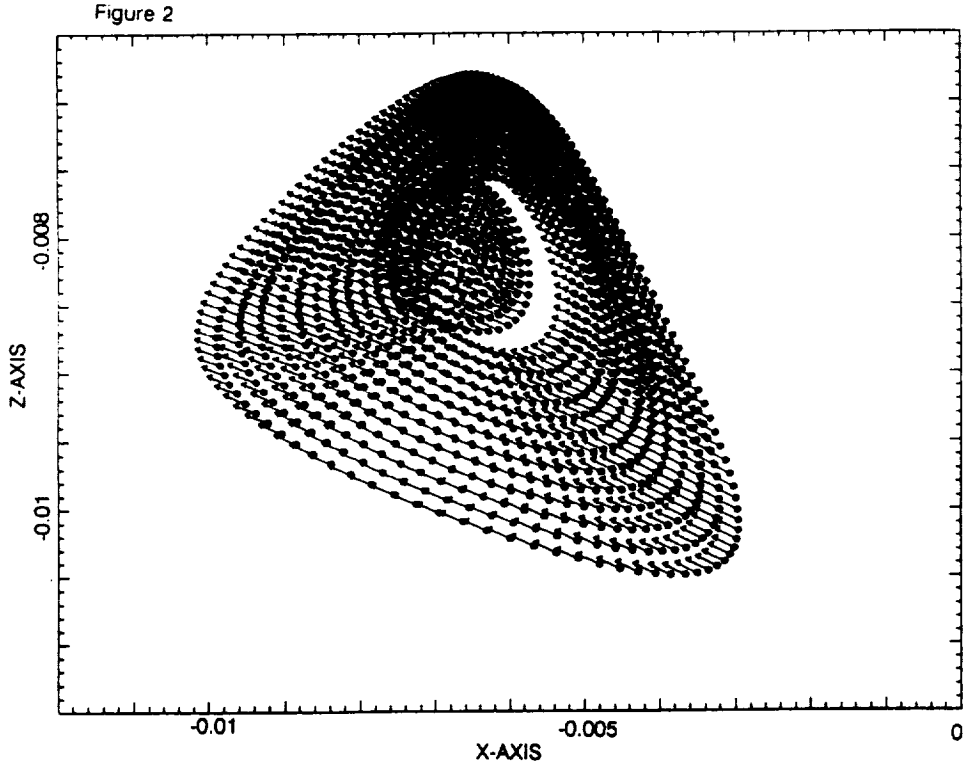

References: (1) Öpik, E.J., 1976, Interplanetary Encounters, Elsevier; (2) Greenberg, R., *et al.*, 1988, Icarus **75**, 1; (3) Wetherill, G.W., and Cox, L.P., 1984, Icarus **60**, 40, and 1985, Icarus **63**, 290.

Runaway Planetesimal Growth: Agreement Between Analytical Solution of the Coagulation Equation and the Results of Numerical Physical Modelling.

G. W. Wetherill, Department of Terrestrial Magnetism, Carnegie Institution of Washington, Washington, D.C. 20015

The growth of a swarm of planetesimals initially of mass m_o by accumulation of one another is often described in terms of a coagulation equation (1,2,3):

$$\frac{d}{dt}n_k = \frac{1}{2}\sum_{i+j=k} A_{ij}n_i n_j - n_k \sum_{i=1}^{\infty} A_{ik}n_i \qquad eqn.\ (1)$$

where the n_k are the number of bodies of mass $m_o k$ at time t, and the "kernel" A_{ij} is the probability of collision of bodies of mass im_o and jm_o per unit time. In general, the A_{ij} are nonlinear functions of the masses, velocities, and physical properties of the planetesimals and no general analytical solution can be found. Analytical solutions have been published only for the cases $A_{ij} \propto (m_i + m_j)$ and A_{ij} = constant. Both of these solutions correspond to orderly, non-runaway growth. Ohtsuki and Nakagawa (4) have demonstrated the usefulness of these solutions as test cases of algorithms also used for simulation of growth using more physically realistic forms of A_{ij}.

The work of Stewart and myself (5,6) shows that as a result of equipartition of energy, orderly growth is not likely to occur. Instead, after an initial orderly stage of growth, one planetesimal begins to grow much faster than its neighbors, leading to only a moderate number (e.g. 10 to 50) of 10^{26} - 10^{27} gram "embryos" in the terrestrial planet region and to a much more rapid time scale of embryo formation. It is therefore of interest to compare our use of a physical model of coagulation with an analytical solution for a case of runaway growth.

Trubnikov (3) shows that an analytical solution of eqn. (1) for the case $A_{ij} = \gamma m_i m_j$ should be of the form:

$$n_k = \frac{n_o k^{k-2}}{k!}\eta^{k-1}e^{-k\eta} \qquad eqn.\ (2)$$

where η is the dimensionless time, $\eta = \gamma n_o t$, γ is a constant, and n_o is the initial number of bodies of mass m_o. When the total number of bodies and mass in the swarm at time t is calculated by summation of eqn. (2) over all values of k, this result is clearly contradictory, because among other things, mass is conserved only up to $\eta = 1$, after which it declines to zero for large values of the time.

It might be thought that this contradiction implies that no analytical solution exists. Use of the physical model (6) for the numerical calculation of this same case suggests, however, that this result does not simply represent a mathematical *reductio ad absurdum*. Instead it is found that eqn. (2) accurately describes the entire mass distribution, except for the largest body, which begins to run away at the critical value $\eta = 1$.

As a result, equations (1) and (2), together with conservation of mass, and proper interpretation, lead to agreement between analytical and numerical calculation of runaway growth, even though the concept of runaway growth is foreign to the formulation of equations (1) and (2). This paradox can be resolved by extension of equation (1) to include a runaway. When this is done, analytic solutions can be found for both the runaway body and for the residual swarm. Both of these solutions are in excellent agreement with the numerical results using the algorithm of the physical model. The same algorithm also provides excellent agreement when applied to the two cases of orderly growth considered by Ohtsuki and Nakagawa.

References

(1) Safronov, V.S. (1962) A particular solution of the coagulation equation. *Doklady Akad. Nauk SSSR* **147**, 64–66.
(2) Safronov, V.S. (1969) *Evolution of the protoplanetary cloud and formation of the Earth and planets.* Transl. 1972 NASA TT F-677, Nauka, Moscow.
(3) Trubnikov, B.A. (1971) Solution of the coagulation equations in the case of a bilinear coefficient of adhesion of particles. *Doklady Akad. Nauk SSSR* **196**, 1316–1319.
(4) Ohtsuki, K. and Nakagawa, Y. (1988) Accumulation process of planetesimals to the planets. *Prog. Theor. Phys. Suppl.* **96**, 239–255.
(5) Stewart, G.R., Wetherill, G.W. (1988) Evolution of planetesimal velocities. *Icarus* **74**, 542–553.
(6) Wetherill, G.W., Stewart, G.R. (1989) Accumulation of a swarm of small planetesimals. *Icarus* **77**, 330–357.

Long-Term Evolution of a Planetesimal Swarm in the Vicinity of a Protoplanet

David M. Kary and Jack J. Lissauer (SUNY at Stony Brook)

Many models of planet formation involve scenarios in which one or a few large protoplanets interact with a swarm of much smaller planetesimals. In such scenarios, three-body perturbations by the protoplanet as well as mutual collisions and gravitational interactions between the swarm bodies are important in determining the velocity distribution of the swarm. We are developing a model to examine the effects of these processes on the evolution of a planetesimal swarm. The model consists of a combination of numerical integrations of the gravitational influence of one (or a few) massive protoplanets on swarm bodies together with a statistical treatment of the interactions between the planetesimals. Integrating the planetesimal orbits allows us to take into account effects that are difficult to model analytically or statistically, such as three-body collision cross-sections and resonant perturbations by the protoplanet, while using a statistical treatment for the particle-particle interactions allows us to use a large enough sample to obtain meaningful results.

Our model follows the interactions between planetesimals and protoplanets in a deterministic manner. Planetesimal orbits are numerically integrated using a predictor-corrector integrator on the three (or in some cases more) body problem. At intervals throughout the calculation, the orbital elements of the individual bodies will be used to develop a swarm density profile binned in both radius and height above the midplane. The associated velocity and size distributions will be recorded for each bin. Such a distribution can, in turn, be used to statistically compute the size and velocity evolution of individual planetesimals as they are affected by inelastic collisions and gravitational scattering with other swarm bodies. This will be accomplished using analytic and semi-analytic formulae analogous to those developed by Stewart and Wetherill (1988, Icarus **74**, 542), but generalized to include the situation where eccentricities can be much larger than inclinations. In such a manner, we will be able to follow the growth of the protoplanet(s) and the evolution of the planetesimal swarm.

This work is supported in part by NASA Planetary Geology and Geophysics grant NAGW-1107.

Accretion Rates of Planets II: Gaussian Distributions of Planetesimal Velocities

Yuval Greenzweig (UC Santa Barbara) and Jack J. Lissauer (SUNY at Stony Brook)

We calculate the accretion rate of a protoplanet embedded in a uniform surface density disk of planetesimals having a Gaussian velocity distribution. The longitudes of the apses and nodes of the planetesimals are uniformly distributed, and the protoplaent is on a circular orbit. We find that the accretion rate of the protoplanet in the two-body approximation is enhanced by a factor of > 2.6 (>2), compared with that of a disk in which all planetesimals have eccentricity and inclination equal to the r.m.s. (mean) values of those variables in the Gaussian distribution disk. For flattened disks ($i \ll e$), this enhancement factor is considerably larger. Numerical simulations are in progress to determine the corresponding enhancement when three-body effects are present. However, in the high random velocity regime we expect the two-body approximation to be good. Thus, the enhanced accretion rate should be incorporated into planetary accretion models.

Support for this project was provided by the NASA Planetary Geology and Geophysics Program under grants NGR-010-05-062 (UCSB) and NAGW-1107 (SUNYSB).

Accretion Rates of Protoplanets

Yuval Greenzweig (UC Santa Barbara) and Jack J. Lissauer (SUNY at Stony Brook)

We calculate the rate at which planetesimals in a uniform surface density disk collide with, and are assumed to be accreted by, a massive protoplanet. The collision cross-section of a protoplanet is enhanced relative to its geometric cross-section due to its gravitational focusing of planetesimal trajectories. The gravitational enhancement factor of a protoplanet's cross-section, F_g, increases as planetesimal random velocities (eccentricities and inclinations) decrease. For large random velocity planetesimals, encounters are sufficiently rapid ($\lesssim 5\%$ of an orbital period) that F_g is well approximated by the two-body "particle in a box" formula, which neglects the gravitational effect of the Sun. As planetesimal velocities decrease, F_g increases to approximately twice the two-body value, and then rises less rapidly than the two-body value, eventually dropping below it and asymptotically approaching a constant for sufficiently small random velocities. We present a scaling argument that generalizes our results to protoplanets of arbitrary mass, radius, and orbital semimajor axis. Gravitational scatterings by a protoplanet prevent random velocities of the planetesimals within its accretion zone from becoming too small. When gravitational stirring is included, the maximum plausible value of the gravitational enhancement factor for rock protoplanets 1 AU from the Sun is $F_g \sim 1000$. If one protoplanet dominates gravitational scatterings in a given region of a protoplanetary disk, we find that planetesimal inclinations are excited much less rapidly than eccentricities, in contrast to the two-body approximation, in which energy is roughly equipartitioned between eccentric and inclined random motions. The resulting skewed velocity dispersion allows for a more rapid rate of protoplanet growth.

AERODYNAMIC AND GASDYNAMIC EFFECTS IN COSMOGONY

S. J. Weidenschilling and D. R. Davis
Planetary Science Institute, 2421 E. 6th St., Tucson, Arizona 85719 U.S.A.

Introduction: The solar system is the product of a primordial nebula that was composed mostly of gas, with only a small admixture of solid matter. The early evolution of solid bodies of various sizes in the disk was dominated by a variety of interactions with the gas., e.g., turbulent transport, differential settling, and orbital decay due to drag. These processes controlled relative velocities, and hence collision rates and outcomes, over a range of particle sizes roughly from μm to km--some 9 orders of magnitude. Small grains, transported and mixed by turbulence, may have also influenced the gas. Since grains provided most of the opacity, their abundance and properties may have determined whether convection occurred in the disk. Earlier suggestions that turbulent viscosity might have caused major redistribution of mass and angular momentum in the solar nebula now seem unlikely, as recent analyses (Cabot et al. 1987) derive much lower convective velocities. However, even these can inhibit settling to the central plane and prevent formation of planetesimals by the "classical" mechanism of gravitational instability. A general feature of solar nebula models is a radial pressure gradient that causes non-Keplerian rotation of the gaseous component. Even in the absence of global turbulence, formation of a relatively dense dust-rich layer would cause shear between it and the surrounding gas, producing localized turbulence sufficient to prevent gravitational instability. Thus, planetesimals probably formed by collisional coagulation, with a range of initial sizes.

Large bodies were also affected by drag, which caused their orbits to decay. There may have been significant radial transport of mass by this mechanism. However the apparent compositional zoning of the asteroid belt and the existence of distinctive types of undifferentiated meteorites places constraints on this process. It is now widely accepted that the giant planets formed by core-accretion. In this scenario, massive ($\sim 10 M_\oplus$) solid cores formed by accretion of planetesimals before capturing gas from the surrounding nebula. A major unanswered question is the timescale for core growth: how could it have occurred before the nebula was dissipated? In order to model this process, we must understand the combined influences of gas drag and gravitational perturbations on planetesimals in the solar nebula.

Evolution of Dust in the Solar Nebula. Most previous studies of coagulation and settling of dust in the nebula have assumed that the gas was laminar (Weidenschilling 1980; Nakagawa et al. 1981; Weidenschilling et al. 1989), despite the probability that some turbulence was present. Weidenschilling (1984) modeled some cases with high turbulent velocities, one third of the sound speed, which effectively precluded settling to the central plane. Mizuno (1989) considered a range of turbulent velocities, but his models were vertically averaged through the disk and did not consider settling. The low convective velocities predicted by Cabot et al. (1987) and the lack of definitive models for generation of

non-convective turbulence have led us to develop a series of "generic" models with arbitrary degrees of turbulence. These are 1-D models of the vertical structure of the gas-dust disk at a given radius. Coagulation of particles is computed in a series of Z-levels. Systematic settling yields drift toward the central plane, while turbulence can transport particle aggregates and mix them downward (always) and upward (if their turbulent diffusion velocities exceed their vertical settling rates). These models feature improved spatial resolution (more levels) and better resolution of the size distribution (more bins) than our previous simulations.

We have run a series of cases for r=1AU, with particle aggregates assumed to have fractal structures of dimension 2.11 at sizes less than 1 mm (Weidenschilling et al. 1989). Growth times are shorter than reported in that work, apparently due to the improved resolution of the model. Cases have been run for turbulent velocities of 0, 10, 100, and 1000 cm/s. The presence of turbulence has little effect on particle relative velocities, because small grains and aggregates are so closely coupled to the gas. However, turbulence strongly affects the vertical distribution of particles, affecting their spatial density and coagulation rate. The particle size distribution varies significantly with distance from the central plane and with turbulent velocity (Figure 1).

In general, higher turbulent velocities lead to longer timescales for concentration of particles to the central plane of the disk; this is because the aggregates must grow to larger sizes before the settling rate becomes comparable to the turbulent diffusion rate. During this time, particles experience inward radial drift due to the non-keplerian rotation of the gas. Plausible fractional deviations from keplerian motion are a few parts per thousand. For the laminar case, no material originally at 1 AU is lost into the Sun before the dust/gas mass ratio exceeds unity in the central plane. For the delayed settling due to turbulence, some fraction of the solids is lost by orbital decay, reaching a few percent for turbulent velocities of 1000 cm/s. However, the diffusion length scale becomes comparable to the heliocentric distance for such cases, suggesting that substantial radial mixings, both inward and outward, would occur. The next stage of investigation will presumably require 2-D modeling of radial and vertical structure of the nebular disk.

REFERENCES

Cabot, W., Canuto, V., Hubickyj, O. and Pollack, J. 1987. Icarus 69, 387.

Mizuno, H. 1989. Icarus 80, 189.

Nakagawa, Y., Nakazawa, K. and Hayashi, C. 1981. Icarus 45, 517.

Weidenschilling, S. 1980. Icarus 44, 172.

_____ 1984. Icarus 60, 553.

Weidenschilling, S., Donn, B. and Meakin, P. 1989. In Formation and Evolution of Planetary Systems, H. Weaver and L. Danly, Eds., Cambridge Univ. Press, pp. 131-150.

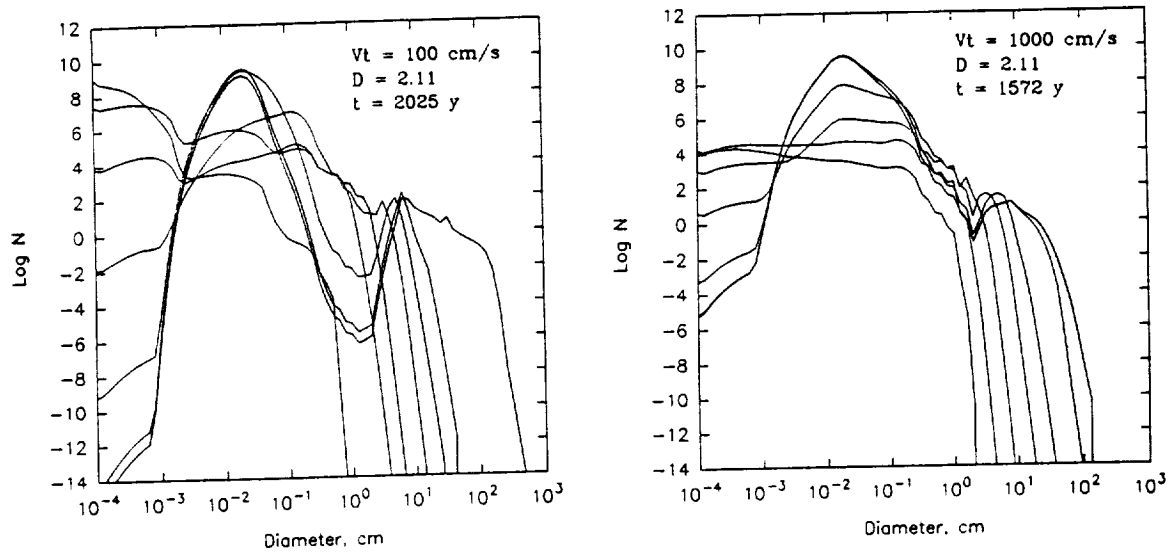

Figure 1. Particle size distributions at various levels in the disk, ranging from Z=0 to Z=2.3 scale heights, for turbulent velocities of 100 and 1000 cm/s. In the central plane, large particles are more abundant, while μm-sized grains are depleted by accretion onto the larger bodies. At large values of Z, small particles are more abundant, while large ones are depleted by settling to lower levels.

Nonaxisymmetric Structure During Solar Nebula Formation

Alan P. Boss, DTM, Carnegie Institution of Washington

Numerical solutions of the equations of hydrodynamics, gravitation, and radiative transfer in three spatial dimensions are used to model the formation and time evolution of the early solar nebula. The models involve solutions for the collapse of spherical clouds with assumed initial density and rotation profiles, onto protosuns of variable mass. Most of the models assume uniform initial density and rotation, and have variations in three other initial parameters (cloud mass, cloud rotation rate, and protosun mass) chosen to simulate a range of possible phases of early solar nebula evolution. Because of the explicit time differencing used in the numerical solution, the models start from initial densities ($\sim 10^{-13} - 10^{-12}$ g cm^{-3}) considerably higher than dense molecular cloud cores.

The primary goal is to learn whether or not gravitational torques between nonaxisymmetric structures in the solar nebula can transport angular momentum rapidly enough to produce nebula clearing on astronomically indicated ($10^5 - 10^7$ years) time scales. While these 3D models are incapable of following nebula evolution over such long time scales, if the initial angular momentum transport rates are maintained, even mildly nonaxisymmetric disks have extrapolated time scales for angular momentum transport consistent with the astronomical time scales; more strongly nonaxisymmetric disks may have time scales as short as 10^3 to 10^5 years.

The models show little tendency for directly forming small numbers of giant gaseous protoplanets through gaseous gravitational instability. Furthermore, the low mass nebula models do not have sufficient surface density at 5 AU to account for the rapid, runaway formation of Jupiter. High mass nebula models do exceed this critical surface density, but a protoJupiter may be lost during subsequent evolution of a massive nebula. Varying the initial density and rotation profiles does not produce enough mass at 5 AU to account for rapid Jupiter formation; it appears that substantial nebula evolution is required to enhance surface densities in the outer solar nebula. Finally, the large amount of compressional energy produced by collapse into the gravitational well of a solar mass protosun appears to be capable of heating the inner nebula to temperatures on the order of 1500 K, in either nearly axisymmetric or strongly nonaxisymmetric nebula models; because of the neglect of heating from the protosun, these temperatures appear to be lower bounds.

Tidal Disruption of Inviscid Protoplanets

A. P. Boss, DTM, Carnegie Institution of Washington

A. G. W. Cameron & W. Benz, Harvard-Smithsonian Center for Astrophysics

The terminal phase of terrestrial planet accumulation is believed to involve impacts at $\sim$ 14 km s^{-1} between growing planets and protoplanets. Such giant impacts are energetically capable of melting planetary bodies, and collisional debris from these impacts may then lead to a population of largely molten protoplanets. Because the area within the Roche limit is about 9 times larger than the cross section for collision, if tidal disruption can occur during passage within the Roche limit, tidal disruption could have a profound effect on the protoplanetary mass spectrum. Previous work by Mizuno and Boss has indicated that dissipative (solid) planetestimals are nearly immune to tidal disruption, but the situation for inviscid (molten) protoplanets has not been studied, except for some preliminary work by K. Nakazawa in 1982.

We have calculated a number of simulations of inviscid tidal disruption using the smoothed particle hydrodynamics (SPH) code developed by Benz and used previously to model impacts between protoplanets. The simulations are fully three dimensional, and model the tidal effects between an intruding protoplanet and an Earth-mass planet; both bodies have iron cores and rocky mantles, with molten temperatures (4000 K) and zero physical viscosity. Three parameters are of most importance: intruder mass, impact parameter, and velocity at infinity (v_∞).

In agreement with an analytical calculation showing that massive bodies are more resistant to tidal disruption than smaller bodies, we have found that relatively massive, inviscid protoplanets do not undergo complete tidal disruption. Previous giant impact models have shown that a 0.16 $M_\oplus$ intruder with $v_\infty = 5$ km s^{-1} and with impact parameter small enough for a grazing collision with the Earth easily survives the encounter. Even with an intruder mass as low as 0.01 $M_\oplus$, little disruption occurs at near-grazing incidence with $v_\infty = 5$ km s^{-1}; only for $v_\infty = 2$ km s^{-1} or less is a 0.01 $M_\oplus$ intruder disrupted into a number of bodies following a grazing encounter. Bodies smaller than this are likely to be subject to collisional disruption anyway. The results imply that tidal disruption is unlikely to have a major effect on planetary accumulation, regardless of whether protoplanets are inviscid or dissipative.

Surface Density and Temperature Profiles in the Early Solar Nebula

Alan P. Boss, DTM, Carnegie Institution of Washington

Models of the formation of the solar nebula through the collapse of very dense, rotating, spherical clouds onto protosuns of variable mass have been calculated through numerical solution of the three dimensional (3D) equations of hydrodynamics, gravitation, and radiative transfer in the diffusion approximation. Previous work has shown the probable importance of nonaxisymmetry (i.e., spiral arms) for angular momentum transport in the nebula [1], and the possibility of relatively high ($\sim$ 1500 K) midplane temperatures [2] in the inner solar nebula.

Calculation of these models with an explicit time differences computer code is made possible only by the *ansatz* of starting the collapse from initial densities ($\rho_i \sim 10^{-13}$ g cm^{-3}) that are considerably higher than those of observed dense molecular clouds. Recently, several axisymmetric (2D) solar nebula models have been computed starting from similarly high initial densities [3,4]. While it can be argued that starting from these densities need not have a major effect on the dynamics and thermodynamics [2], it must be noted that this assumption will *overestimate* nebula temperatures. However, the neglect of heating from the central protosun in the 3D models so far *underestimates* nebula temperatures (cf. [3], where inclusion of this heating produced $T > 1600$ K inside 5 AU). Evidently, further work will be necessary before the thermal structure of these models can be considered definitive.

The original 16 models [1] all started from uniform density ($\rho_i = c$) and uniform rotation ($\Omega_i = c$) initial spheres. In order to learn what effect other initial density and rotation profiles would have on the structure of the nebula, 8 new 3D models have been calculated. Six of these models started with either $\rho_i = c$ and $\Omega_i \propto R$ (R = cylindrical radius) or with $\rho_i \propto r^{-1}$ (r = spherical radius) and $\Omega_i = c$. Two new models were started from $\rho_i = c$ and $\Omega_i = c$, but with large amounts of rotation.

Surface densities in the inner solar nebula are typically high enough to account for terrestrial planet formation [5]. However, in the outer solar nebula, densities are insufficient for rapid formation of Jupiter through runaway accretion [6], unless the nebula is quite massive ($\approx 1 M_\odot$), in which case a Jupiter which has cleared a gap will likely be lost during subsequent evolution of the bulk of the nebula gas onto the sun. Surface densities in these 3D models are in basic agreement with those produced from the isothermal collapse of axisymmetric clouds [7].

The models imply that if outer solar nebula surface densities are ever to reach the required values in a minimum mass nebula, these densities must be increased through subsequent nebula evolution, e.g., through the action of viscous [6] or gravitational torques [1].

A simple time scale argument [2] suggests that compressional energy produced by the collapse of the presolar cloud was trapped within the nebula for $\sim 10^5$ years. If so, this means that certain minimum mass solar nebula models can have midplane temperatures in the inner few AU of $\sim$ 1500 K or more. This result also holds for models starting from alternative initial density profiles Temperatures this high are interesting in light of meteoritical evidence for the condensation of refractory inclusions [9] in a nebula cooling from high temperatures, though such a globally hot nebula would only cool over rather long ($\sim 10^5$ years) time scales. A hot inner solar nebula also may be able to account for the gross depletion (relative to solar) of volatile species in the terrestrial planets [10], because the gaseous C, N, and H_2O may have been removed along with the H and He by the early solar wind.

Midplane temperatures may have been regulated to $\sim$ 1500 K by the thermostatic effect of the opacity. Because the nebula opacity at high temperatures is dominated by iron grains, which vaporize around 1420 K [11], at higher temperatures the opacity drops by a factor of $\sim$ 100, and hence radiative cooling is more efficient. However, should temperatures drop below 1420K, iron grains reform, the opacity rises, radiative losses decrease, and further decrease of the temperature is slowed. This thermostatic effect may ensure the survival of the most refractory interstellar grains, and prevent condensation from establishing a strong compositional gradient by minimizing the radial thermal gradient in the inner solar nebula.

Finally, one may also speculate that Type II Ca-Al-rich inclusions, which are depleted in both the most volatile and the most refractory rare earth elements (REE) [12], owe their peculiar composition to the thermostatic effect. That is, if midplane temperatures in the asteroid zone never exceeded $\sim$ 1500K, the most refractory components of the pre-existing interstellar grains will survive and rapidly sediment to the dust midplane, producing a population of volatile-poor grains (Type III inclusions [13]). After the nebula cools somewhat, newly-condensed grains will be depleted in the most refractory REE as well as the most volatile REE, as in Type II inclusions. If the nebula is removed prior to further cooling (and naked T Tauri star ages are similar to nebula cooling times), then the most volatile species would be removed altogether.

References:

[1] Boss, A. P. (1988), in *Lunar Planet. Sci. XIX*, pp. 122-123. [2] Boss, A. P. (1988), *Science*, **241**, 565. [3] Tscharnuter, W. M. (1987), *Astron. Astrophys.*, **188**, 55. [4] Bodenheimer, P., Różyczka, M., Yorke, H. W., and Tohline, J. E. (1988), in *Formation and Evolution of Low Mass Stars*, eds. A. K. Dupree and M. T. V. T. Lago (Dordrecht: Reidel), pp. 139-151. [5] Goldreich, P. and Ward, W. R. (1973), *Astrophys. J.*, **183**, 1051. [6] Lissauer, J. J. (1987), *Icarus*, **69**, 249. [7] Stemwedel, S. W., Yuan, C., and Cassen, P. (1987), *B. A. A. S.*, **19**, 1092. [8] Weidenschilling, S. J. (1977), *Astrophys. Space Sci.*, **51**, 153. [9] Grossman, L. (1980), *Ann. Rev. Earth Planet. Sci.*, **8**, 559. [10] Prinn, R. G. and Fegley, B., Jr.(1988), in *Origin and Evolution of Planetary and Satellite Atmospheres*, eds. S. K. Atreya, J. B. Pollack, and M. S. Matthews (Tucson: University of Arizona), in press. [11] Pollack, J. B., McKay, C. P., and Christofferson, B. M. (1985), *Icarus*, **64**, 471. [12] Wood, J. A. (1988), *Ann. Rev. Earth Planet. Sci.*, **16**, 53. [13] Boynton, W. V. (1978), in *Protostars and Planets*, ed. T. Gehrels (Tucson: Univ. Arizona), pp. 427-438.

ACCRETION AND EVOLUTION OF SOLAR SYSTEM BODIES

S. J. Weidenschilling, D. Spaute, and D. R. Davis
Planetary Science Institute, 2421 E. 6th St., Tucson, Arizona 85719 U.S.A.

The terrestrial planets formed by accretion from a swarm of many ($>10^{12}$) small (~km-sized) planetesimals. A number of researchers have modeled the earliest stage of growth by collisions and gravitational accretion by statistical approaches, using particle-in-a-box methods (Greenberg et al. 1978, Nakagawa et al. 1983, Wetherill and Stewart 1989). The rate of collisions and gravitational interactions is characterized only by relative velocities (the spatial density of particles is implicitly dependent on velocity). This assumption is valid only over a region of the swarm small enough so that variations in swarm properties, e.g., distributions of size and velocity, can be neglected. These conditions are not met during later stages of accumulation; indeed, the breakdown of spatial uniformity, i.e., the formation of a small number of large bodies (planets or protoplanetary embryos), is the phenomenon of interest.

The final stage of accretion, involving a small number of bodies, has been modeled by explicit computation of keplerian orbits, generally with Monte Carlo treatment of close encounters and collisions (Wetherill 1980, 1986, 1988; Cox and Lewis 1980; Lecar and Aarseth 1986). However, computer capacity limits such simulations to a few hundred bodies. Initial conditions (sizes and orbital distributions) must be assumed, and are not linked directly to the earliest stage of accretion.

We are attempting to bridge (or at least narrow) the gap between early- and late-stage accretion by a new method, using a spatially resolved calculation. The swarm is divided into a series of radial zones in semimajor axis. The evolution of size and velocity distributions in each zone is calculated, considering collisions and gravitational stirring among bodies within a zone, and also interactions with other zones for which orbits overlap (mass can be transferred between zones by collisions or other phenomena such as orbital decay due to gas drag). Unlike the particle-in-a-box method, where interaction probabilities and outcomes are determined solely by a velocity, we compute distributions of orbital elements $\underline{a}$, $\underline{e}$, and $\underline{i}$. We use a Monte Carlo method to find the spatial distribution of collisions and their effects on orbital elements. In the later stages of accretion, we are able to assign orbital elements to individual planetesimals at the large end of the size distribution, and follow their evolution as discrete bodies as they interact with the continuum swarm and each other.

In the past year we have devoted much effort to testing of the numerical methods used in the program. Ohtsuki et al. (1990) described results of a test of a particle-in-a-box type code on a problem for which an analytic solution is known, i.e., coagulation rate proportional to the sum of particle masses. Their algorithm, which used a mass binning method to characterize the size distributions, produced too rapid growth compared with the analytic solution. They found that wider mass bins led to more rapid growth, and suggested that bin widths greater than $\sqrt{2}$ in mass produced spurious "runaway" growth of large bodies. In response, we conducted a series of tests of our own algorithm against the analytic

solution. We found initially that our computed growth rates were too slow, with wider bins yielding slower growth. This behavior, opposite to that found by Ohtsuki et al., appears to be due mainly to different definitions of the mean mass in a bin. They used the arithmetic mean of the upper and lower bounds, while we take the geometric mean. One can show that their effective mass (and hence the coagulation rate) is always greater than our definition.

Another important factor is the treatment mass shifting between bins. This effect is due to the variation of masses across a bin for a continuous size distribution. Accretion of a small body by a larger one always removes the smaller one from its mass bin. The combined particle may fall in the mass bin corresponding to the original target, or in a larger bin if the target was near the top of its range. Greenberg et al. (1978) introduced the concept, but computed mass shift on the assumption of a uniform distribution of particles vs. log (mass) within a bin. We showed (Spaute et al. 1990) that this resulted in an unrealistically large shift. The algorithm used in our spatially resolved program approximates the distribution within each bin as a segment of a power law. We use this assumption, with appropriate weighting of collision probability, to evaluate the fraction of collisions that result in shifting of mass across bin boundaries. We find excellent agreement with the analytic solution for a bin width of 2 (Figure 1); the agreement is actually better than Ohtsuki's result for $\sqrt{2}$. This is a significant improvement, as the running time for simulations increases rapidly with the number of bins.

As a further test, we have compared our program in a single-zone mode with a suite of particle-in-a-box calculations by Wetherill and Stewart (1989). Again the agreement is excellent (Figure 2). The only significant difference is in the latest stage of the simulation. Wetherill and Stewart's calculation showed the largest bodies with masses $\gtrsim 10^{24}$g accreted to form a single $\sim 10^{26}$g body after 2.6×10^5y; our simulation does not show this behavior. Our model allows for the fact that the few largest bodies have different semi-major axes, which lowers their probability of collision and slows runaway growth. Extending these runs to later times than Wetherill and Stewart's calculations shows spreading of the swarm into adjacent zones that were originally empty. This is a physically realistic outcome due to dissipation of energy during collisions (Wetherill 1980). Initial tests of multi-zone simulations are now underway.

REFERENCES:

Cox, L. P. and Lewis, J. S. 1980, Icarus 44, 706; Greenberg, R., Wacker, J., Hartmann, W. and Chapman C. R. 1978, Icarus 35, 1; Lecar, M. and Aarseth, S. 1986, Ap.J. 305, 564; Nakagawa, Y., Hayashi, C. and Nakazawa, K. 1983, Icarus 54, 361; Ohtsuki, K., Nakagawa, Y. and Nakazawa, K. 1990, Icarus 83, 205; Spaute, D., Weidenschilling and Davis, D. R. 1990, in preparation; Wetherill, G. W. 1980, Ann. Rev. Astr. Ap. 18, 77; Wetherill, G. W. 1986, in Origin of the Moon, W. Hartmann, R. Phillips, and G. Taylor, Eds., LPI, Houston, p. 519; Wetherill, G. W. 1988, in Mercury, C. Chapman and F. Villas, Eds., Univ. of Arizona Press, p. 670; Wetherill, G. W. and Stewart, G. 1989, Icarus 77, 330.

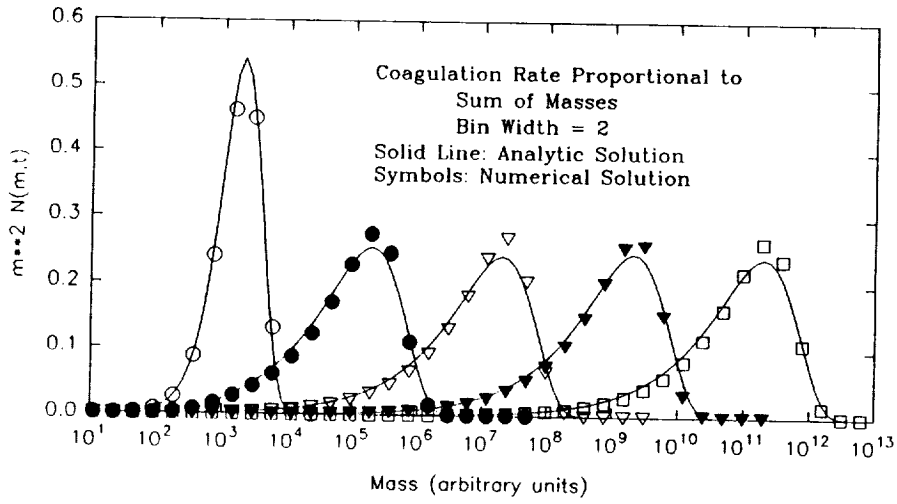

Figure 1: Comparison of analytic and numerical solutions for the case of coagulation rate proportional to the sum of the masses.

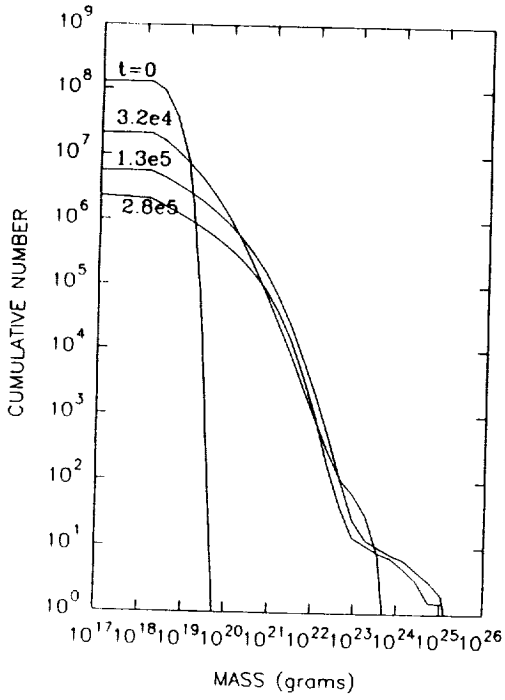

Figure 2a): Cumulative number of bodies vs. mass. Parameters were chosen to match those in Fig. 5 of Wetherill and Stewart, 1989.

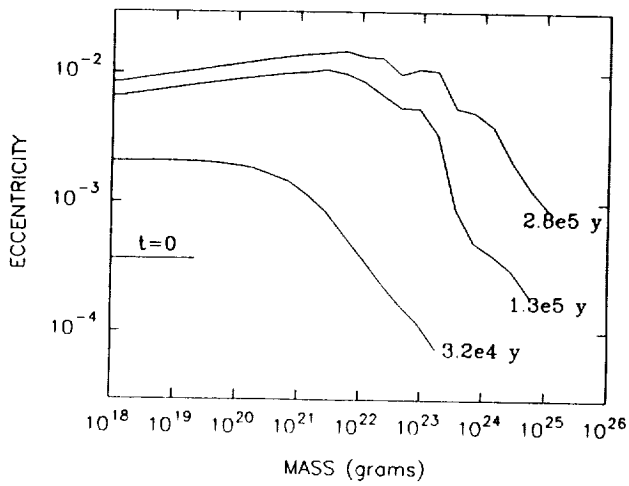

Figure 2b): Eccentricity vs. mass for the same case; compare with Fig. 6 of Wetherill and Stewart, 1989.

Tidal Evolution of Planetary Satellites

William C. Tittemore, Lunar and Planetary Laboratory,
University of Arizona, Tucson, AZ 85721

Ariel may have undergone significant tidal heating during evolution through a 4:1 orbital commensurability with Titania (Tittemore 1988). Based on the rather narrow constraints on the Q of Uranus set by the dynamics of other past resonances among the Uranian satellites ($1.1 \times 10^4 < Q < 3.9 \times 10^4$, Tittemore and Wisdom 1990), this resonance would have been encountered 3.8 billion years or more ago.

There is a significant probability of temporary capture into resonance at this commensurability, leading to a large increase in the orbital eccentricity of Ariel. Initially, the behavior of the satellites can be determined analytically, but at large values of the orbital eccentricity, strong interactions between the primary resonances at the 4:1 commensurability result in the presence of a large chaotic zone. The satellites ultimately escape from the resonance at large eccentricity via a dynamical mechanism first identified in the dynamics of the Uranian satellites, that also explains the anomalously high orbital inclination of Miranda (Tittemore and Wisdom 1989). The trajectory is captured into a secondary resonance between the resonance libration frequency and the frequency splitting the primary resonances. The secondary resonance drags the trajectory into the chaotic zone, allowing Ariel and Titania to escape from the 4:1 commensurability.

During resonance passage, and after escape from the resonance as the orbital eccentricity decayed, the interior of Ariel may have been tidally heated by up to about 20 K. At the time the resonance was encountered, early in the history of the Uranian system, the internal temperature of Ariel would probably have been relatively high due to radiogenic and accretional heating. The increase in the internal temperature of Ariel due to resonance passage may have triggered the geological activity that led to its late resurfacing, by increasing the vigor of solid-state convection in the interior, and by decreasing the thickness of the lithosphere thermally stressing it, facilitating the movement of relatively bouyant, mobile materials such as ammonia hydrates to the surface.

This can explain the discrepancy between the geological histories of Ariel and Umbriel: although both may have been heated at similar rates by radiogenic and accretional sources, only Ariel would have been subjected to the additional tidal heating near the end of the heavy cratering period. Passage through the Ariel-Titania 4:1 commensurability probably did not significantly affect the thermal evolution of Titania, because of its relatively large distance from the planet. Ariel may have encountered many other resonances with the other Uranian satellites (Tittemore and Wisdom 1988, 1990; Tittemore 1990), however, the probability that any of these significantly affected its thermal evolution is small.

References:

Tittemore, W. C. and J. Wisdom 1988. Tidal evolution of the Uranian satellites. I. Passage of Ariel and Umbriel through the 5:3 mean-motion commensurability. *Icarus* **74**, 174-230.

Tittemore, W. C. and J. Wisdom 1989. Tidal evolution of the Uranian satellites. II. An explanation of the anomalously high orbital inclination of Miranda. *Icarus* **78**, 63-89.

Tittemore, W. C. and J. Wisdom 1990. Tidal evolution of the Uranian satellites. III. Evolution through the Miranda-Umbriel 3:1, Miranda-Ariel 5:3, and Ariel-Umbriel 2:1 mean-motion commensurabilities. *Icarus*, in press.

Tittemore, W. C. 1990. Tidal heating of Ariel. *Icarus*, in press.

Thermal and Dynamical Processes in the Evolution of Planets and Satellites.

Gerald Schubert, University of California, Los Angeles, Department of Earth and Space Sciences, Los Angeles, California 90024-1567

Mantle dynamics in Mars and Venus

We used a numerical model of compressible, fully three-dimensional, nonlinear thermal convection in a highly viscous spherical shell to simulate possible convective motions in the mantles of Venus and Mars. The prominent forms of upwelling in the models are cylindrical plumes. Major volcanic centers on Mars, such as Tharsis and Elysium, and the coronae and some equatorial highlands on Venus may be the surface expressions of cylindrical mantle plumes. In models with rigid upper boundaries, as might pertain to Mars, the upper thermal boundary layer surrounding the plumes has uneven thickness, being interspersed with downwelling regions emanating radially from the plumes' axes. This may establish a stress field at the base of hotspot swells that could lead to radial fractures such as those on Tharsis. The models generate about 4 km of dynamic topography, similar to estimates of the uncompensated Tharsis topography. There are no deep-seated, active, linear upwellings in the models that could be associated with linear spreading centers in Aphrodite on Venus. The models contain downwelling cylindrical plumes which might explain the compressional features in western Ishtar Terra. This research is discussed in more detail in the paper "Mantle Dynamics in Mars and Venus: Influence of an Immobile Lithosphere on Three-Dimensional Mantle convection", by G. Schubert, D. Bercovici, and G.A. Glatzmaier (*J. Geophys. Res.*, in press).

Thermal Evolution of Mars

We have developed new models of the thermal history of Mars. In the models, Mars is initially hot and completely differentiated into a core and mantle, consistent with isotope systematics of SNC meteorites suggesting core formation essentially contemporaneously with the completion of planetary accretion. The subsequent thermal evolution of the models involves cooling of the mantle and core by subsolidus mantle convection, differentiation of a crust, and thickening of a rigid lithosphere. Rates of planetary cooling and crustal production are much higher during the first 1 Gyr of cooling than they are during the remainder of the evolution. This is consistent with geological evidence for a general decrease with time in the Martian volcanic flux, and, following a brief initial period of massive crustal formation, early global contraction recorded in the widespread formation of wrinkle ridges on geologically ancient surface units. The sulfur content of the core determines whether the present core is liquid or partially solidified and whether a core dynamo produces a present planetary magnetic field. If the

core dynamo produces a present planetary magnetic field. If the weight fraction of sulfur in the core is 15% or more, then the present Martian core is completely fluid and there is no thermal convective dynamo, consistent with observational evidence of a very weak or nonexistent Martian magnetic field. This work is reported in the papers "Origin and Thermal Evolution of Mars", by G. Schubert, et. al. (in press in the Mars book to be published by University of Arizona Press) and "Thermal History of Mars and the Sulfur Content of its Core" by G. Schubert and T. Spohn (*J. Geophys. Res.*, in press).

Effects of Volatile Exchange Between Atmosphere and Mantle On Planetary Thermal Evolution

We have developed a model to simulate the thermal history of the Earth that accounts for the transfer of volatiles between the mantle and the ocean-atmosphere system and the dependence of mantle viscosity on volatile content. Degassing/regassing rates are a function of convective vigor which depends on mantle volatile content through mantle viscosity. Thus the devolatilization/revolatilization in the model is self-consistently calculated. Model results indicate that mantle degassing/regassing rates quickly equilibrate during an early stage of rapid Earth cooling (lasting a few hundred million years) and adjust to regulate a more gradual cooling of the Earth over most of geologic time. Most of the net volatile release from the mantle occurs early, in accord with isotopic evidence for rapid formation of the atmosphere. When mantle viscosity depends on both volatile content and temperature, changes in volatile content are compensated by changes in temperature so that the mantle evolves with the viscosity and convective vigor required to transfer its internally generated heat. Thus the mantle is hotter (colder) as a consequence of degassing (regassing) compared to a mantle with a volatile independent rheology. This research is discussed in "Thermal Evolution of the Earth: Effects of Volatile Exchange Between Atmosphere and Interior" by P.McGovern and G. Schubert, *Earth Planet. Sci. Lett.*, *96*, 27-37, 1989.

Lunar Orbital Evolution

We modelled the coupled thermal-dynamical evolution of the Earth- Moon system including solid planet tidal dissipation and dissipation by the Earth's oceans. Solid Earth tidal friction has been the main energy sink in the Earth-Moon system; oceanic dissipation has a relatively small effect over geologic time, even though it is important at present. About 90% of the angular momentum transferred from the Earth to the Moon is a consequence of solid-body tidal friction. These results are discussed in more detail in "Evolution of the Lunar Orbit with Temperature and Frequency-Dependent Dissipation," by M. N. Ross and G. Schubert *J. Geophys. Res.*, *94*, 9533-9544, 1989.

Atmosphere-Interior Evolution of Planets and Satellites

We have written a review paper, "Coupled evolution of the atmospheres and interiors of planets and satellites" by G. Schubert, D. L. Turcotte, S. C. Solomon, and N. Sleep., in *Origin and Evolution of Planetary and Satellite Atmospheres*, eds. S. K. Atreya, J. B. Pollack, and M.S. Matthews, University of Arizona Press, Tucson, Arizona, pp. 450-483, 1989 that discusses how the atmospheres and interiors of terrestrial planets evolve in a coupled manner. The physical mechanisms that couple the atmospheres and interiors of planets are analyzed in detail. The major coupling mechanisms involve the dependencies of subsolidus mantle viscosity and degree of partial melting on volatile content.

Tidal Heating in Enceladus

We have investigated tidal heating of Enceladus using multilayered viscoelastic models of the satellite. Dissipation on Enceladus can be as large as about 900 GW at the current eccentricity, nearly a factor of 2000 greater than previously thought. Among the suite of interior structures capable of large amounts of tidal heating is one that includes a sublithospheric internal ocean of accumulated H_3-H_2O eutectic melt. The models suggest that Enceladus' thermal and dynamical evolution may have been relatively simple, involving only Dione in a 2:1 resonance. The results of this study are reported in "Viscoelastic Models of Tidal Heating in Enceladus" by M. N. Ross and G. Schubert, *Icarus*, *78*, 90-101, 1989.

Tidal Dissipation and Shape of Io

We have calculated spatial distributions of tidal heating in layered viscoelastic models of Io. Tidal heating is concentrated at the equator if dissipation occurs mainly in an asthenosphere; heating is ıcentrated at the poles if dissipation occurs throughout Io.Equatorial hotspots and the concentration of Prometheus-type plumes near the equator favor asthenosphere heating. Io's observed figure supports the existence of an Fe-FeS core with a radius of about 1,000 km.

We calculated global topography for multilayer Io models with dissipation occurring in a viscous asthenosphere and a solid mantle. The derived topography was compared with observed topographic variations which feature alternating basins and swells along the equator and moderately elevated or depressed regions at the poles. Theoretical models match observations if about 2/3 of the tidal heating occurs in a partially molten asthenosphere and 1/3 occurs in the underlying solid mantle. In addition, the modelling suggests that Io's lithosphere is compositionally distinct from the asthenosphere. This work is discussed in "Internal Structure of Io and the Global Distribution of its Topography" by M. N. Ross, G. Schubert, T. Spohn and R. W. Gaskell, *Icarus*, in press, 1990.

CAPTURE OF TRITON AND THE GAS DRAG TIMESCALE

Andrew C. Leith and William B. McKinnon, Dept. Earth and Planetary Sciences and the McDonnell Center for Space Sciences, Washington University, Saint Louis MO 63130.

Introduction: Our study of the capture of Triton by a gas drag mechanism, discussed in last year's Reports of Planetary Geology Memorandum and elsewhere [1–3], has been refined to include the influence of solar perturbations on the early evolution of Triton's orbit and Triton's recently determined physical parameters [4]. We have also further evaluated the mechanisms by which Triton may have avoided spiraling into Neptune (the usual end result of gas drag scenarios) and survived to the present time.

Method: As in the original study we reconstruct the protosatellite nebula around Uranus using a minimum mass hypothesis [e.g., 5] and assume that a similar nebula would have existed around Neptune. The resulting "nominal nebula" has a mass of about 40 M_T. We assume that $\sigma \propto r^{-3/2}$, where σ is the surface density, and r is the nebula radius (the value of the exponent is not critical to the results). The model nebula is isothermal and cool (50 K), and truncated at just over 25 R_N (the limit of Oberon's "feeding zone"). We also consider the possibility that the Neptunian protosatellite nebula was enriched in high–Z elements and investigate orbital evolution in a "low–mass" nebula with 1/10th the mass of the "nominal" nebula. We initially set Triton's apocenter at the limit of Neptune's Hill sphere (~4600 R_N) and specify an initial encounter distance (pericenter). For simplicity we also assume that the line of nodes coincides with the line of apses, so that every other passage through the nebula plane occurs at pericenter (the effects of relaxing this condition are discussed later). Early in Triton's orbital evolution when its semimajor axis is still relatively large (> 100 R_N), solar perturbations cause a harmonic oscillation of the specific orbital angular momentum [6]. This oscillation (δh) has a period of half a Neptunian year. The position in the angular momentum cycle at which Triton first passes through the nebula is crucial to its subsequent orbital evolution because the distance of pericenter varies with the angular momentum . Most of our calculations assume that the initial encounter occurs at minimum angular momentum (most negative δh), which means that the first encounter is also the closest. We ignore the effects of solar perturbations on the semimajor axis of the orbit [6], and also the effects of precession. Due to its retrograde nature angular momentum is transferred from Triton's orbit to Neptune, therefore we allow the orbital elements to evolve until the mean angular momentum of the model orbit falls below the actual value for Triton's present orbit.

Results: The time for the orbital angular momentum of a Triton interacting with our "nominal" nebula to be reduced to the present value (the evolution time) is shown plotted against the initial distance of encounter with the nebula in Fig. 1. In all cases the initial encounter took place at minimum angular momentum. Since very little change in orbital inclination occurs after dissipation of the nebula, the starting inclinations were chosen such that the final inclination would be within 0.2° of the present value (157°). As in the original study [1–4] the total change in inclination was never more than 6° and the final eccentricity in all instances was less than 0.15. The low final eccentricities are the result of setting the lines of nodes and apses to be coincident. If the initial encounter with the nebula does not occur at pericenter, the true anomaly, f, increases

C 3

with each passage through the nebula. The result of having non-zero f is that at each passage the pericenter distance is reduced as well as the apocenter distance, leading to greater final eccentricity. Overall results suggest that the post-gas-drag eccentricity, i.e., that remaining when Triton's present-day angular momentum is reached during each calculation, is likely to be more than ~0.2.

The large increase in evolution time for an initial encounter at 25 R_N occurs because the initial encounter just grazes the edge of the nebula. Because the first approach occurs at minimum angular momentum and is therefore the closest that Triton can approach Neptune (until apocenter also falls inside the nebula), many of the subsequent orbits do not encounter the nebula at all. This is true for all initial encounters further out than ~7 R_N, but the further out the first encounter the greater the number of orbits that do not intersect the nebula, and the longer the period for each orbit. Fig. 2, which shows pericenter passage distance versus time for an initial encounter at 24 R_N, illustrates this effect. In the 300 orbits shown, there are only 19 that intersect the nebula.

Although it is possible to extend the evolution time beyond 10^5 years for particular initial conditions, in general gas drag in our nominal nebula is too effective to make Triton's survival likely, unless the lifetime of the nebula is under ~10^4 years. However, the situation is considerably improved if the nebula is less massive than "nominal". We repeated some of the iterations of Fig.1, but for a nebula 1/10th as massive. In addition we considered the effects of Triton's passage on the nebula. At each encounter a cylinder of gas is dispersed. The resulting hole in the nebula is filled by a combination of pressure gradient flow in the azimuthal direction, and viscous spreading in the radial direction. The time for the pressure gradient to equilibrate azimuthally is about 0.1 years or less for our model. Therefore, if the kinematic viscosity of the nebula is low enough, Triton should be able to so deplete the gas in the annular region it interacts with that its orbit cannot evolve further by gas drag. This annular clearing phenomenon is shown in Fig. 3, which is a surface density versus radius plot for the low mass nebula. The results of initial encounters at 7, 10 and 15 R_N are shown. The width of the cleared annulus increases outwards primarily because of the increase in scale height of the nebula. The surface densities in the cleared lanes are all below 100 kg/m^2. Figure 4 shows the evolution times for interactions with the low–mass nebula. As in Fig. 1 initial encounter takes place at minimum angular momentum, but in this case the starting inclination was 160° for all cases. The calculations were halted when on each passage through the nebula the ratio of gas mass encountered to Triton's mass fell below 10^{-7}. At this point the region of the nebula that Triton interacts with has been thinned nearly a thousandfold and orbital evolution by gas drag halts. Initial encounters further out than 15 R_N were not considered, as insufficient energy is dissipated during the initial encounter to make permanent capture likely.

Conclusion: Oscillations of Triton's orbit in and out of the protosatellite nebula can extend the timescale for evolution by gas drag to O 10^5 years for specific initial conditions. While this is still shorter than estimates for the lifetime of the T Tauri phase (which may be indicative of the lifetime of the protosatellite nebula), it may be that capture occurs towards the end of the nebula's lifetime, or turbulent dissipation may cause the nebula to evolve rapidly. Another possibility is that Triton may be able to clear the gas from an annulus about the region it interacts with and "self–terminate" its orbital evolution. This is of particular relevance to low–mass (high–Z element enriched) nebulae, which may be the most likely to have formed around Uranus and Neptune [7].

For "self–termination" to work the nebula kinematic viscosity probably has to be less than O 10^5 cm^2/sec . This is orders of magnitude less than turbulent values estimated for our nebula, but is orders of magnitude greater than molecular values at the relevant conditions, and possibly means that the nebula has to be in its satellite building phase for capture by gas drag. Although none of these results preclude the possibility of capture by collision [6], they do indicate that it is possible to reconcile capture with the gas drag timescale.

References: [1] McKinnon, W.B., A.C. Leith, and S. Mueller (1989) *NASA T.M.* **4130**, 57–59; [2] Leith, A.C., and W.B. McKinnon (1988) *Bull. Am. Astron. Soc.* **20**, 815-816; [3] McKinnon, W.B. (1989) *Bull. Am. Astron. Soc.* **21**, 916; [4] McKinnon, W.B., and A.C. Leith (1990) Gas drag and the evolution of a captured Triton, *Icarus*, in revision; [5] Weidenschilling, S.J. (1982) In *The Comparative Study of the Planets*, pp. 49–59, D. Reidel; [6] Goldreich, P., *et al.* (1989) *Science* **245**, 500–504; [7] Bodenheimer, P., and J.B. Pollack (1986) *Icarus* **67**, 391–408.

Figure 1

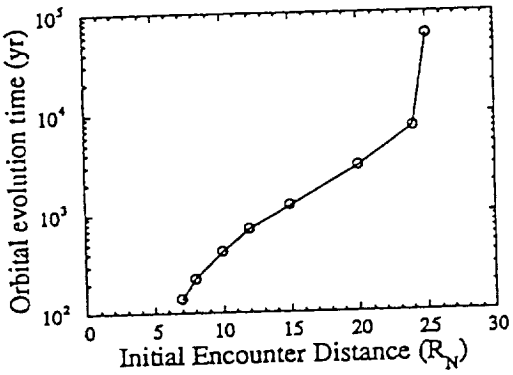

Figure 2

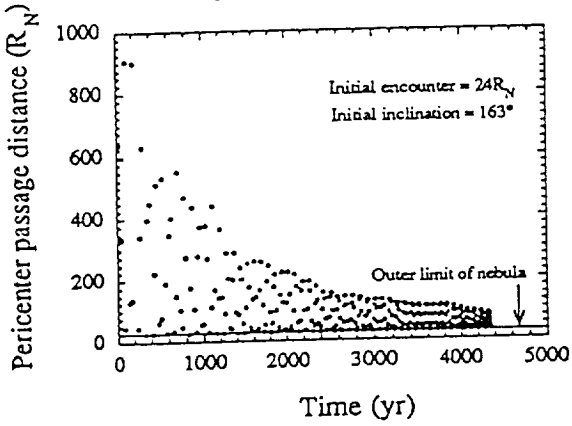

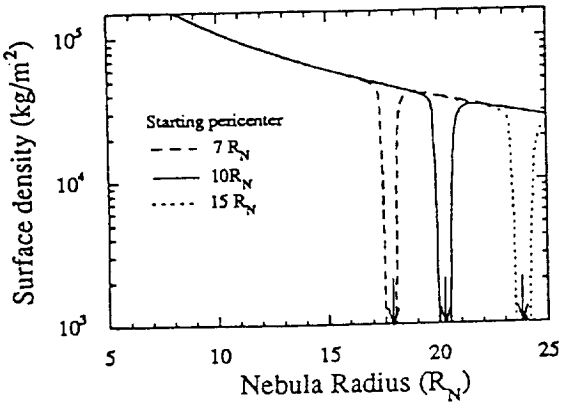

Figure 3

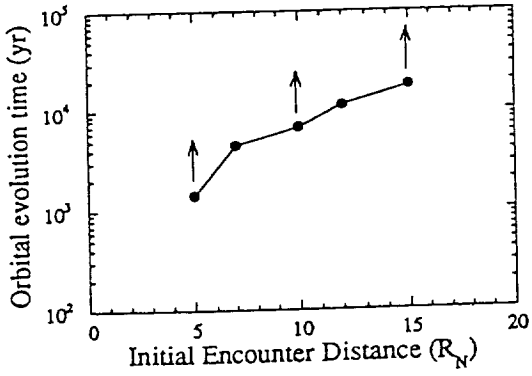

Figure 4

The figures are described in the text.

ON THE TIDAL EVOLUTION OF BINARY ASTEROIDS A.W. Harris, Jet Propulsion Laboratory

One explanation which has been offered for the excess of slowly rotating asteroids is that they are tidally de-spun binaries, like the Pluto-Charon system. I have in the past advocated this mechanism as an explanation for slowly spinning main best asteroids (1,2), but also noted that the near earth asteroids possess an even more bi-modal distribution. Recently, Ostro (3) has obtained strong evidence from radar observations that the near earth asteroid 1989 PB is a binary object, with the components either in or nearly in contact. Furthermore, he notes that radar observations of several other asteroids (e.g., 1627 Ivar, 216 Kleopatra) are suggestive of contact binary objects. A similar model has been proposed for 624 Hektor, based on its lightcurve (4). The purpose of this note is to point out that these two classes of objects, slowly spinning binaries of a few days period, and contact or near contact binaries, are plausible outcomes of the same formation event: a collisional splash-off of debris from a massive collision, such as is now widely believed to have led to the formation of the moon (5).

The "splash-off" collisional mechanism essentially results in a debris blob in a long elliptical orbit with periapse near one radius of the primary. As the blob coalesces into a discrete satellite, the orbital eccentricity rapidly decays to yield a nearly circular orbit at about 2 planet radii, conserving the orbital angular momentum (6). This orbit radius corresponds to a period of about 5 - 6 hours, for bodies of density 2.5 - 3.0. If the primary is spinning more rapidly than that, tidal evolution will be outward, leading either to a tidally locked binary like Pluto/Charon, or to a partially evolved system, like the earth/moon. This configuration has also been suggested for 288 Glauke (7) and 1220 Crocus (8). On the other hand, a rotation period of <6 hours is considerably shorter than the average for all asteroids, hence it is reasonable to conclude that, if these splash-off events occur at all, some may not spin up the primary sufficiently to bring the synchronous orbit radius inside of the satellite orbit. In this case, the tidal evolution will be inward, with the ultimate result that the satellite will evolve into contact with the primary. This evolutionary track has been recognized for a long time (6, 9, 10), but has not been well explored.

Consider a very simple model of a binary with spherical components of equal density and radii R and r, and initially in a circular orbit of radius 2R. Let the secondary have a spin period equal to the orbit period (i.e., it is already tidally locked, like the moon), and the primary has an initial spin period of P_1, greater than the initial orbit period. Tidal evolution of such a system will always result in a contact binary. After the system comes into contact and begins revolving as a single rigid body, and neglecting the deformation of the bodies by the collision, the spin period can be shown to be:

$$P = \frac{1 + \rho^5 + 2.5\rho^3(1+\rho)^2/(1+\rho^3)}{[10\rho^3/(1+\rho^3) + \rho^5][(1+\rho^3)/8]^{1/2} + P_o/P_1} P_o$$

where $\rho = r/R$, and P_o is the orbit period at the surface of a sphere, about 2 hours for a body of density 2.7. A remarkable property of this complicated

experession is that it has a value of about (2-3)P_0 over the entire range of interest here - binaries of size ratio $\rho > 0.5$ and initial planet period slower than about 6 hours (see Figure 1). Hence if a massive binary is formed by the splash-off mechanism, but does not initially settle into an orbit outside of the synchronous limit, the final end state will be a contact binary with a spin period of about 4 to 6 hours. All of the above mentioned possible binary objects have periods in that range (624 Hektor's period of 6.921 hours is only slightly outside). A provocative aspect of this model of formation is that, if it applies to very small asteroids (1627 Ivar, 1989 PB), then it must work in the current regime of very high velocity collisions, since such small bodies are expected to be collisionally young.

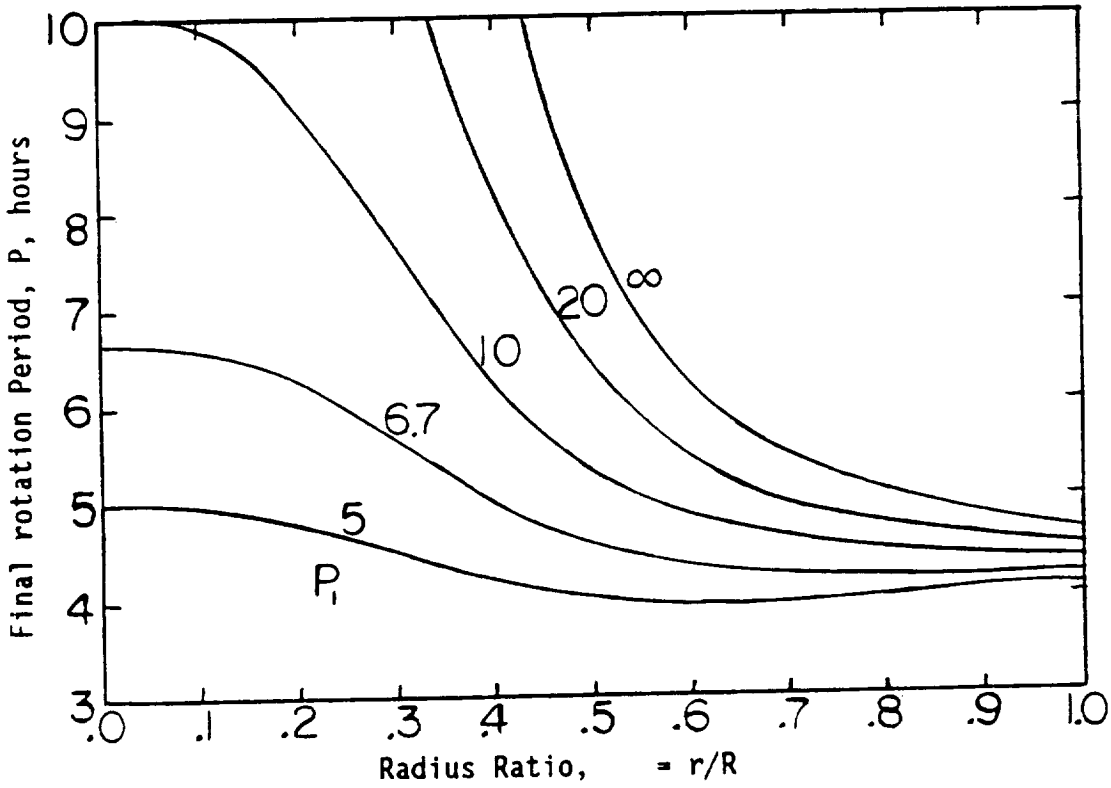

Figure 1. Final rotation period of a contact binary after tidal evolution from an initial orbit at a/R = 2.0. The abscissa is the ratio of the radius of the secondary to that of the primary; the ordinate is the final rotation period of the contact binary. Each curve is for the specified initial rotation period of the primary.

REFERENCES (1) Harris, A.W. (1986) In Asteroids, Comets, Meteors II (Lagerkvist, Lindblad, Lundstedt, Rickman, eds.) Uppsala: Reprocentralen HSC, pp. 35-44. (2) Farinella, P., P. Paolicchi, V. Zappala (1981) Astron. Astrophys. 104, 159-165. (3) Ostro, S.J. (1989) Private Communication. (4) Weidenschilling, S.J. (1980) Icarus 44, 807-809. (5) Stevenson, D.J. (1987) Ann. Rev. Earth Planet. Sci. 15, 271-316. (6) Weidenschilling, S.J., P. Paolicchi, v. Zappalà (1989) In Asteroids II (Binzel, Gehrels, Matthews, eds.) Tucson: Univ. Ariz. Press, pp. 643-658. (7) Harris, A. W. (1983) Bul. Amer. Astron. Soc. 15, 828. (8) Binzel, R.P. (1985) Icarus 63, 99-108. (9) Councelman, C.C. (1973) Astrophys. J. 180, 307-314. (10) Greenberg, R. (1974) Icarus 23, 51-58.

CHAPTER 5

PLANETARY INTERIORS, PETROLOGY, AND GEOCHEMISTRY

PROPERTIES OF PLANETARY FLUIDS AT HIGH PRESSURES AND TEMPERATURES

William J. Nellis, Lawrence Livermore National Laboratory, University of California, Livermore, CA 94550

Observational data obtained by Voyager space probes to the giant planets Jupiter, Saturn, Uranus and Neptune have provided valuable information which is used to refine our picture of the nature of the interiors of these planets. Most timely are the Voyager II flyby's of Uranus in 1986 and Neptune in 1989. Jupiter and Saturn are thought to consist primarily of hydrogen and helium [1]. Uranus is thought to consist of an outer layer primarily of hydrogen and helium and an inner layer rich in the "ices," especially water, possibly mixed with liquid silicates [1,2]. Density distributions calculated for Uranus [2-5] from the gravitational movements derived from the observed precessions of its elliptical rings, and from its mass, radius, and rotational rate are plotted in Fig. 1. Two of the models show a dense "rocky" core, although the sensitivity of the external gravitational field is weak to the relatively small mass at such great depth. The low-density region at radii greater than about 0.75 R_u, where R_u is the radius of Uranus, is the H_2-rich envelope. The region at radii less than about 0.75 R_u is the ice-rich region.

The magnetic fields of these planets are produced by dynamos generated by the convection of high-temperature conducting fluids in the outer ~30% of the planetary radii [6]. Pressures extend up to the 100 GPa (Mbar) range and several 1000 K in these regions. Pressures and temperatures in the deep interiors extend up to several TPa in Jupiter and Saturn and to about 500 GPa in Uranus and Neptune.

Our goal is to obtain equation-of-state (EOS) and electrical conductivity data for planetary "ices" (H_20, CH_4, and NH_3, and their mixtures) and gases (H_2 and He) considered to be major constituents of the giant planets. These data are needed to test theoretical databases used to construct models of the chemical composition of planetary interiors, models which are consistent with observables such as mass, diameter, gravitational moments, rotation rate and magnetic field. The 100 GPa pressures and several 1000 K temperatures in the giant planets can be achieved in the laboratory by the shock compression of liquid specimens.

In the last year four successful EOS experiments were performed on "synthetic Uranus," an H-rich liquid with an H:O composition ratio of 3.5:1 and abundance ratios close to cosmological for O:C(7:4) and O:N(7:1). This liquid mixture, which is representative of Neptune as well, is a solution of water, ammonia, and isopropanol (C_3H_8O) with mole fractions of 0.71, 0.14, and 0.15, respectively. Because these polar molecules are mutually soluable at ambient conditions, high-pressure and high-temperature specimen holders to mix

methane with water and ammonia are not necessary. The new data complement previous single-shock data [7] and a double-shock point for synthetic Uranus to produce a complete (P,V,E) experimental database. The four double-shock points are in the range 0.98 - 2.2 Mbar. Our new 2.2 Mbar experiment achieved a density of 3.1 g/cm^3, which from Fig. 1 probes a depth of about 0.5 R_u. The region for radii >0.5 R_u is the region probed most sensitively by gravitational moments. Our four double-shock EOS points and highest-pressure single-shock point are in excellent agreement with Uranian adiabats calculated by Hubbard and Marley [1]. This agreement suggests that the inner region of Uranus might be composed primarily of the ices. However, chemical compositions cannot be derived uniquely from laboratory data alone. The same density distribution could also be caused by a mixture of hydrogen and rock [2].

We have performed a double-shock temperature experiments on synthetic Uranus, which produced a preliminary temperature of about 3100 K at about 0.75 Mbar. Temperature data are important to provide good estimates of the temperature inside Uranus and Neptune. Internal temperatures are quite uncertain in current planetary models.

We have also just performed the first successful measurement of the electrical conductivity of hydrogen at high shock pressure and temperature. At this juncture in our planetary program, measuring the electrical conductivities and shock temperatures of hydrogen are the most important measurements we can make. These data are important for understanding the magnetic fields of all the giant planets. Because conductivity σ scales sensitively as

$$\sigma \alpha \exp(-E_g/kT),$$

where E_g is the bandgap at density ρ, and T is temperature at density ρ, both σ and T must be measured to check theoretical density dependences of band gap [8,9] and shock temperatures [10]. Once scaling parameters for σ are obtained, an experimentally validated conductivity model will be available for modeling the magnetic fields of the giant planets. These results will also provide a measure of the narrowing of the bandgap of molecular H_2 with density as it approaches metallization, a subject of fundamental scientific interest.

References

1. W. B. Hubbard and M. S. Marley, "Optimized Jupiter, Saturn, and Uranus Interior Models," Icarus 78, 102-118 (1989).
2. A. M. Podolak, W. B. Hubbard, and D. J. Stevenson, "Models of Uranus' Interior and Magnetic Field," preprint (1988).
3. D. J. Stevenson, "Uranus," Bull. Am. Astron. Soc. 19, 851 (1987).
4. M. Podolak and R. T. Reynolds, "The Rotation Rate of Uranus, Its Internal Structure, and the Process of Planetary Accretion," Icarus 70, 31-36 (1987).

5. T. V. Gudkova, V. N. Zharkov, and V. V. Leont'ev, "Models of Uranus and Neptune with Partially Mixed Envelopes," Sol. Sys. Res. 22, 16-29, (1989) [Translation of Russian: Astron. Vestn. 22, 23-40 (1988)].
6. R. L. Kirk and D. J. Stevenson, "Hydromagnetic Constraints on Deep Zonal Flow in the Giant Planets," Astrophys. J. 316, 836-846 (1987).
7. W. J. Nellis, D. C. Hamilton, N. C. Holmes, H. B. Radousky, F. H. Ree, A. C. Mitchell, and M. Nicol, "The Nature of the Interior of Uranus Based on Studies of Planetary Ices at High Dynamic Pressure," Science 240, 779-781 (1988).
8. C. Friedli and N. W. Ashcroft, "Combined Representation Method for Use in Band-Structure Calculations: Application to Highly Compressed Hydrogen," Phys. Rev. 16B, 662-672 (1977).
9. B. I. Min, H. J. F. Jansen, and A. J. Freeman, "Pressure-Induced Electronic and Structural Phase Transitions in Solid Hydrogen," Phys. Rev. 33B, 6383-6390 (1986).
10. M. Ross, F. H. Ree, and D. A. Young, "The Equation of State of Molecular Hydrogen at Very High Density," J. Chem. Phys. 79, 1487-1494 (1983).

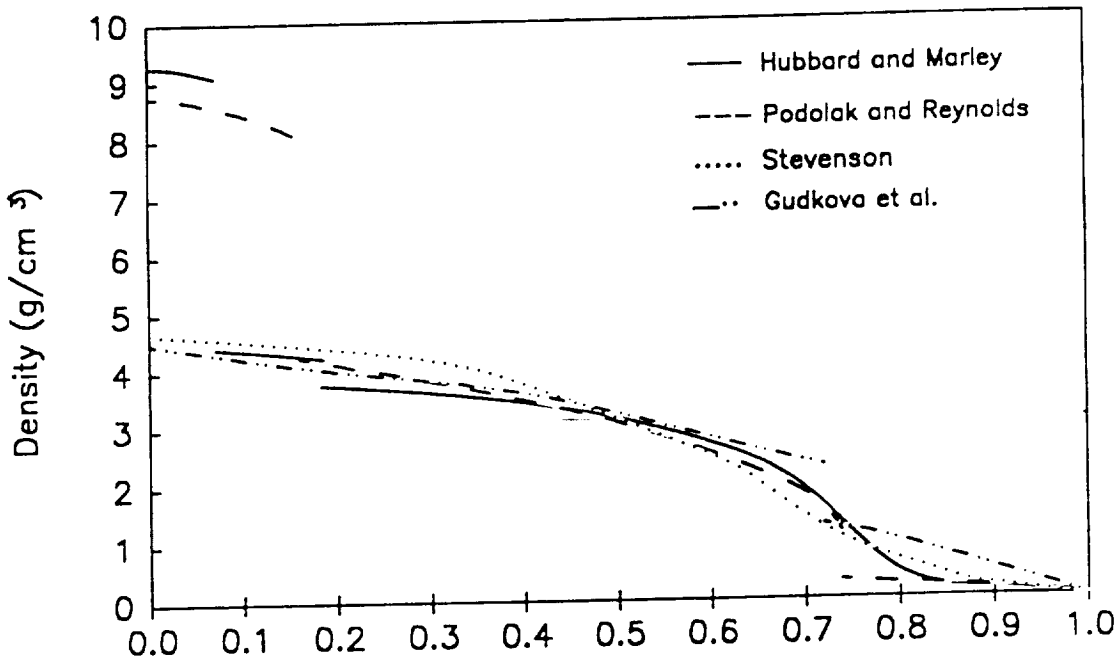

Fig. 1. Density vs normalized radius for Uranus (after Ref. 2)

AMMONIA-WATER DENSITIES AND PHASE RELATIONS TO FOUR KILOBARS D.L. Hogenboom[1] and J.S. Kargel[2]; 1Physics Department, Lafayette College, Easton, PA 18042; 2Lunar and Planetary Laboratory, University of Arizona, Tucson, AZ 85721

Introduction. Ammonia-water cryovolcanism is widely suspected to have been important in the evolution of icy satellites in the outer solar system. We report experimental determinations of ammonia-water liquid densities and solid-liquid phase relations, following from previous work [1-3]. We have determined ice liquidus temperatures for liquids containing 10, 20, and 28.6 wt. % NH_3 at several pressures, and the melting behavior of ammonia hydrates at several pressures for mixtures containing 28.6 and 32.1% NH_3. Our new data cover the entire range of interior pressures in small to intermediate sized icy satellites and in the outer 200 kilometers or so of the largest icy satellites.

The Experiment. Our apparatus and procedure have been modified slightly from those described previously [1]. The essential components of the system are shown in Figure 1. The change in volume of the sample is measured with a transducer which detects the position of an alnico magnet floating on a mercury column. The transducer generates a DC voltage which changes as the sample volume changes. After calibrating with water and correcting for compression of the mercury and sample in the expansion pipe we estimate the uncertainty in our reported densities is less than 0.15%. A comparison of our densities with direct volumetric measurements [3] indicates a similar uncertainty.

Since our last report, the temperature measurement and control system has been improved by placing the silicon diode thermometer in a copper sleeve in good thermal contact with the sample pressure vessel. A heating tape was also used to balance the heat lost to the liquid nitrogen bath, permitting good control of heating and cooling rates.

Liquid and solid volumes. The density, ρ, of 28.6 wt.% NH_3-H_2O at roughly 20 bars is given as a function of temperature, T, by the equation $\rho = 0.997612 - 0.185481\times10^{-3}T - 0.498297 \times 10^{-6}T^2$. The density of the ammonia dihydrate-composition liquid (32.1 wt.% NH_3) at 303.15 K is given as a function of pressure by the equation $\rho = 0.8789 + 0.3645\times10^{-4}P - 0.2434\times10^{-8}P^2$, where P is in kilobars.

Since we can not directly observe the contents of the bomb we rely on the volumetric behavior of the system to infer the identity of solid phases. We observe two solid phases, apparently water ice-I and ammonia monohydrate, which are less dense than co-existing ammonia-water liquids. We also observe solids which are denser than the liquid, apparently including ammonia dihydrate and ices-II, -III, and -V.

Supercooling and crystallization behavior. Samples were quickly cooled (several K/minute) from room temperature to about 120 K, without crystallization, where the temperature then remained more or less constant for several hours, and then began to warm slowly (about 0.03 K/minute). Failure to cool below about 130 K at least for several hours typically failed to result in crystallization of ammonia hydrate. Given the necessary time and temperature conditions we typically observed a 3- to 4-fold increase in the warming rate of the bomb and the enclosed sample in the interval from about 130 to 140 K. This enhanced warming was often accompanied by a slight decrease in voltage. We interpret these effects to be due to the volumetric adjustment and latent heat release caused by the crystallization of ammonia dihydrate.

Solid-liquid phase relations. Figures 2 and 3 show representative temperature-voltage plots for crystallized mixtures containing 28.6 wt.% NH_3 (voltage is inversely related to density). For pressures of one kilobar and lower the melting behavior of mixtures of ice and ammonia dihydrate is simple. The iso-voltaic stretch on the warming curves in Figures 2 and 3 is due to the plugging of the bomb with crystals. Melting at 20 bars occurs cleanly at 176.2 +- 0.2 K, in agreement with the peritectic melting point at 1 atm (20 bars pressure has a negligible effect on the melting point). Melting is indicated by a sharp rise in voltage as the bomb first unplugs and then as ammonia dihydrate yields a less dense peritectic liquid phase plus a small amount of water ice. The melting reaction is reversible (ammonia dihydrate re-crystallizes) if the sample is re-cooled very slowly (0.01 K/min) before all the ammonia dihydrate has melted.

Above one kilobar a more complex (but repeatable) melting behavior is usually observed (Figure 3). The sample apparently crystallizes to ammonia dihydrate but it melts differently. In the first stage of melting the voltage rises sharply. But instead of levelling off at a value near that of the ice melting curve, as it does below 1 kilobar, the voltage continues to rise. The voltage peaks and then, in the second stage of melting, descends toward the ice melting curve. Endothermic effects indicative of a melting reaction, observable as a depression in the warming rate, occur continuously during both these stages of melting. The first stage of melting is consistent with the melting of ammonia dihydrate and its partial re-crystallization to a low-density assemblage of water ice and ammonia monohydrate; this stage apparently is irreversible (ammonia dihydrate does not re-crystallize), since the voltage continues to rise if the sample is slowly re-cooled before the first stage of melting is complete. The second stage of the reaction is consistent with the eutectic melting of ammonia monohydrate and water ice. The second stage is reversible (ammonia monohydrate can be re-crystallized) if the sample is very slowly re-cooled prior to the final disappearance of ammonia monohydrate. Excess water ice melts gradually after the ammonia hydrates have completely melted; the liquidus is indicated in Figure 3 by the break in slope where the warming curve meets the liquid cooling curve.

The observations above seem to imply that ammonia dihydrate is the stable ammoniacal phase near the melting point below 1 kilobar, whereas ammonia monohydrate is stable above 1 kilobar (although ammonia dihydrate may exist metastably above a kilobar). Figure 4 is a phase diagram of the mixture containing 28.6% NH_3. The solidus, including the metastable dihydrate melting curve, has been reproduced in several experiments. The liquidus is preliminary.

In accordance with prior expectations [2] we find that the ice-I liquidus drops to lower temperatures and the peritectic shifts to slightly water-richer compositions as pressure is applied. Apparently around 200 bars the peritectic

composition crosses that of ammonia dihydrate; ammonia dihydrate melting then becomes congruent, and the peritectic becomes a eutectic. This eutectic becomes more water rich as pressure is applied, finally attaining a minimum of about 29% NH_3 at 2 kilobars.

Implications. 1) Igneous distillation of solar system ices by partial melting and then re-melting can yield liquids as ammonia-rich as 35.4 wt.% NH_3 (the monohydrate-dihydrate eutectic) at pressures less than about 200 bars, but above this pressure the accessible liquid compositions are restricted to the water-rich side of the ice-dihydrate eutectic. 2) High-pressure, relatively water-rich eutectic liquids are forced to precipitate water ice as they ascend and de-pressurize, resulting in relatively viscous slurries. 3) A high pressure transition in one of the ammonia hydrates is required at some pressure between 4 and 10 kilobars to fit both these data and those of [2].

Acknowledgements. We thank Guy Consolmagno, Steven Croft, John Lewis, Jonathan Lunine, and Robert Strom for constructive comments and encouragement. This study has been partially supported by the NASA Planetary Atmospheres Program and the Uranus Data Analysis Program.

References. [1] Hogenboom, D.L., J. Winebrake, G.J. Consolmagno, and W. Dalrymple III, LPS XX, 420-421. [2] Cynn, H.C., S. Boone, A. Koumvakalis, M. Nicol, and D.J. Stevenson, 1989, Proc. 19th Lunar Planet. Sci. Conf., G. Ryder and V.L. Sharpton (eds.), Cambridge Univ. Press and Lunar and Planetary Inst. (Publ.), Houston, p. 433-441. [3] Croft, S.K., J.I. Lunine, and J.S. Kargel, 1988, Icarus, 73, 279-293.

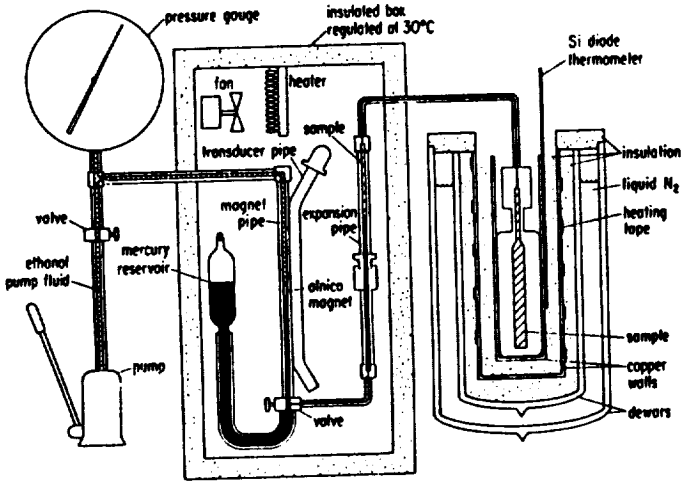

Figure 1. Schematic of high-pressure apparatus.

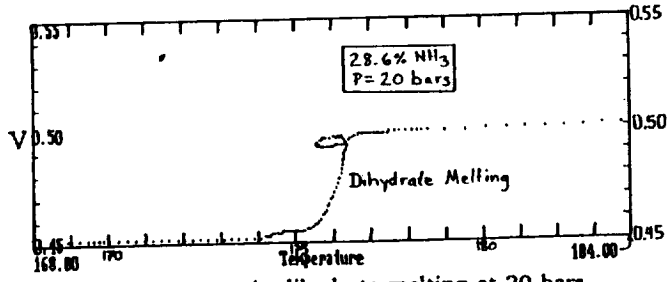

Figure 2. Ammonia dihydrate melting at 20 bars with reversal.

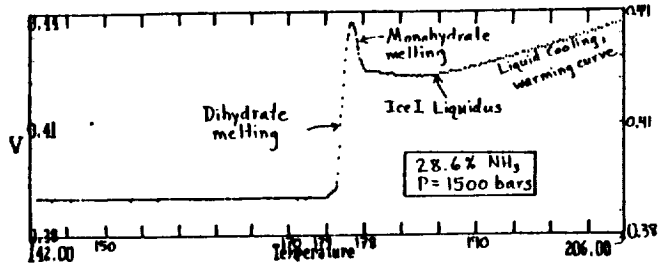

Figure 3. Melting at 1500 bars showing metastable dihydrate melting followed by stable monohydrate melting at their respective eutectics.

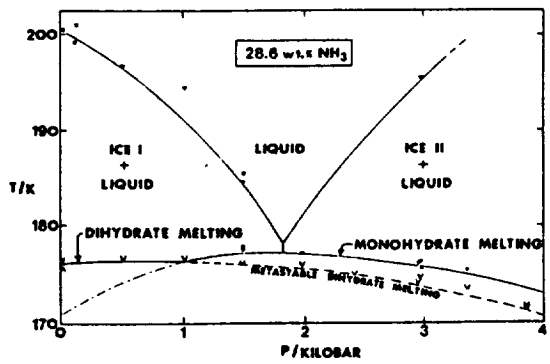

Figure 4. Phase diagram for 28.6% ammonia mixture.

HIGH PRESSURE COSMOCHEMISTRY OF MAJOR PLANETARY INTERIORS: LABORATORY STUDIES OF THE WATER-RICH REGION OF THE SYSTEM AMMONIA-WATER AND METHANE HYDRATE CLATHRATE

Malcolm Nicol and Steven Boone
Department of Chemistry and Biochemistry
University of California, Los Angeles, CA 90024-1569

Ammonia, methane, and water are believed to be major components of primordial solar system ices. Celestial bodies of the outer solar system probably incorporated large amounts of these ices into their interiors during accretion. Our understanding of the histories, dynamics, and structures of these objects depends upon our understanding of phase relationships and thermodynamic properties of mixtures of these materials at high pressures. Few laboratory measurements are available so models of these major planets and satellites make simple, rather arbitrary assumptions concerning their "rock" cores or "ice" layers. Our studies are designed to measure properties of "gas-ice" mixtures at pressures relevant to planetary problems, 1 GPa and higher pressures. We have determined pressure-temperature-composition (P-T-X) diagram of binary mixtures of ammonia (NH_3), water (H_2O), and methane CH_4.

During the past year, Dr. Boone [1989] completed his dissertation research and reported his studies of the phase relations of mixtures of ammonia and water, $(NH_3)_X \cdot (H_2O)_{1-X}$, with compositions $0.32 < X < 0.51$ at pressures to 6.5 GPa and temperatures from 125 to 400 K. He made *in situ* microscopic observations of the samples under polarized light to determine phase boundaries and to identify the stable phases. A major outcome of this study is the first determination of the congruent melting curve of ammonia dihydrate, $NH_3 \cdot H_2O$. Recent models [Lunine and Stevenson, Icarus, 1987] suggest that this dihydrate and ammonia hydrate, $NH_3 \cdot H_2O$, are important in the evolution of the interior and surfaces of the icy satellites. Dr. Boone described his measurements of the melting curve between 0.06 GPa and 179 K to 1.4 GPa and 243 K by the equation $T_m/K = 176 + 60 \times (P/GPa) - 8.5 \times (P/GPa)^2$. He also grew large crystals of this dihydrate for the first time and attempted to measure their x-ray diffraction pattern. However, the available x-ray sources were too weak. Further work will be done when we can obtain time on a diffractometer with a rotating Mo-anode source. From his data and other measurements of equilibrium properties of water ice and ammonia monohydrate made in our laboratory [Johnson et al., 1985; Johnson and Nicol, 1987; Koumvakalis, 1988; Cynn et al., 1989], Dr. Boone constructed a phase diagram for the water-rich ammonia water system to 450 K which will be described in a forthcoming publication.

Dr. Boone also loaded a few samples of methane and water into diamond-anvil cells as solid methane hydrate clathrate, measured their Raman spectra, and observed their behavior at pressures from 0.4 to 5.0 GPa and temperatures from 296 to 323 K. The Raman spectra indicated that methane hydrate clathrate decomposes to high pressure ices and solid methane at pressures above 2.0 GPa at 295 ± 5 K. Visual observations at higher pressures suggest, however, that only one phase was present. Further work on this system is planned.

References

Boone, S.C., 1989. Mixtures of Ammonia and Water and of Methane and Water at High Pressures (University of California, Los Angeles).
Cynn, H., S. Boone, A. Koumvakalis, and M. Nicol, 1989. Proc. 19th Lunar and Planet. Sci. Conf. (Lunar and Planetary Inst., Houston) 433-441.
Johnson, M. L., A. Schwake, and M. Nicol, 1985. in Klinger, J. et al., eds., Ices in the Solar System (D. Reidel, Doerdrecht) 39-47.
Johnson, M.L., and M. Nicol, 1987. J. Geophys. Res. 92, 6339-6349.
Koumvakalis, A., 1988. High Pressure Studies of Ammonia Monohydrate, (University of California, Los Angeles).
Lunine, J.I., and D.J.Stevenson, 1987. Icarus 7, 61-77.

The Interiors of Uranus and Neptune-A Post Voyager Comparison

M. Podolak*, R. T. Reynolds, and R. Young
NASA Ames Research Center, Moffett Field, CA 94035

* NAS/NRC Senior Research Associate. Permanent address: Dept. of Geophysics and Planetary Sciences, Tel Aviv University, Ramat Aviv, Israel

The planets Uranus and Neptune are very similar in mass and radius. They were formed in the same general region of the solar nebula. Their magnetic fields are comparable as well although they differ significantly from those of the other planets. One would therefore expect that their interiors and compositions are also similar. The 18 hr rotation period for Neptune previously deduced from atmospheric motions by Earth-based photometry [1] seemed to require a quite different interior structure for the two planets. Indeed, the assumption of similar interior structure and composition, together with some occultation observations [2] led us to suggest [3] that the 18 hr period referred to the cloud motions, while the body of the planet rotated considerably faster. This suggestion was confirmed by Voyager which measured a rotation period of 16.1 hr [4]. Voyager also measured two of the multipole moments of Neptune's gravitational field, J_2 ($= 3.411 \pm .0010 \times 10^{-3}$) and J_4 ($= -2.6^{+1.2}_{-2.0} \times 10^{-5}$) [5]. These two parameters put useful constraints on the interior density distribution, so improved models of the planet can be computed.

Our models are composed of three layers. The innermost layer is a core of "rock", composed of a mixture of SiO_2, MgO, Fe, and Ni in solar proportions. The middle layer is composed of "ice", a mixture of H_2O, NH_3, and CH_4, also in solar proportions. The outermost layer, or "envelope" is composed of a solar mix of H_2 and He, with H_2O, NH_3, and CH_4 also present and with their abundance relative to H_2 and He enhanced by a factor A over their abundance in solar composition. The models were fit to the observed mass; radius; one-bar temperature; J_2; and J_4. For $A = 1$ (solar abundances), J_2 can be matched with $I/R = 11$. Significantly larger values of A give a J_4 that is too large in absolute value. This is qualitatively similar to the case for Uranus, where the models also require a nearly solar composition envelope [6,7]

The figure shows a density distribution for this model compared to the density distribution for a three shell model of Uranus with $A = 1$ and $I/R = 30$, a model that gives a best fit to that planet. The chief difference between the two planets appears be the value of I/R. It should be noted, however, the density of "ice" is very similar to the density of a mixture of 75% "rock" and 25% "gas" [8]. Thus the middle layer in our models, which we

have assumed to be composed of "ice", may, in fact, represent a mixture of ice, rock and gas, where the ratio of rock to gas is 3:1 by mass.

If we assume that the ice shell is composed of a mass fraction q of ice, $.75(1-q)$ of rock, and $.25(1-q)$ of gas, and that I/R for both Uranus and Neptune is 0.5, roughly the value for Triton and Pluto [9], we find $q = 0.28$ for Uranus and 0.30 for Neptune, so that the q's are nearly equal for the two planets. Other choices of I/R give similar results.

In view of the possibility of very similar structures and compositions for Uranus and Neptune, the difference between the internal heat sources of the two planets is very striking. Neptune, like Jupiter and Saturn, radiates about twice as much energy as it receives from the sun, while Uranus' internal radiation is so low as to be essentially undetectable. If Neptune were to orbit the sun at the distance of Uranus, the ratio of its total emitted energy to absorbed solar energy would be about 1.7, similar to the value for Jupiter. In Jupiter, parts of the interior are stably stratified and the heat flux vector has a significant meridional component, so that the heat flux is shunted to the poles [10]. A condition unique to Uranus is the large tilt of the rotation axis (98°), combined with the long radiative time constants of the atmosphere, which are comparable to or exceed the orbital period at pressure levels greater than 10 mbar [11]. These two proprties of Uranus imply that to a large extent the sun appears to the planet as an almost globally averaged heat source. We suggest that the solar insolation affects the heat transport and therefore statically stable interior regions exist. Since every point in the atmosphere is effectively heated by the sun because of the long radiative time constant, the internal heat flux may be suppressed at all latitudes for Uranus. In contrast, since Neptune has an obliquity of about 29°, most of the solar insolation occurs at low latitudes. The interior heat flux of Neptune should be shunted towards higher latitudes, as apparently occurs for Jupiter.

References

[1]Belton, M. J. S., and R. Terrile, *Uranus and Neptune* NASA CP-2330, edited by Bergstralh, J. T., 327–347, 1984. [2]Hubbard, W. B., *et al.*, *Astron. J.*, *90*, 655–667, 1985. [3]Podolak, M., R. Young, and R. Reynolds, *Icarus*, *63*, 266–271, 1985. [4]Warwick, J. W., *et al.*, *Science*, *246*, 1498–1501, 1989. [5]Tyler, G. L., *et al.*, *Science 246*, 1466–1473, 1989. [6]Hubbard, W. B. and M. S. Marley, *Icarus*, *78*, 102–118, 1989. [7]Podolak, M. and R. T. Reynolds, *Icarus*, *70*, 31–36, 1987. [8]Podolak, M., *et al.*, preprint 1990. [9]Simonelli, D. P., *et al. Icarus*, *82*, 1–35, 1989. [10]Ingersoll, A. P., and C. C. Porco, *Icarus*, *35*, 27–43, 1978. [11]Flasar, F. M., *et al.*, *J. Geophys. Res.*, *92*, 15,011–15,018, 1987.

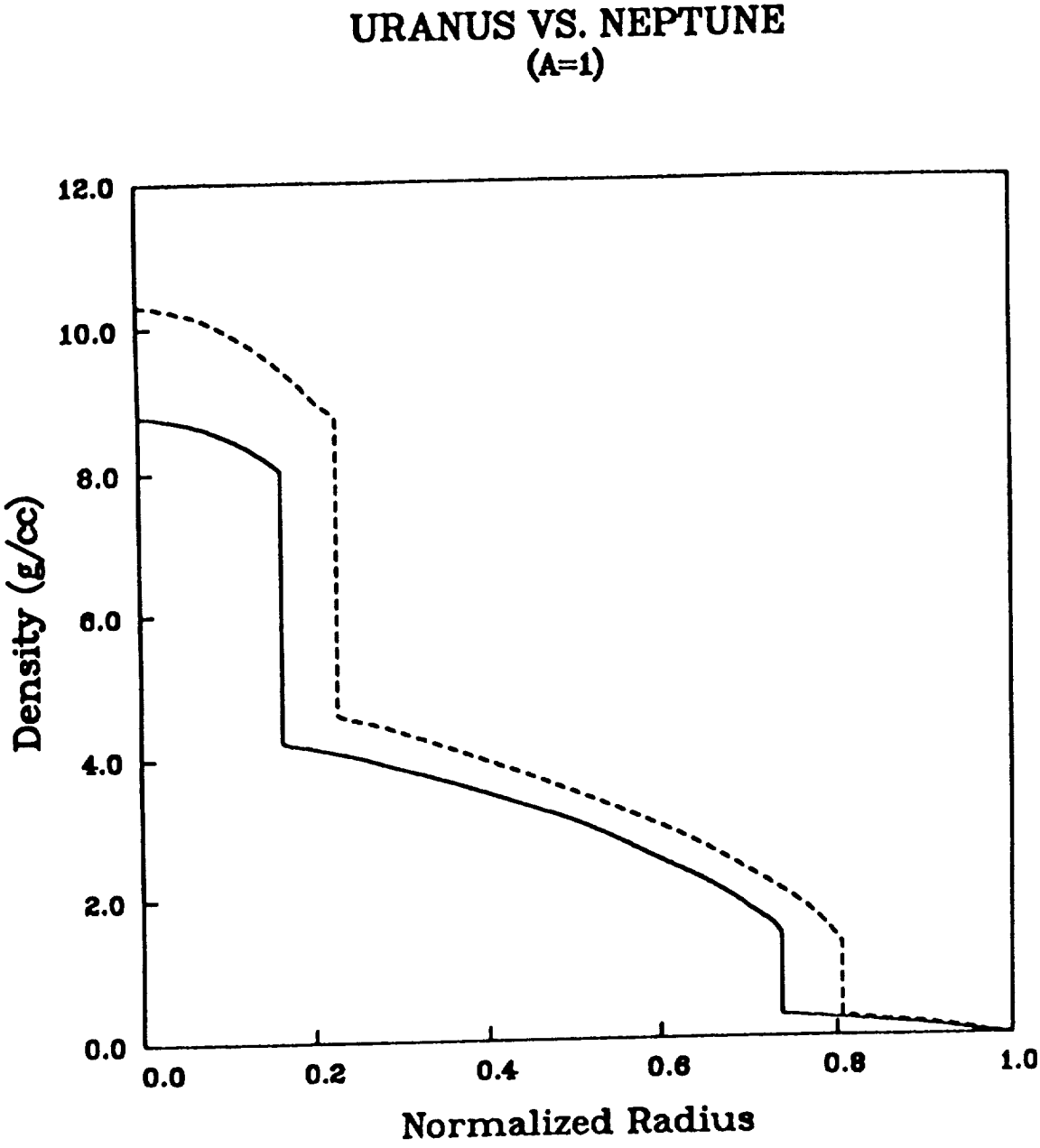

Density as a function of normalized radius for a Neptune model with $A = 1, I/R = 13$ (dashed curve) and for a Uranus model with $A = 1, I/R = 30$ (solid curve).

PLANETARY ICES: A COMPARISON OF RHEOLOGIES AT T < 200 K; W. B. Durham, UCLLNL, Livermore, CA 94550; S. H. Kirby, USGS, Menlo Park, CA 94025

Tectonics on icy bodies at warm temperatures depends strongly on the mechanical properties of water ice because water ice generally dominates both composition and rheology at these temperatures. In contrast, processes at 200 K and below in the outer solar system involve and depend on the properties of a wider range of materials. Given that there is large-scale tectonic activity all the way out to Triton, some fundamental questions about the composition and origin of the icy satellites of Jupiter and beyond can be addressed by studying rheologies at very low temperatures.

In Figure 1 we compare the flow of several important planetary ices as measured in our laboratory over the past several years. The plot includes only the results for T < 200 K, which applies roughly to the near surface of Jupiter's icy moons and to more significant depths in the moons of Saturn and beyond. Our experiments have been done under high pressures and low temperatures that bracket conditions in the interiors and on the surfaces of the icy moons. One shortcoming of the laboratory experiments is that they fail to simulate planetary strain rates. The requirement that we develop observable strains in our samples in a reasonable time forces us to deform our samples at rates that are at best several (> 4) orders of magnitude faster than strain rates expected on the icy moons, which in turn forces us to make very large extrapolations in applying our results to the outer solar system.

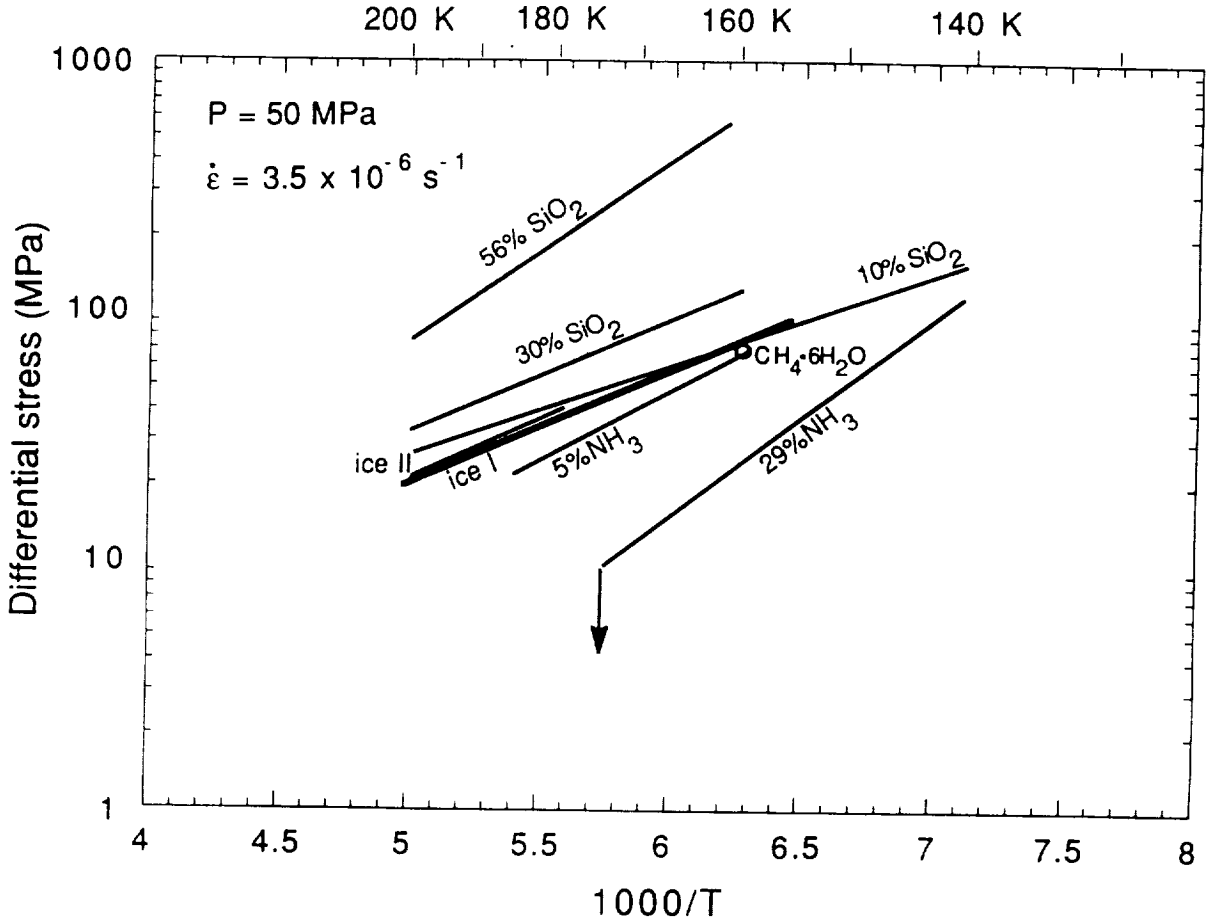

Figure 1. Laboratory results for ductile flow of planetary ices at T < 200 K. Lines shown are approximate straight-line fits to measurements (individual data not shown); no extrapolations are involved. The measurements were made at a fixed hydrostatic pressure of 50 MPa and a strain rate of 3.5×10^{-6} s^{-1} and apply to the so called "steady-state" flow regime thought to apply at absolute strains (measured from the last change in stress) above a few percent. Measurements at faster strain rates (not shown) on all these materials indicate that ductile flow under these conditions is highly non-Newtonian (see text). The downward-pointing arrow on the 29% NH_3 (pure ammonia dihydrate) line corresponds to the appearance of a melt phase that is thought to be responsible for much of the resurfacing seen on icy moons of Saturn and beyond.

RHEOLOGY OF PLANETARY ICES AT T < 200 K: Durham, W. B. and Kirby, S. H.

We have measured the flow and fracture of four varieties of planetary ices in our work to date: (1) pure water ice, including several of its high-pressure polymorphs, (2) mixtures of water ice + particulates, mainly silica, in volume concentrations of <1% to 56%; (3) ices in the system NH_3–H_2O, in concentrations of NH_3 from 1 to 29 wt%; and (4) methane clathrate, with an approximate formula $CH_4 \cdot 6H_2O$.

Because of a logarithmic scale along the differential stress axis in Figure 1, the flow laws for pure water ices I and II, water ice with low concentrations of rock and with low concentrations of NH_3, and the one point for methane clathrate are in close proximity. The differences between these rheologies are more noticeable if one prefers to think in terms of viscosity contrasts because of the strong sensitivity of strain rate ($\dot{\varepsilon}$) to stress (σ). The relationship is observed to be of the form $\dot{\varepsilon} = \sigma^n$ where $n = 4$ to 6 depending on the particular ice involved.

Outside the cluster of rheologies in the center of the figure are a spectrum of planetary materials that is many orders of magnitude more viscous: mixtures of ice and rock at volume concentrations of rock above 30%. These may help explain the slow viscous relaxation of craters on Ganymede and Callisto. There is also a spectrum of much less viscous materials: mixtures of water ice and ammonia dihydrate. The rheological contrast between the NH_3–H_2O mixtures and the other materials confirms the explanation for the absence of a tectonic activity gradient in the outer solar system. In the commonly held understanding of planetary formation, materials with lower melting temperatures condensed farther from the sun and hence have been at a large fraction of their melting points or have melted during their histories, facilitating internal flow. Thus water ice condensed at the orbit of Jupiter, while ammonia dihydrate probably condensed in significant amounts beyond the orbit of Jupiter (1). To a first approximation, the homologous temperature of the outer solar system is constant.

Preliminary results for methane clathrate suggest a break from this simple relationship. Following Lewis's (1) model for equilibrium accretion, methane clathrate is the first methane-rich phase to condense, and, at similar pressures, should appear at solar radii beyond where ammonia dihydrate first condenses. We have observed that methane clathrate at 160 K has approximately the same viscosity as water ice at that temperature (Fig. 1). At 140 K, ductile flow appears to be so difficult under laboratory conditions that brittle failure at high stresses occurs first. Given solar abundances of ammonia, water, and methane, some early models predicted significant if not dominant levels of methane clathrate with respect to ammonia dihydrate on Triton. The magnitude of tectonic activity on Triton shown in the Voyager images allows us to conclude that methane clathrate does not dominate its near-surface (say < 10-km depth) makeup.

Future studies may help clarify the situation. More complex molecules of H, C, N, and O are candidates for solid phases, as are solid N_2 and CH_4 at extremely cold temperatures. Laboratory experiments at lower strain rates will also aid with the extrapolations.

References

(1) Lewis, J. S. (1972) *Icarus, 16*, 241-252.

CLATHRATE STORAGE OF VOLATILES ON MARS:

Donald S. Musselwhite and Jonathan I. Lunine, Lunar and Planetary Laboratory, University of Arizona, Tucson, AZ 85721

Introduction: The polar caps of Mars represent the largest known reservoir for volatiles on the surface of Mars. As such, any attempt to understand the volatile budget of the planet must take into account these vast deposits. The martian polar terrains consist of two components [1]: 1) Remnant ice caps which overlie 2) Polar layered deposits. Both types of units are characterized by numerous laterally extensive horizontal layers each about 10 to 50 meters thick. The north and south terrains are both very young. From their lack of any large craters, their age is less than 10^6 years [2]. The permanent north polar caps are H_2O ice I and dust. This conclusion is based on brightness temperatures and albedo measured in 1976 during Mars' north polar summer [3]. These observations are consistent with Mars Atmospheric Water Detector data for the northern hemisphere summer [4] which detected large amounts of water vapor over the north pole -- consistent with water ice in equilibrium with a water vapor saturated atmosphere.

The composition of the permanent south polar cap is not as clear-cut as that for the northern cap. Summer brightness temperatures, albedo and atmospheric water content are consistent with CO_2 at its sublimation point [5]. But an alternative possibilty is $H_2O{\cdot}CO_2$ clathrate being the main solid volatile phase. Miller and Smythe [6] proposed this idea on the basis of Mariner 7 data and phase stabilitiy experiments for CO_2 and H_2O. The temperature and pressure over the south pole in summer is within the stability field for $H_2O{\cdot}CO_2$ clathrate in equilibrium with CO_2 vapor. In fact, under no conditions can solid CO_2 and H_2O ice coexist stably. The more recent Viking measurements discussed above are also consistent with $H_2O{\cdot}CO_2$ clathrate being the main constituent of the south polar caps. The existence of $H_2O{\cdot}CO_2$ clathrate at the south pole may explain the persistence of lower summertime temperatures above the caps compared with the north polar caps as $H_2O{\cdot}CO_2$ clathrate has approximately one-fifth the heat conductivity of pure H_2O ice.

Storage of Trace Volatiles in the South Polar Caps: To the assess the storage capacity of $H_2O{\cdot}CO_2$ clathrate under the conditions extant on Mars, we have calculated vapor/clathrate partitioning of noble gases, N_2 and CO using the equations developed by Lunine and Stevenson (1985). The abundance ratio of gas species k to l within the clathrate is given by the expression:

$$f_{kl} = \{C_{1k} \cdot P_k (1 + C_{2k} \cdot P_k + C_{2k} \cdot P_l)/ (1 + C_{2k} \cdot P_k + C_{2k} \cdot P_l) + 3 \cdot C_{2k} \cdot P_k \}$$
$$+ \{C_{1l} \cdot P_l (1 + C_{2k} \cdot P_k + C_{2k} \cdot P_l)/ (1 + C_{2k} \cdot P_k + C_{2k} \cdot P_l) + 3 \cdot C_{2l} \cdot P_l \}$$

where: C = Langmuir Constant, P = Partial Pressure, subscripts 1 and 2 refer to sites 1 and 2 in the clathrate.

The abundance ratios for each trace gas species (Ne, Ar, Kr, Xe, N_2 and CO) to CO_2 stored within the clathrate were calculated individually. Langmuir constants are based on the method of [7]. The partial pressure of each species were determined from the volume mixing ratios [8] and the temperature was assumed to be 150°K. Since the Langmuir constants were not originally determined for this temperature, most of them had to be interpolated. The results of these calculations are shown in Figure 1, expressed as moles gas species to moles CO_2 along with the ratio of each gas species to CO_2 in the atmosphere. The concentrations of Kr and Xe relative to CO_2 exceed those in the atmosphere by several orders of magnitude. The concentrations of Ar, N_2 and CO are about 10% of their atmospheric values.

In order to determine the relative importance of the south polar cap as a reservoir for these various gas species *vis a vis* the atmosphere, we need to know the total volume of clathrate in the cap. The thickness of the cap plus layered deposits from Mariner 9 radio occultation data is one to two kilometers [1]. The caps themselves are likely no more than half of this. So an upper limit of one kilometer for the thickness of the $H_2O{\cdot}CO_2$ clathrate is chosen. If the ice cap is much thinner than 10 meters, it probably would have visible bare spots in places. So an extreme lower limit of 10 meters for the thickness of the $H_2O{\cdot}CO_2$ is chosen. The actual cap thickness is presumably somewhere between these two extremes. The concentration of each species in the clathrate was calculated assuming a ratio of $H_2O{:}CO_2$ = 7:1. Calculation of the total abundance of each gas species in the caps compared with the abundance of each species in the atmosphere is shown in Figure 2 for both the upper and lower limits for the cap thickness.

The simple but important lesson to be learned from this exercise comes in assessing the trace volatile budget of Mars based on measurements of the trace volatile abundances in the martian atmosphere. Since, if indeed the south polar cap of Mars is $H_2O \cdot CO_2$ clathrate, then it also represents a more significant reservoir for Xe and possibly Kr than the atmosphere. Thus, the abundances of these gas species in the martian atmosphere are not representative of these abundances for the outgassed portion of Mars.

Figure 1:

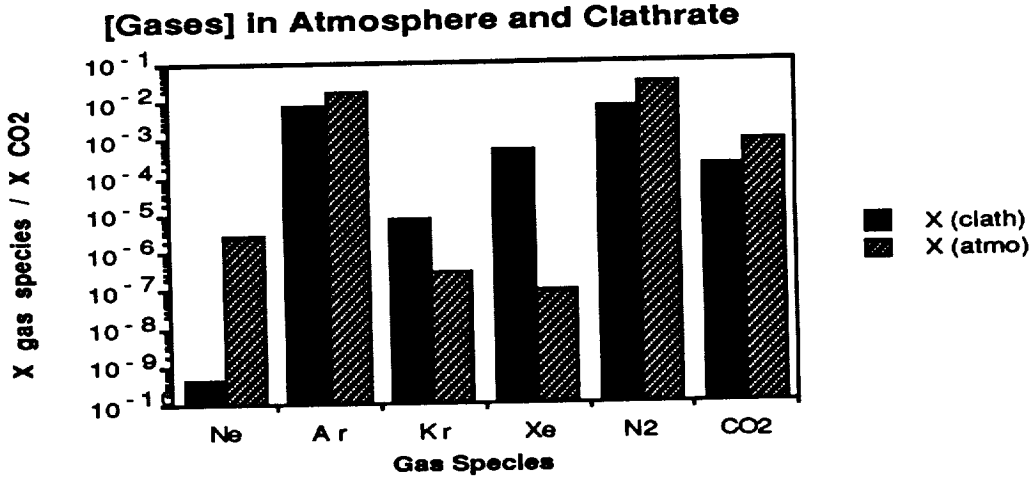

Figure 2:

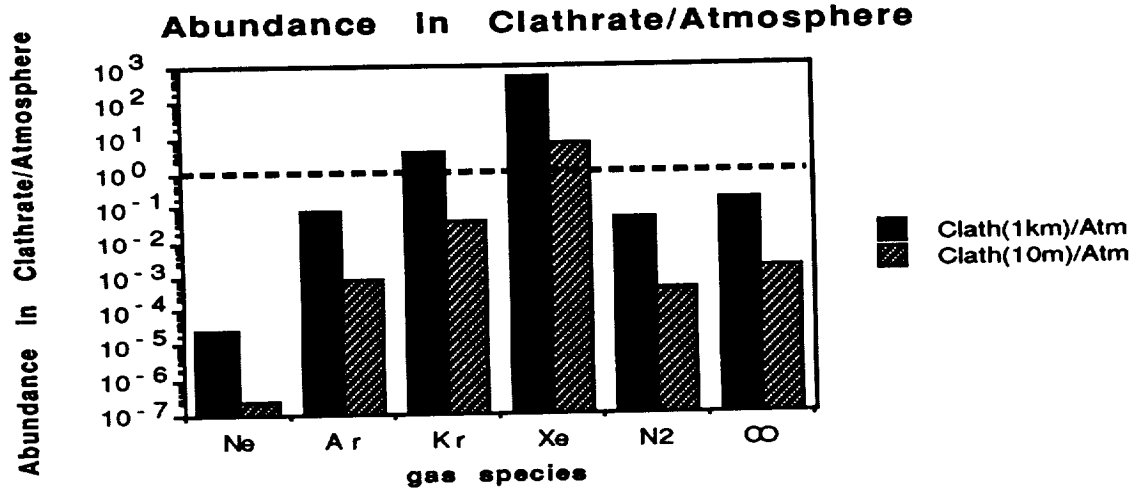

REFERENCES [1] Carr, *The Surface of Mars*, 1981 [2] Cutts *et al.* (1976) *Science*, **194**, p. 1329 [3] Kieffer *et al.* (1976) *Science*, **194**, p. 1341 [4] Farmer *et al.* (1976) *Science*, **194**, p. 1339 [5] Kieffer (1979) Mars south polar spring and summer temperatures: A residual CO_2 frost, *J. Geophys. Res.*, **84**, p. 8263 [6] Miller and Smythe (1970) *Science*, **170**, p. 531 [7] Lunine and Stevenson (1985) *Astrophys. J. Suppl. Ser.*, **58**, p. 493 [8] Chamberlain and Hunten; *Theory of Planetary Atmospheres*, 1987.

Supported by NASA Grants NAG 9-39 and NAGW 1039

ESTIMATES OF MARTIAN "OXIDANT" ABUNDANCES IN SEDIMENT SAMPLES AT THE *VIKING* LANDING SITES

James L. Gooding
SN21/Planetary Science Branch, NASA/Johnson Space Center, Houston, TX 77058.

Introduction. The life-detection experiments on the *Viking* Landers obtained apparently positive responses which, after initial evaluation as possible biological activity, were inferred to be signatures of highly reactive inorganic chemical agents in the Martian sediment samples. As reviewed by Klein [1], the complete set of results indicated that at least two (and possibly three or more) different agents occurred in the samples. Given the fundamentally different nature of the three biology experiments and their results, it was concluded that, at the minimum, the set of reactive agents possessed the capacities to evolve molecular oxygen by reaction with water, to oxidize simple organic compounds in aqueous solution, and to fix gaseous carbon dioxide into forms that are non-volatile under nominal Martian surface conditions. Despite those very different properties, the oxidization reactions received more popular attention and the reactive agents became known collectively as "oxidants". Although the experiment teams explored various explanations for the *Viking* results, derived values for the abundances of the "oxidants" were apparently never published.

The simple calculations presented here purport to use the *Viking* measurements to estimate the concentrations of reactive agents in the original sediment samples. Such estimates are needed both to support preservation plans for returned Martian samples and to assist in design of future Mars surface experiments. As will be shown, there is no single, preferred concentration value. Instead, it is found that the "oxidant" concentrations were probably in the range of a few parts per billion (ppb) to a few hundred parts per million (ppm) by weight.

Data and Assumptions. Upper limits for abundances of the reactants can be estimated from the most active samples (i.e., those giving the greatest "positive" results) in the *Viking* Lander gas-exchange (GEX), labelled release (LR) and carbon assimilation (CA; also known as pyrolytic release, PR) experiments. Other samples showed less activity, presumably because they contained lower abundances of the active chemical agents. Data used here are those reported by the original investigator teams [2-5]. Assuming a bulk density of 1.5 g/cm^3 for the delivered soil samples of specified volume, the masses of the samples analyzed were approximately 1.5 g (GEX), 0.75 g (LR), and 0.38 g (CA/PR), respectively. For simplicity, instrument-based differences between actual decay rates and measured count rates are ignored here for LR and CA/PR.

Most interpreters of the *Viking* biology results have favored one or more metal peroxides or superoxides as the active agents for the observed phenomena. Because computational results of the type presented below depend on the molecular weight (hence, identity) assumed for the oxidant and the stoichiometry assumed for the pertinent reactions, caution must be exercised in interpreting the derived numbers; they are intended to represent only the order-of-magnitude concentrations of the compounds in question. For simplicity, the following results assume the stoichiometry appropriate for alkali-metal peroxides (M_2O_2) as model reactants and express results in equivalent concentrations of H_2O_2. It should not be inferred, however, that this procedure represents an endorsement of H_2O_2 as the active agent in any of the *Viking* biology experiments. Alternative models, based on catalytic properties of clay minerals [6,7] deserve separate attention and are not treated here.

Results for GEX. The GEX, VL-1 "Sandy Flats" (first cycle, humid) sample released 790 nmol O_2 after wetting of 1 cm^3 of soil with 0.56 cm^3 of aqueous nutrients [5]. If evolution of O_2 was an inorganic process, for which the organic nutrients were simply spectators in a water/peroxide reaction, each mole of O_2 produced would require consumption of two moles of peroxide:

$$M_2O_2 + H_2O \rightarrow 1/2\,O_2 + 2\,MOH.$$

Therefore, the abundance of peroxide would be $2(7.9 \times 10^{-7}$ mol)/1.5 g = 1.05×10^{-6} mol/g sample. If the peroxide was H_2O_2 (f.w. 34.0), the implied abundance would be

$(1.05 \times 10^{-6})(34.0) = 36$ ppm.

Using laboratory simulations with photo-oxidized MnO_2 to duplicate the GEX results, Blackburn et al. [8] pointed out that 790 nmol of O_2 could be produced by only 1.9×10^{18} atoms of activated Mn. That amount would correspond to only 1.2×10^{-4} g Mn/g sample, or only 120 ppm Mn in the sample. If the oxidant was MnO_3H (f.w. 103.9), as suggested by Blackburn et al. [8], then its equivalent concentration would have been $(1.2 \times 10^{-4})(103.9/54.9) = 230$ ppm.

Results for LR. The LR, VL-2, under "Notch Rock" (third cycle) sample produced 15,500 dpm of ^{14}C after injection of 0.115 cm^3 of aqueous nutrient onto 0.5 cm^3 of sample [3]. The nutrient consisted of 7 organic compounds, each at a concentration of 2.5×10^{-4} M and with an average labelled activity of 8 μCi/μmol [2].

The carbon gas evolved (presumably CO_2) contained *at the minimum* the number of carbon atoms equivalent to the measured radioactivity. Most likely (but not substantiated by the experiment), the evolved gas also contained non-radioactive carbon in the same proportion as the ^{14}C/(total C) ratio in the original nutrients. Therefore, at least two different estimates for oxidant abundance are possible. The number of ^{14}C atoms should be related to the decay rate according to $N = (1/\lambda)(dN/dt)$, where $\lambda = 1.21 \times 10^{-4}\ y^{-1} = 2.30 \times 10^{-10}\ m^{-1}$. Therefore, using the measured activity, the minimum (all ^{14}C) "efficiency" of carbon consumption was $[(1.55 \times 10^4\ m^{-1})/(2.30 \times 10^{-10}\ m^{-1})]/[(6.02 \times 10^{23}\ mol^{-1})(0.75\ g)] = 1.49 \times 10^{-10}$ mol C/g sample. A second, higher estimate could be made by assuming that the specific activity (on a molar basis) of the evolved gas was not changed by the oxidation reaction(s). (The most plausible change, but one not addressed by the experiment, would have been mass-dependent fractionation of the carbon isotopes by oxidation). The assumption of constant specific activity in the nutrients and the evolved gas permits a gas yield of $[(1.55 \times 10^4\ m^{-1})(1\ m/60\ s)]/[8\ Ci/mol)(3.7 \times 10^{10}\ s^{-1}/Ci)(0.75\ g)] = 1.16 \times 10^{-9}$ mol C/g sample.

If the oxidation reaction involved a 1:1 molecular ratio of oxidant to nutrient (e.g., M_2O_2/HCOONa), then the decarboxylation "efficiency" number also corresponds to the moles of oxidant per gram of sample. Reducing the yields to a basis of H_2O_2 concentrations, as done above for GEX, gives the following two estimated concentrations:

$(1.49 \times 10^{-10})(34.0) = 5.1$ ppb $\qquad$ $(1.16 \times 10^{9})(34.0) = 39$ ppb.

A third estimate can be made by accepting the interpretation [1,2] that the equivalent of one ^{14}C-labelled nutrient was quantitatively oxidized by the most reactive sample. (Although partial oxidation of several different nutrients cannot be excluded by available data, quantitative consumption of the formate nutrient became the favored interpretation, because of the model simplicity offered by a one-carbon compound). Given the concentration and volume of each LR inoculation, the absolute quantity of each nutrient in the subject experiment was $(2.5 \times 10^{-4}\ mol/10^3\ cm^3)(0.115\ cm^3) = 2.9 \times 10^{-8}$ mol. Assuming the same 1:1 stoichiometry for oxidation used above and an H_2O_2 basis, the alternative estimate for the "oxidant" concentration would be

$(2.9 \times 10^{-8})(34.0)/(0.75) = 1.3$ ppm.

Results for CA/PR. The CA/PR, VL-1, "Sandy Flats" (C1) sample produced 842 dpm of ^{14}C (corrected Peak 2) after incubation of 0.25 cm^3 of sample [4] with 20 μl of ^{14}C-labelled CO_2 and CO (98:2 by volume; total activity of 22 μCi) in a 4 cm^3 test cell filled with Martian atmosphere (95% CO_2) at 7.6 mb pressure and a temperature of 17° C [2]. The ^{14}C spike increased the total cell pressure by 2.2 mb [2].

By analogy with LR, the simplest *minimum* estimate for the carbon actually fixed can be found from the number of ^{14}C atoms that were fixed. Following the first-order decay method used for LR, the minimum "efficiency" for carbon fixation in CA/PR was $[(8.42 \times 10^2\ m^{-1})/(2.30 \times 10^{-10}\ m^{-1})]/[(6.02 \times 10^{23}\ mol^{-1})(0.38\ g)] = 1.60 \times 10^{-11}$ mol C/g sample. Again, by analogy with LR (and ignoring possible mass-dependent fractionation of carbon during reaction), an alternative estimate can be made by assuming no change in specific molar activity during carbon fixation (i.e., Martian CO_2 was fixed along with the labelled

CO_2). For ideal gas behavior, the total activity per mole of CO_2 in the cell before reaction would be $(2.2 \times 10^{-5}$ Ci)/[((7.6 + 2.2)/1013 atm)(4 x 10^{-3} l)(0.95)/(8.21 x 10^{-2} l atm K^{-1} mol^{-1})(290 K)] = 1.42 x 10^{1} Ci/mol. From the measured ^{14}C activity in the fixed carbon, the "efficiency" of fixation would follow as [(8.42 x 10^{2} m^{-1})(1 m/60 s)]/[(1.42 x 10^{1} Ci/mol)(3.7 x 10^{10} s^{-1}/Ci)(0.38 g)] = 7.03 x 10^{-11} mol C/g sample.

The experiment team originally suggested [2] a conversion factor of (2.6 x 10^{-11} mol CO_2/81 dpm) = 3.2 x 10^{-13} mol C/m^{-1} ^{14}C which, by the reasoning presented here, would have led to a fixation "efficiency" of (3.2 x 10^{-13})(8.42 x 10^{2})/(0.38) = 7.09 x 10^{-10} mol C/g sample.

On an H_2O_2-equivalent basis, the consequent estimates for fixation-reactant concentration according to these three different model assumptions would be

$$(1.60 \times 10^{-11})(34.0) = 0.54 \text{ ppb} \qquad (7.03 \times 10^{-11})(34.0) = 2.4 \text{ ppb} \qquad (7.09 \times 10^{-10})(34.0) = 24 \text{ ppb.}$$

An additional complication exists in CA/PR because CO is not distinguished from CO_2 among the reactants and products [2,4]. Because the $^{14}CO_2$ in the experimental gas spike possessed a lower specific activity than the ^{14}CO, the three estimates given immediately above could actually be lower (by as much as a factor of 3) if CO was a major reaction participant [4].

It is important to note that, as originally pointed out by the experiment team [2,4], the active agent detected by the CA/PR experiment might not be an "oxidant". In principle, either an oxidizing or reducing agent (or a third category, "organic-synthetic catalyst") might have produced the carbon fixation.

Summary and Conclusions. The simplest interpretations (i.e., those with the fewest model assumptions) of the three *Viking* biology experiments imply abundances for the unidentified oxidants/reactants comprising 36 ppm (GEX), 5 ppb (LR), and 0.5 ppb (CA/PR), when expressed in equivalent concentrations of H_2O_2. The LR and CA/PR results, in particular, are open to a wide range of model assumptions that can support other H_2O_2-equivalent concentrations up to 24 ppb (CA/PR) or 1 ppm (LR). The values so derived are fundamentally uncertain because both the molecular weights of the reactants and the stoichiometry of the subject reactions remain unknown. The important point is not the specific number values but the fact that the chemical agents responsible for the Viking biology results occurred at exceedingly small concentrations. Even if several different oxidants/reactants were involved, they would require either very high molecular weights (at least 10 times that of H_2O_2) or disproportionately large reaction coefficients (i.e., high reactant/evolved-gas ratio) in order for their total concentrations to exceed a few hundred ppm by weight in the samples.

The trace levels of the "oxidants" must be appreciated both for Mars sample-return missions and for design of future *in situ* Mars sample analyzers. It will be scientifically important to carefully preserve at least some subset of samples in a way that maximizes the opportunity to study these rare, metastable compounds in the laboratory; their low abundances will mean that they may be difficult to isolate for identification. Any experiments proposed to identify the "oxidants" *in situ* must be able to perform diagnostic analyses of analytes that occur at the ppb to ppm levels.

References: [1] Klein H. P. (1978) The Viking biological experiments on Mars. *Icarus, 34,* 666-674. [2] Klein H. P., Horowitz N. H., Levin G. V., Oyama, V. I., Lederberg J., Rich A., Hubbard J. S., Hobby G. L., Straat P. A., Berdahl B. J., Carle G. C., Brown F. S., and Johnson R. D. (1976) The Viking biological investigation: preliminary results. *Science, 194,* 99-105. [3] Levin G. V. and Straat P. A. (1976) Viking labelled release biology experiment: interim results. *Science, 194,* 1322-1329. [4] Horowitz N. H., Hobby G. L., and Hubbard G. S. (1977) Viking on Mars: the carbon assimilation experiment. J. Geophys. Res., 82, 4659-4662. [5] Oyama V. I. and Berdahl B. J. (1977) The Viking gas exchange experiment results from Chryse and Utopia surface samples. *J. Geophys. Res., 82,* 4669-4676. [6] Banin A. and Margulies L. (1983) Simulation of Viking biology experiments suggest smectites not palagonites as martian soil analogues. *Nature, 305,* 523-525. [7] Burt D. M. (1989) Iron-rich clay minerals on Mars: Potential sources or sinks for hydrogen and indicators of hydrogen loss over time. *Proc. 19th Lunar Planet. Sci. Conf.,* 423-432. [8] Blackburn T. R., Holland H. D., and Ceasar G. P. (1979) Viking gas exchange reaction: simulation on UV-irradiated manganese dioxide substrate. *J. Geophys. Res., 84,* 8391-8394.

RHEOLOGICAL PROPERTIES OF MARTIAN MAGMAS: EXPERIMENTS AND INFERENCES

Frank J. Spera and Daniel J. Stein, Department of Geological Sciences
and Institute for Crustal Studies, University of California,
Santa Barbara, California 93106, U.S.A.

Virtually every magma transport process of relevance to planetary magmatism and volcanism involves the diffusion of momentum. The rheological properties of both melts (single phase) and magmatic multiphase mixtures (melt plus crystals, melt plus vapor, etc.) are consequently of primary importance when evaluating the thermal history and volcanic evolution of a planetary body. Dynamic processes such as the extraction of melt from a source region, the propagation and ascent of melt or magma filled cracks, the convective dynamics of magma bodies, and the eruption of magma upon the surface of a planet cannot be quantitatively addressed unless accurate constitutive relations which properly account for the variation of rheological parameters with temperature, pressure, bulk composition, oxygen fugacity, the volume fraction and size and shape characteristics of suspended crystals and vapor bubbles are available. An approach based on both theory and experiment has proven to be most fruitful in the search for generally applicable models. Experimental concentric cylinder viscometry on a model Martian mafic magma (MMM) of shergottitic bulk composition (~50% SiO_2, 20% FeO_t, 10% MgO) at a range of hyperliquidus to near liquidus temperatures and fo_2's along QFM indicate that MMM behaves as a Newtonian fluid in the shear rate range 0.5 to 10 s^{-1}. The fraction of ferrous iron relative to total iron as an oxide is about $\omega_{FeO}/(\omega_{FeO} + \omega_{Fe_2O_3}) \approx 0.85$ along QFM (Sack et al., 1980) at 900 to 1300°C with melts being slightly more reduced at the high temperature end of the quoted range and where ω_{FeO} is the mass fraction of FeO in the melt. In the temperature range 1200°C < t < 1300°C, the activation energy is 165 ± 4 kJ/mole and the viscosity is given by $\eta = 2.25 \times 10^{-5} \exp(20150/T)$ where T is in kelvins and η is in Pa•s. The models of Shaw (1972) and Bottinga and Weill (1972) predict viscosity numbers smaller by about a factor of three compared to experimental values; the Shaw model predicts the experimental value of the activation energy within experimental error, however. In other concentric cylinder experiments, the rheometric properties of solid plus melt and melt plus vapor magmatic mixtures have been studied. It is important to note that multiphase suspensions (s + m) and emulsions (m + v) are much more difficult to characterize compared to melts because of a number of experimental difficulties including differential solid-melt velocity, violation of the no-slip velocity boundary condition, the relative instability of bubble emulsions with respect to shear and the difficulty in preparing homogeneous monodisperse melt plus vapor emulsions. Although these are not trivial problems, methods do exist to overcome or at least mitigate them. High-quality rheometric data support the following conclusions. At relatively low shear rate, crystal-melt suspensions behave as Newtonian materials but with an apparent viscosity that depends on the volume fraction (ϕ), size and shape distributions of suspended crystals. Unless particles are highly inequant (e.g., long acicular

needles) treating particles as equivalent spheres is a reasonable approximation. The relative apparent viscosity, defined according to $\eta_r = \eta/\eta_m$ where η is the viscosity of the suspension and η_m is the viscosity of the host melt (which changes with T,P and composition) varies with volume fraction crystals (ϕ) normalized by the maximum solid loading level, ϕ_m according to $\eta_r = (1 - \phi/\phi_m)^{-2}$ (Maron and Pierce, 1956). In monodisperse systems (i.e., same-sized spheres) the theoretical close-packed loading upper bound for ϕ_m is 0.74 corresponding to body-centered cubic packing. A random cubic packing gives $\phi_m = 0.52$ for smooth spheres and 0.44 for rough spheres. Experiments, which naturally allow for micropores and misalignments generally give values in the range $0.60 < \phi_m < 0.70$. In polydisperse systems, maximum loading values are always greater compared to monodisperse values. It is suggested that, for magmatic suspensions of polydisperse, non-spherical crystals, $\phi_m = 0.60$ based on experimental studies. The yield stress concept has been discussed recently in the rheological literature (Barnes and Walters, 1985; Hartnett and Hu, 1989; Astarita, 1990) with the conclusion being that one may assign an apparent yield stress that, in fact, depends on the shear rate range of the experiment. Examination of available data suggests that for $1\ s^{-1} < \gamma < 200\ s^{-1}$ the apparent yield stress (σ_ϑ) varies with ϕ, the fraction of solids according to $\tau_o = 4500\ \phi^{2.7}$ whereas for $10^{-2}\ s^{-1} < \gamma < 1\ s^{-1}$ and $0.1 < \phi < 0.6$ the relation $\tau_o = 750\ \phi^{3.5}$ recovers data better. For $\phi > 0.6$, experiments in this laboratory suggest $\tau_o = 13.8 + 8.1 \ln \phi$ when $\gamma \sim 10 s^{-1}$. Finally, recent experimental work on dilute mixtures of viscous melt plus vapor bubbles indicates linear constitutfive behavior with $\eta_r = (1 - k\phi)^{-5/2}$ with $k \approx 4$ and no detectable yield strength in the range $0.01 < \phi < 0.10$ where ϕ is the volume fraction of vapor in the two phase dilute emulsion.

References

Astarita, G., Letter to the Editor: The Engineering Reality of the Yield Stress, Jour. Rheology 34(2), 275-277, 1990.

Barnes, H.A., et al., The Yield Stress Myth, Rheol. Acta 24, 323-326, 1985.

Bottinga, Y., et al., The Viscosity of Magmatic Silicate Liquids: A Model for Calculation, Am. Jour. Sci., 272, 438-475, 1972.

Chong, J.S., et al., Rheology of Concentrated Suspension, Jour. Appl. Poly. Sci., 15, 2007-2021, 1971.

Hartnett, J., et al., Technical Note: The Yield Stress - An Engineering Reality, Jour. Rheology 33(4), 671-679, 1989.

Maron, S.H., et al., Viscosity of Suspension, J. Colloid. Sci., 8, 80-86 1956.

Sack, R.O., et al., Ferric-Ferrous Equilibria in National Silicate Liquids at 1 Bar, Contrib. Mineral Petrol., 75, 369-376, 1980.

Shaw, H.R., Viscosities of Magmatic Silicate Liquids: An Emperical Method of Prediction, Am. Jour. Sci., 272, 870-893, 1972.

EXPERIMENTAL STUDIES OF MARS (SNC) BASALT PETROGENESIS AND C-O-H GAS SOLUBILITIES. Malcolm J. Rutherford, Marie C. Johnson and Robert A. Fogel, Dept. of Geological Sciences, Brown University, Providence, RI, 02912

INTRODUCTION. The experimental work described in this abstract is primarily from two Ph.D. theses submitted by the second and third authors in 1989 and 1990.

SNC BASALT CRYSTALLIZATION CONDITIONS. The intensive parameters of SNC petrogenesis are difficult to estimate because the SNC's are cumulate rocks and many of them, *i.e.*, Chassigny and the nakhlites, are virtually monomineralic. Clues to these parameters, however, can be deduced from studying melt inclusions, droplets of melt that were trapped by growing phenocrysts, and combining these data with experimental data. Melt inclusions have been identified in Chassigny, Shergotty, and Zagami (1, 2). The melt in these inclusions has crystallized to varying degrees. Since crystallization occurred in a closed system, the phases should reflect the intensive parameters (pressure, temperature, oxygen and water fugacity) that controlled SNC crystallization. As part of this study, the phases within melt inclusions in Chassigny USNM 624-1 and Shergotty USNM 321-1 were extensively analyzed with an electron microprobe. In addition, phase equilibrium experiments were conducted to deduce the intensive parameters associated with SNC petrogenesis and evolution.

SNC MELT INCLUSIONS. Chassigny melt inclusions were trapped by olivine crystals. Most Shergotty melt inclusions were trapped by pigeonite crystals, but some inclusions are found in augite and whitlockite. In both meteorites, the melt inclusions now consist of pyroxenes, amphiboles, oxides, sulfides, phosphates, and glass.

As indicated by previous studies (1, 2), the amphiboles in these inclusions are true kaersutites (>5 wt.% TiO_2) and are hydrous. Core-to-rim traverses across individual kaersutites reveal that they are homogenous. The kaersutites in Chassigny and Shergotty melt inclusions, however, differ (Table 1). A biotite crystal (Table 1) was identified and analyzed in the one of the largest Chassigny melt inclusion. This biotite is extremely titaniferous and has a Mg* identical to the kaersutite.

Both orthopyroxene and clinopyroxene occur in the Chassigny melt inclusions (Fig. 1). These pyroxenes have homogeneous Fe/Mg ratios, but highly variable Al_2O_3 and TiO_2 contents (Fig. 2). The pyroxenes that coexist with kaersutite are indicated by open symbols and these tend to have the highest Al_2O_3 and TiO_2 contents. Host pigeonites and augites and pyroxenes in Shergotty melt inclusions are also plotted in Fig. 1. The host pyroxenes are zoned with MgO-rich cores and FeO-rich rims, but the pyroxenes in the melt inclusions all have Fe/Mg ratios of ~.78. The melt inclusion pyroxenes have widely varying Wo contents reflecting significant differences in CaO (5 - 15 wt.%). These pyroxenes are similar to the extremely FeO-rich pyroxferrites found in some lunar basalts. Averages of all Chassigny orthopyroxenes and clinopyroxenes are reported in Table 1, and a representative Shergotty pyroxene is also listed.

Most of the oxides in Chassigny both within melt inclusions and in the bulk meteorite are chromites. These chromites have highly variable compositions indicating that they were liquidus phases over a significant crystallization interval. Oxides in Shergotty melt inclusions are ilmenites, magnetites, or hercynites. Ilmenite and magnetite are found in the bulk meteorite but hercynite is not. Hercynite often appears as rims on magnetite cores in the inclusions (1).

The crystalline phases in Chassigny and Shergotty melt inclusions are surrounded by a glassy-looking isotropic phase. This phase tends to be homogenous within a melt inclusion but varies in composition between different melt inclusions. In Chassigny, regions with albite stoichiometry were identified as well as low-SiO_2 rhyolitic glasses (Table 1). In Shergotty, high-SiO_2 rhyolitic glasses were identified (Table 1). These isotropic regions are believed to represent the melt inclusion mesostasis that was shock melted and possibly mixed with other shock melted phases.

Mass balance equations involving the compositions of the Chassigny melt inclusion phases were combined with experimentally determined distribution coefficients to calculate the original trapped melt composition for Chassigny (51% SiO_2, 7.6% Al_2O_3, 6.5% CaO, and 1.1 wt. % H_2O). The

Fe/Mg ratio of this liquid was adjusted to be in equilibrium with Fo_{88} olivine. The major element chemistry of this liquid is a very FeO–rich basalt; the closest terrestrial analogue is a boninite.

EXPERIMENTAL RESULTS. The natural melt inclusion minerals constrain the intensive parameters associated with Chassigny and Shergotty crystallization. These constraints were used to guide the phase equilibrium experiments. For example, two pyroxene geothermometry (3) applied to the Chassigny melt inclusion pyroxenes with the lowest Al_2O_3 contents yields temperatures of 1000°C. For Shergotty, two oxide geothermometry and oxygen geobarometry (4) indicate that crystallization temperatures were 960° to 930°C, and the oxygen fugacity was 0.5 log units below QFM. Textural and impact excavation studies both indicate that the SNC's are the products of low–pressure crystallization. Therefore, phase equilibrium experiments designed to stabilize kaersutite in equilibrium with different melts were run at 1 and 2 kbar pressures and buffered at QFM. The amphibole liquidus is 960°C consistent with the temperatures indicated by the natural minerals. Once kaersutite begins to crystallize, the melt SiO_2 contents evolve substantially consistent with the high–SiO_2 glasses found in the melt inclusions. The existence of hydrous igneous kaersutite requires that substantial water (>4 wt.%) was dissolved in the coexisting melt (5). Water undersaturated experiments at 2 kbar indicate that the stability field of amphibole plus melt is drastically limited as water fugacity is reduced. These results suggest that water fugacity was at least 940 bars to stabilize amphibole at the temperatures indicated. Mass balance indicates that the liquid trapped initially contained slightly more than 1 wt. % water.

CO_2 AND CO SOLUBILITY IN SILICIC MELTS. The solubilities of CO_2 and CO in rhyolite liquid have been determined using quantitative fourier transform infrared spectroscopy. Initial experiments were conducted along the 950°C, 1050°C and 1150°C isotherms at pressures between 500 to 6600 bars under CO_2 saturated conditions. The 2350 cm^{-1} band was used for quantitative CO_2 concentration determinations. The 1050°C isotherm was investigated in greatest detail. Along this isotherm CO_2 solubility is ideal (in the Henrian sense) up to roughly 2300 bars. Above this pressure deviations from ideality are prominent, with concentrations less than predicted by extrapolation of the linear form of Henry's Law. Interestingly, the effect of increasing temperature is to decrease the solubility of molecular CO_2, similar to the behavior of albite melts (Stolper et al., 1987). The maximum water contents of the rhyolite were 0.30 wt % and the presence of small amounts of H_2O has no apparent effect on CO_2 solubility.

The solubility of CO_2 in rhyolite can be modeled with a modified Henry's Law equation that covers the entire P-T range investigated. This expression requires the selection of a reference T and P which was chosen as 1323°K and 0 bars, respectively. The data were regressed to determine the partial molar volume ($\bar{v}$) and heat of solution (Δh) of dissolved CO_2 yielding values of 33.62 $\pm$ 0.98 cm^3/mole and -20.18 $\pm$ 3.99 kJ/mole, respectively.

Samples retained their original shapes throughout the experiments. This, as well as the detection of CO_2 diffusion profiles in various samples, indicates that the approach to equilibrium was limited solely by the process of diffusion. The melt viscosities were apparently high enough to hinder CO_2(fluid)-melt equilibration by silicate mixing. The diffusion coefficient of CO_2 in rhyolite at 1050°C was estimated in three charges to be 2.4 ($\pm$ 0.5) X 10^{-8} cm^2/sec, in close agreement with the work of Watson et al. (1982) on CO_2 diffusion in silicate melts of somewhat different composition.

Infrared bands attributable to dissolved carbonate complexes were not detected under any of the experimental conditions. This is consistent with the general decrease in the carbonate to CO_2(molecular) ratio in the sequence basalt, andesite, rhyodacite, rhyolite investigated in this laboratory. Basalt, the most primitive composition, dissolves CO_2 solely in the form of carbonate complexes, whereas the highly evolved member of this sequence, rhyolite, dissolves CO_2 exclusively in the molecular form. A comparison of these new data for CO_2 solubility in rhyolite with data for CO_2 solubility in basalt (Stolper and Holloway, 1988) shows that both on a mole fraction and weight percent basis, slightly more CO_2 dissolves in rhyolite than in basalt. The contention of many

workers that CO_2 is more soluble in mafic magmas than it is in more evolved compositions is clearly incorrect.

REFERENCES. (1) Treiman, A. H. (1985) *Meteoritics, 20*, 229-243. (2) Floran, R. J. et al., (1978) *Geochem. Cosmochem. Acta, 42*, 1213-1229. (3) Lindsley, D. H.(1983) *Amer. Miner., 68*, 477 - 493. (4) Andersen, D. J. and Lindsley, D. H.(1988) *Amer. Miner., 73*, 714 - 726. (5) Merzbacher, C. and Eggler, D. H. (1984) *Geology, 12*, 587 - 590. (6) Stolper, E. et al., (1987) *Am. Mineral., 72*: 1071-1085.

Table 1. SNC melt inclusion compositions.

	SiO_2	TiO_2	Al_2O_3	FeO	MgO	CaO	Na_2O	K_2O	MnO	Tot
					Chassigny					
kaer	39.49	7.00	14.22	10.47	11.53	11.80	2.99	0.33	0.17	98.00
biot	35.71	8.86	13.12	12.12	14.09	0.01	0.17	8.39	0.07	92.55
opx	52.70	0.43	2.86	16.40	25.36	1.61	0.06	0.02	0.50	100.13
cpx	49.70	1.39	4.93	7.64	14.32	20.43	0.58	0.02	0.29	99.74
plag	66.38	0.09	21.07	0.52	0.04	1.19	10.61	0.10	0.00	100.00
glass	71.04	0.18	16.75	0.67	0.06	1.22	5.72	4.37	0.02	100.00
					Shergotty					
kaer	35.15	8.90	15.65	19.79	5.73	11.32	2.32	0.11	0.36	99.31
pyx	47.87	0.50	0.63	38.74	5.86	5.93	0.05	0.00	0.91	100.49
glass	76.66	0.23	12.80	0.95	0.02	1.37	1.96	5.95	0.06	100.00

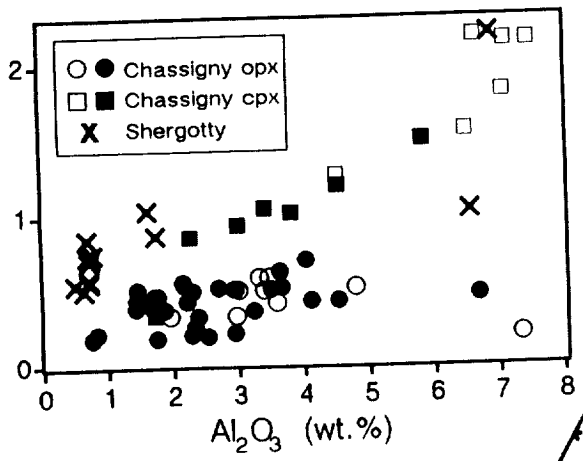

Figure 2

Figure 1

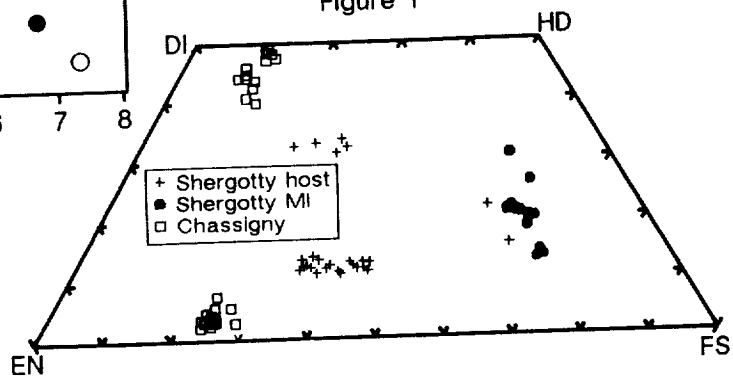

MAGMATIC SULFIDES ON MARS

Roger G. Burns
Department of Earth, Atmospheric and Planetary Sciences,
Massachusetts Institute of Technology, Cambridge MA 02139.

Introduction. Basalts typically contain 0.1-0.2 wt. % sulfur [1]. Shergottite meteorites believed to have originated from Mars rarely exceed 0.2 wt. % S [2]. However, the Viking XRF experiment measured ~3 wt. % S in martian fines [3]. These abundance data summarized in Table 1 for surface materials on Mars pose a dilemma [4]: if the sulfur originated from chemical weathering of basaltic parent rocks, whence did such high concentrations of sulfur in martian regolith originate? One source is SO_2 in volcanic exhalates which, upon reaction with H_2O vapor, produced H_2SO_4 aerosols in acid rain, induced chemical weathering of the surface rocks, and led to the accumulation of sulfate-bearing materials [4].

Another possibility is that deep-weathering reactions of sulfide mineralization associated with underlying ultramafic igneous rocks has generated the oxidized ferric- and sulfate-bearing materials observed on Mars' surface [5]. Clues that these rocks might have been the source of high sulfur contents on Mars are provided by paragenetic relationships between komatiitic basalts and the deduced parent rock-type of martian regolith fines [6,7] and of SNC meteorites [8,9]. On Earth, Archean komatiites host pyrrhotite-pentlandite (± chalcopyrite, pyrite) assemblages which occur as disseminated veins or stratabound lenses at the base of ultramafic flows. The possibility that such Fe-Ni sulfide mineralization occurs in ultramafic and mafic rocks on Mars is examined here.

Since basaltic magma erupting onto surfaces of terrestrial planets such as Mars are partial-melt derivatives of the mantle, properties that need to be evaluated include: (1) the abundance of sulfur in the mantle; and (2) the solubility of sulfur in derived partial melts.

The Sulfur Budget of Mars. Mars probably formed by accretion of carbonaceous chondritic material, so that the abundance of sulfur in the undifferentiated planet would have been ~6 wt. % S. However, core-formation fractionated a considerable proportion of this sulfur into the core; amounts exceeding 15 wt. % S and precluding a solid inner core could explain the apparent lack of a magnetic field on Mars [10]. The observation that SNC meteorites appear to be depleted in several chalcophilic and siderophilic elements has led to the suggestion that such metals are enriched in the sulfur-rich core of Mars, which was estimated to contain 14.24 wt. % S [11]. If the core radius of Mars is assumed to be approximately half the radius of the planet, simple mass balance calculations by the author show that roughly 4.5 wt. % S would remain in the martian mantle after core formation. Therefore, there was probably adequate sulfur remaining in the mantle to be transported to the surface of Mars by magmatic activity.

Sulfur Solubility in Silicate Melts. Experimental measurements [12-17] have demonstrated that the solubility of sulfur in sulfide-undersaturated silicate melts increases with rising temperature, FeO content, and sulfur fugacity, but is reduced by increased silica content, oxygen fugacity, and oxidation of ferrous to ferric iron in the melt. Sulfur solubility is, thus, positively correlated with FeO, TiO_2, MgO and CaO, but negatively with SiO_2, Al_2O_3, Fe_2O_3, Na_2O and K_2O [12]. In sulfide-saturated silicate melts, S solubilities decrease with increasing f_{S2} and decreasing f_{O2}. These trends for S in anhydrous melts are apparent in Table 1 and Figure 1. The effect of increasing pressure, however, remains ambiguous [15-18]. In silicate melts that were equilibrated at oxygen fugacities controlled by the quartz-fayalite-magnetite (QFM) buffer, sulfur predominates as dissolved S^{2-} or HS^- in hydrous magmas [17]. Under more oxidizing conditions corresponding to 2 or more *log* f_{O2} units above the QFM buffer, sulfate species predominate. Compositions of coexisting Fe-Ti oxides in SNC meteorites suggest that they equilibrated under oxygen fugacities near the QFM buffer [2]. Therefore, since SNC meteorites are also volatile-rich [11], the sulfur that was dissolved in parent basaltic melts on Mars probably existed as S^{2-} and HS^-, although a small fraction might have been present as SO_4^{2-} [19].

The ranges of sulfur solubility shown in Figure 1 indicate that melts with 17-22 wt. % FeO (corresponding to compositions of most SNC meteorites and to mafic rocks deduced from XRF measurements of the martian regolith) are saturated with ~0.2 wt. % S at 1200°C. However, the trends suggested by Figure 1 indicate that above 1400°C, an excess of 1 wt. % S could be

dissolved in sulfide-saturated, low Al_2O_3, iron-rich basaltic melts equilibrated at f_{O_2}'s controlled by the QFM buffer.

The Fe/(Fe + Mg) ratio of the martian mantle was deduced to be significantly higher than that of the Earth's mantle [6,20], suggesting that partial melting may have produced iron-rich basaltic magmas with very low viscosities that would possess high sulfur solubilities. Recent experimental measurements suggest that anhydrous martian mantle primary melts formed at a minimum melting temperature of 1400°C at 23 kb contain 23.3 wt. % FeO [21]. Melts formed at comparable P and T but containing only 12 wt. % FeO dissolved ~ 0.23 wt. % S [15]. The sulfur solubilities in more iron-rich martian melts at high pressures could be much higher, perhaps exceeding 1 or 2 wt. % S in hydrous melts, but would probably be unsaturated relative to the ~4.5 wt. % S calculated earlier to remain in the martian mantle after core formation.

Emplacement of Magmatic Sulfides. Terrestrial komatiites provide clues to the emplacement mechanism of sulfur-rich basaltic magma derived by partial melting of the martian mantle. On Earth during the Archean era when radiogenic heat production was significantly higher than it is now, ultramafic magmas formed by rapid adiabatic emplacement from depths exceeding 200 km were extruded at high temperatures (1350-1700°C). Sulfur saturation of the ultramafic magmas occurred as they cooled near the surface, leading to the separation of immiscible FeS liquids, gravitational settling and riffling out of the sulfides as the lavas advanced over surface depressions, and the formation of pyrrhotite-pentlandite deposits. Very low viscosity komatiitic lavas may have flowed turbulently at high extrusion temperatures accompanied by vigorous convection forces with rapid cooling rates [22]. These lavas could also have melted and assimilated large portions of undersaturated sulfur-rich sediments, forming the deep erosion channels into which immiscible FeS liquids subsequently settled.

A similar scenerio has been proposed for Mars [2,8]. Close analogies between certain SNC meteorites and komatiites suggest that volcanism on Mars generated ultramafic lava flows and shallow intrusions, and that *in situ* magmatic crystallization produced pyroxene-olivine cumulate rocks represented by nakhlites and chassignites [8]. Flows of the nakhlite parent magma were envisaged to have erupted from shield volcanos and flood basalt provinces and to have flowed over rough terrains left by previous flows producing magma lakes in which crystal cumulates were formed. Under these conditions, fractional crystallization of sulfides would also occur, leading to localized concentrations of pyrrhotite-pendlandite assemblages by riffling out from successive flows, although the lower gravitational field on Mars would have inhibited massive ore formation. Eruption of these ultramafic lavas as hot, highly fluid, turbulent melts could also account for the enormous lateral extent of martian flows [23], which might have eroded deep channels on Mars, assimilating early sulfate-enriched duricrust and re-precipitating fresh sulfide deposits in structural depressions.

Evolution of Sulfides on Mars. Magmatic sulfide deposits did not evolve on Mars to the same extent as they have on Earth due to insignificant plate tectonic activity there [25]. Interactions of martian mantle with crust, hydrosphere, and atmosphere have been minimal, so that ore deposits such as porphyry copper and molybdenum, granite-hosted mineralization, and sediment-hosted galena-sphalerite assemblages did not form on Mars. Cumulate igneous chromites may occur on Mars, however, as indicated by textures observed in SNC meteorites.

References [1] *Basaltic Magmatism on Terrestrial Planets* (1981); [2] H.Y.McSween, *Rev. Geophys.*, *23*, 391 (1985); [3] B.C.Clark *et al.*, *JGR*, 87, 10059 (1982); [4] B.C.Clark & A.K.Baird, *JGR*, *84*, 8395 (1979); [5] R.G.Burns, *Proc. 18th LPSC*, 713 (1988); [6] T.R.McGetchin & J.R.Smyth, *Icarus*, *34*, 512 (1979); [7] A.K.Baird & B.C.Clark, *Icarus*, *45*, 113 (1981); [8] A.H.Treiman, *GCA*, *50*, 1061 (1986); [9] J. Longhi & V.Pan, *Proc. 19th LPSC*, 451 (1989); [10] G.Schubert *et al.*, *4th Intern. Conf. Mars, Abstr.*, 50 (1989); [11] G. Dreibus & H. Wanke, *Icarus*, *71*, 225 (1987); [12] D.R.Haughton *et al.*, *Econ. Geol.*, *69*, 451 (1974); [13] D.L.Buchanan & J.Nolan, *Canad. Min.*, 17, 483 (1979); [14] H.Shima & A.J.Naldrett, *Econ. Geol.*, 70, 960 (1975); [15] R.F.Wendlandt, *Amer. Min.*, 67, 877 (1982); [16] M.R.Carroll & M.J.Rutherford, *JGR*, *90*, C601 (1985); [17] *Idem, Amer. Min.*, *73*, 845 (1988); [18] B.O.Mysen & R.K.Popp, *Amer. J. Sci.*, 280, 78 (1980); [19] R. Burgess *et al.*, *EPSL*, *93*, 314 (1989); [20] J.W.Morgan & E.Anders, *GCA*, *43*, 1601 (1979); [21] C.M.Bertka & J.R.Holloway, *Proc. 19th LPSC*, 723 (1988); [22] H.E.Huppert *et al.*, *Nature*, *309*, 19 (1984); [23] A.K.Baird & B.C.Clark, *Nature*, *311*, 18 (1984); [24] R.G.Burns & D.S.Fisher, *MEVTV/LPI Tech. Rept.*, *89-04*, 20 (1989), *JGR*, in press; [25] R.J.Floran *et al.*, *Geochim. Cosmochim. Acta*, 42, 1213 (1978); [26]
Supported by NASA grants NSG-7604 & NAGW-1078.

Table 1. Chemical analyses of sulfur-bearing basaltic rocks and melts

	[1]	[2]	[3]	[4]	[5]	[6]	[7]	[8]	[9]
SiO_2	46.5	49.00	44.7	55.5	51.54	39.64	45.6	45.93	41.9
TiO_2	0.2	1.23	0.8	0.4		0.78		3.73	
Al_2O_3	3.6	9.93	5.7	12.0	7.81	29.64	8.75	11.67	11.9
Fe_2O_3	1.0	0.22	18.2					4.06	
FeO	9.4	16.90		9.3	19.50	18.14	12.43	13.36	23.3
MgO	33.0	7.32	8.3	12.6	7.98	0.42	22.95	4.23	12.7
CaO	5.1	11.00	5.6	2.13	11.77	7.73	7.73	8.81	9.4
Na_2O	0.5	1.68	(2.)	4.1		2.64	0.50	2.40	0.8
K_2O	0.2	0.09	<0.3	1.93		0.63		1.28	
others	0.6	1.86	~1.0	0.82				2.07	
S	0.1-0.2	0.22 (0.19)	~2.5-4.0	0.18	0.32	0.245	0.27 (0.47)	0.225 (0.26-0.18)	

[1] Komatiite, Komati, Sth. Africa [ref.1]
[2] Shergottite EETA 79001, lith.B. (lith.A: S = 0.19%) [2]
[3] Viking XRF analysis [3,4]
[4] Chassigny, melt inclusions in olivine [25]
[5] Synth. melt, T = 1200°C, $\log f_{O_2} = -11.50$, $\log f_{S_2} = -3.0$ [13]
[6] Synth. melt, T = 1350°C, $\log f_{O_2} = -8.02$, $\log f_{S_2} = -1.06$ [12]
[7] Synth. ultramafic melt, T = 1450°C, $\log f_{O_2} = -10.4$, $\log f_{S_2} = -2$ (estimated: 0.47% S when $\log f_{O_2} = -9.2$, $\log f_{S_2} = -0.7$) [14]
[8] Goose Is. basalt, T = 1420C, P = 20kb, $\log f_{O_2} = -9$, $f_{S_2} = 1$bar, FeO(melt) = 12 wt,% (At P = 12.5 & 30kb, FeO = 11 & 14%, S = 0.26 & 0.18%) [15]
[9] Estimated martian mantle primary melt [21]

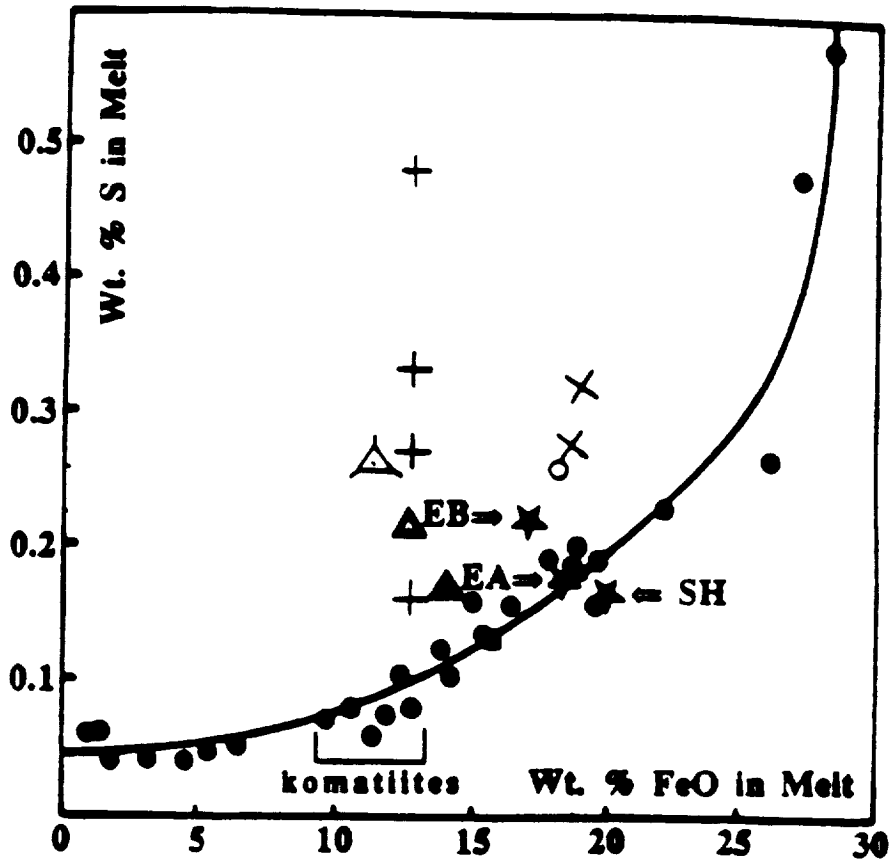

Figure 1. Sulfur solubility versus FeO contents of basaltic melts. O & O: 1200°C & 1350°C [12]; X: 1200°C [13]; +: 1450°C [14]; △, ▲ & ▲: 1420°C at 12.5 20 & 30 kb [15]; SH = Shergotty; EA and EB = EETA 79001, lithologies A and B [2].

CLASTS IN LUNAR IMPACT MELTS AND THE ORIGIN OF LOW-K FRA MAURO BASALT

Spudis P.D.[1], Taylor G.J.[2], McCormick K.A.[2], Ryder G.[3], Keil K.[2], and Grieve R.A.F.[4] 1. U.S. Geological Survey, Flagstaff, AZ 86001 2. Inst. Meteoritics, Univ. New Mexico, Albuquerque, NM 87131 3. Lunar and Planetary Inst., Houston, TX 77058 4. Geophysics Division, GSC, Ottawa K1A OY3

Although "low-K Fra Mauro basalt" (LKFM; [1]) has been recognized as an impact-produced mixture (e.g., [2]), several aspects of its occurrence remain poorly understood. The term LKFM, originally used to describe soil agglutinates [1], is now applied to a variety of impact-melt breccias of basaltic composition that were assembled around 3.8 to 3.9 Ga [2, 3]. More than 90 % of melt breccias in the Apollo sample collections have LKFM composition, but regionally it is rare on the lunar surface [4]. LKFM melt rocks contain clasts of crystalline rock and mineral fragments (no regolith products) and cannot be made by mixing any combination of known pristine rocks [5]; the one or more missing components are rich in transition metals (e.g., Ti, Sc) and KREEP and have a high Mg*. Through an analog study of melt rocks from the terrestrial Mistastin Lake crater [6], we have shown that clasts in impact melts contain information on the path followed by the melt as it traversed the pre-existing target rocks during cratering flow. We here describe results from an ongoing study [7] that uses the same methodology for lunar impact melts.

Bersch [8] has assembled high-precision electron microprobe analyses for the minor-element concentrations in the mineral phases of virtually all known lunar pristine rocks. We analyzed (by microprobe) olivine and pyroxene clasts in lunar impact melts 15445 and 15455 for minor elements, using Bersch's database to establish the affinities of these clasts to the known pristine rock types. We also examined these same data in an attempt to understand the chemical nature of unknown rock types that contribute to the LKFM composition. We chose samples 15445 and 15455 for initial study because they are aphanites, and their entrained clasts can be easily and unambiguously distinguished from the matrix [9]; moreover, they have been interpreted as fragments of the melt sheet of the Imbrium basin [9]. We plan to extend our study of clast compositions to other melt groups from other landing sites, including the Apollo 17 aphanites and the Apollo 16 VHA melts (which could represent Nectaris basin impact melt; [3]).

The dominant mafic mineral occurring as clasts in both 15445 and 15455 is olivine (the olivine/pyroxene ratio in both rocks ~ 5:1). Results of analyses of Cr and Fe in olivine clasts in the two samples are shown in Figure 1. A wide variety of compositions is present; moreover, the composition of clastic olivines falls only partly within the fields defined by the analyses of known pristine rocks [8]. Because even these fields encompass rocks derived from more than one magma source, the olivine clasts in 15445 and 15455 probably are derived from rocks of many different intrusions. The fields defined by the known pristine rocks are probably incomplete; many of the points lie just outside the boundary of the known fields. Some olivines appear to possess high Cr (Fig. 1), an expected characteristic of the "missing" matrix component of LKFM (which has a high concentration of transition metals). However, these clasts probably are *not* derived from a "missing" rock type, because they have no accompanying high Ti (as expected for a transition metal-rich rock type) nor high P (as expected for a KREEP-rich rock). We interpret these clasts as derived from Mg-suite rocks produced by magmas enriched in Cr that have not been sampled as pristine plutonic rocks. The bulk of the olivine clasts appear to be derived from Mg-suite troctolites, with lesser amounts from Mg-suite norites. Only three clasts occur close enough to the ferroan field (Fig. 1) to indicate their derivation from ferroan anorthosites; these clasts (and others that plot directly above them; Fig. 1) may be pieces of unsampled, mafic members of the ferroan suite, such as ferroan troctolite or gabbro. Finally, the proportions of clasts representing identified rock types differ in the two samples; if we generously extend the fields of the known rock types to include the "orphan" points, sample 15445 consists of 79.6 % troctolite and 12.9 % olivine-bearing norite, whereas sample 15455 consists of 62.6 % troctolite and 31.6 % olivine-bearing norite.

As previously observed in the impact melt rocks of Mistastin Lake crater [6], the clasts contained in 15445 and 15455 are derived from a variety of rock types whose proportions differ within samples from the same melt sheet. The clasts appear to be derived largely from a variety of Mg-suite plutonic rocks, only a few of which are represented by samples in the Apollo collections. The Mg-suite probably comprises a wide variety of rocks produced over a long period of time from many magmas that ranged widely in composition. The lithic clasts of 15445 and 15455 are Mg-suite troctolites and norites, the same rock types from which their mineral clasts are derived. These observations support our model for melt formation, whereby the clast population of impact melts reflects the path that the melt followed during cratering flow and its final emplacement [6],

rather than containing a representative population of rock types that have participated in the melt petrogenesis (e.g., [10]). LKFM may represent impact melt produced during the formation of multi-ring basins [3, 9, 11]. In these large events, the scale of crater formation is greater than the curvature of the Moon; impact melt generated at depth that moves laterally outward during crater growth encounters progressively higher stratigraphic levels. Thus, clasts are entrained in the LKFM basin melts during the later stages of crater growth, and they are derived from crustal levels above the mafic, KREEP-rich zone of melt generation. In our model, the "missing" components of LKFM are plutonic rocks that occur in lower parts of the crust, perhaps as deep as its base. We can only infer their properties from geochemical modeling; they are unlikely to be observed as clastic components within the melt breccias.

References. [1] Reid A.R. *et al.* (1972) *Meteoritics* 7, 395. [2] Reid A.R. *et al.* (1977) *PLSC* **8**, 2321. [3] Spudis P.D. (1984) *PLPSC* **15**, *JGR* **89**, C95. [4] Davis P.A. and Spudis P.D. (1987) *PLPSC* **17**, *JGR* **92**, E387. [5] Ryder G. (1979) *PLPSC* **10**, 561. [6] McCormick K.A. *et al.* (1989) *PLPSC* **19**, 691. [7] Ryder G. (1984) *LPS* **XV**, 707. [8] Bersch M.G. (1990) Ph.D. Thesis, Univ. New Mexico, Albuquerque, 188 pp. [9] Ryder G. and Bower J.F. (1977) *PLSC* **8**, 1895. [10] Phinney W.C. and Simonds C.H. (1977) *Impact and Explosion Cratering*, Pergamon Press, 771. [11] Spudis P.D. and Davis P.A. (1986) *PLPSC* **17**, *JGR* **91**, E84.

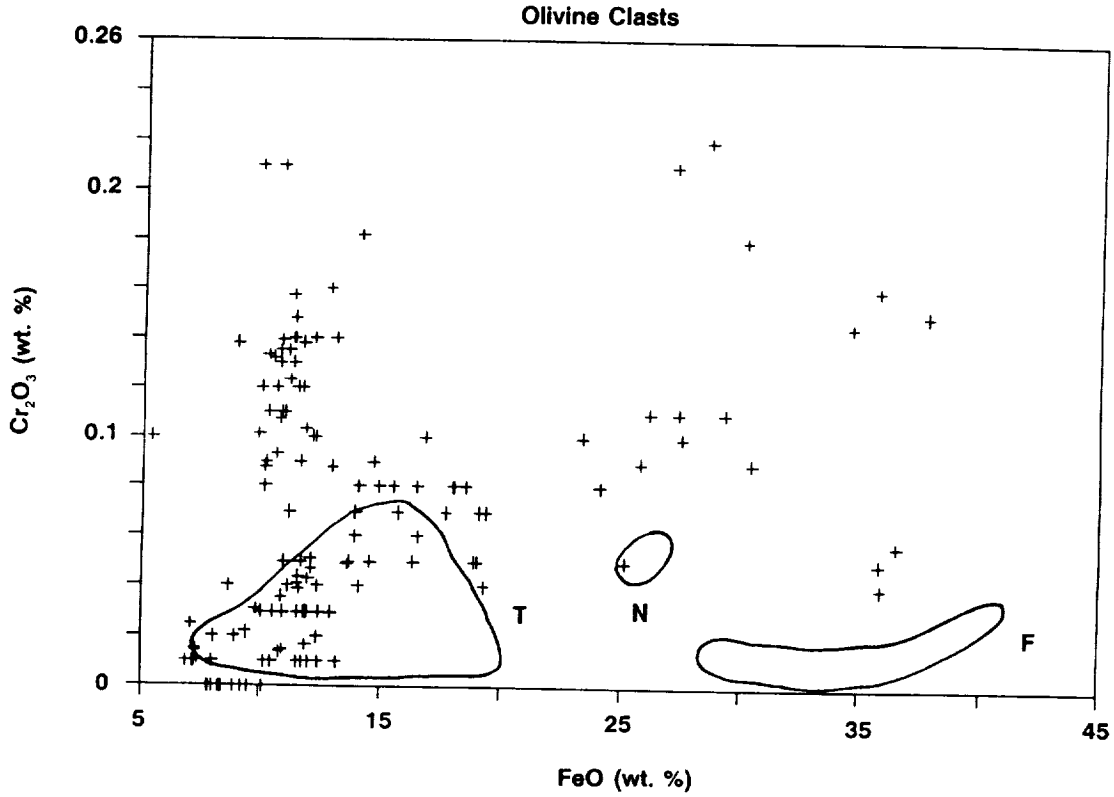

Figure 1. Cr and Fe concentration data for clastic olivines in impact-melt breccias 15445 and 15455. Fields for pristine lunar rocks are taken from the data of Bersch [8]; "T" - Mg-troctolites, "N" - Mg-norites, "F" - ferroan anorthosites.

Measurement of the Electrical Conductivity of an Fe-rich Perovskite-Magnesiowüstite Assemblage

Xiaoyuan Li and Raymond Jeanloz (Both at: Department of Geology and Geophysics, University of California, Berkeley, CA 94720)

$(Mg,Fe)SiO_3$ perovskite and (Mg,Fe)O magnesiowüstite are believed to be the major constituents of the mantles of Venus and Earth; they may also make up the mineralogical assemblage at the base of the mantle in Mars. Thus, a knowledge of the electrical conductivity of these minerals is required for modelling the electromagnetism of terrestrial planetary interiors, as well as for understanding the mineral physics and chemistry of rocky mantles. In this study, we have measured the electrical conductivity of a perovskite-magnesiowüstite assemblage, synthesized from a natural olivine of composition $(Mg_{0.80}Fe_{0.20})_2SiO_4$ extracted from the Eagle Station meteorite. Our data, obtained with the laser-heated diamond cell, yield an electrical conductivity of 1.1 (±0.3) x 10^2 S/m at 77 GPa and 2410 K. We find that the electrical conductivity increases by 4 orders of magnitude as pressure and temperature are increased over the range of our experimental conditions, pressures of 45-80 GPa and temperatures of 298 to 3600 K. From these measurements, we derive an activation energy of 0.2 (±0.1) eV for electrical conduction at elevated pressures.

The perovskite-magnesiowüstite assemblages, analyzed by electron microprobe and scanning electronic microscope (SEM) after the experiments, are uniform in composition at the limit of analytical resolution. Thus, there is no indication of Soret diffusion or of reaction between the unmelted sample and leads (e.g., loss of Fe to Pt) in our experiments on unmelted samples. Some experiments, in which molten perovskite was in contact with Pt, show that limited reaction can occur between the melted sample and leads, and this is visually observed during the conductivity measurements. These results support the reliability of electrical conductivity measurements inside the laser-heated diamond anvil cell.

Comparing the present results with those derived from Fe-poor samples (Li and Jeanloz, 1987, 1990), we find that the electrical conductivity of the perovskite-magnesiowüstite assemblage strongly depends on its iron content: *i.e.*, when Fe/(Mg+Fe) ratio increases from 10% to 20%, the electrical conductivity increases by 5 orders of magnitude. The electrical conductivity values of the 20%-Fe assemblage are compatible with geomagnetically inferred values of the Earth's deep-mantle conductivity (see the attached figure). Assuming that the geomagnetic modelling represents the true distribution of conductivity in the mantle, our results are consistent with the lower mantle being enriched in Fe relative to the Earth's upper mantle, and hence being of lunar-mantle composition (Jeanloz and Knittle, 1989).

Jeanloz, R., and E. Knittle, Density and composition of the lower mantle, *Phil. Trans. R. Soc. Lond. A* **328**, 377-389, 1989.

Li, X., and R. Jeanloz, Electrical conductivity of (Mg,Fe)SiO3 perovskite and perovskite-dominated assemblage at lower mantle conditions, *Geophys. Res. Lett.* **14**, 1075-1078, 1987.

Li, X., and R. Jeanloz, Laboratory studies of the electrical conductivity of silicate perovskites at high pressures and high temperatures, *J. Geophys. Res.*,

in press, 1990.

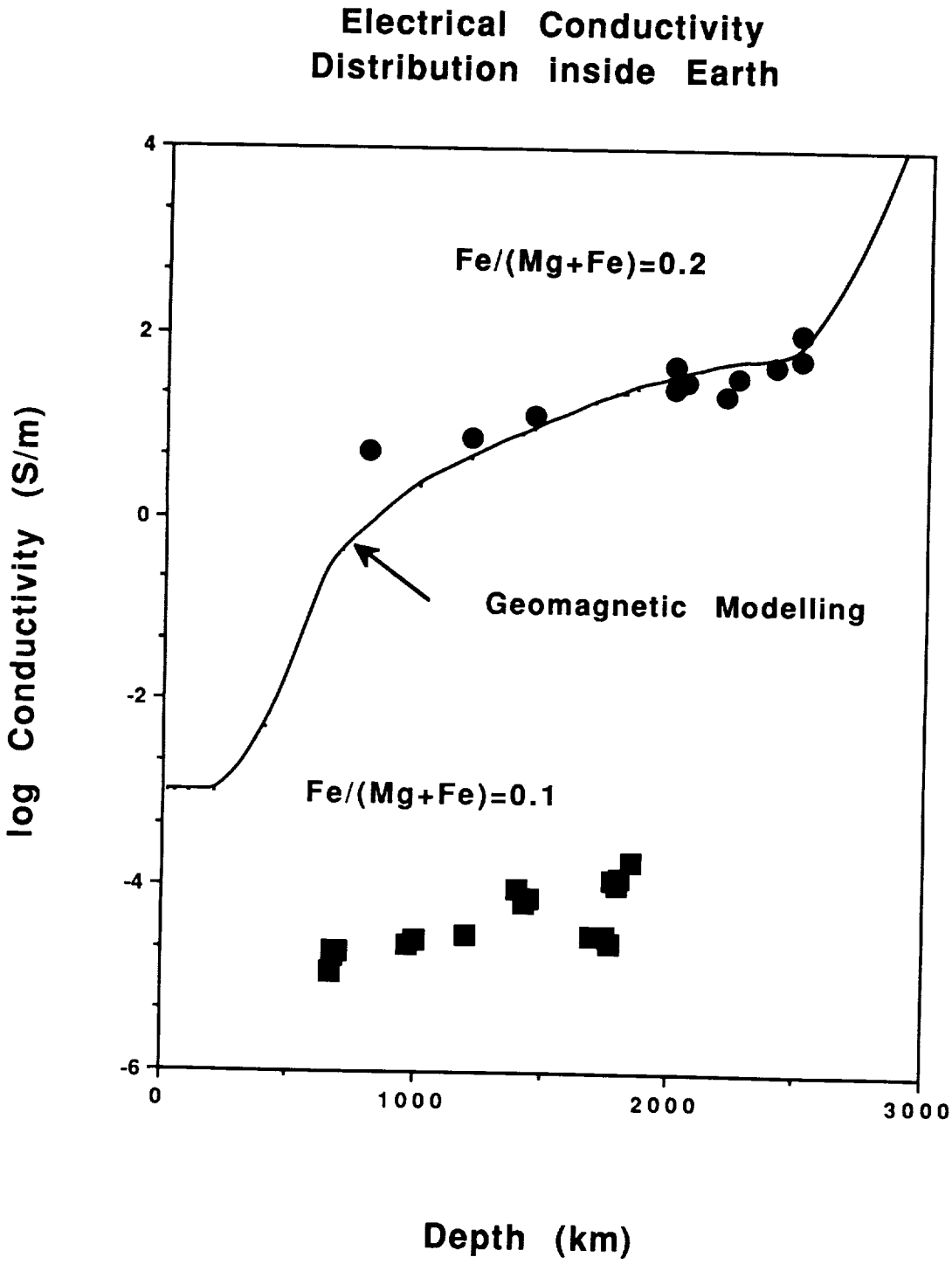

Ultrahigh-Pressure Melting of Lead: A Multidisciplinary Study

B. K. Godwal*, Charles Meade, Raymond Jeanloz (All at: Department of Geology and Geophysics, University of California, Berkeley, CA 94720; *Permanent Address: Neutron Physics Division, Bhabha Atomic Research Center, Trombay, Bombay 400 085, India)

Alberto Garcia, Amy Y. Liu AND Marvin L. Cohen (All at: Department of Physics, University of California, Berkeley, CA 94720, and Materials and Chemical Sciences Division, Lawrence Berkeley Laboratory, Berkeley, CA 94720)

Measurements of the melting temperature of lead, carried out to pressures of 1 Megabar (10^{11} Pascal) and temperatures near 4000 Kelvin by way of the laser-heated diamond cell, are in excellent agreement with the results of previous shock-wave experiments. The data are analyzed by means of first-principles quantum mechanical calculations, and the agreement documents the reliability of current experimental and theoretical techniques for studies of melting at ultrahigh pressures: studies that have potentially wide-ranging applications, from planetary science to condensed matter physics.

MANTLE PLUME DYNAMICS IN THE TERRESTRIAL PLANETS

Peter Olson, Department of Earth & Planetary Sciences,
The Johns Hopkins University, Baltimore, MD 21218 USA

Thermal plumes are an important mechanism for heat and mass transport in planetary mantles. On Earth, mantle plumes are considered to be the source of the global system of volcanic hotspots. Mantle plumes may be even more important in the tectonics of Venus. Transsolidus thermal plumes--localized upwellings of partially molten mantle silicates--may underlie volcanic highlands on Venus. Our calculations indicate these plumes can transport up to 50% of the heat from the Venusian interior (Olson et al., 1990).

Unlike heat transfer in Earth's mantle, heat transfer within the Venusian mantle is evidently not dominated by plate tectonic processes. While there are linear topographic structures on the surface of Venus that may be broadly analogous to mid-ocean ridges on Earth (Head and Crumpler, 1987), we have no evidence that these structures are elements of a global network of mobile plate boundaries (Grimm and Solomon, 1987).

Without rapid plate motions, there is a problem in explaining how heat is lost from the Venusian mantle, since cosmochemical abundances indicate it has an inventory of heat producing elements similar to Earth. In an effectively "single-plate" planet, there are only two mechanisms for efficient heat loss. These are (i) conduction through very thin lithosphere, and (ii) heat loss by magmatic activity.

We have investigated the effectiveness of magmatic heat transport by thermal plumes in the Venusian mantle. We find that this mechanism can account for the observed characteristics of the circular highlands. We suggest that these highlands may be regions of both high heat flow and thick crust, which are maintained dynamically by mantle upwelling and by influx of basaltic melts derived from mantle plumes. Turcotte (1988) calculated the amount of surface volcanism required to balance the internal heat production is equivalent to 1000 Hawaiian hotspots. This level of volcanic activity exceeds, by two orders of magnitude, the rate estimated from absorption of SO_2 (Fegley and Prinn, 1989). Magmatic activity can provide much of the required heat transport, without violating the above constraints, if the magmatism is predominantly intrusive rather than extrusive.

A simplified model for heat transfer by plume-derived melts intruding a thick crust is shown in Figure 1. By virtue of the high surface temperature, upwelling mantle crosses the solidus at a depth of the order of 100 km. The upwelling inevitably produces a three-layer structure. At depth is the subsolidus zone, where the temperature is below the solidus and flow occurs by subsolidus creep only. Above this is the melting zone, with temperatures above the solidus and with equilibrium partial melting. In this zone, the melt migrates vertically through the solid matrix by percolative flow. The surface layer, the crust-lithosphere, is the freezing zone. Here temperatures are below the solidus on average, and the melt derived from below freezes during ascent. Latent heat release in the crust considerably increases the surface heat flux. We find that two steady state configurations are possible for the case of uniform freezing:

one with a very thin (3 km) crust, and one with a moderately thick crust (48 km). Only the thicker crust solution is consistent with the assumption of intrusive magmatism.

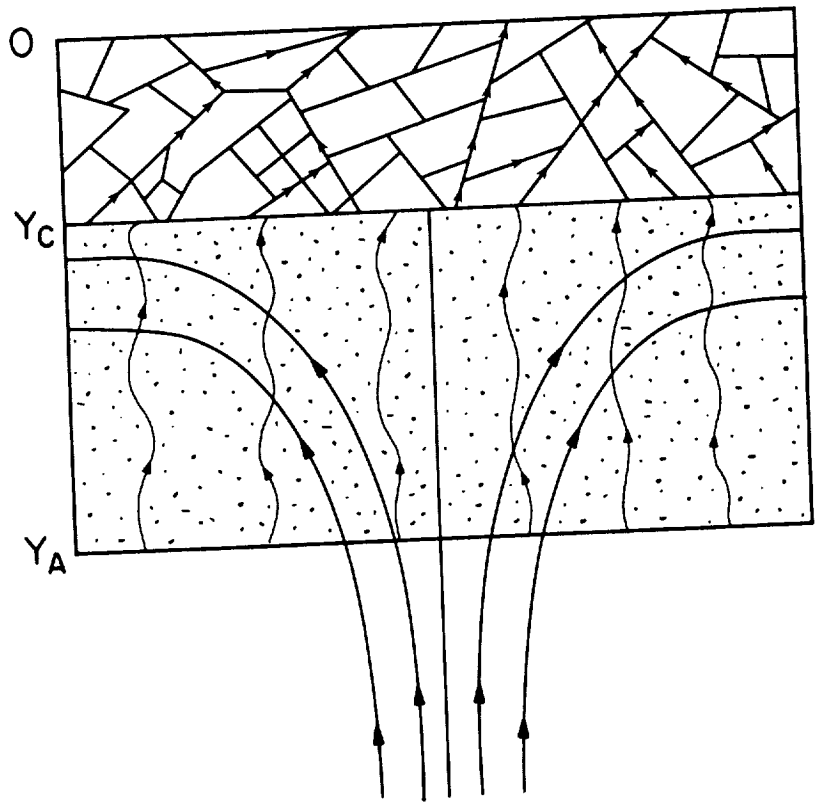

Figure 1. A sketch of the three layer structure produced by a rising transsolidus mantle plume. Lower region is the subsolidus zone, with temperatures below the solidus and solid-state flow as indicated by the streamlines. The region between Y_A and Y_C is the equilibrium melting zone. The zone above Y_C is the crust-lithosphere or freezing zone, with subsolidus average temperatures, and with melt transport and solidification in dikes.

The resulting temperature and porosity distributions are shown in Figure 2. Our calculations indicate that as much as one half of the estimated 40 TW Venusian heat loss can occur at highland regions by this mechanism. An important prediction of this model is that high heat flow, dynamical uplift and thick basaltic crust are present in the highland regions.

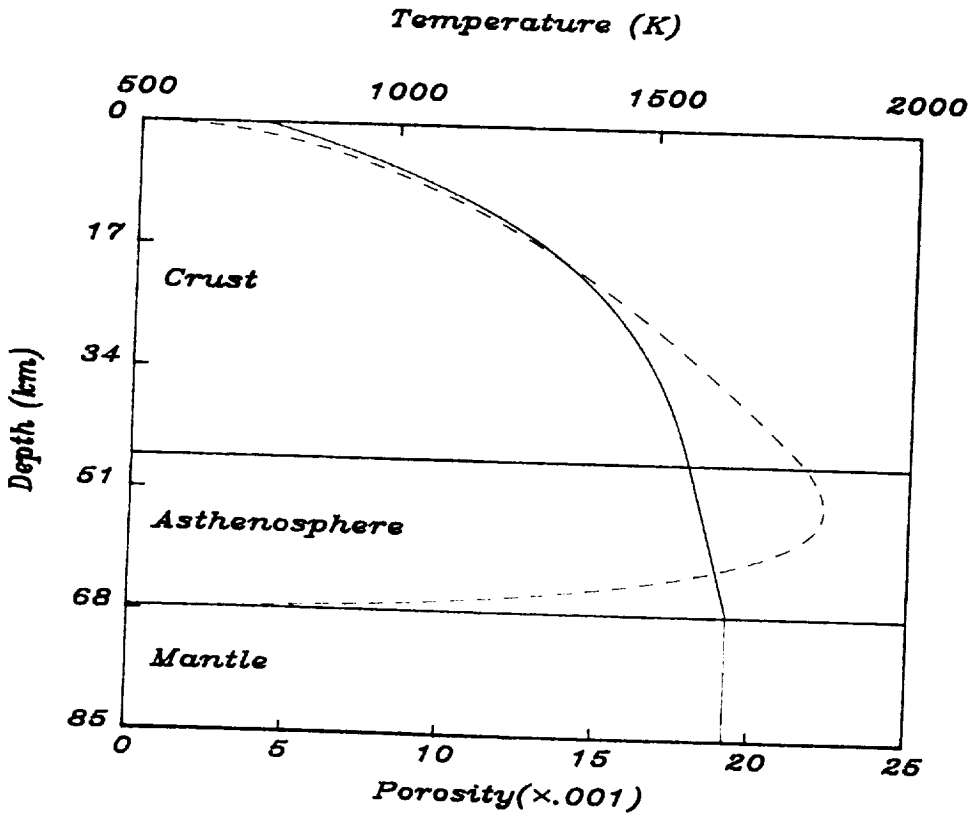

Figure 2. Steady state temperature (solid curve) and melt content, expressed as porosity (dashed curve) for the plume structure shown in Figure 1. Asthenosphere and mantle correspond to melting and subsolidus zones, while the crust corresponds to the freezing zone.

References

Fegley, B. and R. G. Prinn, *Nature* 337, 55-58, 1989.
Grimm, R. E. and S. C. Solomon, *Geophys. Res. Lett.* 14, 538-541, 1987.
Head, J. W. and L. S. Crumpler, Science 238, 1380-1385, 1987.
Olson, P., S. Weinstein, and Y. Zhou, *XXI Lunar Planet. Sci. Conf.*, 919, 1990.
Turcotte, D. L., *XIX Lunar Planet. Sci. Conf.*, 1207-1208, 1988.

Implications of Convection in the Moon and the Terrestrial Planets

Donald L. Turcotte, Department of Geological Science,
Cornell University, Ithaca, NY 14850-1504

During the past year our principal effort has been to use parameterized convection calculations to determine the thermal and chemical evolution of terrestrial planets. The calculations give the secular variation of the internal temperatures, Rayleigh number, viscosity, crustal thickness, lithosphere thickness, and rate of volcanism. The rate of crustal creation on the earth was used as a calabration. Crustal forming volcanics extracts heat producing elements from the mantle to the lithosphere thus reducing the vigor of mantle convection. Plate tectonics returns these elements to the interior of the earth through the subduction process. Without plate tectonics the thermal evolution of a planet may be quite different. Our results for the moon and Mars are generally consistent with observations. For Venus our calculations indicate that without crustal recycling the interior would be fully differentiated and there would have been essentially no volcanism for the last 2 Gyrs. Also, our calculations predict a lithospheric thickness of about 450 km which could explain the high topography and associated gravity anomalies on Venus. This work has been presented at several meetings (1,2).

Our joint paper on the tectonic implications of noble gases in planetary atmospheres has been published (3). A joint paper on the origin and thermal evolution of Mars was presented as a review paper at the Mars Conference held in Tucson in January 1989; this work has subsequently been written up and is in press in the proceedings of the conference (4). Our paper on a heat-pipe mechanism for heat transport to the surface of Venus has also been published (5).

References

[1] D.L. Turcotte (1989) *Thermal evolution of Mars and Venus including irreversible fractionation,* Lunar Planet. Sci. XX, 1138-1139. [2] J. Huang and D.L. Turcotte (1989) *Crustal formation and recycling rates based on parameterized convection calculations,* Trans. Am. Geophys. Un. 70, 478. [3] G. Schubert, D.L. Turcotte. S.C. Solomon, and N.H. Sleep (1989) *Coupled evolution of the atmospheres and interiors of planets and satellites* , in Origin and Evolution of Planetary and Satellite Atmospheres, S.K. Atreya, J.B. Pollack, and M.S. Matthews, eds., University of Arizona Press, Tucson, 450-483. [4] G. Schubert, S.C. Solomon, D.L. Turcotte, M. Drake, and N. Sleep (1989) *Origin and thermal evolution of Mars,* in Mars, University of Arizona Press (in press). [5] D.L. Turcotte (1989) *A heat pipe mechanism for volcanism and tectonics on Venus,* J. Geophysics. Res. 94, 2779-2785.

SPECIATION, REACTION KINETICS, AND DIFFUSION OF WATER IN NATURAL RHYOLITIC GLASSES

Edward Stolper and Youxue Zhang, Division of Geological and Planetary Sciences, 170-25, California Institute of Technology, Pasadena, CA 91125

Water is a major volatile component in natural rhyolitic glasses and melts. It dissolves as two species, molecular water and hydroxyl groups. The two species interconvert to each other and there is an equilibrium between them: $H_2O+O=2OH$, where H_2O is molecular water, OH is hydroxyl groups believed to be associated with SiOH or AlOH, and O is a bridging oxygen in a fully polymerized rhyolitic melt or glass. The presence of water and its speciation greatly affects the physical and chemical properties such as viscosity and phase equilibria of these melts and glasses. The rate of water diffusion is the limiting step to bubble growth, and degassing of water from magma which is related to the early evolution of the atmosphere and ocean. The interplay of the rate of water diffusion and the rate of magma ascending also determines whether enough water overpressure can be built in an ascending magma body to power explosive volcanic eruptions.

In the last one and half years, we have carried out a study on the diffusion of water in rhyolitic glasses, and on the rate of the interconversion reaction between molecular water and hydroxyl groups.

1. Diffusion of water in rhyolitic glasses: Previous extensive studies on water diffusion in synthetic silicate glasses and in rhyolitic melts have shown that the chemical diffusivity of total water increases strongly with water content in the silicates. There have been many speculations on the cause of this strong concentration dependence of water diffusivity. Our study differs from previous ones in that we measured concentration profiles of both molecular water and hydroxyl groups after the diffusion experiments and treated the diffusion profiles with a two-species diffusion problem. One of the unique features of the two water species is that the two species are not at constant proportions at variable water concentrations, but rather, at low water content OH is the dominant species, and at high water content H_2O is the dominant species. This feature allows us to resolve the diffusion coefficients of both species by fitting our experimental diffusion profiles with a two species diffusion treatment.

We dehydrated at elevated temperatures doubly polished natural rhyolitic glass wafers, each of which was initially uniform in water concentration (0.2 to 1.7%). After dehydration for 10 to 50 days, the glass wafer was quenched and a slice was cut perpendicular to the diffusing surfaces and concentration profiles of both H_2O molecules and OH groups were measured. Such concentration profiles were compared to the solution of two species diffusion equation which allows the determination of the diffusivities of both species. Figure 1 shows the measured diffusion profiles of H_2O, OH and total water, and compares them to the solution of two species diffusion model assuming $D_{OH}=0$. From

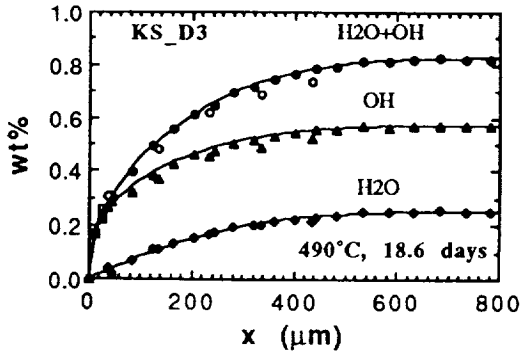

Figure 1: Concentration profiles of H_2O, OH and total water produced in water dehydration experiments. Horizontal axis is distance (μm) away from dehydrating interface. Filled symbols represent measurement from one edge and open symbols represent measurement from the other edge. Lines are the best fit lines to data represented by the filled symbols assuming $D_{OH}=0$

the best fit, we found that $D_{OH)}$ is orders of magnitude smaller than D_{H_2O}, and thus that hydroxyl can be treated as immobile during water diffusion. The OH profile is generated by the reaction to convert OH to H_2O after H_2O diffused away, instead of by OH diffusion. This treatment also successfully fits previous water concentration profiles in diffusion couple experiments. The concentration dependence of D_{H_2O} is small in water concentration range 0.2 to 1.7%. Therefore, the previously observed concentration dependence of total water diffusivity is largely due to the fact that fraction of molecular H_2O increases strongly (almost linearly) with total water concentration.

Figure 2 summarizes our results on the temperature dependence of D_{H_2O}. The activation energy for the diffusion of molecular H_2O is 25 kcal/mol. Figure 3 compares the activation energy of diffusion coefficients of molecular H_2O and of noble gas elements which are generally believed to behave as molecular species. A good relationship between activation energy and radius of a molecular species suggests that H_2O indeed behaves as a molecular species.

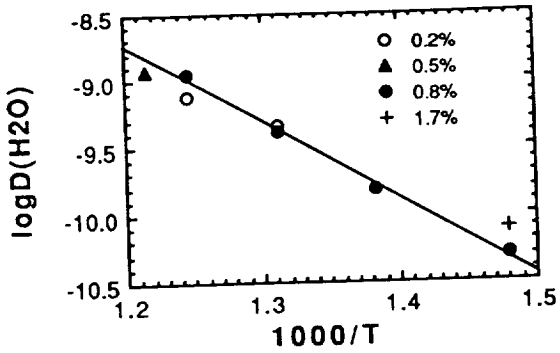

Figure 2: Diffusion coefficients of molecular H_2O vs. 1000/T(°K). Initial water contents of glass wafers are given in the legend

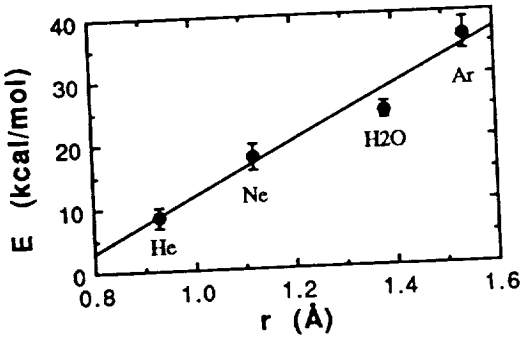

Figure 3: Activation energy for diffusion vs. radius of molecular species

2. <u>The kinetics of the species interconversion reaction:</u> The species equilibrium between OH groups and H_2O molecules has been studied previously. Since in situ measurements of species concentration at elevated temperatures are very difficult, if not impossible, species concentrations at high temperatures (400-850°C) have been determined by quenching experimental charges to glasses. It has been cautioned that the results may have been partly affected by reaction during quench. An understanding of the rate at which OH groups are converted to H_2O molecules and vise versa is important to the assessment of such experimental data. Knowledge on the reaction kinetics may also be used to constrain the thermal history of natural rhyolitic glasses.

Glass wafers with known initial water species concentrations were held at elevated temperatures for a designated period of time. After quench, The species concentrations were measured and hence their variation with time and the rate to reach equilibrium can be determined. We found that the rate of the reaction increases strongly with temperature and water content, as shown in Figure 4 and 5. Figure 4 shows the half time to reach equilibrium at 1.2% total

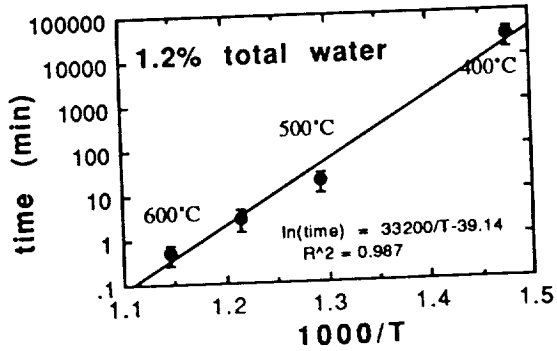

Figure 4: Half time to reach equilibrium (for water reaction $H_2O+O=2OH$) vs. 1000/T (°K) at 1.2 wt % total water

water concentration, which is ~20 days at 400°C, ~0.5 min. at 600°C. The activation energy for the reaction is in the order of 60 kcal/mol. Figure 5 shows the dependence of reaction rate on water content. The reaction was found to be complicated in that the species concentrations do not approach the final equilibrium concentrations monotonically. This behavior is best explained by the presence of at least two different types of OH subgroups that are generated and consumed at different rates by reaction of molecular H_2O with anhydrous oxygen species.

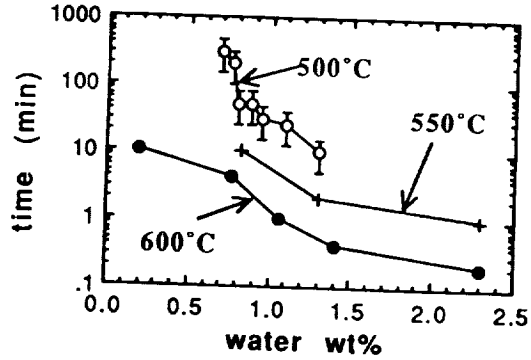

Figure 5: Half-time to reach equilibrium (for water reaction $H_2O+O=2OH$) vs. total water content (wt%) at 500, 550, and 600°C

The preliminary data on the reaction kinetics suggest that care must be taken to quench quantitatively water speciation from high temperature, and indeed, above a certain temperature it may not be possible.

3. Speciation of water in rhyolitic glasses, a refinement: Because reaction kinetics data suggest that previous speciation data at 850°C have been significantly affected by reaction during quench, we obtained more speciation data at lower temperatures (400-600°C) at 0.5 to 4.0% water, with particular attention to demonstrating that the results are unaffected by quenching. There is a clear dependence of the equilibrium coefficient K $\{=[OH]^2/([H_2O][O])$ at equilibrium, where quantities in brackets represent mole fractions$\}$ on temperature and on water concentration. The dependence can be modelled successfully by a regular solution model. Although we note that the regular solution model may not reflect reality, the model can reproduce the experimental temperatures from H_2O and OH concentrations to an average about 5°C; maximum error in reproducing experimental temperature is 20°C. Hence it can be applied to predict the closure temperature of natural water-bearing rhyolitic glasses. Coupled with our data on the reaction rate kinetics, we are now able to infer some details on the thermal history experienced by these glasses.

CHAPTER 6

SPECTROSCOPY AND REMOTE SENSING

VOYAGER DISK-INTEGRATED PHOTOMETRY OF TRITON

J. Hillier, P. Helfenstein, A. Verbiscer and J. Veverka, Center for Radiophysics and Space Research, Cornell University, Ithaca, NY 14853.

We have fit Hapke's photometric model with a thin atmospheric haze layer to Voyager whole-disk observations of Triton (Smith et al., 1989), in the violet (0.41 μm), blue (0.48 μm), and green (0.56 μm) filters in order to obtain estimates of Triton's geometric albedo, phase integral, Bond albedo, and emissivity. Phase angle coverage in these filters ranging from $\sim$ 11° to 159° was obtained by combining narrow- and wide-angle camera data.

Our model is based on van Blerkom's approximation to Chandrasekhar's "planetary problem" (van Blerkom, 1971; Chandrasekhar, 1960). The haze, assumed to be optically thin, is characterized by an optical depth τ_H and a scattering phase function p(cos θ) where θ is the scattering angle. We let i and ϵ be the incidence and emission angles, respectively, and $\alpha = 180° - \theta$ be the phase angle. Rayleigh scattering is negligible in Triton's tenuous atmosphere. The expression for the scattered intensity I(i, ϵ, α) from the combined haze + ground system is approximated by the sum of five terms:

Term 1: Light singly scattered by the haze only;
Term 2: Light scattered by the ground only;
Terms 3 and 4: Light scattered once by haze, either on way out (4) or in (3), and by the ground;
Term 5: Light scattered twice by haze (once on way in and once on way out) and by the ground.

Of these five terms, the last is generally the least significant and begins to play a role only at the highest phase angles. In our model the ground is assumed to scatter incident light according to Hapke's theory (Hapke, 1981; 1986). The upturn seen in the data at the highest phase angles (Fig. 1) can be explained reasonably well by including scattering in a thin atmospheric haze layer with optical depth ranging from $\sim$ 0.06 in the violet to 0.03 for the green filter data. Our best fits for the Hapke and haze parameters are given in Table 1.

TABLE 1: Best-fit Hapke and Haze Parameters for Triton

	Surface			*Haze*	
Filter	Single Scattering Albedo $\tilde{\omega}_0$	Roughness Parameter (°) $\bar{\theta}$	H-G Asymmetry Factor g_{surf}	Optical Depth τ_H	H-G Asymmetry Factor g_H
Green	0.995	14.7	-0.281	0.0325	+0.800
Blue	0.986	13.1	-0.292	0.0415	+0.750
Violet	0.980	11.9	-0.293	0.0625	+0.735

The corresponding geometric albedos and phase integrals are shown in Table 2. Due to the lack of Voyager data below 10° phase, the opposition surge for Triton could not be constrained; therefore, the geometric albedos shown were calculated assuming no opposition surge, and thus yield conservative estimates. However, groundbased observations show that Triton does not have an appreciable opposition surge. The Bond albedo of Triton, calculated from the spherical albedos in Table 2 below, is 0.84 ± 0.05. If the 16 μbar N_2 atmosphere

TABLE 2: Voyager Green-, Blue-, and Violet-Filter Geometric Albedos, Phase Integrals, and Spherical Albedos for Triton

Filter	p	q	pq
Green	0.73	1.19	0.87
Blue	0.68	1.18	0.80
Violet	0.66	1.19	0.78

detected by the Voyager radio occultation experiment (Tyler et al., 1989) is in vapor equilibrium with the surface (therefore implying a surface temperature of ~ 37.7°K), our Bond albedo implies a surface emissivity of 0.54 ± 0.17.

This research was supported by NASA Grants NSG 7156 and NSG 7606.

References

Chandrasekhar, S. (1960). *Radiative Transfer.* Dover, N.Y.

Hapke, B. W. (1981). Bidirectional reflectance spectroscopy. 1. Theory. *J. Geophys. Res. 86*, 3039-3054.

Hapke, B. W. (1986). Bidirectional reflectance spectroscopy 4. The extinction coefficient and the opposition effect. *Icarus 67*, 264-280.

Smith, B. A., et al. (1989). Voyager 2 at Neptune: Imaging science results. *Science 246*, 1422-1449.

Tyler, G. L., et al. (1989). Voyager radio science observations of Neptune and Triton. *Science 246*, 1466-1473.

van Blerkom, D. J. (1971). Effects of haze on visibility of martian surface features. *Icarus 14*, 235-244.

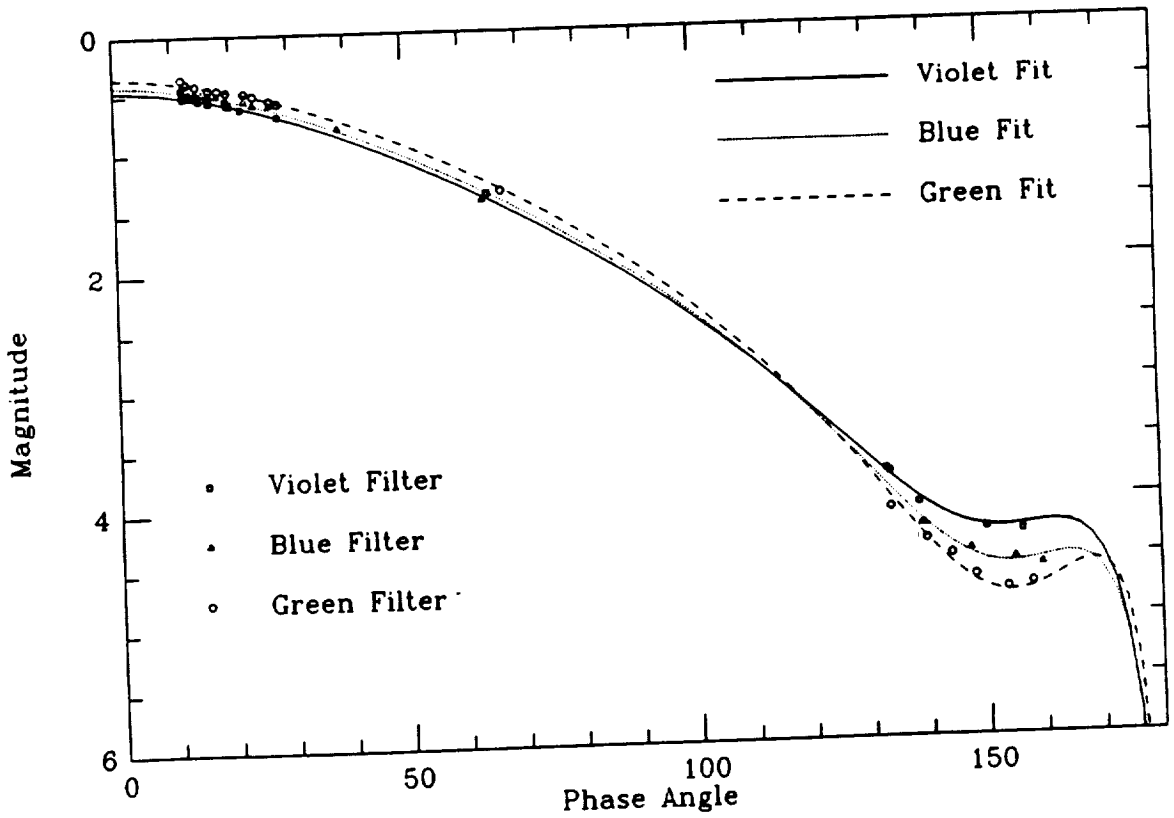

FIGURE 1: Whole-disk phase curves of Triton from Voyager 2 observations fitted with models in which the surface is overlain by a thin haze of optical depth τ_H. The model parameters are listed in Table 1. Rayleigh scattering in Triton's tenuous atmosphere is negligible.

OBERON: COLOR PHOTOMETRY AND ITS GEOLOGICAL IMPLICATIONS.
P. Helfenstein, J. Hillier, C. Weitz, and J. Veverka, Center for Radiophysics and Space Research, Cornell University, Ithaca NY.

Three primary terrain units are exposed at the surface of Oberon--average cratered terrain, bright crater rays, and prominent dark deposits often seen on crater floors[1]. Our preliminary analysis of Voyager broadband images[2] demonstrated that Oberon's bright crater rays are distinctly bluer than average cratered terrains and dark crater floor deposits, in contrast to terrains on other Uranian satellites which exhibit little correlation of color with terrain albedo. In the present detailed analysis, we have applied Hapke's[3] photometric model to observations from Voyager imaging and Earthbased photometry[4] in order to compare photometric properties and colors of Oberon's terrain units to each other, and to those of other Uranian satellites.

Available phase angle coverage of Oberon is adequate constrain all five Hapke parameters (ω_0,h,B_0,θ,g) only at Voyager clear-filter wavelengths (λ=0.48 μm). At other Voyager wavelengths and for individual terrains classes, no opposition surge data are available. In these cases, we have fixed the opposition surge parameters, h=0.007±0.002 and B_0=1.03±0.06, at their global average clear filter values and determined least-squares fit values of ω_0, g, and θ. Table I lists our Hapke parameter fits for Voyager violet- (λ=0.41 μm), clear-, and green-filter (λ=0.56 μm) data. Despite significant variations of ω_0 and g, values of macroscopic roughness are similarly lunar-like ($\theta \simeq 21°$) for all terrains. Values of g from Table I decrease (representing less strongly backscattering particles) with increasing average particle single-scattering albedo.

We've used our Table I results and the highest resolution (5 km/pixel) Voyager color sequence of Oberon (FDS 26836.25;clear, 26836.27;violet, and 26836.29;green) to estimate the distribution of normal albedos and colors of different terrains. Clear-filter albedos range from 0.15 for darkest materials on Oberon to 0.61 for brightest crater ray materials. Fig. 1 shows that average violet and green normal albedos of different terrains systematically vary relative to corresponding clear-filter albedos. The brightest materials on Oberon are most nearly spectrally neutral, while darkest materials are at the same time most red and violet relative to clear filter albedos. Hillier et al.[5] observed a qualitatively similar, but much weaker trend for terrains on Miranda (see Fig. 1). They proposed that this trend is consistent with a mixing model in which differing amounts of material spectrally similar to asteroidal F-material are mixed with a spectrally neutral icy component.

Composite color-ratio and albedo maps assembled from our shading-corrected Voyager images clearly reveal a globally asymmetric spatial distribution of compositionally different materials (see Fig. 2). Vast areas of Oberon's leading hemisphere are covered by low-albedo materials which are spectrally similar

to dark crater-floor deposits. In contrast, the trailing hemisphere of Oberon contains comparatively small, patchy concentrations of dark material, and much greater abundances of a spectrally neutral regolith component. Bright crater materials are the most spectrally neutral of all materials on the surface.

Dark deposits in crater floors on Oberon have been interpreted as volcanic flow materials extruded from depth through fissures[1]. While many of our newly discovered dark surface deposits are associated with crater floors, most occur in large contiguous patches exhibiting no obvious genetic relationship to particular craters. A simple explanation for the origin of dark materials, both in crater floors and on the surface, is that they are volcanic flood deposits analogous to lunar mare. This origin has also been suggested for irregular, quasi-polygonal deposits of unusually dark material in topographically low-lying regions of Umbriel's surface[6]. Alternatively, the dark areas may represent a low-albedo layer of Oberon's lithosphere which has been exposed by preferential impact erosion on its leading hemisphere. In either event, the preferential occurrence of dark materials on the leading hemisphere suggests the presence of a crustal thickness asymmetry. Relatively fresh impact craters have evidently excavated comparatively clean bright ice from a near-surface crustal layer. This clean-ice crust appears to cover a deeper layer of dark material, suggesting that Oberon is at least partially differentiated. The trailing hemisphere appears to be covered by a regolith of bright icy crustal material contaminated by dark surface deposits.

ACKNOWLEDGEMENTS: This research was supported by NASA under Grants NSG-7156, NAGW-1221, and NSG-7606.

REFERENCES: [1]Smith et al.(1986). Science **233**, 43-64. [2]Helfenstein et al.(1989). LPSC XX, 402-403. [3]Hapke(1986). Icarus **67**, 264-280. [4]Goguen et al.(1989). Icarus **77**, 239-247. [5]Hillier et al.(1989). Icarus **82**, 314-335. [6]Helfenstein et al.(1989). Nature **338**. 324-326.

Table I: Hapke Parameters[a] for Terrains on Oberon

Terrain	Filter	ω_0	g	$\bar{\theta}$
Global Average	Clear	0.41±0.01	-0.29±0.03	21±2°
	Green	0.48±0.01	-0.24±0.01	
	Violet	0.33±0.01	-0.35±0.02	
Average cratered	Clear	0.41±0.02	-0.27±0.03	22±4°
	Green	0.53±0.02	-0.21±0.02	
	Violet	0.42±0.03	-0.24±0.04	
Bright craters	Clear	0.50±0.01	-0.23±0.06	21±7°
	Green	0.57±0.06	-0.20±0.07	
	Violet	0.50±0.07	-0.19±0.09	
Dark materials	Clear	0.34±0.02	-0.28±0.05	20±4°
	Green	0.47±0.03	[-0.24][b]	
	Violet	0.31±0.02	[-0.36][b]	

[a]**Hapke parameters:** ω_0=average particle single-scattering albedo, h=opposition surge angular width=0.007±0.002, B_0=opposition surge amplitude=1.03±0.06, g=asymmetry factor in Henyey-Greenstein particle phase function, $\bar{\theta}$=macroscopic roughness
[b]Bracketed values found from empirical $g = -0.1123/\omega_0 - 0.00026$

Fig. 1: Normal albedos (relative to clear-filter) of terrains on Oberon and Miranda[5] as a function of λ.

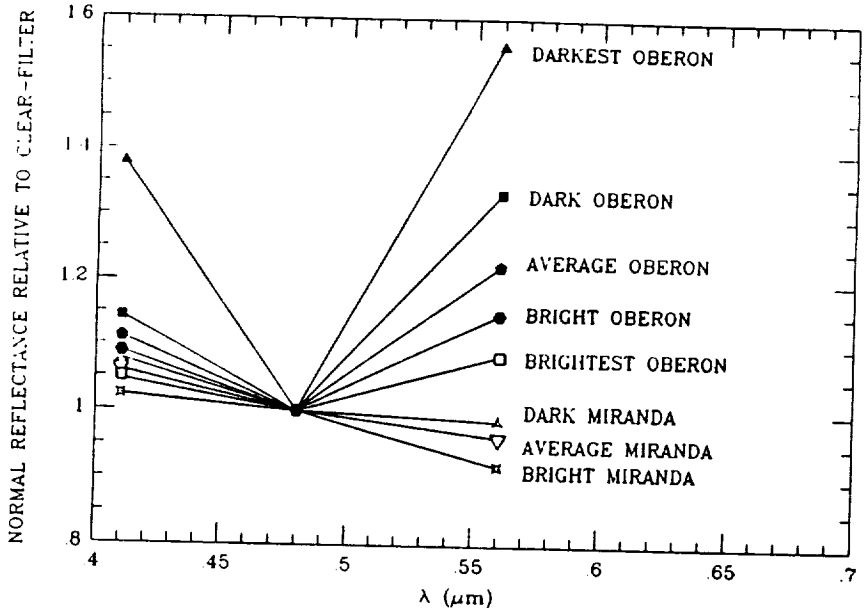

Fig. 2: Geological sketchmap of Oberon showing distribution of material units. This map was assembled on the basis of albedo and color boundaries visible in Voyager images FDS 26836.25 (NA clear), 26836.27 (NA violet), 26836.29 (NA green), and color ratio images constructed from them.

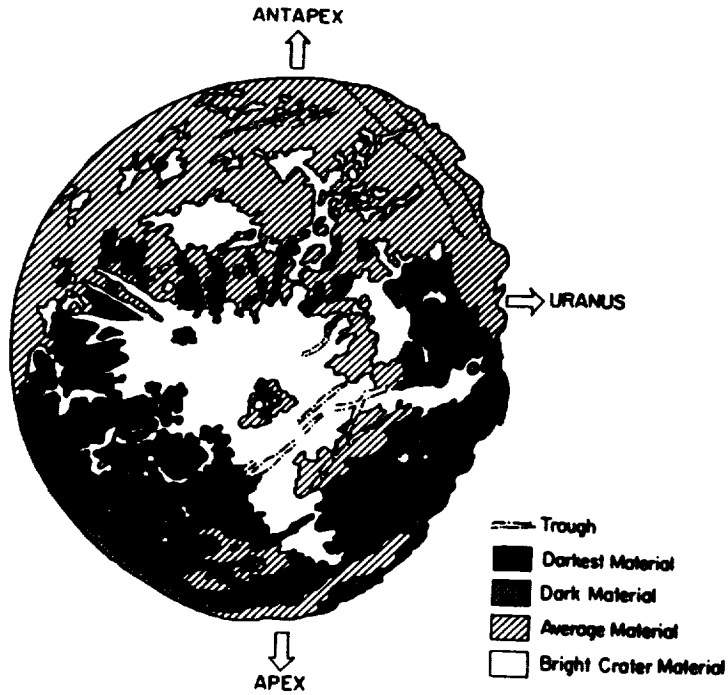

AN IMPROVED PHASE CURVE FOR ENCELADUS

A. Verbiscer and J. Veverka, Cornell University, Ithaca, NY; H. B. Hammel, Jet Propulsion Laboratory, Pasadena, CA; J. J. Klavetter, University of Maryland, College Park, MD.

Voyager observations of Enceladus are limited to phase angles in the range α = 11°-43°, and do not include measurements near opposition. We have supplemented the Voyager imaging data with Earth-based CCD observations (made independently by H.B.H. and J.J.K.) to construct as complete a solar phase curve as possible. To place these Earth-based observations on the Voyager curve, we need spectral data to transfer observations reduced to the standard Johnson V filter (0.55 μm) to the Voyager clear filter (0.48 μm). Additonal telescopic data are available from Franz and Millis (1975) and Koutchmy and Lamy (1975); however, the sub-Earth point at the time of these observations was located in extreme southern latitudes (-30°) compared to about +30° for Voyager. Given that Buratti suggests that the southern hemisphere of Enceladus is 20% brighter than the northern hemisphere, it is difficult to correct the Franz/Millis and Koutchmy/Lamy data reliably to the Voyager aspect. The data from Hammel and Klavetter, however, are from extreme northern latitudes (+30°), just as are most of the Voyager images.

The new combined phase curve is shown in Fig. 1. Orbital phase effects have been removed from the data by normalizing to the brightness at 0° longitude, as described by Verbiscer and Veverka (1990a). The position of the Hammel point at phase angle 0.65° relative to that of the Klavetter data near 4° suggests an opposition surge; however, the Klavetter measurements were made at R, and thus their position in Fig. 1 is strongly dependent on the V-R assumed for Enceladus. The shape of the entire curve is fit to Hapke's equation with the following parameters: single scattering albedo $\tilde{\omega}_0$ = 0.987, macroscopic roughness $\bar{\theta}$ = 0°, and Henyey-Greenstein asymmetry factor g = -0.3, opposition surge angular width h = 0.01 amplitude B_0 = 0.7.

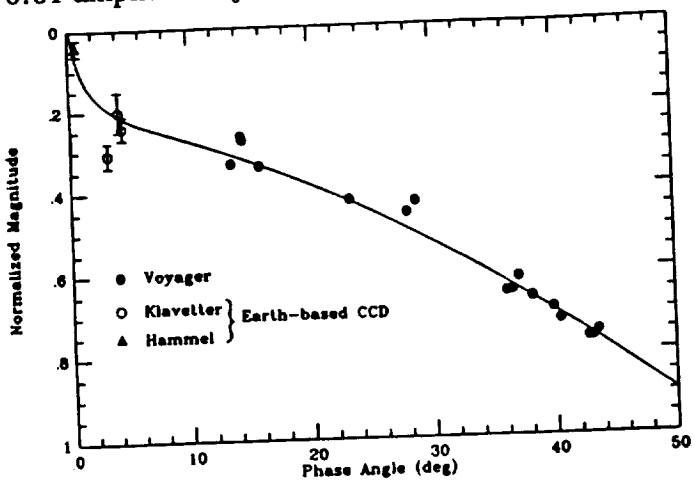

Fig. 1. Disk-integrated solar phase curve of Enceladus with Voyager clear filter (0.48 μm) and Earth-based V-filter (0.55 μm) points from Hammel and Klavetter CCD data. Magnitudes are normalized to -2.5 log p_v where p_v is the geometric albedo in the V-band.

Using the new solar phase curve we calculate a phase integral $q = 0.89$ and a Bond albedo $A_B = 0.89$. The results agree with Voyager IRIS values (Hanel et al., 1982) $A_B = 0.89 \pm 0.02$ and $q = 0.89 \pm 0.09$ (for $p_v = 1.0$, the geometric albedo based on Voyager and Earth-based observations). Our values compare favorably with those of Buratti and Veverka (1984): $A_B = 0.90 \pm 0.01$, $p_v = 1.04 \pm 0.15$, and $q = 0.94 \pm 0.1$. Since the spectrum of Enceladus is fairly flat (Cruikshank, 1980), we assumed that the spherical albedo $A = p_v q$ approximates the Bond albedo.

It is remarkable that an object as bright as Enceladus is so strongly backscattering. Snow and frost surfaces found in nature typically scatter incident radiation in the forward direction (Verbiscer and Veverka, 1990b). The exceptionally high albedo precludes the existence of significant amounts of impurities in the surface of Enceladus. Therefore, the frost itself must be backscattering, unlike known terrestrial analogs (Verbiscer et al., 1990).

This research was supported in part by NASA grants NGT 50482 and NSG 7156.

References

Buratti, B. J. 1984. Voyager disk-resolved photometry of the Saturnian satellites. *Icarus 59*, 392-405.

Buratti, B. J. 1986. Enceladus: Implications of its unusual photometric properties. *Icarus 75*, 113-126.

Buratti, B. J., and J. Veverka, 1984. Voyager photometry of Rhea, Dione, Tethys, Enceladus, and Mimas. *Icarus 58*, 254-264.

Cruikshank, D. P. (1980). Near-infrared studies of the satellites of Saturn and Uranus. *Icarus 41*, 246-258.

Franz, O. G., and R. L. Millis, 1975. Photometry of Dione, Tethys, and Enceladus on the UBV system. *Icarus 24*, 433-442.

Hanel, R., B. Conrath, F. M. Flasar, V. Kunde, W. Maguire, J. Pearl, J. Pirraglia, R. Samuelson, D. Cruikshank, D. Gautier, P. Gierasch, L. Horn, C. Ponnamperuma, 1982. Infrared observations of the Saturnian system from Voyager 2. *Science 215*, 544-548.

Hapke, B., 1986. Bidirectional reflectance spectroscopy 4. The extinction coefficient and the opposition effect. *Icarus 67*, 264-280.

Koutchmy, S., and P. L. Lamy, 1975. Study of the inner satellites of Saturn by photographic photometry. *Icarus 25*, 459-465.

Verbiscer, A., P. Helfenstein, and J. Veverka, 1990. Icy satellites in the outer solar system: A backscattering frost component? Submitted to *Nature*.

Verbiscer, A., and J. Veverka, 1990a. The photometric roughness of Enceladus. In preparation.

Verbiscer, A., and J. Veverka, 1990b. Photometric properties of snow and frost surfaces. *Icarus*, submitted.

THE INTEGRAL PHASE FUNCTION OF EUROPA

D. Domingue and B. Hapke (Department of Geology and Planetary Science, University of Pittsburgh) and W. Lockwood and D. Thompson (Lowell Observatory)

Measurements taken by two of us (W.L. and D.T.) with narrow band filters at 0.47 and 0.55 μm at small phase angles clearly show the existence of a sharp, narrow opposition peak. We have combined this data with Voyager images to give a range of phase angle coverage from 0.3° to 119°. Application of Hapke's photometric theory to this integral data gives the following results. The photometric parameters are remarkably similar for both wavelengths and hemispheres. For example, the values at $\lambda = 0.47$ μm for the leading side are as follows: single scattering albedo $w = 0.913$; opposition effect amplitude $B_o = 0.43$; opposition effect width $h = 0.0016$; double-lobed Henyey-Greenstein forward scattering parameter $b = 0.46$ and back scattering parameter $c = 0.15$; mean roughness angle $\bar{\theta} = 10^{\circ}$. The small roughness implies that the low surface relief seen at kilometer scales in the Voyager images extends down to centimeter scales. The very narrow opposition surge may be caused by some other phenomenon than shadow- hiding; however, if it is due to shadow- hiding, then the porosity of the upper layers of the regolith must be very high, of the order of 96% or more. This is much larger than that of a regolith generated by meteoritic gardening, which would be similar to lunar soil and have a porosity of the order of 60%. However, it is within the range of dry powdered snow or frost. The high porosity implies that the structure of the visible regolith at cemtimeter sclaes is dominated by endogenic processes, such as frost sublimation. The differences between our results and those of other studies are due primarily to the new data at small phase angles, which was not available to previous workers.

Laboratory Reflectance Spectra of Irradiated Ices: Applications to Europa

J.W. Boring, Dept. of Nuclear Engineering and Engineering Physics, University of Virginia, Charlottesville, VA 22901

Much of the information about the character of the surfaces of planetary bodies has been obtained by studying the spectra of reflected sunlight. From these spectra one obtains a feel for the chemical species present on the surface, as well as its topography and crystal structure. However, it has become increasingly apparent that in many cases the surfaces are rather complex, consisting of a mixture of original materials that have been modified over time by various processes. As a result of this complexity it is frequently difficult to assign unambiguously a spectral feature to a definite species and structure without additional information. If we now focus our attention on planetary satellites and rings then one of the processes that is most important in altering the surface is due to its bombardment by ions trapped in the magnetosphere of the planet. These ions become implanted in the surface region, they break chemical bonds in the material (resulting in new species) and they alter the topography and crystal structure of the surface. Because these ions can produce such drastic changes in the character of the surface it is absolutely essential that we have a body of carefully controlled laboratory data for comparison with the direct planetary observations. In the present work we concentrate on one ubiquitous surface material - H_2O and the Jovian satellite Europa. The program involves studying in the laboratory the reflectance characteristics of ice under a variety of conditions both before and after bombardment by keV ions. The first measurements will be made in the ultraviolet and visible. Later the measurements will be expanded to include the infrared.

The experimental system consists of a closed cycle helium refrigerator for producing a target temperature in the range 15-150K, an ion accelerator with energy capability in the range 5-60 keV, a target chamber with UHV capability down to 10^{-10} Torr, light sources in the visible, UV and IR, and VUV and FTIR spectrometers for observing the spectrum of light reflected from a solid H_2O surface.

Preliminary measurements for the effects of ion bombardment on the reflectance of ice have been made in our laboratory by graduate students O'Shaughnessy and Nowakowski. Their results indicate that there may be absorption features produced by both the implantation of atoms such as sulfur and also new species that are produced as a result of the bonds broken in the original H_2O molecules. We are now in the process of doing systematic studies of the reflection of solid

H_2O as a function of ion fluence, growing temperature, bombarding temperature and ion species. The reflectance spectra taken in these measurements are compared to the reflectance from a mirror of known spectral reflectance, thereby determining the absolute shape of the curves.

From our first series of measurements with this system we have made the following observations: (1) In the temperature range 30-90K the films grown at the higher temperatures are more reflecting (no ion bombardment),

with no strong spectral features. (2) Bombardment of a 50 μm film at 60K with ions produces two strong features, one at a wavelength of 0.26 μm and one at 0.36 μm. The 0.36μm feature is remarkable in that it is produced at relatively low fluences and does not get stronger as the fluence is increased, relative to the other parts of the spectrum. (3) Measurements at 30K give similar results but the spectral features are weaker.

PRELIMINARY QUANTITATIVE ASSESSMENT AND ANALYSES OF PHOBOS 88 TERMOSKAN OBSERVATIONS OF MARS

B. H. Betts, T. Svitek, M. L. Santee, B. C. Murray, D. Crisp, California Institute of Technology, D. A. Paige, University of California at Los Angeles, M. Naraeva and A. Selivanov, Institute of Space Devices, Moscow.

In February and March, 1989, the Termoskan instrument onboard the Phobos '88 spacecraft of the USSR acquired a limited set of very high resolution simultaneous observations of the reflected solar and thermal emission from Mars' equatorial region. We have analyzed quantitatively approximately 20% of the entire data set and here present three preliminary analyses: a comparison of Termoskan data with Viking Infrared Thermal Mapper (IRTM) data; an analysis of thermal infrared limb brightening seen on the morning limb and other preliminary limb analysis results; and an analysis of one observation of the shadow of the moon Phobos as observed on Mars by Termoskan.

THE EXPERIMENT: Termoskan was a two channel optical-mechanical scanning radiometer with one visible channel (0.5-1.0 μm and one thermal infrared channel (8.5-12.0 μm). The instrument was fixed to the spacecraft, pointing in the anti-solar direction. Resolution per pixel at nadir was 1.8 km for 3 of the 4 panoramas acquired and 300 meters for the remaining panorama.

COMPARISON WITH IRTM OBSERVATIONS: To determine the absolute accuracy of the Termoskan data set, we compared it with the well calibrated Viking IRTM measurements. We compared brightness temperatures from Termoskan infrared observations to brightness temperatures from IRTM's 11 micron channel (9.8 to 12.5 μm). We constrained the IRTM data to match approximately the Termoskan data in season (L_s), longitude, latitude, and local time of day. In order to compare the two data sets, we degraded the Termoskan resolution to a resolution comparable to Viking. Figure 1 shows a representative Termoskan-IRTM comparison which is consistent with other areas that we have compared. We find that the Termoskan brightness temperatures are approximately 3 K warmer than corresponding IRTM brightness temperatures; that relative features correlate very well in the two data sets; and that Termoskan sees thermal variations even at the limit of its spatial resolution.

TERMOSKAN LIMB PROFILES: Limb brightening in the Termoskan thermal infrared channel from the morning limb was consistently observed. Figure 2 shows a sample morning limb profile. We explain the peak in thermal brightness just off the limb as a consequence of an ice or dust haze in equilibrium with the atmosphere, which is warmer than the pre-dawn surface. Paige used a delta-Eddington spherical shell model developed for the Mars Observer limb sounder PMIRR (Pressure Modulator Infrared Radiometer), and found that a water ice haze with a scale height of 5 km (isothermal atmosphere at 200 K, surface at 175 K) could produce a thermal brightness signature matching the one in Figure 2. The visible channel defines a highly scattering atmosphere to extend 60 to 70 km above the limb. Figure 3 shows a sample evening limb profile. The absence of any infrared evening limb brightening is consistent with a surface which is warmer than the atmosphere . On the evening limb a high haze was observed which may correlate well with that seen by the Phobos '88 AUGUST experiment.

PHOBOS SHADOW MEASUREMENTS: Termoskan observed the shadow of Phobos on the surface of Mars during two of its four scans. Due to the scanning nature of the instrument and the similarity of the spacecraft's orbit to that of Phobos, the shadow appears elongated in the images. We have looked at one shadowed region south of Arsia Mons. We used the observed drop in visible flux within the shadowed area to model the solar insolation as a function of both actual time since the beginning of eclipse and position in the scan. We then used this in an adaptation of the Clifford et al., 1987 one

dimensional, finite difference thermal model for a homogeneous surface [1]. By comparing the model results with the temperature drops observed in the infrared scan we find thermal inertias varying from 0.7 to 1.1 (10^{-3} cal cm^{-2} $s^{-1/2}$ K^{-1}). These values of thermal inertia are lower by factors of 2 to 4 compared to thermal inertias derived from Viking IRTM measurements [2] for the same area. Viking-derived inertias are sensitive to the upper few centimeters of the surface, whereas the Phobos shadow measurements are sensitive only to the upper tenths of a mm of the surface due to the short duration of the eclipse. Our results imply that there is a thin layer of highly insulating material, for example a thin, loosely packed dust layer, on the surface which overlies a layer of less insulating material.

REFERENCES: (1) Clifford, S.M., C.J. Bartels, and E.P. Rubenstein (1987), Lunar and Planetary Institute; (2) Kieffer, H.H., T.Z. Martin, A.P. Peterfreund, B.M. Jakosky, E.D. Miner, F.D. Palluconi (1977), Journal of Geophysical Research, 82 (28), pp. 4249-4291.

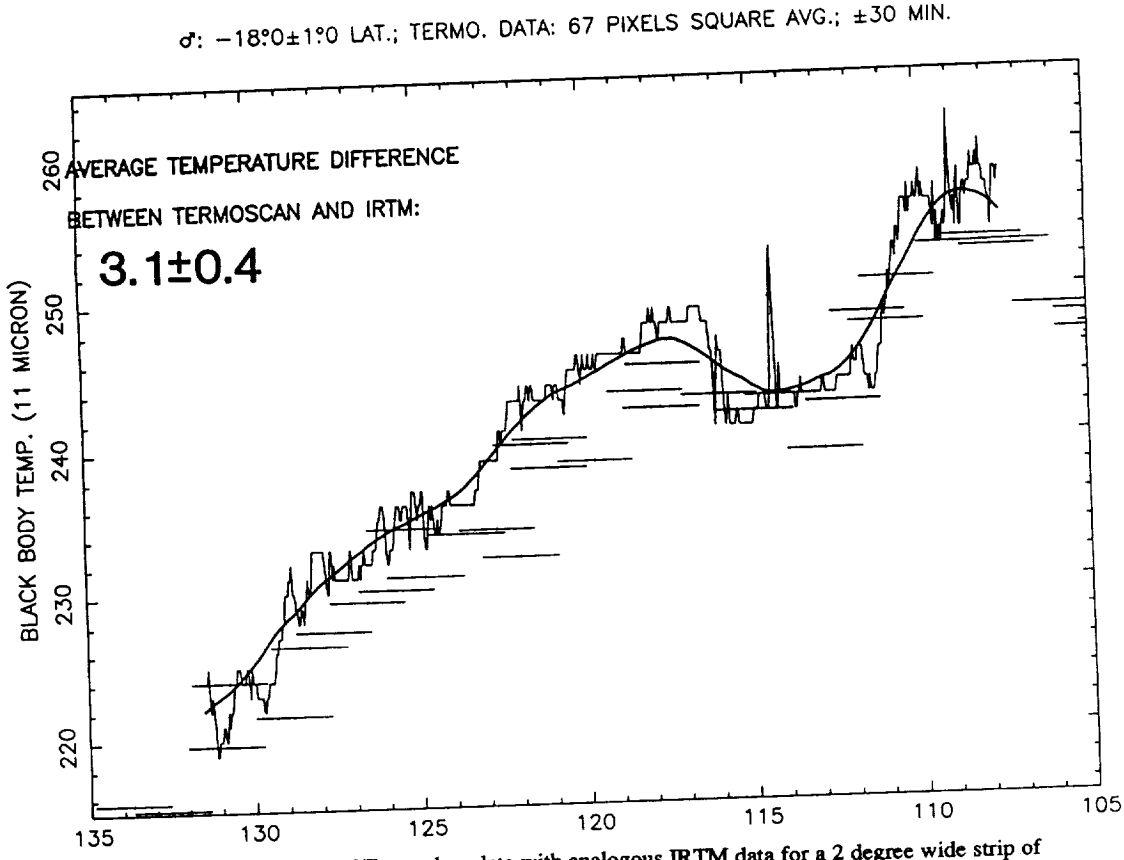

Figure 1: Comparison of Termoskan data with analogous IRTM data for a 2 degree wide strip of constant latitude centered on -18 degrees. The dark line represents a sliding boxcar average of Termoskan data which has been averaged in 2 x 2 degree squares. The lighter line is a 1 pixel Termoskan strip for reference. The points represent IRTM data with the error bars representing the footprint of each IRTM data point. IRTM data is constrained to match the Termoskan data to within ±10 degrees of L_s and to within ±30 minutes of local time. After comparing each IRTM point with the averaged Termoskan point of the same longitude, the average temperature difference between Termoskan and IRTM is 3.1±0.4 K with the Termoskan temperatures being warmer. Local time of day in the data shown ranges from about 8.5 to 10.3.

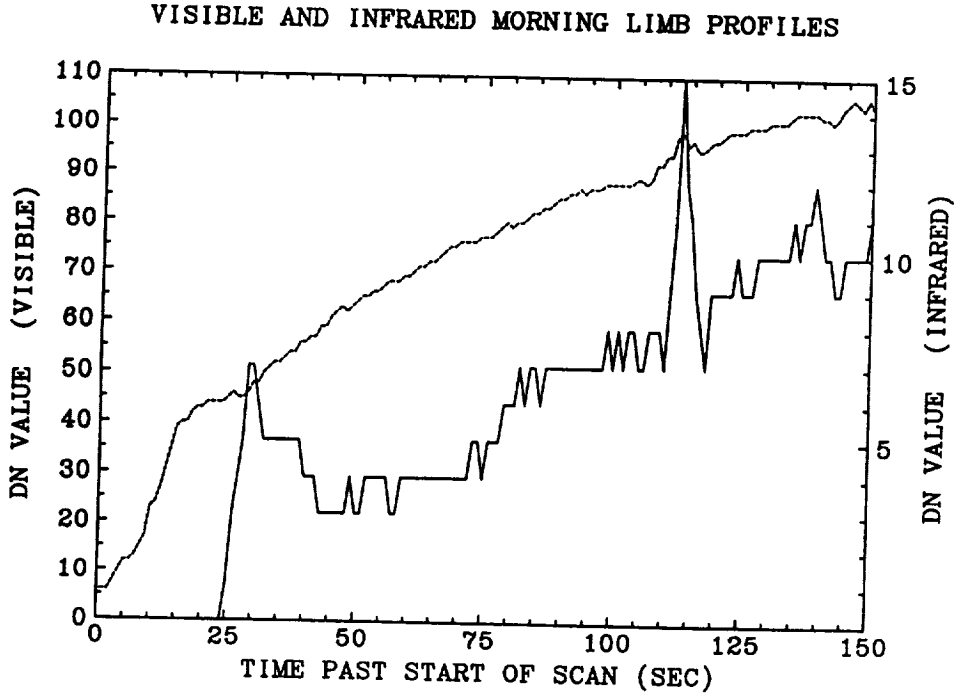

Figure 2: A single morning limb profile for both the visible (dashed curve) and the infrared (solid curve) channels. The solid limb was encountered at approximately 26 seconds after the start of the scan.

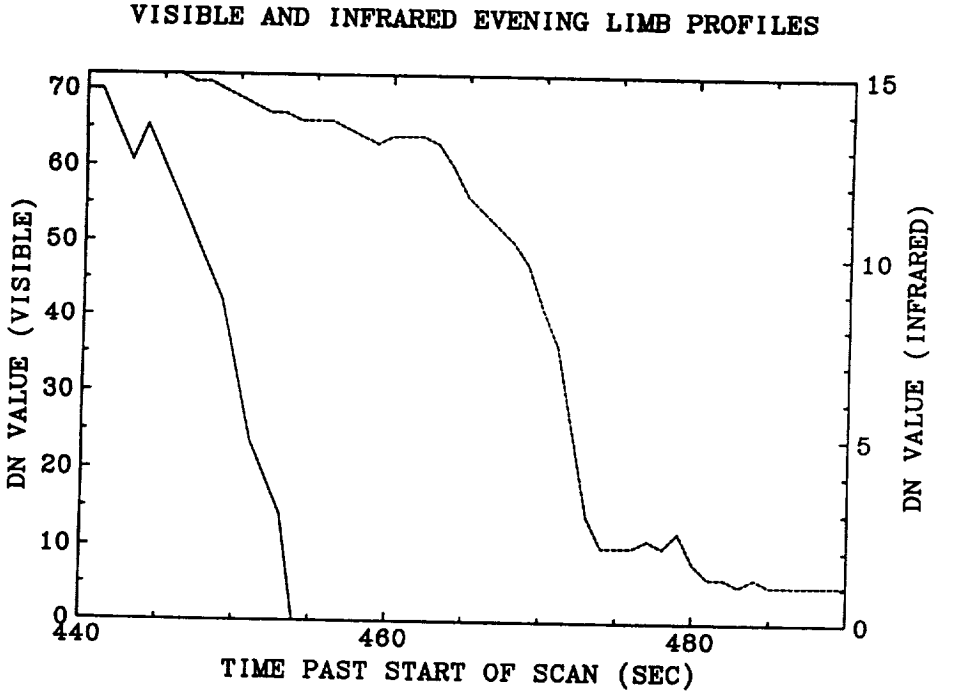

Figure 3: A single evening limb profile for both the visible (dashed curve) and the infrared (solid curve) channels. Note that the times on the horizontal axis are local to the particular data file and do not represent actual times along the scan. Note the peak in visible brightness at 479 seconds which is a distinct cloud feature.

SURFACE HETEROGENEITY AND METEORITE ANALOGS OF PHOBOS: ANALYSIS OF KRFM SPECTRAL RESULTS. D.T. Britt, S.L. Murchie, C.M. Pieters, J.W. Head, P.C. Fisher, S.F. Pratt (Department of Geological Sciences, Brown University, Box 1846, Providence, RI, U.S.A.). L.V. Ksanfomality, A. Zharkov, G. Nikitin, B.S. Zhukov, and A. Kuzmin (Space Research Institute, Profsoyuznaya, 84/32, 117810, Moscow GSP-7, U.S.S.R.).

Introduction: On March 25, 1989 the 10-channel, 0.3-0.6 μm KRFM spectrometer on the Soviet *Phobos* 2 spacecraft acquired spectral data along two groundtracks across the surface of the Martian moon Phobos. Track 1 sampled a swath 0.83 kilometers wide located at 4.5°S, 140°W-242°W; track 2 covered a swath 0.94 kilometers wide located at 2°N, 194°W-227°W [1]. The location of these tracks coincides with areas of surface heterogeneity recognized in VSK visible/near-IR color-ratio images and KRFM radiometer data. The tracks sample three of four color units mapped in the color-ratio images, the "red", "reddish gray", and "bluish gray" units [2]. This analysis will focus on presentation of KRFM spectra of Phobos surface material, comparison with spectra of a suite of possible meteorite analogs, and the mineralogical interpretation of these data for clues to the composition of Phobos. Because of instrumental drop-out in channel 5 and a low signal-to-noise ratio in channel 1, these two channels were not included in this analysis and all data will be presented in an 8-channel format. Calibration of these data are described by Murchie et al. [1] and include use of an internal standard and a composite spectrum of Phobos derived from previous remote observations [3].

Spectral Data: Shown in **Figure 1** are the spectra of ten areas on Phobos and the composite disk-integrated spectrum used as a calibration standard [1]. These spectra are scaled to unity at 0.55 μm (KRFM channel 9) and, for viewing purposes, the reflectance scale is offset by 10% for each spectrum. All Phobos spectra are averages of four adjacent spectra taken at one second intervals, effectively sampling approximately one kilometer along track. Although the spectra exhibit substantial heterogeneity, several general observations can be made. (1) All spectra show a strong UV drop-off, usually beginning between channels 4 (0.363 μm) and 6 (0.410 μm). (2) Most spectra are red-sloped, and the degree of redness tends to increase in a westerly direction along track. This reddening to the west confirms similar results from color-ratio images [2]. (3) Absorption bands are present in spectra of "bluish gray" material (centered in the KRFM spectra on channel 3 at 0.346 μm and channel 10 at 0.6 μm), the "red" material (centered on channel 8 at 0.488 μm), and the "reddish gray" ghost crater (centered on channel 7 at 0.445 μm). The areas characterized by these absorptions correlate with the color units identified using VSK color-ratio data [2].

Shown in **Figure 2** are laboratory spectra of eleven meteorites representing classes of material suggested as possible compositional analogs for Phobos, specifically carbonaceous chondrites [3] and optically altered black chondrites [4]. These spectra were originally obtained at high spectral resolution with RELAB [5], and were resampled into KRFM bandpasses by a computer algorithm based on the KRFM spectral response in each channel. Once again, all spectra are scaled to unity at 0.55 μm and are offset for viewing purposes.

Analysis and Interpretation: A comparison of spectra in **Figures 1** and **2** shows that no single meteorite or group of meteorites has a unique spectral similarity with the Phobos surface material in the wavelength range analyzed by KRFM. Most meteorites exhibit a relatively gradual UV drop-off that begins between 0.55 and 0.6 μm, in contrast to the rapid drop-off below 0.410 μm and the relatively flat spectrum at longer wavelengths that are evident in the Phobos data. In addition, no meteorites exhibit the absorption bands seen in the KRFM data at 0.488 and 0.445 μm. A more modest absorption band at 0.346 microns is seen in both the spectra of the bluish gray unit and in the carbonaceous chondrites Boriskino, Kainsaz, Groznaja, and Orgueil. However, data obtained by the VSK instrument indicates that the bluish gray unit's color-ratio of 1.0-1.1 is outside the range observed in carbonaceous chondrites, but is within the range observed in optically altered mafic silicates such as black chondrites [6]. The two other mapped units sampled by the KRFM ground track, the red and reddish gray units, have color ratios that overlap the range observed in carbonaceous chondrite meteorites and some optically altered black chondrite meteorites. Of the meteorites considered, the black chondrites Gorlovka and Pervomaisky have spectra most similar to those of Phobos surface materials, especially the "bluish gray" color unit.

The spectral similarity of Phobos surface material to meteorite analogs was quantitatively tested using principal components analysis. In this analysis, shown in **Figure 3**, the variance between spectra is transformed into orthogonal principal components and reprojected into statistical space where distance is a measure of relative spectral dissimilarity. The strongly red sloped carbonaceous chondrites plot at a larger distance from the area defined by the KRFM Phobos spectra. Although there is substantial variation between the spectra of the three black chondrites shown in this plot, black chondrites tend to be more similar to Phobos spectra than any carbonaceous chondrites. In addition, the analysis shows that the anhydrous black chondrites and CV and CO carbonaceous chondrites tend to be less dissimilar to Phobos surface material than the hydrous CI and CM carbonaceous chondrites, consistent with the low state of hydration reported by ISM and telescopic observations [7,8].

Conclusions: Analysis of KRFM spectral data show that, among the meteorites studied, there are no unique spectral analogs for Phobos surface material. Currently, the closest spectral analogs are the optically altered black chondrites Gorlovka and Pervomaisky. The weak UV absorption bands in KRFM spectra and the red slope in VSK color-ratio data indicate that carbonaceous chondrite-like material may also be a component of Phobos surface material. However, the lack of close carbonaceous chondrite spectral analogs and the existence of apparent absorption bands in KRFM spectra that are not seen in meteorite spectra suggest that there are processes and/or materials on the surface of Phobos that are not represented in the meteorite collections. The similarities between KRFM spectra of Phobos and the spectra of black chondrites suggest that optically altered mafic silicates may constitute a component of the surface

material of Phobos, and that optical alteration and mixing by regolith processes may be an important factor in the evolution of Phobos surface material.

REFERENCES: [1] Murchie S. et al. (1990a) *LPS XXI*, These volumes. [2] Murchie S. et al. (1990b) *LPS XXI*, These volumes. [3] Pang K. et al. (1978) *Science 199*, 64-66. [4] Britt D. and Pieters C. (1988) *Astron. Vestnik 22*, 229-239. [5] Pieters C. (1989) RELAB Users Manual, available on request. [6] Britt D. and Pieters C. (1990) Unpublished RELAB spectra. [7] Lucy P. and Bell J. (1989) *LPS XX*, 598-599. [8] Bibring J-P. et al. (1989) *Nature 341*, 591-593.

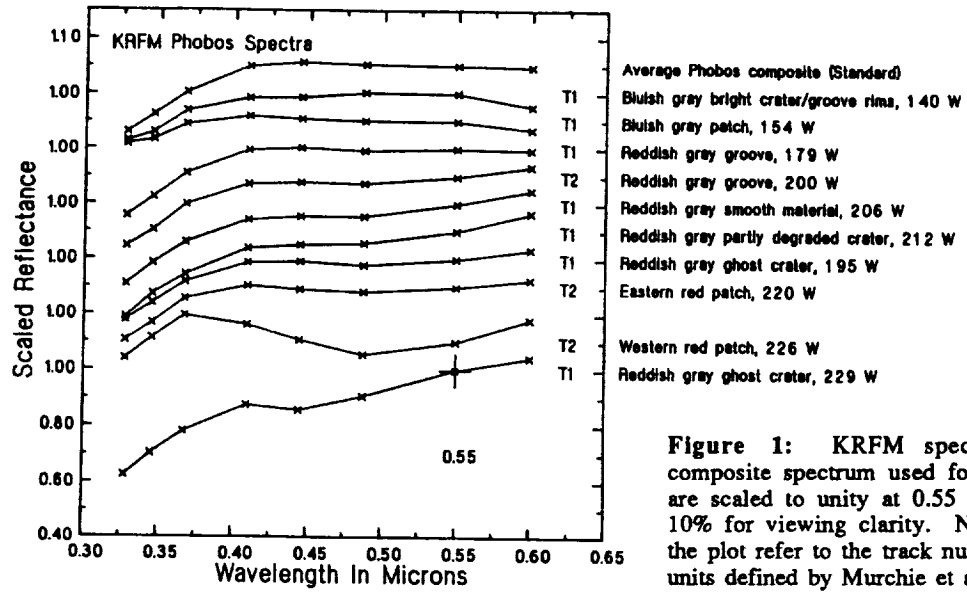

Figure 1: KRFM spectra of Phobos and the composite spectrum used for calibration. All spectra are scaled to unity at 0.55 and each spectra is offset 10% for viewing clarity. Notations on left border of the plot refer to the track number of the data and color units defined by Murchie et al. [2].

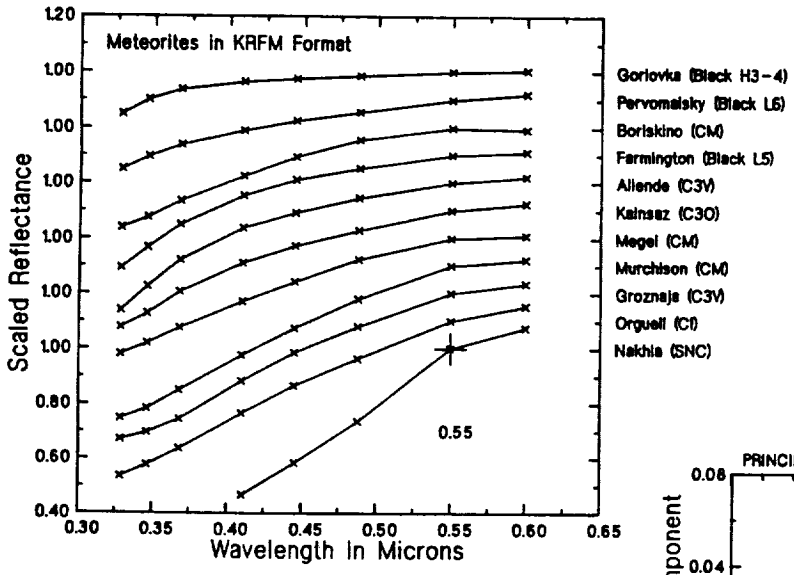

Figure 2: Meteorite laboratory spectra resampled into KRFM spectral bandpasses. All spectra are scaled to unity at 0.55 and each spectra is offset 10% for viewing clarity. Meteorites are arranged roughly in order of decreasing redness.

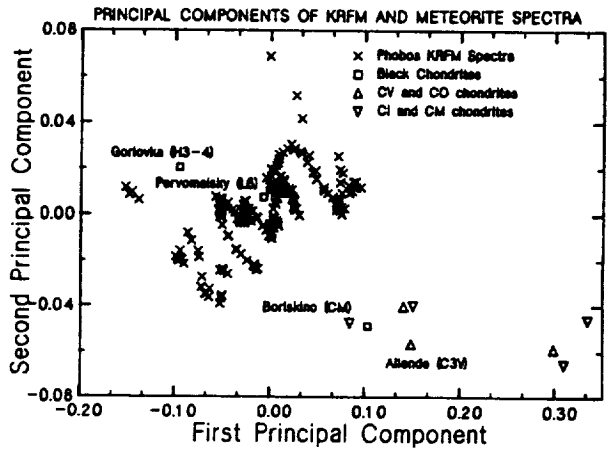

Figure 3: The first two principal components of KRFM and meteorite spectra. The position of an object in the plot is a measure of spectral similarity.

OPTICAL PROPERTIES OF CO_2 ICE AND CO_2 SNOW FROM THE ULTRAVIOLET TO THE INFRARED: APPLICATION TO SURFACE FROST DEPOSITS AND CLOUDS ON MARS

Gary B. Hansen, Geophysics Program AK-50, University of Washington, Seattle, WA 98195 U.S.A.
Stephen G. Warren and Conway B. Leovy, Department of Atmospheric Sciences AK-40,
University of Washington, Seattle, WA 98195 U.S.A.

The planet Mars has a tenuous atmosphere which is ~95% carbon dioxide. The annual variation of atmospheric pressure is about 30% of the mean value of 6 mbar, with most of the variation due to condensation in the winter hemisphere, where radiative cooling lowers the temperature of the surface and/or atmosphere to below the equilibrium condensation point. This condensation controls a major component of the atmospheric circulation (Pollack et al., 1990) and the global atmospheric pressure. Exact modelling of the radiative properties of the CO_2 clouds and frost which determine the rate and altitude of condensation requires the refractive index and absorption coefficient of bulk CO_2 ice as well as particle size distributions and dust optical properties and distribution. These optical properties must be known throughout the visible and near infrared as well as in the thermal infrared, if springtime sublimation of the polar deposits by radiative processes is to be understood.

Warren(1986) has compiled a best estimate of the optical constants of CO_2 ice, which nevertheless contains a large number of gaps and uncertainties. Indications are, however, that the absorption of CO_2 ice is very low in the visible and near ultraviolet and between the strong absorption bands in the infrared. This increases the reflectance and reduces the emissivity of a surface of small particles since photons can pass through more particles and be scattered out of the surface before being absorbed. Using the optical properties from Warren (1986) and the radiative transfer models of Wiscombe and Warren (1980) and Warren and Wiscombe (1980), Warren et al. (1990) calculated the spectral albedo and emissivity of CO_2 snow from 0.2 to 25μm as a function of particle size and dust or water ice contamination. The differences with our more common experience with water snow are striking, with near infrared reflectance > 90% and thermal infrared emissivity < 20% in some spectral regions and for some particle sizes (water snow is 'black' in these regions). Clouds of particles which have low absorption (high single scattering albedo) in the infrared do not act as blackbodies as do water clouds, but instead show low emissivity and are effective at backscattering surface thermal radiation (Hunt, 1980). The strength of these effects is dependent on accurate knowledge of absorption between the strong bands, which is not now available.

A large number of spacecraft measurements have hinted at unusual emissivities or unidentified spectral features which may be attributed to the properties of CO_2 ice. Unexpectedly low brightness temperatures in the polar regions of Mars have been measured in the thermal infrared by both the Mariner 9 and Viking orbiters. For example, measurements from IRTM (a multichannel infrared radiometer on Viking) across the polar regions in the winter and spring show 20μm brightness temperatures significantly lower than the 11μm brightness temperatures (Kieffer et al.,1976; Kieffer, 1979). Recent reexamination of the thermal spectra from the Mariner 9 orbiter reveal similar non-blackbody spectra including those of winter polar regions which show brightness temperatures at wavelengths longer than 20μm below the equilibrium for CO_2 condensation. Among the explanations offered for these observations are low emissivity of the surface (e.g.,

Kieffer et al., 1976; Ditteon and Kieffer, 1979) and CO_2 clouds (e.g., Paige, 1985; Paige, 1989). Calvin(1989), using the scattering model of Hapke(1981), has shown that the spectral reflectance calculated with the Warren(1986) index estimates in the near infrared do not match with the spectra of laboratory frosts or the spectra returned by Mariner 7. The proper modeling of these phenomena will require better knowledge of the optical constants of the CO_2 ice particles on the ground or in the clouds.

It has been proven difficult to grow CO_2 ice in other than thin films. This is apparently due to frost-like non-equilibrium growth or to excessive thermal stresses, which cause clouding or cracking (Ditteon and Kieffer, 1979). The imaginary index of refraction (= linear absorption coefficient $\times \lambda/4\pi$) has therefore been poorly measured or not measured at all where linear absorption < 10 cm^{-1} (imaginary index < 10^{-4} at 1μm) Among the existing measurements of the absorption of CO_2 ice in the regions of low absorption are those from 0.3μm to 1μm with impure ice (Egan and Spagnolo, 1969) and those from 2.5μm to 25μm with cracked and cloudy samples (Ditteon and Kieffer, 1979). However Gaizauskas (1955) succeeded in growing clear crystals of several millimeters thickness to measure the absorption bands near 7μm. Measurements have never been made beyond 25μm, between 1μm and 2.5μm except for the strong bands or between the strong ultraviolet absorption <0.14μm and 0.3μm. Measurements of the real index of CO_2 ice have been made at many temperatures in the visible and have been extended to all wavelengths by the use of accurate knowledge of strong absorptions and Kramers-Kronig analysis (Warren, 1986).

We have found that it is possible to grow large clear samples of CO_2 ice at Mars-like temperatures of 150K-170K if a temperature-controlled refrigerator is connected to an isolated two-phase pure CO_2 system. In this way, the system pressure adjusts to the equilibrium value dictated by the refrigerator temperature and the ice grows at a rate consistant with the gas supply. Samples of up to 18 cm^3 have been grown from ultra-high purity gas in this way. We have designed a chamber for transmission measurements whose optical path between the 13mm diameter windows is adjustable from 1.6mm to 107mm. This will allow measurements of linear absorption down to <0.01 cm^{-1}. The spectral resolution will be provided from the ultraviolet to 5.5μm by a grating monochrometer whose slit image will be focused in the chamber center and on the following detector by mirror optics. The spectral region from 2.5μm to 50μm will be measured by a Fourier transform spectrometer whose interference beam will be focused through the chamber and onto the detector. The absorption coefficient will be determined by a linear fit to the logarithm of the absorption at different optical path lengths for each wavelength. If measurements are made at two distinct temperatures, some estimate of the temperature variation of the coefficients can be made. It would also be useful to devise a way to make an accurate measurement of the real index of refraction at wavelengths between the strong bands other than in the visible, to help constrain the Kramers-Kronig analysis made by Warren(1986).

Once the revised optical constants have been determined as a function of wavelength and temperature, they can be applied to spectral reflectance/emissivity models for CO_2 snow surfaces, both pure and contaminated with dust or water ice, using the delta-Eddington approach of Warren et al. (1990) and/or the modified two-stream approach of Hapke (1981). It will be useful, also, to develop an infrared scattering-emission cloud radiance model (especially as viewed from near the limb) in order to develop a strategy for the identification of CO_2 cloud layers by the PMIRR (atmospheric infrared radiometer) instrument on Mars

Observer. These model results will hopefully also shed light on the unusual measurements made on the previous missions.

Acknowledgements. We are grateful for the use of the laboratory and fabrication facilities at the Jet Propulsion Laboratory, Pasadena, CA, for this study, and the help of Vachik Gharakhanian, Robert Carlson and William Smythe.

REFERENCES

Calvin, W.M., Additions and corrections to the absorption coefficients of CO_2 ice: Applications to the Martian south polar cap, submitted to *J. Geophys. Res.*, 1989.

Ditteon, R., and H.H.Kieffer, Optical properties of solid CO_2: Application to Mars, *J. Geophys. Res.*, **84**, 8294-8300, 1979.

Egan, W.G., and F.A.Spagnolo, Complex index of refraction of bulk solid carbon dioxide, *Appl. Optics*, **8**, 2359, 1969.

Gaizauskas, V., Studies of the infrared and raman spectra of gaseous, liquid and solid carbon dioxide, PhD thesis, Univ. of Toronto, Toronto, Ontario, Canada, 1955.

Hapke, B., Bidirectional reflectance spectroscopy, 1. Theory, *J. Geophys. Res.*, **86**, 3039-3054, 1981.

Hunt, G.E., On the infrared radiative properties of CO_2 ice clouds: Application to Mars, *Geophys. Res. Lett.*, 7, 481-484, 1980.

Kieffer, H.H., Mars south polar spring and summer temperatures: A residual CO_2 frost, *J. Geophys. Res.*, **84**, 8263-8288, 1979.

Kieffer, H.H., S.C.Chase Jr., E.D.Miner, F.D.Palluconi, G.Muench, G.Neugebauer and T.Z.Martin, Infrared thermal mapping of the Martian surface and atmosphere: First results, *Science*, **193**, 780-786, 1976.

Paige, D.A., PhD Thesis, California Inst. of Tech., Pasadena, CA, 1985.

Paige, D.A., An analysis of Viking IRTM observations of the Martian polar regions during the polar night seasons, submitted to *J. Geophys. Res.*, 1989.

Pollack, J.B., R.M.Haberle, J.Schaeffer and H.Lee, Simulation of the general circulation of the Martian atmosphere, 1, Polar processes, *J. Geophys. Res.*, **95**, 1447-1474, 1990.

Warren, S.G., Optical constants of carbon dioxide ice, *Appl. Optics*, **25**, 2650-2674, 1986.

Warren, S.G., and W.J.Wiscombe, A model for the spectral albedo of snow. II: Snow containing atmospheric aerosols, *J. Atmos. Sci.*, **37**, 2734-2745, 1980.

Warren, S.G., W.J.Wiscombe and J.F.Firestone, Spectral albedo and emissivity of CO_2 snow in Martian polar caps: Model results, *J. Geophys. Res.* in press, 1990.

Wiscombe, W.J., and S.G.Warren, A model for the spectral albedo of snow. I: Pure snow, *J. Atmos. Sci.*, **37**, 2712-2733, 1980.

ANALYSIS OF MARINER 6 AND 7 DATA (2-6μm): APPLICATION TO THE MERIDIANI SINUS, OXIA PALUS, HELLAS AND SOUTH POLAR CAP REGIONS OF MARS

Trude V.V. King and Wendy M. Calvin, U.S. Geological Survey, Denver, CO 80225

Studies using the Mariner 6 and 7 data were undertaken to identify previously unrecognized absorption features and to confirm the results of recent ground-based observations. The Mariner data have the advantage that they are not affected by terrestrial atmospheric absorptions, have higher spatial resolution than terrestrial observations, and cover the short wavelength infrared region with reasonably high spectral resolution. However, the Mariner data are subject to a variety of other uncertainties which we have attempted to rectify, as much as is possible twenty years after the original flyby. A major programming effort was required to prepare the data for interpretation.

The Mariner infrared spectrometer data were obtained from Martin (1985) who provided corrections to the current latitude and longitude system and an initial wavelength calibration. However, the initial wavelength calibration was inaccurate. The 2-6μm wavelength region is covered by two halves (1.9-3.7μm and 3.0-6.0 μm) of a circular variable filter wheel. The rotation rate of the wheel seemingly varied non-linearly, thus prohibiting the use of fiduciary spikes in the filter wheel for calibration within or across a wavelength segment. It was necessary to use CO_2 atmospheric absorptions, an absorption in the circular variable filter and fiduciary spikes as inter- and intra- segment calibrations for the two halves of the CVF.

Additional corrections which had to be determined and applied to the data in the 3-6μm wavelength region included removal of a space background signature, correction for the instrument response as a function of wavelength, removal of the thermally emitted component and correction of the reflected solar response to obtain reflectance. The instrument response function, derived from black-body calibration spectra and the space background response (average of six spectra recorded after the flyby) were smoothed using a fast Fourier transform. The solar flux was calculated and adjusted for Mars' distance from the Sun, and the thermal contribution was calculated using temperatures determined by the original instrument team (Pimentel et al., 1974). Two studies using the corrected Mariner data, one of the Martian south polar cap and another of non-icy areas, have been completed.

Calvin (1989,1990) used the processed Mariner 7 data in a study comparing laboratory CO_2 frosts, calculated CO_2 ice reflectances and the Martian south polar cap spectra. Figure 1 shows a calculated ice and a Mariner 7 spectrum of the Mars south polar region. The Mariner 7 data of the south polar cap display spectral trends similar to the calculated frost spectra. Both data sets show: increasing depth of the 2.28 and 2.34 μm features, suppression of the 3-4 μm wavelength region, and reduction of the 3.0 and 3.3 μm band depths, all of which correlate with increasing grain size. The Mariner 7 spectrum indicate an increase in the grain size from 1 or 2 mm to 1 cm or greater across the polar cap. Saturation of absorption bands in the 3-4μm region is the most probable explanation of the behavior of the spectra. However, other factors such as contamination of the CO_2 ice with water or dust may contribute to the observed spectral changes.

Differences between the calculated CO_2 spectra and Mariner spectra in

the 2.43 μm wavelength region were also reported by Calvin (1990). In the calculated spectra the 2.28, 2.34 and 2.43 CO_2 absorptions have the same intensity but in the Mariner spectra the 2.43μm absorption is less than half that of the 2.28 and 2.34μm absorptions. However, the relative intensities of the absorption bands in the spectra of the laboratory CO_2 frost on ice spectra are similar to the Mariner spectra. This suggests, assuming no problems with derived absorption coefficients in this wavelength region, that the Martian polar cap may be composed of CO_2 frost overlying CO_2 ice. The presence of small amounts of water or dust in the CO_2 mixture, or a range of grain sizes in the polar cap may also account for these spectral changes.

In a second study, Calvin and King (1990) reported on the weak absorption features between 2-6 μm in the spectra of non-icy regions of the Martian surface. Many of the weak absorption bands identified in the study occur near or in the middle of atmospheric absorption features. Thus, special care was taken in convolving a model Martian atmosphere, provided by Crisp (1989), to the resolution of the Mariner instrument. The data are discussed in two wavelength segments, 1.9-3.6μm and 3.0-6μm. The short wavelength segment has not undergone any intensity corrections due to a lack of calibration spectra at needed temperatures.

Figure 2 shows the Mariner 7 spectra (1.9-3.6μm) after removal of the model atmosphere. This spectrum shows a sharp absorption at 2.76 μm. This feature is present in all the atmosphere removed spectra and is seen as a change of slope in some of the original spectra. However, given the uncertainties of the atmospheric model, it is possible that the absorption feature may have been introduced by improper removal of atmospheric absorptions. Confirmation using Mariner 6 data was not possible due to the poor signal-to-noise quality of that instrument.

The processed Mariner 7 data confirmed the presence, of absorption features reported by Clark et al. (1990) and by Blaney and McCord (1990) based on terrestrial observations. Blaney and McCord (1990) attribute a feature at 3.8μm to atmospheric CO_2. Calvin and King (1990) corrected the Mariner data for thermal and solar fluxes and removed a continuum for comparison with models of 2 and 4 airmass atmospheres of the Hellas region. Using the 4 airmass atmosphere model, which based on path length and elevation is known to be too much atmosphere for this observation, the 3.8μm absorption remains. Thus the 3.8μm feature appears to be related to a mineralogical component in the atmospheric dust or on the surface. Before a definitive statement can be made on the origin of this feature, the atmospheric models need to be checked for inaccuracies. However, the observation that the atmospheric model is consistent with the depth of the atmospheric absorptions over other regions of Mars supports the mineralogical interpretation of the 3.8μm absorption over Hellas.

Previously unrecognized absorption features were identified in the 5-5.6μm wavelength region of Meridiani Sinus in both the Mariner 6 and 7 data by Calvin and King (1990). Absorption features on either side of the 5.2μm atmospheric CO_2 absorption are apparent in a Mariner 7 spectrum after complete reduction, see Figure 3. The 5.1, 5.35 and 5.45 μm absorptions are not believed to result from incomplete or inaccurate data reduction, but a definitive cause for the absorptions cannot be identified at this time.

Laboratory studies are now underway to determine plausible mineralogical causes for the weak absorption features identified in the Mariner spectra. Preliminary examination indicates that OH- or S- bearing

minerals may be likely candidates. In particular, spectra of hydrous carbonates presented by Miyamoto and Kato (1990) are especially interesting.

Figure 1 shows the calculated 1mm grain size CO_2 frost spectrum (dotted line) and the Mariner 7 spectrum of Mars south polar region (solid line). The Mariner data has been scaled to the reflectance level of the frost for comparison. Comparison of the 2.28, 2.34, 3.0 and 3.3 μm absorptions features suggests that the grain size of the Mariner 7 spectrum is greater than 1mm.

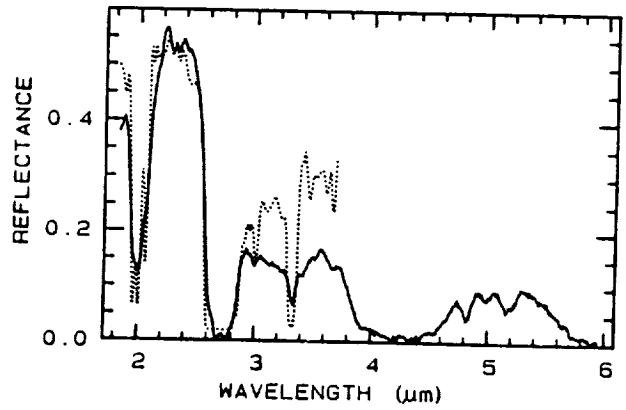

Figure 2 shows the Mariner 7 spectrum (1.9-3.6) after removal of a model atmosphere. The spectrum shows a strong 2.76μm absorption. This feature is present in all atmosphere removed spectra and is suggested in the raw data. The cause of the absorption cannot be resolved at this time.

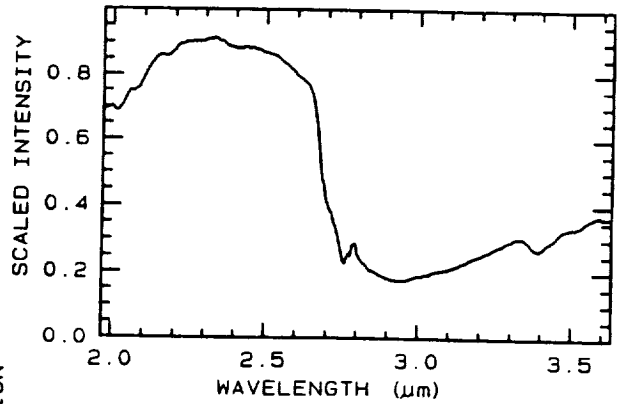

Figure 3 shows the 5-5.6μm wavelength region of Mariner 7 corrected data of Meridiani Sinus (solid line) and a scaled spectrum of the Martian atmosphere (dotted line). The 5.1,5.35, and 5.45 μm absorptions in the corrected Mariner data are not believed to result from incomplete or inaccurate data reduction. However, a definitive cause for these absorptions cannot be identified without additional work.

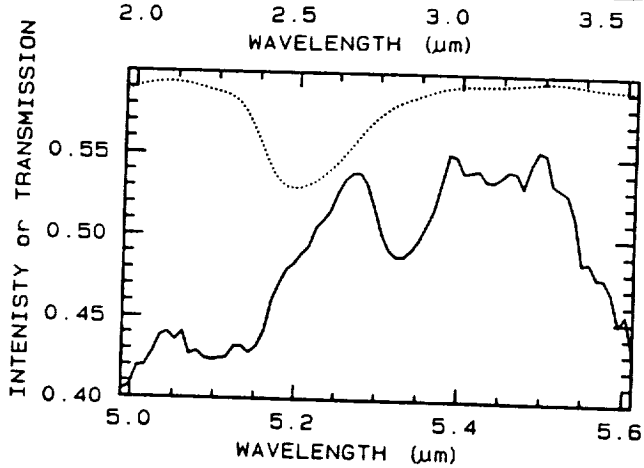

REFERENCES

Blaney and McCord, submitted to *J. Geophys. Res.*, 1990. Calvin, submitted to *J. Geophys. Res.*, 1990. Calvin, *Bull.Am.Astron.Soc.*, p. 978, 1989. Calvin and King, *LPSC XXI*, pp. 153-154, 1990. Clark, Swayze, Singer and Pollack, submitted to *J. Geophys. Res.*, 1990. Crisp, submitted to *J. Geophys. Res.*, 1989. Martin, Mariner 6 and 7 data released under the Pilot Planetary Data System, 1985. Pimentel, Forney, and Herr, *J. Geophys. Res.*, pp. 1623-1634, 1974. Miyamoto and Kato, *LPSC XXI*, pp. 801-802.

APPLICATIONS OF GAMMA-RAY SPECTROSCOPY TO ATMOSPHERIC MEASUREMENTS

Albert E. Metzger, Jet Propulsion Laboratory, Pasadena, CA 91109
and Eldon L. Haines, Sunrise Research Inc., Eugene, OR 97404

We have completed a study into the utilization of gamma-ray observations from orbit above a planet with a thin atmosphere. Three applicable methods have been found for determining atmospheric composition, column mass and surface pressure. These have been evaluated with respect to Mars.

The thin atmosphere at Mars absorbs a portion of the gamma-ray flux emitted from its surface, the proportion depending on the energy of the gamma ray and the thickness of the atmosphere. Two or more lines emitted from the same surface element, or elements related by radioactive decay, may be used to characterize the mean thickness of the atmosphere over the period of observation. This is illustrated in Figure 1 which shows the monotonic relationship between atmospheric thickness over the range expected at Mars and the count rate ratio of four gamma-ray line pairs. Based on an analytic model developed for this study, the sensitivity with which atmospheric thickness may be determined from these pairs for assumed concentrations of 0.45 ppm Th and 0.12 ppm U is shown in Figure 2 together with the sensitivity of the same four pairs taken in combination. Besides Th and U, Fe and Si are also useful for this technique. Iron should provide the most sensitivity unless Th and U concentrations reach several ppm or greater.

Oxygen is not applicable to this technique because it is a major constituent of the atmosphere as well as of surface rock material. We have found however, that one gamma-ray line of oxygen, fortunately the strongest, can be distinguished with respect to its presence in the surface or the atmosphere by virtue of its characteristic decay time. In the atmosphere, the 6129 keV oxygen line is Doppler-broadened, in the surface it is not. The concentration of atmospheric constituents may be measured by gamma-ray spectroscopy in the same manner as surface composition. On the other hand, given the fractional concentration of atmospheric oxygen from other measurements then the intensity of the corresponding gamma-ray line can be interpreted in terms of atmospheric thickness. Figure 3 shows the sensitivity with which atmospheric thickness may be determined from the measurement of the Doppler-broadened atmospheric 6129 keV oxygen line. The observed response as a fraction of the intensity from a thick target (ρ), and the relative sensitivity for 100 hr of accumulation are plotted vs atmospheric thickness. This second technique of direct determination has also been found applicable to atmospheric carbon if carbon is absent from the surface.

If a surface material of known composition is thick enough to maximize emission of a strong characteristic gamma-ray line, or if the mean thickness over an accumulation region is independently determinable, a third method of measuring atmospheric thickness, that of single line attenuation, becomes possible. Given an accurate model value of the emitted gamma-ray flux (also a requirement for elemental analysis), observation of the unbroadened

surface line flux from orbit will yield a signal modulated by its passage through the atmosphere in proportion to atmospheric thickness. This method will be applicable to the CO_2 or H_2O polar caps of Mars using the 6129 keV oxygen line or the 2223 keV line due to hydrogen. It should also be applicable to the layered terrain existing at high latitudes if the GRS can determine the general composition with sufficient accuracy. Figure 4 shows the effect of atmospheric thickness in attenuating the 6129 keV line of oxygen emitted by a thick dust-free CO_2 cap. Plotted are the expected signal count rate, and the relative sensitivity for a 100 hour accumulation. Figure 5 shows the calculated effect of atmospheric thickness on the observed signal strength of the 2223 keV hydrogen line from layered terrain assumed to be 50% H_2O and 50% dry soil, for a 100 hour accumulation. In this application, the uncertainty in composition rather than the uncertainty due to counting statistics (σ_{TS}) will be the dominant factor limiting the measured sensitivity ($\sigma_{T/T}$).

By these methods, it should be possible to track temporal changes in atmospheric mass over broad topographical features, within latitude bands, by hemisphere, and for the entire planet. Surface pressure is readily determinable from atmospheric thickness. It should also be possible to observe the enrichment of argon in south polar regions due to CO_2 precipitation if such an effect is occurring on a large scale.

A complete report of this work will appear in the JGR special issue on the 4th International Conference on Mars.

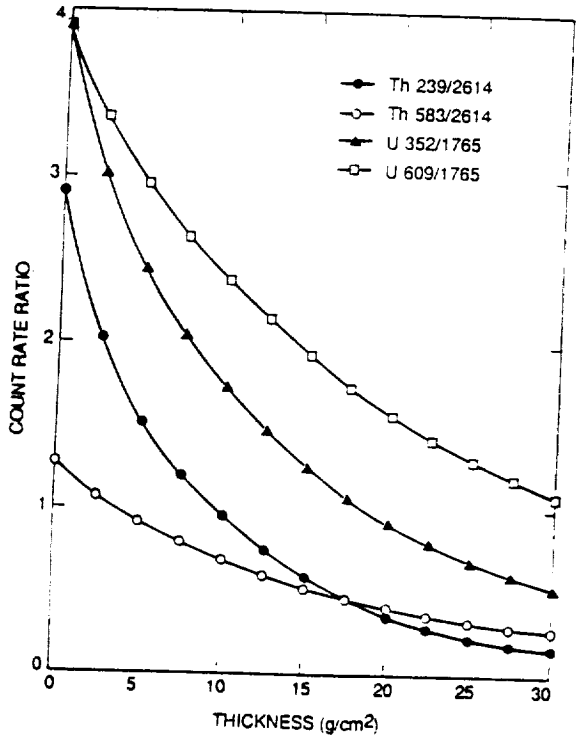

Figure 1

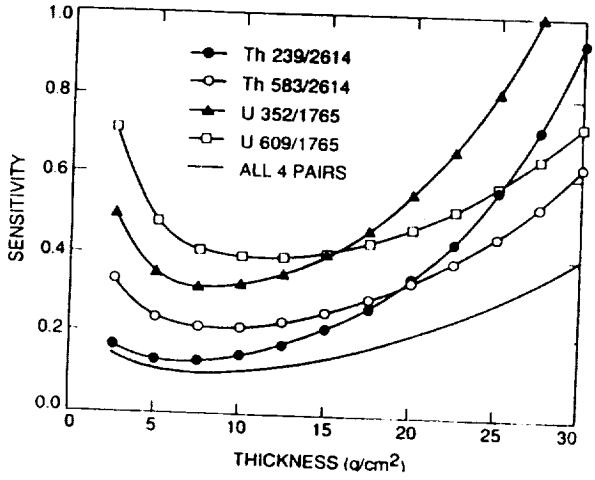

Figure 2

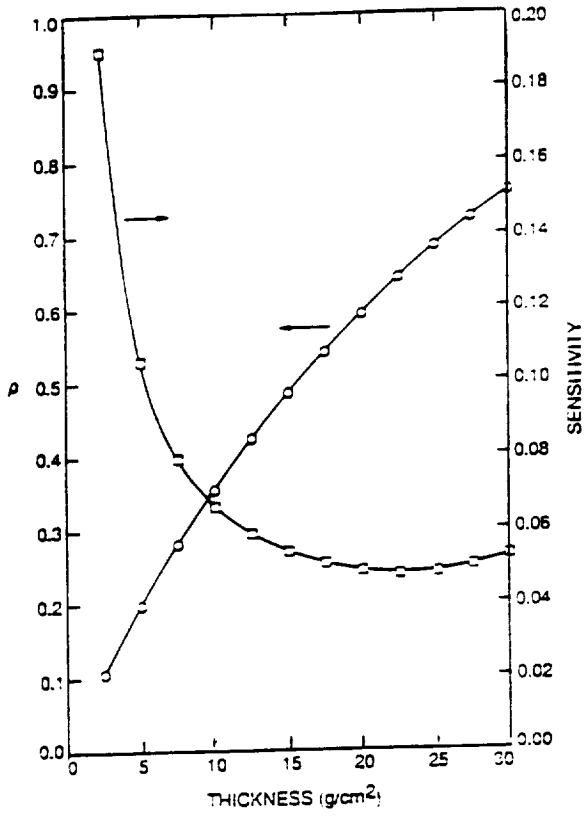

Figure 3

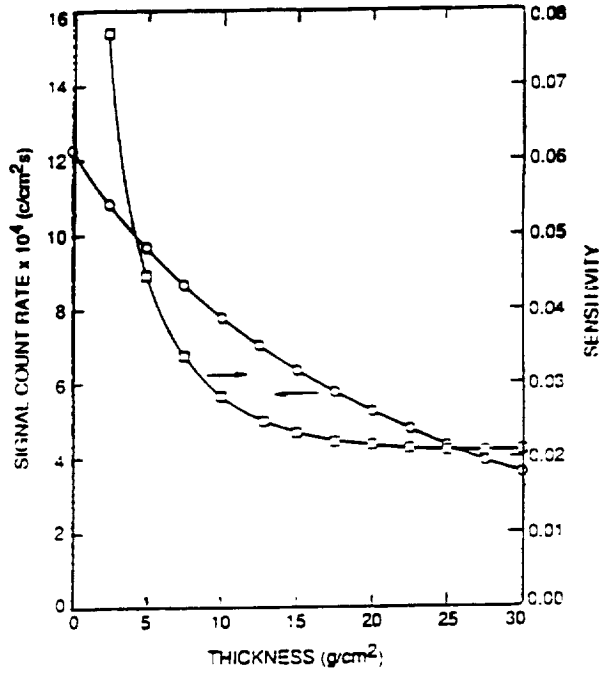

Figure 4

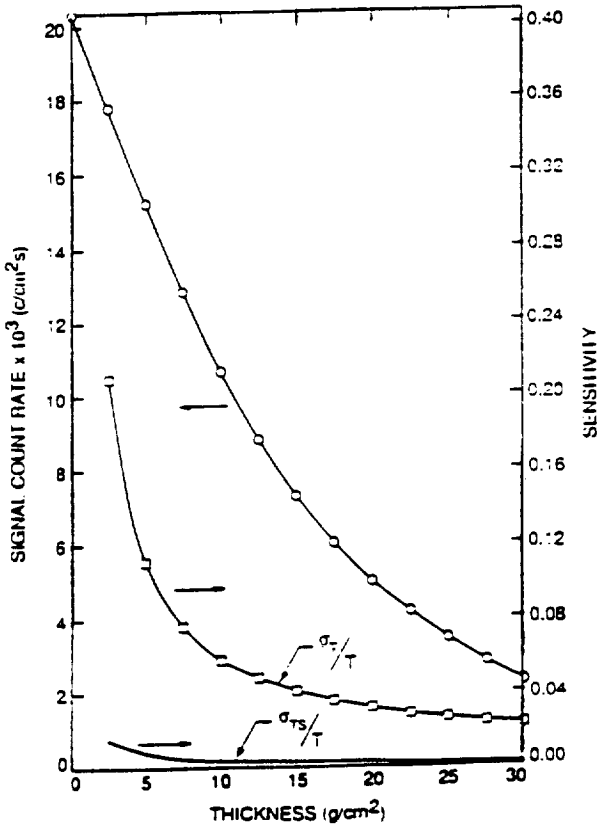

Figure 5

THE THERMAL INERTIA OF MARS: RE-INTERPRETATION USING A BETTER ATMOSPHERIC MODEL; B. M. Jakosky (Laboratory for Atmospheric and Space Physics and Dept. of Geological Sciences, University of Colorado, Boulder, CO 80309) and R. M. Haberle (Space Sciences Division, NASA/Ames Research Center, Moffett Field, CA 94035).

The thermal inertia of the uppermost 1-10 cm of the martian surface has been determined by comparing measurements of the infrared brightness temperature of the surface at many times of day with temperatures predicted from a thermal model. The thermal model accounts for the energy balance at the surface, and includes incoming sunlight, emitted thermal-infrared energy, energy conducted into the subsurface, and energy from the atmosphere to the surface. This latter term includes both infrared emission from the atmosphere to the ground and sensible heat due to near-surface winds, and is usually smaller than the other terms. In the thermal model developed by Kieffer and used in previous determinations of thermal inertia, a constant atmospheric emission term is used as a first-order approximation; based on the large variation in surface properties expected and on the large uncertainties in the values of the thermal inertia, this was a good approximation at that time. Using an atmospheric radiative/convective model, including absorption and emission by both CO_2 and airborne dust, we have calculated the magnitude of the energy exchange between the atmosphere and the surface, and we use this as a basis by which to re-calculate the derived values of surface thermal inertia. Although the global pattern of thermal inertia probably will not change significantly, the actual values of thermal inertia will change, and the physical interpretation in terms of particle sizes will change as well.

The model includes a fully coupled atmospheric radiative transfer model and a surface and subsurface thermal conduction model. The atmospheric model is based on an earlier version of the algorithms currently used in the Ames Mars Atmosphere General Circulation Model. It includes absorption and scattering of incoming sunlight by CO_2 and by dust; absorption, emission and scattering of thermal-infrared energy by CO_2 and by dust; and a near-surface convective adjustment when the temperature gradient exceeds the adiabat. The energy exchange with the surface includes radiation from the atmosphere to the surface as well as sensible heat based on a parameterization of the near-surface boundary layer (this latter term is generally very small). The surface and subsurface model accounts for conduction within the subsurface, and is similar to other thermal models in the literature.

The basic difference between our model and that by Kieffer is in the magnitude of the atmospheric radiation term. Even without dust, the radiation to the surface is roughly twice what was used in his model; the effect of this additional radiation is to spread out the heating of the surface to some extent over all times of day, and to result in a smaller diurnal amplitude of the surface temperature variations. When interpreted using the Kieffer model, then, a higher thermal inertia is required to produce the same surface temperatures. Thus, using our model, the surface thermal inertia is lower than that determined using Kieffer's model.

For a nominal dust opacity of 0.4, similar to that observed at the Viking landing sites, surfaces which were thought to have a thermal inertia of 0.007 cal/cm^2-s$^{1/2}$-K have a recalculated thermal inertia of about 0.005; similarly, an inertia of 0.003 is changed to 0.001. Because of the relationship between particle size and thermal inertia within a surface, the particle sizes inferred for the surface change as well. The effective particle size of the high-inertia surface is changed from about 500 μm to 100-200 μm, and that of a low-inertia surface is changed from about 50 μm to about 5 μm. For the high-inertia surfaces, we caution that other mechanisms such as bonding into a duricrust may be responsible for producing the observed thermal inertia. The particle size of the low-inertia surfaces is now more consistent with that expected due to fallout of airborne dust.

By changing the amplitude of the surface temperature variations, our model also explains a large fraction of the so-called "afternoon cooling" effect, wherein observed mid-afternoon temperatures are lower than predicted using the simple thermal model. As the Kieffer model requires a higher thermal inertia to fit the amplitude, it shifts the noontime peak and afternoon decline in temperatures to later times, producing such an effect. Using the improved atmospheric model can explain about two-thirds of this effect; the remainder may result from mixing of materials at the surface, along with other processes known to occur on Mars.

DERIVATION OF MARS ATMOSPHERIC DUST PROPERTIES FROM RADIATIVE TRANSFER ANALYSIS OF VIKING IRTM EMISSION PHASE FUNCTION SEQUENCES; R.T. Clancy and S.W. Lee, Laboratory for Atmospheric and Space Physics, University of Colorado, Boulder, CO 80309

During the span of the Viking Orbiter missions, several hundred emission-phase-function (EPF) sequences were obtained, in which the IRTM instrument observed the same area of surface as the spacecraft moved overhead. The IRTM data set as a whole is well calibrated, having been corrected for inter-spacecraft, inter-detector, and temporal calibration variations; a conservative estimate for the absolute uncertainty inherent in this data set is 1-2% [1]. The EPF visual brightness observations (passband of 0.3-3.0 μm , effective wavelength of 0.57 μm) present very accurately calibrated albedos of a given region and the atmosphere above it versus emission (and to a lesser extent, incidence) angle. Although these observations were designed for the purposes of surface photometric studies, they are quite suitable for the derivation of atmospheric dust opacities.

We have developed a radiative transfer model of the Mars atmosphere and surface based upon a discrete-ordinates radiative transfer code [2]. Input parameters include the atmospheric dust opacity, the single scattering albedo (ϖ_0) and particle phase function of the atmospheric dust, and the surface bidirectional reflectance. A 16-stream approximation is adopted to adequately represent the model dust and surface phase functions. The surface photometric function is estimated from EPF sequences at low dust opacities and emission angles, where the effects of scattering by atmospheric dust are minimized. The exact behavior of the bidirectional reflectance at large emission angles and/or high dust loading is not critical since the contribution of atmospheric dust scattering dominates the observed reflectance for these regions.

On the basis of an analysis of ~20 separate EPF sequences spanning low and high latitudes, low and high dust opacities, and a wide range of L_S; we find evidence for three distinct aerosol populations. In all three cases it is possible to model the dust scattering with a single dust phase function labelled "IRTM" in figure 1. An empirical phase function representing scattering by non-spherical particles was derived by Pollack et al. [3] to fit the Viking lander observations of dust scattering, and is presented by the solid line in figure 1. The agreement between the "IRTM" and Pollack phase functions is quite good; however the asymmetry factor, g, is 0.55-0.56 rather than the value of 0.79 given by Pollack et al. [3]. A Henyey-Greenstein phase function with g=0.79 is also included in figure 1 to indicate the very large large differences in particle back-scattering implied by g=0.55 versus g=0.79.

We find three separate values of the single scattering albedo, ϖ_0, corresponding to the three aerosol populations. At low-to-mid latitudes for moderate dust opacities (τ = 0.2-1.0), ϖ_0=0.88 fits the EPF observations. Figures 2-4 present a subset of model-data comparisons for this case. At high latitudes (70°-80°N) we find ϖ_0=1.0, indicating that ice clouds are the likely source of particulate scattering. Figure 5b presents a model-data comparison for this case and a best fit attempt with ϖ_0=0.88 (figure 5a). The third aerosol population corresponds to very high dust loading (τ > 2), in which it is necessary to increase ϖ_0 to 0.9-0.92 to fit the data with the "IRTM" dust phase function. Figures 6a and 6b indicate model-data comparisons over Hellas basin in which we attempt to fit the EPF data with ϖ_0=0.88 and ϖ_0=0.92, respectively.

The primary differences between the EPF IRTM and Viking lander derived dust properties are larger ϖ_0 from the EPF analysis (ϖ_0=0.88 versus 0.86) and an increase in ϖ_0 during the peak of the dust storm as found in the EPF analysis (the Viking lander data indicate no such change, J. Pollack, personal communication). It is possible that the distinction of looking from below with lander data and looking from above with the IRTM data may account for these differences. Finer dust (higher ϖ_0 and more backscattering) may be mixed to higher altitudes and may increase during the peak of the dust storms (J. Bergstrahl, personal communication). The downward-looking geometry of the EPF sequences would be more sensitive to a high-altitude, fine component.

This research was supported under NASA Planetary Geology grant NAGW 1378.

REFERENCES: [1] Pleskot, L.K., and E.D. Miner (1981). Time variability of martian bolometric albedo. *Icarus 45*, 179-201. [2] Stamnes, K., S.C. Tsay, W. Wiscombe, and K. Jayaweera (1988). A numerically stable algorithm for discrete-ordinate-method radiative transfer in scattering and emitting layered media. *Appl. Opt., 27*, 2502-2509. [3] Pollack, J. B., D. S. Colburn, F. M. Flasar, R. Kahn, C. E. Carston, and D. Pidek (1979). Properties and effects of dust particles suspended in the martian atmosphere. *J. Geophys. Res., 84*, 2929-2945.

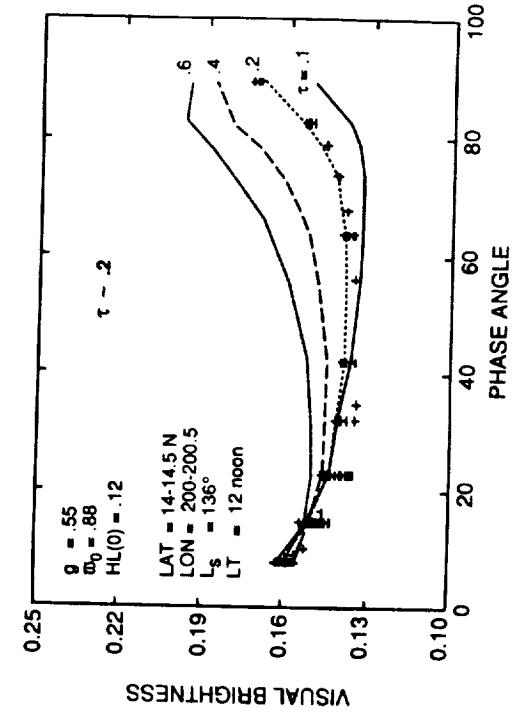

Fig. 2. Observed (crosses) phase function of EPF sequence over Cerberus versus model phase functions with τ=.1,.2,.4, and .6. Best-fit to data gives τ=.2, ϖ_0=.88, g=.55.

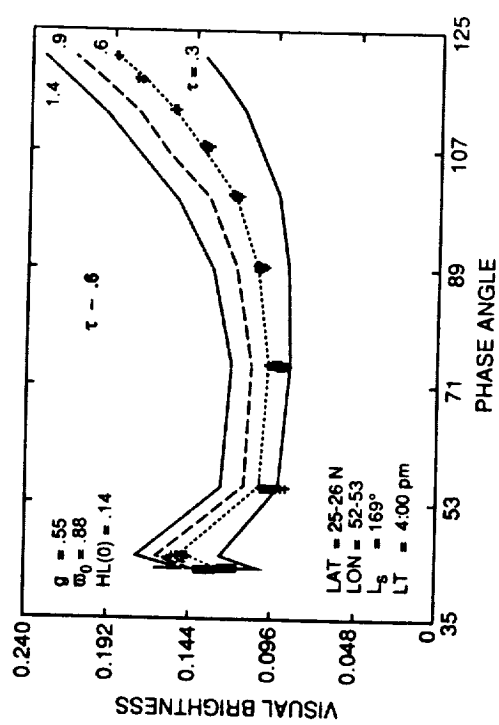

Fig. 4. Observed (crosses) phase function of EPF sequence over Chryse Planitia versus model phase functions with τ=.3,.6,.9, and 1.4. Best-fit gives τ=.6, ϖ_0=.88, g=.55.

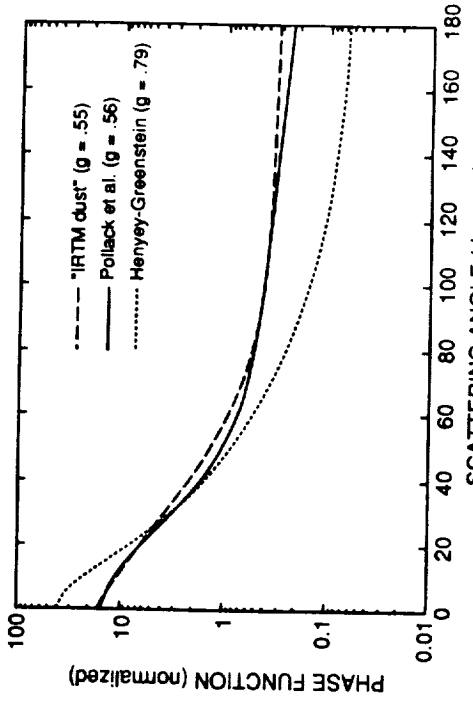

Fig. 1. Mars aerosol phase functions.

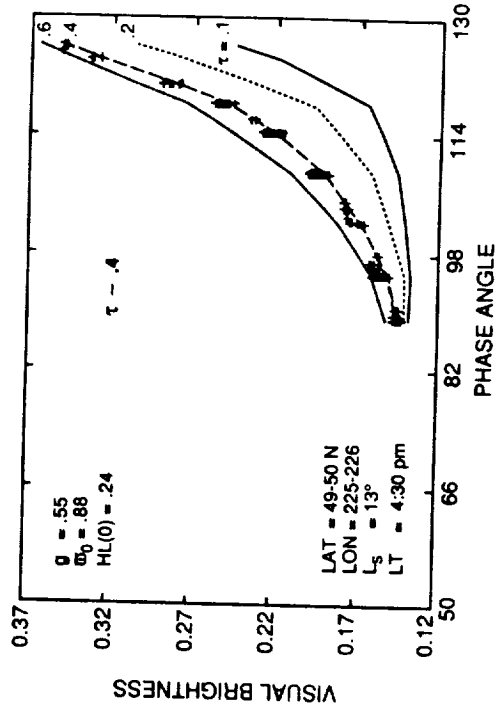

Fig. 3. Observed (crosses) phase function of EPF sequence over Utopia Planitia versus model phase functions with τ=.1,.2,.4, and .6. Best-fit to data gives τ=.4, ϖ_0=.88, g=.55.

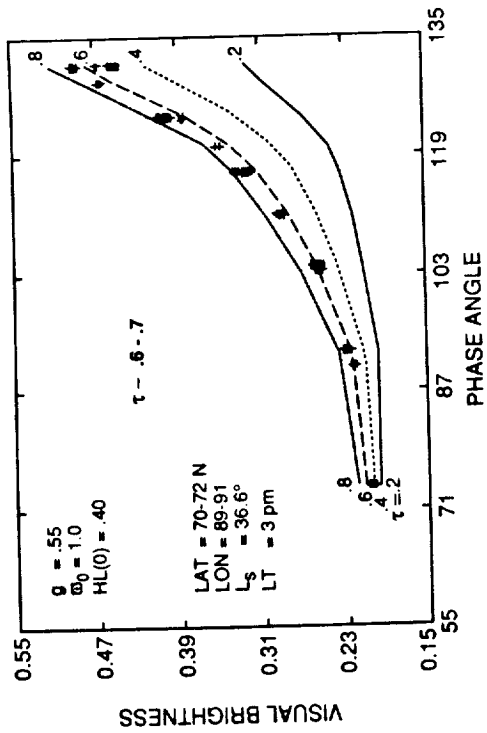

Fig. 5b. Observed (crosses) phase function of EPF sequence over the North polar erg versus model phase functions with τ=.2, .4,.6, and .8. Best-fit to data gives τ=.7, ϖ_0=1.0, g=.55.

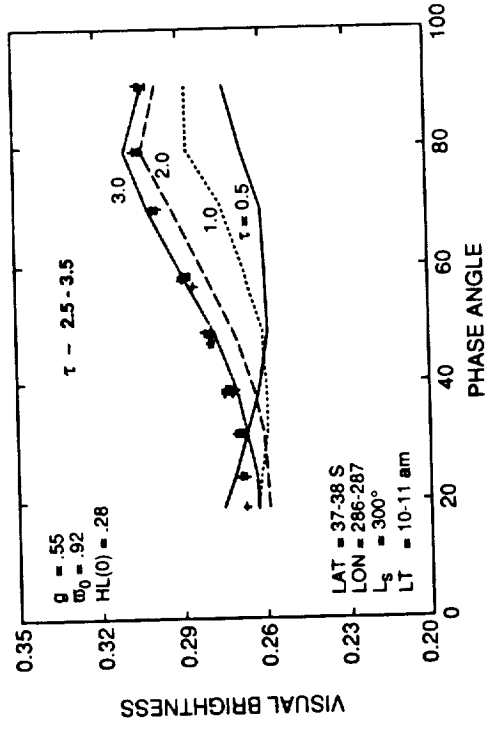

Fig. 6b. Observed (crosses) phase function of EPF sequence over Hellas Planitia versus model phase functions with τ=.5,1.0, 2.0, and 3.0. Best-fit gives τ=3.0, ϖ_0=.92, g=.55.

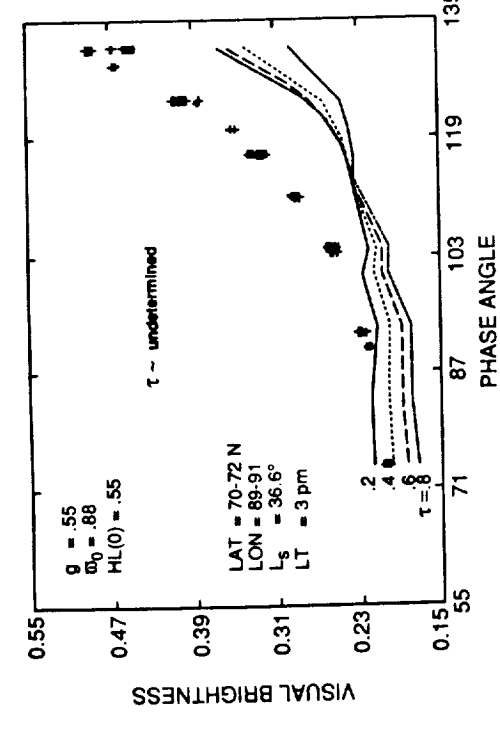

Fig. 5a. Observed (crosses) phase function of EPF sequence over the North polar erg versus model phase functions with τ=.2, .4,.6, and .8. No fit is possible for ϖ_0=.88, g=.55.

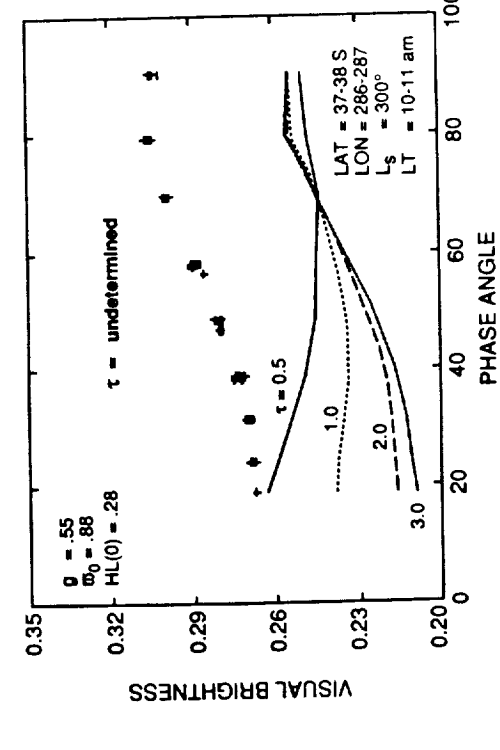

Fig. 6a. Observed (crosses) phase function of EPF sequence over Hellas Planitia versus model phase functions with τ=.5,1.0, 2.0, and 3.0. No fit is possible for ϖ_0=.88, g=.55.

THE EFFECTS OF ATMOSPHERIC DUST ON OBSERVATIONS OF THE SURFACE ALBEDO OF MARS; S.W. Lee and R.T. Clancy, Laboratory for Atmospheric and Space Physics, Univ. Colorado, Boulder, CO 80309

The Mariner 9 and Viking missions provided abundant evidence that aeolian processes are active over much of the surface of Mars [1; 2]. Past studies have demonstrated that variations in regional albedo and wind streak patterns are indicative of sediment transport through a region [3; 4], while thermal inertia data [derived from the Viking Infrared Thermal Mapper (IRTM) data set] are indicative of the degree of surface mantling by dust deposits [5; 6; 7; 8; 9]. The visual and thermal data are therefore diagnostic of whether net erosion or deposition of dust-storm fallout is taking place currently and whether such processes have been active in a region over the long term. These previous investigations, however, have not attempted to correct for the effects of atmospheric dust loading on observations of the martian surface, so quantitative studies of current sediment transport rates have included large errors due to uncertainty in the magnitude of the "atmospheric contamination".

We have developed a radiative transfer model which allows the effects of atmospheric dust loading and variable surface albedo to be investigated [see related abstract, 10]. This model incorporates atmospheric dust opacity, the single scattering albedo and particle phase function of atmospheric dust, the bidirectional reflectance of the surface, and variable lighting and viewing geometry.

The Cerberus albedo feature has been examined in detail using this technique. Previous studies have shown the Cerberus region to have a moderately time-variable albedo [4]. IRTM observations obtained at ten different times (spanning one full martian year) have been corrected for the contribution of atmospheric dust in the following manner:

- A "slice" across the IRTM visual brightness observations was taken for each time step. Values within this area were binned to 1° latitude, longitude resolution.
- The atmospheric opacity (τ) for each time was estimated from [11]. As the value of τ strongly influences the radiative transfer modelling results, spatial and temporal variability of τ was included to generate an error estimate.
- The radiative transfer model was applied, including dust and surface phase functions, viewing and lighting geometry of the actual observations, and the range of τ [10].
- Offsets were applied to the visual brightness observations to match the model results at each τ (Figure 1).
- The "true surface albedo" was determined by applying the radiative transfer model to the offset brightness values, assuming $\tau = 0$ and a fixed geometry (0° incidence, 30° emission). Repetition of this technique for each time step allows values of albedo for specific locations to be tracked as a function of time (Figure 2).

The initial results for Cerberus indicate the region darkens prior to the major 1977 dust storms, consistent with erosion of dust from the surface (possibly contributing to the increasing atmospheric dust load). There is some indication of regional brightening during the dust storms followed by a general darkening, consistent with enhanced dust deposition during the storms followed by erosion of the added dust. There is only minor variability during the second year, consistent with little regional dust transport during that period.

The results of this study indicate that atmospheric dust loading has a significant effect on observations of surface albedo, amounting to albedo corrections of as much as several tens of percent. This correction is not constant or linear, but depends upon surface albedo, viewing and lighting geometry, the dust and surface phase functions, and the atmospheric opacity. It is clear that the quantitative study of surface albedo, especially where small variations in observed albedo are important (such as photometric analyses), needs to account for the effects of atmospheric dust loading. Our future work will expand this study to other regional albedo features on Mars.

This research was supported under NASA Planetary Geology grant NAGW 1378.

REFERENCES: [1] Veverka, J., P. Thomas, and R. Greeley (1977). A study of variable features on Mars during the Viking primary mission. *J. Geophys. Res. 82*, 4167-4187. [2] Thomas, P., J. Veverka, S. Lee, and A. Bloom (1981). Classification of wind streaks on Mars. *Icarus 45*, 124-153. [3] Lee, S.W., P.C. Thomas, and J. Veverka (1982). Wind streaks in Tharsis and Elysium: Implications for sediment transport by slope winds. *J.Geophys. Res. 87*, 10025-10042. [4] Lee, S.W. (1986). Regional sources and sinks of dust on Mars: Viking observations of Cerberus, Solis Planum, and Syrtis Major (abstract), In *Symposium on Mars: Evolution of its Climate and Atmosphere* (V. Baker et al., eds.), pp. 71-72, LPI Tech. Rpt. 87-01, Lunar and Planetary Institute, Houston. [5] Kieffer, H.H., T.Z. Martin, A.R. Peterfreund, B.M. Jakosky, E.D. Miner and F.D. Palluconi (1977). Thermal and albedo mapping of Mars during the Viking primary mission. *J. Geophys. Res. 82*, 4249-4295. [6] Christensen, P.R. (1982). Martian dust mantling and surface composition: Interpretation of thermophysical properties. *J. Geophys. Res. 87*, 9985-9998. [7] Christensen, P.R. (1986). Regional dust deposits on Mars: Physical properties, age, and history. *J. Geophys. Res. 91*, 3533-3545. [8] Christensen, P.R. (1986). The distribution of rocks on Mars. *Icarus 68*, 217-238. [9] Jakosky, B.M. (1986). On the thermal properties of martian fines. *Icarus 66*, 117-124. [10] Clancy, R.T., and S.W. Lee (1990). Derivation of Mars atmospheric dust properties from radiative transfer analysis of Viking IRTM emission phase function sequences. *Reports of Planetary Geology and Geophysics Program*, this volume. [11] Martin, T.Z. (1986). Thermal infrared opacity of the Mars atmosphere. *Icarus 66*, 2-21.

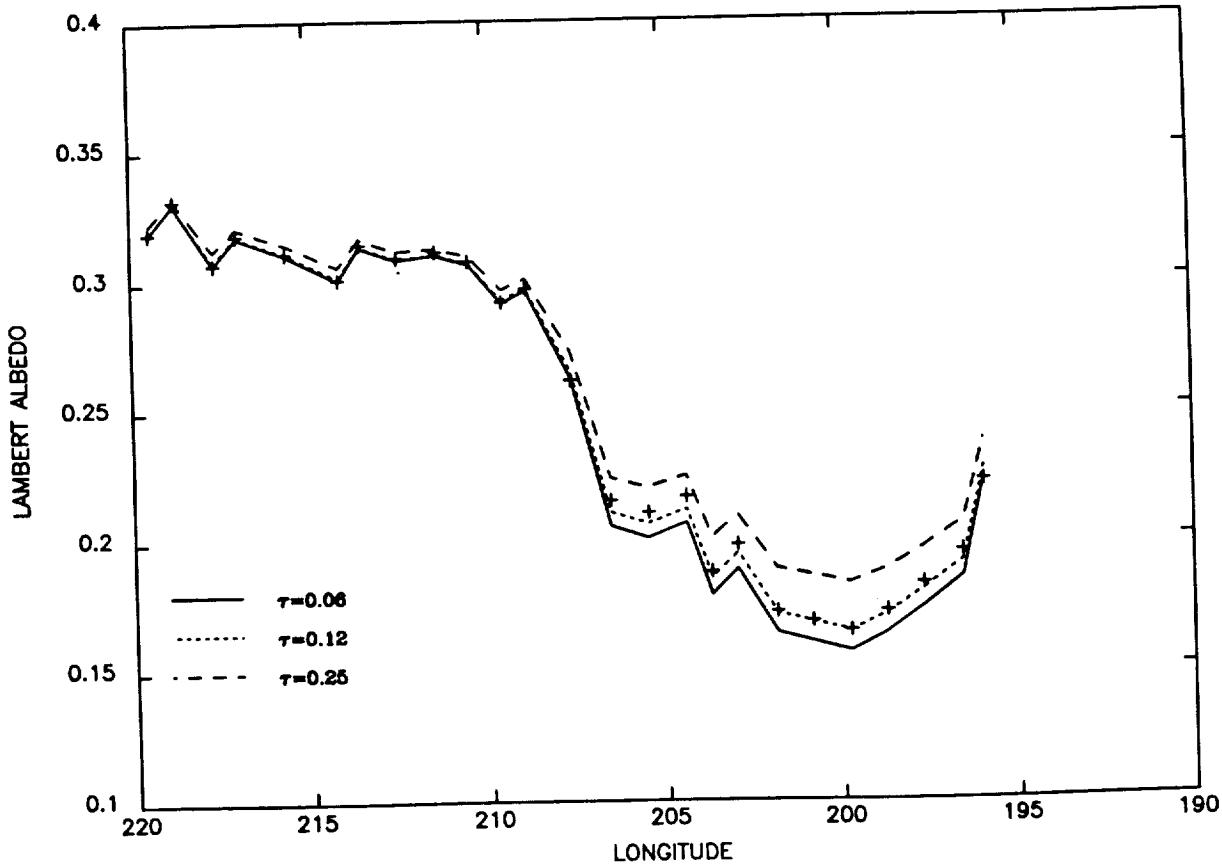

Figure 1: Results of the radiative transfer modelling for an albedo slice across Cerberus (latitude 13° – 14°) at L_S 124°. Crosses indicate the actual observations, and lines denote the model results for three different opacities.

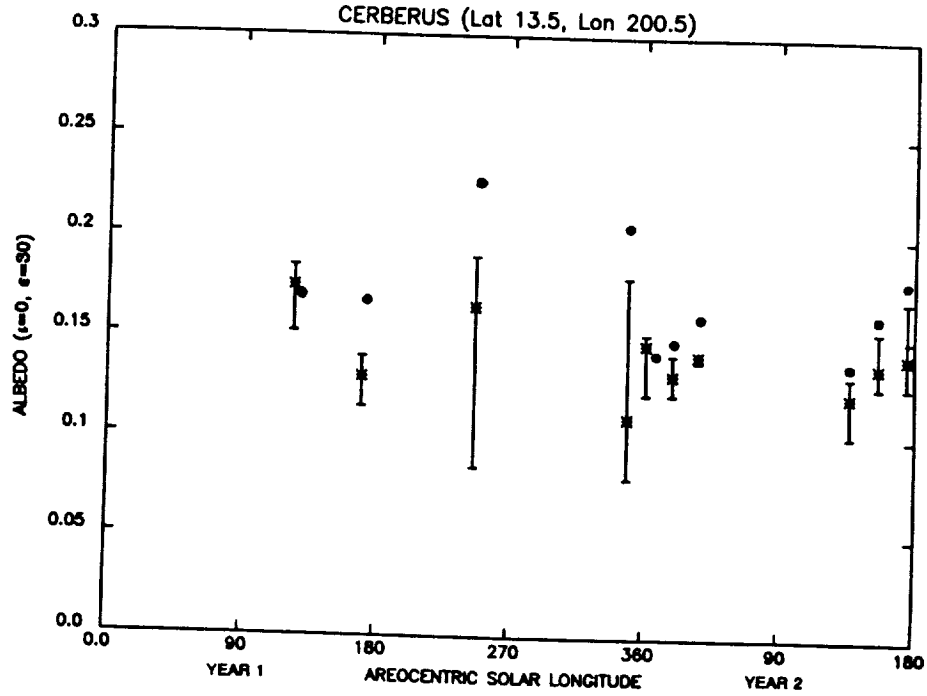

Figure 2a: Temporal behavior of a dark area in Cerberus. "True surface albedos" are denoted by asterisks; error bars indicate uncertainty in τ. Uncorrected albedos are denoted by dots.

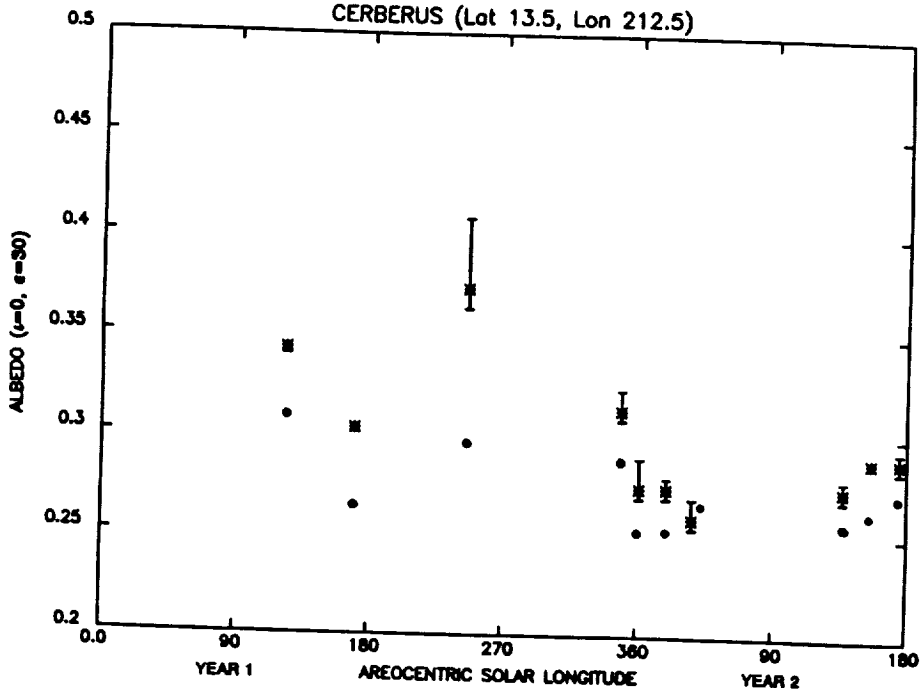

Figure 2b: Temporal behavior of a bright area in Cerberus. "True surface albedos" are denoted by asterisks; error bars indicate uncertainty in τ. Uncorrected albedos are denoted by dots.

LIGHT SCATTERING BY LARGE, IRREGULAR PARTICLES

A. McGuire and B. Hapke (Department of Geology and Planetary Science, University of Pittsburgh)

The light scattering properties of irregular particles that are large compared to the wavelength are of considerable interest to persons who interpret remote sensing observations of planetary regoliths. As part of a research project to investigate these properties, several artificial particles were prepared, and the intensity and linear polarization of the light scattered by them measured as a function of phase angle. Scattering by a clear sphere is described by Mie theory, and is characterized by the following: a weakly negatively polarized, strong forward lobe, due to refracted light transmitted once through the particle; a weakly negatively polarized, weak backward lobe, due to internally-reflected light transmitted twice through the particle; a strongly positively polarized, low intensity component at intermediate phase angles, due to light externally specularly reflected from the surface; plus cloudbows and a glory. If the particle shape is made irregular, or if the surface is roughened, the cloudbows and glories are eliminated, but the general character of the scattering is otherwise similar to that of a sphere, except that the intensity of the forward lobe is decreased, and scattering in intermediate directions somewhat enhanced. Adding internal scatterers (such as cracks, voids, inclusions, grain boundaries or agglomerates) weakens the forward lobe and causes the particle to become more backscattering. However, an extremely high density of internal scatterers is required to eliminate the forward lobe completely. A clear particle, even if it is rough or irregular, will always have a forward scattering lobe. Increasing the absorption decreases the single scattering albedo and decreases the back lobe much more than the forward lobe.

What's Wrong with Photoclinometry?

David G. Jankowski and Steven W. Squyres
Center for Radiophysics and Space Research
Cornell University, Ithaca, NY 14853

Due to its simplicity and speed, photoclinometry has become a popular technique for determination of topography in monoscopic images of planetary surfaces (1-6). However, photoclinometry cannot give reliable results in all cases. Therefore it is important that topographic data derived from photoclinometry, like any other data, be presented with without appropriate error estimates.

Photoclinometrically-determined slopes can contain errors from the following sources:

- Image noise: Image noise is a source of error because it produces spurious intensity fluctuations from pixel to pixel.
- Digitization: The digitization of brightness levels in all spacecraft images results in an inherent slope uncertainty.
- Background: An incorrect dark current will introduce systematic errors.
- Photometric function uncertainties: An an improper photometric function can be a serious source of error.
- Albedo errors: The surface albedo can be a source of error both due to uncertainties in the mean regional albedo (often assumed constant) and due to local albedo variations.
- Atmospheric effects: An atmosphere can be a source of error due both to uncertainties in the mean contribution of light scattered and due to fluctuations of this contribution across an image.
- Scanline misallignment: The most widely-used photoclinometry techniques are one-dimensional, determining the topography only along a specified line. Such techniques are typically restricted to scanlines that travel directly up or down all slopes, so slope errors can occur due to the misallignment of scanlines.
- Viewing and lighting geometry uncertainties: The errors associated with viewing and lighting geometry uncertainties associated with recent spacecraft are for the most part insignificant compared to other errors.

We have performed an investigation of the quantitative effect of each of these error sources on the photoclinometric method. The error contributions due to the above sources are modelled under conditions appropriate for spacecraft images of Ganymede and Mars. The characteristics of Viking Orbiter images are used for modelling Mars and the characteristics of Voyager images are used for Ganymede. The noise characteristics of the Galileo camera are included as a comparison with the Voyager cameras. The "lunar-like" photometric function is used to model the surface of Ganymede (1), and the Minnaert function is used to model the surface of Mars (5).

Photoclinometric slope uncertainties due to the above sources have been calculated for phase angles of 30°, 60°, and 90°. Slope errors are investigated for "actual" slopes of 0°, 10° (sloping away from the sun), and −10° (sloping towards the sun). Slope errors are also investigated for rotation angles (the angle subtended by the scanline direction and the local photometric latitude line) ranging from 30° to −30°.

At small incidence angles, the photometric functions change very slowly; therefore small brightness variations in this region correspond to large topographic slopes. Hence the effects of

albedo variations, atmospheric variations, noise, and digitization are all enhanced near the subsolar point.

The noise levels characteristic of the Viking and Voyager cameras result in significant slope errors at low incidence angles. The errors associated with Viking images are the largest, near 2° at the subspacecraft point at 60° phase. For all images considered, errors associated with digitization and incorrect dark currents are negligible compared to noise errors.

The martian atmosphere clearly can not be ignored when doing photoclinometry. However, with the help of resolved shadows (5), the contribution of the atmosphere can be estimated fairly well in many Viking images. The atmospheric contribution can often be estimated with less than 10% error. Fluctuations within a given image are small, usually much less than 5%. The errors associated with these uncertainties are less than 1°.

Errors due to uncertainties in the Minnaert K parameter are generally not larger than 1°. However, for large slopes and large rotation angles, this error source can become much more significant, even at large incidence angles, where other errors sources disappear.

Errors due to misallignment can be significant if the misallignment angle is larger than about 10°. The errors tend to be larger for the Minnaert function than for the lunar-like function, and they tend to be smaller for lower rotation angles (scanline directions chosen parallel to lines of photometric latitude) for both functions. For the Minnaert function, scanlines pointing away from the sun are more accurate when pointing away from the photometric equator at a given angle than when pointing towards the equator at the same angle.

Slope errors are usually larger for sun-facing slopes than for slopes facing away from the sun. This effect is generally stronger for the lunar-like photometric function than it is for the Minnaert function. The errors associated with uncertainties in the Minnaert K parameter and with scanline misallignment both increase significantly with increasing slope.

Slope errors decrease with increasing phase angle. The optimal phase angle for photoclinometry is about 60°. Smaller phase angles result in larger errors, while larger phase angles result in smaller adequate surface areas and larger geometric foreshortening.

References

1) Squyres, S. (1981) *Icarus* **46** 156-168.

2) Davis, P., Soderblom, L. (1984) *J.Geophys.Res* **89** 9449-9457.

3) Moore, J., McEwen,A., Albin,E., Greeley,R. (1986) *Icarus* **67** 181-183.

4) Jankowski, D., Squyres, S., (1988) *Science* **241** 1322-1325.

5) Tanaka, K., Davis, P. (1988) *J.Geophys.Res* **93** 14893-14917.

6) Schenk, P. (1989) *J.Geophys.Res* **94** 3813-3832.

INFRARED REFLECTANCE SPECTRA OF PLAGIOCLASE FELDSPARS

Douglas B. Nash, San Juan Institute, San Juan Capistrano, CA 92675
John W. Salisbury, Johns Hopkins University, Baltimore, MD 21218

This study addresses mid-infrared reflectance properties of plagioclase feldspars in powdered form for both crystalline and glass phases. It covers the solid-solution series from sodium end-member albite to calcium end-member anorthite. Spectra were measured in the laboratory using the diffuse (biconical) reflectance mode. The study goal is to understand and decipher emission spectra of silicate rocks and their fragmental regolith or soil equivalents in the thermal IR range (generally 5 to 15 μm). The intended application is to identify and map rock and soil composition on surfaces of terrestrial planetary bodies such as the Moon, Mars, and asteroids.

Spectra presented here were obtained using an interferometer (FTIR) spectrometer covering the mid-IR (2.5-25 μm) at a resolution of 4 cm^{-1} [1]. Spectra are obtained by ratioing the sample reflectance to that of a reference standard, gold-coated sandpaper [1]. Samples of plagioclase (Table 1) were prepared by crushing to a particle size <50 μm. The powdered material was very lightly packed in 3-mm-deep sample cups and their top surface placed at the focal plane of the spectrometer. Aliquots of powdered crystalline plagioclase were quick-fused (1 min.) in a resistance strip furnace using a molybdenum-foil crucible in a nitrogen gas atmosphere [2]. Beads of the air-quenched glass were likewise powdered and their spectra determined with the FTIR.

Figure 1 shows the biconical reflectance spectra for the series of plagioclase crystalline samples (top panel) and glass samples (bottom panel). The baseline of each spectrum except the bottom one in each panel is offset 5% vertically for clarity. The spectra are characterized by the following features in the 5 to 15 μm range:

1. Steep fall off in reflectance from 5 to 7.5-8.0 μm due to gradually increasing resonant absorption owing to many molecular vibration (stretch) modes of the Si-0 and A1-0 bonds in silicate materials.

2. Distinct minimum in reflectance near 7.7 to 8.1 μm; the wavelength of this minimum is clearly related to plagioclase composition, shifting systematically from 7.69 μm for albite to 8.03 μm for anorthite. This reflectance minimum (emission maximum) is identified as the Christiansen Frequency (CF), which in spectra of silicate powders has been shown to have important diagnostic implications for remote sensing identification purposes [3], [4], [5], [6]. The results presented here document that the wavelength position of the CF in reflectance is compositionally dependent and can be used to identify plagioclase in terms of its Na or Ca concentration, as suggested by the pioneering work of Conel [3], [4], with transmission spectra of silicate powder films.

3. Structure consisting of a broad reflectance plateau from 8.3 to 12.0 μm; this includes a persistent band gap at 9.2 μm separating stretching vibration bands (reflectance peaks) at 8.7, 9.1, 9.7, and 10 μm in the albite spectrum; the intensity and contrast in these features are clearly related to plagioclase composition and are much more pronounced for the crystalline than for the glass phase. This structure seems to be related to a systematic variation in the relative strength of Restrahlen bands and the so-called transparency peak, which result from variation in strength of several fundamental molecular vibrations (asymmetric stretch modes involving Si-0 and A1-0 bonds) in the silicate lattice [6].

The band structure in the 8.3-12 μm plateau region, shown here most clearly in the case of albite, has been the subject of much research going back many years, and the changes in band position and intensity with Si-Al ordering and Na/Ca ratio are well documented; e.g., Lyon [7] showed from transmission spectra that the double peak in albite at 9.7-10 μm becomes a single peak and shifts to near 10.6 μm in going to anorthite. However, we now know that a highly porous and finely particulate regolith like that on the Moon minimizes the diagnostic importance of these band features and it is for this reason that the Christiansen Frequency has been studied as an alternative key to composition.

In conclusion, these lab results show for the first time in reflectance spectra of powdered plagioclase feldspars that (1) the wavelength position of the Christiansen Frequency migrates systematically with composition ranging from albite to anorthite, and (2) there is no loss of compositional information in the Christiansen Frequency by a change in phase from crystalline to glass, which might be the expected result of hypervelocity impact. Thus, the composition of regoliths with a variety of developmental histories can be examined using mid-IR spectroscopy.

References: [1] Nash, D.B. Appl. Optics 25, 2427-2433, 1986. [2] Nash, D.B. In Advances in X-ray Analysis 7, edited by W. Mueller, Plenum press, 1964. [3] Conel, J.E. J. Geophys. Res. 74, 1614-1634, 1969. [4] Conel, J.E. JPL Space Program Summary 37-63, Vol. III, 7-9, 1970. [5] Logan, L., G. Hunt, J. Salisbury, and S. Balsano. J. Geophys. Res. 78, 4983-5003, 1973. [6] Salisbury, J. and L. Walter. J. Geophys. Res. 94, 9192-9202, 1989. [7] Lyon, R.J.P. Stanford Research Institute Report, Project No. PSU-3943, 139 pp., September, 1962.
Acknowledgements: We thank Jim Conel for helpful discussions. Part of this work was done at JPL. This is SJI contribution 2, supported by NASA Grant NAGW 1350.

Table 1. Sample characterization:

Albite	Amelia County, Virginia
Oligoclase	Bancroft, Ontario
Oligoclase	Mitchell County, N.C.
Labradorite	San Gabriel Mts., Calif.
Labradorite	Nain, Labrador
Bytownite	Crystal Bay, Minn.
Anorthite	Grass Valley, Calif.

(1) Molecular % anorthite; from glass-bead refractive index determination technique.
(2) Weight % SiO_2; from wet chemical analysis by A.G. Loomis.
(3) Wavelength of reflectance minimum (emission max) for powder in air at 25 °C.

(1)	SiO_2 (2)	Reflect. min.(3) cm^{-1}	Reflect. min.(3) μm
An 2.5	68.6	1301	7.69
An 12.5	62.0	1298	7.70
An 24.5	59.5	1289	7.76
An 52.4	54.2	1272	7.86
An 64.5	51.2	1266	7.90
An 80.5	47.3	1258	7.95
An 98.5	42.3	1245	8.03

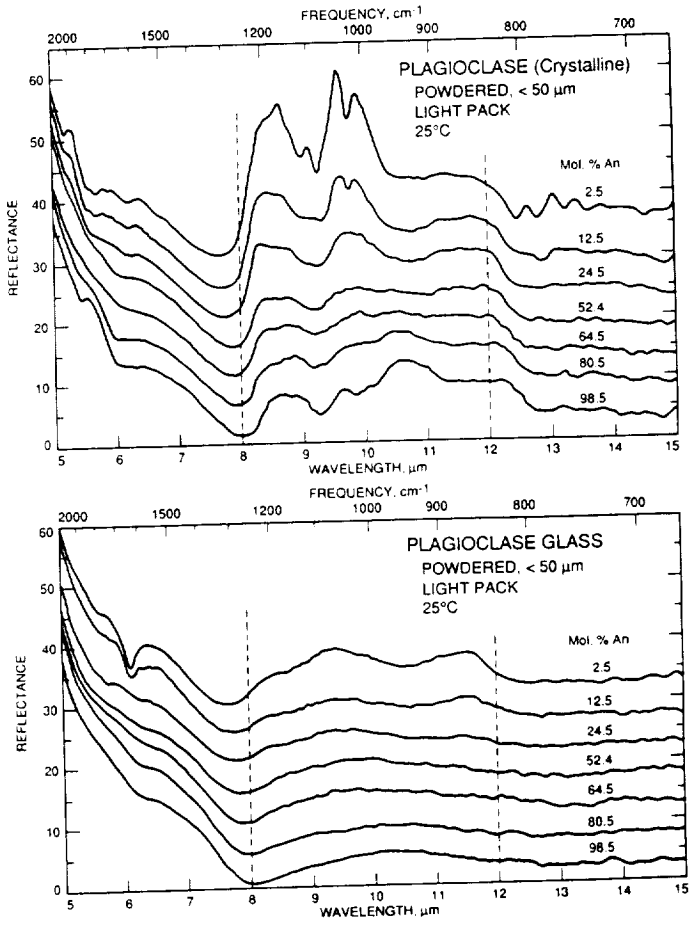

Figure 1. Reflectance spectra of powdered plagioclase (crystalline in top panel, glass in bottom panel), relative to gold-coated sandpaper. Except for bottom spectrum in each panel, baseline for each spectrum is offset vertically 5 % from its neighbor for clarity. Vertical dashed lines are for arbitrary reference only.

AN INFRARED REFLECTANCE STUDY OF LOW ALBEDO SURFACE CONSTITUENTS

Larry A. Lebofsky, Lunar and Planetary Laboratory,
University of Arizona, Tucson, Arizona, 85721

Unaltered asteroids are thought to represent the raw materials available for terrestrial planet formation and so are important to our understanding of the origin and evolution of the Solar System. Compositional variation in the asteroid belt has long been interpreted as primordial, with asteroids becoming more volatile-rich with distance from the sun. Gradie and Tedesco (1982) showed that the asteroid compositional types varied systematically with heliocentric distance and inferred that the asteroids probably formed very close to their present locations in the asteroid belt. From their inferred composition, Gradie and Tedesco also concluded that the outer belt and Trojan asteroids were probably more "primitive" than the C-class asteroids which dominate the main belt. This interpretation was consistent with the earlier laboratory study of asteroid analogs by Gradie and Veverka (1980), who concluded that the low albedo D-class asteroids were probably "ultraprimitive" in composition, *i.e.*, composed largely of hydrated silicates and organic material. However, recent observations (Jones 1988, Jones *et al.* 1990, and Lebofsky *et al.* 1989, 1990) suggest that much of the surface mineralogy seems to be due to alteration events subsequent to formation rather than primordial composition. The distribution of water is the key to understanding the volatile content of the asteroid belt and controls much of the later alteration.

Observational testing of this idea relies on the exploitation of the 3-μm absorption feature in hydrated silicates—the only diagnostic spectral band evident in the dark, volatile-rich CI and CM meteorites (Lebofsky 1978). The existence of the band has demonstrated the presence of hydrated silicates on asteroids (Lebofsky *et al.* 1981, 1989, 1990; Jones 1988; Jones *et al.* 1989). An example of this feature is shown in the spectrum of the CI meteorite Orgueil. The feature is characterized by a sharp reflectance drop at 2.7 μm, due to structural OH, and by an absorption due to H_2O that decreases slowly out to about 3.5 μm. A weak feature at around 3.4 μm is due to organics. In our earlier work (Feierberg *et al.* 1985) we presented spectrophotometric observations of 14 main-belt C-class asteroids. We found that 9 of them had a spectral signature in the 3-μm spectral region indicative of the presence of water of hydration. In that paper we found a positive correlation between the strength of the UV absorption feature shortward of 0.4 μm and the depth of the 3-μm water of hydration feature. Among those asteroids observed, however, there appeared to be no correlation between a hydrated composition and solar distance.

In our present observational program we are expanding our observations to include other low-albedo classes of asteroids, asteroids that range primarily from the middle and outer asteroid belt (>2.5 AU) to the Trojan region at 5.2 AU. Our prelimary results indicate that the outer belt and Trojan asteroids do not show features diagnostic of hydrated silicates and we conclude that these asteroids have not undergone the alteration processes that made the C-class asteroids. We do, however see some features at low signal-to-noise that require further telescopic observations to verify and laboratory studies to identify (Fig. 1–4).

Before the start of our program very little high-resolution reflectance data existed on meteorites and asteroid analogs in the 3-μm spectral region. We now have a large

dataset of laboratory spectra for comparison with our telescopic spectra (Jones 1988, Jones *et al.* 1990). With these data in hand and results from our future efforts, we hope to understand better the composition of the primitive, relatively unaltered asteroids. Coupled with studies of meteorites and new theories of Solar System formation, this picture of asteroid composition may illuminate the materials and source regions for terrestrial planet formation.

At the present time, we are one of the few groups conducting laboratory studies of meteorites and asteroid analogs in the critical 3-μm spectral region. Also, with our new cold chamber, we will be the only group able to study these materials at low temperatures, critical to our understanding of the role of water and ice in clay minerals. Also, we are the only group carrying out a systematic study of low-albedo asteroids to determine the distribution of water in the asteroid belt.

Our previous and current laboratory studies have helped us to refine our telescopic procedures: how low a spectral resolution can still identify a diagnostic 3-μm feature; what other features may be observable in this region, etc. For example, by observing in the 2.7- to 2.9-μm spectral region, we were able to show conclusively that the absorption feature on Ceres is due to hydrated silicates (clays) rather than hydrated salts (Feierberg *et al.* 1985) With further studies of asteroid analogs, especially organic-rich samples and studies at low temperatures, we hope to be able to interpret the spectra we are obtaining on outer belt and Trojan asteroids and thus shed light on our understanding of the distribution of minerals in the asteroid belt.

REFERENCES

FEIERBERG, M. A., L. A. LEBOFSKY, AND D. THOLEN 1985. The nature of C-class asteroids from 3-μm spectrophotometry. *Icarus* **63**, 183–191.

GRADIE, J. C., AND E. F. TEDESCO 1982. Compositional structure of the asteroid belt. *Science* **216**, 1404–1407.

GRADIE, J. C., AND J. VEVERKA 1980. The composition of the Trojan asteroids. *Nature* **283**, 840–842.

JONES, T. D. 1988. An infrared reflectance study of water in outer belt asteroids: Clues to composition and origin. PhD Dissertation, Univ. of Arizona, Tucson. 281 pp.

JONES, T. D., L. A. LEBOFSKY, J. S. LEWIS, AND M. S. MARLEY 1990. The composition and origin of the C, P, and D asteroids: Water as a tracer of thermal evolution in the outer belt. *Icarus*, submitted.

LEBOFSKY, L. A. 1978. Asteroid 1 Ceres: Evidence for water of hydration. *MNRAS* **182**, 17p–21p.

LEBOFSKY, L. A., M. A. FEIERBERG, A. T. TOKUNAGA, H. P. LARSON, AND J. R. JOHNSON 1981. The 1.7- to 4.2-μm spectrum of asteroid 1 Ceres: Evidence for structural water in clay minerals. *Icarus* **48**, 453–459.

LEBOFSKY, L. A., T. D. JONES, AND F. HERBERT 1989. Asteroid volatile inventories. In *Origin and Evolution of Planetary and Satellite Atmospheres* (S. K. Atreya, J. B. Pollack, and M. S. Matthews, Eds.), Univ. of Arizona Press, Tucson, pp 192–229.

LEBOFSKY, L. A., T. D. JONES, P. D. OWENSBY, M. A. FEIERBERG, AND G. J. CONSOLMAGNO 1990. The nature of low albedo asteroids from 3-μm spectrophotometry. *Icarus* **83**, 16–26.

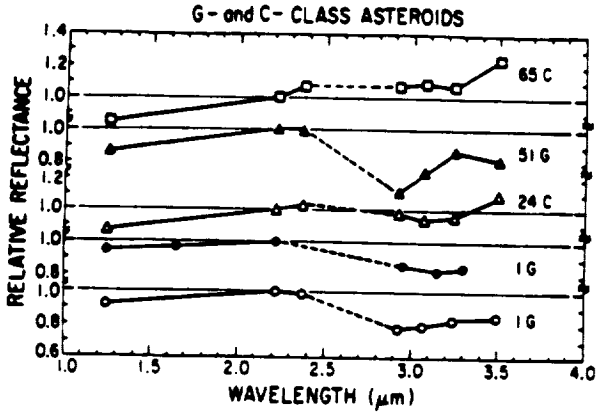

Fig. 1

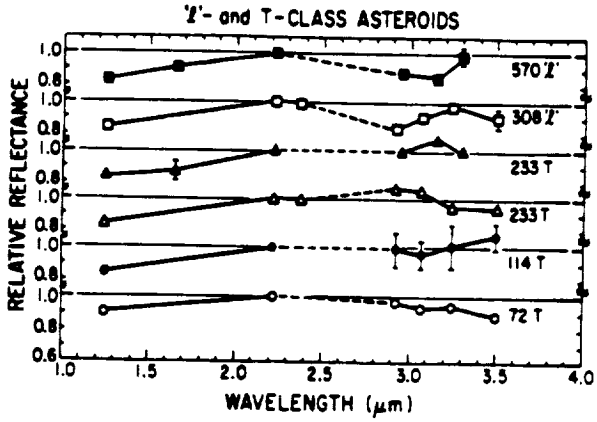

Fig. 2

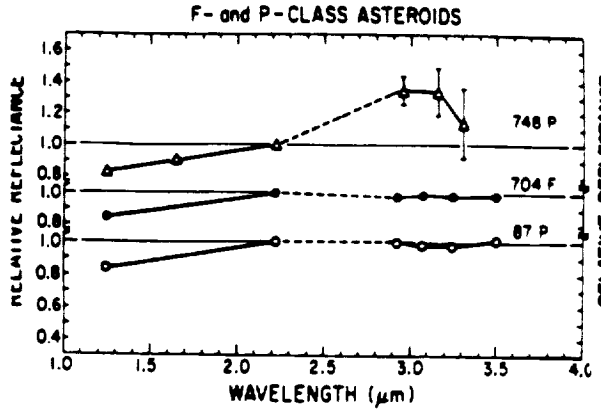

Fig. 3

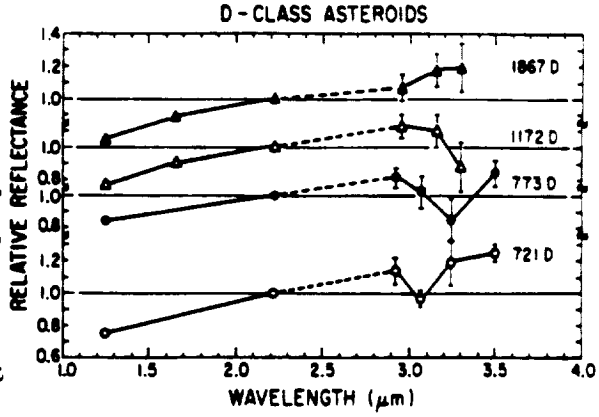

Fig. 4

FIG. 1. Spectra (scaled to 1.0 at 2.2 μm) of the G- and C-class asteroids observed in this program.

FIG. 2. 'l'- and T-class asteroids observed in this program. The 'l' asteroids are actually not a class, but refer to low albedo asteroids that did not fit into the taxonomic classes as defined by Tedesco *et al.* (1989).

FIG. 3. F- and P-class asteroids observed in this program.

FIG. 4. D-class asteroids observed in this program.

ANALYSIS OF POORLY CRYSTALLINE CLAY MINERALOGY: NEAR INFRARED SPECTROMETRY *VERSUS* X-RAY DIFFRACTION

William H. Farrand and Robert B. Singer, Planetary Image Research Laboratory, University of Arizona, Tucson, AZ 85721

Clay minerals are arguably the most abundant group of minerals at the Earth's surface, occurring in hydrothermal alteration zones and a host of sedimentary environments. On Mars, the existence of clay minerals has been hotly debated; their existence or absence has important implications for the type of surface processes which have acted through that planet's history and should provide clues to past climate. Given the importance of clay minerals, it is important to know the capabilities and limitations of various analytic methods that can detect and identity clay minerals. This study makes some direct comparisons between two such laboratory analytic methods, X-ray diffraction (XRD) and near infrared (NIR) reflectance spectrometry.

Before the advent of XRD demonstrated the existance of crystalline structure in clays minerals, they were regarded as being composed of amorphous phases [1]. XRD studies showed that any given clay specimen can be thought of as lying somewhere on a continuum between a highly-crystalline end member and an amorphous endmember. Some of the debate about the existence of "clays" vs. "palagonites" on Mars is semantic, since for different researchers these names imply different regions of this continuum. Nevertheless, the degree of crystallinity of a clay is closely related to its formation conditions, information which we very much wish to decipher.

The data for the comparison of techniques presented here are from an ongoing study of basaltic hydrovolcanism on Earth, with applications to Mars. Hydrovolcanism, the explosive interaction of magma with surface or near surface water [2], commonly produces tuff rings and tuff cones when the magma is basaltic in composition. The alteration product of basaltic glass (sideromelane) is termed palagonite, and a tuff in which the sideromelane has been largely altered to palagonite is called a palagonite tuff. The clay size-fraction (< 2 μm) of such tuffs has, at best, only poorly crystalline clays, and therefore lies toward the "amorphous" end of the continuum discussed above.

For this study, samples from two tuff rings and one tuff cone were analyzed. The tuff rings were Ubehebe Crater, CA and Zuni Salt Lake, NM; the tuff cone was Pavant Butte, UT. The reflectance of ten to twenty powdered samples (grain size < 500 μm) from each area were analyzed in the 0.3 to 2.7-μm wavelength range at RELAB [3]. Most of the highly palagonitized tuff cone sample spectra display a 2.3-μm absorption feature; a typical Pavant Butte palagonite tuff spectrum is shown in Figure 1. The 2.3-μm feature in these samples is due to a combination of the O-H stretch and Mg-OH lattice modes [4], and is characteristic of trioctahedral Mg-bearing clay minerals. In contrast, several of the less-palagonitized tuff ring sample spectra had 2.2 μm absorption features. This indicates the presence of Al-OH bonds and is diagnostic of Al-bearing dioctahedral clay minerals. A typical tuff spectrum from the Zuni Salt Lake tuff ring is also shown in Figure 1. Note that, independent of the difference in cation between these two samples, the more heavily altered (palagonitized) tuff cone material has a much deeper band.

It should be noted that our emphasis is on the 2.2- and 2.3-μm features. These overtones are weaker than the ν_{OH} stretching fundamental at 2.75μm and weaker even than the $2\nu_{OH}$ primary overtone at 1.38μm. However, both of the latter features are obscured by atmospheric water vapor and/or other gases in most remote sensing studies. Consequently, the 2.2- and 2.3-μm features take on a practical significance belied by their relatively shallow band depth. Details in these relatively weak features have also proven to be very diagnostic of mineralogy.

XRD analyses were performed on our samples that showed the strongest 2.2- and 2.3-μm features. XRD analyses of the initial bulk samples produced no peaks characteristic of Al-bearing clay minerals. However, the Pavant Butte samples did give a

7 Å peak that is tentatively assigned to antigorite. The bulk samples were then broken down to sand, silt and clay sized fractions and subjected to XRD analysis in the manner of Starkey et al. [5]. Only in the clay-sized fraction of two of the three tuff-ring samples did even a weak peak in the vicinity of 15 Å appear. This is interpreted as evidence of a smectite and/or mixed layer smectite-illite.

These results demonstrate something that many planetary spectroscopists have noticed for years: reflectance spectrometry is generally a more sensitive indicator of fine-grained and/or poorly crystalline clay-type mineralogy than is the more mature technique of XRD. NIR spectrometry can detect crystalline clays even in bulk samples of poorly crystalline materials. To attempt to detect those minerals with XRD analysis requires time consuming size separation procedures. In fairness, it should also be noted that in one of the Pavant Butte samples, a 15 Å peak indicated the presence of clay minerals whereas the NIR spectrum of that same sample showed no 2.2- or 2.3-μm band. That particular sample had a low reflectance and the lack of spectral features is attributed to masking by opaque minerals. Reflectance spectrometry is not an entirely mature technique, and more attention needs to be paid to issues such as the role that opaque minerals can play in masking diagnostic absorption features. Nevertheless reflectance spectometry should continue to receive serious consideration not only for laboratory use, but for possible in-situ instrumentation on future planetary rovers.

REFERENCES: [1] Eslinger, E. and Pevear, D. (1988) *SEPM Short Course Notes* **22**. [2] Sheridan, M.F. and Wohletz, K.H. (1983) *J. Volc. Geotherm. Res.*, **17**, 1-29. [3] Pieters, C.M. (1983) *J. Geophys. Res.*, **88**, 9534-9544. [4] Hunt, G.R. and Salisbury, J.W. (1970) *Modern Geology*, **1**, 283-300. [5] Starkey, H.C. et al. (1984) *USGS Bull. 1563.*

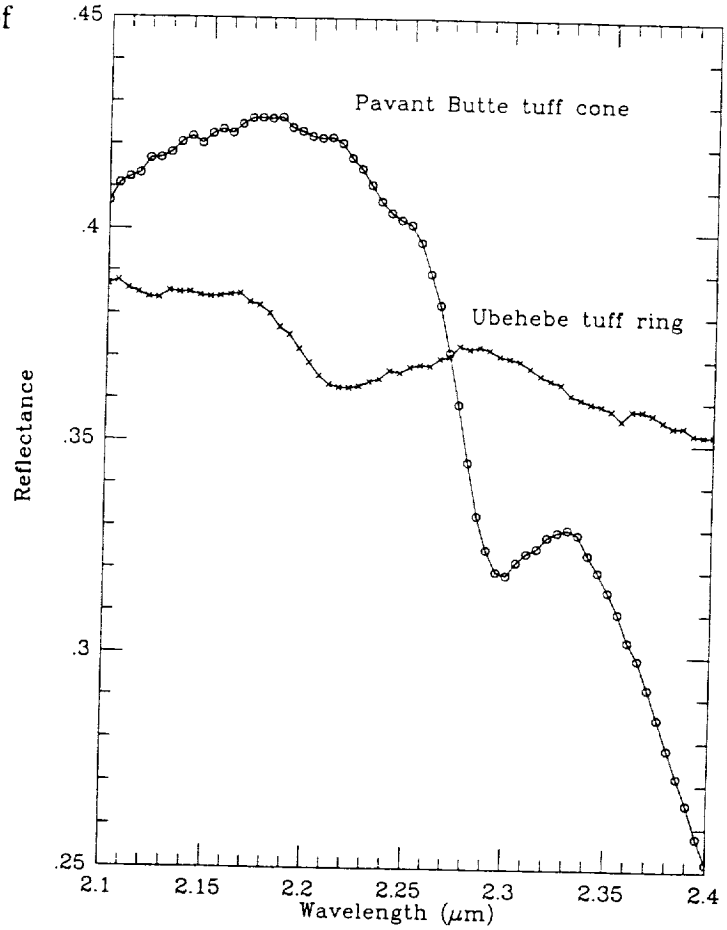

Figure 1. Near infrared reflectance of palagonitized basaltic tuffs from Ubehebe Crater and Pavant Butte. Arrows indicate the presence of 2.2 and 2.3 μm absorption features.

THERMAL INFRARED SPECTROSCOPIC REMOTE SENSING

John W. Salisbury, Department of Earth and Planetary Sciences, Johns Hopkins University, Baltimore, MD 21218

Considerable progress has been made during the past six months in four different areas of thermal infrared spectroscopic remote sensing.

Extraction of Compositional Information From Remotely Sensed Data. Real world, as opposed to laboratory, remote sensing data always pose problems in the extraction of compositional information. One of the classic problems is caused by fine particle size, which greatly reduces the spectral contrast in the fundamental molecular vibration (reststrahlen) bands. The lunar surface offers a prime example of this effect and lunar thermal infrared spectroscopic data have been the subject of confusion and controversy as a result. A group of scientists interested in this problem gathered at the San Juan Capistrano Research Institute at the urging of Doug Nash and reviewed spectral data from telescopic observations of the moon and laboratory measurements of returned lunar samples. The conclusion of this group (Nash et al., 1990) was that diagnostic compositional information exists in lunar emittance in the form of: overtone and combination tone bands in the 4 to 7 μm region of volume scattering; a Christiansen frequency feature associated with a minimum in scattering in the 7 to 8 μm region; and probably residual reststrahlen bands due to surface scattering in the 8 to 12 μm region. As a result, they recommended that a thermal infrared spectrometer be included in the payload of any new lunar orbiter.

Another classic problem results from the fact that emittance is a function of both temperature and emissivity, and one must be known to determine the other. Thus, the problem in compositional remote sensing is to establish the temperature of the emitting surface. There are a number of approaches to estimating temperature, and each involves different assumptions. To document these different approaches and the positive and negative aspects of each, the author gathered another group of scientists at the U. S. Geological Survey laboratory in Golden, CO. A report summarizing the results of this meeting is in preparation and will be the lead article in a special issue of Remote Sensing of Environment devoted primarily to thermal infrared remote sensing.

First Use of New Portable Field Spectrometer. A new, high-resolution field spectrometer funded by another agency has also begun to help strengthen the link between laboratory and real world remote sensing measurements. Use of this new instrument has illustrated how to overcome a third problem in some infrared measurements, which is the role of reflected downwelling radiance. When an atmosphere is present, its infrared emission is reflected from the surface of the target material and this reflected radiation is added to the emitted radiation. The result is reduced spectral contrast and the superimposition of atmospheric emission line structure on the spectral signature of the target. To remove this effect, we have used a diffuse gold surface surface to measure the downwelling radiance directly (Salisbury, 1990), but the downwelling radiance could also be calculated if the profile of atmospheric composition and temperature were known or could be accurately estimated. One other result of these field measurements has been to confirm the accuracy of our directional hemispherical reflectance in predicting emissivity. Removal of downwelling radiance effects yields emissivity values within 1% of those calculated from laboratory reflectance measurements using Kirchhoff's Law (Salisbury, 1990).

New Spectral Data On Minerals and Mineral Mixtures. Work on mixing models in cooperation with Janice Gardiner at Dartmouth has shown that the reststrahlen bands of minerals in solid rocks and in intimate particulate mixtures down to sand size are linearly additive, because this region of the spectrum is dominated by surface scattering (Gardiner and Salisbury, 1989). This linear mixing model is much simpler than the highly non-linear model in the visible/near-infrared made necessary by volume scattering. As particle size decreases, some volume scattering occurs, even in the reststrahlen region, and experiments continue to see how well the linear model applies at fine particle size.

Another interesting research result was obtained in cooperation with Doug Nash. Plagioclase feldspars of different Na/Ca contents can be distinguished in thermal infrared spectra of fine particulates by means of the wavelength position of the Christiansen frequency feature. Interestingly, glassification of these materials does not change the wavelength of this feature, despite the well-known loss of all fine structure in the reststrahlen bands, suggesting that one of the more significant effects of impact

metamorphism may not affect use of this spectral feature in remote sensing (Nash and Salisbury, 1990).

Spectral Libraries. The Second Edition of the mineral library is waiting on some difficult chemical analyses, but should be issued soon. Those researchers interested in the infrared spectrum of a particular mineral can obtain advance hard copy or digital data if desired.

A library of stony meteorite spectra is currently in preparation, along with an interpretative scientific paper. One of the more interesting results of this work is that almost 40% of the 61 meteorite samples examined are significantly contaminated with hydrocarbons, sometimes to the great surprise of the museum curator.

Spectral libraries of metamorphic and sedimentary rocks are under development. Suites of rocks have been assembled, polished sections obtained and spectra run for most samples. Proper characterization, as usual, will take the most time.

References

Gardiner, J. L. and Salisbury, J. W., 1989, Spectral reflectance of mineral mixtures in the mid-infrared (7-25 μm): Abstracts of the ERIM 7th Thematic Conference on Remote Sensing and Exploration Geology, Calgary, Canada, October 2-6, 1989, p. 2.

Nash, D. B. and Salisbury, J. W., 1990, Infrared reflectance spectra of plagioclase feldspars: Abstracts of the Twenty-first Lunar and Planetary Science Conference.

Nash, D. B., Conel, J. E., Christensen, P., Lucey, P.G., and Salisbury, J. W., 1990, Evaluation of thermal emission spectroscopy for compositional mapping of the Moon's surface from a polar-orbiting spacecraft: submitted to EOS.

Salisbury, J. W., 1990, First use of a new portable thermal infrared spectrometer: Abstracts of the IEEE International Geoscience and Remote Sensing Symposium, May 20-24, 1990, College Park, MD (in press).

OXIDIZED PYROXENES: THEIR VISIBLE - NEAR INFRARED REFLECTANCE SPECTRA AND IMPLICATIONS TO REMOTE-SENSING OF MARS

D'Arcy W. Straub and Roger G. Burns
Department of Earth, Atmospheric and Planetary Sciences,
Massachusetts Institute of Technology, Cambridge MA 02139.

Introduction. Pyroxenes are usually the most common and abundant ferromagnesian silicate mineral occurring in primary igneous rocks on the surface of terrestrial planets. As such, pyroxenes contribute significantly to remote-sensed reflectance spectra of planetary surfaces, particularly in the "1 micron" and "2 micron" regions where crystal field (CF) transitions in Fe^{2+} ions form the basis for identifying pyroxene compositions and structures. During extrusion of basaltic magma onto planetary surfaces, however, Fe^{2+} ions in the pyroxenes are vulnerable to oxidation. The ferric iron may remain as Fe^{3+} ions in the pyroxene structure or form a veneer of ferric oxides. Either state of ferric iron could obscure the diagnostic pyroxene Fe^{2+} spectral features.

To assess the effects of aerial oxidation on pyroxene reflectance spectra, visible - near infrared spectral measurements were made on a suite of well characterized pyroxenes that are representative of different structure-types and compositions. Correlations were made with Mossbauer spectra obtained at room temperature and at 4.2K to enable the Fe^{3+}-bearing phases to be identified.

Origins of Pyroxene Spectral Features. In the pyroxene crystal structure, cations occur in two crystallographic positions designated as the M1 and M2 sites. The pyroxene M1 site is only slightly distorted from octahedral symmetry, and cations in this position are located near the center of symmetry of the site. Chains of edge-sharing M1 octahedra zig-zag along the c axis, and relatively short M1-M1 interatomic distances permit $Fe^{2+} \rightarrow Fe^{3+}$ intervalence charge transfer (IVCT) transitions to occur. The pyroxene M2 site, on the other hand, is a very distorted, non-centrosymmetric coordination polyhedron, which causes the Fe^{2+}/M2 site crystal field (CF) bands to be considerably more intense than the Fe^{2+}/M1 site CF bands. Such intensification of Fe^{2+}/M2 site spectra are illustrated for unoxidized pyroxenes in Figure 1. In basaltic orthopyroxenes and also pigeonites, Fe^{2+} ions are strongly enriched in the M2 sites and are responsible for the two intense CF bands centered around 0.9 and 1.8 microns (Figure 1a). In calcic clinopyroxenes, Fe^{2+} ions occupy only the M1 sites when Ca^{2+} ions fill the M2 sites so that the two bands centered around 0.9 and 1.15 microns in the spectra of stoichiometric hedenbergites (Figure 1d) originate from Fe^{2+}/M1 site CF transitions alone. In non-stoichiometric calcic clinopyroxenes, Fe^{2+} ions occupy M2 sites vacated by Ca^{2+} ions. The spectra of sub-calcic hedenbergites (Figure 1c) indicate that the Fe^{2+}/M2 site CF bands occurring near 1.0 and 2.3 microns are more intense than the Fe^{2+}/M1 site CF bands at 0.9 and 1.15 microns even though Fe^{2+} ions are concentrated in the M1 sites.

The presence of ferric iron in pyroxenes raises the possibility of additional spectral features originating from Fe^{3+}/M1 site CF transitions (which yield weak spin-forbidden bands) and from $Fe^{2+} \rightarrow Fe^{3+}$ IVCT. Such $Fe^{2+} \rightarrow Fe^{3+}$ IVCT bands occur near 0.8 microns in the spectra of the sub-calcic augite and hedenbergite shown in figures 1b and 1c.

Spectra of Oxidized Orthopyroxenes. Reflectance spectra of an orthopyroxene, $(Fe_{0.29}Mg_{0.70}Ca_{0.01})SiO_3$, which was heated in air at 600°C for different time periods, are illustrated in Figure 1a. The spectra show that the depths of the 0.9 and 1.8 micron bands are considerably reduced by the oxidation of Fe^{2+} to Fe^{3+} ions. The increased absorption between 0.4 and 0.9 microns may originate from: (1) Fe^{3+} CF transitions within ferric iron remaining in the pyroxene structure after oxidation of ferrous iron; (2) a ferric oxide (e.g. hematite) formed by decomposition of the pyroxene; or (3) a $Fe^{2+} \rightarrow Fe^{3+}$ IVCT transition.

The Mössbauer spectra shown in Figure 2 indicate that nanophase hematite (superparamagnetic at room temperature) is the predominant ferric bearing phase.

Spectra of Oxidized Hedenbergites. The spectra of a Mn hedenbergite, $(Ca_{0.99}Mn_{0.20}Fe_{0.80}Mg_{0.01})Si_2O_6$, heated in air at 500°C are shown in Figure 1d. In this

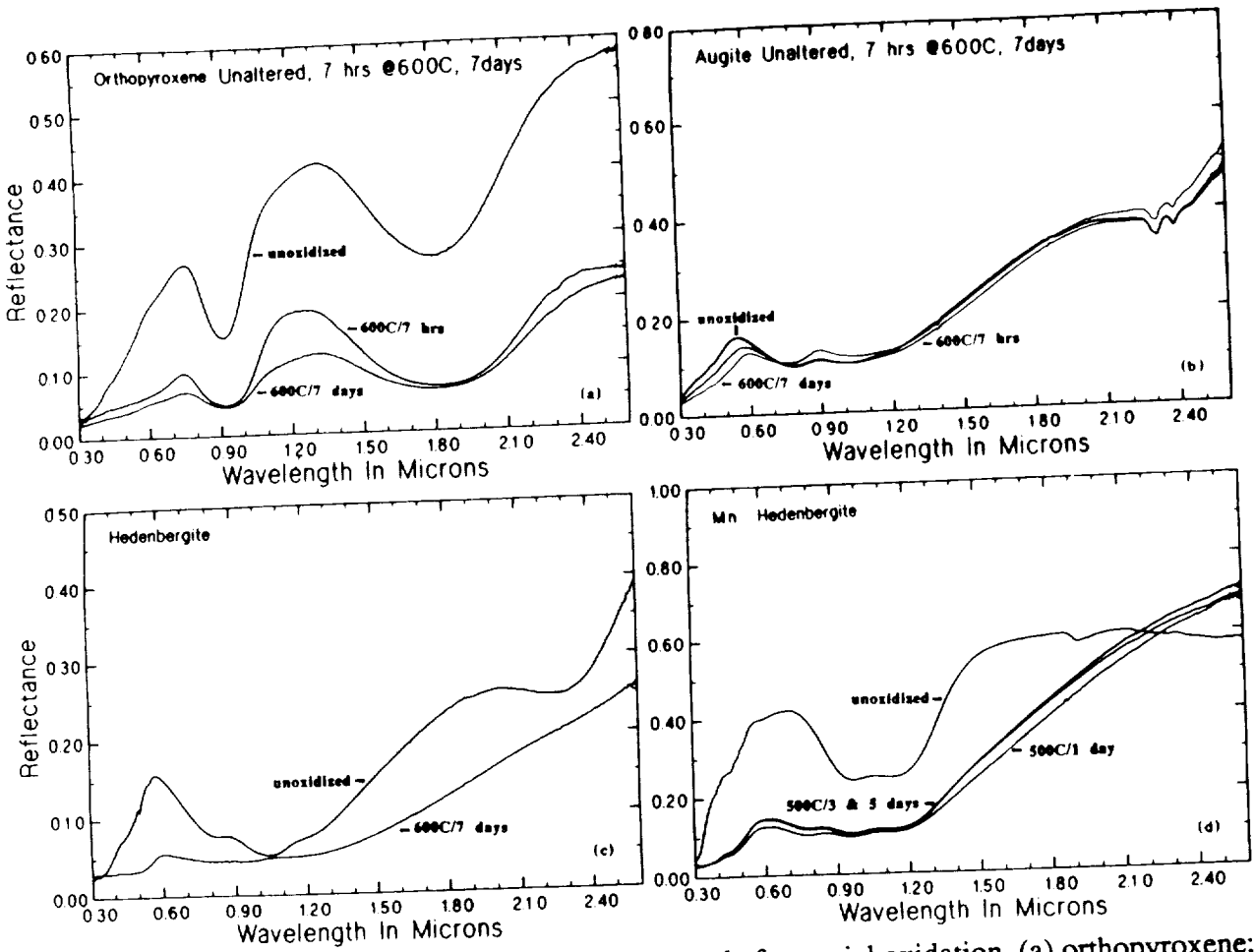

Figure 1. Reflectance spectra of pyroxenes before and after aerial oxidation. (a) orthopyroxene; (b) augite; (c) hedenbergite; and (d) Mn hedenbergite.

hedenbergite, Ca^{2+} and Mn^{2+} ions completely fill the M2 sites so that no Fe^{2+}/M2 site bands at 1.05 and 2.30 microns appear in the spectra. With increased oxidation, the band depths of the Fe^{2+}/M1 site bands at 0.95 and 1.15 microns become diminished and the $Fe^{2+} \rightarrow Fe^{3+}$ IVCT band at 0.8 microns increases in intensity. The Mössbauer spectra at 4.2K (Figure 3), in which magnetic ordering of the M1 site Fe^{2+} ions appears, show the presence of only minor amounts of ferric oxide in the oxidized hedenbergites.

When hedenbergite is strongly oxidized, all Fe^{2+} CF and $Fe^{2+} \rightarrow Fe^{3+}$ IVCT bands become obliterated. Such effects are illustrated in Figure 1c for sub-calcic hedenbergite, $(Ca_{0.95}Fe_{0.85}Mg_{0.20})Si_2O_6$, initially containing ~10% ferric iron. The Mössbauer spectra (Figure 3) show that although significant amounts of ferric oxide (hematite) are formed, a large proportion of Fe^{2+} still remains in the oxidized hedenbergite.

Spectra of Oxidized Augite. The effects of aerial oxidation on the reflectance spectra of an augite, $Fs_{10}En_{41}Wo_{46}$, are shown in Figure1b. The effects of oxidation are to diminish the band depths of the Fe2+/M2 site CF bands at ~1.0 and 2.2 microns, and to broaden the band at ~0.8 microns, perhaps due to several $Fe^{2+} \rightarrow Fe^{3+}$ IVCT transitions involving oxidized Fe^{2+} (now Fe^{3+}) located in both the M1 and M2 sites of the oxidized augites. This assignment is supported by the Mössbauer spectra which indicate that ferric iron formed by oxidation of augite remains predominantly in the pyroxene structure.

Conclusions. The reduced band depths of the pyroxene 1 micron and 2 micron spectral features observed in the reflectance spectra of oxidized pyroxenes may be attributed to two related causes: first, loss of Fe^{2+} ions in the pyroxene M2 sites after they become oxidized to Fe^{3+} ions; and second, increased absorption by the ferric iron, either as structural Fe^{3+} ions in the pyroxenes, or as nanophase Fe_2O_3 phases formed in and on the surfaces of the pyroxene grains.

Crystal field and intervalence charge transfer transitions involving structural Fe^{3+} in pyroxenes and olivine, in addition to CF transitions within ferric oxides, may explain the contrasting reflectance spectral profiles seen between dark and bright regions of Mars.

Our studies also suggest a mechanism for producing the nanophase hematite popularly considered to be responsible for the features observed around 0.65 and 0.87 microns in remote-sensed spectra of Mars: the ferric oxide originates from aerial oxidation of structural Fe^{2+} ions in the ferromagnesian silicates to disseminated Fe_2O_3.

Bibliography. This paper was exhibited as a poster presentation at the 21st Lunar and Planetary Science Conference in the session on "Mars Remote Sensing." Background references appear in *Lunar & Planetary Science, XXI,* 1216-1217 (1990). The research is supported by NASA grant NSG-7604.

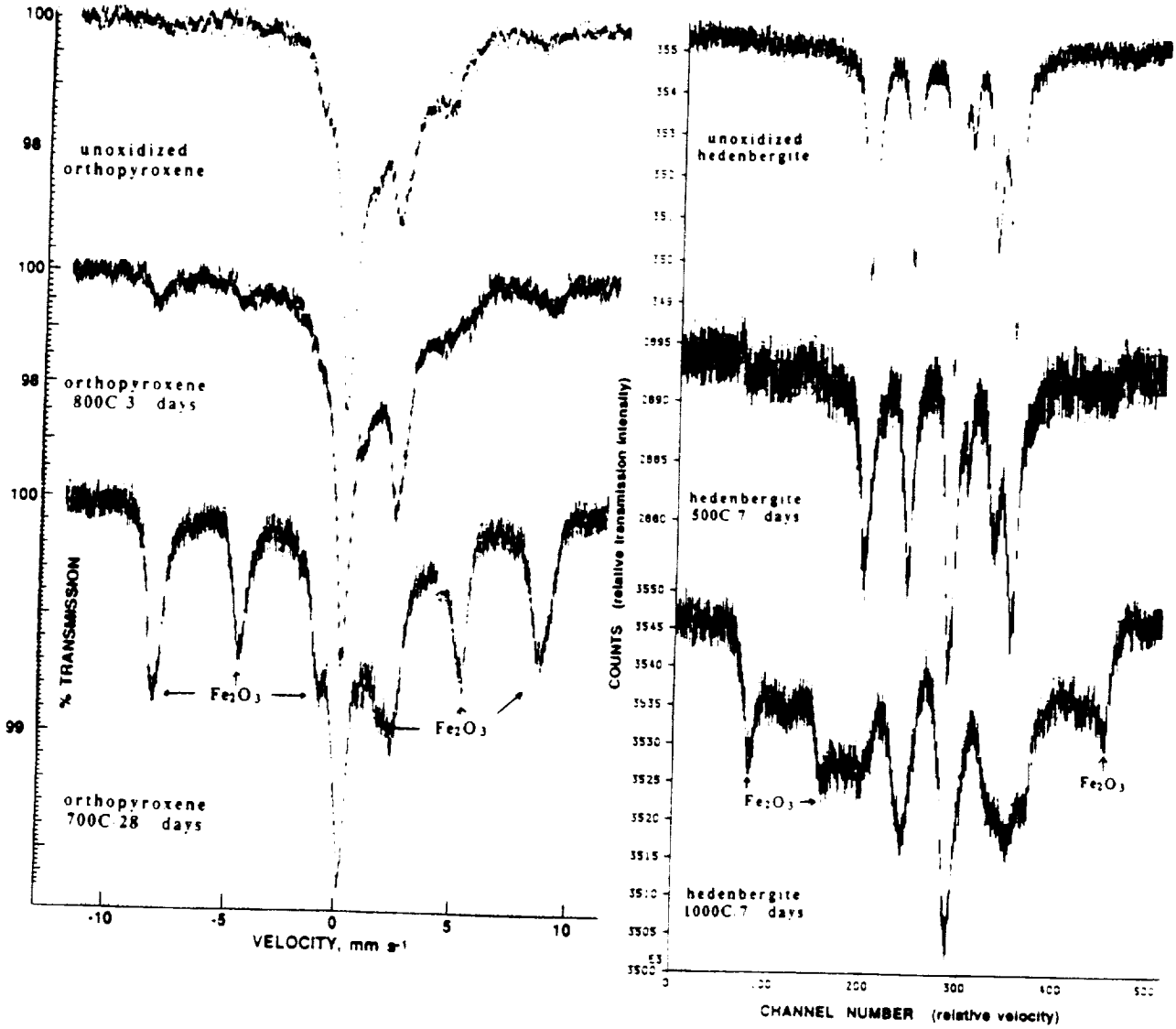

Figure 2. Mossbauer spectra at 4.2K of oxidized orthopyroxenes

Figure 3. Mossbauer spectra at 4.2K of oxidized hedenbergites

MOSSBAUER SPECTRA OF OLIVINE-RICH WEATHERED ACHONDRITES

Sondra L. Martinez and Roger G. Burns
Department of Earth, Atmospheric and Planetary Sciences,
Massachusetts Institute of Technology, Cambridge MA 02139.

Introduction. Olivine, the dominant ferromagnesian silicate in many meteorite-types, is susceptible to oxidative weathering, particularly in aqueous environments. Olivine also predominates in several SNC meteorites believed to have originated from Mars. In studies to assess whether oxidation of olivine has occurred on the frozen surface of Mars, Mossbauer spectral measurements were made on olivine-bearing achondritic meteorites found in Antarctica. Reported here are results obtained from 4.2K and room temperature Mossbauer spectra of a suite of ureilites and most of the SNC meteorites, including several *falls* and *finds* .

Ureilite Mossbauer Spectra. Several ureilites, typically consisting of olivine-pigeonite assemblages in a carbonaceous matrix of graphite, diamond and lonsdaleite plus accessory Fe-Ni metal and sulfides, were acquired for the Mossbauer spectral measurements. They included seven specimens found in Antarctica and the two *falls* Novo-Urei and Haverö. The 295K Mossbauer spectra (Figure 1) are composed of two ferrous and one ferric (shaded) doublets, in addition to the four inner peaks of the metallic Fe sextet spectrum. The relative intensities of the outer and inner ferrous doublets, originating from Fe^{2+} ions in olivine and pigeonite, respectively, indicate that olivine predominates in most of the ureilites, except for two: ALHA 84136 and EET 87517. The Fe^{3+} peaks are also intensified in these two ureilites relative to the other specimens.

The 4.2K spectra (Figures 2) show the appearance of sextets originating from magnetically-ordered Fe(III) oxide phases and from metallic Fe. The ferric sextet peaks are sharper in PCA 82506 and yield a magnetic hyperfine splitting, H, of ~503 gauss indicative of goethite (G), compared to the sextet peaks in EET 87517 with H = ~486 gauss having larger widths and may be indicative of ferrihydrite (F) and, perhaps, akaganeite and nanophase goethite. All of the ureilites, including the two *fall* specimens (Novo-Urei and Haverö), contain ferric oxide sextets. Specimen EET 87517 with the highest ferric iron content shows no Fe sextet, suggesting that any metallic iron originally present in the meteorite has been completely oxidized.

Conclusions. It is apparent from the 295 and 4.2K Mossbauer spectra that several of the ureilites contain major proportions of metallic iron. Much of this metallic phase has resulted from carbon-induced reduction of ferrous iron in the outermost 10-100 microns of olivine grains in contact with carbonaceous material in the ureilites. The cryptocrystalline character of these Fe inclusions in olivine appears to render the metal extremely vulnerable to aerial oxidation, even in ureilites collected as *falls*.

Spectra of SNC and Related Meteorites. Mossbauer spectra measured on six of the eight SNC meteorites (Shergotty, Chassigny, Nakhla, LaFayette, ALHA 77005 "light" and "dark" fractions, and EETA 79001 lithologies A, B and C), together with spectra of related achondrites (Brachina and eucrite ALHA 81002), are illustrated in Figures 3. The 4.2K spectra show that peaks at approx. -7.75 and +8.5 mm s^{-1} indicative of a Fe(III) oxide phase are: (1) conspicuous in Lafayette (found in Indiana) and Brachina (found in South Australia); (2) barely discernable in Nakhla (fell in Egypt, 1911), eucrite ALHA 81002 and Shergotty (fell in India, 1865); and (3) absent in Chassigny (fell in France, 1815) and ALHA 77005 (found in Antarctica). Spectra measured at 295K show that Fe^{3+} peaks observed in Brachina and LaFayette are not obvious in samples of the other SNC meteorites, including the three lithologies of EETA 79001. Fitted 295K Mossbauer spectra of the Chassigny, Nakhla, ALHA 77005 and EETA 79001 samples, however, resolved ~2% ferric iron.

Conclusions. The nanophase goethite identified in Brachina and Lafayette was probably produced by terrestrial weathering before the meteorites were found. Similar oxidation could not have occurred in Chassigny and Nakhla which were collected soon after they fell, so that the ~2 % Fe^{3+} resolved in their 295K Mossbauer spectra must be of extraterrestrial origin. The absence of goethite in the two olivine-bearing Antarctic shergottites (ALHA 77005 and EETA 79001) indicates that oxidative weathering of these metal-free meteorites in the polar icecap was negligible. Again, the ~2 percent ferric iron determined in the 295K spectra of these Antarctic shergottites appears to have originated from oxidation on Mars.

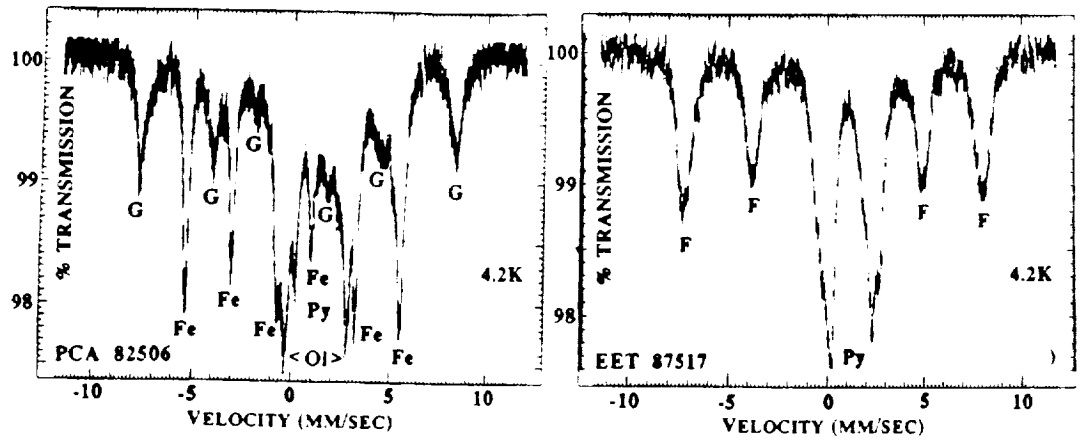

Figure 1. Mossbauer spectra of two ureilites from Antarctica measured at room temperature

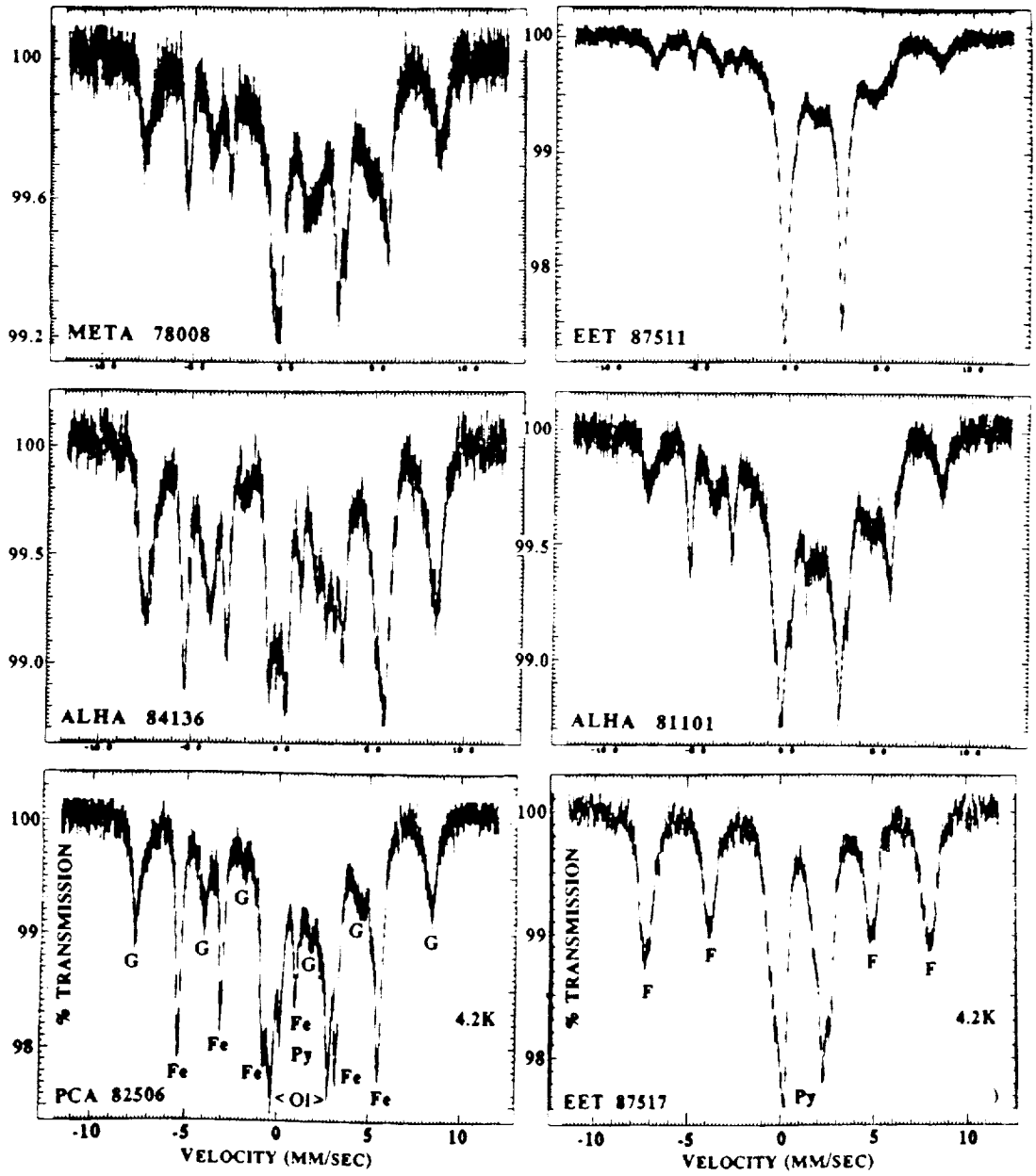

Figure 2. Mossbauer spectra measured at 4.2K of ureilites from Antarctica

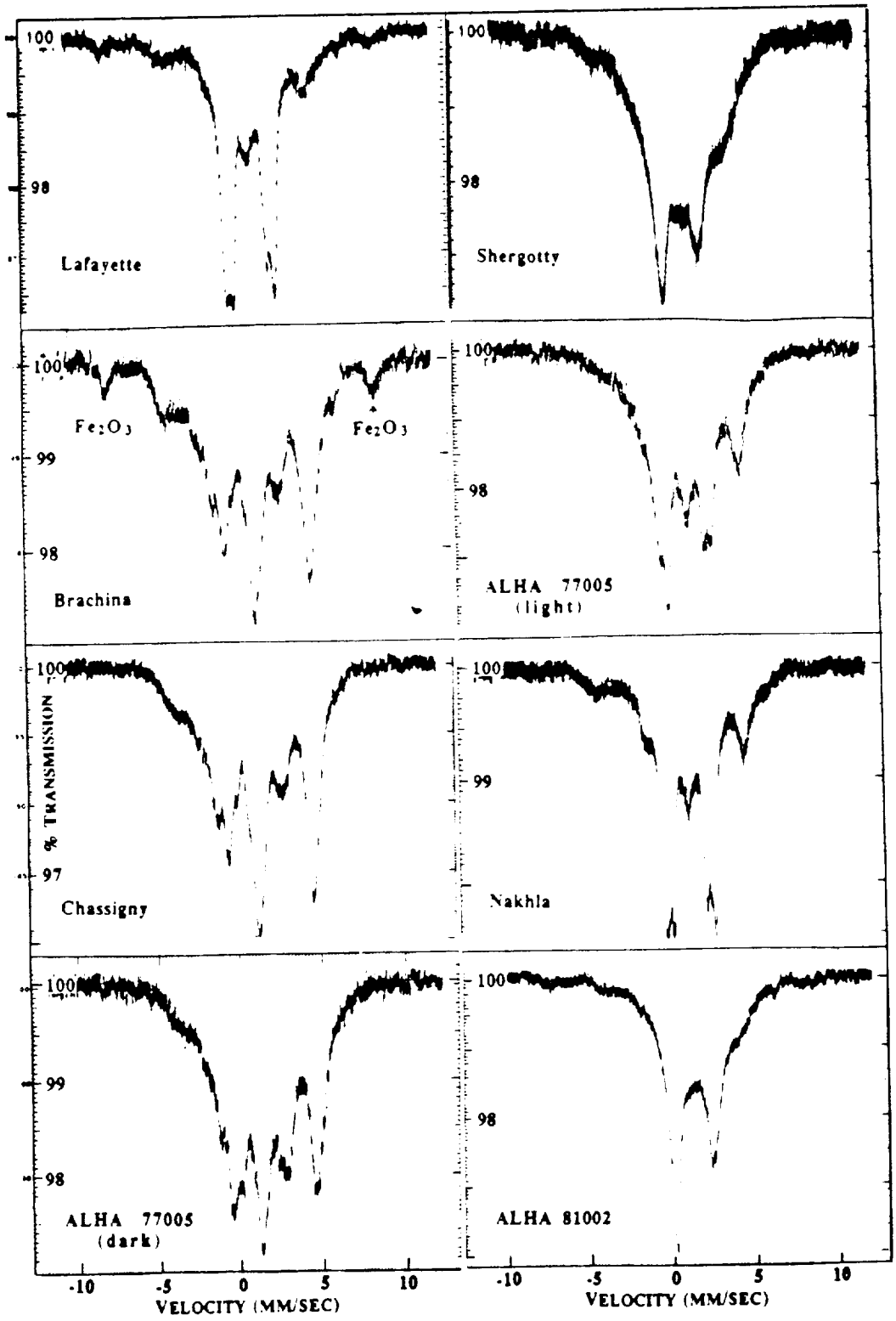

Figure 3. Mossbauer spectra of SNC and related achondrites measured at 4.2K

Bibliography. This paper was exhibited as a poster presentation at the 21st Lunar and Planetary Science Conference in the sessions "MEVTV: Martian Magmatic and Surface Evolution" and "Ureilite - HED." Background references appear in *Lunar & Planetary Science, XXI*, 147-148 and 736-737 (199). The research is supported by NASA Grants NAGW-1078 and NSG-7604

Compositional Variability in Olivine Reflectance Spectra: A New Capability for Lunar Exploration. Jessica M. Sunshine and Carle M. Pieters, Department of Geological Sciences, Brown University, Providence, RI 02912.

New opportunities to explore the lunar surface using remotely acquired reflectance spectra are expected from the deployment of imaging spectrometers on earth based telescopes, the upcoming Galileo lunar encounters, and the Lunar Observer spacecraft. Although reflectance spectra contain features that are diagnostic of individual minerals, spectra of lunar rocks contain combined absorption features from each of the minerals present on the surface. Mineralogic interpretation of these convolved spectral signals depends on our ability to resolve them into quantifiable parameters that are related to specific minerals. Spectra can be deconvolved by representing the individual absorption bands as discrete mathematical distributions and modeling the spectrum as a sum of these distributions using a least-square fitting procedure. An accurate model for electronic transition absorptions has been developed by Sunshine et al., 1990 (J.G.R. in press) which uses modified Gaussian distributions to describe each absorption band in terms of three model parameters; band center, band width and band strength. Sunshine et al. [1] were able to use this modified Gaussian model (MGM) to successfully resolve the spectra of orthopyroxene, clinopyroxene and pyroxene mixtures into individual absorption bands. The study presented here focuses on applying the MGM to olivine reflectance spectra.

Given the relationship between olivine chemistry and the degree of differentiation of a rock, developing the ability to not only identify the presence of olivine, but also to provide constrains on its chemical composition using remotely obtained reflectance spectra would be particularly useful for lunar petrology. However, the spectrum of olivine is complex (see **Figure 1**). It is dominated by an absorption feature near 1.0 μm that consists of three overlapping absorption bands caused by the spin-allowed electronic transition of Fe^{+2} in distorted octahedral (M1 and M2) crystal field sites [2,3]. Previous studies using transmission spectra of oriented olivine crystals have revealed systematic compositional trends in the band centers of individual absorption bands [2,4]. Similarly, in reflectance spectra of particulate olivines, the overall minimum (near 1.0 μm) of the composite absorption feature has also been observed to vary with composition [5].

Because the 1.0 μm olivine feature has three independent absorption bands, there are nine free model parameters (a center, strength, and width for each absorption) all within the 1.0 μm region in any model of the olivine spectrum. It is difficult to resolve these overlapping absorption bands in spectra of multi-component lunar rocks, which include absorption features from other minerals. If quantifiable relationships among the model parameters can be determined for olivine spectra, this problem could be greatly simplified, particularly for data with lower signal to noise ratios.

To investigate the relationships among the model parameters, a suite of twelve olivine samples spanning a wide range of compositions was assembled. (We would like to thank R. Burns, E. Cloutis, and the Harvard Mineral Museum for generously providing several of these samples). Bi-directional reflectance spectra from 0.3 to 2.6 μm were obtained for <45 μm particle size separates of these samples using the RELAB spectrometer [6]. One sample (Fo 43) was excluded from further analysis due to its anomalous spectral characteristics; the cause of this behavior is unknown and being investigated further. The remaining samples were all successfully modeled using five modified Gaussian distributions superimposed on a continuum (see **Figure 1** for example). Three of the absorptions (bands a, b and c) form the primary Fe^{+2} feature, another consistently occurs on the short wavelength wing of this feature (band d), and the fifth represents the charge transfer absorptions at short wavelengths.

Modeling the suite of olivine spectra reveals that the centers and strengths of absorptions vary systematically with chemistry. Analysis of the resultant model parameters also suggests that each absorption band has a fundamental band width and that three of the four major absorption bands have a similar average band widths in energy. The average band widths and their standard deviations are given in wavelength (nm) and energy (cm^{-1}) in the chart below. Bands a, c, and d have band widths of approximately 3000 cm^{-1} while band d has a width of ≈1500 cm^{-1}.

	band a	band b	band c	band d
average band width in nm	228 ± 38	176 ± 8	424 ± 37	115 ± 34
average band width in cm^{-1}	3053 ± 270	1612 ± 24	2870 ± 178	2889 ± 311
approximate band width in energy	3000	1500	3000	3000

Since one would expect the width of an electronic transition absorption to be a function of the crystal field site, the relationships between the average band widths suggest that absorptions a, c and d are from one site and absorption b is from a different site. This is consistent with Burns' assignment of absorption bands a and c to

transitions of Fe^{+2} in the M1 site and absorption band b to transitions of Fe^{+2} in the M2 site based on transmission studies [2,4]. The origin of the smaller absorption, band d, remains unclear. However, the fact that band d has the same average width as bands a and c suggests that absorption band d also arises due to Fe^{+2} in the M1 site.

The suite of olivine spectra was re-modeled using the MGM with the average band widths for the four absorptions given in the chart above. Constraining the band widths reduces the number of free parameters by four, but has little effect on the RMS residual error of fit. The model fit using average band widths for the Fo 97 spectrum is shown, for example, in **Figure 1**. It is possible to model all the olivine spectra except the high iron fayalite spectrum (Fo 01) using the average band widths shown in the chart above. In order to fit the fayalite spectrum it is necessary to relax the constraints on the band widths. This suggest that the presence of a large proportion of iron changes the structure of the crystal field site and thus the width of the absorption band. The spectra of high iron olivines (Fo <36) will need to be analyzed more completely in order to determine when this transition occurs.

Constraining the band widths increases the correlation of band centers and band strengths with composition. The relationship between the band centers of the primary absorptions and chemistry are shown as a function of molar percentage forsterite in **Figure 2**. As was first observed for transmission spectra [4], there is a systematic increase in the wavelength of each of the band centers of the primary absorption bands (bands a, b and c) as the composition becomes increasingly fayalitic. While these band centers are all well correlated to the molar percentage forsterite in the samples, band c has the highest correlation, .975, and spans the largest range of wavelengths.

The high correlation between the band centers of the primary absorption bands in olivine spectra and the chemical composition of the sample suggest that the composition of an unknown olivine sample can be estimated from the position of the band centers derived using the MGM. Recognition of the constant band widths in this analysis of laboratory spectra has reduced the number of free model parameters, which will enhance the accuracy of modelling olivine spectra with lower signal to noise ratios. The results presented here, and in previous study of pyroxene spectra [1], suggest that reflectance spectra can be used to not only identify minerals, but to also estimate their chemical composition by relating their absorption characteristics with those derived from known samples. Expanded studies of the spectral variation of additional minerals over a more complete range of compositions, using terrestrial and returned lunar samples, will provide the capability to obtain compositional information for a larger number of relevant minerals on the lunar surface.

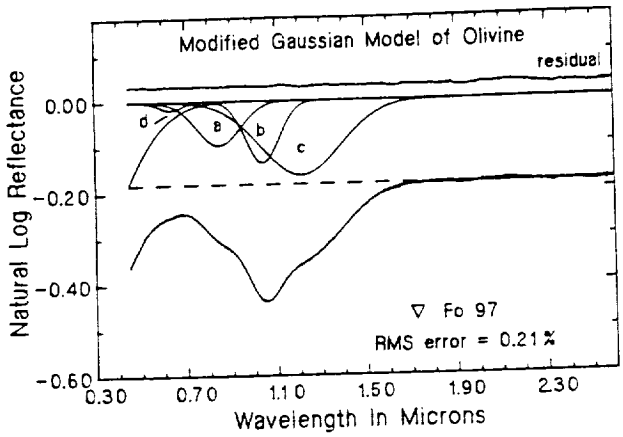

Figure 1. The olivine absorption bands derived from the modified Gaussian model fit to the spectrum of Fo 97 olivine. The band widths used for the primary absorption bands are the average widths indicated in the chart above.

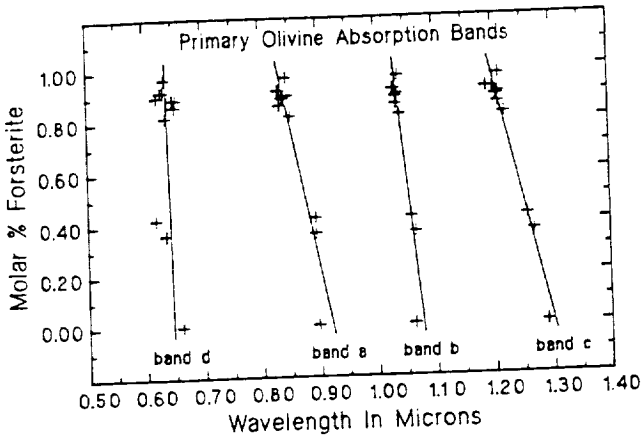

Figure 2. The relationship between band center and composition for the primary absorption bands in olivine reflectance spectra.

References [1] Sunshine, J. M., Pieters, C. M. and Pratt, S. F., *J.G.R.*, 1990 in press. [2] Burns, R. G., *Amer. Min.*, 55, 1608-1632, 1970. [3] Marfunin, A. S., *Physics of Minerals and Inorganic Materials*, 1979. [4] Burns, R. G., *Mineralogical Applications to Crystal Field Theory*, 1970. [5] King, T. V. V. and W. I. Ridley, *J.G.R.*, **92**, 11,457-11,469, 1987. [6] Pieters, C. M. et al., *RELAB Users Manual*, available on request.

THE OLIVINE MOUNTAINS AT COPERNICUS: AN EXPOSED LAYERED PLUTON

C. M. Pieters, S.F. Pratt and J.M. Sunshine, Brown University, Providence RI 02912

Earth-based near-infrared spectrometers have detected olivine as a major component of local rock types at several unsampled sites on the lunar near-side. It is suspected to be abundant in the late Ti-rich basalts of the western mare (1) and is present in deposits from a localized pyroclastic vent in the north polar area (2). Olivine was discovered to be the primary mafic mineral comprising the central peaks of Copernicus (3). It was also found to be a significant component of material excavated along the south rim of Aristarchus as well as a major component of a mountain (massif) on the Aristarchus plateau (4). In all cases, the existence of significant olivine was inferred from the general character of diagnostic absorption features near 1 μm observed in remotely obtained reflectance spectra. To address the more important compositional questions about mineral abundance and mineral composition requires more sophisticated approaches than were previously available. Several techniques for deconvolving mineral mixtures into components and quantifying mineral absorption features have been recently tested and show promise for lunar applications. Presented here is an approach to extract quantified compositional information utilizing the Hapke model for separating components of intimate mixtures (5, 6) and the modified Gaussian model (7) for analyses of mineral composition (8). The discussion below evaluates the composition of the Copernicus mountains.

The central peaks of Copernicus are tens of kilometers in size and represent material excavated from a depth of about 10 km within the crust. The abundance and composition of the olivine is directly related to the origin of this unusual lithology, which in turn bears on the evolution of the lunar crust in this part of the central nearside. A Mg-rich dunite deposit of this size would likely represent a cumulate from a large-scale differentiation event (a pluton or even the mantle formed from a magma ocean). A more Fe-rich olivine deposit would imply extensive intrusion of a rather evolved magma. Although the crater is thought to be about 800 My old (9), the soil at Copernicus is believed to have reached a state of maturity about comparable to typical highland soils, since the optical properties of soil on much of the rim and ejecta is similar to that in the central highlands or at Apollo 16 (10,11).

Regolith Alteration. To extract information about mineral abundances from a composite spectrum requires accurate measurement of the character and the strength of absorption features as well as the overall albedo of the original lithology. Although the soil formation process significantly darkens lunar material and reduces spectral contrast, the residual absorption features retain the characteristics of the original lithology (e.g. 12). The alteration products contained in lunar agglutinates dominate the optical properties. Particle size effects are insignificant due largely to the fact that all soils have a range of particle sizes (13). Shown in Figures 1 and 2 are preliminary results from a two-step approach for removing the effects of alteration from the spectrum for the middle central peak of Copernicus (Cop P3). The first step is to derive a model for the optical properties of the alteration products for typical highland soil. Noritic breccia 67455 was chosen for this preliminary study to represent typical unaltered lithology and soil 62231 was chosen to represent the local mature soil. The intimate mixing model was used to calculate the properties of alteration products required to transform the breccia into mature soil. If particle size and density are comparable, 70% of the synthesized alteration product (ALT) shown in **Figure 1** is required to produce soil 62231. [If the absorbing species in ALT is smaller, the proportion required decreases, but ALT remains the same.] Assuming the same alteration process at Copernicus, the second step is to remove the effects of ALT from the spectrum for Cop P3 using the intimate mixing model (in reverse). In this case, derivation of the unaltered Copernicus P3 spectrum shown in **Figure 2** required removal of 50% ALT from the original telescopic spectrum.

Mineral Abundance. The strength of the broad olivine absorption band near 1 μm in the unaltered Copernicus P3 spectrum is about 40%. Although it can vary with composition, such an absorption strength is typical for particulate monomineralic samples of olivine that contain fine particles (**Figure 3**). A large plagioclase component would be inconsistent with the unaltered Cop P3 spectrum since the plagioclase spectrum (relatively featureless) would dilute the mafic mineral absorption band. In comparison with variations in band strength observed for analogue lunar soil mixtures of plagioclase and pyroxene (13), an upper limit of about 30% plagioclase is estimated for P3. Contrary to previous expectations using simple continuum removal techniques (3, 12), there does appear to be a weak feature in the unaltered Cop P3 spectrum near 2 μm. Two possible causes for this faint absorption are minor components of (1) low-Ca pyroxene or (2) spinel. Pyroxene abundance is simple to estimate and remove with the intimate mixing model. Using the spectrum of a lunar orthopyroxene (separate from 78235), the low-Ca pyroxene component was estimated to be 4-5%. The unaltered Cop P3 spectrum with this minor pyroxene removed is shown in the top of **Figure 2**. Alternatively, trace amounts of spinel could account for the faint 2 μm feature. Only two particulate lunar olivine samples have been available for spectral measurement (72414 and a 76535 separate), both of which exhibited a 2 μm feature and were known to contain noticeable amounts of translucent Cr-spinel. Diffuse transmission measurements on a thinsection of 72415 confirmed the cause of the 2 μm feature to be the spinel in these pristine lunar olivines. Diffuse thinsection spectra and a comparison spectrum from a particulate sample are shown in **Figure 4**. Since the spinel crystals were smaller than the 1 mm beam size, the characteristics of the spinel were calculated from the olivine and the olivine + spinel spectra. In contrast to unmixing pyroxene, however, it is more difficult to confidently remove minor spinel from the Cop P3 spectrum. Reflectance models have not yet been tested that can incorporate these recent thinsection data.

OLIVINE MOUNTAINS AT COPERNICUS

C. M. Pieters et al.

Mineral Composition. Once the olivine has been separated from the other components (ALT, orthopyroxene, spinel), the complex Fe^{2+} olivine feature can be deconvolved into individual absorption bands using the modified Gaussian model (MGM) (7). If P3 band characteristics are adequately constrained within the S/N of the telescopic data, the composition of the olivine at Copernicus can be estimated by comparing P3 band parameters with the systematic variations observed as a function of composition for the terrestrial Fo - Fa suite (8).

Summary. Although the character of ALT is preliminary, these initial results indicate that the centermost, and blockiest, mountain of Copernicus appears to be composed almost entirely of dunite. Plagioclase is not required, but may be present to <30%. The P3 mountain lithology also contains either 4-5% low-Ca pyroxene or trace amounts of spinel comparable to those found in several pristine olivine samples. When the cause of the 2 μm feature is more fully understood, determination of the olivine composition should be possible. It should be noted, however, that P1, the larger olivine-bearing mountain 10 km to the west (11), must contain an abundant feldspar component since the olivine absorption strength observed for P1 is about 1/3 that at P3 and there are no other significant features in the spectrum (11, 12). The spatial relations of such a distinctive compositional sequence is suggestive of an exposed layered pluton, perhaps similar to that found at the Stillwater complex on Earth.

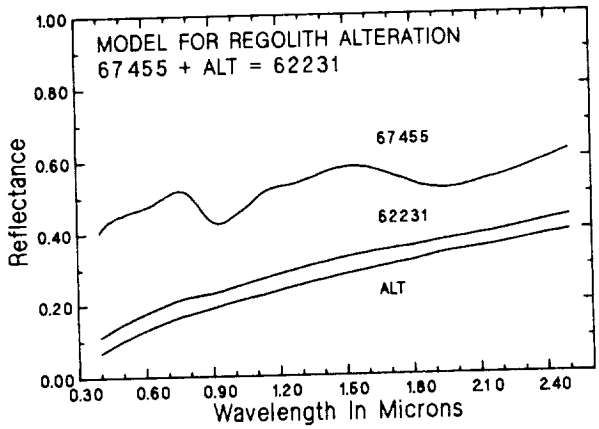

Figure 1. Reflectance spectra of samples used to estimate the required spectral characteristics of materials produced during regolith alteration (ALT). Based on an intimate mixing model, an unweathered breccia (67455) mixed with 70% ALT will produce mature soil (62231).

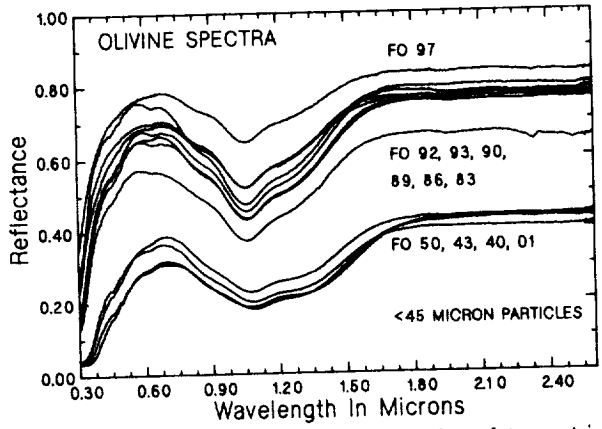

Figure 3. Reflectance spectra of a suite of terrestrial olivines with different compositions [used in Sunshine and Pieters (8)]. All samples have a particle size <45μm.

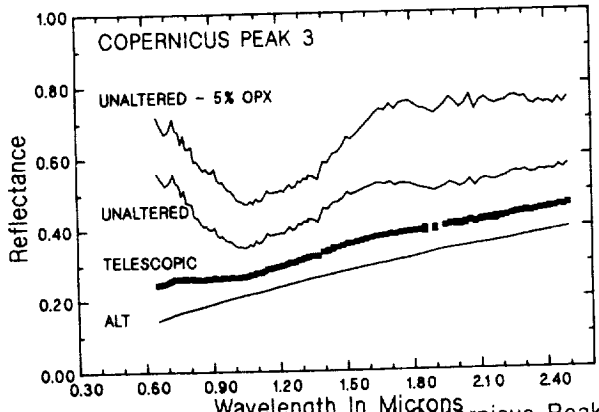

Figure 2. Reflectance spectrum of Copernicus Peak 3 (P3) obtained with earthbased telescopes (with errorbars). Using intimate mixing models, ALT was first removed from Cop P3 to produce a spectrum for unaltered material at P3, then minor (5%) orthopyroxene (78235) was removed resulting in a dunite spectrum (offset upward 0.1).

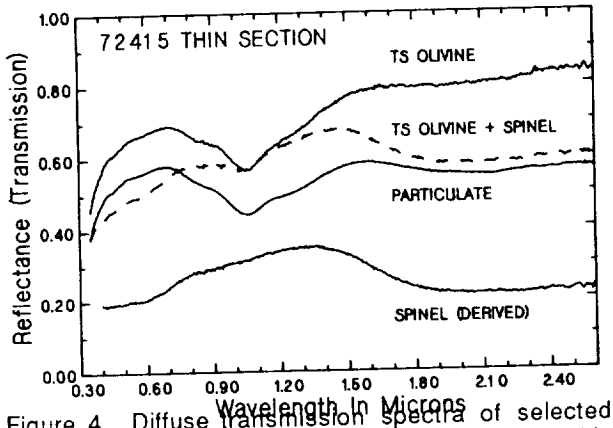

Figure 4. Diffuse transmission spectra of selected areas of olivine and olivine + spinel from a 72415 thin section. The spectral properties of the more absorbing spinel was calculated using linear mixing model. A reflectance spectrum of a particulate sample (<45 μm) of this dunite exhibits a distinct spinel feature near 2 μm.

References: **1**. Pieters C.M. et al. (1980) *JGR*, 85, 3913-3938. **2**. McCord T.B. et al. (1981) *JGR*, 86, 10883. **3**. Pieters (1982) *Science*, 215, 59-61. **4**. Lucey P.G. et al. (1986) *PLPSC16th*, D344-D354. **5**. Hapke B. (1981) *JGR* *86*, 3039-3054. **6**. Mustard J.F. and Pieters (1986) *LPSC17th*, *JGR 92*, E617-E626. --- (1989) *JGR 94*, 13619-13634. **7**. Sunshine J. et al. (1990) *JGR*, in press. **8** Sunshine and Pieters (1990) LPS XXI, these volumes. **9**. Eberhardt et al. (1973) *Moon 8*, 104-114. **10**. McCord et al. (1972) *Moon 5*, 52-89. **11**. Pieters et al. (1985) *JGR*, 90, 813-816. **12**. Pieters (1986) *Rev. Geophys Phys. 24*, 557-578. **13** Crown D.A. and Pieters C.M. (1987) *Icarus 72*, 492-506.

SPECTRAL EMISSIVITY OF FINE-GRAINED SURFACES

S.B. Petroy and R.E. Arvidson; McDonnell Center for the Space Sciences, Earth and Planetary Sciences Department, Washington University, St. Louis, MO, 63130

The high spectral and spatial resolution thermal infrared (TIR) data to be acquired from the up-coming MO-TES mission will help to further constrain the composition and texture of martian sediments, thus allowing for more detailed mapping of the surface. To prepare for these data, portions of two remote sensing field experiments (MFE - 1988, GRSFE - 1989) [1, 2] were conducted to test procedures used to extract surface property information from TIR data. Results from the continuing analyses of Thermal Infrared Multispectral Scanner (TIMS) data and field emission spectra with respect to the physical characteristics (composition, emissivity, etc.) of two playas in southern California and central Nevada are presented below.

TIR data are used not only for lithological discrimination, but also to determine the physical properties of target materials. The major silicate absorption feature in emission spectra (centered at 9.0 μm) results from the fundamental stretching of the Si-O bonds; the location and depth of this feature is diagnostic of the silicate content of the sample. Generally, the minima shifts from left to right as the total silicate content within the sample decreases, thus allowing for general lithologic discrimination between materials [3]. In loose sediments that are compositionally homogeneous, the depth of the minima is diagnostic of particle size and degree of packing [3].

Silver Lake, in southern CA, is bounded on the west by the Soda Mountains (Precambrian and Mesozoic granites and carbonates) and on the east by alluvial fans originating in the Silurian Hills. The western shore of the playa consists of beach ridges and wave cut cliffs, while the eastern shore is marked by a well-sorted quartz sand berm. The surface of the playa is dry, hard packed, and mud-cracked. The soil of the playa is unusually dark as compared to that of most playas in the southern Mojave [4]. Two sites were selected for study; site 1 (south) consists of fine-grained clays and deep mud-cracks and site 2 (north) of slightly coarser sediments and shallower mud-cracks. Compositional analyses of samples collected at both sites were almost identical - predominantly smectites, Ca-muscovite, kaolinite, and quartz; minor amounts of calcite were also detected

Lunar Lake, in central NV, is bounded to the west and north by the Lunar Crater Quaternary basaltic flows and tephra cones and to the southeast by uplifted Tertiary rhyolitic tuffs. Much of the shoreline is marked by a well-sorted, quartz rich sand berm. The surface of this playa is also dry, hard packed, and mud-cracked. However, this playa is very bright in contrast to Silver Lake. Several areas at the southern end of the playa are covered with locally derived basaltic cobbles (2 to 10 cm). Three sites were selected for study at Lunar Lake (all in the southern end) - an undisturbed playa site, a similar site which had been artificially modified (the surface crust broken up and loosened), and a basaltic cobble covered site. Samples were collected from the playa sites and are presently being analyzed for composition.

Field emission data were collected (Feb and July of 1989) at both playas with the JPL Portable Field Emission Spectrometer- the PFES [5] and are shown in Figure 1. The emission

curve for site 1 at Silver Lake exhibits a broad, shallow absorption feature centered at 9.0 μm, characteristic of fine-grained, silicate material. The absorption feature for site 2 is deeper and shifted to slightly longer wavelengths (around 9.5 μm). The difference between the two sites is not compositional, but rather due to the slightly coarser nature of the sediment at site 2. At Lunar Lake, the cobble site emission curve is similar to that of the Cima, CA, mantled flows [6] and is characteristic of a two-component surface (silicate clays and basaltic cobbles). The absorption minima is broad and centered around 9.5 μm; in addition, the emissivity for this site is high at the smaller wavelengths, characteristic of a mafic component. The two undisturbed playa sites exhibit essentially identical emission curves but show a marked contrast from the Silver Lake data. The sediments at Lunar Lake are characterized by a narrow, sharply defined absorption minima at 9.5 μm and high emission at smaller wavelengths (consistent with a more mafic origin of the clays).

These field observations can be empirically related to color composites using the TIMS bands 1, 3, and 5. The green areas within both images correspond to the lowest points on the playas; they consist of the finest clays and the deepest mud-cracks. The red rims around both playas correspond to the well-sorted, quartz rich sand berms observed in the field. The general color trend across both lakes is bluish-purple; slight variations in the amount of red (Silver Lake is "redder") are consistent with compositional differences between the two lakes (more silicates at Silver Lake, more mafics at Lunar Lake).

Within the lakes, however, color variations probably represent textural differences (particle size, packing, mud-cracks, etc.). Stick spectra were extracted from the six-band TIMS image for Lunar Lake at all three test sites (Fig. 2). Spectra for the disturbed playa site are much higher than for the undisturbed site. This observation is consistent with Conel's (1969) work [3] which demonstrated that fine-grained, loose material exhibits a higher emissivity than the same material which is packed down. However, the stick spectra for the disturbed site displays the same general shape as the spectra for the cobble site; thus, it appears that, for low spectral resolution data, compositional and textural effects can mimic each other.

Based on qualitative interpretations of the TIMS data and the field emission spectra, subtle compositional and textural differences across two playas can be recognized. However, care must be taken when using such low spectral resolution data in an attempt to quantitatively separate these two effects.

References

[1] Wall, S., et al. (1988) *Bull. Am. Astr. Soc.*, 20, p. 809. [2] Arvidson, R.E. and D.L. Evans (1989) *GSA Abst. with Prog.*, p. A121. [3] Conel, J.E. (1969) *Jour. Geophys. Res.*, vol. 74, p. 1614-1634. [4] Thompson, D.G. (1929) *U.S. Geol. Survey WS Paper 578* , p. 559-568. [5] Hoover, G. and A.B. Kahle (1987) *Phot. Eng. and Remote Sens.*, vol. 53, p. 627-632. [6] Petroy, S.B. and R.E. Arvidson (1990) *LPSC Abst. with Prog.- XXI*, p. 952-953.

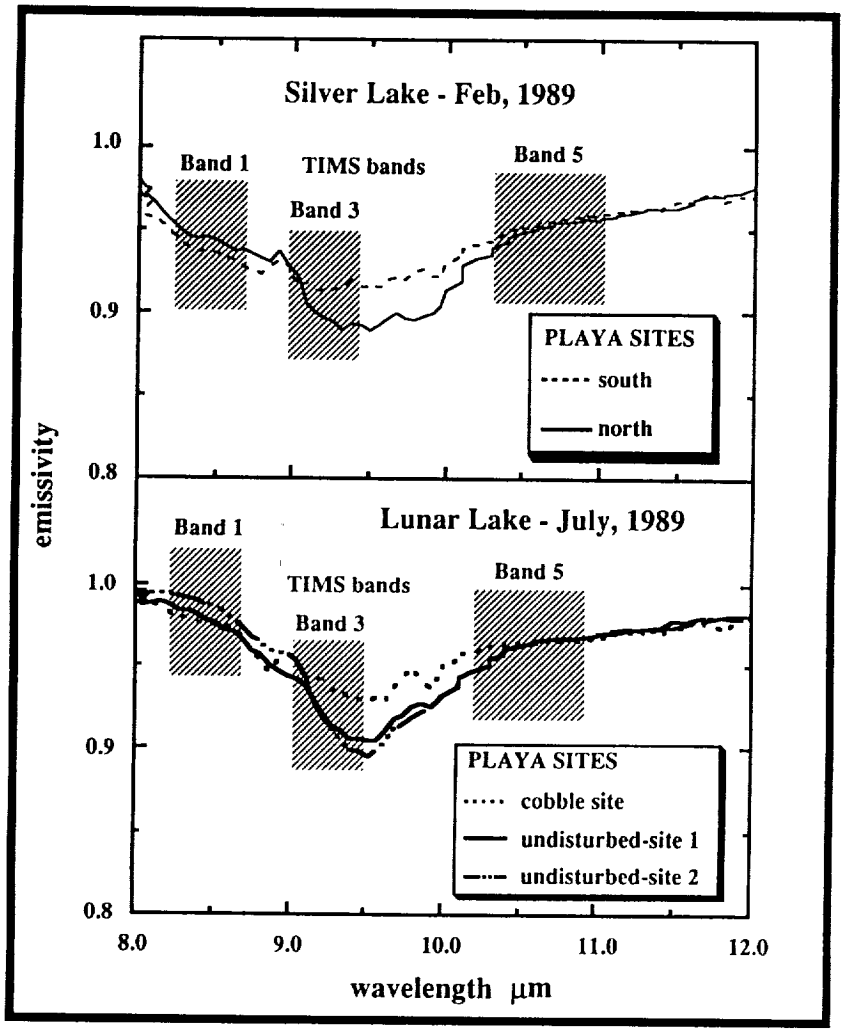

Figure 1: Infrered emission spectra for sites on Silver and Lunar Lake collected with the JPL Portable Field Emission Spectrometer (PFES).

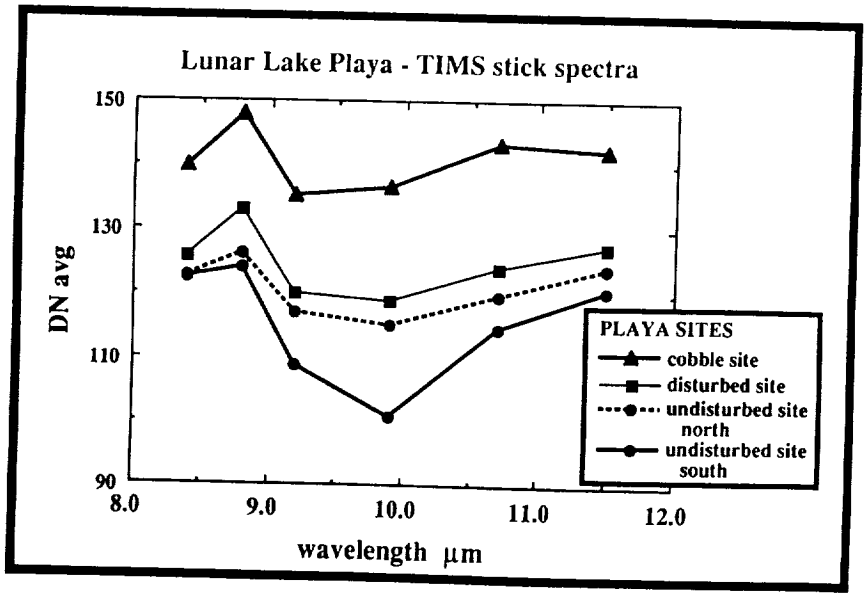

Figure 2: DN extracted from the Lunar Lake TIMS six band data (data are uncalibrated) for each of the three modelling sites. In addition, DN values were extracted from random sites in the northern end of the lake (the green area in the TIMS image of Lunar Lake).

GEOLOGIC REMOTE SENSING FIELD EXPERIMENT

R. E. Arvidson, McDonnell Center for the Space Sciences, Department of Earth and Planetary Sciences, Washington University, St. Louis, Missouri 63130; D. L. Evans, Jet Propulsion Laboratory, 4800 Oak Grove Dr., Pasadena, CA 91108

The Geology Remote Sensing Field Experiment (GRSFE) was designed to acquire remote sensing data from advanced instrumentation over sites of planetary relevance (i.e., basalts, aeolian features, surfaces weathered under arid conditions) in the southwestern United States. The GRSFE archive is meant to be used by the planetary community to test quantitative models for extraction of surface property information (e.g., refractive index, permittivity, grain size and packing, thermal conductivity, microscopic roughness over variety of length scales). The Airborne Visible and Reflected Infrared Imaging Spectrometer (AVIRIS), Thermal Infrared Multispectral Scanner (TIMS), the C.L.P band multiple incidence angle polarimetric SAR, the Advanced Solid-State Array Spectroradiometer (ASAS), airborne laser altimetry (ATLAS), helicopter-borne stereophotography, and associated ground, and associated ground measurements of the atmosphere and surface were conducted. Sites included the Providence Mountain fans, Cima Volcanic Field, Kelso Dunes, Death Valley fans, Death Valley dunes, and the Ubehebe volcanic maar complex in California, and the Lunar Crater Volcanic Field and Railroad Valley fans in Nevada. The derived data will also be used to explore the paleoclimatic and paleotectonic histories of these area. The effort was guided by a Science Steering Group with representatives from Arizona State Univ., Univ. of Colorado, Jet Propulsion Laboratory, Univ. of Arizona, Univ. of Washington, Washington Univ., Stanford Univ., and Goddard Space Flight Center. Data and documentation will be published jointly during the first quarter of FY91 by the NASA Planetary Data System and Pilot Land Data System on a set of 8 CDROMs for general use. For reference, Table A lists the characteristics of the prime target (Lunar Crater Volcanic Field). Table B lists the characteristics of the instruments flown during GRSFE and Table C summarizes the data sets acquired.

TABLE A
GEOLOGIC REMOTE SENSING FIELD EXPERIMENT
Lunar Crater Volcanic Field, Nevada

- 250 km northwest of Las Vegas, NV
- Middle to late Pliocene and Pleistocene (0.015 to 4.2 m.y.) in age
- About 95 vents and at least 35 associated lava flows within a northeast-trending zone, up to 10 km wide and about 40 km long
- Vents include cinder cones, elongate fissures, and at least two maars
- Lava flows range up to 1.9 km wide and 6.1 km long with thicknesses less than 3 m to as much as 25 m
- Cobble-strewn playa located in center of field used as modeling / calibration site
- Progressive degradation of the cones and flows similar to that displayed by other basaltic volcanic fields in the southwest Basin and Range (including the Cima, Crater Flat, and Coso fields)
- Many of the flows in the northeast and central parts of the field are veneered with varying thicknesses of air-fall tephra
- In other areas, all but the youngest flows are mantled with extensive deposits of aeolian silt and fine sand
- Tertiary rhyolite exposures nearby

TABLE B
GEOLOGIC REMOTE SENSING FIELD EXPERIMENT
Aircraft Sensor Characteristics

	Airborne Visible and Infrared Imaging Spectrometer (AVIRIS)	Advanced Solid-State Array Spectroradiometer (ASAS)	Airborne Terrain Laser Altimeter System (ATLAS)
Wavelengths	0.41-2.45 micrometers	0.47-0.87 micrometers	1.06 micrometers
Number of Channels	224	29	1
Swath Width (km)	10	2	N/A
Pixel Size (m)	20	4	1-20 m
Nominal Altitude (km)	20	5	1-10 km
Platform	ER-2	C-130	T-39 Sabre Liner
	Thermal Infrared Multispectral Scanner (TIMS)	Aircraft Polarimetric SAR	
Wavelengths	8.2-11.7 micrometers	5.7, 24, 68 cm	
Number of Channels	6	3	
Swath Width (km)	12	10	
Pixel size (m)	20	10	
Nominal Altitude (km)	8	10	
Platform	C-130	DC-8	

TABLE C
GEOLOGIC REMOTE SENSING FIELD EXPERIMENT
Data Archive

Instrument	Date Volume
AVIRIS (21 scenes @ 141 MB/scene)	3 GB
ASAS (12 scenes @ 83 MB/scene)	1 GB
TIMS (1,685 km)	670 MB
SAR (19 scenes @ 30 MB/scene	570 MB
ATLAS (8 profiles)	96 MB
Helicopter, field, lab data, documentation	200 MB
Total	5.5 GB

USE OF AIRCRAFT MULTISPECTRAL AND MULTIPLE EMISSION ANGLE DATA TO DETERMINE SURFACE ROUGHNESS AND COMPOSITION AT THE LUNAR LAKE PLAYA IN NEVADA

Edward A. Guinness, Raymond E. Arvidson, McDonnell Center for the Space Sciences, Department of Earth and Planetary Sciences, Washington University, St. Louis, Missouri, 63130; and James R. Irons, Biospheric Sciences Branch, David J. Harding, Geophysics Branch, both at Goddard Space Flight Center, Greenbelt, Maryland, 20771.

The Geologic Remote Sensing Field Experiment (GRSFE) was conducted in July and September 1989 to collect data with advanced aircraft instrumentation [1]. One of the main objectives of GRSFE was to acquire both aircraft and ground data needed to test models for determining quantitative surface property information from remotely acquired data, including data to be acquired during the Magellan and Mars Observer missions and existing Viking data. The intent of this abstract is to report preliminary results from analyses of Advanced Solid-State Array Spectroradiometer (ASAS) [2] data to determine surface roughness and composition. The ASAS instrument is designed to collect multispectral and multiple emission angle images of a given ground target with ground resolutions of about 4 meters. The instrument has 29 spectral bands that cover the wavelengths of 0.465 to 0.87 micrometers. ASAS can also be rotated during data collection to view a scene at seven different geometries ranging ± 45° from nadir in 15° increments.

ASAS data were acquired over the Lunar Crater Volcanic Field in Nevada [3]. This is one of the primary GRSFE locations and is about 250 km northwest of Las Vegas. The area has numerous cinder cones, fissures, lava flows, and several maars. In addition to volcanic features, the location contains the Lunar Lake playa, where three detailed modeling surfaces were established for GRSFE. One modeling surface, which is referred to as the cobble surface, consists of basalt fragments with sizes ranging from about a centimeter to several tens of centimeters sitting on a bright silty playa surface. The site also contains several meter size bushes. A second surface, called the smooth playa, consists of a clay-rich playa surface with mud cracks and some centimeter size basalt pebbles. The third surface, called the rough playa, was disturbed and roughened by driving an automobile across the playa surface using a "brody" technique. The rough playa site displayed a range of surface textures such as loose silt and clay powder, clods of playa sediment that were several centimeters in size, and undisturbed playa surface.

ASAS data over the Lunar Crater Volcanic Field were acquired at three different times on July 17, 1989. Flight lines were oriented parallel and perpendicular to the principal plane of the Sun in order to provide a large variety of phase angles. Thus far, one morning scene with the flight line along the principal plane has been analyzed. The incidence angle of the Sun is about 65°. The range in phase angles is 20° to 110°. At these phase angles the contribution due to an opposition effect should be minimal, whereas the contribution due to surface roughness should be significant [4]. In addition to the aircraft data over Lunar Lake, the spectral reflectance of the sites was measured with a Daedalus AA440 field spectrometer, and the optical depth of the atmosphere was measured with a sun photometer at the same time as the ASAS overflight.

Reflectance data for the three modeling surfaces were extracted from ASAS images at the seven different viewing angles. Data from the band centered at 0.693 μm

were used. The LOWTRAN 7 computer code [5] was used to estimate the atmospheric contribution to the ASAS data. Atmospheric parameters were chosen so that the LOWTRAN model results matched the optical depth values measured at Lunar Lake. These parameters were then used to predict the radiance reaching the ASAS sensor (at an altitude of 5 km) from direct and diffuse reflectance off the ground and from single and multiple scattering in the atmosphere. Models were computed for dark and bright surfaces assuming Lambertian scattering at each of the seven emission angles observed by ASAS. The atmospheric modeling indicates that: A) most of the radiance reaching ASAS is from reflection of the direct solar irradiance from the ground; and B) there is no significant variation in radiance as a function of emission angle due to atmospheric scattering. Therefore, no correction was made to the ASAS data for atmospheric scattering in this preliminary analysis.

The ASAS reflectance data were then modeled with the Hapke photometric function [4, 6, 7] to determine differences in the composition and macroscopic roughness of the surfaces. The three surfaces can be distinguished by their composition and scattering characteristics. In addition, there is a correlation between the scale of roughness elements and the magnitude of the Hapke roughness parameter. The smooth and rough playa sites, which have similar compositions, were fit with nearly the same value of single scattering albedo. However, there were significant differences in the roughness parameter and particle phase function of the two playa surfaces. The smooth playa data were modeled with a macroscopic roughness angle of less than 1°, which is consistent with the smooth nature of the surface that exhibits only shallow mud cracks and a few centimeter size rock fragments. In addition, the smooth playa surface had a moderately forward scattering phase function due to an increase in reflectance at large phase angles. The rough playa data were best modeled with a roughness angle of about 15° and a moderately back scattering phase function. Roughness elements on the rough playa surface consist of fine powder and centimeter scale sediment clods. The cobble surface data were modeled with a single scattering albedo much less than the playa sites, with a nearly isotropic phase function, and with a roughness angle of about 40°. The cobble surface had the largest roughness elements, consisting of rock fragments up to several tens of centimeters in size and several meter size bushes.

The results presented above are preliminary. Future work will include: A) analysis of ASAS scenes at several incidence angles, including small incidence and phase angles; B) modification the LOWTRAN code to include the Hapke function so that the atmospheric and surface scattering can be solved for at the same time; and C) consideration of subpixel mixing models. The intent will be to separate textural information from compositional information for the various surfaces.

REFERENCES

[1] Arvidson, R. E., and D. Evans (1989) *GSA Abstracts with Programs, v. 21*, n. 6, A121.
[2] Irons, J., and R. Irish (1988) *SPIE, v. 924*, 109-119.
[3] Dohrenwend, J. C., et al. (1987) *GSA Bulletin, v. 99*, 405-413.
[4] Hapke, B. (1984) *Icarus, v. 59*, 41-59.
[5] Kneizys, F. X., et al. (1988) *Air Force Geophysics Laboratory Technical Report 88-0177.*
[6] Hapke, B. (1986) *Icarus, v. 67*, 264-280.
[7] Hapke, B. (1981) *J. Geophys. Res., v. 86*, 3039-3054.

CHAPTER 7

RADAR APPLICATIONS

ANALYSES OF AIRCRAFT RADAR DATA OF FLOW TEXTURES AND AEOLIAN DEPOSITS AT PISGAH, CA

Lisa R. Gaddis and Ronald Greeley, Department of Geology,
Arizona State University, Tempe, AZ 85287

Analyses of radar data acquired by the NASA/JPL polarimetric Airborne Synthetic Aperture Radar (AIRSAR) for the Pisgah lava field permit mapping of lava flows and aeolian mantling deposits based on the radar response to variations in surface roughness. As part of the Mojave Field Experiment (Wall et al., 1988), the AIRSAR measured scattering matrices at 3 wavelengths (P:68 cm, L:24 cm, C:6 cm) and at multiple angles of incidence (about 20° to 50° across an image). From the scattering matrices, images with a variety of polarizations may be synthesized (Zebker et al., 1987; van Zyl et al., 1987). For this analysis, images with a resolution of about 10 m at direct (HH, VV) and crossed (HV=VH) polarizations were examined. The goal is to determine the best configuration of imaging radar parameters for: (a) mapping lava flows with a variety of surface textures; (b) assessing the effects of aeolian mantling deposits on lava flow discrimination; and (c) mapping and (d) estimating the thickness of aeolian mantling deposits. The results of this study have implications for geologic mapping of terrains influenced by volcanic and aeolian processes using data such as those to be acquired for Earth during the SIR-C and EOS experiments and for Venus during the Magellan mission.

The distribution of Quaternary basaltic lava flows and Recent aeolian mantling deposits at Pisgah is shown on Figure 1. Lava was erupted in three phases: Phase I produced thin (~1 m), flat-surfaced, "platform" pahoehoe; Phase II produced aa flows up to ~5 m thick and local patches of smooth pahoehoe; Phase III lavas mostly formed pahoehoe, with tumuli and pressure ridges up to 5 m high and smoother "platforms" (Wise, 1966). Parts of all flows are mantled by aeolian sediments deposited by the prevailing westerly winds. Although their thicknesses have not been mapped in detail, mantling units range from <1 cm to >1 m in thickness.

Comparison of radar responses to volcanic and aeolian units at 3 wavelengths and at HH and HV polarizations shows that unit discrimination is related to surface texture. The P- and L-band data show a greater sensitivity to larger-scale (>20 cm) roughness in the flow (tumuli, pressure ridges), whereas C-band data show a bright response due to more uniform small-scale (≤10 cm) roughness. The direct-polarized backscatter is due largely to single-reflection response to surface or volume scatterers of a size comparable to that of the radar wavelength, and the cross-polarized radar backscatter results from multiple surface or volume scattering at a range of roughnesses (Fung and Ulaby, 1983).

A greater variation in image brightness is observed among all units on the HV images (Figure 2). Lava flows are generally bright at HH and HV polarizations and at all 3 wavelengths. Most of the smoother alluvial fan and playa surfaces are dark on P- and L-band HH and HV images. Only the playa surface is dark at C-band wavelength at HH and HV polarizations. On HH images, moderate variations in image brightness on the P-, and L-band data are observed but the flow surface is almost uniformly bright on the C-band image, indicating that most units are rough at 6-cm wavelength (C-band). The only generally unmantled lava flow surfaces that have moderately low returns at P- and L-band and lower-than-average returns at C-band are those of the platform pahoehoe flows of Phases I and II (near Lavic Lake playa), and III (near the flow center). These smooth surfaces may act as specular reflectors at the longer P- and L-band wavelengths, and as relatively smooth diffusely scattering surfaces at the C-band wavelength. Although in the P-band HV and HH images the brightest radar units (e.g., the aa of Phase II; tumuli of central Phase III) do correspond to the rougher parts of Phase II and III flows, it is difficult to distinguish these flow types based on their P-band radar brightness. The larger scale of roughness and texture that the P-band radar is responsive to may be comparable on these different lava flows. A similar effect is observed in the L-band HH image in which the rougher flow parts are almost uniformly bright and thus are difficult to separate. However, on the L-band HV image, we see the clearest separation of different flow surface textures [e.g., the boundary between the very rough (bright) aa of Phase

II and the moderately bright pahoehoe tumuli of Phase III lavas are separable in the flow center]. The increased discrimination of lava flow units on the HV L-band image is attributed to the variation in size and spacing of multiple scatterers such as tumuli, pressure ridges, and aa clinker on the surfaces of these different flow units.

Many of the aeolian mantling deposits on the western margin of Pisgah are seen as darkened areas at all 3 wavelengths and at HH and HV polarizations (Figures 1, 2). Detailed examination of color overlays of these data shows that penetration of the aeolian mantles may be occurring. For example, areas along the southern flow margin and west of Pisgah Crater show high backscatter at P-band wavelengths, suggesting that this longer wavelength radar is passing through the mantling material to reflect off of the underlying lava surface. Additional areas west and southwest of Pisgah Crater show moderately high backscatter at both P- and L-band, suggesting that both the 70-cm and 25-cm radar penetrates mantling material. These observations imply that mantling material is thickest (~50 to 70 cm) along the southern margin and in places on the central portion of the flow, of moderate thickness (~20 to 50 cm) west of the cone, and thinnest (~<20 cm) elsewhere along the margin of the flow.

Increased discrimination among lava flows is observed in the cross-polarized radar images due to their greater sensitivity to surface structure than to average roughness. At P-band wavelength, observed flow textures do not correspond well with mapped flow boundaries. At the L-band wavelength, the greatest discrimination among mapped flow textures is observed. At C-band wavelengths the lava flow surface is ~uniformly bright, inhibiting flow discrimination. L-band cross-polarized data is best for discriminating lava flow textures at Pisgah. Aeolian mantling deposits are observable as darker areas at all three wavelengths used here. Detailed observations of radar backscatter along the flow margins permit use of the penetration capability of radar to estimate the thickness of the mantling deposits.

References Cited

Fung, A. K. and F. T. Ulaby, 1983, Matter-Energy Interaction in the Microwave Region, v. 1, *Manual of Remote Sensing*, American Society of Photogrammetry, p. 115.

van Zyl, J. J., H. A. Zebker, and C. Elachi, 1987, Imaging radar polarization signatures, *Radio Science*, vol. 22, pp. 529-543.

Wall, S., J. J. van Zyl, R.E. Arvidson, E. Theilig, and R.S. Saunders, 1988, The Mojave Field Experiment: Precursor to the planetary test site (abstract), *Bulletin of the American Astronomical Society*, v. 20, pp. 809.

Wise,W.S., 1966, Geologic Map of the Pisgah and Sunshine Cone Lava Fields, *NASA Technical Letter 11*, 8 pp.

Zebker, H.A., Jakob J. vanZyl, and Daniel N. Held, 1987, Imaging Radar Polarimetry from Wave Synthesis, *Journal of Geophysical Research*, v. 92, pp. 683-701.

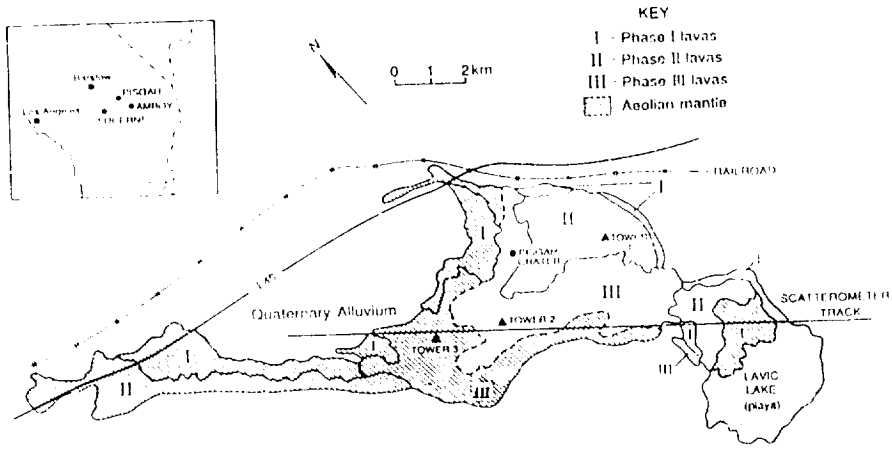

Figure 1: Schematic map showing the distribution of Quaternary basaltic lava flows and Recent aeolian mantling deposits at Pisgah lava field, CA (after Wise, 1966).

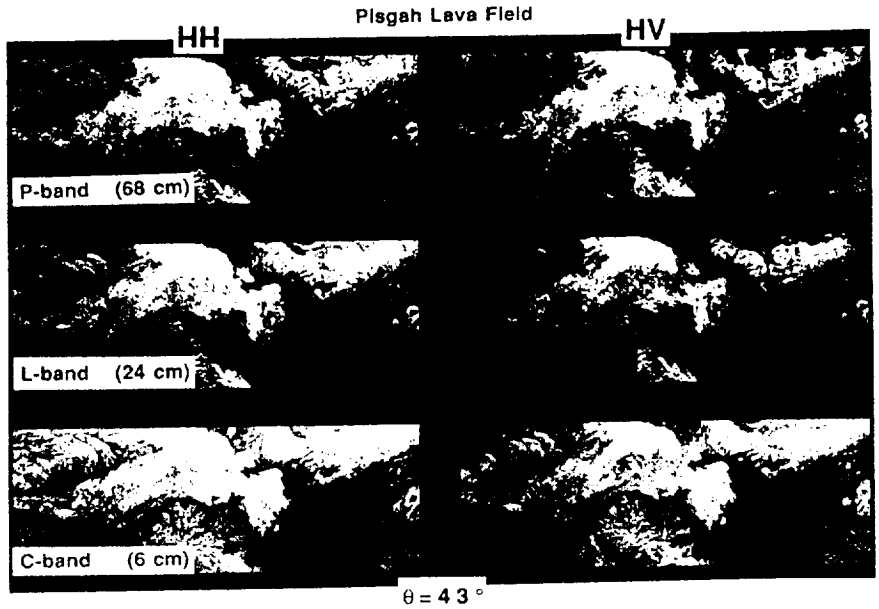

Figure 2: Aircraft radar (AIRSAR) images of Pisgah lava field, acquired at 68-cm, 24-cm, and 6-cm wavelengths (P, L, and C bands), a center incidence angle of 43°, and shown at direct (HH, left) and crossed (HV, right) polarizations.

SLOPE PROPERTIES OF SOME TERRESTRIAL SURFACES AND IMPLICATIONS FOR PLANETARY RADAR INTERPRETATION; T.M. McCollom and B.M. Jakosky, Laboratory for Atmospheric and Space Physics and Department of Geological Sciences, University of Colorado, Boulder, CO 80309-0392

The radar scattering properties of planetary surfaces have been used by many investigators to infer the roughness of the surfaces on the scale of a meter to several tens of meters. The roughness of the surfaces are estimated by comparison of radar spectra with a model of radar scattering developed by Hagfors, and are generally reported as an rms slope. In an effort to test assumptions made by the Hagfors' model and to gain a better understanding of surface roughness estimates, we determined the surface slope distributions of a number of terrestrial surfaces by field measurement.

Slope distributions for the terrestrial surfaces differed considerably from the distributions assumed in the development of the Hagfors' model. In particular, the terrestrial surfaces had fewer flatter slopes and a greater proportion of steep slopes than assumed by the model.

Rms slope values for the measured terrestrial surfaces ranged from 0° for an evaporative basin to 16.5° for sand dunes and a lava flow. By comparison, rms slope values estimated for planetary surfaces have ranged from less than a degree to about 10°, with the majority of planetary surfaces in the lower end of this range (<5°). Only the flattest two measured terrestrial surfaces had rms slope values less than 5°, while half of the measured surfaces had rms slopes >10°.

We also used the Hagfors' model of radar scattering to predict the return that would be expected from planetary surfaces where different surface types were present in the field of view. The expected returns for surfaces with varying fractions of two surface types were modelled by scaling the expected return from each surface separately and adding the results together to estimate the combined return. The shapes of the resulting spectra differed from those predicted by the Hagfors' model for homogeneous surfaces, with the combined spectra having a broader central peak than expected for a homogeneous surface. Since the shape of the spectra is important in determining the rms slope, rms slope values estimated for the combined spectra are lower than the values determined by combining slope distributions and calculating the rms slope directly. These results suggest that the radar-determined rms slope of a rugged area could be substantially underestimated by the presence of a few patches of flat surface in the view area.

Together, these results suggest that current methods of determining surface roughness from radar significantly underestimate the roughness of planetary surfaces. Furthermore, the results indicate that it is not merely a matter of "scaling up" the presently reported rms slopes to get a more satisfactory range of values. Rather, we are unable to ascribe a specific geologic meaning to radar-determined rms slope values, and suggest that rms slope values are most useful in distinguishing geologic units.

RADAR BACKSCATTERING BEHAVIOR IN THE EQUATORIAL REGION OF VENUS - RESULTS FROM CALIBRATED GOLDSTONE OBSERVATIONS

J.J. Plaut, McDonnell Center for the Space Sciences, Department of Earth and Planetary Sciences, Washington University, St. Louis, MO 63130.
R.F. Jurgens, Jet Propulsion Laboratory, 4800 Oak Grove Drive, Pasadena, CA 91109.

A critical aspect of geological interpretation of radar data from Venus is understanding the radar backscattering behavior of the surface. In addition to the large-scale geomorphologic information typically extracted from radar imaging, constraints on physical properties of surface materials can be obtained from calibrated values of radar backscattering cross-section. Since 1972, the Goldstone Solar System Radar has been used to obtain over 50 radar images of Venus during inferior conjunctions. Early observations empolyed a single baseline, two-station interferometer system (1,2), while more recent images were acquired with a three-station interferometry technique (3,4). A geological analysis of the ensemble of data has recently been completed (5). The Goldstone Venus observations are unique among radar datasets for Venus in that they consist of medium-to-high resolution image data (with accompanying altimetry) obtained at small incidence angles, typically less than 10 degrees. In this viewing geometry, the cross-circular polarization backscattered power which the Goldstone system measures is sensitive primarily to the quasi-specular component of the scattering process. The physical controls on backscattered power in this regime are basically limited to (a) regional slopes which affect local incidence angles, (b) slopes with radii of curvature greater than the wavelength (12 cm), and (c) the dielectric permittivity of the surface materials. By contrast, other imaging systems (Arecibo, Magellan) employ much larger incidence angles and have an additional (and in some cases, complicating) sensitvity to wavelength-scale roughness elements. In this study, we have analyzed several sets of Goldstone Venus image data to extract calibrated values of radar backscattering cross-section for a number of geological units found in the equatorial region. Performing this exercise on homogeneous areas that extend over a range of incidence angles, we have filled in portions of the backscatter versus incidence angle curve, to obtain a more complete analysis of the physical basis of the backscattering behavior. This work extends calibrations beyond those reported in (6).

In order to obtain accurate values of radar cross-section (i.e. solve the radar equation), several system and observing parameters must be known. These are:

1. Transmitted power.
2. Antenna gain and receiver collecting area.
3. Distance to the planet.
4. Received power, taking into account noise. This is done by estimating:
   a. Reciever system noise temperature and effective bandwidth.
   b. Signal-to-noise, which is measured during acquisition of each range-power profile.

Once these quantities are known, it is a straightfoward procedure to obtain the normalized cross-section (sigma zero) for the entire spherical cap of the planet being imaged, from nadir out to some angular distance. To extract the value of sigma zero for a particular resolution cell in the area of interest, the power recieved at that delay-Doppler coordinate is calculated in terms of the average cross-section, and then normalized to its corresponding surface area.

Data covering portions of Guinevere and Navkha Planitiae, obtained in 1980 and 1982, were used in this analysis. The observed scattering law for each day's observation was fit to a Hagfors' scattering function to estimate Fresnel reflectivity and rms slopes at scales greater than the wavelength (12.9 cm). Average reflectivity values for these days range from 0.079 to 0.105, fully consistent with values estimated from the Pioneer Venus altimetry experiment (7). Hagfors' C parameter values range from 400 to 100, corresponding to a range of rms slope of 2.9 to 5.7 degrees. Preliminary analysis of the backscattering behavior of individual features and units distinguished in the image data shows that the equatorial plains have significant inhomogeneities in Fresnel reflectivity at length scales of several hundreds of kilometers and smaller. For example, a 600 km ridge structure seen in data of February 4, 1982 has a reflectivity near 0.05, while the surrounding plains value is near 0.10. Similarly, a ring of hilly topography seen in the north on July 2, 1980, shows an unusually high reflectivity near 0.20, compared to the surrounding plains value of 0.08. Fitting the Hagfors' function to these and other features indicates that image brightness variations in the Goldstone data are controlled primarily by differences in Fresnel reflectivity, and not by variations in rms slope. This suggests that surfaces in this region have a similar intermediate-scale structure, yet vary widely in either composition or soil/rock ratio.

REFERENCES:

(1) Rumsey, H.C. et al. (1974). Icarus 23, 1-7.
(2) Goldstein, R.M. et al. (1976). J. Geophys. Res. 81, 4807-4817.
(3) Jurgens, R.F. et al. (1980). J. Geophys. Res. 85, 8282-8294.
(4) Jurgens, R.F. et al. (1988). Geophys. Res. Lett. 15, 577-580.
(5) Arvidson, R.E. et al. (1990). Proc. Lunar Planet. Sci. Conf. 20th, 557-572.
(6) Jurgens, R.F. et al. (1988). Science 240, 1021-1023.
(7) Pettengill, G.H. et al. (1988). J. Geophys. Res. 92, 14,881-14,892.

HIGH RESOLUTION RADAR STUDIES OF IMPACT AND VOLCANIC PHENOMENA ON VENUS AND THE MOON

Bruce A. Campbell and Peter J. Mouginis-Mark, Planetary Geosciences Division, School of Ocean and Earth Sciences and Technology, University of Hawaii, Honolulu, HI 96822.

INTRODUCTION

Earth-based radar observations provide the opportunity to study geographic areas of Venus and the Moon that have not been investigated at high spatial resolution either by the Venera 15/16 spacecraft for Venus or the Lunar Orbiter and Apollo missions in the case of the Moon. As part of an on-going program that is studying the high resolution characteristics of impact and volcanic landforms on the terrestrial planets, we have been using recently obtained radar images, collected by Don Campbell at Arecibo Observatory and Stan Zisk at Haystack Observatory, to study the surface roughness and dielectric properties of geologic units on Venus and the Moon. In the case of Venus, we utilize dual-polarization images, collected during the summer of 1988, to describe the geometry and extent of volcanic deposits in western Eisila Regio. For the Moon, our investigation has concentrated on high-resolution studies of crater ray materials.

DATA SETS

A) A large amount of imaging radar data was collected at Arecibo Observatory during the 1988 conjunction with Venus. The data that we are working with were collected at a wavelength of 12.6 cm, and have a spatial resolution of 1.5 - 2.0 km. A total of 25 individual radar "looks" were collected. A circularly-polarized wave was transmitted, and both senses of circular polarization were received (1). We have used these Arecibo images to study Eisila Regio, which is a broad uplift region to the west of Aphrodite Terra. This area includes two large volcanic edifices, Sif and Gula Montes, which each have basal diameters of ~500 km.

B) The lunar data were collected at a wavelength of 3-cm, and both senses of circular polarization were recorded (2). These data have a spatial resolution of 30 m. To date, with the assistance of Stan Zisk (also at University of Hawaii), we have processed five images, each of which cover about 30 km in range direction and 120 km in azimuth:

1) A region immediately southeast of Bessel.
2) A swath across Menelaus Crater.
3) The crossing of Copernicus and Tycho rays in Mare Vaporum.
4) A Tycho ray near Rosse Crater.
5) An area north of Copernicus Crater.

For both data sets, measurements of the complex radar echo allows a Stokes vector to be calculated for each pixel (either from several looks or from spatial averaging of pixels). The elements of the Stokes vector can be used to isolate the randomly polarized (diffuse) component of the radar echo from the non-diffuse return. Previous studies (2) showed that areas with apparently high double-bounce geometry could be discriminated with this technique.

PRELIMINARY RESULTS

Volcanic Deposits on Venus: The polarization behavior of volcanic deposits in western Eisila Regio can be grouped into three broad categories. The first comprises the highly depolarizing, low polarization ratio (depolarized power divided by polarized power) echoes that are believed to be associated with radar-facing ridge walls or cliffs, and the southern rim of the central circular feature on Sif Mons. The exterior rim deposits and interior peak complexes of large impact craters also demonstrate this type of radar return, but over their entire circumference. Radar-facing topography is thus not adequate to explain the behavior of the crater rim deposits.

The second type of radar return comprises moderately-to-highly depolarizing, moderate-to-low polarization ratio echoes seen for the most of the radial flows from Sif and

Gula Montes. There are spatial variations in radar brightness and ratio within individual flows, consistent with possible changes in surface morphology. The third major type of radar return is the low-brightness, high polarization ratio echo seen for the dark deposits on the flanks and summit of Sif Mons. The central features of these deposits are typically moderately depolarizing, with a low polarization ratio.

There are also a number of features that do not conform to these three simple groupings. In particular, there are small (10 - 50 km) areas on Sif Mons with high depolarized brightness and polarization ratios similar to the darker flows around them. The highly-depolarizing, low polarization ratio summit area of Gula Mons is surrounded by an irregular region of highly depolarizing, high polarization ratio terrain. Finally, the 100-km long feature to the north of Gula Mons has a very high polarized return, but minimal depolarized echo. This attribute sets it apart from the apparent lava flows which trend north from Gula Mons.

Lunar Crater Rays: The area in Mare Serenitatis southeast of the crater Bessel shows a strong depolarized radar enhancement associated with the continuous ejecta of Bessel Crater, as well as a bright trace of the ray which passes to the west of Bessel. The rays have a high polarization ratio (0.75 - 1.0), indicating a large degree of cm-scale surface roughness. This was also evident in the strongly enhanced depolarized echo along the ray seen in previous 3.8-cm radar maps (3).

The Copernicus image (centered at 20.0°N, 18.8°W) reveals a number of continuous radar-bright linear rays. These rays have significantly higher polarization ratios than the surrounding mare, indicating a large degree of cm-scale roughness. We are currently using these new radar data to extend our earlier studies of the Copernicus ray system (4).

The Rosse region (centered at 16.5°S, 36.0°E) represents a Tycho ray at a considerable distance from its source. Only a small portion of this ray was imaged due to the orientation of the radar swath, but a distinct radar-bright region can be seen associated with a group of Tycho secondary craters. Interestingly, we have found that the high radar polarization ratio for this feature continues away from the group of secondary craters, and the depolarized radar brightness remains quite high.

FUTURE WORK

Further investigation of the Venus radar data will focus on detailed mapping and classification of the individual geologic units. We also plan to integrate these radar studies with topographic information and geophysical data derived from the Pioneer Venus Orbiter to help improve our understanding of the style and evolution of volcanism in this region of Venus. For the lunar studies, the radar images will be used to further map the distribution of ejecta deposits associated with secondary craters and to assess the correlation (or lack thereof) between the radar images and the distribution of ray materials as identified on the best available orbital photography. We also intend to investigate the effect of the pyroclastic substrate on the radar backscatter properties of the Menelaus ray at Sulpicius Gallus.

REFERENCES:

1) Campbell, D. B. et al., (1989). Science **246**, p. 373 - 377.
2) Campbell B.A. et al. (1988). LPSC **XIX**, p. 160 - 161.
3) Campbell B. A. et al. (1989). LPSC **XX**, p. 139 - 140.
4) Pieters, C.M. et al. (1985). JGR **90**, p. 12393 - 12413.

COHERENT BACKSCATTER: AN EXPLANATION FOR THE UNUSUAL RADAR PROPERTIES OF OUTER PLANET SATELLITES

Bruce Hapke (Department of Geology and Planetary Science, University of Pittsburgh)

The radar properties of Europa, Ganymede and Callisto are characterized by high reflectivities dominated by a diffuse component, and a large amount of polarization in the opposite sense of that expected if the waves were specularly reflected once. It is pointed out that these are precisely the properties expected when a collimated source illuminates a weakly absorbing, particulate medium in which the scatterers are separated by distances somewhat larger than the wavelength, such as a regolith consisting of silicate rocks an/or voids of sizes comparable with the wavelength imbedded in an icy matrix. No specialized structures are required. Portions of the wave front that are multiply scattered within the medium and that traverse the same path in opposite directions combine coherently in the backscatter direction to produce an increased intensity. The enhancement is different for the two components of polarized reflected radiation and appears to be able to account for the observed polarization ratios. These coherent effects are confined to a peak centered on the backscatter direction of angular width $\lambda/2\pi D$, where λ is the wavelength and D is the photon diffusion length in the medium. Bistatic radar observations would confirm this model and give information on the structures of the regoliths. This same phenomenon may play a role in radar scattering from Saturn's rings and also in the sharp opposition effects observed on outer planet satellites at optical frequencies.

A RADAR-ECHO MODEL FOR MARS; H.J. Moore, U.S. Geological Survey, Menlo Park, CA, 94025 and T.W. Thompson, Calif. Inst. Tech., Jet Propulsion Laboratory, Pasadena, CA, 96011.

We have developed a radar-echo model for Mars based on 12.6-cm continuous-wave radio transmissions backscattered from the planet [1,2]. Our model (1) broadly matches the variations in polarized and depolarized total-radar cross sections with longitude observed by Goldstone in 1986 along 7° S. and (2) yields echo spectra that are generally similar to the observed spectra, with some departures.

In our model, Mars' surface is divided into radar map units that are based on generalized geologic map units [2]; the radar map units are further subdivided using thermal inertias [3]. Thermal inertias are used because the geologic units are not sufficient to account for the quasi-specular echoes and normal reflectivities and thermal inertias are positively correlated along 7° S. (Fig. 1A) and elsewhere [4,5]. For cratered uplands and plains units, model depolarized-echo strengths vary as A*cos[theta] (where [theta] is the incidence angle and A is a parameter assigned to the radar map unit on a degree by degree basis)and polarized diffuse-echo strengths vayr as 3*A*cos[theta]. For most volcanic units, depolarized and polarized diffuse-echo strengths vary as $A*\cos^2[theta]$. Quasi-specular echoes were computed using Hagfors' scattering law [6] (integrated from -30° to +30° theta). Assignments of depolarized echo strengths, normal reflectivities, and root-mean-square (rms) slopes for the radar map units were guided by previous experience [2], thermal inertias [3], and the results from analyses of the quasi-specular echo spectra and then they were adjusted by trial and error methods to best fit the data. Coarse-scale topography is not included in the model.

Radar map units in our model include: (1) an extensive cratered uplands (background) unit with weak depolarized-echo cross sections (0.01), average thermal inertias, moderate normal reflectivities (0.095), and moderate rms slopes (4.0°); (2) the volcanic units of the Tharsis, Elysium, and Amazonis regions with strong depolarized echo cross sections (0.04-0.133), low thermal inertias, low normal reflectivities (0.025-0.050), and large rms slopes (6-20°); and (3) the northern plains units with moderate to strong depolarized-echo cross sections (0.017-0.045), moderate to very high thermal inertias, moderate to large normal reflectivities (0.075-0.15), and moderate rms slopes (3-5°). Arabia, an extensive unit of upland that is mantled by dust, has a low depolarized-echo cross section (0.007), low thermal inertia, small normal reflectivity (0.05), and small rms slope (3.0°). There are additional radar map units - about 140 in all. At this time, our model does not include an equatorial region extending from the vicinity of western Pavonis Mons to S.E. Elysium Planitia that has non existent to very weak depolarized echoes or the strong ones from the poles observed at 3.6-cm wavelength [7].

Like the observations, model total-polarized echo cross sections vary with longitude as a two-cycle curve with maxima near 30° and 240° W. and minima near 130° and 330° W (Fig. 1B); model total-depolarized-echo cross sections vary with longitude as a one- cycle curve with a maximum near 135° and a minimum near 330° W.(Fig. 1C); and, the ratio of total-depolarized and total-polarized cross sections (mu) vary with longitude as a one-cycle curve (Fig. 1D).

Model polarized- and depolarized-echo spectra, as well as ratios of the two, resemble those that are observed (Fig. 2A,B; 2C,D; and, 2E,F, respectively). For smooth regions with moderate thermal inertias and normal reflectivities, the central parts of polarized-echo spectra are dominated by the quasi-specular parts that form tall, narrow peaks and that rest upon low, broad domes of the diffuse echoes (Fig. 2A). In rough regions with low thermal inertias and small normal reflectivities, the quasi-specular echoes form low broad peaks that rest upon and merge imperceptibly with the broad domes of the diffuse part of the echoes (Fig. 2B). Like the observed spectra, the forms of the polarized diffuse echoes tend to mimic the depolarized echoes except near the centers of the spectra where the quasi-specular parts of the polarized echoes totally dominate the spectra. Depolarized spectra dominated by upland and plains are weak (Fig. 2C) while those including volcanic units are strong and peaked (Fig. 2D). For the model and observations, ratios of the spectra of depolarized and polarized echoes are similar (Fig. 2E,F).

Several aspects of our model are instructive and relevant to the interpretation of radar echoes from Mars. These aspects are related to the sizes of the heterogeneous radar map units and the areas sampled by the radar, and the way in which the radar samples the surface; for example: (1) quasi-specular echoes from horizontal surfaces may be asymmetrical with peaks displaced from zero-doppler frequency when the radar samples adjacent units with different roughnesses; (2) quasi-specular echoes from very smooth areas with embedded very rough areas may be so dominated by the smooth areas that the rough areas are not revealed in the spectra; and (3) the diffuse parts of the polarized echoes may contribute substantially to the polarized echoes. Careful examination of observed echoes show that the surface of Mars is, like our model, heterogeneous.

REFERENCES

[1] Thompson, T.W., 1988, LPI Tech. Report 88-05, p. 107-108. [2] Thompson, T.W. and Moore, H.J., 1989, Proc. 19th Lunar and Planet. Sci. Conf., p. 409-422. [3] Palluconi, F.D. and Kieffer, H.H., 1981, Icarus, v. 45, p. 415-426. [4] Jakosky, B.M. and Christensen, P.R., 1986, Icarus, v. 66, p. 125-133. [5] Moore, H.J. and Jakosky, B.M., 1989, Icarus, v. 81, p. 164-184. [6] Hagfors, T., 1964, J.Geophys. Res., v. 69, p. 3779-

3784. [7] Butler, B., Muhleman, D., Grossman, A., and Slade, M., 1989, Eos (Trans. Am. Geophys. Union), v. 70, #43, p. 1171.

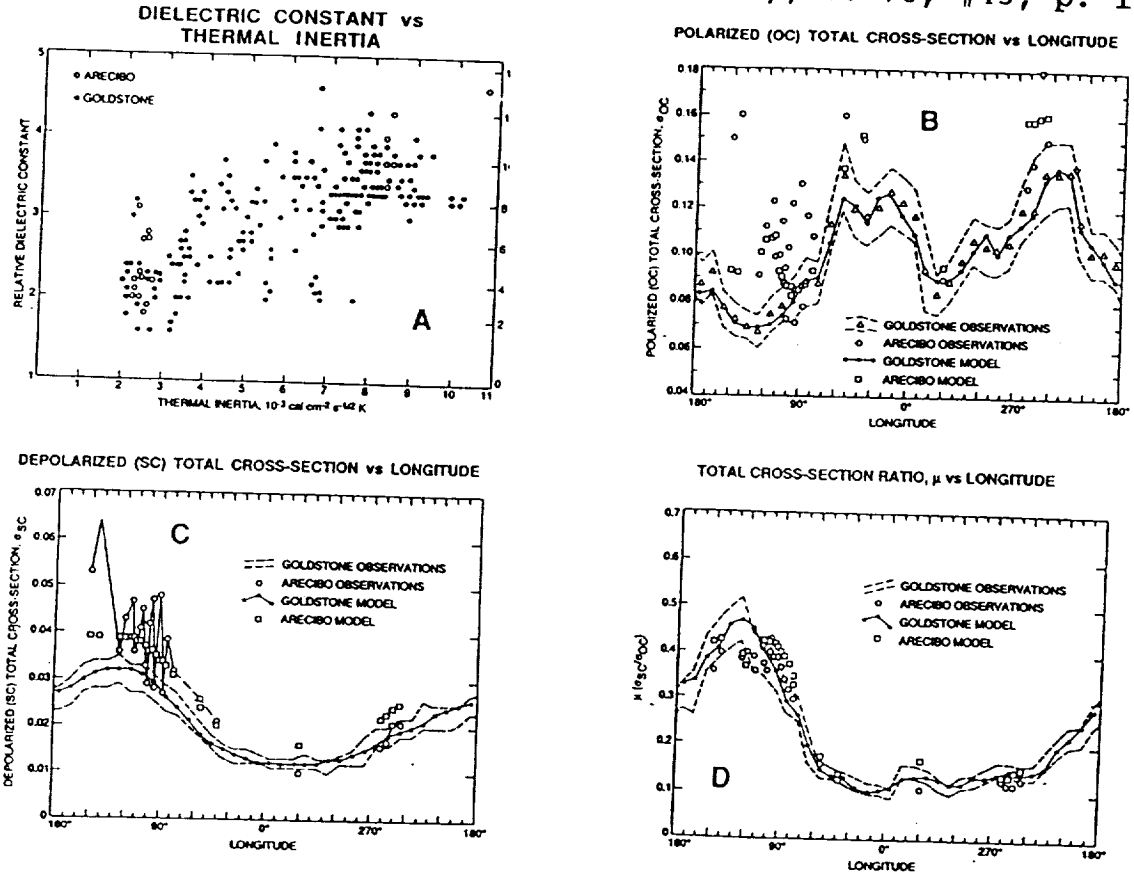

Figure 1. Correlation between dielectric constant and thermal inertia (A) and variation of observed and model polarized total-cross section (B), depolarized total-cross section (C), and mu (ratio of (C) and (B)) with longitude (D).

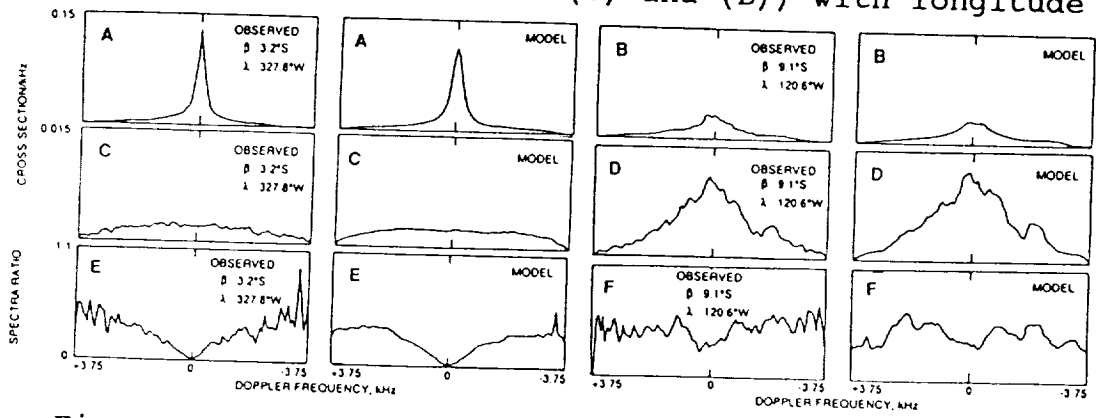

Figure 2. Observed and model spectra for selected polarized echoes (A,B), depolarized echoes (C,D), and echo ratios or mu (E,F).

Numerical Modeling of Radiowave Scattering

R.A. Simpson and G.L. Tyler, Center for Radar Astronomy
Stanford University, Stanford, CA 94305-4055

Radiowave scattering is an effective tool for remotely studying planetary surfaces, particularly at surface scales comparable to and somewhat larger than the radio wavelength. Numerical techniques, in combination with rapidly improving computer technology, now provide an alternative to conventional analytical interpretations of scattering data. Relatively simple and robust algorithms allow us to model physical processes; we construct solutions to relatively complex problems from coherent addition of more elemental results. Although there are but a few analytical solutions which can be used for checking, the clarity with which the problems may be stated plus an understanding of the computer's numerical limitations provide assurance that the results are correct.

Numerical calculations will be of value in interpreting planetary radar data, such as that expected from Magellan. Toward that end we have previously obtained and adapted several numerical codes, including the Numerical Electromagnetic Code (NEC) developed at Lawrence Livermore Laboratory. NEC permits evaluation of scattering from virtually any object that can be (approximately) described in terms of 300 or fewer wire segments or small plates. Relatively large scatterers may be studied, but the component wires or plates must remain less than $\lambda/10$ in size; otherwise, fundamental assumptions regarding electrical phase across individual elements are violated (λ is the radio wavelength). The (present) constraint of 300 elements sets strong limits on the dimensions of objects having arbitrary shape. We have studied scattering from "small" individual cubes, cylinders (tuna cans), and spheres where the characteristic dimension (*e.g.*, the diameter) is less than a wavelength (Simpson and Tyler, 1988, 1989). We found that when this dimension is less than $\lambda/10$ neither the shapes nor the orientations of single targets can be distinguished from their scattering patterns. Our results for these calculations are consistent with both analytic solutions and intuitive understanding of changes expected when scattering objects become small compared with the probing wavelength.

Scattering by two or more bodies (such as by a collection of rocks) is considerably more complex in an analytic sense. Not only must interference effects be included, but there will be coupling so that each body actually influences the responses of its neighbors. Numerically, however, the same physical principles can be applied as with one body. We have constructed numerical models of "rocks" from wire elements (Figure 1), replicated these, and then calculated the scattered field from both individual targets and from pairs. Our objective has been to estimate the "error" introduced by coupling phenomena as compared to a simpler calculation in which only interference is considered.

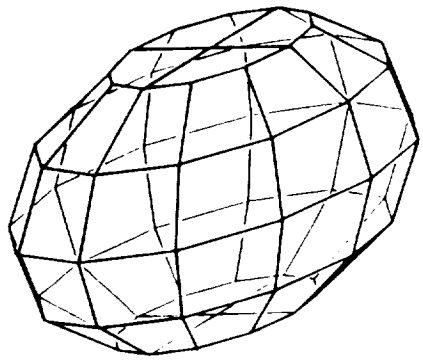

Figure 1: Model "rock" constructed from wire segments. Some wires mimic great circle arcs in longitude, but polar caps have been truncated. Substitution of simple cross-hairs at the poles reduces artifacts resulting from our imperfect model.

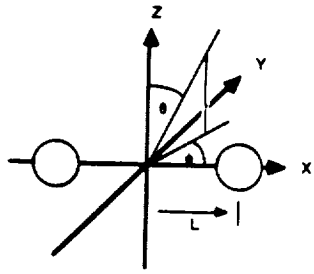

Figure 2: Geometry for scattering calculations. Two spheres are shown on the x-axis, equally spaced by L from the origin. Angles θ and ϕ define directions to the transmitter and observer; for calculations reported here the source was located on the z-axis.

The geometry for these calculations is shown in Figure 2. We assumed two (approximately) spherical targets of equal size (diameter/wavelength = $1/\pi$); distance between their centers is 2L. Our transmitter is on the z-axis; the observer (receiver) is in direction ($\theta=\theta_s,\phi=0$). Both the source and observer are assumed to be at large distance with respect to L. We have used an illuminating wave polarized in the x-direction, and we "measure" the scattered field polarized in the x-z plane (the E_θ component).

To obtain the "exact" solution we applied NEC to the two spheres simultaneously. Results, plotted as a function of separation distance (2L) and parameterized by the scattering angle θ_s, are shown in Figure 3. Squares indicate magnitude of the scattered field from the pair of spheres at each separation distance -- from about 0.34λ (spheres almost touching) to 60λ. Phase of the scattered field is also of interest, but it is less easily interpreted so is not shown here. Maximum field strength is on the order of 80 volts/meter, though it drops for spacings less than λ.

We also calculated the scattered fields expected from each sphere separately and added the results. This yields the constructive and destructive interference expected, but does not account for body-body interactions (coupling). The difference between the "exact" and the approximate solutions for field strength, expressed as a percent of the "exact" value is shown by the diamonds in Figure 3.

The results in Figure 3a provide a measure of the coupling effects, since no interference is expected when the transmitter and receiver are co-located and the spheres are symmetrically placed about the z-axis. The actual field is reduced by about 10% because of coupling when the spheres are almost touching, but the effect drops to about 1% at one-wavelength spacing and is less still at greater spacings. In Figures 3b and 3c the influence of interference can be seen. It is worth noting, however, that the percent error when using the simple field calculation is still less than about 10% *except* when the field itself is weak.

In Figure 3d we show the field strength and the percent error when the spheres lie along the y-axis. In this case the incident electric field is polarized across the axis of the two spheres, rather than along it. Simply adding the responses of two spheres scattering independently would result in an error of almost 30% at close spacings, indicating that the coupling term can be strongly polarization dependent.

These results are not definitive. Considerably more calculations are needed to complete the picture outlined here. We have not studied the effect of the size of the targets in the multiple scattering case nor have we exhausted the possible combinations of polarization, orientation of the sphere pair, and observer position. Nevertheless, the fact that we can obtain a solution at 10-30% accuracy for some simple cases expected in backscatter experiments is encouraging. This indicates that coupling among at least electrically small, discrete objects (such as centimeter-sized rocks on Venus when probed by Magellan radar

signals) may not require elaborate or time consuming calculations -- that the response of an ensemble can be obtained to reasonable accuracy by simply summing the scattering from the individual objects. Calculations for the broader parameter space described above will refine our understanding of the degree to which the simplifications can be applied.

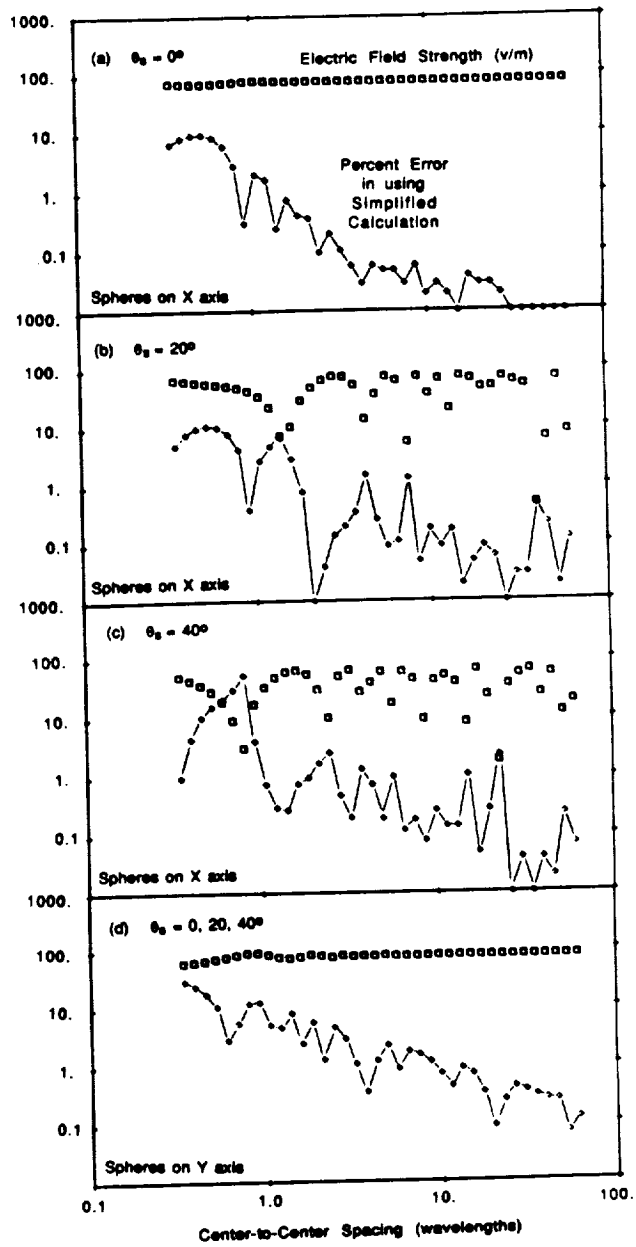

Figure 3: Electric field strength (squares) and percent error (diamonds) from numerical calculations of scattering by a pair of model "rocks" (diameters = λ/π); both quantities are plotted to same scale on left. Error values give the difference between the exact E-field solution and one in which the responses of two separate spheres were simply added (no coupling assumed). Oscillations in E-field show constructive and destructive interference, with minima more closely spaced as viewing angle θ_S increases for orientation shown in Figure 2. For panel (d) the spheres were placed along the y-axis. Lines connecting diamonds are to assist in distinguishing data types; particularly at large separation distances, not enough values have been calculated to show all oscillations.

Simpson, R.A., and G.L. Tyler, Numerical modeling of radiowave scattering, *Bull. AAS* **20**, 838, 1988.

Simpson, R.A., and G.L. Tyler, Numerical modeling of radiowave scattering, in *Reports of Planetary Geology and Geophysics Program - 1988* (NASA Technical Memorandum 4130), 296-298, 1989.

CHAPTER 8

FLUVIAL, PERIGLACIAL, AND AEOLIAN PROCESSES

WEATHERING AND EROSION OF THE POLAR LAYERED DEPOSITS ON MARS

Ken Herkenhoff and Bruce Murray, Division of Geological and Planetary Sciences
California Institute of Technology, Pasadena, CA 91125

The Martian polar layered deposits are widely believed to be composed of water ice and silicates, but the relative amount of each component is unknown. The "conventional wisdom" among Mars researchers is that the deposits were formed by periodic variations in the deposition of dust and ice caused by climate changes over the last 10 to 100 million years (Carr, 1982). It is assumed here that water ice is an important constituent of the layered deposits, that the deposits were formed by eolian processes, and that the origin and evolution of the north and south polar deposits were similar.

Maximum slopes of 10-20 degrees occur on an exposure of layered deposits within the south polar residual cap of Mars. A new photoclinometric technique was used to produce profiles of slope and albedo using high resolution Mariner 9 images (Herkenhoff and Murray, 1990b). Stereophotogrammetry was also used to constrain the photoclinometric solutions, which resolve layer thicknesses of 100-300 meters. Albedo variations are correlated with slope, indicating that frost is present on level areas. The magnitude of the slopes suggests that the layers are competent, perhaps due to the presence of a weathering rind.

Calculations of the stability of water ice in the polar regions of Mars (Toon et al., 1980; Hofstadter and Murray, 1990) indicate that ice should not currently be present at the surface of the layered deposits. The present water ice sublimation rate is high enough to erode the entire thickness of the deposits in about a million years. This result suggests that sublimation of water ice from the layered deposits results in concentration of non-volatile material at the surface of the deposits. Such a surface layer would insulate underlying water ice from further sublimation, stabilizing the layered deposits against rapid erosion.

Five color/albedo units have been recognized and mapped in the southern layered deposits on Mars (Figure 1). Shadow brightnesses were measured and modeled in order to correct for the effects of atmospheric scattering and quantify the albedo and color of the surface (Herkenhoff and Murray, 1990a). The layered deposits appear to be mantled by red dust, except where eolian stripping has exposed the darker, less red underlying bedrock. Frost and bare ground are mixed below the resolution of the images in many areas, some of which appear to be younger than the surrounding layered terrain.

The color and albedo of the layered deposits indicate that bright, red dust is the major non-volatile component of the deposits. However, the differences in albedo and color between mantling dust and exposures of layered deposits in the south polar region and the association of dark dune material with the north polar layered deposits (Thomas and Weitz, 1989) indicates that there is at least a minor component of dark material in the deposits. The dark material may be either sand or dust; each possibility is examined below. The dark material must either be intimately mixed with the bright dust in the layered deposits or occur in layers or lenses less than a few meters in size, or they would be visible in high-resolution Viking Orbiter images.

The presence of small amounts of dark sand in the layered deposits can account for the dark dunes that appear to have sources in the north polar deposits (Thomas and Weitz, 1989). Poleward circulation during the summer is then required to transport sand into the layered deposits. The most significant problem with this hypothesis is the eolian codeposition of sand and dust in the polar regions. It is unlikely that sand can be carried in suspension by even a much denser Martian atmosphere, so that sand must be transported by saltation (Thomas and Weitz, 1989). Saltating sand would eject dust into suspension, hindering codeposition of sand and dust. Although small amounts of sand may have saltated over frozen, cemented dust toward the poles, the difficulties with this scenario prompt consideration of alternative hypotheses. A theory for layered deposit formation and evolution involving only dust (bright and dark) and ice is proposed below.

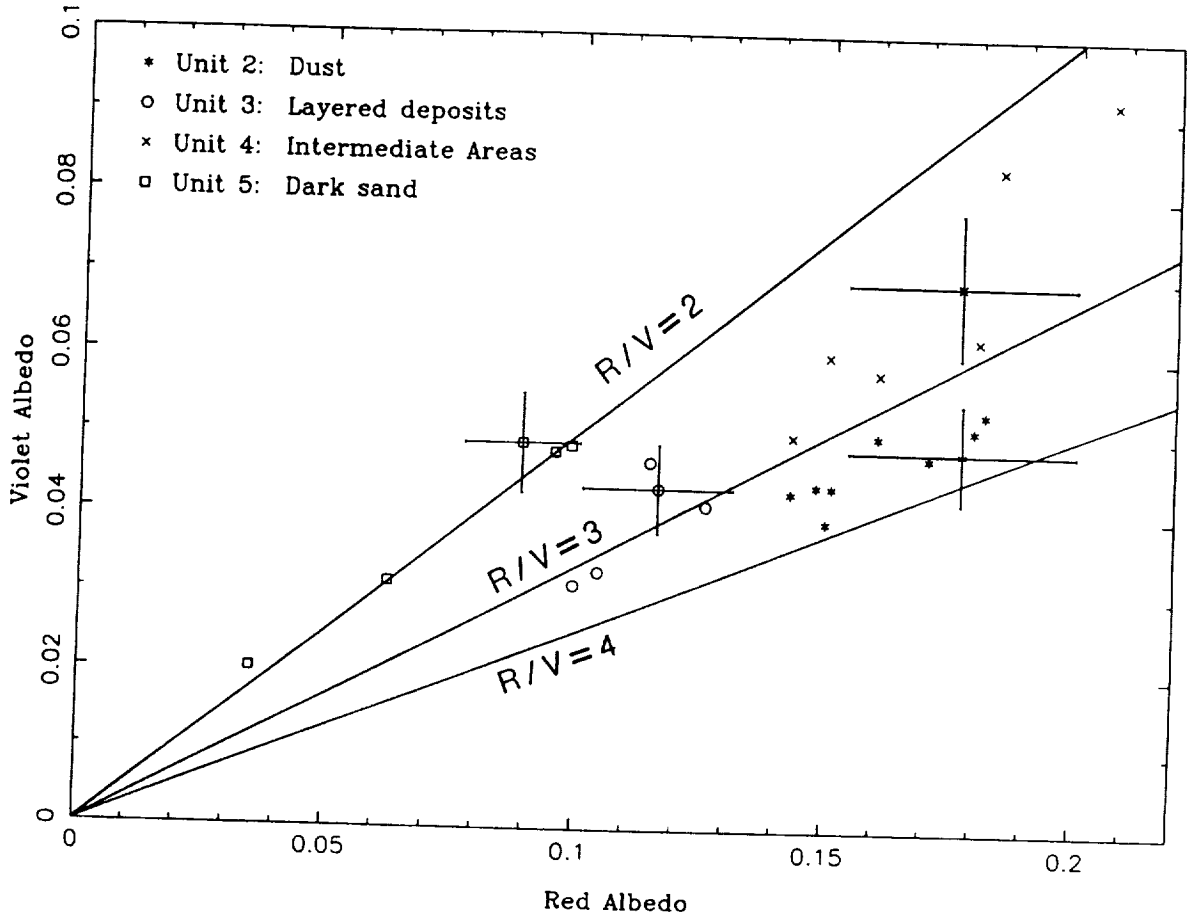

Figure 1: Violet vs. red Lambert albedo for 4 surface units in the vicinity of the south polar residual cap. Unit 1 (polar frost) has higher albedos and plots outside this figure. Error bars represent 13% uncertainty in absolute albedos, sampling noise in 5 x 5 pixel areas in red/violet mosaic.

How can dark dust in the layered deposits form the dunes observed in the polar regions? Sublimation of dust/ice mixtures has been shown to result in the formation of filamentary sublimation residue (FSR) particles about 100 microns in size (Storrs et al., 1988). Such particles can saltate along the Martian surface, and may therefore create dunes (Saunders et al., 1985). In order to form saltating material by this mechanism that is at least 3 times darker (in red light) than the bright dust that mantles much of Mars, dark dust grains must preferentially form FSR particles. Magnetic dust grains would be expected to form FSR more easily than non-magnetic dust, and are probably much darker. Experimental formation of FSR with magnetic material has not been attempted, and should be the subject of future research.

There is direct evidence for 1-7% magnetic material in the surface fines at the Viking lander sites (Hargraves et al, 1979). In addition, analysis of Viking lander sky brightness data indicates that suspended dust over the landing sites contains about 1% opaque phase, perhaps of the same composition as the magnetic material on the surface (Hargraves *et al.*, 1979; Pollack *et al.*, 1979). Within the uncertainties of these measurements, the percentages of magnetic material given above are identical to the volume of dark dune deposits in the polar regions expressed as a percentage of eroded layered deposits (Table 1). This comparison indicates that the presence of magnetic material in the layered deposits is likely, and that formation of sand dunes from dark FSR particles is plausible.

In summary, weathering of the layered deposits by sublimation of water ice can account for the geologic relationships observed in the polar regions. The non-volatile component of the layered deposits appears to consist mainly of bright red dust, with small amounts of dark dust or sand. Dark dust, perhaps similar to the magnetic material found at the Viking Lander sites, may preferentially form filamentary residue particles upon weathering of the deposits. Once eroded, these particles may saltate to form the dark dunes found in both polar regions. Eventual destruction of the particles could allow recycling of the dark dust into the layered deposits via atmospheric suspension. This scenario for the origin and evolution of the layered deposits is consistent with the available data.

REFERENCES

Carr, M. H. (1982). Periodic climate change on Mars: Review of evidence and effects on distribution of volatiles. *Icarus* **50**, 129-139.

Hargraves, R. B., D. W. Collinson, R. E. Arvidson, and P. M. Cates (1979). Viking magnetic properties experiment: Extended mission results. *J. Geophys. Res.* **84**, 8379-8384.

Herkenhoff, K. E. and B. C. Murray (1990a). Color and albedo of the south polar layered deposits on Mars. *J. Geophys. Res.* **95**, 1343-1358.

Herkenhoff, K. E. and B. C. Murray (1990b). High resolution topography and albedo of the south polar layered deposits on Mars. *J. Geophys. Res.*, in press (Mars special issue).

Hofstadter, M. D. and B. C. Murray (1990). Ice sublimation and rheology: Implications for the Martian polar layered deposits. *Icarus*, in press.

Pollack, J. B., D. Colburn, F. M. Flasar, R. Kahn, C. Carlston, and D. Pidek (1979). Properties and effects of dust particles suspended in the Martian atmosphere. *J. Geophys. Res.* **84**, 4479-4496.

Saunders, R. S., T. J. Parker, J. B. Stephens, E. G. Laue, and F. P. Fanale (1985). Transformation of polar ice sublimate residue into Martian circumpolar sand. *NASA Tech. Mem.* **87563**, 300-302.

Storrs, A. D., F. P. Fanale, R. S. Saunders, and J. B. Stephens (1988). The formation of filamentary sublimate residues (FSR) from mineral grains. *Icarus* **76**, 493-512.

Thomas, P. (1982). Present wind activity on Mars: Relation to large latitudinally zoned sediment deposits. *J. Geophys. Res.* **87**, 9999-10008.

Thomas, P. C. and C. Weitz (1989). Dune sand materials and polar layered deposits on Mars. *Icarus* **81**, 185-215.

Toon, O. B., J. B. Pollack, W. Ward, J. A. Burns, and K. Bilski (1980). The astronomical theory of climatic change on Mars. *Icarus* **44**, 552-607.

Table 1

Quantity	Fraction	Reference
Magnetic material in surface fines	1-7 %	(Hargraves *et al.*, 1979)
Opaque phase in atmospheric dust	1 %	(Pollack *et al.*, 1979)
Volume of dark dunes/volume of eroded polar deposits	1-10 %	(Thomas, 1982)

EXPERIMENTAL STUDIES OF ICE SUBLIMATION UNDER MARS-LIKE CONDITIONS: RESULTS OF THE DUST COVER RUNS

Jeffrey M. Moore, Department of Geology, Arizona State University, Tempe, AZ 85287

An apparatus has been fabricated to conduct experiments on ice/non-volatile mixtures by providing a Mars-like environment (3 mbar of CO_2 at ~250 °K) for a 1 m by 50 cm thick sample of H_2O ice and ice mixed and/or covered with non-volatile particles (Moore and Malin, 1988; Moore, 1989). The chamber, enclosed in a "walk-in" freezer, consists of two parts: a lower, plexiglas sample container that holds the ice-rich mixture and an upper, aluminum environmental volume above the sample to which its surface is exposed. A pump can circulate the 3 mbar CO_2 atmosphere between the sample chamber and the H_2O vapor-trapping cold-finger. The first experiments have investigated the properties of a sample of pure 0.25-5.0 mm granular ice with a bulk density of 0.49 g cm^{-3}, covered with increasingly thick layers of 10 μm-sized dust.

Measurements

One clean-ice and three dust-covered (1, 2.5, and 5 mm thick) experiments have been conducted. During each experiment the sublimation rate of a given dust-covered sample was determined for four environmental conditions: 1) isothermal sample with the circulation pump off, 2) isothermal sample with the circulation pump on, 3) sample heated from above for one 24-hour period with the circulation pump off, and 4) sample heated from above with the circulation pump on. The sample was allowed to return to an isothermal state between the third and fourth conditions.

The change in sublimation rate of an isothermal (-20 °C) sample as a function of increasing dust-cover thickness when the circulation pump is off is very small. An exponential curve can be fit to the data with the form:

Sublimation rate, isothermal, circulation off (in 10^{-9} g s^{-1} cm^{-2}) =

$$182.13 \times 10^{(-2.5541 \times 10^{-2}) \times \text{Dust cover thickness (in mm)}}$$

Sublimation rate from isothermal samples increases dramatically when the circulation pump is on. In the case of clean ice, the sublimation rate increased by almost a factor of eight (from 185 x 10^{-9} to 1426 x 10^{-9} g s^{-1} cm^{-2}). The effect of increasing dust-cover thickness on isothermal samples with the circulation pump on is a small decrease at a rate slightly greater than that under isothermal/circulation off conditions. The relationship also has an exponential functional form:

Sublimation rate, isothermal, circulation on (in 10^{-9} g s^{-1} cm^{-2}) =

$$1471.5 \times 10^{(-7.345 \times 10^{-2}) \times \text{Dust cover thickness (in mm)}}$$

When the initially isothermal sample is heated from above (in these experiments, for 24 hours) and the circulation pump is off, a substantial increase in sublimation rate was observed for both the clean-ice and 1 mm-thick dust layer samples, as compared to the two previously discussed environmental conditions. However, with increasing dust cover thickness (>2.5 mm) the sublimation rate of heated samples without circulation is *less* than the sublimation rate of isothermal samples with circulation, by a factor of ~20-25%. The functional relationship is:

Sublimation rate, heated sample, circulation off (in 10^{-9} g s^{-1} cm^{-2}) =

$$2662.7 \times 10^{(-0.15745) \times \text{Dust cover thickness (in mm)}}$$

The heating of an initially isothermal sample for 24 hours with circulation results in the highest rate of sublimation for a given sample under any of the four environmental conditions. In every case, the sublimation rate doubled from the measurements acquired for heated samples

without circulation. In addition, the effect of increasing dust cover on sublimation rate appears to be the greatest under this condition. The exponential curve for this case is:

Sublimation rate, heated sample, circulation on (in 10^{-9} g s^{-1} cm^{-2}) =

$$5152.8 \times 10^{(-0.14055) \times \text{Dust cover thickness (in mm)}}$$

The measurements and associated curves are shown in Figure 1. Uncertainties in both dust thickness and sublimation rate are less than approximately 25%. The convergence of the curves at extrapolated dust cover thickness of 10 mm towards two values, one corresponding to conditions with atmospheric circulation and one without, is interesting but must be verified experimentally.

Discussion

A number of studies have modeled theoretically the sublimation rates of ice, both exposed (e.g. Ingersoll, 1970; Wallace and Sagan, 1979; Haberle and Jakosky, 1990) and covered (e.g. Farmer, 1976; Clifford and Hillel, 1983; Zent *et al*, 1986), under a variety of martian conditions. In order to relate the measured sublimation rates determined by this investigation to these works, formulas from these studies were used to calculate a sublimation rate using parameters matching the conditions of the experiment.

The clean ice sublimation rate (J_c) was calculated using an expression employed by Ingersoll (1970) and subsequently used by many investigators, which as used in this investigation has the form:

$$J_c = 0.17\ (\Delta\rho)\ D_{om}[\ (\Delta\rho\ /\ \rho)\ g\ /\ \upsilon\ 2\ ]\ 1/3$$

where $\Delta\rho$ is the difference between total mixed-gas density at the surface and that of water vapor at the surface, $(\Delta\rho\ /\ \rho)$ is the ratio of the difference between mixed-gas density at the surface and that of water vapor at the surface to the mixed-gas density, D_{om} is the ordinary molecular diffusion coefficient for water vapor in CO_2, υ is the kinematic viscosity of CO_2, and g is the acceleration of gravity at the surface.

The rate of sublimation for ice under a dust cover (J_d) was calculated using an expression from Farmer (1976), also generally adopted by subsequent investigators. It has the form:

$$J_d = D_k\ V\ M_w\ /\ \Pi\ \kappa\ T\ L$$

where D_k is the Knudsen diffusion coefficient appropriate for the pore sizes within the dust layer, V is the saturation vapor pressure of ice for a given temperature, M_w is the molar mass of water, Π is Avagadro's number, κ is Boltzmann's constant, T is the temperature of the gas at the surface, and L is the thickness of the dust layer. The mean free path length of a mixture of H_2O and CO_2 at 3 mbar at -20 °C was calculated to be 28 μm, which is an order of magnitude larger than the effective pore size (~1 μm) given in Clifford and Hillel (1983) for uncompressed, 10 μm diameter dust particles deposited from suspension. Gas diffusion through the dust layer is, as a consequence of the ratio of pore size to the mean free path length, entirely in the realm of Knudsen diffusion.

The calculations for both J_c and J_d assume that water vapor is subliming into a totally desiccated CO_2 atmosphere. To compare the theoretical predictions to the experimentally measured sublimation rate, the results from the environmental condition of the CO_2 gas circulating (via the operation of the circulation pump) over an isothermal sample were used. The circulation pump cycles the entire volume of gas above the sample past the cold-finger and back to the chamber in approximately 70 seconds. This is equivalent to a "surface" wind "velocity" of roughly 1.5 cm/sec, a value only slightly higher than the rate at which H_2O vapor

would be buoyantly lofted away from a surface in a still, desiccated CO_2 atmosphere. The results of the comparison are shown in Figure 2.

Note that, although the experimental conditions should potentially be more conducive to ice sublimation than the theoretical conditions, just the opposite is the actual case: the experimentally-determined sublimation rate is one-sixth that calculated using the most common expression for clean ice sublimation rates. The theoretical and actual values for the sublimation rate of ice under a dust cover appear to converge with increasing layer thicknesses. The sublimation rate of ice under 5 mm of dust has a measured value that is one third the theoretical prediction. Although it is tempting to attribute the difference between the theoretical and experimentally-measured sublimation rates to the inability of the cold finger to completely desiccate the atmosphere in the chamber, the trapping efficiency has been determined through other experiments to be much greater than necessary to remove the small amounts of water evolved during these experiments.

Results

The initial interpretation of the results from these runs are : (1) even thin layers of dust greatly lower the sublimation rate of an underlying ice substrate being heated from above, (2) thin layers of dust only mildly suppress the sublimation rate of an underlying ice substrate when sample is wholly isothermal, (3) even a low-flux, desiccated gas flow over the sample surface significantly increases the sublimation rate of any given sample, and (4) actual sublimation rates are within an order of magnitude but definitely lower than sublimation rates predicted from theoretical treatments.

REFERENCES

Clifford, S.M. and D. Hillel (1983), *J. Geophys. Res., 88*, 2456-2474.; Farmer, C.B. (1976), *Icarus, 28*, 279-289; Haberle, R.M. and B.M. Jakosky (1990), *J. Geophys. Res., 95*, 1423-1437; Ingersoll, A.P. (1970), *Science, 168*, 972-973; Moore, J. M. (1989), in Reports of Planetary Geology Program - 1988, *NASA Tech. Mem. 4130*, 346-348; Moore, J. M. and M. C. Malin (1988), in Reports of Planetary Geology Program - 1987, *NASA Tech. Mem. 4041*, 133-134; Wallace, D. and C. Sagan (1979), *Icarus, 39*, 385-400; Zent, A.P., F.P. Fanale, J.R. Salvail, and S.E. Postawko (1986), *Icarus, 67*, 19-36.

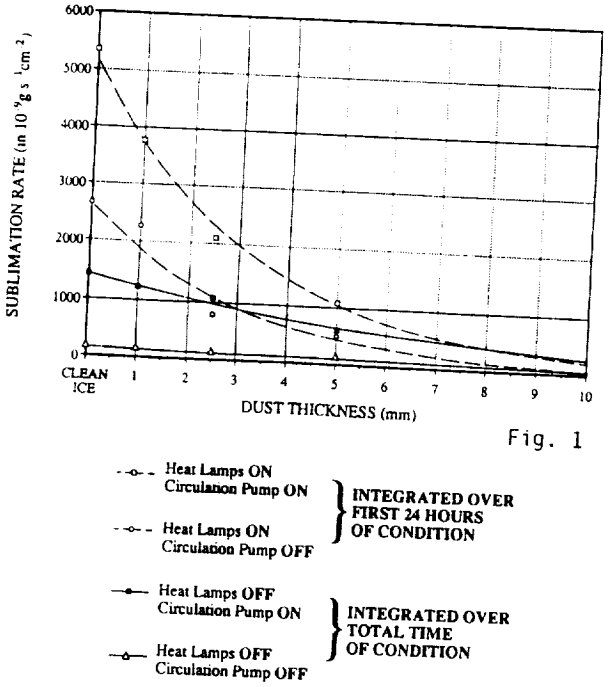

Fig. 1

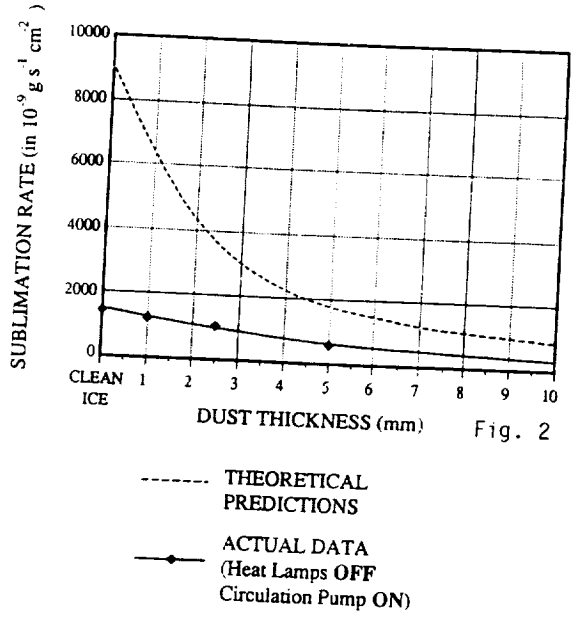

Fig. 2

Ancient Glaciation on Mars J.S. Kargel and R.G. Strom, Lunar and Planetary Laboratory, University of Arizona, Tucson, AZ 85721

Photogeologic evidence for widespread ancient episodes of glaciation has been discovered in Viking spacecraft images of Mars. The principal image base used for this study consists of the USGS 1:2 million scale photomosaics of the MC-26 Quadrangle and the Viking Orbiter images obtained on orbits 349S, 352S, 567B, 568B, 569B, and 574A. We recognize that non-glacial mechanisms may adequately explain certain individual types of landforms discussed below. However, we believe that a glacial hypothesis provides a more acceptable unified explanation, and is consistent with the emerging outlines of a global hydrologic model [1].

Figure 1 is a glaciological map of a region the Charitum Montes and the adjoining Argyre Planitia. The most startling feature in this region is an anastomosing system of sinuous ridges, noted previously [2-5]. The plan of this ridge system (Viking Orbiter frames 352S34 and 567B30-35) is fluvial in character and must therefore have an underlying fluvial explanation (volcano-tectonic processes can not generate this pattern). The possibility that similar ridge systems elsewhere on Mars are glacial eskers has been previously noted [2](eskers are stream deposits of sand and gravel originally layed down on the surface of, within, or beneath stagnant, melting glaciers). The esker hypothesis is lent support by the similarity in length, height, width, overall structural plan, and detailed structure of the Martian features compared to large terrestrial eskers associated with the melting of Late Pleistocene and modern ice sheets on Earth [6, 7].

Figure 1 also shows the characteristic structure of the mountainous inner ring of Argyre, including numerous valleys separating sharp linear to semi-circular ridges. The characteristics of this mountain range, if considered with a terrestrial perspective, are diagnostic of alpine-type glacial erosion. The Charitum Montes appear to be a classic glacial assemblage of horns, cirques, and aretes, with intervening valleys mantled by lobate debris aprons. A prominent cirque near 54°30'S. Lat. 31°30'Long. is intimately associated with a region of fluvial deposition and erosion interpreted to be a glacial outwash deposit (sandur plain). Another region of fluvial erosion and deposition, near 54° S. Lat. 37° Long., emanates from a large glacially modified valley in the Charitum Montes and is interpreted as a glacio-lacustrine delta.

Large-scale glacial fluting was severe in Argyre Planitia during the height of the ancient ice age. The scouring of several large impact crater rims (e.g., frame 568B33) demonstrates that a considerable interval of time elapsed between the Argyre impact and the glacial epoch. In the area mapped in Figure 1 (450,000 km^2) there are seven fresh impact craters larger than 10 km in diameter displaying fresh ejecta and sharp rims and lacking any signs of glaciation, suggesting an early Amazonian termination of the glacial epoch. The extensive ejecta blanket of the large crater Galle (not one of the seven) covers about a third of Argyre Planitia, and clearly mantles many glacial grooves and ridges (e.g., frame 352S39). However, the delta-like fluvial system mentioned above erodes and elsewhere embays the ejecta blanket of Galle; further, smooth layered deposits, interpreted as glacio-lacustrine sediments associated with the esker system, embay Galle's ejecta blanket (frames 567B36 and 568B09); finally, a channel, either glacial or possibly fluvioglacial, incises the rim of Galle (frame 352S24). Hence, Galle dates from the glacial epoch (or an interglacial). Impact into an ice sheet is suggested by the extensive occurrence of ice disintegration features (e.g., kettle holes) on the ejecta blanket of Galle (frame 568B12). Possibly an underlying ice sheet, or perhaps anomalously large quantities of ice entrained in the ejecta itself, later melted or sublimated.

Kettle fields outside the area of Galle's ejecta testify to the retreat of the ice sheet and the stranding of large blocks of ice on Argyre Planitia (frame 568B53). Together with the eskers and outwash deposits these landforms record the melting of the Argyre ice sheet, *indicating a period of relatively warm climate even at moderately high elevations and latitudes*. However, the absence of super-imposed fluvial systems (other than those plausibly related to the melting of ice) indicates that *humid conditions following the ablation of the ice sheet were short-lived*. We note that the northern rim escarpment of Argyre has been fluvially modified and lacks evidence of glaciation, as if it rained there probably at the time that it snowed at higher latitudes.

We have made a preliminary search for possible glaciogenic landforms elsewhere on Mars. The single most diagnostic glaciogenic landform on Mars probably is the esker. Eskers are widespread in the Southern Hemisphere of Mars, often occurring in close association with polar layered deposits and etched (kettled and/or glacially scoured?) terrains; these probably indicate that a vast ice sheet once enveloped much of the Southern Hemisphere down to about 40° S. Lat. Eskers also occur more sparingly in the Northern Lowlands north of 26° in close association with the "thumbprint terrains" (recessional moraine fields?), and in one tropical location.

The final ablation of the southern ice sheet must have occurred under much warmer conditions and under a denser atmosphere than currently prevail. Glaciation and de-glaciation may have been two steps

in a global hydrologic cycle. Possibly Oceanus Borealis [1] supplied the atmosphere with water vapor which then was cold-trapped as snow or frost in the high elevations of the Southern Hemisphere. As the climate warmed due to climatic perturbations related to the formation of Oceanus Borealis the ice sheet eventually melted, charging the cratered uplands with groundwater. Given sufficient permeability this groundwater may have flowed northward to re-charge the equatorial region. Volcanism-driven outbursts of groundwaters may have re-filled Oceanus Borealis, completing the cycle, possibly on a repeating basis [8, 9].

Finally, we suggest that the nature and significance of the lobate debris aprons at high- and mid-latitudes on Mars [10] should be re-evaluated. It is generally thought that these debris aprons are rock glaciers. The outstanding issue is whether they are purely periglacial rock glaciers where down-slope motion is generated by gelifluction (surficial freeze-thaw), or whether the debris aprons are ice-cored rock glaciers where a rocky lag has accumulated on the surfaces of old glaciers by processes of melting and/or sublimation [11]. Figure 1 shows that debris aprons are commonly associated with individual cirques, suggesting a glacial origin.

References. 1) V. Baker et al., 1990, *LPS XX*. 2) M.H. Carr et al., 1980, *Viking Orbiter Views of Mars*, U.S. Gov't. Printing Office, Washington, D.C., p. 136. 3) P.H. Schultz and D. Britt, 1986, *LPS XVII*, p.775. 4) T.J. Parker, 1989, *LPS XX*, p. 826. 5) C.A. Hodges, 1980, Geologic Map of the Argyre Quadrangle of Mars, USGS Map I-1181. 6) R.J. Price, 1973, *Glacial and Fluvioglacial Landforms*, Oliver & Boyd, Edinburgh, 242 pages. 7) H. Lee, 1965, *Geol. Surv. Can. Pap. 65-14*, 1-17. 8) V. Gulick and V. Baker, 1990, *LPS XXI*. 9) G. Komatsu and R.G. Strom, 1990, *LPS XXI*. 10) S.W. Squyres and M.H. Carr, 1986, *Science 231*, 249-252. 11) J.R. Giardino, J.F. Schroder, Jr., and J.D. Vitek (eds.), 1987, *Rock Glaciers*, Allen & Unwin, Boston, 355 pages.

Figure 1. Glaciological map of a portion of Argyre Planitia and the adjoining Charitum Montes.

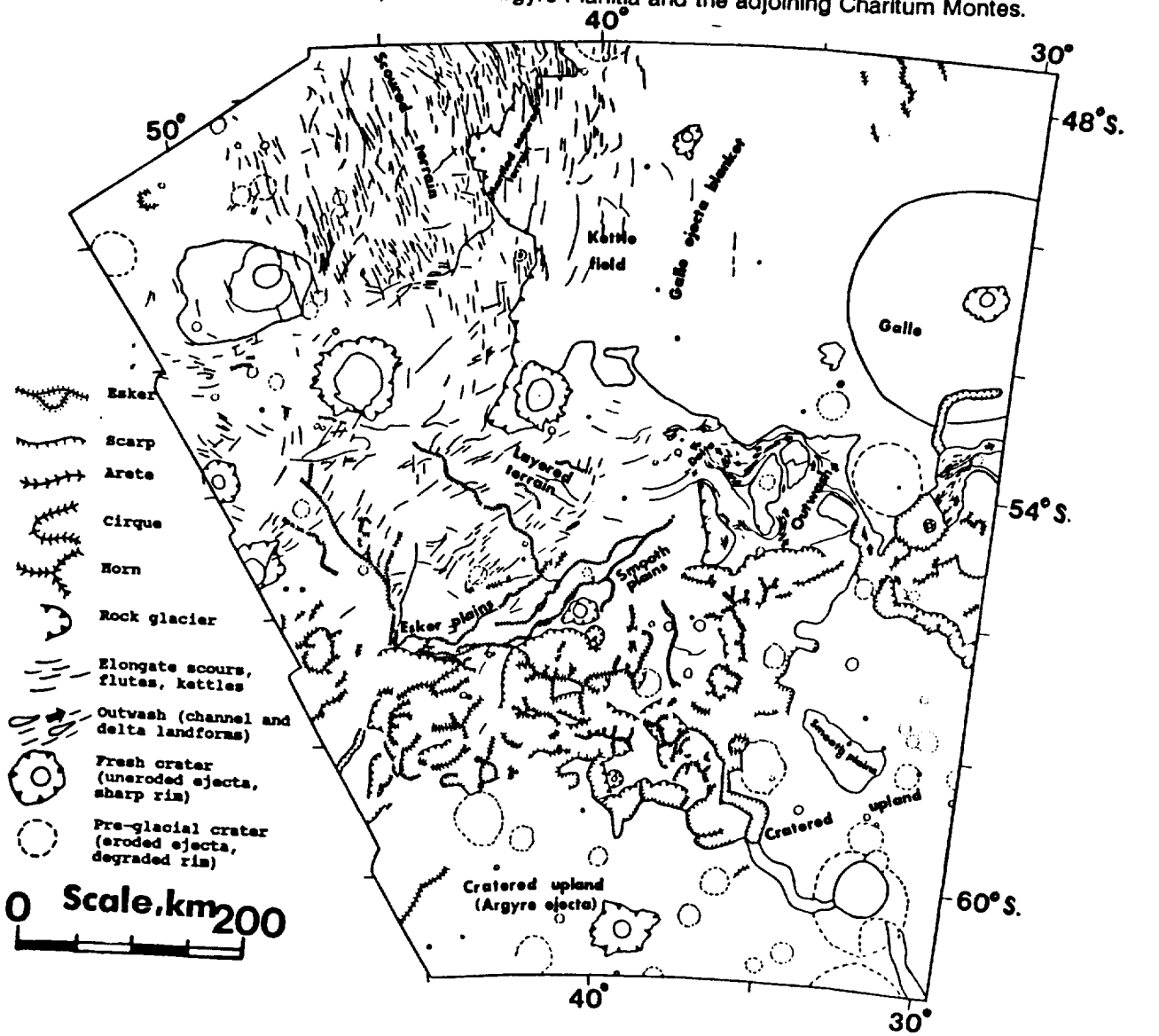

GIANT MARTIAN POLYGONS: ORIGIN BY DESICCATION AND BENDING

George E. McGill and L. Scott Hills
University of Massachusetts, Amherst, MA 01003.

The giant polygons of Acidalia and Utopia planitiae are geometrically most similar to desiccation polygons, but they have also been compared to frost-wedge polygons and columnar joints in lavas (2). Polygonal structures on the earth demonstrate a roughly 4:1 to 10:1 relationship between polygon diameter and the depth of the bounding fractures (1). Transferring this relationship to the giant polygons of the martian northern plains, which are 5-20 km in diameter, requires that fracturing driven by cooling or desiccation penetrate to depths at least as great as 0.5 km, and perhaps as much as 2 km. This is mechanically unlikely, as is convincingly argued by Pechmann (2), who concludes, somewhat reluctantly, that only deep-seated tectonic stresses could account for the fracture depth required to form such large polygons. However, the giant martian polygons do not resemble any known tectonic structures (2,3).

Polygonal terrane corresponds in age to large outflow channels that drain from the highlands into the lowlands (4), and it occurs in the topographically lowest parts of the lowlands (5). It also can be shown that the polygonal troughs formed almost immediately following deposition of these materials (3), a timing that does not rule out a tectonic origin, of course, but which strongly suggests a link between deposition and fracturing. Processes known to occur shortly following deposition of wet sediment are desiccation and compaction. Geological evidence thus favors a model for polygon formation that involves shrinkage stresses due to desiccation of wet sediment. However, most similar structures on earth have dimensions on the order of centimeters to meters; rare large polygons with diameters up to 300 m are known from a few playas (6).

The martian polygonal terrane was deposited unconformably on top of a rugged surface characterized by knobs, mesas, fragments of ancient crater rims, and scattered fresh craters (3,7). This rugged surface is exposed south of the polygonal terrane of Utopia planitia. Northward, the surface is increasingly obscured by younger plains deposits until it disappears completely beneath polygonal terrane (7). Circular troughs present among the more irregularly shaped polygons within polygonal terrane occur above buried fresh craters similar to those exposed to the south. The complete burial of a crater population that includes craters as large as 35 km in diameter requires that polygonal terrain be at least 400 m thick (8). Moreover, the sediments also must be thick enough to cover the crater rims to depths on the order of twice the apparent depths of the circular troughs, implying a total regional thickness of polygonal terrane material of about 600 m. The presence of rugged topography beneath a thick layer of wet sediment will result in the development of drape anticlines and synclines as the sediment compacts because the total downward displacement of an originally horizontal plane within the sediments will vary directly with the thickness of compacting underlying material. These drape folds will superpose bending stresses onto the pervasive tensile stresses due to desiccation shrinkage. The objectives of this research are 1) to test the feasibility of this model by estimating the magnitudes of the stresses involved, and 2) to continue developing an hypothesis for polygon formation that considers both geological and mechanical data.

Because crater morphology is well known (8), and because of the geometric simplicity provided by radial symmetry, our mechanical analysis considers the specific case where a crater 10 km in diameter is covered by sediments thick enough to bury the rim to a depth of 400 m. For purposes of analysis, it is convenient to consider the lower part of the sedimentary layer filling the crater as an "older fill", and the upper part as a "younger cover". This may represent the true geological history of the deposit, but the analysis does not depend on this. The actual history may well have involved many depositional episodes, but the only assumption critically important to our results is the thickness of sediment deposited during the last of these.

Two quantitative models are attempted, one based on plate-bending theory, the other using finite-element methods. Both models draw on the literature of soil mechanics to estimate the rheological properties of polygonal terrane materials. Most normally consolidated sand- and clay-rich soils exhibit Young's moduli in the range 5-75 MPa, and Poisson's ratios between 0.25 and 0.40 (9). Cohesive strengths commonly are negligible, and shear failure is governed by angles of internal friction averaging 30°. The plate bending model considers material above the crater rim to be an elastic plate that is bent as the underlying older fill compacts under the load of the younger cover. Because boundary conditions impose a sinusoidal shape on the bent plate, this approach does not predict a very realistic shape for a drape fold formed over the upward-concave slope of a crater wall. However, the sinusoidal shape underestimates bending stresses, and thus is conservative. The finite-element model considers the three-dimensional elastic deformation of older fill and younger cover as a function of position and time. The buried crater rim is modeled using cubic splines, hence the shape of the resulting drape fold seems very realistic. Because of the flexibility of the finite-element method, various depth-dependent combinations of elastic properties and extent of preconsolidation can be modeled. The assumption of purely elastic compaction, although probably not very realistic, also is conservative.

The two approaches yield similar results. Even when very conservative estimates of compaction of older fill are used (<10%), failure by brittle fracture or by shear is predicted to depths of the right order to account for the troughs bounding the martian polygons. This result is obtained without considering the tensile stresses due to desiccation shrinkage. If these are of the same order as the bending stresses, as seems likely, then not only are the total stresses available adequate to cause failure to the requisite depth, but superposition of these two stress systems will produce significant differences in total tensile stresses available to initiate fracturing at the surface; the probability of fracturing will be enhanced by drape anticlines and domes above crater rims and knobs/mesas, and suppressed by drape synclines between these features. Thus the scale of the polygons relates to the spacing of buried topographic features rather than to the strength/thickness characteristics of the sediment layer.

Compaction and bending must occur quickly enough for elastic strains to build up faster than they can be relaxed by pseudoviscous creep. Equivalent viscosity of soil is rarely determined, but in slow landslides it is estimated to be about 10^5-10^6 MPa-s (10). Maxwell times for materials with equivalent viscosities of 10^6-10^8 MPa-s and Young's moduli of about 10 MPa are months to years. Very large Maxwell times (order of 10^6 years) would thus seem to require unrealistically high equivalent viscosities. Consequently, it appears as if the formation of the martian polygons must be a geologically rapid process.

References

(1) Lachenbruch, A.H., J. Geophys. Res., 66, 4273-4292, 1961.
(2) Pechmann, J.C., Icarus, 42, 185-210, 1980.
(3) McGill, G.E., Geophys. Res. Letts., 13, 705-708, 1986.
(4) Neukum, G., and K. Hiller, J. Geophys. Res., 86, 3097-3121, 1981.
(5) Lucchitta, B.K., et al., J. Geophys. Res., 91, E166-E174, 1986.
(6) Neal, J.T., , et al., Bull. Geol. Soc. America, 79, 69-90, 1968.
(7) McGill, G.E., J. Geophys. Res., 94, 2753-2759, 1989.
(8) Pike, R.J., and P.A. Davis, Lunar Planet. Sci. XV, 645-646, 1984.
(9) Hunt, R.E., Geotechnical Engineering Analysis and Evaluation, McGraw-Hill, 1986.
(10) Iverson, R.M., in Abrahams, A.D., Hillslope processes, Allen & Unwin, 1986.

THICKNESS ESTIMATES FOR CONCENTRIC CRATER FILL IN THE UTOPIA PLANITIA REGION OF MARS

James R. Zimbelman, Center for Earth and Planetary Studies, National Air and Space Museum, Smithsonian Institution, Washington, D.C. 20560

Concentric crater fill (CCF) is one member of a group of distinctive landforms, abundant throughout the mid-latitudes of Mars, that are interpreted to be indicators of the presence of ground ice (1,2). Recently an aeolian alternative has been proposed for the origin of the CCF morphology (3). This work presents topographic data for CCF deposits in Utopia Planitia (36°N, 279°W) that are helpful in evaluating the relative roles of ice-enhanced creep and aeolian deposition/erosion in CCF.

Numerous landforms have been attributed to the presence of ground ice on Mars (e.g. 1-8). It is important to note that for none of these features has an unambiguous connection with ground ice been established, even though the appearance of many of these features is very suggestive of a volatile-related origin. Concentric crater fill (CCF) consists of a concentric pattern of arcuate ridges and grooves in material within craters located between 30° and 60° latitude (9), near other potential indicators of ground ice (1,2). CCF morphology is interpreted to result from the downslope movement of ice-rich materials through creep deformation of the interstitial ice (1,2). High resolution images in and around some CCF craters reveal extensive erosion of a multi-layered mantling deposit, which suggests that some CCF could result from aeolian deposition and erosion in the martian mid-latitudes (3). It seems likely that both ice-creep and aeolian processes may have contributed to the unique character of the mid-latitude terrains, so that a method is needed for evaluating the relative importance of each process. CCF deposit thickness provides a useful parameter for this evaluation.

One of the strongest arguments supporting an ice-creep origin for lobate debris aprons is their lobate profile with a concave terminus, consistent with the profile of terrestrial glaciers (1,2,8). The surface profile of a glacier is, to first order, a consequence of the limitation of the basal shear stress of the ice, beyond which flow occurs if the ice behaves as a perfect plastic (10). Numerical solutions for the thickness of mobile ice over irregular bed topography (11) allows glacier profiles to be computed for specified terrains. This technique was applied to the topography of a flat-floored crater (many CCF deposits are in flat-floored craters), using physical constants appropriate for ice on Mars, to determine the profile of materials that could move as a result of ice-creep (Fig. 1). The ice attains a thickness in excess of 200 m within 1 km of the glacier terminus, regardless of the terminus location within the crater, and the thickness steadily increases toward the crater rim. Inclusion of rocky debris with the ice would increase the average density but this would likely reduce the calculated thickness by a factor of two or less. CCF deposits with thicknesses < 50 m would thus be too thin to be mobile by ice-creep, increasing the probability of an aeolian origin.

Four craters in Utopia Planitia (Fig. 2) were used to obtain topographic profiles through photoclinometry (Fig. 3). Profile calculations assume uniform albedo over a given profile and a Lambertian photometric function for the surface materials. This technique has several inherent sources of potential error (12) so the relative relief of nearby features is much more likely to be realistic than the absolute relief across the entire profile. The observed relative relief of the ridges and grooves in the CCF deposits consistently is < 50 m, and in many cases is < 20 m. This thickness is far too small for ice-creep to be active at the base of the CCF layer, increasing the probability that aeolian processes are dominant at this location. Deposit thickness can be a useful constraint for evaluating the relative role of ice-creep and aeolian processes in CCF (and other proposed ice-rich, mobile features) in the martian mid-latitudes.

REFERENCES: 1) S.W. Squyres and M.H. Carr, Science 231, 249-252, 1986. 2) S.W. Squyres, Icarus 79, 229-288, 1989. 3) J.R. Zimbelman et al., Proc. 19th LPSC, 397-407, 1989. 4) R.P. Sharp, J. Geophys. Res. 82, 4039-4054, 1973. 5) M.H. Carr and G.G. Schaber, J. Geophys. Res. 78, 4073-4083, 1977. 6) L.A. Rossbacher and S. Judson, Icarus 45, 39-59, 1981. 7) B.K. Lucchitta, J. Geophys. Res. 89, B409-B418, 1984. 8) S.W. Squyres et al., in Mars, U of Ar. Pr. (in press). 9) S.W. Squyres, J. Geophys. Res. 84, 8087-8096, 1979. 10) E. Orowan, J. Glaciol. 1, 231-236, 1949. 11) S.C. Ackerly, Bull. Geol. Soc. Am. 101, 561-572, 1989. 12) D.G. Jankowski and S.W. Squyres, LPS XXI, 561-562, 1990.

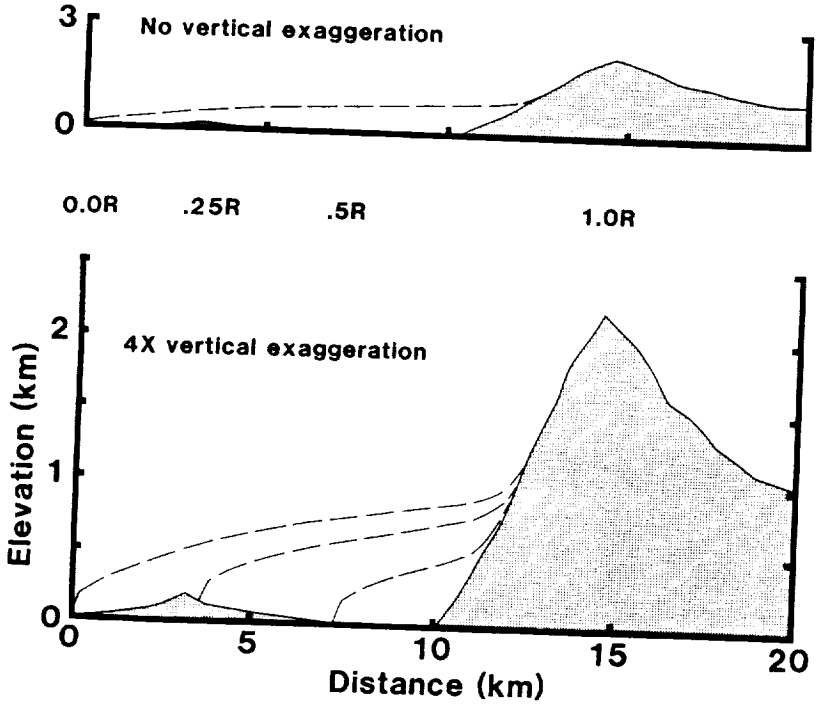

Figure 1. Calculated glacier profiles (dashed lines) within a flat-floored crater under martian conditions. Bottom diagram shows profiles for three termini positions. Thickness of ice exceeds 200 m and it steadily increases toward the crater rim.

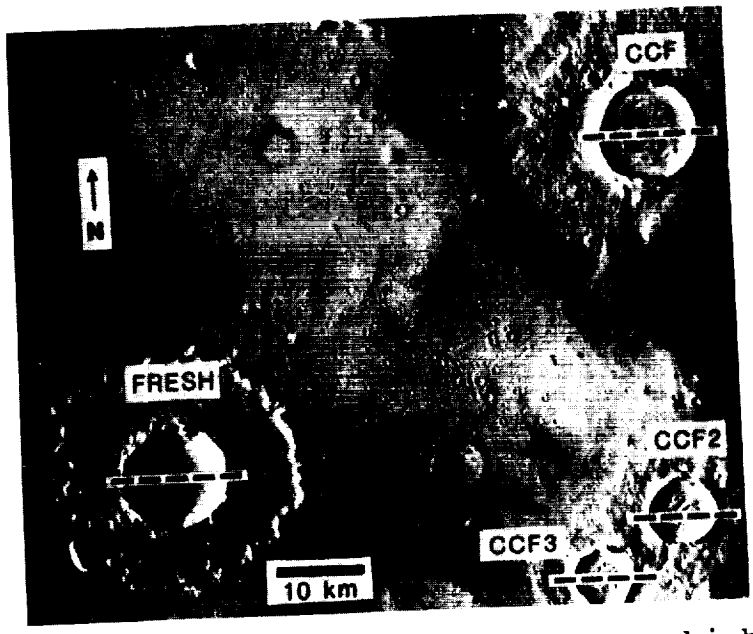

Figure 2. Four craters in Utopia Planitia for which topographic profiles were obtained by photoclinometry. Dashed lines are locations of profiles shown in Figure 3. Crater labeled 'Fresh' lacks CCF. Portion of Viking frame 608A04, 87 m/pixel.

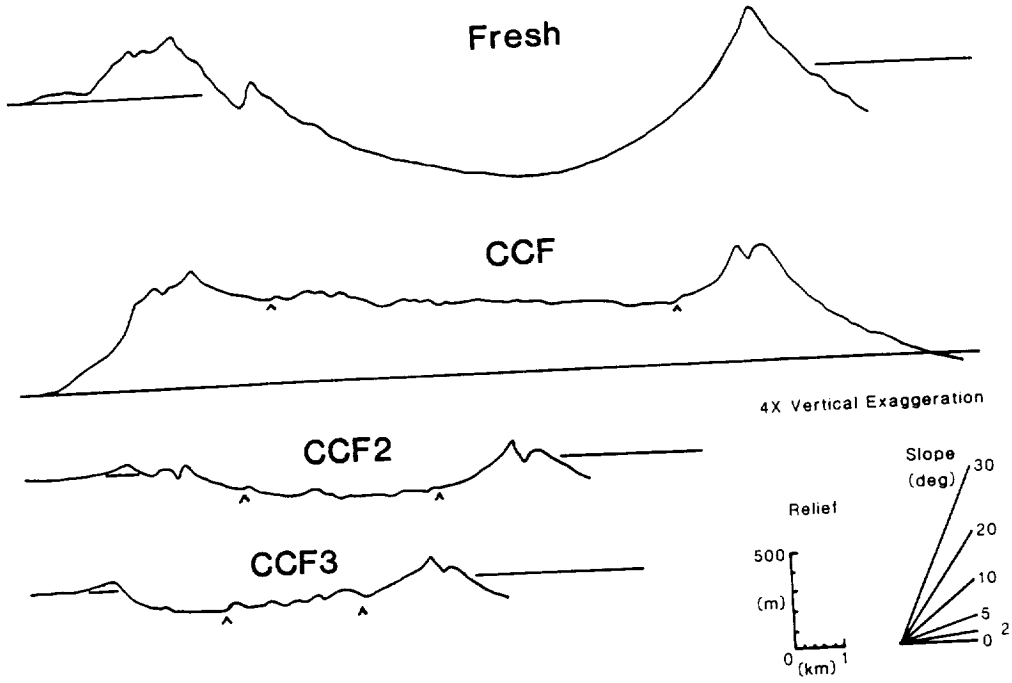

Figure 3. Photoclinometric profiles for four craters in Utopia Planitia. Profiles have 4X vertical exaggeration. Margins of CCF deposits indicated by ^. Local relief of CCF is < 50 m, making it unlikely that the CCF material moved by ice-creep. Compare CCF relief to calculated ice thickness (bottom, Fig. 1).

VOLATILES ON MARTIAN SURFACE. Tomas Svitek and Bruce Murray, California Institute of Technology, Pasadena CA 91125

The focus of our research is on direct determination of crucial microphysics processes which control volatile-related phenomena on Martian surface. Volatiles represent one of most intriguing puzzles on the surface of Mars. What is the reason for asymmetry between residual north and south frosts? How is the presence of water possible in co-existence with the polar cold trap? What is the source of water on seasonal tinescale? Are there low-altitude night fogs? Why dust has such little effect on the atmospheric pressure even if it influences atmosphere and frost in such great extent? How to explain the albedo behavior of residual frost? What is the origin of layered deposists? There could be a long list of questions like this formulated. Obviously, it is beyond the scope of any single study to solve conclusively these critical problems.

Therefore, our approach is to focus on closing the loop — experimental verification of suggested hypothesis. We organize our work in three parts: A) Identification of key questions of microphysical processes related to water and carbon dioxide diurnal and seasonal cycles. B) Feasibility of possible observations and experimental tests to be conducted at Mars during the planned mission of 1990s. C) Experimental investigation of relevant analogs at the terrestrial environment. Our stress is on the small-scale processes which are critical, in our view, for integrating remote sensing data with in-situ observations. Our previous or current investigations included these subjects related to volatiles on Mars:

Viking Lander 2 winter frost. The annual deposition and retreat of the frost layer was observed in-situ by Viking Lander 2. The frost is inferred to be H_2O frost but with some properties suggesting a much thicker layer than would be expected from the simple mass balance calculation. Our original contribution is in considering the effect of cold-trapping (frost redeposition) which has been previously neglected and which enables to reconcile all the observations with environmental conditions. In addition, we believe that this study points to a more general phenomenon of cold-trapping in the Martian environment.

Sublimation of volatile surface under radiation-dominated environment. During the last year we have conducted an investigation of how surface morphology of ice surface will evolve at the sublimation dominated environment. We have proposed a hypothesis that volatile surface under these conditions will always inherently develop towards substantial small-scale surface roughness. This is known to exist at some regions on the Earth and these types of surface features are called penitentes. The presence of these features is caused by positive feedback between roughness and temperature. We have conducted extensive literature search as well as preliminary calculations of this roughness/temperature feedback mechanism. Most importantly, one of us (Svitek) had an opportunity to conduct exploratory field observations and measurements of this effect during 1989/90 season in Antartica. Two conclusions of this investigation are: A) roughness/temperature feedback has dominant effect on small-scale morphology (1-10 cm) of ice surface when radiative heat transfer dominates, and B) further analysis is needed to apply these terrestrial observations to the Martian polar frost. We plan to continue our investigation of micromorphology of volatile surfaces with regard to this temperature/roughness feedback. The next two steps of this effort are: A) To extend our preliminary conclusions based on terrestrial analogs to four combinations possible in Martian environment - H_2O vs. CO_2 and seasonal vs. residual frost. B) To attempt predictions for future missions which will not be able to resolve individual morphological features.

Diurnal and seasonal water cycle. We have concentrated on identifying the key effects which locally control the diurnal water cycle as well as seasonal water vapor exchange between regolith and atmosphere. For example, the effect of inclusion of boundary layer on water vapor, or, the interaction between water and carbon dioxide seasonal frost as seen from correlated MAWD/IRTM/imaging observations by Viking Orbiter. We are also studying possible experimental approaches which would delineate these parameters controlling the diurnal flow of water vapor and interactions between surface and atmosphere. In particular, what role can humidity detector play on some of the proposed platforms for 90s' (balloons, network science, hard landers, etc.). How can we learn about the diurnal cycle from single or multiple humidity detectors? What to look for? What is the proper sensor configuration? What are the requirements on the sensor? We plan to evaluate the techniques of water vapor detection and measurement with the particular emphasis on assessing solid-state sensors which are currently available as commercial units or as prototypes for their application on Martian surface.

EARLY MARS: HEAT FLOW VS. ATMOSPHERIC GREENHOUSE

Fraser P. Fanale and Susan E. Postawko, Planetary Geosciences Div., Univ. of Hawaii, Honolulu, HI 96822

The morphology and distribution of the valley networks seen on ancient martian terrain have been interpreted to indicate a change in erosional style between about 3.8 billion years ago compared to later martian history. While the exact mechanism of the formation of these valley networks in unknown, it appears as though sapping processes rather than precipitation runoff played a dominant role. What does seem clear, however, is that liquid water played a role in their formation. Present conditions on the martian surface seem to preclude the existance of liquid water in the quantities, and for the time periods apparently necessary for the formation of these networks (large quantities of liquid water, such as carved the large outflow channels, and small, transient pockets of water may both be able to exist for very short times under present martian conditions). The mechanism by which these valley networks formed have been the focus of many scientific studies (e.g. 1, 2, 3).

Opinion on the general conditions under which these networks formed is generally divided into 2 camps: one which believes that more clement conditions could have existed on early Mars due to large amounts of CO_2 in the atmosphere, which could have created a large greenhouse warming of the martian surface; and those who do not support a massive greenhouse warming, but advocate warming of the martian surface due to an early, high internal heat flow. In fact, the truth may be a combination of both of these processes. We have derived a quantitative relationship between the effectiveness of an atmospheric greenhouse and internal heat flow in producing the morphological differences between early and late martian terrains.

The relationship between these two mechanisms can be stated in the following way: Although the mean residence time of CO_2 in the early martian atmosphere is not well known, it is almost certainly shorter than the total time over which climatic differences are thought to have occurred (4, 5). Thus, recycling of CO_2 is important in sustaining an early atmospheric greenhouse. Atmospheric CO_2 pressure (and thus surface temperature) may be approximated mathematically as a function of the total degassed CO_2 in the atmosphere plus buried material, and the ratio of the atmospheric and regolith mean residence times. The mean residence time of CO_2 in the regolith can be expressed as a function of heat flow (5). It therefore follows (given assumptions as to regolith conductivity) that the surface temperature may be expressed as a function of heat flow and the total CO_2 in the atmosphere-regolith system. We also know that the depth to the water table (assumed to be the 273K isotherm in this study) can be expressed as a function of heat flow and surface temperature (a boundary condition), again making assumptions as to regolith conductivity. Therefore, for any given values of total available CO_2 and regolith conductivity there exists a set of coupled independent equations which relate heat flow, surface temperature, and depth to the 273K isotherm. This means that for any value of heat flow we can now calculate simultaneous values of surface temperature and depth to the 273K isotherm. Our derivation is

based on relationships already derived in the literature, and only algebraic manipulation of these relationships is necessary for this study. We can utilize these derived relationships to evaluate both the relative and absolute importance of internal heat flow vs. an atmospheric greenhouse effect in producing morphological changes for any value of heat flow, and also for a range of heat flow values reasonable for early Mars.

We have carried out calculations for various values of total available CO_2, regolith conductivity, CO_2 atmospheric mean residence time, and surface temperature-surface pressure relationships (determined by solar output and orbital configuration) for a variety of values of heat flow. Although our exploration of parametric space to date has been somewhat limited, the qualitative characteristics of the system are readily apparent, as illustrated in Figure 1. This figure is for the case of an early cool sun, favorable orbital configuration, and an equatorial site; mean atmospheric residence time of CO_2, and regolith conductivity are the same in both sets of calculations. The figure shows surface temperature (T_s) as a function of depth to the 273 isotherm (Z). The numbers in parentheses indicate heat flow in mW m^{-2}. The figure clearly demonstrates that the relative roles of internal heat flow and atmospheric greenhouse are inextricably interlocked.

Figure 1a is for a total of 3.5 bars of CO_2. According to this figure a heat flow of only about 150 mW m^{-2} (well within the values predicted for early Mars; ref. 6) is more than sufficient to recycle enough CO_2 to keep surface temperatures above freezing. In this case, because we have assumed so much total carbon dioxide, the atmospheric greenhouse plays a dominant role. It has been argued (7) that a water table as deep as 350 meters would still have been capable of creating the observed valley networks by groundwater sapping early in martian history. In this case, the internal thermal gradient would have played a major role in widening the latitude and time bands in which sapping would have been prevalent.

There have been many attempts to estimate the volatile inventory of Mars (e.g. 8, 9, 10, 11). In several of these versions, the total estimated carbon dioxide is 1 bar or less. In Figure 1b we explore the implications of having a low total CO_2 abundance, by assuming a total of 1 bar of CO_2 available to the system. In this case we find that an atmospheric greenhouse effect plays almost no role, and that the depth to the water table is strongly affected by internal heat flow in spite of the fact that surface temperature only varies by a few degrees for reasonable values of early heat flow. For heat flow of about 100 mW m^{-2} the depth to the 273K isotherm is less that 300 m and near the critical depth suggested by (7).

Although our calculations are somewhat sensitive to the values chosen for regolith conductivity, CO_2 atmospheric mean residence time, and total CO_2 inventory, it is clear that heat flow on early Mars plays a key role in both the effectiveness of an early atmospheric greenhouse and in keeping regolith temperatures high enough so that groundwater is closer to the surface. If the total available CO_2 was on the order of 4 bars or more, then an atmospheric greenhouse effect can easily keep near surface temperatures high enough to account for the change in erosional style, and the role of heat flow is to raise groundwater temperatures and extend the space and time regime for

valley network formation. If, however, total CO_2 was on the order of 1 bar or less, then the atmospheric greenhouse does not raise surface temperatures by more than a few degrees, yet a high early heat flow could still keep regolith temperatures high enough to decrease the depth to the water table by a large factor (for reasonable assumptions of regolith conductivity), enabling valley network formation.

References (1) Pieri, D.C. (1980) *Science* **210,** 895-897. (2) Carr, M.H. and G.D. Clow (1981) *Icarus* **48,** 91-117. (3) Baker, V.R. (1982) *The Channels of Mars.* Univ. of Texas Press, Austin, TX, 198p. (4)Fanale, F.P., J.R. Salvail, W.B. Banerdt, and R.S. Saunders (1982) *Icarus* **50,**381-407. (5) Pollack, J.B., J.F. Kasting, S.M. Richardson, and K. Poliakoff (1987) *Icarus* **71,** 203-224. (6) Schubert, G., P. Cassen, and R.E. Young (1979) *Icarus* **38,** 192-211. (7) Squyres, S. (1989) [Abstract] *Fourth International Conference on Mars,* Tucson, AZ. (8) Anders, E. and T. Owen (1977). Mars and Earth: Origin and abundance of volatiles. *Science* **198,** 453-465. (9) Pollack, J.B, and D.C. Black (1979) *Science* **205,** 56-69. (10) Dreibus, G. and H. Wanke (1989) In *Origin and Evolution of the Atmospheres of the Planets and Satellites,* S.K. Atreya, J.B. Pollack, and M.S. Matthews, eds., Univ. of Arizona Press, Tucson, AZ. (11) Pepin, R.O. (1989) To be published in *Icarus.*

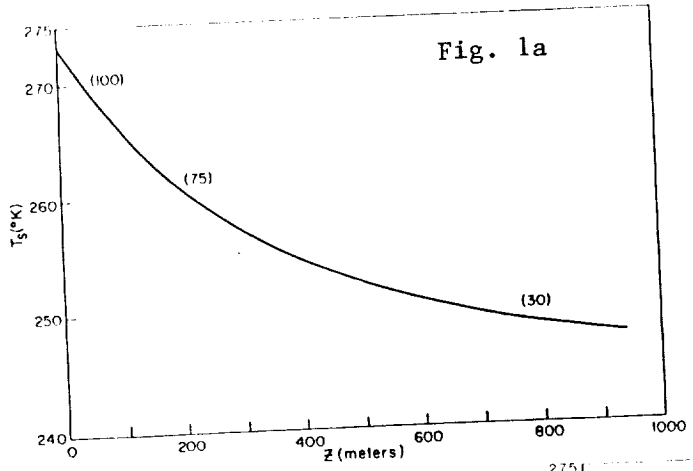

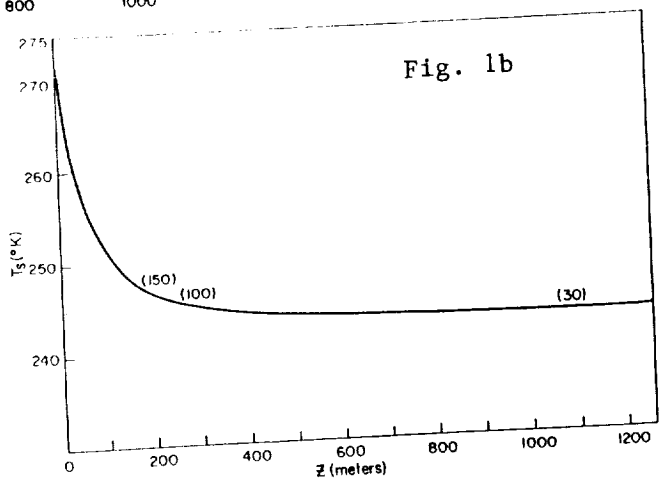

MARTIAN FRETTED TERRAIN: A MINIMUM ESTIMATE FOR THE VOLUME OF MATERIAL REMOVED BETWEEN 270°W AND 360°W

Andrew M. Dimitriou, University of Massachusetts, Amherst, MA 01003.

Since the return of Mariner 9 data, Martian fretted terrain has been a subject of study (1). The morphologic description presented by Sharp (1) of a once continuous heavily cratered plateau which has since been subject to extensive erosion has been accepted in the literature. The plateau remnants stand as positive relief landforms i.e. as "knobs" and "mesas" amidst onlapping stratigraphically younger plains materials. The largest area of fretted terrain on Mars lies between 270°W and 360°W in a 5-10 degree wide zone around 40°N. Studies done in this area have concentrated on the nature and origin of the debris aprons and fretted valley floor lineations (2,3). Principal component analysis (4) was attempted on the outlying "mesas" in order to associate the observed pattern of occurrence with structural trends and erosive events. This abstract describes a method used to estimate the volume of plateau material that has since been removed from this area of fretted terrain. Relatively strict lower limits are placed on these estimates by this method, upper bounds are more uncertain because the extent of plateau material buried beneath plains to the north is difficult to infer. This estimation is useful because the region is a clear source of material that could then be redistributed, and it is possible that the lowlands to the north have been a sink for this material. Comparing these source volumes to the amounts of material inferred to be burying large areas of the lowlands can put this regional contribution into a global context.

Three models are presented for the former extent of a once continuous heavily cratered plateau that has since been dissected and eroded. Within these model areas, outlying "mesas" and "knobs" (hereafter termed mountains) are split into two groups by surface area for analytical purposes. Mountains >40 km^2 are termed large mountains, those <40 km^2 small mountains.

Identical southern and western limits for all three models are defined by the present boundary between fretted terrain and the heavily cratered plateau. The northern limit for all three models is gradational and thus less clear. The northern boundary for the three models between 300°W and 350°W is inferred to be the limit of occurrence of large (>40km^2) mountains. This is an irregular east-west trace at about 49°N. East of 300°W, the three models have different and distinct NE limits, all of which are separate from the present limits of fretted terrain. The model areas are defined by these NE limits.

The smallest area (model 1) is bounded to the NE by a northwestward extension of the NW trending graben on the upland surface at about 38°N, 305°W. Extending a visible upland trend into what is now lowland is necessary if the assumption is made that these graben are the observable traces of a series of NW trending boundary faults that dropped plateau material to the north and east. Many of the long axes of the remnant mesas standing in this area of lowland appear to be oriented parallel to this northwest trend. If this model defines the true initial northern limit of the plateau, then the assumption that a continuous plateau was available for erosion cannot be made north and east of this zone.

Model 2 includes the model 1 area but its northeast limit is farther eastward and is defined by a NW trace at the abrupt limit of occurrence of outlying mountains which is noted most clearly around 43°N, 298°W. One possible explanation for this abrupt loss of mountains is that it represents a rapid drop in basement elevation. For this model, this trace is taken as the limit of a continuous plateau surface which has since been dissected, eroded and embayed by younger materials.

Model 3 includes not only the model 2 area but also an additional zone to the east as far as a NW trace defined by the trend of the large mesas centred on 35°N, 280°W. Wilhelms and Squyres (5) identified these as rim remnants of their putative 7700 km diameter Borealis basin. North and east of this boundary, there is no observable evidence to indicate that a continuous thickness of plateau material was available for removal.

For each of the three model areas, the areal extent was digitised, as were the exposed surface areas of all large mountains within the relevant model. Shadow measurements were made at 16 locations on the continuous plateau boundary scarp and a mean height of 1.42 ± 0.52 km was determined. The quoted error not only includes the standard deviation, but a 2 pixel vertical error to account for slope rounding and shadow margin location problems as detailed by Parker et al. (6). Shadow

measurements were made on 39 large mountains using the same method with the mean height of 1.45 ± 0.69 km agreeing very well with that obtained from the scarp. In order to account for the volume of residual plateau material remaining within the model areas in the form of small (<40km^2) mountains, five small subareas were located where the resolution allows a confident assessment of the surface areas and heights of these small mountains to be made. Across these five subareas an average of 3.3% of the surface is covered by small mountains. This is assumed to be a fair estimate across all three of the model areas. Shadow measurements made on 45 small mountains yielded a mean height of 0.78 ± 0.41 km. Ten shadow measurements were made on the margins of debris aprons visible on the extremely high resolution orbit 461B Viking images and a mean height of 0.07 ± 0.02 km was determined. It was assumed that the entire lowland within each model area was completely buried by a debris blanket of the above thickness. This overestimates the volume remaining in these debris aprons, but removes the necessity for identifying the extent of all debris aprons within the model areas.

Volume removal estimates range from 1.04 ± 0.60 M km^3 for model 1 through 1.53 ± 0.80 M km^3 for model 2 to 1.99 ± 1.10 M km^3 for model 3. This is equivalent to a global layer of between 3 and 21 m of sediment. If the northern lowlands is the sole sink for this material, this represents a layer of between 9 and 60 m. These are minimum estimates for three reasons: (i) the thickness of plateau material measured does not represent the height above pre-plains basement but the height above the younger plains deposits (ii) the northern inferred plateau limit is conservative; more plateau material may lie buried (iii) the mountains were assumed to be flat-topped and have vertical cliff faces but are often conical or significantly rounded in cross-section.

The sediment derived from this area of fretted terrain is only a very small proportion of the total present in the northern lowlands, since the volume of young material that is assumed to be present to the north is significantly greater than that estimated above.

(1) Sharp, R.P., J. Geophys. Res., 78, 4073-4083, 1973.
(2) Squyres, S.W., Icarus, 34, 600-613, 1978.
(3) Squyres, S.W., J. Geophys. Res., 84, 8087-8096, 1979.
(4) Kochel, R.C., and R.T. Peake, J. Geophys. Res., 89, C336-C350, 1984.
(5) Wilhelms, D.E. and S.W. Squyres, Nature, 309, 138-140, 1984.
(6) Parker, T.J., et al. Icarus, 82, 111-145, 1989.

EPISODIC FLOW IN MARTIAN CHANNEL SYSTEMS. R. A. De Hon, Department of Geosciences, Northeast Louisiana University, Monroe LA, 71209.

INTRODUCTION (FLOW THROUGH MARTIAN CHANNELS)

The outflow channels of Mars are compariable to scablands formed by catastrophic floods associated with glacial outbursts on earth (1,2). Because these outflows traverse surfaces unmodified by previous alluvial processes, the flow is consequent. Hence, the flow travels downslope controlled by the natural configuration of the topography. The flood surge may exist as an unconfined or semiconfined flow over much of its length. The surge may be broken into various anastomosing branches that may or may not recombine at lower elevations. In addition, ponding along the various flow reaches retards the flood crests within each reach. The recombined flow at the terminus may appear to be episodic.

Terrestrial analogs of martian outflow systems are seen best in glacial catastropic outflows as in the channeled scablands (1,2) and jokulhlaups in Iceland (3,4). Other analogs of possible significance in understanding the flow history and its erosional and depositional characteristics include the advance of flood crests during spring floods; multiple sequential dam failures along a valley sequence; and, perhaps, interbasinal drainage in arid regions. Martian outflow systems provide an ideal example of drainage development on a previous undeveloped surface.

MARTIAN EXAMPLES

Lunae Planum Outflow Complex. Maja Vallis originates from Juventae Chasma and associated chaotic terrain on the eastern edge of Lunae Planum. The flow is traced northward for about 1000 km along the contact between Lunae Planum ridged plains-forming material and cratered terrain of Xanthe Terra. The flow ponded on northern Lunae Planum (5). It spilled over the Xanthe Terra highlands in numerous subparallel, anastomosing channels and collected in a basin behind the ridge system on the western edge of Chryse Planitia (6,7). As the water level rose, it crested the ridges and continued as a recombined flow northeast into mid-Chryse.

Mangala Vallis. The Mangala Vallis outflow originates in the Memnonia Fosse region in Terra Sirenum. The outflow spreads northward for 450 km where it bifurcates. One segment, Labou Vallis, branches northwestward as the main flow, Mangala, continues to the north. For 350 km, Mangala is traced as multiple channels across cratered terrain to Amazonis Planitia. Craters traversed by Labou are characterized by smooth, sediment-filled floors. Craters traversed by Mangala below the bifurcation are also sediment filled, but some fills are dissected by channels indicating more than one episode of flow through the system.

Kasei Vallis. Kasei Vallis originates on the west side of Lunae Planum. Beginning in a wide box canyon rimmed by chaotic terrain, the outflow scoured a 300 km wide path as it travelled northward and turned eastward to cut across Lunae Planum and Xanthe Terra. The flow finally dissipates 2000 km from its source, in mid-Chryse Planitia (6). Along its path, the flow was split by two major blocks of terrain and by many smaller massifs and craters.

Elysium Channels. Granicus Valles, originating 200-300 km northwest of Elysium Mons, is traced northwestard for about 1000 km. The system appears to begin at grabenlike troughs. Unlike Mangala and Maja, the multiple anastomosing channels are narrow and deeply incised, but like Maja, water flowing through the system would have been split and recombined many times.

EPISODIC FLOW

De Hon, R. A.

FLOOD CREST RETARDATION

A flood crest originating by rapid release at the source will be directed by the natural configuration of the surface. Where hydrologic routing separates the flow into two or more semiconfined or confined flows, the flood waves will traverse each reach at different rates depending on the characteristics and lengths of each segment. Upon rejoining, retardation in one reach in respect to the other results in a prolonged, reduced flow of multiple flood crests in the recombined flow system.

Ponding in flow-breached craters and other natural basins along each segment will temporarily impede the flow until it fills the basin and spills over. Each such basin becomes the origin of a new, but delayed, flood crest. Ponding along individual reaches of a multiple channeled system will further separate the flow crests in the recombined flow regime. Multiple serial ponding may be seen along Labou Vallis, and multiple parallel ponding (ponding in different segments before recombining) may be seen in the lower Mangala Vallis system.

Not all flow is recombined. In some Martian outflow systems, the flow diverges to different terminii. In the Mangala Vallis system, Labou Vallis branches northwestward from Mangala. Further downstream the Mangala system divides again to form two major branches which feed a multitude of smaller distributaries near the lower reaches along the highland escarpment.

IMPLICATIONS FOR EROSION AND SEDIMENTATION

1. The initial outflow has high capacity at release and a correspondingly high erosion rate. If the flow is impounded along its course, sedimentation occurs within the site of ponding. Release from secondary storage results in renewed erosional capacity downstream.

2. Retardation of flow in different drainage courses of an anastomosing system results in episodic flow in the downstream region which looks like prolonged release from the source area. Thus, a single outburst is translated into prolonged flow at great distance from the source. A large number of "baffles" in the system could translate an outburst into a sustained flow with minor surge crests.

3. Retardation by ponding imposes major retardations and correponding large renewed surge crests. Ponding near the terminus translates into a single, delayed surge at the terminus.

4. If the outflow channel has no interuptions, sediments at the downstream terminus could be derived from along the entire length of the system. On the other hand, if the flow ponded, sediments at the terminus are derived from below the last site of impoundment.

5. Erosion and deposition in the terminus reflects varying energies in the system as the flow regimen changes with each surge and nonsurge episode.

6. Floods diverted to multiple terminii result in multiple deposits. If the terminii are sufficiently close together, they may build overlapping deposits which would, at first glance, indicate different periods of activity.

DOWN CHANNEL HISTORY

The record of a flow from its source to terminus need not be uniform. A single outburst can be ponded, routed through multiple channels, and recombined. Near the source the flow history is simple and channeling a result of a single surge and its decreasing volume with time. In the mid-reaches of the flows course, the diversions into multiple channels and multiple retardations by local ponding break the surge into multiple routes and multiple surges. The record of the flow as preserved by erosional and depositional forms becomes more complex downstream.

KASEI VALLES REGION FLOOD FEATURES

Figure 1. Scoured and grooved channel floor; arrows show three directions of water flow possibly indicative of separate flood events (Viking image 226A10, centered near lat 25° N., long 61°).

Figure 2. Impact crater in channel; crater was formed before and degraded by early catastrophic flooding that scoured channel floor (Viking image 664A07, centered near lat 23° N., long 74°).

Figure 3. Impact craters (arrows at A) formed after early high-water stage that deeply eroded terraces; craters have been truncated by later floods along lower part of valley floor. A post-flood crater is shown at B (Viking image 665A20, centered near lat 27° N., long 68°).

CHYRSE BASIN OUTFLOW CHANNELS, MARS: POST-FLOOD MODIFICATION, CHANNEL EVOLUTION, AND SOURCE CONSIDERATIONS

R. Craig Kochel, Department of Geology, Bucknell University, Lewisburg, PA 17837
Jerry R. Miller, Quaternary Sciences Center, Desert Research Institute, Reno, NV 89506

Introduction The channels surrounding southern Chryse Planitia on Mars have been interpreted by most investigators as the erosional product of catastrophic floods which eminated from equatorial source regions of chaotic terrain. Geomorphic interpretations of channel morphology indicate significant flood flows did occur, but there is considerable range in estimates of flow volumes. Carr and others (1987) estimated that the total volume of material eroded in the Chryse region was $4 \times 10^6 km^3$, requiring at least 6×10^6 km^3 of water.

One of the foremost unresolved questions regarding channel evolution is the apparent disparity between the relatively small volumes of source chaos regions and the extensive downstream reaches. In addition, there has been considerable debate regarding mechanisms capable of releasing water at rates consistent with the large-scale flooding dictated by the interpretation of erosional and depositional landforms downstream. Our investigation integrates data from Viking images and flume experiments to suggest that there may be much less disparity between source and channel volumes than previously assumed.

Post-flood Modifications Systematic mapping and interpretation of the channel margins of the Chryse channels show that post-channeling volume modifications have been significant (Table 1). Volume enlargement since flooding along representative mapped reaches varies between 0 - 33%, while weighted averages accounting for the size of the mapped areas within each channel range from 4 - 21%. Channel retreat processes include rockfall, debris flow, slumping, and groundwater sapping. The importance of these processes varies spatially along the channel walls and between channels; possibly giving indications of significant variations in the composition of host terrains, distribution of volatiles (water), or regional geothermal conditions in the Martian regolith.

Kasei Vallis is the most deeply incised of the Chryse channels. Its extreme depth and large volume may be partly attributed to structural extension from the Tharsis uplift (Schumm 1974). Orientations of geomorphic features in Kasei Vallis conform with trends of regional structural features (Kochel and Burgess 1983, Chapman and Scott 1989). Floods in Kasei Vallis probably modified a pre-existing structural trough similar to the Valles Marineris system. The extensive post-flood degradation of valley walls in the Kasei system may have been greatly facilitated because of its extensive incision and intersection with crustal discontinuities (Davis and Golumbek 1989, MacKinnon and Tanaka 1989) not encountered in the other less incised channels to the east.

TABLE 1
POST-CHANNELING ENLARGEMENT

Section	Total Channel Area (km^2)	Post-Channeling Area (km^2)	Enlargement Percent
KASEI VALLIS			
K-1	37,020	3,360	9
K-2	2,124	375	18
K-3	7,261	1,984	27
K-4	204	68	33
K-5	8,986	2,607	29
K-6	26,718	8,544	32
		WEIGHTED PERECENT = 21%	
MAJA VALLIS			
M-1	131	21.4	16
M-2	451	9.3	2
M-3	10,260	616	6
		WEIGHTED PERCENT = 6%	
EASTERN CHANNELS			
E-1	136	10.7	8
E-2	892	185	21
E-3	806	20	2
E-4	28,515	1,549	5
E-5	18,476	0	0
E-6	11,260	961	9
		WEIGHTED PERECNT = 4%	

References Cited

Baker, V.R., and Kochel, R.C, 1978, Proc. 9th Lun. & Plan. Sci. Cf., 3193-3203.
Carr, M.H., 1979, J. Gephys. Res., 84, 2995-3007.
Carr, M.H., Wu, S.S.C., Jordan, R., and Schafer , F.J., 1987, Abs. 18th Lun. & Plan. Sci. Cf., 155-156
Chapman, M.G., and Scott, D.H., 1989, Proc. 19th Lun. & Plan. Sci. Cf., 367-375
Davis, P.A., and Golumbek, M.P., 1989, Abs. 20th Lun. & Plan. Sci., 224-25.
Kochel, R.C., and Burgess, C.M., 1983, NASA TM 85127, 288-290.
Komar, P.D., 1983, Geology, 11, 651-54.
MacKinnon, D.J., and Tanaka, K.L., 1989, J. Geophys. Res., 94, 17,359-17,370
Schumm, S.A., 1974, Icarus, 22, 371-374.
Waitt, R.B., 1980, J. Geology, 88, 653-79.

The disparity between the source area and channel volumes is greatest for Kasei Vallis and assumed Echus Chasma source and least for Maja Vallis and its Juventae Chasma head. Geothermal heating from the Tharsis volcanic region may have produced diffuse but widespread regional thermal degradation of frozen ground along western Lunae Planum. Widespread fretting in the form of arcuate scarps along the upstream segments of Kasei Vallis may represent the last stages of this style of terrain degradation. Water released from this formerly frozen regolith would likely have been ponded in large lakes upstream from the incised reach of Kasei Vallis (near the big bend). Once lake levels overtopped the divide, catastrophic flooding would have occurred in the Kasei structural trough.

In contrast to Kasei Vallis, Maja Vallis and the eastern Chryse channels exhibit much less incision into Lunae Planum host rocks and show less disparity between source and channel volumes. Their increased distance from the Tharsis volcanic center may have precluded wholesale degradation of ground-ice. Melting appears to have been limited to more localized intrusive activity of the scale represented by Juventae Chasma chaos (Maja Vallis) or the Hydaspis Chaos source area of Tiu Vallis.

Channel Evolution Observations of the morphology of outflow chaos source areas are not consistent with models suggested for catastrophic release of fluids from a confined subsurface aquifer (Carr 1979). Chaos typically appears as an assemblage of fractured host terrain which appears to have collapsed, but there is no evidence of significant flows from within the fractures. Evidence of flood flow begins 10's of km downstream where streamlined islands and erosional features are first observed. Many times, these flood features occur immediately downstream of sites interpreted as temporary impoundments (Fig. 1). We propose that water emerged slowly from subsurface reservoirs beneath the chaos through fractured crust and subsequently ponded. The numerous impoundments evident in the eastern Chryse channels may initially have been lows in the Martian terrain or they may have formed by a combination of ice and debris dams during various stages of outflow channel evolution. Periodic decay of these dams would have provided a mechanism for releasing floods episodically down the channels. If dams involved significant quantities of ice, they may have failed periodically when impounded waters reached critical depths enabling them to hydraulically buoy up the ice dam and dump the water in a manner suggested by Waitt (1980) for episodic release of Scabland floods.

Geomorphic evidence for multiple episodes of flooding have been observed in all Chryse outflow channels, including: 1) distinct levels of channeling; 2) distinctive streamlined islands; 3) cross-cutting relationships between channel erosion and mass wasting along channel walls; 4) cross-cutting relationships between flow processes and formation of channel floor chaos; and 5) ponding, divide overflow, and episodic release of impounded water.

Terracing is common along most of the Chryse channels. The presence of terraces implies that flows were either episodic and/or that they occurred concurrent with base level lowering accompanying channel incision during floods of substantial duration. Interaction of flow processes with mass wasting of channel walls (observed in Kasei Vallis and the eastern Chyrse channels) suggests that flood flows were distinctly episodic.

Streamlined Islands and Thermal Erosion Steamlining of objects by fluid flow occurs due to an attempt of the feature to modify its shape into a form exhibiting minimal resistance to flow (Baker and Kochel 1978; Komar 1983), resulting islands of airfoil shape with L/W values between 3 - 4. We performed a series of flume experiments using a variety of resistant obstacles to observe the evolution of streamlined forms in flows of varying discharge and base level conditions. These experiments indicate that significant streamlined island relief (of the style visible in Chryse channels) can only be created during conditions of steadily declining base levels, irrespective of discharge. This is consistent with our model of channel formation by episodic flows of modest discharge. We also observed distinctive alterations in island morphology coincident with minor changes of incident flow approach. The long axis of islands dramatically shifted with minor changes in flow direction.

Abnormally wide islands were formed under conditions of variable flow direction during their evolution. Particularly narrow islands (high L/W ratios) were formed when buried obstacles were exhumed as channels degraded with falling base level. Island extension was faciliated by flow interference with the channel walls in these cases. A similar process may be invoked to explain some of the very long and narrow forms on Mars.

Runs using ice-cemented blocks of sediment also yielded streamlined forms when done under conditions of falling base level. However, the final product was a streamlined island without an apparent upstream obstacle due to its thermal decay. Similar processes may explain many of the Martian forms lacking apparent resistant obstacles at their upstream ends.

There is considerable geomorphic evidence to suggest that the eastern Chryse channels developed by a complicated series of multiple flows, multiple sources, and smaller floods triggered by repeated failure of temporary enchannel impoundments. The assemblage of morphologic observations taken together with the streamlining experiments suggests that observed channel features could have been formed by a series of smaller floods, rather than few exceedingly catastrophic flows. This model provides a reasonable mechanism to avoid difficult arguments requiring catastrophic release of large water volumes from subsurface aquifers and is consistent with the observed morphology of source chaos regions.

Figure 1. Regional view of Tiu and Simud Vallis depicting multiple chaos areas (h) multi-level channels (c), terraces (t), and numerous ponded reaches (p).

HYDROTHERMAL SYSTEMS AND THE FORMATION OF FLUVIAL VALLEYS ON MARS; Virginia C. Gulick and Victor R. Baker; Departments of Geosciences and Planetary Sciences; University of Arizona, Tucson, Arizona, 85721.

On Earth, the formation of fluvial valleys requires replenishment and mobilization of surface-water and ground-water reserves by rainfall-runoff processes. Such a cycle is needed in order to persistently drive water flows in the surface environment sufficient to cause erosion. On Mars, however, it is unclear whether a similar atmospherically-induced hydrologic cycle ever existed or whether such an atmospheric system was even necessary to form the valley networks. Alternatively, the Martian hydrologic cycle may have been driven by endogenetic processes. Localized, but intense hydrothermal systems, such as those produced by impacts or volcanic activity in a permeable water-rich subsurface may be able to generate persistent energy gradients sufficient to form valleys. Hydrothermal circulation can melt and mobilize large amounts of ground water, drive it into the surface environment and subsequently recycle this water over prolonged time periods. To evaluate this possible endogenetic water source, we are studying the small valleys which formed around impact craters and on the flanks of volcanoes. Hydrothermal circulation produced by these particular geologic events are especially conducive to study because the associated thermal anomalies can be estimated.

In order to investigate the potential of hydrothermal systems as a viable way of forming fluvial valleys, we are employing the following techniques: 1) detailed geomorphic mapping of valleys associated with impact craters and volcanoes, 2) developing physical and conceptual models of how valleys can be formed in the presence of active hydrothermal systems, 3) simulating the associated fluid movement and energy transport in the subsurface by numerically modelling hypothesized hydrothermal systems, and 4) evaluating whether the resulting quantities of water and energy delivered to the surface environment over the lifetime of the hydrothermal system are sufficient to erode the landsurface and produce the observed valleys.

Several observations from our photogeologic studies regarding the history of fluvial valley formation on Mars may yield some insight into the environment in which they formed. Valleys developed throughout Mars' history from the Noachian into mid-Amazonian times. During this period valley development went through distinct style changes which appear to be related to major changes in Mars' impacting and volcanic history. These changes are marked by early runoff valley development in Noachian-age terrains, followed by reactivation of these valleys and the formation of the large, structurally controlled valleys (*e.g.*, Nirgal Vallis) during the late Noachian/early Hesperian, and finally a return to runoff valley development, though restricted to isolated regions, from late Hesperian to mid-Amazonian [1]. The youngest and most developed fluvial valleys identified so far are located on a mid-Amazonian aged mantling unit ($\approx$ 440 craters $>$ 1 km in diameter per 10^6 km^2) on the northern flank of Alba Patera. Detailed observations reveal that most of the valleys formed on Mars appear to be associated with contemporaneous heat sources. Many of the Noachian age tributary valleys (where they can be traced) emanate from craters. Valleys are also present on some volcanoes, but not on others, even though they may be similar in age. Large-scale sapping valleys formed in the intercrater plains, a terrain which is thought to be largely volcanic in nature. Any hypothesis invoked to explain valley formation on Mars must be able to account for these observations. An endogenetically-induced hydrologic cycle is consistent with such constraints.

We have developed physical and conceptual models of how hydrothermal circulation may result in the formation of fluvial valleys. Figure 1 is a hypothetical cross-section of an active hydrothermal system as might be produced by a magmatic intrusion associated with volcano formation on Mars. Depending on the size of the intrusion, ground-ice within several tens of kilometers could be melted, providing additional ground water to the system. Heat transfer from the magma to the surrounding region would then produce perturbations in the subsurface flow field resulting in a net flow of water toward the surface. Water may reach the surface in the form of liquid or vapor or both. The time it takes for the water to re-enter the ground water system to repeat the process depends on the surface and near surface lithologic conditions. The path that this hydrothermally derived water takes has important implications for fluvial valley formation. On the left flank, the surface is composed of permeable basalt so water quickly infiltrates and recharges a near surface aquifer. The water again intersects the surface farther down the flank forming a seepage face. At this site, sapping processes (erosion by ground-water outflow at the surface) may eventually form a valley. On the right flank (see also Figure 2), the surface is mantled with ash. This ash, which is much less permeable

than the underlying basalt, allows more water to flow on the surface. With continual surface flow, water will start to concentrate and downcut into this erodible surface and eventually form a runoff valley.

Figure 2 is a model of how fluvial valleys may form by ground-water outflow. Although terrestrial runoff valleys are generally formed by precipitation–runoff, it may also be possible to form runoff valleys from emerging ground-water outflow. If the seepage face intersects the surface environment on a very gently sloping landscape ($< 5°$) and if the surface downslope of the seepage is such that the rate of runoff is greater than the rate of infiltration (*e.g.*, ash mantled), runoff valleys may form. However if the ground water emerges from a spring or seepage face on a cliff or steeply sloping landsurface, headward erosion may occur and result in the formation of sapping valleys. This model of valley pattern development and morphology is consistent with those proposed for small valleys in the heavily cratered terrain [3,1] and on the Martian volcanoes [4,5,6].

As on Earth, Martian hydrothermal systems could affect the local climate. The warmer, more moist environments which develop near regions of vigorous hydrothermal activity, may have induced areas of precipitation particularly along the perimeter of these zones. Even snow accumulation in such regions could yield surface water flow under present climatic conditions [7]. Such activity would result in a fuller, more developed drainage pattern (Figure 2). If hydrothermal systems were particularly widespread as implied by the increased frequency of large impacts and volcanic activity early in Mars' history, then such systems may have induced a temporary global atmospheric hydrologic cycle [2,8]. Similarly, formation of the Amazonian-age Alba valleys might have received additional moisture from outflow channel discharges [4].

Preliminary calculations indicate that typical hydrothermal systems which might have been produced on Mars, should have persisted long enough to have formed the valleys observed on impact craters and volcanoes. Thermal anomalies in a dry, 300 kilometer, impact basin could remain for over 10^8 years [9]. Based on terrestrial models, an active hydrothermal system may decrease this value by a factor of 2 to 3 [7]. Possible hydrothermal systems produced by a volcano (*e.g.*, Alba Patera), assuming a Mauna Loa sized magma chamber (350 km^3) may persist for 10^5 years [11]. However, repeated intrusions of magma would greatly extend the life of the hydrothermal system [12]. In comparison, well-integrated fluvial valleys on Earth can form in approximately 10^5 years. Therefore, typical hydrothermal systems on Mars should have been able to remain active long enough to circulate and focus adequate quantities of fluid up through volcanic or impact structure to form the valley networks. Such a system would be limited only by the quantity of water available and by the rate at which this water can be recycled.

Numerical simulations of idealized hydrothermal systems are currently being carried out to determine volumes and rates at which water can be cycled into and out of the hydrothermal systems. We are assuming appropriate parameters and boundary conditions for the hypothesized Martian hydrothermal systems, including, the melt or magma's latent heat of crystallization and initial temperature, and the density, flow or fracture porosity, and initial permeability of all system components (basalt, fractured basalt, brecciated basalt, regolith, ejecta, gabbro, and gabbroic anorthosite).

As computer modelling continues, we will determine those parameters which influence the hypothesized hydrothermal systems. We will thus determine how important and widespread hydrothermal systems may have been in Mars' fluvial history.

REFERENCES

[1] Gulick, V.C. and Baker, V.R. 1990, *LPSC* **XXI**, 443–444. [2] Gulick, V.C. and Baker, V.R. 1989, *LPSC* **XX**, 369–370. [3] Baker, V.R. and Partridge, J.B. 1986, *JGR* **91**, 3561–3572. [4] Gulick, V.C. and Baker, V.R. 1989, *Nature* **341**, 514–516. [5] Gulick, V.C. and Baker, V.R. (in press) *JGR*. [6] Gulick, V.C. 1987, MS Thesis (Dept. Geosciences, Univ.of Arizona), 102p. [7] Clow, G.D. 1987, *Icarus* **72**, 95–127. [8] Baker, V.R. *et. al.*, 1990, *LPSC* **XXI**, 40–41. [9] Bratt, S.R. and Solomon, S.C. 1981, *LPSC* **XII**, 109–111. [10] Norton, D. 1984, *Ann. Rev.Earth Planet. Sci.* **12**, 155–177. [11] Gulick, V.C. *et al.*, 1988, *LPSC* **XIX**, 441–442. [12] Brikowski, T., and Norton, D., 1989, *Earth Planet. Sci. Lett.* **93**, 241–255.

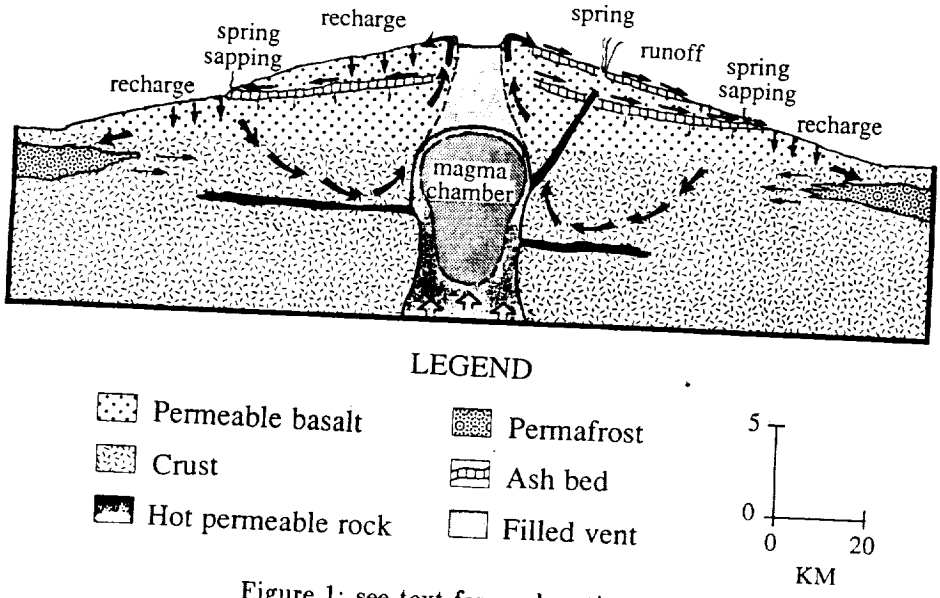

Figure 1: see text for explanation

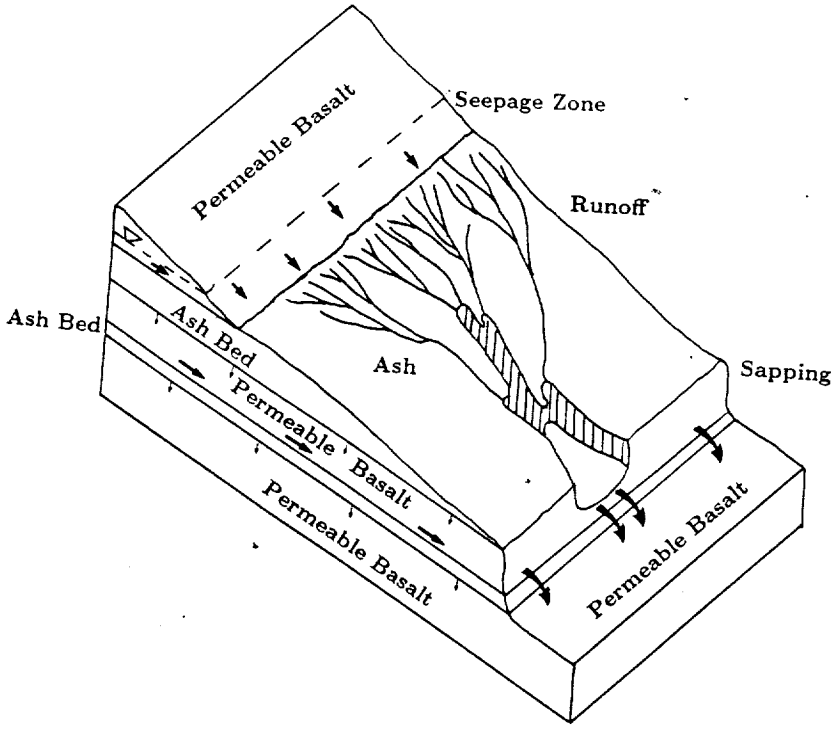

Figure 2: see text for explanation

MARTIAN PALEOHYDROLOGICAL CYCLES

Victor R. Baker, Department of Geosciences
University of Arizona, Tucson, Arizona 85721 U.S.A.

Introduction. Mars is a planet characterized by strange anomalies. Despite its extensive areas of relict heavily cratered terrain and very low average denudation rates (1), Mars has experienced discrete episodes of crater erosion (2,3), including the planation of crater rims, probably by fluvial action (4). Despite its modern cold, dry climate and low atmospheric pressure, Mars displays extensive evidence of periglacial (5,6,7) and ice-related permafrost features (8,9), probable glacial features (10, 11), and lacustrine features (12, 13). Most anomalous are the extensive valley networks (14, 15), which require the persistent action of a hydrological cycle for their origin (16). Groundwater sapping processes are indicated for the genesis of most valleys (14, 17, 18), but sapping cannot be maintained without long-term head differentials to drive water flow in subsurface aquifers. The required persistent flow cannot be achieved by merely melting an ice-rich permafrost. Although most valley networks date from the heavy bombardment period (15, 19) of late Noachian in age, anomalously young valleys formed in the Hesperian (20) and Amazonian (21).

Models that explain valley development on Mars by a warm, wet early climate (22) are inconsistent with anomalously young valley, glacial, periglacial, and lacustrine features on the planet. Endogenetic mechanisms, including thermal effects of cratering (23) and volcanism (24, 25), could produce local hydrothermal cycling of water, but regional patterns then become anomalous. Moreover, the most spectacular fluvial features on the planet, the outflow channels, are highly concentrated in time and space. Originating by cataclysmic water flow from endogenetic sources (26, 17), the outflow channels all debouched their immense discharges to the northern plains. There, ponded sediments (27, 28) imply immense lakes (29) or a single large innundation (30) of temporary duration.

Global Model. Baker, Strom, Croft, Gulick, Kargel, and Komatsu (31) inferred that the ponded water of the northern Martian plains, named Oceanus Borealis, was a key element of a cyclic causative system that ties together the diverse anomalies described above. The ocean-land-atmosphere interactions implied by this model provide a unifying theme binding together diverse consequences and suggesting exciting new connections. Whether one is antagonistic or favorably disposed to this concept, the work toward either its confirmation or rejection will be especially productive for bringing together seemingly unrelated aspects of Martian geomorphology.

In its preliminary form (31) the model involves the concentration of volcanism in the Tharsis area during post-Noachian Martian planetary history. Massive and rapid emplacement of magma beneath this bulging hot spot, perhaps analogous to terrestrial rift volcanism (32), drove out huge quantities of water from subsurface aquifers confined by ground ice (33). Driven by volcanic heat, the cataclysmic flows emanated from the equatorial zone of fractures peripheral to the Tharsis Bulge. The huge water volume concentrated in the fractures plus ponded water in the Valles Marineris (13) all became rapidly transferred to the Northern Plains. The cataclysmic influx of warm flood water would have vaporized the carbon dioxide ice of the north polar cap. Subsequent evaporation of water and sublimation of the Oceanus Borealis ice cover should have occurred at atmospheric pressures elevated well above present conditions. Cataclysmic ocean formation would produce a transient greenhouse atmosphere of water vapor and carbon dioxide. As Martian temperatures rose, other water frozen in permafrost would be released to the Oceanus Borealis. Possible release of adsorbed CO_2 in the previously cold regolith (34) could have provided an additional feedback mechanism. The resulting maritime climate would have made precipitation possible. This maritime climate was probably relatively short-lived, similar to terrestrial glacial climates, and may have been modulated by cycles of planetary obliquity and orbital eccentricity.

A key factor in the duration of an ocean interaction cycle on Mars is the probable very high infiltration capacity of Martian surface materials. Except at local sites with volcanic ash (21) or eolian covers, precipitated liquid water would infiltrate and then suffer prolonged storage in the ground-water zone. As more water became sequestered in the subsurface by recharge into the heavily cratered uplands, the reduction in ocean size probably produced the negative feedbacks that returned the planet to its predominant cool, dry state.

Implications. The above ocean-land-atmosphere cycling is best evidenced by late Hesperian to Amazonian features of Mars. Repeated volcanic activity at Tharsis and Elysium could have produced recurrences of the scenario at varying scales of spatial and temporal effect. Over the entire history of Mars the cycling would occur concurrent with evolutionary changes in impact cratering rates, concentration of volcanism, declining heat flow (35) and atmospheric escape of hydrogen (36) that would reduce the initially high endowment of Martian water (37). During the Noachian there is no direct evidence of a northern plains ocean, but widespread valley network development in the heavily cratered plains implies a pluvial climate of warm, wet persistence. Higher planetary heat flow (35) heavy impact cratering, widespread volcanism in the cratered uplands, and a possible primordial CO_2 greenhouse atmosphere (22) all would favor the development of a persistent ocean. The Noachian ocean was probably progressively initiated by fluvial and ground-water flow to sinks on the Northern Plains and the Hellas Basin. Loss of CO_2 by carbonate formation in this Noachian ocean could have been followed by burial of carbonates beneath the clastic sediments of younger oceans. Alternatively, carbonates may have concentrated in the subsurface by ground-water movement, with local returns to the surface as scapolite (38) formed by volcanic-hydrothermal interactions.

During the Hesperian and Amazonian, ocean formation became sporadic and transient. As cratering rates declined and planetary heat flow was reduced, volcanism became concentrated at Tharsis and Elysium. Ocean formation was by cataclysmic inception via outflow channel activity. The resulting glacial climates were short-lived episodes in an overall period of cold-dry conditions. Valley development was minor and localized, but glacial and especially periglacial conditions were widespread.

The above model has so many rich possibilities for unifying Mars geomorphological studies that it may not be possible to view that planet quite as it had been before. The enigmatic features that seemed to make Mars a strange world now derive naturally as a consequence of planetary water cycling. Even the unusual basal volcano scarps of Olympus Mons (39) fit the model. The large standing bodies of water could also have provided conditions favorable for the inception of life (40). By exhibiting global water cycling in analogous fashion to Earth, Mars provides important clues toward understanding problems of terrestrial global change.

References

1. Arvidson, R.E., Guiness, E.A., and Lee, S.W. (1979), Nature, 278, 533-535.
2. Chapman, C.R. (1974), Icarus, 22, 272-291.
3. Chapman, C.R. and Jones, K.L. (1977), Ann. Rev. Earth Planet. Sci., 5, 515-540.
4. Craddock, R.A. and Maxwell, T.A. (1990), Lunar and Planet. Sci. XXI, 236-237.
5. Carr, M.H. and Schaber, G.G. (1977), J. Geophys. Res., 82, 4039-4054.
6. Squyres, S.W. (1978), Icarus, 34, 600-613.
7. Squyres, S.W. (1979), J. Geophys. Res. 84, 8087-8096.
8. Rossbacher, L.A. and Judson, S. (1981) Icarus, 45, 39-59.
9. Squyres, S.W. and Carr, M.M. (1986), Science 231, 248-252.
10. Lucchitta, B.K. (1982), J. Geophys. Res., 87, 9951-9973.
11. Kargel, J.S. and Strom, R.G. (1990), Lunar and Planet. Sci. XXI, 597-598.
12. Nedel, S.S., Squyres, S.W., and Andersen, D.W. (1987), Icarus, 70, 409-441.
13. Komatsu, G., and Strom, R.G. (1990), Lunar and Planet. Sci. XXI, 651-652.
14. Pieri, D.C. (1980), Science, 210, 895-897.
15. Carr, M.H. and Clow, G.D. (1981), Icarus, 48, 91-117.
16. Baker, V.R. (1985), Lunar and Planet. Inst. Tech. Rept. 85-03, 12-13.
17. Baker, V.R. (1982), The Channels of Mars, Univ. Texas Press.
18. Mars Channel Working Group (1983), Geol. Soc. America Bull. 94, 1035-1054.
19. Baker, V.R. and Partridge, J.B. (1986) J. Geophys. Res. 91, 3561-3572.
20. Grant, J.A. and Schultz, P.M. (1990) Icarus, in press.
21. Gulick, V.C., and Baker, V.R. (1989) Nature 341, 514-516.
22. Pollack, J.B., Kasting, J.F., Richardson, S.M., and Paliakoff, K. (1987) Icarus, 71, 203-224.
23. Brakenridge, G.R., Newsom, H.E. and Baker, V.R. (1985) Geology, 13, 859-862.
24. Gulick, V.C., Marley, M.S. and Baker, V.R. (1988), Lunar and Planet. Sci. XIX, 441-442.
25. Wilhelms, D.E. and Baldwin, R.J. (1989) Proc. 19th Lunar and Planet. Sci. Conf., 355-365.
26. Baker, V.R., and Milton, D.J. (1974), Icarus, 23, 27-41.
27. Jons, H.P. (1985), Lunar and Planet. Sci. XVII, 404-405.
28. Lucchitta, B.K. (1986), Lunar and Plant. Sci. XVIII, 498-499.
29. Chapman, M.G., Scott, D.H. and Tanaka, K.L. (1990) Lunar and Planet. Sci. XXI, 180-181.
30. Parker, T.J., Saunders, R.S. and Schneeberger, D.M. (1989), Icarus, 82, 111-145.
31. Baker, V.R. Strom, R.G., Croft, S.K., Gulick, V.C., Kargel, J.S., and Komatsu, G. (1990), Lunar and Planet. Sci. XXI, 40-41.
32. White, R.S. and McKenzie, D.P. (1989), J. Geophys. Res., 94, 7685-7729.
33. Carr, M.H. (1979), J. Geophys. Res., 84, 2995-3007.
34. Fanale, F.P. and Cannon, W.A. (1979), J. Geophys. Res., 84, 8404-8414.
35. Schubert, G. et. al. (1989), 4th Internat. Conf. on Mars Abstracts, 50-51.
36. Hunten, D.M., Donahue, T.M., Walker, J.C.G. and Kastning, J.F. (1989) in Origin and Evolution of Planetary Atmospheres (ed. S.K. Atreya, J.B. Pollack, and M.S. Matthews), Univ. Arizona Press, 386-422.
37. Carr, M.H. (1987), Nature, 326, 30-34.
38. Clark, R.B., et al., (1989), 4th Internat. Conf.on Mars Abstracts, 82-83.
39. Hodges, C.A. and Moore, H.J. (1979), J. Geophys. Res., 84, 8061-8074.
40. Oberbeck, V.R., Marshall, J.R. and Schwartz, D.E. (1990), Lunar and Planet. Sci. XXI, 905-906.

GROUNDWATER AND FLUVIAL EROSION ON MARS: RECHARGE OR DEWATERING?

Alan D. Howard, Department of Environmental Sciences, University of Virginia, Charlottesville, VA 22903.

A wide variety of landforms on Mars have been attributed to the action of processes related directly or indirectly to the presence of groundwater or permafrost (1,2), including the widespread occurrence of channels of probable fluvial origin (3,4,5). However, a considerable range of uncertainty exists about the environment prevailing on Mars during formation of the fluvial channels and about the available quantity of water or ice (1,2,6).

Most current models of fluvial erosion on Mars invoke groundwater or ground ice as a reservoir and source of water. However, with the exception of (7) and (9), little attention has been directed towards groundwater flow mechanics on Mars. Preliminary simulations of two simple transient groundwater flow models have been made to assess the timescales of groundwater flow on Mars and the recharge rates that would be necessary to maintain active groundwater flow early in Mars' history. The models are cross-sectional models assuming shallow flow in a sloping aquifer. Flow is assumed to obey the Dupuit-Forchheimer assumptions for unconfined flow. In one model the horizontal permeability, k, and the porosity, η, are assumed to be uniform areally and constant with depth. The areally constant aquifer thickness is T, the length is L, and the surface elevation change over the length of the aquifer is H:

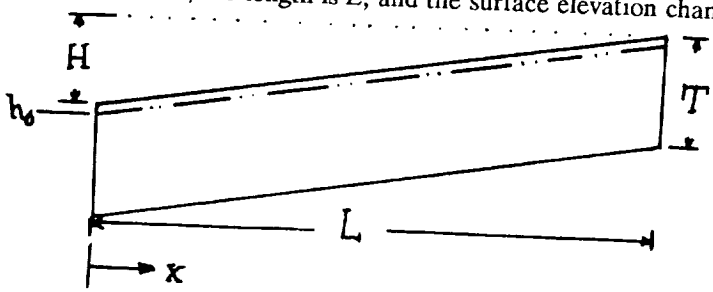

The initial conditions are that the aquifer is initially filled with water to within 100 m of the surface. The simulation is conducted with the outlet level of the water, h_0, at $x=0$ assumed to remain constant, and the water drains laterally through this face. The upstream face at $x=L$ is assumed to be a groundwater divide (no-flow). The proportion of the total water volume in the aquifer that is above h_0 (and therefore can flow out of the simulated section) is ϵ. Simulations have shown that the time, t_δ, required for δ percent of the available groundwater to flow out of the aquifer is given by:

$$t_\delta = T_\delta L^2 \nu \eta \epsilon / (kgH) .$$

Note that the times do not depend explicitly upon the aquifer thickness, T. The discharge per unit width, q, through the lower face of the aquifer is given by:

$$q_\delta = Q_\delta kgHT/(\nu L) ,$$

where g is the gravitational constant and ν the water viscosity. The following table (linear case) shows values of Q_δ and T_δ for several values of δ when H and L are measured in km, k in darcies, and t in years (for martian gravity and water just above freezing).

A similar set of simulations was conducted with the assumption that the permeability and porosity decrease exponentially with depth, h_S-h, beneath the surface, h_S:

$$\eta = \eta_0 e^{-\beta(h_S-h)} \text{ and } k = k_0 e^{-\beta(h_S-h)} .$$

The timescale, t_δ, can be expressed by an equivalent formula to that for the linear case if k_0 and η_0 are used. The appropriate formula for discharge estimation is:

$$q_\delta = Q_\delta k_0 e^{-\beta(h_S - h_W)} gHT/(\beta\nu L),$$

where h_W is the outlet water surface elevation. Simulation results (Exponential) are shown in the table.

	Linear		Exponential	
δ	T_δ	Q_δ	T_δ	Q_δ
10%	0.14	1.0	0.13	1.0
50%	0.84	0.74	0.76	0.74
75%	1.73	0.32	1.46	0.37
90%	3.00	0.14	2.12	0.14

Timescales of Aquifer Dewatering: A representative scenario for martian global flow would have L≈3000 km, H≈5 km, T≈10 km, and η≈0.1. For these conditions, the timescale for 75% dewatering of the aquifer via lateral flow is ~10^6 years for permeability of 1 darcy, 1,000 years for 10^3 darcies (Carr's (7) assumed permeability for the martian regolith), and 10^9 years for 10^{-3} darcies. These results apply both to the homogeneous aquifer and to porosity and permeability decreasing exponentially with depth. MacKinnon and Tanaka (9) propose another model with a 1-2 km thick ejecta with permeability ~ 0.01 darcies and porosity ~0.15 overlying a 10 km fractured basement with permeability ~10^3 darcies and porosity ~0.01. Under these two-layer conditions, the effective relaxation timescale of the aquifer will be the maximum of the timescale for lateral drainage of the aquifer through the lower high permeability basement and the timescale for vertical drainage of the ejecta layer. If the basement aquifer is not completely confined then the effective time scale will be hundreds of years. However, since the porosity of the basement is so low, filling of the fractures in the bedrock by calcite, other mineralization, or weathering products (10) might effectively seal this layer and increase timescales for dewatering to 10^8 or 10^9 years.

Implications for Valley Network Development: There are several possible sources and release mechanisms for water forming valley networks:

1) *Sapping with groundwater recharge:* It is instructive to calculate the amount of recharge that would be required to maintain near-saturated conditions in the aquifer considered above. For 1 darcy permeability the recharge would be ~0.04 cm/yr, ~4×10^{-5} cm/yr for 10^{-3} darcies, and 40 cm/yr for 10^3 darcies. Thus the possibility of widespread groundwater seepage in an unconfined martian groundwater system depends critically on the regolith permeability. If it is high the groundwater table will be very low, and seepage will occur only at the lowest elevations on the planet (assuming recharge <1 cm/yr). If it is low (<1 darcy), groundwater levels will be high and seepage widespread but in small volumes. Modest groundwater-fed flow in the valley networks with ~5-20 km spacing between valleys would require recharge rates of 1 to 100 cm/yr.

2) *Erosion by runoff:* This is the typical terrestrial situation and requires either occasional intense rains (sufficient that precipitation rates exceed infiltration capacity) or seasonal melting of water-rich "snows" (11). Either scenario requires an atmosphere considerably denser than at present and abundant water; whether such conditions ever occurred is a topic of considerable debate. Runoff would be encouraged by sufficient surface weathering to form near-surface clay or caliche horizons to retard infiltration. A shallow permafrost would also encourage runoff.

3) *Development from hydrothermal waters:* Under this scenario the formation of valley networks is suggested to be due to groundwater sapping resulting from local releases of melted permafrost by volcanic intrusions (12,13) or impact-generated heat (14,15). Some of the collapsed terrains are likewise suggested to be due to lava intrusions as sills (16). These processes can operate under atmospheric pressures and surface temperatures similar to those at present. However, a number of concerns may be raised. Mechanisms for incorporation of volatiles into the surface ejecta have not been elaborated. If the near-surface ejecta were ever unfrozen over large areas for a few thousand years much of the water would have been drained from the martian highlands if permeability is as high as (7) and (9) assume. Early in Mars' history permafrost would be thin due to high thermal gradients. Terrestrial hydrothermal systems generally involve meteoric water circulating under groundwater gradients developed by recharge. Therefore, in the absence of recharge by some such mechanism as

vapor phase transport (8), only regolith water above the level of surface seeps would be available for mobilization. Such mechanisms might be adequate for development of channel systems on the lower flanks of volcanic shields and valleys such as Nirgal Valles, which heads in a large undissected upland. However, the Noachian valley systems have much smaller contributing areas and the channels often extend almost to crater rims. Erosion of channels by runoff or seepage probably requires volumes of water 10^2 to 10^5 times the volume of eroded solids (17); furthermore, the extent and depth of fluvial dissection in the cratered terrain may be greater than previously estimated (18).

In summary, erosion of valley networks by runoff or sapping with surface recharge seem most consistent with hydrological considerations. Atmospheric conditions conducive to recharge need not have lasted long ($\sim 10^6$ to 10^7 years in total) and could have been episodic depending upon impact and volcanic history (19,20).

Implications for Outflow Channel Development: The distinctive characteristic of the outflow channels is the need for rapid mobilization of large quantities of water and debris. Supply of water from hydrothermal melting of permafrost is common to many of these models. Again, a number of possible release mechanisms have been proposed:

1) *Release from confined aquifers:* In this scenario water is confined by permafrost (7) or a relatively impermeable ejecta regolith (9). Sudden release of water is due to aquifer pressures exceeding the overburden weight. Permeability must be very high ($\sim 10^3$ darcies) to release sufficient water, and the confining permafrost or ejecta must be monolithic to prevent slower dewatering. Otherwise very rapid hydrothermal melting would be required over time periods $< 10^3$ years to counterbalance lateral drainage. As discussed above, the retaining of large volumes of groundwater in high permeability aquifers well above global baselevel is problematic. It has been suggested that occurrence of massive debris flow might relieve the large discharge requirement (9).

2) *Release from surface storage:* One-time or episodic breaching of tectonic, thermokarstic, or ice-dammed depressions (e.g. Valles Marineris and chaotic terrain) via surface or subsurface drainageways is another possibility. Some outflow valleys are not obviously connected to an appropriate surface reservoir except by putative subterranean routes. This mechanism has the advantage of not requiring sudden mobilization of groundwater. This might be an effective mechanism if combined with recharge from melting of southern latitude ice deposits (21,22).

3) *Tectonic uplift:* Direct aquifer pressuring due to land uplift and tilting could only occur if the aquifer were either very impermeable or tightly confined both vertically and laterally, due to the slowness of tectonic deformation.

4) *Tectonic fracturing:* Large fractures would serve as very effective conduits for groundwater flow (9,23). If these intersected surface storage or confined aquifers then rapid outflows could occur. If the original basement rock were initially impermeable, then new fractures could provide rapid drainage of the overlying ejecta zone due to the reduction in effective length scales.

In summary, the major difficulty with a direct groundwater source for large floods in outflow channels is providing large reservoirs of groundwater in aquifers of high permeability while maintaining artesian aquifer pressures.

References: (1) Squyres, S.W., 1989, *Icarus,* 79, 229-288; (2) Carr, M.H., 1986, *Icarus,* 68, 187-216; (3) Baker, V.R., 1982, *Channels of Mars,* U. Tex. Press; (4) Carr, M.H., 1981, *Surface of Mars,* Yale U. Press; (5) MCWG, 1983, *Geol. Soc. Amer. Bull.,* 94, 1035-54; (6) Greeley, R., 1987, *Science,* 236, 1653-54; (7) Carr, M.H., 1979, *J. Geophys. Res.,* 84, 2995-3007; (8) Clifford, S.M., 1987, *J. Geophys. Res.,* 92, 9135-52; (9) MacKinnon, D.J. and K.L. Tanaka, *J. Geophys. Res.,* 94, 17,359-70; (10) Soderblom, L.A. and D.B. Wenner, *Icarus,* 34, 622-37; (11) Clow, G.D., 1987, *Icarus,* 72, 95-127; (12) Schultz, P.H. *et al,* 1979, *LPSC X,* 1075-77; (13) Wilhelms, D.E. and R.J. Baldwin, 1988, *LPSC XIX,* 1270-71; (14) Brakenridge, G.R. *et al.,* 1985, *Geology,* 13, 859-62; (15) Gulick, V.C. *et al.,* 1988, *LPSC XIX,* 441-2; (16) Squyres, S.W. *et al.,* 1987, *Icarus,* 70, 385-408; (17) Howard, A.D., 1988. *NASA SP-491,* 1-5; (18) Craddock, R.A. and T.A. Maxwell, 1990, *LPSC XXI,* 236-7; (19) Carr, M.H., 1989, *Icarus,* 79, 311-27; (20) Postawko, S.E. and F.P. Fanale, 1989, *NASA TM 4130,* 429-30; (21) Baker, V.R. *et al., LPSC XXI,* 40-41; (22) Kargel, J.S. and R.G. Strom, *LPSC XXI,* 597-8; (23) Tanaka, K.L. and D.J. MacKinnon, 1989, *NASA TM 4130,* 323-4.

PRELIMINARY MODEL OF PROCESSES FORMING SPUR-AND-GULLY TERRAIN

Alan D. Howard, Department of Environmental Sciences
University of Virginia, Charlottesville, VA 22903 U.S.A.

The walls of Valles Marineris are generally dissected by intricate digitate scarps (spurs) extending downslope from the scarp crests; these are bordered laterally and downslope by concave gullies and talus which has accumulated at the angle of repose. Mass wasting of the spurs has created the talus slopes, which gradually bury the scarp base. This *spur-and-gully* topography (1-4) is one of the youngest landforms on Mars, and therefore is potentially informative about the late stage mass wasting environment on Mars. Similar landforms occur in terrestrial arctic and alpine environments (5-9) and miniature analogs of spur-and-gully topography are found in slightly cohesive sediments (10). Studies of these landforms to date are descriptive.

The processes responsible for this intriguing landform remain obscure, although it is clear from the topography, deposits, and terrestrial analogs that physical weathering mass wasting by rockfall and debris avalanches, and talus accumulation predominate (5-9). The range in scale from tiny forms in sand to spurs with characteristic spacing of 0.5 to 10 km on Valles Marineris scarps suggests that the size and shape of these landforms may be informative about material properties and/or weathering environments on Mars.

A number of approaches would be useful for explicating these processes, including terrestrial field study, controlled experiments, theoretical modeling, and measurement and mapping of Martian examples. In this abstract a theoretical approach is taken to examine a class of processes that appear to be sufficient to explain development of spur-and-gully topography.

Examination of Viking images and photos of terrestrial analogs indicates that the upper slopes of spur-and-gully topography is organized into steep, primitive basins with divides at the scarp crest and along the crests of spurs extending down the slope. Topographic profiles from the scarp or spur crusts are concave, with the upper portions being very steep (45-90°) and bedrock floored, giving way abruptly downslope to talus at the angle of repose (30-45°, depending upon talus angularity and grain size range). Two classes of models explanation might explain the development of basin forms. One possibility is that stress-strain-failure relationships in near surface rocks coupled with topography, spatially variable rock resistance or fracture patterns, and surface-directed weathering processes might develop spur and gully forms independent of direct involvement of mass-wasting processes. Although not specifically applied to spur-and-gully forms, a number of investigators have proffered such arguments for development of crenulated forms of alpine relief (12, and references therein). The other possibility is that the rockfall and avalanche processes are erosive, such that the basins develop due to economy of scale in the erosive processes similar to that responsible for creation of fluvial drainage basins (5-9). The models proposed here fall into the second category. Observations of spur and gully morphology and processes occurring in miniature analogs support the latter interpretation. The depressions (chutes) in the floor of these steep basins are fairly smooth in profile and lack sharp bends. Furthermore in larger basins several chutes may converge in a crudely branched pattern. In the damp sand miniature analogs the chutes are clearly preferred pathways for sand flows originating from slope crests. Finally in both miniature analogs and larger terrestrial and martian forms the talus accumulations clearly radiate from the major chutes.

Theoretical Model: The basic driving process is assumed to be a surface-directed physical weathering process (e.g., frost wedging, progressive failure, etc.). In the present model rock shearing is modeled by Coulomb failure with a linear relationship between maximum shearing strength, τ_f, and normal stress, σ_f, on the failure plane:

$$\tau_f = c + \sigma_f \operatorname{Tan} \psi, \qquad [1]$$

where c is cohesion and ψ is the angle of internal friction. Weathering is assumed to slowly reduce cohesion through a characteristic thickness, d, of the exposed rock while ψ remains constant:

$$c = c_0 \exp\{-\alpha(t-t_0)\} \qquad [2]$$

where c_0 is the initial cohesion at time t_0 and α is a characteristic rate of weathering. Individual failures are assumed to be thin ($d << H$, the scarp height) so that a potential failure plane parallel to an infinite slope can be assumed. Under these conditions failure occurs if:

$$1 > (c + \rho g d \text{ Cos } \theta \text{ Tan } \psi)/(\rho g d \text{ Sin } \theta + \tau_S), \quad [3]$$

where θ is the local slope gradient and τ_S is a surface shear exerted by mass-wasting debris shed from higher on the slope. If a section of scarp becomes unstable due to decreasing c the debris shed from the slope is routed downslope. Models of avalanche motion (13-15) suggest the following form for flow resistance:

$$\tau_r = \rho g d \text{ Cos } \theta \text{ Tan } \mu + \rho C_f V^2, \quad [4]$$

where μ is a coefficient of sliding friction, V is mean velocity, and C_f is a coefficient of "turbulent" friction. A theoretical basis for C_f is not firmly established and may represent air drag, internal frictional dissipation, and "plowing" of surface material (13). Some models (13,15,18) suggest an additional "laminar" frictional term proportional to velocity. Empirical estimates in snow avalanching suggest Tan $\mu \approx 0.15$ and $\xi = g/C_f \approx 1500$ m/s^2 (12-17). In rock avalanches air drag is generally unimportant so that τ_S is equated with τ_r in the model. Change in flow momentum equals the difference between downslope gravitational force and flow resistance, such that:

$$dV^2/ds = 2g[(\text{Sin } \theta - \text{Tan } \mu \text{ Cos } \theta) - V^2/\xi d], \quad [5]$$

where s is downslope distance. The simplifying assumption is made that ρ and d remain constant during the downslope motion. Eroded material is deposited where V decreases to zero, generally on the talus slope.

In addition to mass wasting erosion being caused by the destabilizing influence of moving avalanche debris [3], surface shear may also erode the rock surface at a rate proportional to the frictional stress, τ_r:

$$\Delta n = -\beta \tau_r \lambda / V, \quad [6]$$

where Δn is the amount of erosion normal to the surface for a given avalanche event, λ is the length of the moving block of avalanche material, and β is a rate constant which can be assumed to be an inverse function of the cohesion, c.

Simulation Model: The above assumptions are incorporated into a 2-D simulation model. Initial conditions are a scarp of height H extending above a flat valley floor with constant initial gradient θ_0, ψ=45°, and randomly assigned values of c_0 (values are assumed to be lognormally distributed with a specified mean and variance). The values of c_0 are chosen to assure initial slope stability. The simulation model progressed through iterations, with weathering gradually reducing the strength of the surface layer as indicated above. Once an avalanche occurs on a given segment of slope, flow of that plug of material is routed downslope and the factor of safety is determined for each slope segment traversed by the flow. In general the value of τ_S is sufficiently large that a number of downslope segments also fail. Erosion and debris production may also occur due to [6]. Debris from the additional failed or eroded segments is also routed downslope (for simplicity it is assumed that each plug moves independently, although observations suggest an almost simultaneous movement of all portions of the slope involved in an individual avalanche. Once the surface skin of thickness d is removed from the slope, weathering of the underlying layer begins, with a value for c_0 assigned randomly as discussed above. In the simulations provision is made for lack of flow contact and weathering exposure in overhangs and momentum loss at sudden decreases of slope angle.

Case I: One simulation was run in which there was no erosion due to avalanche movement (β=0) and no instability due to surface stress (τ_S=0). In this case the valley wall retreats by parallel motion until the rock wall reaches the limiting angle ψ. The toe of the slope is gradually mantled by the accumulating talus. Under these conditions there is no enhanced downslope erosion and

spur-and-gully topography would be unlikely to form in the 3-D case. Note that the assumed value of the dynamic friction angle μ gives a talus slope that is unrealistically gentle; either rockfalls are characterized by a larger μ and/or flow over talus has a larger friction angle than flow over rock.

Case II: *In this case surface avalanche erosion was equal zero* ($\beta=0$), but instability due to surface stress by moving debris was permitted, with $\tau_S=\tau_r$. The important feature of this case is the the valley wall steeping through time due to greater chances for instability at the base of the slope due the the V^2 dependence of τ_S. This is the type of economy of scale that can result in deepening of flow chutes. In three dimensions the scale economy would be magnified by the potential for avalanche flow convergence into established chutes.

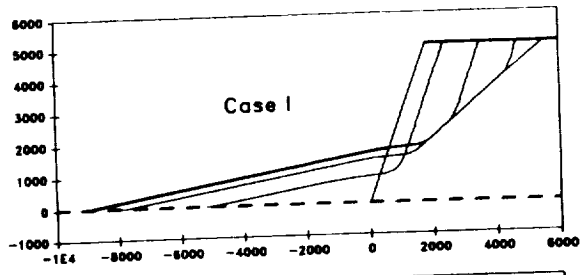

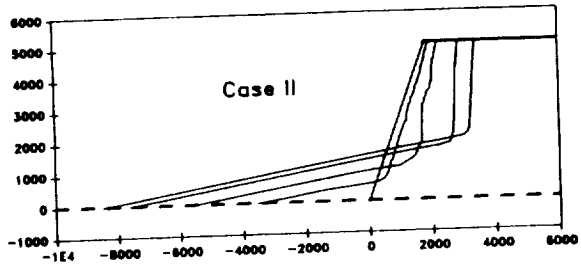

Case III: In this case surface erosion was permitted ($\beta>0$), but movement-induced instability was disallowed ($\tau_S=0$). The results are very similar to Case II in that the scarp steepens as it retreats. Therefore both Case II and Case III (or a combination of the two) seem capable of explaining development of spur-and-gully landforms.

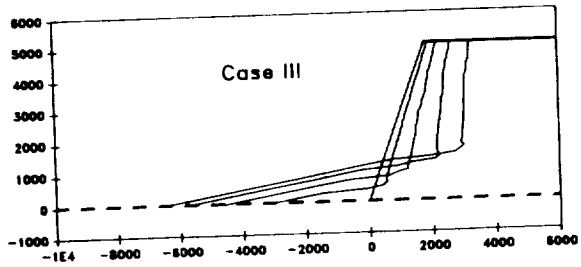

Future Modeling Efforts: Unfortunately, 3-D simulations are difficult because slope angles approach and exceed 90°, making the usual areal mesh discretization impractical. A vertical mesh was used in the present simulations, and could be used for the 3-D case, but this does not allow the possibility for slopes facing backwards. A surface-conforming mesh would be best, but is difficult to implement.

Conclusions: Field observations and the simulation modeling suggest that spur and gully topography is created due to enhanced erosion from movement of rockfall debris. However, at least two distinct erosion models with different dependencies upon rock and avalanche properties could produce spur-and-gully topography. Further field or experimental study is required to pick a realistic model and to constrain model parameters. One this has been done, it would be possible to make inferences about rock properties, weathering processes, and rockfall mechanics on martian scarps.

References:

(1) Sharp, R. P., 1973, *J. Geophys. Res.* 78, 4063; **(2)** Sharp, R.P. and M.C. Malin, 1975, *Geol. Soc. Amer. Bull.*, 86, 593-609; **(3)** Blasius, K.R. et al., 1977, *J. Geophys. Res.*, 82, 4067-4091; **(4)** Lucchitta, B.K., *J. Res., U.S. Geol. Survey*, 6, 651-662; **(5)** Blackwelder, E., 1942, *J. Geomorph.*, 4; **(6)** Matthes, F.E., 1938, *Int. Assoc. Sci. Hydrol. Bull.*, 23, 631-637; **(7)** Akerman, H.J., 1984, *Geograf. Annal.*, 66A, 267-284; **(8)** Rudberg, S., 1986, *Geograf. Annal.*, 68A, 41-63; **(9)** Rapp, A., 1960, *Geograf. Annal.*, 42, 73-200; **(10)** Howard, A.D., 1989, *Reports of the Planetary Geology Program -- 1988, NASA TM 4130*, 355-357; **(11)** Patton, P.C., 1982, *Repts. Planetary Geol. Prog. 1982, NASA TM 85127*, 242-243; **(12)** Whalley, W.B., 1984, in *Slope Instability* (D. Brunsden and D.B. Prior, eds), Wiley, Chichester, 217-256; **(13)** Perla, R. et al., 1980, *J. Glaciol.*, 26, 197-206; **(14)** Dent, J.D. and T.E. Lang, 1980, *J. Glaciol.* 26, 131-140; **(15)** Martinelli, M. Jr. et al., 1980, *J. Glaciol.* 26, 109-119; **(16)** Buser, O. and H. Frutiger, 1980, *J. Glaciol.* 26, 121-130; **(17)** McClung, D.M. and P.A. Schaerer, *Ann. Glaciol.* 4, 170-173; **(18)** McEwen, A.S. and M.C. Malin, 1990, *J. Volcan. Geotherm. Res., in press.*

PROSPECTS FOR SIMULATION MODELING OF VALLEY NETWORKS ON MARS

Alan D. Howard, Department of Environmental Sciences, University of Virginia, Charlottesville, VA 22903

The valley systems of Mars remain an enigma. They mostly formed during late stages of heavy bombardment, but understanding of the morphology and environment of these fluvial networks is hampered by the extensive modification by cratering, volcanic activity, tectonism, and eolian erosion-deposition. The climatic environment during this time is highly uncertain, with various lines of evidence suggesting conditions ranging from a cold surface and thin atmosphere to a relatively warm, moist climate. Valley system development under the former scenario has been suggested to be due to sapping processes resulting from hydrothermal melting of ground ice by volcanic intrusions or crater impact (1,2). Under moist conditions runoff processes might occur, possibly from snowmelt (3). Carr (4) suggests an intermediate scenario regulated by CO_2 scavenging by carbonate formation by surface waters, with temperatures regulated to hover near the melting point of water.

The scenario to be investigated here is that most of the valley networks resulted from weathering and runoff processes that were arrested at an early stage by a deteriorating environment. A recent study has suggested widespread degradation of Noachian cratered terrain, probably by fluvial erosion (5). Some high relief areas of the cratered uplands have been dissected sufficiently that graded slopes and well-defined drainage divides have formed, such as a zone about 30-70 km wide centered along the Loire Valley channel (615A45). Unfortunately, analogous terrestrial fluvial systems are rare, not because of a lack of stream systems in early stages of development, but because Earth lacks the suitable initial conditions of fresh cratered surfaces. Rudimentary stream networks on terrestrial volcanic constructs are more common and morphometric comparisons have been made to dissected martian volcanos (6).

Cratering produces a constructional surface that is characterized by numerous enclosed basins (craters and inter-crater basins), locally steep topography (crater rims), a richly textured surface of ejecta, and considerable variability of composition and erosional susceptibility of material. It is likely that large spatial variations in drainage density and degree of dissection, as well as a fragmented drainage network would result during early stages of dissection of a cratered landscape. Recent advances in computer capabilities has made feasible the simulation modeling of cratered-surface dissection. Similar modeling of volcanic dissection is already in progress (7). This abstract discusses general discussion of the representation of drainage basin processes in simulation models and provides examples of a partial simulation model of drainage basin development.

A multiplicity of processes must be accounted for in drainage basin development. In the absence of significant contributions by glacial, eolian, volcanic, tectonic, and marine-lacustrine processes the following processes must be accounted for:

- Weathering
  - Physical [rock slopes, exfoliation, tafoni, some bedrock streams]
  - Chemical [groundwater sapping, karst]
- Entrainment
  - Solution [karst]
  - Rainsplash [badland slopes]
  - ***Running water*** [piping, rills, bedrock streams]
  - Regolith failure [rockfall, landslides]
- Transport and Deposition
  - Rainsplash [badland slopes]
  - Mass-wasting
    - ***Creep & flows*** [convex slopes, solifluction]
    - Debris Flows [talus, earthflows, lahars]
  - Fluvial [alluvial channels and floodplains, fans, deltas]

In any location within a landscape one of these processes (weathering, entrainment, or transport & deposition) is the limiting factor in overall erosion rate, and the resulting morphology of the landform

element is largely determined by the limiting process (examples are given in brackets). In some cases two process classes are inseparably linked (e.g. solutional weathering and entrainment in groundwater). Landform elements limited by weathering rate generally expose rock, those limited by entrainment are generally regolith covered, and those limited by transport and deposition have a colluvial or sediment mantle. Clearly a comprehensive model is impractical, although one approach to slope modeling has been to try to parameterize all important processes for particular circumstances **(8,9)**. The approach suggested here is to explicitly include only those processes that are limiting factors, and to implicitly model other processes. In fact, only running water entrainment and creep transport (bold italics in above table) are included in the preliminary model discussed below.

Drainage basins result from simultaneous action of diffusional and concentrative processes. For example, creep, rainsplash, and possibly some forms of overland flow are diffusional, whereas most fluvial processes (excepting fans and deltas) are concentrative.

A Preliminary Model: The simulation model reported here includes creep (diffusional) and runoff (concentrative) erosion. Weathering is assumed not to be a limiting factor and is not explicitly modeled. Creep is assumed to be limited to surface soil layers, and thus is independent of total soil depth. The creep flux $\boldsymbol{q}$ is a function of the slope gradient, $\boldsymbol{S}$: $\boldsymbol{q} = K_S \boldsymbol{S}^{\alpha}/(1-K_t S^{\epsilon})$, where K_S is a rate constant, α and ϵ are constant exponents, and a constant $K_t>0$ allows for threshold limiting slopes (bold type indicates vector quantities). The rate of erosion due to creep, E_S, equals the divergence of creep, $\nabla \cdot \boldsymbol{q}$. Channels and rills are assumed to be bedrock-floored, with channel erosion rate, E_C, depending upon overland flow shear stress, τ: $E_C = K_C (\tau-\tau_C)^{\beta}$, where τ_C is a critical shear stress and β is a constant exponent. Simple hydraulic geometry arguments permit quantification of τ as a function of contributing drainage area, A, and local gradient, S: $\tau = K_e A^{\gamma} S^{\delta}$ **(10)**. The assumption of bedrock-floored channels means that explicit sediment routing in channels is not required. The total erosion at any location, E_t, equals E_S if $E_C=0$, otherwise it is $E_S/\eta + E_C$, where $\eta>1$ models the easier erosion of soil debris than bedrock.

Simulations have been conducted with this model on a 100x100 matrix. The simulations generally assume one boundary is a horizontal outflow which is lowered at a constant rate, E_b. The opposite boundary is a drainage divide, and the side boundaries are periodic. Initial conditions are a very low relief with a random drainage pattern. The simulation is run to a nearly steady-state topography (≈1500 iterations). The simplest model assumes $\alpha=1$, $\tau_C=0$, $K_t=0$, $\eta=1$, and $\beta=1$. For an assumed grid spacing of unity the following values give a reasonable drainage density: $K_C=K_e=1$, $K_S=2$, $\gamma=0.7$, $\delta=0.35$ with an erosion rate $E_b=1$ **(Figure 1)**. A badlands-like topography is formed if $\eta=6$ and $\tau_C=2.5$ **(Figure 2)**.

Application to Mars: The use of simulation models of landform development permit the testing of hypotheses regarding erosional processes and comparison of model results with observed martian valley systems. For example, notable characteristics of the valley systems are large areal variations in drainage density and degree of dissection, irregular basin shape, apparent strong structural control of valley alignment, and small, variable junction angles. Noachian valley system development was rudimentary by terrestrial standards, so that the steady-state topography of Figures 1 and 2 is clearly an inappropriate analog. However, the same model can be run to show initial stages of development from an irregular initial surface, as shown in **Figure 3**. Although this model is not optimized to simulate the presumed martian conditions, erosion of an irregular surface results in considerable areal variation in depth of dissection and drainage density, as is observed on the martian heavily-cratered terrain.

Several steps are required to develop a simulation model specifically for Mars. First, initial conditions must be specified, both in terms of topography and erosion characteristics of surficial materials. An appropriate choice would be a cratered surface, possibly with local volcanic flooding. Sources for cratered topography include measured planetary topography, surfaces created in the laboratory, or simulated surfaces. A cratered surface poses some modeling difficulties, since enclosed depressions will be numerous. This means that the model must be capable of handling surface water flow into depressions (searching for the outlet and possibly allowing for loss of water due to infiltration and evaporation). In addition sediment transport and deposition must be accounted for, with attendant possibilities of fan, playa, delta and lacustrine sedimentation. The model discussed above is not

presently capable of treating enclosed depressions.

Furthermore, assumptions must be made about the hydrologic and erosional processes that are acting on the landscape and their appropriate mathematical formulation. Given our uncertainty about early conditions on Mars, the best approach is to test a variety of process assumptions and compare the resulting simulated landforms with martian prototypes. For example, the simulations reported here assume surface and/or throughflow runoff as the dominant contributor to erosion and transport by running water. A contrasting hypothesis would be areal recharge of a regolith aquifer with seepage discharge and erosion; this could be modeled by a regional flow and seepage erosion model similar to an existing scarp erosion model (11). The basic model could also be expanded to include valley widening by fluvial lateral erosion, weathering and mass-wasting of steep bedrock slopes (e.g., crater walls), cratering and ejecta mantling continuing during fluvial erosion, and hydrothermal effects due to cratering or volcanism, *inter alia*.

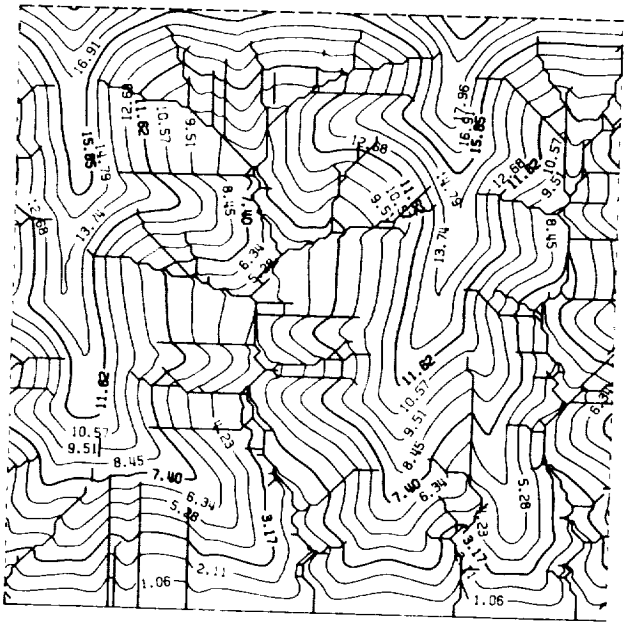

Figure 1

References: (1) Brackenridge, G.R., H.E. Newsom and V.R. Baker, 1985, *Geology*, 13, 859-862; (2) Wilhelms, D.E. and R.J. Baldwin, 1988, *LPSC XIX*, 1270-1271; (3) Clow, G.D., 1987, *Icarus*, 72, 95-127; (4) Carr, M.H., 1989, *NASA TM 4130*, 427-428; (5) Craddock, R.A. and T.A. Maxwell, 1990, *LPSC XXI*, 236-237; (6) Kochel, R.C.and J.F. Piper, 1986, *J. Geophys. Res.*, 91, E175-E192; (7) .Seidl, M.A., D.S. Loewenherz, and W.E. Dietrich, 1989, *EOS*, 70, 1125; (8) Kirkby, M.J., 1985, *Models in Geomorphology (Woldenberg, ed.)*, Allen & Unwin, 213-237;Kirkby, M.J., 1986, *Hillslope Processes (Abrahams, ed.)*, Allen & Unwin, 203-222, (9) Ahnert, F., 1987, *Geomorphological Models, Catena Suppl. 10*, 31-50; (10) Howard, A.D. and G. Kerby, 1983, *Bull. Geol. Soc. Amer.*, 94, 739-752; (11) Howard, A.D., 1989, *NASA TM 4130*, 355-357.

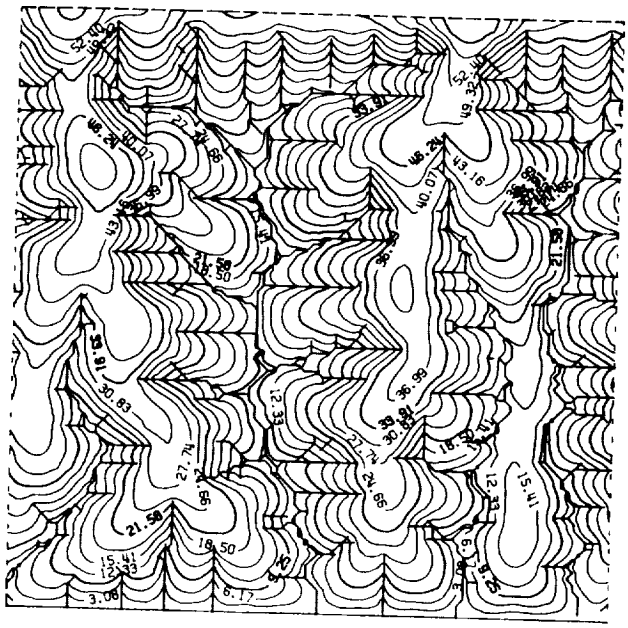

Figure 2

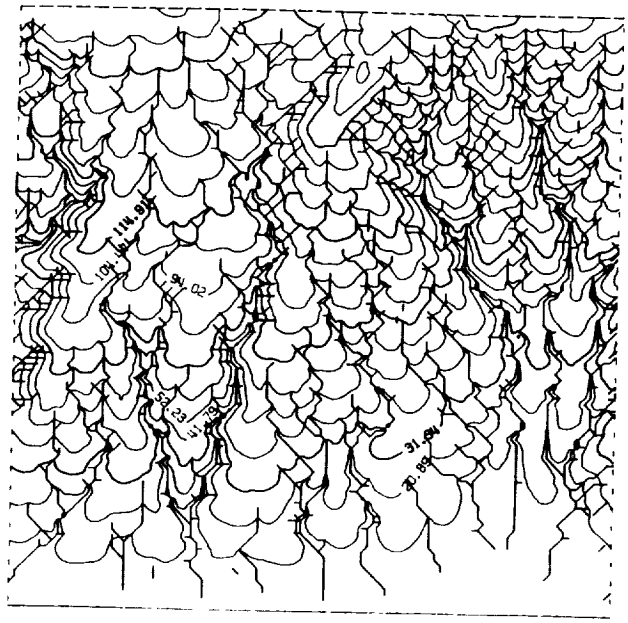

Figure 3

EVALUATIONS OF FLOODS ON EARTH AND MARS BY FLOW-COMPETENCE TECHNIQUES

Paul D. Komar, College of Oceanography
Oregon State University, Corvallis, Oregon 97331

We are limited in our ability to quantitatively assess the hydraulic parameters of extreme floods, whether they have occurred on Earth or Mars. The desire is to be able to examine the erosional features or sediment deposits associated with the flood, and to use that evidence to evaluate flow velocities, bed stresses, depths and discharges. The overall objective of my recent research has been to improve techniques for evaluating the hydraulic parameters of major flood events so as to enhance reconstructions of flows that eroded the outflow channels on Mars. This research has led to a series of publications – the present abstract summarizes that work.

The technique of flow competence relates the sizes of the largest sediment particles transported by a flood to the flow's magnitude, its mean velocity and discharge, or mean bed stress. For example, Bradley and Mears (1980) applied competence calculations to boulders up to 2.3 meters diameter found adjacent to Boulder Creek where it flows through Boulder, Colorado, in an attempt to evaluate the extreme flood conditions responsible for their transport. Prior to my work, such assessments utilized empirical correlations between the mean velocity or stress and the diameters of the largest particles transported, based on data from terrestrial floods. I found that those simple empirical correlations do not adequately account for particle sorting in rivers, and would generally yield flood estimates that are an order-of-magnitude too large (Komar 1987a, 1987b). However, as shown in Figure 1, data for gravel entrainment from various rivers and for movement by ocean currents can be made to converge if normalized to the respective bed-material median grain sizes, $\bar{D}_B$, yielding the relationship (Komar, 1989)

$$\theta_{tm} = 0.045(D_m/\bar{D}_B)^{-0.65} \qquad (1)$$

where D_m is the diameter of the largest particle transported and $\theta_{tm} = \tau_{tm}/(\rho_s - \rho)gD_m$ is the dimensionless Shields entrainment function (τ_{tm} is the mean stress experted by the flow, ρ_s and ρ are respectively the grain and water densities, and g is the acceleration of gravity). Using this definition for θ_{tm} , equation (1) can be rewritten as

$$\tau_{tm} = 0.045(\rho_s - \rho)g\bar{D}_B^{0.65}D_m^{0.35} \qquad (2)$$

This relationship provides the best empirical evaluation of both selective entrainment and flow competence, and has the advantage that it is dimensionally homogeneous and accounts for the gravity field so that it can be used on Mars as well as Earth.

An example of the use of these relationships is provided by the Pleistocene spillways that were eroded by the rapid drainage of Glacial Lake Regina in Saskatchewan, Canada, studied by Lord and Kehew (1987). The largest boulder in the Souris Spillway has a diameter D_m =

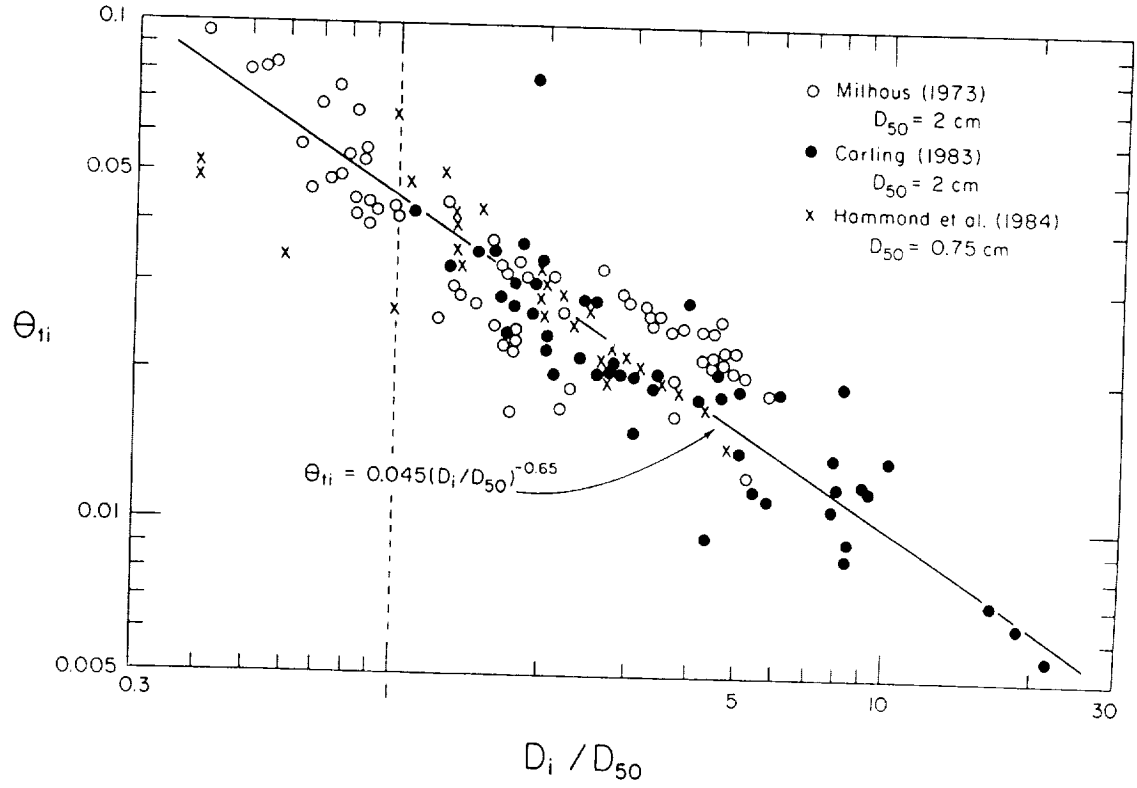

Figure 1: Test of equation (1) with gravel-entrainment data from streams and under ocean currents. [Komar (1989)]

1.54 m, and the median diameter of the deposit as a whole is $\bar{D}_B$ = 0.03 m. This yields τ_{tm} = 91 N/m^2 from equation (2) as the estimated mean-flow stress, and the corresponding mean velocity is estimated to have been 2.6 m/sec and the depth 45 m (Komar, 1988). This calculated depth is essentially the same as that established by Lord and Kehew in their field measurements of the eroded channel, providing partial confirmation of the flow-competence assessments using equation (2).

The above relationships can be used in reverse to estimate sizes of particles that were transported by the floods on Mars that eroded the outflow channels. Using my previous analyses of flow stresses of those floods derived from channel dimensions (Komar, 1979), the maximum-size boulders transported would have been on the order of 5 meters diameter. This illustrates the extreme magnitudes of the Martian floods and their abilities to entrain and transport very large materials, leading to the rapid excavation of the outflow channels. When future missions to Mars yield data on actual particle sizes transported, we will be able to utilize the above flow-competence equations to directly infer mean bed stresses, and then to estimate mean velocities and discharges from the flow equations.

Although the above relationships account for the observed patterns of selective

entrainment of coarse materials in streams, the equations are still empirical. This limits their serving as a foundation for a better understanding of the actual processes of grain entrainment, and raises concern in their use to evaluate floods on Mars, an application which requires extrapolations beyond the existent data base. To overcome this deficiency, I have undertaken detailed analyses of models for particle entrainment involving grain pivoting, rolling and sliding (Komar and Li, 1988). These models were as successful as the empirical equations when compared with the existing data, while providing a firmer understanding of the physical processes involved in flow-competence estimates. Another short-coming of the existing flow-competence analyses is that they rely solely on the maximum particle sizes transported, whereas it is clear that the competence of a flood must be reflected in the total distribution of transported grain sizes. This has been demonstrated for the bedload gravels in Oak Creek, Oregon, where there is a systematic variation in grain-size ranges and in the overall form of the grain-size distribution with changing flow stage (Shih and Komar, 1990). We have been able to use this pattern of changing grain sizes as the basis for computations of transport rates of different size fractions (Shih and Komar, in press). We are now comparing those results with similar data from Great Eggleshope Beck, England, a comparison that is of special interest due to contrasting fabrics of bed materials in these two streams and resulting differences in grain-sorting patterns.

References

Bradley, W.C., and Mears, A.I., Calculations of flows needed to transport coarse fraction of Boulder Creek alluvium at Boulder, Colorado, *Geol. Soc. Amer. Bull.*, 91, 135-138, 1980.

Komar, P.D., Comparisons of the hydraulics of water flows in Martian outflow channels with flows of similar scale on Earth, *Icarus* , 37, 156-181, 1979.

Komar, P.D., Selective grain entrainment by a current from a bed of mixed sizes: A reanalysis, *Journal of Sedimentary Petrology*, 57, 203-211, 1987a.

Komar, P.D., Selective gravel entrainment and the empirical evalaution of flow competence, *Sedimentology*, 34, 1165-1176, 1987b.

Komar, P.D., Discussion (of paper by Lord and Kehew), *Geol. Soc. Amer. Bull.*, 100, 1311-1312, 1988.

Komar, P.D., Flow competence evaluations of the hydraulic parameters of floods: An assessment of the technique, in *Floods: Hydrological, Sedimentological and Geomorphological Implications*, K. Beven and P. Carling (editors), John Wiley & Sons, 107-134, 1989.

Komar, P.D., and Li, Z., Applications of grain-pivoting and sliding analyses to selective entrainment and flow-competence evaluations, *Sedimentology*, 35, 681-695, 1988.

Lord, M.L., and Kehew, A.E., Sedimentology and paleohydrology of glacial-lake outburst deposits in southeastern Saskatchewan and northwestern North Dakota, *Geol. Soc. Amer. Bull.*, 99, 663-673, 1987.

Shih, S.-M., and Komar, P.D., Hydraulic controls of grain-size distributions of bedload gravels in Oak Creek, Oregon, *Sedimentology*, 1990.

Shih, S.-M., and Komar, P.D., Differential bedload transport rates in a gravel-bed stream: A grain-size distribution approach, *Earth Surface Processes and Landforms*, in press.

Ancient Aqueous Sedimentation on Mars

Jules M. Goldspiel and Steven W. Squyres
Center for Radiophysics and Space Research
Cornell University, Ithaca, NY 14853

Quasi-dendritic valley systems are common in the ancient cratered terrain of Mars. These valley systems are the result of fluvial erosion and have been interpreted as evidence for a period very early in martian history when the climate was significantly warmer, wetter and more Earth-like than it is at present. Examination of Viking orbiter images shows that the valley systems in some instances debouch into closed depressions which can act as local ponding basins for flow. These depressions hence can be expected to be sites of aqueous sedimentation. In some cases these sites are ancient craters, while in others they are local topographic lows nestled among crater rims. Because they are low-lying, closed depressions, they are also sites favorable to accumulation of low-viscosity lavas. A number of them appear to have undergone volcanic filling subsequent to the cessation of fluvial activity.

Using the Viking orbiter images, it is possible to calculate approximate volumes for the inflow valleys, and hence to estimate the amount of material eroded from them. A sediment transport model can then used to estimate the amount of water necessary to remove such a volume of debris from the valleys. The results for four basins having especially well-developed inflow networks suggest sediment thicknesses in the basins of tens to hundreds of m, and indicate that the water involved in the transport process would have been enough to fill the basins to a depth of several kilometers had it all been present simultaneously. This analysis does not provide any information on the instantaneous water depth at any time, of course, and allows the possibility that most basins were more like terrestrial playas than true lakes. In a few instances, however, the water appears to have overtopped the basin rim and eroded down to a lower base level, attesting to the attainment of significant water depths at some point in the past. The valleys seen in the ancient highlands are most likely the result of basal sapping (Pieri, 1980; Laity and Malin, 1985; Howard *et al.*, 1988). The water volume estimates can hence be compared to the megaregolith porosity (Binder and Lange, 1980; Clifford, 1981) to investigate whether aquifer recharge was required for their formation. The total water volumes are strong functions of the mean size of transported sediment, but the calculations suggest that unless the transported sediments were particularly fine, the quantities of water required to transport the sediment are greater than that which can result from a single discharge of the associated aquifers.

Although no conclusive evidence has been found yet in the geologic record for a more Earth-like early martian environment, outgassing arguments and greenhouse calculations have been presented in support this hypothesis (Pollack *et al.*, 1987). The current surface pressure is 7 mbar, so where a postulated early $\sim$ 1 bar CO_2 atmosphere could reside is a major problem; the polar caps and regolith are inadequate repositories (Fanale *et al.*, 1982) and thermal escape to space is negligible over the age of the planet. Ancient aqueous sedimentation basins could provide an additional sink for atmospheric CO_2, as the dissolved gas can react with cations brought in by the inflowing streams to form carbonate minerals. Using the calculated water volumes, it is possible to evaluate the carbonate precipitation potential of observed ancient aqueous sedimentation basins and assess their climatological significance. Such calculations indicate that the maximum mass of carbonates which could reasonably have been precipitated in these basins is equivalent to only a few millibars of atmospheric CO_2. The observed basins account for only a trivial fraction of the proposed early dense atmosphere. Ancient carbonate sediments would be very important if they exist, however, since they could contain information concerning the chemical and climatological conditions on the planet at the time of their deposition, and hence could provide direct evidence for the postulated early warmer and wetter environment.

References

Binder, A. B., and M. A. Lange 1980. *J. Geophys. Res.* **85**, 3194-3208.

Clifford, S. M. 1981. LPI Contribution 441, 46-48.

Fanale, F. P., *et al.*, 1982. *Icarus* **50**, 381-407.

Howard, A. D., R. C. Kochel, and H. E. Holt (Eds.) 1988. NASA SP-491.

Pieri, D. C. 1980. *Science* **210**, 895-897.

Laity, J. E., and M. C. Malin 1985. *Geol. Soc. Amer. Bull.* **96**, 203-217.

Pollack, J. B., *et al.*, 1987. *Icarus* **71**, 203-224.

ELYSIUM BASIN, MARS: IMPLICATIONS OF A DEEP, INTERMITTENT LAKE SYSTEM; Mary G. Chapman, David H. Scott, and Kenneth L. Tanaka, U.S. Geological Survey, Flagstaff, AZ 86001.

The Elysium basin, one of the largest depositional basins on Mars, is the only one exhibiting direct geologic and topographic evidence of former water levels. Data have been presented previously that suggest the past existence of large standing bodies of water on Mars (Haberle, 1986; Carr et al., 1987; Goldspiel and Squyres, 1989). That the Elysium basin may have been the locus of an ephemeral sea or large lake has important climatic and biological implications. Ice-covered lakes could have held liquid water at 0 °C that may have significantly extended the period when biological habitats could persist (McKay et al., 1985; Wharton et al., 1987; McKay and Nedell, 1988). Gas-concentration mechanisms operating in these lakes could have enhanced atmospheric gases and provided a source of biologically important gases (pricipally CO_2 and N_2) as the Martian atmosphere thinned (McKay and Stoker, 1989).

Our study of the Elysium basin has two objectives, to determine (1) the maximum extent of the basin and (2) the former volume of water in the basin and the sources of this water. To fulfill the first objective and part of the second, we have compiled a preliminary map of the basin on nine 1:2,000,000-scale quadrangles to determine its maximum shoreline on the basis of geologic indicators. To fulfill the second objective, we are examining and mapping source channels in the circumbasin materials. Our final products will be a geologic map and a physiographic-topographic map, both showing the entire basin at 1:5,000,000 scale. The second map, compiled on a new topographic base (U.S. Geological Survey, in press and work in progress in the Memnonia and Amazonis subquadrangles) shows former shorelines, basin extent, and drainage channels.

Our study indicates that the highest shoreline of the basin lay between 1,000 and 500 m below the Martian datum. Etched lava flows having parallel terraces occur at lat 2° S., long 197° (Viking Orbiter image 725A21) near an elevation of -1,000 m. Eroded possible shoreline material is found near lat 1° N., long 184° at an approximate elevation of -500 m. Two spillways are observed that lead into northern Amazonis Planitia at about lat 24° N., long 176° (Viking Orbiter image 545A22); these spillways lie above an elevation of -1,000 m. (A southern spillway lies at about lat 10° N., long 175°.) Because the deepest part of the basin lies below an elevation of -2,000 m, water depth may have been as great as 1,500 m.

Was the Elysium basin an intermittent or a persistent lake system? Three different ages of inflow from channel systems into the area suggest that a lake recurred in the basin. Initially, before the formation of the basin and the Elysium volcanic rise, many small, dendritic channels of probable Noachian age drained from the highlands into a broad lowland plain. During the Hesperian, after the basin had become well defined, large outflow channels such as Ma'adim and Al-qahira Valles funneled highland waters into the basin (Scott et al., 1978; Greeley and Guest, 1987). Finally, lake filling in Amazonian time is indicated by several lines of evidence. (1) Amazonian-Hesperian volcanic flows of Apollinaris Patera blocked the mouth of Ma'adim Vallis, and later sapping fluids cut around Apollinaris and flowed out into the basin. (2) Channels within the Amazonian Medusae Fossae

Formation drained toward the basin. (3) Fluids flowed into the basin from the north, cutting streamlined features into Amazonian volcanic flows of the Elysium rise at lat 9° N., long 204° (Viking Orbiter image 883A30).

Simple life forms may have evolved on Mars during a more hospitable climate in the ancient past. If such life had developed the capability to remain dormant for extremely long periods until conditions for metabolism were favorable, biologic activity may have been reawakened (McKay and Stoker, 1989). Our evidence for episodic lake filling in the Elysium basin throughout much of Martian history provides a mechanism for possible periodic biologic activity, perhaps even close to the present.

References

Carr,M.H., Wu, S.S.C., Jordan, Raymond, and Schafer, F.J., 1987, Volumes of channels, canyons and chaos in the circum-Chryse region of Mars (abs.): 18th Lunar & Planet. Sci. Conf., p. 155-156.

Haberle, R.M., 1986, The climate of Mars: Sci. Amer., v. 254, p. 54-73.

Goldspiel, J.M., and Squyres, S.W., 1989, Ancient lakes on Mars? (abs.): NASA Conf. Publ. 10027, p. 26.

Greeley, Ronald, and Guest, J.E., 1987, Geologic map of the eastern equatorial region of Mars: U.S.G.S. Misc. Inv. Ser. Map I-1802-B, scale 1:15,000,000.

McKay, C.P., Clow, G.D., Wharton, R.A., Jr., and Squyres, S.W., 1985, Thickness of ice on perennially frozen lakes: Nature, v. 313, p. 561-562.

McKay, C.P., and Nedell, S.S., 1988, Are there carbonate deposits in Valles Marineris, Mars?: Icarus, v. 73, p. 142-148.

McKay, C.P., and Stoker, C.R., 1989, The early environment and its evolution on Mars: Implications for life: Rev. of Geophys., v. 27, no. 2, p. 189-214.

Scott, D.H., Morris, E.C., and West, M.N., 1978, Geologic map of the Aeolis quadrangle of Mars: U.S.G.S. Misc. Inv. Ser. Map I-1111, 1:5,000,000 scale.

Wharton, R.A., Jr., McKay, C.P., Mancinelli, R.L., and Simmons, G.M.,Jr., 1987, Perennial N_2 supersaturation in an Antarctic lake: Nature, v. 325, p. 343-345.

U.S. Geological Survey, in press, Topographic maps of the Aeolis NE and NW and the Elysium NE, SE, and SW quadrangles of Mars: U.S.G.S. Misc. Inv. Ser. Maps I-2118, I-2121, I-2126, I-2127, and I-2128, respectively. 1:2,000,000 scale.

WIDESPREAD RESURFACING IN THE MARTIAN HIGHLANDS

Robert A. Craddock and Ted A. Maxwell, Center for Earth and Planetary Studies, National Air and Space Museum, Smithsonian Institution, Washington, DC 20560

The southern cratered highlands of Mars contain a large population of flat-floored, rimless craters which occur on a variety of Noachian geologic materials (Fig. 1). Previously these craters have been interpreted to have formed by aeolian mantling [1] or flood volcanism [2]; however, neither of these geologic processes accurately explains the observed morphology or the crater statistics. Determining the distribution of the flat-floored, rimless craters, the timing of the process responsible for their formation, and the actual process involved in their formation is important for understanding the geomorphic evolution of most of the southern cratered hemisphere of Mars. Our initial investigation concentrated on the analysis of the Amenthes and Tyrrhena regions near the dichotomy boundary [3,4,5]. Currently we have begun investigations into other areas including Mare Australe, Eridania, Arabia, Noachis, and Memnonia.

The geologic analysis of these regions was based on the published 1:15M geologic maps of Mars and was limited to two materials: the Noachian cratered unit (Npl_1; 6) and the Noachian dissected unit (Npld; 6). Although flat-floored, rimless craters occur on other Noachian geologic materials as well, the interpretations of these units [7,8,9] includes resurfacing by processes we feel are separable from a larger, more extensive process. The Noachian cratered unit (Npl_1) and the Noachian dissected unit (Npld) are distinguished by the absence or presence of ancient valley networks (i.e., runoff channels), respectively [6]. Together these units make up a bulk (~70%) of the surface area of the southern cratered hemisphere.

The termination of the resurfacing event represented by the cumulative size-frequency curves of superposed, fresh craters was not a catastrophic, global event (Fig. 2). Resurfacing ceased during the late Noachian to early Hesperian in the regions analyzed. In general, resurfacing ceased in the Npld materials later than in the Npl_1 materials, suggesting that the ancient valley networks represent the late stages or a change in the resurfacing process. These observations correlate well with other work suggesting that the ancient valley networks ceased to form by the early Hesperian [6].

A proposed mechanism responsible for martian highland resurfacing must be able to explain not only the morphology of the flat-floored, rimless, craters, but also the timing of the process between regions and the bendover in crater size-frequency distribution curves of highland materials [e.g., 5] as well. Although a bulk of the cratered highlands may be composed of volcanics [e.g., 10], volcanism does not produce flat-floored, rimless craters except in very rare circumstances. Aeolian erosion/deposition is also a very active process on Mars as evidenced by the seasonal dust storms and a variety of landforms [e.g., 11]; however, unlike what has been suggested by Wilhelms and Baldwin (1) aeolian fallout would not only be deposited up to the rim crest of craters but <u>on</u> the rims of craters as well. The result is not to produce a flat-floored, rimless crater, but to subdue the morphology of the crater. Volcanic and aeolian resurfacing do not produce a bendover in the cumulative size-frequency curves either. In both processes a crater is either buried, or it is not,

in which case it is still counted. We propose a fluvial process capable of eroding the rims of the craters primarily from the outside, thus reducing the apparent diameter of the craters. The eroded material is redistributed, inundating the smaller craters before they are eroded completely. Such a complicated process not only explains the morphology of the flat-floored, rimless craters, but also the bendover in the cumulative size-frequency curves and potentially the timing of the process between regions.

These results were presented at the 21th Lunar and Planetary Science Conference, Houston, Texas, March, 1990. Supported by NASA Grant NAGW-129.

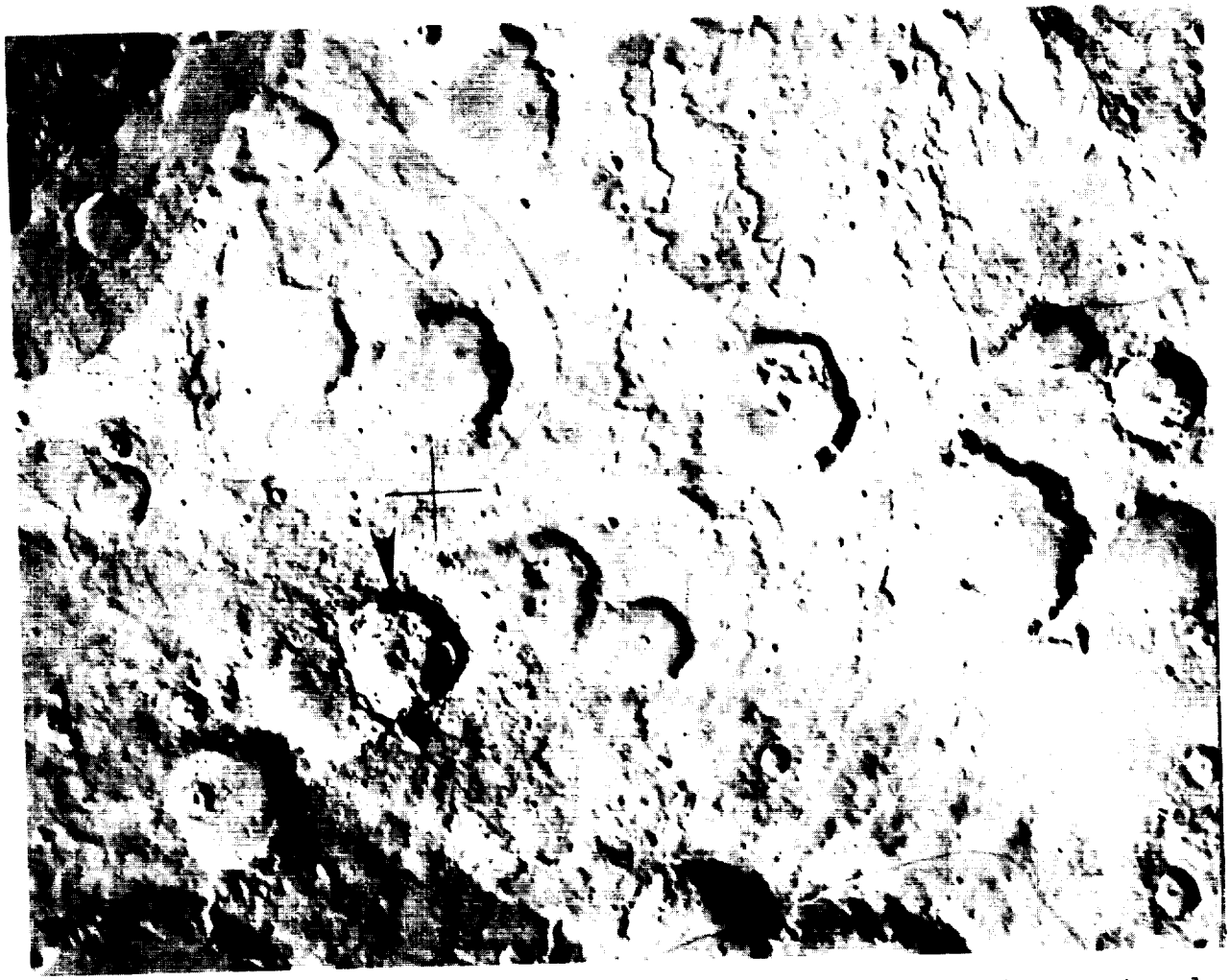

Figure 1. Flat-floored, rimless craters in the martian cratered highlands. The morphologic differences between these craters and a fresh, superposed lunar-like crater (black arrow) is indicative of a major resurfacing event in the early history of Mars. Continued investigations will allow the timing, extent, and mechanism of resurfacing to be determined.

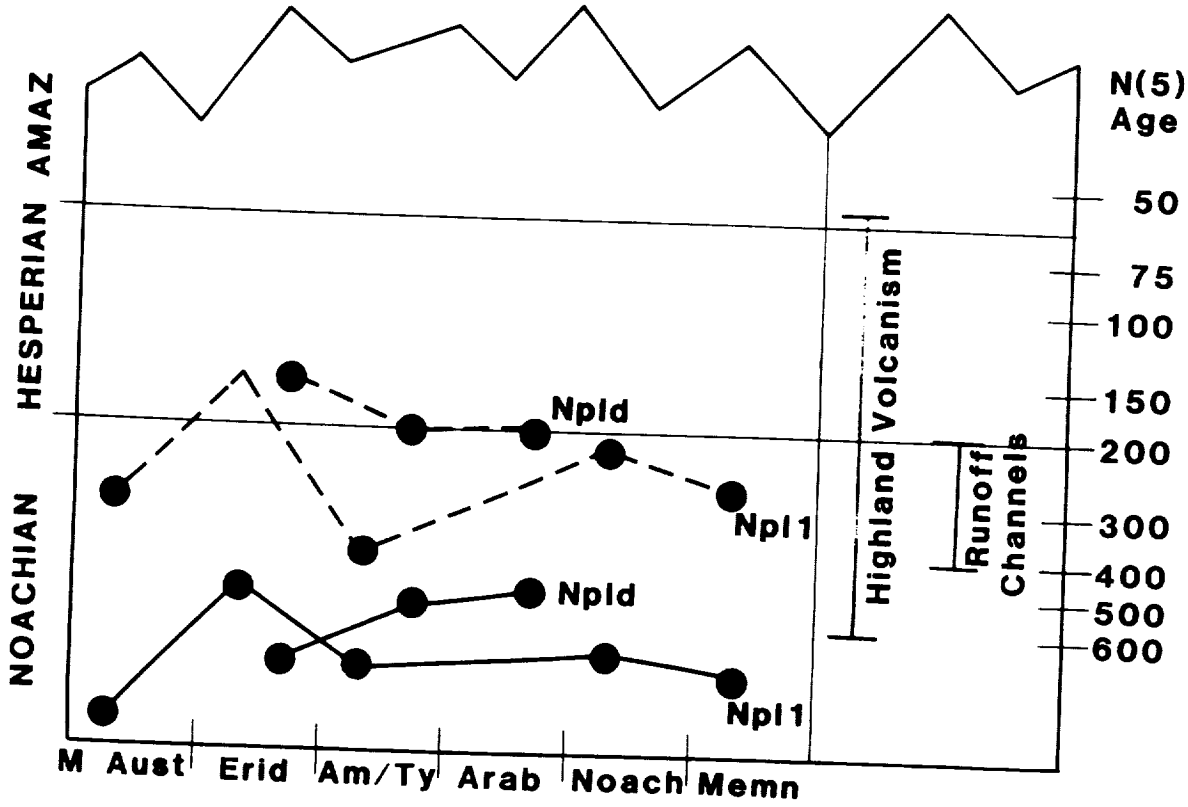

Figure 2. Timing of resurfacing in the areas mentioned in text. N(5) ages represent the number of craters >5-km-diameter per million square kilometers. Solid lines represent age of material based on all craters. Dashed lines represent termination of resurfacing event based on fresh, superposed craters.

REFERENCES: [1] Wilhelms, D.E. and R.J. Baldwin, Proc. Luanr Planet. Sci., 19th, 355-365, 1989. [2] Hartmann, W.K. et al., In Basaltic Volcanism on the Terrestrial Planets, Chap. 8, pp. 1049-1127, Pergamon, New York, 1981. [3] Craddock, R.A. and T.A. Maxwell, Lunar Planet. Sci., 20, 191-192, 1989. [4] Maxwell, T.A. and R.A. Craddock, Lunar Planet. Sci., 20, 646-647, 1989. [5] Craddock, R.A. and T.A. Maxwell, Resurfacing of the martian highlands in the Amenthes and Tyrrhena region, J. Geophys. Res., in review. [6] Tanaka, K.L., Proc. Lunar Planet. Sci. Conf., 17th, in J. Geophys. Res., 91, E139-E158, 1986. [7] Scott, D.H., and K.L. Tanaka, Geologic map of the western equatorial region of Mars, 1:15M scale, U.S.G.S. Map I-1802-A, 1986. [8] Greeley, R. and J.E. Guest, Geologic map of the eastern equatorial region of Mars, 1:15M scale, U.S.G.S Map I-1802-B, 1987. [9] Tanaka, K.L. and D.H. Scott, Geologic map of the polar regions of Mars, 1:15M scale, U.S.G.S. Map I-1802-C, 1987. [10] Greeley, R. and P.D. Spudis, Rev. Geophys. Space Phys., 19, 13-41, 1981. [11] Thomas, P., J. Geophys. Res., 87, 9999-10,008, 1982.

THE EFFECTS OF FLOODS, VOLCANISM AND POLAR PROCESSES ON THE D/H RATIO IN THE MARTIAN ATMOSPHERE. M. H. Carr, U. S. Geological Survey, Menlo Park, CA 94025.

Water in the martian atmosphere is 5.1 times more enriched in deuterium than terrestrial water (Owen et al., 1988; Bjoraker et al., 1989). The enrichment has been previously attributed to either massive loss of water early in the planet's history (Owen et al., 1988) or to the presence of only a very small reservoir of water that has exchanged with the atmosphere over geologic time (Yung et al. 1988). However, early massive loss of nearly all the planet's water appears inconsistent with abundant evidence for the action of water throughout Mars history, and exchange of only small amounts of water with the atmosphere is contrary to interpretation of channels as water worn, and interpretation of the poles as a sink for water. Here we examine what effect geologic processes might have on D/H in the atmosphere, and assess whether the geologic model for the evolution of the Mars surface that has been developed over the last two decades needs major revision.

Outflow channels are generally believed to have been formed by large floods. A large flood would immediately inject a substantial amount of water into the atmosphere, then in the long term water would sublime into the atmosphere from the ice rich deposits that must have formed where the water pooled after the flood was over. To estimate the amount of water injected into the atmosphere, a flood was divided into three stages. Assuming present conditions on Mars at the time of a flood, and using previously derived techniques for determining sublimation rates (Toon et al., 1980), it was estimated that roughly 10^{17} g of water would evaporate into the atmosphere in the active stage, while the flood was in progress. This water probably would have frozen out rapidly at the poles to form an ice layer a few centimeters thick. In the second stage, the lake that formed at the end of the flood channel freezes, and the thermal anomaly created by the presence of the lake dissipates. It was estimated that in a typical flood the terminal lake would take about one year to freeze solid and the thermal anomaly would take about 6 years to dissipate during which time about another 10^{17} gm of water would evaporate into the atmosphere and be precipitated out at the poles. The long term fate of the terminal ice deposits would depend on their latitude and thickness of any superimposed dust. Most of the floods in Elysium and Hellas, and around Chryse Planitia appear to have pooled at high latitudes (McGill, 1985; Lucchitta et al., 1986). Dust would affect the stability of ice deposits by reducing daily temperature excursions and inhibiting movement of water vapor from the buried ice to the surface. These effects were modeled using the techniques developed by Clifford and Hillel (1983) and some results are shown in Figure 1. For an ice deposit at 50^{o} latitude, covered with a few tens of centimeters of dust, sublimation rates are estimated to be extremely low, in the range of 10^{-7} to 10^{-8} g cm^{-2} yr^{-1}. Sublimation rates at the equator are over 100 times higher. Thus, the immediate effect of a flood on the atmospheric D/H would be to reset the atmospheric D/H to the value for groundwater. The long-term effect would depend on the latitude of the terminal ice deposit. Sublimation rates are so low for high latitude deposits that the D/H in the atmosphere could become enriched with respect to groundwater in response to upper atmosphere losses. If the terminal ice deposit were at low latitude, the atmosphere would be maintained at the D/H value for groundwater until the deposit had fully sublimed.

Volcanism is likely to have episodically introduced water into the atmosphere throughout the history of the planet. Greeley (1987) estimates that 25 to 41 m of water averaged over the whole planet have been introduced onto the surface by volcanism during the last 3.5 Ga. Judging from the size of lava flows, individual eruptions could almost instantaneously introduce 10^{13} to 10^{17} gm of water into the atmosphere. The larger eruptions would inject enough water into the atmosphere to reset its D/H ratio to that of juvenile water. Much of the erupted water would have rapidly frozen out at the poles without having its D/H ratio changed.

The effect of polar processes on D/H in the atmosphere depends on how actively water at the poles is exchanging with the atmosphere. If the Yung et al. (1988) estimates of loss of hydrogen from the upper atmosphere are correct, and water at the poles has actively interchanged with the atmosphere, then the poles can contain no more than 0.2 m of water averaged over the whole planet. But this conclusion is inconsistent with evidence of introduction of water onto the surface by floods and volcanism, and with the current perception of the polar layered terrains as ice rich. Jakosky (in press) suggested that Yung et al (1988) had underestimated hydrogen loss rates. He suggested that loss rates at high obliquity could be 100 times present rates, and the time averaged value 20 times the present rate. If so, then the reservoir of water at the surface would be correspondingly increased. An alternative explanation of the inconsistency is that exchange of water between the poles and the atmosphere is minimal, and restricted to the upper few centimeters of the polar deposits. Thus, new ice added to the polar deposits as a result of floods or volcanism, retains its initial D/H ratio except for the upper surface. In this case, the D/H in the atmosphere evolves almost independently of the poles, and reveals little about the inventory of water at the surface. Such a scenario is consistent with the crater ages of Plaut et al. (1989), which suggest that the polar layered terrains are older than formerly thought.

We can conclude that the D/H enrichment of the atmosphere is not necessarily that of the bulk of the near surface water. The evolution of D/H in the atmosphere is likely to have been episodic. Floods and eruptions would have periodically reset the atmospheric D/H to the groundwater and juvenile values respectively. Between these events the atmosphere would have become enriched in deuterium at a rate dependent on the rate of interchange of water between the atmosphere and other surface reservoirs such as the poles.

REFERENCES. Bjoraker, G. 1., Mumma, M. J., and Larson, H. P., Proc. 4th Int., Conf. on Mars, Tucson, 69-70 (1989). Clifford, S. M., and Hillel, D., J. Geophys. Res., 88, 2456-2474 (1983). Greeley, R., Science, 236, 1653-1654 (1987). Jakosky, B. M., J. Geophys. Res. (in press). Lucchitta, B. K., LPSC XVII, 498-499 (1986). Mc Gill, G. E., LPSC XVI, 534-535 (1985). Owen, T., Maillard, J. P., deBergh, C., and Lutz, B. L., Science, 240, 1767-170 (1988). Plaut, J. J., Kahn, R., Guiness, E. A., and Arvidson, R. E., Icarus, 76, 357-377 (1988). Toon, O. B., Pollack J. B, Ward, W., Burns, J. A., and Bilski, K., Icarus, 44, 552-607 (1980). Yung, Y. L., Wen, J., Pinto, J. P., Allen, M., Pierce, K. K., and Paulsen, S., Icarus, 76, 146-159 (1988).

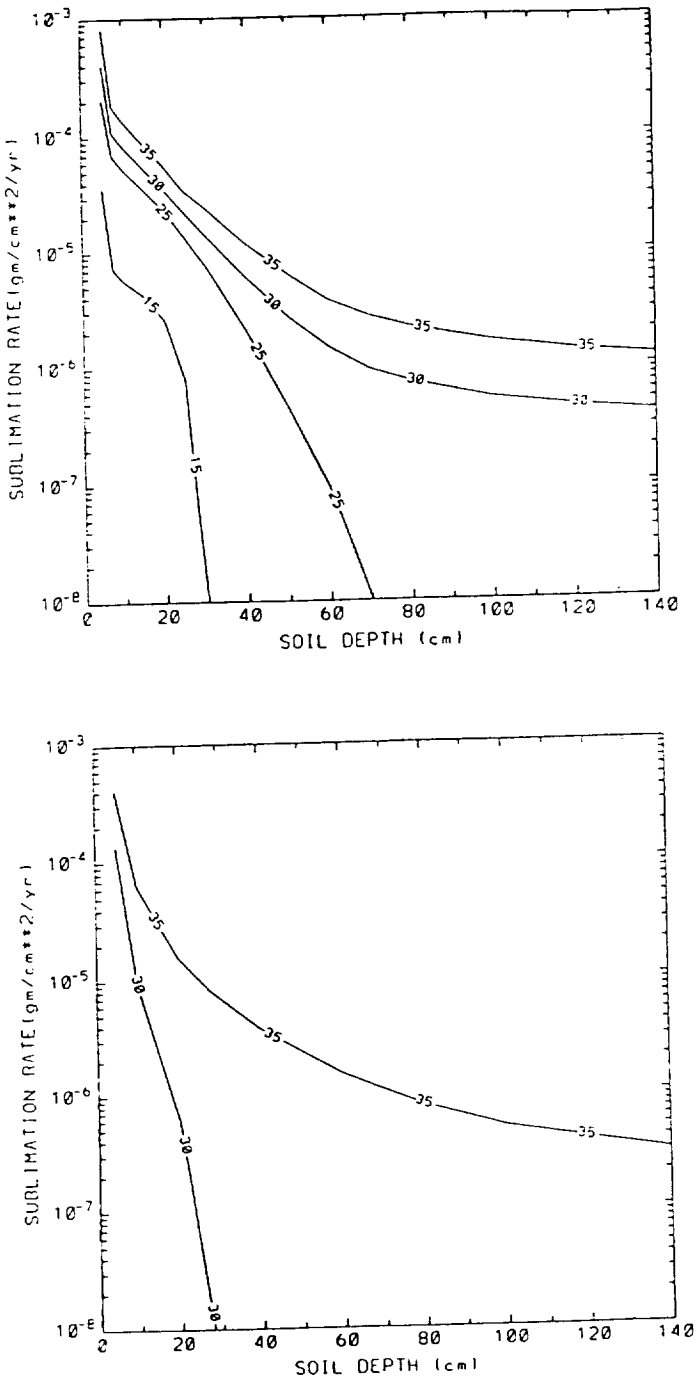

Figure 1. Sublimation rates of ice as a function of the thickness of the overlying dust. Different curves are for different obliquities. Upper graph is for 40^{o} latitude. Lower graph is for 60^{o} latitude.

Characteristics of the Martian Atmospheric Surface Layer

Gary D.Clow (U.S. Geological Survey, MS946, Menlo Park, CA 94025)
Robert M.Haberle (NASA/Ames Research Center, Moffett Field, CA 94035)

We extend elements of various terrestrial boundary layer models to Mars in order to estimate sensible heat, latent heat, and momentum fluxes within the martian atmospheric surface ("constant flux") layer. The atmospheric surface layer consists of an interfacial sublayer (#1) immediately adjacent to the ground and an overlying fully turbulent surface sublayer (#2) where wind-shear production of turbulence dominates buoyancy production. Within the interfacial sublayer, sensible and latent heat are transported by non-steady molecular diffusion into small-scale eddies which intermittently burst through this zone. Both the thickness of the interfacial sublayer and the characteristics of the turbulent eddies penetrating through it, depend on whether airflow is aerodynamically smooth or aerodynamically rough, as determined by the Roughness Reynold's number. Within the overlying surface sublayer (#2), similarity theory can be used to express the mean vertical windspeed, temperature, and water vapor profiles in terms of a single parameter, the Monin-Obukhov stability parameter.

To estimate the molecular viscosity and thermal conductivity of a CO_2-H_2O gas mixture under martian conditions, parameterizations were developed using data from the TPRC Data Series [1] and the first-order Chapman-Cowling expressions; the required collision integrals were approximated using the Lenard-Jones (12,6) potential. Parameterizations for specific heat and binary diffusivity were also determined. The Prandtl and Schmidt numbers derived from these thermophysical properties are found to range 0.78 - 1.0 and 0.47 - 0.70, respectively, for Mars. Brutsaert's model for sensible and latent heat transport within the interfacial sublayer for both aerodynamically smooth and rough airflow has been experimentally tested under similar conditions [2], validating its application to martian conditions. For the surface sublayer (#2), we modify the definition of the Monin-Obukhov length to properly account for the buoyancy forces arising from water vapor gradients in the martian atmospheric boundary layer. This length scale is then utilized with similarity-theory turbulent-flux profiles with the same form as those used by Businger *et al.* [3] and others.

We find that under most martian conditions, the interfacial and surface sublayers offer roughly comparable resistance to sensible heat and water vapor transport and are thus both important in determining the associated fluxes. Airflow over surfaces similar to terrestrial polar snow (surface roughness length z_0 approx. 0.03 cm) is generally found to be aerodynamically smooth at low martian pressures (P<30 mb) but aerodynamically rough at high pressures (P>300 mb); airflow at the Viking Lander sites is aerodynamically transitional under current martian conditions. For aerodynamically smooth airflow, the thickness of the interfacial sublayer is found to be up to 100 times thicker for Mars than is typical for the Earth. At low pressures (P<30 mb) and high temperatures (T>250 K), buoyancy forces due to water vapor gradients can become so high on Mars that the surface sublayer (#2) essentially disappears (the Monin-Obukhov length becomes comparable to the thickness of the interfacial sublayer). At this point, the atmospheric boundary layer transitions to the "free convection" regime [4]. Free convection sensible and latent heat fluxes are smaller than those for the case when the surface sublayer (#2) is present. As expected, friction velocities u_* and the sensible and latent heat fluxes are found to be extremely sensitive to the Monin-Obukhov stability parameter for stable atmospheric conditions and mildly sensitive for unstable conditions.

The ability to predict heat losses across an interfacial boundary layer and to predict the shapes of the windspeed and temperature profiles in the atmospheric surface layer, should prove useful for estimating heat losses from engineering structures deployed on the martian surface and for improving our understanding of water vapor transfer rates from icy surfaces (such as the polar caps) to the atmosphere.

References: [1] Touloukian, Y.S. (1972) **Thermophysical Properties of Matter: The TPRC Data Series,** vol.3,6,11; [2] Brutsaert, W. (1975) **Water Resour. Res.,11**,543-550; [3] Businger *et al.*(1971) **J.Atmos.Sci.,28**,181-189; [4] Clow, G.D. and R.M. Haberle (1990) **Lunar and Planet. Sci. XXI,** in press.

Free Convection in the Martian Atmosphere

Gary D.Clow (U.S. Geological Survey, MS946, Menlo Park, CA 94025)
Robert M.Haberle (NASA/Ames Research Center, Moffett Field, CA 94035)

We investigate the "free convective" regime for the martian atmospheric boundary layer (ABL). This state occurs when the mean windspeed at the top of the ABL drops below some critical value U_c and positive buoyant forces are present. Such forces can arise either from vertical temperature or water vapor gradients across the atmospheric surface layer. During free convection, buoyant forces drive narrow plumes that ascend to the inversion height with a return circulation consisting of broad slower-moving downdraughts. Horizontal pressure, temperature, windspeed, and water vapor fluctuations resulting from this circulation pattern can be quite large adjacent to the ground (within the surface layer). These local turbulent fluctuations cause non-zero mean surface stresses, sensible heat fluxes, and latent heat fluxes, even when the mean regional windspeed is zero. Although motions above the surface layer are insensitive to the nature of the surface, the sensible and latent heat fluxes are primarily controlled by processes within the interfacial sublayer immediately adjacent to the ground during free convection. Thus the distinction between aerodynamically smooth and rough airflow within the interfacial sublayer is more important than for the more typical situation where the mean regional windspeed exceeds the value U_c. Buoyant forces associated with water vapor gradients are particularly large on Mars at low pressures ($P<30$ mb) and high temperatures ($T>250$ K) when the surface's relative humidity is 100%, enhancing the likelihood of free convection under these conditions. On this basis, Ingersol [1] postulated the evaporative heat losses from an icy surface on Mars at 273 K and current pressures would exceed the available net radiative flux at the surface, thus prohibiting ice from melting at low atmospheric pressures.

Recently, Schumann [2] has developed equations describing the horizontal fluctuations and mean vertical gradients occurring during free convection. However, his model is limited to the case where free convection is driven solely by thermal buoyancy and the surface is aerodynamically rough. Within these restrictions, model results compare very well with those of a detailed large-eddy simulation (LES) which in turn generally agree with available atmospheric observations [3]. Despite large horizontal wind velocities associated with the updraughts, the LES demonstrates that the time-derivatives for horizontal motion in the surface layer are small, validating the use of Monin-Obukhov theory in the model.

We have generalized Schumann's model to include convection driven by water vapor gradients and to include the effects of circulation above both aerodynamically smooth and rough surfaces. Applying the model to Mars, we find that nearly all the resistance to sensible and latent heat transfer in the ABL occurs within the thin interfacial sublayer at the surface. Free convection is found to readily occur at low pressures and high temperatures when surface ice is present. At 7 mb, the ABL should freely convect whenever the mean windspeed at the top of the surface layer drops below about 2.5 m s^{-1} and surface temperatures exceed 250 K. Mean horizontal fluctuations within the surface layer are found to be as high as 3 m s^{-1} for windspeed, 0.5 K for temperature, and 10^{-4} kg m^{-3} for water vapor density. Airflow over surfaces with a surface roughness length z_0 of about 0.03 cm (similar to the Antarctic Polar Plateau) is found to be aerodynamically smooth on Mars during free convection for all pressures between 6 and 1000 mb while surfaces with $z_0=1$ cm are aerodynamically rough over this pressure range.

Free convective latent-heat fluxes are of particular interest because they establish the *minimum* evaporative heat losses that will occur from an icy surface at a given temperature. Fig.1 shows the predicted latent heat fluxes during free convection for the limiting case where the ABL is isothermal and the surface temperature is 273 K. For a surface resembling average terrestrial polar snows (curve A), our predicted fluxes are a factor of 4 smaller than those given by Eq.(1) of Ingersol [1], making it proportionally easier to melt ice on Mars. Fig.2 shows the albedo required for the net radiative flux at the surface to just balance the predicted latent heat losses at 273 K at the time of maximum incoming solar radiation. The lowest albedo that can be achieved for martian ice surfaces is about 0.2 [4]. Hence, atmospheric pressures need to be at least 100 mb at the poles and about 6 mb at the equator before ice can melt under the best of conditions.

References: [1] Ingersol, A.P. (1970) **Science, 168**, 972-973; [2] Schumann, U. (1988) **Boundary-Layer Meteorol., 44**, 311-326; [3] Schmidt, H. and U. Schumann (1989) **J.Fluid Mech., 200**, 511-562; [4] Clow, G.D. (1987) **Icarus, 72**, 95-127.

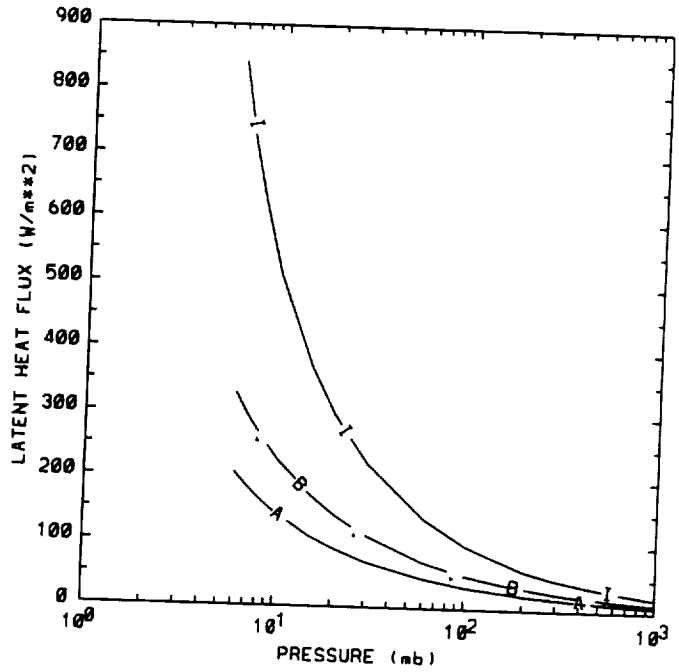

Fig.1: Predicted latent heat fluxes at 273 K for a surface with z_0=0.03 cm (curve A) and z_0=1 cm (curve B). Shown for comparison are the free convection predictions of Ingersol [1], (curve I).

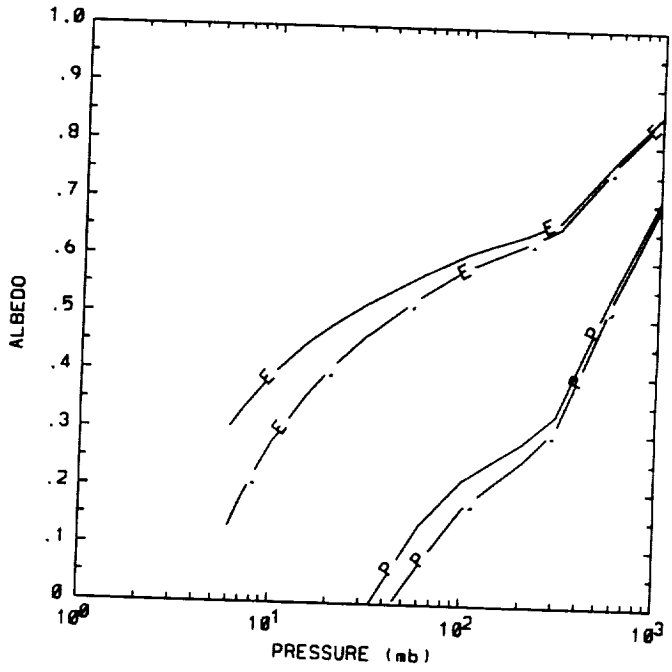

Fig.2: Highest albedos for which ice can melt under optimal conditions in the equatorial regions (curves E) and the polar regions (curves P). Solid lines refer to aerodynamically smooth surfaces while dashed lines are for aerodynamically rough surfaces.

DISCRIMINATION OF ACTIVE AND INACTIVE SAND FROM REMOTE SENSING: THE KELSO DUNES, MOJAVE DESERT, CALIFORNIA

Elizabeth C.I. Paisley, Lisa R. Gaddis, and Ronald Greeley, Department of Geology, Arizona State University, Tempe, Arizona 85287 U.S.A.

Aeolian deposits are observed on the Earth and Mars and they may exist on other planets or satellites. Although planetary surface processes are not dominated by aeolian activity, it is important to consider such activity because the bedrock geology may be altered and/or obscured by aeolian deposits. The ability to identify and to characterize aeolian deposits by remote sensing will help with assessment of recent sediment transport and interpretation of regional geologic histories. Previous research in the Gran Desierto, Mexico has demonstrated the capability of spectral discrimination between active and inactive sand [Blount, 1988]. In that area, active sand is spectrally brighter than inactive sand because of texture and composition. Texturally, the active sand has a higher proportion of saltation-sized grains (125-250 mm) and a more unimodal distribution than the inactive sand, which has more coarse (>250 mm) and fine (<62 mm) grains. Compositionally, the inactive sand contains a higher percentage of dark lithics in the coarsest and finest size fractions. The objective of this study is to assess further the utility of remote sensing techniques to identify active and inactive sand surfaces in the Kelso dunes. The study represents our preliminary results in the effort to characterize the origin and evolution of sediments in and around the Kelso dunes of the Mojave Desert, California.

A Landsat TM image of the Kelso region (acquired April 13, 1987) was processed to use as a study base. A Gaussian stretch of the image was implemented, with bands 5, 4, and 1 as the red, green and blue color bands. Potential units of active and inactive sand were identified and mapped using brightness and textural patterns as criteria for differentiation. To test the identification of these units, field work was conducted in the Kelso dunes area from April 21 to April 25, 1989. Eighty-five (85) surface sand samples and one rock sample were collected. The site of each sample was described as active, stabilized/subdued, inactive, or sand sheet by noting the type and abundance of vegetation, dune morphology, and presence of slip faces and/or active ripple marks. In general, it was observed that previously identified active and inactive units agreed well with those identified in the field.

Laboratory analysis of the field samples was performed to quantify texture and composition, and consisted of grain-size analysis and point-counts. Results of the grain-size analysis agreed with those in the Gran Desierto; inactive sand samples at Kelso are more bimodal, containing a higher percentage of both finer and coarser sand than the active samples. Compositionally, Kelso samples have a high percentage of quartz. Although the Kelso samples contain more dark grains in the finer size fractions, as in the Gran Desierto, they do not have the large amount of dark grains in the coarse size fraction observed in the Gran Desierto. This

example, and other compositional differences between the Kelso area and the Gran Desierto, are due to different regional source materials in each area. The source of the coarse, dark grains at the Gran Desierto is basalt, weathered from the near-by Pinacate volcanic field and brought into the outskirts of inactive sand. Another important difference is that the active sand at Kelso has concentrated lag deposits of magnetite, weathered from the surrounding mountains. This has a significant effect on the laboratory spectra of the active units.

High-resolution spectra of the units were obtained from the RELAB facility at Brown University. The spectra were deconvolved to TM equivalent 6-point spectra and corrected for viewing geometry. After atmospheric corrections were applied to the image [Chavez, 1988], DN values were converted to reflectance, giving TM 6-point spectra for each unit. Comparison of these spectra show the effect of the magnetite concentrations in the active units at Kelso. A small percent of magnetite in a sample can flatten spectral absorption bands (quartz and atmospheric water) and greatly decrease the spectral brightness [Singer, 1981]. This has the effect of decreasing the spectral brightness in the active samples so that they appear darker, more like the inactive samples. RELAB spectra are influenced to a greater degree than the TM spectra, no doubt because small sampling sites do not always prove equivalent to the large areas viewed by the TM.

Examination of plots of unit characteristics versus degree of activity show, several trends. As sand becomes more stabilized: sorting decreases, percent of fines increases, percent of vegetation increases, DN brightness decreases, percent of active ripple marks decreases, and percent of active slip faces decrease. The sand in the Kelso region is not as obviously active or inactive as in the Gran Desierto, but represents varying degrees from active to inactive. Because of regional differences in source materials, the use of remote sensing to discriminate active and inactive sand in the Kelso area is more difficult than in the Gran Desierto, but still possible.

References

Blount, H.G., 1988, Regional aeolian dynamics from remote sensing: Origin of the Gran Desierto, Sonora, Mexico, Ph.D. dissertation, Arizona State University.

Chavez, P.S., 1988, An improved dark-object subtraction technique for atmospheric scattering correction of multispectral data, Remote Sensing of Environment, v. 24, pp. 459-479.

Singer, R.B., 1981, Near-Infrared spectral reflectance of mineral mixtures: Systematic combinations of pyroxene, olivine, and iron oxides, J. Geophys. Res., v. 86, pp. 7967-7982.

MARTIAN DUST THRESHOLD MEASUREMENTS - SIMULATIONS UNDER HEATED SURFACE CONDITIONS

Bruce R. White, Department of Mechanical Engineering,
University of California, Davis, CA 95616 and
Ronald Greeley and Rodman N. Leach, Geology Department,
Arizona State University, Tempe, AZ 85201

Diurnal changes in solar radiation on Mars set up a cycle of cooling and heating of the planetary boundary layer, this effect strongly influences the wind field. The stratification of the air layer is stable in early morning since the ground is cooler than the air above it. When the ground is heated and becomes warmer than the air its heat is transferred (by molecular conduction action - no flow at the ground) to the air above it. The heated parcels of air near the surface will, in effect, increase the near surface wind speed or increase the aeolian surface stress the wind has upon the surface when compared to an unheated or cooled surface.

This means that for the same wind speed at a fixed height above the surface, ground-level shear stress will be greater for the heated surface (unstable case) than an unheated surface. Thus, it is possible to obtain saltation threshold conditions at lower mean wind speeds when the surface is heated. Even though the mean wind speed is less when the surface is heated, the surface shear stress required to initiate particle movement remains the same in both cases.

To investigate this phenomenon, low-density surface dust aeolian threshold measurements have been made in the MARSWIT wind tunnel located at NASA Ames Research Center, Moffett Field, California. The MARSWIT is an open circuit wind tunnel that is operated within a large pressure chamber (4000 m^3) that allows a range in operating pressure from a few millibar to one atmosphere of pressure (Greeley et al., 1977). The current experiments were carried out with both heated and unheated surface temperature conditions. The heated surface condition represents or models diurnal surface heating by radiation from the sun. The unheated surface represents a neutrally stable condition. The heating of the floor primarily affects the vertical turbulent structure of the boundary layer. The exact level of heating is unknown under Mars surface conditions; however, it is expected to produce a maximum temperature difference of 25 K between the surface and the atmosphere above it. (Hess et al. 1977; Ryan and Henry, 1979).

Limited vertical temperature profiles also were measured under several heating conditions which enabled a determination of friction speed, u_* as a function of freestream speed at a specified heating condition. Additionally, the surface material temperature was measured with a thermocouple from which the value of bulk Richardson number was determined.

On Mars, from the Viking Landers, there are no direct data available as to the mean wind speed and surface temperature when the initial dust movement occurred. However, Arvidson, et al. (1983) estimate that winds of 25 to 30 m/s would be needed to initiate particle motion of optimum sized surface material (i.e., about 100 microns in mean diameter). Presumably this would occur at Mars noon when the temperature difference between the surface and Lander was a maximum. For the Lander case this corresponds to a bulk Richardson number of about -0.02 at threshold.

The experiments were carried out for two different sized particles, one having a mean diameter of about 105 microns while the other sample material had a mean diameter of about 11 microns. Threshold measurements were made under two surface temperature conditions: one where the surface was not heated (i.e., uniform temperature throughout the boundary layer profile) and the other where the surface was heated. The amount of surface heating was varied for each experiment and approximately represents a value of bulk Richardson number from zero to -0.02 which is believed to be in the range that exist on the surface of Mars near the Viking Lander sites.

The first series of tests examined threshold values of the 100 micron sand material. At 13 mb surface pressure the unheated surface had a threshold friction speed of 2.93 m/s (and approximately corresponded to a velocity of 41.4 m/s at a height of 1 meter) while the heated surface, equivalent bulk Richardson number of -0.02, yielded a threshold friction speed of 2.67

m/s (and approximately corresponded to a velocity of 38.0 m/s at a height of 1 meter). This change represents an 8.8% decrease in threshold conditions for the heated case. The values of velocities are well within the threshold range as observed by Arvidson et al., 1983. Figure 1 presents this data. As the surface was heated the threshold speed decreased. At a value of bulk Richardson number equal to - 0.02 the threshold friction speed and threshold wind speed appeared to level-off to a constant value.

This trend also was observed in the MARSWIT experiments involving the 11 micron sized-silt material. Although we were not able to directly measure extensive numerical values to support this trend, it was readily observed in the tunnel testing. Note, it is extremely difficult to maintain constant ambient chamber pressure while continuously increasing the wind flow through the tunnel. Figure 2 does, however, present the two data points that have been measured to date. The threshold friction speed at 6.7 mb pressure of the 11 micron dust material was found to be 9.4 m/s with the unheated surface. When the surface was heated to a value of bulk Richardson number equal to -0.01, the friction threshold speed was reduced by 18% to a value of 7.7 m/s. Unfortunately, this is the only ambient chamber pressure (6.7 mb) that the MARSWIT was able to achieve threshold conditions.

The data results suggest that as the surface is heated the threshold wind speed will decrease. The amount reduction in threshold wind speed appears to be a function of bulk Richardson number as well as the mean size of the test material. The smaller sized materials will tend to experience more of a reduction in threshold wind speed. It is anticipated that for larger size particles there will be negligible difference between heated and unheated surfaces (larger than 1 mm in diameter) in values of threshold wind speed.

REFERENCES

Arvidson, R.E., E.A. Guinness, H.J. Moore, J. Tillman, and S.D. Wall, Three Mars Years: Viking Lander I Imaging Observations, Science, Volume 222, Number 4623, pp. 463-468.

Greeley, R., B.R. White, J.B. Pollack, J.D. Iversen, and R.N. Leach, Dust Storms of Mars: Considerations and Simulations, NASA Tech. Memo., TM 78423, 1977.

Hess, S.L., R.M. Henry, C.B. Leovy, J.A. Ryan, and J.E. Tillman, Meterological Results From the Surface of Mars: Viking 1 and 2, Journal of Geophysical Research, Volume 82, No. 28, pp. 4559-4574.

Ryan, J.A. and R.M. Henry, Mars Atmospheric Phenomena During Major Dust Storms, as Measured at Surface, Journal of Geophysical Research, Volume 84, No. 86, pp. 2821-2829.

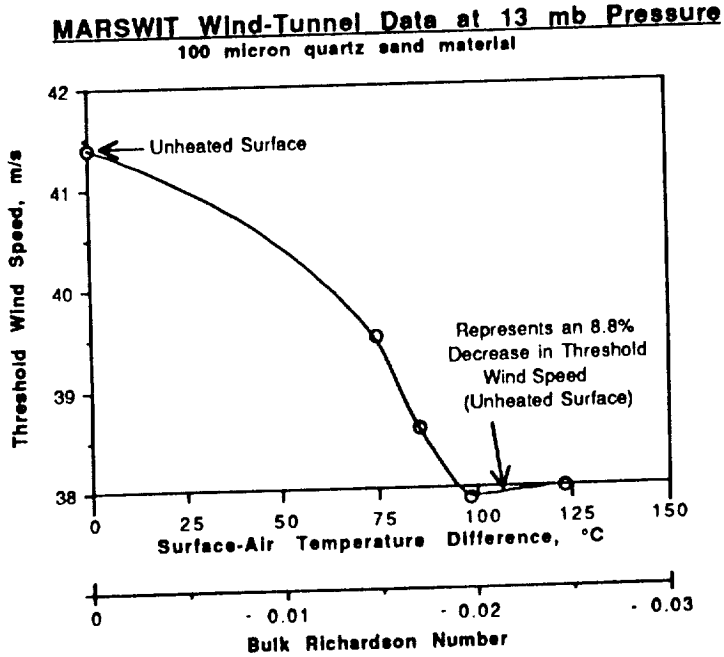

Figure 1. Threshold wind speed as a function of temperature difference (surface and free-stream) and Bulk Richardson Number for 100 micron diameter Quartz sand material at an ambient pressure of 13 mb.

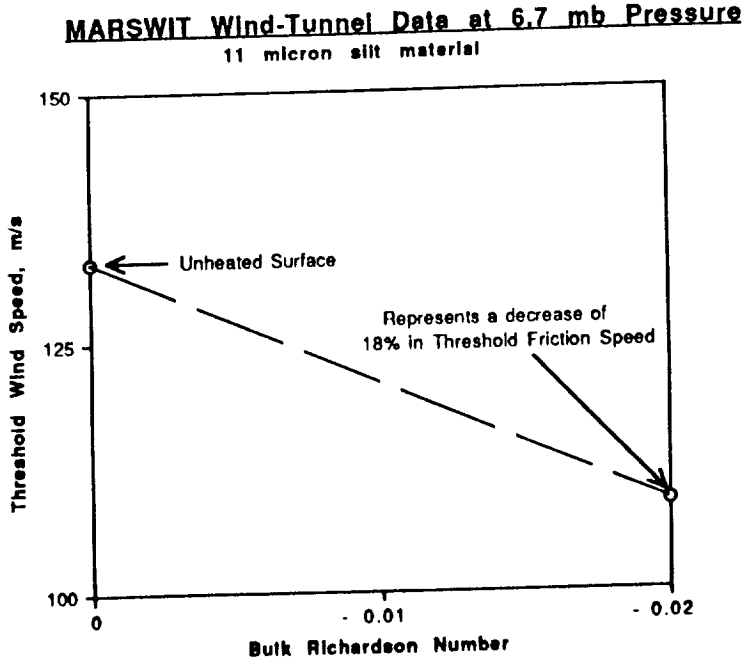

Figure 2. Threshold wind speed as a function of approximate Bulk Richardson Number for 11 micron diameter silt material at an ambient pressure of 6.7 mb.

THE EFFECT OF SURFACE ROUGHNESS ON THRESHOLD VELOCITY AND FLUX AT EARTH AND MARTIAN ATMOSPHERIC PRESSURES

Bret Boundy, Department of Geology and Geophysics,
University of Wyoming, Laramie, Wyoming 82071
Rodman Leach, Department of Geology, Arizona State University, Tempe, Arizona 85287-1404

One of the many parameters affecting aeolian processes on Mars is the natural surface roughness provided by the rock-strewn surface. A wind tunnel investigation of the effect of surface roughness on saltation threshold velocity and flux of fine sand at both terrestrial and martian atmospheric density was conducted in the Martian Surface Wind Tunnel (MARSWIT) at NASA Ames Research Center. Surface roughness was provided by a pattern of regularly spaced blocks fastened to the wind tunnel floor. The blocks were 5.7 cm high, 3.8 cm wide, and 1.9 cm thick (dimension ratio of 3:2:1), oriented with the 3.8 cm side facing the wind. The space between the blocks in the cross-wind direction was 11.4 cm (3 block widths) and the space between the rows in the wind direction was 11.4 cm with the blocks spaced alternately from row to row. Quartz foundry sand with a median size of 145 microns was used in the experiments. The blocks were installed in the first six meters of the wind tunnel with the sand placed uniformly over the last 2.5 meters of the blocks (the downwind end of the bed of blocks). Different levels of block exposure were produced by two different methods for the Earth pressure runs. The first method involved spreading the sand smooth, flush with the top of the blocks, and allowing the wind to progressively expose the blocks by deflation. The second method was to spread the sand in a smooth layer to a depth which allowed the blocks to project to the desired uniform height. With both methods the saltation threshold velocity and the flux at 1.2 times the threshold velocity was measured for different block projection heights.

Saltation threshold velocity for the sand placed flush with the top of the blocks and deflated by the wind decreased slightly as the blocks were exposed, but then increased rapidly as the block exposure increased, and finally reached a velocity 20% above the initial velocity (Fig. 1). Saltation threshold velocity for sand placed by the second method (smoothed bed) also decreased slightly as the block exposure was increased, but then remained nearly constant for increasing exposure. At each block exposure the threshold velocity became nearly identical with a wind-deflated bed value after running for a short time at 1.2 times threshold velocity (Fig. 1). This is due to the fact that sand is removed by the wind from those areas where the local surface stress is large, and not from those areas where it is low. With the wind-deflated bed those areas of higher surface stress are soon depleted from sand (some of which is deposited in areas of lower surface stress), and higher winds are required to remove the remaining sand. With the smoothed beds, initially there is always sand in areas of high surfaces stress which is removed quickly by the wind.

For the martian pressure runs only the first method was used (sand initially placed flush with the top of the blocks and the wind used to deflate the sand, progressively exposing the blocks). Instead of exposing all of the blocks uniformly as in the Earth pressure runs, a mound of sand remained 0.3 meter from the upwind end of the sand bed and only the sand upwind and downwind of the mound was deflated. There was no initial decrease in saltation threshold velocity, but rather a continual increase with average block exposure (Fig. 2). A second run was made in which the downwind 2.5 meters of blocks were removed and the sand was placed on the wind tunnel floor downwind of the 3.5 meters of remaining blocks. In this test the sand deflated more uniformly, and threshold velocity was obtained as a function of the difference of height of the top of the blocks and the height of the bed of sand. The threshold velocity increased initially as the bed of sand deflated, and then remained constant (Fig. 3).

Flux was measured for each block exposure for the Earth runs at threshold and 1.2 times the threshold velocity. In both of the martian runs the total flux was measured for the entire run for all block exposures at 1.2 times threshold velocity (Fig. 4).

Previous tests indicated that saltation threshold for martian pressures required about the same dynamic pressure for saltation threshold at terrestrial pressures (Greeley, 1980). If the ambient pressure were reduced from 1 bar to 10 mb the required velocity would be expected to increase by a factor of 10. In these tests with the large surface roughness, the wind velocity only needed to be increased by a factor of 8. This indicates that surface roughness is more effective in initiating saltation threshold on Mars than on Earth.

References

Greeley, R., R. Leach, B. White, J. Iversen, and J. Pollack, 1980. Threshold windspeeds for sand on Mars: Wind tunnel simulations, *Geophys. Res. Lett.*, 7, 121-124.

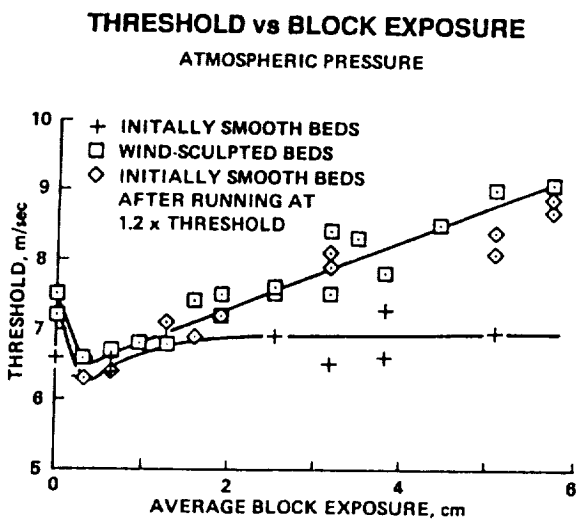

FIGURE 1

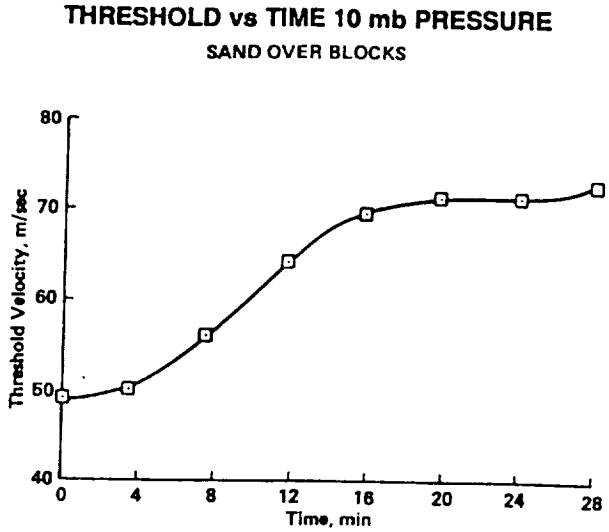

FIGURE 2

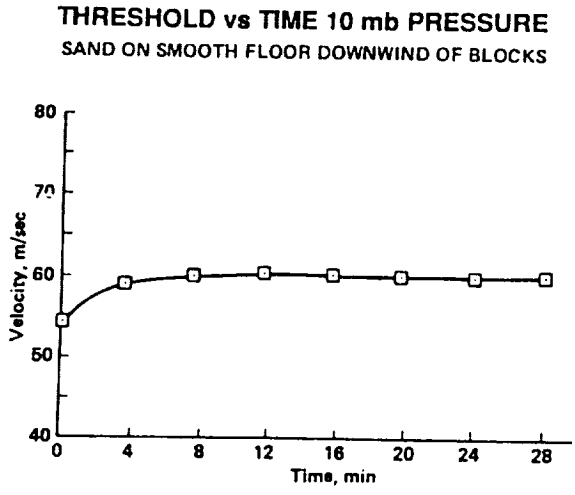

FIGURE 3

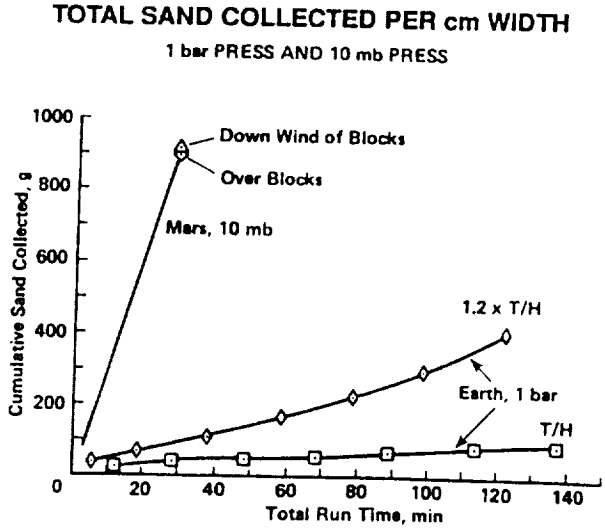

FIGURE 4

EFFECTS OF ROUGHNESS ELEMENTS ON SALTATION

J. D. Iversen*, R. Greeley**, W. P. Wang*, R. Leach***
*Iowa State University, Ames, Iowa
**Arizona State University, Tempe, Arizona
***NASA, Ames Research Center, Moffett Field, California

The aerodynamic characteristics of boundary layer surface protrusions and their effects on aeolian transport are problems of continuing significance. Recent experiments have been performed concerning both (1) the local effects of single roughness elements on drift topography and (2) the effects of distributed roughness on aeolian transport rates and threshold speeds.

For single elements, the flow pattern, and therefore the drift topography and time-dependent progress toward equilibrium, depend considerably on the obstacle shape. A series of experiments was conducted using circular cylinders of varying aspect ratios (i.e., height-diameter ratio). Results are shown in Figs. 1 and 2. Fig. 1 illustrates the growth of erosion volume as a function of time (presented here in dimensionless form) for the upwind erosional moat [1]. The initial slopes of these curves are plotted in Fig. 2. For very short cylinders (aspect ratio less than 0.15), the windward erosional moat ceases to exist and deposition occurs immediately upwind. The upwind separation (horseshoe) vortex increases rapidly in strength with increase in aspect ratio from 0.15 to about one, and the erosion rate increases accordingly, as shown in Fig. 2.

Recent threshold experiments with rectangular block arrays [2] complement earlier experiments with circular cylinders [3]. The effect of multi-element roughness beds on erodible material emplaced between the elements is to increase the threshold shear stress. This effect is shown in Fig. 3 for relatively sparse element arrays. The increase in threshold is a complex function of element shape, aspect ratio, and density. Some degree of correlation is achieved by presenting the data as a function of the ratio of element frontal (windward) area to total surface area.

References

1. J. D. Iversen, W. P. Wang, K. R. Rasmussen, H. E. Mikkelsen, and R. Leach, "Roughness element effect on local and universal saltation transport," NATO Advanced Research Workshop on Sand, Dust, and Soil in Relation to Aeolian and Littoral Processes, Sandbjerg, Denmark, May 1990.
2. B. Boundy and R. Leach, "The effect of surface roughness on flux and threshold velocity of 145 micron sand at atmospheric and Martian pressures," Informal report, NASA, Ames Research Center, 1989.
3. L. Lyles, B. E. Allison, "Wind erosion: uniformly spacing nonerodible elements eliminates effects of wind direction variability," Journal of Soil & Water Conservation, 30, 225-226, 1975.

Figures

1. Upwind dimensionless erosional volume versus dimensionless time for cylinders of various aspect ratios.
2. Dimensionless erosion rate versus aspect ratio. Data points are the initial slopes of the curves in Fig. 1.
3. Ratio of threshold friction speed in the presence of uniform roughness arrays as a function of effective element density.

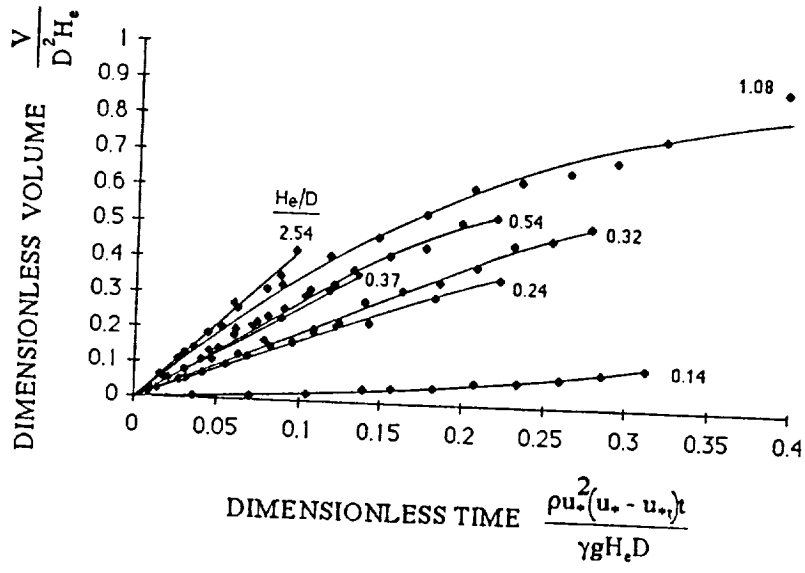
DIMENSIONLESS VOLUME $\frac{V}{D^2H_e}$
1
0.9
0.8
0.7
0.6
0.5
0.4
0.3
0.2
0.1
0
0
0.05
0.1
0.15
0.2
0.25
0.3
0.35
0.4
$\frac{He/D}{2.54}$
1.08
0.54
0.37
0.32
0.24
0.14
DIMENSIONLESS TIME $\frac{\rho u_*^2(u_* - u_{*t})t}{\gamma g H_e D}$

1.

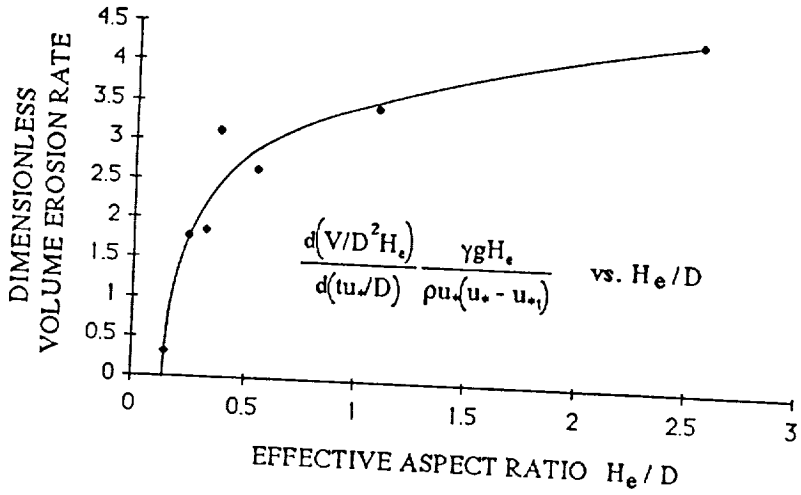
DIMENSIONLESS VOLUME EROSION RATE
4.5
4
3.5
3
2.5
2
1.5
1
0.5
0
0
0.5
1
1.5
2
2.5
3
$\frac{d(V/D^2H_e)}{d(tu_*/D)} \frac{\gamma g H_e}{\rho u_*(u_* - u_{*t})}$ vs. H_e/D
EFFECTIVE ASPECT RATIO H_e / D

2.

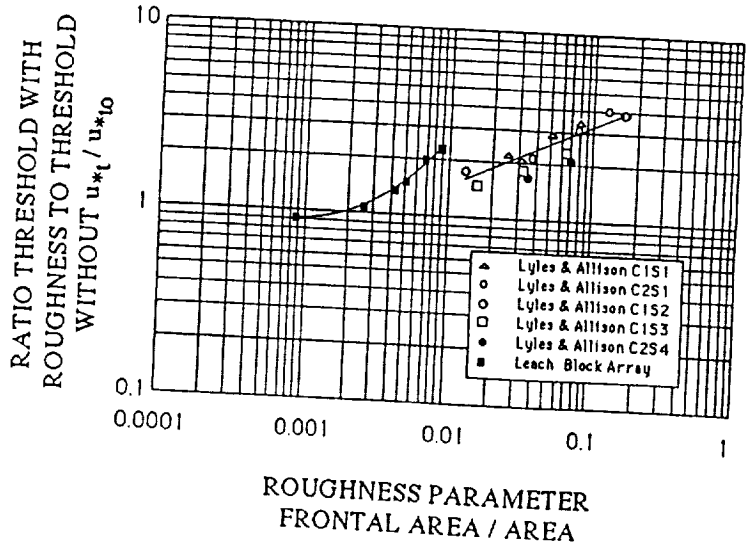
RATIO THRESHOLD WITH ROUGHNESS TO THRESHOLD WITHOUT u_{*t} / u_{*to}
10
1
0.1
0.0001
0.001
0.01
0.1
1
Lyles & Allison C1S1
Lyles & Allison C2S1
Lyles & Allison C1S2
Lyles & Allison C1S3
Lyles & Allison C2S4
Leach Block Array
ROUGHNESS PARAMETER
FRONTAL AREA / AREA

3.

CHAPTER 9

VOLCANIC PROCESSES AND LANDFORMS

WHAT IF DEPOSITS IN THE VALLES MARINERIS ARE VOLCANIC?

Baerbel K. Lucchitta, U.S. Geological Survey, Flagstaff, Ariz. 86001

An intensive study of high-resolution stereoscopic images found that the deposits inside the Valles Marineris include two major types: an older layered sequence that forms high, eroded mesas approaching the elevation of the bounding plateaus [1,2] and a younger sequence composed of varied materials deposited on a deeply eroded surface whose elevation is close to that of the present trough floors. Both may be, at least partly, of volcanic origin.

The older layered deposits were emplaced during or shortly after erosion of the trough walls into spurs and gullies. They consist of dark and light layers. The dark layers are generally thin and some are resistant to erosion; the light layers are thick, poorly stratified, and highly susceptible to wind erosion. These layered deposits, because of their apparent horizontality and lateral continuity, may be lacustrine [3]. However, the volume of interior deposits is too large to have come solely from chemically precipitated [4], inflowing fluvial, or masswasted materials. The amount of eolian material that may have foundered through an ice cap on a lake [2] is probably also insufficient. The existence of resistant, thin, dark units, the susceptibility to deflation of thick, light units, and the volumetric insufficiencies of alternative processes support a volcanic origin for at least some of the layered deposits [5,6]; perhaps the even layering is due to eruption into a paleolake [2].

After the troughs had nearly reached their present configuration through late-stage faulting and erosion, new deposits of diverse morphology and albedo were emplaced [7]. These deposits are generally thin, but in western Candor Chasma they may reach thicknesses of 3 km. Light materials are locally massive bedded or wind fluted; some have lobate fronts. Dark deposits are spectrally nearly gray, have an albedo as low as 5 percent [8], and preferentially occur along fault lines. The younger deposits are not readily explained as lacustrine in origin, because they were emplaced late in Martian history when surface water was unstable in equatorial latitudes. They are too rugged and diverse to be solely eolian. Debris-flow origin is also unlikely because the deposits embay other masswasted features such as talus slopes on the walls of tributary canyons and landslides, and the deposits have no obvious source scars. A volcanic origin is consistent with the apparent flow lobes, the spectral signatures of the dark materials that suggest mafic compositions, the association of the dark materials with structures, and with deflation fluting similar to that seen on terrestrial tuffs in arid regions.

What are the implications if some of the interior deposits are indeed of volcanic origin?

(1) The Valles Marineris grabens would be more like terrestrial rifts that commonly contain volcanic rocks.

(2) Volcanism in this region of Mars would have taken place throughout the history of the Valles Marineris, extending from Early Hesperian to Late Amazonian and perhaps even to recent times.

(3) Early volcanism would have produced voluminous eruptions of flows and light-colored tuffs that formed evenly layered sheets over thousands of square kilometers. These deposits may have been subaqueous.

(4) Later, subaerial volcanism would have produced materials of diverse composition and morphology, including mafic pyroclastic and effusive products, and it would have emplaced voluminous ash-like deposits that flowed readily for tens of kilometers.

Questions arising from these implications include the following: (a) Can the even layering be explained by subaerial volcanism, or need subaqueous volcanism be invoked? If so, how would subaqueous volcanism function in the Martian environment? (b) If the light-colored deposits are indeed ash-flow tuffs, what is their composition? If they are silicic, the discovery would alter our perception of volcanism on Mars. (c) Can some of the ash production be explained by an unusually high volatile content of the magma or by interaction of the magma with the ice-rich regolith [9]?

Overall, the evidence points toward the presence of at least some volcanic rocks inside the Valles Marineris. If so, the timing of the eruptions, the composition of the rocks, and their emplacement mechanisms set important constraints on the magmatic evolution of Mars. The exploration of these possibly volcanic rocks should be a high priority on future missions to Mars.

References

[1] McCauley J.F. (1978) Geologic map of the Coprates quadrangle of Mars. U.S. Geological Survey Miscellaneous Investigations Series Map I-897, scale 1:5,00,000. [2] Nedell S.S., Squyres S.W., and Anderson D.W. (1987) Origin and evolution of the layered deposits in the Valles Marineris. Icarus 70, 409-441. [3] McCauley J.F., Carr M.H., Cutts, J.A., Hartmann W.K., Masursky Harold, Milton D.J., Sharp R.P., and Wilhelms D.E. (1972) Preliminary Mariner 9 report on the geology of Mars. Icarus 17, 289-327. [4] McKay C.P. and Nedell S.S. (1988) Are there carbonate deposits in Valles Marineris, Mars? Icarus 73, 142-148. [5] Peterson, Christine (1981) A secondary origin for the central plateau of Hebes Chasma. Lunar and Planetary Science Conference 12th, Proceedings, Geochimica et Cosmochimica Acta, 1459-1471. [6] Lucchitta B.K. (1987) History of Valles Marineris (abs.). In Lunar and Planetary Science 18, 572-573. [7] Lucchitta B.K. (1987) Recent mafic volcanism

on Mars. Science 235, 565-567. [8] Geissler P.E., Singer R.B., and Lucchitta B.K. (1989) Valles Marineris: Compositional constraints from Viking multispectral images (abs.). In Fourth International Conference on Mars, (Tucson, Arizona: Jan. 10-13, 1989), 111-112. [9] Wilson L. and Head J.W. (1983) A comparison of volcanic eruption processes on Earth, Moon, Mars, and Venus. Nature 302, 663-669.

OLD FAITHFUL GEYSER: WHAT IF IT (HAD) ERUPTED ON MARS (ON A WARM DAY)?

Susan Werner Kieffer, Department of Geology, Arizona State University, Tempe, AZ 85287-1404

Because of the strong indications of correlation between volcanic activity and subsurface water on Mars (for example, pseudocraters in the Chryse Planitia region; small ubiquitous cones in the Utopia-Isidis-Elysium Planitia; braided channels on thin flows in the vicinity of Elysium Mons), the possibility and nature of geothermal activity on Mars is considered. The combination of volcanoes and water usually leads to hydrothermal and phreatic activity. It is, therefore, of interest to compare not only processes of and features from silicate volcanism (e.g., lava flows) on the Earth and Mars, but also styles of phreatic activity.

As an example of the similarities and differences that might be expected between terrestrial and martian geothermal features, the fluid dynamic behavior of Old Faithful geyser is extrapolated to Mars, and the influence of several different martian atmospheric pressure-temperature conditions is examined. The constraint is imposed that a "warm" martian day be considered, where "warm" means that the temperature of the atmosphere into which the geyser erupts at the triple point of water. This constraint allows one to simplify the plume dynamics by ignoring heats and kinetics of ice formation.

On Earth, the water at the base of Old Faithful's conduit decompresses from 116 to 93° C (0.07 bars pressure) at the exit plane (vent). The enthalpy change from 116 to 93° C places an upper limit on the exit plane velocity of u = 88 m/s. Thermodynamic equilibrium conditions during the decompression would allow formation of a jet that is 96 weight percent liquid and 4% vapor, with a bulk density, ρ_o, of 11 kg/m^3 at the vent. Ambient atmospheric density, ρ_a, is 0.7 kg/m^3, and so the jet is negatively buoyant. J.S. Turner (J. Fl. Mech., 26, 779-792, 1966) gives the following equation for jet height:

$$x = 1.85\, F^{1/2}\, D$$

where D is the diameter of the vent, and F is the densimetric Froude number (a parameter that contains only the densities of the jet and atmosphere, the acceleration of gravity, g, and D). (This equation is strictly valid only when the density ratio $\rho_a / \rho_o \sim 1$. Using the values given above, a height x = 50 m, and a value of D = 1.1 m (the average diameter of Old Faithful's fissure-like vent that measures 1.5 by 0.6 m at 0.5 m depth), the calculated exit-plane velocity is 78 m/s--a value in reasonable agreement with the velocity available from enthalpy. This agreement gives some confidence that thermodynamic equilibrium assumptions and simple fluid dynamics relations derived largely at the laboratory scale hold for Old Faithful.

If Old Faithful erupted on Mars into an atmosphere at 0.1° C (the triple point of H_2O), the conversion of enthalpy would produce a jet composed of 16 weight-percent vapor with a density of 0.03 kg/m^3. The maximum jet velocity at the vent would be about 385 m/s. At present, near-surface martian atmospheric density is about 0.015 kg/m^3, half that of the jet. Using a velocity of 350 m/s (thus allowing for some small energy losses in the conduit), the jet from an Old Faithful-like eruption on Mars would rise to about 485 m. The calculated height of the eruption is strongly dependent on the assumed atmospheric density and its vertical gradient. For example, if the atmospheric density were so low that a ballistic equation could be applied to the ejecta from the vent, an Old Faithful-like eruption could produce a plume 20 km high on Mars! Because of the simplifying

thermodynamic and fluid dynamic assumptions, these conclusions must be taken as only indicative of general trends, but they demonstrate clearly that planetary atmospheric pressure and temperature have a significant influence on eruption fluid dynamics and, by implication, on ejecta stratigraphy and morphology.

Dark Materials in Valles Marineris: Indications of the style of Volcanism and Magmatism on Mars

Paul E. Geissler, Robert B. Singer (Planetary Image Research Laboratory, L.P.L., University of Arizona) and Baerbel K. Lucchitta (U.S. Geological Survey, Flagstaff, Arizona).

Rifting on the equatorial canyon system of Valles Marineris provides a unique view of the interior of the martian crust to depths reaching 7 kilometers, exposing several in-situ bedrock units which testify to past volcanic and magmatic processes on Mars. Dark, relatively gray materials, believed to be among the least altered of martian crustal components, are found in a variety of geologic settings in Valles Marineris. These include in-situ wall-rock layers exposed during the formation of the canyon system, canyon floor covering deposits such as eolian dunes, and volcanic materials, possibly indicating relatively recent volcanism in the Valles [1]. Using Viking Orbiter apoapsis color images, we have studied the spectral reflectance and spatial distribution of these materials in an attempt to understand their relation to past episodes of volcanism, tectonism, igneous intrusion, and eolian redistribution in the canyon system.

A series of cliffs in the Ophir Chasma wallrock is interpreted to be exposures of resistant bedrock; the spectral signature of this massive and uniform unit most closely resembles that of terrestrial mafic rocks altered to or coated by crystalline hematite. These Ophir Chasma cliffs may be erosional scars exposing fresh bedrock beneath more weathered wallrock of a similar composition, or they could be a physically and compositionally distinct unit, produced, for example, by igneous intrusion prior to the formation of the Valles.

Application of multispectral mapping techniques to probable young volcanic materials in the Central Troughs yields an inferred distribution of volcanic activity consistent with an interpretation of extrusion along faults near the margins of the canyon floors. Terrestrial examples of similar relationships between tectonism and volcanism include the African Rift Valleys and the Basin and Range Province in the southwest of the U.S., both areas of crustal extension. Since there is no a-priori reason to expect this relationship to occur if the Valles were generated by fluvial erosion or by subsidence of karst or thermokarst, the inferred distribution of volcanism appears to support the hypothesis [2] that the Valles originated through tectonic extension and graben subsidence. While the age of this volcanism is at present poorly constrained, photogeologic indications that it may be relatively recent [1] could suggest that tensional rifting and canyon formation may be ongoing processes.

A thick, regionally extensive deposit observed in outcrops in Juventae Chasma and in a wallrock layer in Coprates is interpreted to be composed of mafic glass on the basis of spectral reflectance, incompetent erosional morphology and marked tendency for eolian redistribution, indicating that the material is easily broken down into sand-sized grains capable of saltation. Multispectral mapping suggests that the eolian floor-covering materials in the lower canyons several hundred kilometers to the east are derived from sources in Juventae and Coprates Chasmata. The interpretation of this unit as volcanic ash requires that the deposits were produced in pyroclastic eruptions at what was once the surface of the planet, and later buried by almost 3 kilometers of plains materials including the 400 to 600 meters of Hesperian lavas believed to resurface the Lunae-Sinai Planum region. The deposits in Coprates and Juventae Chasmata are thus probably among the oldest of martian volcanic materials.

Voluminous regional deposits of basaltic ash have no terrestrial analogue, although they are common on the Moon [3-8] and may be present on Mercury as well [9]. If we tentatively accept the identification of massive mafic ash deposits on Mars, the Moon and Mercury, then the absence of such deposits from the inventory of

present day crustal materials on Earth requires explanation. One possibility is that the processes which produce large pyroclastic eruptions from mafic magmas are confined to smaller terrestrial planets, perhaps because of their reduced gravitational acceleration and atmospheric pressure [10]. Another possibility is that these processes could be confined to the early stages of planetary evolution. By analogy with the lunar mantling deposits, the materials exposed in the layer in Coprates Chasma and in Juventae may represent a relatively volatile-rich phase of volcanism early in the history of Mars, possibly even the late stages of planetary outgassing. The absence of extensive deposits of mafic glass associated with more recent volcanism on Mars and the Moon (and, perhaps, the Earth) might then be due to a diminishing supply of juvenile volatiles. It is interesting to speculate that massive basaltic ash deposits might once have been common on Earth, and later obliterated from the geologic record along with the evidence for an early period of heavy bombardment by impactors.

References cited:

[1] Lucchitta, B.K., Science, 235, 565-567, 1987.
[2] Carr, M.H., J. Geophys. Res., 79, 3943-3949, 1974.
[3] Wilhelms, D.E., U.S. Geol. Survey Prof. Paper 599-F, 1970.
[4] Wilhelms, D.E. and J.F. McCauley, U.S. Geol. Survey Misc. Geol. Inv. Map I-548, 1971
[5] El Baz, F., Lunar Science IV, 217-218, 1973.
[6] Heiken, G.H., D.S. McKay, and P.W. Brown, Geochim. Cosmochim. Acta, 38, 1703-1718, 1974.
[7] Head, J.W., Proc. Lunar Sci. Conf., 5th, 207-222, 1974
[8] Gaddis, L.R., C.M. Pieters, and B.R. Hawke, Icarus, 61, 461-489, 1985.
[9] Schultz, P.H., Phys. Earth Planet. Int., 15, 202-219, 1977
[10] Wilson, L., and J. W. Head, Nature, 302, 663-669, 1983.

STATE OF STRESS AND ERUPTION CHARACTERISTICS OF MARTIAN VOLCANOES. Patrick J. McGovern and Sean C. Solomon, Dept. of Earth, Atmospheric, and Planetary Sciences, Massachusetts Institute of Technology, Cambridge, MA 02139.

Introduction. The growth of a large volcano exerts a load on a planetary lithosphere that can give rise to flexural deformation and faulting. Lithospheric stress, in turn, can influence the state of stress within the volcano and thus the characteristics of eruptions and the deformation and growth of the construct. Previous studies of the stress state within and beneath terrestrial volcanoes have been of two main types: (1) models of plate flexural stresses in isolation [1,2], or (2) finite element models of volcanic bodies with rigid lower boundary conditions [3,4]. We seek a model which couples the stress and displacement fields of both the plate and volcano structures, in order to understand the behavior of Martian volcanoes and the relationship of eruption styles to evolving local and regional stress.

Method. We use the finite element code TECTON, written by H.J. Melosh and A. Rafesky [5,6], to construct axisymmetric models of volcanoes resting on an elastic lithospheric plate overlying a viscoelastic asthenosphere. This code can model buoyancy forces supporting the plate, thus allowing a proper representation of plate flexure. Several values of the ratio of volcano size to lithospheric thickness were considered. The thickness of the strong upper lithosphere was taken from flexure models [7]. The viscoelastic layer was taken to extend to a sufficient depth so that a rigid lower boundary has no significant influence on the results. The code first calculates elastic deformations and stresses and then determines the time-dependent viscous deformations and stresses. Time in the model scales as the Maxwell time in the asthenosphere.

Results. The deviatoric stress field (principal stress directions) resulting from the elastic deformation induced by a volcano 20 km in height and 400 km in diameter on a strong lithosphere 40 km thick (parameters appropriate to Ascraeus Mons) is shown in Fig. 1. The stress field after the plate has flexed under the volcanic load is shown in Fig. 2. We note two effects of plate flexure with increasing time: (1) the deviatoric stresses in the surface region grow quite large; and (2) the area where the principal compressive direction is parallel to the surface extends progressively deeper, eventually reaching into the crust beneath the construct. Also, at large times, the boundary between the area of rotated stress directions and the underlying area of 'normal' stress orientations (compression axis vertical) is a region of low deviatoric stress. We find that plate deflections and stresses within the lithosphere are in qualitative agreement with those of flexural models [7].

Discussion. The above effects of flexure on the volcano stress field may have important implications for the history of volcanic events. It has been suggested [1] that time-dependent flexural stresses at the top of the elastic lithosphere beneath the Hawaiian volcanic chain control the history of eruptions at individual volcanoes, with eruptions ceasing during intervals when the two principal horizontal stress deviators are compressive and of significant magnitude. Applied to our model, this would imply that at early times after an interval of significant shield-building eruptions, the horizontal stress deviators within and beneath the volcano are tensional, so magma ascent to high-level chambers within the construct is favored. At later times, the stress directions in and beneath the volcano rotate such that the most compressive axis is nearly horizontal, so high-level magma bodies and summit eruptions would not be expected unless the ascending magma is significantly overpressured. In contrast, given that magma propagates through conduits oriented perpendicular to the least compressive stress, the stress orientations shown in Fig. 2 imply that flank eruptions are preferred at this stage of development. The

young ages of the volcanic units surrounding Olympus Mons and Tharsis Montes are consistent with such an evolution in eruptive style [8].

Conclusions. These initial models suggest that the state of stress during volcano growth and lithospheric flexure can have an important influence on volcano evolution on Mars. Further models are planned to examine the roles of magma chamber overpressure and evacuation and near-surface faulting on the stress orientations presented here.

References. [1] U.S. ten Brink and T.M. Brocher, *JGR, 92,* 13687, 1987; [2] C.H. Thurber and A.E. Gripp, *JGR, 93,* 4721, 1988; [3] L. Chevallier and W.J. Verwoerd, *JGR, 93,* 4182 1988; [4] J.H. Dieterich, *JGR, 93,* 4258, 1988; [5] H.J. Melosh and A. Rafesky, *GJRAS, 60,* 333, 1980; [6] H.J. Melosh and A. Rafesky, *JGR, 88,* 515, 1983; [7] R.P. Comer et al., *Rev. Geophys., 23,* 61, 1985; [8] D.H. Scott and K.L. Tanaka, *Icarus, 45,* 304, 1981.

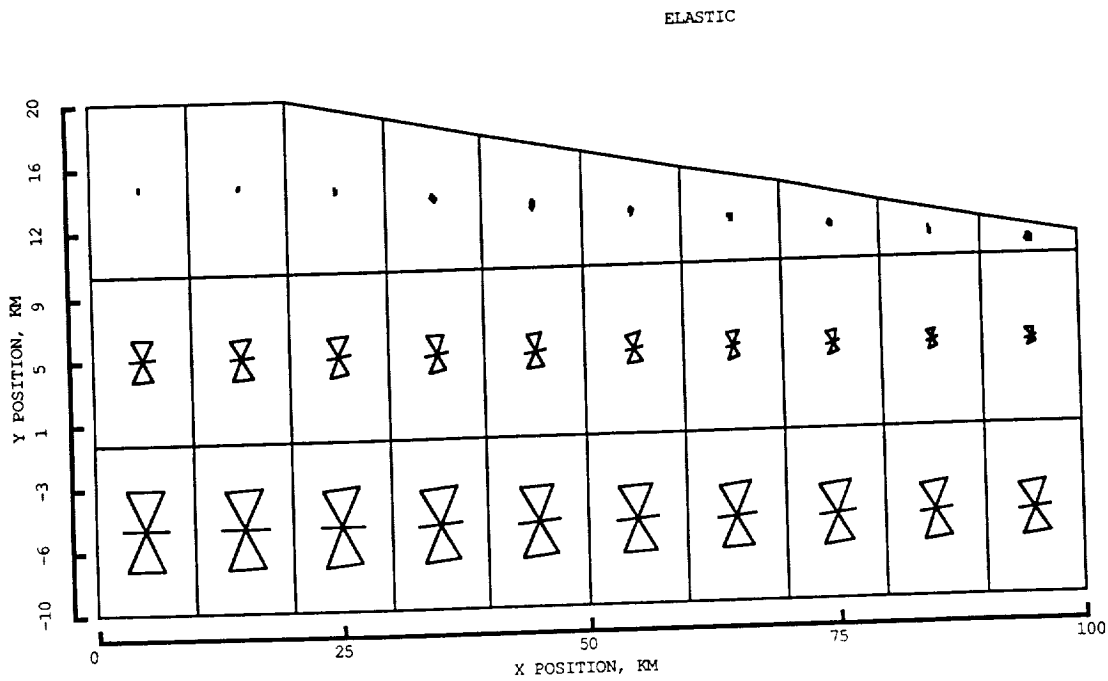

Figure 1. Close-up view of the deviatoric stress field in the volcano after the initial elastic deformation. An hourglass shape denotes the principal axis of compression, a bar denotes the principal axis of tension; the size of each symbol is proportional to deviatoric stress magnitude. The axis of rotational symmetry is x=0.

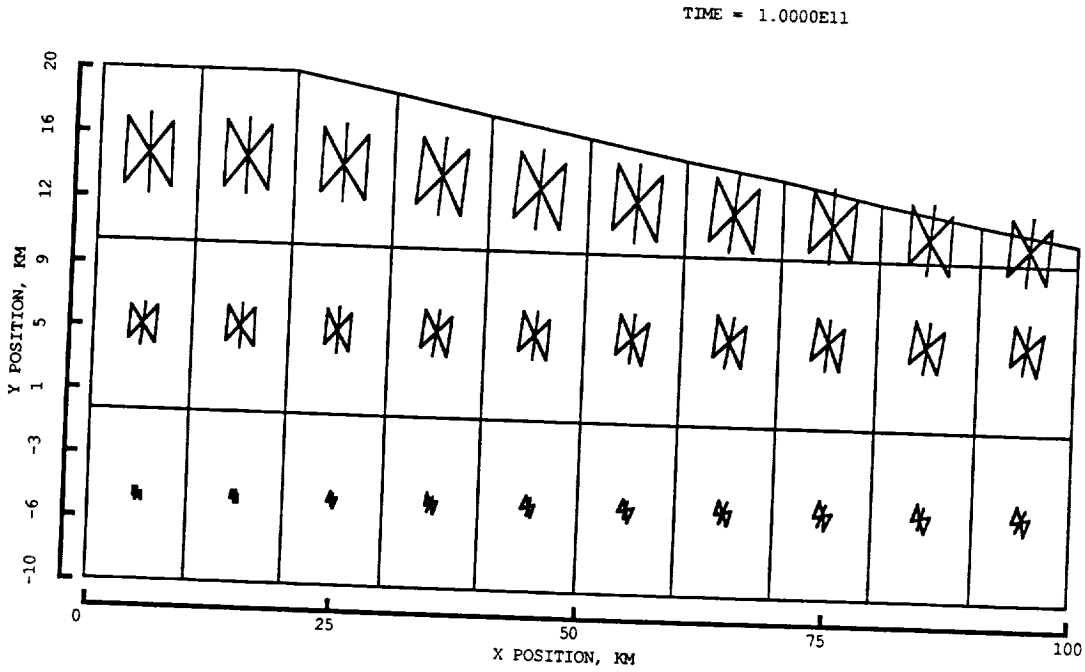

Figure 2. Deviatoric stress field in the volcano after flexure. The time elapsed is on the order of 100 Maxwell times. Rotation of the stress axes extends downward to the top layer of the plate (below y=0).

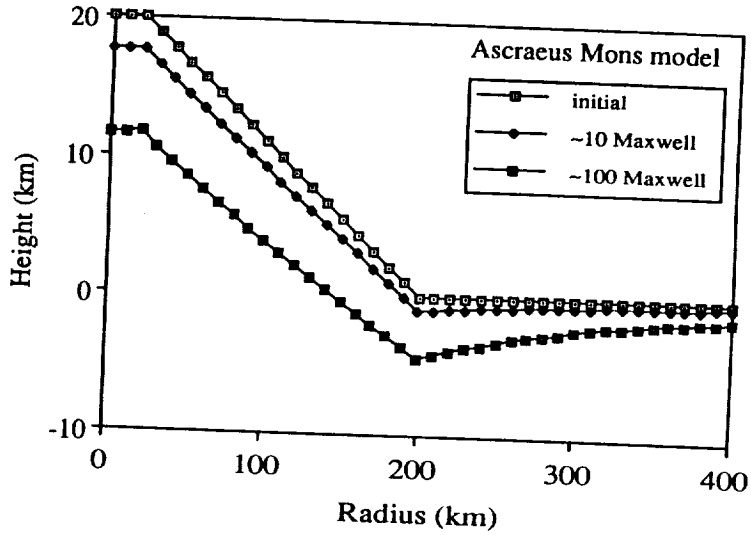

Figure 3. Surface topography as a function of time. Flexure significantly lowers the elevations of the volcano and surrounding area at timescales on the order of hundreds of Maxwell times.

CONSTRAINTS ON THE DEPTH AND GEOMETRY OF THE MAGMA CHAMBER OF THE OLYMPUS MONS VOLCANO, MARS FROM TECTONIC FEATURES IN THE SUMMIT CALDERA.

M.T. Zuber, Geodynamics Branch, Code 621, NASA/Goddard Space Flight Center, Greenbelt, MD 20771, *and P.J. Mouginis-Mark*, Planetary Geosciences Division, Hawaii Institute of Geophysics, University of Hawaii, Honolulu, HI 96822.

The summit caldera of the Olympus Mons volcano exhibits one of the clearest examples of tectonic processes associated with shield volcanism on Mars [1,2]. Within the 80 km diameter structure are six nested craters that indicate that the volcano edifice has undergone multiple collapse episodes [1]. Also found within the caldera are numerous compressional (ridges) and extensional (graben) tectonic features. Analysis of the topography of the caldera as derived from stereophotogrammetry [3] shows that the central portion of the largest (and oldest) crater, which contains radial and concentric ridges, represents a topographic low, while the crater perimeter, which is characterized by concentric graben, forms a topographic high. The relationship of the summit topography to the tectonic features, in combination with photogeologic evidence for basalt-like resurfacing of the caldera floor [4,5], is believed to indicate that a large lava lake has cooled and subsided due to pressure reduction in the underlying magma chamber.

The radial distance from center of the transition from concentric ridges to concentric graben within the oldest crater provides a constraint on the geometry and depth of the subsurface magmatic reservoir at the time of subsidence. In this study we use this constraint to investigate the size, shape and depth of the reservoir. Our approach consists of calculating radial surface stresses (σ_{rro}) corresponding to a range of subsurface pressure distributions representing an evacuating magma chamber. We then compare the stress patterns to the observed radial positions of concentric ridges and graben. We solve the problem by employing a finite element approach using the program TECTON [6]. An axisymmetric geometry and linear elastic material properties are assumed. The magma chamber is modeled as an elliptically-shaped source; nodes within the ellipse are characterized by a stress condition that represents an instantaneous pressure drop. Parameters of interest include the horizontal (a) and vertical (b) dimensions of the magma chamber and the depth to the top of the chamber (d). The following boundary conditions are imposed: vanishing horizontal (u) displacements at the center of symmetry of the volcano; vanishing vertical (w) displacements at depths much greater than the crater radius; and vanishing horizontal and vertical displacements at radial distances far from the crater rim. Numerical analyses were performed to assure that solutions were not sensitive to the far field boundary conditions.

Examples of radial surface stress distributions for a series of magma chamber depths with $a=R_c$ (where R_c is the crater radius) and $b/a=0.5$ are shown in Figure 1. The state of stress as inferred from the ridges and graben changes from compression (-) to extension (+) at a radial distance (r) of approximately $0.53R_c$ [5], where R_c is the crater radius (32 km). For these assumed parameters, the corresponding pattern of stresses indicates that the top of the magma chamber at the time of subsidence was located at a depth of less than $0.5R_c$ (best-fit range $8 \le d \le 16$ km). The best-fit depth is not very sensitive to the aspect ratio of the chamber (Figure 2), the difference in Young's Modulus between the chamber and surroundings (for $E_{mc}/E_s < .1$), or details of the imposed pressure distribution. However, as shown in Figure 3, depth is highly sensitive to magma chamber width. The magma chamber is unlikely to be markedly narrower than the crater; if it is wider, then Figure 3 illustrates that a shallower maximum depth than determined from Figure 1 is implied. We thus conclude that if concentric ridges and graben within the largest and oldest crater in the Olympus Mons caldera complex formed as a consequence of subsidence related to magma chamber withdrawal, then the magma chamber was located within the volcanic edifice, at a depth less than half the crater radius. With appropriate scaling for the difference in gravity between Mars and Earth, this depth is similar to that observed for the magma chamber beneath the Kilauea caldera [7], which would suggest a gross similarity of internal structure of the two shields.

References: [1]Mouginis-Mark, P.J., *Proc. Lunar Planet. Sci. Conf. XII,* 1431-1447, 1981. [2]Mouginis-Mark, P.J., et al., submitted to *Mars,* University of Arizona Press, Tucson, 1989. [3]Wu, S.S.C., et al., *Nature, 309,* 432-435, 1984. [4]Greeley, R., and P.D. Spudis, *Rev. Geophys., 19,* 13-41, 1981. [5]Mouginis-Mark, P.J., submitted to *LPSC XXI*, 1990. [6]Melosh, H.J., and A. Raefsky, *Geophys.*

J. R. ast. Soc., 60, 333, 1980. [7]Ryan, M.P., et al., *J. Geophys. Res., 88,* 4147-4181, 1983.

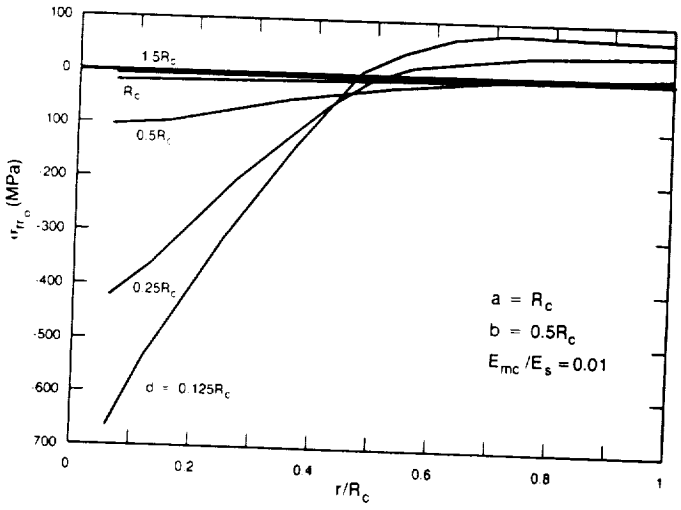

Figure 1. Radial surface stress (σ_{rro}) vs. distance from the crater center (r/R_c, where R_c = crater radius) due to deflation of a subsurface magma chamber. Stress patterns are shown for a range of depths (d). Assumes an elliptical chamber with width $a=R_c$ and height $b=0.5a$. Negative stresses are compressional and positive stresses are extensional.

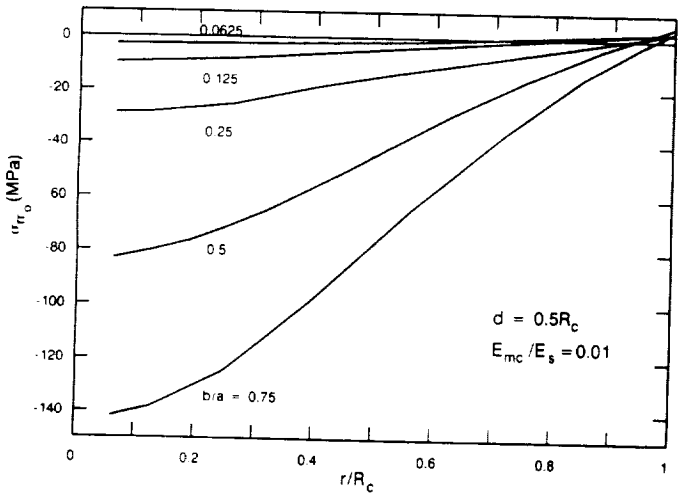

Figure 2. Plot of σ_{rro} vs. r/R_c for a range of magma chamber aspect ratios (b/a) assuming $a=R_c$ and $d=0.5R_c$. Note that the transition from compression (-) to extension (+) is not sensitive to this parameter except for very small b/a.

Figure 3. Plot of σ_{rro} vs. r/R_c for a range of magma chamber widths (a) assuming $b=d=0.25R_c$. Note that a wide magma chamber undergoes the transition from compression (-) to extension (+) at greater distances from the crater center than a narrow magma chamber. Therefore a chamber with $a>R_c$ must be shallower than a chamber with $a=R_c$ to explain the transition from concentric ridges to concentric graben at $r\sim0.5R_c$ in the Olympus Mons caldera.

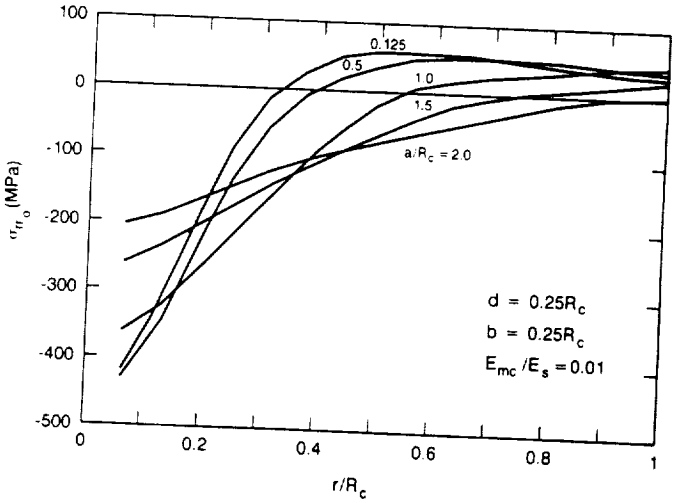

VOLCANIC GEOLOGY OF THE MARTIAN HIGHLAND PATERAE

David A. Crown and Ronald Greeley, *Department of Geology, Arizona State University, Tempe, Arizona 85287*

The highland paterae are being investigated in order to determine the styles and evolution of volcanic activity associated with the Hellas basin in the ancient, southern cratered highlands of Mars. The highland paterae are low-relief, areally-extensive features with central calderas and radial channels and ridges [1,2]. Four of these volcanoes, Hadriaca, Tyrrhena, Amphitrites, and Peneus Paterae, are associated with inferred rings of the Hellas basin [3,4]. Their morphometry [5] and the erosional characteristics of Tyrrhena Patera [2] have been used as evidence that they are composed of ash. Analyses of the energetics of eruption and flow processes have shown that the distribution of units at Hadriaca and Tyrrhena Paterae is consistent with an origin by the emplacement of gravity-driven pyroclastic flows and that explosive eruptions driven by magmatic volatiles or groundwater could provide sufficient energy [6-9]. The supply of groundwater for hydromagmatic eruptions has been considered; large volumes of water could accumulate rapidly over geologic time at flow rates determined for Mars [9-11]. Recent work includes geologic mapping of the Hadriaca Patera region [12] and syntheses of the photogeologic and modeling studies of Hadriaca and Tyrrhena Patera in order to examine volcanism in the eastern Hellas region [13].

Geology of the East Rim of the Hellas Basin

The Hellas basin is a ~2000 km impact structure with possible rings extending 4260 km in diameter [3]. The east rim of Hellas (27.5-42.5°S, 260-275°W) is a complex geologic region affected by volcanism, tectonism, and channeling [12]. Major units include Hesperian volcanics associated with Hadriaca and Tyrrhena Paterae in the north and Hesperian and Amazonian channeled plains and outflow channels in the south. Remnants of Noachian mountains and plateaus are found throughout the region [14]. A large flank flow containing lava flow lobes and leveed channels, the first definitive evidence of effusive activity associated with the highland paterae, extends for over 1000 km from Tyrrhena Patera to the southwest adjacent to Hadriaca Patera. Remnants of an extensive mantling deposit and smooth deposits filling craters may be indicative of widespread aeolian activity, presumably related to the dust storms originating in the Hellas region [15].

Based upon photogeologic mapping the geologic history of the east rim of Hellas has been derived. Uplift of Noachian mountains and plateau materials occurred in association with the Hellas impact event. The locations of mountains identify possible basin rings, which may have produced zones of weakness providing access to the surface for the magmas forming Hadriaca and Tyrrhena Paterae in Hesperian time. Erosion by runoff and/or sapping modified the plains and flanks of the volcanoes, followed by the formation of Dao and Harmakhis Valles. The presence of volatile-rich surface materials and possible fluvial or periglacial activity is suggested by the deflation and collapse of the channel deposits [11], the style of erosion of the channeled plains, and the debris aprons and pitted materials observed in association with the older units.

Tectonism in Eastern Hellas

Impact basin control of volcanism and tectonism is evident on the Moon [16], and relationships between martian basins and surface processes have been identified [4, 17]. In eastern Hellas, Hadriaca and Tyrrhena Paterae are observed in association with the ridged plains of Hesperia Planum. Zones of weakness generated by the Hellas impact event may have produced conduits for the magmas forming these deposits. The structure of Hellas has clearly influenced the shapes of the paterae, which are elongated downslope toward the basin, as well as the positions of the volcanic source vents. The orientations of 243 ridges have been mapped in the Hadriaca [260-275° W, 27.5-42.5° S] and Tyrrhena [247.5-265° W, 15-30° S] regions. The 219 ridges contained within volcanic units have a wide range of orientations but exhibit trends which are approximately radial (NE-SW) and concentric (NW-SE) to Hellas. Although orthogonal and

parallel alignments between ridges and the regional slope and lava flow directions in the flank flow unit at Tyrrhena are also observed, basin-related tectonism is considered the primary factor governing ridge orientation because the regional slope is a consequence of the basin and has controlled the emplacement of the volcanic units. The NE-SW and NW-SE ridge orientations measured agree with previously documented trends for Hesperia Planum [18] and indicate the effects of the Hellas impact event over a wide region of the southern highlands and the persistence of the tectonic signature of the basin over geologic time.

Volcanic Geology of Hadriaca Patera

Volcanic units in the Hadriaca Patera region include the flank flow from Tyrrhena Patera and the caldera-filling and volcanic flank materials of Hadriaca Patera. The caldera at Hadriaca Patera is ~70 km across and filled with smooth, relatively featureless deposits. A well-defined caldera wall is observed to the west and south; to the north and east the caldera wall is not apparent, possibly due to either overflow or mantling by volcanic materials. Within the caldera, scarps are evident and extend into the surrounding flanks of the volcano. Although many of the scarps appear to be erosional, a large scarp near the southwestern margin of the caldera may be a flow margin of ponded lavas or ash. Surrounding the caldera are the channeled flanks of the volcano. Hadriaca Patera is ~290 by 570 km across and asymmetric to the southwest along the regional slope into the Hellas basin [19]. Flank slopes range from ~0.05° in the north to ~0.60° in the west and south [6]. On the west and south flanks the spacing between the channels is smaller and the number of exposed layers greater than to the north, where the observed scarps (defining the ridges between channels) do not form a distinct radial pattern and only one or two layers are evident. The channels are commonly not continuous along the flanks, and several channels extend from topographic highs, such as the rims of small impact craters. In the lower part of the southwest flank of Hadriaca Patera, several ridges trending NE-SW and deeper dissection by the channels are observed. No evidence for flank eruptions is apparent. The morphology of the channels and related scarps and the presence of remnants of the ridges suggest an erosional process, presumably sapping. The erosional characteristics in combination with similar morphometry to large terrestrial ash sheets [5] and the absence of primary lava flow features (except in the flank flow unit) suggest that Hadriaca Patera is composed primarily of ash [8].

Assuming that eruptions occurred near the present summit region, the dimensions of Hadriaca Patera can be used to constrain possible explosive eruption mechanisms [6-8]. An air-fall origin for most of the deposits can be dismissed because the eruption cloud heights required (comparable to the maximum flank width of ~450 km) are unreasonable for the martian atmosphere [20]. Models for the emplacement of gravity-driven flows resisted by a frictional force [21] indicate that the dimensions of Hadriaca Patera require initial velocities as high as 350 - 550 m/sec (for a slope of 0.25° and coefficients of friction between 0.05 - 0.10). Theoretical analyses of hydromagmatic eruptions indicate that these velocities could be produced for < 12% conversion of a magma's thermal energy into the kinetic energy of a pyroclastic flow, which is in agreement with experimental results [22]. The requisite amount of water to produce Hadriaca Patera by hydrovolcanic phenomena could accumulate rapidly over geologic time at water flow rates determined for Mars [6,8]. A magmatic eruption with an exsolved volatile content of > 1%, a mass eruption rate of > 10^7 kg/sec and a 70 km eruption cloud height would also generate sufficient energy [23].

Volcanic Evolution of Eastern Hellas

Cross-cutting relationships determined from geologic mapping of eastern Hellas [9,12-13] indicate that the ridged plains of western Hesperia Planum and the flank flow unit at Tyrrhena Patera are younger than the basal and summit shield units, suggesting a transition from explosive to effusive volcanism. The erosion of the flanks of Hadriaca Patera pre-dates the erosion of the channeled plains to the south. The erosion on the plains (presumably by runoff) and the eventual formation of the Dao Vallis outflow system continues through the formation of the flank flow. Thus, the erosional processes affecting Hadriaca and Tyrrhena Paterae and the plains were

probably active, at least in some areas, after the emplacement of the flank flow. This relationship supports the interpretation of the dissected units at Hadriaca and Tyrrhena Paterae as ash rather than eroded lavas because the flank flow unit should have been subjected to similar degradational processes, at least in the south near Hadriaca Patera. The presence of volatile-rich surface materials in the region is strongly supported by the morphologies of the channeled plains and Dao Vallis [11-12]. In addition, debris flows and pitted plains associated with Noachian mountains near Harmahkis Vallis illustrate the influence of near-surface volatiles. The transition from explosive to effusive volcanism (from the low shields of the paterae to the flank flow unit and the ridged plains of Hesperia Planum) can be interpreted as the result of the cessation of magma-volatile interactions. Groundwater could have been concentrated by the topography of Hellas and would have moved easily in the fractured highland crust. The interpretation of the caldera-filling materials at the paterae as late-stage lavas [9] is consistent with this scenario, as the rising magma could eventually seal the conduit from further inflow by water [24]. In addition, as the volcanoes increased in size, water would tend to flow away from the structures, and even if contact occurred beneath the surface, explosive eruptions could be suppressed by the increasing weight of the volcano. Explosive eruptions at Tyrrhena Patera would have ceased first due to its distance from Hellas.

The style of eruptive activity in eastern Hellas has implications for the general evolution of martian volcanism. If magmatic eruptions generated the pyroclastic flows forming the paterae, this suggests an evolution in magma types from Hesperian to Amazonian time, when the Tharsis and Elysium volcanics formed, and/or the existence of spatial heterogeneities in the mantle from which the magmas were derived. Hydromagmatic origins for the paterae imply an evolution from volatile-rich to volatile-poor eras in the near-surface environment of Mars, in accordance with proposed global climatic changes [25]. While the observed morphologies and the energetics of explosive eruptions are consistent with both magmatic and hydromagmatic origins of Hadriaca and Tyrrhena Paterae, consideration of the regional geologic setting supports the role of magma-volatile interactions in the volcanism of the eastern Hellas region.

References:

[1] Plescia, J.B. and R.S. Saunders, *Proc. Lunar Planet. Sci. Conf., 10th*, 2841-2859, 1979. [2] Greeley, R. and P.D. Spudis, *Rev. Geophys. Space Phys., 19*, 13-41, 1981. [3] Peterson, J.E., *Proc. Lunar Planet. Sci. Conf., 9th*, 3411-3432, 1978. [4] Schultz, P.H., *Lunar Planet. Sci. Conf., XV*, 728-729, 1984. [5] Pike, R.J., *Proc. Lunar Planet. Sci. Conf., 9th*, 3239-3273, 1978. [6] Crown, D.A., R. Greeley, and M.F. Sheridan, *Lunar Planet. Sci. Conf., XIX*, 229-230, 1988. [7] Crown, D.A. and R. Greeley, *LPI Technical Report 89-04*, 29-31, 1989. [8] Crown, D.A. and R. Greeley, in *MEVTV Workshop on the Evolution of Magma Bodies on Mars*, L.P.I., in press, 1990. [9] Greeley, R. and D.A. Crown, *J. Geophys. Res.*, in press, 1990. [10] Carr, M.H., *J. Geophys. Res., 84*, 2995-3007, 1979. [11] Squyres, S.W., D.E. Wilhelms, and A.C. Moosman, *Icarus, 70*, 385-408, 1987. [12] Crown, D.A., K.H. Price, and R. Greeley, *Lunar Planet. Sci. Conf., XXI*, 252-253, 1990. [13] Crown, D.A. and R. Greeley, *Lunar Planet. Sci. Conf., XXI*, 250-251, 1990. [14] Greeley, R. and J.E. Guest, *U.S. Geol. Survey Misc. Inv. Series Map I-1802B*, 1987. [15] Zurek, R.W., *Icarus, 50*, 288-310, 1982. [16] Solomon, S.C. and J.W. Head, *Rev. Geophys. Space Phys., 18*, 107-141, 1980. [17] Schultz, P.H., J.L. Rogers, and R.A. Schultz, *Lunar Planet. Sci. Conf., XIII*, 700-701, 1982. [18] Watters, T.R. and D.J. Chadwick, *LPI Technical Report 89-06*, 68-69, 1989. [19] U.S. Geological Survey, *Topographic Map of Mars-Eastern Region*, 1:15M, 1987. [20] Mouginis-Mark, P.J., L. Wilson, and J.R. Zimbelman, *Bull. Volcanol., 50*, 361-379, 1988. [21] Malin, M.C. and M.F. Sheridan, *Science, 217*, 637-640, 1982. [22] Wohletz, K.H., *Bull. Volcanol., 48*, 245-264, 1986. [23] Mouginis-Mark, P.J., L. Wilson, and J.W. Head, *J. Geophys. Res., 87*, 9890-9904, 1982. [24] Sheridan, M.F. and K.H. Wohletz, *J. Volcanol. Geotherm. Res., 17*, 1-29, 1983. [25] Clifford, S.M., R. Greeley, and R.M. Haberle, *EOS (Trans. Amer. Geophys. Union), 69*, 1988.

ANALYSES AND MORPHOLOGY OF A LAVA FLOW, ASCRAEUS MONS, MARS; H.J. Moore, U.S. Geological Survey, Menlo Park, CA, 94025 and P.A. Davis, U.S. Geological Survey, Flagstaff, AZ, 86001.

We have obtained some 32 profiles of lava flows on Mars using photoclinometry [1]. These photoclinometric profiles were leveled by adjusting them until the levee crests had the same elevations. Here, we compare our lava-flow dimensions and rheologic analyses for one profile on Ascraeus Mons with previous results using dimensions from images and shadow techniques [2, profile E5] (fig. 1, Table 1). In our rheological analyses, we use a wide-flow model [3], Hulme's model [4], and model 1 of Baloga and Crisp [5]. Effusion rates are estimated by using an unmixed-cooling model [6] and calibrated by using Hawaiian flows [7] and a Graetz-number model [4,8]. Our Graetz-number effusion rates are about 3.9 times larger than previous ones [7] because of a corresponding increase in thermal diffusivity.

In general, our results are compatible with the previous ones [2] (Table 1). Yield strengths are about 1 to 10 kPa, and Bingham viscosities are about 1 to 10 MPa*s. Newtonian viscosities for the wide-flow model are about 4 times larger than Bingham viscosities. Rates of shear are very small (5×10^{-8} s^{-1}). Both Newtonian viscosities and rates of shear are comparable to those expected for basaltic flows just before they stop [9,10].

Morphologies of flow E (fig. 1) and of many other flows near the summit of Ascraeus Mons are complex and similar to those of Hawaii [11] and Etna [12]. For both types of flows, morphologies indicate the presence of overflow levees, sheets, and lobes, breached lava ponds and breakouts; locally, channels appear clogged (profile A, fig. 1) and, in other places, drained (profile B, fig 1); and tips of flows are commonly multilobed (fig. 1). Interpretation of these flows introduces uncertainties into the appropriate flow dimensions to be used in the rheologic models. Additional uncertainties exist that are related to effusion-rate models and parameters, flow lengths and areas, and measurement techniques. Thus, the compatibility of the results from our rheologic analyses and the previous results [2] is surprising.

REFERENCES

[1] Davis, P.A., et al., 1984, J. Geophys. Res., v. 89, p. 9449-9457. [2] Zimbelman, J.R., 1985, J. Geophys. Res., v. 90, Suppl. D, p. D157-162. [3] Moore, H.J., et al., 1975, Proc. 6th LSC., p. 101-118.. [4] Hulme, G., 1974, Geophys. J. Roy. Astron. Soc., v. 39, p. 361-383. [5] Baloga, S.M. and Crisp, J., 1988, unpubl. rept., 35 p. [6] Pieri, D.C., et al., 1986, J. Volc. Geotherm. Res., v. 30, p. 29-45. [7] Moore, H.J., et al., 1989, Repts. Planet. Geol. Geophys. Prgm.-1988, NASA TM 4130, p. 387-389. [8] Hulme, G., et al., 1977, Phil. Trans. Roy. Soc., Lond., ser. A, v. 285, p. 227-234. [9] Moore, H.J., 1987, USGS Prof. Paper 1350, p. 1569-1588. [10] Walker, G.P.L.,

LAVA FLOW, ASCRAEUS MONS: Moore, H.J. and Davis, P.A. 1967, Nature, v. 213, p. 484-485. [11] Lipman, P.W., et al., 1987, USGS Prof. Paper 1350, p. 1527-1567. [12] Kilburn, C.R.J., et al., 1988, J. Geopys. Res., v. 93, p. 14759-14772.

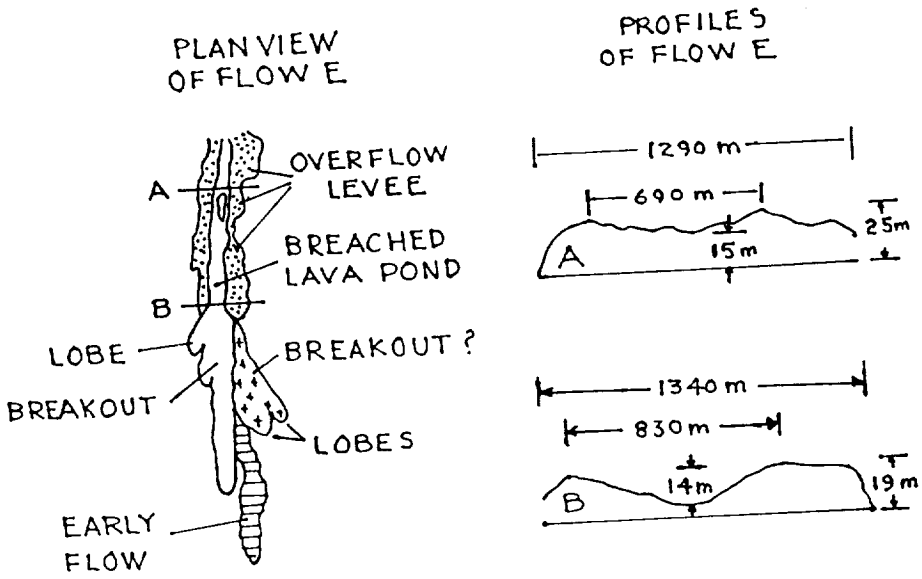

Figure 1. Plan view and photoclinometric profiles of Flow E of Zimbelman [2]. Profile B is same as E5 of Zimbelman [2]; Zy=15 m in Table 1 estimated from profile A.

Table 1. Comparison of dimensions and rheologies for profile E5 of Zimbelman [2] and this work. Equations used to calculate yield strengths (Y1, Y2, and Y3) and Bingham viscosities are given in Zimbelman [2].

Source	Flow Dimensions						Slope Angle	Effusion Rates	
	Zy m	Zl m	Zf m	Yc m	Yf m	Xf km	Theta deg.	Fc m^3/s	Fg m^3/s
Zimbelman	25	25	na	470	1350	14.8	5.0	59	
This work	15	19	29	830	1340	15.4	3.8	120	96

	Yield Strength (kPa)				Bingham Viscosity (Mpa) Graetz (Fc)			Cooling (Fc)		
	Y1[1]	Y2	Y3[2]	Y4[3]	E1[2]	E2[2]	E3[2]	Ew[1]	Eh[2]	E4[3]
Zimbelman	21	4	63		12	3	36			
This work	8	2	19	4	12		19	9	14	4

[1] Wide-flow model. [2] Hulme model. [3] Baloga and Crisp Model.

1967, Nature, v. 213, p. 484-485. [11] Lipman, P.W., et al., 1987, USGS Prof. Paper 1350, p. 1527-1567. [12] Kilburn, C.R.J., et al., 1988, J. Geopys. Res., v. 93, p. 14759-14772.

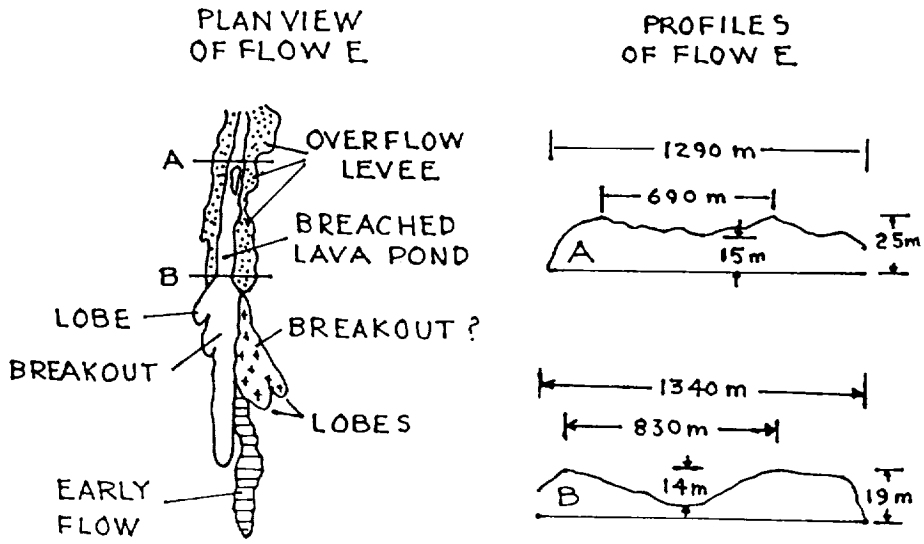

Figure 1. Plan view and photoclinometric profiles of Flow E of Zimbelman [2]. Profile B is same as E5 of Zimbelman [2]; Zy=15 m in Table 1 estimated from profile A.

Table 1. Comparison of dimensions and rheologies for profile E5 of Zimbelman [2] and this work. Equations used to calculate yield strengths (Y1, Y2, and Y3) and Bingham viscosities are given in Zimbelman [2].

Source	Flow Dimensions						Slope Angle	Effusion Rates	
	Zy m	Zl m	Zf m	Yc m	Yf m	Xf km	Theta deg.	Fc m^3/s	Fg m^3/s
Zimbelman	25	25	na	470	1350	14.8	5.0	59	
This work	15	19	29	830	1340	15.4	3.8	120	96

Source	Yield Strength (kPa)				Bingham Viscosity (Mpa) Graetz (Fc)			Cooling (Fc)		
	Y1[1]	Y2	Y3[2]	Y4[3]	E1[2]	E2[2]	E3[2]	Ew[1]	Eh[2]	E4[3]
Zimbelman	21	4	63		12	3	36			
This work	8	2	19	4	12		19	9	14	4

[1] Wide-flow model. [2] Hulme model. [3] Baloga and Crisp Model.

YOUNG FLOOD LAVAS IN THE ELYSIUM REGION, MARS

J. B. Plescia, Jet Propulsion Laboratory, California Institute of Technology, Pasadena, CA 91109.

The nature and origin of a smooth plains unit (the Cerberus Plains) in southeastern Elysium and western Amazonis is reported here. The Cerberus Plains cover >100,000 km^2 and extend an east-west distance of nearly 3,000 km; the plains are about 700 km wide in a north-south direction near longitude 195°. The unit is uncratered and exhibits lobate albedo patterns and embayment relations with older terrane. Morphologic characteristics suggest fluidized emplacement and the unit is interpreted to be formed by the eruption of large volumes of very low viscosity lava. A volcanic origin for this unit was also suggested by Schaber (1980), but he felt that the unit had been heavily modified by aeolian processes and he did not discuss its origin in detail. Tanaka and Scott (1986) and Tanaka (1986) reached a different conclusion and interpreted the material to be sedimentary, deposited during a fluvial episode.

The Cerberus Plains are one of the youngest units on Mars, crater numbers of 89 ±15 craters >1 km/10^6 km^2 were measured during this study. Carr and Clow (1981) cite 1 km crater numbers of <600; and Scott and Tanaka (1986) cite numbers of <50. Embayment relations indicate the Cerberus Formation overlies all other units in the Elysium region and western Amazonis (Greeley and Guest, 1987; Scott and Tanaka, 1986).

The Cerberus Plains are characterized by distinct linear albedo patterns independent of the wind streaks associated with aeolian processes. These patterns suggest an eastward flow across the Cerberus Plains, then a northeastward flow through a topographic low in the knobby terrane (exploiting a series of older channels carved into knobby terrane and ridged plains during an earlier period), and then out into Amazonis Planitia. In the east the albedo patterns are regionally organized forming bands up to 40 km wide; in the western areas, the albedo patterns are complex and intricate with high-frequency digitate boundaries varying from narrow, meandering patterns to broad, equant "ponded" shapes.

Small-scale surface texture of the plains is difficult to resolve; only in the highest resolution images are the relevant morphologic details observable. Near 19°N, 174°W the unit fills a channel cut through older plains and knobby terrane; here the channel floor appears smooth whereas the surrounding terrane has significant texture and numerous 400-600 m diameter craters. Apparently the original floor is covered by material younger than the surrounding plains. At the southern margin of the Cerberus Plains the surface shows a myriad of surface details indicative of a lava flow--pressure ridges, flow fronts, and flowage around obstacles; a festoon pattern is observed locally indicative of flowage up against the topographically higher areas. Morphology suggestive of a volcanic origin is also observed in western Amazonis Planitia (near 22°N, 170°W) where the distribution of material indicates flow and where the material terminates in a series of digitate and lobate fronts about 10 m high.

Six eruptive vents have been identified; the morphology of these features is suggestive of low shields--constructional volcanic features a few hundred meters high having lava flows emanating both as floods from a central vent and through a tube and

channel system (e.g., Mauna Ulu and Mauna Iki; Greeley, 1982). Some of the Cerberus shields are elongate having elliptical vents; others are more symmetric. Summit vents range from 1-2 km diameter for circular vents; up to 15 km in length for elongate vents.

The morphology of the Cerberus Plains suggests it is an example of flood basalt volcanism; the morphology of western part indicates plains style volcanism. Terrestrial examples of flood basalts include the Deccan Traps and the Columbia Plateau (specifically the Yakima Basalt). Flood basalt provinces (Greeley, 1976, 1982) are characterized by flows 5-45 m thick extending over large areas and exhibiting little relief. Eruption rates for flood basalts are many times greater than for central volcanoes and the vents are fissure systems typically tens to hundreds of kilometers long in zones several kilometers wide. Western Cerberus Plains (near longitude 200°) appears to be a basaltic lava plains style of volcanism (e.g., the Snake River Plains of Idaho; Greeley, 1976, 1982). Plains volcanism is characterized by a overlapping and coalescing low shields with intervening tube-fed flows The low eruption rates and intermittent nature of eruptions favors the construction of low shields and the development of channelized and tube-fed flows. Plains volcanism eruption rates are lower than for flood volcanism.The bulk of the volcanics were probably erupted from linear fissures, which may correspond to the present location of Cerberus Rupes. The eruptive fissures were probably relatively narrow; for example the lunar mare fissures are probably 10-25 m wide (Schaber et al., 1976). Typically, in both lunar and terrestrial flood basalt provinces the fissure vents are hidden.

A fluvial origin for the Cerberus Plains, as proposed by Tanaka and Scott (1986) and Tanaka (1986), appears inconsistent with the observed morphology. Although a fluvial episode did occur in the area, it predates the formation of the Cerberus Plains. The absence of a recognized source region for the fluid (presumably water); the absence of a recognized sink; and the burial of channel floors and the channels themselves by the Cerberus Plains are not consistent with a fluvial origin. Channels cut into the knobby terrane can not be traced to the southwest into their source region, nor to the northeast into the debouchment area; presumably they are overlain by the younger plains. In western Cerberus Plains, narrow channels (a few kilometers wide) are cut into exposures of older plains. However, these channels are traceable only for short distances and only on the older plains; the channels abruptly end at the contact with the Cerberus Plains.

The interpretation that Cerberus Plains results from flood plains style volcanism late in martian history carries implications for martian thermal history and volcanic evolution on a global scale. Although central construct volcanism (e.g., Olympus Mons) has long been recognized as occurring late in time, flood volcanism has not. Flood volcanism in the period <700 Ma indicates that, at least in the Elysium region, sufficient heat remained to generate large quantities of lava having low viscosity and erupted at high rates. Flood volcanism has been suggested as the origin of the ridged plains units (e.g., Lunae Planum, Solis and Sinai Planum). This type of volcanic activity generally occurred early, and in Tharsis the style of volcanism evolved from flood eruptions into centralized eruptions which built the large Tharsis Montes and Olympus Mons shields. Volcanism in the Elysium region seems to have followed a similar trend from flood eruptions to central construct building. But, the Cerberus Plains indicate that the volcanic style returned to flood eruption again after central constructional volcanism had ended.

REFERENCES:

Carr, M., and Clow, G. (1981) *Icarus*, **48**, 91-117.
Greeley, R. (1976) *Proc. 7th Lunar Planet. Sci. Conf.*, 2747-2759.
Greeley, R. (1982) *J. Geophys. Res.*, **87**, 2705-2712.
Greeley, R. and Guest, J. E. (1987) U. S. Geological Survey Miscellaneous Investigation Series Map I-1802B.
Schaber, G. G., (1980) *Icarus*, **42**, 159-184.
Schaber, G. G., Boyce, J. M., and Moore, H. J. (1976) *Proc. 7th Lunar Planet. Sci. Conf.*, 2783-2800.
Scott, D. H., and Tanaka, K. L. (1986) U. S. Geological Survey Miscellaneous Investigation Series Map I-1802A.
Tanaka, K. L. (1986) *Proc. 17th Lunar Planet. Sci. Conf., Part I, J. Geophys. Res.*, **91**, E139-E158.
Tanaka, K. L., and Scott, D. H. (1986) *Abstracts, 17th Lunar Planet. Sci. Conf.*, 865-866.

Layered deposits with volcanic intrusions in Gangis Chasma, Mars.

G. Komatsu and R.G. Strom. Lunar and Planetary Laboratory, University of Arizona, Tucson, AZ 85721.

Layered terrains on the floor of Valles Marineris were first recognized in the Mariner 9 Images. They are about 100-200km long, 50km wide and 1-5km high, and characterized by well-developed, near-horizontal layers. Proposed origins are summarized by the following hypotheses:

1.Erosional remnants of the surrounding plains. This hypothesis is probably incorrect because the erosional style is very different than that of the canyon walls ([1],[2]). 2.Eolian deposits. Peterson [1] suggested that crossbedding in the Candor and Ophir layered terrains could be explained by global dust storm deposition, but Nedell, et al. [2] argued against this idea because of the lack of similar deposits on the surrounding plains and walls. 3.Pyroclastic deposits. A pyroclastic origin by ash fall or flow is based on the similarity between the erosional pattern of terrestrial ash flow and welded tuff and that of the resistent layer in the Hebes layered terrain [1]. However, because there are no similar deposits on the surrounding plains and no evidence for an associated caldera, Nedell, et al. [2] rejected this hypothesis. 4.Lacustrine deposits. This hypothesis is favored because it can explain the location, near horizontality, lateral continuity, great thickness and stratigraphic relationship ([2],[3],[4]). Moreover, a substantial subsurface aquifer system may have supplied water to fill or partially fill the canyons at or near the time of outflow channel and canyon formation [2].

Geologic setting of Gangis layered terrain. The area surrounding the Gangis layered terrain show a variety of geologic features relevant to its origin (Fig. 1). The canyon walls are about 2km high and show gully and spur topography and landslides. Fewer craters on the canyon floor than on the surrounding plains suggests that the floor is younger, possibly as a result of fluvial or eolian processes. A large crater on the southern upper plain shows evidence of ponding and outburst of water to the east forming an outflow channel. On the western part of the canyon floor are blocky mesas a few to 20km across and about 1km high. Their morphology is similar to the mesas of chaotic terrains thought to be the source of outflow channels. To the south and southeast of the layered terrain there are clusters of small hills 1-5km wide and a few hundreds of meters high. These may also be eroded remnants of chaotic terrain or they could be volcanic constructs. Their color is similar to the canyon floor.

Gangis layered terrain. The approximate size of Gangis layered terrain is 100km, 40-50km wide, and 1.5-2.0km high. To the west, the terrain seems to have been more eroded than to the east. The relatively gentle south- facing side has a slope of a few degrees, and is conspicuously fluted. This fluting could be due either to wind scouring or to the seepage of ground water. On the eastern part of the south-facing side are two blocky slabs, each about 10km wide. Their blocky nature and fold-like texture in them suggest they may be large landslide masses that have been subsequently shaped by erosion. Extending in a north-south direction from the summit of the layered terrain to near its base are several lines of darker domes and ridges. In some cases, areas of dark material surround the domes. These structures may be volcanic domes and dikes intruded into the layered deposits and subsequently exposed by the erosion which shaped the present-day layered terrain. The associated dark deposits could be erosional products from the structures or pyroclastic material. Part of slope has texture smoother than the fluted area. This region could be covered by the pyroclastic material suggesting volcanism could have been active until recently. The layered terrain itself can be divided into three main stratigraphic units (A,B,C in Fig.1) based on the erosional morphology. Each main unit consists of other less well-defined units not shown in Fig.1. The upper two layers are relatively thin and have steeper slopes than the lower unit. Strata within the middle unit(B) appear to thin and pinch out against the upper unit(C) suggesting an angular unconformity (arrow 1). Similarly, a dark layer within the lower unit (A) appears truncated by the middle unit indicating another angular unconformity (arrow 2). To the west, these three main units disconformably overlie a heavily eroded base rock that might be ancient cratered terrain. The angular conformities between the main stratigraphic units suggest that there were at least two intervals of erosion between the deposition of these three units. Domes, ridges and dark materials suggest that volcanism has modified the Gangis layered terrain. Whether Gangis layered terrain was laid down in a lake is still controversial, but assuming it originated as sedimentary deposits in the lake and the angular unconformaties are real, then the following sequence of events appears to apply.

1.Formation of early closed Gangis Chasma and filling with water from subsurface. Hills and mesas may be remnants of chaotic terrain associated with this event. 2.Layer A deposited. 3.Draining or evaporation of lake and erosion of layer A during minor tectonic tilting. 4.Refilling of canyon with water from subsurface and deposition of layer B uncomfomably on layer A. 5.Draining or evaporation of lake and erosion of layer B during minor tectonic tilting. 6.Refilling of canyon with water from subsurface and deposition of layer C unconformably on layer B. 7.Intrusion of volcanics into layered deposits. 8.Catastrophic draining of lake to the east and erosion of layered deposits to expose volcanic intrusions.

Layered terrains may provide important clues for understanding the history of canyon formation and the Martian hydrologic cycle. Our current interpretation suggests multiple cycles of canyon filling and draining. This may be consistent with the proposed cycles of ancient oceans in the northern plains [5].

REFERENCES [1]Peterson, C. (1981). Proc. Lunar Planet. Sci. 12B, p.1459-1471. [2]Nedell, S.S., et al. (1987). Icarus, 70, 409-441. [3]Lucchitta, B.K. (1982). Report of Planetary Geology Program, p.233-234. NASA- TM 85127 [4]McCauley, J.F. (1978). Geologic map of the Coprates quadrangle of Mars. U.S. Geological Survey, Misc. Inv. Map I-897. [5]Baker, V.R., et al. (1990). Lunar and Planet. Sci. XXI.

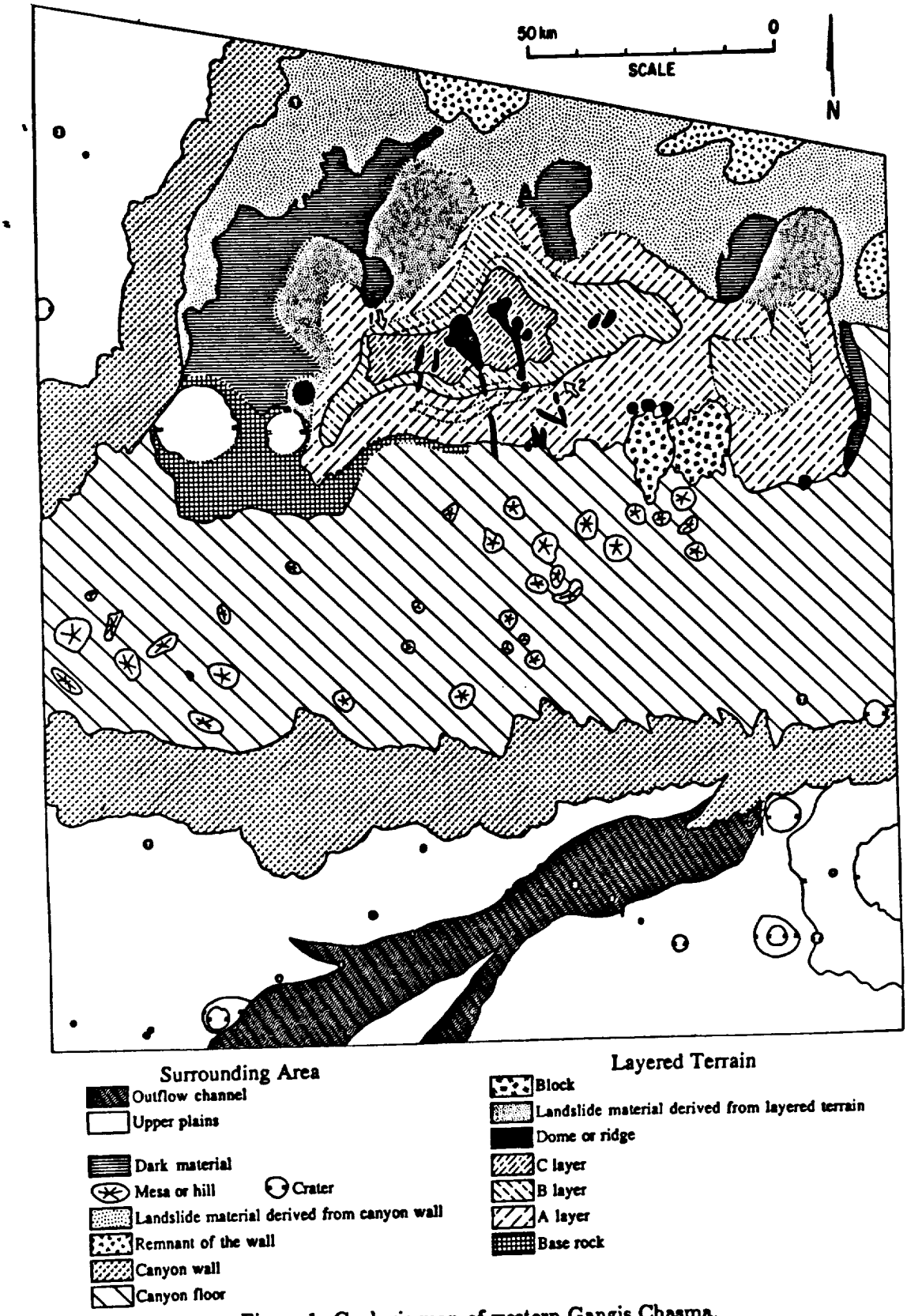

Figure 1. Geologic map of western Gangis Chasma.

THREE PYROCLASTIC DEPOSITS IN THE NECTARIS REGION.

Cassandra R. Coombs[1], B.Ray Hawke[2], Chris A. Peterson[2], and Paul G. Lucey[2], [1]SN15 Johnson Space Center, Houston, TX 77058; [2]Planetary Geosciences Division, Hawaii Institute of Geophysics, Honolulu, HI 96822.

INTRODUCTION

Lunar pyroclastic deposits vary in size and are widespread about the lunar nearside. These deposits may be associated with irregular depressions, sinuous and arcuate rilles, and/or floor fractures, and are most commonly found in the floors of large craters of Imbrian age or greater. Three such deposits have been identified in the Nectaris region (34°E, 16°S). The presence of these dark mantling deposits has been mentioned several times in relation to other studies,[e.g.,1,2] however, to date no detailed remote sensing studies have yet been undertaken of them.

This study incorporates a variety of geologic and remote sensing data of the dark mantling deposits in the Nectaris region. Goals of this project were to: (1) determine which of the deposits are of pyroclastic origin; (2) determine the composition of the pyroclastic deposits; (3) investigate the eruption mechanisms responsible for the emplacement of the pyroclastic deposits; (4) investigate the relationships among the pyroclastic deposits and the mare basaltic deposits in Nectaris; (5) investigate the factors that may or may not have influenced the distribution of the deposits; and (6) investigate the origin of those that are not of pyroclastic origin.

METHOD

Geologic maps of the region were constructed using Earth-based and spacecraft photography. In addition, various spectral data sets were utilized. These data sets include: (1) near-infrared reflectance spectra (0.6-2.5 μm); (2) multispectral images (0.40/0.56 μm, 0.56 μm, 0.95/0.56 μm); and (3) Whitaker's lunar color difference photograph.[3] Radar images obtained from Zisk et al.[4] provided information about the surface roughness of the study region.

RESULTS AND DISCUSSION

Criteria established by Head and Wilson[5] were used to help identify the endogenic (pyroclastic) deposits within the Nectaris study region. These criteria distinguish an impact induced crater from the volcanic or endogenically derived craters. In general impact craters are more circular than endogenic craters and have distinguishable crater rays, a feature lacking around endogenic craters. In addition, the pyroclastic deposits peripheral to irregular source vents mantle or subdue the surrounding terrain. Also, the composition of the pyroclastic deposit will differ from that of an impact crater.

Both localized and regional pyroclastic deposits were identified in this study. Regional dark mantle deposits (DMD) are extensive (thousands to tens of thousands of km^2) mantling units that may originate from one or more vents whereas, localized pyroclastic deposits are small (<250

km^2) mantling units with a single source vent. The localized deposits examined in this study include the Bohnenberger DHC, the Gaudibert B volcanic complex, the Gaudibert crater DMD and a deposit on part of the Daguerre rim.

Multispectral ratio images of the localized deposits exhibit relatively low values in the 0.40/0.56 μm range. Near-infrared spectra (0.6-2.5 μm) for various portions of the Gaudibert B pyroclastic deposit fall within the Group 1 spectral group as defined by Hawke et al.[1] These spectra typically exhibit 1.0 μm absorption bands centered near 0.93-0.95 μm with depths of approximately 4-5%. These bands are generally asymmetrical and have been described as "checkmark-like" with a straight, steep, short-wavelength edge followed by a shallower, straight long-wavelength edge. The Group 1 band parameters indicate the presence of feldspar-bearing lithologies with mafic assemblages dominated by orthopyroxene.

Another, much larger, deposit of possible pyroclastic origin is located southeast of Nectaris. This possible regional dark mantling unit exhibits unusual values in the multispectral images and color-difference photographs. Additionally, depolarized 3.8 cm radar backscatter images of this unit exhibit relatively low values, similar to other known regional pyroclastic deposits. Further telescopic studies will help determine the composition of this unit.

REFERENCES

(1) B.R. Hawke, C.R. Coombs, P.D. Owensby (1989) *Proc. Lunar and Planet. Sci. Conf. 19th*, 255. (2) D. Wilhelms and J. McCauley (1971) *U.S.G.S. Map I-703*. (3) D. Wilhelms (1987) *U.S.G.S. Prof. Paper 1348*, 302pp. (4) S. Zisk *et al.* (1974) *Moon, 10*, 17. (5) J. Head and L. Wilson (1970) *Proc. Lunar and Planet. Sci. Conf. 10th*, 2861.

Regional Dark Mantling Deposits Located in the North-Central Region of the Lunar Nearside.

Cassandra R. Coombs, SN15, Johnson Space Center, Houston, TX, 77058
B.Ray Hawke, Chris A. Peterson, Stan H. Zisk, Planetary Geosciences Division, Hawaii Institute of Geophysics, Honolulu, HI, 96822.

Introduction.

With the U.S.A. entering a new era of space exploration and considering the establishment of a permanent lunar outpost, the investigation of lunar resources has become more important. Resources are needed to sustain life in the reduced gravitational and atmospheric environment as well as to maintain operations in low-Earth and near-Earth space.[1] Liquid oxygen is just one of the many resources potentially avialable on the lunar surface. With minimum processing the liquid oxygen might be used for spacecraft propellant and other things such as life support systems. One such source for this oxygen may be ilmenite-rich material. Ilmenite-rich deposits would also provide Fe and Ti, both materials useful in space construction.[1,2] Efforts to locate such deposits thusfar have focused on the high-titanium mare deposits located on the lunar nearside.[3,4,5] However, we have recently suggested that an excellent source for the ilmenite-rich material would be those regional pyroclastic deposits that are rich in ilmenite. These volcanic deposits are unconsolidated, extensive, and relatively thick and may prove to be excellent sites for the establishment of permanent lunar bases.[2] Also, many by-products may be produced from these resource-rich deposits. This abstract presents the results of recent Earth-based remote-sensing studies of these potentially important ilmenite-rich regional pyroclastic deposits.

Method.

Data used in this study included a variety of remote-sensing data as well as spacecraft and Earth-based photographs. Multispectral images presented by McCord *et al.*[6] were utilized as were both near-infrared (0.6-2.5 μm) and UV-VIS (0.35-1.1 μm) spectral reflectance data. The near-IR and UV-VIS spectral were collected for a several selected regional pyroclastic deposits using the Planetary Geosciences Division spectrometers at the U.H. 2.2-m telescope facility on Mauna Kea. Additionally, radar data (3.8-cm) collected by Zisk *et al.*[7] were analyzed. Also, new, high-resolution 3.0-cm radar data collected at the Haystack Observatory were examined in order to better characterize the surface properties of the regional pyroclastics.

Discussion.

Apollo 17 (A17) sampled the dark mantle deposit at Taurus-Littrow to see if, in fact, it was of pyroclastic origin as was thought during premission analyses.[8] Partially crystallized black spheres and orange glass droplets, identified as pyroclastic components in the deposit were also collected at the A17 landing site.[9] Chemically, these two components are indistinguishable. Their only difference is that the black spheres are largely crystallized and consist of very fine intergrowths of ilmenite and euhedral crystals of olivine. These A17 black spheres are similar, though not identical, in composition to the A17 high-Ti mare basalts, and are rich in TiO_2 (9-10%) and ilmenite. A comparison of laboratory reflectance spectra for the A17 samples with telescopic spectral measurements

of the Taurus-Littrow deposit has demonstrated that the A17 black spheres are the characteristic component of the pyroclastic mantling deposit at Taurus-Littrow.[8,10,11,12]

The Taurus-Littrow deposit covers an area greater than 4,000 km^2 and is many tens of meters thick. In the depolarized 3.8-cm radar maps of Zisk *et al.*[7], the Taurus-Littrow deposit exhibits very weak to non-existent echoes. This poor signal return is thought to be due to a lack of signal-scatterers in the 1 to 50 cm size range on the surface of the pyroclastic deposit. As a result, a very low degree of surface roughness and a relatively block-free surface are indicated.

Besides the Taurus-Littrow regional pyroclastic deposits, there are many others on the lunar nearside. Among these include: Aristarchus Plateau, Southern Sinus Aestuum, Southern Mare Vaporum, Rima Bode, and Sulpicius Gallus. Each of these deposits subdues, or mantles the underlying terrain and have low albedoes (0.079-0.096). These deposits, too, have low radar backscatters.

Spectral studies of these deposits indicate that several of these large deposits are composed of high-titanium, ilmenite-rich spheres of pyroclastic origin.[2,8,10] These such deposits include: (a) Rima Bode; (b) Taurus-Littrow; (c) Southern Sinus Aestuum; and (d) Southern Mare Vaporum. Each of these deposits correlates with the lunar "black spots" as identified by Pieters *et al.*[10] Analysis of recently obtained near-IR spectra of the Southern Sinus Aestuum and Southern Mare Vaporum deposits fully support our previous interpretations for these two sites. Based on the old UV-VIS spectra and our newly obtained near-IR spectra, the surfaces of these regional deposits are strikingly uniform in composition. Vertical mixing and/or lateral transport have resulted in little or no contamination of these surfaces by non-pyroclastic material. This finding is also supported by two newly collected UV-VIS spectra collected for separate portions of the Southern Sinus Aestuum dark mantle deposit.

Two newly collected UV-VIS spectra for the pyroclastic deposit on the west flank of Gambart crater appear to contain a significant amount of ilmenite-rich black spheres. The surface of the Gambart deposit is however, contaminated by variable amounts of highland debris.

3.0-cm radar data for a portion of the Rima Bode dark mantle deposit have also been obtained. The spatial resolution of this new data is an order of magnitude greater than that presented earlier by Zisk *et al.*[7] (120 m vs. 1 km) These new high-resolution depolarized radar images confirm that the Rima Bode deposit is deficient in surface scatterers in the 1-50 cm size range. Also, the data suggest that the deposit is composed of loose, unwelded "soil" fragments.

References.

(1) Mendell W. (1985) *Lunar Bases and Space Act. in the 21st Cent.* (2) Hawke B. *et al.* (1990) *PLPSC 20.* (3) Cameron E. (1988) *Lunar Bases II*, p. 47. (4) Busarev V. and Shevchenko V (1988) *Lunar Bases II*, p. 44. (5) Shevchenko V. and Busarev V (1988) *Lunar Bases II*, p. 219. (6) McCord T. *et al.* (1976) *Icarus*, 29, p. 1. (7) Zisk S. *et. al.* (1974) *The Moon*, 10, p. 17. (8) Gaddis L. *et al.* (1985) *Icarus*, 61, p. 461. (9) Heiken G. *et al.* (1974) *GCA*, *38*, p. 1703. (10) Pieters C. *et al.* (1973) *JGR*, *78*, p. 5867. (11) Pieters C. *et al.* (1974) *Science*, *183*, p. 1191. (12) Adams J. *et al.* (1974) *PLSC* 5, p. 171. (13) Wilhelms D. and McCauley J. (1971) *USGS Map I-703.*

YOUNG DARK MANTLE DEPOSITS ON THE MOON. Paul D. Spudis, U.S. Geological Survey, Flagstaff, AZ 86001

Dark mantling deposits were recognized and postulated to be of volcanic origin during the geologic mapping of the Moon (e.g, [1]). Based on a general belief that "dark" = "young" (see [1,2]), they were considered to be the youngest products of lunar volcanism. The Apollo 17 mission was sent to the Taurus-Littrow Valley to sample the extensive dark mantle deposits in this region that were inferred to be young [3-5]. Samples returned from that mission showed that the Taurus-Littrow dark mantle is the product of pyroclastic volcanism that occurred over 3.7 billion years ago [6]. It has been widely assumed that lunar pyroclastic volcanism was confined to the "main phase" of mare volcanism, i.e., from around 3.8 to 3 billion years ago. Subsequent reinterpretations of other lunar dark mantle deposits [7], the stratigraphy of Mare Serenitatis [8], and crater densities in the Apollo 17 region [9] all concluded that lunar pyroclastic deposits are old (> 3 Ga) and that "young" dark mantling deposits probably do not exist.

Estimating the age of dark mantle deposits on the Moon is difficult. Because these units are fine-grained, unconsolidated debris in which craters are eroded very rapidly, crater densities are of little value [9]. The only way to estimate the age of unvisited dark mantle deposits is to bracket them stratigraphically with units that can be dated by crater densities. I here discuss two dark mantle deposits on the east limb of the Moon that occur in different geological settings and attempt to determine their ages. Although they are of small extent, their presence suggests that explosive volcanism on the Moon continued to as recently as about 1 billion years ago.

Dark mantle deposits of Mare Smythii. Mare Smythii is a circular mare on the equatorial east limb of the Moon [10, 11]. Several dark deposits are evident on high-sun-illumination photographs of the region. In particular, dark mantle deposits occur around the margins of the inner basin ring (370 km dia.) near the craters Haldane, Kiess, and McAdie. These deposits are closely associated with the mare fill of the Smythii basin. Within the basin, the dark mantle material underlies the mare in some places (e.g., west rim of McAdie at 3° N, 93° E), while it overlies mare basalt elsewhere (e.g., near a volcanic vent north of Haldane at 0, 83° E). It thus appears that eruption of mare basalt in the Smythii basin was accompanied by eruptions of dark mantling material; such a relation is similar to that evidenced at the Apollo 17 site, where dark mantle pyroclastics are of similar age (and composition) to the local mare basalts.

Dark mantle deposits within Taruntius crater. The crater Taruntius (5.6° N, 46.5° E; 55 km dia.) is a floor-fractured impact crater [12] of Copernican age. A low-albedo deposit is associated with irregularly shaped craters and fractures on the floor of Taruntius. This deposit is similar to localized dark mantle deposits [13] that occur within crater floors elsewhere on the Moon, which are probably deposits from vulcanian eruptions [13] associated with the injection of magma beneath the crater floor, floor uplift, and fracturing [12]. Taruntius dark mantle deposits are also associated with minor mare basalt flooding of portions of the crater floor. All of these volcanic events post-date the formation of the crater Taruntius, which appears to be about the same age as Copernicus.

Ages of the Smythii and Taruntius dark mantle deposits. I have attempted to determine the ages of these two deposits by measuring the crater densities on units that have a clear stratigraphic relation to the dark mantle (Figure 1). The Smythii mare basalts (point "Mare Smythii" in Fig. 1) are among the youngest on the Moon; an estimate based on known ages of the Apollo mare sites and inferred ages of Copernicus and Tycho (850 Ma and 100 Ma, respectively [15]) suggests an age of about 1.2 ▪ 0.3 Ga for the basalts of Mare Smythii. Because the dark mantle deposits of the Smythii basin are contemporaneous with the basalts, a similar age for the dark mantle is inferred, i.e., about 1.5 Ga to less than 1 Ga. Similarly, the crater density and inferred absolute age of Taruntius suggest that it is about the same age as the crater Copernicus (about 1 Ga [15]). The dark mantle on the floor of Taruntius post-dates the crater; thus, these volcanic deposits must be younger than 1 Ga. The dark mantle deposit within Taruntius is the youngest recognized volcanic unit on the Moon, possibly younger than the mare flow that embays Lichtenberg crater [14].

Although these dark mantle deposits are not extensive, their existence indicates that very late volcanism on the Moon exhibited the same styles of eruption and emplacement of earlier epochs of mare volcanism. Both of the two major types of occurrence determined for explosive volcanic deposits on the Moon [13] are displayed by these two pyroclastic deposits.

References. [1] Wilhelms D.E. and McCauley J.F. (1971) USGS Map I-703. [2] Mutch T.A. (1970) Geology of the Moon. Princeton Univ. Press, 324 pp. [3] Carr M.H. (1966) USGS Map I-489. [4] Scott D.H. et al (1972) USGS Map I-800. [5] Greeley R. and Gault D.E. (1973) EPSL 18, 102. [6] Taylor S.R. (1982) Planetary Science, LPI Press, 481 pp. [7] Head J.W. (1974) PLSC 5th, 207. [8] Howard K.A. et al. (1973) Apollo 17 PSR, NASA SP-330, p. 29-1. [9] Lucchitta B.K. and Sanchez A. (1975) PLSC 6th, 2427. [10] Wilhelms D.E and El-Baz F. (1977) USGS Map I-948. [11] Spudis P.D. and Hood L.L. (in press) Lunar Bases II. [12] Schultz P.H. (1976) Moon 15, 241. [13] Hawke B.R. et al. (1989) PLPSC 19, 255. [14] Schultz P.H. and Spudis P.D. (1983) Nature 302, 233. [15] BVSP (1981) Basaltic Volcanism, Pergamon Press, Ch. 8.

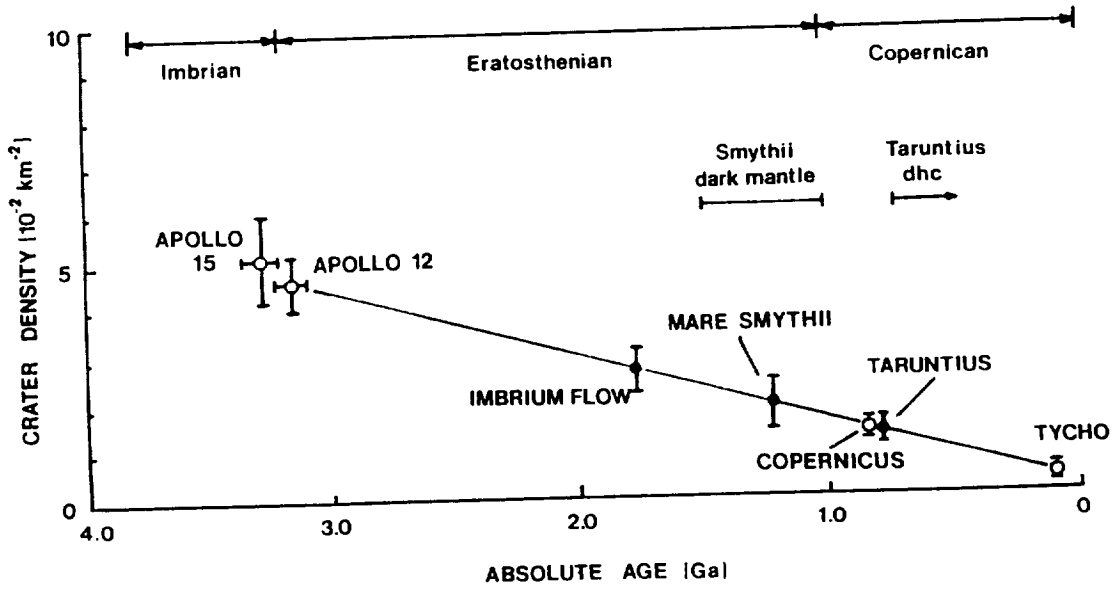

Figure 1. Crater densities and absolute ages for sampled units (open circles) and inferred ages for unsampled units (solid circles) on the Moon. Dark mantle deposit ages (above curve) are inferred from stratigraphic evidence. Lunar stratigraphic divisions shown at top. After [14].

MORPHOLOGIC AND SPECTRAL CHARACTERISTICS OF IGNIMBRITES

David A. Crown, Ronald Greeley, and Michael F. Sheridan, *Department of Geology, Arizona State University, Tempe, AZ 85287 and* ***Raul Carrasco,*** *Servicio Geologico de Bolivia, La Paz, Bolivia*

Ignimbrites in the Central Andes are being investigated as analogues for potential ash deposits on Mars and other planetary surfaces. Currently, a remote sensing study of the Frailes Formation in Bolivia is being undertaken to determine morphologic and spectral criteria for the identification and analysis of large ignimbrite sheets. A primary objective is the assessment of the utility of LANDSAT Thematic Mapper (TM) data in mapping volcanic materials in order to make interpretations regarding the eruption and emplacement processes leading to their formation.

The Frailes Formation (19°30'S, 66°30'W), an extensive ignimbrite plateau greater than 100 km in diameter, is located along the western margin of the Eastern Cordillera of the Andes in southern Bolivia. The Frailes Formation is among the largest ignimbrite deposits in the world and resides in the central volcanic zone of the Andes (16°-28°S) [1]. The ash-flow sheets comprising the Frailes Formation cover ~8,500 km^2 and were erupted in late Miocene time (5-8 Ma) [2-4]. These silicic tuffs display various degrees of welding with exposures averaging 100 m in thickness and reaching a maximum of ~1 km. The Frailes Formation overlies Paleozoic shales, sandstones, and carbonates of the Eastern Cordillera, which were folded and faulted during the Cenozoic in response to subduction along the western margin of South America.

Previous studies in this area include regional mapping by the Servicio Geologico De Bolivia, reconnaissance remote sensing, and geochemical analyses. The 1:100,000 geologic maps published in 1962 consider the entire ignimbrite plateau as a single unit consisting of ash with small occurrences of silicic lavas. The majority of the tectonic features are associated with the development of the Eastern Cordillera and are aligned parallel to its NW-SE trend. The tuffs of the Frailes Formation commonly contain between 65 and 69 wt. % SiO_2 and range in composition from dacite to rhyolite [5]. These ash-flow sheets are crystal-rich, containing phenocrysts of biotite, quartz, and two feldspars in a glassy to devitrified matrix. Based upon K-Ar and fission track dating, age relationships between the Frailes Formation and surrounding volcanic deposits and the evolution of volcanism within parts of the plateau have been determined [3-4].

Geologic Mapping Using Thematic Mapper Data. A mosaic of three LANDSAT TM quarter frames (Y5052213592/4, Y5051513531/3, and Y5086713403/1) has been generated for analysis of the Frailes Formation. The spatial resolution (28.5 m/pixel) and spectral variations of the TM data allow mapping of the units and identification of sub-units within the ignimbrite plateau. Interpretations are supported by reconnaissance field work. Volcanic materials associated with the Frailes Formation are easily distinguished from the surrounding sedimentary rocks in the fold belts of the Andes and on the surface of the Altiplano. Sedimentary sequences in the Eastern Cordillera can also be delineated. In addition, effusive volcanic materials associated with the Frailes Formation can be distinguished from the ash deposits. Most of the exposed horizontal rock surfaces of the Frailes Formation are of the partially-welded, columnar-jointed interior of the tuffs (the upper non-welded zone presumably has been stripped off). In several areas where the non-welded base of the flows are exposed they can easily be identified and differentiated from outcrops of partially-welded ash.

Discrimination of probable ignimbrite source areas from other eruptive centers is based upon examination of TM images and field observations. Five major eruptive centers and their associated flow materials can be identified. To the north in the Frailes Formation are two quasi-circular regions, which appear spectrally different than the main part of the plateau due to the presence of a well-developed glacial deposit. These areas (Cerro Livicucho and Cerro Condor Nasa/Cerro Chokkota) are apparently older, self-contained eruptive centers with the extrusions at their summits representing post-Frailes eruptions at the locations of ignimbrite source vents. The main part of the plateau consists of 2 overlapping ash shields with sources represented by Cerro Villacollo, a cone of lava with a prominent summit crater, and Cerro Pascual Canaviri, a large, high-standing dome complex. A fifth and the youngest eruptive center is the Nuevo Mundo Province, a complex of large rhyolite domes and related ash deposits at the southern margin of the Frailes Formation.

Wind-blown, weathered ash from this area blankets much of the SE part of the plateau. Identification of the units within the Frailes Formation and interpretations of the age relationships on the plateau using TM data are generally in agreement with previous remote sensing [6] and geochemical [4] studies.

Morphologic Characteristics of Ignimbrites. The volcanic materials of the Frailes Formation exhibit diverse morphologies which are a reflection of their emplacement history and post-depositional modification. The observed morphologic properties are similar to those of other ignimbrite deposits which have been identified in the Central Andes [6-7]. Knowledge of the relationship between the morphology, as observed in aerial photographs or in spacecraft images, and the eruption and emplacement processes is essential for analyses of large or inaccessible volcanic deposits and for accurate interpretations of the volcanic histories of other terrestrial planets. The following morphologic characteristics of ignimbrites erupted from central vents are apparent from analysis of the Frailes Formation: 1) ash-flow sheets form low-profile shields around and sloping away from their eruptive centers; 2) eruptive centers are identified by post-ignimbrite extrusives forming domes and cones, which have steeper slopes and are more resistant to erosion than the surrounding ash deposits; 3) erosion of ignimbrites is strongly influenced by topography; a radial drainage pattern extending from the eruptive center is common. Regional tectonism may also affect the erosion of ignimbrites; 4) partially welded ash-flow interiors produce cliff-forming exposures, whereas the nonwelded bases are slope-forming units; 5) nonwelded ash varies in thickness with distance from its source and may mask the underlying topography by filling valleys and ponding in depressions. Welded ash is typically more uniform in thickness and mimics or subdues the terrain on which it is emplaced; and 6) partially welded zones of ash flows are more resistant to weathering than nonwelded zones, allowing erosional outliers of ignimbrite with welded caps to be preserved.

Spectral Properties of Ignimbrites. The spectral variations in TM images can be used to identify and map volcanic deposits and allow discrimination of the units within the Frailes Formation. Interpretations of the TM data are supported by visible and near-infrared laboratory reflectance spectra of samples collected in the field. Bidirectional reflectance meaurements made relative to halon have been acquired from the RELAB (Reflectance Experiment Laboratory) at Brown University for fresh and weathered surfaces of the following volcanic rock types present in the Frailes region: dacite lava, altered dacite lava, welded ash, nonwelded ash, and altered ash. Spectra of windblown ash, lichen, and Cretaceous redbed sequences have also been obtained. Spectra of Frailes ash are relatively featureless because quartz and feldspar, the two major components of the ash, do not have strong absorption bands at visible and near-infrared wavelengths. Spectra of weathered, non-welded ash, wind-blown, weathered ash, and weathered, welded ash are similar, exhibiting a 1.4 μm OH band, a 1.9 μm H_2O band, and a band at 2.2 μm due to hydroxyl or water overtones. On TM images wind-blown and non-welded ash are noticeably brighter than welded ash. The increase in brightness from welded to wind-blown to non-welded ash, as seen in the spectra, is attributed to a decrease in the effective particle size. All of the spectra of the Frailes ash can be distinguished from spectra of lavas found in the plateau. Dacite spectra exhibit a band near 0.9 μm due to crystal field transitions of Fe^{2+}, whereas hydrothermally-altered dacite spectra exhibit a 0.85 μm band due to Fe^{3+}. Altered dacite is bright, and its spectrum contains prominent OH and H_2O absorptions. Dark, non-altered dacite spectra exhibit a weak H_2O feature at 1.9 μm. Spectra of hydrothermally-altered ash are very different from spectra of non-altered ash. They are dominated by water and hydroxyl absorptions at 1.4, at 1.9, and beyond 2.0 μm and are significantly brighter than non-altered ash beyond ~0.7 μm. In addition, a weak Fe^{3+} band at 0.85 μm is present. Spectra of redbeds are very similar to that of the altered ash (and to the altered dacite), and this similarity is evident in TM data. The spectrum of lichen contains strong OH and H_2O absorptions but can be distinguished from altered volcanic materials by its higher reflectance between 0.7 and 1.1 μm and the absence of an Fe^{3+} band.

Effects of Weathering on the Spectral Signature. It is most appropriate to compare laboratory spectra of weathered materials to TM data; however, fresh exposures may exist and it is important to understand if and in what manner weathering alters the spectral characteristics of

various deposits. Changes in particle size and/or composition resulting from weathering may have significant effects on reflectance spectra. For both ash and lava the effect of weathering is to decrease the reflectance at visible wavelengths. In addition, the strength of absorption features is also slightly reduced in spectra of weathered samples. For dacite the overall brightness of the spectra is also decreased.

Thematic Mapper Band Ratioing. The 1, 4, and 5 (blue, green, red) band combination utilizes bands of high individual variance in the visible, near-infrared, and short-wavelength infrared regions to produce color images which allow geologic interpretations to be made from morphologic and spectral information. By using band ratios the effects of topography are reduced and the spectral characteristics are emphasized. To determine which band ratio images most effectively illustrate spectral differences for the Frailes Formation, six-point spectra equivalent to the TM data have been generated from the laboratory measurements by convolving the lab spectra with the TM band filters. Band 6, the lower resolution, mid infrared band, has not been used. All possible band ratios have been computed and plotted according to the sample type.

In the 7/5 ratio lava is distinguished from ash, which has a higher reflectance in band 7. This ratio does not separate weathered and fresh deposits or nonwelded and welded ash. The ratios 7/4, 7/3, 7/2, 7/1, 5/4, 5/3, 5/2, and 5/1 do not show significant differences between ash and lava but do show a progression in brightness from weathered to fresh and welded to nonwelded ash samples. Weathered, welded ash spectra have the lowest reflectances. Reflectances of weathered, nonwelded ash, windblown ash, and fresh, welded ash are similar. Fresh surfaces of nonwelded ash are the brightest. Bands 1, 2, 3, and 4 are strongly correlated, but ratios show the progression in reflectance among the ash spectra. Lavas and lichen generally have a high reflectance in band 4 relative to ash. The 4/1 ratio shows the greatest separation between the various fields for these bands. Ratios of bands 1, 2, and 3 are not particularly useful in distinguishing differences between the rock types represented.

In general, weathering is observed to reduce the reflectance in bands 1 - 5 for dacite and welded, nonwelded, and altered ash, while increasing the reflectance in bands 1 - 7 for redbeds. The reduction in reflectance can be attributed to an increase in particle size due to the formation of a dark coating and possible absorptions due to Fe^{2+}. The redbeds are a friable deposit which, upon weathering, break down thus increasing their reflectance. The spectral effect of welding on ash is to reduce the reflectance in bands 1, 2, 3, and 4, which can be attributed to a decrease in particle size. Hydrothermal alteration of dacite generally increases the reflectance in bands 1 - 5, and alteration of ash increases reflectance in bands 4, 5, and 7. This results from the removal of dark, mafic materials, replacement by brighter Fe^{3+} oxides, and possibly a decrease in particle size.

A color ratio image for the Cerro Villacollo region has been generated using the ratio of bands 4/1, band 5, and the ratio of bands 7/5 (blue, green, and red) to illustrate spectral differences suggested in band ratio scatter plots. In this color ratio image the ignimbrite plateau is easily distinguished from sedimentary deposits on the Altiplano. Non-welded ash is visible as a light orange patch southwest of Cerro Tihua Alto. A similar color is apparent along many of the riverbeds extending west from the Frailes Formation, indicating that these materials are derived from the ignimbrite. The ratio image separates lava from ash more distinctly than in a band 1, 4, and 5 color image. Dacites at Cerro Tihua Alto are readily apparent as bright blue areas. A bluish color is evident for the deposits at the summit of Cerro Villacollo and to the northeast in pre-Frailes volcanics. The existence of dacite lavas is also suggested on the western margin of the plateau to the northwest of Cerro Villacollo. The brown areas surrounding the dacites are exposures of welded Frailes ash. The spectral variations observed in this band ratio combination assist in mapping the Frailes Formation and are especially useful for separating ash from lava as indicated by the 7/5 band ratio scatter plot.

References: [1] Thorpe, R.S. et al., 1982, in *Andesites*, ed. R.S. Thorpe, John Wiley & Sons, Great Britain, 187-205. [2] Evernden, J.F. et al., 1977, *Econ. Geol., 72*, 1042-1061. [3] Schneider, A., and Halls, C., 1985, *Communicaciones, 35*, 217-224. [4] Schneider, A., 1987, *Revista Geologica de Chile, 30*, 27-33. [5] Ericksen, G.E. et al., 1985, *U.S. Geol. Surv. Open-File Report 85-258*, 12 pp. [6] Baker, M.C.W., 1981, *J. Volcanol. Geotherm. Res., 11*, 293-315. [7] Francis, P.W. et al., 1978, *Nature, 274*, 749-751.

Mapping of textural variations in the Bishop Tuff related to welding and vapor-phase crystallization using Landsat TM data

Michael F. Sheridan and Alan H. Levine, Department of Geology, Arizona State University, Tempe, AZ 85287-1404

The Bishop Tuff is a Pleistocene (0.74 Ma) ignimbrite sheet exposed in an apron extending radially up to 50 km from the rim of Long Valley Caldera in eastern California. Erosion has stripped the non-welded upper ash from many parts of the sheet exposing at the surface the interior, which has undergone various degrees of welding and secondary crystallization. A few canyons have cut deep (up to 150 m) gorges through the sheet, but the upper surface is relatively flat. In lower elevations (1,200 m to 1,700 m) there is only sparse vegetative cover of sage and rabbit bush but at higher elevations there is a pinyon, juniper, and ponderosa forest that covers the tuff.

Visible to near-infrared reflectance, spectral data were obtained from RELAB facility on samples from all of the significant textural facies of the Bishop Tuff. The samples with a vitric matrix are easily distinguished from those with a crystalline matrix by the presence of water absorption bands at 1.4, 1.9, and 2.2 um. The albed of samples decreased with the degree of welding. Oxidation or reduction of the tuff could be measured by the reflectance slope near 0.7 um. A steep slope is indicative of the ferric iron absorption band, and the slope decreases as more iron is reduced. The data from the samples provide an excellent basis for interpretation of remotely obtained spectral data.

Spectral reflectance data recorded by the Landsat TM likewise is sensitive to textural changes caused by welding and secondary crystallization. TM data was useful where the vegetation was sparse at low elevations, and over 400 km^2 were mapped, but the signal from the tuff was strongly masked in the pine forest of higher elevations. Several facies of the tuff were recognized and mapped on processed images: (1) non-welded vitric tuff, (2) vitric partly-welded tuff, (3) partly-welded tuff with a crystalline matrix, (4) moderately crystalline vapor-phase tuff, (5) strongly welded vapor-phase tuff, (6) vapor-phase tuff with oxidized iron, and (7) fumarolic mounds (Sheridan, 1970). In addition, three different types of alluvial deposits were recognized, and correlated with different lithological source areas.

The map made from TM data compared favorably with the published geologic map of the area (Crowder and Sheridan, 1974) and actually displayed considerably more detail. The TM map allowed some new interpretations regarding the Bishop Tuff: (1) individual emplacement lobes could be distinguished by their different levels of oxidation, (2) the degree of vapor-phase crystallization could be accurately mapped to permit estimations of amount of hot gas that permeated through the upper parts of the tuff, (3) the depth of erosion could be qualitatively determined by the facies of tuff exposed at the surface, (4) a previously unrecognized thin sheet of obsidian-bearing gravel on top of the Bishop Tuff sheds new light on the drainage history of a Pleistocene Long Valley Lake, and (5) the timing of faulting of the ignimbrite sheet could be related to various deposits of alluvial materials on the tuff surface.

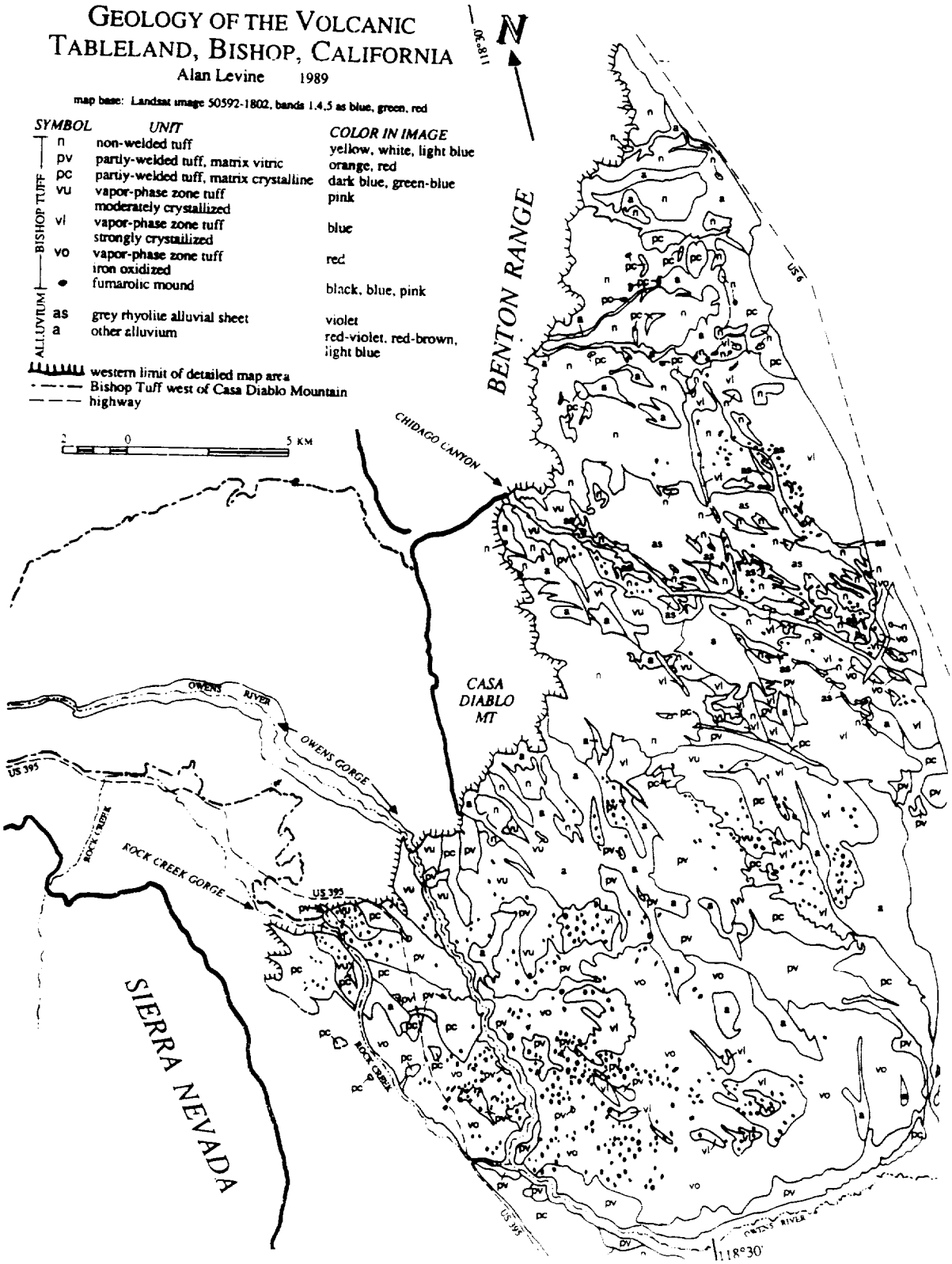

ORIGINAL PAGE IS
OF POOR QUALITY

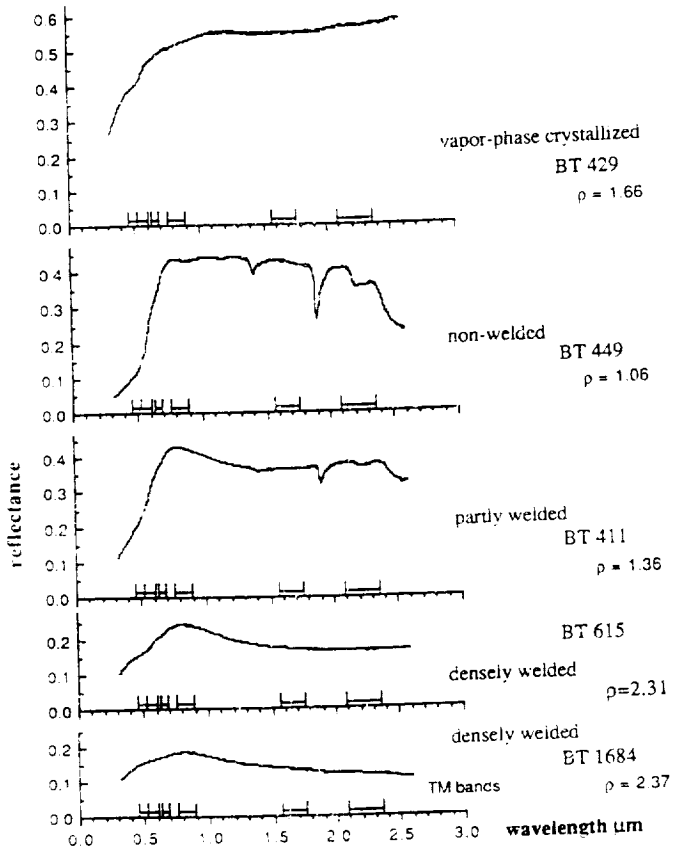

Figure 1. RELAB reflectace spectra of welded and vapor-phase crystallized Bishop Tuff. Vertical axis is reflectance in units of 0.1 (10%) relative to halon standard. Bars indicate wavelength of TM bands. Reflectance decreases with degree of welding and the 1.4 and 1.9 um H_2O and 2.2 um OH- bands decrease in depth. The steep slope near 0.7 um decreses as iron changes from oxidized (hematite) in the non-welded tuff to reduced (magnetite) in densely welded tuff. Reflectance of vapor-phase crystallized tuff is similar to reflectance spectra of quartz and sanidine. P = density in g/cm^3.

References:

Crowder, D.F. and Sheridan, M.F., 1974. Geologic Map of the White Mountain Peak Quadrangle, California. U.S. Geological Survey Geol. Quad. Map GQ-1012, scale 1:62,500.

Sheridan, M. F., 1970. Fumarolic mounds and ridges of the Bishop Tuff, California. Geological Society of America Bull., 81:851-868.

PREDICTING EXTRA-TERRESTRIAL LAVA FLOW MORPHOLOGY

J.H. Fink and N. Bridges, Geology Dept., Arizona State Univ., Tempe, AZ 85287

The morphology of lavas is controlled in large part by relative rates of crust growth and surface deformation within the flows. Laboratory and theoretical studies show that a progression of common lava flow features can be formed by varying either the cooling rate or the local flow rate (or both)[1,2]. If cooling rates are relatively high, surface crust growth inhibits the radial or lateral spreading of flows, and the resulting morphology consists of short bulbous lobes like those found in submarine pillow basalts and subaerial "toey" pahoehoe flows. Persistence of these conditions over an extended period of basaltic extrusion can lead to large-scale delta-like constructs such as those seen on the north flank of Mauna Loa Volcano [3] and on submarine portions of Kilauea Volcano [4]. Slower crust growth rates in basalts favor the formation of surface folds and levees, and produce longer, narrower flows and lower volcanic constructs. For silicic compositions, more efficient cooling results in the formation of endogenic domes in which new lava is added to the dome interior without substantial fracturing of the crust. Slower cooling of silicic extrusions yields exogenous domes and flows in which the crust cracks frequently, allowing hot interior lava to cool faster.

In the laboratory, transitions from one morphologic type to another correspond to specific ranges of two dimensionless parameters, Π and τ_s, where Π is a modified Peclet Number relating effusion rate to cooling rate, and τ_s is the time required for the surface to solidify, which combines ambient, eruption, and solidification temperatures. As shown in Fig. 1, the transitions occur at discrete values of a third parameter, Ψ, which describes the dimensionless distance from the vent at which surface crust first appears. For lavas erupted at or near solidus temperatures or in very cold environments, crust appears relatively close to the vent. In contrast, super-liquidus flows or those emplaced in a hot environment will not develop crust until the lava has travelled a greater distance. The morphology of larger-scale volcanic constructs should also reflect these conditions.

In laboratory simulations of lava flows in which polyethylene glycol is injected into a cold sucrose solution, four principal transitions can be noted: (1) flows without crust first develop levees when Ψ=55, (2) folds appear on leveed flows when Ψ=30, (3) rift-like fractures disrupt folded flows if Ψ=13, and (4) rifted flows become pillow-like when Ψ=3. Calculations of comparable parameters for a submarine basalt flow [4] yield a point well within the pillow regime (Ψ=1). Similar calculations for growth of the Mount St. Helens dome also indicate conditions within the rifting regime. We are currently collecting eruption data to allow us to plot conditions for a large enough number of eruptions to test the applicability of Figure 1 to natural terrestrial flows.

There are three main differences between terrestrial and extra-terrestrial conditions which must be considered before these results can be used to interpret flows on other planets: gravity, ambient temperature (T_a), and cooling mechanism. Considering a basalt flow erupted under water on earth [2,4] yields a Π of 8.8×10^6, τ_s of 3.6×10^{-2}, and Ψ of about 5. If we calculate these groups for Venus by substituting g=8.8 m-s^{-2} and T_a=457°C, and assuming that cooling in the dense, hot venusian atmosphere is primarily by convection, we obtain $\Pi=2.3 \times 10^7$, $\tau_s=2.4 \times 10^{-2}$, and Ψ of about 9. These values indicate that solidification of a basaltic crust is about two times slower on Venus than on earth so that for comparable effusion rates and compositions, volcanic constructs on Venus should be broader and lower with proportionally more structures like folds and levees, and should exhibit fewer pillow-like or rift-like forms. Comparable calculations for Mars using g=3.7 and T_a=-73°C show that sub-aerial crust growth may under certain circumstances be slower on Mars than on earth, depending on the heat transfer mechanism assumed for the thin martian atmosphere. Thus lava flows on Venus and Mars may look more like each other than they do flows on earth.

Ongoing laboratory simulations and calculations for a variety of eruption scenarios should allow our model of morphologic dependence on crust growth and effusion rates to first be calibrated and then used to interpret the appearance of extra-terrestrial lava flows and volcanic constructs.

REFERENCES: [1] Fink JH, Griffiths RW (1989) Laboratory simulations of lava flows with solid crusts. *Lunar Planet. Sci. Conf.* XX, 285-286. [2] Fink JH, Griffiths RW (1990) Radial spreading of viscous gravity currents with solidifying crust. *Jour. Fluid Mechanics* (in press). [3] Malin MC, pers. commun., 1983. [4] Tepley L, Moore JG (1974) Fire under the sea (16 mm motion picture) Moonlight Prods., Mountain View, CA.

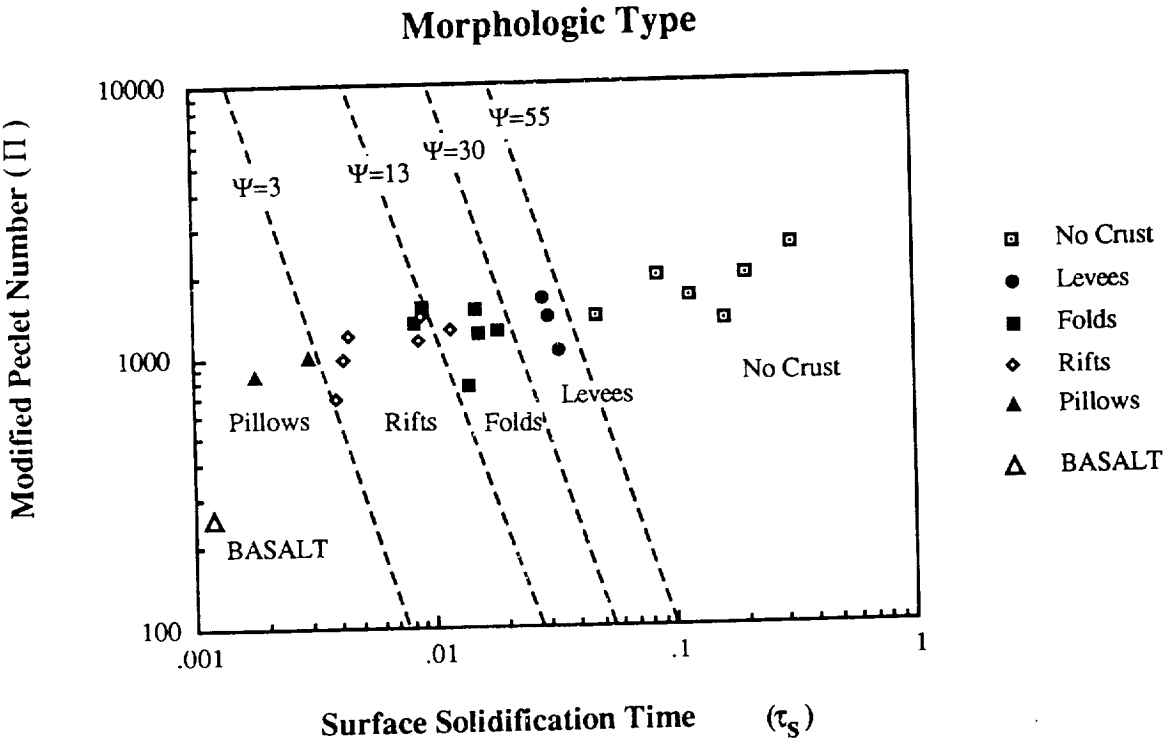

FIGURE 1. Plot showing extrusion type and experimental conditions for 21 laboratory simulations of lava effusion. Data expressed in terms of a modified Peclet Number, Π, and a dimensionless time to solidification, τ_S. Lines representing constant Ψ separate the different morphologic fields. Large circle represents calculated values for terrestrial basalt flow emplaced under water by a combination of rifting and pillow formation.

Time and Space Dependent Two-Component Thermal Model for Lava Flows

S. Baloga, J. Crisp, J. Plescia, R. Lopes, Jet Propulsion Laboratory
California Institute of Technology, Pasadena CA

Understanding the physical processes that control the dimensions of terrestrial lava flows is essential for the development of models that can be applied to planetary data. The post-emplacement dimensions of terrestrial basaltic lava flows exhibit a high degree of variability when mapped and analyzed in detail. Figures 1 and 2 show, for example, the variations of flow width and pre-existing slope as a function of distance from the source for Episode 18 of the recent Puu Oo eruption. A detailed statistical analysis of such data for a number of flows indicates that the variability in the local dimensions (height and width) cannot be attributed to local topographic changes derived from 20 m contour maps [1]. Data from other volcanoes produce similar results. On the basis of the data analyzed to date, the inescapable conclusion is that the dimensions of lava flows are controlled by small scale topographic variations (on the order of meters or less) or variability associated with critical physical processes, such as thermal losses. In this abstract we examine one model related to the latter case.

The importance of treating space and time as independent variables in models of flow emplacement processes has been discussed theoretically (e.g., [3]) and in field studies of active flows [4, 5]. To explain the type of variability shown in Figures 1 and 2, it is clear that mathematical models need to include both space and time, independently, and permit the incorporation of stochastic processes into the formulation (e.g. [6]) of the model.

We have recently proposed a model that assumes that cooling by Stefan-Boltzmann radiation is the dominant physical process controlling the dimensions of lava flows [7]. This model considers the insulating effect of a cooler crust on the heat loss from the inner core. Here, we present a new governing equation for the core temperature of a lava flow. This formulation can be simplified and used to estimate eruption rates of planetary flows [2] with currently available data.

The model shown below extends the two component thermal model to two independent variables, time and distance from the vent. To derive the governing equation for the temperature of the core of the lava flow, we use a control volume as shown in Fig. 3. The variables h, δ, and T are all considered to be functions of x and t. The heat content of the core includes the following considerations. First, it may change with time due to the flow of material through the vertical faces. Second, the control volume itself may diminish with time as the location of the upper horizontal surface advances down. Finally, the upper control surface permits a radiative heat loss from a fractional area f. Thus,

$\rho\ C_p\ \partial/\partial t\ [\ (h-\delta)\ T\ ]\ W\ dx$ = time rate of change of heat in the control volume (e.g., ergs/s)

$-\ \rho\ C_p\ u\ \partial/\partial x\ T\ dx$ = net flux through vertical faces with area $(h-\delta)\ W$ of control volume due to the flow of lava (e.g., ergs/cm^2 s)

$-\ q$	= net flux through the part of the upper face with area (1-f)Wdx that shields the core. This flux is due to the downward advance of the upper control volume surface
$-\ \epsilon\ \sigma\ T^4$	= net heat flux through upper surface of control volume with area f W dx

By equating the time rate of change of the total heat content to the total net flux into the control volume, the governing equation for the temperature of the core is obtained

$$\rho C_p \left[\partial/\partial t \left\{ (h-\delta)\ T \right\} + u\ \partial/\partial x \left\{ (h-\delta)\ T \right\} \right] = -\ (1-f)q - f\epsilon\sigma T^4 \qquad (1)$$

If we now require T to be constant for f=0, i.e., no direct exposure of the inner core, then

$$q = \rho\ C_p\ T \left\{ \partial\delta/\partial t + u\ \partial\delta/\partial x - \partial h/\partial t - u\ \partial h/\partial x \right\} \qquad (2)$$

Substituting Eqn (2) into Eqn (1) and simplifying the results for a flow that maintains a constant thickness gives the governing equation

$$(h-\delta) \left\{ \partial/\partial t + u\ \partial/\partial x \right\} - fT \left\{ \partial\delta/\partial t + u\ \partial/\partial x \right\} = -\ f(\rho\ C_p)^{-1}\ \epsilon\sigma\ T^4 \qquad (3)$$

This equation for the temperature of the core requires a supplementary boundary condition, such as the time behavior of the temperature at the vent. Crisp and Baloga [7] investigated in detail the case of heat transport through the crust by Fourier conduction. We will use the notation $T(x=0,t) = \Psi(t)$ for the magma temperature at the vent with the understanding that Ψ is a prescribed function. In addition, $\delta(x,t)$ must also be specified or derived from another independent governing equation. Although Eqn (3) appears formidable, it is readily solved analytically by putting it in the form

$$\left\{ \partial/\partial t + u\ \partial/\partial x \right\}\ (h-\delta)^f\ T = -\ f\ \epsilon\ \sigma\ T^4\ (h-\delta)^{f-1}\ /\ \rho\ C_p \qquad (4)$$

and making the substitution

$$\eta = (h-\delta)^f\ T \qquad (5)$$

thus we obtain

$$\left\{ \partial/\partial t + u\ \partial/\partial x \right\}\ \eta = -\ f\ \epsilon\ \sigma\ \eta^4\ (h-\delta)^{-(1+3f)}\ /\ \rho\ C_p \qquad (6)$$

and the equivalent system of ordinary differential equations

$$dt/1 = dx/u = -\ \rho\ C_p\ (h-\delta)^{1+3f}\ d\eta\ /\ f\ \epsilon\ \sigma\ \eta^4 \qquad (7)$$

Explicit solutions to this "Cauchy problem" can be obtained for the case of a crustal boundary layer that changes in any fashion. The solutions to this system can embrace systematic and random variations in both the magma temperature at the vent and the degree of core exposure along the path of the flow during emplacement. The detailed mathematical

solutions and the degree to which they explain data as shown in figures 1 and 2 will appear elsewhere.

References: [1] Wolfe, E.W. et al., 1989, US Geol. Surv. Prof. Pap. 1463, 1-98 [2] Crisp and Baloga, 1990, A method for estimating eruption rates of planetary lava flows, to appear in Icarus. [3] Baloga, S., 1987, J. Geophys. Res., 92:9271-9279 [4] Guest, J.E. et al., Bull. Volc. 49, 527-540 [5] Moore, H., 1987, U.S. Geol. Surv. Prof. Pap., 1350, 1569-1588 [6] Schuss, Z., 1980, Theo. and Appl. Stochastic Diff. Eqs. [7] Crisp and Baloga, 1990, Jour. Geophys. Res., 95, 1255-1270.

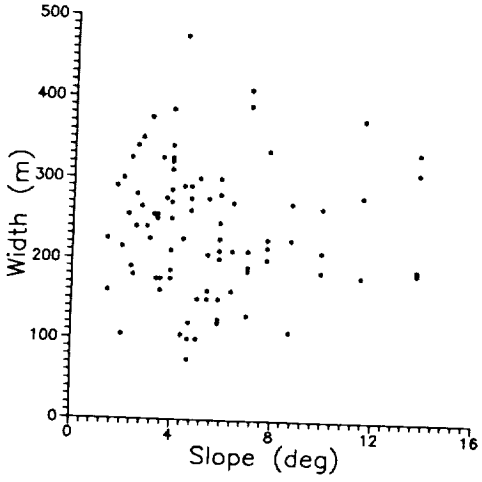

Figure 1

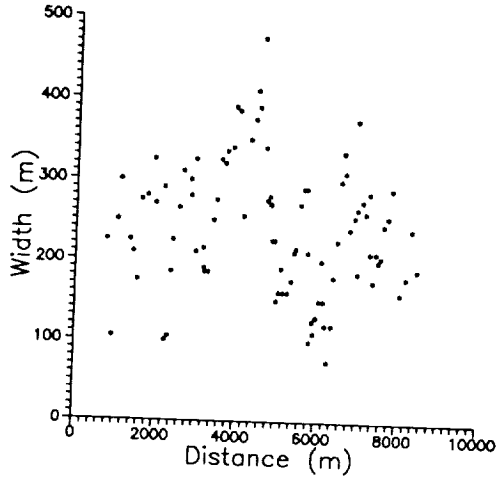

Figure 2

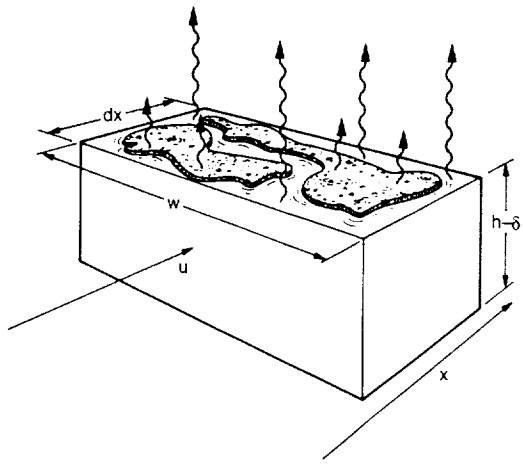

Figure 3. Control volume construction used for developing the heat balance for the core. Flow of lava is in the x-direction. Large arrows indicate radiation directly from the core. Small arrows indicate radiation from the cooler crust, which may grow with time, or with distance from the vent, in an arbitrary manner.

COMPOSITION-SPECIFIC PATTERNS OF TEXTURAL DISTRIBUTION ON SILICIC LAVA FLOW SURFACES

J.H. Fink and S.W. Anderson, Dept. of Geology, Arizona State Univ., Tempe, AZ 85287

Silicic lava flows and domes have not yet been identified on Mars or Venus, either because they do not occur [1], or because the resolution of available images is too poor. Assuming the latter to be the case, we are undertaking a series of studies designed to characterize the surface appearance of silicic extrusions, in anticipation of higher resolution data from the Magellan and Mars Observer missions. Here we report on characteristic patterns of vesicular texture observed on terrestrial dacite and rhyolite flows and domes which may be used as diagnostic indicators of composition.

The crystal-rich Mount St. Helens dacite dome, which grew episodically from 1980 to 1986, provided an unrivaled opportunity to study the formation of surface textures in silicic lava [2]. Two distinctive textures, smooth and scoriaceous, developed throughout the growth of the dome. Smooth lava has less than 30 volume percent vesicles whereas scoria has more than 50 per cent. The two lava types can be easily identified, both on the ground and in aerial photographs. The large contrast in roughness suggests that the textures could also be distinguished in synthetic aperture radar (SAR) images.

Analysis of photographs and observations taken during emplacement of the nearly 20 lobes of the Mount St. Helens dome reveals that the textures occur in three distinct patterns depending on the underlying slope and the water content of the magma. When an active lobe emerges on a slope of more than 20 degrees, a predominantly scoriaceous surface develops, with only a small amount of smooth lava located over the vent and occasionally near the flow front. We refer to this as a Type I extrusion.

If a flow forms on a shallow slope of less than 20 degrees, the extruding lava spreads laterally away from the vent in opposite directions, separated by a prominent feature called a "crease structure", which consists of two paired convex-upward fractures [3]. Inward growth of this rift-like structure keeps pace with emergence of the lava and takes place in very small steps. This incremental exposure of new lava rapidly cools the flow surface, preventing vesiculation and the formation of scoria. The result is a bilaterally-symmetric smooth lobe cut by a prominent medial fracture. We call this a Type II lobe.

During some extrusions, water content progressively increases because the earliest lava degasses as it rises to the surface [4]. As a result, the last lava to appear in some Type II lobes is sufficiently water-rich to vesiculate, even though it has been rapidly cooled by growth of a crease structure. In these cases the pattern consists of a scoriaceous central area surrounded by smooth outer margins. The medial fracture may be partly or totally destroyed by the late-stage vesiculation. We can thus further differentiate between "dry" Type IIA lobes with smooth central regions, and "wet" Type IIB with scoria over the vent.

In contrast to dacites, the higher viscosities and more rapid cooling of rhyolite lavas cause them to retain volatiles more effectively. As a result, the upper surfaces of rhyolite flows tend to be composed mostly of light-colored, finely vesicular pumice (FVP). Once formed, this rigid carapace acts as a barrier to upward migration of volatiles released by crystallization within the flow interior, leading to the growth of a water-rich zone 10 to 20 meters beneath the surface [5]. As the volatile content of this zone increases, the lava gets less and less dense. When it becomes sufficiently buoyant, regularly spaced, sub-circular diapirs of very dark, coarsely vesicular pumice (CVP) up to 100 meters in diameter may rise to the flow surface. The periodic spacing of these outcrops [6], coupled with the large albedo contrast between CVP and FVP are diagnostic of lavas with very high silica contents. CVP and FVP may also be distinguishable on SAR images, because of large

differences in average vesicle size, and because the FVP tends to break up more readily into large blocks. Although dacite lavas may also develop diapirs of CVP, the surfaces of such intermediate composition flows tend to have much smaller contrasts in albedo.

These characteristic textural distributions allow terrestrial rhyolite and dacite flows to be distinguished from each other and from more mafic compositions. High-resolution images of relatively fresh lava flows from Mars or Venus could be examined together with estimates of surface slope to look for some of these diagnostic patterns. Textural information combined with a description of the suite of surface structures found on a flow [7] may provide important constraints on extra-terrestrial lava composition.

REFERENCES: [1] Francis, P.W. and Wood, C.A. (1982) *J. Geophys. Res.* **87**:9881-9889. [2] Anderson, S.W. and Fink, J.H. (1989a) *in* Fink, J.H. (ed.) Lava flows and domes, *IAVCEI Proc.Volcanology* **2**:25-46. [3] Anderson, S.W. and Fink, J.H. (1990) Crease structures as indicators of emplacement rates and surface stress regimes of lava flows, *Geol. Soc. America Bull.*, (submitted). [4] Anderson, S.W. and Fink, J.H. (1989b) *Nature* **341**:521-523. [5] Fink, J.H. and Manley, C.R. (1987) *in* Fink, J.H.(ed.) The emplacement of silicic domes and lava flows, *Geol.Soc. America Spec. Paper* **212**:77-88. [6] Baum, B., Krantz, W., Fink, J.H. and Dickerson, R. (1989) *J. Geophys. Research* **94**: 5815-5828. [7] Fink, J.H. and Griffiths, R.W. (1990) Radial spreading of viscous gravity currents with solidifying crusts, *J. Fluid Mechanics* (in press).

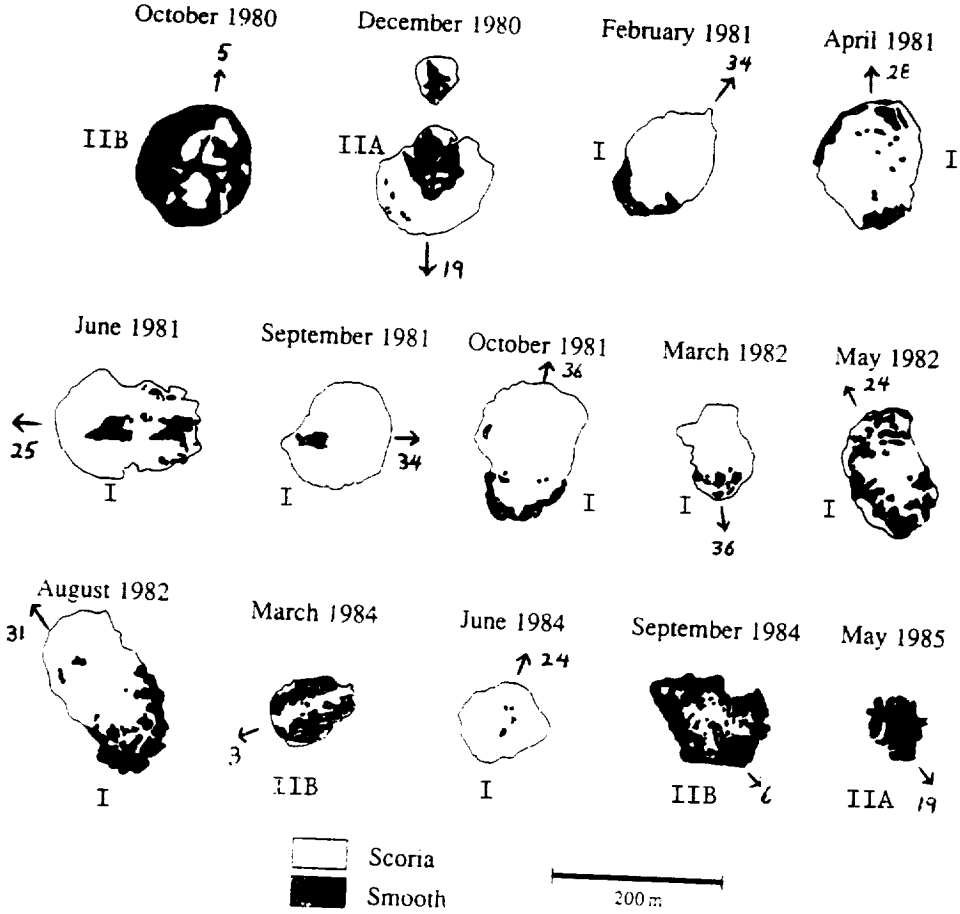

Figure 1. Maps showing the distribution of smooth and scoriaceous textures on various lobes of the Mount St. Helens dome. Arrows point in downslope directions and numbers are slope angles in degrees. Roman numerals refer to lobe type.

MAPPING TEXTURAL VARIATIONS ON SILICIC LAVA FLOWS WITH THERMAL INFRARED SPECTROMETRY

J. Ondrusek, J.H. Fink, and P.R. Christensen, Department of Geology, Arizona State University, Tempe AZ 85287-1404 BITNET: AGJXO @ ASUACAD

Available photogeologic evidence for rhyolitic and dacitic volcanic deposits on Mars is equivocal at best. However, anticipated spectroscopic data from the Thermal Emission Spectrometer (TES) instrument on the Mars Observer mission should permit a more effective search for silicic deposits. The purpose of our investigation is to establish a strategy for using spectroscopic data to identify silicic lava flows and domes.

We have shown earlier (Ondrusek et al., 1989) that small variations in the vesicularity of silicic lava flows have a profound effect on the thermal infrared spectral signature measured. While the Thermal Infrared Mapping Spectrometer (TIMS) can readily distinguish compositional variations in crystalline and, to some degree, glassy rocks, this sensitivity is greatly reduced in vesicular lavas. Coarsely vesicular pumice (CVP) makes up a sizable portion of the surfaces on most terrestrial silicic lava flows. Similar textures on martian flows would prevent successful identification of composition by TES.

To study the effect of vesicularity on infrared imagery in more detail, spectral data from areas of known texture were collected from TIMS scenes of Little Glass Mountain (LGM), Crater Glass flow (CG), and Medicine Lake Dacite Flow (MLDF), all located on the Medicine Lake Volcano in northern California. These flows are ideal for studying textural variations because each flow consists of lava of only one composition but a range of textures including CVP, finely vesicular pumice (FVP), and glassy obsidian. LGM and CG flows are rhyolitic and MLDF is dacitic in composition.

Digital numbers from 10-15 locations in each textural type were collected and averaged for each flow. These data are plotted as six-point TIMS spectra to better show spectral variations due to textural control. Figure 1 is a plot of averaged DN's of the six TIMS bands for both pumiceous textures on all three flows. In general, the CVP texture (open symbols) has a higher emissivity than the FVP texture, regardless of composition. Comparison of different textures within a single flow reveals variations in the slope between TIMS bands 1 and 2, 3 and 4, and 5 and 6.

Experimentation with ratio images indicates that ratios of TIMS bands 3 and 4 produce images which accurately differentiate between CVP and FVP textures on flows of both rhyolitic and dacitic compositions. This discriminatory facility has been tested on images of Glass Mountain, another large flow at Medicine Lake consisting of both textures and several compositions. The band 3 to 4 ratio image accurately shows the distribution of coarse and fine pumiceous textures where they are known from field work. Comparable distinctions cannot be made using aerial photographs.

Mapping the location of the textures present on silicic lava flows allows the image analyst to avoid the areas of CVP which are unsuitable for compositional determinations and concentrate on those portions of the flow where such mapping may be successful. In addition, the detailed knowledge of the distributions of coarse and fine pumiceous textures has relevance in various models of silicic lava emplacement and volatile migration. We are now developing appropriate image processing techniques to produce accurate maps of compositional variation.

Reference:

Ondrusek, J.V., Christensen, P.R., and Fink, J.H. (1989) Composition and textural variations in Glass Mountain, California lava: Evidence from thermal spectroscopy. NASA TM 4130, Reports of Planetary Geology and Geophysics Program - 1988, p. 416.

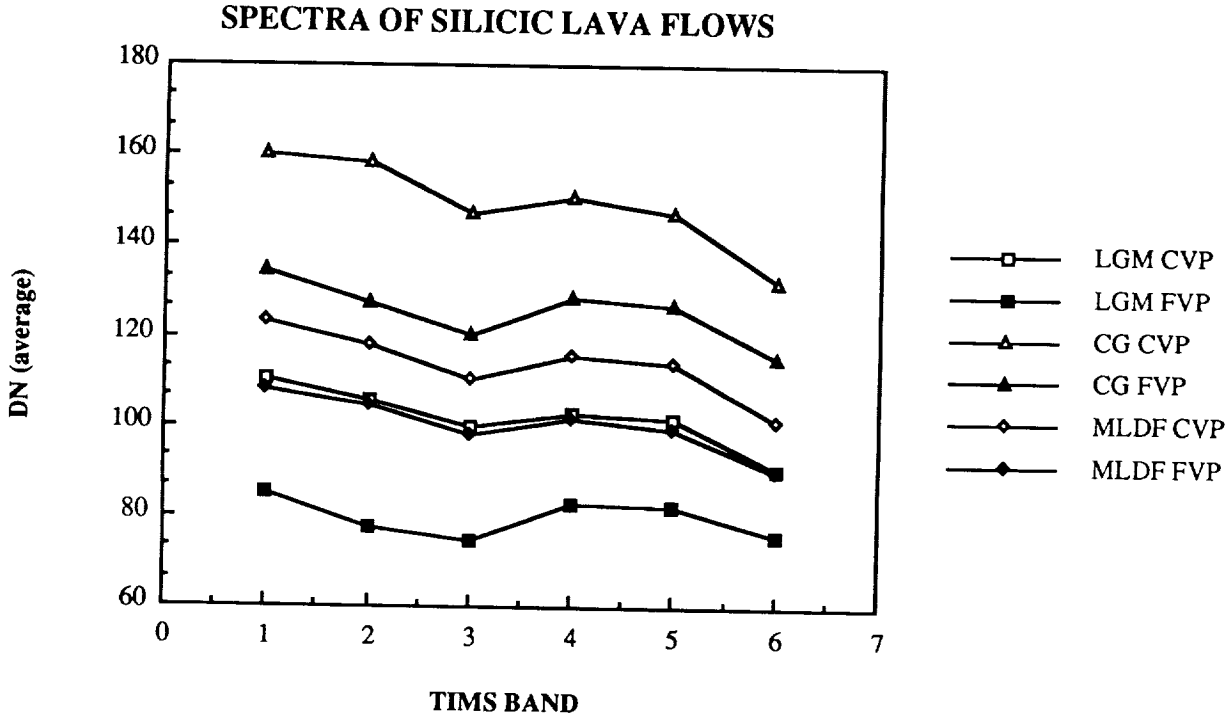

Figure 1. Plot of TIMS spectra for two different lava textures (CVP = coarsely vesicular pumice; FVP = finely vesicular pumice) from lava flows of two different compositions: LGM = Little Glass Mountain (rhyolite); CG = Crater Glass Flow (rhyolite); MLDF = Medicine Lake Dacite Flow (dacite). Note that coarse pumice samples have consistently higher emissivity values than corresponding fine pumice, allowing the two textures to be distinguished on TIMS images.

CHAPTER 10

CRATERING PROCESSES AND CHRONOLOGIES

THE CRATERING RECORD ON TRITON; R. G. Strom, S.K. Croft, Lunar and Planetary Laboratory, Univ. of Arizona, and J. M. Boyce, NASA Headquarters

Impact craters on Triton are rare to nearly absent at the 3 to 1.8 km resolutions acquired on the mapping sequence of Voyager 2. There are no multiring or peak-ring basins. Fresh impact craters displaying sharp rims with bowl-shaped interiors, or flat floors with central peaks, range in size from the resolution limits of the images (about 1 km) up to 27 km. The transition diameter from simple to complex craters occurs at a diameter of about 11±2 km, which is consistent with the transition diameters for craters on other icy satellites when their surface gravities are taken into account. The depth/diameter ratio of Triton's impact craters (6 measurements) is commensurate with the depth/diameter ratios on other icy satellites. For example, a 15 km diameter complex crater is about 1.4 km deep, and a 5 km diameter simple crater is about 0.65 km deep. The craters do not show recognizable ejecta blankets or interior terraces, but this is probably due to the low resolution of the images. Lunar craters of comparable diameter also do not show ejecta blankets or terracing at similar resolutions. The craters also do not display either light or dark rays. This could be due to the high albedo of the surface and/or darkening of light rays by micrometeorite gardening or radiation darkening. The lack of dark ray craters, which are apparent on other icy satellites at comparable resolutions, may place constraints on models of dark ray formation. There are several large circular features up to about 50 km in diameter in the frost-covered southern hemisphere and near the "cantaloupe" terrain that could be impact craters dating from an earlier period of heavy bombardment. However, these features have been so degraded and modified by internal processes, possibly including viscous relaxation, that all morphological signatures ,except their circularity, have been erased. Whether these structures are ancient impact craters is highly uncertain at this time.

The imaged surface of Triton was divided into four areas, indicated by solid outlines in figure 1. Area 1 is the most heavily cratered region and occurs between about 30 and 70 degrees longitude. Area 2 is the most lightly cratered region and coincides with the lake-like features between about 0 and 30 degrees longitude. Area 3 is largely the "cantaloupe" terrain, and Area 4 is a portion of the frost covered southern hemisphere. At this time crater counts on the "cantaloupe" terrain are unreliable and, therefore, are not shown. Because of the nature of this terrain and the low resolution at which most of it was imaged, impact craters are extremely difficult to recognize with any degree of certainty. Although impact craters probably occur on this terrain, their number and diameters are uncertain at this time and comparisons with other areas could lead to erroneous interpretations. However, a small portion of this terrain imaged at a resolution of about 2 km has a very low crater abundance possibly comparable to that of area 2.

Figure 2 is an R plot of the crater size/frequency distribution for Areas 1,2, and 4 compared with those of the lunar highlands, the lunar post-mare and the fresh crater population on Miranda. The crater density for the most heavily cratered terrain (Area 1) is essentially the same as that of the lunar post-mare over the same diameter range. Although the statistics are poor, both Area 2 and Area 4 are at about the same longitude and have the same crater density suggesting that the frost covered southern hemisphere and the "lake" region are about the same age. They have a crater density about half that of Area 1. Furthermore, the crater density on the "lakes" near the terminator is much lower (only two craters) than on the smooth terrain immediately to the east, indicating the "lakes" are younger. Although Area 1 is the most heavily cratered region on Triton's imaged surface, it is not necessarily the oldest surface. This part of Triton constitutes the leading hemisphere in its orbit around Neptune and therefore impacts will be more frequent and at higher velocities than elsewhere on the satellite. The crater frequency should decrease from the apex to the antapex of motion as observed. Furthermore, the three largest craters observed all occur within about 50 km of each other and nearer the apex of motion than most other craters in the region. Therefore, the relatively high crater density in Area 1 compared to other areas could be wholly or partly due to a leading/trailing asymmetry in the crater production rate. If this is the case then determining relative ages form crater abundances on relatively widely separated terrains could lead to erroneous results. This method of age dating should only be attempted for adjacent terrains at similar longitudes. Even then the uneven resolution and very low crater abundances make this method very uncertain.

We attempted a more refined estimate of the leading-trailing asymmetry by counting craters in the areas denoted by dashed lines in figure 1. These areas were chosen to encompass similar geologic provinces to eliminate real geologic age differences as much as possible. The approximate bounding longitudes and cumulative number of craters above 4 km in diameter of each area are, respectively: 60-75° and 13±3 /10^6 km^2, 30-60° and 12±3 /10^6 km^2, and 0-30° and 6±2 /10^6 km^2. These statistics are marginal but broadly consistent with a factor of 2 decrease in crater density between the leading edge and the boundary between the leading and trailing hemispheres.

A comparison of Triton's and Miranda's cratering record sheds some light on the origin of the impacting objects. The crater statistics in lightly cratered areas are too poor and have too small a diameter range to be much help in determining the crater size/frequency distribution, thus only Triton's most heavily cratered

terrain (Area 1) is considered to provide a fairly reliable indication of the crater size/frequency distribution. Figure 2 shows the impact crater size/frequency distribution for the craters in area 1 on Triton and for fresh craters on Miranda. Both distributions have about a differential -3 slope, and an upper diameter cut-off of about 25-30 km. The density of the fresh craters on Miranda is about an order of magnitude higher than the craters on Triton. The distribution for craters on the lunar maria, also shown in figure 2, has a slope and density similar to Triton's, but the upper diameter cut-off is near 100 km. The largest undisputed crater on Triton is 27 km in diameter, and Triton is large enough that craters larger than 30 km should occur if sufficiently large projectiles were present in the impactor population. Thus the lower cut-off for crater (and impactor) sizes on Triton and Miranda relative to the Moon could be real and reflect a difference in the respective impactor size distributions. On the Moon this population must contain a substantial number of asteroids which are not present at Uranus and Neptune.

In addition to similar population statistics, both the craters on Triton and the fresh craters on Miranda appear to exhibit leading-trailing asymmetries. Since Miranda is in prograde orbit, the leading/trailing asymmetry most likely indicates a source population external to the uranian system: i.e., comets. The possible leading/trailing asymmetry for Triton's craters is also consistent with a cometary origin, but unfortunately not diagnostic. This is because Triton's orbit is retrograde and therefore planetocentric objects in prograde orbits (which were almost certainly present) will also preferentially impact on its leading hemisphere. This is consistent with Goldreich's (1) model for Triton's capture, which proposes an initial eccentric orbit and tidal heating followed by circularization of the orbit and sweep-up of objects in prograde orbits. Therefore, the cratering record could be the result of sweep-up of the prograde planetocentric objects near final circularization of Triton's orbit and after resurfacing. Thus, even though similarities of Triton's and Miranda's fresh crater populations favor a similar cometary origin for both, a planetocentric origin for the craters on Triton cannot be ruled out.

REFERENCES

1. Goldreich, P. et al., Science, 245, pp. 500-504, August 4, 1989.

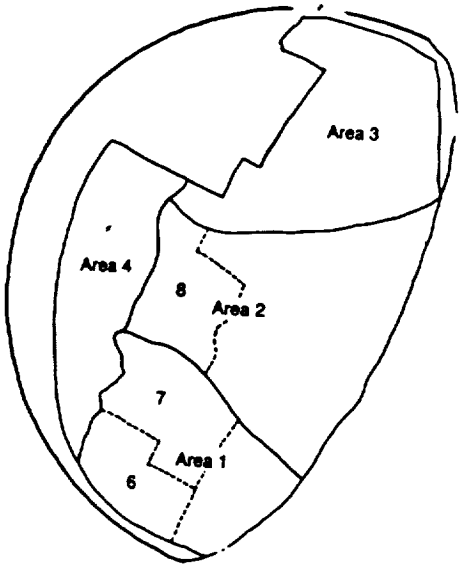

Figure 1. Location map of areas on which crater counts were performed. Area 1 is the most heavily cratered and corresponds to the Triton HC curve in Figure 2. Area 2 is lightly cratered and corresponds to the Triton LC curve in Figure 2. Area 3 is the Cantaloupe terrain and not yet fully analyzed. Area 4 is a portion of the frost covered southern hemisphere and corresponds to the Triton SH curve in Figure 2. The dashed areas (6,7 and 8) are the areas counted to determine if a gradient in the crater density exists. These areas all consist of similar terrain.

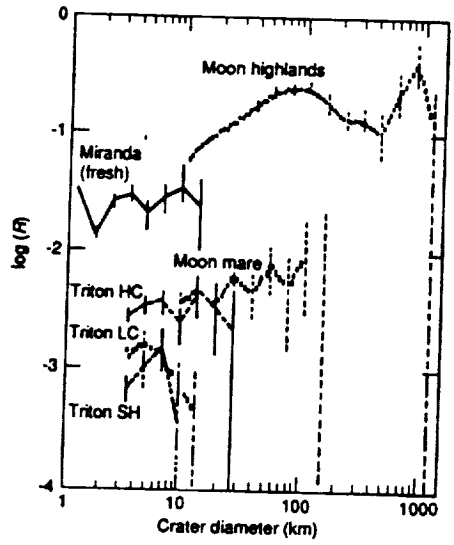

Figure 2. R plot of the Triton crater size/frequency distribution for Area 1 (Triton HC), Area 2 (Triton LC) and Area 4 (Triton SH) compared with the fresh crater population on Miranda, the lunar highlands and the lunar post-mare.

IMPACT AND COLLISIONAL PROCESSES IN THE SOLAR SYSTEM

Thomas J. Ahrens, Seismological Laboratory 252-21, California Institute of Technology, Pasadena, CA 91125.

We are carrying out experimental research on mechanical and thermodynamic aspects of shock and impact cratering and accretionary processes in solid planets, and their atmospheres and satellites. Experiments are being conducted to understand impact induced melting and vaporization of minerals on the terrestrial planets, their satellites and the icy satellites of the outer solar system. Recent theories of the impact origin of the moon and impact devolatilization of Mercury need to be tested with these data.

We measure the shock pressure, and hence, infer corresponding impact velocities of infalling planetesimals during planetary accretion which are required to induce melting of iron, sulfides, and oxides which precedes planetary core formation. We are studying the release of volatiles by impact on water-, carbon dioxide-, sulfur-bearing minerals, and hydrocarbons in the laboratory because this process is believed to underlie the accretion of planetary atmospheres. Studies of noble gas devolatilization are conducted to constrain theories of atmospheric evolution. We combine experimental data on shock induced melting and vaporization and theories of planetary atmospheric growth to understand the chemistry of interaction of hot proto-planetary surfaces with proto-atmospheres. To understand impact production of melt and vapor from silicates and formation of magma oceans on the earth, Moon, and Venus, we are studying shock temperatures in the minerals of planetary crusts and mantles. We are conducting shock loading experiments on rocks in order to understand and be able to describe their mechanical response which gives rise to the observed negative Bouguer gravity anomalies observed over impact craters on the earth and moon and seismic velocity deficits beneath impact and explosion craters.

1) We have carried out the first experimental studies of the solubility of Ar in carbon glass in order to both understand how noble gases become dissolved in carbonaceous material in the solar nebulae and to provide sample material to conduct impact devolatilization experiments.

2) New gas recovery shock devolatilization experiments were conducted on serpentine, serpentine enriched in D, and Murchison carbonaceous chondrite. All three materials demonstrate that incipient to complete loss of water occurs upon subjecting these materials to shock pressures in the range of 100 to 300 kbar. This is in approximate agreement with previous experiments in which only the solid phase was recovered and analyzed. Marked depletion of the evolved water and hydrogen in deuterium by as much as $\Delta\delta D = -100‰$ was discovered. We attribute the preferential partitioning of deuterium into the solid phase as a result of a kinetic effect in the reaction of iron with water during the shock devolatilization process. If this process occurs during planetary accretion, it leads to a new scenario in which the early deuterium depleted atmosphere is lost by Jeans' loss or by hydrodynamic escape and a later forming atmosphere has a greater D/H ratio. We propose that such a scenario might have occurred on Mars and Venus.

3) New Hugoniot equation of state data for brucite $Mg(OH)_2$ to 60 GPa demonstrate that like MgO, this mineral does not undergo a phase change over this pressure range. Moreover, these shock data when analyzed in terms of possible breakdown to $MgO + H_2O$ may permit determination of whether water remains associated in the solid state at high pressures in planetary mantles. The release isentrope data for brucite shows strong evidence for

devolatilization upon pressure release and needs to be analyzed in detail and compared to previous shock recovery data.

4) We have nearly completed construction of VISAR (Velocity Interferometer System for a Reflecting Surface) which will be used to conduct a rigorous program of study of the impact vaporization of rocks. Virtually no experimental data on the conditions for impact volatilization of rocks are available, yet the most recent theories of the origin of the moon and the devolatilization of Mercury appeal to this, at present, poorly understood process.

5) We have conducted a series of impact experiments on blocks of San Marcos gabbro and Bedford limestone which demonstrate 30 and 50% crack-induced reduction in P-wave velocity due to 900 MPa shock pressures. One-dimensional spall experiments to relate dynamic tensile stress to the resulting velocity deficit and crack density are also being conducted on these rocks.

We propose to:

1) continue our initial study of the uptake of Ar and other noble gases in carbon and hydrocarbons and study their devolatilization both via shock and via annealing. We expect to start dissolving noble gases in silicates and also study the devolatilization behavior of other minerals. In collaboration with Professor Frank Podosek and Dr. Thomas Bernatowicz, we expect to study the impact devolatilization of noble gases from primitive meteorites.

2) search for and analyze the solid phases ($MgSiO_3$, Mg_2SiO_4, $Mg_3Si_2O_5(OH)_4$) remaining upon partial devolatilization of serpentine and Murchison meteorites. The serpentine is predicted to be enriched in D/H. We propose to also study the gaseous species produced upon shocking Murchison meteorite and elucidate the chemistry and isotopic variations which appear to occur in the gas phase.

3) conduct further analysis of the equation of state of brucite and construct a model which describes the release isentropes in terms of the equation of state and thermodynamic properties of MgO and H_2O.

4) conduct further experiments on the cracking and hence density and seismic velocity deficit induced by shock waves in both hemispherical and planar geometry in dry and wet rocks. We expect to examine the data prescribing the regions of velocity deficits beneath such craters as the Ries and Meteor crater and determine what constraints these anomalies can place on the impact process.

5) Conduct further experimental impact studies of rocks and determine the effects of velocity and size scaling on the production of aerosol-sized ejecta.

References

1. Lange, M. A. and Ahrens, T. J., 1987, Impact experiments in low temperature ice, *Icarus*, **69**, p. 506-518.
2. Tyburczy, J. A. and Ahrens, T. J., 1988, Dehydration kinetics of shocked serpentine, *Proceedings of the 18th Lunar and Planetary Science Conference*, Cambridge Univ. Press, p. 435-442.
3. Schmitt, D. R. and Ahrens, T. J., 1988, Shock temperatures in silica glass, *J. Geophys. Res.*, in press.
4. Tyburczy, J. A., Krishnamurthy, R. V., Epstein, S., and Ahrens, T. J., 1989, Impact induced devolatilization and hydrogen isotopic fractionation of serpentine: Implications for planetary accretion, submitted, *Earth Planet. Sci. Lett.*
5. Tan, H. and Ahrens, T. J., 1989, Shock-induced polymorphic transition in quartz, carbon, and boron nitride, *J. Appl. Phys.*

IMPACT CRATERING CALCULATIONS

Thomas J. Ahrens, Seismological Laboratory 252-21, California Institute of Technology, Pasadena, CA 91125.

To describe and understand the physics of impact cratering, both normal and oblique, on planetary surfaces composed of solid silicates, ices, and their regoliths, as well as impacts into planetary atmospheres and proto-atmospheres and into the ocean. On a larger scale we expect to constrain impact conditions for partial and complete loss of atmospheres as well as whole planet, devolatilization melting and/or disruption. This includes determining energy partitioning, ejecta distributions (with regard to size, velocity, energy content, and sorting), and condensation physics of impact produced vapor as well as the impact production of aerosols from the liquid and solid state.

Accomplishments:

1) Developed a computer model which can explicitly describe impact onto a self gravitating exponential planetary atmosphere and the resulting solid ejecta-atmosphere interaction. Calculated impact-induced flow from a large (10 km-diameter, 20 km/sec) bolide onto an earth-sized planet with an exponential atmosphere. We have determined that some 6% of bolide energy couples to the atmosphere. This is close to the value, 5.3%, inferred from similarity variable analysis of the hemispherical shock wave in the air.

2) We have begun test calculations using a new smooth particle hydrodynamic code capable of studying atmospheric loss and total planet melting and disruption upon impact of two like-sized self gravitating planetary-sized objects.

3) Determined, via finite-difference calculations, the effect of planetary crustal strength and planetary gravity and/or impactor energy on the transition between cratering controlled by strength, versus, that controlled by gravity. Quantitatively demonstrated how planetary gravity, strength and crater scale gives rise to gravity-induced crater rebound. We have demonstrated that the crater diameter for transition from simple to complex craters varies as g^{-1} for silicate terrestrial planets and varies from $g^{-0.3}$ to $g^{-1.0}$ for icy satellites depending on the effective viscosity of the satellite.

4) In analyzing the effect of impact of a large, Cretaceous-Tertiary sized-, impactor on the earth, we have examined the experimental data for impact induced fine ejecta in the aerosol (<1μm) range and find that only 10^{-5} of the 3-20 x 10^{18} g of ejecta from a K/T impactor is in fines < 1 μm. This is a factor of 10^2 to 10^3 less than previous estimates of optically dense material lofted into the stratosphere.

We propose to:

1) Conduct atmospheric impact cratering calculations to determine the mass of atmosphere ejected and lost from a planet (with exponential atmospheres) upon impact of different density, diameter, and velocity bolides.

2) Complete a study of the effect of gravity, velocity target strength, and projectile dimensions on the depth of excavation and crater shape upon impact of large bolides on planetary surfaces. The major effect we expect to study is the scaling appropriate for high velocity impacts where shock-induced vaporization accounts for a major fraction of the crater volume.

3) We propose to study very large body impacts with our self-gravitating smooth particle hydrodynamic code. We expect to examine partitioning of energy and momentum for different velocity, impact angle and equation of state, as well as the degree of planetary melting and devolatilization.

References

1. Ahrens, T. J., O'Keefe, J. D., and Lange, M. A., 1989, Formation of atmospheres during accretion of the terrestrial planets, *Planet and Satellite Atmospheres: Origin and Evolution*, ed. S. Atreya and J. Pollack, U. Ariz. Press, Tucson, AZ., in press.
2. Lange, M. A. and Ahrens, T. J., 1989, Atmospheric blow-off during accretion of the terrestrial planetary atmospheres, submitted to *Icarus*.
3. O'Keefe, J. D. and Ahrens, T. J., 1989, Impact produced condensate and droplet size distributions, submitted to *Icarus*.
4. O'Keefe, J. D. and Ahrens, T. J., 1989, Impact production of CO_2 by the K-T extinction bolide and the sudden heating of the Earth, *Nature, 338*, 247-249.

ATMOSPHERIC EFFECTS ON CRATERING EFFICIENCY: P.H. Schultz, Brown University, Dept. of Geological Sciences, Providence, RI 02912

Introduction: The presence of an atmosphere can affect cratering efficiency (displaced target mass in projectile masses) through at least three processes: static atmospheric overpressure (P_o) adding to the lithostatic overburden; dynamic pressure acting on ejecta (P_e); and changes in coupling due to projectile–atmosphere interactions. Separation of these three processes are difficult because they involve many of the same controlling variables. Previous studies reported the possible roles of static atmospheric pressure (1, 2) and dynamic pressure (3). Observed contradictions with earlier studies (1) and systematic departures within new data (3), however, required assessing the potential effects of projectile–target interactions. This contribution reviews the relative role of the three processes based on laboratory experiments designed to isolate their effects for cratering in particulate targets.

Experimental Approach: The impact experiments were performed with the NASA–Ames Vertical Gun, a facility uniquely suited for exploring the role of an atmosphere on gravity–controlled crater growth. Different combinations of environmental (atmosphere), target, and impactor variables permitted resolving the three controlling processes. The role of static atmospheric pressure can be isolated by minimizing the effects of both dynamic pressure and projectile–atmosphere interaction. With a working model of the independent variables controlling static pressure, the number of experiments also can be reduced by examining the effects at a given value of the assumed controlling parameter. The present analysis followed the approach of Holsapple (1) who proposed that static atmospheric pressure can be described by a dimensionless parameter comparing ambient pressure (P) with bulk target density (δ) multiplied by the specific energy Q, i.e., $1/2v^2$ for impact velocity of v. This approach was shown to be equivalent to the more classical description where atmospheric pressure adds to the lithospheric overpressure, thereby changing the effective depth of burst (1). This approach also indicated, however, that atmospheric pressure has little effect on cratering efficiency.

Results: The effect of P_e was minimized by the use of an atmosphere with low density (helium) and ejecta with large sizes (coarse sand). The potential effect of projectile–atmosphere interactions also was minimized by using helium (high mach number) and low impact velocities (2 km/s). Figure 1 summarizes these results and reveals that ambient atmospheric pressure alone reduces cratering efficiency with $(P/\delta v^2)$ raised to a power law of $-\beta \simeq -0.23$ for both pumice and fine sand targets.

Dynamic pressure effects can be expressed in terms of a dimensionless drag parameter (d/g) where drag deceleration, d, is scaled to gravitational acceleration, g (4, 5). Such effects can be explored simply by expressing the data in terms of this ratio, but it is more useful to view it as a modification to the π_2 parameter as gravity–controlled growth becomes drag–controlled growth for d>>g. The observed cratering efficiencies were corrected for P_o using the exponent derived above and then plotted against (d/g). Three different expressions for (d/g) can be given for contrasting environmental and target conditions. First, the small ejecta size ($a \sim 85\mu$) and low ejection velocities (50–100 cm/s) at late stages for a pumice target result in a drag coefficient that varies inversely proportional to the Reynolds number, R_e. It can be shown that the resulting expression for (d/g) for a given target simply depends on μv_e where μ is the viscosity of the ambient atmosphere; this also can be expressed as $\mu R_v^{1/2}$ where R_v is the radius of the crater had it formed in a vacuum through scaling relations (5, 6). Second, conditions leading to a narrow range of R_e result in a constant drag coefficient; hence (d/g) can be shown to vary with ρR_v for a given target where ρ is the ambient atmospheric density. And third, targets with different size ejecta should result in (d/g) varying as $\mu R_v/a^2$ if the drag coefficient is inversely proportional to the R_e. Figure 2 illustrates this third approach. All three approaches indicated that drag affects cratering efficiency with the same exponent, $-\alpha$, as g in the π_2 parameter for vacuum conditions.

The data were tested for consistency by plotting cratering efficiency corrected for P_o and P_e against the Reynolds number. If the approach taken was valid and if no other processes were involved, then the ordinate becomes the inverse of the drag coefficient, and the data should show no systematic variations. Systematic departures dependent on atmospheric composition, however, did emerge. Moreover, augmentation (rather than reduction) in cratering efficiency was consistently observed under certain conditions, and the results for P_o still conflicted with previous studies (1). These observations required exploring alternative approaches for relevant scaling parameters as well as possible clues for other controlling processes.

High–frame photography clearly revealed a bright ionized wake trailing the impactor at high velocities (>4 km/s) and ambient pressures (>0.5 bars) that appeared to modify crater formation (7). New experiments were designed to separate the projectile from its wake, thereby establishing its possible role in crater excavation. This approach revealed two effects. At lower mach numbers (<6) and ambient pressures (<0.5 bars), the wake is injected into the growing cavity created by the projectile and adds a backpressure (Figure 3). Stagnation pressure created by hypervelocity impingement of a gas jet on particulate surfaces (8) provided an expression for this backpressure as $P_o \gamma M^2(\gamma - 1)$ where M is mach number and γ is the ratio of specific heats for the gas. This backpres-

sure augments cratering efficiency with a power-law exponent identical to but opposite in sign, to ambient pressure effects. Hence, collision by the projectile wake can be viewed as a process decoupled from the projectile. The observed offsetting effects of backpressure and ambient pressure may provide an explanation for previous studies (1) indicating minimal ambient pressure effects. With increasing mach numbers and pressures, however, cratering efficiency once again decreases. On the basis of previous experience with clustered impacts (9), low-density collisions have little effect on cratering efficiency if referenced to the cluster diameter. Hence the projectile wake at high mach numbers and ambient pressures was assumed to be coupled to the projectile, thereby increasing the projectile radius, r_p, to an effective radius, r_e. The resulting expression was found to accommodate the data with an exponent equivalent to $-\alpha$.

Concluding Remarks: The effect of an atmosphere on cratering efficiency in particulate targets at laboratory scales can be separated into three dimensionless pressure parameters (ambient, dynamic, and wake pressures) that can be expressed formally in terms of previously derived scaling parameters for gravity-controlled crater growth. It can be shown that ambient pressure should not affect cratering efficiency on the Earth and present-day Mars but could be very different on Venus. The effect of aerodynamic drag, however, could be important with (or producing) fine-size ejecta (see 10). Potential projectile wake effects have been previously explored for Venus in terms of a strong atmospheric blast (11). From the experimental results, here, it is possible that the wake modifies overall coupling at impact and could result in crater shapes and morphologies unique to Venus.

References: (1) Holsapple K.A. (1980) In *Proc. Lunar Planet. Sci. 11th*, 2379-2401, Pergamon N.Y. (2) Schultz, P.H. and Gault, D.E. (1982) *Lunar and Planet. Sci. XIII*, LPI, Houston, 694-695. (3) Schultz, P.H. (1988) *Lunar and Planet. Sci. XIX*, LPI, Houston, 1039-1040. (4) Tauber, M.E. *et al.* (1978) *Icarus 33*, 529-536. (5) Schultz, P.H. and Gault, D.E. (1979) *J. Geophys. Res. 84*, 7669-7687. (6) Housen, K.R. *et al.* (1983) *J. Geophys. Res. 88*, 2485-2499. (7) Schultz, P.H. and Gault, D.E. (1982) *Geol. Soc. Amer. Sp. Paper 190*, 153-174. (8) Land, N.S. and Clarke, L.V. (1965) NASA TND-2633. (9) Schultz, P.H. and Gault, D.E. (1985) *J. Geophys. Res. 90*, 3701-3732. (10) Schultz, P.H. (1990) *Lunar and Planet. Sci. XXI*, LPI, Houston (this volume). (11) Ivanov, B.A. *et al.* (1988) *J. Geophys. Res. 91*, (B4), D413-430.

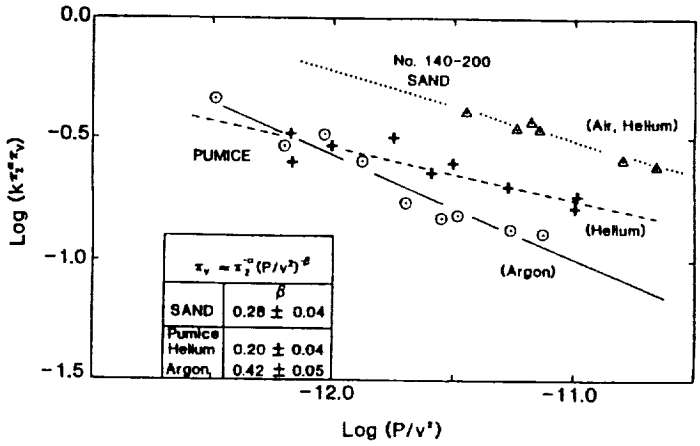

Figure 1. Effect of atmospheric pressure of different densities on cratering efficiency (π_v) corrected for gravity scaling (π_2) for compacted pumice targets. Atmospheric pressure (P_o) is incorporated in a dimensionless scaling parameter ($P_o/\delta v^2$) incorporating bulk target density, δ, and impact velocity, v. Here, density has not been included in order to separate data more clearly. Low-density helium atmosphere exhibits a clear effect on cratering efficiency with high-density argon indicating additional processes.

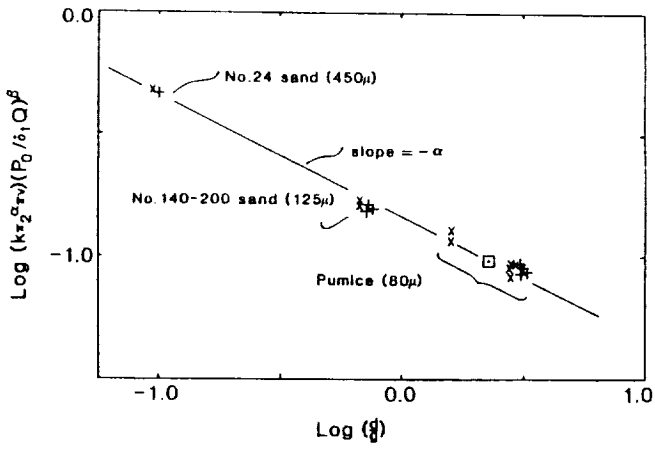

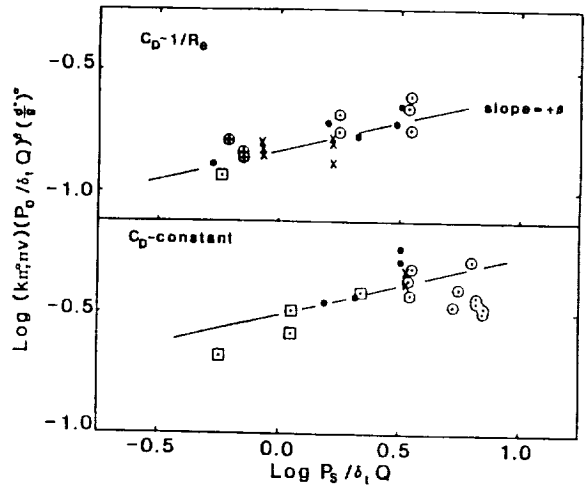

Figure 3. Effect of wake stagnation backpressure (P_s) on cratering efficiency (π_v) corrected for dimensionless scaling parameters for gravity (π_2), ambient pressure ($P_o/\delta Q$), and drag pressure (d/g). The top half shows a broad range of Reynolds numbers (R_e), where the bottom restricts the range in R_e. Backpressure created by the projectile wake appears to offset ambient pressure effects with the same exponent, β. At high Reynolds numbers, this trend is reversed due to direct coupling with energy/momentum transfer by the projectile.

Figure 2. Effect of aerodynamic drag on cratering efficiency (π_v) corrected for gravity (π_2) and ambient pressure ($P/\delta Q$) where Q is the specific energy ($1/2v^2$). Drag deceleration (d) is scaled to gravitational acceleration (g) and shown for targets with different particle sizes. The resulting exponent, $-\alpha$, for drag-controlled scaling is the same as for gravity-controlled scaling.

Cratering on Callisto and Ganymede: a Progress Report

Croft, S.K., R.G. Strom, S. Pozio* and S. Dekle. Lunar & Planetary Laboratory, Univ. of Arizona, Tucson, AZ 85721. *Reparto di Planetologia, Viale dell' Universita 11, 00185 Roma, Italy.

Over the last several years we have carried out an ongoing effort to improve crater statistics on Ganymede and Callisto, the giant icy satellites of Jupiter. There are several objectives in this study: 1) to improve the absolute values of the statistical data over as large a diameter range as possible to provide the best characterization possible of the crater populations (and indirectly the impactor populations) in the jovian system for comparison with the crater populations in the inner solar system. These data are important in determining whether differences exist in crater populations, and presumably in origins of the impactors, in different parts of the solar system. We have paid particular attention to the large diameter craters on Ganymede and Callisto because they provide the largest heavily cratered surface areas (and hence the best statistics) in the outer solar system. 2) To search for apex-antapex and equator-pole variations that would give indications of the sources of the impactor population(s). 3) To search for local variations in crater density that would be indicative of endogenic resurfacing. Resurfacing has been long recognized on Ganymede and postulated, but never directly found, on Callisto. Previous progress reports have been published (1,2,3,4).

Here we report on recent crater counts on Callisto. We were interested in improving our small crater statistics and in testing for any pole-equator variations, thus we rechecked and redivided the original data presented in Strom et al.(ref. 5) according to latitude, which were along the terminator observed by Voyager II at longitude 273 W between about 50 S and 60 N. We also did a new set of counts on images (FDS# 16425.14,.16,.18,.20,.22,.24,.26) along the terminator observed by Voyager I at longitude 312 W between 25 N and the pole. We found no equator-pole variations (we really didn't expect any), but the new crater densities found along the Voyager I hemisphere were systematically higher than the Strom et al. data by a factor of two at diameters below about 60 km. Initially, we could not find a reason for the discrepancy. The two counting areas are only about 40° apart and show no morphologic differences possibly attributable to resurfacing. the theoretical resolution is about twice as good in the Voyager I images than in the Voyager II images, but the former are somewhat smeared, reducing the effective resolution. Further, new counts on images chosen for sharpness in each hemisphere with the resolution differences comparable to the two terminator data sets (FDS# 16424.46 in the Voyager I data, about 50° from the terminator, and FDS# 20616.53 in the Voyager II data, about 40° from the terminator) gave densities similar to each other and to the densities of Strom et al.. We made an independent recount (i.e., a count by a different person) of one Voyager I image (FDS# 16425.24) and obtained even higher densities.

Finally we noted that the Voyager I data were all taken within about 12° of the terminator while the Voyager II data extended out 30° to 45° from the terminator. Therefore we independently recounted two Voyager II images (FDS# 20616.57 & 20617.25) and divided the data into two strips along the terminator: 1) craters within 12°, and 2) craters between 12° and about 26° of the terminator. The densities near the terminator matched the higher Voyager I densities while the densities including data farther from the terminator matched the lower Strom et al. densities. We therefore conclude that the earlier counts of Strom et al. are too low because they counted areas far enough from the terminator to introduce substantial data loss due to the high sun angle.

Our current preferred crater statistics for Callisto are given in Table 1 and shown in Figure 1. The data are compiled from: 1) the Voyager I terminator counts up to 54 km, 2) Voyager I hemisphere counts (4) up to 152 km, and 3) global coverage counts (4) at larger diameters. The cited numbers below 60 km may still be 20% to 30% low because of the conservative nature of the initial Voyager I counts. Refinements are in progress.

We also found variations in density between individual counting areas (nominally 10^5 km^2 in area) on the order of 20% to 30%, but the variations appeared stochastic and did not show any of the trends characteristic of resurfacing. We chose FDS# 20616.57 to count again because of some small-scale textural differences between the west and east sides (the east is smoother) of the image that might indicate large areas of low viscosity flooding. Stooke (6) has also suggested some flooding in the area. In addition to the bands relative to the terminator, we marked out a few of the smoothest patches for counting. There were differences in crater density, but the differences vary with respect to the terminator and not obviously with local smoothness. The putative smooth patches did not differ in

density from other areas at similar distance from the terminator. Thus we conclude that the differences apparent to the eye are probably related to the changing sun angle across the image and degradation by the ejecta of large impacts, and not due to endogenic resurfacing.

Discussion. The new Callisto curve now reaches up to and crosses the density curve for Rhea (figure 1), previously recognized as the most heavily cratered surface in the solar system (7). This accords with the visual impression that both bodies are roughly equally heavily cratered at smaller diameters. The differential log slope of the new curve is about -5.1 between about 60 km and 150 km and "bends over" to about -3 below about 50 km. One interpretation of the curve is that it represents a production function over its entire length. This view implies that the curve on the dark terrain on Ganymede, which shows a similar bend over -albeit starting and peaking at larger diameters than on Callisto (4)- is the same population (with the exception of the palimpsests, see ref 4), but at lower crater density. Some loss of smaller craters due to surface flooding on Ganymede is also implied (see ref. 2). However, theoretical simulations (8) indicate that production functions with slopes more negative than -3 bend over to form branches with slopes near -3 below the diameter at which saturation is reached. More recent simulations (9) reach similar results and indicate that saturation densities should be near R = 0.3, just about the density of the -3 branches of the Rhea and Callisto curves. Further, the lack of large craters in or near the counting areas capable of 'resetting' the saturation level (cf. 9) or evidence of widespread flooding implies that the smaller craters may be saturated. This suggests an alternative interpretation: that the -5 part of the curve is the production function and that the bend-over in crater density below about 50 km is indeed a saturation effect. This accords with the idea that Rhea and now Callisto have near-saturation density populations at smaller diameters. The problem is that now the craters on the dark terrain on Ganymede (fig. 1), which at a density of about 1/6 that of Callisto are certainly not saturated, apparently represents a second, later population. The possibility of two populations in the jovian system (an earlier internal population and a later external population, see ref. 4) has been suggested on the basis of apex-antapex variations, but flooding on Ganymede has partially obscured the cratering record. A -5 population curve is different from that seen anywhere else in the solar system, but is similar to that expected from runaway accretion (10). Further, there is growing evidence that the slope of the cometary population, which would be responsible for recent impacts in the jovian system, is near -3 (11). Consequently, the population on Ganymede could be a later, flood modified population of craters due to comets, while the -5 population on Callisto could be accretional remnants that (earlier) reached saturation at small diameters. While there is consistency to the two-population scenario, it is by no means proven. Work is continuing.

References. 1) Croft, S.K. 1985. Ripple Ring basins on Ganymede and Callisto. Reports Planet. Geol. Geophys. Prog.-1984, NASA TM 87563, p. 206-208. 2) Croft, S.K. & B.N. Goudreau 1987. Tectonism and volcanism in Ganymede's dark terrain. Lunar Planet Sci. XVIII, 209-210. 3)Croft, S.K. 1988. Icy Satellites: Cratering and Volcanism, Reports of PGGP-1987, p. 404-406. 4) Croft,S.K. & E.D. Duxbury 1988. Crater and Crater forming populations on Ganymede and Callisto, Lunar Planet. Sci. XIX, 227-228. 5) Strom,R.G., A. Woronow and M. Gurnis 1981. Crater populations on Ganymede and Callisto. J. Geophys. Res.,86: 8659-8674. 6)Stooke, P.J. (1989) Volcanism on Callisto. Lunar & Planet. Sci. XX, 1073-1074. 7) Strom, R.G. 1987. The solar system cratering record: Voyager 2 results at Uranus and implications for the origin of impacting objects. Icarus 70:517-535. 8) Woronow, A., R.G. Strom and M. Gurnis (1982) Interpreting the cratering record: Mercury to Ganymede and Callisto. In Satellites of Jupiter, p. 237-276, Univ. of Arizona Press. 9) Chapman, C.R. and W.B. McKinnon (1986) Cratering of Planetary Satellites. In Satellites, p, 492-580, Univ. of Arizona Press. 10) Davis, D.R., C.R. Chapman, S.J. Weidenshilling and R. Greenberg (1985) Collisional history of asteroids: evidence from Vesta and the Hirayama families. Icarus 62:30-53. 11) Strom, R.G., S.K. Croft and J. Boyce (1990) The cratering record on Triton. Lunar Planet. Sci. XXI, p. 1218-1219.

Table 1. "Best" Callisto Crater Densities (as of 3-90)

D_{avg}	N	R	δD	Area, $10^6 km^2$
19.03	478	0.2904	0.0133	1.71
26.91	271	0.3293	0.0200	1.71
38.05	116	0.2819	0.0262	1.71
53.82	47	0.2284	0.0333	1.71
76.11	51	0.05426	0.0076	15.6
107.63	12	0.02554	0.0074	15.6
152.22	12	0.0157	0.0045	51.0
215.27	2	0.0052	0.0037	51.0
304.44	1	0.0052	0.0052	51.0
430.54	2	0.0209	0.0148	51.0
608.87	4	0.0835	0.0418	51.0
861.08	0	0.000	0.000	51.0
1217.75	2	0.167	0.118	51.0

Figure 1. R - Plot contrasting the new and old crater densities on Callisto. Crater densities on Rhea and the dark terrain on Ganymede are also shown for comparison.

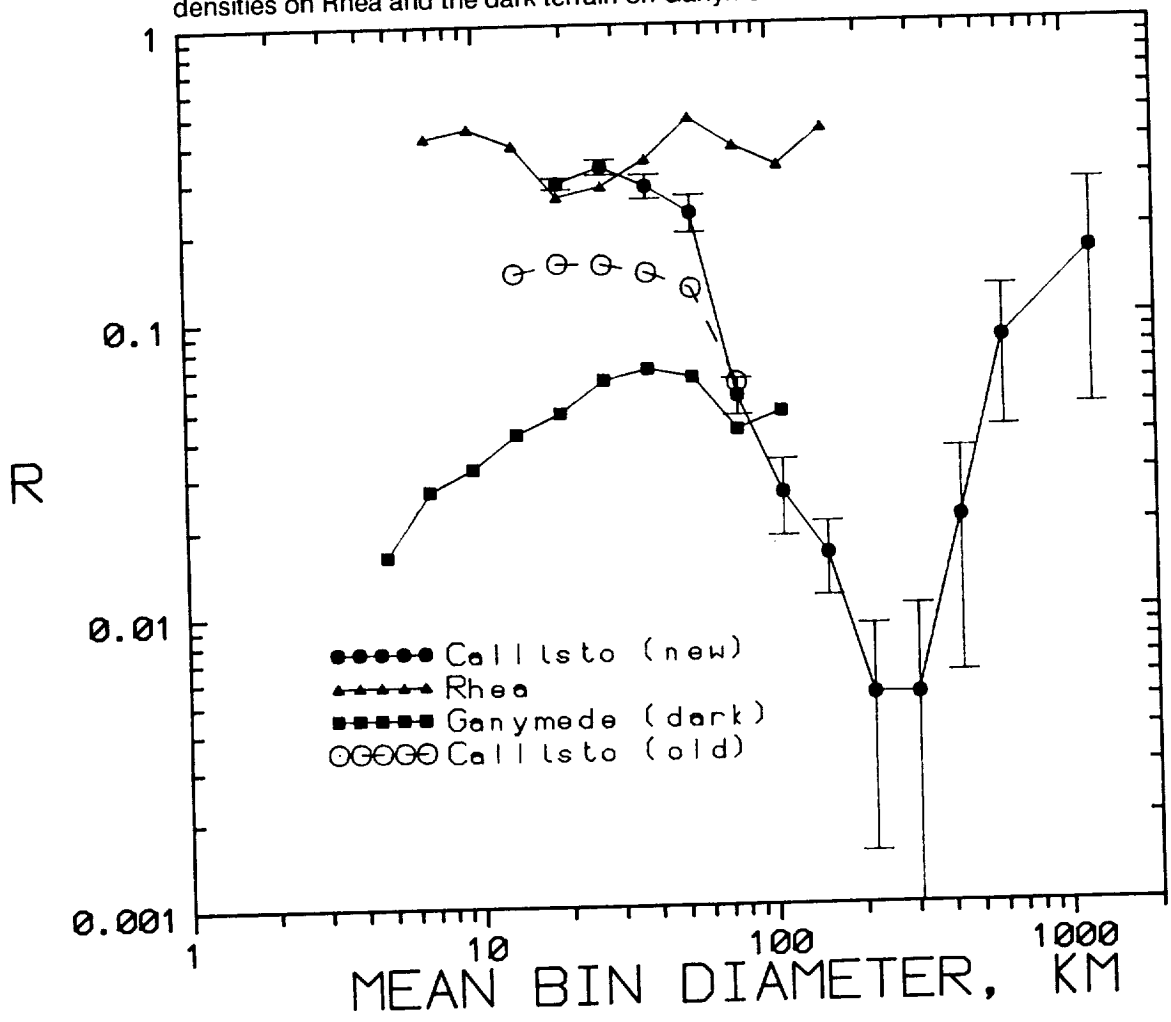

Formation of Crater Palimpsests on Ganymede

Paul J. Thomas
Dept. of Physics and Astronomy, University of Wisconsin, Eau Claire, WI 54702
Steven W. Squyres
Center for Radiophysics and Space Research, Cornell University, Ithaca, NY 14853

Crater palimpsests on Ganymede are circular features of very subdued relief that are apparently vestiges of ancient impact craters. Where they lie in dark cratered terrain, they are rendered easily visible by a high albedo relative to their surroundings. In the few cases where palimpsests lie in the brighter resurfaced terrain, no obvious albedo boundary is present, and they are visible only as subtle topographic forms. Some palimpsests in both settings are clearly observed to consist of broad, low, dome-like deposits of some small but finite thickness. Two models have been suggested for the origin of palimpsests. In one (1), the margin of the palimpsest is envisioned to be the rim of the original crater. In the other (2), the margin of the palimpsest is the limit of continuous ejecta. Both models face difficulties. For the first, several lines of evidence (discussed below) suggest that the margin of the palimpsest in fact extends well beyond the original crater rim. For the second, one must consider that the limit of continuous ejecta on craters elsewhere in the solar system is typically ragged and irregular, while palimpsest margins are very clearly defined, smoothly curved, and nearly circular.

We have re-examined the distribution and dimensions of all the palimpsests on Ganymede, updating the original survey of Passey and Shoemaker (2). The base maps used were the fifteen USGS quadrangle maps of Ganymede. We measured four characteristics: palimpsest diameter, diameter of the smooth central region of the palimpsest, apparent diameter of the original crater rim where a vestige of it appears, and diameter of the secondary crater field. We find linear relationships between several of these parameters. Where a smooth central region is present, it typically has a diameter 1/4 to 1/3 that of the palimpsest. Where a vestige of the original crater rim appears to be present within the palimpsest, its diameter is typically about half that of the palimpsest. The smallest craters for which palimpsests are observed have diameters of about 40 km.

We have found three palimpsests that have sufficiently defined secondary crater fields for us to measure their dimensions with confidence. Assuming that the ratio of secondary field diameter to crater diameter is the same as is observed for the rest of Ganymede, we find again that the original crater diameter is about half that of the palimpsest. This observation strengthens our confidence in the identification of crater rims well inside the outer edge of the palimpsest.

As an alternative to the two hypotheses for palimpsest formation mentioned above, we suggest that the outer margin of a palimpsest instead represents the limit of a volcanic deposit triggered by a large impact event early in Ganymede's history. We suggest that palimpsest formation may be a straightforward result of cratering during an early period of intense activity within the satellite. Accretional heating of Ganymede would have led to substantial early warming of the satellite's outer layers, producing a thick, warm, mobile zone overlain by a relatively thin, rigid "lid". The material below the lid may have been solid, or might have been partially liquid for a short time. In the case of solid but warm ice, the material would clearly have been buoyant relative to the cold lid above it. In the case of liquid, a small amount of silicates in the lid would be required for buoyancy. Small impacts would not have penetrated the lid, and would have produced normal craters. Larger impacts, however, would have penetrated it, allowing any buoyant, mobile material to ascend to the surface. Crater excavation depths for 40 km craters are expected to be $\sim$10 km, comparable with estimates for the thickness of both the mechanical and thermal lithospheres 4 Gy ago. As the lithosphere cooled and thickened, palimpsest formation would have ceased, consistent with the observed concentration of palimpsest formation in the earliest part of Ganymede's recorded geologic history.

Constraints on the nature of the extruded materials may be derived from the mechanics of their emplacement. We first consider the case of extrusion of solid ice. Extrusion would be driven by the density difference between the lithosphere and the underlying mobile material. For ice at a plausible sublithospheric temperature of 250 K (corresponding to a viscosity of $\sim 10^{15}$ Pa s), extrusion through a 40 km diameter conduit will extrude what we believe to be a typical palimpsest volume ($\sim 10^{13}$ m^3) in a time much shorter than the conductive cooling time for the flow. Because the flow is much thinner than the conduit, cooling of the flow will control extrusion.

We are able to determine the aspect ratio γ (maximum height divided by radius) of palimpsests in only one case. The value is about 0.02, but this palimpsest may be an unusually thick one. The smallest values may be in the vicinity of 0.005 (typical thickness of 500 m for a 100-km radius palimpsest), but accurate measurements cannot be made from Voyager data. A simple model for axisymmetric spreading of a Newtonian viscous material (3) and the requirement that the flow is emplaced in one cooling time for a layer of appropriate thickness would imply a bulk viscosity for the flow of 10^{15} Pa s for $\gamma = 0.02$. For $\gamma = 0.005$, however, the value would be about 10^{12} Pa s.

While the former viscosities are consistent with glacial viscosities of ice (and the assumed extrusion viscosities), the latter values are too low for subsolidus flow. If typical aspect ratios really are as low as 0.005, we must then instead consider flow in a partially liquid state. In this case, the behavior of the spreading material might best be described by a Bingham rheology. Using this rheology, we can determine the yield strength of such a partial melt from the dimensions of the palimpsest. For a 100 km radius palimpsest with $\gamma = 0.005$, the yield strength would be $\sim$1 kPa. This is lower than is typical for the yield strength of even very mobile silicate lavas, but may be reasonable for an H_2O water/ice slush.

We believe that formation of crater palimpsests by volcanic extrusion of buoyant, mobile subsurface materials is the model most consistent with their morphology. It also readily explains the concentration of palimpsest formation in the early part of the satellite's history. In order to better constrain the mode of emplacement (solid or liquid) of palimpsest deposits, an important objective for the *Galileo* mission will be to obtain accurate measurements of the aspect ratios of the deposits.

References

1) Hartmann, W.K., *Icarus* **60**, 56-74, 1984.

2) Passey, Q.R., and E.M. Shoemaker, in *Satellites of Jupiter*, (D. Morrison ed.), pp. 379-434, Univ. of Arizona Press, 1982.

3) Huppert, H.E., *et al.*, *J. Volcanol. Geotherm. Res.* **14**, 199-222, 1982.

EVIDENCE FOR ATMOSPHERIC EFFECTS ON MARTIAN CRATER SHAPE: P.H. Schultz, Department of Geological Sciences, Brown University, Providence, RI 02912.

Introduction: An atmosphere affects the over-all cratering efficiency by adding an ambient pressure to the lithostatic overburden (1, 2, 3), reducing the ballistic flow of ejecta (3, 4), and modifying the coupling between impactor and target (4, 5). Laboratory experiments using the NASA-Ames Vertical Gun Range also reveal that the presence of an atmosphere introduces systematic changes in crater shape. Such changes can be understood in terms of modification of crater growth, and dimensionless scaling relations indicate that the observed laboratory-scale phenomena should be identifiable at planetary scales. As a test, the laboratory results are applied to Mars where eolian processes can produce a fine-grained substrate leading to modification by drag deceleration without the complicating effects of ambient pressure and projectile-atmosphere interactions.

Laboratory Results: Separate contributions summarize the approach and results for atmospheric modification of over-all cratering efficiencies observed in the laboratory (3, 4). Here, we focus on atmospheric effects on crater shape expressed in terms of apparent crater diameter and depth. Laboratory experiments (e.g., 6) and finite-element models (e.g., 7) reveal that impact craters under vacuum conditions first grow hemispherically and then expand laterally after achieving a maximum depth. Most of the impact displaced mass occurs at late stages during lateral expansion until gravity or target strength limits further growth. Consequently, the role of ambient atmospheric pressure or aerodynamic drag on cratering efficiency should be expressed principally by a reduction in crater diameter, rather than depth. The possible role of the projectile wake (4) is not considered here. The combined effects of atmospheric pressure and drag on crater shape can be written as:

$$\left(\frac{D_A}{d_A}\right)\left(\frac{P_o}{\delta v^2}\right)^{\beta/2} \sim \left(\frac{d}{g}\right)^{-\alpha/2}$$

where D_A and d_A are the observed diameter and depth, respectively, under atmospheric conditions; P_o, the ambient pressure; δ the bulk target density; v, impact velocity; d, drag deceleration on ejecta; and g, gravitational acceleration. The exponents β and α are derived for over-all cratering efficiency; a square root (rather than cube root) dependence is used due to the effect solely on diameter, not depth and diameter.

As a test, Figure 1 shows the change in diameter and depth as a function of ambient pressure alone. This is possible because the range in values for the dimensionless ambient pressure parameter in the laboratory for compacted pumice targets far exceeds the available range for aerodynamic drag. Figure 1 reveals three important trends. First, crater diameter decreases with increasing values of $P/\delta v^2$ with a power-law consistent with $-\beta/2$. Second, crater depth is essentially constant. And third, systematic offsets dependent on gas composition indicates that a residual factor related to aerodynamic drag may be hidden. If crater shape is now corrected for ambient pressure effects, then evidence for drag can be tested. Figure 2 includes two alternative expressions for d/g: the first expression uses a constant drag coefficient over a narrow range (<15%) of Reynolds numbers, R_e (upper half, Fig. 2); the second, a broad range in R_e where the drag coefficient depends on $1/R_e$. Both data sets confirm the predicted power-law dependence where α represents the exponent derived for vacuum conditions when g dominates.

It is emphasized that these results apply only to compacted pumice. Such a target exhibits a large angle of internal friction, thereby preserving the transient crater shape. Impacts under vacuum conditions reveal, however, that the target exhibits gravity-controlled growth similar to sand with an exponent of $\alpha = 0.518$. Use of loose sand targets with a low internal angle of friction exhibit rim collapse and shallowing after achieving a crater aspect ratio similar to compacted pumice.

Planetary Signatures: Although the Earth and Venus seem to provide the most ideal environments for testing such predictions, all three pressure effects acting simultaneously (further complicated by modification, erosion, and imaging) lessen their usefulness as an initial test. Mars, however, provides ideal conditions for considering just the effects of drag, even under its presently tenuous atmosphere (8). Extrapolating conditions leading to $(d/g) \gtrsim 0.5$ from the laboratory to current martian conditions predict that drag-modified scaling should become important for craters larger than 1 km in diameter formed in substrates producing sand-size (~500μ) ejecta. Larger craters should show a progressively deeper profile up to diameters exceeding an atmospheric scale height and/or the onset of rim/wall collapse limit. The current martian atmosphere is nevertheless too tenuous to result in significant scaling changes due to either static ambient pressure or the impactor wake. Consequently, crater depths were measured for different diameter craters formed in contrasting lithologies in order to isolate the one remaining variable, ejecta size.

Previous studies revealed the enigmatic relation between crater depth and diameter on Mars (9, 10): depths of complex craters at a given diameter exhibited considerable variation; depths of simple craters appeared to increase more rapidly than diameter; and systematic differences were recognized between craters on plains (volcanic combined with other origins) and highlands. These dif-

ferences were generally attributed to the role of volatiles, whether enhancing crater collapse (10) or impact vaporization (9). Here, depth–diameter relations are contrasted between plains of well–established volcanic origin (Lunae Planum, Syrtis Major Planitia, lava flows) and probable sedimentary origin (easily eroded unconformable deposits and the fractured plains of Casius). Figure 3 reveals that this approach significantly reduced the dispersion in data for a given lithology. Moreover, craters on the fractured plains exhibit systematically deepening craters with increasing diameter. The laboratory results predict that crater growth unaffected by aerodynamic drag should exhibit d ~ D up to the onset of rim/wall collapse or other scaling changes. Crater growth affected by drag, however, should increase as $(1 + \alpha/2)$ for craters larger than a critical size (D_{At}) dependent on ejecta size for a given atmospheric density. From laboratory–based scaling relations, α is about 0.5, and Figure 3 includes the resulting slope of 1.25 fit to the data. The resulting intercept corresponds to a mean ejecta size approximately 80μ, a value consistent with a sedimentary origin. The absence of a departure for craters on volcanic plains indicate a mean size exceeding 0.2 cm.

Concluding Remarks: While previous studies proposed that the observed diameter–depth relations on Mars may require water–saturated substrates in order to enlarge crater diameters and reduce depths (9, 10), this study suggests that drag scaling controlled by the size distribution in the substrate reduces diameter while maintaining depth for simple craters. Such a proposal is consistent with predictions from laboratory experiments, the narrow dispersion in observed diameter–depth data for clearly distinguished lithologies, and the clear contrast between lithologies likely characterized by coarse (basalts) and fine (sediments) ejecta. The observed effects are reflected in crater statistics and may provide a means to identify changes in atmospheric conditions through time as well as probing physical characteristics of impacted substrates.

References: (1) Herr, R.W. (1971) *NASA TRR-366*. (2) Holsapple, K.A. (1980) in *Proc. Lunar Planet. Sci. 11th*, 2379–2401, Pergamon, N.Y. (3) Schultz, P.H. (1988) *Lunar and Planet. Sci. XIX*, LPI, Houston, 1039–1040. (4) Schultz, P.H. (1990) *Lunar and Planet. Sci. XXI*, LPI, Houston (this volume). (5) Gault, D.E. and Sonett, C. (1982) in *Geol. Soc. Amer. Sp. Paper 190*, 69–92. (6) Gault, D.E. *et al.* (1968) in *Shock Metamorphism of Natural Materials* (B.M. French *et al.*), Mono Books, Baltimore, 87–100. (7) Grieve, R.A.F. *et al.* (1980) in *Proc. Lunar Planet. Sci. Conf. 11th*, 2309–2323, Pergamon, N.Y. (8) Schultz, P.H. and Gault, D.E. (1979) *J. Geophys. Res. 84*, 7669–7687. (9) Cintala, M. and Mougins-Mark, P. (1980) *Geophys. Res. Lett. 7*, 329–332. (10) Pike, R.J. (1980) in *Proc. Lunar Planet. Sci. Conf. 11th*, 2159–2189, Pergamon, N.Y.

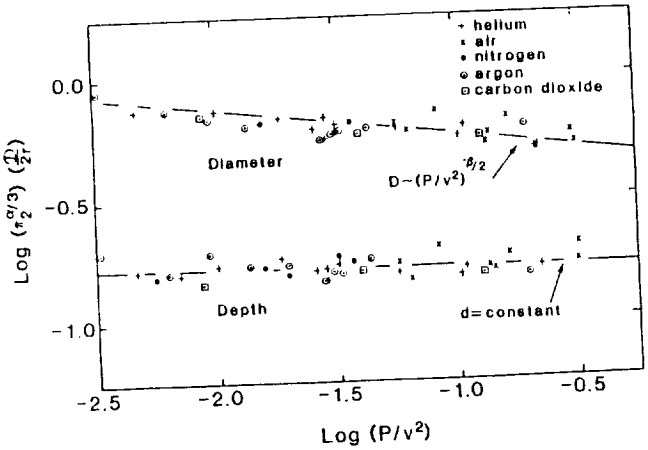

Figure 1. Effect of ambient atmospheric pressure, P, on crater diameter, D, and depth, d, for impacts into compacted pumice for different atmospheric compositions. Diameter and depth are given relative to vacuum conditions (π_2). Pressure can be given in a dimensionless form as $P/\delta v^2$ (δ is bulk target density and v is impact velocity) which varies as P/v^2 for a given target.

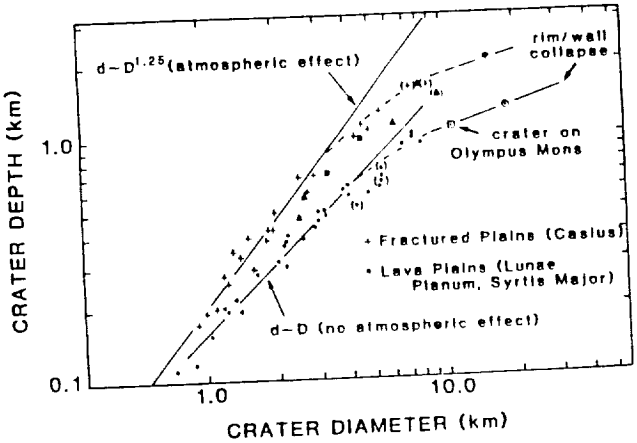

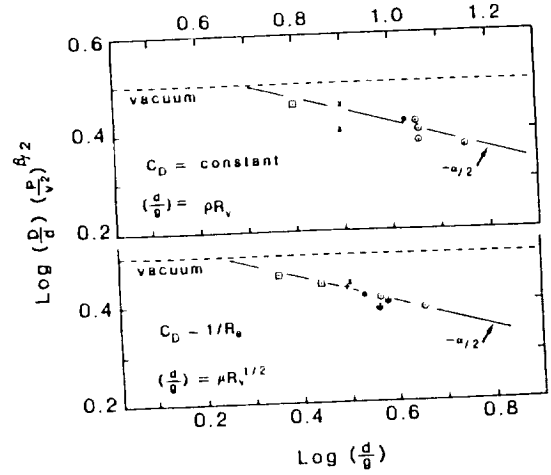

Figure 2. Effect of aerodynamic drag, d, relative to gravitational acceleration, g, on crater shape corrected for atmospheric pressure effects (Figure 1). Top half shows data over a narrow range of Reynolds numbers such that the drag coefficient (C_D) is essentially constant, thereby resulting in d/g depending on atmospheric density and crater size, R_v, had it formed in a vacuum. Bottom half includes a broader range of Reynolds numbers such that the drag coefficient varies inversely with Reynolds number. In this case, d/g can be reduced for convenience to varying with $R_v^{1/2}$ and viscosity (μ).

Figure 3. Depths and diameters for well–preserved craters on clearly identified volcanic plains and probable sediments. Squares indicate craters on the sedimentary fill of Isidis, while triangles indicate data for unconformable and friable airfall deposits. Parentheses and circles represent craters exhbiting partial and extensive rim/wall collapse. The clear separation of the data can be interpreted in terms of drag–controlled crater growth for probable sedimentary lithologies contrasted with no drag effects on lava lithologies.

IMPACT GENERATION OF ORBITING DEBRIS AROUND MARS: P.H. Schultz and D.A. Crawford, Brown University, Providence, R.I. 02912 and D.E. Gault, Murphys Center of Planetology, Murphys, CA 95247.

Collisions have been invoked to create planetary rings around solid planets (1, 2) and the gaseous giants (3) early in their history. As summarized in (4), orbital insertion of debris from gas expansion above a vertical impact requires impactors exceeding 10^{-3} M_e (for a terrestrial impact). Laboratory experiments (5), however, are revealing new information on the partitioning of energy and basic phenomena associated with oblique impacts that may significantly lessen requisite large masses. Here we explore the implications of these observations for major oblique impacts on Mars.

Oblique Impact Phenomena: Impact vaporization is observed to increase with decreasing impact angles for volatile-rich targets (water, carbonates) with the vapor-cloud energy increasing as $1/2\cos^2\theta$ for impact angles (referenced to the horizontal) from 45° to 15° (5). This increase is attributed to energy partitioned into shear heating along the projectile/target interface, a process separate from jetting created by converging oblique shocks. Energy partitioned to internal energy of the projectile, however, decreases as $\sin^2\theta$ as revealed by decreased fragmentation (size and number) and increased kinetic energy retained in ricochet debris. Even impacts into non-volatile solid aluminum targets exhibit the same decrease in projectile internal energy and perhaps an increased role of heating by mechanical shear. High frame-photography reveals that the impact-generated vapor cloud in volatile-rich targets is not stationary, as in vertical impacts, but moves downrange while expanding and rising. Additionally, trajectories of spalled projectile fragments entrained in this cloud are deflected by gas drag (6). These observations can be used to parameterize the first-order effects of impact angle on orbital insertion of material.

Numerical Model: From the laboratory results, we model the impact-generated vapor as a hemispherically expanding cloud with a center of mass moving downrange at an angle 1/2 the initial impact angle and with a velocity equal to the ricochet velocity, i.e., $v_{cm} = 0.12v_i/\tan\theta$ for $\theta > 7.5°$ ($0.9v_i$ for $\theta < 7.5°$). The maximum energy partitioned to the vapor cloud is assumed to be 50% of the impactor energy, increasing as $\cos^2\theta$ down to 7.5° with the vaporized mass fraction (projectile masses) approximated by $11\cos^2\theta\ (v_i/7.5)^2$ for v_i in km/s. As assumed in (4) the vapor cloud of mass M_v expands with a velocity of $(5/3 \cdot 2E_c/M_v)^{1/2}$ over a time equal to a radius R_c defined by $(3/4\pi \cdot M_v/\rho)^{1/3}$ where ρ is the density when gravitational forces begin dominating over hydrodynamic effects (assumed to be about 0.1 g/cm³).

The probability of achieving orbit depends on the height (h) achieved by the cloud above the surface when gravitational forces control expansion. For vertical impacts, conditions leading to orbital injection depend on h/R_p, where R_p is the radius of the planet (4). For oblique impacts, however, this height is controlled by $R_c + H_{cm}$ where H_{cm} is now defined as the height of the center of mass when gravitational forces begin to dominate hydrodynamic forces. Keplerian trajectories of elements in this downrange-moving cloud were then traced numerically in spherical coordinates with conditions for orbital insertion identical to those assumed in (4).

Because of the excessive number of oblique impacts on Mars (7) and the possible impact signature of Mars orbiting debris on Phobos (8), calculations were made for 20, 50, and 100 km diameter bodies colliding Mars with velocities at 7.5, 10, and 15 km/s. Figure 1 illustrates the effect of impact angle on projectile masses achieving orbit for different size projectiles at 15 km/s, whereas Figure 2 shows the effect of impact velocity for 20 km and 100 km-diameter impactors. In contrast with vertical impacts, we find that relatively small oblique impacts can potentially inject significant material into orbit. This greater probability of achieving orbit principally reflects the combination of the tangential velocity of elements in the cloud subtracted from (sharp maximum at 15° in Fig. 1) or added to (lesser maximum at 30°) the velocity of the center of mass.

Discussion and Implications: Figures 1 and 2 reveal that significant quantities of orbiting debris may be generated by oblique basin-forming collisions on Mars. Such collisions are not hypothetical. Orcus Patera is an oblong crater (150 km x 450 km) with all the signatures of a very low angle impact (6). For an isotropic flux, we should expect about one third of the martian basin-forming impactors (100-500 km) to contribute orbiting debris during the first 0.5 billion year history. The ubiquitous occurrence of smaller grazing impacts (7) may be a signature of this debris, rather than an incom-

References: (1) Cameron, A.G.W. and Ward, W.R. (1976) *Lunar and Planet. Sci. VII*, LPI, Houston, 120–122. (2) Cameron, A.G.W. (1985) *Icarus 62*, 319–327. (3) Cameron, A.G.W. (1975) *Icarus 24*, 280–284. (4) Stevenson, D.J. *et al.* (1986) In *Satellites* (J.A. Burns and M.S. Matthews, eds.), 39–88. (5) Schultz, P.H. and Gault, D.E. (1990) In *Proc. of Catastrophes in Earth History*, *Geol. Soc. Amer. Sp. Paper* (in press). (6) Schultz, P.H. (1988) In *Lunar and Planet. Sci. XIX*, LPI, Houston, 1039–1040. (7) Schultz, P.H. and Lutz-Garihan, A. (1982) *J. Geophys. Res. 87*, A84–A96. (8) Schultz, P.H. and Crawford, D.A. (1989) *Am.Astron. Soc. Bull. 21*, p. 932.

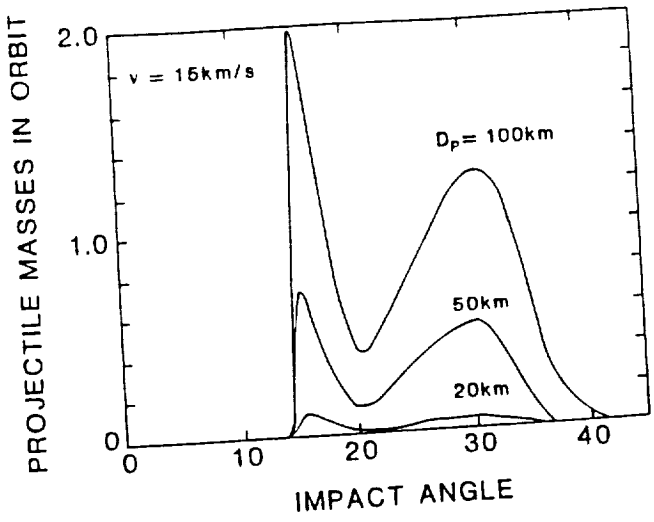

Figure 1. Effect of impact angle on mass achieving orbit (in projectile masses) for different diameter impactors on Mars at 15 km/s.

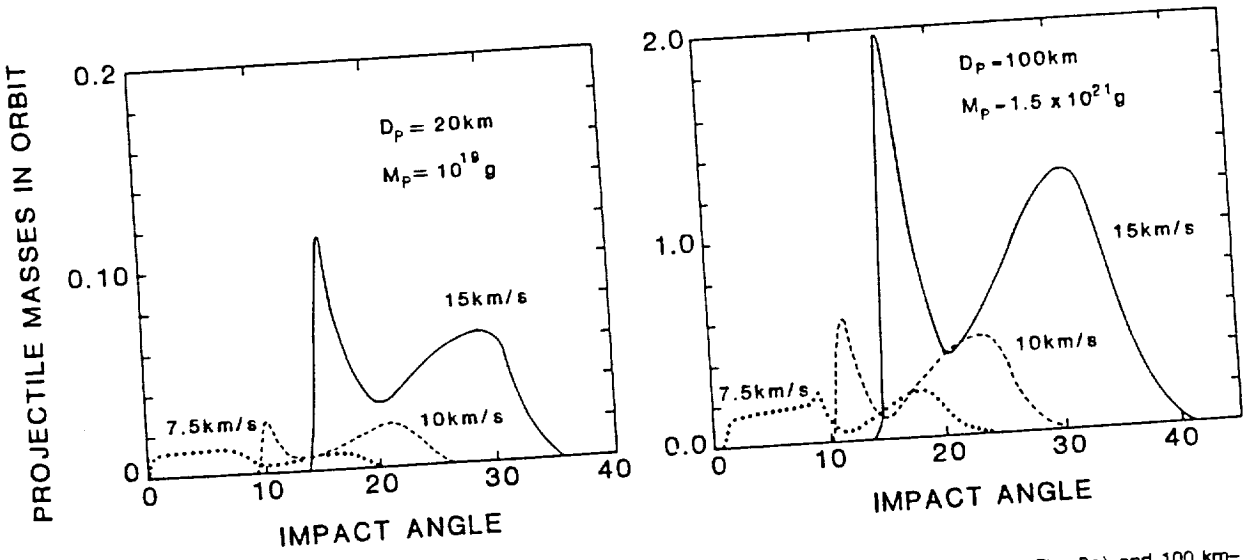

Figure 2. Effect of impact angle on mass achieving orbit (in projectile masses) for a 20 km–diameter (Fig. 2*a*) and 100 km–diameter impactor (Fig. 2*b*) on Mars at different impact velocities. Figures 1 and 2 show that relatively small impactors can inject significant quantities of debris into orbit. The narrow range of favored impact angles, however, indicate that such events would be episodic through time but increase in likelihood for early Mars due to the greater likelihood for large impactors.

ORIGIN OF ANOMALOUS CRATER CHAINS AND THEIR IMPLICATIONS FOR THE CRATERING RECORD; C.W. Halfen, P.H. Schultz (Brown Univ), and D.E. Gault (Murphys Center for Planetology)

Background: Crater chains, or catenae, are present on most planetary bodies. Although many can be associated with large craters or basins, a number of large chains on Callisto have not been correlated with any known basin (1). Recent laboratory studies (2,3) reveal that it is possible for large, nearly equal-size fragments of a projectile to survive collisions at low impact angles. Consequently, anomalously large crater chains on the Moon, Mercury, Ganymede and Callisto were examined to determine plausible modes of origin, including secondary ejecta from basins and re-impacts by projectile ricochet.

Observations: Because of the wide range of resolution for different planets, we restricted our study to chains of five or more members which were contiguous or closely spaced with the largest member crater >20 km in diameter. On Callisto seven chains met the selection criteria (table 1). They varied in length from 150 to 1150 km. The diameter of the largest member crater typically exceeded the smallest by a factor of ~2; the one exception had a ratio of 4 with member diameters ranging from 10 to 40 km. Individual crater widths of Gipul Catena systematically increase along the chain (north to south) from 28 km to 74 km near the middle of the chain, but systematically decrease to 25 km at the south end. Three of the chains had bright rays associated with them. On Ganymede the presence of the nearly ubiquitous grooves and furrows made location and identification of crater chains difficult. To avoid ambiguity, all chains following local groove/ridge sets were excluded. Only one chain on Ganymede was found that fits our criteria (4). This 100 km long chain had a ratio of widths of only ~1.5, with individual craters ranging from 35-50 km in width (table 1). This chain also had bright rays extending 50-100 km beyond the crater rims. The circular central pits and ejecta distribution at either end indicate a more vertical impact.

Neither the Moon nor Mercury had any chains that could meet our selection criteria. All other large chains greater than 20 km across could be traced to a basin or a large crater. In addition to anomalous chain craters, we measured the sizes of the largest secondaries in crater chains associated with large basins for each of the four planets. These secondaries ranged from 10 km on Ganymede to 25 km on the Moon. The width ratios for these chains ranged from ~2 to >4 on all of the bodies, but the crater widths varied randomly along the chain length.

In summary, only the icy satellites had chains meeting our criteria. Callisto had both the widest and longest of any examples. In comparison with strings of secondary craters, anomalous chains had larger members, had less variation in their diameters, and were typically longer. In Figure 1 we have plotted the diameters of the largest two member craters and largest secondary crater against the diameter of the largest basin on each planet. The diameters of crater chains on Callisto and Ganymede plot well above the secondary craters of any of the bodies, whereas secondary craters plotted against their parent basin diameter increase with increasing basin size.

Discussion: We considered four possible origins for the anomalous crater chains: a) secondary ejecta from (unknown) basins; b) fragmented bodies caused by tidal disruption (5); c) ricochet fragments which re-impacted the surface on a given satellite; or d) ricochet fragments from another planetary body.

If the anomalous crater chains on Callisto and Ganymede are secondaries, they should resemble other secondary chains. Secondary chains are radial to a basin (or large crater) and exhibit a large variation in crater widths, with the largest member less than 5% of the basin diameter. In Figure 1, the anomalous chains plot well above the position of typical secondaries, and use of stereonets failed to reveal probable primary basins consistent with preservation state. If Gipul Catena were a secondary chain following the trend from well-established secondaries in this figure, then its parent basin would had exceeded the diameter of the planet.

Formation of the chain-forming fragments by tidal disruption would probably provide roughly equant sizes with minimal velocity dispersion. However, the spacing achieved prior to impact for non-orbiting objects would be too small unless the disruption were violent. Tidal disruption by a near-miss of another large nearby planetary body might be necessary. This is consistent with the occurrence of chains on Callisto and Ganymede, but is inconsistent with the lunar record unless the chains were lost (or represented) in later basin-forming events.

The possibility of re-impacting ricochet might account for the largest chains on Callisto. Low-angle impacts can create large fragments relative to their parents due to spallation, and the fragments can disperse in a linear pattern (2). If the 75 km crater from Gipul were created by ricochet fragment, its parent projectile would only had to have been 55 km in diameter based on direct extrapolation of experimental results. More likely a much larger parent is required due to increased failure expected at larger scales. In addition, we would have to assume that analogous ricochet debris from the Moon and Mercury was lost since no record was found.

Impacts from ricochet from another body is plausible provided that the body is nearby (to maintain the close spacing of fragments), that the impact angle was sufficiently small (to reduce shock disruption), and that its impact velocity was relatively low. Experiments (2) indicate that projectile fragments for very low angle ($<7.5^{o}$)

impacts leave at a velocity nearly the same as the initial impact velocity and with little dispersion. Such events would be most probable early in planetary history (small fraction of a high flux).

Implications: Presumably, if large planetary catenae were formed by ricochet of material from rare grazing ($<10^{o}$) impacts, then there would be evidence for smaller ricochet fragments produced by higher angle impacts as well. This means that the cratering record in a satellite system (and perhaps the Solar System) will reflect not only a "parent" population(s) of impactors, but additional craters from "sibling" impactors as well. From laboratory studies (2), a 5 km/sec projectile impacting at 15^{o} would ricochet 20 fragments greater than 1.0% of the original mass. Without introducing rate-dependent or scaling effects (or further tidal disruption), this translates to 20 fragments of ~10 km diameter created by ricochet from a single 50 km impactor. Such a sibling population is used to explore the possible effects on a cratering record due to a separate parent population on the Moon. The probability of an impact angle $<15^{o}$ is 8.5% for an isotropic flux. From the observed record of lunar basins, three basin-size projectiles may have produced a sibling population of high velocity impactors. The sum of the sibling and primary populations establishes a new crater production function.

Figure 2 shows a distribution solely from a primary population derived from the highlands cratering record and includes two illustrative cases. First, we used the ten largest fragments, with the largest having 3% of the initial projectile mass, as our sibling population. Since larger bodies are inherently weaker, a second possibility considered a slightly different case where the largest fragments were only 1% of the original mass but produced ~20 fragments. The resulting effect resembles, to first-order, the shape of the observed highland crater size-frequency distribution. Increasing disruption of the parent impactor will further decrease the diameter of maximum departure from an uncontaminated parent population. Consequently, it is intriguing to speculate that ricochet siblings could have contributed to the distinction between early (Population I) and late (Population II) parent populations discussed in (6).

References: 1) Passey, Q.R. and E.M. Shoemaker (1982) in *Satellites of Jupiter* pp.389-392. 2) Schultz and Gault (1989) in *Proc. of Catastrophes in Earth History*. 3) Schultz and Gault (1990) in this volume. 4) Schultz, P.H. (1988) in *Mercury* p.311. 5) Stevenson, D.J. et al (1986) in *Satellites* pp.55-56. (6) Strom, R.G. et al. (1981) *JGR*, pp. 8656-8674.

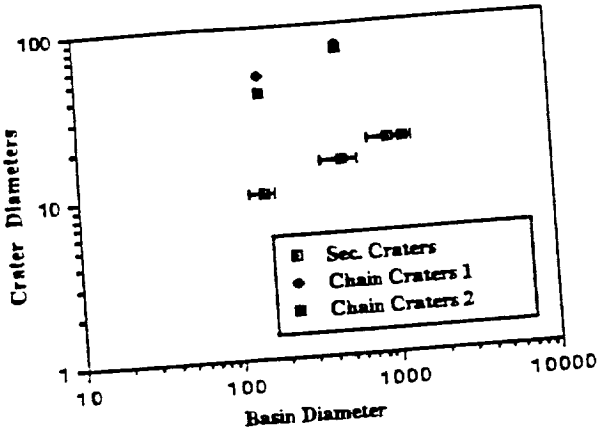

Figure 1. Plot of two largest chain craters and largest secondary crater vs. largest basin diameter for each planet. Error bars reflect uncertainty in diameter of basin.

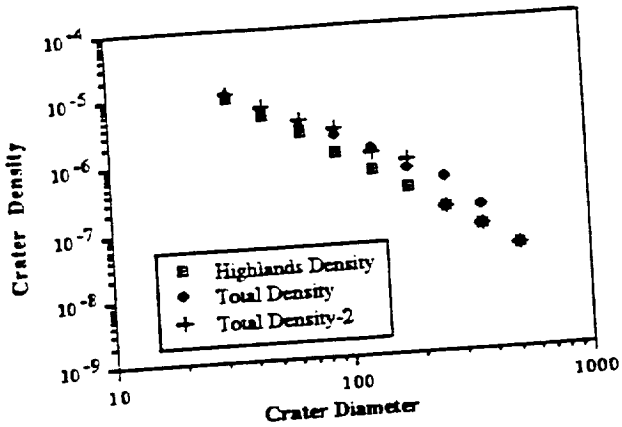

Figure 2. Cumulative distribution of craters from three populations. The highlands curve is a log distribution. The total density curves show the effect of adding sibling fragments to primary population.

Table 1. Anomalous Crater Chains

Planet	Longitude	Latitude	Length (km)	Max Diam (km)	Min Diam (km)
Callisto	0.00	70.50	1000.00	100.00	50.00
	0.00	66.00	800.00	100.00	50.00
	355.00	64.00	150.00	35.00	35.00
	60.00	68.00	1150.00	74.00	28.00
	55.50	44.00	430.00	25.00	15.00
	62.00	13.00	195.00	76.50	60.00
	345.00	-9.00	375.00	20.00	20.00
Ganymede	355.00	15.00	100.00	50.00	35.00

GLOBAL ASSOCIATIONS OF VOLCANIC VENTS TO FRACTURES RADIAL TO LARGE IMPACT BASINS ON MARS

Byron D. Schneid and Ronald Greeley, Department of Geology
Arizona State University, Tempe, Arizona 85287 USA

Volcanic vents have been related to martian impact basins in previous studies (Albin and Greeley, 1986; Albin, 1986; Craddock et al., 1990; Schultz et al., 1982; Schultz, 1984; Wichman and Schultz, 1989). It has been asserted that the concentric fractures around impact basins extend into the crust and may localize some features, including volcanoes (e.g. Schultz et al., 1982). This study has attempted to assess the possibility that radial fractures, inferred to be associated with major impact basins are an additional control on the location of volcanoes on Mars. Geologic mapping at 1:2 million scale enabled over 200 central and fissure vents to be identified.

The pattern of vent distributions upon a globe shows that most vents occur on three distinct circles. The first is a great circle which passes through the Tharsis Montes, Tempe Fossae, along Protonilus Mensea, through Syrtis Major, Hadriaca Patera, and through a series of small central vents and fissure vents to the southwest of Tharsis. A similar great circle trends SW to NE from the Hellas Basin through Hadriaca Patera, Tyrrhena Patera, northern Elysium, Alba Patera (which is approximately antipodal to Hellas Basin), southern Tempe Fossae, the eastern Valles Marineris chaotic region, and the Amphitrites Patera vents on the southwest rim of the Hellas Basin. The third series of vents is located on a small circle ~4800 km in diameter centered at ~104°W, 2°N. The circle is centered near the maximum of the Tharsis gravity anomaly and the loci of associated tensile stresses (Phillips and Lambeck, 1980; Phillips and Ivins, 1979). Most fissure vents are located on the small circle or on the great circle associated with Tharsis.

There are two more possible great circles which may be superimposed onto the martian globe. The first is associated with the Isidis impact basin and can be traced through Tyrrhena Patera, some small central vents in Eridania, across Icaria, fractured terrain in the Solis Planum area (a possible fissure vent source area), Juventae Chasma, and then along the north-south dichotomy escarpment. This circle may reflect the role of inferred radial fractures in modifying the surface in ways which are not necessarily volcanic, as many of the features are structural. The second possible great circle passes through the Hellas Basin, some unnamed central vent volcanoes in Eridania, a group of fissure vents to the northwest of Olympus Mons, across the escarpment north of Alba Patera and the Tempe Fossae region, into Acidalia Planitia, and near some fissure in Arabia. Acidalia Planitia is also along the trend of the Tharsis chain of volcanoes and may indicate a major impact site centered near 30°W, 60°N.

Although concentric fractures of smaller impact basins may influence vent positions locally, the global setting appears to be governed by fractures radial to major impact sites. This is supported by the association of one or perhaps two great circles with the Hellas impact basin, and possible great circles associated with the Isidis Basin and Acidalia Planitia. Distribution of the vent sites also suggests that larger impacts produce larger fractures and can, therefore, accommodate more volcanic activity. Isidis, Argyre, Procellarum, and Hellas basins in that order, appear to have increasing numbers of vents inferred to be associated with them.

References

Albin, E., Masters Thesis, ASU Press, 1986.

Albin, E. and Greeley, R.,Mars: Volcanic Plains in the Cratered Uplands and Possible Tectonic Associations, Proc. LPSC. XVII, pp.7-8, 1986.

Craddock, R.A.,Greeley, R., Christensen, P.R., Evidence for an Ancient Impact Basin in Daedalia Planum, Mars, LPSC XX abs., pp. 195-6, 1989.

Phillips, R.J. and Ivins, E.R., Geophysical Observations Pertaining to Solid State Convection in the Terrestrial Planets, Physics of Earth and Planetary Interiors, 19, pp.107-148, 1979.

Phillips, R.J. and Lambeck, K., Gravity Fields of the Terrestrial Planets: Long Wave Anomalies and Tectonics, Reviews of Geophysics and Space Research, 18, pp.27-76, 1980.

Schultz, P.H., Impact Basin Control of Volcanic and Tectonic Provinces on Mars, LPSC XV abs., pp.728-9, 1984.

Schultz, P.H., Schultz, R.A., and Rogers, J., The Structure and Evolution of Ancient Impact Basins on Mars, JGR, 82, B12, pp.9803-20, 1982.

Wichman, R.A. and Schultz, P.H., Sequence and Mechanisms of Deformation Around Hellas and Isidis Impact Basins on Mars, JGR, 94, B12, pp. 17333-17357, 1989.

POSSIBLE DEFICIENCY OF LARGE MARTIAN CRATERS AND RELATIVE CRATERING OF THE TERRESTRIAL PLANETS. *Richard A. Schultz, Geodynamics Branch, NASA Goddard Space Flight Center, Greenbelt, MD 20771.*

The relative size-frequency distribution of impact craters and basins on Mercury, the Moon, and Mars is remarkably similar [1], suggesting that all three bodies were bombarded by the same population of objects early in solar system history [2]. However, Mars appears to be deficient in large craters relative to Mercury and the Moon [3,4]. Part of this difference appears to be observational because large partly buried or eroded craters may not always be included in crater inventories [e.g., 5]. The relative deficiency of large craters on Mars conflicts with the interpretation of a common population of impactors within the early inner solar system [1,2] and suggests either of two possibilities. If the apparent deficiency of martian craters is real then the population of impactors at Mars differed significantly from that closer to the Sun. If the apparent deficiency is not real then the complete crater inventory of Mars should be similar to those of Mercury and the Moon, supporting the interpretation of a single population of impactors. These alternative possibilities can be tested by comparing revised inventories that include partly buried or eroded craters to an estimate of Mars' possible relative crater deficiency.

The number of "deficient" martian craters was estimated by subtracting binned lunar crater counts from the binned martian counts and propagating their uncertainties [6]. All counts were normalized by the surface area of Mars. Comparison of *Barlow's* [5] crater and basin inventory for Mars to the lunar one shows the apparent deficiency [3,4] of large martian craters having diameters ~100 km < D < 1000 km relative to the Moon (Fig. 1a, b). The mercurian curve (not shown) is indistinguishable statistically from the lunar curve [1]. All three bodies contain the same relative number of large basins (D > 1000 km). Lateral shift of the martian curve to the next larger diameter bin in order to compensate for lower relative impact velocity [3] eliminates the deficit for craters less than 250 km ($log\ D$ = 2.4) in diameter (Fig. 1b). Revision of the multi-ring basin record [4] does not affect the deficit significantly. The difference between the lunar and martian crater counts shows that a considerable number of large martian craters may remain uncounted.

Best-fit polynomials to cumulative size-frequency crater distributions have been used to define 'standard crater curves' [e.g., 7]. These curves are somewhat artificial because they incorporate crater data from geologic units having different counting areas and absolute ages. Nevertheless, they can be useful for interplanetary comparisons and resurfacing studies. The *Neukum and Hiller* 1981 and *Neukum* 1983 fits were determined by using smaller craters (< 20 km in diameter), and the revised 1983 fit increased the order of the best-fit polynomial from 7 to 11. However, neither curve fits martian crater data at diameters larger than 100-300 km. A new "Mars reference curve" was obtained by converting the binned crater data [5,4] into log-log cumulative form and obtaining best-fitting polynomials by using weighted least squares. The martian crater and basin record can be adequately represented by either a single cubic equation (1) or two equations (2) (see Fig. 2):

$$\Sigma N = 3.40 + 3.47\,D - 2.68\,D^2 + 0.42\,D^3 \qquad 8 \le D < 5000 \text{ km} \qquad (1)$$
$$\chi^2 = 16.8$$

or

$$\Sigma N = 4.67 + 0.70\,D - 0.77\,D^2 \qquad 8 \le D < \sim 500 \text{ km} \qquad (2)$$
$$\chi^2 = 21.2$$
$$\Sigma N = 4.96 - 1.21\,D \qquad D > 500 \text{ km}$$
$$\chi^2 = 0.646$$

These best-fit curves are simpler than previous fits that were restricted to small crater data. Equation (1) or something similar would be appropriate if the apparent crater deficiency is

observational; additional counts of large craters may reduce the knee near 200 km (Fig. 2a: *log D* = 2.3). Equations (2) would be appropriate if the apparent crater deficiency is real and the associated impactor population thereby different than that for Mercury and the Moon. Equations (1) and (2) are better fits to the data than a simple D^{-2} distribution (Fig. 2c). These results provide a means to test the interpretation of a common source of impactors within the early solar system once more complete crater counts for older martian terrains become available.

REFERENCES: [1] Strom, R.G., *Icarus, 70*, 517-535, 1987. [2] Wetherill, G.W., *Proc. Lunar Sci. Conf., 6th*, 1539-1561, 1975. [3] Strom, R.G., S.K. Croft, and N.G. Barlow, in *Mars*, Univ. of Arizona Press, in press. [4] Schultz, R.A. and H.V. Frey, *J. Geophys. Res.*, submitted, 1989. [5] Barlow, N.G., *Icarus*, 75, 285-305, 1988. [6] Bevington, P.R., *Data Reduction and Error Analysis for the Physical Sciences*, p. 60-61, 1969. [7] Neukum, G. and K. Hiller, *J. Geophys. Res.*, 86, 3097-3121, 1981.

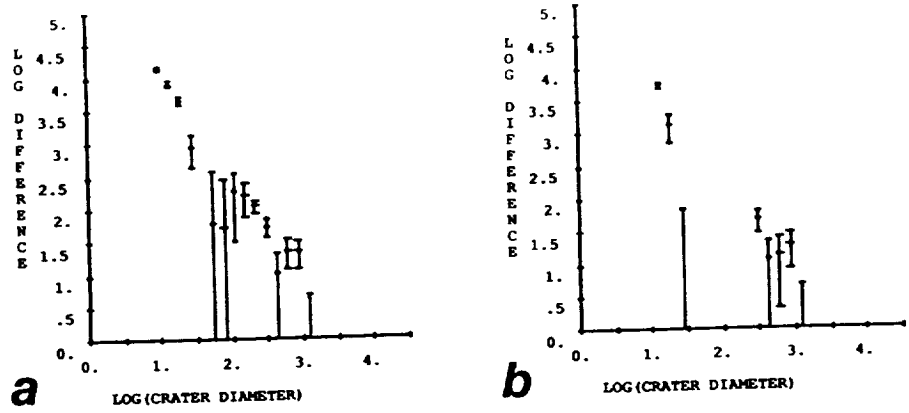

Fig. 1. Plots of difference between number of lunar and martian craters vs. binned crater diameter. All data normalized to surface area of Mars. (a) Direct subtraction. (b) Subtraction after correction for suggested differences in heliocentric impactor velocity.

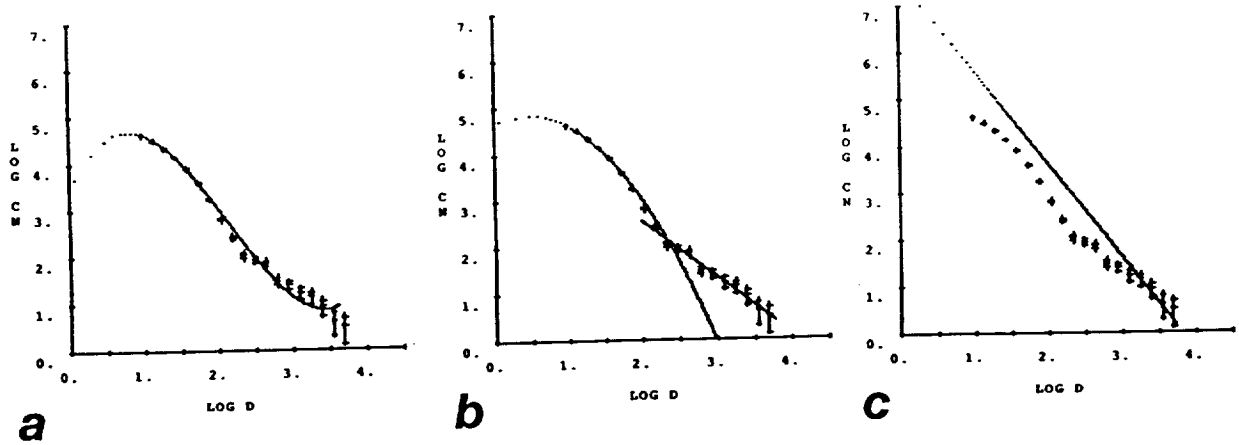

Fig. 2. Cumulative frequency plots of martian craters and basins; data from [5,4]. (a) Cubic best fit, equation (1). (b) Best fit if two impactor populations are defined; equations (2). (c) D^{-2} curve with intercept $a_o = 7.6$.

EARLY INTENSE CRATERING OF THE EARTH-MOON SYSTEM

William K. Hartmann, Planetary Science Institute, Tucson, AZ
David G. Grinspoon, NASA-Ames Research Center, Moffett Field, CA

Following earlier work by Hartmann, we have reconstructed the early cratering history of the earth-moon system by fitting the curve of cratering rate vs. time, derived from Apollo data back to about 4 Gy ago, to a data point for 4.5 Gy ago derived from the mass flux needed to accrete Earth in the measured formation interval of about 70 My. We have refined earlier treatments by careful consideration of the sweep-up times for interplanetary bodies scattered by the growing planets, as calculated by Wetherill. The time-behavior of this curve is crucial to planetary evolution, as evidenced by recent papers that attribute to the early intense flux many important effects, such as impact frustration of the origin of life on Earth and Mars, primordial climate effects induced by dust palls, heterogeneities introduced into the primordial Earth's crust, creation of Earth's oceans by comet impacts, and other effects.

To first order, our derived curve is remarkable for having an empirical mean half-life of declining flux of about 25 My, just the value calculated independently by Wetherill for sweep-up of terrestrial zone planetesimals in orbits scattered by Earth. However, we refine earlier work in several ways. We point out that many of the earlier studies mentioned above were based on assumption of a constant half-life, and hence underestimated the earliest flux. We developed a more realistic curve of continually lengthening half-life which permits, we believe, more realistic quantitative modeling of early impact effects. Second, we note that the widely postulated impact "cataclysm" -- a short-lived overwhelming cratering episode of unknown origin at 4.0 to 3.8 Gy ago -- is not needed to explain available data such as lunar rock ages. Third, we respond to recent criticisms by Graham Ryder, which not only postulate the "cataclysm", but also propose that there was essentially zero cratering for the first 600 My before the cataclysm. This would be difficult to understand in view of the dynamical calculations of the sweep-up of planetesimals left over from the planet-forming process. We believe the quantitative model we propose for declining flux in the first 600 My, with constantly lengthening half-life, permits more realistic modeling of the early planetary environment.

FORMATION OF MAGNETIC ANOMALIES ANTIPODAL TO LUNAR IMPACT BASINS

Lon L. Hood, Lunar and Planetary Laboratory
University of Arizona, Tucson, Arizona 85721, U.S.A.

Many observations suggest an important role for impact processes in producing lunar crustal magnetization. If this role is verified, then basic consequences would follow for the interpretation of paleomagnetism on airless or nearly airless planetary bodies in the solar system. Specifically, it has been shown that the largest regions of strong lunar crustal magnetization detected by electron reflection magnetometry on the Apollo subsatellites are located near the antipodes of four young large impact basins: Orientale, Imbrium, Serenitatis, and Crisium [Lin et al., 1988]. Medium-amplitude orbital anomalies correlate in many cases with surface exposures of primary and secondary basin ejecta including the Fra Mauro and Cayley formations [Hood et al., 1979]. Sample paleointensity data imply a wide range of lunar field amplitudes and indicate that significant fields have existed at the lunar surface in relatively recent times. In particular, 70019, an Apollo 17 impact glass sample dated as < 200 m.y. old, yielded a Thellier paleointensity of 0.025 gauss, which is about eight times the largest measured surface crustal field [Sugiura et al., 1979]. On the other hand, lunar sample paleointensities indicate a possible high field epoch between about 3.9 and 3.6 Ga, suggesting a former core dynamo magnetic field [Cisowski and Fuller, 1986].

Theoretically, the major aspect of meteoroid impacts that leads to plasma and magnetic field effects is the production at vertical impact velocities greater than about 10 km/s of a hot cloud of vaporized rock in addition to solid and molten ejecta (see, e.g., Melosh [1989]). A preliminary model was proposed for the formation of large lunar magnetization concentrations (or 'magcons') in which the partially ionized vapor cloud produced in a basin-forming impact expands around the Moon forcing a pre-existing ambient magnetic field to be compressed near the boundary of the cloud. An especially large compression of the magnetic field was expected to occur antipodal to the impact point. Magnetization acquisition in basin antipode zones and peripheral to the basins was suggested to occur by relatively rapid shock or thermal remanence due to impacts of solid secondaries and to compressive stresses generated by the convergence of seismic waves.

At the laboratory scale, some progress toward experimental detection of plasma, magnetic field, and rock magnetization effects associated with hypervelocity impacts onto basalt targets has been reported. In particular, Crawford and Schultz [1988] have recently documented electrical currents and spontaneous magnetic fields generated by thermal pressure gradients within the impact plasma cloud itself. They have also detected magnetic fields resulting from interaction of the impact plasma with applied external magnetic fields.

In order to investigate quantitatively magnetic effects of large impacts on airless planetary bodies such as the Moon, numerical model calculations were made of the expansion and interaction with a lunar-sized body of a basin-scale impact plasma cloud. Results show that the outer periphery of the cloud remains completely vaporized and expands around the body at a speed comparable to the incident impact velocity. For example, at impact velocities of 15 to 20 km/s, basin-scale silicate impactors (50 to 75 km in radius) produce a vapor cloud that converges on the antipode in a time of approximately 400 to 450 seconds

after the impact.

Fields Within the Plasma Cloud: Transient electrical currents are generated in the plasma cloud itself by strong temperature and density gradients combined with the basic difference in ion and electron mobilities. A scaling analysis of the governing equations yields an estimate for the saturation magnetic field amplitude, $| B_s | \sim (ck/e)(\Delta T/VL)$, where c is the speed of light, k is Boltzmann's constant, e is the electron charge, $\Delta T/L$ is a typical cloud temperature gradient, and V is a representative gas expansion velocity. Although generated field amplitudes can be large for laboratory-scale events, $| B_s |$ decreases as L increases while ΔT and V remain relatively constant. In the basin-scale impact plasma cloud calculation described above, after 64 seconds the size of the cloud is comparable to half the lunar diameter. Maximum temperatures near the impact point are $\sim 10^4$K and decrease to much smaller values in a distance of $\sim$ 1000 km. Typical expansion velocities are $\sim$ 10 km s^{-1}. Substitution into the above expression yields $| B_s | \sim 10^{-6}$ G. Even at times of $<$ 10 seconds after the impact, the estimated field amplitudes remain $< 10^{-4}$ G. It is therefore concluded that large-scale impacts on airless planetary surfaces are unlikely to produce significant large-scale magnetizing fields within the impact plasma cloud itself. This result is generally consistent with the absence of correlations between lunar orbital magnetic anomalies and impact crater locations [Hood et al., 1979].

External Fields: At least three initial plasma and magnetic field environments of an airless planetary body may be considered. First, the body may have no large-scale intrinsic magnetic field but may be exposed to the solar wind plasma and its embedded magnetic field (e.g. the present-day Moon for most of its orbit). Second, the body may possess an intrinsic field and be exposed to plasmas in its own magnetosphere (e.g. Mercury). Third, the body may have no intrinsic field but may spend part or all of its time within the magnetosphere of a planet (e.g. satellites of the outer planets). In any of these cases, the external medium consists of a plasma with an embedded magnetic field. A magnetohydrodynamic shock wave will therefore develop ahead of the expanding impact plasma cloud. Within the shocked layer, the field is amplified while outside the shock wave, the plasma and field environment is unperturbed. A case in which the body is immersed in the solar wind (i.e. the typical lunar case) is illustrated in the figure. The inner dashed line represents the outer boundary of the impact plasma cloud and the outer dashed line represents the external shock. In this example, the external plasma medium is moving at 400 km/s relative to the Moon and the ambient magnetic field is uniform and oriented perpendicular to the solar wind velocity vector. The largest field amplification occurs antipodal to the impact point and can reach values of several hundred times the ambient field amplitude. Although other initial plasma and field conditions result in different compressed external field configurations, antipodal field compression is found to occur in most cases. This result combined with observational evidence for magnetization concentrations antipodal to lunar impact basins suggests that external field compression is the most important magnetic field effect of large-scale impacts on airless planetary surfaces. Heating and weak shock effects of converging seismic waves in basin antipode zones provides one plausible mechanism for imparting magnetization to crustal materials.

References:

Cisowski, S. M. and M. Fuller, Lunar paleointensities via the IRMs normalization method and the early magnetic history of the Moon, in *Origin of the Moon*, edited by W. K. Hartmann, R. J. Phillips, and G. J. Taylor, p. 411-424, Lunar and Planetary Institute, Houston, 1986.

Crawford, D. A. and P. H. Schultz, Laboratory observations of impact-generated magnetic fields, *Nature, 336*, 50-52, 1988.

Hood, L. L., Magnetic field and remanent magnetization effects of basin-forming impacts on the Moon, *Geophys. Res. Lett., 14*, 844-847, 1987.

Hood, L. L., P. J. Coleman, Jr., and D. E. Wilhelms, Lunar nearside magnetic anomalies, *Proc. Lunar Planet. Sci. Conf. 10th*, 2235-2257, 1979.

Lin, R. P., K. A. Anderson, and L. L. Hood, Lunar surface magnetic field concentrations antipodal to young large impact basins, *Icarus, 74*, 529-541, 1988.

Sugiura, N., Y. M. Wu, D. W. Strangway, G. W. Pearce, and L. A. Taylor, A new magnetic paleointensity value for a young lunar glass, *Proc. Lunar Planet. Sci. Conf. 10th*, 2189-2198, 1979.

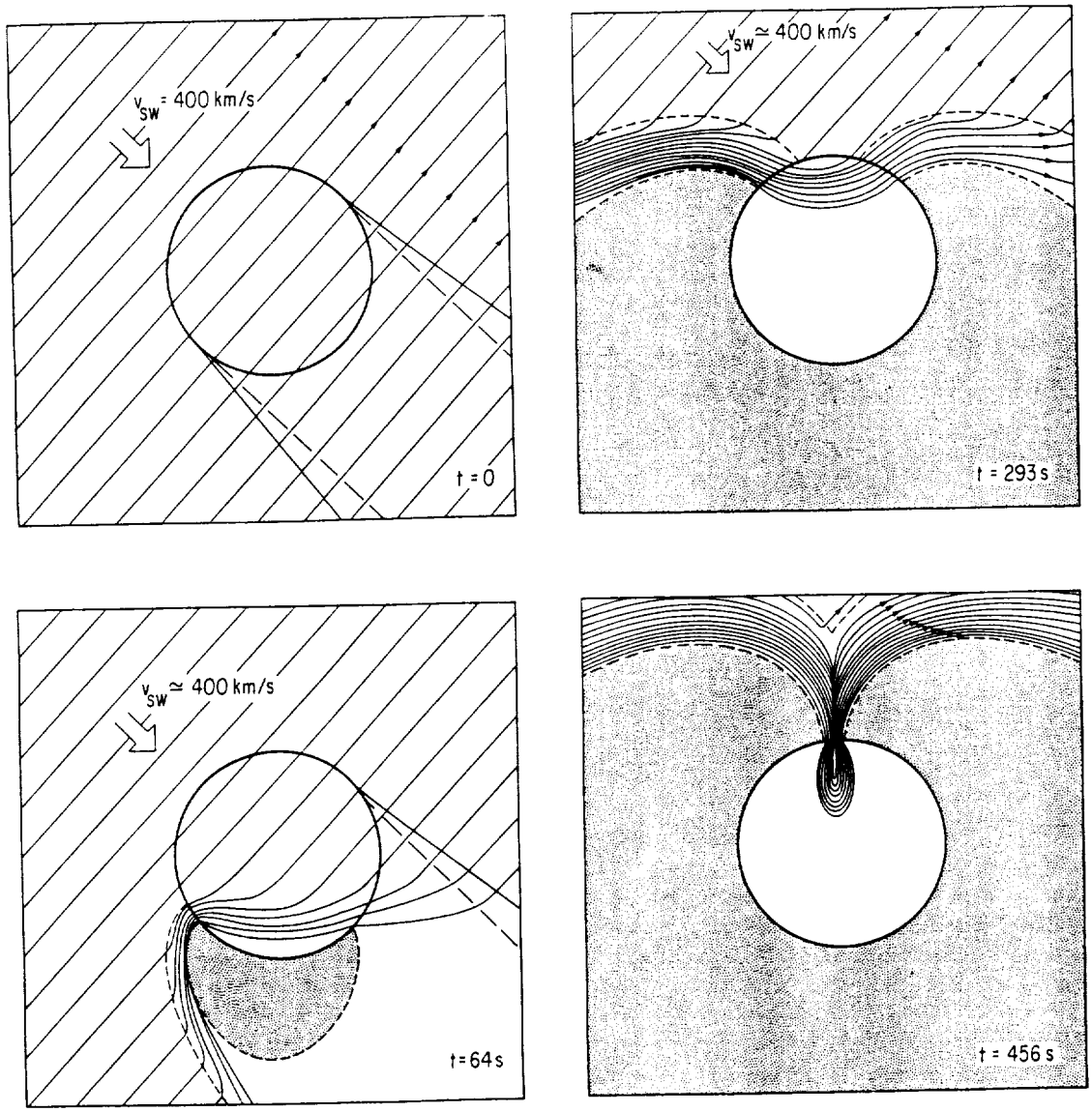

SEARCHING FOR CRISIUM BASIN EJECTA: CHEMISTRY AND AGES OF LUNA 20 IMPACT MELTS Swindle T.[1], Spudis P.D.[2], Taylor G.J.[3], Korotev R.[4], Nichols R.H.[4], and Olinger C.T.[4] 1. Univ. of Ariz., Tucson, AZ 85721 2. U.S. Geological Survey, Flagstaff, AZ 86001 3. Univ. New Mexico, Albuquerque, NM 87131 4. Washington Univ., St. Louis, MO 63130

We have studied fragments of impact melt rocks separated from Luna 20 samples. One of our goals was to identify samples of the impact melt sheet of the Crisium basin, which has not yet been characterized. Studies of Apollo 15 and 17 samples (e.g., [1-3]) have shown that the Imbrium and Serenitatis melt sheets differ in composition (though both are LKFM) and age. Apollo 16 samples contain impact melts richer in Al_2O_3 ("VHA basalt"), suggesting that the melt sheet of the Nectaris basin differs in composition from the melt sheets of both the Imbrium and Serenitatis basins [4]. We also wished to constrain the age of the Crisium basin by dating fragments of its basin melt. The only age data previously available for Luna 20 samples indicate that an impact occurred at 3.86 Ga ([5]; recalculated using decay constants of [6]), a date contemporaneous with the formation of the Serenitatis basin [2, 3]. This Luna 20 melt rock is interpreted as Crisium ejecta by some [7], but it could be from another basin or a crater.

From the Luna 20 coarse fines, we hand-picked six fragments (A-F, Table 1) that macroscopically appear to be fine-grained crystalline rocks. These samples were irradiated for INAA and ^{40}Ar-^{39}Ar analyses. Enough remained of fragments A and B to prepare thin sections; both samples are highland impact melts. Formation ages of these six samples are shown in Table 1; some selected chemical data are presented in Figure 1.

Our results, combined with published data for other Luna 20 samples [8, 9], indicate the presence of at least three distinct melt groups and a large cluster of loosely associated rocks. The three labelled groups of Fig. 1 are composed of impact melts that have homogeneous major and trace-element compositions; the age of at least one sample in each group has been determined. We interpret these three groups as representing three separate impact events. Group 3 overlaps the field for the Apollo 17 poikilitic impact melts, interpreted to be of Serenitatis basin origin [2, 3]. Sample 22007,1 was dated at 3.86 Ga [5], an age indistinguishable from that of the Serenitatis basin. Group 2 forms a tight compositional cluster and is dated at 3.72 Ga. Group 1 consists of only two members, but sample B is a fine-grained melt rock with bulk chemistry approximating "anorthositic norite" [10], and it has a well-determined age of 3.92 Ga (Table 1). Among our other samples, C and D have indistinguishable ages of about 3.7 Ga, and A and E have young ages close to 0.4 Ga. However, because the rocks are compositionally distinct, each represents a separate impact.

The Crisium basin predates the Imbrium basin (3.85 Ga) and possibly the Serenitatis (3.87 Ga) basin [7]; the age of our Group 2 melt sample F (3.72 Ga) precludes a Crisium basin origin. Group 2 likely represents the melt sheet of a post-basin crater somewhere in the vicinity of the Luna 20 site. Group 3 has a chemical composition and an age indistinguishable from those of the impact melts of the Serenitatis basin [2, 3]. Although Group 3 contains the sample suggested by Wilhelms [7] to be from the Crisium basin, we tentatively identify our Group 3 with the Serenitatis impact (despite the considerable distance (750 km) of the Luna 20 site from the rim crest of Serenitatis). Although sparsely populated, Group 1 contains an impact melt (sample B) with a precise age (3.92 Ga) and a composition similar to that of another Luna 20 sample. Group 1 is definitely older than both the Imbrium and Serenitatis impacts and is contemporaneous with the Nectaris impact. This group is distinctive chemically in that its composition does not resemble either the LKFM composition associated with the Imbrium and Serenitatis basins [1-3] or the VHA basalt composition associated with the Nectaris basin [4]. Group 1 corresponds chemically to "anorthositic norite," a polymict composition long recognized as a major component of the lunar highlands [10].

We tentatively associate Group 1 impact melt with the Crisium basin. The Luna 20 site is either inside the topographic basin [7] or on its rim crest [11]; thus, impact melt from Crisium should constitute at least some of the Luna 20 samples. If Group 1 is Crisium melt, its aluminous composition could result from the formation of the Crisium basin in a thicker, more anorthositic crust, farther away from the central near side of the Moon than Imbrium or Nectaris [7]. The association of Group 1 with the Crisium basin also suggests that Crisium, although younger than Nectaris [7], formed fairly soon afterwards, both impacts having occurred around 3.92 Ga.

LUNA 20 IMPACT MELT ROCKS: Swindle T. *et al.*

Two Luna 20 samples, A and E, have exceptionally young ages, 0.46 Ga and 0.35 Ga, respectively, and represent crater (rather than basin) impacts. The samples are compositionally distinct and probably represent two separate impacts. Sample A is a relatively coarse grained impact melt and formed during an impact into an anorthosite-rich terrain. We have no petrographic information about sample E, but macroscopically it also appears to be an impact melt. Both samples have cosmic-ray exposure ages equal (within errors) to their formational ages, indicating that (1) they represent the upper meter of their respective melt sheets, (2) they formed as meter-sized molten ejecta, or (3) they were ejected from their melt sheets by a subsequent impact soon after their formation.

References [1] Ryder G. and Spudis P. (1987) *PLPSC* **17**, *JGR* 92, E432. [2] Winzer S.R *et al.* (1977) *EPSL* **33**, 389. [3] Spudis P.D. and Ryder G. (1981) *PLPSC* **12A**, 133. [4] Spudis P.D. (1984) *PLPSC* **15**, *JGR* **89**, C95. [5] Podosek F.A. *et al.* (1973) *GCA* **37**, 887. [6] Steiger R.H. and Jäger E. (1977) *EPSL* **36**, 359. [7] Wilhelms D.E. (1987) *USGS Prof. Paper* **1348**, 303 pp. [8] Laul J.C. and Schmitt R.A. (1973) *GCA* **37**, 927. [9] Smith M.R. *et al.* (1983) *LPS* **XIV**, 716. [10] Taylor S.R. (1982) *Planetary Science*, LPI Press, 481 pp. [11] Spudis P.D. *et al.* (1989) *LPS* **XX**, 1042.

Table 1. ^{40}Ar-^{39}Ar Ages of Luna 20 Impact Melts

Sample	T (Ga)
A	0.46 ± 0.01
B	3.92 ± 0.03
C	3.71 ± 0.04
D	3.67 ± 0.05
E	0.35 ± 0.10
F	3.72 ± 0.03
22007,1*	3.86 ± 0.03
22006,1*	3.86 ± 0.03

* from Podosek et al. [5]

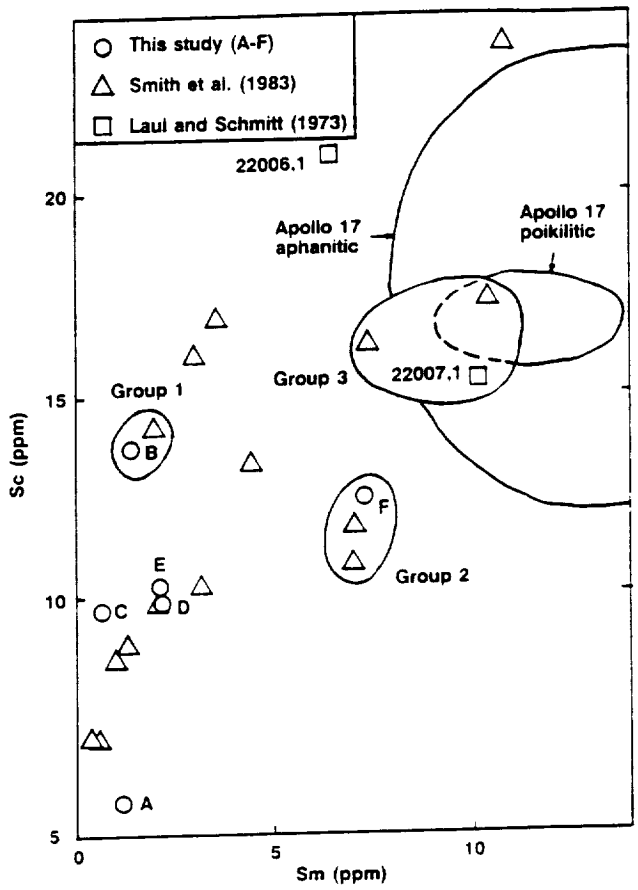

Figure 1. Sc and Sm concentrations in Luna 20 rock samples.

CRATER SIMULATIONS IN SUBSCALE JOINTED ROCK: PRELIMINARY RESULTS

Robert M. Schmidt, M/S 3H-29, Boeing Aerospace & Electronics, Seattle WA 98124

There is much conjecture about the effect of joint spacing on the effective strength of rock and its consequences on scaling. To date, all impact experiments in rock have been conducted in small, and therefore rather homogeneous, samples. The problem with such experiments is that they don't correctly model the joint/fracture characteristics of rocky materials involved in large scale impacts. In order to simulate large events, it is necessary to fabricate samples which are fractured at the appropriate spacing and have the low porosity associated with rock. This requirement has presented a difficult experimental hurdle. The approach being investigated here is to use targets consisting of layers of prefractured tempered glass plates. The layers provide a controlled vertical spacing of fractures. Additionally, the plates can be prefractured with a small explosive charge buried deep enough so as not to significantly disturb the sample surface. This abstract presents a summary of some preliminary experiments designed to test this method of sample fabrication. Seven impact tests have been performed, some using prefractured glass plates and some using "virgin" plates for comparison.

Brief description of experiments: All impactors were 6.35 mm diameter. **763-IAGS** Al sphere, 3.6 km/s, 1G. Target was alternating layers of 2.3 mm thick annealed glass and 1.5 mm thick layers of basalt fines that passed a #100 sieve. Test of virgin glass soil model. **764-I762** Al sphere, 3.5 km/s, 1G. Target same as shot 763, but had been rubblized by a buried charge forming a crater which was later filled back in. Provided a comparison of rubblized targets with virgin glass soil model. **766-I764** Al cylinder, 1.8 km/s, 1G into same rubblized target as shot 764 above, where again the crater was filled back in. Tested effect of impact velocity on rubblized target. **770-I766** Al cylinder, 1.9 km/s and 523G into same rubblized target as shot 766 above, where the crater was yet again filled back in. Tested effect of gravity on rubblized target. **767-I765** Al cylinder, 1.7 km/s, 1G. Target was 3.3 mm thick layers of tempered glass, previously fractured but not cratered by a very deeply buried explosive charge. Only a slight mound was evident on the surface. Tested effect of prefracturing the glass model. **769-I768** Al cylinder, 1.8 km/s, 520G. Target prepared as described for 767. Test effect of gravity on prefractured glass. **771-IVTG** Al cyl., 1.8 km/s, 520G. Target was 3.3 mm thick layers of virgin tempered glass. Compare with 769 for effect of prefracture.

The figure below shows how the cratering efficiency for the various shots compares with the previous results for dry sand and wet sand. It appears that interlocking of joints and block overturning might provide a significant strength even when materials are highly fractured.

To validate the suitablity of any of the jointed rock simulants, comparison is also being made with existing explosive events that have been performed in rock in the field. Of particular interest is the cratering series conducted at Buckboard Mesa in a jointed basalt on the Nevada Test Site.

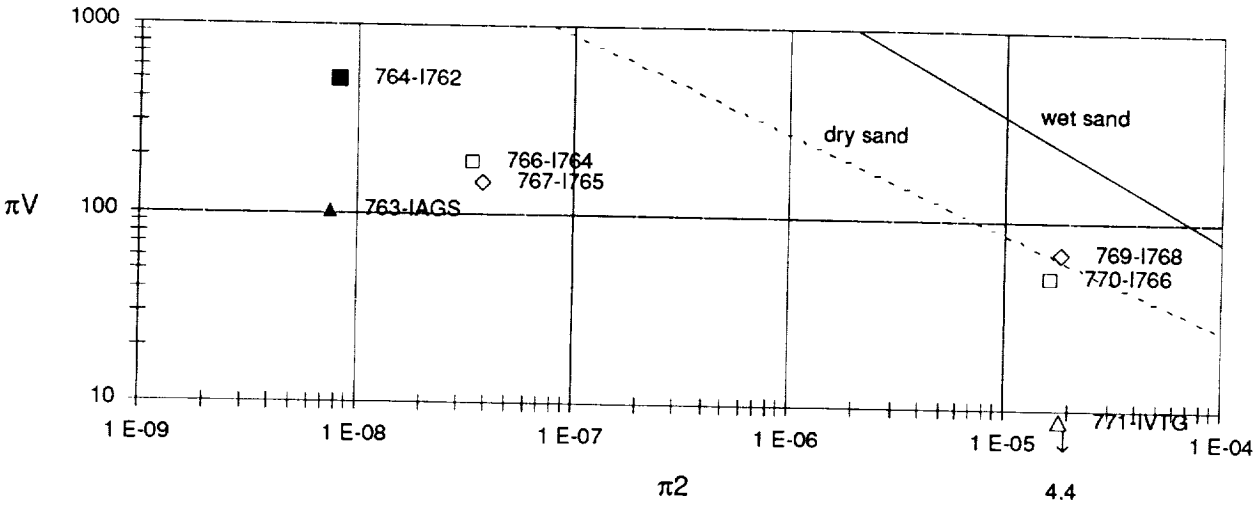

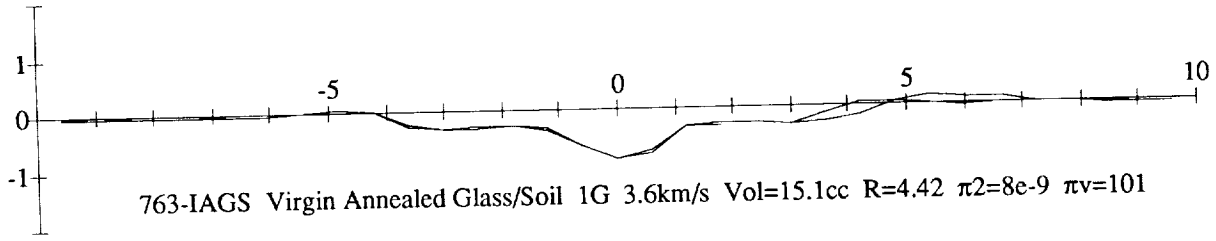

763-IAGS Virgin Annealed Glass/Soil 1G 3.6km/s Vol=15.1cc R=4.42 π2=8e-9 πv=101

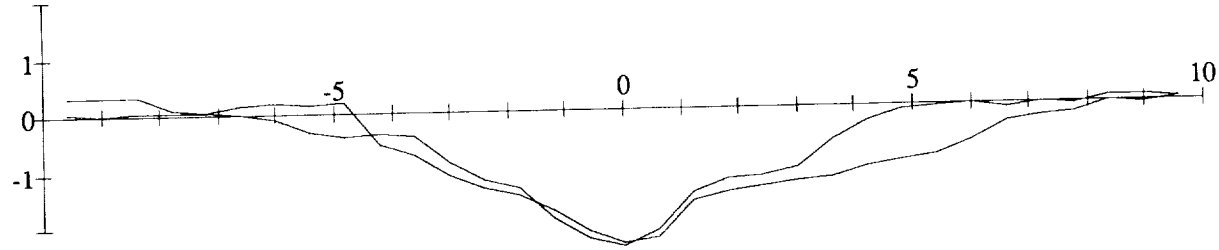

764-I762 Rubble Annealed Glass/Soil 1G 3.5km/s Vol=86.3cc R=6.32 π2=8e-9 πv=508

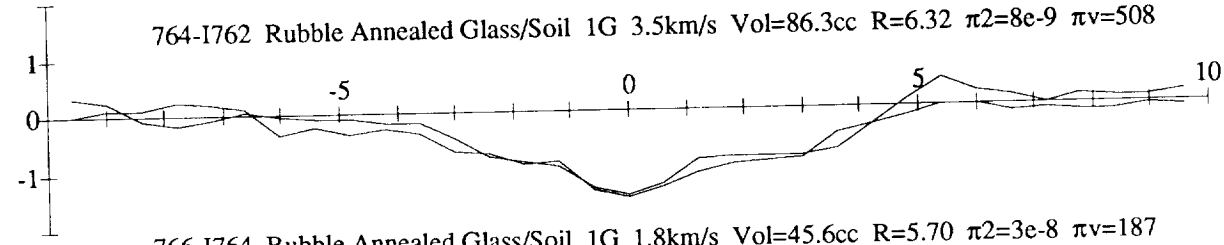

766-I764 Rubble Annealed Glass/Soil 1G 1.8km/s Vol=45.6cc R=5.70 π2=3e-8 πv=187

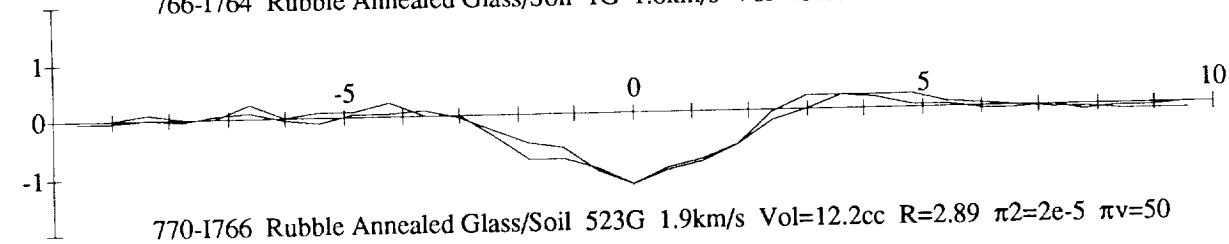

770-I766 Rubble Annealed Glass/Soil 523G 1.9km/s Vol=12.2cc R=2.89 π2=2e-5 πv=50

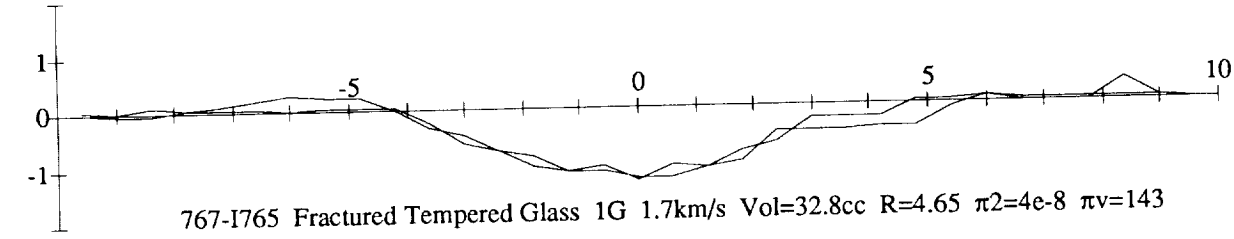

767-I765 Fractured Tempered Glass 1G 1.7km/s Vol=32.8cc R=4.65 π2=4e-8 πv=143

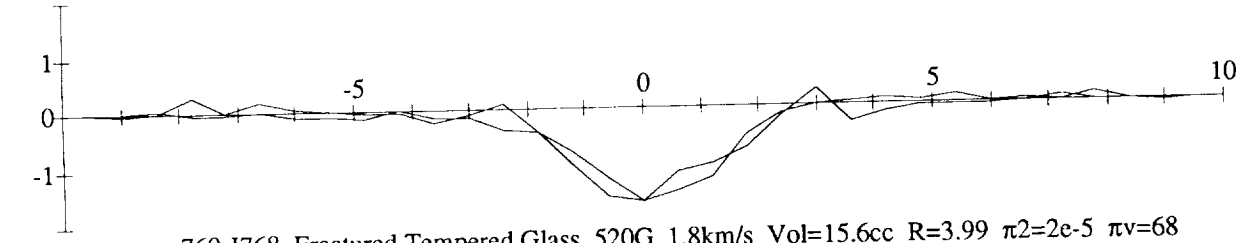

769-I768 Fractured Tempered Glass 520G 1.8km/s Vol=15.6cc R=3.99 π2=2e-5 πv=68

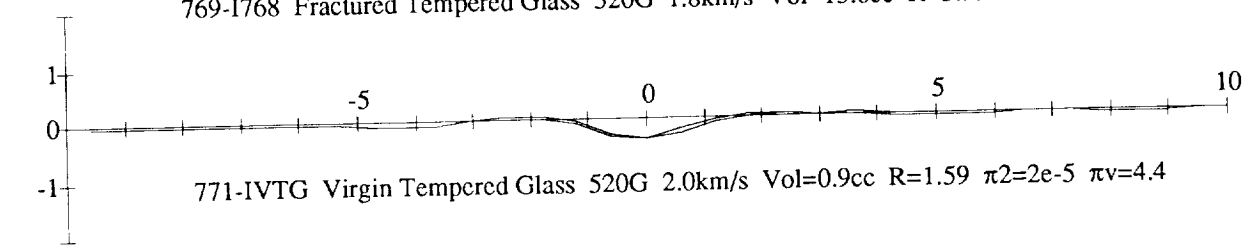

771-IVTG Virgin Tempered Glass 520G 2.0km/s Vol=0.9cc R=1.59 π2=2e-5 πv=4.4

LANGMUIR PROBE MEASUREMENTS OF IMPACT-GENERATED PLASMA. D. A. Crawford and P. H. Schultz, Dept. of Geological Sciences, Brown University, Providence, RI 02912.

Laboratory experiments at the NASA Ames Vertical Gun Range demonstrate that macroscopic hypervelocity (4.5 - 6.0 km/s) impacts can generate magnetic fields in low ambient field environments[1,2]. Nonaligned electron density and temperature gradients within the impact-generated plasma provide a possible source of these fields[3]. In the past, we inferred the presence of impact-generated plasma by noting the high electrical conductivity of the impact-induced vapor cloud[4]. Quantifying various plasma parameters such as the electron density and electron temperature potentially provides a measure of the internal energy distribution within impact-generated vapor. The plasma's electron density and temperature have been measured directly in new experiments (suggested by L. Srnka) by means of an electrostatic (Langmuir) probe.

A Langmuir probe was used to establish the electron density and temperature by measuring the current that flows between the probe and plasma as a function of an applied, variable potential. Since the lifetime of impact-generated plasma could be measured in milliseconds, it was necessary to sweep the applied probe potential rapidly while simultaneously measuring the probe current. In order to accurately determine plasma parameters, the characteristic dimension of an electrostatic probe must be much larger than the Debye length, $\lambda_d = (kT_e/4\pi e^2 N_e)^{1/2}$ and much smaller than the electron mean-free-path, λ_e[5].

A cylindrical probe 11.4 cm long and 0.028 cm diameter was located 7 cm downrange and 15.5 cm above the low-angle (15° from horizontal, 5.44 km/s) impact point of a 1/4 inch aluminum projectile into a solid aluminum target. Since we had no prior knowledge of λ_d and λ_e, several experiments with different probes determined the best probe size. The probe was connected to a 5 kHz sinusoidal voltage source. It was enveloped by the impact-generated plasma for approximately 3 ms and emerged unscathed. Both the probe potential and current were sampled every 2 μsec by A/D converters. Fig. 1 is a graph of probe current vs. potential for this particular impact. The curve has been shifted so that the probe's floating potential (at which no current flows) corresponds to zero volts. The probe current is dominated by electron current when the probe potential is positive (i.e. when the probe attracts electrons) and can be given by:

$$I_p - I_e = I_0 \exp\left(\frac{e(V_p - V_a)}{kT_e}\right) \qquad 0 < V_p < V_a \tag{1}$$

where

$$I_0 = - N_e\, e\, A_p \sqrt{\frac{kT_e}{2\pi m_e}} \tag{2}$$

where I_p = probe current, I_e = electron current, e = electronic charge, V_p = probe potential, V_a = plasma potential (from Fig. 2), k = Boltzmann's constant, T_e = electron temperature, N_e = electron number density, A_p = area of probe (1.0 cm^2) and m_e = mass of electron[5].

Figure 2 is a plot of $\ln(I_p)$ vs. V_p. The linear slope in Fig. 2 yields an electron temperature (T_e) of approximately 4500 K which is probably an overestimate. Applying equation (2) yields an electron number density (N_e) of approximately 10^9 cm^{-3} which is probably an underestimate. For a cloud density only slightly greater than that of the residual atmosphere in the impact chamber (about 10^{16} cm^{-3}), only about 1 part in 10^7 of the impact-generated vapor cloud is ionized. Under these conditions, the Debye length (λ_d) is less than 0.02 cm and the electron mean-free-path (λ_e) is between 0.3 and 1.0 cm.

Further experimental and analytical work should improve these results, but it is unlikely that our estimate of N_e will change by more than about two orders of magnitude *for this type of impact.* Since λ_d and λ_e are so close in magnitude, the use of greatly different probe sizes is restricted. Future work will focus on isolating the several possible mechanisms for producing ionization at such low impact velocities. The most likely mechanism intrinsic to the impact process may be a broad energy distribution within the impact-generated vapor cloud allowing ionization of a small fraction of the overall vapor. Other contributing mechanisms include ionization in the wake of the projectile as it travels through the residual atmosphere and ionization in the wake of the jetting phase. Ongoing experiments should resolve the relative importance of these mechanisms.

Other impact experiments indicate that higher velocities or the use of other projectile/target materials such as dry-ice, water-ice, calcium carbonate and powdered dolomite substantially

increase the amount of vaporization[6]. As indicated by the degree to which the ambient magnetic field is excluded from the impact region[4], the electrical conductivity during these impacts is comparable to, if not greater than, the analyzed case of an aluminum projectile impacting into solid aluminum. Hence, the degree of ionization is probably greater in these cases than in the example discussed here. The large amount of neutral vapor produced by such vapor-generating impacts, however, tends to reduce the electron mean-free-path, thereby reducing the effectiveness of the electrostatic probe method to obtain meaningful values of the plasma parameters. Nevertheless, careful probe design and placement should permit characterizing such parameters in the future.

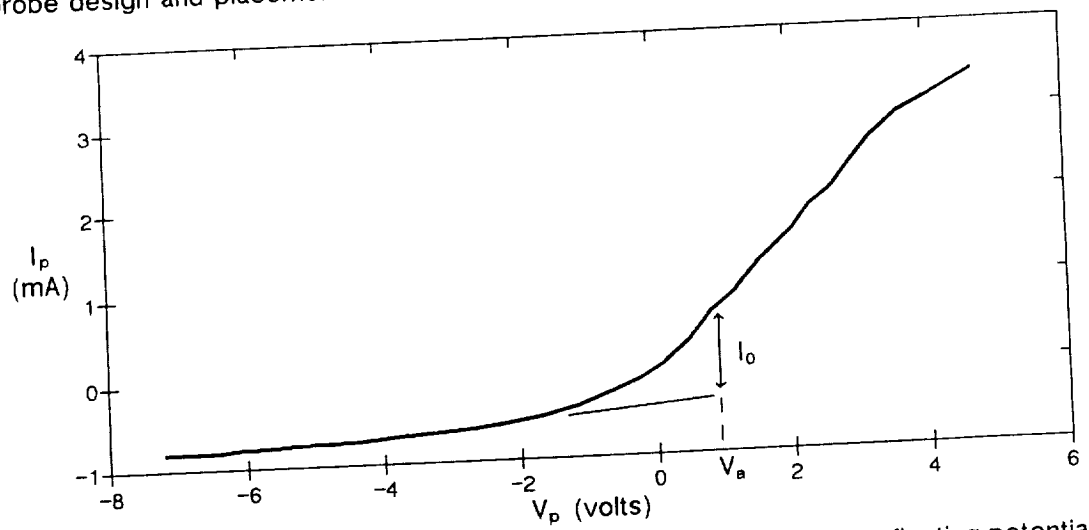

Fig. 1 Langmuir probe characteristic. V_p is the probe potential relative to floating potential (at which no current flows). I_p is the current flowing into the probe. I_o is the electron current flowing into the probe at V_a, the plasma potential.

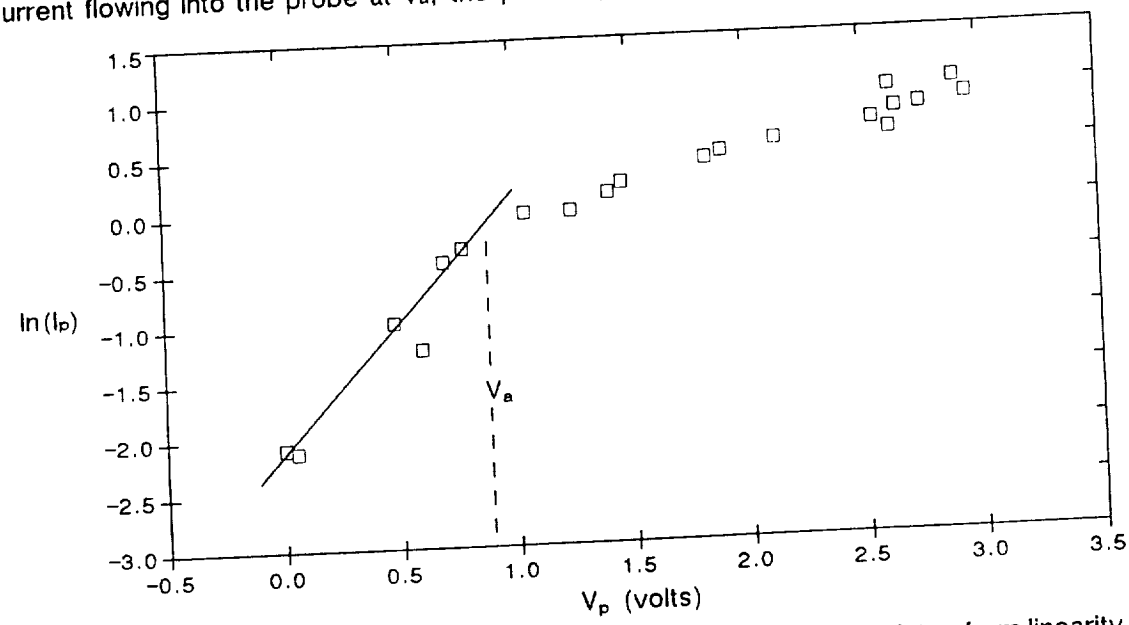

Fig. 2 Plot of ln(I_p) vs. V_p. V_a (plasma potential) is where the graph deviates from linearity.

[1] Crawford, D. A. and Schultz, P. H., *Nature* **336**, 50-52 (1988). [2] Crawford, D. A. and Schultz, P. H., *Lunar Planet. Science* **20th**, 197-198 (1989). [3] Srnka, L. J., *Proc. Lunar Science Conf.* **8th**, 893-895 (1977). [4] Crawford, D. A. and Schultz, P. H., *Lunar Planet. Science* **19th**, 217-218 (1988). [5] Swift, J. D. and Schwar, M. J. R., *Electrical Probes for Plasma Diagnostics*, London iLiffe Books Ltd. (1970). [6] Schultz, P. H., *Lunar Planet. Science* **19th**, 1039-1040 (1988).

DECAPITATED IMPACTORS IN THE LABORATORY AND ON THE PLANETS: P.H. Schultz, Brown University, Providence, RI 02912 and D.E. Gault, Murphys Center of Planetology, Murphys, CA 95247.

Background: The partitioning of energy during oblique impacts is very different from vertical impacts. For vertical impacts into sand, about 73% of the initial impactor energy is expended in target displacement including 20% in compaction and 53% in ejecta (1). The remaining energy (27%) is partitioned into waste heat and kinetic energy of the projectile. At low impact angles (15° from the horizontal), however, most of the impactor energy occurs as kinetic energy in ricocheted debris (2, 3). Internal energy in the projectile decreases as $\sin^2\theta$ until ricocheting nearly intact at very low impact angles (<7.5°), even at hypervelocities (>6 km/s) into non-porous targets (3). Oblique impacts of ductile aluminum into solid aluminum targets have been observed to consistently produce nearby downrange pits (2, 4). Because these enigmatic pits occur within a few projectile diameters of first contact, they cannot be caused by hypervelocity ballistic ejecta from the target. They appeared to be produced instead by decapitation of the projectile due to spallation.

Laboratory Experiments: Positioning the target edge close to the expected downrange rim of the primary crater permitted isolating the downrange impacting fragments from the first impact. Vertical witness plates placed farther downrange recorded the dispersion and trajectories of these isolated fragments. High-frame rate imaging from 35,000 fps to 2 x 10^6 fps (frames per second) constrained their velocity within about 5% and permitted deriving the size of the fragments from the size of the impact pits through scaling relations for identical materials (5). Aluminum and pyrex spheres (0.635 cm spheres) were launched at hypervelocities (~5 km/s) in order to contrast the response of ductile and brittle materials. Aluminum targets included a range of thicknesses (from 0.079 to 2.5 cm) in order to explore first-order effects of initial contact. Different targets (soft aluminum, sand, and water) were also used to calibrate compositional effects.

High velocity impact (5–6 km/s) of 0.635 cm aluminum spheres into 2.5 cm thick aluminum targets produce a characteristic ricochet pattern with a horizontal concentration and vertical strings of more isolated impact pits. Isolation of the downrange second impacts, however, produced only a faint horizontal line of very small pits. In such cases, the largest pits occurred well below the impact surface plane and only slightly (but significantly) above the projected intercept of the original impactor trajectory. For thin targets (less than 0.5 projectile diameter), the observed vertical offset depended more on proximity to the target edge than on target composition or thickness. The vertical offset resulting from impacts into thick aluminum targets typically correspond to a 10° change from the original trajectory. High frame-rate photography revealed that the velocity of the fragments were indistinguishable from the launch velocity, i.e., a loss of no more than 300 m/s. This record also clearly distinguished the high-speed (9 km/s) jetting component from a lower speed (~3 km/s) cloud of expanding self-luminous ejecta directed along the impact plane. The latter component was observed to uniformally plate the witness plate and pits with a microscopically thin layer of aluminum.

Discussion: The laboratory experiments clearly demonstrated that the downrange ricochet pits indeed result from spallation of the top of the projectile. At a 15° impact angle, decapitation produces a bimodal distribution with 4 to 8 fragments of nearly equal size and numerous smaller debris. Because these fragments did not impact the target surface, larger fragments survive (Figure 1). The small near-vertical velocity component of the spalled debris is generally consistent with calculated peak pressures based on the approach of Gault and Heitowit (6) modified to include only the vertical velocity component. For 5 km/s impact velocities, the shock created by first contact reaches the top of the projectile before it has penetrated 10% of its diameter into the surface. Even brittle and fragile pyrex spheres exhibited surviving fragments 10–20% of the original projectile diameter at 5.4 km/s and 15°. We note that oblique impacts into easily volatized targets (plasticene, water, carbonates) in addition produce a significant boost to the spall velocity, most likely due to acceleration in the observed impact-generated vapor cloud (7).

Hence, internal energy losses in the projectile appear to decrease for oblique impacts owing to spallation of the free surface. Several observations suggest, however, that internal energy losses along the projectile/target interface increase. First, the photographic records reveal a self-luminous ejecta cloud separable from the jetting phase that expands non-ballistically—even below the target reference surface. Second, aluminizing of thin pyrex witness plates placed just 2.5 cm above the impact indicate considerable internal but little kinetic energy in the expanding ejecta cloud. And third, downrange discoloration of the target occurs within a broad parabolic-shaped fan. This discoloration suggests brief but intense heating related to ejecta, not target-transmitted shock heating. Hence, the decrease in projectile fragmentation with decreasing impact angle down to 15° is paradoxically accompanied by an increase in heating, even for impacts into aluminum where calculated peak shock pressures are sufficient to induce only partial melting (1). This heating is expressed not only by jetting but also by fine incandescent (perhaps even melted and vaporized) aluminum ejecta. We attribute such heating to mechanical shear, a process commonly used to weld dissimilar materials, and we suspect that internal losses by shear heating may exceed shock-induced losses for impact angles less than 20–30°.

The downrange patterns resulting from projectile spallation observed in the laboratory have

striking analogs in the planetary record. Re-examination of the oblique impact record on the Moon and Mars reveals numerous examples of downrange re-impacts. The specific pattern depends on local topography and crater size. On flat surfaces, nearby and downrange oblique impact are readily recognized (Fig. 2a). At low impact angles, however, local slopes can significantly affect not only the distance between first and ricochet impact but also can change the impact angle of decapitation fragments. Ricochet from oblique impacts on the floors of several large martian craters exhibit re-impact craters on the facing wall that are even larger than the crater resulting from the initial impact. In contrast, downslope collisions have produced a succession of smaller, shallower impacts (Fig. 2b). At the broadest scales, the initial impact and downrange re-impact merge. Orcus Patera (450 km x 150 km) on Mars exhibits the diagnostic ejecta pattern for an oblique impact and a series of smaller coalescing impacts downrange. The crater Schiller on the Moon is accompanied by a series of larger downrange, coalescing craters due to the topographic effects of the facing wall/ring of Schiller basin. Both morphologies can be understood in terms of the processes observed in the laboratory. Although it can be argued that such (or some) companion impacts reflect multiple impacts by tidally disrupted or binary asteroids, the consistent pattern of smaller/shallower impacts downrange on flat surfaces, the sequence of impact, and the observed controlling effects of topography all support a process analogous to projectile decapitation observed in the laboratory.

Concluding Remarks: Laboratory experiments reveal fundamental differences in the partitioning of energy with impact angle and can be supported by both first-order theoretical considerations and planetary analogs. We feel that the process and observed phenomena provide more than just an explanation for enigmatic or unique impact structures. The decreased disruption and ricochet of a single basin-forming impactor at low angles (<15°) could contribute significantly to a sibling population of impactors, particularly in satellite systems (see 8). The increased partitioning of energy into shear heating at more modest angles (10-30°) could affect the formation and recycling of planetary atmospheres (9). Finally, the combination of vapor release and embedded projectile ricochet provides a mechanism for episodically creating orbiting debris around solid-surface planets that could evolve into a short-lived ring (3, 10).

References: (1) Braslau, D. (1970) *J. Geophys. Res.* 75, 3987-3999. (2) Gault, D.E. and Wedekind, J. (1978) *Proc. Lunar Planet. Sci. Conf. 9th*, 3843-3875. (3) Schultz, P.H. and Gault, D.E. (1990) in *Proc. of Catastrophes in Earth History*, *Geol. Soc. Sp. Paper* (in press). (4) Summers, J.L. (1959) NASA TND-94. (5) Denardo, B.P. *et al.* (1967) *NASA TND-4067*. (6) Gault, D.E. and Heitowit, E.D. (1963) *Proc. Sixth Hypervelocity Impact Symp.*, Vol. 2, 419-456. (7) Schultz, P.H. (1988) in *Lunar and Planet. Sci. XIX*, LPI, Houston, 1039-1040. (8) Hallen, C. *et al.* (1990) in *Lunar and Planet. Sci. XXI*, LPI, Houston (this volume). (9) Schultz, P.H. (1988) *Eos*, 69, p. 388. (10) Schultz, P.H. *et al.* (1990) in *Lunar and Planet. Sci. XXI*, LPI, Houston (this volume).

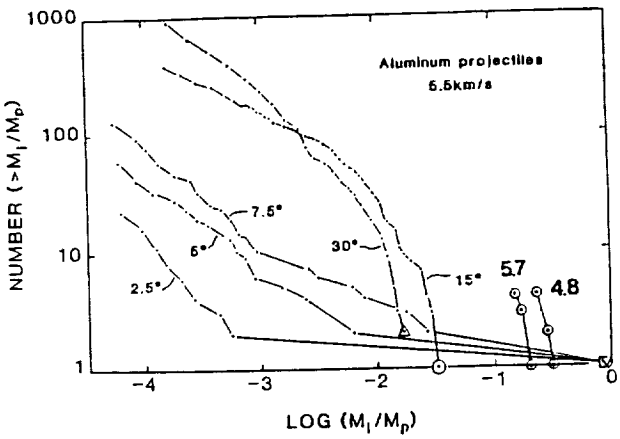

Figure 1. Size distribution of ricocheting projectile resulting from oblique impacts (referenced to horizontal) of sand (dots) and 2.5 cm-thick aluminum (large filled circles) targets. For impacts into aluminum targets, the ricochet component was prevented from re-impacting the target surface, thereby preserving the actual size and trajectory of the spalled projectile. Only the four largest spall fragments are shown for two different velocities.

Figure 2a. Numerous craters on Mars exhibit evidence for downrange impact by spall fragments from the top of the projectile. Figure 2a shows a 4.2 x 5.5 km diameter crater with companion downrange impact (387B06).

Figure 2b. Illustrates a 15 x 35 km-diameter crater that impacted the downsloping wall of Kasai Vallis (519A27). Although appearing to be the consequence of multiple impacts, the same pattern can be reproduced in the laboratory by successive spallation and impact of a single projectile.

AMOUNTS AND STYLES OF EJECTA EROSION AT METEOR CRATER, ARIZONA;
J.A. Grant and P.H. Schultz, Brown University, Providence, RI 02912.

INTRODUCTION: Two independent studies constrain average erosion from much of the ejecta surrounding the 50,000 year old (1,2) Meteor Crater, thereby supporting our preliminary contention (3) that the majority of the ejecta retains a largely pristine morphology. Most erosion occurred during a brief period following impact and under wetter conditions ~24,000–12,000 years ago. Preserved morphology indicates that fluvial run–off and eolian processes have dominated denudation with insignificant erosion by groundwater sapping processes and mass–wasting. Our conclusions are supported by the scale of preserved primary ejecta features.

AMOUNT OF EROSION: Average erosion of ejecta (comprised of predominantly Kaibab fragments) beyond ~0.25R from the rim crest is 60 +/–30 cm based on: A) the relative coarsening of ejecta surface lag deposits at various grain scales as compared to unweathered ejecta drainage systems/densities; B) the volume of locally eroded sediments within a semi–enclosed drainage basin west of the crater; and C) the persistence of small distal ejecta blocks on pre–impact surfaces and distal ejecta deposits in exposed locations on top of, and a ballistic shadow downrange of a pre–existing ridge located ~1 km from the crater rim (3). Less resistant and areally limited outcrops of ejecta dominated by Coconino debris fragments are estimated to have been eroded an average 1.5–3.0 m.

In contrast with processes responsible for formation of coarse–grained surface lag deposits in most arid environments (4,5), lag–forming processes on the widespread Kaibab ejecta at Meteor Crater are dominated by unconfined run–off, deflation, and weathering. Upward clast migration and downslope creep of saturated soils were most active during the early history of the crater, but have played only minor roles. Because lag–forming processes on the ejecta result primarily in downwasting, we can assume that the lags formed largely by differential transport of the finer matrix and *in situ* accumulation of coarse–grains. Hence, their development provides a measure of erosion after correcting for losses due to *in situ* weathering processes. Thirty samples from a variety of locations and depths demonstrate that the grainsize characteristics of the unweathered ejecta are fairly uniform (for the Kaibab and Coconino ejecta, respectively). Erosion estimates based on comparison of coarse–grained lag deposit and unweathered ejecta grainsize characteristics were made using ~50 samples in pairs/trios from around the crater. Analyses of sediments in alluvium eroded from the ejecta reveals that blocks >20 cm are infrequently carried. Blocks larger than 20 cm therefore, collect *in situ* on gully floors as finer material is removed. Because block densities per channel volume preserved on gully floors are indistinguishable from block concentrations in unweathered ejecta, only minor amounts of erosion in addition to that required for gully formation can have occurred overall (3).

Mapping of depositional environment and trenching were used to constrain the initial volume of sediments within the semi–enclosed basin. These initial volumes were then corrected for five other contributions and losses. First, deposits adjacent to the basin were included in order to account for sediments transported outside through minor divide breaches. Second, corrections were made for sediments lost by eolian deflation from the exposed ejecta and the various deposits using: the degree of coarsening relative to subsurface alluvium in lag deposits on alluvial fans; the height of phreatophyte mounds in areas of distal, diffuse drainage; and comparison of these results with amounts of erosion indicated by the present windstreak northeast of the crater. Third, volumes were modified to account for material deflated from surfaces prior to burial by the observed deposits. Fourth, a similar adjustment was made to account for buried colluvium. Finally, corrections were made to account for losses due to chemical dissolution.

STYLES OF EROSION: Fluvial run–off and eolian processes have dominated ejecta denudation with fluvial activity controlling erosion of the higher gradient upper rim (<0.5R). Overall, the two processes have operated at about equal intensities on the lower rim and distal ejecta (>0.5R). Dissection of the ejecta has occurred along ~75 small gullies incised into the outer crater flanks. Gullies are generally incised to depths of less than 1 to 2 m and merge with alluvial fans and areas of diffuse drainage near the base of the outer rim. The drainage density around the crater out to 0.6R from the rim is 8.6 km/km^2 (3) and associated drainage basins have an average relief ratio of 0.7, indicating

the ejecta is well drained and adjusted to low frequency, high magnitude events. Divides between adjacent drainage basins are typically delineated by topographic variations in the primary ejecta. Many of the alluvial fans around the crater are presently inactive as demonstrated by: A) headward fan incisement by Holocene activity resulting in only minor, more distal deposition; B) little variability between proximal and distal fan/diffuse drainage grainsize distributions; C) coarse-grained lag accumulations on fan surfaces and an absence of small scale (5–10 cm) flow features; and D) late Pleistocene soils on most fans (6–8). Together with soil studies, present fan morphology indicates that formation occurred mainly during the wetter pluvial between 24,000–12,000 years ago. The change from active fan formation to present headward incisement indicates a change from frequent, relatively sediment rich run-off in the past to less frequent, higher intensity, clear water run-off (4). Similarly, fans formed in the southwest during the pluvial exhibit little variation in down-fan grainsize owing to reduced run-off and stream power caused by the more extensive vegetation and thicker soils that existed (5). Because precipitation 50,000–25,000 years ago was probably similar to today (Forester 1983, written comm.), significant fan formation then is unlikely.

Eolian activity over the past 10,000–12,000 years has produced the currently observed patchy windstreak northeast of the crater. Several lines of evidence indicate that the windstreak is now largely inactive: there is little active transport during high wind events; a paucity of active bedforms on the surface; and abundant vegetation. From the preserved record, windstreak formation is apparently not continuous through time, but undergoes periods of formation and preservation followed by epochs of enhanced erosion. Formation continues until the supply of fine-grained sediments, supplemented by the prior increased intensity of gradational processes (i.e. fluvial), is depleted.

Ejecta aquifer properties are equivalent to a fairly homogeneous, pure sand or sandstone aquifer (9), indicating that surface infiltration rates are high. Together with the absence of characteristic sapping morphology, these properties demonstrate the insignificance of erosion by groundwater processes. Only 5–10 cm chemical dissolution has occurred as indicated by: A) chert nodule relief on Kaibab blocks; B) survival of small (10–15 cm) Kaibab blocks on pre-impact surfaces; and C) and fragments spalled off large Kaibab ejecta blocks that can be easily traced to their original position. Little evidence was found around the crater exterior for modification by mass-wasting processes.

Erosion under present climate conditions has been minimal as demonstrated by the largely inactive fans and windstreak. Because precipitation between 50,000–25,000 is thought to have been generally similar to present amounts, denudation rates were probably similarly low. Maximum erosion occurred during the pluvial when rates were 2–3X present values and during a brief period following crater formation prior to surface stabilization.

CONCLUSIONS: Ejecta surrounding Meteor Crater has remained remarkably unmodified. The widespread coarse-grained surface lags on the Kaibab ejecta resulting from small amounts of erosion forms an armor that protects underlying ejecta and whose resistance may approach that of *in situ* Kaibab formation. Erosion was greatest during the pluvial and has been dominated by fluvial run-off and eolian processes. This study provides a framework for comparing the gradational history of other terrestrial and martian impact craters in order to understand their erosional/climate histories.

REFERENCES: (1) Sutton, S.R., 1985, Thermoluminescence measurements on shock-metamorphosed sandstone and dolomite from Meteor Crater, Arizona: 2. Thermoluminescence age of Meteor Crater: Jour. Geophys. Research, v. 90, No. B5, p. 3690–3700. (2) Nishiizumi, K., Kohl, C.P., Shoemaker, E.M., Arnold, J.R., Lal, D., Klein, J., Fink, D. and Middleton, R., 1989, In Situ ^{10}Be–^{26}Al exposure ages at Meteor Crater, Arizona: p. 792–793, in Lunar and Planet. Sci. XX (abstracts), Lunar and Planetary Institute, Houston, Texas. (3) Grant, J. A. and Schultz, P. H., 1989, The erosional state and style of Meteor Crater, Arizona: p. 355–356, in Lunar and Planet. Sci. XX (abstracts), Lunar and Planetary Institute, Houston, Texas. (4) Cooke, R.U. and Warren, A., 1973, Geomorphology in Desserts: Los Angeles, California, Univ. of California Press, 394p. (5) Dohrenwend, J.C., 1987, Basin and Range, in Graf, W.L., ed., Geomorphic Systems of North America, Centennial Special Volume 2: Boulder, Colorado, Geological Society of America, p. 303–342. (6) Shoemaker, E.M., 1960, Impact mechanics at Meteor Crater, Arizona: PhD Dissertation, Geology, Princeton Univ., Princeton, N.J., 55p. (7) Shoemaker, E.M., 1987, Meteor Crater, Arizona, in Beus, S.S., ed., Centennial Field Guide, v. 2, Rocky Mountain Section of the Geological Society of America: Boulder, Colorado, Geological Society of America, p. 399–404. (8) Shoemaker, E.M. and Kieffer, S.E. (1974), Guidebook to the geology of Meteor Crater, Arizona: Arizona State University Center for Meteorite Studies Pulication 17, Tempe, AZ., 66p. (9) U.S. Dept. of the Interior (1977), Ground Water Manuel: A Water Resources Technical Publication, U.S Government Printing Office, Washington, D.C., 480p.

ORIGIN OF THE BUSHVELD AND VREDEFORT COMPLEXES, SOUTH AFRICA BY MULTIPLE IMPACTS: EVOLUTION OF A CONCEPT

Wolfgang E. Elston and Jonathan Sadow, Department of Geology, University of New Mexico, Albuquerque, New Mexico 87131, and David Twist, Institute for Geological Research on the Bushveld Complex, University of Pretoria, Pretoria 0001, South Africa

An impact origin for the Bushveld Complex was mentioned in passing by Schwarz (1909); that of the Vredefort Ring was discussed in detail by Daly (1947). Impact origin of Vredefort has been accepted by those later workers who treated discoveries of pseudotachylite dikes, shatter cones, shock lamellae, coesite, and stishovite as diagnostic. Although leading workers since the 1920's have considered Bushveld and Vredefort to be cogenetic, an impact origin for the Bushveld has not been widely accepted or even discussed. The complexity of the Bushveld is one reason. Nobody has attempted a synthesis since Hall (1932); subsequent geophysical studies have shown his reconstruction to be untenable. We are attempting an impact model based on the published literature and tested by our own investigations.

Vredefort-Bushveld events deformed ~100,000 km^3 of otherwise stable Kaapvaal craton ~2.05 Ga ago. If endogenic, they may have involved processes new to geology (Nicolaysen, 1985); if exogenic, they involved multiple impacts by a disintegrating bolide and energy levels orders of magnitude above those of other proposed astroblemes. "When one is dealing with an extraordinary phenomenon, no possibility is too extraordinary to be worthy of consideration." Thus wrote Shand (1916) about pseudotachylite of the Vredefort Ring. In 1947, Shand recognized the resemblance between pseudotachylite veins in rocks "subjected to violent mechanical shock" and dark veins in meteorites "produced by the sudden disintegration of some larger celestial body." He failed to make the mental leap from meteorites to their targets but Daly (1947) cited pseudotachylite among the evidence for impact origin of Vredefort.

In 1922, A.L. Hall and G.A.F. Molengraaff had guided Daly through the Vredefort Dome and the much larger (400 km diameter) Bushveld Complex. Daly had cited Hall and Molengraaff in his 1928 Bushveld synopsis as regarding Vredefort and Bushveld as cogenetic and "nearly if not quite contemporaneous," yet he never made the mental leap to interpreting Vredefort and Bushveld as results of contemporaneous impacts. That connection was left to Dietz (1962).

In 1928, Daly had invoked orogenic uplift, centripetal tangential stresses, and rising magmas to explain the Bushveld Complex; in 1947, he enumerated these very forces as inadequate to explain Vredefort. Why did he not apply his later thinking to the Bushveld? Although he recognized many of the features later cited by others as evidence for impact, Daly interpreted the Bushveld Complex as a modified lopolith (i.e., a lava flow of layered gabbro many kilometers thick with a differentiated felsic crust) that filled a 60,000+ km^2 basin and was fed by a central vent. Later geologic mapping and gravity, magnetic, electrical resistivity, and seismic-reflection surveys have shown that mafic rocks are inward-dipping intrusive sheets and probably absent in the center of the Bushveld Complex. They end abruptly at 11-13 km depth against a disturbed zone that may form the collar around a central uplift. Dietz (1962) still had a lopolith in mind when he attributed the Bushveld Complex to a bolide that penetrated the mantle and left a crater flooded with mafic magma. French (1968) accepted Cousins' (1960) interpretation of mafic rocks in overlapping ring complexes; he visualized them on the periphery of central uplifts of impact craters. Hamilton postulated impacts by four comet fragments, to produce Vredefort and three overlapping Bushveld basins; mafic Bushveld rocks were interpreted as accumulations in ring synclines.

"Fragments" of intensely disturbed basement, tens of km in diameter, occur within the Bushveld Complex; Daly (1928) interpreted them as enormous

xenoliths floated to the mafic-felsic interface of the gigantic lava flow. Other workers regarded them as roof pendants. French (1968), Hamilton (1970) and Rhodes (1975) interpreted them as parts of central uplifts of impact craters. We interpret them as segments of the deformed zone between transient and modified impact cavity, peripheral to central uplifts. By our interpretation, Vredefort represents a central uplift and deformed collar at a deeper erosion level; in the Bushveld Complex the central uplift(s) is (are) covered by later rocks. This would explain occurrences of shock phenomena at Vredefort and their absence in the Bushveld.

The felsic crust of Daly's lava flow (Rooiberg Felsite) has turned out to be older than, and intruded by, mafic magmas. The interpretation of this 5-km succession of high-temperature melts (Twist and Elston, 1989) is critical to any interpretation of the Bushveld Complex. French (1968) wondered if it might be fallback breccia, analogous to the Onaping Formation at Sudbury; French and Hargraves (1971) and French (in press) unsuccessfully searched for shock effects. Hamilton (1970) generally accepted Daly's interpretation but also raised the possibility of fallback breccia. In a more detailed study, Rhodes (1975) interpreted the lower part of Rooiberg Felsite as shock-induced impact melt, the upper part as a volcanic-like rock "....that was extruded over its own solidified crust after the impact event." We tentatively attribute the huge initial volume (~300,000 km^3, ~20% of the Bushveld Complex), chemistry, and high temperature of Rooiberg Felsite to massive crustal melting in an impact cavity excavated to isotherms above the ambient-pressure liquidus of granite.

Current investigations have centered on part of the Marble Hall "fragment," where layered gabbro is missing and pre-Bushveld sedimentary rocks (Pretoria Group) grade into Rooiberg Felsite. Over a vertical distance of 15-20 m, orthoquartzite and subgraywacke (Fig. 1) are progressively (1) recrystallized to metaquartzite with sutured grain boundaries (Fig. 2a), (2) cataclastically deformed, (3) recrystallized into a network of quartz needles (Fig. 2b), and (4) partly melted and quenched. The quartz needles are interpreted as paramorphs of quartz after tridymite; they indicate temperatures between 870°C (ß quartz-ß tridymite inversion) and 1700°C (melting temperature of SiO_2). Where melting is complete, quench textures indicate temperatures >1100°C. Quartz needles are so ubiquitous that sediment and meltrock are difficult to distinguish. Deformation and recrystallization on such a scale are unknown beneath conventional siliceous volcanic flows. Additional evidence for unusual processes can be found in locally intense brecciation or ductile deformation of basement sedimentary rocks, the incorporation of quartzite xenoliths > 100 m into felsite, and chemical composition of some felsite varieties appropriate for melted sedimentary rocks (Rhodes, 1975).

References: Cousins, C.A., 1960, Geol. Soc. South Africa Trans. 62. Daly, R.A., 1928, Geol. Soc. America Bull. 39; 1947, Jour. Geol. 55. Dietz, R.S., 1962, Jour. Geol. 70. French, B.M., 1968, in Shock Metamorphism of Natural Materials, Mono Book Corp., Baltimore; in press, Tectonophysics. French, B.M. and Hargraves, R.B., 1971, Jour. Geol. 79. Hall, A.L., 1932, Geol. Survey South Africa Mem. 28. Hamilton, W., 1970, Geol. Soc. South Africa Spec. Pub. 1. Nicolaysen, 1985, South African Jour. Sci. 81. Rhodes, R.C., 1975, Geology 3. Schwarz, E.H.L., 1909, Jour. Geol. 17. Shand, S.J., 1916, Geol. Soc. London Quart. Jour. 72; 1947, Eruptive Rocks, J. Wiley, New York. Twist, D. and Elston, W.E. 1989, New Mexico Bureau of Mines and Mineral Resources Bull. 131.

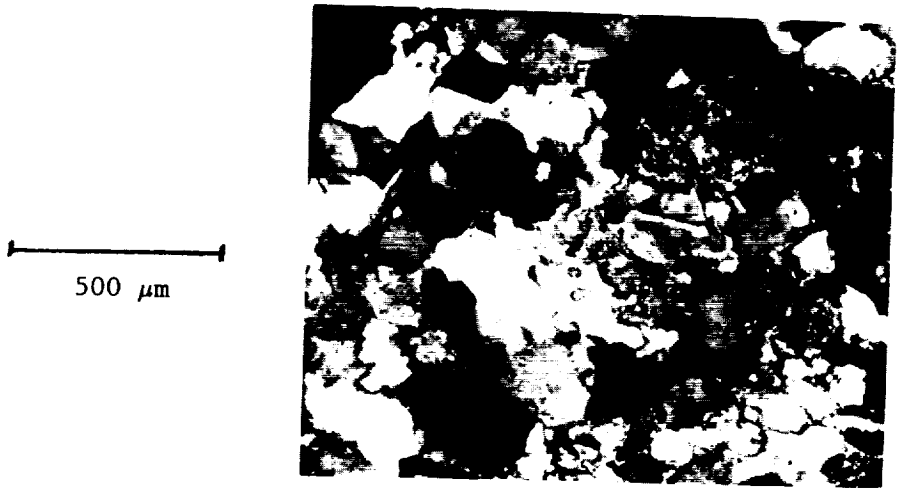

Figure 1. Arenite of Pretoria Group with incipient recrystallization, about 10m below contact with Rooiberg Felsite, Farm Riffontein 706 KS, 15 km north of Marble Hall, Transvaal. Crossed polars. Rock is subgraywacke with subangular to subrounded quartz and minor plagioclase in a matrix of sericite and minor calcite. In the middle of the field of view, quartz has recrystallized to an aggregate with sutured grain boundaries.

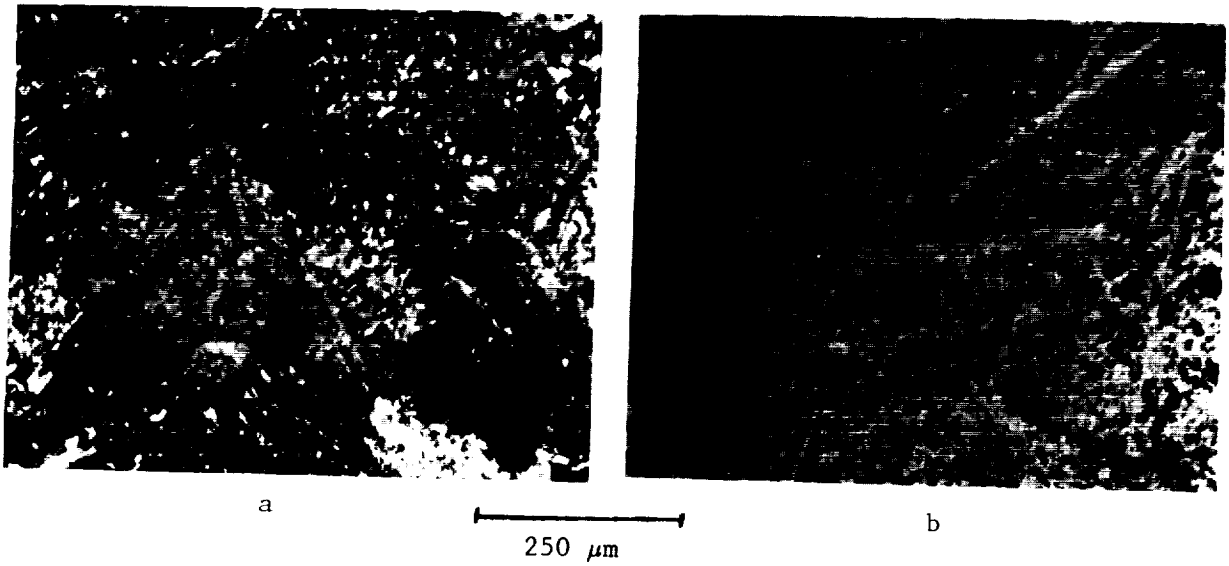

Figure 2. Arenite of Pretoria Group with advanced recrystallization, about 15 m below contact with Rooiberg Felsite, Farm Palmiefontein 708 KS, 15 km north of Marble Hall.

a. Transmitted light crossed polars. Sutured quartz grain boundaries are indistinct, sericite is dispersed through quartz grains.

b. Same view as 2a, reflected light, which shows quartz grains to have been recrystallized to a network of quartz needles paramorph after tridymite. The needles disregard the indistinct (relict) grain boundaries seen in transmitted light.

CHAPTER 11

STRUCTURE AND TECTONICS

VALLES MARINERIS TECTONISM

B.K. Lucchitta, U.S. Geological Survey, 2255 North Gemini Drive, Flagstaff, Ariz.

Introduction: The Valles Marineris system, just south of the Martian equator, extends for 4,000 km, from longitude 40° to 110°. It includes a series of troughs that trend approximately N. 75° W. Individual troughs are generally 50 to 100 km wide, but in the central part of the system, they merge to form a depressed area 600 km wide. Depths of as much as 8 km below the plateau surface are common, and locally they may reach 10 km. The troughs are interconnected and open toward the east, except for Hebes Chasma, which is entirely enclosed, and Echus and Juventae Chasmata, which open toward the north. The troughs appear to lie on a regional high extending eastward from the Tharsis rise [1,2], and they are paralleled by many shallow grabens that are part of a system radial to Tharsis [3,4,5,6].

Geologic Setting: The Valles Marineris troughs disrupted the Lunae and Syria Planum plateaus of Early Hesperian age [7,8] and, accordingly, may be as old as Early Hesperian. The Noctis Labyrinthus troughs, which disrupted Upper Hesperian or Lower Amazonian lavas [9], may thus be of Early Amazonian age. Interior layered deposits were emplaced mainly in the central trough region shortly after the troughs opened. These deposits may be lake sediments or volcanic rocks with contributions of mass-wasted or eolian material. Deposition of the layered materials probably extended through Late Hesperian and possibly into Early Amazonian time. After the troughs were filled nearly to their rims by layered deposits, unknown processes removed parts of these deposits, leaving many as isolated tablelands surrounded by newly formed depressions, the so-called moats. The removal process may have been erosional, but structural disruption is a possible alternative. In the latter case, interior deposits may have filled only older, smaller troughs, and later faulting may have widened the original depressions to form the moats. Landslides, dated as Middle to Late Amazonian [10], fell into the newly created voids. After landslide emplacement, a new unit, several kilometers thick in places, was deposited on the trough floors; its dark patches and lobate fronts suggest that this unit may be volcanic [11].

Tectonism apparently occurred throughout the history of the Valles Marineris. If the interior deposits are partly of volcanic origin, volcanism may gave extended over roughly the same period.

Structure and Tectonics: The Valles Marineris troughs lie along a structural trend that is radial to Tharsis [4,12,13,14,15]. This trend is expressed by many shallow grabens on the surrounding plateau. Within the troughs, linear boundary faults at the base of the walls extend parallel to these grabens for hundreds of kilometers, and locally the faults cut lower spurs to form triangular facets [4,16]. Such scarps are conspicuous on the north slopes of Coprates Chasma and eastern Candor Chasma, although on the south side of Coprates the faults are en echelon [17]. More commonly, the boundary-fault trace is expressed as straight wall segments lining up across wide landslide reentrants. Other faults parallel the boundary faults. Some of these faults bound subsidiary troughs parallel to the major ones [18]. These troughs may have formed from successive structural collapse along parallel faults. Curved wall segments, such as the south wall of Melas Chasma, may follow faults that were influenced by buried crater or basin structures.

The attitude of the boundary faults is not certain. Carr [19] noted that the faults appear to be vertical. Photoclinometric measurements of Davis and Golombek [20] indicate dips of 60°, perhaps suggesting opposing fault scarps associated with simple grabens and a discontinuity at depth [20,21,22]. If the Valles Marineris faults are near vertical, collapse into voids at depth without interaction with a discontinuity, becomes more likely [23].

Although trough floors lie as much as 10 km below the adjacent plateau surface at many places, their depths decrease to about 4 km in eastern Coprates Chasma. Such depths are not unusual for deep terrestrial grabens. Deposits of wall and plateau material on trough floors indicate that structural relief in the Valles Marineris may have been on the order of 2 to 3 km in the eastern troughs that are transitional to outflow channels, and 8 to more than 10 km in the central troughs. The Valles Marineris void is apparently not compensated, as shown by a negative line-of-sight gravity anomaly [24], an observation that supports a thick, rigid crust in this area. Minor topographic rises on the surrounding plateau near the trough edges, observed in several places, could be caused by incipient isostatic adjustments that are compensating for the void.

A genetic link between the Tharsis rise and the Valles Marineris has long been suspected because of the alignment of their major trends. Stress models of the Tharsis rise relate the parallel shallow grabens on the adjacent plateaus to a tensional stress regime caused by dynamic uplift or isostatic loading of the Tharsis area [5,6,25,26,27,28,29]. However, why did only the Valles Marineris, and no other fractures radial to Tharsis, open into deep troughs? The extraordinary trough depth, much deeper than that of the shallow grabens on the adjacent plateau, has been attributed to possible keystone collapse along the crest of an arch or bulge [1,2,4,5].

Tharsis stress patterns have also influenced the trend of wrinkle ridges on the plateau, which is generally nearly perpendicular to that of the shallow grabens [30,31]. This trend also appears to have influenced the structure of the Valles Marineris: the trend parallels the blunt ends of troughs and many smaller faults and lineations inside the troughs. However, many structures within the troughs and on the surrounding plateau diverge from the general trend [17]. An analysis of the adjacent grabens and wrinkle ridges suggests that wrinkle ridges developed first; grabens, second [30]; and the Valles Marineris, last [17,32].

Because of the size of the grabens and their location over an arch, the origin of the Valles Marineris has frequently been ascribed to aborted planetary rifting [4,13,15,33,34]. Arches are characteristic of terrestrial rifts [34,35]. However, in detail the Valles Marineris are different from terrestrial plate-tectonic rifts. Most terrestrial rifts have many en echelon faults that taper out along strike. Also, their beds are tilted [34]. By contrast, in the Valles Marineris, faults are more widely spaced, trough ends are blunt and bounded by cross faults, fault planes may be near vertical, and few beds are tilted. Perhaps the difference is due to the thick crust on Mars [36], which Frey [34] estimated to be 50% thicker than Earth's crust in the African rift-zone. Also, rifts on Earth are invariably associated with volcanism, whereas the occurrence of volcanism inside the Valles Marineris [11,37,38,39] is still conjectural.

Another proposed origin of the Marineris troughs is tectonic collapse due to withdrawal of subsurface material. Possible transfer of

magma into the region of the Tharsis rise has been proposed by McCauley et al. [12], Sharp [14], and Schonfeld [33], but their hypotheses have never been analyzed in detail. A variant of the tectonic-collapse hypothesis involves collapse of materials into voids that were created at depth by the opening of tension fractures [23]. This hypothesis is based on the inference that pit chains, which most likely formed by collapse, are transitional to the troughs, and that therefore the troughs probably formed by similar processes. However, Schultz [17] showed that pit chains and troughs are different in trend as well as morphology, so that their developments may be unrelated.

Overall, the Valles Marineris troughs show a clear imprint of tectonism and influence by Tharsis radial extensional stresses that predisposed their location and may have initiated their formation. Other mechanisms that possibly aborted tectonic rifting, collapse along the crest of a bulge, and subsurface withdrawal of material.

References

(1) Christensen, E.J. 1975, JGR 80, 2909-2913; (2) U.S. Geological Survey. 1986, USGS Misc. Inv. Ser. Map I-1712; (3) Carr, M.H. 1974, JGR 79, 3943-3949; 4) Blasius, K.R., Cutts, J.A., Guest, J.E., and Masursky, Harold 1977, JGR 82, 4067-4091; (5) Wise, D.U., Golombek, M.P., and McGill, G.E. 1979, Icarus 38, 456-472; (6) Plescia, J.B., and Saunders, R.S. 1982, JGR 87, 9775-9791; (7) Scott, D.H., and Tanaka, K.L. 1986, USGS Misc. Inv. Ser. Map I-1802-A, scale 1:15,000,000; (8) Tanaka, K.L. 1986, LPSC 17 Proc., JGR 91, E139-E158; (9) Tanaka, K.L., and Davis, P.A. 1988, JGR 93, 14893-14917; (10) Lucchitta, B.K. 1979, JGR 84, 8097-8113; (11) Lucchitta, B.K. 1987, Science 235, 565-567; (12) McCauley, J.F., Carr, M.H., Cutts, J.A., Hartmann, W.K., Masursky, Harold, Milton, D.J., Sharp, R.P., and Wilhelms, D.E. 1972, Icarus 17, 289-327; (13) Hartmann, W.K. 1973, Icarus 19, 550-575; (14) Sharp, R.P. 1973, JGR 78, 4063-4072; (15) Masson, Phillipe 1977, Icarus 30, 49-62; (16) Spencer, J.R. 1984, NASA TM 86246, 243-245; (17) Schultz, R.A. 1989, MEVTV Workshop on Tectonic Features on Mars, 21-22; (18) Lucchitta, B.K., and Bertolini, L.M. 1989, LPSC 20, 590-591; (19) Carr, M.H. 1981, The Surface of Mars: New Haven, Yale University Press, 232 pp.; (20) Davis, P.A., and Golombek, M.P., JGR, in press; (21) Golombek, M.P. 1979, JGR 84, 4657-4666; (22) Golombek, M.P. 1985, JGR 90, 3065-3074; (23) Tanaka K.L. and Golombek, M.P. 1989, LPSC 19, Proc., 383-396; (24) Scott, D.H., and Tanaka, K.L. 1980, LPSC 11th, Proc., 2403-2421; (25) Phillips, R.J., and Lambeck, K. 1980, Rev. Geophys. Space Phys. 18, 27-76; (26) Banerdt, W.B., Phillips, R.J., Sleep, N.H., and Saunders, P.S. 1982, JGR 87, 9723-9733; (27) Solomon, S.C. and Head, J.W. 1982, JGR 87, 9755-9774; (28) Masson, Phillipe 1985, Advances in Space Research 5, 83-92; (29) Sleep, N.H., and Phillips, R.J. 1985, JGR 90, 4469-4489; (30) Watters, T.R., and Maxwell, T.A. 1983, Icarus 56, 278-298; (31) Chicarro, A.F., Schultz, P.H., and Masson, Phillipe 1985, Icarus 63, 153-174; (32) Schultz, R.A. 1989, LPSC 20, 974-975; (33) Schonfeld, E. 1979, LPSC 10th, Proc., 3031-3038; (34) Frey, H. 1979, Icarus 32, 142-155; (35) Baker, B.H., Mohr, P.A., and Williams, L.A. 1972, GSA Spec. Paper No. 136, 67 p.; (36) Milanovsky, E.E., and Nikishin, A.M. 1984, LPSC 15, 548-549; (37) Peterson, Christine 1981, LPSC 12th, Proc., 1459-1471; (38) Nedell, S.S., Squyres, S.W., and Anderson, D.W. 1987, Icarus 70, 409-441; (39) Witbeck, N.E., Tanaka, K.L., and Scott, D.H., USGS Misc. Inv. Ser. Map I-2010, scale 1:2,000,000, in press.

INTERIOR STRUCTURES OF VALLES MARINERIS, MARS

B.K. Lucchitta, U.S. Geological Survey, Flagstaff, AZ 86001 and
L.M. Bertolini, University of Arizona, Tucson, AZ 85721.

The origin of the Valles Marineris troughs has been attributed to both erosional and tectonic processes. Whereas some early investigators proposed formation by erosional processes such as melting of ice-saturated megaregolith followed by mass wasting, sublimation of water or ice, and deflation of the remaining dust [1], other workers, especially those using Viking images, favored tectonism as the major process [2]. Proposed tectonic mechanisms include the formation of grabens due to crustal spreading and rifting [3,4] or collapse following magma withdrawal at depth [5]. However, the extent to which the troughs were later enlarged or modified by erosion is still questioned, and an origin due entirely to mass-wasting processes (collapse of surface rocks into subsurface voids) has recently been advocated [6].

Two observations support the notion that erosion played a major role in forming the present configuration of the troughs. One observation pertains to the formation of depressions that separate interior layered deposits from chasma walls, the so-called moats; the other pertains to the formation of a semicircular wall segment along the south rim of Melas Chasma; this shape initially appeared to be more compatible with erosion than with faulting. New observations suggest that both features may be primarily of structural origin.

The origin of the moats is poorly understood: wind erosion appears to be an insufficient cause, as is erosion by water resulting from drainage of a hypothetical paleolake [7,8]. Also, erosion by water is improbable for the formation of the moat in Hebes Chasma, which is entirely enclosed by wall rock. Sublimation of ice has been proposed as an alternative mechanism for moat formation [9], but volumetric problems remain, such as the difficulty of removing all materials by sublimation and deflation. We here proposed that the moats are primarily of structural origin. This hypothesis is based on recent geologic mapping of Ophir and Candor Chasmata combined with a study of elevations on topographic maps [10].

The elongate, east-west trending trough of eastern Candor Chasma is divided lengthwise into southern and northern segments. The southern segment, extending across one-half to two-thirds the width of the chasma, is filled with interior layered deposits (hereafter called basin beds) that form a high-level bench. The bench has surface elevations about 4 km above the Martian datum, and it abuts the walls of the adjacent plateau to the south. The northern chasma segment is lower, having surface elevations of generally 0 to -2 km, and it forms a subsidiary trough about 5 km lower than the southern bench. This trough contains several erosional remnants displaying spur-and-gully morphology, an erosional form characteristic of chasma wall rock but not of basin beds. Also, no layered basin beds crop out within it. These observations suggest that the northern trough is underlain dominantly by wall rock. A critical relation is observed in one place: a hill composed of wall rock lies directly adjacent to the bench underlain by

basin beds; both rise to similar elevations. This outcrop relation precludes extension of the wall rock underneath the baisn-bed bench at the same stratigraphic level; the wall rock underneath the bench has to be at greater depth. The outcrop relation therefore suggests that the wall rock in the northern trough and the basin beds on the southern bench are in fault contact; thus, the northern trough, though topographically lower, is structurally higher than the southern bench. To obtain this configuration, the original Candor Chasma may have occupied only the area of the southern bench, forming an ancestral trough that became filled with basin beds. The northern trough segment apparently dropped after the deposition of these beds. The formation of this later, subsidiary trough appears to have postdated the emplacement of layered basin beds, as none are seen on its floor. These geologic relations indicate that in eastern Candor Chasma the linear depression forming the moat between basin beds and chasma wall is primarily of structural origin.

The configuration of Ophir Chasma is similar to that of eastern Candor Chasma. Again, the southern two-thirds of the chasma is occupied by basin beds; the northern third is deeper and forms a linear trough between basin beds and chasma wall, the so-called moat. No wall rock remnants are seen on the floor of this depression, because its floor is buried by young landslide deposits. However, the geologic and topographic setting is similar to that of eastern Cnador Chasma and suggests that Ophir Chasma may have developed similarly to Candor and that the depression along the north side of Ophir Chasma may also have been a later, subsidiary, structural trough.

The interior mesas of Candor Mensa, Baetis Mensa, and an unnamed interior mesa farther east are separated by north-trending valleys 4-5 km deep. Even though some evidence points toward later fluvial activity within one of these valleys [11], their primary origin is unknown. On the floor of these valleys occur numerous lineations and minor offsets that trend parallel to the long axes of the valleys. These structures suggest that tectonism was also involved in the formation of the valleys, even though erosion by unknown processes may have aided significantly in their formation. However, a north-trending depression between basin beds and wall rock along the west closure of Ophir Chasma is paralleled by two faults and by tilted beds in chasma wall and basin beds, a relation suggesting that this moat is also primarily of structural origin.

Southern Melas Chasma, like eastern Candor and Ophir Chasmata, is also occupied by a bench. This bench, having surface elevations of 1-2 km, lies about 2 km above northern Melas Chasma, which has surface elevations of -1 to -2 km. Again, whereas the outcrops on the bench are of basin beds, those of the topographically lower Melas Chasma floor to the north are dominantly wall rock. These relations, similar to those of Candor Chasma, suggest that the northern bench margin is a fault. The idea that the margin follows a structure is also supported by its shape: the bench margin forms a semicircular curvature that approximately parallels the curvature of the south boundary of Melas Chasma and the curvature of several grabens on top of the plateau to the

south. The margin of the bench, the chasma rim, and the grabens are apparently controlled by a circular structure in the basement, most likely a buried ancient crater or basin underlying southern Melas Chasma and the plateau to the south. This observation also supports the concept that the southern curved reentrant of Melas Chasma is primarily structural, representing a wall segment where the fault bounding the chasma became locally diverted by planes of weakness related to an ancient impact. Erosional modifications were apparently relatively minor.

In summary, two major features of the interior of the Valles Marineris, previously attributed mainly to erosion, are here shown to be primarily of structural origin. These observations support those hypotheses suggesting that the present configuration of the Valles Marineris is dominantly due to tectonism and that erosional modifications were only subsidiary.

References

[1] McCauley et al. 1972, Icarus 17, 289; [2] Blasius et al. 1977, JRG 82, 4067; [3] Hartman 1973, Icarus 19, 550; [4] Frey 1979, Icarus 37, 142; [5] Sharp 1973, JRG 78, 4063; [6] Tanaka and Golombek, 19 LPSC Proc., 383; [7] McCauley 1978, USGS Map I-897; [8] Lucchitta 1982, NASA TM 85127, 233; [9] Nedell et al. 1987, Icarus 70, 409; [10] U.S. Geological Survey 1986, Map I-1712; [11] Lucchitta 1987, Icarus 72, 411.

CANYON SYSTEMS ON MARS

B.K. Lucchitta[1], G.D. Clow[2], S.K. Croft[3], P.E. Geissler[3], A.S. McEwen[1], R.B. Singer[3], S.W. Squyres[4], K.L. Tanaka[1]; [1]USGS Flagstaff, Ariz.; [2]USGS Menlo Park, Calif.; [3]LPL, Univ. of Ariz., Tucson, Ariz.; [4]Cornell, Ithaca, New York

The canyon system of Mars, just south of the equator, extends approximately east-west for about 4,000 km (from about long 40° to 110°). It includes the network of Noctis Labyrinthus in the west, the linear troughs and enclosed depressions of the Valles Marineris chasmata in the center, and the eastward-widening troughs, transitional to outflow channels, in the east. The chasmata are as much as 100 km wide and 8 km deep and are located along the crest of a regional rise 2-4 km high that extends eastward from the Tharsis topographic high.

Origin of Valles Marineris: The opening of deep troughs parallel to shallow graben systems radial to Tharsis disrupted the Lunae Planum and Sinai Planum volcanic plateaus of Late Noachian to Late Hesperian age (1,2). Because no plateau lavas are seen to spill into the troughs, we know that the disruption postdated emplacement of these lavas. Incipient opening of the troughs may have taken place as early as Late Noachian time, but it most probably occurred during the Early Hesperian; Noctis Labyrinthus may have opened during the Late Hesperian (3). The troughs disrupted lava caprock of Lunae Planum and impact breccia of the underlying megaregolith (4).

The formation of the chasmata has been attributed to erosional or tectonic (5) processes. Erosional processes may have involved melting of ice-saturated material of the megaregolith, followed by mass wasting, sublimation of water or ice, and deflation of the remaining dust (6). Tectonic processes are assumed to have been initially related to tensional stresses associated with emplacement of the Tharsis dome to the west (7); however, the precise mechanism that caused the Valles Marineris to attain their exceptional depth is not clear. It could be due to rifting, crustal spreading (8), collapse following magma withdrawal (9), or tensional fracturing at depth (10). A gravity profile over the central Valles Marineris shows a negative anomaly (11), but its significance remains poorly explored. Most likely, a combination of tectonic and erosional processes took place, but faulting dominated, as evidenced by the generally straight wall segments in central Valles Marineris. Eosion along structural lines of weakness may have widened the troughs in places and removed most material in Noctis Labyrinthus and in tributary canyons. Sapping processes, ice-lubricated creep, sublimation, subsurface drainage, and karst collapse (12) may have contributed to the removal of material. In the eastern chasmata, channel-forming processes probably enlarged the troughs.

Interior Layered Deposits: Simultaneous with early faulting, the canyon walls were eroded into spurs and gullies, and the troughs were filled by interior deposits to elevations close to those of the present chasma rims. The interior beds, which locally overtopped eroded wall-rock remnants, consist of alternating dark and light layers. The dark layers are generally thin and resistant to erosion, and the light layers

are more massive and highly susceptible to wind erosion. McCauley et al. (6) suggested that the deposits are lacustrine because of their apparent horizontality and lateral continuity. However, the volume of the interior deposits is too large to have come from inflowing or mass-wasted (13) materials alone, because tributary valleys are short and spur-and-gully erosion on the walls probably caused only minor recession. The amount of eolian material that may have foundered through the ice cap on a lake (14) is probably also insufficient. Deposition of carbonates (15) may have helped to alleviate the volume constraints; the presence of carbonates is supported by bright, white layers in Ganges and Capri Chasmata (16). However, the existence of resistant dark units and volumetric insufficiences support a volcanic origin for some of the material (17); perhaps the even layering is due to eruption into a paleolake (14).

After emplacement of the layered deposits, deep "moats" developed locally between wall rock and interior deposits, leaving interior mesas standing as high as 6 km above the trough floors. The origin of the moats is poorly understood: wind erosion appears to be an insufficient cause, and sublimation of ice has been proposed as an alternate mechanism (14). The moats may be partly structural, because some are bordered by faults. Shortly after the formation of the moats, the hypothetical lake noted above may have drained through Coprates Chasma (18), perhaps resulting in a last gigantic flood through Simud and Tiu Valles.

Irregular Floor Deposits: After the troughs had nearly reached their present configuration, new deposits consisting of diverse dark and light materials were emplaced on their floors. These deposits rest unconformably on older units and embay interior mesas, landslides, and tributary canyons. The deposits are generally thin, but in western Candor Chasma they may reach thicknesses of 3 km. Most of the dark material may be wind drifts derived from outcrops of older dark layers interbedded in wall rock or interior deposits, but dark material along faults could have come from volcanic vents (19). Also, the spectra of the dark materials are compatible with mafic volcanic rock or glass (20). Superposition of these deposits on young landslides and a dearth of superposed craters suggest a Late Amazonian age.

A thin mantle of dark material covers the floors in most low areas, suggesting emplacement by saltation of wind-drifted materials. Dunes are also dark and relatively blue, and their shape indicates wind directions along the troughs. By contrast, the interior mesas are covered by light-colored dust that is relatively red. Interior deposits show deflation flutes, but landslides, talus slopes, and wall rock appear unaffected by wind erosion.

Mass-Wasting Processes: Mass wasting modified the troughs and contributed to their widening. Most of the walls are eroded into spurs and gullies at slope angles below or near the angle of repose. Tributary canyons have V-shaped cross profiles, low gradients, and local hummocky floor deposits that probably formed by sapping of ice or water-rich wall materials (9). The Noctis Labyrinthus canyons and other narrow canyons that parallel the major chasmata appear to have formed by

collapse and subsurface drainage. After the formation of the interior mesas, massive landslides from the chasma walls formed debris aprons that extend as much as 100 km across the chasma floors. A slope-stability analysis suggests that the wall rock is fairly strong to a depth of several kilometers (21), in spite of the susceptibility of the walls to sliding. The landslides appear to have contained some ice or water, as indicated by channels emerging from them, but the quantity of fluid was probably small. Because it is unlikely that the landslides were saturated with water, the size-dependent fluidization mechanisms for dry-rock debris (22) may help explain the extensive runout distances.

Conclusion: The Valles Marineris are dominantly fault troughs whose walls were modified by mass-wasting processes. They evolved through the last two-thirds of Martian history in a complicated interplay of tectonism, deposition of interior materials, volcanism, and erosion, including mass wasting and the action of ice and water. Wind erosion was probably minor. Bedrock exposures in the chasmata offer a unique opportunity to determine their compositions during future Mars missions.

References

(1) Scott and Tanaka 1986, USGS Map I-1802A; (2) Tanaka 1986, JGR 91, E139; (3) Tanaka and Davis 1988, JGR 93, 14893; (4) Carr 1979, JGR 84, B6, 2995; (5) Blasius et al. 1977, JGR 82, 4067; (6) McCauley et al. 1972, Icarus 17, 289; (7) Wise et al. 1979, JGR 84, 7934; (8) Frey 1979, Icarus 37, 142; (9) Sharp 1973, JGR 78, 4063; (10) Tanaka and Golombek 1989, 19 LPSC Proc., 383; (11) Tanaka et al. 1986, NASA TM 88383, 603; (12) Croft 1989, Fourth Int. Conf. on Mars, 10-13 Jan 1989, Tucson, Ariz., 88; (13) Carr 1981, Yale Univ. Press, 232 p.; (14) Nedell et al. 1987, Icarus 70, 409; (15) McKay and Nedell 1988, Icarus 73, 142; (16) McEwen and Soderblom 1989, Fourth Int. Conf. on Mars, 10-13 Jan. 1989, Tucson, Ariz., 138; (17) Peterson 1981, 12 LPSC Proc.. 1459; (18) Lucchitta and Ferguson 1983, JGR 88, A553; (19) Lucchitta 1987, Science 235, 565; (20) Geissler et al., 1989, Fourth Int. Conf. on Mars, 10-13 Jan. 1989, Tucson, Ariz., 111; (21) Clow and Moore 1988, LPSC 19, 201; (22) Melosh 1987, GSA Reviews Eng. Geol. 7, 41.

COMPLEX EARLY RIFTING IN VALLES MARINERIS: RESULTS FROM PRELIMINARY GEOLOGIC MAPPING OF THE OPHIR PLANUM REGION OF MARS, 1:500,000 SCALE.

Richard A. Schultz, Geodynamics Branch, NASA Goddard Space Flight Center, Greenbelt, MD 20771.

Ophir Planum is a relict plateau bounded on three sides by Valles Marineris troughs (Coprates, Melas, and Candor/Ophir Chasmata). The plateau is deformed by a distinctive array of grabens whose orientations differ by as much as 30° from the overall trend of the troughs. Photogeologic mapping of the Ophir Planum quadrangle (MTM -10067; Fig. 1) was undertaken to solve two main problems: (1) What controlled the location, orientation, and growth of Ophir Planum grabens? and (2) How are the grabens and trough faulting related?

Geology within the quadrangle is surprisingly diverse (Fig. 2). The Ophir Planum plateau is capped by plains materials that embay more rugged and densely cratered materials. New crater counts suggest that these plains materials are correlative to Early Hesperian ridged plains on Lunae Planum to the north [1] but significantly, no wrinkle ridges are found on Ophir Planum. The densely cratered materials are probably Noachian (Npl2?) in age, as is the trough wall rock beneath the plateau. Five units are identified in Coprates Chasma: cratered plains (Hpf in Fig. 2), 2 facies of basin beds (Hvl), landslide materials (As), and young possible volcanics (Avsd; see [2]). A third facies of basin bed is distinguished in Ophir Chasma to the north. Crater counts suggest that Hpf in Coprates is also of Early Hesperian age, implying that the Coprates trough floor is structurally lowered caprock of "Lunae Planum" age.

Well defined fault scarps divide Ophir Planum from Coprates Chasma. These trough bounding normal faults change strike from nearly east-west in the eastern part of the quadrangle (Fig. 1) to northwest. The orientations of grabens on Ophir Planum plateau mirror this change and plateau faults locally merge with trough bounding faults. These relationships suggest that plateau grabens are as old as the trough bounding normal faults and that they probably formed under the same stress regime. Ophir Planum grabens probably did not result from either lateral unloading due to landsliding or sliding of caprock into the troughs [3] because (a) their age is older than the periods of landsliding or development of spur-and-gully topography on trough walls, which occurred after downfaulting in the troughs; (b) they do not always parallel the plateau bounding scarp, as required by the mechanisms of [3]; and (c) stress analysis of lateral unloading shows that the grabens occur too far from bounding scarps to have resulted from scarp retreat.

The grabens on Ophir Planum define an echelon set and their changing orientations within the stepover are consistent with mechanical interaction between grabens as they grew into the echelon array [e.g., 4] (Fig. 3). The overall orientation of Valles Marineris troughs is consistent to first order with a spatially uniform, Tharsis generated remote stress state in the region containing the troughs [e.g., 5]. The curving geometries of Ophir Planum grabens and trough bounding faults in Coprates both indicate that the local stress state in this area was spatially variable during the time of Valles Marineris faulting and trough growth. The cause of this spatial variability is still uncertain although stress pertubation by growing troughs that also interact mechanically is an attractive possibility.

The rich geologic history of the Ophir Planum quadrangle (Table 1) underscores the fundamental importance of faulting in the early growth of Valles Marineris.

REFERENCES: [1] Tanaka, K.L., *Proc. Lunar Planet. Sci. Conf., 17th*, in *JGR, 91*, E139-E158, 1986. [2] Lucchitta, B.K., *Science, 235*, 565-567, 1987. [3] Witbeck, N.E., K.L. Tanaka, and D.H. Scott, Geologic map of the Valles Marineris region, Mars, *USGS Map I-2010*, in press. [4] Pollard, D.D. and A. Aydin, *JGR, 89*, 10,017-10,028, 1984. [5] Banerdt, W.B. et al., *JGR, 87*, 9723-9733, 1982.

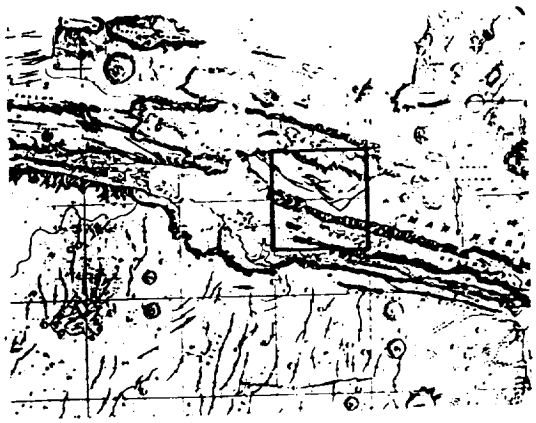

Fig. 1. Quadrangle location.

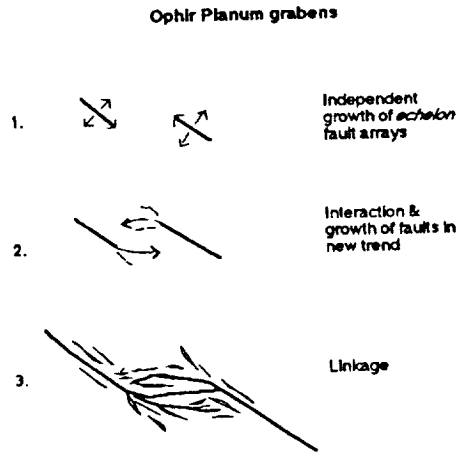

Fig. 3. Growth model for Ophir Planum grabens.

Fig. 2.

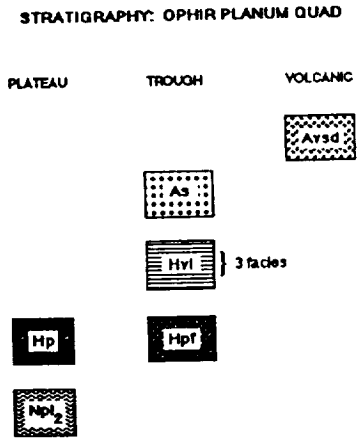

Table 1: Geologic Synopsis.

1. FORMATION OF OLDER NOACHIAN UNITS
- ◊ Npl_2, Noachian wall materials

2. DEPOSITION OF OPHIR PLANUM PLATEAU UNIT
- ◊ Resurface and embay Npl_2
- ◊ No wrinkle ridges

3. FAULTING

Trough Formation
- ◊ Growth of Coprates, bounding faults- linear to concave NE
- ◊ Ophir Planum relatively undeformed
- ◊ Minor faulting & volcanism (pits, flows) on OP // to Coprates

Deformation of Ophir Planum
- ◊ Growth of oblique graben arrays on & beyond OP
- ◊ Graben depth ~1 km < D < 5 ?? km

4. TROUGH MODIFICATION
- ◊ Erosional retreat of wall scarps
- ◊ Deposition of regional & local floor layers (Hvf)
- ◊ Faulting of basin beds, wall scarps (?)
- ◊ Erosion of most Hvf in Coprates, minor in Melas
- ◊ Landslides; mafic volcanism (?)

MEVTV STUDY: EARLY TECTONIC EVOLUTION OF MARS - CRUSTAL DICHOTOMY TO VALLES MARINERIS; H. V. Frey and R. A. Schultz, Geodynamics Branch, Goddard Space Flight Center, Greenbelt MD 20771

In this study we addressed several fundamental problems in the early impact, tectonic and volcanic evolution of the martian lithosphere: (a) origin and evolution of the fundamental crustal dichotomy, including development of the highland/lowland transition zone; (b) growth and evolution of the Valles Marineris; and (c) nature and role of major resurfacing events in early martian history. Below we briefly summarize our results in these areas.

(a) Origin and Evolution of the Martian Crustal Dichotomy

Both internal and external processes have been invoked to explain this fundamental characteristic of the martian lithosphere. We suggest that major, basin-forming impacts have played a prominent role in the origin and development of the crustal dichotomy (1,2,3). Our study revealed little direct support for the single giant impact hypothesis (4), but did suggest a number of new, previously unrecognized large impacts basins (5). Independent evidence for the Daedalia, Utopia and Elysium Basins has been presented by others (6,7,8). Most of the largest recognized basins are in the northern or western hemispheres; we believe that the overlap of these basins is responsible for the lower topography and prolonged volcanism which characterizes the northern lowland plains, and perhaps also for the growth of major volcano-tectonic complexes such as Elysium and Tharsis (3,9). A speculative model for the evolution of the northern lowlands in the Utopia-Elysium region was developed within this context (9,10). More work needs to be done to refine the inventory of major impact basins for Mars and to relate these basins to the earliest crustal development of the planet. We have found evidence in the cumulative frequency curves as well as in the morphology of the basins for a signficant change in properties at Argyre-sized basins (D~1850 km) and at Chryse size basins (D~3600 km) (5). These changes may be related to lithospheric structure at the time of basin formation or to fundamental differences in the impacting population.

(b) Growth and Evolution of the Valles Marineris

Valles Marineris is a complex system of ancient grabens that were modified by erosion and deposition. Our detailed studies addressed several fundamental issues on trough origin and growth. Relative orientations of Coprates Chasma and wrinkle ridges and grabens located on the adjacent southern plateau suggest that the ridges and grabens grew under multiple stress states and probably predate Coprates Chasma itself (11). New structural mapping of the region (12,13) details the discontinuous distribution and interrelationships of wrinkle ridges, grabens and pit-crater chains around the troughs. Although the trough system is often assumed to have nucleated as small pit-craters, pit-crater chains appear to be distinct structures, not trough precursors (14). Unambiguous evidence for strike-slip faulting was found in Early Hesperian ridged plains materials to the south in Coprates (15,16,17). Detailed mapping of the echelon set of plateau grabens located on Ophir Planum and the adjacent Coprates trough bounding faults is unravelling the sequence of faulting in central Valles Marineris. The curving geometries of grabens in Ophir and trough faults near Melas Chasma indicate that the local stress state was spatially variable, but probably regionally uniform, during early trough growth (18). Our work reveals unexpected complexities in the growth and tectonic development of the Valles Marineris region.

(c) Major Resurfacing Events in Martian History

Resurfacing has been a major process during most of martian history, but detailing the characteristics of major events has been difficult. We have adapted the Neukum and Hiller technique (19) for larger crater diameters in order to study older terrains and the resurfacing which has modified them. We showed that a major resurfacing event within and around the highland/lowland transition zone occured at the time of ridged plains emplacement in Lunae Planum and elsewhere (20). Similar study of the Tempe Terra region in western Mars shows

that comparable resurfacing at about the same time occurred there (21) as well as in Xanthe Terra, Lunae Planum and Coprates (22,23). It appears that there was a major, perhaps planet-wide resurfacing on Mars corresponding to the eruption of Lunae Planum Age (LPA) ridged plains. We also find evidence for an older resurfacing event which can be related to intercrater plains development (cratered plateau material) recognized in geologic studies (24). In the Tempe region a common-age resurfacing event younger than LPA affecting the cratered terrain and adjacent plains-forming lowland units appears to correlate with the Vastitas Borealis Formation (21,24). We have also extracted information on the thickness of materials associated with different resurfacing events from the cumulative frequency curves. Thicknesses associated with the major LPA resurfacing vary greatly depending on location: in the Lunae Planum, Tempe and Coprates ridged plains 350-600 m is common (21,23,25) but in the adjacent cratered terrain in Xanthe Terra, Tempe Terra and elsewhere the correpsonding value is less than 100 m. These results can provide an independent stratigraphy based on major resurfacing events correlated at many places around Mars, which can both date the resurfacing events and also locate the depth to older, now buried surfaces.

In a related study (26) we find evidence that what have been mapped as Noachian age ridged plains in Memnonia and Argyre may be Early Hesperian in age. These plains are sufficiently thin that a large number of medium-sized craters show through from an older surface below. This may mean that the eruption of ridged plains was more temporally confined than previously thought, which would have important implications for the thermal history of Mars.

References: (1)Frey, H. and R. A. Schultz, GRL 15, 229-232, 1988. (2)Frey, H. and R. A. Schultz, MEVTV Workshop on Early Tectonic and Volcanic Evolution of Mars, LPI Report 89-04, p35-37, 1989. (3)Frey, H. and R. A. Schultz, 4th Internat. Conf. on Mars, 106-107, 1989. (4)Wilhelms, D. E. and S. W. Squyres, Nature 309, 138-140, 1984. (5)Schultz, R. A. and H. V. Frey, JGR submitted, 1989. (6)Craddock, R. A., R. Greeley and P. R. Christensen, JGR in press, 1990. (7)McGill, G. E., JGR 94, 2753-2759, 1989. (8)Schultz, P. H., LPS XV, 728-729, 1984. (9)Frey, H. and R. A. Schultz, LPS XX, 315-316, 1989. (10)Frey, H. and R. A. Schultz, JGR submitted, 1989. (11)Schultz, R. A. and H. V. Frey, EOS Trans. Am Geophys. Un. 69, 389-390, 1988. (12)Schultz, R. A. and H. V. Frey, 4th Internat. Conf. on Mars, 183-184, 1989. (13)Schultz, R. A. and H. V. Frey, LPS XX, 974-975, 1989. (14)Schultz, R. A., MEVTV Workshop Tectonic Features on Mars, 12-22, 1989. (15)Schultz, R. A., MEVTV Workshop Tectonic Features on Mars, 23-25, 1989. (16)Schultz, R. A., Nature 341, 424-426, 1989. (17)Schultz, R. A., LPS XXI(this volume), 1990. (18)Schultz, R. A., LPS XXI(this volume), 1990. (19)Neukum, G. and K. Hiller, JGR 86, 3097-3121, 1981. (20)Frey, H. V., A. M. Semeniuk, J. A. Semeniuk and S. Tokarcik, Proceed. LPSC 18th, 679-699, 1988. (21)Frey, H. V. and T. D. Grant, JGR submitted, 1989. (22)Grant, T. D. and H. V. Frey, EOS Trans. Am. Geophys. Un. 68, 1342, 1987. (23)Frey, H. V. and T. D. Grant, LPS XX, 313-314, 1989. (24)Tanaka, K. L. Proceed. LPSC 17th, JGR 91, E139-E158, 1986. (25)Frey, H. V., J. A. Semeniuk and T. D. Grant, MEVTV Workshop on Early Tectonic and Volcanic Evolution of Mars, LPI Report 89-04, p38-40, 1989. (26)Frey, H. V., C. E. Doudnikoff and A. M. Mongeon, LPS XXI(this volume), 1990.

ORIGIN OF THE ECHELON GEOMETRIES OF JOINTS AND FAULTS ON PLANETARY SURFACES.

Richard A. Schultz, Geodynamics Branch, NASA Goddard Space Flight Center, Greenbelt, MD 20771.

It is well known that the map traces of joints and strike-slip faults are characteristically discontinuous and that fracture segments or strands are noncolinear (e.g., ref. [1,2]). Adjacent discrete segments step aside and overlap slightly to form what is commonly known as *echelon* joint or fault geometry. This conspicuous geometry is quite common on Earth [3,4], Mars [5], and Europa [6]. Echelon stepovers in map view are found in joints, continental and oceanic rifts, and strike-slip faults and in the down-dip direction of joints and dip-slip faults [7]. The underlying mechanical controls on the development of echelon geometries are similar for both joints and faults [8,9]. An important characteristic of echelon geometry is its scale independence. Echelon stepovers are found along micron sized cracks in glass as well as in kilometer scale oceanic spreading centers [10,11], giving rise to fractal descriptions of joint and fault geometry. Plots of the overlap and separation of echelon fractures (e.g., ref. [4,9,5]) suggest that formation of the echelon geometry is related to the local stresses associated with the tips of joints and faults (e.g., ref. [12]). The process of mechanical interaction between closely spaced joints and faults can produce echelon geometry [8,9] and details of the analysis can be found in those papers.

Briefly, consider two echelon fractures having lengths $2b$, center spacing $2k$, overlap $2o$, and separation $2s$ (Fig. 1). I use the displacement discontinuity version of the boundary element method [13] to calculate the stress fields near echelon fractures. This method is superior to the finite element method for solving elastic crack and fault problems because the inner boundary conditions are easily specified and the displacements along the fractures are efficiently calculated. The displacement discontinuity method is based on the displacement potential functions for a line segment (boundary element) with constant displacement discontinuity (i.e., dislocation) in an infinite linearly elastic plate. In this analysis, the fractures are idealized as cracks in an elastic two dimensional plate and are divided into several elements. Far field remote loading induces displacements across the fractures. These displacements produce a stress concentration around fracture tips. The magnitude of stress concentration at the inner tips of echelon fractures is related to the stress intensity factor, K, which is calculated here from near-tip displacements [14]. Mechanical interaction between echelon fractures is modeled by relating K to the strain energy release rate, or "fracture propagation energy", G (Fig. 2). Fracture growth occurs when G exceeds the critical value for a given material, G_{crit}. These calculations show that growth of the inner tips of closely spaced echelon fractures is first enhanced by interaction, then impeded, so that an overlapping echelon geometry results.

Mechanical interaction between growing joints, veins, and dikes is an important sorting process that controls joint size, spacing, frequency, and rock strength [1]. Interaction between growing strike-slip faults profoundly influences the occurrence and self-similarity of pull-apart basins and push-up ranges [9] as well as the seismicity associated with normal and reverse faults (see ref. [7]). Echelon fracture geometry is found on planetary bodies having different surface gravities and compositions (e.g., Mars, Europa), suggesting that the mechanics of fracture growth and brittle deformation is similar on many, if not all, solar system bodies. Rock mechanics testing of ice-rich mixtures (e.g., ref. [15]) provides an important link between quantification of planetary fractures and remote stresses necessary for growth of the observed fracture systems. These calculations show that important quantitative information on brittle deformation can be obtained from the mechanical analysis of common joint and fault geometries.

REFERENCES: [1] Segall, P., *Geol. Soc. Am. Bull., 95*, 454-462, 1984. [2] Sharp, R.V., *USGS Open File Report, 79-1239*, 1979. [3] Pollard, D.D. and A. Aydin, *Geol. Soc. Am. Bull., 100*, 1181-1204, 1988. [4] Aydin, A. and A. Nur, *Tectonics, 1*, 11-21, 1982. [5] Schultz, R.A., *Nature, 341*, 424-426, 1989. [6] Schenk, P.M. and W.B. McKinnon, *Icarus, 79*, 75-100, 1989. [7] Aydin, A. and A. Nur, in *Strike-Slip Deformation, Basin Formation, and Sedimentation*, SEPM Spec. Publ., 37, 35-44, 1985. [8] Pollard, D.D., P. Segall, and P.T. Delaney, *Geol. Soc. Am. Bull., 93*, 1291-1303, 1982. [9] Aydin, A. and R.A. Schultz, *J. Struct. Geol.*, in press, 1989. [10] Pollard, D.D. and A. Aydin, *J. Geophys. Res., 89*, 10,017-10,028, 1984. [11] Sempere, J.-C. and K.C.

Macdonald, *Tectonics*, 5, 151-163, 1986. [12] Segall, P. and D.D. Pollard, *J. Geophys. Res.*, 85, 4337-4350, 1980. [13] Crouch, S.L. and A.M. Starfield, *Boundary Element Methods in Solid Mechanics*, George Allen & Unwin, 1983. [14] Schultz, R.A., *Int. J. Fracture*, 37, R31-R34, 1988. [15] Beeman, M., W.B. Durham, and S.H. Kirby, *J. Geophys. Res.*, 93, 7625-7633, 1988.

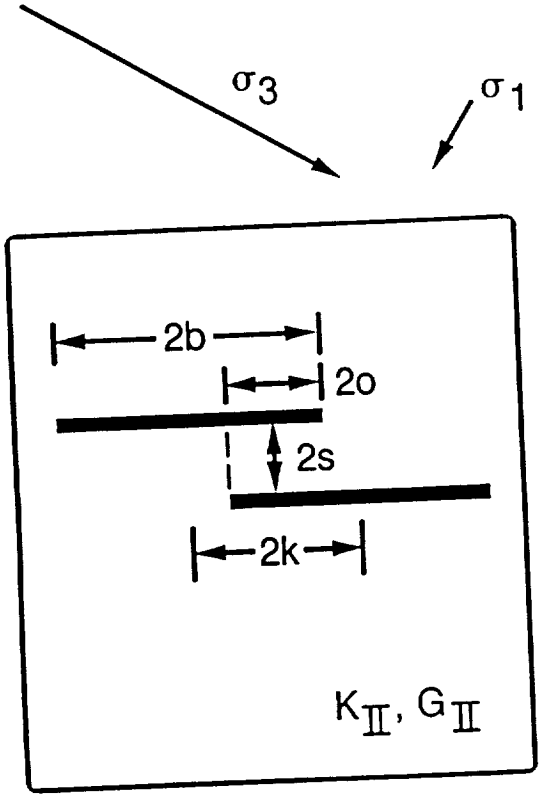

Fig. 1. Geometry of echelon fractures. Far field loading by remote principal stresses σ_3 and σ_1.

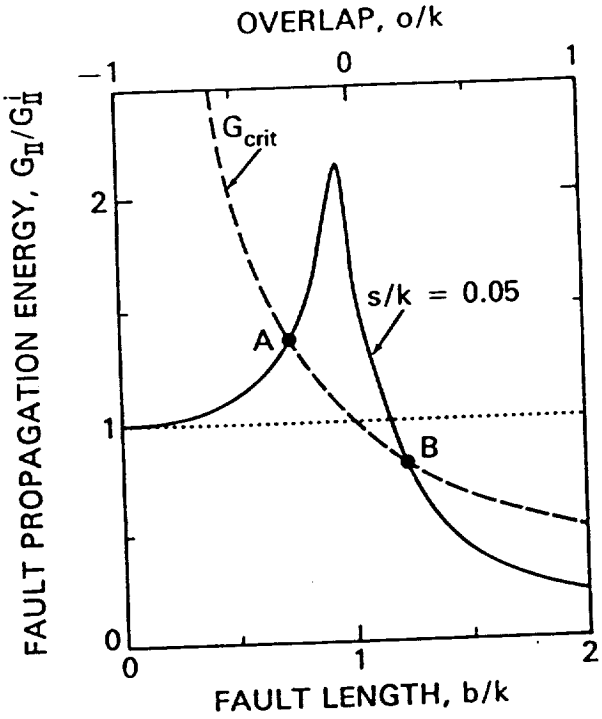

Fig. 2. Dependence of fault propagation energy G on length b/k and separation s/k of echelon faults. Overlap of inner fault tips occurs for positive values of o/k. Fault growth begins at A and stops at B, producing an overlapped geometry.

GEOPHYSICS AT MARS: IMPORTANT ISSUES

R.J. Phillips, Department of Geological Sciences, Southern Methodist University, Dallas, TX 75275.

Introduction. The tectonic and volcanic evolution of Mars is strongly coupled to the evolution of the martian mantle, which has delivered mass and heat to the martian lithosphere over geological time. Understanding the evolution of the martian mantle and unraveling the tectonic and volcanic history are tightly coupled because in the absence of seismic data, surface information and gravity data are the major ways to constrain interior processes. The overall problem is highly underdetermined, but some progress has been made in the sense that there are not an infinite number of interior models that will satisfy the topographical, gravitational and geological constraints available.

Model results for the Global Dichotomy Boundary (GDB) are limited. There is general agreement that this boundary is isostatically compensated, and any scenario that attempts to explain the gross differences between the two hemispheres must include processes that extend to at least the crust-mantle boundary. The global center-of-figure to center-of-mass offset is explained by a combination of an isostatically compensated GDB and a nearly compensated Tharsis.

Most geophysical modeling of Mars has concentrated on the Tharsis and Elysium provinces. Central to these considerations are the relative roles of structural uplift and volcanic construction in the creation of immense topographic relief [1,2]. The origin, classification, and relative timing of tectonic features has also been a subject of focused study [3,4].

Stress Modeling. The observation of grossly organized tectonic patterns associated with Tharsis (and to a lesser extent Elysium) have led to the formulation of a number of theoretical elastic and isostatic models of the interior [5-8]. Such models are constrained by the observed gravity and topography, satisfy the equations of mechanical equilibrium, and are used to predict stress type, magnitude, and direction in the lithosphere. The results depend on the estimate of the non-hydrostatic component of the second zonal harmonic gravity, J_2. This estimate and the corresponding estimate of the mean moment of inertia have been the subject of recent debate [9,10].

If tectonic features on Tharsis can be separated into stratigraphic groups with relative age firmly established [3], and if these groups can be related to specific mechanical models of the interior, then scenarios for interior evolution can be worked out. Generally, three types of mechanical models have been recognized: (i) isostatic, (ii) flexural loading, and (iii) flexural uplift. In model (i) the flexural rigidity D is set to zero and the stress distribution is governed solely by membrane and gravitational forces. Addition of a non-zero D leads to a different stress distribution, which depends on whether the lithosphere is loaded from above [model (ii); e.g., volcanic piles] or loaded from below [model (iii); e.g., buoyant uplift]. Model (i) cannot distinguish isostatic loading from isostatic uplift.

Graben in the Claritas Fossae region of Tharsis are mapped as Early Noachian in age [3]. Flexural uplift models predict extensional stresses at Claritas Fossae [8] that are approximately orthogonal to the mapped tectonic features [11]. This suggests that flexural uplift was an early phase in the tectonic evolution of Tharsis. To first order, radial graben and fractures on the

C-6

periphery of Tharsis are consistent with flexural loading models [5-7], while tectonic features in the immediate Tharsis area are best explained by isostatic models [6,7]. *Detailed* matching of stress predictions with tectonic features is more problematical. This is partly due to the extremely poor knowledge of martian topography and partly because all modeling efforts have no choice but to use the present-day values of the gravity field and topography to predict ancient stress fields. The most complete modeling to date uses spherical harmonic coefficients of the field quantities to degree and order eight [8]. While this model has more resolution than earlier fourth degree models, it may also be noisier. Locally, predictions are successful in some regions but do not match as well as earlier models do in other regions (e.g., Valles Marineris). Attempts to match stratigraphically assigned fracture/graben sets to either flexural loading or isostatic models have also not been successful because of inadequate azimuthal resolution of the stress trajectories in the two types of models.

Petrological Models Related to Geophysics. All of the mechanical models carry an interior density distribution required to match the gravity and topography boundary conditions. Isostatic models, for example, are composed of a low density Pratt-like region in the upper mantle and a thinned crust beneath Tharsis. Flexural loading models carry a thickened crust. The Pratt zone in the isostatic model can be interpreted in terms of a low density mantle residuum formed by partial melting that produced basaltic magmas [12]. Isostatic models have been formulated that satisfy the gravity and topography boundary conditions and conserve mass in a partial melting sequence. More recent work [11] has concentrated on the implications of a requirement for uplift, as suggested by the fault distribution and elevation of Claritas Fossae. While most of the buoyancy for uplift is provided by a low density residuum, a crustal extrusive load will strongly counteract this effect unless it is only a small portion of the melt products generated beneath Tharsis. Thus most of the Tharsis magmas may have ended up as intrusive bodies in the crust and upper mantle. During the period of intense tectonism of Tharsis (Hesperian time and earlier), volcanism was not as active at Tharsis as it was on other parts of Mars [13]. Later (Late Hesperian, Amazonian), Tharsis accounted for about half of the planet's volcanism. The picture that is emerging is that early in the history of Tharsis, massive intrusion led to tectonic disruption of the surface. Subsequently, magmas made their way to the surface and tectonism waned. The reason for this evolution may have been decreasing melt density as the partial melting process evolved toward lower iron content of basaltic magmas. The concept of massive intrusion leading to the immense relief of Tharsis blurs the distinction between uplift and constructional models.

Future Directions. While geological mapping of Tharsis has reached a high level of maturity, there are major areas of geophysical modeling yet to be carried out. Time-dependent thermoelastic modeling has not been considered, nor has stress modeling with the majority of the flexural load in the form of intrusive bodies. Considerable work on the spatial and temporal variation of elastic lithospheric thickness [14] and inferred temperature gradient [15] has not been incorporated into the regional-scale stress modeling described above. The accuracy and resolution of stress modeling will undergo marked improvement with the topography and gravity field information to be acquired by Mars Observer. Finally, some of the models for the origin and evolution of Tharsis, which predict specific differences in magma composition as a function of age, can possibly be tested with data acquired by the remote sensing instruments on Mars Observer.

References. [1] Solomon, S.C., and J.W. Head, *JGR, 87*, 9755, 1982; [2] Phillips, R.J., *et al.*, *JGR, 78*, 4815, 1973; [3] Tanaka, K.L., and P.A. Davis, *JGR, 93*, 14893, 1988; [4] Tanaka, K.L., *Proc. Lunar Planet Sci. Conf. 20th*, in press, Cambridge Univ. Press, 1990; [5] Willemann, R.J., and D.L. Turcotte, *JGR, 87*, 9793, 1982; [6] Banerdt, W.B., *et al.*, *JGR, 87*, 9723, 1982; [7] Sleep, N.H., and R.J. Phillips, *JGR, 90*, 4469, 1985; [8] Banerdt, W.B., *et al.*, in *Mars*, University of Arizona Press, in press, 1990; [9] Kaula, W.M., *et al.*, *GRL, 16*, 1333, 1989; [10] Bills, B., *GRL, 16*, 385, 1989; [11] Phillips, R.J., *JGR, 95*, in press, 1990; [12] Finnerty, A.A., *et al.*, *JGR, 93*, 10225, 1988; [13] K.L. Tanaka, personal communication, 1989; [14] Comer, R.P., *et al.*, *Rev. Geophys., 23*, 61, 1985; [15] Solomon, S.C., and J.W. Head, *JGR, 95*, in press, 1990.

THE THARSIS STRESS PARADOX: A POSSIBLE SOLUTION

W. B. Banerdt and M. P. Golombek, Jet Propulsion Laboratory,
California Institute of Technology, Pasadena, CA 91109

Introduction: Tharsis is intensely fractured by long, narrow grabens that extend radially hundreds of kilometers beyond the rise and is ringed by mostly concentric wrinkle ridges that formed over 2,000 km from the center of the rise. Its size, involving a full hemisphere of Mars, gives it a central role in the thermal and tectonic evolution of the planet. This has stimulated a number of studies attempting to determine the sequence of events responsible for this unique feature [e.g., 1–5]. Many of these investigations relied on the distinct stress patterns generated by various mechanisms for topographic support to help constrain the relative timing of phases in the history of Tharsis. Recent mapping results, however, have cast doubt on the validity of this exercise. In this abstract we first review the constraints that gravity and topography data place on the current structure of Tharsis, along with the results of theoretical deformation models. We then compare these constraints with insights into its development derived from comparisons of detailed regional mapping of faulting, and describe the so–call "stress paradox". Finally, a self–consistent model for the structure of Tharsis is proposed which provides a possible solution.

Gravity and Topography: The gravity and topography of Tharsis show a high degree of correlation, with a large proportion of the spectral power contained in the lowest harmonics (degrees 2–3). The apparent depth of compensation derived from the spectral admittance depends strongly on wavelength, ranging from over 1000 km at degree 2 to about 100 km for the shorter wavelengths [6]. Stated plainly, there is a large excess of gravity at long wavelengths relative to that which can be explained by simple compensation models. There are a limited number of ways to realistically accommodate this. One is isostatic compensation utilizing a density dipole, with a shallow positive anomaly overlying a deeper negative anomaly [4, 7]. This model requires massive removal of crustal material and static support by a thick (~300–400 km), immobile layer of magmatically depleted mantle. Another approach is dynamic support by mantle convection [8, 9]. This would imply a single immense plume that has not moved significantly with respect to the lithosphere since the Noachian. The third possibility is partial flexural support of the load [2]. In this case a modestly thicker crust is required with a >100 km thick lithosphere that is capable of supporting stresses of several hundred MPa.

Faulting: The timing and extent of faulting around Tharsis is both long–lived and varied, involving both local/regional events and full hemispheric events [1, 10–12]. For hemisphere–wide patterns relevant to the theoretical stress models, three distinct events have been recognized. In the upper Noachian, a radial system of grabens formed that marks the first unequivocal tectonic event in the formation of Tharsis. This fracture system, centered on Syria Planum [10], can be traced from near the center of the rise to beyond its flanks in exposed Noachian–aged units. In the lower Hesperian, massive outpourings of fissure volcanics formed the surface now recognized as Lunae Planum and similarly–aged plains surrounding Tharsis (the so–called ridged plains). Shortly after deposition of the plains, concentric wrinkle ridges formed [11] that are also centered in Syria Planum. By upper Hesperian times another enormous radial normal faulting event occurred, this time centered near Pavonis Mons [10]. This was followed by long–lived volcanism (throughout the Amazonian) to form the prominent central volcanoes of Tharsis and their aprons. One other faulting event has been related to stress models. A system of E–W trending normal faults formed in Claritas Fossae, an uplifted horst of Noachian–aged terrain that is covered by all Hesperian and Amazonian units [5, 12].

These faults are consistent with a Tharsis–concentric pattern, but this fracture system is only found in a limited area, so its regional significance is unclear.

Stress calculations: These two types of information, gravity/topography and surface strain, can be linked in a complementary fashion via theoretical stress modelling [2, 4]. In broad terms, three distinct fault patterns can be generated at the surface of a spherical shell that supports a roughly circular, long–wavelength topographic high by static means. If the topography is due to uplift of the lithosphere, circumferentially oriented extensional features within the uplifted portion and radially oriented compressional features in the periphery are predicted. In contrast, a surface load that causes subsidence of the lithosphere predicts the opposite sense of faulting, with circumferential ridges within the load region and radial extensional faulting farther out. Isostatic support of topography generates a stress field that predicts radially oriented normal faulting in a region around the topographic center and circumferential ridge formation near its edges. In addition, the isostatic stresses are much smaller in magnitude than those for the flexural cases (~50 MPa vs. 200–400 MPa). Stresses due to convective support of topography are still under study, but the patterns are likely to be similar to those of the uplift case.

These results place some strong constraints on the evolution of Tharsis as reflected in its structural record. Only the uplift case (and, possibly, convective support) can form circumferentially oriented grabens [2]. Such grabens have tentatively been identified only in the oldest (early Noachian) units in Claritas Fossae [5, 12]. Thus this mechanism can be ruled out for all but perhaps the earliest stages of formation. Circumferentially oriented ridges near the edge of the rise are a feature of both the isostatic and subsidence cases, with the former extending the ridge zone outward and the latter extending it inward [2, 4]. Thus the distribution of ridges is broadly consistent with either isostasy or flexure, but tends to marginally favor an isostatic regime. The most clear–cut distinction between these two cases, however, is in the respective regions of radial extensional faulting. Inner radial faulting is possible only in the isostatic case, whereas outer radial faulting can occur only in the subsidence case [2, 4]. This result led to the expectation that the relative timing of radial faulting episodes determined from geologic mapping would provide the key needed to construct the tectonic history of Tharsis [2].

Stress paradox: The conditions under which the inner and outer radial faulting form in a spherical lithosphere have been shown to be mutually exclusive, and cannot exist coevally. However recent stratigraphic mapping has shown that both inner and outer radial faulting have occurred contemporaneously over a considerable interval of Tharsis history [13]. Thus there is a fundamental contradiction between apparently robust model results and observation that must be resolved in order to understand the evolution of this crucial region.

Proposed model: The cause of this contradiction must lie in the limitations of the global elastic lithosphere models used to generate the stress results. The stress models described above assume that the load is supported by a homogeneous elastic shell. But the actual rheology of the lithosphere is undoubtedly more complex [e.g., 13–15]. Laboratory and field measurements on Earth indicate that the strength of rocks in the shallow lithosphere is generally limited by frictional sliding on preexisting faults, giving a strength that increases with depth. At the higher temperatures characteristic of the lower portions of the lithosphere ductile creep becomes the strength–limiting factor, with the conductive thermal gradient causing a decrease in strength with depth. In addition, ultramafic minerals characteristic of mantle rocks have a considerably higher creep resistance than those minerals common in crustal rocks. Thus the lithosphere may have two strength maxima separated by a ductile layer in the lower crust. The existence and strength of this ductile layer will depend on the crustal thickness and thermal

gradient, with larger values of either of these parameters making such a layer more pronounced.

The gravity observations described above, along with the difficulties inherent in creating a realistic isostatic structure, argue for current flexural support of the Tharsis load. In addition, most of the regional tectonic deformation, with the notable exception of the inner radial faulting, is consistent with subsidence of the lithosphere. Thus most evidence, again with the exception of the inner radial faulting, is consistent with a major component of flexural support since the late Noachian. We contend that the formation of the inner radial fault pattern is a natural consequence of the thickened crust and higher heat flow resulting from the extrusive and intrusive volcanic construction of the Tharsis rise.

As Tharsis is formed by construction, it acts as a flexural load on the elastic lithosphere [3]. Far from Tharsis, where the crust is relatively thin and the heat flow modest, the lithosphere is made up of a single mechanical unit consisting both the crust and upper mantle. However within Tharsis itself the thickened crust and high heat flow that are characteristic of prolonged magmatism will act to form a weak lower crustal layer that will decouple the brittle upper crust from the strong zone in the upper mantle. In this situation the upper mantle strong layer, which constitutes most of the lithosphere in either case, will deform as part of the global shell, transferring flexural stresses and displacements to the rest of the shell. But the relatively thin, brittle upper crustal layer will deform not as part of the greater shell, but rather as a spherical cap with a lubricated lower surface and a peripheral boundary which is fixed to the global shell. Thus it will respond primarily to isostatic or downslope spreading forces [16] and to increases in its radius of curvature induced by the subsidence of the lower lithosphere [17, 18]. Both processes induce circumferential extension within the cap, and have sufficient magnitude to lead to radial faulting within the highland area. Outside this region of decoupled crust, faulting will be due to flexural stresses caused by the overall lithosphere depression. Radial compression is likely to be concentrated near the boundary of the two regions.

The lithospheric model proposed here is supported by a recent analysis by Solomon and Head [15] of elastic lithosphere thickness estimates. They found that the range of thicknesses derived from flexural modelling of volcanic and basin loads [19] could be explained by thicker crust and higher heat flow beneath the volcanic provinces of Tharsis and Elysium, resulting in a mechanical decoupling of the upper crust from the mantle.

Thus a model in which Tharsis was formed primarily as a flexural load on the lithosphere through massive extrusive and intrusive magmatism appears to be consistent with most geophysical and geological constraints.

References: [1] Wise et al., *Icarus* **38**, 456, 1979; [2] Banerdt et al., *JGR* **87**, 9723, 1982; [3] Solomon and Head, *JGR* **87**, 9755, 1982; [4] Sleep and Phillips, *JGR* **90**, 4469, 1985; [5] Phillips et al., *JGR*, in press, 1990; [6] Phillips and Saunders, *JGR* **80**, 2893, 1975; [7] Sleep and Phillips, *GRL* **6**, 803, 1979; [8] Bills et al., *LPSC XVII*, 48, 1986; [9] Kiefer and Hager, *MEVTV: Early Tect. Volc. Evol. Mars*, 48, 1988; [10] Plescia and Saunders, *JGR* **87** 9775, 1982; [11] Watters and Maxwell, *JGR* **91** 8113, 1986; [12] Tanaka and Davis, *JGR* **93**, 14893, 1988; [13] Banerdt et al., Stress and Tectonics, *Mars*, in press, 1990; [14] Brace and Kohlstedt, *JGR* **85**, 6248, 1980; [15] Solomon and Head, *JGR*, in press, 1990; [16] Artyushkov, *JGR* **78**, 7675, 1973; [17] Turcotte, *Geophys. J.* **36**, 33, 1974; [18] McKinnon,.*Proc. LPSC 12th,* 1585, 1981; [19] Comer et al., *Rev. Geophys.* **23**, 61, 1985.

SYMMETRY OF INFERRED STRESS FIELDS IN THE THARSIS REGION OF MARS. Thomas R. Watters and Michael J. Tuttle, Center for Earth and Planetary Studies, National Air and Space Museum, Smithsonian Institution, Washington, D.C. 20560, and Francis J. Kiger, Department of Geology and Astronomy, West Chester University, West Chester, Pennsylvania, 19383

Understanding the origin of the stresses that generated the radial fracture system and circumferential wrinkle ridge system on the Tharsis Plateau is key to unraveling the tectonic evolution of the region. Banerdt et al. (1,2) and Sleep and Phillips (3) have proposed models for the origin of the stresses and calculated stress trajectories that can be compared to the observed tectonic features. The stress fields predicted in these models are strongly radial to an area near Pavonis Mons. If these models are correct, the stress inferred from the structures should be strongly radial to this area.

The radial nature of the inferred stresses has been analyzed using a stereonet in a number of studies (4,5,6,7). In a recent study, Golombek (8), using graben data compiled by Plescia and Saunders (5) and ridge data subsampled into length-weighted vector means compiled by Watters and Maxwell (6), concluded that the graben and wrinkle ridges define a significantly radial system. With respect to the wrinkle ridges, this conclusion is in contrast to the findings of Watters and Maxwell (6) and is not the result of a net manipulation error as reported by Golombek (8). The method used by Golombek (8) involves fitting great circles with the correct angular relationship on the net to the vector normals. The resulting great circles are then geographically correct traces of the inferred principal stress on the surface. Watters and Maxwell (6) used the azimuth of the vector normals to fit the great circles. This method does not generate geographically correct traces of the inferred stresses, but can be used to test radial symmetry.

In an effort to address the question of the significance of the radial symmetry of the system of structures, a wrinkle ridge data set consisting of 1845 ridge segments and a graben data set consisting of 6841 fault segments is used in a beta analysis. Great circles that are geographically correct traces of the inferred principal stresses (8) are fit to each graben segment and the normals to each ridge segment. The 1.7 million intersections of the ridge data are distributed in a broad girdle with a maximum concentration of 5% per 1% area centered at approximately 5°S, 110°W (fig. 1). The 32 million intersections of the graben data are distributed in a symmetric pattern, elongated in a N-S direction with a maximum concentration of 12% per 1% area roughly centered at 3°S, 110°W (fig. 2).

The agreement between the locations of the maximum concentrations of intersections for the two systems of structures supports models where isostatic and flexural loading stresses result from the observed topography and gravity (1,2,3). However, in the isostatic case of Banerdt et al. (2), the predicted compressional stresses would result in a strongly radially symmetric ridge system (maximum concentration of 45% per 1% area located at roughly 5°N, 105°W). Even when the predicted stress trajectories are varied by as much as 10°, the maximum concentration does not approach 5%.

A possible explanation for the difference between the predicted stresses and those inferred from the observed structures is that some component of the total stress responsible for the wrinkle ridges is not accounted for in the models. Additional components of stress may have resulted from: 1) gravitationally induced down-surface slope stresses (9) generated when the

regional topographic slope was greater than at present, and 2) local and/or regional subsidence.

References Cited: (1) Banerdt, W.B., R.J. Phillips, N.H. Sleep, and R.S. Saunders, *JGR, 87*, 9723-9733, 1982. (2) Banerdt, W.B., M.P. Golombek, and K.L. Tanaka, submitted to *Mars*, University of Arizona Press, Tucson, 1989. (3) Sleep, N.H. and R.J. Phillips, *JGR, 90*, 4469-4489, 1985. (4) Wise, D.U., M.P. Golombek and G.E. McGill, *Icarus, 38*, 456-472, 1979. (5) Plescia, J.B. and R.S. Saunders, *JGR, 87*, 9775-9791, 1982. (6) Watters, T.R. and T.A. Maxwell, *JGR, 91*, 8113-8125, 1986. (7) Schultz R.A., *JGR, 90*, 1985. (8) Golombek, M.P., *LPSC XX*, 345-346, 1989. (9) Elliott, D., *JGR, 81*, 949-963, 1976.

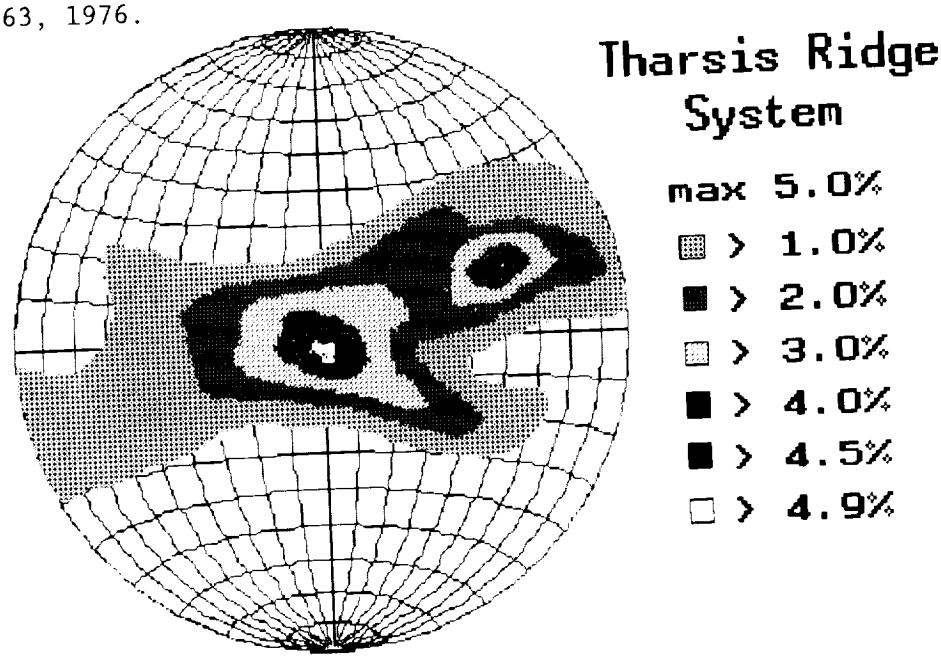

Fig. 1. Contours 1-2-3-4-4.5-4.9% per 1% area.

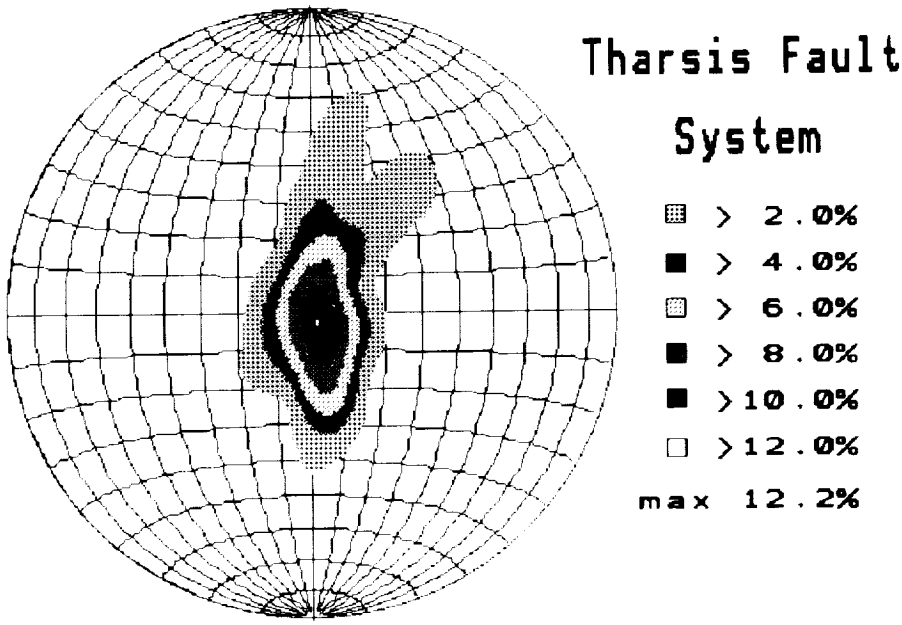

Fig. 2. Contours 2-4-6-8-10-12% per 1% area.

DISTRIBUTION OF STRAIN IN THE FLOOR OF THE OLYMPUS MONS CALDERA. Thomas R. Watters and D. John Chadwick, Center for Earth and Planetary Studies, National Air and Space Museum, Smithsonian Institution, Washington, D.C. 20560, and Michael C. Liu, Department of Astronomy, Cornell University, Ithaca, NY 14853

The Olympus Mons caldera is made up of six coalescing volcanic craters (fig. 1). Based on comparisons with terrestrial volcanoes, such as Mauna Loa, Hawaii (1, 2), the volcanic craters are interpreted to be the result of collapse of a solidified lava lake due to evacuation of the magma chamber during late-stage summit activity (3). The floors of several of the craters are characterized by a large number of deformational features in the form of graben and wrinkle ridges. The largest and oldest of the volcanic craters (crater 6, see 3), approximately 65 km in diameter, has a well developed circumferential graben system in the margins of the floor (fig. 1). Wrinkle ridges are present in the interior of the floor but have been sharply truncated by at least three successive collapse episodes.

The origin of the stresses that generated the observed structures is likely the result of subsidence of the central portion of crater floors (3). Using topography derived by Wu et al. (4), subsidence is evident across the floor of the large crater (fig. 2, 5X vertical exaggeration). The cause of the subsidence is presumed to be loss of support of the caldera floor by withdrawal of the underlying magma, probably the result of flank eruptions. In a finite element analysis, Zuber and Mouginis-Mark (5) have shown that compressive and extensional stresses compatible with the generalized location of the structures can be generated by subsidence. A detailed assessment of the location of the wrinkle ridges and graben relative to the topography is useful in refining such models.

The distribution of the circumferential graben on the floor of large crater is not uniform. Mouginis-Mark (3) notes that the widths of graben are greatest near the crater edge and narrow toward the center of the floor. The most extensive fracturing of the floor is on the southern edge, near the rim of the of crater 3 (fig. 1). The average slope of the floor in the area of these graben is roughly 4° (fig. 2), the largest slopes observed on the floor. On the northern edge, there are fewer graben and the average slope of the floor is less (roughly 3°). Thus, the areas of greatest slope and possibly greatest flexure of the floor correspond to areas with the greatest observed extension. This correlation supports the assumption that the structures are the result of downward displacement of the floor. As noted by Zuber and Mouginis-Mark (5), many of the wrinkle ridges occur in topographic lows. In contrast to the circumferential graben, the ridges are not strongly radially distributed, but are confined to a roughly E-W oriented trough (fig. 2). The most prominent wrinkle ridge on the crater floor is located close to the area of lowest elevation. The average slope of the floor in area of the ridges is $\leq 2°$. Preliminary estimates of the bulk horizontal shortening and extension in the crater floor, using average values of the shortening across the ridges (see 6) and the extension across the graben (see 7), are roughly compatible at 1.5-2.0 km. Based on the topography and the distribution of structures, the subsidence appears to have been asymmetric with greater downward displacement and deformation of the southern half of the floor.

References Cited:
(1) Carr, M.H., *JGR, 78*, 4049-4062,1973. (2) Greeley, R., *Geology, 1*, 175-180, 1973. (3) Mouginis-Mark, P.J., *Proc. LPSC XII*, 1981. (4) Wu, S.S.C., P.A. Garcia, R. Jordan, F.J. Schafer and B.A. Skiff, *Nature, 309*, 432-435, 1984. (5) Zuber, M.T. and P.J. Mouginis-Mark, *LPI Tech. Rep. No. 89-06*, 74-75, 1989. (6) Watters, T.R., *JGR, 93*, 10,236-10,254, 1988. (7) Golombek, M.P., *JGR, 84*, 4657-4666, 1979.

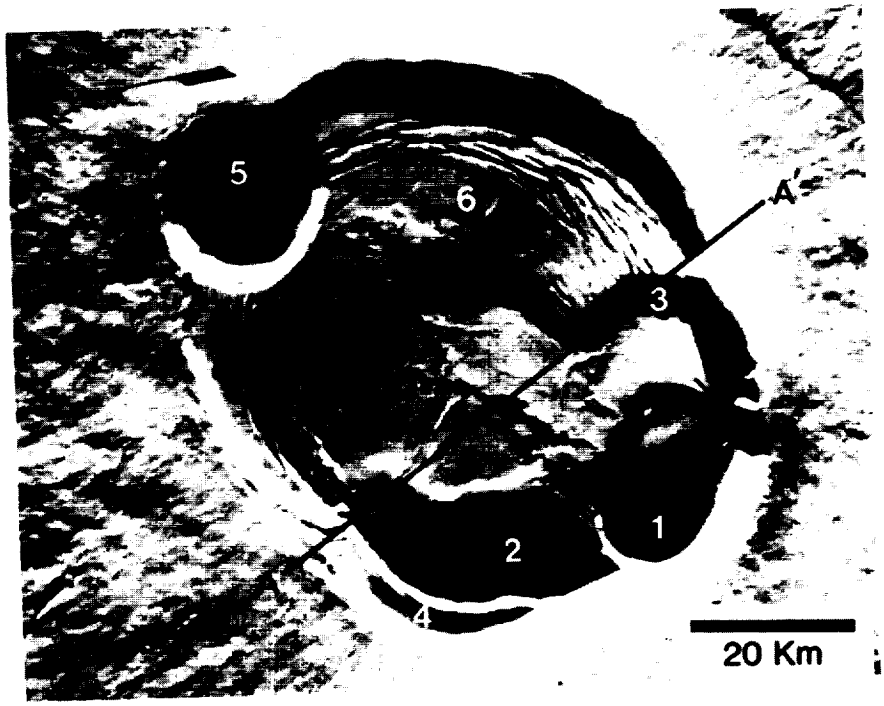

Fig. 1. Nested summit caldera of Olympus Mons.

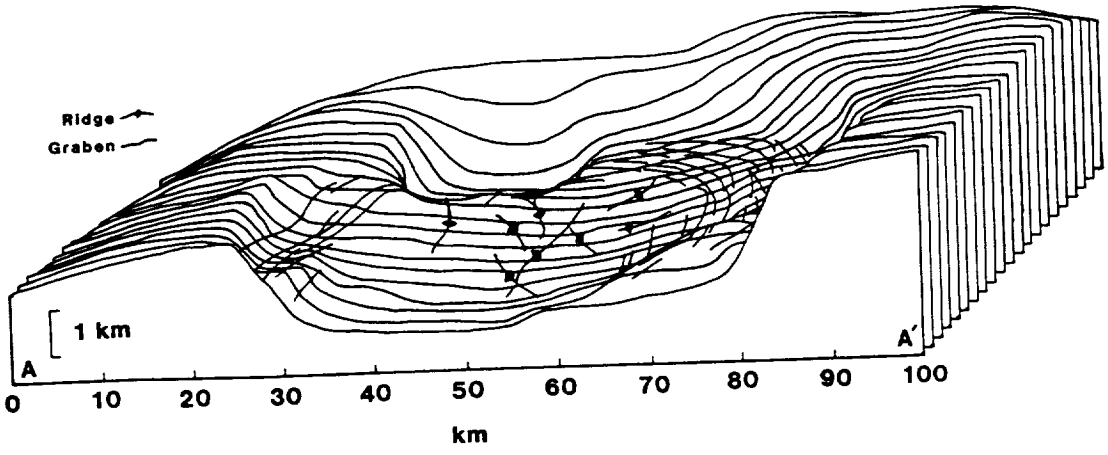

Fig. 2. Topographic profiles of a portion of the caldera with the location of prominent wrinkle ridges and graben.

Flank Tectonics of Martian Volcanoes

Paul J. Thomas
Dept. of Physics and Astronomy, University of Wisconsin, Eau Claire, WI 54702
Steven W. Squyres
Center for Radiophysics and Space Research, Cornell University, Ithaca, NY 14853
Michael H. Carr
U.S. Geological Survey, Menlo Park, CA 94025

Olympus Mons exhibits a series of terraces on its slopes, concentrically distributed around the caldera. The base of each terrace is marked by a modest but abrupt change in slope. Above the base, the slope decreases gradually with height, creating a gentle, convex topographic profile. In some locations, several terraces are located one above another. They occur in a region roughly 25% to 75% of the radius from summit to base.

The sharp break in slope at the base of the terraces and the apparent dislocation of some flows suggests an origin by faulting. However, the faulting does not appear to be analogous to the "pali" around the periphery of the Hawaiian shields, which result from normal faulting associated with outward movement of the shield flanks. Normal faults typically are marked by a steep escarpment with sharp breaks in slope at their base and crest. This is true of the peripheral faults on Kilauea and Mauna Loa, and is true also of the numerous normal faults on Mars. In contrast, the terraces on Olympus Mons have a sharp break in slope at their base, and gentle convex upward profiles. Here we explore the possibility that the breaks in slope are caused by thrust faults that formed penecontemporaneously with emplacement of the flows on the volcano flanks, due to compressional failure of the cone.

In an attempt to understand the mechanism of faulting and the possible influences of the interior structure of Olympus Mons, we have constructed a numerical model for elastic stresses within a martian volcano using an incompressible, Eulerian finite element formulation (1,2).

For Olympus Mons, our model represents the volcano as an axisymmetric truncated cone, 21 km in height, with upper and basal radii of 50 km and 250 km, respectively. The cone rests upon a base 100 km thick and 500 km in radius. The base is constrained below and at its outer edge by rigid boundary conditions. Numerical tests show that the base is sufficiently large to completely avoid edge effects.

The model incorporates a magma chamber. The magma chamber has a diameter equal to that of the caldera, $\approx$ 100 km. Given this diameter, the magma chamber clearly is far from spherical; we model it as an oblate spheroid. For the case of Kilauea, accurate measurements of surface tilting are best explained by pressurization of a magma chamber at a depth of 2 – 6 km (3). This requires that the chamber be within the edifice, raised above the surrounding plains. The vertical location of the magma chamber probably is controlled by the buoyancy of the magma, as it ascends though material of decreasing density (4). The variation in density with depth is predominantly due to the closing of voids by hydrostatic pressure at depth. Scaling the depth of the Kilauea magma chamber (4) for gravity, we find that an appropriate vertical extent is 5 – 15 km below the summit. This implies that the magma chamber is elevated over 10 km above the surrounding plains.

The magma chamber in the model may be vacant, filled but unpressurized, or pressurized. Pressurization of the magma chamber is simulated by specifying normal stresses as boundary conditions on the magma chamber walls. The density of the material throughout the volcano is 2050 kg m^{-3}, and a value of Young's modulus appropriate to basalt, 9×10^{10} Pa s, is adopted.

For a full magma chamber, the stress environment at the surface is dominated by a region of compressive stress occupying the middle portion of the slope, appropriate to the formation of thrust faults there. Maximum compressive stresses are $\sim$250 MPa. These stresses arise from the

general elastic deformation of the cone, and represent a net reduction in surface area. In addition to these prominent stress features, there is a region of compressive tangential stress at the summit, ringed by a region of extensional stress. However, the stresses here are much smaller ($\sim$10 MPa). The location of the greatest extensional stresses is found on the lower slopes of the cone when the chamber is filled, occupying roughly the lowest third of the flanks. The stresses here are < 30 MPa.

A similar stress distribution is observed when the cone contains a vacant magma chamber. In this case, however, compressive stresses tend to be more equally distributed over the volcano slopes, and no extensional stress is evident on the lower slopes. This is apparently because the presence of a vacant magma chamber permits increased compression of the edifice and, accordingly, more pronounced compression on the slopes. Assuming that the escarpments on Olympus Mons are indeed the expressions of the thrust faults, we find that a full chamber produces a stress distribution most consistent with the observed distribution.

If the magma chamber is pressurized, additional extensional stresses can occur at the summit and the upper slopes of the cone. For a magma chamber pressure of 100 MPa (twice the overburden), the maximum extensional stress is $\sim$200 MPa. While such stresses could readily cause extensional faulting, it is unlikely that the material of the volcano could support such large overpressures without extrusion taking place.

Terraces like those on the flanks of Olympus Mons are also observed on three other martian volcanoes: they are very prominent on Ascraeus Mons, and present but less well-developed on Arsia Mons and Pavonis Mons. Alba Patera, which has a diameter over twice that of Olympus Mons, does not have them. If the occurrence of these features, which we believe are due to thrust faulting, is related to edifice size, then clearly large diameter alone is not a sufficient requirement. We therefore considered the influence of both diameter D and mean slope h/D, where h is the edifice height, on flank stresses.

Calculations for a range of h/D and D show that the maximum compressive stress found on the flanks is a simple linear function of these parameters. By modeling volcanoes with various diameters and slopes, then, we can extend the results obtained for Olympus Mons to the other martian volcanoes. We find that the four volcanoes with the largest stresses are the only ones on which concentric flank terraces are observed, lending considerable support to the view that these features form by thrust faulting.

It is useful to compare our calculated maximum stresses to laboratory data for the strength of basalt. Estimates for the unconfined uniaxial compressional strength of basalt vary from 124 MPa (5) to 262 MPa (6) for basalts with densities similar to that assumed for this model. We can then investigate the range of edifice dimensions h/D and D that will produce flank stresses that meet or exceed this failure strength. Dimensions of the major martian volcanoes are taken from Pike (8). All four volcanoes that exhibit flank terraces lie well within the regime where failure, and hence thrust faulting, is expected. All other martian volcanoes, which are free of terraces, have flank stresses below the failure strength of basalt. Simplifying assumptions of this model, in particular incompressibility (7) and neglect of lithospheric flexure, have the effect of understimating stresses on the volcano flanks, and do not alter this conclusion.

References:

1) Thompson, E.G. & M.I. Haque (1973) *Int. J. Num. Methods Eng.*, **6**, 315-321.

2) Thompson, E.G. (1975) *Int. J. Num. Methods Eng.* **9**, 925-932.

3) Macdonald, G.A. (1961) *Science*, **133**, 673-679.

4) Ryan, M.P. (1987) *U.S. Geol. Surv. Prof. Pap. 1350*, vol. 2, 1395-1447.

5) Hathaway, A.W. & G.A. Kiersch (1982) in *Handbook of physical properties of rock*, CRC Press.

6) Handin, J. (1966) in *Handbook of Physical Constants*, GSA Memoir 97.

7) Deterich, J.H. (1988) *J. Geophys. Res.*, **93**, 4258-4270, 1988.

8) Pike, R.J. (1979) in *Proc. 9th Lunar Planet. Sci. Conf.*, pp. 3239-73, Pergamon, New York.

THE NATURE AND ORIGIN OF PERIODICALLY SPACED WRINKLE RIDGES ON MARS. Thomas R. Watters, Center for Earth and Planetary Studies, National Air and Space Museum, Smithsonian Institution, Washington, D.C. 20560.

Over 3% of the surface of Mars is covered by smooth plains material characterized by landforms analogous to mare wrinkle ridges. Although the exact nature of these ridged plains materials has not been directly determined, indirect evidence suggests they are the result of flood volcanism (1,2,3). The origin of wrinkle ridges is also not agreed upon, and recent debates have focused on the role of buckling and reverse or thrust faulting (3,4,5). However, the general consensus is that wrinkle ridges are tectonic in origin resulting from horizontal compressive stresses.

The largest known occurrence of wrinkle ridges on the terrestrial planets, observed within a distinct physiographic province, is on the Tharsis Plateau of Mars (6). The average spacing, evaluated in six provinces of the Tharsis ridge system, is 30 km (2,934 measurements), equal to the average spacing of the crosscutting wrinkle ridges of Hesperia Planum (7). There have been a number of buckling models proposed to explain the periodic nature of the wrinkle ridges (8,9,10,11,12) and some recent debate as to whether the lithosphere is involved in the deformation (thick-skinned) or not (thin-skinned). One reason for considering models that do not require wrinkle ridges be rooted in the lithosphere is the unlikelihood that stresses penetrating both the crust and lithosphere were involved in the deformation of ridged plains units well distant from Tharsis, particularly the many relatively small, isolated areas of ridged plains material that occupy topographic lows within intercrater plains.

In the models evaluated in this study, it is assumed that the ridged plains material behaves as both a single member and a multilayer with frictionless contacts, resting on a mechanically weak megaregolith substrate of finite thickness that has buckled at a critical wavelength of folding. The basement does not directly participate in the deformation that results in the ridges, thus no assumption of whole or partial lithosphere deformation is necessary to explain the periodic spacing. Free slip between layers is assumed based on the possible existence of mechanically weak interbeds in the ridged plains sequence separating groups of flows. Interbeds separating groups or units of flows are not uncommon within mare basalts on the Moon or in terrestrial continental flood basalt sequences (13,14,15) and may contribute to the localization of buckling (16). The rheologic behavior of the ridged plains and megaregolith are approximated by a linear elastic and linear viscous material. The models are examined for a range in: 1) the strength contrast between the ridged plains material and the underlying megaregolith of 100, 1,000 and 5,000; 2) thickness of the ridged plains material of 250 to 3,500 m; 3) thickness of the megaregolith of 1,000 to 5,000 m; and 4) number of layers (n) of 1 to 12. For the elastic case, wavelengths consistent with many of the observed spacings are obtained at critical stresses below the yield-strength of a basalt-like material for $n > 5$. For $n = 8$, wavelengths range from 27 to 42 km for thicknesses of the ridged plains material ranging from 1,900 to 3,500 m over a range in thickness of the substrate of 1,000 to 5,000 m and ratio in Young's modulus of 1,000 to 5,000. The cases of $n = 1$ (i.e., a single member) through 5 do not yield admissible wavelengths. At the upper limit of the model parameters, the average thickness of the ridged plains necessary to account

for the minimum average spacing of the ridges (20 km) is roughly 1,700 m. If the ridge spacing is the result of elastic buckling, the relatively high contrast in Young's modulus required ($\geq$ 1,000) is only possible if there were high pore-fluid pressure within the megaregolith at the time of deformation that reduced the effect of the overburden.

Over the same range in values of the parameters, viscous buckling is much less restricted than the elastic case. The observed wavelengths can be accounted for over almost the entire range of viscosity contrast, ridged plains material thickness and substrate thickness for either a single layer or a multilayer. The minimum average spacing of the ridges can be explained with a single layer (n = 1) at the lower limit of the estimated thickness of the ridged plains material (250 m), at the upper limit of the substrate thickness and viscosity contrast. In addition, viscous buckling is viable if the megaregolith were dry, water-rich or ice-rich at the time of deformation.

References Cited:

(1) Greeley, R., E. Theilig, J.E. Guest, M.H. Carr, H. Masursky and J.A. Cutts, *JGR, 82*, 4039-4109, 1977. (2) Scott, D.H. and K.L. Tanaka, *USGS Map I-1802-A*, Denver, Colo., 1986. (3) Watters, T.R., *JGR, 93*, 10,236-10,254, 1988. (4) Plescia, J.B. and M.P. Golombek, *GSA Bull., 97*, 1289-1299, 1986. (5) Sharpton, V.L. and J.W. Head, *Proc. LPSC IX*, 307-317, 1987. (6) Watters, T.R. and T.A. Maxwell, *JGR, 91*, 8113-8125, 1986. (7) Watters T.R. and D.J. Chadwick, *LPI Tech. Rep. No. 89-06*, 68-70, 1989. (8) Saunders, R.S. and T.E. Gregory, *NASA Tech. Memo. TM82385*, 93-94, 1980. (9) Watters, T.R. and T.A. Maxwell, *LPSC XVI*, 897-898, 1985. (10) Watters, T.R., *Fourth International Conference on Mars*, 206-207, 1989. (11) Zuber, M.T. and L.L. Aist, *LPSC XX*, 1261-1262, 1989. (12) Zuber, M.T. and L.L. Aist, submitted to *JGR*, 1989. (13) Peeples, W.J., R.W. Sill, T.W. May, S.H. Ward, R.J. Phillips, R.L. Jordan, E.A. Abott, and T.J. Killpack, *JGR, 83*, 3459-3468, 1978. (14) Reidel, S.P., T.L. Tolan, P.R. Hooper, K.R. Fecht, M.H. Beeson, R.D. Bentley, and J.L. Anderson, *GSA Sp. Paper 239*, in press, 1989. (15) BVSP, 1286 pp., Pergamon Press, New York, 1981. (16) Watters, T.R., *GSA Sp. Paper 239*, in press, 1989.

PHOTOCLINOMETRIC ANALYSIS OF WRINKLE RIDGES ON LUNAE PLANUM, MARS

J. Plescia, Jet Propulsion Laboratory, California Institute of Technology, Pasadena, CA 91109

Wrinkle ridges are common morphologic features on Mars. Both volcanic and tectonic mechanisms have been suggested to explain their origin (e.g., Quaide, 1965; Strom, 1972; Scott, 1973, Muehlberger, 1974; Lucchitta, 1976, Bryan, 1973); recent work has focused on a compressional origin (Maxwell et al., 1975; Lucchitta, 1977; Sharpton and Head, 1982, 1988, Watters, 1988; Plescia and Golombek, 1986). Analysis of terrestrial analogs has greatly influenced and aided the understanding of wrinkle ridge formation (Plescia and Golombek, 1986). An important aspect necessary to interpret structure is topography. Topographic profiles across ridges can provide important constraints for models of internal structure and analyzing deformation associated with ridges.

Topographic maps for Mars are too coarse (contour interval 1 km) to resolve the topography of individual ridges, therefore, monoscopic photoclinometry (Davis and Soderblom, 1984) was used to derive topographic profiles for the ridges in. Profiles spaced a few kilometers apart were obtained for each ridge; the number depended on ridge length, morphology and albedo variation. Photoclinometry relies on pixel brightness variations which results from topography (the assumption of the technique), albedo, or both. Because of the albedo variations, photoclinometric profiles can not be extended across large distances, such as between adjacent ridges (about 20-80 km). However, the technique is applicable to shorter distances, such as the distance across typical ridges. Profiles were measures across the ridge and extended a few kilometers on either side, including all visible components of the ridge.

The data indicate that ridge relief varies from 27-370 m; average relief is 130±74 m; mean width measured is 5±2 km; the maximum width measured is 14 km. The superposed hill and crenulation are well-defined by the topographic profiles of the wrinkle ridges. The superposed hill and crenulation have slopes of 1° to 9°; in a few locations the slopes locally exceed 10°. The profiles are generally asymmetric, with slopes steeper on one side than on the other. Lunae Planum ridges are characterized by an elevation offset, that is, the plains on one side of the ridge have an elevation distinctly different from the elevation of the opposite side. The offset is similar to that observed for lunar ridges. Measured offsets vary from 0 to as much as 250 m; the average offset is about 30 m to 100 m, with a mean of 57±46 m. The sense of offset does not change abruptly or randomly. Locally, changes in the direction of offset are observed, but these are characterized by a corresponding change in the ridge morphology and a decrease in both ridge relief and width. The elevation offset is generally continuous away from the ridges for at least several kilometers (the length of the photoclinometric profiles).

The elevation offset is an important point in the consideration of models of their internal structure (c.f. Watters, 1988 and Plescia and Golombek, 1986). The offset is most easily explained by a fault beneath the ridge separating structural blocks at different elevations. The study of earth analogs suggests that the broad, low-relief structure characteristic of wrinkle ridges is most compatible with folding and faulting over thrust faults. In this model, a thrust fault at depth dips beneath the high side of the ridge producing the elevation offset. Since the elevation offset persists away from the

ridge, the fault producing the offset must be uniform over these scales (kilometers to tens of kilometers) and the fault dip can not decrease at a shallow depth. The complex surface morphology of wrinkle ridges in which different morphologies are observed for each ridge and at different points along the same ridge is interpreted to be the result of splays from the master thrust fault. These splays have a variety of dips and senses of displacement and deform the surface in a unique manner.

Using such a model for the internal structure and the topographic profiles it is possible to estimate the shortening due to folding and faulting (Table 1). Shortening due to folding is estimated by simply unfolding the surface profile across the ridge, assuming conservation of line length; shortening due to faulting at depth is proportional to fault dip. Although the fault dip at depth is not directly observable, theoretical failure criteria and observed angle of normal faults on the moon and Mars suggest a dip of about 25° for thrust faults.

Data (Table 1) indicate that folding shortening varies from <1m-75m; mean 10±10 m. Assuming fault dips of 25°, faulting shortening varies from 0-540m, mean 122±98 m. The average ratio of shortening due to faulting versus folding is about 12. Shortening due to faulting significantly exceeds that due to folding; shortening due to faulting would exceed that due to folding by a factor of 3 to 6 even for fault steeper dips (i.e., 35°). These estimates suggest that a model wherein the fault breaks the surface and a substantial portion of the shortening is expressed by slip on faults at the surface is appropriate for martian ridges.

The shortening data can be used to estimate strain. Individual ridges exhibit a local (single ridge) folding strain of 0.05% to 0.5%, a faulting (displacement) strain of 1.0% to 5.0%, to produce a total strain of 1.4% to 5%. These estimates are broadly consistent with previous estimates of strain of a fraction of a percent to a few percent (e.g., Bryan, 1973; Muehlberger, 1974; Watters, 1988). Ridges on Lunae Planum generally trend north-south indicating an east-west compressional stress field. At 20°N latitude, there are 12 major ridges between Echus Chasma-Kasei Vallis on the west and the heavily cratered terrain on the east. Assuming each ridge is typical (131 m total shortening/ridge), the total shortening across Lunae Planum is 1600 m; corresponding regional compressive strain is 0.2% to 0.5%.

References:

Bryan, W. B., *Proc. 4th Lunar Sci. Conf.*, 93-106, 1973.
Davis, P., and Soderblom, L. A., , *J. Geophys. Res.*, **89**, 9449-9457, 1984.
Lucchitta, B. K., *Proc. 7th Lunar Sci. Conf.*, 2761-2782, 1976.
Lucchitta, B. K., *Proc. 8th Lunar Sci. Conf.*, 2691-2703, 1977.
Maxwell, T. A., F. El-Baz, and S. H. Ward, *Geol. Soc. Amer. Bull.*, **86**, 1273-1278, 1975.
Muehlberger, W. R., *Proc. 5th Lunar Sci. Conf.*, 101-110, 1974.
Plescia, J. B., and M. P. Golombek, *Geol. Soc. Amer. Bull.*, **97**, 1289-1299, 1986.
Quaide, W., *Icarus*, 4, 374-389, 1965.
Scott, D. H.,*Apollo 17 Prelim. Sci. Rep., NASA SP-330*, 31/25-31/28, 1973.
Sharpton, V. L., and J. W. Head, *J. Geophys. Res.*, **87**, 10,983-10,998, 1982.
Sharpton, V. L., and J. W. Head III, *Proc. 18th Lunar Planet. Sci. Conf.*, 307-317, 1988.
Strom, R. G., The Moon, IAU Symposium no. 47, 187-215, 1972.

Watters, T. R., *J. Geophys. Res.*, **89**, 10,236-10,254, 1988.

TABLE 1

RIDGE LOCATIONS (number of profiles)	HEIGHT (M)	WIDTH (KM)	OFFSET (M)	HIGH SIDE	SHORTENING FOLD (M)	SHORTENING FAULT (M)	SHORTENING COMBINED (M)
MC10NW							
20.5°N; 71°W (27)	204±52	5.3±1.0	105±44	E	17±10	225±95	242±101
20.5°N; 70.5°W (26)	197±81	5.0±1.5	94±65	E	22±19	209±142	232±153
20°N; 69°W (13)	152±31	6.4±1.5	58±32	E	9±3	25±52	134±52
17°N; 71.3°W (23)	146±41	6.8±1.9	75±32	E	7±3	160±70	168±71
MC10NE							
20.5°N; 66°W (13)	69±29	5.1±2.4	30±22	E	3±1	63±47	65±48
21°N; 65°W (6)	102±20	4.7±1.3	48±28	E	5±2	103±61	108±62
21°N; 64.5°W (7)	131±106	5.0±3.9	52±38	W	9±9	112±81	121±87
21.5°N; 62.5°W (6)	55±14	3.0±0.8	19±12	W	3±2	41±2	44±24
22°N; 62°W (7)	147±46	5.8±1.5	64±22	E	8±5	136±48	142±49
22°N; 59.5°W (4)	169±41	4.0±1.0	68±45	E	10±5	90±6	100±2
17°N; 66.2°W (6)	79±36	3.7±0.9	33±16	W	5±4	71±31	76±33
MC10SE							
14°N; 66.5°W (7)	75±19	3.3±1.1	39±20	W	3±1	84±44	87±44

(±standard deviation of measurements around means)

MORPHOLOGIC COMPONENTS AND PATTERNS IN WRINKLE RIDGES: KINEMATIC IMPLICATIONS;

Jayne C. Aubele, Dept. Geological Sciences, Brown University, Providence, R.I. 02912

INTRODUCTION The origin and mechanism of formation of planetary wrinkle-ridges has been in question since the initial discovery of these features on the moon. Subsequently, ridges similar in form and appearance to lunar mare ridges have been identified on Mercury, Mars and Venus and, in a few instances, on Earth. Theories of the origin of wrinkle-ridges can be classified into tectonic, volcanic, or combined processes. Sharpton and Head [1] have summarized and evaluated the evidence for lunar mare wrinkle-ridge origins proposed by other workers and have concluded that mare ridges and their characteristic morphology are the surface expressions of tectonic deformation. Previously proposed structural models have described thrust faults [1,2,3,4], stike-slip faults [5], vertical faulting [6], keystone-style splay faults [1], anticlinal folding [7,8] and upwarp due to underlying topography [9]. Many workers have compared the morphology of mare-type ridges on the other planets with similar features on Earth formed by known mechanisms, such as thrust fault deformation associated with recent earthquakes, anticlinal folding in the Columbia Plateau flood basalts, deformation on the surface of a collapsed lava lake, and small-scale pavement folds due to landslide movement [4,7,10]. All of the structural models and terrestrial analogues involve compression.

Mare type wrinkle-ridges were originally described [11,12] as composed of three morphologic parts or, as they will be referred to here, components; 1) a broad linear rise, which may not always be present or may be visible only under low illumination angles; 2) an arch, which may be up to 200m high and 7 km wide; and 3) a crenulated ridge which may be up to 100 m high and 1.5 km wide and may be central or marginal to the position of the arch. In cross section, the arch may appear symmetrical or asymmetrical with alternating scarp directions [13].

Wrinkle-ridges on all planets exhibit this characteristic morphology. In fact, it is by this morphology alone that they are identified. Understanding this morphology, then, is necessary to understanding the ridges themselves. Furthermore, any regular pattern in the morphology should be indicative of the kinematics of wrinkle-ridge formation. For this reason, the morphological components of a large number of lunar and Mars ridges have been mapped in detail and these components and their patterns have been characterized.

OBSERVATIONS A wrinkle ridge can be treated as a system of related individual components, as previously described by Aubele [14], or as an "assemblage", as described concurrently by Watters [15]. All of the morphologic components, rise, arch and crenulated ridges occur as segmented features along the general trend of the wrinkle ridge, with individual component segment lengths that are shorter than the overall length of the wrinkle ridge. Each component segment tends to be arcuate to sinuous in map view, with sinuosity increasing with decreasing size. In map view, the entire wrinkle ridge can be modeled as a series of individual parabolic curves of different sizes and alternating orientations. All component segments overlap, so that minor (small) crenulated ridges can be thought of as being superimposed on major (large) crenulated ridges which are superimposed on arches which, in turn, occur on rises. The only exceptions to this generalization are minor crenulated ridges (less than 200 m wide) which sometimes occur off the arch, either parallel to or at some angle to the main trend of the wrinkle ridge.

The crenulated ridge component segments of a typical wrinkle-ridge occur in a range of sizes that can be divided into general categories: major ridges ($\geq$ 0.2 km in width); and minor ridges ($\leq$ 0.2 km in width), as named by Aubele [14] or 1st, 2nd and 3rd order ridges, as named by Watters [15]. As illustrated in Figure 1, the major crenulated ridges tend to occur along the outer margins of the arch, frequently crossing from one side to the other in a sinuous or en echelon pattern. Where a crenulated ridge is superimposed at one margin of an arch and then crosses to the other margin, it gives the entire wrinkle ridge a general appearance of asymmetrical and alternating scarps. In cross-section, however, each component of a wrinkle ridge can be individually modeled as a symmetrical curve, or an anticlinal fold, while the overlap of individual components presents a somewhat misleading appearance of assymetry in the wrinkle ridge when viewed as a whole. In general, there is a direct relationship between widths of arch and major crenulated ridge segments within a wrinkle ridge.

The orientation of the major crenulated ridge segments and the arch segments of a wrinkle ridge form a distinct and regular pattern (Fig. 1, close-up A and B). The crenulated ridge segments occur either: 1) generally parallel to the arch in a sinuous map pattern, first along one margin and then along the other margin of the arch (Fig. 1A); or 2) at some angle to the main trend of the arch in an en echelon pattern (Fig. 1B). In fact, when tangents are drawn along the major crenulated ridge segments of an entire wrinkle-ridge, they are all oriented in the same general direction, regardless of the orientation of the main trend of the arch. The arch tends to follow pre-existing structure; for example, the circumference of basins or the rims of buried

craters. The crenulated ridge segments tend to occur oriented in a dominant direction along the entire length of the wrinkle-ridge. When the strike of both arch and crenulated ridge segments coincide, then the crenulated ridges occur in their sinuous pattern moving from margin to margin of the arch (Fig. 1A). When the strike of the arch and crenulated ridge segments diverge, then the crenulated ridges continue to follow their original strike and occur in a series of en echelon segments crossing the strike of the arch (Fig. 1B).

ANALYSIS The regular pattern in crenulated ridge and arch orientation, is an indication of the kinematics of wrinkle ridge formation. The orientation of the crenulated ridge component appears to be related to a dominant direction of regional compression. For example, the crenulated ridge segments of the wrinkle-ridges in southern Serenitatis are predominantly oriented in a N-S direction, while the arch, and the general wrinkle-ridge system itself, is apparently aligned with the circumferential basin margin or buried basin ring. This supports previous work [16] that identified the N-S trending wrinkle ridges in the center of several lunar basins as indicating a dominant E-W compressive stress regime which existed during the formation of the wrinkle-ridges. The major crenulated ridge component segments, therefore, apparently exist perpendicular to the dominant direction of compression; the arch component segments can be affected by local stress, and can exist either perpendicular to the direction of compression or at some oblique angle to the direction of compression. In ordinary circumstances, strike-slip movement might be expected along the oblique angle segments. Experiments in clay [17,18] have shown that en echelon folds can occur as initial conjugate features along a zone which is oblique to a dominant direction of compression and undergoing shear. These are known as "pre-peak" structures, referring to the fact that they occur just before the shear strength is exceeded. No strike slip fault forms when the total strain is very small and the shear strength of the material is not exceeded. This implies that minimal strain is associated with the formation of the en echelon segments of lunar wrinkle-ridge morphology, which agrees with previous estimates of small percentages of surface shortening and horizontal deformation of craters [13,1].

Any mechanism of formation for wrinkle ridges must take into account the existence and observed characteristics of the morphologic components that make up wrinkle ridges; the change in wrinkle ridge morphology with change in terrain or geologic unit; the primary occurrence of wrinkle ridges on planetary plains units, basins, and volcanic calderas; and the fact that recognizable wrinkle ridges are infrequently observed on Earth. In addition, the relationship in width of the crenulated ridge and arch components, and their regular and predictable patterns implies that the components are related during formation but are capable of reacting in different ways to the mechanism of formation. The pre-peak en echelon folds imply minimal strain associated with formation. This evidence indicates that wrinkle ridges are not the direct result of a major thrust fault breaking the surface, but rather the indirect result of some subsurface fault that is manifested as associated minor ruptures and slip close to the surface and folds at the surface (Fig. 2). This type of structural movement has been observed in terrestrial anticlines formed in layered material and as a precursor surface manifestation of thrust faults that have not yet propagated to the surface [A. Johnson, pers. comm., 1989]. Three conditions are necessary for this type of structure: (1) layered stratigraphic sequence with intercalated incompetent beds that can act as slip planes; (2) no pre-defined major fractures of joints in the stratigraphic sequence; and (3) a subsurface disturbance, either a compressional fault or subsidence over pre-existing topography, that causes folding of the stratigraphic sequence above it. In response to the subsurface disturbance, the layered sequence experiences minor converging or diverging ruptures, called symmetrical overthrusting, along slip planes. These faults are detached from, but related to, the major subsurface fault or disturbance and may alternate in orientation to produce surface anticlinal folds of sizes related both to the growth of the wrinkle ridge structure and the thickness of the layers experiencing folding. This model would predict the existence of layered plains units and subsurface discontinuities wherever planetary wrinkle ridges are observed; and explains the morpologic components, their patterns, the change in morphology with change in terrain, and the lack of recognition of these features on Earth with its active erosional regime.

CONCLUSIONS Wrinkle-ridges consist, not of random combinations of scarps and "wrinkles", but of consistent patterns of (1) morphology, (2) trends of morphologic components, and (3) trends between morphologic components. The typical wrinkle-ridge morphology can be produced by small compressive strains. The entire wrinkle-ridge structure appears to be the result of "pre-preak" compression of the surface. The amplitude of the stress field at the surface, generated by faulting or displacement along pre-existing structures at depth, does not exceed the shear strength of the surface material. As a consequence, the surface warps, "wrinkles" and experiences minor ruptures and multiple sytles of deformation at the surface. Any major rupture at depth need not break the surface. It appears that a dominant direction of regional compression generates the consistently oriented major crenulated ridge components, while local compressive influences affect the arch components. Where the crenulated ridge and arch component segments are at an angle to each other, then they represent a general zone of incipient transpression and the crenulated ridge components form en echelon conjugate compressive features perpendicular to the dominant direction of compression.

Based on this study, the major crenulated ridge components, not the entire wrinkle-ridge, should be used to indicate the direction of regional compression.

References [1] Sharpton, V.L. and Head, J.W., 1987, Proc. LPSC, 18th [2] Conel, J. E., 1969, Jet Propulsion Laboratory Space Program Summary 37-56, v.111, p.58-63. [3] Howard, K.A. and Muehlberger, W. R., 1973, Apollo 17 Prelim. Science Report, NASA SP-330, p. 31/22-31/25. [4] Plescia J.B. and Golombek, M.P., 1986, G.S.A. Bull, v. 97, p. 1289-1299. [5] Tjia, H.D., 1970, G.S.A. Bull., v. 81, p. 3095-3100. [6] Luchitta, B.K., 1976, Proc. Lunar Science Conference, 7th, p. 2761-2782. [7] Watters, T.R. and Maxwell, T.A., 1985, Reports Planetary Geology and Geophysics Programs, 1984, NASA T.M.87563, p. 479-481. [8] Watters, T.R., 1987, G.S.A. Abst.w/programs, v.19, p. 883. [9] Solomon, S.C. and Head, J.W., 1979, J. Geophys. Res., 84, p. 1667-1682. [10] Greeley, R. and Spudis, P.D., 1978, Lunar Science Conference, 9th (Abst.), p.411-412. [11] Strom, R.G., 1972, *in* Runcorn, S.K. and Urey, H.C., (eds.), The Moon, IAU Symposium no. 47, p.187-215. [12] Hodges, C.A.,1973, Apollo 17 Prelim. Sci. Report, NASA SP-330, p. 31-12 to 31-21. [13] Lucchita, B.K., 1977, Proc. Lunar Science Conference, 8th, p. 2961-2703. [14] Aubele, J.C., 1988, LPSC 19 (abst), p. 19-20. [15] Watters, T., 1988, LPSC 19 (abst), p. 1245-1246. [16] Fagin, S.W., et al., 1978, Proc. LPSC, 9th, p. 3473-3479. [17] Tchalenko, J.S., 1970, G.S.A. Bull., v.81, p.1625-1640. [18] Wilcox, R.E., et al., 1973, AAPG Bull. v.57, no 1, p. 74-96.

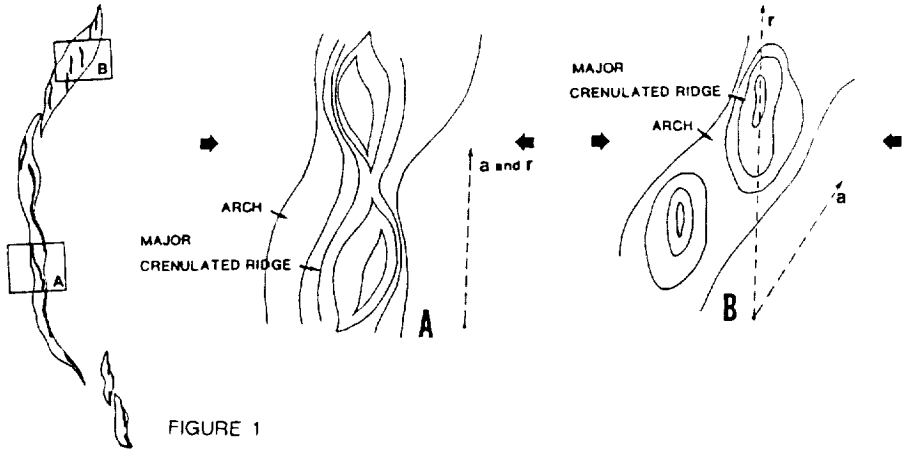

FIGURE 1

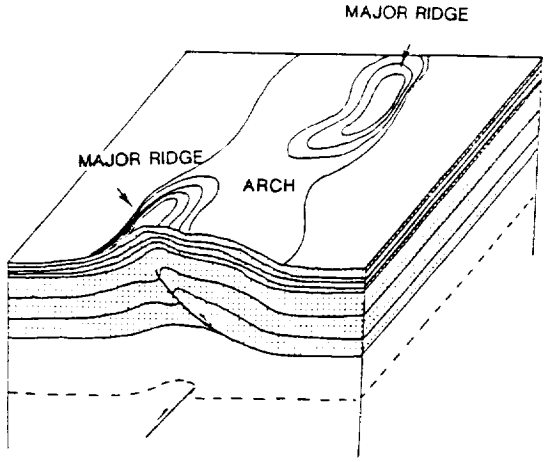

FIGURE 2

FIGURE 1. Schematic morphologic map of a typical lunar wrinkle-ridge showing the arch and crenulated ridge components. Narrow black lines outline arch component segments. Thick black lines represent major (large) crenulated ridge component segments.
CLOSE-UP A and B. Crenulated ridge superimposed on arch is indicated by generalized contour lines. Dashed arrows indicate strike of arch component (a) and crenulated ridge component (r). Large arrows indicate direction of regional compression.
FIGURE 2. Block diagram of proposed model. Only one of many related minor ruptures is shown. A converging overthrust in a direction opposite to the one shown, and occurring behind the plane of the paper, would account for the major ridge component at far right. Minor ridge components, not shown, would be produced by slip and ruptures between layers closer to the surface.

DOMAINS OF REGIONAL PURE SHEAR ON THE TERRESTRIAL PLANETS.

Thomas R. Watters and Michael J. Tuttle, Center for Earth and Planetary Studies, National Air and Space Museum, Smithsonian Institution, Washington, D.C. 20560

Tectonic domains where major fold and thrust fault trends are transected by conjugate strike-slip faults have been documented within fold-thrust belts on the Earth (1,2). The geometric relationships between the structures is best explained by a pure shear mechanism because of the limited extent and lateral displacements of the strike-slip faults (see 2). Given a N-S directed compressive stress, the system of structures possible includes E-W trending first-order folds and first-order right-lateral and conjugate left-lateral strike-slip faults with an angle θ to the primary stress direction. The angle θ is constrained by the Coulomb-Navier criterion where θ is related to the coefficient of internal friction μ. For typical values of μ between 0.58 and 1.0, θ is in the range of 22.5°-30°.

Yakima Fold Belt, Columbia Plateau, Earth

The anticlinal ridges in the continental flood basalts of the Columbia Plateau (or Columbia Basin) are long, narrow, periodically spaced structures with broad relatively undeformed synclines. The anticlinal ridges are believed to be the result of initial buckling in response to a horizontal compressive load followed by dominantly reverse to thrust faulting (3). Numerous strike-slip faults have been mapped in the southern portion of the fold belt (4). The lateral displacement along the most extensive faults is typically small (< 1 km). The strike-slip faults can be classified as either tear faults, faults of limited extent or regional faults (5). As part of this study, over 80 lineaments have been mapped, 73 of which are located in the southern portion of the fold belt. Many of these correspond to previously mapped right-lateral strike-slip faults. The mean direction of the known and suspected strike-slip faults in the southern portion of the fold belt is N37°W. Taking the normal to the mean direction of the anticlines to be the approximate direction of the principal compressive stress, the mean direction of the known and suspected right-lateral strike-slip faults is within the range for θ. The anticlinal ridges of the Columbia Plateau are good analogs to first-order ridges in wrinkle ridge assemblages that occur in the ridged plains material on Mars (6).

Wrinkle Ridge Assemblages, Mars

Wrinkle ridges occur in smooth plains material that is inferred to be volcanic in origin. These ridges are also believed to form in response to horizontal compression with reverse or thrust faulting developed as a result of buckling (flexure-fracture) or buckling the result of reverse or thrust faulting (fracture-flexure) (6,7). If the ridged plains material has deformed in a similar style to the basalts of the Columbia Plateau, then strike-slip faults and their associated secondary structures may be common on Mars. Lineaments that transect wrinkle ridges have been found in medium and high resolution Viking Orbiter images. Some are comparable in scale to strike-slip faults associated with the anticlines on the Columbia Plateau. Lineaments of limited areal extent that sharply truncate both *en echelon* stepping and individual ridge segments are interpreted to be tear faults. Crosscutting lineaments of greater areal extent ($\leq$ 100 km) occur near or within the expected range for θ and are interpreted to be strike-slip

faults consistent with a domain of regional pure shear. Like their analogs on the Columbia Plateau, the strike-slip faults accommodate a portion of the relatively low bulk strain apparent in the ridged plains. Other evidence of strike-slip faulting on Mars has been recently reported by Forsythe and Zimbelman (8) and Schultz (9).

Ridge Belts, Venus

Parallel to subparallel ridges form the prominent ridge belts identified in Venera 15/16 images. Although the role of extension (10) and compression (11,12) in origin of the ridge belts is under debate, the similarity in morphology of the ridges to wrinkle ridges suggests that they are the result of horizontal compression. Frank and Head (11) describe some of the ridges as broad arches and compare them to arches associated with maria wrinkle ridges. Crosscutting lineaments are common in the ridge belts (11,12). These lineaments often occur in conjugate sets and evidence of strike-slip motion has been reported (11,12), however we observe little or no apparent displacement along the lineaments studied thus far. The areal extent, limited apparent displacement and the estimated values of θ determine for the lineaments are consistent with the development of strike-slip faults in a domain of regional pure shear. Based on the assumption that the morphology and fold geometry of the ridges is similar to that of wrinkle ridges, crude estimates of the bulk strain within the ridge belts in the Pandrosos and Ahsonnutli Dorsa regions are as high as 7% (see 6), as compared to a maximum of roughly 2% estimated bulk strain for ridged plains of Tharsis and 5% for the deformed basalts of the Columbia Plateau.

References Cited:

(1) Tirrul, R., I.R. Bell, R.J. Griffis and V.E. Camp, *GSA Bull., 94*, 134-150, 1983. (2) Sylvester, A.G., *GSA Bull., 100*, 1666-1703, 1988. (3) Watters, T.R., in *GSA Sp. Paper 239*, in press, 1989. (4) Anderson, J.L., Ph.D. dissertation, Univ. South. CA, 1987. (5) T.L. Tolan, J.L. Anderson and M.H. Beeson, this volume. (6) Watters, T.R., *JGR 93*, 10,236-10,254, 1988. (7) Plescia, J.B. and M.P. Golombek, *GSA Bull., 97*, 1289-1299, 1986. (8) Forsythe R.D. and J.R. Zimbelman, *Nature, 336*, 143-146, 1988. (9) Schultz, R.A., *Nature, 341*, 424-426, 1989. (10) Sukhanov, A.L. and Pronin, A.A., *Proc. LPSC XIX*, 335-348, 1989. (11) Frank, S.L. and J.W. Head, *Venus Geoscience Tutorial, LPI No. 708*, 13-14, 1989. (12) Kryuchkov, V.P., *LPSC XX*, 546-547, 1989.

STRIKE-SLIP FAULTING, WRINKLE RIDGES, AND TIME VARIABLE STRESS STATES IN THE COPRATES REGION OF MARS.

Richard A. Schultz, Geodynamics Branch, NASA Goddard Space Flight Center, Greenbelt, MD 20771.

The existence of strike-slip faults has recently been documented in two locations on Mars [1,2]. In this abstract I review two clear examples located southeast of Valles Marineris and present preliminary evidence for more widespread strike-slip deformation elsewhere in Coprates.

Strike-slip faults and wrinkle ridges both deform Early Hesperian plains materials in eastern Coprates between 20-25° S and ~55° W [2]. The strike-slip faults are defined by echelon arrays of linear structures that bound polygonal or rhombohedral plateaus located within their stepovers. The faults are oriented obliquely (~60°) to the overall, north-south trend of the wrinkle ridges. The plateaus were probably formed within contractional strike-slip stepovers rather than by simple lateral or vertical offset of pre-existing markers. Crustal shortening along each echelon fault array may exceed 1-2 km. Northwest trending strike-slip faults in this area are left lateral, as inferred by their sense of step and type of stepover, whereas northeast trending faults are right lateral. The lack of orthogonal fault-ridge intersections implies that the faults did not serve as passive transforms during wrinkle ridge deformation. Indeed, some wrinkle ridges located at fault terminations occur in the fault's compressional quadrants and have angular relationships to the strike-slip faults suggesting that they may have nucleated as a result of the localized strike-slip activity. Strike-slip faulting in this part of Coprates may have predated or overlapped episodes of wrinkle ridge growth and was probably also driven by Tharsis generated stresses.

Strike-slip faulting becomes more complex near 26-28° S in Coprates (Fig. 1). Here, northeast trending linear zones that look like wrinkle ridge material appear to be closely spaced strike-slip faults. Wrinkle ridges that cross these zones are not noticeably offset, suggesting that the zones occurred before the ridges. In contrast, left lateral strike-slip faults occurring in the same area appear to offset at least one ridge, and portions of many other ridges appear defined by scarps of similar orientations to these faults. Inferred remote stress states for the three sets of structures (Fig. 1a, b) are comparable to those predicted from Tharsis deformation models. It appears that right lateral strike-slip faulting first occurred in the curvilinear zones, then was replaced by coeval left lateral strike-slip faulting and wrinkle ridge growth.

Most wrinkle ridges south of Valles Marineris trend northeast but older, northwest trending ridges are also present [e.g., 3]. Fig. 3 shows the geometry of some large ridges southeast of Melas Chasma. Crosscutting relations indicate that northwest ridges formed first (Fig. 2a), so a change in remote stress orientation over time is implied. A resolved shear stress may have acted along or within northwest trending ridges during superposition of the second wrinkle ridge producing stress state. This would explain the growth of short oblique "crenulations" on the southern ridge (Fig. 2b) and growth of some northeast trending ridges in the inferred compressional stress quadrants of older ridges (see [2]). This example differs from the previous two in that discrete strike-slip faults are not observed. Instead, the lateral growth of wrinkle ridges appears to have been locally influenced by the relative orientations of ridges and remote principal stresses [e.g., 4-6]. Interestingly, the older northwest trending ridges with inferred left lateral shear strain parallel the left lateral strike-slip faults to the east [2, Fig. 1].

The first two examples show that strike-slip faulting occurred in a broad zone east of the Coprates Rise spanning ~400 km east-west by perhaps 1000 km north-south. The last example suggests that the growth of major wrinkle ridges throughout Coprates may have been influenced by horizontally directed shear stresses and that more than one generation of ridges was produced. Thus, "compressional" deformation of ridged plains south of Valles Marineris was spatially heterogeneous and a temporal change in stress state may have been involved.

REFERENCES: [1] Forsythe, R.D. and J.R. Zimbelman, *Nature, 336*, 143-146, 1988. [2] Schultz, R.A., *Nature, 341*, 424-426, 1989. [3] Watters, T.R. and T.A. Maxwell, *Icarus 56*, 278-298, 1983. [4] Tija, H.D., *Geol. Soc. Am. Bull., 81*, 3095-3100, 1970. [5] Raitala, J., *Moon Planets, 25*, 105-112, 1980. [6] Aubele, J.C., *Lunar & Planet. Sci., XIX*, 19-20, 1988.

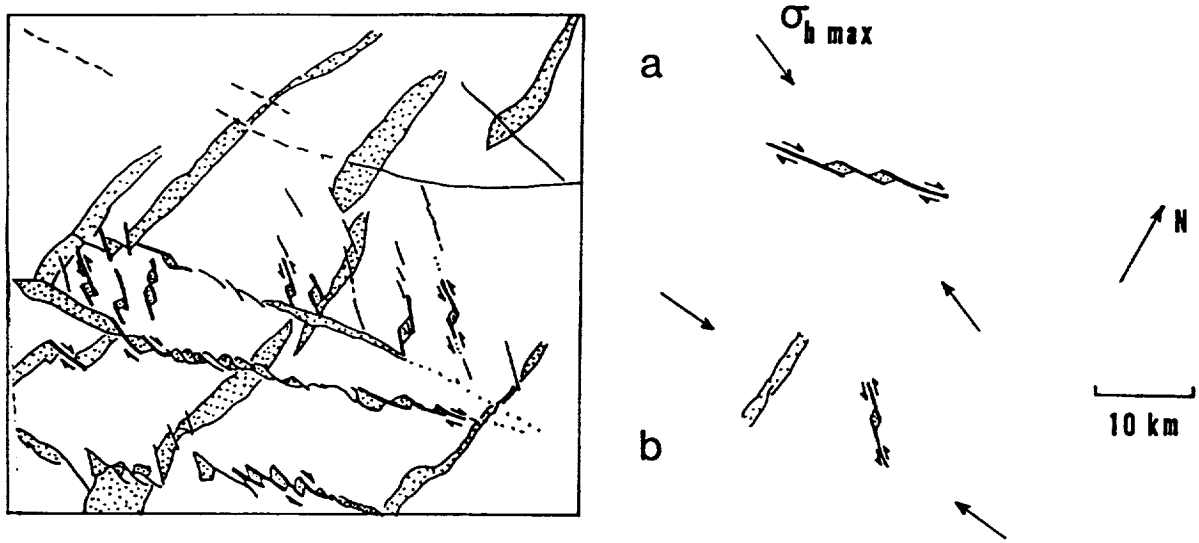

Fig. 1. Sketch map showing relationships between strike-slip faulting and wrinkle ridge growth in Coprates. Wrinkle ridges are stippled. Deformation inset (a) preceeded deformation (b). Viking orbiter images 610A27, A44.

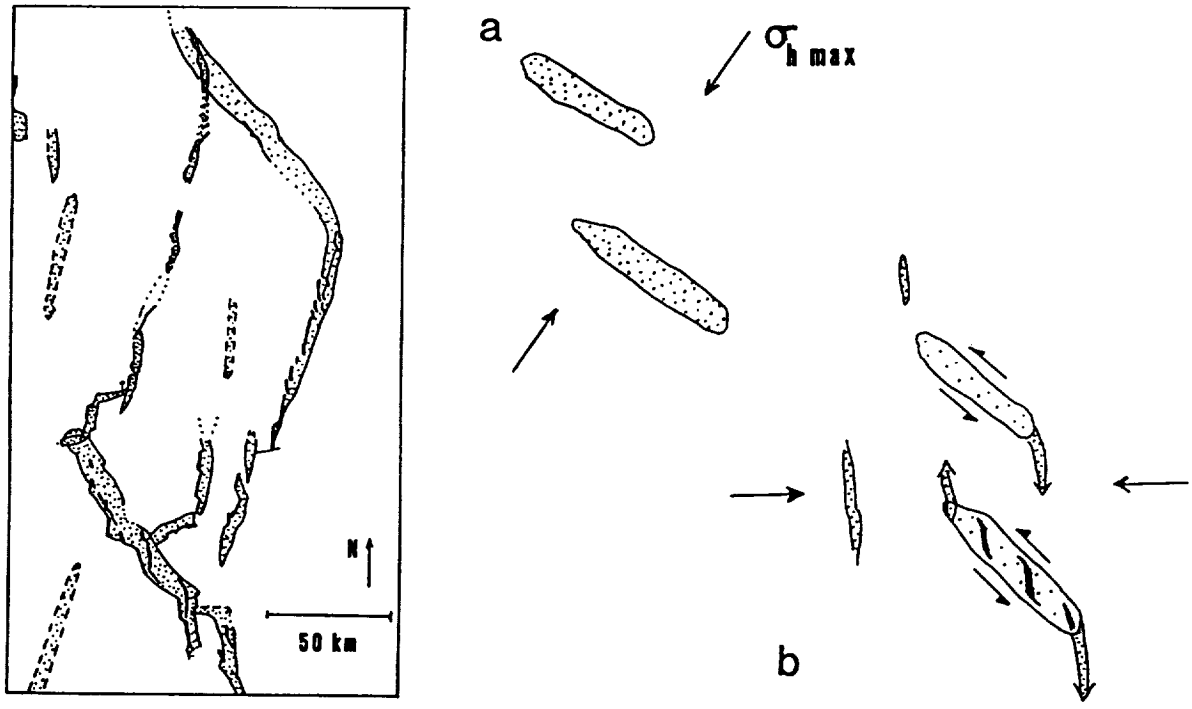

Fig. 2. Northeast trending regional set of wrinkle ridges are superimposed on northwest trending ridges. Insets show inferred time variation of associated stress states. Viking image 608A51.

ORIGIN OF CURVILINEAR GRABEN IN SOUTHWEST LUNAE PLANUM, MARS.

Thomas R. Watters and Michael J. Tuttle, Center for Earth and Planetary Studies, National Air and Space Museum, Smithsonian Institution, Washington, D.C. 20560

The southwest Lunae Planum region of the Tharsis Plateau is being mapped at the 1:500,000 scale as part of the Mars Geologic Mapping program. The western margin of the ridged plains and plateau plains units in this region is marked by a steep, 3 km high erosional scarp. The plateau units in this region are cut by sets of curvilinear graben that occur within a 150 km zone of the scarp. There are three sets of graben in the region, set A cuts Noachian cratered uplands, set B cuts Hesperian plateau material and set C cuts both Hesperian plateau and ridged plains material (see A, B and C, fig. 1). The graben in set A have a mean direction of N12°E and are partially covered by ridged plains material that embays the cratered uplands (fig. 1, see A). Graben set B cuts plains material that appears to be continuous with the ridged plains material but lacks wrinkle ridges (fig. 1, see B). The trend of many of these graben (mean direction N10°E) are parallel to those in the adjacent cratered uplands. This suggests that these graben are the result of reactivation of a preexisting extensional fabric.

The orientation of graben in set A and B is not consistent with any phase of Tharsis radial extension (1). Circumferential oriented extensional stresses are predicted in this region in isostatic adjustment models (2,3,4), however, the curvature of the graben suggests that they were part of a circular swarm with a radius of approximately 300 km. Circular graben swarms are not uncommon in the Tharsis region. The most likely origin of the extensional stresses is local uplift resulting from the emplacement of an intrusive body. If this is the case, the initial intrusion may have coincided with some of the earliest tectonic activity in the Tharsis region.

The third set of graben (C) cut ridges plains material forming non-orthogonal ridge-fault crosscutting angular relationships (fig. 1, see C). This clearly indicates that graben formation postdates the deformation that resulted in the wrinkle ridges (5). The orientation of the graben in set C (mean direction N49°E) is also not consistent with Tharsis radial extension. However, unlike the other graben sets, the C graben parallel the scarp (mean direction of scarp segments is N52°E). Although the graben in set C do not appear to be related to the other sets, the orientations of the graben in sets B and C become parallel where they cut the same unit (fig. 1, see arrow). This suggests that in this area, the graben in set C were influenced by the same preexisting extensional fabric. The parallel nature of the graben and scarp suggests that the two are related. Possible explanations are: 1) the graben influenced scarp retreat, or 2) graben formation was influenced by, or a result of, the scarp. Extensional stresses near the scarp will result from the release of confining pressure, however, the magnitude of the stress would be expected to decay rapidly with distance from the wall. Another possibility is that extensional stresses resulted from loss of support. If the ridged plains overlie a thick megaregolith that was exposed by erosion, material may have been removed by undercutting and/or sapping. A finite element analysis is planned to determine under what conditions, if any, graben could form at the observed distances from the scarp.

CURVILINEAR GRABEN: Watters, T.R., and M.J. Tuttle

References Cited:
(1) Plescia, J.B. and R.S. Saunders, *JGR, 87*, 9775-9791, 1982. (2) Banerdt, W.B., R.J. Phillips, N.H. Sleep, and R.S. Saunders, *JGR, 87*, 9723-9733, 1982. (3) Banerdt, W.B., M.P. Golombek, and K.L. Tanaka, submitted to *Mars*, University of Arizona Press, Tucson, 1989. (4) Sleep, N.H. and R.J. Phillips, *JGR, 90*, 4469-4489, 1985. (5) Watters, T.R. and T.A. Maxwell, *Icarus, 56*, 278-298, 1983.

Fig. 1. Photomaps of southwest Lunae Planum. The three sets of graben in the region are marked A, B and C.

FORMATION OF RHYOLITIC RIDGES ON MARTIAN BASALTS. T.K. Porter and P.H. Schultz, Dept. of Geology, Brown University, Providence, RI 02912

Introduction: Martian lava flows centered at approximately 3° N, 140° W are characterized by steep, thick flow fronts, large areal extents, and distinctive textures. These flows are strikingly different from other martian flows (see Figures 1a and b). The texture has been interpreted as festoon or pressure ridges [1] like those on terrestrial pahoehoe basalts - yet the martian ridges are the same scale as those on terrestrial rhyolite flows [2]. As discussed in [3], the height and spacing of the ridges is controlled by the thickness of the chilled upper margin of the flow and the viscosity ratio (the viscosity of the chilled crust of the flow vs. the viscosity of the flow interior). A thick crust and high viscosity ratio are conditions that favor the formation of high ridges with long wavelengths. Here, analytical modeling and preliminary experimental results suggest that the martian flows could not have developed a crust sufficiently thick to form the observed ridges if the flows were emplaced subaereally, and that instead the flows may have been emplaced under a unit of ice-rich dust.

Viscosities of Martian Flows: We used high resolution Viking Orbiter photographs to determine an average ridge spacing of 175.5m and an average ridge height of 13.9m. These dimensions are one to two orders of magnitude greater than the ridge dimensions of typical terrestrial basalts and are similar to ridge dimensions found on terrestrial rhyolites ([2], [3]). They are unlike any lunar basalts. We inserted the values found in Table 1 into analytical models ([1], [2], [3]) to obtain viscosities (Table 2). The lower viscosities are high for terrestrial basalts ([1], [4]) while the larger viscosity values approach the terrestrial rhyolite viscosities [2]. But these flows are undoubtedly basaltic: observed lava channels and abundant evidence for tube-fed flow are distinctive characteristics of basalts [5]. The long flow distances (up to 6000km^2) over low gradients combined with the large areal extent of these flows (1000 to 4000km^2) indicate a low-viscosity lava; paradoxically, the steep flow fronts, ridge dimensions and analytical models suggest a high-viscosity lava [6]. Recent experiments with molten carbowax [7] indicate that ridge creation is favored if the flow rate is "sufficiently slow" and the ambient temperature is "sufficiently low." Therefore, forming a thick chilled crust on the martian lavas may impart a high-viscosity appearance to a low-viscosity flow. A low-viscosity lava can form steep, thick flow fronts if the flow cools quickly enough. Icelandic table mountains, for example, are basalts that erupted subglacially, producing steep-sided, flat-topped mountains ([8], [9]). The slopes of the steeper terrestrial table mountains are approximately 32° [8]. For comparison, we derive flow front slopes of about 36° for the martian lavas (see Fig. 1a.), in contrast to the thickest lunar flows which have flow front slopes of about 14°.

Apparent High Viscosity from Low Viscosity Flows: The high-viscosity appearance of the martian flows might be produced by quickly and efficiently cooling the surface of a low-viscosity flow. Rapid cooling of the flow surface could be achieved by emplacing the flow under a material with high heat capacity and high thermal diffusivity This would create a thick chilled crust and, by exerting a downward force, could increase the drag component on the surface; both conditions enhance ridge formation. Many of the observed flows are surrounded by easily eroded deposits and the surfaces of some flows exhibit heavily eroded impact craters indicating differential removal of a friable surface deposit at least 300m thick. Models of the rate of cooling of terrestrial lava flows [7] permit calculating the thermal diffusivity of the boundary environment for the martian flows. Using this model and the parameters in Table 1, and then solving for the thermal diffusivity yields a value that is a hundred times too high for air, water or ice and is a hundred times too low for most rock. An ice-rich dust may produce the appropriate thermal diffusivity.

Preliminary experimental results suggest that overburden pressure on the lava flow may play an important role in creating the observed textures. By simulating lava flows with molten carbowax, we have found that efficient cooling alone is not enough to produce the large-scale ridge texture and the steep flow fronts at this scale. To determine the first-order trends of ridge formation, we have emplaced the molten wax in varying conditions such as: subaeral with ambient temperatures varying from -2° to 20° C; under water varying from 0° to 25° C; under powdered dry ice, snow and foam to simulate a material with high heat capacity but low thermal diffusivity. Cooling the wax flows with dry ice or 0°C air is not as efficient at producing large ridges and steep flow fronts as is cooling the flows with ice water - even though the thickness of the chilled margin is roughly the same in all cases.

Conclusion: The observed martian flows have large areal extents and flow lengths, indicating a fluid basalt; the same flows paradoxically have steep flow fronts and a long ridge wavelength, indicating a highly viscous (almost rhyolitic) lava. A low-viscosity basalt may resemble a high-viscosity lava if the flow cools quickly and efficiently enough to produce a thick surface crust, and if thereby exerting drag force on the crust once formed. Preliminary experimental results suggest that overburden pressures also may be important to ridge formation. If emplaced under a mantle of ice-rich dust, then the martian flows could have cooled quickly and have been sujected to sufficient overburdon pressure.

References: [1] Theilig and Greeley (1986) *Proc. LPSC XVII.* [2] Fink (1980) *Geology*, **8**. [3] Fink and Fletcher (1978) *Jour. of Volc. and Geotherm. Res.*, **4**. [4] *Basaltic Volcanism Study Project* (1981). [5] Greeley (1980)

Volcanic Features of Hawaii. [6] *Hawaiian Planetary Conference.* (1974). [7] Fink and Griffiths (1989) *LPSC XX.* Abs. [8] Allen (1979) *Jour. Geoph. Res.* [9] Hodges and Moore (1979) *Jour. Geoph. Res.*, 84.

Parameter	Number of Samples	Avg. Value
Ridge spacing	1840	175.5m
Ridge height	8	13.9m
Flow thickness	16	62.5m
Flow front slope	8	36°

Table 1. Parameters obtained using high-resolution VO photographs.

Model	Viscosity in Pa•s	
	Interior	Exterior
Fink and Fletcher (1978)	$5.4 * 10^4 - 8.7 * 10^6$	$3.4 * 10^5 - 5.5 * 10^8$
Fink (1980)	$1.5 * 10^6 - 2.3 * 10^8$	$9.7 * 10^6 - 1.5 * 10^9$
Theilig and Greeley (1986)	$1.4 * 10^7 - 2.3 * 10^9$	$1.5 * 10^8 - 2.5 * 10^{10}$

Table 2. Viscosities obtained from the parameters in Table 1 and the models in [1], [2] and [3].

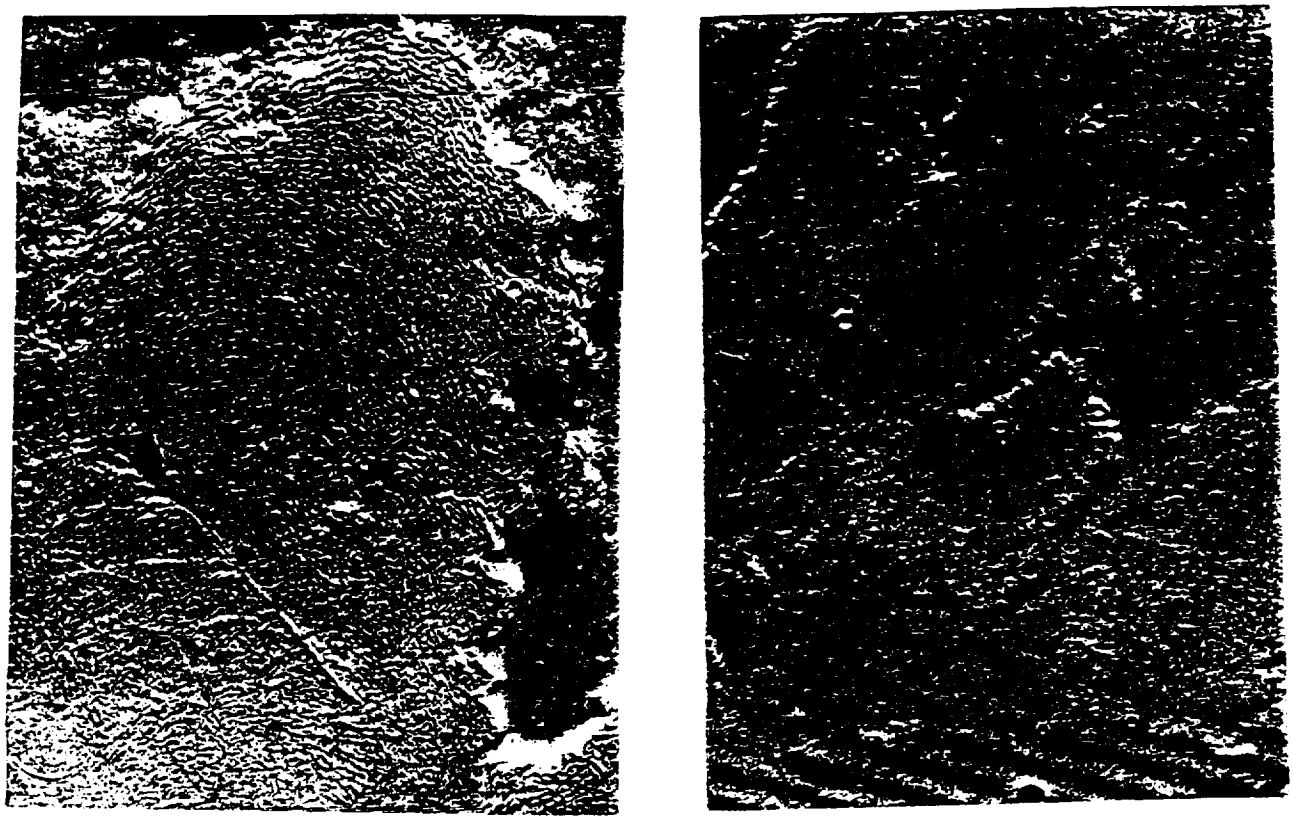

1a. 1b.

Figures 1a. and b. Fig. 1a is a mosaic of 731A03 and 731A04; INA = 75.4°. Note relief and spacing of ridges and steep flow fronts. Fig. 1b. is a portion of 387B13; INA = 72.0°. Here, note flow fronts with less abrupt termini and absence of texture. Scale bar is 10 km for both figures.

SHALLOW CRUSTAL DISCONTINUITIES IN THE ALBA PATERA-TEMPE TERRA REGION OF MARS
Philip A. Davis and Kenneth L. Tanaka, U.S. Geological Survey, Flagstaff, Arizona 86001

INTRODUCTION: In a recent paper [1], morphometric data were presented for several types of erosional and collapse features within Syria, Sinai, and Lunae Plana that suggest the existence of three mechanical discontinuities within the shallow Martian crust. The depths of these discontinuities are 0.5, 1.0 and 2-3 km, which correspond, respectively, to the thickness of the ridged plains unit, to the depth of a widely proposed interface within the regolith, and to the base of the regolith. The 1-km depth of the regolith discontinuity was also strongly suggested by tectonic model calculations in which the morphometric data for grabens were used to estimate the depth to the mechanical discontinuity that initiated faulting. This 1-km discontinuity may represent an interface between ice-laden and dry regolith, ice-laden and water-laden regolith, or pristine and cemented regolith.

According to hypotheses based on vapor diffusion and on surface and subsurface thermal models [2-6], the depth of the cryosphere was about 1 km at the equator and increased to about 3 km at the poles in early Martian geologic history. This depth should correspond to that of the regolith discontinuity, but in the areas of our previous study [1] (between 15° S. and 23° N. latitude), we did not find that the depth of the regolith discontinuity increases toward higher latitudes. However, this depth may remain relatively constant at these low latitudes and increase only north of 30° latitude, as suggested by [4].

APPROACH: To test the hypotheses concerning the cryosphere, we obtained detailed morphometric data, mostly for grabens and pit chains, but also for various erosional and collapse features, within the Alba Patera-Tempe Terra region [7-10] between 25° and 45° N. latitude. We obtained photoclinometric profiles [method described by 11-12] across 172 simple grabens in eastern Alba Patera. We used the width, depth, and wall-slope data for each graben in model calculations [13-14] to estimate the depth to the mechanical discontinuity that initiated normal faulting (assuming a 60° dip for bounding faults). We also measured the average spacing between pits for many segments along all pit chains on the flanks of Alba Patera. Laboratory experiments by [15] indicated that average pit spacing along pit chains formed in cohesionless material are directly related to the thickness of the material or regolith that overlies the opening fracture. The spacing of pits (as well as the width of grabens) at Alba Patera may be governed by the depth to a discontinuity. Although the patera is covered by lava flows, their strength at kilometer scale may be comparable with that of cohesionless sand at centimeter scale. Also, the flows are underlain probably by ancient regolith material and possibly by poorly consolidated pyroclastic material [16]. At depth, tension fractures may accommodate the collapsed material [17].

The Alba Patera region covers 15° of latitude; it ranges in elevation from 3 to 7 km. To determine possible effects of latitude and thickness of volcanic material, we recorded the map coordinates and elevation [from 18] of each graben and pit-chain measurement. We also measured the scarp heights of various collapse and erosional features within the study area. Almost all of these features are contained in the older plains units within the Tempe Terra region. The scarps may indicate either the thickness of the plains units or

a base level of erosion represented by the same mechanical discontinuity that controlled development of the grabens and pit chains.

RESULTS: We found that the scarps around the "islands" of Hesperian ridged plains material along the south border of Tempe Terra are consistently between 0.4 and 0.6 km high, a range similar to that of the scarp heights found on this unit in Lunae Planum [1]. Scarp heights along the east edge of the Tempe Terra plateau are as much as 1.1 km, which corresponds closely to thicknesses of the ridged plains unit near 30° N. latitude; these thicknesses were calculated from diameters and exposed rim heights of partly buried craters and a relation between crater diameter and rim height [19].

The six flat-floored troughs that we examined within Tempe Terra have two depth ranges: three smaller troughs have depths near 0.4 km, and three larger troughs have depths of 1.3-1.6 km. Because all six troughs are mutually adjacent, it is unlikely that the two depths represent the same interface. The shallower one probably represents the thickness of one of the plateau units that occur in the area (either the lower member of the Tempe Terra Formation or the cratered plateau unit [20]). The greater depth may indicate the thickness of the entire sequence of Tempe Terra plateau units or the depth to a mechanical discontinuity within the regolith. The single flat-floored trough that occurs within Alba Patera (37.9° N. latitude, 103.6° longitude) has a depth of 1.3 km, which suggests that the larger trough depths within Tempe Terra probably represent a mechanical discontinuity, because Alba Patera and Tempe Terra do not have the same stratigraphy.

The 172 estimated depths to the mechanical discontinuity that initiated faulting within Alba Patera range between 1 and 6 km. They have a modal value of about 1.6 km (compared with 1.0 km near the Martian equator [1]) and an average of 2.3 km (compared with 1.5 km near the Martian equator [1]). The pit spacings along the three large catenae and several smaller pit chains within Alba Patera range between 1.0 and 3.2 km and average 1.6 km. If the laboratory experiments of [15] are analogous to Martian regolith processes, then these pit-spacing values indicate the thickness of the regolith above major tension fractures that caused regolith collapse. Because the depth estimates from both the graben measurements and the pit spacings result in similar values, we believe that the same crustal discontinuity is involved in both processes.

The average depths to the mechanical discontinuity that initiated faulting found for the Martian equatorial region (1.0-1.5 km [1]) and for 30°-40° N. latitude (1.6-2.3 km) correspond closely to thickness estimates of the Martian cryosphere for this latitude range [2,4-6]. However, our detailed examination of depths to a mechanical discontinuity (by both graben and pit-spacing measurements) found no obvious correlation with latitude between 30° and 45° N. Our detailed comparison of depths to a mechanical discontinuity with change in elevation within Alba Patera found no apparent correlation, which suggests that this mechanical discontinuity formed after Alba Patera and was not dependent on regolith composition. This study and that of [1] indicate that the mechanical discontinuity that initiated faulting and pit-chain development was associated with the Martian cryosphere, either directly or indirectly.

REFERENCES: [1] Davis, P. A., and M. P. Golombek, Discontinuities in the

shallow Martian crust at Lunae, Syria, and Sinai Plana, J. Geophys. Res., in press. [2] Fanale, F. P., Martian volatiles: Their degassing history and geochemical fate, Icarus, 28, 179-202, 1976. [3] Carr, M. H., and G. G. Schaber, Martian permafrost features, J. Geophys. Res., 82, 4039-4054, 1977. [4] Rossbacher, L. A., and S. Judson, Ground ice on Mars: Inventory, distribution, and resulting landforms, Icarus, 45, 39-59, 1981. [5] Clifford, S. M., and D. Hillel, The stability of ground ice in the equatorial region of Mars, J. Geophys. Res., 88, 2456-2474, 1983. [6] Fanale, F. P., J. R. Salvail, A. P. Zent, and S. E. Postawko, Global distribution and migration of subsurface ice on Mars, Icarus, 67, 1-18, 1986. [7] Wise, D. U., Geologic map of the Arcadia quadrangle of Mars, scale 1:5,000,000, U. S. Geol. Surv. Misc. Invest. Ser. Map, I-1154, 1979. [8] Witbeck, N. E., and J. R. Underwood, Geologic map of Mare Acidalium quadrangle, Mars (revised), scale 1:5,000,000, U.S. Geol. Surv. Misc. Invest. Ser. Map, I-1614, 1984. [9] Scott, D. H., and J. M. Dohm, Faults and ridges: Historical development in Tempe Terra and Ulysses Patera regions of Mars, Proc. 20th Lunar and Planet. Sci. Conf., Lunar and Planetary Institute, Houston, 503-513, 1990. [10] Tanaka, K. L., Tectonic history of the Alba Patera-Ceraunius Fossae region of Mars, Proc. 20th Lunar and Planet. Sci. Conf., Lunar and Planetary Institute, Houston, 515-523, 1990. [11] Davis, P. A., and L. A. Soderblom, Modeling crater topography and albedo from monoscopic Viking Orbiter images -- I. Methodology, J. Geophys. Res., 89, 9449-9457, 1984. [12] Tanaka, K. L., and P. A. Davis, Tectonic history of the Syria Planum province of Mars, J. Geophys. Res., 93, 14,893-14,917, 1988. [13] Golombek, M. P., Structural analysis of lunar grabens and the shallow crustal structure of the Moon, J. Geophys. Res. 84, 4657-4666, 1979. [14] Golombek, M. P., and G. E. McGill, Grabens, basin tectonics, and maximum total expansion of the moon, J. Geophys. Res. 88, 3563-3578, 1983. [15] Horstman, K. C., and H. J. Melosh, Drainage pits in cohesionless materials: Implications for the surface of Phobos, J. Geophys. Res. 94, 12,433-12,441, 1989. [16] Mouginis-Mark, P. J., L. Wilson, and J. R. Zimbelman, Polygenic eruptions on Alba Patera, Mars, Bull. Volcanol., 50, 361-379, 1988. [17] Tanaka, K. L., and M. P. Golombek, Martian tension fractures and the formation of grabens and collapse features in Valles Marineris, Proc. 19th Lunar and Planet. Sci. Conf., Lunar and Planetary Institute, Houston, 383-396, 1989. [18] U.S. Geological Survey, Topographic map of the western equatorial region of Mars, scale 1:15,000,000, U.S. Geol. Surv. Misc. Invest. Ser. I-2030, sheet 2, 1989. [19] Plescia, J. B., and R. S. Saunders, Estimation of the thickness of the Tharsis lava flows and implications for the nature of the topography of the Tharsis plateau, Proc. 11th Lunar and Planet. Sci. Conf., 2423-2426, 1980. [20] Scott, D. H., and K. L. Tanaka, Geologic map of the western equatorial region of Mars, scale 1:15,000,000, U.S. Geol. Surv. Misc. Invest. Ser. Map I-1802-A, 1986.

VALLES MARINERIS LANDSLIDES: EVIDENCE FOR MECHANICS OF LARGE ROCK AVALANCHES; A. S. McEwen, U. S. Geological Survey, Flagstaff, AZ 86001.

The mechanism of transport of large rock avalanches has been the subject of considerable interest and controversy in recent decades. On Earth, the observed runout lengths (L) for large rock avalanches, relative to the height of drop (H), are much greater than can be explained by either sliding or dispersive grain-flow mechanisms. Most natural rock types have coefficients of friction (either sliding or internal friction) of 0.6 or higher, so movement is expected only over terrain with an average slope of at least 30° (or H/L at least 0.58); this expectation is confirmed for rock avalanches of relatively small volume and for other flows of dry, granular material. However, as rock avalanches increase in volume, H/L decreases to values as low as 0.1 or less, and a log-log plot of H/L versus volume shows a linear correlation [1,2].

Planetary comparisons under different conditions of gravity, atmospheric pressure, and volatile inventory may prove essential to resolving this question of mechanism. Mars is the only planetary body other than Earth known to have long-runout landslides; they are abundant in the equatorial canyon system of the Valles Marineris. Were the Valles Marineris landslides "wet" or "dry"? ("Wet" is taken to mean that the mass was saturated with water, thus eliminating or greatly reducing grain-to-grain contacts.) Lucchitta [3] thought that they were probably wet, whereas McEwen [4] concluded that they were probably dry. It has even been suggested that the landslides were subaqueous, collapsing into lakes [5]. However, the landslides are among the geologically youngest features on Mars [6]; they clearly postdate the interior layered deposits (of possible lacustrine origin), and there is no evidence for liquid water on the surface of Mars at the time of their formation.

Landslide properties were measured in three regions of Valles Marineris, where 1:500,000-scale topographic maps with 200-m contour intervals are available: (1) the Tithonium and Ius Chasmata region from about lat -9° to -4°, long 83° to 88° [7]; (2) an additional part of Tithonium Chasma from lat -7.5° to -4°, long 80° to 85°; and (3) a region including Ophir Chasma and part of Candor Chasma from lat -7.6° to -3°, long 70° to 75.1°. (Work on maps of the last two regions is in progress by the U.S. Geological Survey.) Within these regions, 25 landslides having identifiable source locations and avalanche deposits were studied. All of the relatively high resolution (200 m/pixel or better) Viking Orbiter images of these areas were utilized.

Landslide volumes were estimated by two methods. For the large landslides with well-defined slump scars, the volume missing from the scars was estimated. For the smaller landslides, the scars are too small relative to the topographic data for the missing volume to be estimated, but the deposits appear to have uniform thicknesses; thus the volumes were estimated from the landslide-deposit area times the estimated height of the flow front. The errors in the volume estimates are small compared

with the variations in landslide volume (more than 5 orders of magnitude.

If we assume a Bingham rheology for the avalanche and uniform, steady flow conditions, then the yield strength, K, may be estimated by $K = \rho g D \sin\beta$, where ρ is the flow density, g is the gravitational acceleration (3.72 m/s for Mars), D is the height of the flow front, and β is the ground slope at the flow front. For ρ, 2000 kg/m^3 was assumed, which is characteristic of terrestrial rock avalanches. Yield-strength estimates range from 10^4 to 10^5 Pa. Terrestrial dry-rock avalanches are characterized by yield strengths near 10^4 Pa, whereas water-saturated debris flows have yield strengths typically from 10^2 to 10^3 Pa. Therefore, even with an uncertainty in the yield-strength estimates of an order of magnitude, the values are clearly consistent with the yield strengths typical of dry rock debris.

Trends of decreasing H/L with increasing volume are obvious from both the terrestrial and the Valles Marineris observations. Least-square fits to the datasets give linear correlation coefficients of 0.82 for the terrestrial points and 0.90 for the Valles Marineris points. The slopes of the two trends are nearly identical. These relations are very different from those seen in wet debris flows, where H/L is almost always less than 0.1 irrespective of volume. If the Valles Marineris landslides were either wet debris flows or subaqueous flows, then the points would be expected to plot below the terrestrial values for dry rock avalanches. Instead, the Valles Marineris trend plots above the terrestrial trend.

Although the slopes of the terrestrial and Valles Marineris trends are nearly identical, there is clearly an offset between the trends. At a given value of H/L, the Martian landslides are typically about 50 to 100 times more voluminous than the terrestrial counterparts, or, at a given volume, H/L is typically about two times larger on Mars. The offset might be explained by the effect of a lower g on flows with high yield strengths. Although this explanation does not answer the more fundamental question of how friction is overcome in large dry-rock avalanches, it does suggest that the correct model should be consistent with the presence of high yield strengths in the moving flows. Fluidization by a gas, for example, eliminates the yield strength in an active flow and is not consistent with the evidence presented here.

[1] Scheidegger, A. E., 1973, Rock Mechanics 5, 231-236.
[2] Hsu, K. J., 1975, Geol. Soc. America Bull. 86, 129-140.
[3] Lucchitta, B. K., 1987, Icarus 72, 411-429.
[4] McEwen, A. S., 1989, Geology 17, 1111-1114.
[5] Shaller, P. J., Murray, B. C., and Albee, A. L., 1989, Lunar and Planetary Science XX, 990-991.
[6] Lucchitta, B. K., 1979, J. Geophys. Res. 84, 8097-8113.
[7] U. S. Geological Survey, 1980, Misc. Inv. Ser. Map I-1294.

DETERMINATION OF COHESION AND ANGLE OF INTERNAL FRICTION OF MARTIAN SLOPE MATERIALS. *Robert Sullivan and Michael Malin, Department of Geology, Arizona State University, Tempe, AZ, 85287.*

Previous work on steep martian slopes, especially the walls of the Valles Marineris, has sought to identify the processes responsible for scarp recession (dry mass wasting has remained the preeminent hypothesis[1]) and the patterns of slope evolution.[2-8] The research reported here has a different objective: the determination of quantitative information about the characteristics of martian materials, using steep slopes only as the most viable setting in which to attempt this. Because of this difference in approach, certain features of steep martian slopes that so far have been less important to previous workers in their efforts become relatively more important in this investigation. The steepest slopes within the Valles Marineris occur just below scarp brinks and are characterized by fine scale crenulations (previously described as U-shaped chutes[1], fluted scarps[2], rocky ribs[3], etc.); these features have received relatively little attention thus far. On close inspection, these small gullies typically have narrow triangular or half hour-glass shapes, with the acute (but usually open) ends pointing downslope, generally resembling terrestrial landslide scars. These features are of similar form to the much larger, more heavily studied (spurs and) gullies, although they are less arcuate, more acute, and occur on generally steeper slopes subjacent to scarp brinks. These fine scale gullies or chutes occur within each of the three main categories of Valles Marineris wall morphology (around the rim and especially at the heads of major gullies, along the walls of tributary canyons, and rimming the headscarps of massive landslide scars) and are characteristic of steep slopes elsewhere on Mars, including the interior walls of the Olympus Mons and Ascraeus Mons calderas, certain places along the basal scarp of Olympus Mons, the walls of channels in the Kasei area, and the interior walls of some large, fresh craters.

The hypothesis investigated in this research is that spur and gully morphology is the result of repeated catastrophic mass-wasting governed by development of a "soil" mantle of reduced strength (compared to the original bedrock) on steep slopes. The mass wasting cycle is defined by a weak mantle layer developing and thickening at the expense of the underlying sloping rock, until the layer fails catastrophically under its own weight down the mantle/rock interface. The shape of the slip surface is largely, but not entirely, defined by the mantle/rock interface. Steep slopes, with correspondingly steep mantle/rock interfaces, will only be able to develop relatively thin mantles before layer failure occurs, producing relatively shallow, narrow gullies from nearly flat slip surfaces, and tightly-spaced, shallow spur and gully slope morphology. The hypothesis also implies that gentler slopes will require thicker soil development for failure to occur, resulting in relatively deeper, wider gullies, with significant curvature to their slip surfaces.

The hypothesis is supported by evidence for considerable soil production on Mars. Direct evidence is supplied by in situ detection and characterization of soils at the Viking Lander sites,[9] observations of large dust storms,[10] observations of aeolian features,[11] and, indirectly, indications of a .1 - 2 m mantle of fine particles covering much of the martian surface.[12] Soils generally have significantly lower strengths than the rock they are derived from, and periodic catastrophic mass-movement of developing soil of reduced strength seems inevitable if the resulting soil is weak enough and slopes are steep enough.

The strength of geological materials can be described by the well-known Coulomb equation:

$$\tau = c + \sigma \tan \phi$$

where τ = shear stress, c = cohesion, σ = normal stress, and ϕ = angle of internal friction. Values of cohesion, c, for common geological materials range across three orders of magnitude; angles of internal friction range from about 7 to 50 degrees.[13] Although different rock groups have their own ranges of c and ϕ, and some groups overlap one another, many rock groups can be distinguished readily from one another on the basis of their strength parameters. An important consequence of the wide range of rock types and c and ϕ values is that it is not necessary to determine c and ϕ values themselves with great precision to identify likely candidates for analogs to martian materials.

The stability of several standing (whole) slopes in Noctis Labyrinthus and several large wall failures with small displacements in the Tithonium-Ius Chasmata region has been evaluated

previously by assuming material homogeneity and log-spiral potential failure surfaces.[8] The present work differs significantly in that the hypothesis investigated: (1) focuses on the fine scale mass-wasting chutes on the steepest slopes (no talus components) immediately subjacent to scarp brinks; and (2) requires failure surfaces that reflect material inhomogeneities by following mantle/rock interfaces, resulting in failure surfaces that are not log-spiral but planar over considerable percentages of their profiles. The procedure employed in this study for analysis of the martian mass wasting features is, in some ways, the inverse of standard civil engineering practice, which typically determines the factor of safety of a slope that has not yet undergone failure. As slope failure for the martian chutes has already occurred, the factor of safety is set = 1. The gradient of these chutes can be inferred from one published and two preliminary high resolution 1:500K topographic maps covering portions of the Valles Marineris.[14,15,16] An infinite slab analysis (setting the factor of safety = 1) is used together with the thickness of the slide mass indicated from orthographic Viking images to solve for likely pairs of c, ϕ values. The state of progress of this research does not yet support conclusive generalizations, but preliminary results indicate: (1) friction angles of about 30° or less are implied for much of the spur and gully slope mantle material for which we have topographic data; and (2) in many cases c, ϕ values of martian slope mantle material indicate that soft glacial clay, stiff glacial clay, and glacial till serve as the closest terrestrial mechanical analogs. Ongoing work includes the application of this analysis to additional slope localities on Mars, the comparison of infinite slope analysis used here with the Morganstern-Price technique[17] for chutes with relatively high thickness:profile length ratios, and the analysis of the stability of the standing walls of these fine-scale chutes.

Sample calculation

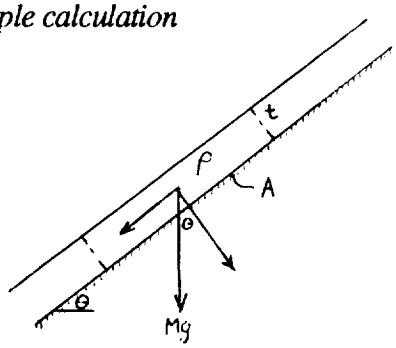

At failure, $\tau = c + \sigma \tan\phi$, so $\frac{\rho g A \sin\theta}{A} = c + \frac{\rho g A \cos\theta}{A} \cdot \tan\phi$

which yields: $t = c / (\rho g \cos\theta(\tan\theta - \tan\phi))$. For mass movement indicated at lat -3.91, lon 74.58 (VO915A10, MTM -05072, preliminary topographic map), $\theta \sim 33$ deg, t indicated ~ 140 m.

For $\rho \sim 1220$ kg/m^3 (terr.), then possible c,ϕ = (50 kPa, 29.2 deg)
For $\rho \sim 1840$ kg/m^3 (terr.), then possible c,ϕ = (55 kPa, 30.2 deg)
For $\rho \sim 2040$ kg/m^3 (terr.), then possible c,ϕ = (60 kPa, 30.3 deg)

In each case the values for c,ϕ lie within the range of terrestrial soft glacial clay (the corresponding terrestrial density is ~1220 kg/m^3).

References

[1] Sharp, R. P., *J. Geophys. Res. 78*, pp. 4063-4072, 1973. [2] Blasius, K. R., J. A. Cutts, J. E. Guest, and H. Masursky, *J. Geophys. Res. 82*, 4067-4091, 1977. [3] Lucchitta, B. K., Intreragency Report: Astrogeology 83, 51 pp., 1977. [4] Lucchitta, B. K., *Jour. Res. U. S. Geol. Survey, 6*, No. 5, pp. 651-662, 1978. [5] Patton, P. C., *in Reports of Planetary Geology Program - 1981, NASA Tech. Mem. 84211*, 324-325, 1981. [6] Patton, P. C., *in Reports of Planetary Geology Program - 1982, NASA Tech. Mem. 85127*, 242-243, 1982. [7] Patton, P. C., *in Reports of Planetary Geology Program - 1983, NASA Tech. Mem. 86246*, 324-325, 1984. [8] Clow, G. D., H. J. Moore, P. A. Davis, and L. R. Strichartz, (abstract), *in Lunar Science XIX* (Lunar and Planetary Institute, Houston), 201-202, 1988. [9] Moore, H. J., R. E. Hutton, G. D. Clow, C. R. Spitzer, *U. S. Geological Survey Professional Paper 1389*, 222 pp., 1987. [10] Slipher, E. C., 1962, *The Photographic Story of Mars*, Northland Press, Flagstaff, AZ. [11] Greeley, R., and J. Iversen, *Wind as a Geological Process*, (Cambridge: Cambridge University Press), 333 pp., 1985. [12] Christensen, P. R., *J. Geophys. Res. 91*, 3353-3545, 1986. [13] Hoek, E., and J. Bray, *Rock Slope Engineering*, 3rd ed., (London: Institution of Mining and Metallurgy) , 358 pp., 1981. [14] U. S. Geological Survey, Topographic orthophoto mosaic of the Tithonium Chasma region of Mars, 1:500K, Map I-1294, 1980. [15] U. S. Geological Survey, Preliminary topographic map of the Candor Chasma part of the Valles Marineris region of Mars, 1:500K, 1989. [16] U. S. Geological Survey, Preliminary topographic map of lon -2.5 to -7.5, lat 80 to 85, Mars, 1:500K, 1989. [17] Morganstern, N. R., and V. E. Price, *Geotechnique,15*, pp. 79-93, 1965.

"BLACKHAWK-LIKE" LANDSLIDES ON EARTH AND MARS

Philip J. Shaller and Bruce C. Murray, Division of Geological & Planetary Sciences, California Institute of Technology, Pasadena, CA 91125

Long-runout landslide deposits on Earth and Mars share a common range of morphologies. **Figure 1** illustrates one common morphology type that occurs on both planets. The deposits are characterized by thick, distal debris heaps which thin toward the headscarp. Headward of the distal heap, the deposits are marked by thin debris sheets bracketed by distinct lateral levees which nearly match the height of the distal heap. These deposits are referred to as "Blackhawk-like" because the Blackhawk landslide in southern California is the most familiar terrestrial example of this morphology type (Shreve, 1968a). Other terrestrial examples occur in the Sierras Pampeanas of northern Argentina (Fauque and Strecker, 1988). One martian and one terrestrial example are bi-lobate, but otherwise share the same characteristic features. Second-order characteristics of the "Blackhawk-like" landslides include faint alternating radial light and dark bands on the distal heaps and transverse distal heap ridges, which are clearly exhibited only on the Blackhawk and Silver Reef landslides in California.

A characteristic difference between the martian and terrestrial "Blackhawk-like" landslides is the greater thickness of the martian landslides as determined from shadow measurements on high-resolution Viking Orbiter images of the deposits. The distal heaps of many terrestrial deposits measure about 30 m in thickness, while 80 m is common in martian landslides. This thickness difference may be a response to the difference in gravity between the two planets. Martian gravity is 0.38 the terrestrial value.

The distribution of martian "Blackhawk-like" landslides is not characteristic of other martian landslide deposits, which are concentrated in Valles Marineris. None of the six martian examples lie in Valles Marineris; five are in the old cratered highlands, and one is situated in the caldera of Olympus Mons. The landslides therefore occur on both the oldest and youngest geologic units on the planet. None of these deposits appear to be of great age because they exhibit few or no impact craters and have clear, unmodified morphologies. These geologically recent landslides therefore were probably emplaced under essentially modern martian climatic conditions.

Figure 2 plots log(volume) versus the ratio of runout length to fall height for six terrestrial and six martian "Blackhawk-like" landslides. The plot illustrates that the commonly observed correlation between increasing volume and long-runout for large landslides holds for both the martian and terrestrial deposits (Hsü, 1975). However, the trends in **Figure 2** are parallel rather than co-linear. This indicates that, for a given volume and fall height, the martian "Blackhawk-like" landslides will not travel as far as their terrestrial counterparts. This is probably related to the observation that martian landslides are several times thicker than their terrestrial counterparts. Thus, the martian deposits do not spread out as much as do landslides on Earth and the slides do not extend as far from the headscarp.

Figure 3 interprets the morphological development of "Blackhawk-like" landslides during deposition. Immediately following the initial slope failure, the landslides take up a bulbous shape distally and begin to deposit a thin sheet of rubble bracketed by sharp lateral levees. As motion continues, deposition of the thin sheet and levees proceeds, while the bulbous distal heap shrinks in relative

dimensions. Apparently, debris in the thin sheet and levees is derived from the distal heap, which shrinks as motion and deposition continue. Given a sufficiently high ratio of fall height to volume, the process will continue until the distal heap is used up. The resulting deposit is an elongate ring of debris. Given varying starting conditions, a "Blackhawk-like" landslide may be frozen in place at any step in this progression.

Several conclusions can be drawn about the nature and mechanics of "Blackhawk-like" landslides from the above data. The first conclusion is that the landslides are dry at emplacement. This is argued for the terrestrial examples (Shreve, 1968a; Fauque and Strecker, 1988) and is supported for the martian landslides by their geographic distribution. All the martian "Blackhawk-like" landslides originated in surficial deposits in low latitude regions thought to be dessicated to considerable depth. From 35° to 0° latitude, Mars is considered dessicated to a depth of 40 to 120 m respectively (Fanale, et al., 1986). Near-surface liquid water is particularly unlikely for the deposit in the caldera of Olympus Mons, which originated in basaltic talus and bedrock at an altitude of 25 km.

The occurrence of geologically recent "Blackhawk-like" landslides on Mars is also significant for evaluation of the air-layer lubrication theory of long-runout. Shreve (1968a,b) developed the theory to explain the long-runout and unusual sedimentological and morphological features of the Blackhawk landslide. However, only under exceptional circumstances can air-layer lubrication operate on Mars with its current thin atmosphere. In air-layer lubrication, a landslide must capture and retain beneath it a pressure of gas equivalent to its weight. At the datum elevation on Mars (6.1 mbar pressure), an 80 m-thick breccia sheet would have to trap a 40 m high column of atmosphere per unit area of landslide to support a 0.3 m compressed gas cushion beneath the landslide. In comparison, a 30 m breccia sheet on Earth need only capture a 0.8 m column of air per unit area of landslide (Shreve, 1968b). Even given a high launching ramp, which occurs for some of the deposits, collecting the required volume of gas per unit area is difficult. However, given a suitable captured gas layer and an 80 m thick debris sheet of 1 darcy permeability, leakage would be slow enough to allow air-layer lubrication on Mars.

Other characterisites of "Blackhawk-like" landslides are also difficult to reconcile with air-layer lubrication. One factor is the 2.6 times greater thickness of martian landslides compared with terrestrial examples. This variation cannot be explained by the air-layer theory. Also, the martian deposits and at least one terrestrial example fail to exhibit tranverse ridges, which are attributed to catastrophic slowing of air-lubricated landslides when the air layer leaks out. Further, the time-variable morphologic development of the "Blackhawk-like" landslides inferred in **Figure 3** does not agree with the model developed by Shreve (1968a). Also, there is no apparent relation between the height of cliffs jumped (or not jumped) by the martian deposits and the runout lengths of the landslides, as might be anticipated in a gas-starved environment.

Though the mechanism of long-runout and morphology development of the "Blackhawk-like" landslides is not yet clear, the martian examples appear to rule against air-layer lubrication. The morphological similarities between the martian and terrestrial examples implies that the same mechanism operates for all "Blackhawk-like" landslides. Any viable mechanism must account for the observed characteristics as well as explain why all landslides do not form the "Blackhawk-like" morphology during deposition.

References:

Fauque, L. and M. R. Strecker, 1988. Large rock avalanche deposits (Sturzströme, sturzstroms) at Sierra Aconquija, northern Sierras Pampeanas, Argentina, Eclogae geol. Helv., 81(3), 579-592.

Fanale, F. P., et al., 1986. Global distribution and migration of subsurface ice on Mars, Icarus, 67, 1-18.

Hsü, K. J., 1975. Catastrophic debris streams (Sturzstroms) generated by rockfalls, G. S. A. Bull., 86, 129-140.

Shreve, R. L., 1968a. The Blackhawk landslide, G. S. A. Spec. Pap. 108, 47 p.

Shreve, R. L., 1968b. Leakage and fluidization in air-layer lubricated avalanches, G. S. A. Bull., 79, 653-658.

Figure 1: Generalized Morphology of "Blackhawk-Like" Landslides

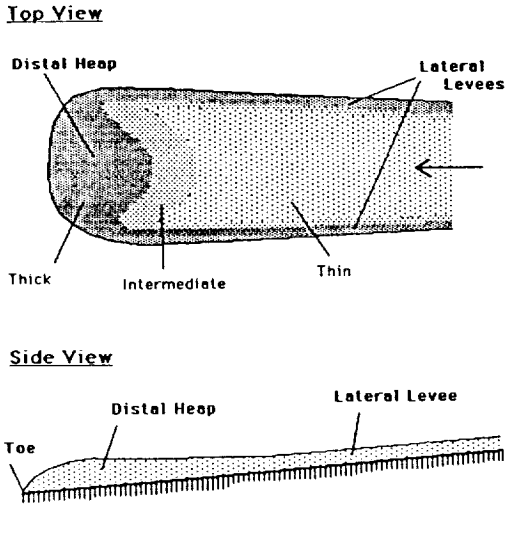

Figure 2: Plot of Volume vs. Runout Length to Fall Height Ratio for Martian and Terrestrial "Blackhawk-Like" Landslides

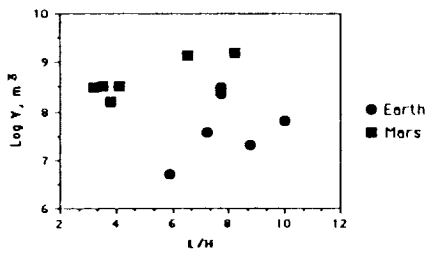

Figure 3: Interpretation of Development of "Blackhawk-Like" Morphology

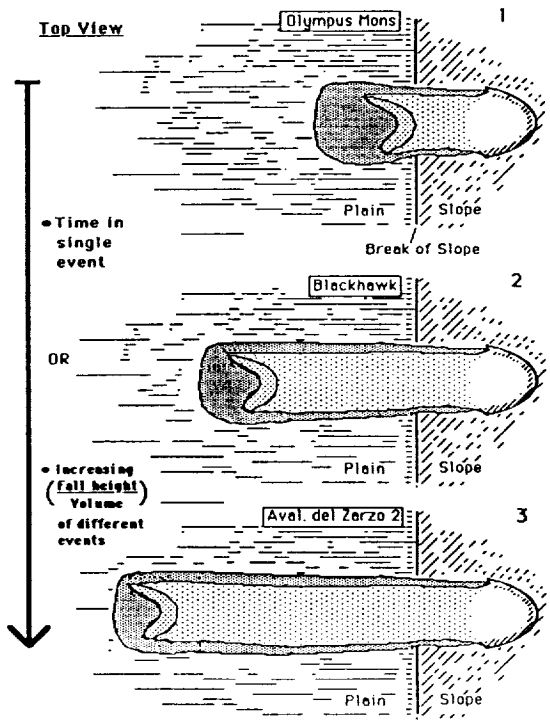

LARGE SCALE COMPRESSION STRUCTURES IN THE ERIDANIA–PHAETHONTIS REGION: MORE EVIDENCE FOR POLAR WANDERING. R. W. Wichman and P. H. Schultz. Dept. of Geological Sciences. Brown University, Providence R.I.

INTRODUCTION: Although most tectonic structures on Mars can be associated with stresses due to either Tharsis formation (1,2,3,4) or basin modification (4,5,6), some structures in the martian highlands appear to be independent of both stress sources. Two major systems of ridges and scarps rival the lobate scarps of Mercury in size and indicate that a large, regional–scale compressional event occurred in the Terra Cimmeria/Terra Sirenum region (7). These structures cannot be explained by either Tharsis–centered or basin–centered regional stress models, but may reflect deformation due to polar wandering as predicted by Melosh (8). If the Tharsis Province was not so interesting tectonically, the size and isolation of these features would have attracted immediate attention and possibly stimulated discussions comparable to those of the mid–1970's for Mercury. In this abstract, we use crater deformation to estimate the amount of crustal shortening across these scarp/ridge systems and reconsider the possible sources the causative compressional stress field.

FEATURE DESCRIPTION: The ridge systems described here are Eridania Scopulus and a system of scarps and ridges located near the Copernicus impact basin. The two systems are of similar age with crater dates (derived from linear crater counts (6,9)) of ~381 ± 270 and ~341 ± 240 $N(>5)/10^6$ km^2, respectively. The Copernicus ridge system is at least 840 km in length, whereas Eridania Scopulus extends over 1000 km. Shadow measurements indicate typical scarp and ridge heights of 500–700 m with a maximum relief exceeding 1 km. The systems are thus comparable in size and scale of deformation to the mercurian lobate scarps, which are typically several hundreds of kilometers in length and range in relief from a few hundreds of meters to one or two kilometers (10,11). The martian systems differ, however, in detailed morphology from the mercurian lobate scarps. The mercurian scarps are typically more rounded and flatter in profile than the martian features; and while the mercurian scarps occur as long, individual features, the martian systems are continuous bands of deformation 100 to 200 km wide containing between 2 and 5 distinct, parallel to subparallel structures. In general, these structures are scarp–like with a backslope away from the scarp on the uplifted side. Where they cross the floors of large craters (>20 km diameter) or intercrater plains units, scarp expression is subdued and more rounded. In some plains regions the scarps then merge into wrinkle ridge systems of the same orientation. Finally, the martian scarp systems coincide with or form apparent linear topographic highs (figure 1). Such behavior is not characteristic of the mercurian lobate scarps and may reflect the combined effects of uplift across individual structures in the martian systems.

CRUSTAL SHORTENING: The nature and degree of deformation in the martian ridge/scarps are best revealed by the modification of craters. Deformation most commonly joins scarps of higher relief on each side of the crater with a linear, asymmetric ridge cutting directly across the crater floor. This pattern resembles crater deformation along the mercurian lobate scarps (11), but differs from the typical deformation associated with smaller wrinkle ridges, which tend to curve around a crater interior instead of cutting directly across it (4,12). A less common modification along the martian ridge/scarps preserves partial craters on the elevated side of a scarp but does not preserve the corresponding down–thrown rim sections (figure 1). Three craters appear foreshortened due to compressional deformation; one of these also shows an offset rim along the scarp resembling deformation of the Guido d'Arezzo crater by the Vostok scarp on Mercury (11). For initially circular craters with no extension perpendicular to compression, the difference between the long and short axes of a deformed crater provides a measure of the regional shortening across the structure. Such measurements for these three craters indicate on the order of 1.5–3 km of crustal shortening across individual scarp features. This is comparable to the values derived by Strom et al (10) for Mercury, where approximately 1–2 km of shortening is estimated for individual mercurian lobate scarps.

The linear nature of deformation in crater interiors and the preservation of uplifted partial craters are consistent with compression by deep–seated thrust or reverse faulting. Consequently, the observed scarp relief helps to constrain fault models for comparison with the observed crater shortening. For a reverse fault with a dip of 60° and a scarp 500 m in elevation, we would expect ~290 m of shortening, a value some 5 to 10 times smaller than that indicated by the deformed craters. Alternatively, a thrust fault with a dip of 25° and scarp relief of 500 m would indicate ~1000 m of shortening, consistent with the estimated crater deformation. Therefore, a thrust fault model for these scarps appears consistent with the observed deformation, and the parallel scarps in the Eridania and Copernicus–Newton systems might represent systems of associated thrust sheets. If the shortening over each thrust is on the order of 1–2 km, in keeping with the crater deformation, such systems could accomodate up to 5 to 10 km of regional shortening perpendicular to the scarp trends.

DISCUSSION: The timing of this compressional event can be derived from the crater ages of the two systems and is broadly correlated to the time of Tharsis formation (figure 2). Due to the large error bars, however, these age determinations encompass both the time of ancient Tharsis faulting and the later main phase of Tharsis radial fracturing. Although coincident in time with Tharsis–centered

deformation, the scarp/ridge systems occur over 70° from the center of Tharsis. Of the Tharsis load models developed by Banerdt et al (3), only the isostatic load model could provide compressive stresses at this distance from Tharsis. Based on the observed deformation east of Tharsis, however, Banerdt et al argue that this model only applies to regions less than 40° from the Tharsis center. Furthermore, the two scarp/ridge systems occur at a distinct angle to each other; neither trend is consistent with the Tharsis stress orientations. Because the systems are well removed from the nearest recognized large impact basins (Hellas, Isidis), basin-centered stresses also seems negligible. Even if a large buried basin did exist in the region, current models of basin-centered deformation (6) could not account for the observed pattern of regional compression.

Some significant regional stress field independent of both Tharsis and basin-controlled deformation thus appears responsible for the formation of these ridge/scarp systems. The global contraction mechanism proposed for Mercury (10,11) seems unlikely on Mars given the early timing and regional scale of the ridge/scarps as well as the widespread contemporary extension associated with Tharsis. Polar wandering, however, can simultaneously produce regions of compressive and tensile stress at the several kilobar level (8), thereby producing the scale of deformation indicated by the crater shortening data. The location and orientation of the scarp/ridge systems are consistent with polar wandering in response to Tharsis development (7), as is the correlation in age of ridge formation with initial Tharsis activity.

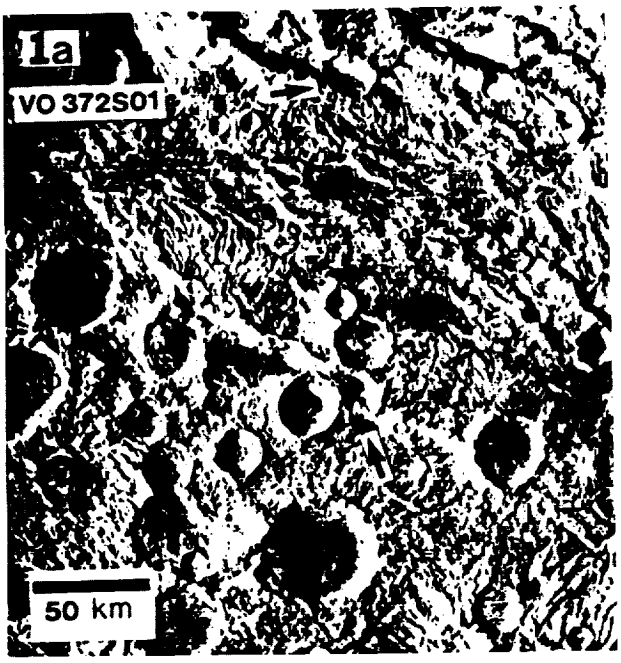

Figure 1. Parts of the Copernicus system (a) and Eridania Scopulus (b). Arrows indicate craters modified by scarp formation.

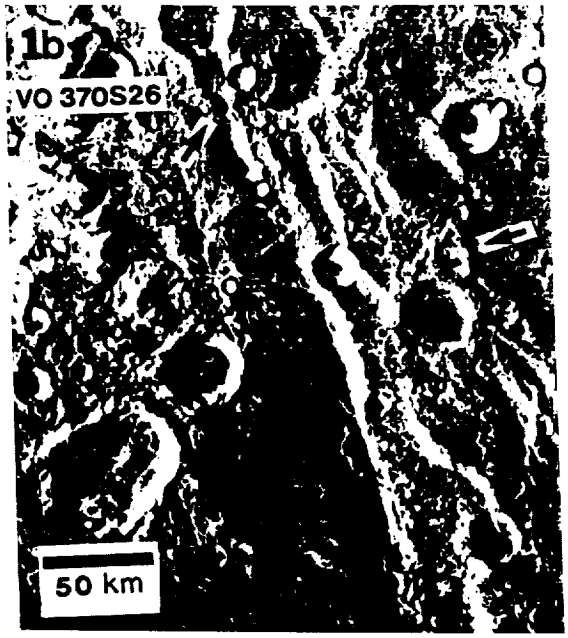

CONCLUSIONS: Large ridge/scarp systems in the Terra Cimeria/Terra Sirenum region appear to reflect a major regional event of compressional deformation with regional crustal shortening of up to 5–10 km. Although contemporary with Tharsis fracturing, ridge system formation appears to be independent of Tharsis stress fields and is more consistent with deformation expected in the polar wander scenario of Schultz and Lutz (7).

REFERENCES: 1)Wise et al (1979) *Icarus 38*, 456-472. 2)Plescia and Saunders (1982) *J. Geoph. Res. 87*, 9775-9791. 3) Banerdt et al (1982) *J. Geoph. Res. 87*, 9723-9734. 4) Chicarro et al (1985) *Icarus 63*, 153-174. 5) Wichman and Schultz (1987) *Lunar Planet. Sci. Conf. 18*, 1078-1079. 6) Wichman and Schultz (1989) *J. Geoph. Res. 94*, 17333-17357. 7) Schultz and Lutz (1988) *Icarus 73*, 91-141. 8) Melosh (1980) *Icarus 44*, 745-751. 9) Wichman and Schultz (1986) *Lunar Planet. Sci. Conf. 17*, 942-943. 10) Strom et al (1975) *J. Geoph. Res. 80*, 2478-2507. 11) Strom (1978) *Space Sci. Rev. 24*, 3-70. 12) Schultz (1976) *Moon Morphology*.

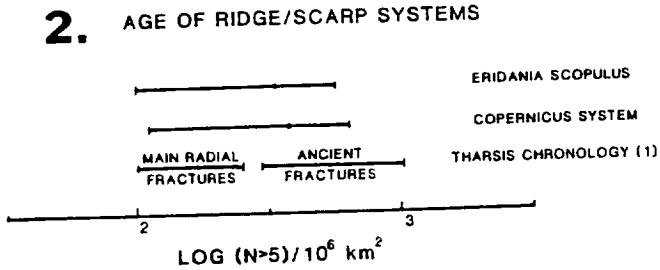

Figure 2. Crater ages derived from linear crater counts (6) for the scarp/ridge systems compared to the Tharsis tectonic history of Wise et al (1).

A MODEL FOR CRUSTAL SUBDUCTION BY LARGE IMPACTS; R. W. Wichman and P. H. Schultz. Dept of Geological Sciences, Brown University, Providence, R.I. 02912.

Introduction: In the standard model of crater excavation, ballistically ejected material represents only about half the volume of the transient cavity (1). The other half corresponds to downwardly displaced, shock-compressed material driven beneath the transient cavity (e.g., 1, 2, 3, 4, 5). In large craters, the final crater then forms by the collapse of this transient cavity with uplift and inward flow of the shocked, displaced material comprising the crater floor (6). Although this idealized model of crater formation fits most well-preserved planetary impact structures, it implicitly assumes an elastic halfspace beneath the target surface which may be inappropriate for modeling the largest early basin-forming impacts. For these very large impacts, the depth of the transient cavity may excede the lithospheric thickness and, at least on Mars, such cavities apparently can interact with underlying viscous mantle regimes during basin formation (7). The extreme size of these cratering events also challenges some of the assumptions concerning cavity growth and collapse extrapolated from smaller structures (8). In this abstract, we propose that viscous deformation beneath very large impacts can allow emplacement of vertically displaced crustal material in the mantle, and we speculate on the implications such "impact subduction" might have for subsequent mantle evolution.

Subduction Model: Although material flow fields result in ballistic trajectories for most near-surface regions of the transient cavity, a full target section is preserved under the center of the impact. In the case of an elastic half space, compression of this section against undeformed rocks at greater depth enhances lateral flow, disrupting the column and spreading it across the base of the transient cavity. If viscous flow occurs beneath the impact, however, downward displacement of this crustal section is partly accomodated by lateral flow in the mantle below. This process transfers impact deformation from the lithospheric section to the mantle and results in the emplacement of shocked crustal material into rocks of the upper mantle or asthenosphere. Although later dynamic rebound might limit the depths such material could reach, rebound uplifts the region beneath the crater as a whole (not the displaced elements of the transient cavity alone) and the sub-impact crustal section initially should stay in the mantle.

Viscous deformation of the mantle during impact is thus a necesary condition for the emplacement of crustal sections at depth. The probability of such deformation can be evaluated by comparing the duration of the impact event to the Maxwell time (T_m) of the mantle: $T_m = \tau/2\mu\dot{\epsilon}$ where τ is applied shear stress, μ is shear modulus (~ 10^6 MPa) and $\dot{\epsilon}$ is strain rate of deformation. The Maxwell time is defined as the time required for viscous creep under stress to equal elastic strain (9); consequently, viscous behavior occurs when deformation times are greater than T_m. Deformation is essentially elastic for timescales less than T_m (9). If an impact generates shear stresses of over 10 kilobars (10^3 MPa), strain rates in an olivine mantle range from 10^{-2} to 10^{-4} /s for mantle temperatures of 800-1000°C (10). These values translate to Maxwell times on the order of 1-100 seconds. Because mantle flow requires that the duration of impact exceed T_m, only large, low-velocity (5-6 km/s) impactors (which have impactor penetration times of several tens of seconds (8)) are likely to induce such a viscous mantle response.

The extent of viscous deformation beneath an impact depends on the impact angle and the duration of the impact relative to T_m. If we define d as the depth of the transient cavity (roughly the penetration depth of the projectile into the target), for near-vertical (>60°) impacts, d can be approximated by the projectile diameter (D_p) but d decreases significantly as the impact angle is then reduced to 5° (11). While rare, near-vertical impacts are not improbable and are the most likely to emplace material at depth in the mantle. For a near-vertical impact with a duration equal to T_m, therefore, we expect viscous mantle deformation comparable to the size of the impact cavity extending to depths of ~D_p beneath the base of the transient cavity. Since the thickness of the down-driven core is of the same scale as the mantle deformation, the crustal section remains near the base of the transient cavity and is likely to be embedded in the basin floor after dynamic rebound. If the duration of the impact is significantly greater than T_m, however, lithospheric material can penetrate the mantle to depths of several D_p. We propose that mantle flow will engulf this displaced crustal section outright with depths of crustal burial in the range of ~ $0.5D_p$ to $2D_p$. This burial of crustal material in the mantle is reminiscent of terrestrial plate subduction and, for a projectile 200 km in diameter, such "subduction" could bury crust to depths of between 100 and 400 km.

The requirement of large, low-velocity impacts for this subduction mechanism limits the extent of this process in planetary history. First, impacts of sufficient size are restricted to the period of basin-forming impacts before ~3.7 Ga. The low impact velocity, however, is a stronger constraint on the occurrence of impact subduction, since only a few planetary impactor populations permit impacts at 5-6 km/s. The planet most likely to have experienced such collisions is Mars, where impact velocities range down to ~5 km/s for co-orbiting, heliocentric objects (12). The coincidence in age of these basins with a time of predicted high mantle temperatures (13) also favors subduction by this mechanism. On the Earth and Venus, impact velocities range from 15-40 km/s and 17-44 km/s, respectively (8,14) and impact subduction is much less likely. Although viscous deformation beneath the impact is still possible at velocities of 15 km/s (for mantle temperatures on the order of

1300–1400°), the increased extent of of vaporization and melting beneath the impact may preclude preservation of a lithospheric section in the mantle during cavity collapse. Some contamination of the mantle by projectile or crustal components might still be expected, however. On Mercury, the predicted impact velocities for comets and earth-crossing asteroids (~34–44 km/s (8)) probably preclude impact subduction. Nevertheless, impactors from the postulated population of Vulcan asteroids (15) should have had much lower velocities, so impact subduction is also possible for Mercury. The probability of subduction on the Moon (impact velocities down to ~6 km/s (12)), depends more strongly on the state of the lunar interior. Thinner lithospheres associated with a magma ocean might permit early subduction events, but the growth of the lithosphere over time would inhibit mantle flow and prevent later subduction.

Implications: Unlike the more continuous subduction of oceanic plates observed on Earth, impact subduction is randomly located and episodic on a global scale. Hence only random and isolated regions of a planetary mantle can be modified by this process. Long-term effects of oceanic subduction such as repeated passage of melts into island arcs or convection beneath back arc basins are thus unlikely to occur for impact subduction. In further contrast, mantle cooling associated with subduction of cold lithospheric plates should not occur with impact subduction due to both shock heating and shear deformation in the subducted section. To first order, this section is presumed to be in thermal equilibrium with normal mantle temperatures at the time of emplacement. Although such a view is over simplistic, the mantle evolution sequence presented below can be regarded as indicative of the relative time scales required to achieve various mantle states.

Impact subduction can potentially influence mantle evolution in two ways. Injection of crustal radiogenic elements into the mantle could affect the long-term thermal history, whereas the introduction of crustal volatiles could affect the melting sequence. In the first case, a crustal block would begin to melt in ~4–6 Ma for subduction to 10 kb pressure with an initial post-impact temperature of 1000°C. Total equilibrium melting then would occur in 9–11 Ma. Significant mantle melting is unlikely to result in this time, since ~16 Ma are needed to achieve lherzolite melting temperatures outside a subducted crustal block. The melting of embedded crustal material, however, will influence the long term thermal evolution of the surrounding mantle. Since a fraction of melt is trapped along grain boundaries during porous flow, we can approximate the mantle composition after crustal melting by mixing a disseminated crustal component into the mantle. For mantle-crust ratios of 100:1, such mixing can double the abundance of heat producing elements in the mantle and these added heat sources eventually can induce mantle partial melts some 100–500 Ma after the subduction event.

The subduction of volatile concentrations could produce mantle melts on much shorter time scales. Although water is unlikely to be a major constituent of the crustal section as a whole, water or ice may be concentrated in near surface regions. For a volatile-rich regolith 500 m thick with 25% porosity, subduction under a 100-km radius projectile can subduct over 1000 km^3 of water. If the projectile caps the subducted section and drives it into the mantle, this volatile phase may not escape into the transient cavity and will be trapped instead near the top of the crustal section. Addition of such a vapor phase to surrounding mantle compositions significantly reduces the solidus temperatures and, at 1000°C and 10 kb, can initiate immediate mantle melting. If carbonates are present in the martian regolith, the associated fluid-rich and volatile phases could possibly acheive a kimberlitic character.

Conclusions: Large, low velocity impacts may inject significant crustal sections into a planetary mantle, but this process will be most efficient if the mantle yields viscously around impact-driven subsidence. Such behavior is most likely before 3.7 Ga on Mars, but also may have occurred on Mercury or the early Moon. The depth of subduction is dependent on the relative scale of impact and mantle flow regimes, but can achieve depths of over 100–200 km for projectiles over 100 km in radius. The effects of such subduction on mantle evolution are unlike those observed in terrestrial subduction zones and primarily reflect the effects of subducted volatile and radiogenic isotope concentrations. Escape of vapor into the mantle should produce kimberlite-like mantle melts soon after impact. Crustal melts develop some 5–10 Ma after impact and enrich higher mantle regions in radiogenic isotopes. Finally, isotopic heating of this enriched mantle may lead to renewed mantle melting several hundred million years after the original impact event. Such a mantle melt sequence may fit the general sequence of highland volcanism observed on Mars where explosive, patera volcanism evidently preceded formation of most of the basaltic shields and ridged plains (16).

REFERENCES: 1) Stoffler et al (1975) *J. Geophys. Res. 80*, p. 4062–4077. 2) Gault et al (1968) In *Shock Metamorphism of Natural Materials* (R.M. French and N.M. Short, eds.) p. 87–99. 3) Dence et al (1977) In *Impact and Explosion Cratering* (D.J. Roddy, R.O. Peppin and R.B. Merrill, eds.) p. 247–275. 4) Schultz et al (1981) *Proc. Lunar Planet. Sci. 12A*, p. 181–195. 5) Croft (1981) *Proc. Lunar Planet. Sci. 12A*, p. 207–225. 6) Grieve (1981) *Proc. Lunar Planet. Sci. 12A*, p. 37–57. 7) Wichman and Schultz (1989) *J. Geophys. Res. 94*, 17333–17357. 8) Schultz (1988) In *Mercury* (F. Villas, C.R. Chapman and M.S. Matthews, eds.) p. 274–335. 9) Melosh (1989) *Impact Cratering*, p. 156. 10) Stocker and Ashby (1973) *Rev. Geophys. Space Physics 11*, p. 391–426. 11) Gault and Wedekind (1978) *Proc. Lunar Planet. Sci. Conf. 9*, 3843–3875. 12) Hartmann (1977) *Icarus 31*, 260–276. 13) Schubert et al (1979) *Icarus 38*, 192–211. 14) Shoemaker (1977) *Impact and Explosion Cratering* (Roddy, D.J., Peppin, R.D., and Merrill, R.B., eds) pp. 617–628. 15) Leake et al (1987) *Icarus 71*, 350–375. 16) Greeley and Spudis (1981) *Rev. Geoph. Space Phys. 19*, 13–41.

HYPOTHESES FOR THE ORIGIN OF THE MARTIAN CRUSTAL DICHOTOMY

George E. McGill, Department of Geology and Geography, University of Massachusetts, Amherst, MA, and Steven W. Squyres, Center for Radiophysics and Space Research, Cornell University, Ithaca, NY

The martian crustal dichotomy has been explained by three general types of hypotheses: endogenic, single impact, and multiple impact. Wise et al. [1,2] propose that the contrast in crustal thickness was caused by local subcrustal erosion over a large, first-order mantle convection cell that existed prior to core formation; this model thus implies an early origin for the dichotomy. McGill and Dimitriou [3] argue that the geological evidence points to an endogenic origin after the end of primordial bombardment. Wilhelms and Squyres [4] propose that the crust was locally thinned and the lowland created by a single gigantic impact event, forming the Borealis basin. Finally, Frey and Schultz [5] argue that the crustal dichotomy and its associated lowland can be explained as due to a small number of large (but not gigantic) overlapping basin impacts. Both impact hypotheses involve processes that must have occurred before the end of primordial bombardment, and thus they also imply an early origin for the dichotomy.

Any hypothesis for the origin of the martian global dichotomy should survive three elementary tests: 1. How well the observed plan shape and apparent depth of the martian lowland are explained. 2. Consistency with reasonable physical processes. 3. Compatibility with geological and geophysical observations. The very existence of three contrasting hypotheses, each with convinced partisans, emphasizes the complexity and incompleteness of the data needed to determine the origin of the martian crustal dichotomy.

A single, gigantic impact obviously will produce a very large, deep, roughly circular depression. However, any attempt to circumscribe the northern lowland with a single circle demonstrates that the lowland departs rather dramatically from a circular shape in places [e.g., 5]. Many of these deviations are easily accounted for as due to the effects of later, but still primordial, basin impacts cutting the perimeter of the circle. Some additional deviations from a circular shape may be due to later erosion modifying parts of the dichotomy boundary. However, deviations from circularity, as in the general region of Chryse and Acidalia planitiae where even a possible Chryse basin does not fully account for the shape of the lowland, remain as problems. But large basins are not necessarily circular when formed, as exemplified by a number of well documented lunar examples [6]. Whether a truly gigantic basin such as Borealis should be more or less circular than merely large basins is not known. Answering this question would be a useful objective for a modeling study.

Currently evolving models for the accretion of terrestrial planets [7] clearly support the high probability of one or more truly giant impacts occurring late in the accretionary process. There is thus support from cosmology for the physical reasonableness of a Borealis basin despite its unusually large size.

The geological evidence for Borealis consists primarily of 5 massifs that lie on the same small circle [4]. No evidence for an ejecta blanket has been described, even though the volume of crust that must be displaced to produce the northern lowland is on the order of 10^9 km^3 [3], and analogy with ordinary large lunar basins suggests that most of this ejected crust should be found in an annulus around the lowland. But the Borealis impact very likely occurred almost immediately after the ~4.55 Ga origin of Mars, and thus the textural criteria for an ejecta blanket would likely be destroyed by younger intense bombardment. Furthermore, because Borealis is so large, it is at least possible that its ejecta were more uniformly distributed around the globe, effectively resurfacing the planet with a layer of average thickness about 7 km. This last hypotheses is in need of quantitative modeling.

Unlike for Borealis, endogenic hypotheses imply no *a priori* tendency towards a roughly circular plan shape for the martian northern lowland. On the contrary, the observed plan shape is a major constraint on the geometry of the convection cell or plume causing the dichotomy. The local details of lowland shape are again easily ascribed to the few known large basins that lie partially or entirely within the lowland, or to local younger erosion.

There is abundant geological evidence for internally driven tectonic events that are areally related to the northern lowland or its boundary, and that clearly occurred after the end of primordial bombardment. Of particular interest are extensive fracturing and related igneous activity of late Noachian to early Hesperian age [3,8,9,10]. Critical to the interpretation of these observations is whether they actually require, rather than simply permit, origin of the crustal dichotomy after the end of primordial bombardment; if they require it, then both impact hypotheses are untenable. Where the dichotomy boundary is defined by abrupt scarps in places exterior to the proposed Borealis basin rim the similarity of the fractured ancient surfaces on the upland and lowland sides seems to require that the boundary be due to post-primordial bombardment faulting or flexing because neither an original basin nor post-basin erosion can account for the observations [3]. Furthermore, the existence of boundary segments where there is simply a gradual transition from upland to lowland, such as east of Chryse planitia, is entirely consistent with an endogenic origin for the lowland but very hard to explain by any impact mechanism. Unequivocal evidence that large segments of the dichotomy boundary resulted from post-primordial bombardment faulting or flexing would constitute very convincing support for an endogenic hypothesis. Even though determination of the structural cause and age of the dichotomy boundary is exceedingly difficult with existing data, there is a reasonable probability that continued careful geological studies can improve substantially on our present understanding of this problem.

Large-scale stretching and internal redistribution of lithospheric, including crustal, material is commonly invoked in tectonic models for the earth. It is abundantly clear that we do not entirely understand what mantle processes are directly responsible for the earth's tectonics, but there does seem to be general agreement that mantle convection, as cells or as plumes, is at least indirectly involved. Consequently, proposing a similar cause for the most fundamental crustal structure on Mars certainly is physically reasonable. Because the creation of a core constitutes a singularity in Mars' history, it is tempting to explain the crustal dichotomy, a large structural singularity, as somehow related to core formation. But isotopic and petrologic arguments for early core formation based on the inference that the SNC meteorites are derived from Mars [11] imply that the peak in tectonic and thermal activity in late Noachian and early Hesperian cannot be related to core formation. This is not fatal to endogenic hypotheses for the origin of the crustal dichotomy [9], but it does eliminate the most satisfying geophysical explanation for the size and shape of the lowland.

The strongest evidence favoring the origin of the lowland by multiple impact is the obvious correlation of large portions of the dichotomy boundary with the inferred rims of several large impact basins [5]. But there are large parts of the northern lowland exterior to the rims of these basins. If the martian lowlands were formed by only these few large basins, then their rims and inner ejecta should stand as high or higher than the uplands. This is clearly not the case for the large basins that have been identified in the lowlands; for example, most of the rim and inner ejecta of the probable Utopia basin are much lower than the uplands [13]. Furthermore, there are areas well within the northern lowland that are external to all these basins; these areas must be underlain by multiple overlapping ejecta blankets and should thus stand higher than the original planetary surface rather than lower. One such area is centered near 120° West, 60° North. Except where much younger volcanics and polar deposits are present, this region of overlapping ejecta blankets is not higher than the original martian surface, as expected. On the contrary, it averages 2 or more km lower than the original martian surface. Even though erosion or other processes on Mars very likely will reduce the magnitude of the initial basin relief,

without transporting material to an even lower lowland somewhere else on Mars (or assuming that the ejecta blankets simply were never there) the entire area affected by basin impact cannot be reduced to a level below that of the pre-impact surface.

Thus in order to support origin of the northern lowland by multiple impact it is necessary to support one of two hypotheses: 1) that most of the ejecta from the known basins within the northern lowland were transported completely away from the lowland; or 2) that there are additional large basins within the northern lowland for which the definitive topographic evidence has been obliterated. Hypothesis 1) is implied by Frey and Schultz [14] who represent basins as large holes without ejecta blankets. A quantitative model explaining why the ejecta from martian basins would be completely removed from the vicinity of the basin rims is clearly needed because this runs counter to experience on the moon. Hypothesis 2) requires clustering of impacts. Clustering implies either that the additional basins impacted on the northern third of Mars purely by chance or that there was some sort of cosmic mechanism that focused impacts onto the northern third of Mars. One of these is required because if basins are to contribute to the anomalous lowness of northern Mars, there cannot be equivalent basin formation in the southern highlands. If there were equivalent basin formation in the highlands there could not be significant net transport of material out of the northern lowlands. Neither clustering hypothesis is defensible.

The evidence supposedly supporting origin by multiple impact is really evidence for the existence of several large basins within the northern lowland. The presence of these basins can be incorporated easily within either of the other two hypotheses; that is, the known basins within the northern lowland are responsible for many of the topographic and geologic details, but not for the lowland itself. Unlike for the other two hypotheses, gathering new geological data is not likely to help very much because most of us already agree that basins exist within the lowland; models to explain the required unexpected behavior of basin impacts on Mars are needed instead.

References

1. Wise, D.U., M.P. Golombek, and G.E. McGill, Icarus, 38, 456-472, 1979.
2. Ibid, J. Geophys. Res., 84, 7934-7939, 1979.
3. McGill, G.E., and A.M. Dimitriou, J. Geophys. Res., in press.
4. Wilhelms, D.E., and S.W. Squyres, Nature, 309, 138-140, 1984.
5. Frey, H., and R.A. Schultz, Geophys. Res. Letts., 15, 229-232, 1988.
6. Wilhelms, D.E., U.S. Geol. Survey Prof. Paper 1348, 392p., 12 pl., 1987.
7. Wetherill, G.W., Science, 228, 877-879, 1985.
8. Greeley, R., Science, 236, 1653-1654, 1987.
9. Tanaka, K.L., N.K. Isbell, D.H. Scott, R. Greeley, and J.E. Guest, *Proc. 18th. Lunar Planet. Sci. Conf.*, 665-678, 1988.
10. Wilhelms, D.E., and R.J. Baldwin, Proc. 19th. Lunar Planet. Sci. Conf., 355-365, 1989.
11. McSween, H.Y., Jr., Rev. Geophys., 23, 391-416, 1985.
12. Schubert, G., D. Bercovici, and G. Glatzmaier, Lunar Planet. Sci. XX, 966-967, 1989.
13. McGill, G.E., J. Geophys. Res., 94, 2753-2759, 1989.
14. Frey, H., and R.A. Schultz, Lunar Planet. Sci. Conf. XX, 315-316, 1989.

MODELLED AND MEASURED STRAIN IN TWO MASCON BASINS ON THE MOON

M. Golombek, Jet Propulsion Laboratory, Caltech, Pasadena, CA 91109

The close association of wrinkle ridges and grabens with mascon basins on the Moon has suggested that the responsible compression and extension resulted from basin subsidence and peripheral flexing of the lithosphere. The distribution of grabens and wrinkle ridges associated with mascon basins has been further used along with elastic plate bending models to constrain the thickness of the lithosphere at the time of their formation (Solomon and Head, 1979, 1980). Kinematic models for basin subsidence have also been developed and compared with strains inferred from grabens and wrinkle ridges (Bryan, 1973; Golombek and McGill, 1983). Note that kinematic models may be preferable to dynamic models because the strain associated with tectonic features can be compared directly with model predictions and because fewer assumptions are required for their calculation, such as perfect elasticity and specific values of the elastic moduli. In addition, if the results from kinematic models compare favorably with the strain estimated across tectonic features on the Moon, then a global strain (or stress) field, proposed by a number of workers, may not be necessary. In this preliminary abstract, the strain inferred for wrinkle ridges and grabens has been compared to that calculated from a simple kinematic subsidence model for two mascon basins on the Moon.

The kinematic model used is conservative (described as model 1 in Golombek and McGill, 1983). Briefly, the model assumes an initial basin that is a couple of kilometers deep (2.5 km) at its center, tapering towards the edges (approximated by a segment of a sphere with a larger radius of curvature than the original lunar surface). The basin center is assumed to subside 1-2 km from loading of the lithosphere, which is 50-100 km thick (Solomon and Head, 1980), with all points moving towards the center of the Moon. The radial strain due to shortening of the arc (membrane) and that due to unbending are calculated for the interior of the basin. Hoop strains are calculated from the corresponding decrease in circumference of interior small circles around the basin center. Radial extensional bending strains at the edge of the basin are calculated from the flexure of the lithosphere over the width of the graben zone (typically about 50 km) due to subsidence of the basin. To first order, the total radial compressional strain from the center of a basin to its edge (one half of a basin) and the peripheral radial extensional bending strain are the quantities most easily compared with the compression across concentric wrinkle ridges within the basin and the extension across concentric grabens at the basin margin.

Determining the extension across grabens on the Moon is straightforward. The bounding faults dip about 60°, so the extension on each fault is a simple function of the depth of the graben floor (see Golombek, 1979 for specific method). Calculations are based on specific measurements already made (where topographic data exist) or by an estimate based on the apparent depth of a graben (where topographic data does not exist).

Determining the shortening across wrinkle ridges is less well constrained. A number of different methods have been used to obtain the compressional strain, and most methods suggest between a fraction of a percent to a few percent (Bryan, 1973; Muehlberger, 1974; Watters, 1988; Golombek et al., 1988). For this application, the method of Golombek et al. (1988) is used, which is based on topographic profiles across wrinkle ridges, the presence of an elevation offset, and assumptions about underlying fault structure and dip. Because many basins are not covered by adequate topographic coverage, a general relationship is used between wrinkle ridge width and shortening based on a set of 31 lunar ridges with detailed topographic data (Golombek and Franklin, 1987) and shortening estimates that suggest wider ridges have more shortening than smaller ridges. This relationship equates shortening with the ridge width times 0.009 plus 57 m; it is derived from linear regression analysis and has a correlation coefficient of 0.66. For each basin, a number of 30 km wide transects were drawn from the center of the basin to its edge. Within each swath, compression across the widest part of each ridge that is crossed and extension across the deepest part of each graben that is crossed is estimated at each distance from the center of the basin where the structures are found. Using the widest parts of the ridges and the deepest segments of the grabens results in a maximum estimate of strain across these structures. Note also that the method for calculating shortening across wrinkle ridges assumes a shallowly dipping thrust fault at depth (25°), which also tends to maximize the strain. In addition, comparison will be made with a model lithosphere thickness of 50 km, which minimizes the bending strains relative to a thicker lithosphere, which yield proportionally larger bending strains. As a result, if minimized model strains and maximized measured strains across the basins are comparable, the need for global stresses may be eliminated.

For the Humorum basin model (200 km radius), results indicate total radial shortening across a half basin is 300-600 m and extension of the edge is 250-500 m for 1-2 km of subsidence. The eastern side of Humorum has 3 to 5 ridges that add up to about 535 m of shortening. The eastern edge of the basin has 4 grabens (Hippalus) that add up to about 470 m of extension. The western side of Humorum has 2 or 3 wrinkle ridges that add up to about 215 m of shortening and the margin has about 3 grabens (Palmieri, De Gasparis, and Mersenius) that add up to about 400 m of extension. These estimates of strain in the Humorum basin are very similar to the model results.

For the Serenitatis basin model (325 km radius), results indicate total radial shortening across a half basin is 270-540 m and extension along the edge is 180-370 m for 1-2 km of subsidence. The eastern and western sides of Serenitatis each have 2 to 3 wrinkle ridges that add up to about 570 m of shortening. The best developed grabens around Serenitatis are to the east; about 4 grabens (Littrow) add up to about 330 m of extension. To the southwest and southeast, smaller graben zones (Sulpicius Gallus and Plinius) are found to each add up to about 200 m of extension. These estimates of strain in the Serenitatis basin are also quite similar to the model results. The models also predicts about one degree of tilting at the edge of the basin due to flexure of the lithosphere, a value in accord with

interpretations of subsurface reflectors identified in Apollo Lunar Sounder Experiment data (Phillips and Maxwell, 1978; Sharpton and Head, 1982).

In summary, preliminary results of a conservative and fairly simple kinematic model of basin subsidence (1-2 km) indicates modest radial shortening across a 300 km half basin of between 300 and 600 m and extension of 200 to 500 m along the basin margin. Comparisons with estimates of the amount of shortening across wrinkle ridges and the amount of extension across grabens in the Humorum and Serenitatis basins are very similar to subsidence model predictions. The similarity of modelled and measured strain, at least for these two basins, does not seem to require superposition of global strains to account for the strain accommodated by the wrinkle ridges and grabens. This work is in progress and further comparisons between basin subsidence model results and strains across grabens and wrinkle ridges will be undertaken for other basins on the Moon.

References:

Bryan, W. B., 1973, Wrinkle-ridges as deformed surface crusts on ponded mare lava: Proc. 4th Lunar Sci. Conf., p. 93-106.

Golombek, M. P., 1979, Structural analysis of lunar graben and the shallow crustal structure of the moon: J. Geophys. Res. v. 84, p. 4657-4666.

Golombek, M., Plescia, J., and Franklin, B., 1988, Relative importance of faulting versus folding in the formation of planetary wrinkle ridges (expanded abstract): Lunar Planet. Sci. XIX, p. 395-396.

Golombek, M., and Franklin, B., 1987, Physiographic constraints on the origin of lunar wrinkle ridges (expanded abstract): Lunar Planet. Sci. XVIII, p. 339-340.

Golombek, M. P., and McGill, G. E., 1983, Grabens, basin tectonics, and the maximum total expansion of the moon: J. Geophys. Res., v. 88, p. 3563-

Muehlberger, W. R., 1974, Structural history of southeastern Mare Serenitatis and adjacent highlands: Proc. 5th Lunar Sci. Conf., p. 101-110.

Phillips, R. J., and Maxwell, T. A., 1978, Lunar Sounder revisited: Stratigraphic correlations and structural inferences (exp. abs.): Lunar Planet. Sci. IX, p. 890-892.

Sharpton, V. L., and Head, J. W., 1982, Stratigraphy and structural evolution of southern Mare Serenitatis: A reinterpretation based on Apollo Lunar Sounder Experiment data: J. Geophys. Res., v. 87, p. 10,983-10,998.

Solomon, S. C., and Head, J. W., 1979, Vertical movements in mare basins: Relation to mare emplacement, basin tectonics, and lunar thermal history: J. Geophys. Res., v. 87, p. 1667-1682.

Solomon, S. C., and Head, J. W., 1980, Lunar mascon basins: Lava filling, tectonics and evolution of the lithosphere: Rev. Geophys. Space Phys., v. 18, p. 107-141.

Watters, T. R., 1988, Wrinkle ridge assemblages on the terrestrial planets: J. Geophys. Res., v. 93, p. 10,236-10,254.

CHAPTER 12

GEOLOGIC MAPPING, CARTOGRAPHY, AND GEODESY

SURFACE-MATERIAL MAPS OF VIKING LANDING SITES ON MARS; H.J. Moore, U.S. Geological Survey, Menlo Park, CA, 94025; J.M. Keller, Stanford University, Stanford, CA, 94309.

We have mapped the surface materials at the Viking landing sites because a review of the literature reveals that such maps have not been made and better information on the types of materials and their abundances should lead to a better understanding of the geology and remote-sensing signatures of the sites. The maps extend to 9 m in front of each lander and are about 15 m wide -- an area comparable to the area of a pixel in the highest resolution Viking Orbiter images of the Lander 1 site. Figure 1 shows our map of the Lander 2 site.

The maps are divided into near and far fields (Fig. 1). Data for the near fields are from: 1/10-scale maps [1], unpublished maps, and lander images. Data for the far fields are from: 1/20-scale contour maps [2], lander camera mosaics with overlain contours [2], and lander images. Rocks were located on these maps using stereometric measurements and the contour maps. Rocks form the control for delineation of other surface materials.

Map units are: (1) fine, (2) soillike, and (3) rock materials. Coordinates, length (l), width (w), and height (h) for each rock are recorded in a file for computational purposes. For many rocks, l or w was estimated. The rocks are assumed to be ellipsoids. Size-frequency and area-covered distributions of rocks are derived from the file according to the surrounding map unit, field, and size. All rocks mapped within fine material and all rocks >0.25 m in the near and far fields are included in the distributions, but rocks <0.25 m in the far fields are assumed to have the same distribution as rocks <0.25 m in the near fields. Areas covered by fine materials and rocks and soillike materials and rocks are measured on the maps. Areas covered by fine and soillike materials are obtained by subtraction of the area covered by rocks.

The forms of our size-frequency distributions of rocks are similar to previous ones [1,3]. Frequencies of rocks > 0.18 m are larger at Lander 2 than Lander 1, but the reverse is true for smaller rocks. Fractions of area covered by the larger rocks in logarithmic size-bins are irregular and yield no simple relations for extrapolations to larger sizes of rocks, but the areas covered by small rocks diminish rapidly with decreasing size. Our fractions of area covered by centimeter-size and larger objects and rocks are about 11.5% at Lander 1 and about 16% at Lander 2. Outcrops of rock cover an additional 4.5% of the area at the Lander 1 site. At Lander 1, about 18% of the surface is covered by thick deposits of fines and 40% by both thick and thin fines. At Lander 2, about 30% of the surface is covered with fine material.

Although there are questions about the physical properties

of the materials mapped beyond the sample fields, we assume that the fine materials are loose fine-grained powders with a small thermal inertia like that previously assumed for drift material [4]. If this assumption is correct, our results suggest that the thermal inertias of crusty to cloddy and blocky materials [1] may be larger than previously estimated [4] and that the amounts of SO_3 plus chlorine in the soillike materials [5] are directly proportional to their thermal inertias. These differences do not substantially alter the previous conclusions of Moore and Jakosky [4].

Preliminary analyses of our data suggest that polarized- and depolarized-radar-echo cross sections and normal radar reflectivities for the Lander 1 site should be about the same at 3.5- and 12.5-cm wavelengths. For Lander 2, polarized- and depolarized-echo cross sections are smaller and the quasi-specular cross section is larger at 3.5-cm wavelength than at 12.5-cm wavelength. These relations are chiefly related to the areal distributions of rocks and the model used to calculate the radar cross sections [5,6]. For Lander 2, the fraction of area covered by "wavelength-size" rocks, or diffuse scatterers, is smaller for the 3.5-cm wavelength than the 12.5-cm wavelength; for Lander 1, these areas are about the same for both wavelengths. For Lander 2, the fraction of area of large rocks contributing to the quasi-specular echo is greater at the 3.5-cm wavelength than at the 12.5-cm wavelength; for Lander 1 these areas are about the same at both wavelengths. Finally, the three types of surface materials and "wavelength-size" rocks contribute to the bulk quasi-specular radar echoes in complicated ways.

REFERENCES

[1] Moore, H.J., et al., 1987, U.S. Geol. Prof. Paper 1389, 222p. [2] Liebes, S. Jr., 1982, NASA CR 3568, 290p. [3] Binder, A., et al., 1977, J. Geophys. Res., v. 82, p. 4439-4451. [4] Moore H.J. and Jakosky, B.M., 1989, Icarus, v. 81, p. 164-184. [5] Evans, J.V. and Hagfors, T., 1964, Icarus, v. 3, p.151-160. [6] Campbell, M.J. and Ulrichs, J., 1969, J.Geophys. Res., v. 74, p. 5867-5881.

Figure 1 (on following page). Surface-material map at Viking 2 site. Mapped area is divided into a near field (A) and a far field (B). The population of rocks <0.25 m within the soillike areas of the far field were assumed to be the same as those in the near field. Fine ridges are crests of ripple-like bedforms; sinuous trough may partly outline ice polygon. Coordinates are in meters from center of Lander 2 (0,0). Note that mapped area is about 9 by 15 m. (Map prepared by John M. Keller).

SURFACE-MATERIAL MAPS, MARS: Moore, H.J. and Keller, J.M.

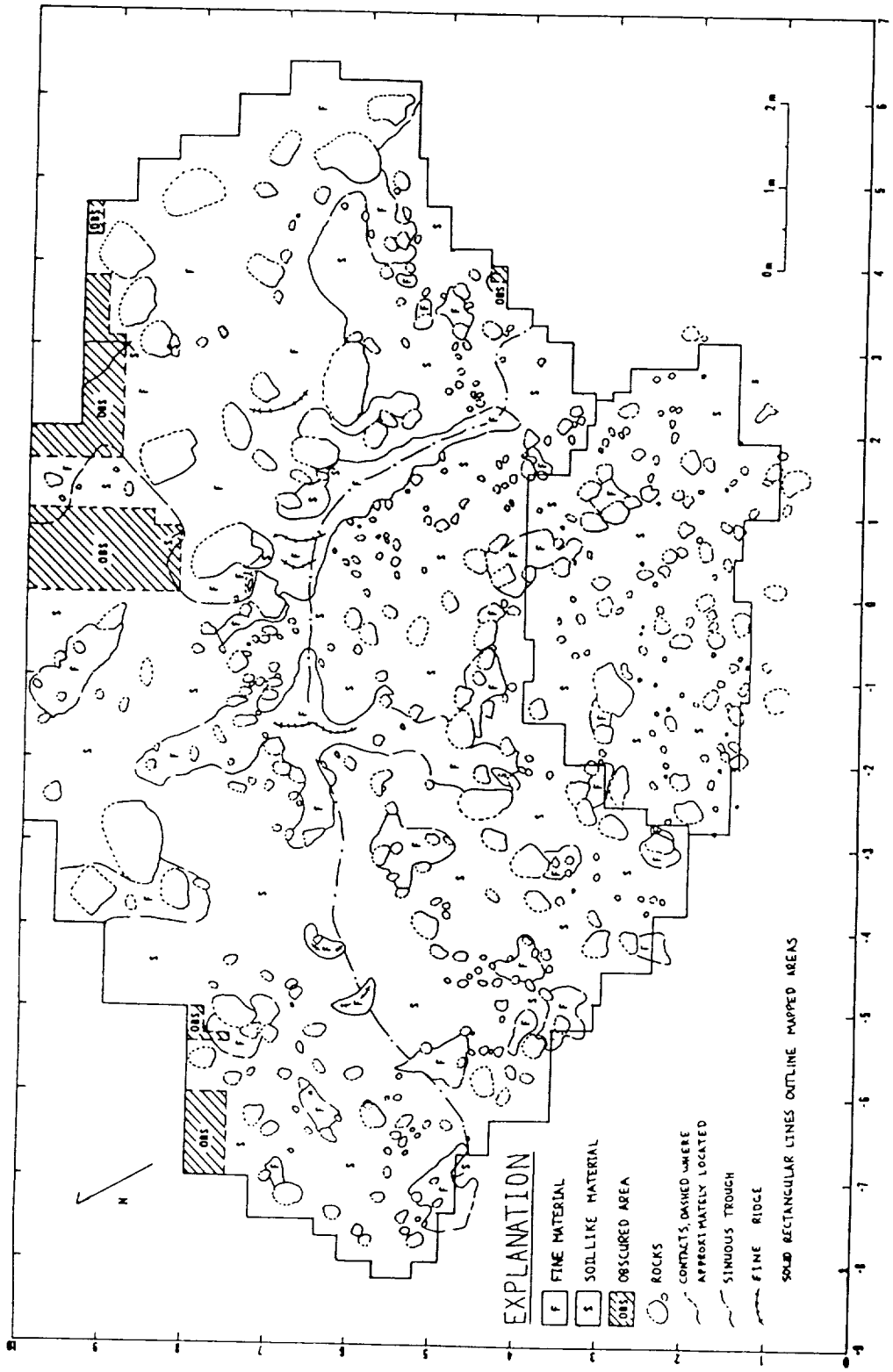

GEOLOGIC MAP OF THE GALAXIAS REGION OF MARS. R. A. De Hon, Department of Geosciences, Northeast Louisiana University, Monroe LA, 71209, and P. M. Mouginis-Mark, Planetary Geoscience Division, Hawaii Institute of Geophysics, University of Hawaii, Honolulu HA 96822.

Introduction: The Galaxias region (MTM 35217) is one of a series of 1:500,000-scale science study areas on Mars sponsored by NASA Planetary Programs. This map is part of an east-west strip which includes Hecates Tholis and a mixture of volcanic and nonvolcanic terrains near the northern limit of the Elysium lava flows. Resolution on the images used in the Viking photomosaic base ranges from 160 to 40 meter per pixel, and the solar illumination angle is not constant. Thus, visible surface detail varies considerably.

Some of the map units (Fig. 1) correspond or are partially equivalent to units of Elston (1), Scott and Carr (2), Greeley and Guest (3), and Tanaka et al. (4). Established terminology is followed where feasible, but the scale of this map requires that some new units be introduced and that some previous terminology be redefined.

Geologic Setting and Physiography: The Galaxias region is located along the transition zone between the broad Elysium Mons rise to the southeast and Utopia Planitia to the northwest. The regional topography consists of a uniform, gentle slope to the northwest upon which is superimposed a moderately smooth to rugged surface consisting of lava plains in the south and a mixture of rolling plains, rugged "badlands", and subdued knobby terrains to the north. The entrenched Hrad Vallis heads in the region and continues 500 km to the northwest. Galaxias Fossae, for which the map is named, consists of a parallel family of deep fissures in the southern part of the region and a long, linear fissure in the northern part of the map area.

Stratigraphy: The chief stratigraphic units in the region are flows from Elysium Mons and possible volcaniclastic units associated with the Elysium activity (Fig. 1). All materials other than craters are Amazonian in age. The oldest flow material (Unit Ael1) covers much of the southern third of the map. More pristine lobate flows (Unit Ael2) are superposed on the older flows. Coarse and smooth members of the Elysium Formation (Units Aelc and Aels) form much of the surface in the northern part of the map. Smooth materials may be of clastic origin (volcaniclastic, mudflow, loess, fluvial, etc.) based on the apparent ease of dissection. The coarse member is expressed as rugged "badlands" topography that appears to form at the expense of the smooth member. Breakup of older lava flows into polygonal blocks is mapped as polygonally grooved materials (Unit Apg) along the northern edge of the flows. This material grades northward into either knobby plains material (Unit Apk) or a mixture of coarse and smooth members of the Elysium formation. Locally, lumpy plains materials (Unit Apl) consisting of closely-spaced small hillocks overlie grooved materials. Smooth plains-forming material (Unit Aps) forms broad plains and floors some basins. Fluvial materials occur as slope and floor material of the incised Hrad Vallis (Unit Ach) and as floodplain material (Unit Achp). Fluted plains material (Unit Apf) near the head of Hrad Vallis may be a lahar originating from Hrad Vallis. A unique mound of rugged ridge material (Unit Arr) stands above the plains in mid-quadrangle. Gullied or fluted slopes suggest that this material is easily eroded and may be friable volcaniclastic material or gullied domed plains material. A smaller mound is located to the southeast, and a long ridge with similar gullied or scalloped flanks is located to the east.

Craters: Most impact craters within the region are small, fresh-appearing Amazonian craters (Unit Ac). Amazonian craters have sharp rim crests and textured ejecta blankets. Some ejecta blankets extend greater than one crater diameter from the crest. Secondary crater fields are scarce. A few craters, which are partially buried by Amazonian plains-forming materials, have uncertain stratigraphic bases. These craters are designated as Amazonian and Hesperian crater material (Unit AHc).

De Hon R. A. and Mouginis-Mark, P. M.
GALAXIAS REGION OF MARS

Structure: The dominant structural trend is parallel to the regional slope. Fissures, graben, and faults trend dominantly northwest with a lesser orthogonal trend. Galaxias Fossae consists of a system of parallel and alined fissures trending northwest in the southern part of the map region and a 300 km long fissure trending west-northwest in the northern part of the region. The northwest trend is accentuated by parallel alinement of other linears such as the long axis of the rugged ridge material, other ridges, valleys, and flow lobes.

Some features present in the region are of undetermined origins. Small (1 to 3 km basal diameter) oval to elongate hillocks with apical fissures are common in the northeastern portion of the region. They may be pingos. Small ridges (less than a kilometer in width) of questionable origin occur along the edge of the smooth plains material near its contact with polygonal plains materials in the eastern portion of the area.

Channels and Hydrologic History: Hrad Vallis and an unnamed flood plain are prominent drainage courses within the map. Both drainages trend parallel to the regional slope and parallel to the dominant structural trend of fissures, faults, and lineaments. In addition, parts of Galaxias Fossae may have carried flowing water.

Hrad Vallis heads in a fissure-like depression that is locally associated with collapsed terrain. The channel is a well-defined, incised, sinuous channel flanked by a broad, paired terrace along most of its course. Slumping along the walls of the valley has left small islands of terrace material within the channel. Cut-off loops attest to an earlier period of channeling before the present channel was fully established.

East of the Hrad Vallis a flat-floored, broad, irregular depression reaches from the southeast portion of the quadrangle to beyond the central northern border. The depression has a smooth floor with some minor scour and channeling that indicates that this depression carried water. The primary source of water is a 10 km diameter depression at the northern limit of the Elysium flows, but water may have been released all along the egde of the polygonally grooved terrain. A delta and levee complex leads from the source basin into the drainage course (5). Locally, the waters embayed isolated blocks of the grooved terrain.

Geologic History: In this region, the interplay of volcanism, near surface volatiles, and surface runoff is evident. Major units were emplaced as lava flows associated with Elysium volcanism and clastic deposition as either sediment or volcaniclastic processes. Surface modification by fluvial processes and possibly by karst/thermokarst action has been responsible for the development of moderately rugged topography.

REFERENCES

(1) Elston, W. E., 1979, Geologic Map of the Cebrenia Quadrangle of Mars: U.S. Geol. Surv. Misc. Inves. Map I-1140 (MC7).

(2) Scott, D. H. and M. H. Carr, 1978, Geologic Map of Mars: U.S. Geol. Surv. Misc. Inves. Map I-1083.

(3) Greeley, R. and J. E. Guest, 1987, Geologic Map of the Eastern Equatorial Region of Mars: U.S. Geol. Surv. Misc. Inves. Map I-1802-B.

(4) Tanaka K. L., M. G. Chapman, and D. H. Scott, 1989, Geologic Map of the Elysium Region of Mars: U.S. Geol. Surv. Misc. Inves. Map I-xxxx (in press).

(5) Mouginis-Mark, P. M., 1985, Volcano/Ground Ice Interactions in Elysium Planitia, Mars: Icarus 64, 265-284.

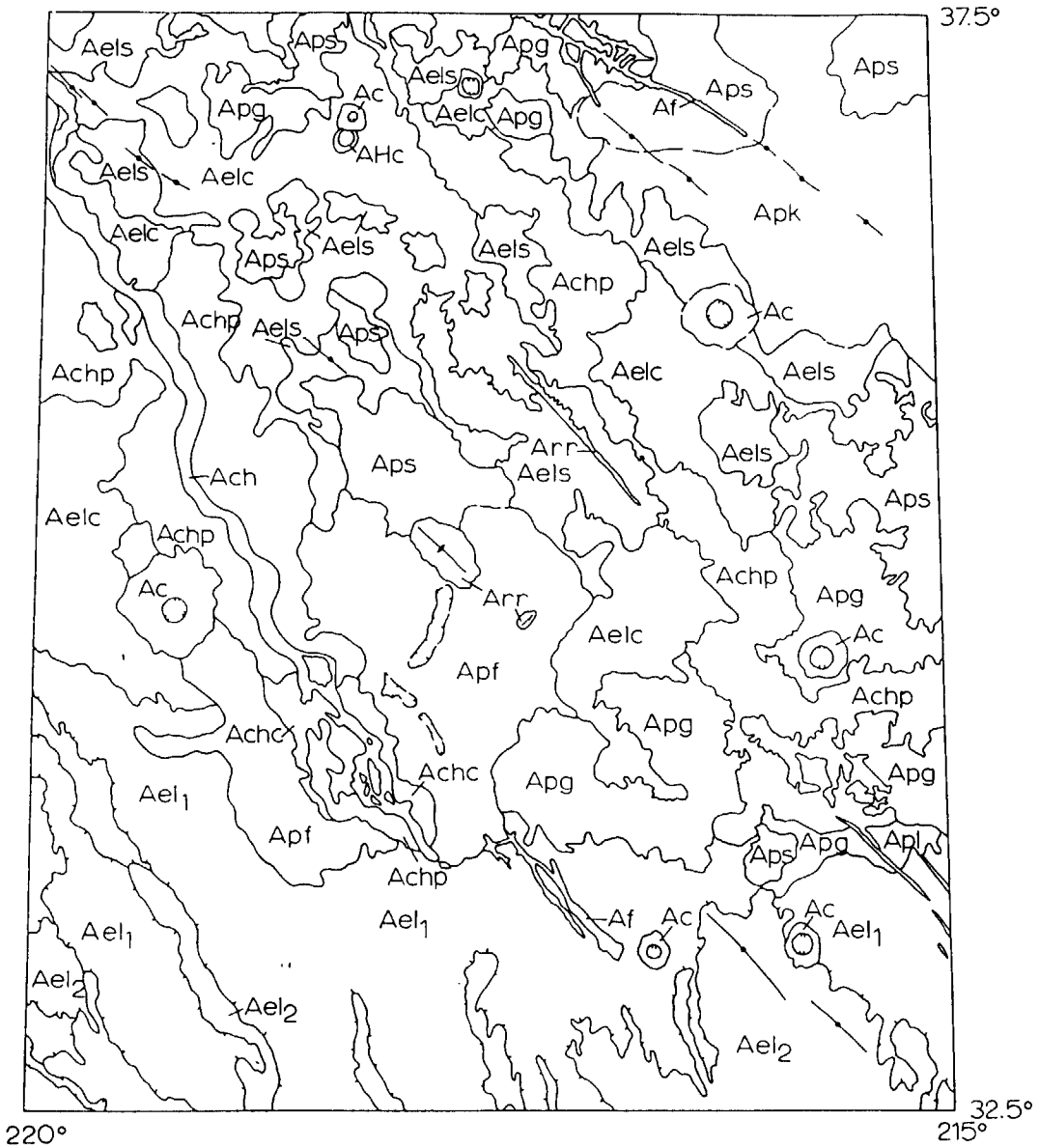

MAP UNITS

LOWLAND MATERIALS

Aps	Smooth Plains Material
Apl	Lumpy Plain Material
Apf	Futed Plains Material
Af	Fissure Material
Arr	Rugged Ridge Material
Apk	Knobby Plains Material
Apg	Grooved Plains Material

EASTERN VOLCANIC ASSEMBLEDGE

Elysium Formation

Aelc	Coarse Member
Ael_2	Member 2
Aels	Smooth Member
Ael_1	Member 1

CHANNEL MATERIALS

Ach	Channel Material
Achp	Flood Plain Material
Achc	Chaotic Channel Material

IMPACT CRATER MATERIALS

Ac	Amazonian Crater Material
AHc	Amazonian and Hesperian Crater Material

FIGURE 1. Geologic sketch map of the Galaxias Region of Mars (MTM35217).

Geologic Map of the Hebes Chasma Quadrangle, VM 500K 00077

Steven K. Croft. Lunar & Planetary Laboratory, University of Arizona, Tucson, AZ 85721.

Introduction. This map uses a base map constructed from medium and high resolution Viking images. The feature of primary interest is Hebes Chasma, which at about 100 km wide, 300 km long, and up to 6 km deep, is the largest of the closed depressions on Mars. Hebes Chasma is part of the Valles Marineris complex of canyons. The small depressions in the complex are appear as simple sink holes or chains of scallop-sided depressions, while the large canyons are straight sided and appear largely tectonic in origin. Hebes occupies a unique position, being both intermediate in size and morphology between the small circular depressions and the large straight canyons. Thus Hebes was chosen for study as an important structure in constructing a model for canyon formation.

Physiographic Setting. The quadrangle includes a portion of the crest of a topographic ridge that extends east from the Tharsis Montes and part of the ridged plains of Lunae Planum which comprises the north slope of the ridge. The slope is part of the large depression associated with the Chryse impact basin. Hebes Chasma is incised into the high plains and is aligned east-west along the main trend of the Valles Marineris. The "head" of Echus Chasma is also in the quadrangle. Its alignment is north-south, perpendicular to the main trends of the canyons, and joins into Kasei Valles to the north.

Stratigraphy. Relative ages of the geologic units are determined from crater densities and superposition relationships. The units are assigned to the formal stratigraphic systems (Noachian, Hesperian, and Amazonian) formulated by (1). Many of the more specific units are adopted from (2). Noachian age units comprise the oldest materials visible on the surface of Mars. Noachian units in the quadrangle include an nunutak of rugged cratered terrain in the NE and the rocks of the lower walls of the chasmata. The wall rocks occur with two characteristic surface morphologies: smooth arcuate scarps 4 - 6 km high with slope angles of 35°-45°, and rugged "spur and gully" slopes with heights and slope angles similar to the arcuate scarps. The latter form appears to be eroded examples of the former. The stresses in the lower portion of the scarps approach half a kilobar, far too high a stress to be supported by sediments cemented by interstitial ice (i.e., permafrost materials, see ref. 3). Only competent rock is strong enough to support the walls.

The wall rocks are overlain by a layer of Hesperian age plains materials one to two kilometers thick (estimated from exposures in the canyon walls and the widths of the smaller surface grabens) whose top layer comprises Lunae Planum. About half of the plains materials in the quadrangle are designated ridged, while the rest are designated fractured plains because of the complex network of grabens that break the surface. The materials are interpreted as successive volcanic flood eruptions from Tharsis that covered almost the whole region. A few small Hesperian age channels dissect the plains materials. Two small exposures of Hesperian age chaotic materials occur on the floor of Hebes Chasma. The characteristic linear dimension of the hillocks are 1 - 2 km in the southern exposure and 0.5 to 1 km in the northern exposure.

The chaotic floor materials are unconformable overlain by the late hesperian layered deposit running along the axis of the chasma. The layered unit is a single bedded deposit 40 - 50 km wide, about 110 km long, and 4 - 5 km high. The top of the deposit almost reaches the height of the surrounding plateau. The uppermost unit of the deposit has a rounded soft texture and is estimated to be a few hundred meters thick. It appears to sit unconformably on top of a massive bedded unit three to four km thick that erodes into a characteristic rilled or fluted surface. Individual beds in the layered deposit vary in albedo and thickness, from the limit of resolution (tens of meters) to hundreds of meters. The morphology of the massive unit is strongly reminiscent of the distinctive rills found on steep slopes in typical "badlands" terrains on the Earth. Terrestrial badlands develop in soft, relatively impermeable rocks exposed to rapid fluvial erosion (4). The climate necessary to produce badlands morphology is arid to semi-arid: seasonal precipitation interspersed with long dry periods (4,5). If the correlation is valid, the erosional state of the massive unit implies the presence of a semi-arid climate at the time of its formation. A potentially important point is the absence of another typical badlands feature: the gullies in the presumed runoff area on the chasma floor. If the rills are due to fluvial erosion, gullies should be present. Their absence suggests that the floor materials, specifically the chaotic materials, are highly permeable, allowing the runoff to be released through the subsurface.

A number of lobate deposits extend away from the base of the massive deposit. The units seem to connect without discontinuity into the massive deposit and lie unconformably on the subjacent floor deposits. The most distinctive of the lobate deposits extends about 20 km across the floor of Hebes to the chasma wall. It is about 5 km wide, several hundred meters high, and has surface transverse ripples spaced about one km apart on the distal half. The morphology of the unit suggests emplacement as a mobile flow. The origin of the layered and lobate materials is still undecided: the deposits may be sedimentary, specifically lacustrine (6), in which case the lobate deposits are probably large mud flows. While it is true that the badlands rills form mostly in sedimentary rocks on the earth and thus might be considered as supporting a sedimentary origin, similar features occur on the steep slopes of volcanic table mountains in Iceland. The resemblance between the Hebes layered deposit and some icelandic table mountains like Sellandafjall is uncanny, even to wall fluting, variable albedo layering, and soft cap deposit (with no obvious volcanic vent). These parallels suggest a second possible origin for the layered deposits as volcanic. In this case the lobate flows would be interpreted as viscous volcanic flows. The ripple spacing suggests viscosities appropriate for acidic materials. If so, this would be nearly the only example of acidic volcanism (with all that implies for internal evolution) on Mars. The elevation of the subjacent chaotic terrains on either side of the layered deposit differ by about one kilometer, and a large fault

(indicated by the presence of collapse features to the east) runs right down the center of Hebes underneath the layered deposit. Thus the deposit has formed along the axis of a major fault with differential vertical motion, an appropriate location for a volcanic eruption.

The most recent materials (amazonian) in the quadrangle are represented by various floor and landslide deposits. Floor deposits in Hebes rough materials, which are probably older landslide, smooth materials, which appear to be eolian (or possibly pyroclastic), and fluted materials which have flutes parallel to the rills in the layered materials. The spacing and detailed structure of the flutes is not the same as the rills, and the fluted materials are mostly perched on the chasma wall disconnected from the central layered deposit. Thus the two units are not interpreted to be erosional remnants of a single unit. If so, the problem is to account for the similar orientations, which may be related to preferred directions of eolian erosion or to an underlying tectonic fabric. No explanation is wholly satisfactory at present. The smooth materials in the lowest section of the floor of Hebes are somewhat unique, appearing as a fairly thin layer of soft material overlying a somewhat rougher surface below. There is some evidence of incipient runoff channels and a surrounding bench of rougher material. The ensemble is reminiscent of dried terrestrial lake beds.

Hebes Structure and Canyon Development. Several processes that have operated in enlarging Hebes are illustrated in figure 1 by geologic/topographic profiles taken from various locations on Hebes' walls. 1) Block slumps are found in at least two places along the north wall, the blocks being identified by surfaces capped with plateau material and by repetition of the layered sequence from the top of the canyon wall along the subsided block edge. The blocks are 10 - 12 km wide. 2) Thick debris landslides are found in several locations, the thicknesses estimated from the heights of the edges of the deposits. Replacing the volume of the landslides onto the head scarp implies widths of the failed wedges of 4 - 6 km. 3) Lobate landslides and debris aprons originating in gullies in the chasma wall are found in a few places; they are volumetrically small. 4) Sapping/karstic processes have also widened Hebes somewhat, but these also are volumetrically small. Hebes is a closed canyon, thus these processes only laterally enlarge a canyon already in existence. Karstic collapse can remove some material via underground water systems, however other purely karstic depressions in the Valles Marineris area are only 10^2 to 10^3 km^3 in volume, while Hebes is 10^5 km^3 in volume. Tectonic subsidence is another means of removing material (straight down), and this seems to be the primary mode of canyon formation for the larger canyons which have volumes of 10^6 km^3 or more (3). The subsidence blocks show that this process has operated to a certain extent in Hebes also. There is additional evidence for subsidence in Hebes. The two blocks of chaos material are at different topographic levels, and both are 4 - 5 km below the original surface. Comparable chaos areas to the east generally occur at levels much closer to the original plateau surface. Further, the floor at the east end of the canyon is lower still and is separated from the rest of the floor by a mantled scarp about a kilometer high. These observations suggest that the central floor of Hebes has differentially settled vertically by several kilometers in 3 to 4 discreet blocks, and that this accounts for most of the volume of the chasma. This is consistent with the model suggested by (3) that true karst processes produced the depressions in the 100 to 1000 km^3 range while larger features are primarily due to tectonic subsidence. This interpretation is shown in the cross sections of various features in the Valles Marineris area in figure 2: pits and catenae form as collapse structures over caverns formed by ground water along major faults through soluble rocks whereas the major canyons form initially as subsidence structures (like grabens) that are subsequently enlarged somewhat by solution-driven mass wasting.

The floor of Hebes, which as a whole is quite rough and topographically variable, provides striking contrast with the smooth, flat floor of the adjacent section of Echus Chasma (which is characteristic of most of the floors of the canyons of Valles Marineris). Echus' floor lies about 2 km in elevation above the floor of Hebes and its surface is covered by albedo patterns reminiscent of fluvial networks in terrestrial deserts. The unique nature of Hebes' floor is interpreted to relate to its condition as a closed depression. Echus is an open canyon and is undoubtedly the headwater source for the floods that swept through Kasei Vallis, thus the flat floor is likely the result of the flow of large amounts of water out of subterranean conduits (likely sources are the sapping canyons in the SW corner of Echus) that erased any floor irregularities. Water in Hebes, on the other hand, could not leave the canyon in a surface flow, but had to seep out through fissures and porous material under the canyon floor, thus no fluvial erosion occurred.

References. 1) Scott, D.H. & M.H. Carr (1978) Geologic Map of Mars. U.S. Geological Survey Map I-1083. 2). Scott, D.H. & K.L. Tanaka (1986) Geologic map of the western equatorial region of Mars. U.S. geological Survey Map I-1802-A. 3) Croft S.K. (1989) Spelunking on Mars: the carbonate-tectonic hypothesis for the origin of Valles Marineris. In Tectonic Features on Mars, MEVTV Workshop on Mars, LPI Tech. Rpt. #89-06, p. 21-24. 4) Campbell, I.A. (1989) Badlands and badland gullies. In Arid zone geomorphology, D.S.G. Thomas, ed., p.159-183. 5) Graf, W.L. (1988) Fluvial processes in dryland rivers, Springer-verlag, Berlin. 6) Nedell, S.S., S.W. Squyres and D.W. Anderson (1987) Origin and evolution of the layered deposits in Valles Marineris, Mars. Icarus 70:409-441.

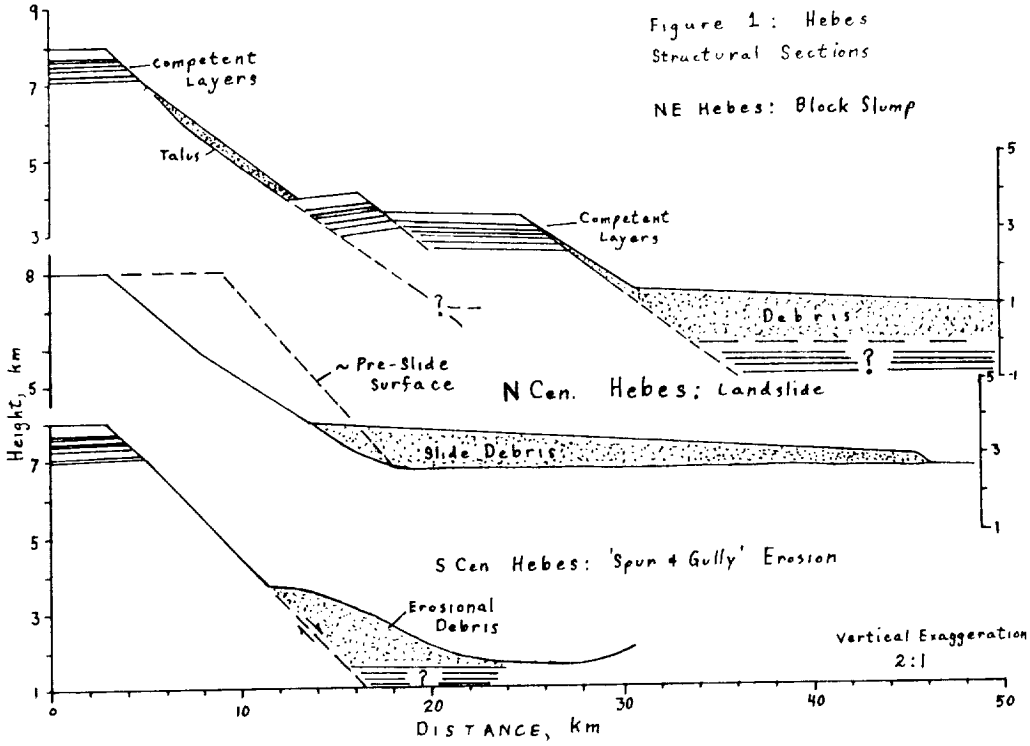

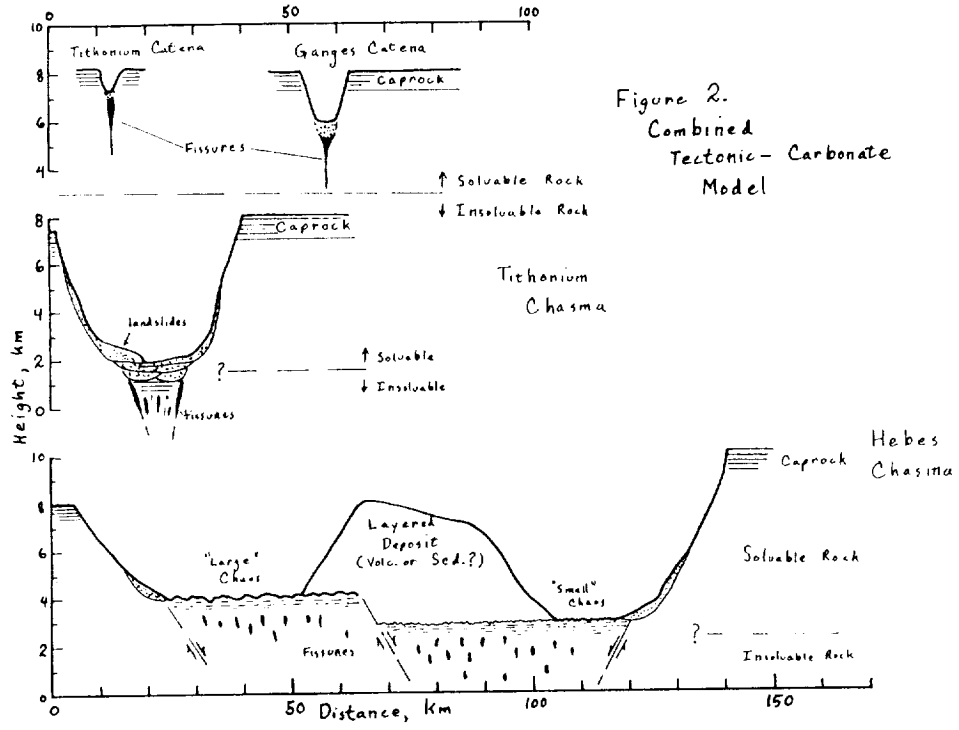

THE STRATIGRAPHY OF THE MC5SE SUBQUADRANGLE, MARS: EVIDENCE FOR DICHOTOMY BOUNDARY FORMATION IN THE UPPER NOACHIAN/LOWER HESPERIAN

Andrew M. Dimitriou, University of Massachusetts, Amherst, MA 01003.

The Ismenius Lacus SE (MC5SE) subquadrangle (292.5°W - 315°W, 30°N - 47.5°N) contains the trace of the global boundary between southern heavily cratered upland and northern sparsely cratered lowland. The dichotomy is well exposed along a series of NW trending scarps that approximate 1.4 km in mean height (1). To the northwest and southeast of the boundary defined by the scarps, areas of "fretted terrain" (2) make this upland/lowland boundary difficult to locate. Lucchitta mapped the entire MC5 quadrangle (3) at a scale of 1:5M using Mariner 9 imagery. This area was also covered in the 1:15M scale geologic map of the Martian eastern hemisphere as compiled by Greeley and Guest (4). This abstract presents the results of a stratigraphic and tectonic study of this area using the published 1:2M photomosaic and the highest available resolution Viking imagery. A detailed relative age sequence of the geologic units identified has been drawn up. This allows the fracturing and tectonic history of this area to be constrained more precisely than before. The cumulative crater plots generated were compared with the Neukum and Hiller curve (5) and stratigraphic ages assigned with reference to Tanaka (6).

Within the uplands, a distinctive population of "rimless" craters is recognised which has also been noted in Amenthes (7). It is assumed here that these craters represent an old population lying at a relatively uniform and shallow depth beneath the present plateau surface units. When relative ages are determined, either by considering the plateau surface as a whole or by separating populations based on the observable geologic units, counts yield a Lower Noachian age.

A number of geologic units can be identified above the Lower Noachian surface based on differences in surface morphology. A smooth plateau unit is located along the fretted northern boundary of the plateau and as a capping unit on the outlying mesas. This is identified as volcanic and/or aeolian material and yields a crater age of Lower Amazonian. This unit truncates a boundary between two units tentatively identified as volcanic.

One of the volcanic units occupies the central portion of the upland in this subquad and is characterised by the presence of low relief irregular scarps. It is identified as a ridged plateau unit. Crater counts yield a spread of ages as derived from curve splitting (5) ranging from Upper Noachian through Lower Amazonian. This indicates that lava may have continued to flood this surface with decreasing volumes over a long period of time competing with the decreasing impact crater flux. This unit is fractured and truncated along its eastern margin by boundary scarps which drop into lowland materials. The second volcanic unit truncated by the smooth plateau unit is material characterised by a hummocky surface at km scale and is thus identified as a hummocky unit. This is located in the central and eastern portion of the upland where its eastern margin is also dissected and truncated by boundary scarps. Crater counts yield a range of ages from Upper Noachian through Upper Hesperian for this unit.

In the southern region of the subquad a complexly differentially eroded surface is identified as an etched unit. This unit consists of ridged and possibly smooth plateau material that has been differentially eroded leaving irregular and circular positive relief landforms. Crater ages from this unit range from Lower Hesperian through Lower Amazonian, but the relative youth indicated is almost certainly due to removal of craters by the complementary processes of erosion and deposition. The stratigraphic age of the materials visible is older. These erosional and depositional processes have however allowed a fairly clear boundary to be drawn between the etched and ridged units.

Within the lowland along the upland/lowland boundary, a unit which is characterised by the presence of bright, very sparsely cratered material is identified. This material includes not only the debris aprons present at the base of the scarp and of many outlying mountains, but also the bright deposits mantling the floors of fractures and irregular valleys which penetrate into the uplands. Crater counts proved impossible on this unit due to the low number of superposed craters present.

North and west, three lowland plains units are identified: a smooth plains unit, a very smooth plains unit and an etched plains unit. Crater counts are only possible on the first two units and yield ages

that range between Upper Noachian and Middle Amazonian. Reworking of the surface materials appears to be a very young process as many of the fresh appearing craters at moderate resolution show fine scale mantling at higher resolution as noted by Williams and Zimbelman (8). The possibility also exists that the Upper Noachian age determined within the plains units represents an old population superposed on a shallowly buried surface unconformably underlying the plains. The etched plains unit is not exposed over a large enough area to permit crater counting and is characterised by the presence of small (< 10km long axis) cuspate positive relief features that suggest differential erosion of plains materials. The morphological differences between the first two units is based on the apparent relative abundance of small mountains that are scattered through the lowland plains. These mountains are taken to represent remnants of older material. Within the areas where these mountains abruptly disappear, the very smooth plains unit was identified. These differences are inferred to represent variations in sub-plains basement elevation, within the very smooth plains unit the remnant mountains are more deeply buried.

A unit that consists of large groups of mostly rounded mountains scattered in a discontinuous but wide zone roughly paralleling the present trace of the upland/lowland scarp is interpreted to be remnants of an older surface that has been partially buried and embayed by the unconformable younger plains materials. Crater remnants are visible in the eastern portion of the subquad and counts over these areas yield a population that fits the Neukum and Hiller production curve (5) very well. The age determined is Lower Noachian. Therefore, the surface that lies at a shallow depth on the plateau is also present at a shallow depth in the eastern portion of the lowlands, an elevation difference of at least 1.4 km.

In order to account for this observation, this area is proposed to have experienced crustal downwarping in the southern portion of the subquad as the topographic map by Wu (9) indicates. In the central and northern parts of the subquad normal faulting occurred which accommodated the structural relief by downthrow to the northeast. This model must also take into consideration the timing and origin of the downdropping event. Judging from the fractures visible which cut upland surfaces, these fractures were initiated around the Upper Noachian/Lower Hesperian boundary. Recent work by McGill and Dimitriou (10) suggests that the northern lowlands formed around this time as a response to large scale subcrustal erosion and that the dichotomy boundary zone shows evidence of significant fracturing and resurfacing in different regions during Upper Noachian/Lower Hesperian time. This work provides support for the relatively late formation of the global dichotomy boundary in this area.

(1) Dimitriou, A.M., Lunar and Planet Sci. Conf. XXI (abs), 291-292, 1990.
(2) Sharp, R.P., J. Geophys. Res., 78, 4073-4083, 1973.
(3) Lucchitta, B.K., Geol. Map Ismenius Lacus Quadrangle of Mars, Map I-1065, 1978.
(4) Greeley, R. and J.E. Guest, Geol. Map of Eastern Equatorial Regions of Mars, Map I-1802B, 1987.
(5) Neukum, G., and K. Hiller, J. Geophys. Res., 86, 3097-3121, 1981.
(6) Tanaka, K.L., J. Geophys. Res., 91, E139-E158, 1986.
(7) Maxwell, T.A. and R.A. Craddock, Lunar and Planet Sci. Conf. XX (abs), 646-647, 1989.
(8) Williams, S.H. and J.R. Zimbelman, Lunar and Planet Sci. Conf. XXI (abs), 1341-1342, 1990.
(9) Wu, S., Topographic map of Mars, Map I-2030, 1989.
(10) McGill, G.E. and A.M. Dimitriou, J. Geophys. Res., in press, 1990.

ARE NOACHIAN-AGE RIDGED PLAINS (*Nplr*) ACTUALLY EARLY HESPERIAN IN AGE? H. V. Frey, C. E. Doudnikoff and A. M. Mongeon, Geodynamics Branch, Goddard Space Flight Center, Greenbelt MD 20771

Ridged Plains of Noachian Age?

The prominant ridged plains of Lunae Planum, Coprates, Hesperia Planum and elsewhere are generally considered to have erupted in the Early Hesperian (1,2) and are generally taken to define the base of that stratigraphic system (3). These plains are widespread, covering over 4 x 10^6 km^2 in western Mars alone (1) and are broad, planar surfaces with some flow lobes and parallel, linear to sinuous ridges similar to lunar mare ridges with a spacing of 30 to 70 km. The general interpretation is that the ridged plains (unit *Hr*) are due to relatively rapid eruptions of low viscosity lavas (1,2), and their occurance at the base of the Hesperian represents a major volcanic episode in martian history (3).

In some areas these plains are gradational with another ridged plains unit, mapped as *Nplr*. The ridges of these apparently Noachian-age plains are generally further apart with rougher, more heavily cratered inter-ridge areas (1,2). *Nplr* terrains are widely distributed in both hemispheres of Mars but cover much less area than the more common *Hr* unit. The type area in Memnonia lies southwest of Tharsis in heavily cratered terrain (*Npl1*, *Npl2*). Other major occurances are further south in Sirenum, between the Argyre and Hellas Basins in Noachis, in the southern portion of Cimmeria Terra and in the northeastern portion of Arabia (1,2). The Noachis and Cimmeria outcrops are distributed roughly concentrically about the Hellas impact basin at approximately 1 and 2 basin diameters, respectively.

The stratigraphic position of these apparently older ridged plains is **Middle Noachian**; in the current geologic maps the unit does not extend into the Upper Noachian and appears temporally unrelated to the more common Hesperian ridged plains (*Hr*) even though these two units are sometimes gradational. The assignment of stratigraphic position is based on superposition relationships and total crater counts; the high density of impact craters on *Nplr* would certainly suggest a Noachian age.

But total crater counts can be misleading: if multiple resurfacing or other crater depopulation events occur and successfully compete with crater production, a given terrain may have an apparently young total crater age even though very old surfaces remain partially exposed in the form of very large craters. Inefficient resurfacing events allow older surfaces to show through and give old crater retention ages based on total crater counts, which may not accurately reflect the age of the major terrain unit. In this paper we examine whether or not the *Nplr* units in Memnonia and Argyre truly represent ridged plains volcanism of Noachian age or are simply areas of younger (Early Hesperian age) volcanism which failed to bury older craters and therefore have a greater total crater age than really applies to the ridged plains portion of those terrains.

Resurfacing in Memnonia and Argyre

We used the Neukum and Hiller (4) technique to determine the number of preserved crater retention surfaces in the Memnonia and Argyre regions where Scott and Tanaka (1) show *Nplr* units to be common. The Memnonia outcrops are the type example of this unit, and we subdivided the study area in MC 16 into two broad units: cratered terrain *Npl* (mostly *Npl1* and *Npl2*) and the ridged plains *Nplr*. Our mapping is similar to but not identical with that previously done (1). We counted craters larger than 3 km in diameter and plotted cumulative frequency curves for each terrain unit, then broke these curves into separate branches where they departed from a standard production curve (4, 5). This departure is interpreted to be due to resurfacing, and breaking the curves into separate branches allows determination of the crater retention age of each post-depopulation "surface" independent of previous history (the survivors are subtracted and remaining craters compared independently to the crater production curve). Table 1 summarizes the results for cratered terrain (*Npl*) in Memnonia and for ridged plains (Nplr) in both Memnonia and Argyre, and compares these with similar results obtained by us for Tempe

Terra (6) and Lunae Planum (the type area for the Lunae Planum Age [LPA] ridged plains [*Hr*] resurfacing).

In Lunae Planum no craters larger than 50 km exist within the ridged plains; in Memnonia and Argyre there are craters as large as 117 and 100 km that survive in the *Nplr* unit. The population of old, large craters contributes to the total crater counts which suggest the *Nplr* unit is of Noachian age. We find the cumulative frequency curves for the ridged plains in Argyre/Memnonia can be broken into four branches which have remarkably similar crater retention ages N(1): an oldest branch ~[121,000/115,000], a branch with N(1) = [80,200/76,500], a "Lunae Planum Age" branch at [28,100/22,100], and a still younger branch at N(1) = [6700/6200]. Note that the Argyre ages for *Nplr* are consistently slightly older. These ages compare with resurfacing ages for the cratered terrain *Npl* in Memnonia of N(1) = [226,900], [76,000], [27,900], and [6300]. For all but the oldest (and most poorly determined) branch, the crater retention ages for the different branches are extremely similar from one area to the next.

The craters which determine the ridged plains resurfacing age (those superimposed on the ridges as opposed to showing through the plains) define the N(1) = [25,000 +/- 3000] age branch for both Memnonia and Argyre. This age is nearly identical (with the precision this technique affords) with the oldest branch we find for Lunae Planum: N(1) = [25,700], even though the craters which define this age branch (10-20 km in Argyre, 8-15 km in Memnonia) are significantly smaller than in Lunae Planum (25-50 km). This implies that the thickness of the *Nplr* ridged plains in Argyre and Memnonia is significantly less than we estimate (4,5) for Lunae Planum (350- 600 m). This reduced thickness is what allows the older craters to show through, preserving the older crater retention surfaces at N(1) = [78,000 +/- 2000] and [118,000 +/- 3000]. These older preserved craters contribute to the high total crater counts that suggested the *Nplr* were of Noachian age.

We suggest that for these two areas at least the *Nplr* ridged plains are the same age as those (*Hr*) in Lunae Planum, Tempe and elsewhere: N(1) = [25,000 +/- 3000]. If this conclusion holds in general for the other outcrops of those units mapped as *Nplr*, it may imply that the eruption of ridged plains volcanism was more restricted in time than previously thought. This would have interesting implications for models of the thermal history of Mars, and would make the ridged plains even more important as a stratigraphic marker in martian history.

Table 1. Resurfacing Ages for Memnonia and Argyre

AREA	UNIT	CRATER RETENTION AGE N(1)			
Memnonia	Npl	226,858	75,980	27,866	6,343
Memnonia	Nplr	115,221	76,445	22,062	6,223
Argyre	Nplr	121,300	80,200	28,100	6,700
Lunae Planum	Hr	--	--	25,700	10,100
Tempe	Hr	--	--	22,100	6,500

References: (1) Scott, D. H. and K. L. Tanaka, Geol. Map Western Equatorial Region of Mars, USGS Map I-1802-A, 1986. (2) Greeley, R. and J. E. Guest, Geol. Map Eastern Equatorial Region of Mars, USGS Map I-1802-B, 1987. (3) Tanaka, K. L., Proceed. LPSC 17th, JGR 91, E139-E158, 1986. (4) Neukum, G. and K. Hiller, JGR 86, 3097-3121, 1981. (5) Frey, H., A. M. Semeniuk, J. A. Semeniuk and S. Tokarcik, Proceed. LPSC 18th, 679-699, 1988. (6) Frey, H. and T. D. Grant, submitted to JGR, 1989.

EXTENT OF BEDROCK EXPOSURE IN THE SINUS MERIDIANI REGION OF THE MARTIAN HIGHLANDS

James R. Zimbelman and Robert A. Craddock, Center for Earth and Planetary Studies, National Air and Space Museum, Smithsonian Institution, Washington, D.C. 20560

A major objective for remote sensing studies of Mars is to provide constraints on the properties and composition of the bedrock materials. However, the active aeolian environment and the ubiquitous presence of dust on Mars make the realization of this objective difficult at best, and impossible at worst. Here we present estimates of the amount of possible bedrock exposures visible in the highest resolution Viking imaging data for comparison with results obtained from remote sensing studies in and around the Sinus Meridiani region.

The location chosen for this study (15°N to 15°S, 330° to 360°W) includes portions of the classical low albedo regions of Sinus Meridiani and Sinus Sabaeus and the high albedo region of Arabia (Fig. 1), and is entirely within the cratered highlands of Mars. This region has been included in several spectral reflectance studies (1-5), as well as in global studies at thermal infrared (6-10) and radar (11-13) wavelengths. The results from these studies have important implications for the aeolian environment on Mars (e.g., 1,4-6,9,14) but the degree to which the data can be directly related to bedrock that underlies the aeolian cover is the subject of the present investigation.

Most studies of visual reflectance conclude that low albedo regions are "less" obscured by the dust that dominates the high albedo regions (e.g., 1-3). However, what fraction of the martian surface (having either low or high albedo) has a reasonable likelihood of providing information about the rocks associated with the terrains present on various geologic units? Presley and Arvidson (4) used visual and thermal infrared data to infer that the surficial units exposed in western Arabia and Sinus Meridiani (including a large fraction of the present study area) are mixed aeolian deposits, predominantly decoupled from the underlying bedrock. Thus, bedrock exposures should be small compared to the scale of the data used in that study (hundreds of meters to kilometers, 4). Thermal infrared measurements at multiple wavelengths indicate that from 5% to 20% of the martian surface consists of material much more competent than dust or sand (15), with the low albedo regions generally having more exposed competent materials than the high albedo regions (10). The competent materials observed by this technique may be either rocks (10,15) or indurated sediments (16).

What do we look for in the images as representing possible exposures of bedrock? Bedrock is defined as "the solid rock underlying the soil and other unconsolidated materials, or appearing at the surface where these [unconsolidated materials] are absent" (17). Thus, we looked for locations with the least likelihood of having an overlying accumulation of unconsolidated materials. The images examined have resolutions of from 8 to 36 m/pixel, so we were unable to identify features smaller than several tens of meters in dimension, so it is possible that any

given picture element can include a mixture of both small bedrock outcrops and aeolian dust or sand. However, it seems likely that steep slopes will shed most unconsolidated materials downslope and thus provide the "cleanest" surface that might reasonably be expected to include bedrock. This assumption means that our results likely represent only upper limits.

We examined over 400 high resolution Viking images within the study area, estimating the percentage of the area of each frame that was a possible exposure of the underlying bedrock. Interior walls of impact craters (e.g., Viking image 748A12) provided the most numerous exposures of steep slopes of competent material. However, even the best images had smooth-textured surfaces covering the majority of crater interiors -- areas that probably include some talus accumulations but which also might be mantled by dust -- that were not considered to be good candidates for possible bedrock exposure. Walls of channels and other cliffs provided additional candidate sites. We also noted steep slopes on materials that are easily eroded and appear to be superposed on the surrounding terrain (e.g., Viking image 708A25). These materials appear to result from depositional events within the region; this material is probably more competent than the aeolian dust but it is unlikely that it will be related to the local bedrock. The entire image set provided the following results: 42% had <1% bedrock exposure, 91% had <5% bedrock exposure, and 15% bedrock exposure was the maximum value (Fig. 2). The high resolution images covered about 10% of the total study area but we believe they are representative of the region as a whole. We found no significant difference in exposures between high albedo and low albedo regions (Fig. 1) and no apparent correlation between bedrock occurrence and the units defined by spectral reflectance studies (1-5), although competent depositional layers are more common in low albedo regions associated with high thermal inertias (e.g., 0^{o} to 8^{o} N, 350^{o} to 360^{o} W). These results will be compared to high resolution thermal infrared data to assess whether the competent depositional layers are exposures of competent 'duricrust' (16).

REFERENCES: 1) L.A. Soderblom et al., Icarus 34, 446-464, 1978. 2) T.B. McCord et al., J. Geophys. Res. 87, 10129-10148, 1982. 3) R.E. Arvidson et al., J. Geophys. Res. 87, 10149-10157, 1982. 4) M.A. Presley and R.E. Arvidson, Icarus 75, 499-517, 1988. 5) E.L. Strickland, LPS XX, 1077-1078, 1989. 6) H.H. Kieffer et al., J. Geophys. Res. 82, 4249-4291, 1977. 7) J.R. Zimbelman and H.H. Kieffer, J. Geophys. Res. 84, 8239-8251, 1979. 8) F.D. Palluconi and H.H. Kieffer, Icarus 45, 415-426, 1981. 9) J.R. Zimbelman and R. Greeley, J. Geophys. Res. 87, 10181-10189, 1982. 10) P.R. Christensen, Icarus 68, 217-238, 1986. 11) G.S. Downs et al., Icarus 18, 8-21, 1973. 12) G.S. Downs et al., Icarus 26, 273-312, 1975. 13) G.S. Downs et al., J. Geophys. Res. 87, 9747-9754, 1982. 14) P.R. Christensen, J. Geophys. Res. 91, 3533-3545, 1986. 15) P.R. Christensen, J. Geophys. Res. 87, 9985-9998, 1982. 16) B.M. Jakosky and P.R. Christensen, J. Geophys. Res. 91, 3547-3560, 1986. 17) Webster's Third New Int. Dictionary, G.&C. Merriam Co., Springfield, Mass., p. 196, 1971.
[This work was supported by NASA grant NAGW-1804].

Figure 1. Footprint map of high resolution images examined in this study. Regional albedo features are labeled in capital letters; dotted circles show rim crests of three named impact craters. Patterns are a general guide to the spatial distribution of bedrock exposures.

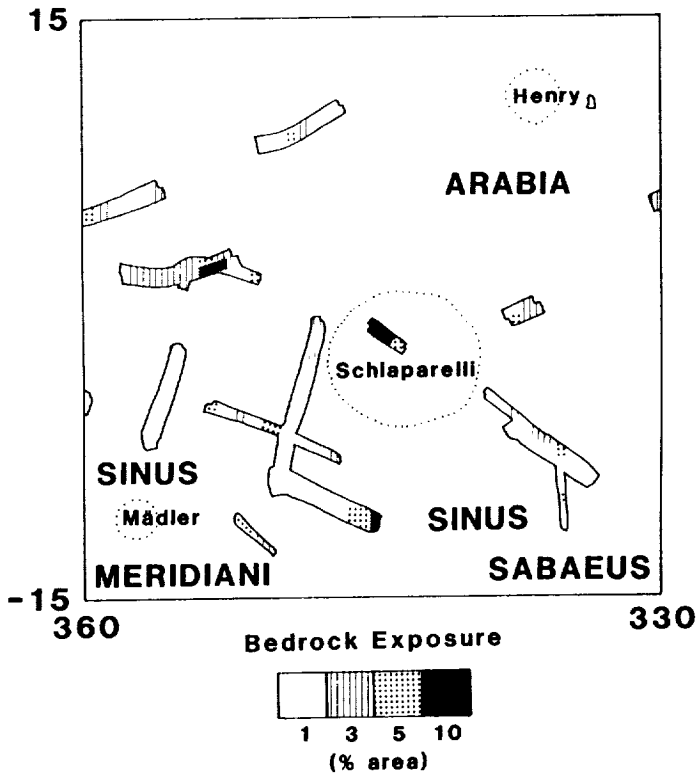

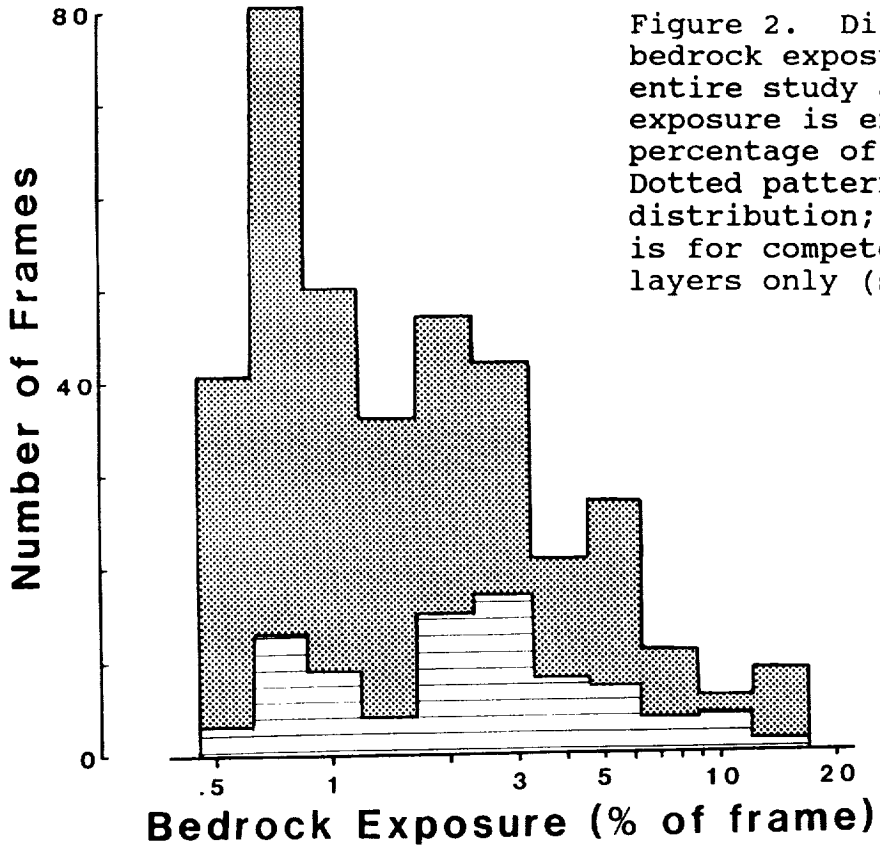

Figure 2. Distribution of bedrock exposures for the entire study area. Bedrock exposure is expressed as the percentage of the frame area. Dotted pattern is cumulative distribution; lined pattern is for competent depositional layers only (see text).

PRELIMINARY GEOLOGIC MAP OF CENTRAL MANGALA VALLES, MARS

James R. Zimbelman, Center for Earth and Planetary Studies, National Air and Space Museum, Smithsonian Institution, Washington, D.C. 20560.

Geologic mapping of the southern and central portions of Mangala Valles at a scale of 1:500,000 has been carried out as part of the Mars Geologic Mapping program. Three adjacent geologic maps have been prepared by researchers at NASM and at Arizona State University (1-3); the work described here corresponds to the northernmost of the three maps (MTM sheet -10147). Physiography around the central reaches of Mangala Valles is dominated by exposures of ancient Noachian material that are severely disrupted by arcuate, lobate scarps (Fig. 1). The scarps are interpreted here to be faults within the oldest materials, similar to those observed around southern Mangala Valles (1-3). The scarps in MTM -10147 lack the km-scale vertical relief of scarps to the south (4,5) but they are still prominent topographic features, cutting across large craters in the Noachian materials. The arcuate planimetric form and the lobate shape of the scarp fronts suggest a compressional origin. The orientation of the scarps in MTM -10147 changes from a north-south trend prominent to the south (1-3) to a northeast-southwest trend (Fig. 1). Both trends may reflect the influence of an ancient impact basin in Daedalia Planum (6). Amazonian-Hesperian materials associated with Mangala Valles embay the western margin of the Noachian materials (Fig. 1). Hesperian intercrater plains north of the Mangala Valles materials are scoured by overland flow likely associated with Mangala Valles flood events; the fluvial scour on these plains extends into the map to the north (7). Amazonian-Hesperian plains traceable to the Tharsis region embay the eastern margin of the Noachian materials (Fig. 1). Researchers at the U.S. Geological Survey in Flagstaff (8) are working on maps immediately west of the map described here. When completed, the detailed geologic maps on eight adjacent MTM sheets will provide a comprehensive view of the intricate history of the Mangala Valles region that could be of great value for planning of future sample-related missions.

REFERENCES: 1) R. Greeley and R.A. Craddock, Geologic map of the southern Mangala Valles region of Mars (MTM -20147), submitted to U.S. Geological Survey. 2) J.R. Zimbelman, R.A. Craddock, and R. Greeley, Geologic map of the south-central Mangala Valles region of Mars (MTM -15147), submitted to U.S. Geological Survey. 3) J.R. Zimbelman, Lunar Planet. Sci. XX, 1239-1240, 1989. 4) J.R. Zimbelman, Trans. AGU 69(16), 390, 1988. 5) R.A. Craddock, J.R. Zimbelman, and R. Greeley, Lunar Planet. Sci. XXI, 240-241, 1990. 6) R.A. Craddock, R. Greeley, and P.R. Christensen, Lunar Plant. Sci. XIX, 213-214, 1988 (submitted to J. Geophys. Res.). 7) M.G. Chapman, H. Masursky, and A.R. Dial, Jr., Misc. Invest. Series Map I-1962, U.S. Geological Survey, 1989. 8) K.L. Tanaka and M.G. Chapman, Geologic maps of MTMs -05152 and -10152, in preparation.

[This work was supported by NASA grant NAGW-1390].

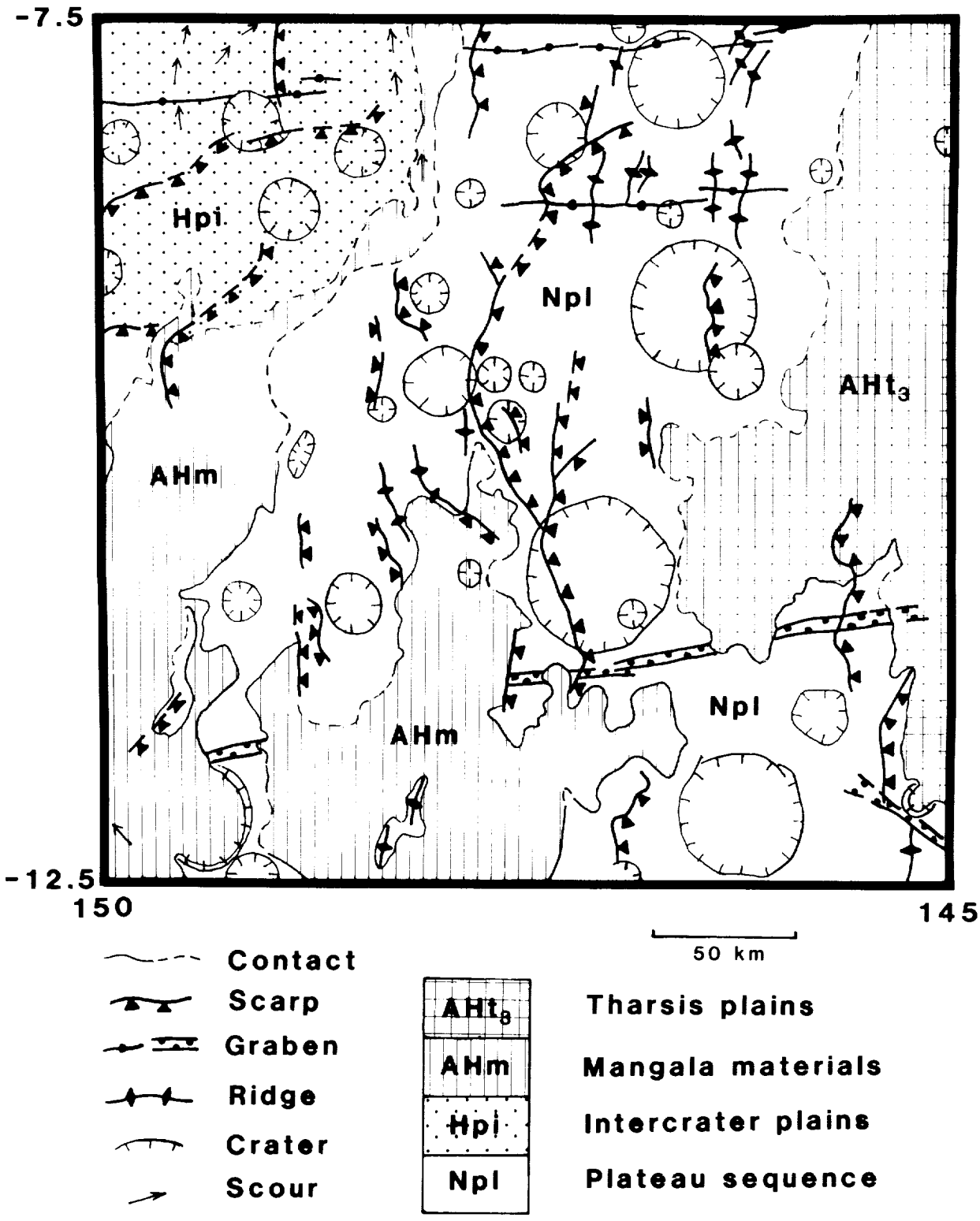

Fig. 1. Simplified geologic map of MTM -10147. Scarps are prominent in the Noachian and Hesperian materials, in places deflecting younger Amazonian-Hesperian materials from Mangala Valles (to the west) and the Tharsis region (to the east).

PRELIMINARY GEOLOGIC MAPPING OF MTM QUADS 40292 AND 40297, NORTH OF THE NILOSYRTIS MENSAE, MARS.

Steven H. Williams, Lunar and Planetary Institute, 3303 NASA Road 1, Houston, TX 77058 and James R. Zimbelman, Center for Earth and Planetary Studies, National Air and Space Museum, Smithsonian Institution, Washington, DC 20560.

Introduction. Geologic mapping of the MTM quads 40292 and 40297 (37.5-42.5^{o}, 290-300^{o}; 1:500,000 scale) is underway as part of the Mars Geologic Mapping program. The map area is in southwestern Utopia Planitia, immediately north of the Nilosyrtis Mensae. The goals of the geologic mapping are to identify and correlate the major geologic units and features in order to determine the sequence and scope of the geologic events that have modified the lowland side of the global dichotomy boundary in this region.

Background. The map area was mapped previously in three separate studies. The first were the maps prepared from Mariner 9 images that were based on surface morphology (1,2). The map area was also included in a global view of martian stratigraphy (3,4). The study area was mapped in (3) as having three units: rolling plains and knobby terrain, both of Hesperian age, and Amazonian-age cratered plains. In (4), the Hesperian-age units are grouped together as undivided material of Noachian/Hesperian age and the plains in the northern part of the map area are identified as Amazonian-age smooth and etched plains. The knobs prevalent throughout the map area are thought (2) to be due to the differential erosion of either: a) pre-existing topography protruding through (hence, older than) the Hesperian-age plains, b) remnants of Noachian-age plateau material common south of the map area, or c) igneous intrusions.

Results. Two important observations have arisen from this study: a) almost the entire map area is veneered by a fine-grained, erodible deposit of irregular thickness and late Amazonian age, and b) the unit immediately beneath the veneer is a late Hesperian-age plains unit, probably a flood basalt, that is younger than the breakup of the Noachian-age plateaus to the south.

The veneer unit has several distinctive features. Most important is its young age; there is not a single crater larger than 1 km diameter emplaced on top of the veneer. Every crater that size and larger in the map area appears to have been partially filled by the veneer. Many of the larger craters contain fill with ridges arranged in a crude circular pattern termed "concentric crater fill" by others (5,6,7). It is likely that the ridges are the eroded edges of a multiply-layered, airfall-type deposit (7) rather than compressional features caused by mass wasting of crater rim materials (5,6). An excellent example of crater fill that cannot have been derived from the rim is shown in Figure 1. Another important observation is that the mantling veneer was probably volatile-rich, as indicated by the presence of a few broad, flat-floored channels cut into its surface and the formation of lobate debris aprons around some of the knobs (Figure 2). Some such aprons are presumably caused by volatile-enhanced mass wasting of the veneer material mantling the knobs (after 5,6). The veneer is obviously much more readily eroded than is the plains unit beneath it.

The volcanic plains unit in the map area has a N(2) crater age of ~500 (late Upper Hesperian) and a N(1) crater age of ~1200 (middle Lower Amazonian); there is an insufficient number of 5 km diameter craters in the map area to give a meaningful N(5) age. The N(2) age is considered more accurate because many 1

km diameter craters are buried by the veneer or have been removed by erosion. The plains also contain several clusters of secondary craters that are probably associated with the Lyot impact (Lower Amazonian; 8). The interpretation of the plains as (basaltic) flood volcanics is bolstered by the presence of numerous wrinkle ridges.

The knobs found throughout the area are probably remnants of ancient terrain that protrude (or almost protrude) through both the veneer and the plains. While some knobs have lobate debris aprons, others appear to be lapped by plains units or surrounded by ridges that may be either the distal margins of eroded aprons or the eroded edges of mantling units (Figure 2). The distribution of the knobs suggests that they may reflect buried ancient cratered terrain (after 9); presumably the same that underlies the plateau units to the south of the map area. The relationship between the plateau and the plains is a critical piece of evidence in constraining the crustal dichotomy dilemma. Both are apparently underlain by heavily cratered terrain and, south of the map area, it appears that the plains butted up against and embayed the eroding plateau margin, which has erosionally retreated further south since the emplacement of the plains (Figure 3). Hence, the erosion of the plateau margin along the dichotomy boundary predates the plains.

References. 1. Lucchitta, B.K., 1978, Geologic map of the Ismenius quadrangle of Mars, USGS Map I-1065. 2. Greeley, R., 1978, Geologic map of the Casius quadrangle of Mars, USGS Map I-1038. 3. Scott, D.H. and M.H Carr, 1978, Geologic map of Mars, USGS Map I-1083. 4. Greeley, R. and J.E. Guest, 1987, Geologic map of the eastern equatorial region of Mars, USGS Map I-1802-B. 5. Squyres, S.W., 1979, The distribution of lobate debris aprons and similar flows on Mars, *Journal of Geophysical Research, 84*, 8087-8096. 6. Squyres, S.W., 1989, Urey Prize lecture: Water on Mars, *Icarus, 79*, 229-288. 7. Zimbelman, J.R., S.M. Clifford, and S.H. Williams, 1989, Concentric crater fill on Mars: An acolian alternative to ice-rich mass wasting, *Proceedings, 19th Lunar and Planetary Science Conference*, 397-407. 8. Tanaka, K.L., 1986, The stratigraphy of Mars, *Journal of Geophysical Research, 91*, B13, E139-E158. 9. McGill, G.E., 1986, The giant polygons of Utopia, northern martian plains, *Geophysical Research Letters, 13*, 705-708.

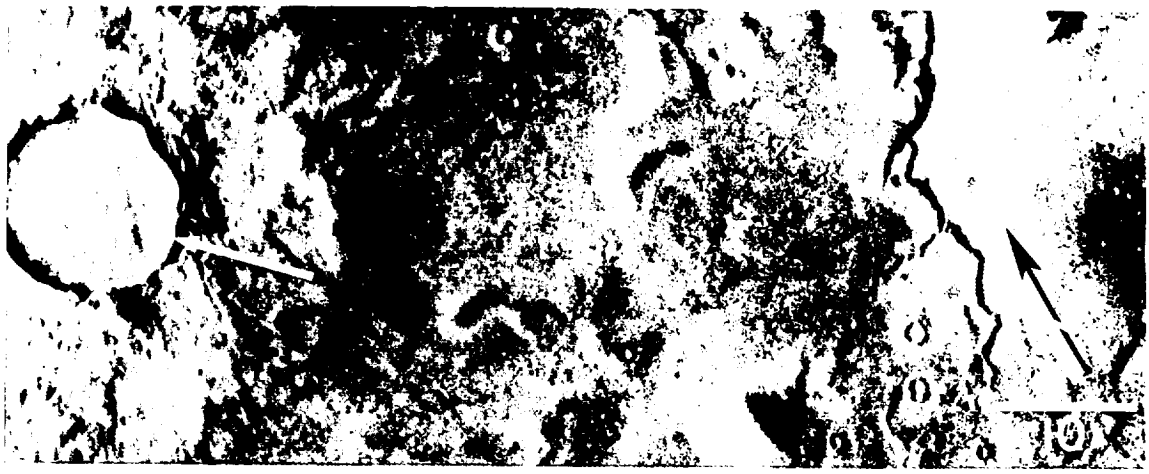

Figure 1. Some crater fill is obviously related to the Upper Amazonian-age veneer deposits. In this example (arrow), there is no ridge structure (insufficient erosional sculpting), the fill is not "concentric," and it is too voluminous to be mass wasted rim debris. This is a portion of Viking frame 11B44.

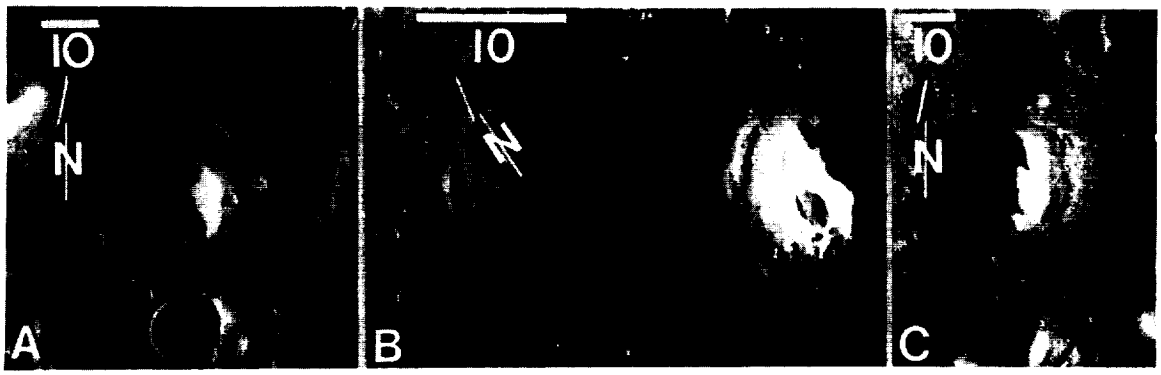

Figure 2. There are several features of interest that surround the knobs in the map area. A) Some knobs are flanked by lobate debris aprons (arrow) that are presumably formed by mass wasting of the volatile-rich knob or, more likely, veneer material. Below the knob is a crater with concentric fill. This is a portion of Viking frame 234S74. B) Some knobs are lapped by the Hesperian-age volcanic plains (arrows). This is a portion of Viking frame 11B44. C) In some cases, it is not possible to tell whether the ridges (arrow) that surround the knob are the distal margins of eroded lobate debris aprons or the eroded edges of veneer materials that once draped more completely over the knob. This is a portion of Viking frame 234S78.

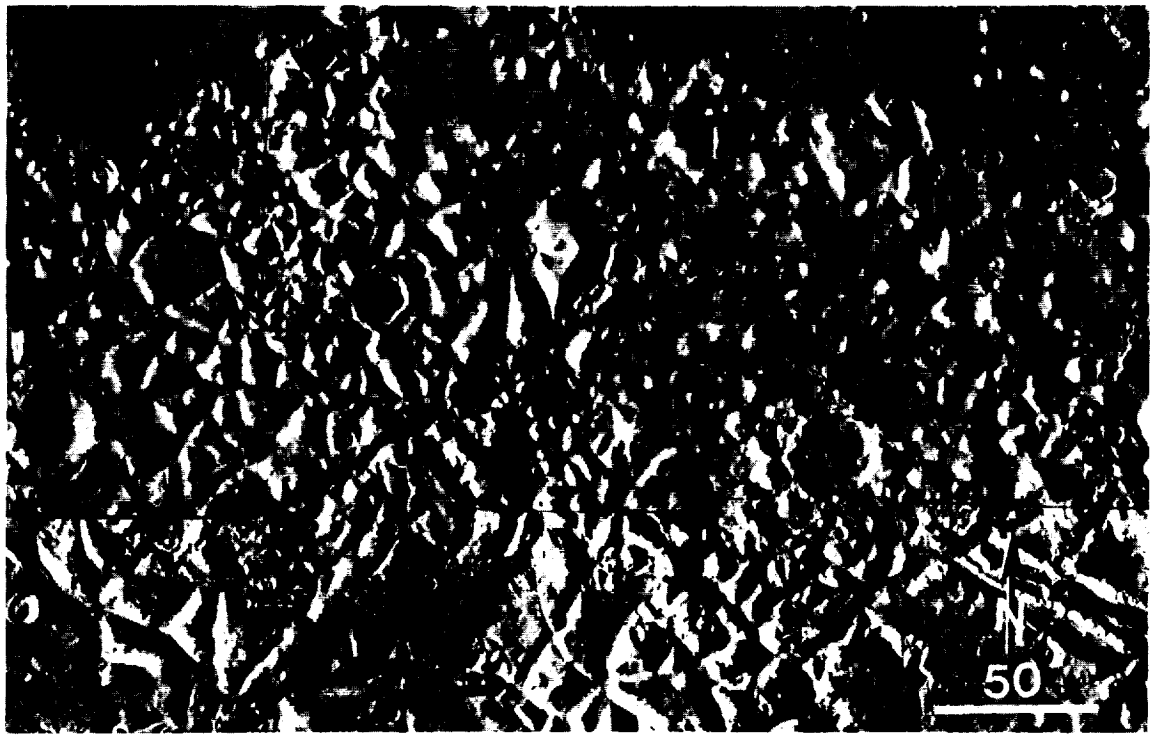

Figure 3. South of the map area, it appears that the Hesperian-age volcanic plains were emplaced against the eroding margin of Noachian-age plateau units (arrows). Subsequently, erosion of the plateau margin southward and several mantling episodes occurred. These are portions of Viking frames 34A01-06.

MOTTLED TERRAIN: A CONTINUING MARTIAN ENIGMA.
D.H. Scott[1] and J.R. Underwood[2], (1) U.S. Geological Survey, Flagstaff, Ariz. and (2) Kansas State University, Manhattan, Kansas

The northern lowlands of Mars are largely covered by plains materials that overall are mottled light and dark, a characteristic that is apparent on both Mariner and Viking images. The mottled terrain material (1) that makes up most of the northern lowlands is probably the most ambiguous material on all Martian images (2). Early studies, e.g., (3), used Mariner 9 images, which showed a hummocky, mottled surface encircling the planet between about lat 50° and 70° N. The Mariner pictures were degraded in this zone by atmospheric haze and high sun angles, which blurred them and produced high albedo contrasts; because significant morphologic variations were not recognized, the entire region was mapped as mottled plains material, a single geologic unit. Although image quality was poor, the mottling of the plains could be seen to result from albedo contrasts between numerous bright crater-ejecta blankets and dark intercrater plains material; also contributing to this effect were many dark-crested knobs, some having long, narrow, bright windstreaks or summit craters with bright interiors. The mottled plains were variously interpreted to consist of lava flows and knobby remnants of the highlands to the south (3), eolian and volcanic materials (4,5,6), ancient terrain and pedestal craters exhumed by wind erosion (7), eolian material cemented by permafrost (8), or volatile-rich deposits (9).

Debris mantles, suggested by (1) to have been derived from polar deposits, are distributed more or less symmetrically around the poles, extending as far as 30° toward the equator. These authors further suggested that the northern hemispheric mantle blankets the mottled plains and masks small (≤10-km diameter) craters on both young and old terrains.

I have described several geologic problems in the Martian northern plains, including that of the origin of the mottled material (2); I suggested that the plains "... may be an eroded remnant of the highlands that have survived a tectonic period of crustal separation caused by drifting or downfaulting followed by erosion."

The presence of lobate debris aprons, concentric crater fill, and terrain-softening poleward of lat 30° N. and S. suggested to (10) that topography in these regions has relaxed through quasi-viscous flow in ice-rich surface and near-surface materials. Support for this idea was provided by theoretical studies (11), which showed that ground ice should be present on Mars at middle and high latitudes. Dial (12) thought that permafrost and highly altered volcanic materials form the mottled plains.

Recent global geologic mapping of Mars (13,14,15), using high-resolution and high-quality Viking images, has subdivided the mottled terrain as originally mapped (3) into four members that constitute the Vastitas Borealis Formation of Late Hesperian age. The members intergrade and are largely distinguished by secondary morphologic characteristics, such as pronounced albedo contrasts, whorled patterns

of ridges, knobby hills, and irregular troughs having polygonal outlines in places. Although the formation has been postulated to consist of lava flows, fluvial deposits, and eolian materials within a permafrost zone (13), its surface is highly degraded, and the composition and origin of its component members remain uncertain.

Mapping problems still exist where image quality and resolution are adequate to determine textural characteristics of individual units but do not reveal the nature of their boundaries, stratigraphic relations, modes of formation, and processes responsible for their characteristic morphologies. The mottled plains material, as originally mapped and recently subdivided into members of the Vastitas Borealis Formation, continues to remain the most enigmatic geologic material in the northern hemisphere of Mars. Clarification of the origin of the mottled plains is critical, because this large, low, comparatively flat and unobstructed region may well provide the most suitable locations for successful landing and sample-return missions on Mars.

REFERENCES

(1) Soderblom, L.A., J.J. Kreidler, and H. Masursky (1973) J. Geophys. Res., 78, 4117-4122. (2) Scott, D.H. (1979) Proc. Lunar Planet. Sci. Conf. 10, 3039-3054. (3) Scott, D.H., and M.H. Carr (1978) U.S. Geol. Surv. Misc. Inv. Ser. Map I-1083. (4) Greeley, R., and J.E. Guest (1978) U.S. Geol. Surv. Misc. Inv. Ser. Map I-1038. (5) Lucchitta, B.K. (1978) U.S. Geol. Surv. Misc. Inv. Ser. Map I-1065. (6) Morris, E.C., and K.A. Howard (1981) U.S. Geol. Surv. Misc. Inv. Ser. Map I-1286. (7) Underwood, J.R., Jr., and N.J. Trask (1978) U.S. Geol. Surv. Misc. Inv. Ser. Map I-1048. (8) Elston, W.E. (1979) U.S. Geol. Surv. Misc. Inv. Ser. Map I-1140. (9) Wise, D.U. (1979) U.S. Geol. Surv. Misc. Inv. Ser. Map I-1154. (10) Squyres, S.W., and M.H. Carr (1986) Science, 231, 249-252. (11) Fanale, F.P., J.R. Salvail, A.P. Zent, and S.E. Postawko (1986) Icarus, 67, 1-18. (12) Dial, A. (1984) U.S. Geol. Surv. Misc. Inv. Ser. Map I-1640. (13) Scott, D.H., and K.L. Tanaka (1986) U.S. Geol. Surv. Misc. Inv. Ser. Map I-1802-A. (14) Greeley, R., and J.E. Guest (1987) U.S. Geol. Surv. Misc. Inv. Ser. Map I-1802-B. (15) Tanaka, K.L., and D.H. Scott (1987) U.S. Geol. Surv. Misc. Inv. Ser. Map I-1802-C.

THE FIGURE OF PHOBOS

T. Duxbury
Jet Propulsion Laboratory

Analytic expressions were derived to model the surface topography and the normal vector to the surface of Phobos. The analytic expressions are comprised of a spherical harmonic expansion for the global figure of Phobos, augmented by addition terms for the large crater Stickney and other craters. Over 300 craters were measured in more than 100 Viking Orbiter images to produce the model. In general, the larger craters were measured since they have a significant affect on topography. The derived topographic model has a global spatial and topographic accuracy ranging from about 50m in areas having the highest resolution and convergence coverage up to 500m in the poorest areas.

These analytic expressions, together with camera and viewing geometry parameters, are used to simulate the Soviet Phobos Mission images of Phobos with good success. A Hapke-Irvine scattering law is used to study the surface brightness (albedo) of Phobos at the pixel level. The Figure shows a real image on the left and the simulated image on the right. The derived volume from the model yields a density of $1.90 \pm 0.05 g/cm^3$. The model predicts a forced rotational libration amplitude of about 0.9 deg as compared with the observed value of about 0.8 deg, supporting Phobos having a uniform density throughout its interior.

The Soviet Phobos mission imaging data will be used to improve the figure model accuracy and add higher frequency details. Also, an attempt will be made to determine if there is an offset between the center-of-mass and the center-of-figure to give additional information on the Phobos interior.

The Shape of Deimos.

P. C. Thomas, Center for Radiophysics and Space Research, Cornell University, Ithaca, NY 14853

Deimos is a very irregularly shaped object and ellipsoidal approximations to its form have restricted mapping and quantitative study of its surface and structure. An approximate shape has been generated from the 12 best images by matching limbs and by stereogrammetric measures. Initial references are the control points measured by Duxbury and Callahan (1989). The shape is stored as a latitude-longitude grid of radii and allows direct calculation of volume, moments of inertia, surface normals, and slopes (including tidal effects on local g). An example view is shown in Figure 1. This is not the finally smoothed and checked product, but local errors to be removed are of 200 m or less.

The mean radius is 6.2 km, essentially identical to that given in Duxbury and Callahan (1989). A density of 1.9 gm/cm^3 would give surface gravity that varies from 0.27 to 0.34 cm/s^2 over the surface. Regional slopes are commonly over 15° and correlate well with the directions of bright streamers thought to show movement of surface material downslope (Thomas and Veverka, 1980).

It is interesting that a shape grossly similar to the laboriously determined one in Fig. 1 can be obtained by starting with an ellipsoid of 7.5, 6.1, and 6.4 km (b < c here), and "applying" two impact craters: an 11.2 km one, 2.7 km deep, near the south pole, and a 12 km, 1 km deep one near the north pole. This result encourages speculation that the overall shape might have been the result of the very large southern crater and an antipodal spallation. There are some geological reservations to this story, but the shape data will allow testing of the likely dispersal of the debris on the surface.

The shape data need fine tuning with even more images, and will allow real photometric measures to be made of the different materials on the surface in addition to the tracking of debris movement over the surface.

Supported by NASA grant NAGW-111.

References

Duxbury, T. C., and Callahan, J. D. 1989. Phobos and Deimos control networks. *Icarus 77*, 275-286.

Thomas, P. C., and Veverka, J. 1980. Downslope movement of material on Deimos. *Icarus 64*, 414-424.

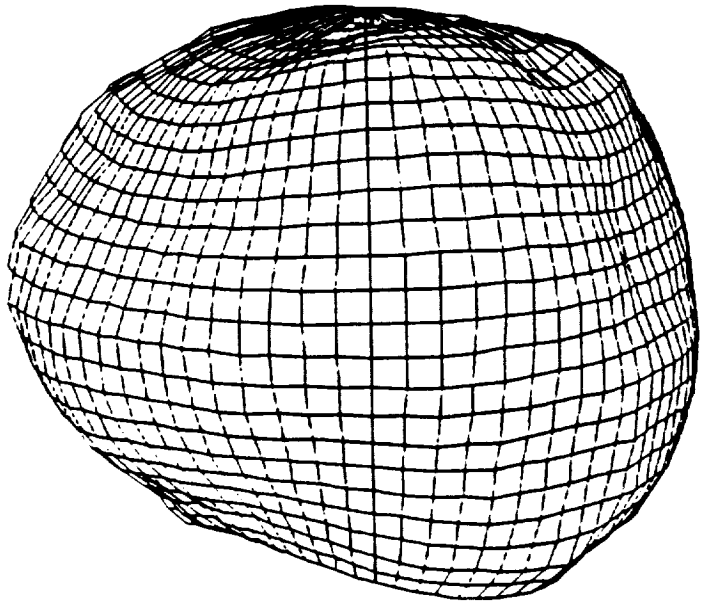

Figure 1. View of the approximate shape of Deimos.

TOPOGRAPHIC MEASUREMENTS OF MARTIAN VOLCANOES AND IMPACT CRATERS

Peter J. Mouginis-Mark, Mark S. Robinson, and Joan Hayashi-Smith, Planetary Geosciences Division, School of Ocean, Earth Science and Technology, University of Hawaii, Honolulu, HI 96822

INTRODUCTION:

Quantitative topographic measurements have previously been used to classify and interpret martian volcanic (1 - 3) and impact (4, 5) craters. In most cases, these measurements have relied on analysis of hard-copy images, where the measurement of shadows can be difficult due to contrast stretches that can make determination of the shadow edge inaccurate. We have initiated a program using digital versions of Viking Orbiter images to make shadow length measurements, and derive topographic profiles using photoclinometry, to add further constraints to the mode of formation and evolution of volcanic and impact craters on Mars via an analysis of their height/depth and topographic slopes.

Shadow length measurements can provide very precise height determinations if the following conditions are met: 1) low sun angle above the horizon; 2) pixel size is much smaller than the size of the feature being measured; and 3) relatively distortion free viewing geometry (low emission angle). Fortunately, Viking images exist that meet these criteria for the volcanoes Apollinaris Patera, Tyrrhena Patera, and for many impact craters within Hesperia Planum (~21 - 34°S, 233 - 248°W). To determine accurate shadow lengths, we measured actual data number (DN) values from calibrated Viking images (6). Errors for these measurements is determined from the assumption that the top and bottom of the shadow can each be located to within 0.75 pixel accuracy (total error 1.5 pixels).

In the case of the photoclinometric measurements (6, 7, 8), in order to determine an accurate slope, all changes in brightness on the image must be the result of a change in slope, not albedo. Inspection of Viking images from multiple passes at several wavelengths for some of our study areas (Apollinaris and Tyrrhena Paterae) reveals no gross change in brightness other than that due to change in slope across the measured profiles. Eight different orbits were used for Apollinaris patera, and five were used for Tyrrhena Patera. Estimation of the flat field (DN value of a flat surface) was done by examining the DN values of caldera floors and at breaks in slope (e.g., the rim of a caldera or impact crater). The validity of the flat field can be checked by taking a profile across a fresh bowl-shaped crater, or by comparing photoclinometrically derived heights with shadow measurements. If the profile across a fresh bowl shaped crater determines that the opposite rims of the crater are at the same height, and the shadow measurement corresponds to the profile height, then a confidence level can be placed upon the flat field value.

For the Hesperia Planum impact craters, we wish to explore an earlier concept (5) that martian impact craters display a gradual transition with increasing crater size from larger depth/diameter ratios at small diameters to lower values for larger craters. Our sample contains 61 craters in the diameter range 2.00 - 48.72 km. Of these craters, 26 are morphologically very fresh, possessing complete rims, well preserved ejecta blankets with radial striations or sharp distal ramparts, and have no superposed impact craters. These freshest craters are 2.44 - 14.28 km in diameter, and are used here to investigate the possible role of volatiles in influencing impact crater geometry. Shadow length measurements of crater depth/diameter were made from Viking Orbiter images that have a resolution of ~95 m/pixel and INA = 64 - 72°. Visual inspection of these images identified that either some of the SEDR solar azimuth angle files are incorrect, or that we had not accounted for the oblique viewing geometry, so we estimated the solar azimuth for each frame by taking the perpendicular to rim shadows for near-circular impact craters. The average of three crater diameters was used for each crater, one diameter being measured in the same direction as the sun azimuth angle and two at about ± 45° to the solar azimuth. In all cases, the rim crest of the crater was taken to be the point where

there was a rapid variation in the DN values. The rapid increase in DN values was also used to determine the edge of the shadow and, from simple trigonometry, the height of the crater rim. For a few of the craters larger than ~4 km diameter, it was also possible to obtain measurements of the height of the far rim above the surrounding terrain.

RESULTS

Apollinaris Patera: Shadow measurement (635A57 INA=79.5°, Res.=250 m/pixel) indicate a minimum relief of 5100 ± 90 m for the west flank of the volcano. The slope of the volcano under the shadow must be greater than the angle of the sun above the horizon, 10.5°. Shadow measurements were also taken of the caldera wall, producing a height estimate of 770 ± 90 m. Photoclinometric profiles show a distinct break in slope ~12 km from the summit plateau. The lower slopes must have a minimum slope of 3.70 ± 0.4°, while the upper regions have a minimum slope of 5.7° ± 0.6° (actual slopes are greater due to the oblique angle of the profile to the topographic slope).

Tyrrhena Patera: Both high and moderate resolution low-sun angle images of Tyrrhena Patera were used to determine flank slopes and caldera scarp heights. Shadow measurements from orbit 445A (INA = 68°, res. 60 m/pixel) indicate that the caldera scarp is typically 400 m high, with a maximum relief being 470 ± 35 m. Photoclinometric profiles (image 087A14, res. 230 m/pixel) indicate that the maximum slope on the measured flank is 3.6° ± 0.5°.

Hesperia Craters: Our preliminary analysis of the depth diameter ratio of the Hesperia Planum craters (Fig. 1) fails to identify the gradual transition from small craters formed within a shallow (top few hundred meters) permafrost layer within the target to larger craters formed with deeper, volatile-poor, strata below the permafrost (perhaps at depths of a few hundred meters). Based on our estimates of depth and rim height, several of the freshest craters would penetrate the entire thickness of the ridged plains materials (estimated to be ~400 m thick; ref. 9), excavating the crater floor within the basement materials.

CONCLUSIONS

The lower slopes of Apollinaris Patera are comparable to the slopes measured for Tyrrhena Patera, suggesting a similar evolution. The break in slope on Apollinaris may reflect a change in the style of eruption from an early stage of explosive activity similar to that proposed for Tyrrhena Patera (10, 11) to a later stage that included effusive eruptions. This model for the evolution of Apollinaris is thus similar to that which we have proposed for the evolution of Alba Patera (12).

Although we cannot at this time identify the reason for the disparity between our results for the geometry of impact craters within Hesperia Planum and earlier ideas, we offer two possible explanations:

1) Cintala and Mouginis-Mark (ref. 5) measured craters on a variety of geological units, some of which may have contained fewer volatiles than did other units.

2) Our analysis has concentrated on the youngest, best-preserved craters within Hesperia Planum, specifically to avoid complications in crater geometry that may have been caused by erosion or subsequent infilling. Our criteria for recognizing these craters will thus bias our sample to preferentially include only the most recent craters, which may have formed at a time when the ridged plains materials of Hesperia Planum had become dessicated. By studying craters of different degradation states, it may still be possible to investigate the temporal evolution of the hypothesized volatile layer provided that subaerial modification processes can be accounted for.

FUTURE WORK

In addition to the volcanological interpretation of the derived topographic measurements for the volcanoes, we also plan to make a comparison between the derived topography and Earth based radar profiles for the same area. In this manner, we hope to assess possible averaging effects when measuring landforms of approximately the same size as the radar resolution cell. Recent radar studies of impact craters (13) can provide a good test can for this investigation.

For the Hesperia Planum craters, it is evident that the early conclusions (5) about the effects of near-surface volatiles influencing impact crater geometry were at best a fortuitous observation that combined data for craters on many different geologic materials. Our more geographically constrained data set, along with the digital nature of our data base, indicates that a larger data base has to be derived in order to prove/disprove the possibility of near-surface volatiles affecting cratering events. We thus intend to extend our Hesperia Planum study to first include a greater number of craters in this region, and then extend our data base to include other areas of ridged plains materials on Mars.

REFERENCES

1) Pike, R.J. (1978). Proc. LPSC 9th, p. 3239 - 3273.
2) Pike, R.J. and Clow, G.D. (1981) U.S. Geological Survey Open File Report, **81-1038**.
3) Blasius, K.R. and Cutts, J.A. (1981) Icarus, 45, 87 - 112.
4) Pike, R.J. (1980). Proc. Lunar Planet. Sci. Conf. 11th, p 2159 - 2189.
5) Cintala, M.J. and Mouginis-Mark, P.J. (1980). Geophys. Res. Lttrs, **7**, p. 329 - 332.
6) USGS Astrogeology (1987). *Planetary Image and Cartography System Manual.*
7) Davis, P.E., and Soderblom, L.A. (1984). JGR, **98**, 9449 - 9457.
8) Davis, P.A. and Tanaka, K.L. (1988). MEVTV Workshop on Nature and Composition of Surface Units on Mars (Abs). LPI Report 88-05, 49 - 50.
9) De Hon, R. A. (1985). Rpt. Plan. Geol. Prog., 1984, **NASA TM-87563**, p. 242 - 244.
10) Greeley, R., and Spudis, R. (1981). Revs. Geophys. Space Phys., **19**, 13 - 41.
11) Greeley, R. and Crown, D.A. (in press). Volcanic geology of Tyrrhena Patera, Mars. JGR.
12) Mouginis-Mark, P.J. et al. (1988). Bull Volcanol. **50**, 361 - 379.
13) Roth, L.E. et al. (1989). Icarus **79**, 289 - 310.

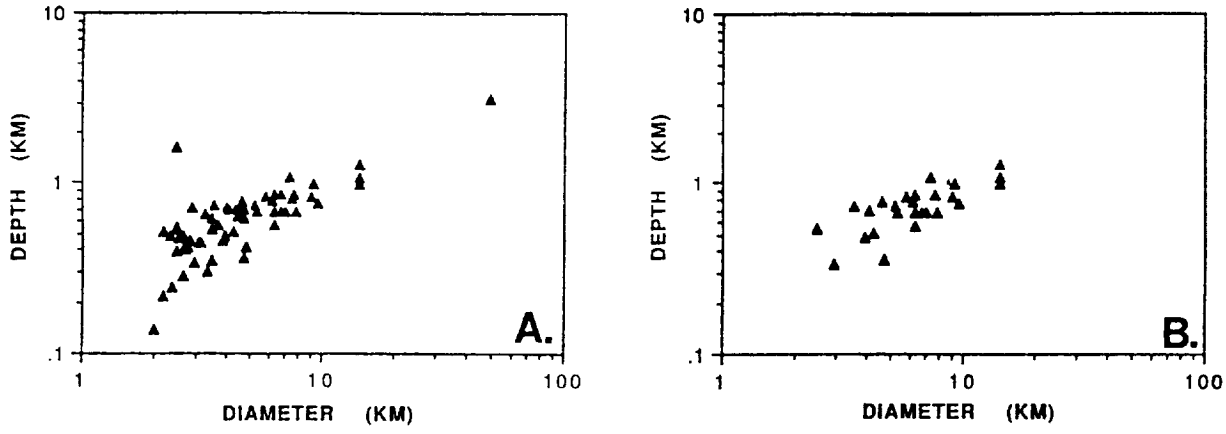

Fig. 1: A) Depth - diameter plot of all craters measured in this analysis. B) Depth - diameter plot of only those craters considered to be "pristine" in this analysis.

Distortions and photometric errors in the Voyager imaging subsystem

Robert W. Gaskell (JPL/Caltech)

Introduction. Determination of satellite shape and topography from Voyager imaging data requires finding landmark and limb locations to sub-pixel accuracy. It also requires that corrections be made for distortions introduced during readout, when the image on the focal plane is translated into electronic signals. The vidicon (TV) tubes used for this purpose on the Voyager spacecraft have reseaux fixed in the camera's focal plane and which appear in the final image. For most purposes, distortions can be computed by interpolating between these reseaux, whose true locations were measured before launch. If very accurate measurements are to be made, simple interpolation between reseaux is not sufficient. Beam bending, a local distortion of the readout electron beam caused by the charge on the vidicon's target, must be modeled.

A simple beam bending model was developed and successfully used to determine landmark locations on Io (Gaskell, 1988). These data were then used to find the shape of Io (Gaskell et al, 1988). When limb data was added to the data set, inconsistencies began to appear. Either limbs were not being found to high enough accuracy or there were distortions not predicted by the model.

A more satisfactory vidicon model now being developed accounts very well for observed beam bending effects (Gaskell, 1989). It also predicts photometric corrections which could significantly alter albedo and color measurements. A computer simulation can now translate small portions of a focal plane brightness distribution into the corresponding digital image data. Analysis of these processes is complicated by the finite size of the beam.

Vidicon operation. The optical-electronic interface occurs at the vidicon target, a thin layer of selenium-sulfur lying in the camera focal plane (Figure 1). The target's resistivity is very high in the absence of light, but falls dramatically when it is illuminated. During the "prepare cycle", the beam side of the target is repeatedly swept with an electron beam until it is fully charged. During the "write cycle", the target is illuminated, allowing electrons to leak through the target from the beam side to the tin oxide conducting layer on the camera side. During the "read cycle", the beam steps across the target through 800 positions in each of 800 lines, representing the picture elements (pixels) of the final digitized image. At each step, the beam reads for $11.57\mu s$ and then takes five times as long to move to the next pixel. Electrons are redeposited on the beam side, capacitively inducing a current in the tin oxide layer on the camera side. This current is a measure of the brightness at that pixel.

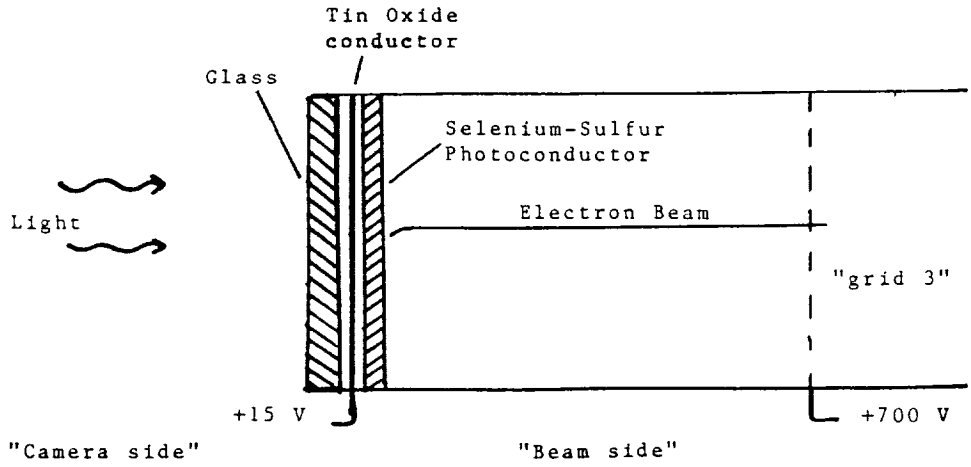

Figure 1. Target portion of vidicon tube.

By the time it leaves the final grid (grid 3), about 5 mm (360 pixels) away from the target, an electron has been accelerated to about 700 eV. It then decelerates, approaching the target with only a few eV. At the same time, it is deflected sideways with an acceleration proportional to

$$\int d^2r'\sigma(\vec{r'}+\vec{r})\vec{r'}\frac{d}{dz}(r'^2+z^2)^{-3/2} \tag{1}$$

where $\vec{r}$ is in the plane of the target and z is normal to it. The target's surface charge density σ is reflected through the tin oxide conducting layer to produce an effective dipole sheet.

Beam deflection. If the acceleration in the z-direction is uniform, and if the beam trajectory is nearly linear, the beam deflection at the target is found to be

$$\vec{s} = K\int d^2r\frac{\vec{r}}{r^3}\phi(\frac{r}{z_g},\lambda)\sigma(\vec{r}+\vec{r}_t) \tag{2}$$

where the beam lands at $\vec{r}_t$, $\lambda = \dot{z}_t/\dot{z}_g$ and z_g is the distance from the target to grid 3. The constant in equation (2) is $K = z_g/4\pi cV_g$ where c is the capacitance per unit area of the target and V_g is the potential at grid 3. The beam bending differs from previous inverse square models by the slowly varying factor

$$\phi(\alpha,\lambda) = \alpha^3\lambda\int_0^1 d\eta\frac{(\alpha^2+\eta^2)^{-3/2}-(\alpha^2+1)^{-3/2}}{[\eta+\lambda^2(1-\eta)]^{3/2}} \tag{3}$$

Photometric errors. The transverse velocity $\dot{\vec{s}}$ of the beam at the target, relative to the beam velocity at grid 3, is given by

$$\frac{\dot{\vec{s}}}{|\dot{z}_g|} = \vec{\rho}(\lambda) = \frac{K}{z_g}\int d^2r\frac{\vec{r}}{r^3}\chi(\frac{r}{z_g},\lambda)\sigma(\vec{r}+\vec{r}_t) \tag{4}$$

where

$$\chi(\alpha,\lambda) = 3\alpha^3\int_0^1 d\eta\eta(\alpha^2+\eta^2)^{-5/2}(\eta+\lambda^2(1-\eta))^{-1/2} \tag{5}$$

Energy conservation demands that $\lambda^2+\rho^2(\lambda) = 4\pi K\sigma/z_g$. This can be used iteratively with equation (4) to determine λ. It also shows that the charge can only be read down to a cutoff $\sigma \approx \rho^2(0)z_g/4\pi K$. In areas where beam bending is large, this leads to significant photometric errors. The beam deflection is also related to the transverse velocity by

$$(1-\lambda^2)\vec{s}(\lambda) = \vec{s}(0) - 2z_g\lambda\vec{\rho}(\lambda) \tag{6}$$

Beam shape. The first line of each Voyager frame is significantly brighter than those following. The values are consistent with a readout beam between two and three pixels in diameter. Roughly speaking, the first line is bright because it represents a wide swath of target being recharged by the beam. Subsequent sweeps recharge only the one pixel wide differential region. A similar phenomenon is observed for the first column of each picture. The situation is complicated by differential beam bending, which causes distortion of the beam.

Simulation results. A computer model has been constructed incorporating these effects. Additional corrections have been made for the target thickness and for slightly nonlinear beam trajectories. Each beam pulse is broken up into six time periods, allowing for changes in the target charge distribution during reading.

To within a factor of two, a saturated image (255 DN) corresponds to about 6 volts so that c, the target capacitance per unit area, is about 40 DN/V. With $z_g = 360$ pixels and $V_g = 700V$, K is about 10^{-3} pixel/DN. This constant was also determined by comparing reseau locations in several pictures taken at approximately the same time. Best fits for K were within 20 percent of the value above for all Voyager cameras. Observed brightness distributions around reseaux and near limbs were reproduced with the same value for K.

Work is currently underway to speed up the simulation process. For example, the simple approximations $\phi(\alpha, \lambda) \approx 2(1 - \lambda(\alpha/2 + \lambda^2)^{-1/2})$ and $\chi(\alpha, \lambda) \approx (\alpha/2 + \lambda^2)^{-1/2}$ can be used to compute the bending analytically in the beam landing region. Approximate simulations will be tested against the current "exact" simulation.

Discussion. It is doubtful whether any control network based on vidicon data can achieve sub-pixel accuracy without properly modeling beam bending. Limb measurements are even more suspect, due to additional photometric effects and there may be significant errors in color and albedo determinations. Finally, the very nature of the readout process is nonlinear. Modeling it as convolution between the target brightness and a pointspread function, as is commonly done for limbs and stars, is inappropriate. The development of a fast vidicon simulator could reduce the errors in a variety of planetary and satellite measurements by at least a factor of three.

References.

M. Benesh and P. Jepsen, *Voyager imaging science subsystem calibration report* (618-802), JPL, (1978).

R.W. Gaskell, S.P. Synnott, A.S. McEwen and G.G. Schaber, "Large-Scale Topography of Io: Implications for Internal Structure and Heat Transfer", *Geophys. Res. Lett.* **15**, 581-584, (1988).

R.W. Gaskell, "Digital identification of cartographic control points", *Photogrammetric Engineering and Remote Sensing*, **54**, 723-727, (1988).

R.W. Gaskell, "Electronic distortions in the Voyager vidicon", JPL EM 314-459, (1989).

B. Kazan and M. Knoll, *Electronic Image Storage*, Academic Press, New York, (1968).

TRITON MAPPING

R.M. Batson, P.M.Bridges, Kathleen Edwards, and J.L. Inge, U.S. Geological Survey, Flagstaff, AZ 86001

Maps of Triton based on Voyager 2 data have been compiled and are in review. Publication in both airbrushed "pictorial" and controlled photomosaic versions is anticipated by October of 1990. The maps are in Mercator and Polar Stereographic (south polar region only) projections at a scale of 1:15,000,000. A third map, in Mercator projection at a scale of 1:5,000,000, is centered on 8° S and 8° E; it extends from 45° N to 60° S and from 285° E to 90° E, enclosing the area of highest resolution Voyager 2 coverage. All projections are based on a sphere with a diameter of 2,700 km. Because of the retrograde rotation of Triton, longitude increases to the east, in accordance with astronomical convention.

Digital mosaics were assembled at a scale of 1/32° (1.3 km) per pixel according to methods described by Batson (1987) and Edwards (1987). Planimetric control was based on ephimerides provided by the Navigation Ancilliary Information Facility (NAIF) of the Jet Propulsion Laboratory. NAIF parameters (spacecraft position, camera orientation, and position and orientation of Triton) were used for the single Voyager frame (1550N2-001) covering the Neptune-facing hemisphere at the highest available resolution, as were spacecraft positions of all other frames. Camera orientations for frames in the mosaic were modified from NAIF data as required to fit the control frame. The average positional error of the mosaic with respect to the control frame is less than 6 km. After compilation, the mosaics were transformed to map projections defined above.

The pictorial maps were prepared according to methods described by Inge and Bridges (1976). Landforms are shown as if illuminated from the south. Surface markings are also shown.

References

Batson, R.M., 1987, Digital cartography of the planets: new methods, its status, and its future: Photogrammetric Engineering and Remote Sensing, vol. 53, no. 9, p. 1211-1218.

Edwards, Kathleen, 1987, Geometric processing of digital images of the planets: Photogrammetric Engineering and Remote Sensing, vol. 53, no. 9, p. 1219-1222.

Inge, J.L., and Bridges, P.M., 1976, Applied photo interpretation for airbrush cartography: Photogram. Eng. and Remote Sensing, v. 42, no. 6, p. 749-760.

PLANETARY ATLASES

R.M. Batson, J.L. Inge, and H.F. Morgan, U.S. Geological Survey, Flagstaff, AZ 86001

Two kinds of planetary map atlases are in production. The first kind, produced as NASA Special Publications, contains reduced-scale versions of previously published maps in hard-bound books with dimensions of 11 X 14 inches. These atlases are intended (1) to provide concise but comprehensive references to the geography of the planets needed by planetary scientists and others and (2) to allow inexpensive access to the planetary map dataset without requiring acquisition and examination of tens or hundreds of full-size map sheets. Two such atlases have been published (Batson et al., 1979, 1984) and a third is in press (Batson and Inge, 1990). We have just begun work on an Atlas of the Satellites of the Outer Planets, which we hope to complete in about one year.

The second kind of atlas is a popular or semi-technical version designed for commercial publication and distribution. One such atlas, The Atlas of the Solar System, by Greeley and Batson, is in preparation. This volume will have dimensions of 12 X 18 inches. Its emphasis is on a global view of each solid-surface body of the Solar System: it will contain, for each such body, brief descriptions, a large number of color maps and illustrations, simplified geologic maps, and shaded relief maps. All of the maps are on equal-area projections. Scales are 1:40,000,000 for the Earth and Venus; 1:2,000,000 for the Saturnian satellites Mimas and Enceladus and the Uranian satellite Miranda; 1:100,000 for the Martian satellites, Phobos and Deimos; and 1:10,000,000 for all other bodies. The giant gaseous planets are portrayed with small-scale, uncontrolled color mosaics.

Map compilations are virtually complete for this second kind of atlas. Text-writing is in progress. The goal is to have the book available to the public on October 12, 1992, in commemoration of the 500th anniversary of the Columbus voyages.

References

Batson, R. M., Bridges, P. M., Inge, J. L., 1979, Atlas of Mars: The 1:5,000,000 Map Series: National Aeronautics and Space Administration Special Pub. 438, 146 p.

Batson, R.M., Lee, E.M., Mullins, K.F., Skiff, B.A., Bridges, P.M., Inge, J.L., Masursky, Harold, and Strobell, M.E., 1984, Voyager 1 and 2 atlas of six Saturnian satellites: National Aeronautics and Space Administration Spec. Pub. 474, 175 p.

Batson, R.M. and Inge, J.L., eds., (in press), Atlas of Mars: the Viking global survey: National Aeronautics and Space Administration Special Publication.

THE MARS DIGITAL CARTOGRAPHIC DATABASE

R.M. Batson and Kathleen Edwards, U.S. Geological Survey, Flagstaff, AZ 86001

A global digital image model (DIM) of Viking Orbiter images of Mars is being compiled according to the plan described by Batson (1987). This mosaic is a refined digital version of the 1:2,000,000-scale controlled photomosaic series. The database is being distributed on digital tapes to nine institutions, including the National Space Science Data Center. Each tape contains a single "MC" quadrangle, partitioned according to the 1:2,000,000-scale quadrangle format. Figure 1 is an example of the photographic image of the MC29SW DIM. Compilation is 88% complete, and 60% of the DIMs have been released and distributed. A final distribution of the remaining DIMs is scheduled for November 1, 1990. Production is on schedule, so there should be no problem in meeting that deadline.

The DIM is tied to the topographic control net for Mars. The published standard error of this net is about 5 km (Wu and Schafer, 1984; Davies and Katayama, 1983) for the control base, which represents 20 pixels in the DIM. Discrepancies between adjacent frames are far less than 20 pixels over most, but not all, of the planet. We attempted to distribute the error so that it was not obtrusive in the mosaics, but this was not possible in some areas. The error can be attributed to a lack of precise knowledge of the spacecraft location in space at the time each image was taken and to parallax in oblique images of rugged terrain. Camera locations can be derived only by tracking the spacecraft continuously and precisely during its active lifetime, which was not always possible. Given camera positions, camera orientations can be derived by reducing to their minima the discrepancies between images in overlapping frames and the control net.

The individual frames incorporated in the global DIM will be distributed on October 31, 1991. These are radiometrically and cosmetically corrected image frames. They have not been resampled (i.e., no geometric correction has been made), nor have they been spatially filtered. They therefore display the highest resolution possible for each frame. The digital label for each of these frames contains corrected camera orientation information (i.e., a refined supplemental engineering data record, or "SEDR") derived during the compilation of the DIM. This can be used to project each image to its exact location in the DIM.

First-order photometric corrections were performed and contrast ranges were normalized based on solar illumination geometry. These corrections were made on the frames only as they were mosaicked into the DIM. The individual versions of these frames will not be distributed.

A high-resolution DIM is being compiled of areas selected to support specific scientific studies (figure 2). This compilation is a digital continuation of the 1:500,000-scale mosaic (MTM) series begun in

1984. Whereas the resolution of the global DIM is normalized to 1/256 deg/pixel (231 m/pixel on Mars), the high-resolution DIMs are normalized to the highest resolution available in each area covered. This may be as small as 1/2056 deg/pixel, or about 30 m/pixel. These high-resolution mosaics are tied to the medium-resolution DIM discussed above.

The 5-km global error becomes particularly obtrusive in the high-resolution DIMs; at 30 m/pixel, for example, 5 km is nearly 200 pixels. Such a large discrepancy between adjacent frames is clearly unacceptable. Where discrepancies of this magnitude occur, therefore, the high-resolution parts of a mosaic are tied to the medium-resolution parts at only one or two points, resulting in small frame-edge discrepancies within high-resolution mosaics, and large (some very large) discrepancies between high-resolution and medium-resolution frame boundaries.

References

Batson, R.M., 1987, Digital cartography of the planets: New methods, its status, and its future: Photogrammetric Engineering and Remote Sensing, vol. 53, no. 9, p. 1211-1218.

Davies, M.E., and Katayama, F.Y., 1983, The 1982 control network of Mars: Jour. Geophys. Res., vol. 88, no. B9, pp 7403-7404.

Wu, S.S.C., and Schafer, F.J., 1984, Mars control network: American Society of Photogrammetry, in Technical papers of the 50th annual meeting of the American Society of Photogrammetry, v. 2, Washington, D.C., March 11 - 16, 1984, p. 456-463.

Illustrations

Figure 1. Photographic image of part of a medium-resolution DIM of Mars (MC29SW). Projection is Sinusoidal Equal-Area centered on long 225° W.

Figure 2. Status of Mars 1:500,000-scale mapping, including both DIMs and manual mosaics. Quadrangles assigned to geologic mappers are solid black.

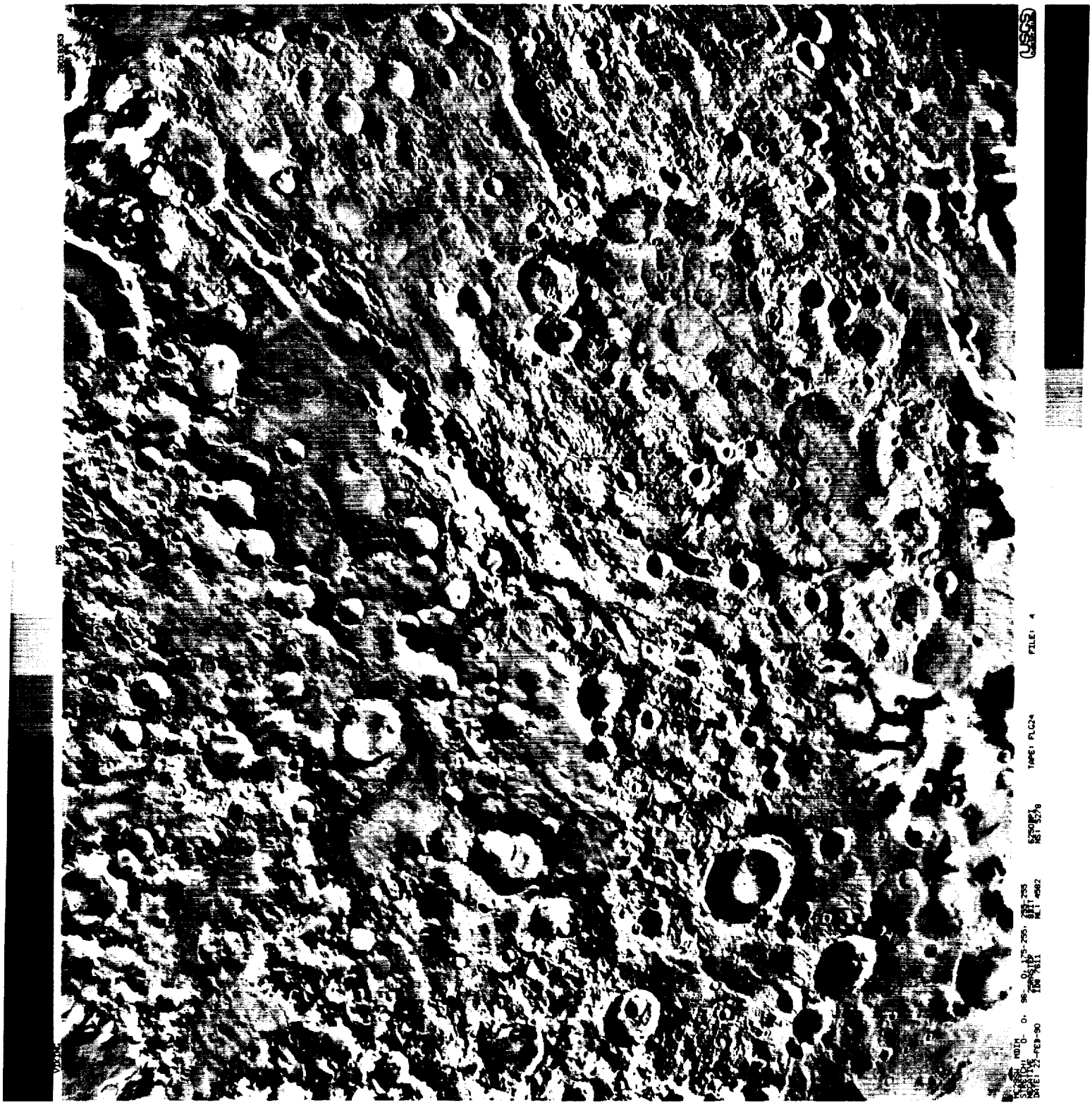

ORIGINAL PAGE
BLACK AND WHITE PHOTOGRAPH

MARS 1:500,000-SCALE MOSAICS PUBLISHED

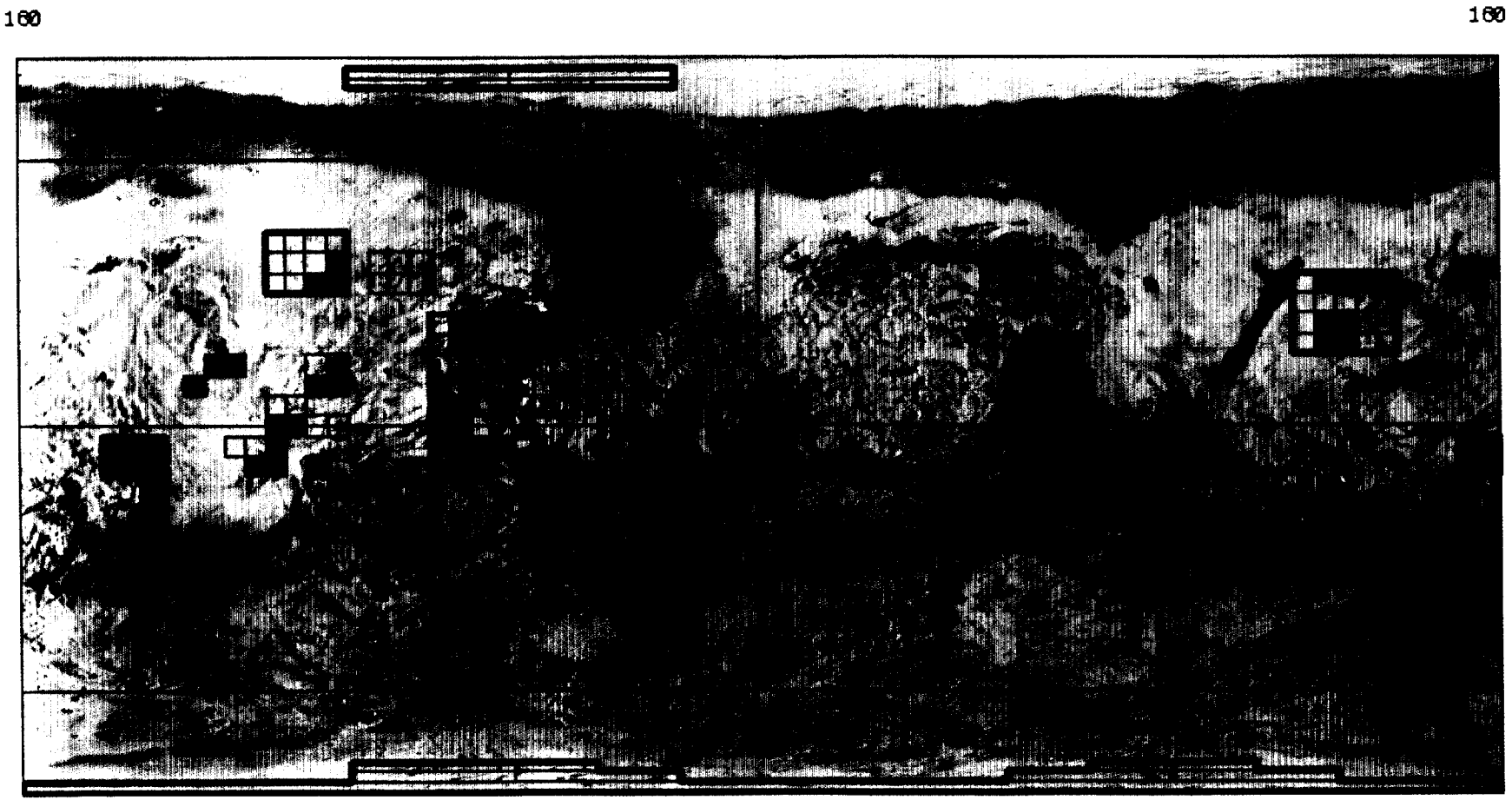

HIGH RESOLUTION DIM PLANNED OR IN PROGRESS: □

COMPLETE: ■

A NEW SHADED RELIEF MAP OF THE LUNAR NEAR SIDE

R.M. Batson and P.M. Bridges, U.S. Geological Survey, Flagstaff, AZ 86001

A new shaded relief map of the lunar near side has been prepared at a scale of 1:5,000,000. This map completes a set consisting also of the far side and the polar regions of the Moon (USGS, 1980, 1981). The maps are in the format of a set prepared primarily from telescopic photographs by the USAF Chart and Information Center (ACIC, 1970a, 1970b, 1970c), now out of print. When completed, this new shaded relief map will be digitized for inclusion in a completely new digital database for the Moon. The new map is required for general scientific use and to support new lunar exploration initiatives.

A mosaic provided by the Defense Mapping Agency Topographic Command was used as a control base. A wide variety of Lunar Orbiter images (primarily LO 4) images were examined in the interpretation.

Although westerly illumination is normally used for lunar and planetary maps, relief in the new map is illuminated from the east for consistency with the series' far side and polar maps.

References

Aeronautical Chart and Information Center, U.S. Air Force, 1970a, Lunar earthside chart, LMP 1, 1:5,000,000 scale, 2nd edition.

Aeronautical Chart and Information Center, U.S. Air Force, 1970b, Lunar polar chart, LMP 3, 1:5,000,000 scale, 2nd edition.

Aeronautical Chart and Information Center, U.S. Air Force, 1970c, Lunar farside chart, LMP2, 1:5,000,000 scale, 2nd edition.

U.S. Geological Survey, 1980, Map showing relief and surface markings of the lunar far side, 1:5,000,000 scale, I-1218A, I-1218B

U.S. Geological Survey, 1981, Map showing relief and surface markings of the lunar polar regions, 1:5,000,000 scale, I-1326A, I-1326B.

STATUS OF THE 1:2,000,000-SCALE TOPOGRAPHIC MAP SERIES OF MARS

Sherman S. C. Wu, Karyn K. Ablin, Patricia A. Garcia, and Raymond Jordan, U.S. Geological Survey, Flagstaff, AZ 86001

We have developed special photogrammetric techniques (Wu et al., 1982) for systematically mapping Mars' topography at a scale of 1:2,000,000 from high-altitude Viking Orbiter images. Seven quadrangles have been published and technical review is complete for an additional 57; these 64 quadrangles cover the Mars equatorial band (lat 30°N to 30°S). By the end of fiscal year 1990, 56 more quadrangles will have been completed for compilation on the analytical stereoplotters. The remaining 20 quadrangles, which cover the two polar regions of Mars, will be completed in fiscal year 1991.

Elevations on the maps are relative to the Mars topographic datum (Wu, 1981). The Mars planetwide control net (Wu and Schafer, 1984) is used for the control of compilation. The maps have a contour interval of 1 km and a vertical precision of ± 1 km, and thus are more detailed than previous maps.

References

Wu, S. S. C., 1981, A method of defining topographic datums of planetary bodies: Annales de Geophysique, AGEPA 7, Tome 37, fasc. 1, p. 141-160.

Wu, S. S. C., and Schafer, F. J., 1984, Mars control network, in Technical Papers of the 50th annual of the American Society of Photogrammetry and Remote Sensing, Washington, D.C., March 11-16, 1984, v. 2, p. 456-463.

Wu, S. S. C., Elassal, A. A., Jordan, Raymond, and Schafer, F. J., 1982, Photogrammetric application of Viking orbital photography: Planetary and Space Science, v. 30, no. 1, p. 45-55.

QUANTITATIVE ANALYSIS OF MARS' TOPOGRAPHY

Sherman S. C. Wu, Annie Howington-Kraus and Karyn Ablin, U.S. Geological Survey, Flagstaff, AZ 86001

A new global topographic map of Mars has been published (USGS, 1989). The map, at a scale of 1:15 million with a contour interval of 1 km, was compiled by the synthesis of data acquired from various scientific experiments of both the Mariner and Viking Missions (Wu et al., 1986). Contour lines of the map are referred to the Mars topographic datum (Wu, 1981). Those in the equatorial belt (between lat 30°N. and 30°S.) were extracted from 1:2 million-scale contour maps compiled by stereophotogrammetric methods using Viking Orbiter pictures. The planetwide control net was used for control (Wu, and Schafer, 1984).

From the global topographic map, a Mars Digital Terrain Model (DTM) has been derived (Wu and Howington-Kraus, 1987). From the DTM, we calculated the distribution of Mars' volume above and below its datum. We first mosaicked data from the western and eastern hemispheres with data from the two polar regions and converted the result from the Mercator projection to a Sinusoidal Equal Area projection. We then calculated volumes in 36 separate blocks, each covering 30° of latitude and 60° of longitude (Fig. 1). The volumes were calculated by multiplying each 1-km^2 area by the surface elevation above or below the datum. In Table 1, total volumes of the six longitudinal zones (each comprising six blocks) are listed in the bottom two rows, and total

Table 1. Volume Distributions of Mars Topography. (All values are X 10^6 km^3.)

Longitude(w)	180°-120°	120°-60°	60°-0°	360°-300°	300°-240°	240°-180°	0°-360°
Latitude							
N90°-60°	+0 -3.135	+0.027 -2.393	+0.017 -3.758	+0.070 -2.433	+0.064 -2.099	+0.006 -4.185	+0.183 -18.003
N60°-30°	+1.228 -5.776	+10.728 -0.384	+0.095 -6.144	+3.768 -1.067	+0.931 -4.901	+0.747 -5.330	+17.497 -23.601
N30°-0°	+9.645 -5.016	+25.687 -0.029	+1.842 -4.526	+9.485 -0.027	+6.910 -4.506	+2.850 -4.837	+56.419 -18.940
S0°-30°	+22.919 -0.001	+42.109 -0.044	+10.006 -0.852	+20.113 -0.006	+18.405 -0.052	+14.215 -0.762	+127.768 -1.716
S30°-60°	+22.146 -0	+24.022 -0	+14.206 -0	+14.769 -1.420	+6.652 -4.616	+18.751 -0	+100.545 -6.036
S60°-90°	+6.844 -0	+6.197 -0	+5.980 -0	+5.258 -0	+5.807 -0	+7.237 -0	+37.324 -0
N90°-S90°	+62.783 -13.927	+108.769 -2.849	+32.145 -15.280	+53.463 -4.952	+38.770 -16.173	+43.805 -15.114	+339.735 -68.296

Note: Positive volumes are solid mass above the topographic datum, whereas negative volumes are empty space below the topographic datum.

volumes of the six latitudinal bands (each comprising six blocks) are listed in the last column. The western hemisphere is about 72 million km^3 greater in volume than the eastern, because it contains the Tharsis bulge. The southern hemisphere is about 244 million km^3 greater in volume than the northern, and its average elevation is 3 to 4 km higher, because Mars' center of mass is shifted about 3.5 km to the north of its center of figure.

Total global topographic volumes are 339.7 million km^3 above the datum and 68.3 million km^3 below it. A total solid volume below the Mars topographic datum is calculated to be about 162.9×10^3 million km^3. Therefore, the total solid volume, including topographic irregularities, is 163.2×10^3 million km^3. The total area of Mars' surface at the datum is about 144.2 million km^2. The mean elevation above the datum is then about 1.9 km.

References

U.S. Geological Survey, 1989, Topographic maps of the western, eastern equatorial, and polar regions of Mars: Misc. Inv. Ser. Map I-2030, 3 sheets, 1:15,000,000.

Wu, S. S. C., 1981, A method of defining topographic datums of planetary bodies: Annales de Geophysique, Centre National de la Recherche Scientifique, Numero 1, Tome 37, p. 147-160.

Wu, S. S. C., and Howington-Kraus, A. E., 1987, Digital presentation of Mars topography, XVIII Lunar and Planetary Science Conference, p. 1108-1110.

Wu, S. S. C., and Schafer, F. J., 1984, Mars control network: American Society of Photogrammetry and Remote Sensing in Technical Papers of the 50th annual meeting of the American Society of Photogrammetry, Washington, D.C., March 11-16, 1984, v. 2, p. 456-463.

Wu, S. S. C., Jordan, Raymond, and Schafer, F. J., 1986, Mars global topographic map: 1:15,000,000 scale: National Aeronautics and Space Administration Technical Memorandum 88383, p. 570-571.

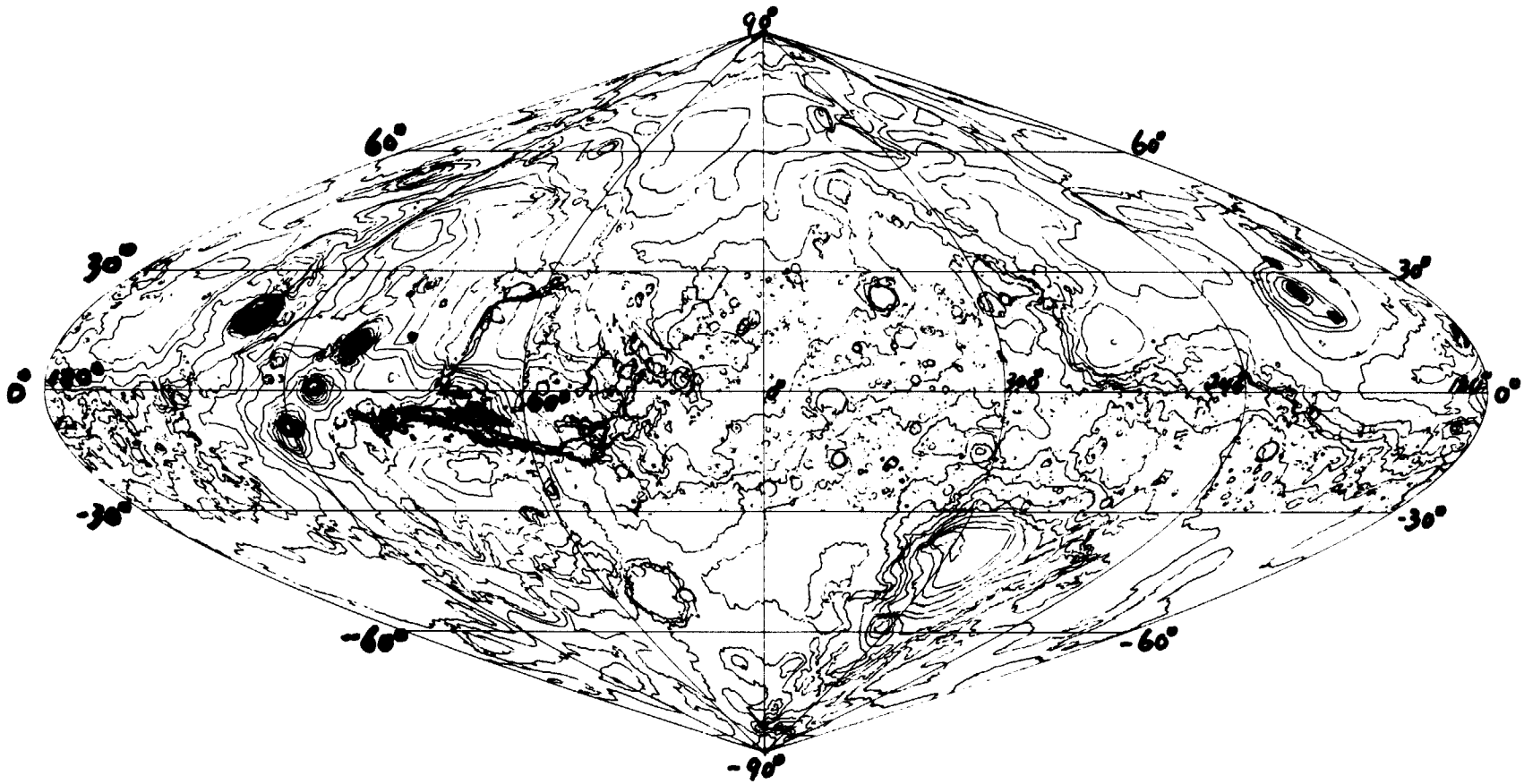

Figure 1. The global topographic map of Mars in Sinusoidal Equal Area projection.

PUBLICATION OF THE MARS CONTROL NETWORK

Sherman S. C. Wu, Jennifer S. Billideau, Annie Howington-Kraus, and Beth A. Spare, U.S. Geological Survey, Flagstaff, AZ 86001

The planetwide control network of Mars (Wu and Schafer, 1984) is based on 1,157 high-altitude Viking Orbiter images and contains 4,502 control points covering the entire surface of Mars. The network is not only instrumental in the compilation of maps at various scales, but it is also widely used in other research such as the study of Mars' gravity and atmosphere.

Since the autumn of 1989, we have been formatting the control network for a NASA Special Publication, which will be useful for planetary studies as well as for planning future Mars missions such as the Rover/Sample Return Mission. We have completed the precise marking of control points on the half-tone bases of 1:2,000,000-scale photomosaics that were prepared for the Mars Atlas (Batson and Inge, in press). Figure 1, an example of these mosaics, shows 105 control points on MC 18E (a combination of MC18-NE and -SE); each point appears on at least two images. The final adjusted ground coordinates and elevations of the control points are shown in Table 1. The last column in the table lists the topographic datum (zero elevation) that can be used to compute the solid radius of the control point from the center of mass of Mars.

The NASA Special Publication will also include information such as the adjusted C-matrices of each image, description of the methods used and their accuracy, and guidelines for users. It will be submitted by the end of fiscal year 1990 for publication.

References

Batson, R. M., and Inge J. L., in press, Atlas of Mars: The Viking Global Survey, NASA Special Publication.

Wu, S. S. C., and Schafer, F. J., 1984, Mars control network, in Technical Papers of the 50th Annual Meeting of the American Society of Photogrammetry and Remote Sensing, Washington, D.C., March 11-16, 1984, v. 2, p. 456-463.

Table 1. Control point information (picture numbers, ground coordinates, and topographic datum)

ID	PICTURE NOS.						LON	LAT	ELEV (M)	DATUM (M)
59	655A82	663A04	663A46	663A48			58 12 29.843	-4 56 18.270	4108.850	3393505.626
61	4A01	620A64	663A48	655A84	7A01		48 08 30.199	-3 07 38.290	3087.196	3393368.234
446	701A31	655A81					65 10 59.409	-21 25 59.191	5854.858	3391438.904
448	663A05	701A31	407B08	334S86	407B06		57 30 46.844	-26 13 54.690	7550.493	3390193.308
3777	655A81	701A31	53A07	40A47	53A17		65 55 14.474	-17 48 32.540	6519.155	3392174.669
3778	663A05	655A81					56 28 51.807	-18 48 12.622	4100.514	3391770.454
11816	663A44	663A04	701A31				61 51 23.436	-11 20 11.978	6260.060	3393047.888
11820	701A36	663A44	663A46	655A82	663A04	684A50	65 02 03.509	-1 55 55.704	5821.576	3393831.876
11821	701A36	663A44	655A82	6630A4	663A46		62 41 46.994	-7 39 32.297	6269.208	3393447.823
11823	663A44	620A62	655A82	663A04	655A81	701A31	62 14 11.284	-10 57 17.953	7147.707	3393103.807
11860	663A46	655A82	620A62	663A04	666A03		58 33 54.762	-1 35 29.081	3640.644	3393635.633
11861	701A36	663A04	663A46	655A82			62 15 37.722	-4 15 35.905	3458.563	3393657.745
11862	620A62	663A04	663A46	4A01	663A48	655A82	55 21 31.398	-4 09 11.905	3586.583	3393471.654
11863	655A82	663A04	663A48	663A46	663A05	620A62	56 23 31.971	-7 29 47.583	4268.167	3393289.115
11864	663A05	620A62	663A46	663A48	4A01	620A64	53 28 59.556	-6 22 59.323	3867.147	3393304.853
11865	663A04	663A48	620A62	663A05	4A01	12A01	51 42 51.786	-5 33 48.165	4122.821	3393320.426
11866	663A04	663A48	663A05	655A85	4A01	620A62	50 03 38.610	-7 26 53.517	214.679	3393162.785
11867	620A63	663A48	620A62				52 23 17.810	13 2529.766	3682.406	3392562.793
11873	663A46	655A81					64 06 29.040	-16 0048.861	5979.953	3392439.020
11878	663A05	663A48	32A08				50 49 32.507	-16 50 31.192	3616.617	3392018.080
11879	663A05	663A48	32A08				53 33 13.930	-17 08 09.092	4181.816	3392013.229
11880	663A05	663A46	655A81				59 10 39.990	-14 22 52.917	4889.051	3392569.267
20189	53A07	407B06	334S86	40A72	407B04		66 26 10.760	-26 01 35.272	6162.946	3390413.366
20274	663A05	663A48	32A08	407B08			45 49 46.370	-20 28 29.689	2689.788	3391296.947
21061	663A05	32A08	407B08				47 42 25.134	-22 29 10.321	2989.837	3390906.231
21062	32A08	407B08					46 09 25.676	-25 01 25.849	3487.769	3390331.600
21063	407B08	32A08					47 29 59.823	-25 55 57.310	3245.672	3390133.016
21064	663A05	407B08	32A08				49 03 56.003	-22 38 41.574	4120.550	3390887.812
21065	663A05	32A08	407B08				50 40 38.796	-22 57 42.542	3670.461	3390839.759
21067	663A05	663A48	32A08				51 07 08.347	-17 25 50.979	3571.655	3391922.712
21069	663A05	663A48	32A08				49 21 58.029	-21 11 56.211	3534.166	3391191.910
21070	663A05	663A48	407B08	32A08			46 38 12.410	-18 53 01.371	2685.596	3391606.682
21071	663A05	663A48	32A08	407B08			48 25 16.138	-18 53 30.129	2920.530	3391625.718
21072	663A05	663A48	32A08	407B08			48 46 18.708	-20 03 46.931	3596.825	3391409.270
21073	663A05	663A48	32A08				45 23 55.357	-19 13 20.329	3848.198	3391531.756
21075	663A05	655A85	4A01	32A08			47 31 30.691	-13 21 16.617	-910.376	3392497.852
21076	663A05	663A48	655A85	4A01	32A08		47 34 14.542	-15 04 42.712	-15.860	3392252.875
21082	663A48	4A01	586A24	655A85	620A64	620A63	45 32 35.133	-10 55 04.126	3375.725	3392772.994
21084	663A48	4A01	12A01	620A64	586A24	655A85	45 31 15.747	-7 18 01.656	2851.986	3393108.854
21971	407B08	40A59					45 15 14.432	-27 01 14.467	3770.347	3389853.966
21972	663A05	407B08	32A08				46 07 49.315	-22 41 52.102	3046.436	3390845.489
21973	663A05	407B08	32A08				47 27 59.122	-23 50 21.346	3687.793	3390610.819
21974	407B08	40A59					48 29 32.272	-29 00 54.853	3446.433	3389387.556
21981	32A08	40A12	407B08	40A59			51 05 36.511	-26 15 04.188	3793.170	3390096.656
21982	40A59	40A12					52 58 50.687	-25 59 29.086	3568.705	3390182.705
21983	663A05	32A08	407B08				52 13 51.946	-24 09 26.017	3370.741	3390596.892
21984	32A08	40A12	40A59	407B08			51 53 32.940	-27 32 02.685	3793.170	3389795.085
21985	32A08	40A59	40A12	407B08			53 09 29.364	-28 39 56.761	4017.580	3389527.552
21986	663A05	663A48	32A08	407B08			53 33 58.257	-22 00 29.032	3257.546	3391084.243
21987	40A59	40A12					55 00 56.823	-27 44 53.422	4999.051	3389783.116
21988	663A05	32A08	40A59	40A12			54 28 08.228	-26 03 57.679	3853.159	3390185.847
21989	663A05	407B08	40A59	40A12	701A31		55 53 42.311	-26 57 37.904	4185.809	3389990.622
21992	40A59	40A12					56 07 45.036	-28 05 50.322	3982.286	3389711.648
21993	663A05	407B08	40A12	40A59			56 48 22.897	-28 02 32.542	4860.847	3389735.552
21998	40A59	40A12	334S86	365B42	407B06	365B56	58 09 50.019	-28 37 31.803	5093.788	3389608.281
21999	40A12	40A59					59 11 37.232	-28 16 55.307	5041.592	3389712.373
22000	40A12	40A59					60 07 22.899	-26 31 22.859	5351.681	3390167.449
22002	701A31	40A12	655A81	407B06	334S86		60 58 37.736	-23 37 50.733	5639.877	3390864.492
22003	334S86	407B06					60 59 32.700	-23 34 58.898	5835.797	3390875.568
22006	40A59	40A12					61 09 03.232	-27 44 09.300	5334.839	3389884.159
22007	365B42	407B06					62 51 21.009	-28 02 17.384	5999.515	3389838.100
22009	407B06	365B42					65 01 42.020	-27 57 23.653	6200.063	3389899.919
22011	40A12	655A81	407B04	334S86			64 25 35.606	-23 48 02.211	6280.430	3390898.654
22013	701A31	40A12	334S86	53A07			65 55 29.007	-23 37 52.638	6504.331	3390971.038
22014	40A12	701A31	407B04	407B06	53A07	334S86	66 15 28.494	-24 46 40.047	6638.028	3390711.122
22202	334S86	40A72	53A07				67 19 57.796	-26 22 40.472	6530.704	3390345.615
23046	655A84	7A01	12A01	4A01	666A03	620A64	47 46 09.715	- 0 53 48.304	3106.962	3393408.177
23047	666A03	620A64	655A84	4A01	12A01		49 26 45.267	-1 36 08.717	3071.760	3393426.771
23048	4A01	12A01	663A04	620A64	655A84	666A03	50 58 05.785	-1 14 45.172	2670.605	3393459.923
23049	4A01	12A01	620A64	663A48	655A84	7A01	46 28 37.916	-3 32 49.946	495.144	3393329.732
23050	665A83	655A86	620A66	7A01	4A01	655A84	45 10 21.482	-1 08 47.023	3067.347	3393369.844
23051	620A62	4A01	12A01	663A04	620A64	666A03	52 36 46.778	-1 57 31.746	3211.081	3393481.212
23056	4A01	663A04	12A01	620A62	620A64	663A48	51 21 37.011	-3 37 38.468	2709.679	3393406.787
23057	4A01	12A01	620A64	655A84	7A01	663A48	47 43 28.872	-4 03 38.551	2409.862	3393327.337
23074	663A05	32A08	407B08				55 28 27.031	-22 59 15.274	3926.260	3390905.424
23075	40A12	407B08	40A59	365B56	365B58	365B42	59 32 42.709	-28 36 59.087	4899.960	3389632.625
23076	663A05	663A46	32A08	701A31	655A81		59 32 28.278	-18 33 56.160	5886.795	3391878.319
23080	663A05	655A81	701A31	407B08	334S86	407B06	59 07 52.956	-22 19 00.357	5574.394	3391117.344
23284	663A46	701A31	655A81				63 32 52.802	-17 52 50.116	4833.903	3392099.496
24004	663A44	663A46	396A48	701A31			66 38 26.305	-9 33 18.785	7957.323	3393392.984
24009	663A44	663A46	655A82	701A31			65 23 06.943	-9 51 15.913	7086.234	3393321.208
24014	663A44	663A46	655A81	701A31			64 27 11.446	-11 05 13.219	7016.872	3393152.948
24015	663A44	663A46	701A31	655A81			65 14 37.335	-12 33 06.771	-356.565	3392991.054
24068	655A81	701A31	334S86	53A07	40A47	53A17	65 39 12.426	-19 52 51.198	5977.181	3391770.639
24069	701A31	655A81	40A47	53A07	53A17		66 05 56.072	-17 44 37.434	6074.528	3392191.411
24070	663A05	663A46	655A81	701A31			62 16 28.328	-15 53 35.851	5396.817	3392410.551
24071	663A05	663A46	655A81	701A31			62 18 16.635	-14 55 25.939	5772.602	3392565.751
24072	663A05	663A46	620A62	655A81			59 23 48.215	-12 27 29.349	4646.797	3392842.335
24073	663A05	663A46	620A62	701A31	655A81		60 06 20.584	11 59 24.658	4890.913	3392920.333
24074	663A46	620A62	663A05				61 50 59.280	-11 19 57.089	6069.927	3393048.199
24075	663A46	663A48	663A05	620A62			55 10 14.592	-10 53 16.555	3794.492	3392934.324
24076	663A46	663A48	663A05	620A62			54 56 25.282	-10 25 24.004	4061.798	3392980.811
24082	663A04	620A62	663A48	663A05	663A46		57 10 06.979	-9 23 06.172	4373.627	3393139.406
24083	663A05	663A46	620A62	655A82	663A04	655A81	60 11 04.184	-8 26 09.795	5070.964	3393307.481
24085	663A46	701A31	655A81				64 58 22.907	-15 58 13.980	6277.326	3392469.724
24086	663A05	663A46	701A31	655A81			60 15 32.870	-16 19 58.125	5985.467	3392287.997
24087	655A81	701A31					65 20 56.997	-21 52 57.589	5650.133	3391346.677
24091	663A05	620A62	663A48	4A01	620A64		51 03 00.733	-10 17 43.191	2922.470	3392918.895
24114	655A81	40A12	407B04	53A07	407B06	334S86	64 16 47.952	-23 56 59.283	6269.791	3390861.175
24115	40A12	701A31	655A81	334A86	407B06		62 24 12.149	-22 12 25.423	5744.268	3391209.198
24132	663A05	663A48	32A08	655A81			55 18 47.673	-17 51 56.858	3611.192	3391918.400
24133	663A05	663A46	32A08	655A81			57 59 51.153	-16 22 58.484	5315.160	3392227.804
24134	663A05	663A46	620A62	663A48	32A08		54 34 07.012	-13 09 09.210	3729.864	3392641.091
24135	663A05	701A31	655A81	32A08			58 53 40.170	-19 46 53.775	5341.431	3391632.923
24139	663A05	663A46	663A48	4A01	32A08		50 20 38.764	-13 48 20.931	-1130.820	3392476.115

ORIGINAL PAGE
BLACK AND WHITE PHOTOGRAPH

Figure 1. Distribution of Control Points in MC 18E

THE CONTROL NETWORK OF MARS: MARCH 1990

Merton E. Davies and Patricia G. Rogers
The RAND Corporation, Santa Monica, CA 90406-2138

The preliminary control network of Mars was established by photogrammetric determination of the areographic coordinates of features on Mariner 6 and 7 images. Mariner 9 images, with resolutions of 1-2 km/pixel and coverage of almost the entire martian surface, led to the first planetwide high-resolution control net. Systematic mapping of the entire Martian surface by the Viking Orbiters produced high-resolution images (10-200 m/pixel) which greatly improved the accuracy and distribution of the control network.

The coordinate system of Mars defines the prime meridian by the crater Airy-O located just south of the equator. The reference spheroid for defining areographic coordinates has an equatorial radius of 3393.4 km and a polar radius of 3375.8 km (de Vaucouleurs et al., 1973). Analysis of radio tracking data from the Viking landers led to accurate measurements of Mars' rotational period, spin axis, and the lander coordinates relative to the inertial reference frame (Mayo et al., 1977; Michael, 1979).

The control net forms the basis of a least squares solution determined by analytical triangulation after the pixel measurements are corrected for geometric distortions and converted to millimeter coordinates in the camera focal plane. This analysis is performed in the J2000 coordinate system.

Viking images (~250 m/pixel) have been used to create high-resolution photogrammetric strips encircling Mars at the equator and at 60° north and south. These are tied together by meridian strips occurring every 90° of longitude. High-resolution strips at 30° north and south are currently being added. High resolution images (7-9 m/pixels) in the Viking 1 lander area are tied into and thereby strengthen the overall net. The Viking 1 lander was located on the surface by Morris and Jones, 1980. The coordinates of control points in this area are accurate to approximately 100 m; whereas, accuracies elsewhere are estimated to be 3 km along the strips and 6 km throughout the rest of the planets' surface.

The following represents the current status of the control network calculations:

9333	Points
2497	Pictures (1054 Mariner 9, 1443 Viking)
62,404	Observation Equations
26,157	Normal Equations
2.39	Overdetermination
14.07	Standard Error (μm)

Through high-resolution imaging of the Viking lander sites, future missions could improve the overall accuracy of the Mars control network.

References

Davies, M. E., "The Prime Meridian of Mars and the Longitudes of the Viking Landers," *Science*, 197, 1277, 1977.

de Vaucouleurs, G., M. E. Davies, and F. M. Sturms, Jr., "Mariner 9 Areographic Coordinate Systems," *J. Geophys. Res.* Vol. 78, No. 20, 4395-4404, July 10, 1973.

Mayo, A. P.; W. T. Blackshear; R. H. Tolson; W. H. Michael, Jr.; G. M. Kelly; J. P. Brenkle, and T. A. Komarek, "Lander locations, Mars physical ephemeris, and solar system parameters: Determination from Viking lander tracking data," *J. Geophys Res.* 82, 4297-4303, 1977.

Michael, William H., Jr., "Viking Lander Tracking Contributions to Mars Mapping," *The Moon and Planets* 20, 149-152, 1979.

Morris, E. C. and K. L. Jones, "Viking I Lander on the Surface of Mars: Revised Location," *Icarus* 44, 217-222, 1980.

C7

A UNIFIED LUNAR CONTROL NETWORK: MARCH 1990

Merton E. Davies and Tim R. Colvin, The RAND Corporation, Santa Monica, CA 90406

Donald L. Meyer, Defense Mapping Agency, Aerospace Center, St. Louis AFS, MO 63118

This program has been designed to combine and transform many control networks of the Moon into a common center-of-mass coordinate system. The first phase, dealing with the near side, has been completed and published (Davies, et al., 1987). Coordinates of 1166 points on the near side of the Moon are given.

The most accurately defined points on the Moon are locations of the laser ranging retroreflectors (Ferrari, et al., 1980) and the VLBI measurements of the locations of the Apollo 15, 16, and 17 ALSEP stations (King, et al., 1976). Recent values for the coordinates of the retroreflectors have been received from Williams and Dickey, 1986. The accuracy of these locations is about 30 m and their locations are used to define the center-of-mass and, hence, the origin of the unified lunar coordinate system. The coordinates of the retroreflectors are given in both principal axes and mean Earth/Polar axis systems. Mean Earth/Polar axis coordinates have been recommended by the IAU (Davies, et al., 1989) for the moon. The difference in the coordinates is important, more than 600 m in latitude and longitude.

The Apollo 15, 16, and 17 ALSEP stations have been identified on Apollo panoramic photography and their locations transferred to Apollo mapping frames. Thus, their coordinates are available in the control network computations. Transformation parameters involving translation, rotation, and scale were derived to best fit the control network coordinates to the three ALSEP station coordinates. The DMA/603 transformed system was selected as the primary control for the unified network.

The telescopic network of Meyer, 1980 was selected to transform from center-of-figure to center-of-mass coordinates. 130 points common to Meyer's and the Apollo networks were selected and transformation parameters computed to shift Meyer's coordinates to the transformed Apollo network. The RMS of the residuals of this transformation is 808 m. The mean shift of the coordinates was 1352 m, with a maximum of 2336 m and a minimum of 803 m.

The Mariner 10 control network has been tied to this system through common points and the coordinates of ten points in the north polar region have been computed. Our report contains coordinates of 130 Apollo points, 1026 telescopic points, and ten Mariner 10 points. These results were published in Davies, et al., 1987.

The Apollo control network does continue around the east limb and the far side to longitude 180° and beyond. Thus, the unified network can be extended onto the farside with the Apollo data. This has now been done.

The measured Apollo points are usually pug holes drilled on film in overlapping areas and transferred to new pictures using a stereocomparitor. Thus, these points are identified on just one set of pictures and it is difficult to describe the location of the points. For this reason, it was decided to determine the coordinates of points (usually craters) that were defined in the Lunar Positional Reference System (1974), 1975. This control network covers the entire near and far sides of the Moon and is based on 40 Lunar Orbiter pictures and one Apollo 16 trans-Earth frame. The estimated accuracy of the coordinates of the Positional Reference System (PRS) points vary from 1 km to 16 km. In the region of the Apollo networks, the estimated accuracy is 1 km to 6 km.

Coordinates of 159 PRS points have been computed in the unified coordinate system. These coordinates have then been compared to the PRS coordinates by computing the distance between them. 60 points had a shift over 10 km; we suspect that identification errors account for many of these. 43 points had a shift between 6 km and 10 km, and 48 fell between 3 km and 6 km. Only 8 points had a shift less than 3 km.

References

Catalog of Lunar Positions Based on the Lunar Positional Reference System (1974), Defense Mapping Agency Aerospace Center, St. Louis AFS, MO 63118, April 1975.

Davies, M. E., T. R. Colvin, and D. L. Meyer, "A Unified Lunar Control Network: The Near Side," *J. Geophys. Res.*, Vol. 92, No. B13, December 10, 1987, pp. 14177-14184.

Davies, M. E., et al., "Report of the IAU/IAG/COSPAR Working Group on Cartographic Coordinates and Rotational Elements of the Planets and Satellites: 1988," *Celestial Mechanics and Dynamical Astronomy*, Vol. 46: 187-204, 1989.

Ferrari, A. J., W. S. Sinclair, W. L. Sjogren, J. G. Williams, and C. F. Yoder, "Geophysical Parameters of the Earth-Moon System," *J. Geophys. Res.*, Vol. 85, No. B7, July 10, 1980, pp. 3939-3951.

King, R. W., C. C. Counselman III, I. I. Shapiro, "Lunar Dynamics and Selenodesy: Results from Analysis of VLBI and Laser Data," *J. Geophys. Res.*, Vol. 81, No. 35, December 10, 1976, pp. 6251-6256.

Meyer, Donald L., "Selenocentric Control System (1979)," Defense Mapping Agency, DMA TR 80-001, April 1980.

Williams, J. G. and J. O. Dickey, "Coordinates of the Lunar Laser Retroreflectors," Letter to M. E. Davies, June 18, 1986.

IMPROVEMENTS TO MERCURY'S GEODETIC CONTROL NETWORK: MARCH 1990

Merton E. Davies and Patricia G. Rogers
The RAND Corporation, Santa Monica, CA 90406

Mariner 10 imaging data of Mercury, acquired during three flybys from 1974-1975, revealed approximately 45 per cent of the planet's surface topography. Features identified on these high-resolution images (0.5-2.0 km/pixel) form the basis of Mercury's planetwide control network.

Hun Kal, a small crater located near the equator defines the 20° meridian on Mercury (Murray, et al., 1974). The planet's spin axis is assumed normal to the equatorial plane and its rotational period is 58.6462 days.

In 1979, the International Astronomical Union (IAU) recommended that the standard inertial coordinate system be based on the epoch of 2000 January 1.5 (Julian date 241545.0). Since 1984, all tables and other data in the Astronomical Almanac have been given in J2000 coordinates. The control network computations of Mercury have been converted to the J2000 coordinate system.

Control network computations involve photogrammetric determination of control point coordinates, and an analytical triangulation solution similar to that used for Mars' control network (Davies et al., 1973). Currently, these calculations include:

2393	Points
811	Pictures
26,142	Observation Equations
7,219	Normal Equations
3.62	Overdetermination
21.54	Standard Error of Measurement (μm)

A mean radius of 2439 km, based on limb measurements and the radio occultation experiment, was used in the control network computations. However, we've modified the radii at 60 points in the current control network solutions using radar altimetry profiles from Arecibo and Goldstone radar observations (Harmon, et al., 1986; Zohar and Goldstein, 1974).

In order to confirm that the mass of Mercury had been correctly determined by the Mariner 10 radio science team, Anderson, et al. (1987) recomputed the trajectories of the first and third flybys. These improved trajectories resulted in the determination of two second degree gravity harmonics. This new trajectory data has been incorporated into our latest control network computations.

We observed a 0.1° to 0.3° longitude shift when comparing the USGS H-6 quadrangle map to the control network. This corresponds to a similar longitude displacement (0.4°) noted by Harmon, et al. (1986) between

Arecibo radar data and the USGS map. Latitudes for features in the control network and the USGS map differed by approximately 0.4°. This latitude shift was not apparent on the 1:15 M map of Mercury.

REFERENCES

Anderson, J. D.; G. Colombo; P. B. Esposito; E. L. Lau; and G. B. Trager, "The Mass, Gravity Field, and Ephemeris of Mercury," *Icarus*, 71, 337-349, 1987.

Davies, M. E. and D. W. G. Arthur, "Martian Surface Coordinates, *J. Geophys. Res.*, 78, 4355, 1973.

Davies, M. E. and R. M. Batson, "Surface Coordinates and Cartography of Mercury, J. Geophys. Res., 80, 2417-2430, 1975.

Harmon, J. K., D. B. Campbell, D. L. Bindschadler, J. W. Head, and I. I. Shapiro, "Radar Altimetry of Mercury: A Preliminary Analysis," *J. Geophys. Res., 91, 385-401, 1986.*

Murray, J. B., M. J. S. Belton, G. E. Danielson, M. E. Davies, D. E. Gault, B. Hapke, B. O'Leary, R. G. Strom, V. Suomi, and N. Trask, "Mercury's Surface: Preliminary Description and Interpretation from Mariner 10 Pictures," *Science*, 185, 169-179, 1974.

Zohar, S., and R. M. Goldstein, "Surface Features on Mercury," *Astron. J.*, 79, 85-91, 1974.

CHAPTER 13

SPECIAL PROGRAMS

IMAGE RETRIEVAL AND PROCESSING SYSTEM (IRPS) FOR THE REGIONAL PLANETARY IMAGE FACILITIES: A PROGRESS REPORT

B. Weiss, S. Slavney, E. A. Guinness, M. Dale-Bannister, R. E. Arvidson, McDonnell Center for the Space Sciences, Department of Earth and Planetary Sciences, Washington University, St. Louis, Missouri, 63130

This abstract is a progress report on the Image Retrieval and Processing System (IRPS) software under development by Washington University.

IRPS provides access to a database of information about the planetary images, planetary maps, and image data products maintained by the Regional Planetary Image Facilities (RPIFs). It also includes descriptive information about planets and satellites; planetary missions (and the various mission phases for each); spacecraft and spacecraft imaging instruments; and general information on the RPIFs, including address, phone number and names of Director and Data Manager for each. IRPS has been designed so that it is compatible with the Planetary Data System (PDS).

The IRPS prototype effort concentrated on Viking and Voyager missions data products and information, since digital image data and documentation from those missions were most accessible. Version 1 (August 1989) added the Apollo 4-17, Apollo-Soyuz Test Project, Lunar Orbiter 1-5, Mariner 1-10, Pioneer 1-4, Project Mercury (some), and Surveyor 1-7 missions; and the most recent (March 1990) version of IRPS also includes the Galileo, Gemini 1-12, Magellan, Pioneer 5-11, Pioneer Venus Orbiter and Multiprobe, Project Mercury (complete), Ranger 1-9, and Skylab 1-4 missions. Thus, this latest version describes in some detail all U. S. space missions and spacecraft (except the Space Shuttles), as well as the data products generated by those missions.

A print-out of data included in the March 1990 version of IRPS has been mailed to a select group of our peers. Once they have reviewed it and sent their comments to us, we will make appropriate changes and/or additions to the database and then distribute the updated IRPS to PDS and those RPIFs who have the hardware and software necessary to utilize it.

For a description of IRPS software, and hardware needed to run same, see "Reports of Planetary Geology and Geophysics Program -- 1988" (NASA Technical Memorandum 4130), pp. 611-612.

A QUICK AND DIRTY WAY OF READING THE BROWSE FILES ON THE "VOYAGER TO THE OUTER PLANETS" CD-ROM DISCS ON A MSDOS PC.

James L. Whitford-Stark, Department of Geology, Sul Ross State University, Alpine, Texas 79832

The recently released CD-ROM discs containing the Voyager information on the outer planets contain "convenient" browse files which can be viewed without decompressing an image to see if it contains the desired data. The inconvenience arises in trying to remember the totally unmemorable names of the individual browse files when accessing them from your image processing program. This article describes a simple and efficient method of creating a batch file for use by the IMDISP image processing program by employing a word processing program. This example uses the Wordstar program but similar attributes are available in other word processing programs.

Firstly, access the appropriate directory of your CD-ROM drive. In my case this is with the command:-

L:

CD \BROWSE\MIRANDA

Next, create a file containing the names of all the files within the subdirectory:-

DIR>C:\IMDISP\MIRANDA.CMD

This will create a file called Miranda.cmd in the imdisp directory of your C drive

Now, open your word processing file **in the non-document mode** calling Miranda.cmd. Use the ^Y (erase to end of line) command to remove the first four lines of the file which are

Volume in drive L is VG003

Directory of L:\BROWSE\MIRANDA

. <DIR> 11-03-88 10:50a

.. <DIR> 11-03-88 10:50a

and the last line of the file which is:

92 File(s) 0 bytes free

Return to the top of the file and place your word processor into column mode if it is not already in it. In Wordstar, this is the command

^K^N (where ^ represents the control key)

Place the cursor over the first number denoting the size of the file on line one of the program (in this case the four in 43200) and type

^K^B (to mark begining of block)

Scroll to the end of the file and place the cursor after the last date which in this case is 9-12-88 and type:

^K^K (to mark the end of the column)

Type **^K^Y** (to erase the block)

In this case the program responds with

Too large to undo later, delete anyway (Y/N)?

to which you respond **Y**.

Return to the begining of the file and enter the find and replace capability. In Wordstar,

^QA

At find, type **_I** (where _represents a blank space)
At replace, type **.I**
At options, type **UGN** (for upper or lower case, throughout file, replace without asking).
Return to top of file and type again
^QA
At find, type **C**
At replace, type **L:\BROWSE\MIRANDA\C**
At options, type **UGN**
Return to the top of the file and for the third time type
^QA
At find, type **G**
At replace, type G^P^M^P^JDISP DSS 200 DSL 200^P^M^P^JERA
At options, type **UGN**
This will place a carriage return and line-feed after the G of IBG, insert the line Disp DSS 200 DSL 200 for displaying the image at location 200,200 on your screen, and insert the line ERA, for erasing the image after it is displayed. Some care will have to be displayed if the planet or satellite has a G in its name (e.g., U_RINGS).
The program is now a completed batch file so save it and leave the word processing program. Enter **IMDISP** and type the command **BATCH MIRANDA.CMD**. As the images scroll by, press the space bar (or any other key) to stop at a file you would like to decompress, and record its number.

JOINT US/USSR STUDIES OF MARS LANDING SITES. Michael H. Carr, U. S. Geological Survey, Menlo Park, CA 94025

On April 15 1987, the United States and the Soviet Union signed an agreement on the exploration and use of outer space for peaceful purposes. A Joint US/USSR Working Group was established to oversee implementation of those items concerning Solar System exploration. The Joint Working Group is chaired by Dr. G. A. Briggs (NASA Hq.) and Dr V. I Barsukov (Vernadsky Institute). One activity identified in the agreement is "Joint studies to identify the most promising landing sites on Mars". To effect this item, a joint implementation team was formed to discuss Mars landing sites. The team is chaired by J. Boyce (NASA Hq.) with M. Carr (USGS) as deputy. Subsequently, discussion of the Mars environmental model was included under the responsibility of the team. Normally the implementation team meets at the time of the Joint Working Group Meeting and at the time of the LPSC. Additional meetings are convened as required. During 1989, three formal meeting were held to discuss landing sites, and several informal exchanges took place concerning the Mars Environmental Model.

The main current concern is with landing sites for the Mars-94 mission. Landing sites need to be chosen for balloons, penetrators, and meteorology stations. Each has a different set of requirements and constraints. The choice of landing sites will inevitably be a compromise between the desire to maximize safety and the desire to meet different science objectives. From a safety standpoint, the preferred landing sites for the Mars-94 balloons are regions of low altitude (< 2km below datum), low thermal inertia, low regional slopes, minimum blockiness, and where no topographic obstacles higher than +2km are likely to be encountered during the projected 10 day lifetime of the balloons. These conditions are highly restrictive. The altitude constraint restricts sites to high northern latitudes, except in the Chryse, Amazonis and Elysium Planitiae where acceptable altitudes can be found as far south as 10^{o}N. The relative merits of different sites in these regions were discussed, and the US provided a variety of data to the Soviets in order that they may better evaluate the sites. These data included high resolution images and mosaics, GCM forecasts of wind magnitudes and direction, and maps of elevation, block frequencies, and wind streak directions.

Each of the Mars-94 spacecraft will deploy 2-3 penetrators before MOI. Preliminary indications are that these sites must lie on a circle centered roughly at 9^{o}S, 90^{o}W, and such that the angle subtended at the center of the planet by the circle center and its circumference is 78^{o}. The radius of the circle is controlled by the need for a 20^{o} entry angle for the penetrators into the upper atmosphere. The longitude of the center of the circle can change slightly according to the specific day that the penetratators are released, but the time of day is tightly controlled by the need to have critical communication times coincide with overlap of the soviet DSN stations, so that dual coverage is assured. A number of sites that met these criteria were examined by the joint implementation team, and the US provided data to the Soviets for their further study. The criteria for the siting of the meteorology stations have yet to be determined.

Landing sites for mission other than the Soviet Mars-94 mission are also being studied. The main purpose is to accumulate a data base that can be used for mission studies, and to have a list of sites of special interest in order that they can be more closely observed by Mars Observer. The science community has been queried for suggestions on possible landing sites, and a catalog of potential landing site is being maintained by Dr. R. Greeley at Arizona State University.

Both the US and the Soviets have published updated versions of a Mars Environment Model (Kaplan, 1988; Moroz et al., 1988). Copies of the models have been exchanged and differences between the two models are being discussed.

REFERENCES

Kaplan, D., 1988, Environment of Mars, 1988. NASA Tech. Memo 100470

Moroz, V. I., Izakov, M. N., and Linkin, V. M., 1988, Engineering model of the atmosphere of Mars. Space Research Institute, Moscow.

THE GALILEAN SATELLITE GEOLOGICAL MAPPING PROGRAM, 1990

B.K. Lucchitta, U.S. Geological Survey, Flagstaff, Arizona 86001

The Galilean Satellite Geological Mapping Program was established by the Planetary Geology Programs Office of NASA to illuminate detailed geologic relations on the four large satellites of Jupiter: Io, Ganymede, Europa, and Callisto. The program is administered by the U.S. Geological Survey, and it involves about 40 investigators from various universities, research institutes, and government offices in the United States, England, Germany, and Italy. Originally, a total of 24 researchers were assigned to map Ganymede, 15 to map Io, and 3 to map Europa. The maps are at a scale of 1:5 million except for three on Io that cover selected areas where high-resolution pictures permit compilation at scales of 1:2 million and 1:1 million. The production of 1:15,000,000-scale global maps of Io, Callisto, and Ganymede was added to the Program in 1989.

Of the 1:5,000,000- and larger-scale maps, 5 have been published, 1 is in press, 2 are in USGS editorial review, 2 are undergoing authors' revision, 5 are in technical review, 2 are in progress, and 2 have been reassigned. Of the 1:15,000,000-scale global maps, that of Io is in USGS editorial review and those of Callisto and Ganymede are in progress.

Published are:

Greeley, Ronald, Spudis, P.D., and Guest, J.E., 1988, Geologic map of the Ra Patera area, Io (Ji2a): U.S. Geol. Survey Misc. Invest. Map I-1949.

Guest, J.E., Bianchi, R., and Greeley, Ronald, 1988, Geologic map of the Uruk Sulcus quadrangle, Ganymede (Jg8): U.S. Geol. Survey Misc. Invest. Map I-1934.

Moore, H.J., 1987, Geologic map of the Maasaw Patera area, Io (Ji2c): U.S. Geol. Survey Misc. Invest. Map I-1851.

Murchie, S.L., and Head, J.W., 1989, Geologic map of the Philus Sulcus quadrangle, Ganymede (Jg4): U.S. Geol. Survey Misc. Invest. Map I-1934.

Schaber, G.G., Scott, D.H., and Greeley, Ronald, 1989, Geologic map of the Ruwa Patera quadrangle, Io (Ji2): U.S. Geol. Survey Misc. Invest. Map, I-1980.

In press is:

Whitford-Stark, J.L., Mouginis-Mark, P.J., and Head, J.W., Geologic map of the Lerna region quadrangle, Io (Ji4): U.S. Geol. Survey Misc. Invest. Map I-2055.

MARS GEOLOGIC MAPPING AND SCIENCE SITE PROGRAMS STATUS (1:500,000 scale)
David H. Scott, U.S. Geological Survey, Flagstaff, AZ 86001.

The Mars Geologic Mapping (MGM) Program was introduced by NASA in 1987 as a new initiative in the Planetary Geology and Geophysics (PGG) Program. The purpose of the Mars mapping program is to support research on topical science studies that address specific scientific questions and problems in areas that will contribute information to the planning of Mars missions. Geologic mapping is being done on Mars Transverse Mercator(MTM) photomosaic bases at 1:500,000 scale. At the close of FY1989 more than 20 investigators were participating in the geologic mapping of some 50 Martian quadrangles; 5 of these maps have been completed through the coordinator and technical review process. In addition to the on-going geologic mapping, about 40 new areas have been prepared and approved for new MTM base map construction.

A parallel but separately organized geologic mapping program at 1:500,000-scale of areas that are considered to be candidate science sites for a Mars sample return mission is also being directed by the project chief of the MGM Program. At present, 8 investigators and 14 map areas are included in this project which will probably be completed in FY1991. Five of the science site maps are in press.

The geologic maps resulting from both of these programs will be published by the U.S. Geological Survey as Miscellaneous Investigation Series I-maps.

PLANETARY NOMENCLATURE; M.E. Strobell and Joel Russell, U.S. Geological Survey, Flagstaff, Ariz.

A detailed history and description of methodology used for planetary nomenclature, by Mary E Strobell and Harold Masursky, is included in "Planetary Cartography"; this book by Raymond Batson and Ronald Greeley will be published by Cambridge University Press in the spring of 1990.

About 100 names requested by geologists for features in the northern hemisphere of Venus, as well as names chosen earlier for nearly 300 features, are shown on the the Magellan Planning Chart, published in late June, 1989.

Nomenclature for about half of the maps that will appear in the forthcoming Atlas of the Solar System has been completed and sent to the publishers in Tucson, Arizona. To date, nomenclature has been completed for maps of Mercury, the Jovian satellites, five of the Saturnian satellites, the Martian satellite Phobos, and five Uranian satellites.

Work is continuing on the series of 1:500,000-scale maps of Mars. As the mosaic of each maps is completed and a cronaflex becomes available, an ozalid copy showing the adopted nomenclature is sent to the geologist compiling the map; he indicates additional features that he wants to have named; names are chosen for these features, and the names are proposed to the proper committees of the International Astronomical Union. In the last year about 30 names on 15 maps in this series have been proposed.

Nomenclature was also checked on all 1:5 million-scale maps of Callisto and Ganymede; these maps are being published separately at this scale, and will also be included in the Solar System Atlas.

Nomenclature for the Neptunian satellites Triton and 1989 N1 (provisionally named "Proteus") has been selected and is in the process of being provisionally adopted by the IAU. Names for features on these satellites will be made available to the planetary community as soon as they have been finalized.

The Gazetteer of Planetary Nomenclature is in the final stages of editing; it will be submitted to NASA for publication in 1990.

Also in 1990, nomenclature will be updated for the Solar System Atlas on maps of Earth, Venus, the Moon, and Hyperion; these maps will also be published separately as USGS I-series maps. A voluminous new nomenclature is expected to be needed for features on Venus discriminated by the higher resolution radar imaging system of the Magellan spacecraft. Some additional nomenclature will probably be requested by geologists working on maps in the 1:500,000-scale series of Mars.

In the past, much of the work of choosing and submitting names to the IAU was done by Harold Masursky, the President of the IAU's Working Group for Planetary system Nomenclature since 1976. However, Masursky retired last year. Although he has Scientist Emeritus status, he continues as Co-President of the Working Group until the IAU's triennial meeting in 1991,

he expects to take a greatly diminished part in Working Group proceedings. His assistant, Mary Strobell, also retired in 1989 but will continue to support the nomenclature effort through June 1990. Much of the development of new nomenclature will now be done by chairmen of the IAU Task Groups for each planetary system; names proposed by the Task Groups will continue to be ratified by the Working Group, now directed by its Co-President, Dr. Kaare Aksnes. Flagstaff will continue to manage and distribute copies of the master nomenclature file of adopted names and all ancillary files of provisional names, as well as "name-bank" files of appropriate names reserved for future use. Flagstaff will also communicate (largely by computer mail) and coordinate the nomenclature effort with IAU personnel. New programs are being developed for an updated digital filing system and for a new planetary geographic information system that will call up specific planetary features on a computer screen.

Except for requests for features to be named on 1:500,000-scale maps of Mars, all matters pertaining to nomenclature should be addressed to the Co-President of the Working Group or to the appropriate Task Group Chair:

Dr. Kaare Aksnes, Co-President, Working Group for Planetary System Nomenclature
Institute of Theoretical Astrophysics
University of Oslo
P.O. Box 1029
Blindern 0315 Oslo 3, Norway

Dr. V.V. Shevchenko, Chairman, Lunar Task Group
Sternberg State Astronomical Institute
Moscow University
Leninskije Gory
Moscow - 234, U.S.S.R.

Dr. Mikail Ya. Marov, Co-Chair, Venus Task Group
Chief, Department of Planetary Physics
Institute of Applied Mathematics
USSR Academy of Sciences, Musskaya Square 4,
Moscow A-47, U.S.S.R.

Dr. Harold Masursky, Co-Chair, Venus Task Group
U.S. Geological Survey
2255 Gemini Drive
Flagstaff, AZ 86001 U.S.A.

Dr. Bradford Smith, Chairman, Mars Task Group
Department of Planetary Sciences
University of Arizona
Tucson, AZ 85721 U.S.A.

Dr. Tobias Owen, Chairman, Outer Solar System Task Group
Institute of Astronomy
2680 Woodlawn Dr.
Honolulu, HI 96822 U.S.A.

CHAPTER 14

LATE ABSTRACTS

ORIGIN AND EVOLUTION OF TRITON AND PLUTO

William B. McKinnon and L.A.M. Benner, Department of Earth and Planetary Sciences and McDonnell Center for the Space Sciences, Washington University, Saint Louis, MO 63130; and Steve Mueller, Department of Geological Sciences, Southern Methodist University, Dallas, TX 75275.

Triton's ice/rock ratio

Our prediction for the density of Triton, based on the assumptions that it was captured from solar orbit by Neptune and thus has a rock/ice ratio similar to that of the Pluto–Charon system (McKinnon and Mueller 1989), proved remarkably accurate. The figure below, redrawn from Fig. 1 in McKinnon and Mueller (1989), gives the density of rock-rich ice-rock satellites as a function of radius. Solid parametric curves are labeled for a range of anhydrous rock mass fractions. Pluto 1 and Pluto 2 mark the size of Pluto and the mean density of the Pluto–Charon system as determined by Tholen and Buie (1987) and (1988), respectively. We predicted that Triton should fall within the shaded region if it is similar to Pluto in bulk composition. Triton's density, determined by Voyager 2 (Smith *et al.* 1989), falls dead center in the shaded region, albeit with large errors due mainly to uncertainties in Triton's size. This number will no doubt be refined. Also plotted (arrow) is the latest mutual event solution to the density of Pluto–Charon (Tholen and Buie 1989). This is formally very well determined, but there remain systematic uncertainties due to Pluto's atmosphere (e.g., Elliot *et al.* 1989) and in the calibration of the overall scale of the Pluto–Charon system. The latter is presently done by speckle interferometry, but the best determination will be made with HST. Thus, within the errors, Pluto–Charon and Triton have extremely similar ice/rock ratios. Whether they remain similar depends on further analysis. It also depends on the evolutionary tracks the two worlds took. For example, although the contours in the figure are given in terms of anhydrous rock, the models at the left end of the figure were calculated with cores whose silicates were partially hydrated. This may be quite applicable to Pluto (McKinnon and Mueller 1988), but the tidal heating Triton likely underwent could easily have melted its core (McKinnon 1988), which at

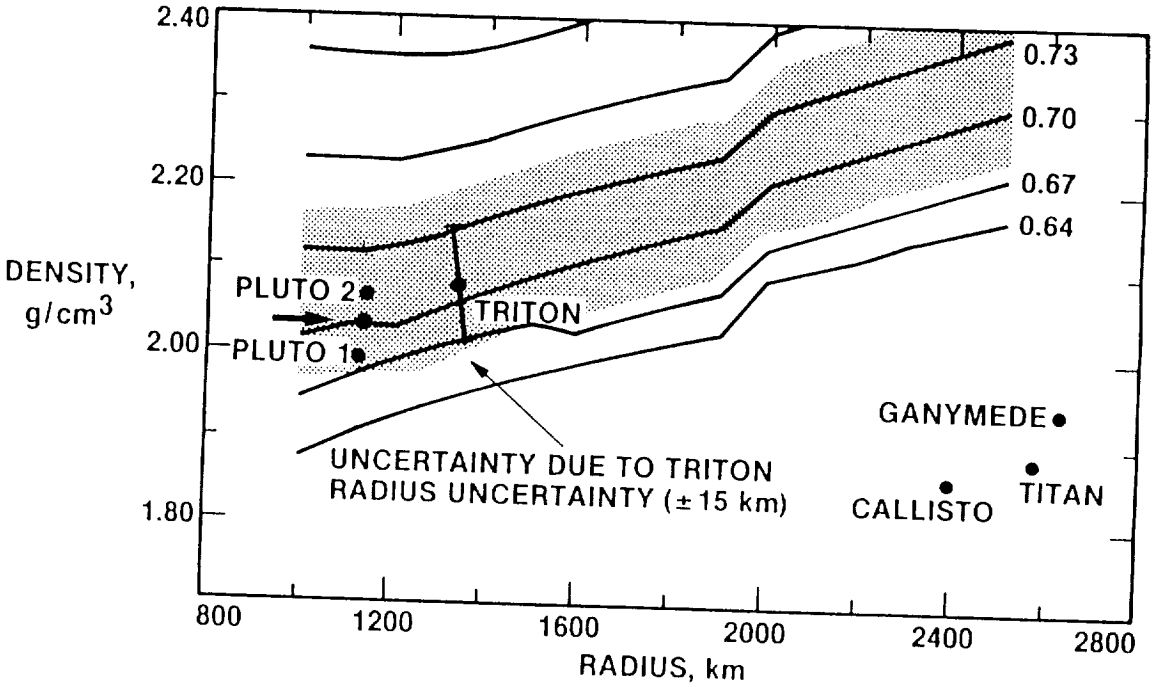

present would be anhydrous and contain an Fe-S inner core. Under these circumstances, its derived rock/(rock + ice) ratio would be 0.65 ± 0.03. Potentially, Triton is less rock rich than Pluto–Charon, which may have suffered a loss of icy material. One mechanism for producing this loss, impact jetting, is discussed below.

Impact jetting of water ice — Application to the accretion of icy planetesimals, Pluto, and Triton

Jetting can occur during oblique impacts of water ice bodies at relative velocities as low as ~500 m s^{-1}, because of the low Hugoniot elastic limit and high compressibility of ice compared to rock (McKinnon 1989). In jetted ice, incipient melting, complete melting, and incipient vaporization occur, upon release to low pressure, at impact velocities of 1.3, 2.0, and 2.7 km s^{-1}, respectively, much less than the 3.4, 4.4, and 5.3 km s^{-1} required in head-on collisions. Uncertainties in the shock equation-of-state may allow complete melting during jetting at relative velocities as low as 1.2 km s^{-1}. Because jet speeds exceed impact speeds, often by a factor of several, during the accretion of icy bodies greater than a few 100 km in radius there may be a significant loss of icy material. This is more true if the accreting body is large enough to differentiate so that its surface layers are closer to pure ice in composition, and especially true if bodies of comparable size are involved, which emphasizes the obliqueness of the collision. I suggest that it is jetting during a Charon-forming collision (and not vaporization) that may account for Pluto–Charon's relatively large rock/ice ratio, should the C/O ratio of the solar nebula turn out to be too low to sufficiently raise the rock/ice ratio of outer solar nebula condensates by formation of non-condensable CO (Anders and Grevesse 1989). Triton's high density, determined by Voyager 2 to be close to that of Pluto–Charon, is consistent with a solar nebula origin for Triton. It might also imply that a physical fractionation mechanism is not necessary to explain Pluto–Charon's density. However, Triton may have suffered catastrophic collisions during and subsequent to capture, so its original rock/ice ratio may have been lower as well.

Aspects of Triton's post-capture thermal history

A captured Triton would likely undergo massive heating as its orbit was circularized and shrunk by tides raised on it by Neptune (McKinnon 1984). The time scale of tidal evolution is an important quantity to estimate (McKinnon and Benner 1990). The simplest model of the dissipation of tidal energy assumes that Triton remains solid throughout its orbital evolution, with a constant Q/k; Q is the tidal dissipation factor (assumed to be 100) and k is the potential Love number (assumed to be appropriate for a uniform, solid rock-ice body). Such a model predicts that a Triton with an extremely elongated elliptical orbit, extending to the edge of Neptune's gravitational sphere of influence, takes almost 10^9 yr to evolve inward and have its orbit circularize. This time scale is (1) more than twice as long as estimated in McKinnon (1984), because Triton's radius was then thought to be near 1750 km, and (2) much longer than the estimated duration of heavy cratering in the outer solar system (~500 million years). Thus, the "new," smaller Triton could have stayed hot well beyond the era of heavy cratering, and it could be predicted that little if any of the heavily cratered terrains seen on nearly all of the other icy satellites would be observed on Triton by Voyager. Such simple models cannot be correct in detail, however, because so much of Triton's orbital energy is dumped into the satellite that it must melt. We determine how soon Triton begins to melt once tidal evolution starts, that is, after the capture collision or after gas drag evolution ceases (assuming its original accretional heating has not already triggered differentiation). Triton is so rock-rich that it is likely that Triton would begin to melt its ice and unmix, or differentiate, spontaneously, due to radiogenic heating alone. Only by deliberately choosing parameters that lower Triton's internal viscosity is it possible to build an internal model of Triton that convects without melting. However, even for very elongated initial orbits that extend to the edge of Neptune's sphere of

influence, the tidal energy dissipated during individual passes close to Neptune is, time-averaged, comparable to the power due to radioactive element decay. Therefore, it is very unlikely that melting can be significantly delayed. Only if Triton is captured cold will melting be put off, perhaps ~100 m.y. The best estimate is that Triton will begin to melt promptly. At the onset of melting, differentiation is partially self-sustaining as the gravitational energy of unmixing is approximately 30% of that needed to melt Triton's ices. Dissipation increases dramatically once melting commences: the Maxwell time of water ice at near-solidus temperatures is shorter than the effective tidal forcing period at perihelion, unmixing creates many transient and dissipative multiphase regions (e.g., ascending slush and descending mud diapirs), and the opening up of an internal ocean allows k to increase substantially. The result is a differentiated Triton in under 10^7 yr (and possibly much less), with a liquid water ocean, approximately 350–400 km deep, capped by a thin, dissipative, conductive ice shell, overlying a rock core. Continued tidal heating in the core causes it to heat up and melt as well. The ultimate tidally heated configuration for Triton is nearly totally molten. A thin water-ice shell tops a liquid water mantle, and thin rock shell tops a liquid silicate core; there may be an inner core of liquid iron-sulfur, but no iron shell. Subsequent orbital evolution slows considerably, as has been discussed previously (McKinnon 1988). A nearly totally molten Triton may stay hot for an extended length of time, greater than 500 million years. Thus, as with the simple model of tidal heating above, it is predicted that Triton should not have retained any early record of heavy cratering. The geological evidence from Triton is consistent with massive tidal heating (Smith *et al.* 1989). Whether tidal heating is *required* to explain the absence of heavily cratered terrains depends on the composition of the surface (McKinnon and Benner 1990). If there is a crust of lower melting point ices greater than a few km thick, then continuing volcanic and other activity can probably destroy any ancient crater population. If, however, portions of Triton's exposed surface are water-ice "bedrock," then tidal heating is necessary.

References

Anders, E., and N. Grevesse (1989). Abundances of the elements: Meteoritic and solar, *Geochim. Cosmochim. Acta*, **53**, 197–214.

Elliot, J. L., E. W. Dunham, A. S. Bosh, S. M. Slivan, L. A. Young, L. H. Wasserman, and R. L. Millis (1989). Pluto's Atmosphere. *Icarus* **77**, 148–170.

McKinnon, W.B. (1984). On the origin of Triton and Pluto. *Nature* **311**, 355–358.

McKinnon, W.B. (1988). Coupled thermal and orbital evolution of a captured Triton. *EOS Trans. AGU* **69**, 1297.

McKinnon, W.B. (1989). Impact jetting of water Ice — Application to the accretion of icy planetesimals and Pluto. *Geophys. Res. Lett.* **16**, 1237–1240.

McKinnon, W.B., and L.A.M. Benner (1990). Triton's post-capture thermal history. *Lunar Planet Sci. XXI*, 777–778.

McKinnon, W. B., and S. Mueller (1988). Pluto's structure and composition suggest origin in the solar, not a planetary, nebula. *Nature* **335**, 240–243.

McKinnon, W. B., and S. Mueller (1989). The density of Triton: A prediction, *Geophys. Res. Lett.* **16**, 591–594.

Smith, B.A., and the Voyager Imaging Team. (1989). Voyager 2 at Neptune: Imaging science results. *Science* **246**, 1422–1449.

Tholen, D. J., and M. W. Buie (1987). Pluto and Charon: Radii, density, and orbital elements from mutual event photometry through 1987. *Bull. Am. Astron. Soc.* **19**, 859–860, 1987.

Tholen, D.J., and M.W. Buie (1988). Circumstances for Pluto–Charon mutual events in 1989. *Astron. J.* **96**, 1977–1982.

Tholen, D. J., and M. W. Buie (1989). Further analysis of Pluto-Charon mutual event observations — 1989. *Bull. Am. Astron. Soc.* **21**, 981–982.

CRATERING OF THE URANIAN SATELLITES

William B. McKinnon, Department of Earth and Planetary Sciences and McDonnell Center for the Space Sciences, Washington University, Saint Louis, MO 63130; Clark R. Chapman, Planetary Science Institute, 2421 E. 6th St., Tucson, AZ 85719; and Kevin R. Housen, Shock Physics and Applied Mechanics, MS 3H–29, Boeing Aerospace Co., Seattle, WA 98124.

The study of impact craters and planetary and satellite bombardment histories have benefited greatly from the data gained at Uranus by Voyager 2 and the subsequent analysis and interpretation of this data. The following is a summary of our recent review paper, which appears in the University of Arizona Space Science Series volume *Uranus*.

Simple, bowl-shaped craters on the middle-sized icy satellites of Uranus and Saturn are shallower than simple craters on the terrestrial planets and satellites. The best explanation is that the breccia lenses of icy craters are thicker because the coefficient of friction of ice is less than that of rock (this promotes greater infilling); we also explore the possibility that the presumably dominant impactors, comets, are of low enough density to cause the excavation to be intrinsically shallow. Complex craters — those created by the gravitationally driven modification, or collapse, of craters above a certain threshold size — are dominated structurally by central peaks on the middle-sized icy satellites. Only for the largest craters observed on these satellites do rim slumping and terrace formation become significant. On these satellites complex craters, except for the largest, do not appear to widen significantly compared with their transient forms, and the effect on observed depth-diameter relations is such that they become deeper with increasing size more rapidly than complex craters do on the Moon or other terrestrial planets.

We present more realistic scaling relations for complex craters on icy satellites based on these new observations. Most complex craters can be adequately scaled with the same law used for simple craters. Only for large craters and those on Ganymede and Callisto is a scaling necessary that explicitly takes into account collapse and widening. Even here, the formula we recommend is closer to simple crater scaling than we have advocated in the past.

Observations of central-peak transitions on the satellites of Uranus are consistent with those measured for the satellites of Saturn and Jupiter and with the model that predicts this transition is close to an inverse function of gravity; central pit craters are not observed, except possibly for the very largest craters, and this is also consistent with observations at Saturn. Ejecta blankets and rays are definitely observed on the Uranian satellites, so the difficulty of observing them on the Saturnian satellites lies not with the non-retention of ejecta on low-gravity worlds, but the with processes that prevent or erase morphological, albedo, and color distinctions among ejecta deposits and between them and surrounding terrain; notable Uranian satellite crater deposits are the dark ejecta for some Miranda craters, due to excavation of similar subsurface material, and dark floors for some craters on Oberon, possibly related to some type of "carbonaceous" volcanism.

A plains unit on Ariel has been identified where several craters are anomalously shallow compared to fresh craters of the same size. If these craters are viscously relaxed, then the implied effective viscosity argues for a surface material less viscous than water ice, perhaps ammonia-water ice. More significant, viscous relaxation may have been an important crater removal process, and thus affected observed crater size-frequency distributions on Uranian satellites that have been geologically active, such as Ariel and Titania.

We describe the very largest craters identified on each of the Uranian satellites, as well as some features whose identities as impact features range from tentative to tenuous. On the Uranian satellites, there is no obvious remaining geological evidence for catastrophic effects due to very large impacts, with the possible exception of Miranda. This may not be surprising given the relative size of the crater necessary to cause such effects, as calibrated from the better imaged Saturn system. Judging from the effects that the formation of Odysseus had on Tethys, we estimate that a middle-sized icy satellite's global geology would be reorganized by a crater with a diameter equal to the satellite radius.

An important part of our chapter is devoted to understanding the origin of the crater populations observed on the satellites. There are substantial disagreements between the published counts by various investigators, especially for Titania and the cratered terrain on Miranda. However, the various counts for heavily cratered Oberon and Umbriel, which defined a Uranian "Population I" to the Voyager investigators, are consistent given plausible systematic errors (these satellites were poorly imaged). Furthermore, the Oberon and Umbriel counts are consistent with each other and an incremental size-frequency power-law of slope close to –3 (horizontal on the relative or "R"-plot). Miranda's heavily cratered terrain may also be consistent with such a power-law; some counts imply a somewhat shallower slope, but we are not convinced that this is not due to diameter-dependent, endogenic crater filling and erasure (possibly blanketing). Counts for Miranda's (resurfaced) coronae and for the freshest craters on the cratered terrain also follow a –3 slope.

We compare various outer solar system crater populations, using our improved understanding of scaling. Craters formed on Rhea are larger than craters formed on Callisto, for heliocentric impactors, so if the scaling is applied and if the largest craters on Rhea are included, the relative plots for both satellites become quite similar (except in overall density). Scaling Oberon and Umbriel to Rhea conditions shows that the counts on the three satellites are compatible, but the limited diameter range of the Oberon and Umbriel data precludes a more definitive assessment. Interestingly, Titania's crater(ed terrain) population is not that different from Rhea's when scaled.

Titania's and Ariel's crater populations have been described as a Uranian "Population II," because they may lack larger craters compared with Uranian Population I, but their somewhat steeper slopes (over limited diameter ranges) may not be statistically different from –3, either. If the steeper slopes are real, then they could be due to a preferential loss of large craters, such as caused by viscous relaxation (as on Ariel), or Uranian Population II may actually be the production population, with saturation at smaller diameters producing a more shallowly sloped Population I. Alternatively, Population II may be a planetocentric population possibly derived

from large cratering events or the collisional breakup of satellites. If Uranian Populations I and II are equivalent, however, given the compatibility of (scaled) crater populations from different satellite systems, the implication is that a single impactor population, comets, could have been responsible for nearly all the cratering in the outer solar system.

With respect to satellite breakup, whether any of the major satellites of Uranus have been catastrophically fragmented depends on the poorly known shape of the crater production population at large diameters (>100–200 km). There is evidence for a relative lack of craters in the ~150-km-diameter range, corresponding to incremental power-law slopes steeper than –3, which lowers the probabilities for breakup relative to that calculated by Shoemaker and co-workers. However, the production population also appears to turn up again at still larger diameters, which means the crater populations on the heavily cratered middle-sized satellites of Uranus and Saturn could be in "saturation equilibrium," their surfaces saturated many times over. Scaling directly from the observed craters on Oberon, we find that the same bombardment that formed Oberon's craters probably catastrophically fragmented Miranda.

We address the scaling of catastrophic breakup for icy satellites. Careful consideration is given to the roles of gravity and strain-rate- and size-dependent strength. Two regimes, a gravity regime and a strength regime, are defined, and the functional dependencies of the threshold specific energy necessary for catastrophic disruption, Q^*, on impactor velocity, U, and target size, R, are derived for each. In all cases Q^* is a slowly increasing function of U because higher velocities are less efficient at fracturing. In the gravity regime Q^* is also an increasing function of R due to gravitational self-compression In the strength regime, though, for our preferred strain-rate-dependent strength model, Q^* decreases slowly with increasing target (or satellite) size, because larger sizes imply lower strain rates and ice (and rock) are intrinsically weaker at lower strain rates.

Estimates of the disruption threshold are calibrated from laboratory experiments. A range of velocities, 0.2–20 km s^{-1}, covering planetocentric and heliocentric impactors, are considered. The transition from the strength to the gravity regime should occur for (icy) satellites in the 10–50-km-radius range. The major satellites of Uranus are all gravity dominated; the smaller satellites discovered by Voyager could be affected by strength, but for all but the smallest, only if the fracture of ice is *not* strain-rate dependent. Our threshold disruption scaling also predicts the crater size these impacts would produce in an infinite half-space target. The threshold "crater"-diameter-to-satellite-radius ratio turns out to be a constant independent of satellite size or impact velocity, with a value of ~1. For smaller, strength-dominated satellites, the cumulative effect of more numerous "sub-catastrophic" collisions may be more important than catastrophic ones, and sub-catastrophic collisions may also be important for the surface geological evolution of gravity-dominated satellites.

THE FATE OF EJECTED MERCURY MANTLE MATERIAL FROM A GIANT IMPACT.

W. B. Tonks[1], H. J. Melosh[1], and W. B. McKinnon[2]. [1]Lunar and Planetary Laboratory, University of Arizona, Tucson, Az. 85721. [2]Dept. of Earth and Planetary Sciences and McDonnell Center for the Space Sciences, Washington University, St. Louis Mo. 63130.

It is well known that Mercury has an anomalously high uncompressed density (~5.3 g/cm^3). Benz *et al.* (1988) argued that this high density might result from a giant impact of Mercury with a large planetesimal in early Solar System history. They investigated the detailed circumstances that would allow formation of a planet with Mercury's present characteristics from such an impact. The success of this scenario depends critically upon the fate of the material ejected into Mercury-crossing orbits. No net change in Mercury's Fe/Si ratio can occur unless most of the material ejected from Mercury is removed from the Solar System. Because of its position as the innermost planet of the Solar System and its high orbital eccentricity, Mercury has the ability to eject material from the Solar System without substantial reaccretion. Our Monte-Carlo orbital simulations reported here shows that ~90% of material ejected into interplanetary space from Mercury by a meteorite impact is subsequently ejected from the Solar System itself. This ejection is largely due to the cumulative effects of Mercury perturbations. Our calculations also show that the other terrestrial planets do not have this ability.

Our method of calculation is based on the two-body approximation of Öpik (1976). A brief description of the method, the algorithm, and other results have been previously reported (Finney et al, 1989; Tonks and Melosh, 1989). A detailed description is forthcoming (Tonks and Melosh, 1990). This approach provides a statistical treatment of the orbital evolution of interplanetary material and is essentially the same approach that has been taken by Wetherill over many years in the study of meteorite dynamics (see Wetherill and Chapman, 1988 for a list of references). The code requires the input of the orbital elements of an arbitrary group of particles in interplanetary space. To obtain such a group of particles, an auxiliary program calculates the orbital elements of a set of particles ejected from a particular planet. This program assumes that particles are ejected from the planet in random directions in a reference frame at rest with respect to the planet. Each particle is given a specified post-escape ejection speed (v_∞).

The present version of the code includes evaluation of the Tisserand criterion (see e.g. Moulton, 1914) as a check of the coordinate transformations performed in the code as well as the inherent error produced by the two-body approximation of Öpik. This criterion is a conserved quantity in the restricted 3 body problem. It would not be strictly conserved due to 3 body effects not accounted for in the Öpik formulation and due to the eccentricities of the planets (especially highly eccentric Mercury). However, changes in the criterion should be small. Most perturbations in our calculation produced changes of <2%. There were a few perturbations by Mercury that produced changes of 10-15%. These larger changes occurred when the eccentricity was very high, >0.9. However, large 3 body effects would be expected at these high eccentricities. Because the Tisserand criterion is conserved to within a few percent, we have confidence that the basic approach is sound and that the necessary coordinate transformations are correct.

We have extended the application of this model to study the fate of material ejected into interplanetary space from each of the terrestrial planets. We performed 3 runs of ejecta from each of the terrestrial planets. Each run consisted of 5000 particles and assumed post-escape velocities of 0.25, 2, and 5 km/sec. These represent a large spectrum of possible speeds from a giant impact. Additionally, we performed runs at post-escape ejection speeds 0.25 and 2 km/sec for ejecta from a hypothetical planet the size and density of Earth, but at the orbit of Mercury. The rest of the Solar System was kept as at present. Figure 1 summarizes the results of the runs. The ejecta's source planet is plotted on the horizontal axis. The vertical axes show the percentage of that ejecta which is ejected from the Solar System. Figure 1 shows that particles ejected from Mercury are subsequently ejected from the Solar System much more readily than ejecta from the other planets. Only about 10% eventually impact other planets. Detailed examination of the fate of this material shows that Mercury itself only retains some 5-7%. Additionally, Mercury readily

ejects material from the other planets from the Solar System. The other terrestrial planets retain a much higher percentage of their own ejecta as well as ejecta from other planets. The other terres-

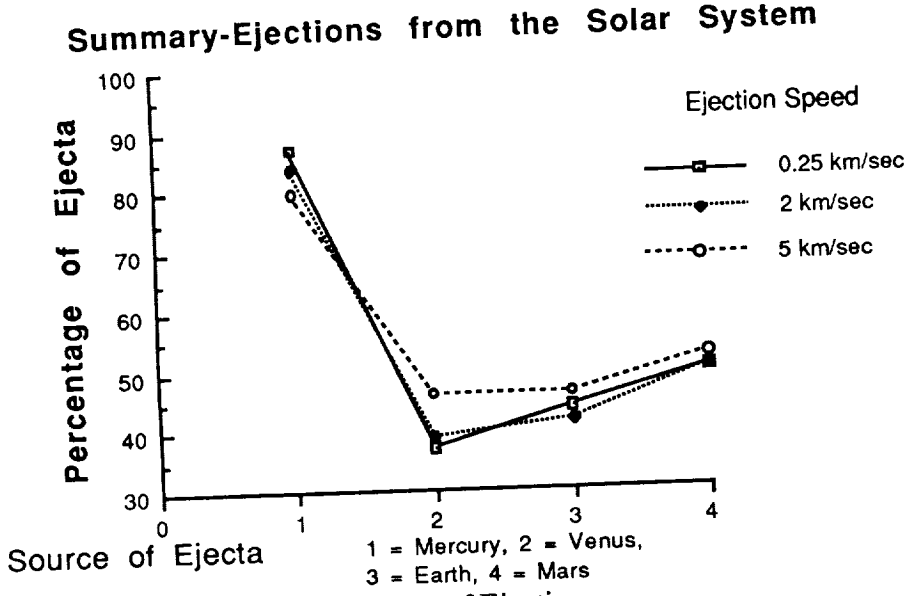

Figure 1: Summary of Ejections

trial planets are very poor at ejecting material from the Solar System. The material from these planets that is lost from the Solar System is ejected almost exclusively by Jupiter or Mercury.

Both runs using the hypothetical planet with the size and density of the Earth show the same basic result. Over 90% of ejecta from this planet is removed from the Solar System at both run speeds. This planet is slightly more efficient at sweeping up its own material than is Mercury but the difference is not striking. The reason for this remarkable effect is probably due to the encounter velocity changing substantially at different positions on Mercury's highly eccentric orbit. Our code randomly choses the arguments of perihelion of the particle and planet's orbit and the anomaly where the two orbits intersect, then calculates the actual encounter velocity from celestial mechanics rather than from the average encounter velocity given by Öpik's (1976) equations. Indeed, when we reduced Mercury's eccentricity to 0, no particles were ejected by Mercury and virtually all reaccreted to Mercury. Note that particles are not ejected by a single interaction with Mercury. Ejection is a consequence of the cumulative effect of a large number of different encounter speed perturbations. Mercury's position as the innermost planet also has an effect. When the eccentricity of the Earth was increased to Mercury's present eccentricity, it ejected a only a small amount of material. This, however, was because the material was quickly perturbed into orbits that crossed the other planets.

These calculations show that Mercury has the unique ability to eject its own material without significant reaccretion. Indeed, if Mercury's anomalous density was created by a giant impact as argued by Benz *et al.*, our calculations indicate that the vast majority of the material would be removed from the Solar System. Our calculations thus significantly strengthen the plausibility of this scenario as an explanation the planet's anomalous density. The calculations also permit depletion of Mercury's mantle by a large number of smaller collisions: the innermost planet is uniquely vulerable to such loss. The general features observed with Mercury should be likewise be seen in the satellite systems of the outer planets. Ongoing work includes further refinement and testing of the code and its application to the these satellite systems.

REFERENCES: Arnold, J. 1965. *Astrophys. J.*, **141**, 1536-1547. Benz, W., Slattery, W. L., and Cameron, A. G. W. 1988. *Icarus* **74**, 516-528. Finney, S. A., Tonks, W. B., and Melosh, H. J. 1989 *LPSCXX Abstracts*, pp.287-288; Moulton, F. R. 1914. *Celestial Mechanics*, MacMillian Publishing Co. p. 297; Öpik, E. J. 1976. *Interplanetary Encounters*, Elsevier Scientific Publishing Company, Amsterdam; Tonks, W. B. and Melosh, H. J. 1989. EOS Trans. Amer. Geophys. Union, 24 Oct, p 1173; Tonks and Melosh, 1990 in preparation.; Wetherill, G. W. and Chapman, C. R. 1988. in *Meteorites and the Early Solar System*, pp. 35-67.

Atmospheric Erosion by Impacts: Evidence for an Early, Dense Atmosphere on Mars

A. M. Vickery and H. J. Melosh (Lunar and Planetary Lab, University of Arizona, Tucson, AZ 85721; 602-621-2703)

We investigate the possibility that Mars had a much denser atmosphere early in its history, much of which has been lost due the erosive effects of large impacts. The transfer of impact energy to the atmosphere can be divided into three phases: first, the incoming projectile compresses and heats the atmosphere ahead of it; second, the impact-generated vapor plume overruns and accelerates overlying atmosphere; and third, the solid ejecta compresses and heats the atmosphere ahead of it. The first and the third mechanisms have been shown to be ineffective at removing atmosphere from a planet [*Walker*, 1986][*Melosh and Vickery*, 1988]. We therefore investigate the effect of the vapor plume.

We assume that the vapor plume can interact with, at most, the atmospheric mass lying above the plane tangent to the planet at the point of impact (M_{tp}). This is a conservative assumption because, when the acceleration due to pressure gradients within the plume declines to values comparable to that due to gravity, the plume will be accelerated below the tangent plane. We divide the momentum of the vapor plume by the sum of the masses of the plume plus overlying atmosphere to find a mean velocity. If this velocity is greater than Mars' escape velocity (5 km/sec), then the overlying atmosphere is lost from the planet. We estimate the minimum impactor mass and velocity required to blowoff the entire atmospheric mass above the tangent plane, neglecting smaller, more numerous impacts that result in partial loss. We then concatenate this information with estimates of the impact flux on Mars to estimate the cumulative effect of impacts over time.

We assume that the impactor and an equal mass of the target are vaporized to the highest internal energies indicated by impedance matching; this assumes that the most highly shocked material is ejected first without significant mixing with less highly shocked material, which may nevertheless be vaporized. We further assume that this vapor expands as a hemisphere according to the Zel'dovich and Razier model for a perfect gas, with $\gamma = 9/7$[*Zel'dovich and Razier*, 1966]. According to this model, the r.m.s. expansion velocity of the plume is

$$u_\infty = \sqrt{2\varepsilon_o}$$

where e_0 is the initial internal energy of the vapor. Requiring that $u_\infty \geq u_{esc}$ gives the minimum impact velocity such that more than half the mass of the plume has velocity $\geq u_{esc}$. In the simplest approximation, we assume that the ejection of M_{tp} requires a mass of impact-generated gas m* equal to $M_{tp} \cong 4 \times 10^{13}$ kg.

From the lunar crater density as a function of age, we derive an expression for the cratering flux as of impactor mass and time, $N_{cum}(m,t)$:

$$N_{cum}(m,t) = a\left[1 + Be^{-\lambda(t+4.6)}\right]m^{-b}$$

where $a = 1.55 \times 10^{-23}$ $kg^b m^{-2} sec^{-1}$, B = 2,300, $\lambda = 4.53$ Gyr^{-1}, and b = 0.47. Assuming that the Martian flux is approximately equal to the lunar flux, the rate of change of the atmospheric mass M_{atm} with time is $-N_{cum}(m^*,t) \times 4\pi R^2 \times M_{tp}$, where R is Mars' radius and $M_{tp} \cong M_{atm}(H/2R)$. We integrate from the present time (t=0, when $M_{atm} = M_O$) to t = -4.5 Gyr to find $M_{atm}(t)/M_O$:

$$\frac{M}{M_o} = \frac{P}{P_o} = \left[1 - \frac{t}{t_*} - \frac{Be^{-4.6\lambda}}{\lambda t_*}\left(1 - e^{-\lambda t}\right)\right]^{1/b}$$

where

$$t_* = \frac{1}{2\pi ab(RH)^{1-b}}\left(\frac{2\pi P_o}{g}\right)^b$$

Our results indicate that Mars' atmospheric pressure may have been 100 times its current value at -4.5 Gyr and declined rapidly to nearly its present value at -3.5 Gyr [*Melosh and Vickery*, 1989].

This model for atmospheric blow-off does not take into account the variation of atmospheric mass with zenith angle θ. We therefore calculate $M_{atm}(\theta)$ for the present atmosphere and redo the blow-off calculation numerically. We find that the minimum impact velocity remains nearly the same; the minimum impactor mass required increases by about an order of magnitude at the lowest impact velocities but is nearly equal to M_{tp} for impact velocities appropriate for comets. Increasing the ratio m^*/M_{tp} increases t^* by the same factor. This implies that the earliest Martian atmosphere may not have been as massive as the previous calculations suggested, and that the rate of decline in atmospheric pressure was not as great [*Vickery and Melosh*, 1989].

It should be noted that these calculations consider only the effect of impact erosion on Mars' atmospheric pressure with time, neglecting other processes that may have affected both the atmospheric pressure and chemistry. If liquid water were stable at the surface of Mars, then chemical weathering probably acted to deplete CO_2 from the atmosphere on time scales of $\sim 10^7$ yr [*Pollack, et al.*, 1987]. If geomorphic evidence for the persistence of liquid water for $\sim 10^9$ yr is correctly interpreted, and both impact erosion and chemical weathering were depleting the atmosphere, then there must have been sources of resupply, e.g.[*Carr*, 1989].

REFERENCES

Carr, M. H., Recharge of the early atmosphere of Mars by impact-induced release of CO2, *Icarus*, *79*, 311-327, 1989.

Melosh, H. J. and A. M. Vickery, Atmospheric Erosion by High Speed Impact Ejecta, *EOS*, *69*, 388, 1988.

Melosh, H. J. and A. M. Vickery, Impact erosion of the primordial atmosphere of Mars, *Nature*, *338*, 487-489, 1989.

Pollack, J. B., J. F. Kasting, S. M. Richardson and K. Poliakoff, The case for a wet, warm climate on early Mars, *Icarus*, *71*, 203-224, 1987.

Vickery, A. M. and H. J. Melosh, Atmospheric erosion by impacts; Evidence for an early, dense atmosphere on Mars, *EOS*, *70*, 1172, 1989.

Walker, J. G. C., Impact Erosion of Planetary Atmospheres, *Icarus*, *68*, 87-98, 1986.

Zel'dovich, Y. B. and Y. P. Razier, *Physics of Shock Waves and High-Temperature Hydrodynamic Phenomena*, 464 pp., Academic Press, New York, 1966.

JETTING AND THE ORIGIN OF TEKTITES

A. M. Vickery, Lunar and Planetary Laboratory, University of Arizona, Tucson, AZ 85721

The origin of tektites was a hotly debated subject for many years. Tektite strewn fields extend hundreds to thousands of kilometers across the earth's surface, and the problem of propelling molten material through the earth's atmosphere without disrupted it into a fine mist (1) led a number of investigators to propose an extraterrestrial origin for tektites (2,3). A large amount of geochemical evidence, however, strongly suggests that tektites were produced by the (presumable impact-induced) melting of terrestrial sediments (4), and most people now believe that the terrestrial origin of tektites has been proved beyond a reasonable doubt (e.g.5). The most widely-cited mechanism for tektite production is jetting during the early stages of impact, although the only previous dynamic study of jetting with regard to this problem (1) concluded that the jet would break up into a fine mist. The problem is compounded by the evidence from the primary shapes and ablation characteristics of the australites, which stongly suggests that they solidified as spheres (implying extremely low differential pressures) and subsequently entered the earth's atmosphere from above (2).

In this study, the theory of jetting due to the collision of thin plates (6-10) was extended to the case of the impact of a sphere at arbitrary impact speed U and angle α from the vertical onto a half-space (c.f. 11).The tangent to the sphere at the locus of intersection is assumed to correspond to the upper plate and the surface of the target, to the lower plate. There are two frames of reference that are typically used in jetting studies: In the standard frame, the two plates converge with equal and opposite velocities v_p perpendicular to the plates, the jet is directed along the bisector of the angle (2θ) between the plates, and the locus of intersection P moves forward as the plates converge. Jetting will only occur if $\theta > \theta_{crit}$ (7-9), where θ_{crit} is a function of v_p. The jet velocity is

$$v_j = |v_p| \left(\frac{1 + f\cos\theta}{\sin\theta} \right)$$

where f~1 from experiments. In the collision frame, the material in the plates moves with a velocity $v_o = v_p \cot\theta$ along the plates into the now stationary intersection P. The jet velocity in this frame $v_1 = fv_o \sim v_o$, combined with information on the jet width (10) essentially gives the rate at which material is fed into the jet. In addition to these to frames of reference, the current problem requires the target frame, in which the target half-space is stationary, and the convergence velocity depends on both the impact velocity and the current geometry (the degree of penetration of the sphere into the half-space). The jet velocity in this frame is the ejection velocity relative to a stationary target and is initially unknown. A vector v_t is derived to translate from the target frame to the standard frame, which requires the assumption of differential slip within the jet (asymmetric jetting (7)). The translation vector is then applied in reverse to v_j to get the jet velocity in the target frame v_j'; v_j' is not directed along the bisector of the angles between the converging surfaces nor is it directly radial from the center of impact. Similarly, the relation between the target and collision frames permits an estimate of the mass flux into the jet. Because jetting is asymmetric, the projectile and target contribute different amounts of mass to the jet.

The pressure at the stagnation point P was estimated using the method of (12) using a piece-wise linear shock velocity-particle velocity equation of state for olivine. It was assumed that release from pressures of 7.3×10^{10} Pa, 1.0×10^{11} Pa, and 5.0×10^{11} Pa would result in melting, incipient vaporization, and complete vaporization, respectively. A computer code was developed that calculates the mass ejected, its phase, the ejection speed, elevation and azimuthal ejection angles, and projectile fraction within the jet as functions of

time. Mass averages of these quantities were calculated for each timestep and for the entire duration of jetting.

Because jetting is a hydrodynamic process, the mass jetted scales rigorously with the mass of the impactor; thus all the calculations involve an impactor with radius 100 m (density 3200 kg/m^3). Impact velocities of 15, 20, and 25 km/s and impact angles ranging from 0° (vertical) to 75° in 15° increments were used.

RESULTS: (1) Overall Mass Averages: The total mass jetted increases with impact velocity (U_i) and decreases (slightly) with increasing obliquity of impact for α = 0 - 60°, then increases for α = 75°. The increase is more pronounced at lower U_i. In all cases, vapor dominates the jet, most strongly at higher U_i and low α. Overall jet velocity increases with U_i and decreases with increasing α. Again, vapor strongly dominates axcept at α = 75°. The mean elevation angle of the jet increases with α from ~7° at α = 0° to 20-25° at α = 75°, with melt generally ejected at higher angles than the vapor. The projectile fraction in the jet (Fp) varies between 0.40 and 0.50 and increases slightly with α; Fp in the melt ranges from ~0.2 at high U_i and low α to > 0.5 at high α. Jetting is azimuthally symmetric for α = 0°, and becomes increasingly focussed downrange with increasing α. In general, the melt fraction is more concentrated downrange than the vapor fraction.

(2) Time Dependence: The mass flux is maximum at the onset of jetting and declines more rapidly for more nearly vertical impacts. Except for α = 0°, the mass flux either levels off, or goes to a local minimum and then increases slightly before a final decline; this effect is less pronounced at higher impact velocities and smaller α. Similarly the jet velocity is greatest at the onset of jetting; the lower α, the greater the initial velocity and the more rapid its decline. Vapor is ejected first and at the highest velocities. At U_i = 15 km/s, the elevation angle is initially < 5° for all α and increases with time and α to a maximum of ~35° at α = 75°. The azimuthal extent of jetting decreases with increasing obliquity and with time at a given obliquity.

APLICATION TO TEKTITE FORMATION: Although these results are preliminary, they suggest that for reasonable asteroidal impact velocities, a very high velocity vapor jet is produced that, as it expands adiabatically, can engulf and accelerate a significant volume of ambient atmosphere away from the impact site. The melt fraction of the jet is thus ejected into a much rarified ambient atmosphere, suppressing break-up of the molten jet. The fact that the jetted material comprises, on average, approximately one-half projectile material, whereas tektites show no detectable projectile contamination, rules out jetting as a source of tektites. Jetting may, however, have been responsible for the thick spherule beds recently found in Africa and Australia, which are heavily contaminated with siderophile elements (13,14).

REFERENCES:

(1) E. Adams (1965) *N. Jb. Miner. Mh.* **9**, 332.
(2) D. R. Chapman and H. K. Larson (1963) *J. Geophys. Res.* **68**, 4305.
(3) J. A. O'Keefe (1976) Tektites and Their Origin, Elsevier, N.Y.
(4) S. R. Taylor (1973) *Earth Sci. Rev.* **9**, 101.
(5) R. Brett and M. Sato (1984) *Geochim. Cosmochim. Acta* **48**, 111.
(6) G. Birkhoff et al. (1948) *J. Appl. Phys.* **19**, 563.
(7) J. M. Walsh et al. (1953) *J. Appl. Phys.* **24**, 349.
(8) W. A. Allen et al. (1959) *Phys. Fluids* **2**, 329.
(9) L. V. Alt'schuler et al. (1962) *Sov. Phys. JETP* **14**, 986.
(10) F. H. Harlow and W. E. Pracht (1966) *Phys. Fluids* **9**, 1951.

(11) H. J. Melosh and C. P. Sonnet (1986) in: Origin of the Moon (Hartmann, Philips, and Taylor, eds.) L.P.I., Houston.
(12) S. W. Kieffer (1977) in: Impact and Explosion Cratering (Roddy, Merrill, and Pepin, eds.) Pergamon, N.Y.
(13) D. R. Lowe and G. R. Byerly (1986) *Geology* **14**, 83.
(14) D. R. Lowe et al. (1989) *Science* **245**, 959.

FINITE ELEMENT MODELING OF VENUSIAN CORONAE. D.M. Janes and H.J.Melosh, Lunar and Planetary Laboratory, University of Arizona, Tucson, AZ 85721

Coronae are large circular features discovered in the Venera 15 and 16 radar images of Venus in areas adjacent to Ishtar Terra and Tethus Regio. They are generally characterized by a set of concentric ridges and grooves having diameters of 150 to 530 km standing 0.7 to 2.0 km high; their centers are typically somewhat depressed but nonetheless stand above the level of the surrounding terrain (1,2), and they are often surrounded by a broad moat, typically about 50 km wide but less than 0.5 km deep (3). Radar signatures indicate that similar materials make up the coronae and the surrounding plains (4). Together with the morphology of the region, this suggests that both may be volcanic in nature.

We use finite element modeling to examine the tectonics and topographic evolution of a large volcanic construct emplaced suddenly on a lithosphere. We first model the volcano itself to determine the state of stress within it and the sense and orientation of any resulting tectonic features. The volcanos treated as axisymmetric and initially parabolic in profile. It has a crust of finite thickness with an exponential viscosity profile (decreasing downwards). We vary the initial aspect ratio, the boundary condition beneath the volcano, whether or not a central pipe containing the viscous interior material reaches the surface, and the thickness of the crust.

Figure 1 shows the stress field within the surface elements at various times for a volcano with a 1 km central height and a radius of 200 km. The lithosphere beneath the volcano is rigid, there is no central pipe, and the crust has a thickness of 250 m. At time t = 0, gravity is turned on resulting in simple self-compression of the load and (since Poisson's ratio is taken to be 0.25) the radial and hoop stresses are 1/3 the vertical, gravitational,

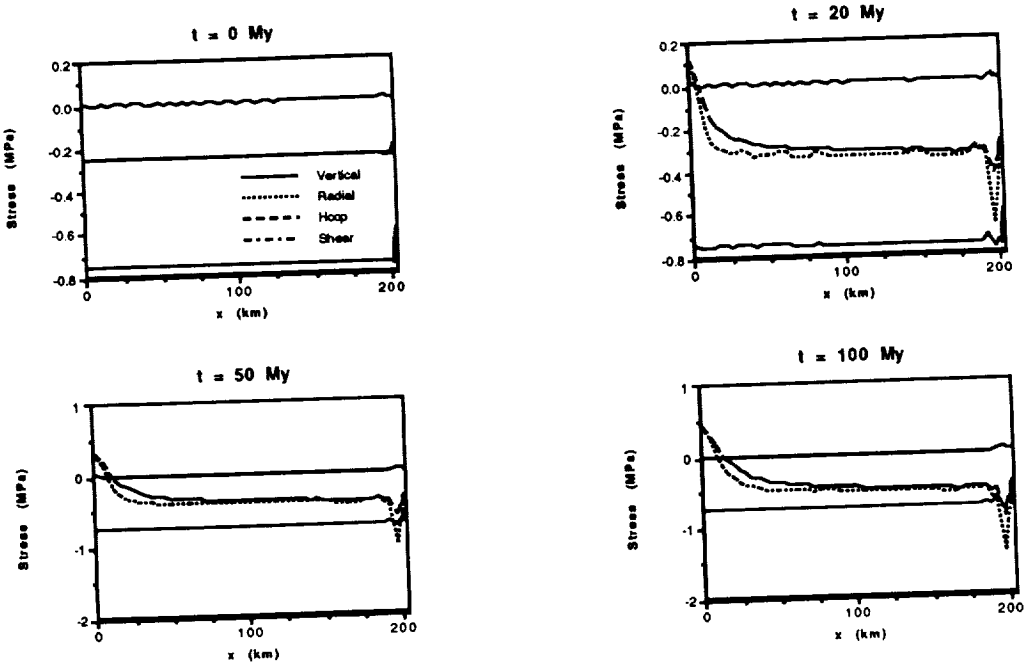

Figure 1: Stress evolution within a 1 km high, 200 km wide volcano

stress. As the load is allowed to relax through time, the radial stress becomes extensional near the volcano center and compressional throughout most of the volcano's upper layers, as required to form concentric compressional features, particularly at the volcanos periphery, where, after 50 My, the radial stress becomes the most compressional, leading to the possibility of buckling parallel to the volcano's edge. However, in each case the radial stress is the intermediate principal stress axis. The hoop stress is the least compressive principal

stress and the vertical is the most compressive. This should lead to normal faulting oriented radially to the load center.

Varying the initial aspect ratio and the crust thickness by factors of two in each direction produces similar results, namely that the hoop stress is always the least compressional while the vertical stress is the most compressional. Nor does the addition of a central pipe of viscous material affect the relationship that the radial stress is intermediate between the vertical and hoop stresses. Allowing the load to move freely over the underlying surface produces extensional radial and hoop stresses throughout the crust of the load at all timesteps but does not alter the relationship between the principal stress axes. Thus the formation of the concentric ridges and grooves around the coronae does not seem to be the result of a simple tectonic response of an elastic crust to relaxation over time.

Alternative possibilities for the formation of the concentric ridge and grooves are that initially radial fractures open, breaking the crust into several discrete wedge-shaped pieces that then slide off over the viscous interior inducing radial compression and folding at the volcano's periphery. Perhaps the simplest explanation is that the ridges and grooves are viscous folding produced during overland lava flow similar to pahoehoe lavas and rhyolitic flows (5) but on a much larger scale.

We also examine the effect of the load on the lithosphere to find the characteristics of any lithospheric flexure. We model the volcanic a corona as an axisymmetric parabolic load 1 km high and 200 km wide emplaced on lithospheres of varying thicknesses overlying a viscous asthenosphere. At the end of 100 My, moats develop which for all lithospheric thicknesses are approximately 0.5 km deep but are broader for thicker lithospheres. In general, the slope in the surrounding lithosphere as it bends under the weight of the load is initially much shallower than the slope of the load itself and continues to be significantly shallower for periods of 10's of millions of years. Models varying lithospheric thickness, rheological profile, and initial load height show similar results. Only for loads substantially larger than those observed and for relatively thin lithospheres do the slopes leading into the moat from the load and exterior sides approach the same steepness. With closer determination of the depth, breadth and relative steepness of the two sides of the moat by the Magellan mission, further constraints can be placed on the age of the coronae and the thickness of the lithosphere beneath them.

References: (1) Barsukov, V.L., *et al.*, The Geology of the Venus Surface as Revealed by the Radar Images Obtained by Veneras 15 and 16, *JGR*, **91**, No. B4, 378-398, (1986); (2) Basilevsky, A.T., *et al.*, Styles of Tectonic Deformations on Venus: Analysis of Venera 15 and 16 Data, *JGR*, **91**, No. B4, 399-411 (1986); (3) Stofan, E.R. and J.W. Head, Coronae of Mnemosyne Regio, Venus: Morphology and Origin, *LPSC XX*, 1061-1062, 1989; (4) Bindschadler, D.L. and J.W. Head, PV Characteristics of Venera Units, *Icarus*, **77**, 3-20, (1989); (5) J. Fink, Surface Folding and Viscosity of Rhyolite Flows, *Geology*, **8**, 250-254, (1980)

PLANETARY GEOLOGY AND GEOPHYSICS PROGRAM: A SUMMARY, FY 89

James R. Underwood, Jr., Code EL, NASA Headquarters,
Washington, D. C. 20546, now Department of Geology,
Kansas State University, Manhattan, KS 66506

A congressionally mandated reduction of $10 M in FY 89 funds incurred by the Solar System Exploration Division resulted in the decision to shift most anniversary dates of research projects supported by the four Planetary Science core programs (Planetary Astronomy, Planetary Atmospheres, Planetary Materials and Geochemistry, and Planetary Geology and Geophysics) to October 1 or November 1. Thus, most Principal Investigators (PI's) were funded for fewer than 12 months from FY 89 funds but did not have an unfunded period inasmuch as FY 90 funding began on the new anniversary date in the fall of 1989. These changes were necessary if Planetary Geology and Geophysics (PG&G) research programs were to remain strong during the FY 89 period of drastically reduced budgets.

The massive shift in FY 89 of research-project anniversary dates necessitated a shift around the calendar in the dates of submission and review of proposals. Thus, on April 1, 1989 all proposals - new and renewal full proposals together with progress reports - were due at the Lunar and Planetary Geoscience Review Panel (LPGRP) office at the Lunar and Planetary Institute (LPI). The 1989 LPGRP met May 20-26 at LPI to review 348 proposals for FY 90 funding. The PG&G program office and the LPGRP made every effort to see that PI's were not disadvantaged by the changes in the anniversary and review dates of their proposals.

The FY 89 support level for the PG&G program was $10.2 M, down from the FY 88 level of $10.5 M. The effective support level, however, was approximately $11.6 M, made possible by the FY 89 reduced-funding periods for most projects. In FY 89, 170 PG&G PI's were involved in 240 research projects. The distribution of PG&G funding by organization is shown in Figure 1, and the distribution of PG&G PI's by organization is provided by Figure 2. A histogram, Figure 3, shows the number of projects funded at various levels from FY 89 funds.

Ten new PI's whose proposals had received high ratings by the LPGRP in their September 1988 meeting, were included in the FY 89 program; start-up support levels averaged $20 K. Joint funding of several projects was continued, and some of the new projects also were jointly funded. These involved cooperation with the Planetary Atmospheres and Planetary Materials and Geochemistry programs of the Solar System Exploration Division and the Land Processes Branch of the Earth Science and Applications Division.

The Planetary Geology and Geophysics Working Group maintained active oversight of the PG&G program during FY 89, holding two meetings - one in Washington, fall 1988, in conjunction with the Planetary Materials and Geochemistry Working Group and the other in March 1989 just prior to Lunar and Planetary Science Conference XX. Special topics reviewed were NASA and PG&G student-support programs, the goals and operations of the Lunar and Planetary Institute, and the Planetary Data System.

A major expense incurred by the PG&G program beginning in FY 89 was the requirement to re-certify the several wind tunnels and experimental chambers

used by PG&G PI's at the Ames Research Center. Total cost will be $200 K over a five-year period.

FY 89 was the third year of the Mars Geologic Mapping (MGM) program (1:500,000 scale); support level was $95 K. A total of 15 PI's, working on 17 projects have now participated in this program, designed not for routine geologic mapping but for mapping those quadrangles for which a geologic map may serve to answer a specific scientific question of importance. The MGM program continued its support of the Mars Rover/Sample Return (MRSR) program by providing information relative to selection of sites for martian landings, sample collection, and rover traverses.

Mars, Evolution of Tectonism and Volcanism (MEVTV), the current Mars data analysis program, sponsored two workshops in FY 89. The first, at the Tidewater Inn in Easton, Maryland, October 5-7, 1988, was titled: "Early Tectonic and Volcanic Evolution of Mars." Twenty-eight papers were presented, and ample time was available for discussion and debate by 40 - 50 participants. The second event was the "Workshop on Tectonic Features on Mars," April 20-22 at the Hanford Science Center, Richland, Washington. This meeting involved some 30 participants, two days of presentations and discussion, and a one-day field trip to the Yakima fold belt to look at possible terrestrial analogs of martian wrinkle ridges.

A PG&G brochure, outlining the program goals, structure, scope, and support facilities, was published and distributed to PI's and to the regional planetary image facilities. Additional copies are available from the Program Office. IMPACT, the PG&G newsletter, was published three times during FY 89, and continued to play an important role in communication within the PG&G program. The "bluebook," Reports of Planetary Geology and Geophysics - 1988, published and distributed early in FY 89, provided an overview of the broad spectrum of activities in the PG&G program in 1988.

The PG&G community of scientists continued to be only partly utilized by NASA, i.e. there was considerable research capability beyond that which NASA had money to support. Furthermore, the community was characterized by a need for additional graduate student and post-doctoral student support and by a critical need for funds to maintain, update, and replace equipment.

Nevertheless, the PG&G community of research scientists and their students and associates made significant contributions to planetary science in FY 89, as testified by their vigorous participation in the annual meetings of the Geological Society of America, the American Geophysical Union, and the Division of Planetary Sciences of the American Astronomical Society, and also by their service on a host of advisory boards, review panels, and working groups. Many of them were involved in activities related to missions, e.g. Voyager, Phobos, CRAF/Cassini, Magellan, Galileo, Mars Observer, and MRSR. The list of PG&G accomplishments in FY 89 was impressive and reflected great credit on a dedicated community of scientists and students.

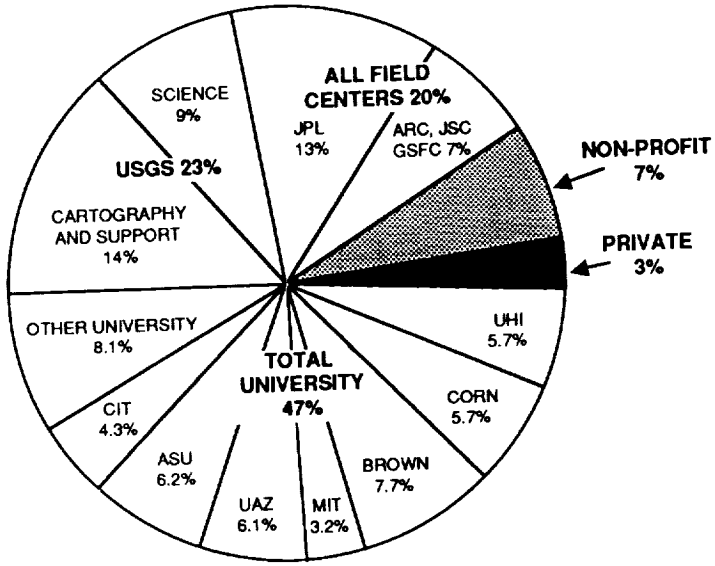

Figure 1. FY89 PG & G Funding By Organization

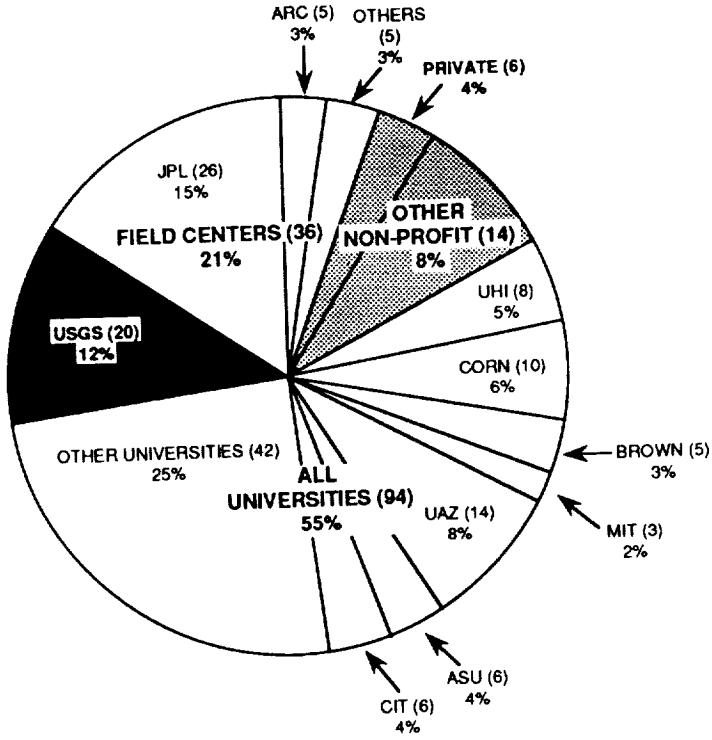

Figure 2. FY89 PG & G Principal Investigators by Organization

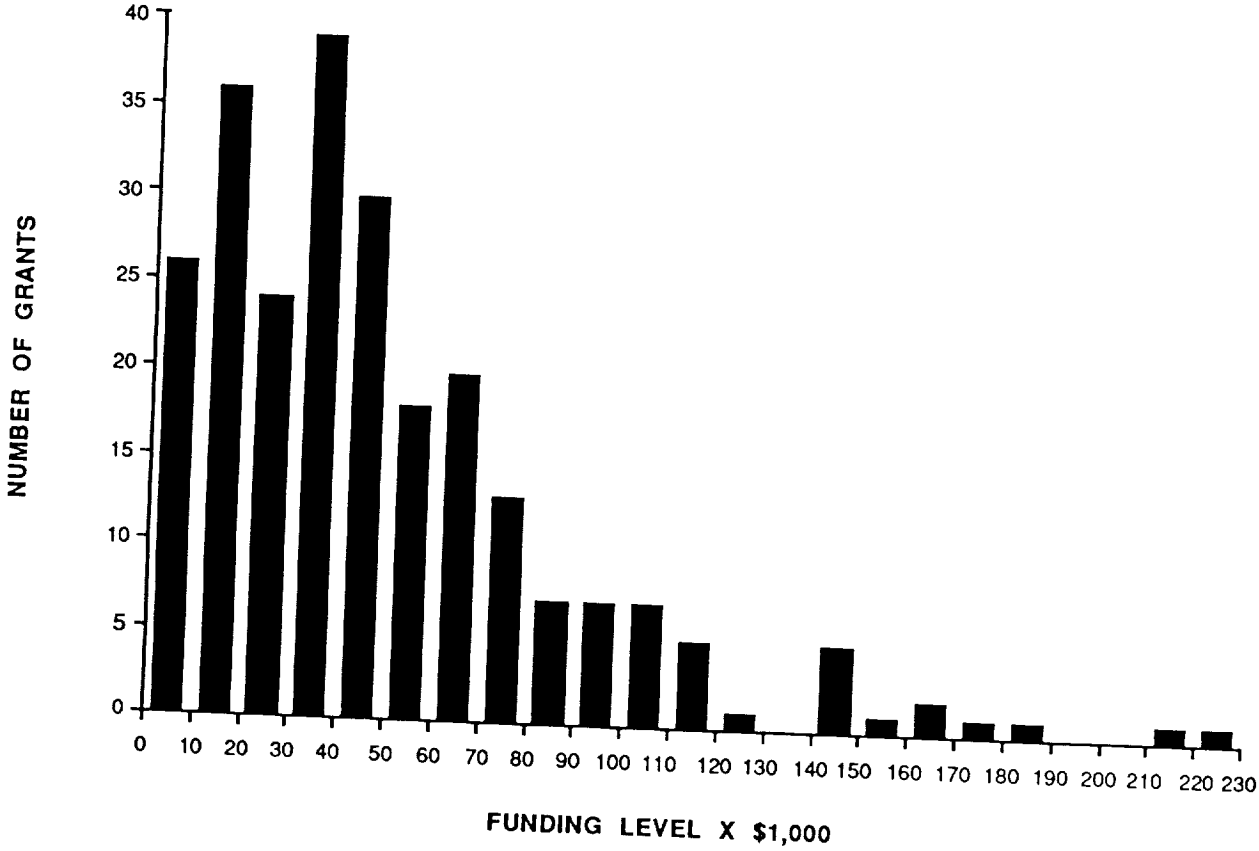

Figure 3. FY89 Funding - Level Distribution Planetary Geology & Geophysics

AUTHOR INDEX

Report Documentation Page

NASA National Aeronautics and Space Administration

1. Report No. NASA TM-4210	2. Government Accession No.
3. Recipient's Catalog No.	
4. Title and Subtitle: Reports of Planetary Geology and Geophysics Program - 1989	5. Report Date: July 1990
	6. Performing Organization Code: SL
7. Author(s): Henry Holt, Editor	8. Performing Organization Report No.
	10. Work Unit No.
9. Performing Organization Name and Address: NASA Office of Space Science and Applications, Solar System Exploration Division	11. Contract or Grant No.
	13. Type of Report and Period Covered: Technical Memorandum
12. Sponsoring Agency Name and Address: National Aeronautics and Space Administration, Washington, DC 20546	14. Sponsoring Agency Code

15. Supplementary Notes

16. Abstract

This document is a compilation of abstracts of reports from Principal Investigators of NASA's Planetary Geology and Geophysics Program. It is a summary of the research conducted under this program during 1989. Each report includes significant accomplishments in the area of the author's funded grant or contract.

17. Key Words (Suggested by Author(s)): planetary geology; planetary geophysics; evolution of planets; comets; asteroids	18. Distribution Statement: Unclassified - Unlimited; Subject Category 91		
19. Security Classif. (of this report): Unclassified	20. Security Classif. (of this page): Unclassified	21. No. of pages: 620	22. Price: A99

NASA FORM 1626 OCT 86

Available from the National Technical Information Service, Springfield, VA 22161